Edited by
Arpan Kumar Nayak
Niroj Kumar Sahu

NANOSTRUCTURED MATERIALS FOR VISIBLE LIGHT PHOTOCATALYSIS

ELSEVIER

Micro & Nano Technologies Series

Nanostructured Materials for Visible Light Photocatalysis

https://www.twirpx.org & http://chemistry-chemists.com

Micro and Nano Technologies

Nanostructured Materials for Visible Light Photocatalysis

Edited by
Arpan Kumar Nayak
Niroj Kumar Sahu

https://www.twirpx.org & http://chemistry-chemists.com

Elsevier
Radarweg 29, PO Box 211, 1000 AE Amsterdam, Netherlands
The Boulevard, Langford Lane, Kidlington, Oxford OX5 1GB, United Kingdom
50 Hampshire Street, 5th Floor, Cambridge, MA 02139, United States

Copyright © 2022 Elsevier Inc. All rights reserved.

No part of this publication may be reproduced or transmitted in any form or by any means, electronic or mechanical, including photocopying, recording, or any information storage and retrieval system, without permission in writing from the publisher. Details on how to seek permission, further information about the Publisher's permissions policies and our arrangements with organizations such as the Copyright Clearance Center and the Copyright Licensing Agency, can be found at our website: www.elsevier.com/permissions.

This book and the individual contributions contained in it are protected under copyright by the Publisher (other than as may be noted herein).

Notices

Knowledge and best practice in this field are constantly changing. As new research and experience broaden our understanding, changes in research methods, professional practices, or medical treatment may become necessary.

Practitioners and researchers must always rely on their own experience and knowledge in evaluating and using any information, methods, compounds, or experiments described herein. In using such information or methods they should be mindful of their own safety and the safety of others, including parties for whom they have a professional responsibility.

To the fullest extent of the law, neither the Publisher nor the authors, contributors, or editors, assume any liability for any injury and/or damage to persons or property as a matter of products liability, negligence or otherwise, or from any use or operation of any methods, products, instructions, or ideas contained in the material herein.

Library of Congress Cataloging-in-Publication Data
A catalog record for this book is available from the Library of Congress

British Library Cataloguing-in-Publication Data
A catalogue record for this book is available from the British Library

ISBN: 978-0-12-823018-3

For information on all Elsevier publications
visit our website at https://www.elsevier.com/books-and-journals

Publisher: Matthew Deans
Acquisitions Editor: Simon Holt
Editorial Project Manager: Andrea Dulberger
Production Project Manager: Kamesh Ramajogi
Cover Designer: Greg Harris

Typeset by STRAIVE, India

https://www.twirpx.org & http://chemistry-chemists.com

Contents

https://www.twirpx.org & http://chemistry-chemists.com

https://www.twirpx.org & http://chemistry-chemists.com

https://www.twirpx.org & http://chemistry-chemists.com

https://www.twirpx.org & http://chemistry-chemists.com

https://www.twirpx.org & http://chemistry-chemists.com

https://www.twirpx.org & http://chemistry-chemists.com

https://www.twirpx.org & http://chemistry-chemists.com

https://www.twirpx.org & http://chemistry-chemists.com

Contributors

K.C. Barick
Chemistry Division, Bhabha Atomic Research Centre, Trombay; Homi Bhabha National Institute, Anushaktinagar, Mumbai, India

Ajit Behera
Department of Metallurgical and Materials Engineering, National Institute of Technology, Rourkela, India

Susanta Kumar Bhunia
Department of Chemistry, School of Advanced Sciences, Vellore Institute of Technology, Vellore, India

Dipti Bidwai
Centre for Nanotechnology Research, Vellore Institute of Technology, Vellore, Tamil Nadu, India

Rishika Chakraborty
Department of Chemistry, National Institute of Technology Meghalaya, Shillong, Meghalaya, India

Jih-Hsing Chang
Department of Environmental Engineering and Management, Chaoyang University of Technology, Taichung, Taiwan

Maya Devi
Department of Physics, School of Applied Sciences, KIIT Deemed to be University, Bhubaneswar, Odisha, India

Jagriti Gupta
Chemistry Division, Bhabha Atomic Research Centre, Trombay, Mumbai, India

P.A. Hassan
Chemistry Division, Bhabha Atomic Research Centre, Trombay; Homi Bhabha National Institute, Anushaktinagar, Mumbai, India

Min Hee Joo
Department of Chemistry; Department of Chemical Engineering and Applied Chemistry, Chungnam National University, Daejeon, Republic of Korea

https://www.twirpx.org & http://chemistry-chemists.com

Abhijit N. Kadam
Department of Chemical and Biological Engineering, Gachon University, Seongnam-si, South Korea

Himani Kalita
Department of Chemistry, Savitribai Phule Pune University, Pune, Maharashtra, India

Mohammad Mansoob Khan
Chemical Sciences, Faculty of Science, Universiti Brunei Darussalam, Brunei Darussalam

Mohanraj Kumar
Department of Environmental Engineering and Management, Chaoyang University of Technology, Taichung, Taiwan

Jinhyeok Lee
Department of Chemical and Biological Engineering, Gachon University, Seongnam-si, South Korea

Sang-Wha Lee
Department of Chemical and Biological Engineering, Gachon University, Seongnam-si, South Korea

Sutripto Majumder
Department of Materials Science and Engineering, Chungnam National University, Daejeon; Department of Physics, Yeungnam University, Gyeongsan, Republic of Korea

S.R. Meher
Department of Physics, School of Advanced Sciences, Vellore Institute of Technology, Vellore, India

Abhaya Kumar Mishra
Materials Science Centre, Indian Institute of Technology, Kharagpur, West Bengal, India

Saralasrita Mohanty
School of Physical Sciences, National Institute of Science Education and Research, HBNI, Jatni, India

Ranjan K. Mohapatra
Department of Chemistry, Government College of Engineering, Keonjhar, Odisha, India

Arpan Kumar Nayak
Department of Physics, School of Advanced Sciences, Vellore Institute of Technology, Vellore, Tamil Nadu, India

Sandip V. Nipane
Department of Chemistry, Smt. Kasturbai Walchand College, Sangli, MS, India

https://www.twirpx.org & http://chemistry-chemists.com

So Jeong Park
Department of Chemistry, Chungnam National University, Daejeon, Republic of Korea

Manoj Patowary
School of Engineering, MIT-ADT University, Pune, Maharashtra, India

Mukul Pradhan
Department of Chemistry, National Institute of Technology Warangal, Warangal, Telangana, India

Swetapadma Praharaj
Department of Physics, School of Applied Sciences, KIIT Deemed to be University, Bhubaneswar, Odisha, India

Sathish Rajendran
Department of Chemistry, School of Advanced Sciences, Vellore Institute of Technology, Vellore, India

Barkha Rani
School of Electronics Engineering; Centre for Nanotechnology Research, Vellore Institute of Technology, Vellore, Tamil Nadu, India

Ankur Rastogi
Department of Physics; Center for Functional Materials, Vellore Institute Technology, Vellore, India

Dibyaranjan Rout
Department of Physics, School of Applied Sciences, KIIT Deemed to be University, Bhubaneswar, Odisha, India

Rajashree Sahoo
Department of Physics, School of Applied Sciences, KIIT Deemed to be University, Odisha, India

Niroj Kumar Sahu
Centre for Nanotechnology Research, Vellore Institute of Technology, Vellore, Tamil Nadu, India

Shan-Yi Shen
Department of Environmental Engineering and Management, Chaoyang University of Technology, Taichung, Taiwan

Brijesh Kumar Singh
Department of Physics, Central University of Rajasthan, Ajmer, India

Sarika Singh
Department of Chemistry, Manipal University Jaipur, Jaipur, India

https://www.twirpx.org & http://chemistry-chemists.com

Tridib Kumar Sinha
Department of Materials Engineering and Convergence Technology, Gyeongsang National University, Jinju, South Korea

Youngku Sohn
Department of Chemistry; Department of Chemical Engineering and Applied Chemistry, Chungnam National University, Daejeon, Republic of Korea

G. Swati
Centre for Nanotechnology Research, Vellore Institute of Technology, Vellore, Tamil Nadu, India

Varsha UshaVipinachandran
Department of Chemistry, School of Advanced Sciences, Vellore Institute of Technology, Vellore, India

Ju Hyun Yang
Department of Chemistry; Department of Chemical Engineering and Applied Chemistry, Chungnam National University, Daejeon, Republic of Korea

https://www.twirpx.org & http://chemistry-chemists.com

1 Fundamentals principle of photocatalysis

Barkha Rani[a,b], Arpan Kumar Nayak[c], and Niroj Kumar Sahu[b]

[a]SCHOOL OF ELECTRONICS ENGINEERING, VELLORE INSTITUTE OF TECHNOLOGY, VELLORE, TAMIL NADU, INDIA [b]CENTRE FOR NANOTECHNOLOGY RESEARCH, VELLORE INSTITUTE OF TECHNOLOGY, VELLORE, TAMIL NADU, INDIA [c]DEPARTMENT OF PHYSICS, SCHOOL OF ADVANCED SCIENCES, VELLORE INSTITUTE OF TECHNOLOGY, VELLORE, TAMIL NADU, INDIA

1 Introduction

Photocatalysis is a combination of two words: photo and catalysis. Photo stands for light and catalysis is a process to enhance the chemical reaction rate by dropping the activation energy for the primary reaction to begin [1]. In the catalysis process, a substance is introduced in the reaction which enhances the rate of transformation of reactant to a product without being altered in the end [2]. These substances are known as catalysts, which are semiconducting in nature [3]. A fundamental distinction between conventional catalysis and photocatalysis is the usage of photons or light in place of heat for the activation of the catalyst. Hence, photocatalysis is a process of activating the catalyst by the application of light, which further improves the rate of the reaction without being self-involved.

Photocatalytic oxidation or the advanced oxidation process (AOP) has been studied extensively from the past five decades for the elimination of harmful microorganisms, pigments, contaminants, and toxic substances from polluted water [2–7]. In this process, the molecular transformation or photo-driven chemical reaction takes place in the catalyst or its surfaces. The aforementioned process is divided into two categories: sensitized and catalyzed photoreaction depends on whether the first excitation happens at the catalyst, surface or on the adsorbate molecules [8]. A sensitized photoreaction occurs when photoexcitation initiates in the catalyst substrate and then the energy is transferred in the form of an electron (e^-) which migrates from the valence band (VB) to the conduction band (CB). In contrast, a catalyzed photoreaction occurs in an adsorbate molecule which further reacts with a catalyst substrate. The adsorption of reactants and the absorption of photons are the two key factors of the photocatalysis process. The photo sorption and desorption can take place either in a solid catalyst or liquid phase. In the case of the solid phase, irradiation of photon energy equal to or greater than the bandgap energy (E_g) of the catalyst results in the formation of e^- and h^+ pairs. A photoelectron is generated in the CB whereas photogenerated h^+ presents in the VB of the catalyst. This photogenerated

Nanostructured Materials for Visible Light Photocatalysis. https://doi.org/10.1016/B978-0-12-823018-3.00009-9
Copyright © 2022 Elsevier Inc. All rights reserved.

https://www.twirpx.org & http://chemistry-chemists.com

electron-hole pair (PEHP) reacts with oxygen and hydroxyl molecules to form highly active radicals. These radicals further react with toxic reactants and transform them into nontoxic ones [9]. However, in the fluid phase, an instantaneous absorption occurs and e^- and h^+ transfer take place in between acceptor and donor molecules, depending on the redox potential of each adsorbate. The e^- migrates toward acceptor molecules whereas positive h^+ migrates toward donor molecules and formed reactive ions. These reactions are explained below:

$$\text{Light} + \text{semiconductor catalyst} \rightarrow \text{electron}^- + \text{hole}^+ \tag{1}$$

$$\text{Acceptor (adsorbed)} + \text{electron}^- \rightarrow \text{Acceptor}^- \text{ (adsorbed)} \tag{2}$$

$$\text{Donor (adsorbed)} + \text{holes}^+ \rightarrow \text{Donor}^+ \text{ (adsorbed)} \tag{3}$$

These ions and free radicals are subsequently reacted to form intermediate and final products. Sometimes, the efficiency of the photoreaction is reduced due to the recombination of PEHP. This recombination converts the photoelectrical energy into heat.

$$\text{Electron}^- + \text{hole}^+ \rightarrow \text{neutral} + \text{heat/phonon} \tag{4}$$

In photocatalysis, radiation is used for the acceleration of chemical reactions. The radiation is broadly divided into two regions: ultraviolet and visible, which are prominently selected based on the catalyst E_g. Only 4% of the solar spectrum comes under the UV region. Hence, the fundamental principles, mechanism, kinetics, and parameters that adversely impact on the photoactivity of the catalytic process along with the strategy to utilize solar spectrum for photocatalysis are explained in detail in this chapter.

2 Basic principle for photocatalytic reactions

In a photocatalytic reaction, a photocatalyst acts as a substrate that gets activated by the application of photon light and subsequently produces highly active radicals. The generated radicals and ions react further with toxic organic molecules and break them into CO_2 and H_2O. Generally, transition oxide-based materials like ZnO, TiO_2, SnO_2, etc. are used as the substrate, and water and oxygen are used as the adsorbate [10]. The reactions involved in the process of dye removal are as follows:

$$\text{Substrate} + \text{photon} \rightarrow \text{substrate}\,(e^- + h^+) \tag{5}$$

$$e^-_{ads} + \text{oxygen} \rightarrow O_2^- \tag{6}$$

$$h^+_{ads} + \text{water} \rightarrow H^+ + OH^- \tag{7}$$

$$h^+_{ads} + OH^- \rightarrow OH^\bullet \tag{8}$$

$$OH^\bullet + O_2^- + \text{toxic dyes} \rightarrow CO_2 + H_2O \tag{9}$$

The abovementioned equations suggest the necessity of interaction between the photocatalyst and adsorbed (acceptor or donor) molecules. Sometimes these interactions

https://www.twirpx.org & http://chemistry-chemists.com

are induced by either electrostatic forces or chemical bonding such as dipole-dipole interaction, van der Waal forces, ion exchange, hydrogen bonding, and adsorbed hydrophobicity. It can be observed from Eq. (5) that the irradiation of photon energy ($h\nu \geq E_g$) causes the creation of e^- and h^+ pairs in the photoactive materials. The energy to generate a photoexcited pair in a catalyst is directly related to the wavelength (λ) of the light by this relation:

$$\lambda \leq \frac{hc}{E_g} \tag{10}$$

$$\lambda \leq \frac{1240}{E_g} \tag{11}$$

where c and h are the velocity of light and Plank's constant, respectively. The wavelength in Eq. (11) is in nanometer units. The overall photocatalytic reaction is based on two mechanisms: direct or indirect photocatalytic mechanisms. These mechanisms are explained in detail below.

2.1 Direct photocatalytic principle

Two different models (the Langmuir-Hinshelwood and Eley-Rideal processes) have been used to describe the direct photocatalytic pathway of the reaction. In the Langmuir-Hinshelwood (L-H) model, the photocatalyst is activated by photons and produces e^- in CB and h^+ in VB. Furthermore, the adsorbed species act as traps for photogenerated h^+ and create a reactive radicals state on the surface of the catalyst, which further decays due to the recombination of e^- and h^+. This recombination again regenerates the catalyst material. The abovementioned model provides the relation between the reaction rate and initial solute concentration [11, 12]. The L-H model can be explained by the following relation [13]:

$$^1\!/_r = {}^1\!/_{K_r} + {}^1\!/_{K_r K_a C} \tag{12}$$

where r is the reaction rate (mg/L min), K_r is the specific reaction rate constant (mg/L min), K_a is the equilibrium constant (l/mg), and C is the concentration of dye. However, in the Eley-Rideal (E-R) model, the free carriers get trapped by surface defects. The degradation path followed in E-L process is as follows: (i) trapping of photogenerated h^+ by surface defect (s); (ii) formation of surface-active centers (s^+); (iii) reaction between s^+ and chemisorbed dye ($dye_{ads})^+$; (iv) formation of adduct species such as ($s\text{-}dye_{ads})^+$; (v) decomposition of ($s\text{-}dye_{ads})^+$; and (vi) production of product and surface defect sites [12].

2.2 Indirect photocatalytic principle

In this method, the PEHP is generated on the surface of the semiconductor. The photo-induced h^+ reacts with the adsorbed water molecules or moisture to form hydroxyl

https://www.twirpx.org & http://chemistry-chemists.com

radicals. Moreover, the PEHP is allowed to produce H_2O_2, which further breaks and produces more reactive radicals (OH^-) for the oxidation of dye molecules [14]. The overall steps can be explained as follows:

$$\text{Semiconductor} + \text{photon} \rightarrow \text{semiconductor}\,(e^- + h^+) \tag{13}$$

$$h^+ + \text{water}_{ads}/\text{moisture} \rightarrow H^+_{ads} + OH^\bullet_{ads} \tag{14}$$

$$e^- + \text{oxygen} \rightarrow O_2^- \tag{15}$$

$$O_2^- + H^+ \leftrightarrow HO_2^\bullet \tag{16}$$

$$2HO_2^\bullet \rightarrow H_2O_{2\,ads} + O_2 \tag{17}$$

$$H_2O_{2\,ads} + \text{photon} \rightarrow 2OH^\bullet_{ads}/OH^\bullet \tag{18}$$

$$2OH^\bullet_{ads}/OH^\bullet + \text{dye} \rightarrow CO_2 + H_2O \tag{19}$$

3 Reaction pathways for photogenerated electron-hole pair

3.1 Pathways of PEHP within a semiconducting catalyst

The irradiation of photon energy over catalyst surface results in a number of reactions given in Fig. 1A. Initially, the semiconducting photocatalyst absorbs the photon energy which results in the excitation across the bandgap depending upon whether $h\nu \geq E_g$. The e^- transfers to CB and a positive h^+ is generated in VB. PEHP has a sufficient time in the range of nanoseconds to undergo charge transfer to adsorbed species on the catalyst surface from solution or gas phase contact [15]. During de-excitation, the e^- and h^+ can follow various paths such as: (i) migration of e^- or h^+ to the photocatalyst surface for the transfer of e^- to adsorbed organic or inorganic species or solvent; (ii) surface or volume recombination of PEHP which releases heat; (iii) donation of e^- at the catalyst surface to reduce O_2 to ions; and (iv) migration of h^+ to the surface where an e^- from a donor species can combine with the surface h^+, thus oxidizing the donor species. These migrations and transformations depend upon the e^- and h^+ position and redox potential level of the adsorbate species [8]. The potential level of acceptor species should be lower than the CB potential of the semiconductor. However, the band position of donor species should be above the VB to donate an e^- to the vacant h^+. The band edge position of the photoactive material changes with the changing pH of the electrolyte with respect to the redox potential of the adsorbate molecules [8].

3.2 Charge carrier trapping

The reaction with the adsorbed species and efficient charge transfer is the mandatory condition for PEHP. The lifetime of PEHP before recombination falls in the range of microseconds to nanoseconds. It can be increased by trapping the charge carriers, which delays the

https://www.twirpx.org & http://chemistry-chemists.com

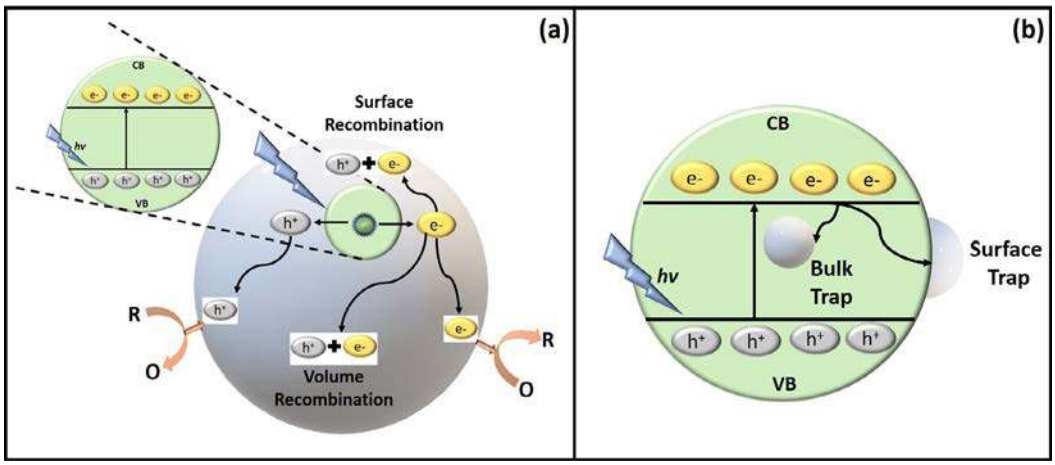

FIG. 1 Schematic of (A) photoexcitation and de-excitation in a catalyst material and (B) surface/bulk charge carrier trapping. *Concept adapted from A. L. Linsebigler, G. Lu, J. T. Yates, Photocatalysis on TiO2 surfaces: principles, mechanisms, and selected results, Chem Rev 95 (1995) 735–758.*

recombination process by a fraction of a nanosecond. Synthesized colloidal or polycrystalline photocatalysts exhibit some defects in their crystal structure or crystal lattice; they also have some irregularity in their surface and bulk. These distortions result in the formation of e^- states at the surface, which are distant compared to the bulk semiconductor's energy band. The abovementioned states work as a trap for PEHP and reduce their recombination. There are mainly two types of traps present in the semiconducting catalyst: bulk traps and surface traps (Fig. 1B) [8]. The trap sites for both models are localized and present within the E_g of the catalyst. The PEHP become trapped in particular sites and form localized states either in bulk or at the surface. The population of traps depends upon the energy difference between the CB and traps. Trapping of photoexcited e^- minimizes the entropy of the system [16].

4 Fundamental principles based on the type of catalyst

Photocatalysts exhibit properties such as: (i) efficient absorption of photons; (ii) effective charge separation of PEHP; (iii) facile migration or diffusion of mobile charges; and (iv) rapid charge transfer, which results in the fast transformation of chemical species. These characteristics depend upon the material and vary greatly with changes to the material specification. For example, the light absorption process of the semiconductor catalyst is different than that of the plasmonic catalyst. Moreover, the lifetime of PEHP in semiconductors is in the range of picoseconds to microseconds whereas it is more than 100 femtoseconds for plasmonic materials [17]. Therefore, a detailed study of the principle that governs the photocatalytic process in different classes of material such as bulk semiconductors, quantum dots, and two-dimensional material is crucial.

https://www.twirpx.org & http://chemistry-chemists.com

4.1 Semiconductor-based photocatalyst

The photocatalytic principle for semiconductor material has been widely researched and studied extensively. In n-type semiconductors, the concentration of e^- is higher than that of h^+. The addition of an n-type semiconductor in the electrolyte results in a more negative value of Fermi level (E_F) than the electrochemical potential of the electrolytes. This causes the formation of the Schottky junction [18]. Under dark conditions, e^- starts migrating from the semiconductor toward the electrolyte, which creates the equilibrium at the interface. This results in a bending of the band upward at the electrode/electrolyte interface and looks like the Schottky junction, which forms at the semiconductor/metal interface. Illumination results in the photoactivation of the catalyst surface and generation of PEHP. This PEHP is separated in the depletion region due to the presence of an internal built-in field (E_b). Doping level and degree of band bending are the deciding factors for the width (W) of the depletion region [19]. Here, the charges are removed to either the bulk or the solid/liquid interface with the help of E_b [20]. The diffusion length (D) of the mobile charge is the distance from the depletion region and it depends solely on the lifetime and mobility of the charge carriers [21]. The total number of charges produced within the D and the depletion region can only participate in the chemical reactions. This collective width ($W + D$) is associated with the penetration depth of the photons and subsequently provides the adsorption coefficient (α) of the material. High efficiency is only observed in those materials which have a higher value of total width ($W + D$) than optical depth ($1/\alpha$). A similar phenomenon can be correlated to p-type materials by only spinning the polarities of mobile charge carriers [20].

4.2 Quantum dot-based photocatalyst

Energy state quantization is a prominent phenomenon observed in the quantum dot-based photocatalyst. The reason for this is the size of the material which is comparable with the Bohr radius of the material. It gives perfect alignment of the energy state of the charge carriers to the molecular orbital of the targeted reactants. This quantization provides an additional advantage in terms of selective oxidation [22, 23]. Zhao et al. [22] reported the selective oxidation of alcohols for hydrogen production by CdSe quantum dots (QDs). Moreover, these QDs are used as sensitizers and frequently used as cocatalysts where they act as light absorbers for the second catalyst material. The quantization of electronic states results in the tuning of optical adsorption edges. Generally, the photoactivation of QDs results in the generation of e^- which is injected into the CB of the supporting semiconductor. However, photogenerated h^+ is present in the VB of the QD and requires a sacrificial e^- donor group. This case creates the internal built-in barrier at the interface of the QD/semiconductor, which significantly increases the lifetime of charge carriers [24]. An increase in an E_g (1.9–2.4 eV) is observed in CdSe with the change in size. The change in the size of CdSe makes CB more negative whereas VB is constant throughout the variation. This causes a substantial potential difference between the QD and semiconducting TiO_2 surface, and increases the charge transfer rate of the reaction [24].

https://www.twirpx.org & http://chemistry-chemists.com

4.3 Two-dimensional material-based photocatalyst

Separation and migration of the charge carriers in the two-dimensional material are different from the bulk semiconductor and quantum dot-based photocatalyst. The reduction in the thickness and the layered morphology results in a change in the bandgap as well as the presence of anisotropic properties in the two-dimensional materials. Li et al. [25] demonstrated the different charge separation in the layered BiOCl particles. Different crystal orientation causes a variation in charge separation and further changes the rate of reaction as well as the lifetime of the charge carriers [26, 27]. Moreover, defects present in the two-dimensional material affect the charge distribution and subsequently a drastic change is seen in the charge behaviors. For example, an oxygen vacancy is created in the two directions (010) and (001) of the BiOCl, causing a change in the surface potential. Furthermore, water molecules get adsorbed at the vacancy sites of the BiOCl-001 whereas dissociation adsorption appears on the vacancy sites of the BiOCl-010 surface. Xie et al. reported a similar approach for improving the charge separation in $ZnIn_2S_4$ [28]. Zhang et al. [29] described the photoactivity of a 2D composite in which $Zn_{0.8}Cd_{0.2}S$ was deposited over the reduced graphene oxide. The composite showed an easier migration of e^- from the CB of $Zn_{0.8}Cd_{0.2}S$ to rGO layers.

5 Factors affecting the photocatalysis reaction

The efficiency, rate, and percentage degradation of photocatalytic reaction depend upon several factors such as the quantity of catalyst, dye concentration, pH of the solution, temperature, additives, wavelength, and intensity of the light source. The effects of these factors are explained in detail.

5.1 Effect of quantity of catalyst

The mass of photocatalyst directly influences the initial rate of the reaction. A greater number of catalysts results in the presence of a huge number of adsorption sites, which further increases the rate of the photocatalytic reaction [30, 31]. However, after a high dose of catalyst, the reaction rate becomes independent of the mass. This range relies on the working condition and geometry of the photoreactor [32]. A higher amount of catalyst results in the masking of photosensitive surfaces, which hinders the efficient absorption of photons as well as reducing the light penetration in the reactor [33–35]. Furthermore, agglomeration of the particles is also observed in the case of high doses which lowers the effective surface area of the catalyst [36]. Herrmann [32] performed the reaction in two different reactors (batch reactor and CPC solar reactor) and optimized the amount of TiO_2 catalyst for the degradation process. He found that a small quantity of TiO_2 (0.2 g/L) is enough to give higher efficiency in a CPC solar reactor than the batch reactor (2.5 g/L). He also concluded that the optimum amount of photocatalyst depends upon the initial concentration of solute. Rauf et al. [37] varied the amount of TiO_2/V_2O_5

https://www.twirpx.org & http://chemistry-chemists.com

catalyst from 10 to 40 mg/20 mL and found that the percentage of decolorization is increased with increasing dose and again starts falling. This increment is attributed to the presence of a large number of active sites for dye adsorption. In addition, it causes the generation of a higher number of hydroxyl radicals for the reaction. Saquib et al. [38] and Qamar et al. [39] also reported that the degradation rate increases with increasing catalyst dosage.

5.2 Effect of wavelength and intensity of light

The wavelength and intensity of light sources also have an impact on the photocatalytic reaction. Photoexcitation energy equal to or more than the E_g is required for the transition of e^- from VB to CB. TiO_2 has an E_g of 3.2 eV, thus it requires a wavelength of a minimum of 400 nm (UV) for photoactivation of the catalyst. Ollis et al. [40] divided the intensity of a light source into three regions (low, intermediate, and high) and explained their effect on the catalytic process. Ollis stated that at low intensity (0–20 mW/cm^2), the rate of reaction is increased linearly with increasing light intensity and follows the first order of the reaction. At intermediate state, it follows the half order reaction, i.e., the rate of the reaction relies on the square root of the light intensity. However, an independency in the rate of reaction is observed at high intensity due to the complete utilization of active sites of the material. Neppolian et al. [41] performed the degradation of three textile dyes using the TiO_2 catalyst by irradiating solar and UV light. They showed that UV light is more adequate than solar irradiation. They also varied the intensity of solar radiation and found that the percentage degradation increases with increasing light intensity. High intensity of light results in the formation of more e^--h^+ along with a negligible recombination rate. At lower intensities, PEHP separation competes with recombination, causing the slow formation of free radicals which results in less percentage degradation of the dyes [42]. Rani et al. [43] used SnO_2 nanoparticles as a catalyst for the removal of methylene blue dye. They examined the effect of wavelength by irradiating 254 and 365 nm light and found that the efficiency is higher in the case of 254 nm wavelength. This behavior was attributed to the presence of a wider absorption band which further results in the generation of a greater number of PEHP. Liu et al. [44] performed the experiment in three different intensities and showed that the decolorization of azo dye increases with increasing light intensity. Increasing light intensity also enhances the decolorization rate [45, 46].

5.3 Effect of pH

The photocatalytic process is governed by three reactions: (i) direct oxidation by the positive charge carrier; (ii) direct reduction by negative charge carrier; and (iii) hydroxyl radical attack. All these reactions depend upon the nature of the substrate and pH of the solution [47]. The pH of the solution tunes the electric double layer and changes the surface charges at the solid-liquid interface. This modification further changes the potential of catalytic reaction, absorption-desorption process, and the separation of PEHP at the

https://www.twirpx.org & http://chemistry-chemists.com

surface of the catalyst. Metal oxide and hydroxide materials exhibit an amphoteric nature which develops either positive or negative charge at the surface [48–51]. Hence, variation in the pH of the solution shows an impact on the adsorption process [49]. Dye degradation is restrained by the H^+ ions in the acidic medium, which subsequently reduces the efficiency of the photocatalytic process. However, in a basic medium, a greater number of hydroxyl ions are present which nullifies the acidic by-product generated during the dye degradation process as well as potentially resulting in the formation of more hydroxyl radicals. The nature of dye is equally crucial for its percentage degradation at higher pH. Some of the dyes are highly stable in the basic medium. Their chromophores are intact even after the irradiation of light and consequently the degradation rate decreases [52]. Bubacz et al. [53] examined methylene blue degradation and found that the rate of degradation increases with an increase in pH. Rani et al. [43] observed that the SnO_2 nanoparticles show fast degradation in the basic medium. This behavior is due to the electrostatic interaction between the anionic catalyst and cationic dye, which results in the high adsorption of the dye molecules over the catalyst surface [54, 55]. Baran et al. [56] reported a sixfold increment in adsorption efficacy during the acidification of the solution from pH 8 to 4.5. This increment is attributed to a change in charge of the dye (bromocresol purple). Many studies reported the high efficiency of positive TiO_2 catalyst in an acidic medium compared to an alkaline medium [57, 58]. They observed more adsorption of dye molecules at lower pH due to the presence of a negative charge in their structure [59].

5.4 Effect of the initial concentration of dye

Generally, the efficiency of dye degradation reduces with increasing concentration of dye [33]. The high concentration of dye results in more adsorption of dye over the catalyst surface. This hinders photons in reaching the catalyst surface and thus reduces the generation of hydroxyl radicals for the photocatalytic reaction. Rauf et al. observed that the percentage decolorization of dye decreases with increasing dye concentration [37]. Neppolian et al. [41] worked on three different dyes (Reactive Yellow 17, Reactive Red 2, and Reactive Blue 4) and studied the effect of dye concentration on the catalytic rate. They found that percentage degradation decreases with increasing concentration in all cases. This result is in agreement with other studies [60–63]. Various reasons reported by the literature for less activity are: (i) absorption of a photon by dye molecules hinders the penetration of light to catalyst surface [59, 62, 64]; (ii) blocking of active sites by dye molecules results in the inefficient generation of hydroxyl radicals [65]; (iii) dye molecules work as a barrier between hydroxyl radicals, PEHP, and catalyst, which further reduces the reaction PEHP to adsorbed species [48]; (iv) high concentration shields the photon and resultantly the path length of the photons reduces; and (v) lesser generation of hydroxy radicals causes less availability of free radicals for reacting dye molecules.

The reaction of the hydroxyl radicals with dye molecules directly influences the rate of the reaction. Initially, the rate of dye degradation increases with increasing the initial concentration of dye due to the presence of more dye molecules and it follows the first-order kinetics [66]. In this case, dyes are being adsorbed on the surface of the catalyst and forming

https://www.twirpx.org & http://chemistry-chemists.com

monolayers which do not restrict the penetration of photons. However, the rate is maximal and shows zero-order kinetics after reaching a critical level of dye concentration [32, 59]. A similar pattern is found by Saquib et al. [38] and Kiriakidou et al. [59]. Saquib et al. experimented by varying the dye concentration from 0.18 to 0.5 mM and they observed that the rate increased with increasing concentration up to 0.25 mM and then abstained.

5.5 Effect of temperature

Temperature also has a significant impact on the rate of photocatalytic reaction. Recombination of charge carriers enhances with an improvement in temperature. Moreover, the desorption process of adsorbed species is increasing with the temperature which results in less catalytic activity of the materials. The photocatalytic reactor does not require any heating element and works at room temperature. The true activation energy (E_T) and apparent activation energy (E_A) are two factors that are used for explaining the effect of temperature on the catalytic reaction. At moderate temperatures (20–80°C), E_T is nil and E_A is very small. However, an increment in E_A is observed at low temperatures (−40°C to 0°C), which is further used to heat the adsorption species [32]. The heating of the solution causes an increase in the rate constant of the photodegradation process. However, lowering the temperature results in a spontaneous exothermic reaction which favors the adsorption of reactant species. It also supports the adsorption of the final product. On the other side, when the temperature reaches the boiling point of the water, the reaction becomes limited and does not support the adsorption of reactant species [67]. Soares et al. [68] found that the optimum temperature for the photocatalytic reaction is 40–50°C for a TiO_2 catalyst.

5.6 Effect of additives

Efficiency and photocatalytic rate are also influenced by the presence of additives in the solution matrix. Additives are initially added to the dye solution for improving the industrial process. They are ionic compounds and present as an ion in the dye solution such as Zn^{2+}, Na^{+}, Fe^{2+}, Cl^{-}, persulfate ions, and so on. However, the abovementioned addition had a negative impact on the efficiency of the photocatalytic reaction. For example, Fe^{2+} ions reacted with highly active hydroxyl radicals and formed OH^{-} and Fe^{3+} [69]. This results in lowering the concentration of hydroxyl radicals and thus decreases the efficiency of the photocatalytic process. Numerous studies have reported the scavenging effect of h^{+} and $OH^{\bullet}$ due to the presence of Cl^{-}, SO_4^{2-}, CO_3^{2-}, and HCO_3^{-} [37, 70, 71]. Rauf et al. [37] reported the e^{-} scavenging by bromate ions which further reduces the degradation efficiency of the reaction. They showed that the bromate ions reacted with six e^{-} and formed bromide ions which further react with hydroxyl radicals and minimize the percentage degradation of dye molecules.

However, some oxidants such as H_2O_2 and O_3 increase the rate of reaction by trapping the e^{-}, which further prevents the recombination of PEHP. Moreover, they contribute to the generation of more traps e^{-} as well as oxidizing radicals for the degradation process.

https://www.twirpx.org & http://chemistry-chemists.com

Even air and oxygen have significant impacts on the dye degradation process [72–74]. Photogenerated e^- reacts with oxygen and forms superoxide ions, which further react with adsorbed species and complete the degradation process. However, in the absence of oxygen the percentage degradation decreases, and the recombination rate increases. Oxygen gets adsorbed on the surface of the catalyst and acts as a trap for photogenerated e^-. On the other side, hydrogen peroxide increases the generation of $OH^\bullet$ either by self-decomposition or reduction at CB [46]. The low concentration of H_2O_2 favors the efficient formation of $OH^\bullet$ and restrains the recombination of PEHP. However, at high concentration, it reacts with the excess H_2O_2 present in the solution.

5.7 Quantum size effects

The reduction in the size of semiconductor catalyst (<10 Angstrom) shows the quantization effect. These effects are prominent when the size of the particle is comparable to the De Broglie wavelength of the charge carriers. The PEHP induced in these particles experiences confinement in potential as well as in geometry. This confined PEHP does not experience bulk electronic states (CB and VB); instead, it produces a quantization of discrete electronic states and increases the effective E_g of the catalyst [75, 76]. Many researchers have examined the size-dependent properties of semiconducting catalysts and compared them with the bulk properties [76–78]. Brus theoretically and experimentally explained how effective E_g is changing with size [78]. Reduction in the size of CdS from 100 to 26 Angstrom results in a blue shift in absorption and emission spectra, which indicates the increase in effective E_g of the materials (Fig. 2). Wang et al. [79] showed that the reduction in the size of PbS from bulk to 13 Å results in an increase in E_g by six factors from 0.4 eV (bulk).

5.8 Effect of other parameters on the photoactivity of catalyst

Surface area, particle size, lattice mismatch, distorted structure, and presence of impurity are the critical factors that influence the catalytic activity of the semiconducting material. These factors have a significant impact on the adsorption process as well as on the recombination rate of PEHP [80]. The large surface area of the catalyst results in the presence of more active sites for the adsorption of dye molecules and thus promotes the speed of the reaction [81]. Muggli et al. [82] claim that the TiO_2 particles with mixed (rutile and anatase) phases are more efficient than the individual one.

6 Strategies for enhancement of photocatalytic properties of semiconducting materials

The efficiency of the photocatalysis process is determined by the quantum yield, i.e., the number of reactions involved per photon absorbed. These reactions mainly depend on: (i) the E_g of photocatalyst; (ii) the rate of generation of PEHP; and (iii) the fate of migration.

https://www.twirpx.org & http://chemistry-chemists.com

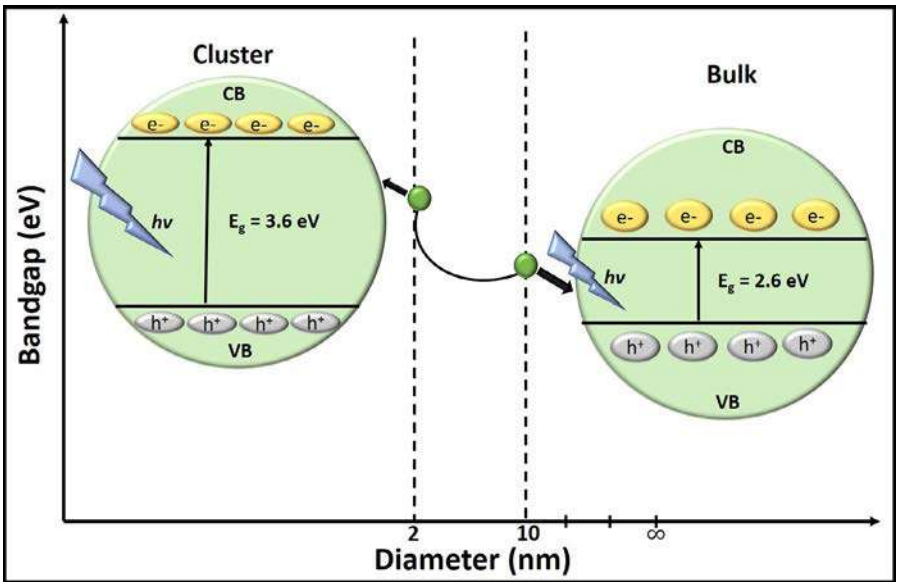

FIG. 2 Effect of quantum size on CdS bandgap. *Concept adapted from A. L. Linsebigler, G. Lu, J. T. Yates, Photocatalysis on TiO2 surfaces: principles, mechanisms, and selected results, Chem Rev 95 (1995) 735–758.*

The rate of generation of PEHP depends on the irradiation condition (photon energy, flux) and optical absorption characteristics (surface area, E_g, size), whereas the fate of migration depends on whether the reaction occurs at the surface of the particles or within the photocatalyst. Surface recombination of PEHP results in the generation of heat, which reduces the efficiency of the photocatalytic process. This recombination can be decreased by increasing the crystallinity of the lattice, reducing catalyst size, or increasing the transfer rate [8]. If the material is highly crystalline, then there are minimal chances of the presence of an impurity, surface defects, and bulk defects, whereas the reduction in the size induces the point defects in the particles which further act as traps for e^- or h^+ and reduce the rate of recombination. These trapped present in the localized energy level in the E_g region and trapped the charge carriers for a microsecond and nanosecond [83]. The efficiency of the reaction can be improved further by preadsorption of the species on the photocatalyst surface [84]. Moreover, the addition of dopants, metals, or forming a heterojunction also reduces the recombination of PEHP, thereby increasing the efficiency of the photocatalytic process.

Until now, TiO_2-based photocatalysts have been extensively used for the removal of dye or toxic containments from wastewater [85]. TiO_2 has a wide E_g of 3.2 eV and photoactivation is only possible by the irradiation of UV light, which employs only 4% of the solar spectrum [86]. Currently, researchers are more focused on the usage of visible light-driven photocatalyst (VLDP) since it covers the largest fraction of the solar spectrum. Bi_2O_3 [87], WO_3 [88], Bi_2WO_6 [89], CdS [90], and C_3N_4 [91] are a few examples of VLDP. Although many experiments have been performed on the preparation of VLDP, their applications are still

https://www.twirpx.org & http://chemistry-chemists.com

limited due to the constrained absorption of visible light and short PEHP lifetime. Various strategies have been adapted to overcome these issues, such as doping, textural design, or constructing a heterojunction by coupling with secondary substance. Among these, the formation of a heterojunction is more efficient for improving the efficiency of photocatalytic reactions [92–94]. The formation of a heterojunction catalyst can be categorized into four parts: (a) a semiconductor-semiconductor heterojunction (Sc-Sc H) which creates sufficient built-in potential (V_b) for an oxidation-reduction reaction as well as providing high absorption of the solar spectrum; (b) a semiconductor-metal heterojunction (Sc-M H) which causes an effective transition and separation of PEHP; (c) a semiconductor-carbon group heterojunction (Sc-C H) which results in sufficient migration and separation of PEHP; and (d) a multicomponent heterojunction (McH) which improves the absorption capacity of material and also broaden the range for UV/visible light absorption. The principles of all these categories are illustrated in Figs. 3 and 4.

6.1 Semiconductor-semiconductor heterojunction (Sc-Sc H)

p-n Sc-Sc H and non-p-n Sc-Sc H are two class of Sc-Sc H. Construction of a p-n junction provides advantages in terms of: (i) high adsorption capacity; (ii) efficient collection and separation of charge carriers; (iii) longer lifetime of the PEHP; and (iv) fast charge transfer to the catalyst. Moreover, it separates the localized inappropriate oxidation and reduction reactions in the nano space. Basically, when n-type and p-type semiconductors come in contact, they create a space charge region at the interface due to the diffusion of e^- and h^+. This results in the generation of V_b which further directs the e^- and h^+ to migrate in the

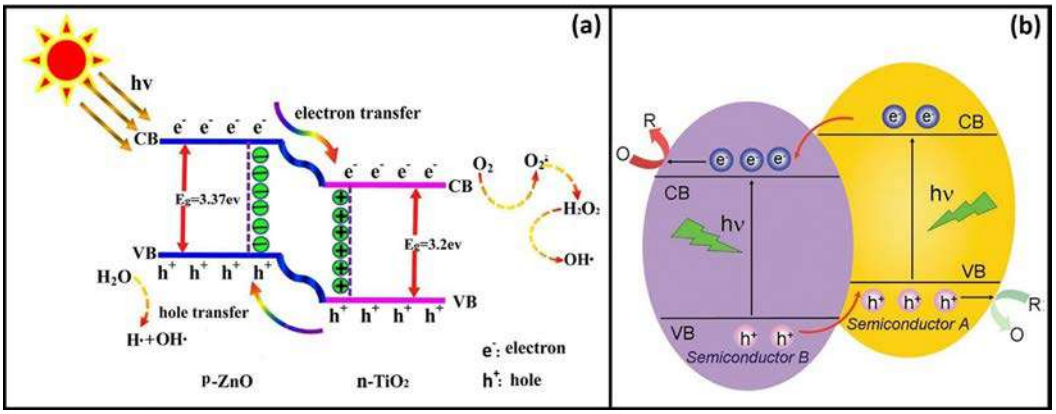

FIG. 3 Schematic structure of (A) p-n semiconductor-semiconductor heterojunction and (B) non-p-n semiconductor-semiconductor heterojunction. *Reprinted with permission from H. Wang, L. Zhang, Z. Chen, J. Hu, S. Li, Z. Wang, et al. Semiconductor heterojunction photocatalysts: Design, construction, and photocatalytic performances. Chemical Society Reviews 2014;43:5234–5244. https://doi.org/10.1039/c4cs00126e and R. Zha, R. Nadimicherla, X. Guo, Ultraviolet photocatalytic degradation of methyl orange by nanostructured TiO_2/ZnO heterojunctions, J Mater Chem A 3 (2015) 6565–6574*

https://www.twirpx.org & http://chemistry-chemists.com

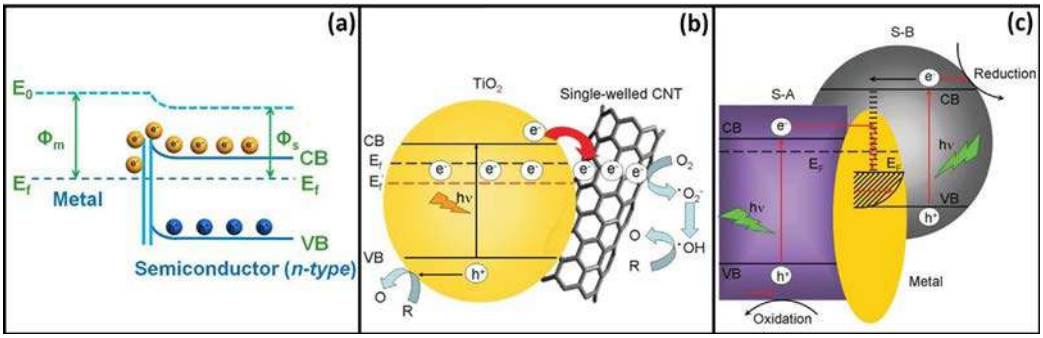

FIG. 4 Schematic structure of (A) semiconductor-metal heterojunction, (B) semiconductor-carbon heterojunction, and (C) multicomponent heterojunction. *Reprinted with permission from H. Wang, L. Zhang, Z. Chen, J. Hu, S. Li, Z. Wang, J. Liu, X. Wang, Semiconductor heterojunction photocatalysts: design, construction, and photocatalytic performances, Chem Soc Rev 43 (2014) 5234–5244 and S. Liu, C. Han, Z. Tang, Y. Xu. Heterostructured semiconductor nanowire arrays for artificial photosynthesis. Materials Horizons 2016;3:270–282. https://doi.org/10.1039/c6mh00063k.*

opposite direction. The irradiation of light in the p-n heterojunction with the energy higher than the E_g of the catalyst causes a quick separation of PEHP by the built-in electric field. This electric field directs the electrons to migrate to the CB of the n-type semiconductor and h^+ to the VB of the p-type semiconductor [95]. Another type of heterojunction formed in the semiconductors is non-p-n-type, in which both semiconductors (A and B) forming the heterojunction are the same types, i.e., either n-type or p-type. Here, two different semiconductors with matched potential are bonded together to form the heterostructures. If the CB level of A is higher than the CB of B, then the transition of e^- from the CB of A to the CB of B is observed in the heterostructure with irradiation of photons. However, when the VB of A is higher than the VB of B, the h^+ starts migrating from the B to the A semiconductor. This results in the presence of a vast number of e^- on the surface of the B semiconductor and h^+ on the A semiconductor. Hence, efficient separation of PEHP by the internal field is obtained in the photocatalyst, which further reduces the recombination rate and promotes the photocatalysis process. Shang et al. [96] reported enhanced photocatalytic activity in Bi_2WO_6-TiO_2 by eight orders compared to bare Bi_2WO_6 under visible light irradiation. Wang et al. [97] demonstrated higher efficiency in SnO_2-TiO_2 heterostructure toward Rhodamine B degradation than bare SnO_2 and TiO_2. Wang et al. [98] showed the enlargement in the absorption range due to the formation of a Bi_2O_3-Bi_2WO_6 heterojunction which results in a 2.7-fold increase in the degradation rate of Bi_2WO_6.

6.2 Semiconductor-metal heterojunction (Sc-M H)

Another way to increase charge separation and reduce recombination of PEHP is by forming an Sc-M H. In this type of contact, e^- start to flow from one catalyst to another depending on their Fermi levels. Generally, the work function of the metal is higher than the n-type semiconductors such as TiO_2 and SnO_2, and e^- start to migrate to the metal from

https://www.twirpx.org & http://chemistry-chemists.com

semiconductor to balance the Fermi energy levels. This creates the Schottky barriers at the interface where the semiconductor has excess h^+ charge whereas the metal has excess e^-. Moreover, this barrier acts as a trap for e^- and reduces the recombination of PEH. Wang et al. [99] reported high decomposition of methylene orange dye by Ag-AgCl. They compared their result with N-doped TiO_2 and found eight times higher activity for dye degradation. Lu et al. [100] compared their finding with bare AgBr and N-doped TiO_2. They found that the activity of Ag-AgBr increased 1.5 times to AgBr and 13 times to N-doped TiO_2 for the removal of Rhodamine B dye under visible light irradiation. Improved activity in these materials is mainly due to: (i) the localized surface plasmons resonance effect; (ii) better quantum efficiency; and (iii) improved light absorption.

6.3 Semiconductor-carbon heterojunction (Sc-C H)

Various types of carbon material such as graphene, reduced graphene oxide, activated carbon, and CNT have been used for making heterojunctions. Carbon-based materials exhibit high surface area, which results in the adsorption of more pollutants and thus improves the photoactivity of the catalyst material [101]. Graphene and CNT have a metallic structure and formed a Schottky barrier at the interface of semiconductor/CNT. This junction causes an improvement in the recombination time. Apart from this, CNT allows more photoexcited e^- from a semiconductor due to its huge e^- storage capacity which hinders the recombination of PEHP [3]. Generally, photoexcitation of the catalyst results in the generation of e^- in the semiconductor. Electrons presents in the space-charge regions start migrating from the CB of semiconductor to CNTs for balancing the Fermi level, whereas h^+ present in the semiconductor continuously participates in the redox reaction [102]. The formation of a heterojunction with graphene provides key advantages to semiconductor photocatalyst such as: (i) high conductivity; (ii) high surface area; (iii) extended absorption wavelength; (iv) promoted charge transfer; and (v) restrained recombination of PEHP. These advantages result in higher photocatalytic activity in the composite material compared to the bare one. Moreover, the interaction of graphene with semiconductors causes a shift in the Fermi level, which further reduces the CB potential of the semiconducting material. This reduction allows the fast migration of photoinduced e^- and suppresses the recombination of charge carriers. Gao et al. [103] reported the Bi_2WO_6 incorporated graphene sheet as a photocatalyst for the removal of Rhodamine B dye. They found that the composite exhibited three times higher activity than the bare Bi_2WO_6 under visible light irradiation. This behavior was mainly attributed to the efficient absorption of photons, fast e^- transportation, and the reduction in the CB potential. A similar result was also reported by Du et al. [101]. They reported an 11-fold increase in the activity of TiO_2-graphene compared to the bare TiO_2 for removal of methylene blue dye.

6.4 Multicomponent heterojunction (McH)

Various types of materials are extensively studied and developed for efficient use of the solar spectrum. But they are suffering in terms of a limited area for visible light photoresponse. In

https://www.twirpx.org & http://chemistry-chemists.com

this direction, the McH-based system plays a significant role in which two or more VLDPs and an e^- migrating system are integrated [104, 105]. Generally, two semiconductors have different absorption ranges and can be excited by visible or UV light. The combination of these two semiconductors results in the widening of photoexcitation of the material. The irradiation of photons in the catalyst causes the generation of e^- and h^+ in both semiconductors, and two types of e^- transfer are observed in these systems. Firstly, the photoexcited e^- of semiconductor A start migrating to the metal through Schottky barriers because the CB of semiconductor A is higher than the Fermi level of metal. The rate of transferring e^- in semiconductor A is faster than the recombination of PEHP. Consequently, a massive number of h^+ are present in the VB of the semiconductor for participating in the redox reaction, and the life span of PEHP also increases [106]. On the other side, the Fermi level of metal is above the VB of semiconductor B, which results in the migration of h^+ from semiconductor B to the metal and reduces the recombination of PEHP in semiconductor B. This results in the presence of a greater number of photoexcited e^- in the CB of semiconductor B which further react with O_2 and air, and generate O_2^-. Hence, the use of visible/UV light results in both the generation of PEHP in the semiconductors and the simultaneous e^- transfer from semiconductor A to the metal to semiconductor B. Here, conjugation of the metal in the semiconductors provides several advantages in terms of: (i) storage system; (ii) recombination center for h^+ in the VB of semiconductor B and e^- in the CB of semiconductor A; (iii) improving the interfacial charge transfer; and (iv) a complete separation of e^- in CB of semiconductor B and h^+ in the VB of semiconductor A which further participated in the redox reaction. Tada et al. [104] demonstrated dye degradation by using the multicomponent system CdS-Au-TiO_2, in which CdS and TiO_2 act as semiconductors A and B, and Au is conjugated with them. Tada et al. reported higher activity in the McH than the single component (CdS or TiO_2) or binary components (Au-TiO_2, CdS-TiO_2).

7 Conclusion

In this chapter, the basic principle for photocatalytic reaction, pathways followed by photoinduced charge carriers, and various strategies to improve the photocatalytic activity of semiconductors were explained in detail. The fundamental principle and mechanisms based on the class of catalysts such as semiconductors, quantum dots, and two-dimensional structures were also discussed. Moreover, the impacts of various parameters such as pH, initial concentration of dye, amount of catalyst, and the intensity of wavelength on the rate of reaction were explained. The formation of heterostructure increases the percentage degradation of dye as well as providing efficient usage of the solar spectrum by broadening the absorption range of the photocatalyst and enhancing the separation and life span of charge carriers. This overview should help the reader to develop a stable VLDP with a high degree of oxidation for the removal of toxic dyes.

https://www.twirpx.org & http://chemistry-chemists.com

References

[1] Qu Y, Duan X. Progress, challenge and perspective of heterogeneous photocatalysts. Chem Soc Rev 2013;42:2568–80.

[2] Legrini O, Oliveros E, Braun AM. Photochemical processes for water treatment. Chem Rev 1993;93:671–98.

[3] Hoffmann MR, Martin ST, Choi W, Bahnemann DW. Environmental applications of semiconductor photocatalysis. Chem Rev 1995;95:69–96.

[4] Carey JH, Lawrence J, Tosine HM. Photodechlorination of PCB's in the presence of titanium dioxide in aqueous suspensions. Bull Environ Contam Toxicol 1976;16:697–701.

[5] Rani B, Thamizharasan G, Nayak AK, Sahu NK. Degradation mechanism of organic dyes by effective transition metal oxide. In: Photocatalysts in Advanced Oxidation Processes for Wastewater Treatment. Wiley; 2020. p. 197–228.

[6] Reiche H, Bard AJ. Heterogeneous photosynthetic production of amino acids from methane-ammonia-water at platinum/titanium dioxide. Implications in chemical evolution. J Am Chem Soc 1979;101:3127–8.

[7] Fujishima A, Honda K. Electrochemical photolysis of water at a semiconductor electrode. Nature 1972;238:37–8.

[8] Linsebigler AL, Lu G, Yates JT. Photocatalysis on TiO_2 surfaces: principles, mechanisms, and selected results. Chem Rev 1995;95:735–58.

[9] Low J, Yu J, Jaroniec M, Wageh S, Al-Ghamdi AA. Heterojunction Photocatalysts. Adv Mater 2017;29:1601694.

[10] Thongam DD, Gupta J, Sahu NK. Effect of induced defects on the properties of ZnO nanocrystals: surfactant role and spectroscopic analysis. SN Appl Sci 2019;1:1030.

[11] Silva CG, Faria JL. Photochemical and photocatalytic degradation of an azo dye in aqueous solution by UV irradiation. J Photochem Photobiol A Chem 2003;155:133–43.

[12] Serpone N, Emeline AV. Suggested terms and definitions in photocatalysis and radiocatalysis. Int J Photoenergy 2002;4:943970.

[13] Machado AEH, Miranda JA, Freitas RF, Duarte ETFM, Ferreira LF, Albuquerque YDT, Ruggiero R, Sattler C, Oliveira L. Destruction of the organic matter present in effluent from a cellulose and paper industry using photocatalysis. J Photochem Photobiol A Chem 2003;1:231–41.

[14] Yue B, Zhou Y, Xu J, Wu Z, Zhang X, Zou Y, Jin S. Photocatalytic degradation of aqueous 4-chlorophenol by silica-immobilized polyoxometalates. Environ Sci Technol 2002;36:1325–9.

[15] Nosaka Y, Fox MA. Kinetics for electron transfer from laser-pulse irradiated colloidal semiconductors to adsorbed methylviologen: dependence of the quantum yield on incident pulse width. J Phys Chem 1988;92:1893–7.

[16] Rothenberger G, Moser J, Graetzel M, Serpone N, Sharma DK. Charge carrier trapping and recombination dynamics in small semiconductor particles. J Am Chem Soc 1985;107:8054–9.

[17] Fan W, Zhang Q, Wang Y. Semiconductor-based nanocomposites for photocatalytic H_2 production and CO_2 conversion. Phys Chem Chem Phys 2013;15:2632–49.

[18] Gelderman K, Lee L, Donne SW. Flat-band potential of a semiconductor: using the Mott–schottky equation. J Chem Educ 2007;84:685.

[19] Yang X, Wang D. Photophysics and photochemistry at the semiconductor/electrolyte Interface for solar water splitting. Semicond Semimet 2017;97:47–80.

[20] Lin Y, Xu Y, Mayer MT, Simpson ZI, McMahon G, Zhou S, Wang D. Growth of p-type hematite by atomic layer deposition and its utilization for improved solar water splitting. J Am Chem Soc 2012;134:5508–11.

https://www.twirpx.org & http://chemistry-chemists.com

[21] Hodes G, Kamat PV. Understanding the implication of carrier diffusion length in photovoltaic cells. J Phys Chem Lett 2015;6:4090–2.

[22] Zhao L, Meng Q, Fan X, Ye C, Li X, Chen B, Ramamurthy V, Tung C, Wu L. Photocatalysis with quantum dots and visible light: selective and efficient oxidation of alcohols to carbonyl compounds through a radical relay process in water. Angew Chem Int Ed 2017;56:3020–4.

[23] Olshansky JH, Ding TX, Lee YV, Leone SR, Alivisatos AP. Hole transfer from photoexcited quantum dots: the relationship between driving force and rate. J Am Chem Soc 2015;137:15567–75.

[24] Robel I, Kuno M, Kamat PV. Size-dependent Electron injection from excited CdSe quantum dots into TiO_2 nanoparticles. J Am Chem Soc 2007;129:4136–7.

[25] Li H, Li J, Ai Z, Jia F, Zhang L. Oxygen vacancy-mediated Photocatalysis of BiOCl: reactivity, selectivity, and perspectives. Angew Chem Int Ed 2018;57:122–38.

[26] Li R, Zhang F, Wang D, Yang J, Li M, Zhu J, Zhou X, Han H, Li C. Spatial separation of photogenerated electrons and holes among ⟨010⟩ and ⟨110⟩ crystal facets of $BiVO_4$. Nat Commun 2013;4:1432.

[27] Yu J, Low J, Xiao W, Zhou P, Jaroniec M. Enhanced photocatalytic CO_2-reduction activity of Anatase TiO_2 by coexposed ⟨001⟩ and ⟨101⟩ facets. J Am Chem Soc 2014;136:8839–42.

[28] Yang W, Zhang L, Xie J, Zhang X, Liu Q, Yao T, Wei S, Zhang Q, Xie Y. Enhanced photoexcited carrier separation in oxygen-doped $ZnIn_2S_4$ nanosheets for hydrogen evolution. Angew Chem Int Ed 2016;55:6716–20.

[29] Zhang J, Yu J, Jaroniec M, Gong JR. Noble metal-free reduced graphene oxide-$Zn_xCd_{1-x}S$ nanocomposite with enhanced solar photocatalytic H_2 - production performance. Nano Lett 2012;12:4584–9.

[30] Herrmann JM. Heterogeneous photocatalysis: an emerging discipline involving multiphase systems. Catal Today 1995;24:157–64.

[31] Muruganandham M, Swaminathan M. Photocatalytic decolourisation and degradation of reactive Orange 4 by TiO_2-UV process. Dyes Pigments 2006;68:133–42.

[32] Herrmann JM. Heterogeneous photocatalysis: fundamentals and applications to the removal of various types of aqueous pollutants. Catal Today 1999;53:115–29.

[33] Macedo LC, Zaia DAM, Moore GJ, Santana HD. Degradation of leather dye on TiO_2: a study of applied experimental parameters on photoelectrocatalysis. J Photochem Photobiol A Chem 2007;185:86–93.

[34] Kamble SP, Sawant SB, Pangarkar VG. Batch and continuous photocatalytic degradation of Benzenesulfonic acid using concentrated solar radiation. Ind Eng Chem Res 2003;42:6705–13.

[35] Gogate PR, Pandit AB. A review of imperative technologies for wastewater treatment I: oxidation technologies at ambient conditions. Adv Environ Res 2004;8:501–51.

[36] Kaneco S, Rahman MA, Suzuki T, Katsumata H, Ohta K. Optimization of solar photocatalytic degradation conditions of bisphenol a in water using titanium dioxide. J Photochem Photobiol A Chem 2004;163:419–24.

[37] Rauf MA, Bukallah SB, Hamadi A, Sulaiman A, Hammadi F. The effect of operational parameters on the photoinduced decoloration of dyes using a hybrid catalyst V_2O_5/TiO_2. Chem Eng J 2007;129:167–72.

[38] Saquib M, Muneer M. TiO_2-mediated photocatalytic degradation of a triphenylmethane dye (gentian violet), in aqueous suspensions. Dyes Pigments 2003;56:37–49.

[39] Qamar M, Saquib M, Muneer M. Photocatalytic degradation of two selected dye derivatives, chromotrope 2B and amido black 10B, in aqueous suspensions of titanium dioxide. Dyes Pigments 2005;65:1–9.

[40] Ollis DF, Pelizzetti E, Serpone N. Photocatalyzed destruction of water contaminants. Environ Sci Technol 1991;25:1522–9.

https://www.twirpx.org & http://chemistry-chemists.com

[41] Neppolian B, Choi HC, Sakthivel S, Arabindoo B, Murugesan V. Solar/UV-induced photocatalytic degradation of three commercial textile dyes. J Hazard Mater 2002;89:303–17.

[42] Bahnemann D. Photocatalytic detoxification of polluted waters. In: Boule P, editor. Environmental Photochemistry. Berlin, Heidelberg: Springer Berlin Heidelberg; 1999. p. 285–351.

[43] Rani B, Punniyakoti S, Sahu NK. Polyol asserted hydrothermal synthesis of SnO_2 nanoparticles for the fast adsorption and photocatalytic degradation of methylene blue cationic dye. New J Chem 2018;42:943–54.

[44] Liu C, Hsieh Y, Lai P, Li C, Kao C. Photodegradation treatment of azo dye wastewater by UV/TiO_2 process. Dyes Pigments 2006;68:191–5.

[45] Sakthivel S, Neppolian B, Shankar MV, Arabindoo B, Palanichamy M, Murugesan V. Solar photocatalytic degradation of azo dye: comparison of photocatalytic efficiency of ZnO and TiO_2. Sol Energy Mater Sol Cells 2003;77:65–82.

[46] So CM, Cheng MY, Yu JC, Wong PK. Degradation of azo dye procion red MX-5B by photocatalytic oxidation. Chemosphere 2002;46:905–12.

[47] Tang WZ, Zhang Z, An H, Quintana MO, Torres DF. TiO_2/UV photodegradation of azo dyes in aqueous solutions. Environ Technol 1997;18:1–12.

[48] Poulios I, Avranas A, Rekliti E, Zouboulis A. Photocatalytic oxidation of Auramine O in the presence of semiconducting oxides. J Chem Technol Biotechnol 2000;75:205–12.

[49] Wang N, Li J, Zhu L, Dong Y, Tang H. Highly photocatalytic activity of metallic hydroxide/titanium dioxide nanoparticles prepared via a modified wet precipitation process. J Photochem Photobiol A Chem 2008;198:282–7.

[50] Guillard C, Lachheb H, Houas A, Ksibi M, Elaloui E, Herrmann J. Influence of chemical structure of dyes, of pH and of inorganic salts on their photocatalytic degradation by TiO_2 comparison of the efficiency of powder and supported TiO_2. J Photochem Photobiol A Chem 2003;158:27–36.

[51] Zielińska B, Grzechulska J, Kaleńczuk RJ, Morawski AW. The pH influence on photocatalytic decomposition of organic dyes over A11 and P25 titanium dioxide. Appl Catal B Environ 2003;45:293–300.

[52] Tsui SM, Chu W. Quantum yield study of the photodegradation of hydrophobic dyes in the presence of acetone sensitizer. Chemosphere 2001;44:17–22.

[53] Bubacz K, Choina J, Dolat D, Morawski AW. Methylene blue and phenol photocatalytic degradation on nanoparticles of Anatase TiO_2. Pol J Environ Stud 2010;19:685–91.

[54] Ling CM, Mohamed AR, Bhatia S. Performance of photocatalytic reactors using immobilized TiO_2 film for the degradation of phenol and methylene blue dye present in water stream. Chemosphere 2004;57:547–54.

[55] Rani B, Jadhao CV, Sahu NK. Tetramethylene glycol mediated hydrothermal synthesis of defect-rich SnO_2 nanoparticles for fast adsorption and degradation of MB dye. AIP Conf Proc 2018;1942:050023.

[56] Baran W, Makowski A, Wardas W. The effect of UV radiation absorption of cationic and anionic dye solutions on their photocatalytic degradation in the presence TiO_2. Dyes Pigments 2008;76:226–30.

[57] Kansal SK, Kaur N, Singh S. Photocatalytic degradation of two commercial reactive dyes in aqueous phase using Nanophotocatalysts. Nanoscale Res Lett 2009;4:709.

[58] Tanaka K, Padermpole K, Hisanaga T. Photocatalytic degradation of commercial azo dyes. Water Res 2000;34:327–33.

[59] Kiriakidou F, Kondarides DI, Verykios XE. The effect of operational parameters and TiO_2-doping on the photocatalytic degradation of azo-dyes. Catal Today 1999;54:119–30.

[60] Saggioro EM, Oliveira AS, Pavesi T, Maia CG, Ferreira LFV, Moreira JC. Use of titanium dioxide photocatalysis on the remediation of model textile wastewaters containing azo dyes. Molecules 2011;16:10370–86.

https://www.twirpx.org & http://chemistry-chemists.com

[61] Daneshvar N, Salari D, Khataee AR. Photocatalytic degradation of azo dye acid red 14 in water: investigation of the effect of operational parameters. J Photochem Photobiol A Chem 2003;157:111–6.

[62] Giwa A, Nkeonye PO, Bello KA, Kolawole EG. Solar photocatalytic degradation of reactive yellow 81 and reactive violet 1 in aqueous solution containing semiconductor oxides. Int J Appl Sci Technol 2012;2:1–16.

[63] Zhang T, Oyama TK, Horikoshi S, Hidaka H, Zhao J, Serpone N. Photocatalyzed N-demethylation and degradation of methylene blue in titania dispersions exposed to concentrated sunlight. Sol Energy Mater Sol Cells 2002;73:287–303.

[64] Augugliaro V, Baiocchi C, Prevot AB, Garcı´a-López E, Loddo V, Malato S, Marcı´ G, Palmisano L, Pazzi M, Pramauro E. Azo-dyes photocatalytic degradation in aqueous suspension of TiO_2 under solar irradiation. Chemosphere 2002;49:1223–30.

[65] Grzechulska J, Morawski AW. Photocatalytic decomposition of azo-dye acid black 1 in water over modified titanium dioxide. Appl Catal B Environ 2002;36:45–51.

[66] Avasarala BK, Tirukkovalluri SR, Bojja S. Synthesis, characterization and photocatalytic activity of alkaline earth metal doped titania. Indian J Chem Sect A: Inorg, Phys Theor Anal Chem 2010;49:1189–96.

[67] Mehrotra K, Yablonsky GS, Ray AK. Macro kinetic studies for photocatalytic degradation of benzoic acid in immobilized systems. Chemosphere 2005;60:1427–36.

[68] Soares ET, Lansarin MA, Moro CC. A study of process variables for the photocatalytic degradation of rhodamine B. Braz J Chem Eng 2007;24:29–36.

[69] Yoon J, Lee Y, Kim S. Investigation of the reaction pathway of OH radicals produced by Fenton oxidation in the conditions of wastewater treatment. Water Sci Technol 2001;44:15–21.

[70] Muruganandham M, Swaminathan M. Photocatalytic decolorization and degradation of reactive orange 4 by TiO_2-UV process. Dyes Pigments 2006;68:133–42.

[71] Rauf MA, Ashraf SS. Fundamental principles and application of heterogeneous photocatalytic degradation of dyes in solution. Chem Eng J 2009;151:10–8.

[72] Alnuaimi MM, Rauf MA, Ashraf SS. A comparative study of neutral red decoloration by photo-Fenton and photocatalytic processes. Dyes Pigments 2008;76:332–7.

[73] Ramirez JH, Maldonado-Hódar FJ, Pérez-Cadenas AF, Moreno-Castilla C, Costa CA, Madeira LM. Azo-dye Orange II degradation by heterogeneous Fenton-like reaction using carbon-Fe catalysts. Appl Catal B Environ 2007;75:312–23.

[74] Dammala P, Machado J, Rani B, Murali S, Devi S, Luwang MN, Sahu NK. Synthesis of biphasic nanomaterials based on ZnO and SnO_2: application towards photocatalytic degradation of acid red dye. Nano-Struct Nano-Objects 2019;18:100292.

[75] Kubo R, Kawabata A, Kobayashi S. Electronic properties of small particles. Annu Rev Mater Sci 1984;14:49–66.

[76] Henglein A. Mechanism of reactions on colloidal microelectrodes and size quantization effects. In: Steckhan E, editor. Electrochemistry II. Topics in Current Chemistry, 143. Berlin, Heidelberg: Springer; 1988. p. 113–80.

[77] Spanhel L, Haase M, Weller H, Henglein A. Photochemistry of colloidal semiconductors. 20. Surface modification and stability of strong luminescing CdS particles. J Am Chem Soc 1987;109:5649–55.

[78] Brus LE. Electron–electron and electron-hole interactions in small semiconductor crystallites: the size dependence of the lowest excited electronic state. J Chem Phys 1984;80:4403–9.

[79] Wang Y, Suna A, Mahler W, Kasowski R. PbS in polymers. From molecules to bulk solids. J Chem Phys 1987;87:7315–22.

[80] Thongam DD, Gupta J, Sahu NK, Bahadur D. Investigating the role of different reducing agents, molar ratios, and synthesis medium over the formation of ZnO nanostructures and their photocatalytic activity. J Mater Sci 2018;53:1110–22.

https://www.twirpx.org & http://chemistry-chemists.com

[81] Watson SS, Beydoun D, Scott JA, Amal R. The effect of preparation method on the photoactivity of crystalline titanium dioxide particles. Chem Eng J 2003;95:213–20.

[82] Muggli DS, Ding L. Photocatalytic performance of sulfated TiO_2 and Degussa P-25 TiO_2 during oxidation of organics. Appl Catal B Environ 2001;32:181–94.

[83] Shkrob IA, Sauer MC. Hole scavenging and photo-stimulated recombination of Electron – hole pairs in aqueous TiO_2 nanoparticles. J Phys Chem B 2004;108:12497–511.

[84] Matthews RW. An adsorption water purifier with in situ photocatalytic regeneration. J Catal 1988;113:549–55.

[85] Fujihira M, Satoh Y, Osa T. Heterogeneous photocatalytic oxidation of aromatic compounds on TiO_2. Nature 1981;293:206–8.

[86] Chen C, Cai W, Long M, Zhou B, Wu Y, Wu D, Feng Y. Synthesis of visible-light responsive graphene oxide/TiO_2 composites with p/n heterojunction. ACS Nano 2010;4:6425–32.

[87] Jiang H, Liu J, Cheng K, Sun W, Lin J. Enhanced visible light photocatalysis of Bi_2O_3 upon fluorination. J Phys Chem C 2013;117:20029–36.

[88] Nayak AK, Pradhan D. Microwave-assisted greener synthesis of defect-rich tungsten oxide nanowires with enhanced photocatalytic and photoelectrochemical performance. J Phys Chem C 2018;122:3183–93.

[89] Huang C, Chen L, Li H, Mu Y, Yang Z. Synthesis and application of Bi_2WO_6 for the photocatalytic degradation of two typical fluoroquinolones under visible light irradiation. RSC Adv 2019;9:27768–79.

[90] Hussain W, Malik H, Bahadur A, Hussain RA, Shoaib M, Iqbal S, Hussain H, Green IR, Badshah A, Li H. Synthesis and characterization of CdS photocatalyst with different morphologies: visible light activated dyes degradation study. Kinet Catal 2018;59:710–9.

[91] Wang X, Maeda K, Thomas A, Takanabe K, Xin G, Carlsson JM, Domen K, Antonietti M. A metal-free polymeric photocatalyst for hydrogen production from water under visible light. Nat Mater 2009;8:76–80.

[92] Zhang L, Li J, Chen Z, Tang Y, Yu Y. Preparation of Fenton reagent with H_2O_2 generated by solar light-illuminated nano-Cu_2O/MWNTs composites. Appl Catal A Gen 2006;299:292–7.

[93] Gao H, Wang H, Jin Y, Lv J, Xu G, Wang D, Zhang X, Chen Z, Zheng Z, Wu Y. Controllable fabrication of immobilized ternary CdS/Pt–TiO_2 heteronanostructures toward high-performance visible-light driven photocatalysis. Phys Chem Chem Phys 2015;17:17755–61.

[94] Zhang L, Wong K, Yip H, Hu C, Yu JC, Chan C, Wong P. Effective photocatalytic disinfection of E. coli K-12 using AgBr-ag-Bi_2WO_6 nanojunction system irradiated by visible light: the role of diffusing hydroxyl radicals. Environ Sci Technol 2010;44:1392–8.

[95] Jiang L, Zhou G, Mi J, Wu Z. Fabrication of visible-light-driven one-dimensional anatase TiO_2/Ag heterojunction plasmonic photocatalyst. Catal Commun 2012;24:48–51.

[96] Shang M, Wang W, Zhang L, Sun S, Wang L, Zhou L. 3D Bi_2WO_6/TiO_2 hierarchical Heterostructure: controllable synthesis and enhanced visible photocatalytic degradation performances. J Phys Chem C 2009;113:14727–31.

[97] Wang C, Shao C, Zhang X, Liu Y. SnO_2 nanostructures-TiO_2 nanofibers Heterostructures: controlled fabrication and high photocatalytic properties. Inorg Chem 2009;48:7261–8.

[98] Wang H, Li S, Zhang L, Chen Z, Hu J, Zou R, Xu K, Song G, Zhao H, Yang J, Liu J. Surface decoration of Bi_2WO_6 superstructures with Bi_2O_3 nanoparticles: an efficient method to improve visible-light-driven photocatalytic activity. CrystEngComm 2013;15:9011–9.

[99] Wang P, Huang B, Qin X, Zhang X, Dai Y, Wei J, Whangbo M. Ag@AgCl: a highly efficient and stable photocatalyst active under visible light. Angew Chem Int Ed 2008;47:7931–3.

https://www.twirpx.org & http://chemistry-chemists.com

[100] Lu W, Qin X, Li H, Asiri AM, Al-Youbi AO, Sun X. One-step hydrothermal synthesis of ag nanoparticle decorated submicrometer-scale spherical AgBr colloids: a highly efficient visible light plasmonic photocatalyst for degradation of organic dyes. Part Part Syst Charact 2013;30:67–71.

[101] Du J, Lai X, Yang N, Zhai J, Kisailus D, Su F, Wang D, Jiang L. Hierarchically ordered macro-mesoporous TiO_2-graphene composite films: improved mass transfer, reduced charge recombination, and their enhanced photocatalytic activities. ACS Nano 2011;5:590–6.

[102] Woan K, Pyrgiotakis G, Sigmund W. Photocatalytic carbon-nanotube–TiO_2 composites. Adv Mater 2009;21:2233–9.

[103] Gao E, Wang W, Shanga M, Xua J. Synthesis and enhanced photocatalytic performance of graphene-Bi_2WO_6 composite. Phys Chem Chem Phys 2011;13:2887–93.

[104] Tada H, Mitsui T, Kiyonaga T, Akita T, Tanaka K. All-solid-state Z-scheme in CdS–au–TiO_2 three-component nanojunction system. Nat Mater 2006;5:782–6.

[105] Elahifard MR, Rahimnejad S, Haghighi S, Gholami MR. Apatite-coated Ag/AgBr/TiO_2 visible-light photocatalyst for destruction of Bacteria. J Am Chem Soc 2007;129:9552–3.

[106] Hirakawa T, Kamat PV. Charge separation and catalytic activity of Ag@TiO_2 Core – Shell composite clusters under UV – irradiation. J Am Chem Soc 2005;127:3928–34.

https://www.twirpx.org & http://chemistry-chemists.com

2

Nanomaterials aspects for photocatalysis

Sarika Singh[a] and Brijesh Kumar Singh[b]

[a]DEPARTMENT OF CHEMISTRY, MANIPAL UNIVERSITY JAIPUR, JAIPUR, INDIA [b]DEPARTMENT OF PHYSICS, CENTRAL UNIVERSITY OF RAJASTHAN, AJMER, INDIA

1. Introduction to nanomaterials and photocatalysis

In the present scenario, continuous growing technology demands efficient solar energy harvesting to achieve sustainable solutions in science and industries. The rapid escalation of industrialization toward developing society and unavoidable human activity cause serious environmental pollution that results in serious threats to human beings. In particular the coloring effluents containing dyes discharged from different sources such as textile, chemicals, mining, and metallurgical industries generate the breakdown of organic products of dyes which are toxic and carcinogenic to life mainly due to the presence of naphthalene, benzamine, and other organic products [1, 2]. Nanotechnology is an emerging field which has played a vital role in protection of the environment in last few years. Nanoscience has attracted much attention from researchers because of materials that are nano in size and have unique properties compared to their bulk counterpart. The unique and unusual properties are due to surface and quantum size effect. At nanoscale level, many thermodynamic laws are broken down. It is well-known that the thermodynamic phenomenon is a collective phenomenon, for example, phase transition. Nanomaterials exhibit a higher surface area to volume ratio in their conventional form, which impacts the thermodynamic behavior of the materials. Nanomaterials having the interactions of atoms at interfaces and the structure of these interfaces determines the properties of nanomaterials. Nanomaterials influence not only physical but also chemical properties. The most important unusual property of nanomaterials is quantum size effect, which shows that electrons are localized in metals and semiconductors. It is represented like electrons in a box model, and electrons at different states then combine to extend the bandgap. At nanoscale, the size of the box is approximately the same as the atomic size; as a result, the particles become pseudo atoms and electrons are quantized similar to atoms or molecules. Thus, all the properties of nanomaterials are due to electron activities such as electromagnetic wave interaction, ionization potential, and electron affinity, which are different from activities of macroscopic molecules. Furthermore, three different methodologies for synthesis of nanomaterials have been applied:

Nanostructured Materials for Visible Light Photocatalysis. https://doi.org/10.1016/B978-0-12-823018-3.00015-4
Copyright © 2022 Elsevier Inc. All rights reserved.

https://www.twirpx.org & http://chemistry-chemists.com

(1) top-down
(2) bottom-up
(3) virtual

The top-down approach is the traditional technique for synthesis of nanoparticles via lithographic tools. The bottom-up approach is used to build up nanomaterials from bottom, i.e., atom by atom, leading to formation of self-assemblies and clusters of atoms/molecules. Furthermore, the morphology of nanomaterials can be easily tuned in different shapes such as rod, thin film, sphere, cube, wire, tube, etc. [3–5]. Fullerene is the primary nanomaterial which was developed at the beginning of the nanoscience era in 1985. The structure of fullerene is stable but chemically reactive because of the presence of an electron-deficient C═C (double) bond in C_{60}. The invention has been further developed to the structure of other allotropes of carbon such as one-dimensional (1D) carbon nanotubes (CNTs) and two-dimensional (2D) graphene sheets. These materials show high electrical conductivity due to the presence of free electrons. Recently, it has been identified that carbon-based nanoparticles exhibit interesting optical properties which have not been observed in macroscopic particles [6]. For examples, carbon quantum dots show high optical properties due to *n*-plasmon absorption in core carbon nanoparticles and exhibit a wide range of the UV/visible spectrum. The unique properties of nanostructured materials lead to enhanced chemical reactivity and affect their properties such as tunable photoactivity, strength, and other interesting characteristics. Nanomaterials are considered to play a key role in shaping our current environment, by providing new materials and remediation techniques. For detoxification of industrial effluents from groundwater and surface water, several cost-effective and environmentally friendly techniques and processes such as adsorption, chemical precipitation, ion exchange, reverse osmosis, membrane based-filtration, solvent extraction, etc. have been used [7–9]. Among several techniques, photocatalysis is a conventional and efficient technique which solves many environmental problems. It has proven very effective since it can be used to degrade and mineralize dyes and chemicals into CO_2 and H_2O, and some other small molecules which are stable and further cannot be degraded by other processes. This process utilizes UV and visible light.

Over the last few decades, various efforts have been made to make organic, inorganic, ceramic, and inorganic polymeric-based nanomaterials. A broad range of materials like calcogenides, metal-carbide, metal-sulfide, metal-nitride, and metal-phosphide, and many kinds of heterogeneous and plasmonic conjugated polymers, have been addressed to solve environmental problems. Among the various kinds of nanoadsorbents, metal oxide-based semiconductors have attracted extensive research interest due to their high photosensitivity, large adsorption capacity, and nontoxic and long-term use without loss of photocatalytic activity. These semiconducting materials have capabilities of absorbing UV light and visible light. The main disadvantage of these materials is low quantum yield, which results from charge carrier recombination and use of UV light. In order to overcome these difficulties, numerous strategies and modifications on nanoscale have been

https://www.twirpx.org & http://chemistry-chemists.com

employed via doping and surface modification to produce visible light-active photocatalysts. Broad research has been conducted on nonmetal doped TiO_2 like N, C, and S, and modification by metal nanoparticles like Ag, Au, Cu, Pt, and Bi enhanced the visible light photocatalytic activity. However, research in this area is still not enough for commercial applications. Therefore, efforts are being made to design and develop novel materials that increase catalytic efficiency under visible light. Several strategies including novel metal loaded catalysts, heterojunctions, and cocatalysts, which provide charge carrier separation, have been developed to investigate new visible light-active photocatalytic materials. In this chapter, our focus is on promising strategies for the development of novel high-performance nanostructured materials of well-matched photo absorption with solar spectrum, photo-excited charge separation to minimize electron-hole pairs recombination, and sufficient energy of charge used for photodegradation of dyes and other toxic chemicals.

2. Mechanism of photocatalysis

In the semiconductor process, a chemical reaction occurs when electrons shift from valence band (VB) to conduction band (CB). The transfer of electrons from the VB to the CB decreases the energy as the number of electrons in the highest occupied molecular orbital (HOMO) and the lowest unoccupied molecular orbital (LUMO) increases. In this process, the light of energy greater or equal to the bandgap of semiconducting materials excites the electron from the VB to the CB, leaving a hole in the VB. Hafmann et al. [10] found that the photogenerated electrons and holes recombine to release heat in 10–100 ns by measuring flash laser photolysis. The recombination of charge carriers leads to low quantum efficiency.

$$\text{Metal oxide} + h\nu \rightarrow e^- + h^+ \tag{1}$$

$$e^- + h^+ \rightarrow \text{heat} \tag{2}$$

The electron-hole pair recombination in semiconductors can be reduced by adding suitable scavengers, creating defects, incorporation of some traps sits on the surface or surface adsorbents. Typically, in the photocatalysis process, two reactions are involve: the first is oxidation of dissociatively absorbed H_2O molecules, and the second is reduction of electron acceptors by photogenerated electrons. These two reactions lead to the production of reactive oxygen species (ROS) such as hydroxyl radicals ($^{\cdot}OH$) and superoxide radicals anion ($^{\bullet}O_2^-$), respectively [11]. The formation of ROS depends on types of materials and irradiated light. These two ROS react with organic pollutants, leading to complete mineralization. A schematic diagram of photocatalysis process is shown in Fig. 1.

The possible reactions scheme involved in the photocatalysis process is shown in Eqs. (3)–(8).

$$h^+ + H_2O \rightarrow H^+ + OH^- \tag{3}$$

https://www.twirpx.org & http://chemistry-chemists.com

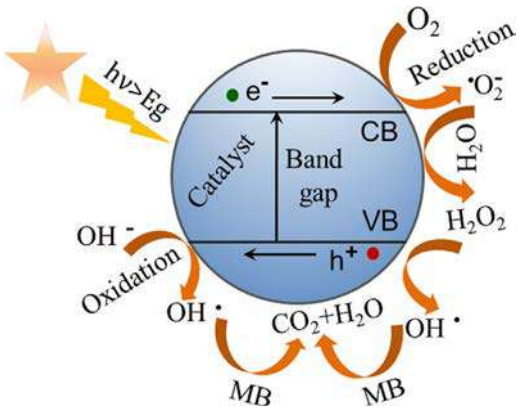

FIG. 1 Mechanism of photocatalytic activity. The mechanism of photocatalytic degradation of dye (MB) on the surface of semiconductor metal oxide under light irradiation.

$$h^+ + OH^- \rightarrow {}^{\cdot}OH \tag{4}$$

$$e^- + O_2 \rightarrow {}^{\cdot}O_2{}^- \tag{5}$$

$$2e^- + {}^{\cdot}O_2{}^- + 2H^+ \rightarrow H_2O_2 \tag{6}$$

$$e^- + H_2O_2 \rightarrow OH^- + {}^{\cdot}OH \tag{7}$$

$$\text{Organic pollutants} + OH^{\cdot} + O_2 \rightarrow CO_2 + H_2O + \text{other degradation products} \tag{8}$$

The organic pollutants get absorbed on the catalyst's surface via oxygen at the surface.

3. Influence of different parameters on photocatalysis

The different parameters like catalyst loading, surface area and morphology, pH, temperature, contaminant concentration, light intensity, and light wavelength play important roles in the degradation of pollutants. Changing the different parameters impacts the degradation efficiency.

3.1 Catalyst loading

One of the important parameters for photocatalytic activity in degradation of organic pollutants is catalyst concentration. The amount of catalyst loading is based on the initial concentration of pollutants and solution volume. It has been observed that the rate of degradation of dyes rises when increasing the loading amount of catalyst, due to an increase in the active surface site on semiconducting materials, which helps in the formation of hydroxyl and superoxide radicals. Further increasing the catalyst loading above the optimal value does not result in a further increase in the degradation rate [12]. This is because the high concentration of catalyst increases the turbidity in the solution, which blocks the

https://www.twirpx.org & http://chemistry-chemists.com

active site of the catalyst and scatters the UV light. Also, a high catalyst concentration leads to agglomeration of the nanoparticles, which results in a decrease in the available active surface area for intake of light and hence reduces the production of photogenerated electron-hole pairs and decreases the photocatalytic activity.

3.2 Surface area and morphology

Photocatalytic activity strongly depends on the surface sites and structural properties of materials such as surface area, crystal composition, pore size, adsorption capacity, band-gap, and intensity of light. Furthermore, photocatalytic activity can be enhanced by modifying the shape and morphology of nanomaterials since the photocatalysis process involves the surface of the catalyst [3]. Not only morphology but even the size of the photocatalyst affects the photocatalytic activity. The catalytic activity increases when decreasing the size of the photocatalyst. The surface area of the catalyst increases with decreasing the size of nanomaterials, which enhances the photocatalytic activity. Thus, semiconducting materials with a large surface area provide a greater number of active surface sites and surface reactivity to enhance the photodegradation of organic pollutants [13]. Dong et al. reported different morphologies of Ag_3PO_4 such as tetrapods, nanorods, and triangular prisms, and investigated their photocatalytic activity under visible light [14]. They showed that branched and porous nanostructure of Ag_3PO_4 exhibit higher photocatalytic activity compared to other structures; this is because of their large surface area. Furthermore, Li et al. [15] synthesized helix W-N codoped TiO_2 to improve the photodegradation of phenol under visible light irradiation. They attributed the enhancement of the photoactivity to the large surface area, special twisting morphology, and pore size.

3.3 Effect of pH

The pH is another important factor which has a significant impact on photocatalytic activity in the presence of catalysts. The pH affects the surface properties of catalysts and dissociates the organic contaminants on the surface of metal oxides as well. Qamar et al. [16] stated that the surface charge of TiO_2 can be protonated in acidic conditions and deprotonated under alkaline conditions as represented in Eqs. (9) and (10).

$$TiOH + H^+ \rightarrow TiOH_2{}^+ \tag{9}$$

$$TiOH + OH^- \rightarrow TiO^- + H_2O \tag{10}$$

Thus, the surface of the catalyst becomes positively charge in a acidic medium and negatively charged in a basic medium. Furthermore, Abbasi et al. [17] prepared decorated ZnO nanoparticles with different amounts of SnO_2 and evaluated how the pH of the medium influences the photocatalytic degradation of methyl orange. They described the higher photodegradation efficiency of ZnO@SnO_2 at neutral pH (pH 7) as compared to pH 4 and pH 10 due to the surface charge of nanoparticles. The surface charge as well as dispersion of particles in an aqueous solution are affected by the acidity of the suspension

https://www.twirpx.org & http://chemistry-chemists.com

solution. Thus, the dispersion of the nanoparticles increased in the acidic medium with respect to the basic medium, and hence enhanced photocatalytic activity in acidic conditions (at pH = 4) compared to alkaline conditions (pH = 10). Byrappa et al. [18] reported that the photocatalytic reaction was enhanced in a alkaline medium and observed that this could be caused by an increase in the hydroxyl ions which give rise to the formation of more hydroxyl radicals ($HO^{\bullet}$) whereas in an acidic medium, the perhydroxyl radicals ($HOO^{\bullet}$) can form hydrogen peroxide (H_2O_2), which induces the formation of hydroxyl radicals. Thus, the rate of reaction increases in both acidic and basic conditions because of the formation of hydroxyl radicals.

3.4 Effect of temperature

Another important factor which contributes to the photocatalysis process is the temperature parameter. One of the key factors which drive the photocatalysis process is dissolved oxygen. It acts as a scavenger to traps the photogenerated electrons from CB, leading to the production of hydroxyl radicals. The degradation rate in the photocatalysis reaction process changes when the temperature is varied. The degradation rate decreases at very high temperatures because of desorption of organic pollutants at the surface of the catalyst.

Regarding the increase in the temperature, Mills and Hunte in 1977 [19] described that the photocatalytic reaction was completed more efficiently by increasing the temperature, which could be attributed to the electron-holes pair recombination.

3.5 Effect of contaminants concentration

One more factor which impacts the degradation rate of organic pollutants is contaminants concentration. Commonly, the degradation rate increases with increasing the concentration of dyes. The degradation rate increases at a certain critical concentration level of dye; however, at high concentrations of dye the photocatalysis process is activated and the degradation rate decreases. Mostly, the photodegradation process proceeds through pseudo-first-order reactions kinetics, as given by Eq. (11).

$$\ln(C_0/C) = kt \tag{11}$$

where k is the photodegradation rate constant and t is the time required for the initial concentration of pollutants to reduce to the final concentration (C).

3.6 Effect of calcination temperature

The calcination temperature is also one of the factors which influences the degradation rate. The photocatalytic performance increases with increasing the calcination temperature of the sample to some extent (~300–500°C) and then sharply decreases with further increases in the calcination temperature. This is because calcination increases the crystallinity of the sample and removes the impurities which are loosely bound. The as-prepared

https://www.twirpx.org & http://chemistry-chemists.com

sample without calcination contains excess moisture (water molecules) which blocks the active surface sites, thus reducing the photocatalytic activity. At very high temperatures (above 600°C), the mesoporous structure collapses and decreases the specific surface area, hence reducing the degradation rate [20, 21]. Thus, the two main factors to improve photocatalytic activity are high surface area, which increases the number of active sites for absorption of dyes on the catalyst surface, and crystallinity, which allows electron-hole pairs recombination to be minimized, subsequently increasing the photocatalytic activity [22].

4. Structured photocatalysts for removal of contaminants under visible light

4.1 Visible light-active noble metal catalysts

Noble metals have been proven as suitable semiconductors for metallization. The effect of these catalysts improves photocatalytic performance. Among the most used semiconductors oxides such as TiO_2 and ZnO, which absorb UV light, have possibilities to perform under visible light when these semiconductors are metalized with noble metals (Ag, Au, Pt, Pd). It has been suggested that metal in an oxidized state has a tendency to respond under visible light by photo-exciting the surface of plasmons in the metal atoms and enhancing photocatalytic efficiency. Several synthesis methodologies have been adopted for the formation of metal decorated onto the surface of metal oxides like impregnation, deposition, precipitation, solvent extraction, chemical reduction, and photo deposition. The metallic particles on semiconductor metal oxide surface act as a trapping center for capturing of photogenerated electrons and holes during the photocatalysis process, thus leading to improve the catalytic activity. The photocatalytic activity depends on the type of oxide substrate. Fig. 2 shows a possible mechanism that takes place in a semiconductor coupled with a metal.

Metal ions having suitable redox potential can be reduced by electrons in the conduction band (Eq. 12). It has been observed that metal nanoparticles with potential of more than 0.4 eV on TiO_2 surface can only reduce.

$$M^{n+} + e^{-(CB)} \rightarrow M^{n-1} \tag{12}$$

Metal ions can further be oxidized by hole or hydroxyl radicals ($^{\cdot}OH$) in the valence band (Eq. 13).

$$M^{n+} + h^{+(VB)} / {}^{\cdot}OH \rightarrow M^{n+1} \tag{13}$$

The colored wastewater discharged from the manufacturing of textile and other industries, mainly dyes, is significantly growing, thus leading to environmental threats because it is very difficult to remove these contaminants. The most commonly dye used in the coloring process is azo dye molecules. The mechanism involved in degradation of dye

https://www.twirpx.org & http://chemistry-chemists.com

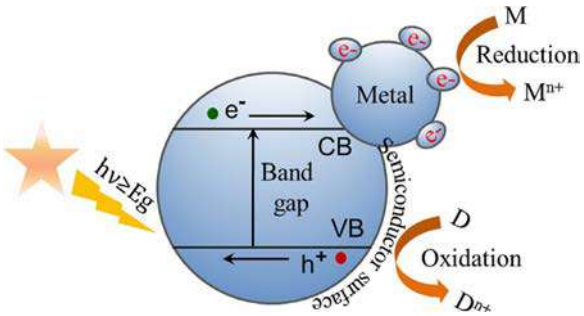

FIG. 2 Visible light-active noble metal catalysts. Photoreduction of metal on semiconductor surface.

molecules consist of different stages in which dye can be either oxidized by ·OH radicals or reduced by the electrons in the conduction band of semiconducting materials. After breaking the azo bond and opening the aromatic ring by oxidation reaction induced by ·OH radicals, dyes are then mineralized by production of CO_2 and H_2O and some small products which can not be further degraded after exposure to light. Sanzone et al. reported visible light-driven Ag-TiO_2 nano-engineered film for photocatalysis [23]. They revealed that coupling of Ag metal with TiO_2 may enhance photocatalytic activity under visible light due to intrinsic electronic transition in silver as well as localized surface plasmons resonance. Similar results were also observed by Wen et al. [24] using modified TiO_2 with Au, which increased the photocatalytic performance under visible light. Thus, noble metal nanoparticle deposited TiO_2 could be a suitable approach to increase photocatalytic performance.

4.2 Structured TiO_2 photocatalyst and its modifications under visible light

Titanium oxide (TiO_2) is a highly efficient material used in the photocatalysis process due to its wide bandgap and being a photocatalytically active, environmentally friendly, stable, and cost-effective material. The drawback of this material is related to low quantum efficiency; it is activated only under UV radiation ($\lambda \leq 387$ nm and its bandgap *Eg* of 3.2 eV). This shows that only 5% of the solar spectrum can be utilized for this purpose, while 43% of the solar spectrum corresponds to visible light. Thus, numerous efforts and strategies have been focused on TiO_2-based photocatalysts that extend absorption of light from UV to the visible region. So far, visible light activity has arisen by depressing the bandgap of photocatalytic materials by surface modification via doping, codoping, self-doping, defect engineering, or developing nanocomposite.

https://www.twirpx.org & http://chemistry-chemists.com

4.3 Cation-doped semiconductor photocatalyst

The energy bandgap can be shifted by adding a dopant to a semiconductor which creates a Fermi level below the conduction band (n-type) or above the valence band (p-type), thus minimum energy is needed to promote the electron from the VB to the CB. The doping of metal ions into TiO_2 favors the creation of imperfections in the crystal lattice, which affects the phase stability and electronic structure. As a result, the surface defects such as oxygen vacancies induced on the semiconductor surface traps the photo generate electrons to reduce charge carriers recombination. The doping of cations such as Ag, Au, Pt, Pd, and Bi ions in Ti^{4+} are about the same size. Various methodologies have been reported for synthesis of metal-incorporated TiO_2 materials. These approaches include electronic and morphological modifications that lead to absorption of light in the solar range and also a porous structure, which is responsible for adsorption of large amounts of pollutants. Thimsen's group reported that doping with Fe content decrease the bandgap energy of anatage TiO_2 [25]. Moreover, metal doping also creates phase transformation, which produces crystal defects and surface modifications and hence changes the activation energy of the reactions. For example, Lv et al. [13] reported the effect of alkaline earth metals doping on TiO_2 with honeycomb-like inverse opal structure that enhanced photocatalytic activity. As shown in Fig. 3, the concentration of rhodamine B (RhB) slightly decreased

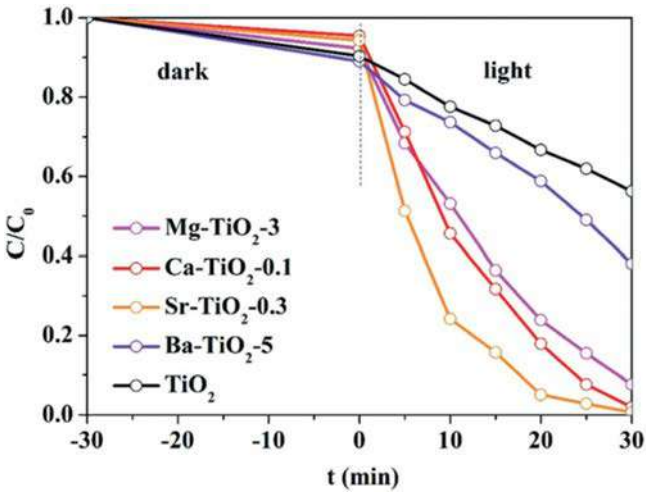

FIG. 3 Cation-doped semiconductor photocatalyst. Photodegradation of RhB in the presence of Mg-TiO_{2-3}, Ca-$TiO_{2-0.1}$, Sr-$TiO_{2-0.3}$, and Ba-TiO_{2-5} and TiO_2 under visible light. *From Alkaline-earth-metal-doped TiO_2 for enhanced photodegradation and H_2 evolution: insights into the mechanisms. Catal Sci Technol 2019;9:6124–6126. https://doi.org/10.1039/C9CY01687B.*

https://www.twirpx.org & http://chemistry-chemists.com

with the increased alkali metal doping concentration, showing the effect of alkali metals on RhB and the adsorption capability of catalysts. The special structural feature and unique morphology of alkali metal-doped TiO_2 extend the light absorption under visible light, increase carrier separation, and improve the absorption of organic pollutants. The superior photocatalytic activity could be attributed to the high surface area and porous structure, which provides more sites for adsorption and degradation of reactants.

The photocatalytic activity of a semiconductor depends on various factors such as dopant concentration, electronic configuration of dopants, distribution of dopants, and position of energy level of dopants. Thus, photocatalytic activity can be improved by intensely creating a defect state within the bandgap by doping of transition metal, or a nonmetal or intrinsic defect state related to shape, size, and morphology.

4.4 Anion-doped semiconductor photocatalysts

Some of the remarkable modifications such as doping of nonmetals such as C, N, S, and B and halides (F, Cl, Br, I) in TiO_2 relate to interesting photocatalysts that have been developed and considered as effective ways to extend the absorption of light from UV to the visible range [26]. The main aim of doping consists of substitution of the oxygen lattice of TiO_2 altering both the electronic and structural properties of TiO_2. This results in narrowing of the bandgap and creation of oxygen defect sites. Zou et al. studied N-doped TiO_2 with different surface morphology synthesized by a hydrothermal method [27]. The optical absorption edge red-shifted in the presence of N-doped TiO_2 and thereby improved the photocatalytic performance. Ramacharyulu et al. adopted a sol gel process followed by hydrothermal treatment to prepare N- and S-doped TiO_2 nanoparticles. They suggested that N and S atoms substituted to the oxygen lattice site narrowed the bandgap due to mixing of N2p and O2p states. The doping in TiO_2 creates oxygen vacancies at the surface which stimulates absorption of sunlight and promotes the electrons to the conduction band [28]. McManamon et al. [29] reported that TiO_2 having an excitation wavelength of 388 nm ($E_g = 3.2$ eV), after doping with sulfur atom, extended into the visible region at 410 nm ($E_g = 1.7$ eV), covering all the visible light spectrum shown in Fig. 4. Zha et al. [21] synthesized S-doped TiO_2 by a solvothermal method using DMSO as a source of sulfur and a solvent as shown in Fig. 5. The sulfur atom substituted into the lattice of TiO_2 exhibited superior and long-term stable photocatalytic performance for degradation of dyes under visible and indoor sunlight illumination compared to the commercial P25 TiO_2 due to the special "tail-like" feature and narrowing of the bandgap. The authors observed that the prepared catalyst is still highly photoactive even after exposure to indoor sunlight irradiation for several months.

Chen et al. [30] prepared B-doped TiO_2 using a sol gel method. The B atom is presented as B^{3+} and is able to occupy into the interstitial position of the TiO_2 structure. These nanoparticles have been investigated for photoregeneration of reduced nicotinamide adenine dinucleotide (NADH).

https://www.twirpx.org & http://chemistry-chemists.com

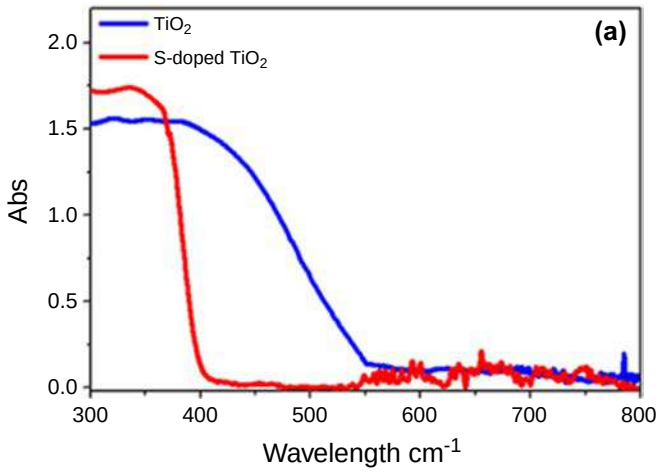

FIG. 4 UV-visible absorption spectra. UV-visible absorption spectra of TiO_2 and S-doped TiO_2 nanoparticles. *From McManamona C, O'Connella J, Delaneya P, Rasappa S, Holmes DJ, Morrisab AM. A facile route to synthesis of S-doped TiO_2 nanoparticles for photocatalytic activity. J Mol Catal A: Chem 2015;406:51–7. https://doi.org/10.1016/j.molcata.2015.05.002.*

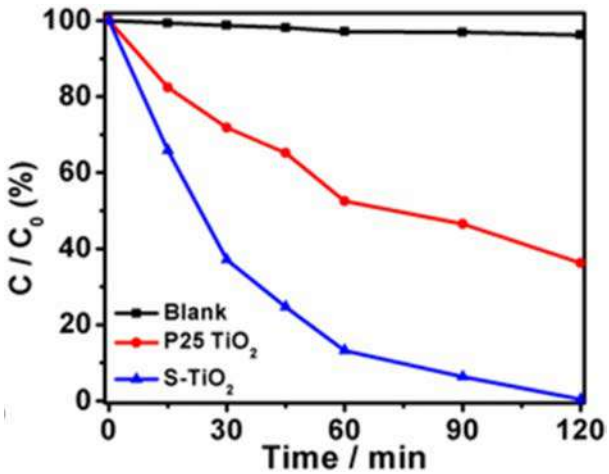

FIG. 5 Photocatalytic activities for the degradation of MB. Photocatalytic activities for degradation of MB pollutants without catalysts and with commercial P25 TiO_2 and S-TiO_2 catalysts under visible light ($\lambda \geq 400$ nm) irradiation. *From Zhu M, Zhai C, Qiu L, Lu C, Paton SA, Du Y, et al. A new method to synthesize S-doped TiO_2 with highly efficient and stable indoor sunlight photocatalytic performance. ACS Sustain Chem Eng 2015;3:3123. https://doi.org/10.1021/acssuschemeng.5b01137.*

4.5 Codoping semiconductor

The doping of two different kinds of suitable atoms such as Ag-Au, Ag-Cu, Au-Cu, or Ag-Pt in a semiconductor, known as codoping, has received considerable attention because of enhanced photocatalytic activity under the visible region compared to a single metal-doped

https://www.twirpx.org & http://chemistry-chemists.com

semiconductor. For example, Yang et al. [31] reported F-S-codoped TiO_2 for photocatalytic degradation of methylene blue under visible light. They proposed that codoping induces a localized state either below the conduction band or above the valence band of the semiconductor. Thus, codoping in metal oxides creates surface oxygen vacancies which are responsible for absorption of visible light and promote the electrons from the localized states to the conduction band. Valentin et al. [32] studied TiO_2 codoped with N-F enhanced photocatalytic activity in the visible region compared with nitrogen-doped TiO_2 only. They found that Ti^{3+} species are formed in association to substitution of F doping. As a result, no more oxygen vacancies are required to induce extra electrons available to fill the N2p states. The relevant consequence is that a small number of oxygen defects should be present in the bulk of N-F-codoped TiO_2 samples with respect to an N-doped counterpart. This may explain the enhancement of photocatalytic activity of N-F-codoped TiO_2. Li et al. [15] investigated helix structure of W-N-codoped TiO_2 for enhancement of photocatalytic activity under visible light. This result is attributed to large surface area, structural morphology, pore size, and high crystallinity. Jia et al. [33] mentioned that substitution of Fe in N-doped TiO_2 increased photocatalytic activity under visible light with respect to N-doped TiO_2. They found that codoping leads to lattice distortion, which changes the dipole moment and increases the separation of electron-holes pairs.

4.6 Self-doping/defect engineering

The self-doping of TiO_2 has proved an effective technique to extend light absorption under the visible region. The bandgap of TiO_2 can be tuned by using an electron beam, which creates a defect in semiconducting materials, and by nonstoichiometric formulation of TiO_2 (containing Ti^{3+}, different from the perfect TiO_2), which by self-doping could create oxygen vacancies. Self-doping can easily be modulated through a synthesis method, process control, and precursor. Jun et al. [34] reported radiation-induced effects in TiO_2 crystal structure. They showed that the photocatalytic activity of the electron beam-treated TiO_2 was tested for photodegradation of methylene blue. Theoretically, it was proven that interstitial Ti^{3+} can cause an impurities level below the CB and vacant Ti^{3+} creates impurity energy levels just above the VB [35, 36]. The concept of self-doping is that electrons can be trapped by oxygen vacancies, thereby reducing Ti^{4+} to Ti^{3+}, whereas hole oxidize superoxide ion (O_2^-) to produce superoxide radicals ($^{\bullet}O_2^-$) which trapped hole or O_2 gases.

5. ZnO and its modifications

Zinc oxide (ZnO) nanoparticles are an alternative to TiO_2. It is most attractive and extensively studied semiconductor materials because of easy crystallization and anisotropic growth process. ZnO possesses unique electrical and optical properties which are used in many optoelectronic devices. ZnO is an n-type semiconductor with a wide bandgap ($\lambda = 387$ nm corresponds to $Eg = 3.2$ eV) having a wurtzite structure [37]. ZnO exhibits

https://www.twirpx.org & http://chemistry-chemists.com

emission and absorption bands in the wavelength range of UV and visible regions, which make it suitable for photocatalysis. The deep level emission originates from a point defect present in ZnO such as oxygen vacancies (V_o), oxygen interstitial (O_i), zinc vacancies (V_{Zn}), and zinc interstitial (Zn_i). The native point defect could be created during crystal growth process [38]. The presence of a point defect in ZnO provides high electron mobility, which could be beneficial in transferring electrons from the valence band to the conduction band, thus it could provide considerable photocatalysis properties. Furthermore, ZnO has high redox potential which could drive various oxidation and reduction reactions in the photocatalysis process that can be utilized. Apart from that, ZnO nanoparticles can be prepared by a variety of methods with different morphologies [3, 18]. All these properties make it a suitable candidate for photocatalysis application.

However, although ZnO has several unique properties which make it suitable for the photocatalysis process, it also has some drawbacks. ZnO absorbs only UV light, which comprises a small portion of the solar spectrum, and the high recombination rate of ZnO prevents the path of electron-holes outward and thus reduces photocatalysis efficiency. The major drawback of ZnO is photo-corrosion when dipped in a solvent under solar light. Another disadvantage of ZnO is that it can dissolve in more acidic and basic solvents under irradiation of light. All these difficulties can be solved by doping of metals and nonmetals in ZnO which could minimize the charge carrier recombination rate, thus improving the photocatalysis performance. Furthermore, the photocatalysis efficiency of ZnO could also be improved by surface modification via combination with another semiconductor, metal deposition onto ZnO, or hybridization with another oxide to form new composite materials. All these processes can suppress the recombination rate and shift the absorption band from the UV region to the visible region.

The doping of some elements such as Mn, Mg, Cd, Co, and Ag could tune the bandgap of ZnO and increase the absorption of light under the visible range, thus improving photocatalytic activity. Etacheri et al. [39] synthesized Mg-doped ZnO nanoparticles via the coprecipitation method. They found that the doping of Mg in ZnO revealed a blue-shift near the band edge emission (NBE) and a decrease of PL intensities. As a result, the photocatalytic decomposition of MB was enhanced under sunlight compared with pure ZnO. The superior catalytic performance of Mg doped in ZnO is attributed to widening of the bandgap, greater textural properties, and efficient electron-hole pairs separation. Pradeev Raj et al. [40] observed that Mg^{2+} doping in ZnO creates defect density by occupying Zn^{2+} vacancies with Mg^{2+} ions and enhances photocatalytic activity. Furthermore, RuhUllah et al. [41] reported that doping of ZnO with Mg forms a tail state in the vicinity of the valence band and reduces the bandgap of ZnO. They observed a faster degradation rate of Mn-doped ZnO compared with undoped ZnO. This may be ascribed to an increase in the defect sites caused by doping with Mn^{2+}, which leads to enhanced light absorption in the visible region. However, some results show that transition metal (Co, Ni, Mn)-doped mesoporous self-aggregated ZnO decreases photocatalytic activity under UV light compared to undoped ZnO [42]. This may be attributed to fast electron-hole pairs recombination resulting in changes to the absorption characteristics due to Mn^{2+} doping.

https://www.twirpx.org & http://chemistry-chemists.com

Similar results were also found by Qiu et al. [43], where Co doping can act as a recombination center of electron-holes, hence significantly suppressing the photodegradation of RhB.

6. TiO_2- and ZnO-based heterostructure photocatalysts

The combination of two semiconductor oxides has the ability to increase photocatalytic activity. Considerable effort has been devoted to preparing semiconductor heterostructures in order to enhance photocatalytic efficiency and extend the visible light response. Three different types of semiconductor heterostructures are possible: straddling gap (type I), staggered gap (type II), and broken gap (type III), as shown in Fig. 6. In type II, the location of the valence band and conduction band of semiconductor 2 is higher than the location in semiconductor 1.

Another advantage of type II is that the difference between chemical potentials of semiconductor 1 and 2 causes band bending at the interface. This band bending at the interface causes a field to be built which produces photogenerated electrons and holes that move in opposite directions, leading to spatial separation of charge carriers on the side of the heterojunction. Thus, type II is an effective way to enhance charge separation and improve photocatalytic performance. The two essential conditions to prepare a visible light-driven type II heterostructure are the outer shell materials, which have a strong visible light response, and band alignment at the interface which satisfies the type II condition. The difference in the lattice spacing of two different types of semiconductor at the interface induces a lattice mismatch. This creates defects at the interface which traps the photogenerated carriers, preventing electron and hole recombination. Furthermore, UV

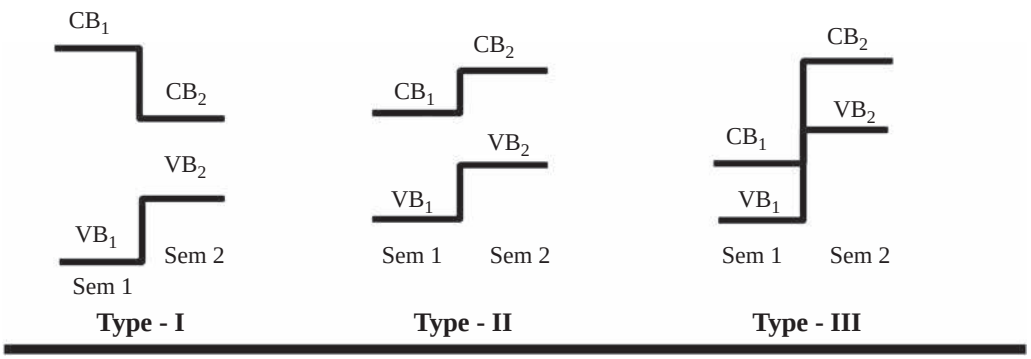

FIG. 6 Energy band diagram of three different types of semiconductor heterostructures. Energy band diagram of three types of semiconductor heterostructures. CB1 and VB1 represent the conduction band and valence band of semiconductor 1, and CB2 and VB2 represent the conduction band and valence band of semiconductor 2, respectively.

https://www.twirpx.org & http://chemistry-chemists.com

light-activated semiconductors like TiO_2 and ZnO are coupled with the visible light-activated semiconductors such as SnO_2, CdS, CdSe, ZnSe, CuO, ZnS, MoS_2, and WS_2 to form type II semiconductor heterostructures. For example, in the ZnO/SnO_2 type II heterostructure shown in Fig. 7, the photogenerated electrons present in the highest conduction band energy (CB of ZnO) of semiconductor 1 transfer into the minimum conduction band energy (CB of SnO_2) of semiconductor 2, while the photogenerated holes existing in the minimum valence band energy (VB of SnO_2) of semiconductor 2 migrate to the maximum valence band energy (VB of ZnO) of semiconductor 1.

A network structure of SnO_2/ZnO heterojunction nanocatalysts was synthesized by Lirong Zheng and his coworkers through a simple solvothermal method [44]. They reported that an SnO_2/ZnO heterojunction increases the separation of photogenerated electron-hole pairs due to the potential difference of two semiconductors and enhances photocatalytic activity. Moonsub Shim et al. [45] described how the lattice strain established the electric field, which enhanced the separating and directing of photogenerated carriers. Meng et al. [46] synthesized double-shelled TiO_2@CdS and CdS@TiO_2 hollow spheres using SiO_2 as a template. These have visible light response and exhibit the best photocatalytic performance for degradation of RhB compared with their counterpart. This is possibly due to coupling of TiO_2 with CdS, which induces an internal field at the interface of two semiconductors, which in turn causes the photogenerated electrons and holes to migrate in different field directions. The chemical potential of the conduction band of CdS is 0.5 eV higher than for TiO_2; therefore, valence band electrons of CdS are photoexcited into CB and subsequently transfer electrons into the CB of TiO_2 under visible light

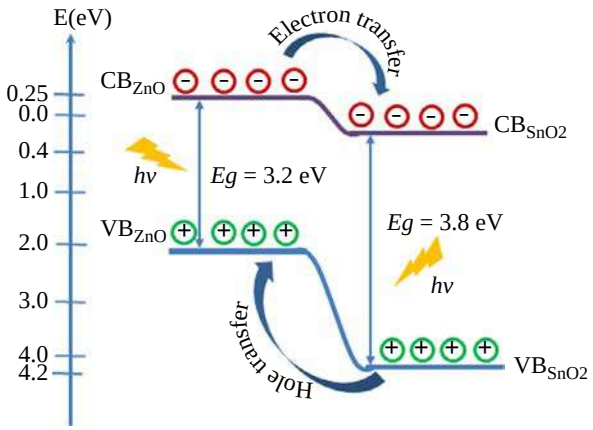

FIG. 7 Band energy diagram of type II heterostructure in ZnO/SnO_2 semiconductor Schematic band energy diagram of type II heterostructure in ZnO/SnO_2 semiconductor.

https://www.twirpx.org & http://chemistry-chemists.com

irradiation, which increases the charge separation. Furthermore, Yu and coworkers [47] prepared a CdSe/TiO_2 heterostructure by an ultrasound solution method. The photocatalytic activity of the CdSe/TiO_2 heterostructure shows higher degradation efficiency of 4-chlorophenol compared with pure TiO_2 due to quantum size effect, which plays an important role in increasing the charge separation and improving photocatalytic activity. Moreover, Wingkei Ho's group [48] studied the nanocluster of MOS_2 and WS_2 coupled with TiO_2 via an in-situ photoreduction deposition method. They evaluated their photocatalytic activity for degradation of methylene blue and 4-chlorophenol under visible light illumination. It was found that the quantum size effect altered the energy level of the valence band and conduction band edge in the semiconductor system which favored interparticle electron transfer. In addition, the coupled system increased the carrier charge separation and reduced the recombination rate.

Heterostructured hybrid layered ZnO and MoS_2 composites were prepared by Benavente and coworkers via varying MoS_2 amounts [49]. They showed that the photogenerated electrons transferred from hybrid layered ZnO to MoS_2 nanosheets, facilitating an interfacial electron transfer and suppressing the recombination of charge carriers during the photocatalytic process. Another kind of heterostructure based on type II is ZnO embedded in graphene. Junli Xu's group [50] prepared ZnO/graphene composites through a simple method and explored their efficiency for degradation of methyl orange and water splitting. Graphene plays an important role in absorbing light in the visible region and narrowing the bandgap of a heterostructure. The presence of graphene in semiconducting materials enhances the separation of photogenerated charge carriers, and suppresses the recombination process that enhances photocatalytic activity. Furthermore, our group [51] has also reported in-situ growth of ZnO nanoclusters deposited onto the reduced graphene oxide (RGO) surface through a simple soft chemical approach. It has been observed that the nanostructure of ZnO is changed by varying the concentration of RGO, thus RGO controls the morphology of ZnO. The ZnO-RGO nanohybrids are formed by the chemical interaction between RGO and ZnO, which gives rise to the difference in the work function of graphene (−4.42 eV), i.e., lower than that of the conduction band of ZnO (−4.05 eV). This drives an excess π electrons cloud from RGO to ZnO and creates a potential barrier at the interfaces, trapping photogenerated electrons. The succeeding increase of RGO in ZnO shifted the absorption band in the visible region (Fig. 8A). These nanohybrids were investigated for their catalytic activity for degradation of methylene blue (MB) under UV light, visible light, and without exposure to light (Fig. 8B). The highest concentration of RGO in ZnO-RGO nanohybrids (ZnO-RGO-100) shows excellent degradation behavior even without exposure to light, compared to their individual counterparts. The MB solution decolorized (10 ppm) suddenly (i.e., in a few seconds) by addition of these nanohybrids. This might be because of combined effects of unique structural properties of ZnO, higher electrical conductivity of RGO, and strong interfacial interaction.

https://www.twirpx.org & http://chemistry-chemists.com

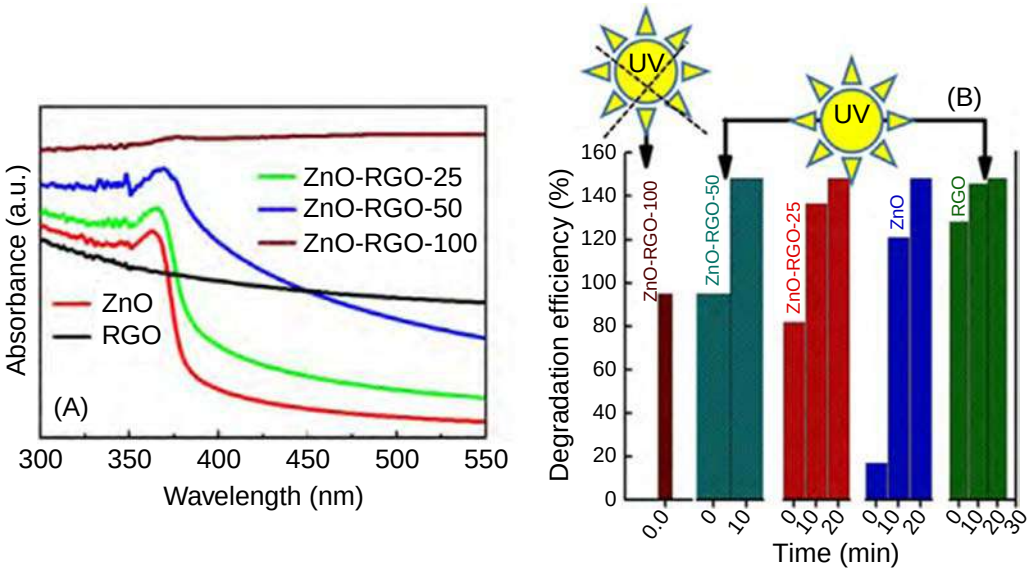

FIG. 8 Heterostructure ZnO-RGO nanohybrid. UV-visible absorption spectra of ZnO-RGO nanohybrids with different concentrations of RGO. (B) Photocatalytic efficiencies of MB in the presence of ZnO-RGO nanohybrids, ZnO and RGO under dark and UV light. *From Prakash A, Singh S, Gupta J, Bahadur D. Highly efficient zinc oxide-reduced graphene oxide nanohybrids for photocatalytic degradation of dye under dark and UV light. Mater Res Exp 2020;6:1250b1. https://doi.org/10.1088/2053-1591/ab6256.*

7. Non-TiO_2- and ZnO-based new visible light-active catalysts

To develop the visible light-active photocatalyst, two methods have been implemented. The first method is modification technologies to extend absorption of light in the visible region, for example, TiO_2 and ZnO doped with metals and nonmetals. Another approach is directed toward the development of new semiconducting materials capable of absorbing visible light. Some visible light-active semiconductor photocatalysts have been developed such as WO_3, Ag_3PO_4, $BiVO_4$, SnO_2, g-C_3N_4, V_2O_5, Sb_2O_3, V_2O_3, Cu_2O, and perovskite, which possesses suitable energy band configurations.

7.1 Ag_3PO_4 photocatalysts

Ag_3PO_4 is an emerging material for researchers because of its high oxidation and excess of oxygen evolution under visible light. In 2010, Yi et al. [52] reported a visible light-driven Ag_3PO_4 photocatalyst for oxidation of water and photodegradation of organic compounds. High quantum efficiency is achieved for Ag_3PO_4 under visible light irradiation. The quantum efficiency of this new catalyst was observed to be around 90%, which is superior to that of other reported catalysts such as $BiVO_4$ and N-doped TiO_2. The different morphology of Ag_3PO_4, such as tetrapod, porous structure, hierarchical structure of

https://www.twirpx.org & http://chemistry-chemists.com

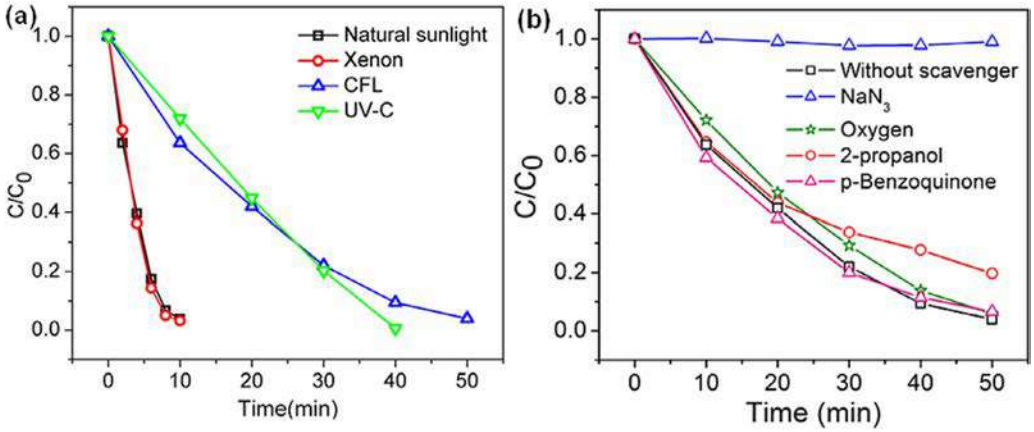

FIG. 9 Ag_3PO_4-based photocatalysts. (A) Photodegradation of methylene blue in the presence of Ag_3PO_4 under different light sources. (B) Determination of ROS using Ag_3PO_4 along with various types of quenchers/acceptors in the photocatalytic process for degradation of methylene blue dye under a CFL lamp. *From Thiyagaraja S, Singh S, Bahaddur D. Reusable sunlight activated photocatalyst Ag_3PO_4 and its significant antibacterial activity. Mater Chem Phys 2016;173:390. https://doi.org/10.1016/j.matchemphys.2016.02.027.*

microcubes, and nanorod, has been reported [53–55]. Very recently, Shankar et al. [56] prepared roughly spherical Ag_3PO_4 nanoparticles by a surfactant free soft chemical approach. They showed that these nanoparticles have the ability to absorb a broad range of the solar spectrum. Therefore, Ag_3PO_4 is highly efficient for photodegradation of different dyes like MB, RhB, and methyl orange under sunlight compared to UV-C light and visible light, as represented in Fig. 9A. The higher degradation efficiency of Ag_3PO_4 is due to the production of ROS, specially singlet oxygen radicals. The detection of ROS is confirmed from electron spin resonance (ESR) spin trapping techniques and using different types of quenchers and acceptors, as shown in Fig. 9B. Furthermore, the role of charge carriers in the photocatalysis process is determined using electron scavenger like $K_2S_2O_8$ that trap the photogenerated electrons, and holes are refrained from recombination leaving them free, thus, holes playing the main role in degradation. Dong et al. [57] prepared various morphologies (branch, tetrapod, nanorod, triangular prism) of Ag_3PO_4 by a facile soft chemical method and observed a morphological effect on photocatalytic activity. They found that branch-shaped Ag_3PO_4 with a porous structure exhibited the highest photocatalytic activity among the other crystals of Ag_3PO_4.

To understand the mechanism of highly photo-oxidative activity of Ag_3PO_4 under visible light, theoretical analysis is concentrated mainly on the energy band diagram. When the energy of an incident photon is higher than that of the bandgap of materials, this produces photo-excited charge carriers. Furthermore, the photogenerated electron can be

https://www.twirpx.org & http://chemistry-chemists.com

transferred to oxygen molecules only when there is a suitable large negative offset of the conduction band minimum. The photogenerated hole combines with the water molecules when the large positive offset of the valence band is at the maximum.

7.2 $BiVO_4$ photocatalyst

Bismuth vanadate ($BiVO_4$) is one of the most efficient semiconducting materials having a visible light response due to a narrow bandgap, low toxicity, high photostability, and resistance to photo-corrosion with good response to visible light. $BiVO_4$ exists in three different crystal structure forms: tetragonal zircon phase (t-z), monoclinic scheelite phase (m-s), and tetragonal scheelite phase (t-s). Among these structures, the monoclinic scheelite phase (m-s) exhibits high catalytic activity in the presence of visible light illumination because Bi6s orbital in $BiVO_4$ semiconductor exhibits lone pair distortion. Thus, the interaction of Bi6s and O2p orbitals in the valence band is beneficial for the mobility of charge carrier to improve photocatalytic performance. $BiVO_4$ is considered an n-type semiconductor with high chemical stability and photo-stability. It has variable optical and electrical properties with a direct bandgap of 2.4 eV. In general, it is believed that a larger surface area and porous structure increase photocatalytic activity. Therefore, various shapes of nanostructures such as micro-tubes, nano-fibers, micro-ribbons, dendritic, hollow spheres, and flower-like microspheres have been fabricated to increase the surface area and pore size. Wang et al. [58] prepared different shapes of $BiVO_4$ hierarchical structures like olives, spherical, cuboids, and dendritic by varying the pH of the medium via a hydrothermal process, and investigated their photocatalytic activity for degradation of methylene blue (MB). Among these, olive-like $BiVO_4$ showed higher catalytic activity under visible light due to its large surface area. In addition, the dendritic morphology of $BiVO_4$ was synthesized by Perez et al. [59] by a hydrothermal method using polyethylene oxide/polyethylene oxide/polypropylene oxide triblock copolymer as surfactants; the authors evaluated their photocatalytic activity for RhB under visible light. These group have compared the photocatalytic activity of as prepared dendrite $BiVO_4$ obtained through hydrothermal method with $BiVO_4$ obtained from solid state reaction process.

7.3 WO_3 photocatalyst

WO_3 is one of the metal oxides used in photocatalysis. It has several advantages including large specific surface area and high absorption capacity, and is used as invisible materials. The bandgap of WO_3 is 2.8 eV and it is stable. The crystal structure of WO_3 exists in different phases: monoclinic, triclinic, orthorhombic, tetragonal, and cubic. Among these, monoclinic consistently shows the best photocatalytic activity. WO_3 is an n-type semiconductor with an electronic bandgap corresponding to the difference between the energy level of the valence band from O2p and the conduction band filled by the empty W5d orbital. The conduction band edge of WO_3 is located slightly more positively than the

https://www.twirpx.org & http://chemistry-chemists.com

reduction potential of H_2/H_2O, which makes WO_3 more efficient for oxidizing a wide variety of organic pollutants under the visible region. The synthesis of nanosized WO_3 particles and controlled morphology are important for improving photocatalytic activity. Furthermore, Farhadian et al. [60] prepared different morphologies such as nanorod, nanosphere, and nanosheet nanostructure of WO_3 by a hydrothermal method and showed how photocatalytic activity for degradation of RhB was influenced by changing the different morphologies of WO_3. They reported that nanoplates have higher degradation efficiency than other forms. This is because of their low coordination number; atoms located in the edges and corners of WO_3 nanoplates have the ability to adsorb more RhB and thus increase the photocatalytic activity of WO_3 nanoplates. Dongqin Bi et al. [61] studied the photocatalytic process of WO_3 for organic degradation in the presence of H_2O_2 via clustered Fe_2O_3. Xiaolei Liu et al. [62] reported synthesis of WO_3 doped with Fe^{3+} and Pt for ethylene degradation under visible light irradiation. They showed that Fe doping enhanced the visible light response and stability of the photocatalyst. The loading of Pt acting as a cocatalyst promoted the transfer of photogenerated electrons and reduced the photo-corrosion of WO_3. Zhao and Miyauchi et al. [63] also reported Pt loaded porous WO_3 nanotubes for photocatalytic activity under visible light.

8. Summary

Visible light-active photocatalysts are highly desirable materials that can enable the degradation of a wide range of organic pollutants. The designing and development of such materials have seen several key advances over the last decade that have served to limit degradation efficiency and stability. This chapter pointed out how the scientific community designed and modified semiconducting materials having UV absorption extended into the visible region. A variety of strategies, such as doping, codoping, self-doping/defect engineering, coupling with metal nanoparticles, and heterostructures, were explored to enhance photocatalytic activities. This chapter enumerated various visible light-active catalysts for degradation of various organic pollutants. This chapter also discussed how different parameters such as catalyst loading, surface area and morphology, pH, temperature, contaminant concentration, and calcination temperature influence the catalytic activity of the catalyst. In addition to modified TiO_2- and ZnO-based photocatalysts, another WO_3, Ag_3PO_4, and $BiVO_4$ visible light photocatalysts were also reported.

References

[1] Esther F, Tibor C, Gyula O. Removal of synthetic dyes from wastewaters: a review. Environ Int 2004;953–71. https://doi.org/10.1016/j.envint.2004.02.001.

[2] Pradeep K, Prasad B, Mishra IM, Shri C. Decolorization and COD reduction of dyeing wastewater from a cotton textile mill using thermolysis and coagulation. J Hazard Mater 2008;635–45. https://doi.org/10.1016/j.jhazmat.2007.09.007.

[3] Singh S, Barick KC, Bahadur D. Shape-controlled hierarchical ZnO architectures: photocatalytic and antibacterial activities. CrstEngComm 2013;15:4631–9. https://doi.org/10.1039/c3ce27084j.

https://www.twirpx.org & http://chemistry-chemists.com

[4] Singh S, Zubenko D, Rosen BA. Influence of $LaNiO_3$ shape on its solid-phase crystallization into coke-free reforming catalysts. ACS Catal 2016;6:4199–205. https://doi.org/10.1021/acscatal.6b00673.

[5] Dinh CT, Nguyen TD, Kleitz F, Do TO. Shape-controlled synthesis of highly crystalline titania nanocrystals. ACS Nano 2009;3:3737–43. https://doi.org/10.1021/nn900940p.

[6] Hu S. Tuning optical properties and photocatalytic activities of carbon-based\quantum dots/through their surface groups. Chem Rec 2016;16:219–30. https://doi.org/10.1111/tcr.201500225.

[7] Chen S, Zou Y, Yan Z, Shen W, Shi S, Zhang X, et al. Carboxymethylated-bacterial cellulose for copper and lead ion removal. J Hazard Mater 2009;161:1355–9. https://doi.org/10.1016/j.jhazmat.2008.04.098.

[8] Maliyekkal SM, Lisha KP, Pradeep T. A novel cellulose-manganese oxide hybrid material by in situ soft chemical synthesis and its application for the removal of Pb (II) from water. J Hazard Mater 2008;2010181:986–95.

[9] Song J, Oh H, Kong H, Jang J. Polyrhodanine modified anodic aluminum oxide membrane for heavy metal ions removal. J Hazard Mater 2011;187:311–7. https://doi.org/10.1016/j.jhazmat.2011.01.026.

[10] Hoffmann MR, Martin ST, Choi W, Bahnemann DW. Environmental applications of semiconductor photocatalysis. Chem Rev 1995;95:69–96. https://doi.org/10.1021/cr00033a004.

[11] He W, Kim HK, Wamer WG, Melka D, Callahan JH, Yin JJ. Photogenerated charge carriers and reactive oxygen species in ZnO/Au hybrid nanostructures with enhanced photocatalytic and antibacterial activity. J Am Chem Soc 2014;136:750–7. https://doi.org/10.1021/ja410800y.

[12] Sarika S, Barick KC, Bahadur D. Novel and efficient three dimensional mesoporous ZnO nanoassemblies for envirnomental remediation. Int J Nanomed 2011;10:1001–5.

[13] Lv C, Lan X, Wang L, Yu Q, Zhang M, Sun H, et al. Alkaline-earth-metal-doped TiO_2 for enhanced photodegradation and H_2 evolution: insights into the mechanisms. Cat Sci Technol 2019;9:6124–35. https://doi.org/10.1039/c9cy01687b.

[14] Dong L, Wang P, Wang S, Lei P, Wang Y. A simple way for Ag_3PO_4 tetrahedron and tetrapod microcrystals with high visible-light-responsive activity. Mater Lett 2014;134:158–61. https://doi.org/10.1016/j.matlet.2014.07.094.

[15] Li J, Xu J, Dai WL, Li H, Fan K. One-pot synthesis of twist-like helix tungsten-nitrogen-codoped titania photocatalysts with highly improved visible light activity in the abatement of phenol. Appl Catal Environ 2008;82:233–43. https://doi.org/10.1016/j.apcatb.2008.01.022.

[16] Qamar M, Saquib M, Muneer M. Photocatalytic degradation of two selected dye derivatives, chromotrope 2B and amido black 10B, in aqueous suspensions of titanium dioxide. Dyes Pigments 2005;65:1–9. https://doi.org/10.1016/j.dyepig.2004.06.006.

[17] Abbasi S, Hasanpour M. The effect of pH on the photocatalytic degradation of methyl orange using decorated ZnO nanoparticles with SnO_2 nanoparticles. J Mater Sci Mater Electron 2017;28:1307–14. https://doi.org/10.1007/s10854-016-5660-5.

[18] Byrappa K, Subramani AK, Ananda S, Lokanatha Rai KM, Dinesh R, Yoshimura M. Photocatalytic degradation of rhodamine B dye using hydrothermally synthesized ZnO. Bull Mater Sci 2006;29:433–8. https://doi.org/10.1007/BF02914073.

[19] Mills A, Le Hunte S. An overview of semiconductor photocatalysis. J Photochem Photobiol A Chem 1997;108:1–35. https://doi.org/10.1016/S1010-6030(97)00118-4.

[20] An T, Liu J, Li G, Zhang S, Zhao H, Zeng X, et al. Structural and photocatalytic degradation characteristics of hydrothermally treated mesoporous TiO_2. Appl Catal Gen 2008;350:237–43. https://doi.org/10.1016/j.apcata.2008.08.022.

[21] Zhu M, Zhai C, Qiu L, Lu C, Paton AS, Du Y, et al. New method to synthesize S-doped TiO_2 with stable and highly efficient photocatalytic performance under indoor sunlight irradiation. ACS Sustain Chem Eng 2015;3:3123–9. https://doi.org/10.1021/acssuschemeng.5b01137.

https://www.twirpx.org & http://chemistry-chemists.com

[22] Bunsho O, Yoshimasa O, Sei-ichi N. Photocatalytic activity of amorphous–anatase mixture of titanium(IV) oxide particles suspended in aqueous solutions. J Phys Chem B 1997;3746–52. https://doi.org/10.1021/jp962702+.

[23] Sanzone G, Zimbone M, Cacciato G, Ruffino F, Carles R, Privitera V, et al. Ag/TiO_2 nanocomposite for visible light-driven photocatalysis. Superlattice Microst 2018;123:394–402. https://doi.org/10.1016/j.spmi.2018.09.028.

[24] Wen Y, Liu B, Zeng W, Wang Y. Plasmonic photocatalysis properties of Au nanoparticles precipitated anatase/rutile mixed TiO_2 nanotubes. Nanoscale 2013;5:9739–46. https://doi.org/10.1039/c3nr03024e.

[25] Thimsen E, Biswas S, Lo CS, Biswas P. Predicting the band structure of mixed transition metal oxides: theory and experiment. J Phys Chem C 2009;113:2014–21. https://doi.org/10.1021/jp807579h.

[26] Xu P, Xu T, Lu J, Gao S, Hosmane NS, Huang B, et al. Visible-light-driven photocatalytic S- and C-codoped meso/nanoporous TiO_2. Energ Environ Sci 2010;3:1128–34. https://doi.org/10.1039/c001940m.

[27] Li G, Zou B, Feng S, Shi H, Liao K, Wang Y, et al. Synthesis of N-doped TiO_2 with good photocatalytic property. Phys B Condens Matter 2020;588. https://doi.org/10.1016/j.physb.2020.412184.

[28] Ramacharyulu PVRK, Nimbalkar DB, Kumar JP, Prasad GK, Ke SC. N-doped, S-doped TiO_2 nanocatalysts: synthesis, characterization and photocatalytic activity in the presence of sunlight. RSC Adv 2015;5:37096–101. https://doi.org/10.1039/c4ra08858a.

[29] McManamon C, O'Connell J, Delaney P, Rasappa S, Holmes JD, Morris MA. A facile route to synthesis of S-doped TiO_2 nanoparticles for photocatalytic activity. J Mol Catal A Chem 2015;406:51–7. https://doi.org/10.1016/j.molcata.2015.05.002.

[30] Chen D, Yang D, Wang Q, Jiang Z. Effects of boron doping on photocatalytic activity and microstructure of titanium dioxide nanoparticles. Ind Eng Chem Res 2006;45:4110–6. https://doi.org/10.1021/ie0600902.

[31] Yang G, Jiang Z, Shi H, Jones MO, Xiao T, Edwards PP, et al. Study on the photocatalysis of F-S co-doped TiO_2 prepared using solvothermal method. Appl Catal Environ 2010;96:458–65. https://doi.org/10.1016/j.apcatb.2010.03.004.

[32] Di Valentin C, Finazzi E, Pacchioni G, Selloni A, Livraghi S, Czoska AM, et al. Density functional theory and electron paramagnetic resonance study on the effect of N-F codoping of TiO_2. Chem Mater 2008;20:3706–14. https://doi.org/10.1021/cm703636s.

[33] Jia L, Wu C, Han S, Yao N, Li Y, Li Z, et al. Theoretical study on the electronic and optical properties of (N, Fe)-codoped anatase TiO_2 photocatalyst. J Alloys Compd 2011;509:6067–71. https://doi.org/10.1016/j.jallcom.2011.03.012.

[34] Jun J, Dhayal M, Shin JH, Kim JC, Getoff N. Surface properties and photoactivity of TiO_2 treated with electron beam. Radiat Phys Chem 2006;75:583–9. https://doi.org/10.1016/j.radphyschem.2005.10.015.

[35] Xing M, Fang W, Nasir M, Ma Y, Zhang J, Anpo M. Self-doped Ti3+-enhanced TiO_2 nanoparticles with a high-performance photocatalysis. J Catal 2013;297:236–43. https://doi.org/10.1016/j.jcat.2012.10.014.

[36] Wen P, Zhang Y, Xu G, Ma D, Qiu P, Zhao X. Ti3+ self-doped TiO_2 as a photocatalyst for cyclohexane oxidation under visible light irradiation. J Materiomics 2019;5:696–701. https://doi.org/10.1016/j.jmat.2019.04.009.

[37] Guo L, Yang S, Yang C, Yu P, Wang J, Ge W, et al. Highly monodisperse polymer-capped ZnO nanoparticles: preparation and optical properties. Appl Phys Lett 2000;76:2901–3. https://doi.org/10.1063/1.126511.

[38] Singh S, Barick KC, Bahadur D. Fe_3O_4 embedded ZnO nanocomposites for the removal of toxic metal ions, organic dyes and bacterial pathogens. J Mater Chem A 2013;1:3325–33. https://doi.org/10.1039/c2ta01045c.

https://www.twirpx.org & http://chemistry-chemists.com

[39] Etacheri V, Roshan R, Kumar V. Mg-doped ZnO nanoparticles for efficient sunlight-driven photocatalysis. ACS Appl Mater Interfaces 2012;4:2717–25. https://doi.org/10.1021/am300359h.

[40] Pradeev Raj K, Sadaiyandi K, Kennedy A, Suresh S, Zaman CZ, BJR M, et al. Influence of Mg doping on ZnO nanoparticles for enhanced photocatalytic evaluation and antibacterial analysis. Nanoscale Res Lett 2018. https://doi.org/10.1186/s11671-018-2643-x.

[41] Ullah R, Dutta J. Photocatalytic degradation of organic dyes with manganese-doped ZnO nanoparticles. J Hazard Mater 2008;156:194–200. https://doi.org/10.1016/j.jhazmat.2007.12.033.

[42] Barick KC, Singh S, Aslam M, Bahadur D. Porosity and photocatalytic studies of transition metal doped ZnO nanoclusters. Microporous Mesoporous Mater 2010;134:195–202. https://doi.org/10.1016/j.micromeso.2010.05.026.

[43] Qiu X, Li G, Sun X, Li L, Fu X. Doping effects of Co^{2+} ions on ZnO nanorods and their photocatalytic properties. Nanotechnology 2008;19.

[44] Zheng L, Zheng Y, Chen C, Zhan Y, Lin X, Zheng Q, et al. Network structured SnO_2/ZnO heterojunction nanocatalyst with high photocatalytic activity. Inorg Chem 2009;48:1819–25. https://doi.org/10.1021/ic802293p.

[45] Shim M, McDaniel H, Oh N. Prospects for strained type-II nanorod heterostructures. J Phys Chem Lett 2011;2:2722–7. https://doi.org/10.1021/jz201111y.

[46] Meng HL, Cui C, Shen HL, Liang DY, Xue YZ, Li PG, et al. Synthesis and photocatalytic activity of TiO_2@CdS and CdS@TiO_2 double-shelled hollow spheres. J Alloys Compd 2012;527:30–5. https://doi.org/10.1016/j.jallcom.2012.02.043.

[47] Yu JC, Wu L, Lin J, Li P, Li Q. Microemulsion-mediated solvothermal synthesis of nanosized CdS-sensitized TiO_2 crystalline photocatalyst. Chem Commun 2003;3:1552–3. https://doi.org/10.1039/b302418k.

[48] Ho W, Yu JC, Lin J, Yu J, Li P. Preparation and photocatalytic behavior of MoS_2 and WS_2 nanocluster sensitized TiO_2. Langmuir 2004;20:5865–9. https://doi.org/10.1021/la049838g.

[49] Benavente E, Durán F, Sotomayor-Torres C, González G. Heterostructured layered hybrid ZnO/MoS_2 nanosheets with enhanced visible light photocatalytic activity. J Phys Chem Solid 2018;113:119–24. https://doi.org/10.1016/j.jpcs.2017.10.027.

[50] Junli X, Ya C, Yide H, Men H, Xia Z. ZnO–graphene composites with high photocatalytic activities under visible light. RSC Adv 2016;96778–84. https://doi.org/10.1039/C6RA19622E.

[51] Prakash A, Singh S, Gupta J, Bahadur D. Highly efficient zinc oxide-reduced graphene oxide nanohybrids for photocatalytic degradation of dye under dark and UV light. Mater Res Express 2020;6.

[52] Liu Y, Withers RL, Kikugawa N, Kako T, Ouyang S, Stuart-Williams H, et al. An orthophosphate semiconductor with photooxidation properties under visible-light irradiation. Nat Mater 2010;9:559–64. https://doi.org/10.1038/nmat2780.

[53] Liu JK, Luo CX, Wang JD, Yang XH, Zhong XH. Controlled synthesis of silver phosphate crystals with high photocatalytic activity and bacteriostatic activity. CrstEngComm 2012;14:8714–21. https://doi.org/10.1039/c2ce25604e.

[54] Wang H, He L, Wang L, Hu P, Guo L, Han X, et al. Facile synthesis of Ag_3PO_4 tetrapod microcrystals with an increased percentage of exposed {110} facets and highly efficient photocatalytic properties. CrstEngComm 2012;14:8342–4. https://doi.org/10.1039/c2ce26366a.

[55] Wang J, Teng F, Chen M, Xu J, Song Y, Zhou X. Facile synthesis of novel Ag_3PO_4 tetrapods and the {110} facets-dominated photocatalytic activity. CrstEngComm 2013;15:39–42. https://doi.org/10.1039/c2ce26060c.

[56] Thiyagarajan S, Singh S, Bahadur D. Reusable sunlight activated photocatalyst Ag_3PO_4 and its significant antibacterial activity. Mater Chem Phys 2016;173:385–94. https://doi.org/10.1016/j.matchemphys.2016.02.027.

https://www.twirpx.org & http://chemistry-chemists.com

[57] Dong P, Wang Y, Li H, Li H, Ma X, Han L. Shape-controllable synthesis and morphology-dependent photocatalytic properties of Ag_3PO_4 crystals. J Mater Chem A 2013;1:4651–6. https://doi.org/10.1039/c3ta00130j.

[58] Wang B, Guo L, He T. Fabrication of an olive-like $BiVO_4$ hierarchical architecture with enhanced visible-light photocatalytic activity. RSC Adv 2016;6:30115–24. https://doi.org/10.1039/c5ra21687g.

[59] García-Pérez UM, Martínez-De La Cruz A, Sepúlveda-Guzmán S, Peral J. Low-temperature synthesis of $BiVO_4$ powders by Pluronic-assisted hydrothermal method: effect of the surfactant and temperature on the morphology and structural control. Ceram Int 2014;40:4631–8. https://doi.org/10.1016/j.ceramint.2013.09.002.

[60] Farhadian M, Sangpout P, Hosseinzadeh G. Morphology dependent photocatalytic activity of WO_3 nanostructures. J Energy Chem 2015;24:171–7. https://doi.org/10.1016/S2095-4956(15)60297-2.

[61] Bi D, Xu Y. Improved photocatalytic activity of WO_3 through clustered Fe_2O_3 for organic degradation in the presence of H_2O_2. Langmuir 2011;27:9359–66. https://doi.org/10.1021/la2012793.

[62] Liu X, Zhai H, Wang P, Zhang Q, Wang Z, Liu Y, et al. Synthesis of a WO_3 photocatalyst with high photocatalytic activity and stability using synergetic internal Fe^{3+} doping and superficial Pt loading for ethylene degradation under visible-light irradiation. Cat Sci Technol 2019;9:652–8. https://doi.org/10.1039/c8cy02375a.

[63] Zhao ZG, Miyauchi M. A novel visible-light-driven photochromic material with high-reversibility: tungsten oxide-based organic-inorganic hybrid microflowers. Chem Commun 2009;2204–6. https://doi.org/10.1039/b823346b.

https://www.twirpx.org & http://chemistry-chemists.com

3 Synthesis methods of nanomaterials for visible light photocatalysis

Sutripto Majumder[a,b]

[a]DEPARTMENT OF MATERIALS SCIENCE AND ENGINEERING, CHUNGNAM NATIONAL UNIVERSITY, DAEJEON, REPUBLIC OF KOREA [b]DEPARTMENT OF PHYSICS, YEUNGNAM UNIVERSITY, GYEONGSAN, REPUBLIC OF KOREA

1 Introduction

Pollution is the contamination of naturally occurring chemical, physical, geochemical, and biological matter in our atmosphere which affects the usual environmental processes. In other words, when the environment cannot able to compete the damage created through the excess usage of natural resources is the consequence of human activities termed as environmental pollution. Therefore, with the development of human society, environmental pollution is becoming a curse to us. Depending upon the nature of the pollutants, environmental pollution can occur as air, water, soil, noise, radioactive, and thermal pollution. Water is an essential requirement for all life forms on earth. About 72% of the earth's crust, which is roughly 1.332 billion cubic km, is filled with water. About 97% of this is salty oceanic water; therefore, attaining a decent quality of water is a huge challenge for developing countries [1]. The usage of contaminated water affects about 1.2 billion people through waterborne diseases which directly increase the deaths of infants [2]. Discharging different organic wastes from various industries such as textile, leather, and paint generates serious problems for human health, aquatic life, and microbial growth in water bodies [3–5]. The effects of these pollutants result in toxicity, color, odor, chemical oxygen demand, and biological oxygen demand [6, 7]. Conventional physical methods such as adsorption, reverse osmosis, coagulation, and filtration are used to transform the above-stated pollutants by transforming them from one phase to another [8]. Nowadays different advanced oxidation processes (AOPs) result in the formation of hydroxyl species which removes the organic pollutants by oxidation [9, 10]. The most effective among all these AOPs is photocatalysis; this is a relatively popular method to remove pollutants since it does not leave any harmful intermediates. In photocatalysis, when light strikes the catalyst the electrons present at the valence band (VB) absorb energy which is equal to its bandgap energy gets excited. These excited electrons move toward the conduction band (CB), leaving holes at the VB. As a result, electron-hole pairs are created in the photocatalytic system. Now, these photogenerated electron-hole pairs react with oxygen molecules which further produce highly reactive oxygen species such as hydroxyl or

Nanostructured Materials for Visible Light Photocatalysis. https://doi.org/10.1016/B978-0-12-823018-3.00008-7
Copyright © 2022 Elsevier Inc. All rights reserved.

https://www.twirpx.org & http://chemistry-chemists.com

superoxide anion radicals. In the end, these newly formed oxygen species will decompose the organic pollutants via oxidation [11–13]. To date, many metal oxide materials with different nanostructures have been used as photocatalysts for the removal of organic pollutants from wastewater. Wide bandgap materials such as TiO_2, ZnO, and SnO_2 are commonly used materials for photocatalysts. However, all of these materials are restricted to use only of the UV portion of the complete solar spectrum to achieve photoactivation. This chapter deals with different synthesis methods for the preparation of powdered nanostructured materials for visible light photocatalysis.

2 Synthesis methods

The synthesis methods have been divided into two parts. Firstly we will understand how to synthesize nanopowders for the visible light photocatalyst? Secondly we will try to explore the different methods for the preparation of the nanostructured thin films for visible light photocatalysis.

2.1 Synthesis of Nanopowders

The following sections set out the methods which are commonly used for the preparation of nanopowders that are applied for visible light photocatalysts.

2.1.1 Precipitation method

The precipitation method was introduced by Marcilly in 1984 [14]. He has pointed out two elementary processes: (a) nucleation and (b) agglomeration of the particles within the mother solution. Fundamentally, when the concentration of the compound within the solution exceeds its solubility limit, precipitation occurs. The process of nucleation starts with Ostwald ripening (i.e., the larger particles tends to grow once on account of fewer) which results in the formation of clusters of the species, which increases the critical size of the particles, consequently precipitate starts aging [15]. The smaller clusters begin to dissolve again while the bigger clusters keep expanding. The aging process (i.e., the time for which the precipitate is left in the mother solution) leads to aggregation of the colloidal particles due to Brownian movement or mechanical forces imposed over the particles in the solution. In short, precipitation involves the formation of the separated phase of the solid from the homogeneous solution. This phase separation occurs soon after the solution reaches its supersaturated level. Therefore, high supersaturation phenomena in the precipitation process are significant. The preparation of powder photocatalyst through the precipitation method is presented in Fig. 1.

The features that affect the morphology of precipitate are as follows: (i) concentration of initial precursor solutions; (ii) change in pH of the solution; (iii) nature of solvent; and (iv) change in the temperature of the solution. A precipitation technique is used to prepare oxides of aluminum, iron, silicon, and titanium [16]. This procedure used to fabricate pure and homogeneous photocatalysts is the only advantage whereas (a) the separation of the

https://www.twirpx.org & http://chemistry-chemists.com

FIG. 1 Precipitation method. Flowchart of the precipitation process.

solid phase and (b) the difficulty of tracing out of extra volumes of salt-containing solutions which were formed during the process are the chief disadvantages of this process.

Synthesis of brown $MnWO_4$ nanoparticles was carried out with different capping agents such as valine, glycine, and asparagine added into the equimolar mixed solution of sodium tungstate and manganese nitrate [17]. The final solution was then agitated thermally followed by centrifugation. Further, in order to form the composite of $MnWO_4$/BiOI, the BiOI was coated by using facile deposition over $MnWO_4$ at room temperature. In this deposition method initially, bismuth nitrate and potassium iodide were mixed in the ethylene glycol, which was then added dropwise into the solution of $MnWO_4$. This composite was used as an efficient photocatalytic activity under the radiation of visible light.

Zhu et al. had prepared $AgPO_4$ nanoparticles by dropwise adding of disodium hydrogen phosphate into a suspension of $Ag(NO_3)$ [18]. The final solution was kept for mechanical agitation followed by centrifugation, washing, and drying for a speculated time and temperature. The prepared Ag_3PO_4 was applied as the photocatalytic decolorization of a cationic azo dye.

Kumar et al. reported the green approach for the synthesis of CuO/Ag composite which acts as a *Z*-scheme for visible light decay of methyl orange [19]. Preparation of the composite takes place on adding an ammonia solution to the mixture of curcumin and copper nitrate; this was stirred at 65°C then centrifuged and annealed at 50°C in a vacuum oven for 24 h.

2.1.2 Coprecipitation method

Similar to the precipitation method, coprecipitation also works under the condition of supersaturation where the products are produced as the insoluble species. Formation of the photocatalyst through coprecipitation involves the following vital steps: (a) nucleation; (b) growth; (c) coarsening; and (d) agglomeration. Mixing up two or more salt constituents in their solution phase to form a homogeneous coprecipitate depends upon the differences in the solubility of the constituents and the precipitation kinetics. The precipitation kinetics typically deals with the nucleation and growth of precipitate particles, which strongly depend upon

https://www.twirpx.org & http://chemistry-chemists.com

FIG. 2 Coprecipitation method. Flowchart of the coprecipitation process.

the pH, degree of solute supersaturation, etc. [20]. Formation of the visible light photocatalyst through the coprecipitation method is illustrated in Fig. 2.

The coprecipitation method was reported for the preparation of the composite Ag_3VO_4/Ag_2CO_3 were done by adding the proper ratio of $Na_3VO_4/NaHCO_3$ into the solution of $AgNO_3$. The precipitate was collected through centrifugation followed by washing and drying [21]. Furthermore, in their reports authors have noted various degradation pathways of the composite.

Talukdar et al. have reported the synthesis of a solid-state *Z*-scheme system of Ag_3PO_4/Fe_3O_4/bamboo-derived activated biochar (BAB) for a visible light photocatalyst [22]. Synthesis of BAB was done by carbonizing of biomass feedstock under an argon atmosphere, which was then chemically functionalized through H_2SO_4/HNO_3 with the ratio 1:3 at 80°C for 3 h. They synthesized Fe_3O_4 nanoparticles separately made from the solution of ferric/ferrous chloride precursors with hydrochloric. The solution was stirred by adding sodium hydroxide dropwise for 3 h. At the end, the powder of Fe_3O_4 and functionalized BAB was ultrasonicated by adding silver nitrate solution. The complete solution was stirred after dropwise adding of $Na_2HPO_4 \cdot 12H_2O$ solution to form an Ag-Fe@BAB photocatalyst, which was washed with DI water several times and dried in a vacuum oven after magnetic separation. From an application point of view, the Ag-Fe@BAB composite is used in the degradation of bisphenol A.

https://www.twirpx.org & http://chemistry-chemists.com

Advantages of the coprecipitation method are as follows: (i) preparation of products is simple and swift; (ii) stress-free control over the size and the composition of the particles; (iii) low temperature; (iv) numerous options to regulate the particle surface state uniformity; and (v) relatively low-temperature process with no use of organic solvent.

The disadvantages of this method lie in the following facts: (i) this process takes a lot of time; (ii) there is a problem of reproducibility; (iii) there are chances of precipitation of impurities with the final products; (iv) coprecipitation will not happen well if the initial reactant species have different rates of precipitation; and (v) proper monitoring of the complete process is essential so that readjustment of the pH of the solution is carried out to achieve high-quality products.

2.1.3 Sol-gel method

Ebelman first introduced sol-gels in 1845 [23]. The sol-gel process deals with three vital steps: (i) preparation of a sol; (ii) gelation of the sol; and (iii) removal of the solvent. Sols are the dispersion of a colloidal suspension that can be obtained from liquid solutions of inorganic precursors (i.e., metal alkoxide and metal chlorides). This discontinuous phase is so limited that the gravitational forces do not exist only, Van der Waals forces and surface charges (i.e., columbic repulsive forces) are present within the mono-sized nanoparticles. Sol is the molecular suspension of the amorphous particles ranging from 1 nm to 1 μm. Gels are highly viscous materials solid solvent encapsulating matrix. In general, the gel is the semirigid mass that is left over when the solvent from the sol begins to evaporate. On evaporation of the solvent, these uniform particle-sized sols connect to each other to form aggregates, joining together to form a network of gel particles.

In the sol-gel process, sol is prepared through hydrolysis or partial condensation of alkoxides or inorganic salts. Gel formation occurs through a polycondensation process that results in the creation of metal-oxo-metal or metal-hydroxy-metal bonds. The transformation of the liquid solution to the cross-linked gels may take a few minutes to a few hours; this period of time is called gel time or gelation time. A further process of condensation often shrinks it, resulting in solvent expulsion. The drying process will then lead to liquid phase removal within the gel. If these gels are dried at ambient pressure, xerogel is formed, whereas under supercritical conditions this drying step results in aerogel formation. On calcination, these gel networks with uniform nanopores that are connected between different aggregates to form large interparticle spaces start to collapse. This calcination step also enhances the mechanical properties of the nano-sized particles. In most cases, particle calcination at a higher temperature of around 800°C was used to remove metal hydroxide groups from the surface [24]. This heating at high temperatures decreases the surface area of the particles.

From the above explanation, it is clear that the important parameters—precursor type, solvent type, pH of the solution, solvent and precursor concentration, reaction temperature, and reaction time—had great impacts on the sol-gel process. Preparation of the visible photocatalyst through the sol-gel method is shown in Fig. 3.

https://www.twirpx.org & http://chemistry-chemists.com

FIG. 3 Sol-gel method. Flowchart of the sol-gel process.

The sol-gel method may be classified into aqueous and nonaqueous sol-gel processes. The aqueous route involves water as a solvent whereas in the nonaqueous route the type of solvent is alcohol. In the aqueous route, due to the presence of water, amorphous precipitates are mostly produced, which is the major disadvantage of the aqueous route over the nonaqueous route.

The equimolar ratios of bismuth nitrate and ammonium vanadate were separately dissolved with nitric acid and ammonium hydroxide solution, respectively [25]. These two solutions were mixed together with ethanol to obtain a yellow solution and stirred for 1 h. As soon as glacial acetic acid was added to the above sol, it started transforming into the gel. Finally, in order to obtain $BiVO_4$, powder gel was dried and calcined at 400°C for 2 h which was then utilized as a visible light photocatalyst.

The preparation of the CdSe photocatalyst using tri-block copolymer, namely poly(ethylene glycol)-*block*-poly(propylene glycol)-*block*-poly(ethylene glycol), abbreviated as F127, which acts as the structural directing mediator, was employed through

https://www.twirpx.org & http://chemistry-chemists.com

the sol-gel method [26]. At the start CH_3COOH, HCl, CH_3CH_2OH, and F127 were dissolved by moderate stirring. Then $CdCl_2$ powder was dissolved in the above solution followed by dropwise adding of the Na_2SeSO_3, which was then transferred into the petri dish and the temperature was raised to 65°C for 24 h. Finally, the above-dried gel was treated at 320°C for 4 h to transform into the highly crystalline CdSe and to eliminate F127. The prepared CdSe was then employed as photocatalyst for improved oxidative desulfurization of thiophene.

Peymanfar et al. reported the formation of the $CuCr_2O_4$ nanoparticles through the sol-gel method [27]. A typical synthesis of $Cu(NO_3)_2.3H_2O$ and $Cr(NO_3)_3.9H_2O$ was dissolved with sucrose for 1 h and the pH was altered by adding NaOH. Finally, the dark precipitate obtained was washed several times with various solvents and was used for the degradation of water pollution.

For the preparation of Li_2MnO_3 nanostructures, an equimolar ratio of mixed metallic salts (i.e., $Mn(NO_3)_2$, Li_2CO_3): ethylene glycol: citric acid was taken and the pH was adjusted through an ammonia solution [28]. The sol was then heated at 80°C to transform into gel followed by 4 h calcination at 700°C. Finally, a prepared photocatalyst was applied for organic dyes degradation.

A stoichiometric composition of Fe $(NO_3)_3.9H_2O$, La $(NO_3)_3$, and citric acid was liquefied to form an aqueous solution which was adjusted at pH 7 by adding ammonium hydroxide [29]. The solution was kept stirred at 60°C to form a sol which was again heated slowly and successively to transform into a solid dry gel due to auto-ignition, followed by activation at 500–900°C for 2 h to form nanocrystalline $LaFeO_3$ powders, which act as photocatalysts for water decomposition.

$Fe(NO_3)_3.9H_2O$, $Sr(NO_3)_2$ and citric acid were stirred at 60–70°C [30]. Soon after, the proper proportion of citric acid/polyethylene glycol was added to the above solution whose pH was maintained by the addition of an NH_3 solution. Then the sol was transformed to a viscous gel and then to a dry gel. Calcination of the dry gel at 700°C for 8 h led to the formation of $SrFe_2O_4$ nanoparticle powder which was applied as a visible light photocatalyst. Synthesis of Mo-doped $BiVO_4$ was reported by the sol-gel method [31]. Firstly, the equimolar concentrations of $Bi(NO_3)_35H_2O$ and NH_4VO_3 were taken separately. Bismuth solution was made in the presence of the concentrated HNO_3. Then citric acid was added to both solutions. In addition, the pH was altered by adding an NH_3 solution. Subsequently, the bismuth solution was mixed with the vanadium solution slowly before drying, washing, and grinding to obtain $BiVO_4$ powders which were impregnated in molybdic acid and kept for calcination at 375°C for the doping of Mo.

The combination of $La(NO_3)_3{\cdot}6H_2O$, $Zr(NO_3)_4{\cdot}5H_2O$, and citric acid was dissolved in deionized water [32]. Then the dropwise addition of ethylene glycol into the above solution was done, whose pH was kept at 2.78 by adding NH_3 water. The collosol was prepared by maintaining a temperature of 70°C for 4 h. This was then dried at 125°C for 6 h to form a gel. Finally, heated at 800°C for maintaining 1 h to obtain $La_2Zr_2O_7$ powder. In the same report, $La_2Zr_2O_7$/GO was prepared by adding GO into the $La_2Zr_2O_7$ collosol, which was ultrasonically treated for 2 h, vacuum dried for 6 h, and then applied for photocatalytic

https://www.twirpx.org & http://chemistry-chemists.com

visible light degradation of tetracycline. A bismuth solution was prepared by adding $Bi(NO_3)_3$ salt with HNO_3, which was then introduced to an aqueous solution of tannic acid [33]. Subsequently, a vanadium solution was made by combining $Cu(NO_3)_2$ and NH_4VO_3 salt with tannic acid. The vanadium solution was finally introduced to the bismuth solution and ethylenediamine. Afterward, the aqueous copper solution was applied to the above mixture, which was then heated at 100°C for 2 h to form a gel. Lastly, calcination of the powder was conducted at 750°C for 2 h to form a $CuO/BiVO_4$ nanocomposite applied for photocatalytic desulfurization of thiophene under visible light.

For the preparation of the boron-doped $C_3N_4/NiFeO_4$ nanocomposite, initially, BCN was ultrasonicated and then $NiCl_2$ and $FeCl_3{\cdot}9H_2O$ were added with continuous stirring [34]. A particular amount of NaOH was added to the above emulsion for adjusting the pH to 13. The emulsion was stirred soon after drying and calcined for 3 h at 450°C to form the required nanocomposite which was then applied for degradation of methylene blue.

The advantages of the sol-gel method of preparing visible light catalytic materials are as follows: (i) tuning of the pore size distribution and pore volume; (ii) opportunities to prepare samples at low temperatures; (iii) possibility to regulated the size, shape, and structure; and (iv) high control of pure products by appropriate choosing of the initial precursor.

Only disadvantage is that synthesis of precipitates takes a longer time, which is also the difficulty of sol-gel synthesis.

2.1.4 Hydrothermal/solvothermal method

A famous geologist named Roderick Murchison introduced the term "hydrothermal" [35]. In his work, he described how the action of water from any water bodies on Earth at elevated temperatures and pressures creates rocks and minerals at the Earth's crust. The same idea of hydrothermal was adopted for the preparation of different nanostructures.

The hydrothermal method is a technique in which an aqueous precursor solution is preserved in a sealed chamber maintaining high temperatures and high vapor pressure of the aqueous precursor solution. To carry out this reaction, autoclaves, stirred reactors, and bath reactors are used. Among all these, autoclaves or bombs are most common in use because they are comprised of thick-walled steel cylinders with an airtight seal. The walls of the steel cylinders are very thick and can survive at very high temperatures and pressure for a long period. For the synthesis of different nanostructured photocatalysts, the temperature varies between 100°C and 800°C, while the pressure that is popularly used is in the range of few bars to 2.5 Kbar [36, 37].

Hydrothermal synthesis has been typically performed below 300°C; this is due to the ionic product which has a maximum value between 250°C and 300°C. Adschiri et al. reported that at the supercritical state, the solubility of water reduces, which in turn enhances the formation of ultra-fine particles with controlled morphology [38]. Another factor is the temperature gradient, which develops between the hotter and the cooler ends of the autoclave. Maintaining this temperature gradient of the autoclave (or reaction chamber), the hotter end of the nutrient dissolves while the cooler ends cause more

https://www.twirpx.org & http://chemistry-chemists.com

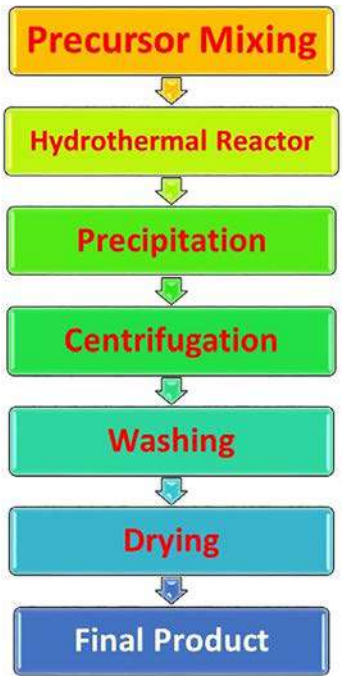

FIG. 4 Hydrothermal/solvothermal method. Elementary steps of the hydrothermal process for the preparation visible-photocatalyst.

growth of grains. This results in the formation of the visible photocatalyst. Preparation of the visible photocatalyst through the hydrothermal method is represented in Fig. 4.

A $BaBiO_3$ perovskite structure was prepared with an equimolar amount of barium nitrate and bismuth nitrate which was mixed with ammonium hydroxide to maintain a pH of 8 [39]. The complete solution was put into the hydrothermal reactor at different temperatures, starting at 130–170°C for 6 h. Subsequently, the $BaBiO_3$ powders were centrifuged, washed, and dried at 80°C. The prepared $BaBiO_3$ perovskite powder was applied for water splitting and removal of rhodamine B from aqueous systems. The preparation of Zn_2GeO_4 nanorods was reported by using equimolar salts of Na_2GeO_3 and $Zn(NO_3)_2$ as an initial precursor complexed with the proper ratio of HMT [40]. The above solution was stirred and shifted to the Teflon-lined autoclave and was kept at 100°C for 12 h. When the reaction was completed, the white solid was collected through a sieve, washed, and dried at 60°C overnight. If organic solvents are used instead of water, then the process is termed as solvothermal method. Individually, if the solvent that is used is alcohol or glycerol, then the process is known as alcohothermal or glycothermal, respectively. Therefore, it is understood that the solvent plays a vital role, since it provides a reaction medium as well as helps to keep high pressure [41]. Bi_3NbO_7 porous nanosheets were synthesized by preparing $Bi_2(NO_3)$ in an acetic acid solution; this solution was then added to a niobium oxalate solution which was dissolved in methanol [42]. Vigorous mechanical agitation was applied to the above mixture after adding benzyl alcohol. In the end, urea as a fuel and

https://www.twirpx.org & http://chemistry-chemists.com

potassium hydroxide were added before transferring the complete mixture solution to the Teflon-lined autoclave for 24 h at 180°C. After cooling at room temperature, the products were collected and washed with water and ethanol, and then dried at 60°C for 6 h. The formation of Bi_2WO_6 QDs/magnetic carbon nano onions photocatalyst was done through a stepwise synthesis of Bi_2WO_6 QDs in which $Bi(NO_3)_3$ were ultrasonically mixed with sodium oleate to form a uniform emulsion [43]. At the same time Na_2WO_4 was mixed with MCNO ultrasonically and then injected to the above-made emulsion; this was stirred and transferred into the Teflon-lined autoclave for 18 h at 160°C. The products were well washed by n-hexane and ethanol several times and placed into the freeze-drying chambers, which were then used for photocatalytic activities.

Composite g-C_3N_4 nanosheets/$BiVO_4$ were prepared by the hydrothermal method [44]. Here the preparation of CNNS was done by grinding the mixture of melamine and ammonium chloride first and then annealing at 550°C for few hours. Subsequently, $BiVO_4$ was formed by adding HNO_3 into an equimolar solution of $Bi(NO_3)_3$ and NH_4VO_3. The surfactant SDBS was added to the above mixture which was adjusted to a pH of 6 using dropwise addition of NaOH solution. The heterojunction which was formed showed the *Z*-scheme for the photocatalytic synthesis of imines.

Aforementioned protocol for the preparation of g-CN nanopowders were adopted. Then after La_2O_3 modified g-CN nanocomposite was fabricated by suspending g-CN powders to the mixed solution of $La(NO_3)$ and ammonia solution [45]. The solution was sonicated and transferred in the Teflon-sealed autoclave, which was kept for 150°C for 6 h. Finally, the powder was procured by centrifugation followed by consecutive washing and drying. The synthesized powders were used in visible light irradiation for the oxidation of various organic contaminants. The formation of the porous oxygen-doped carbon nitride was synthesized by the hydrothermal method [46]. For that, a transparent solution of dicyandiamide was made which was kept at 180°C for 16 h. The precipitate of dicyandiamide was collected by evaporating at 100°C. Finally, oxygen doping in the g-CN nanopowders was achieved by annealing the above-prepared powders at 550°C for 2 h. O-doped g-CN nanopowders were used for photocatalytic applications.

A metal sulfide heterojunction was also reported by preparing e-WS_2 first and then coating it with Bi_2S_3 for improved photocatalytic activity [47]. e-WS_2 was prepared through an aqueous solution of WCl_6, C_2H_5NS, and HCl; after stirring for a few minutes the solution was transferred to the Teflon-lined stainless steel autoclave at 190°C for 24 h, which was then centrifuged, washed, and dried at 140°C for 6 h. In order, the synthesis of Bi_2S_3/e-WS_2 heterojunction previously made e-WS_2 powders was made a homogeneous solution by mixing it well with the aqueous solution of $Bi(NO_3)_3$and Na_2S added with concentrated HCl. The reaction mixture was transferred to a Teflon-lined stainless autoclave maintained at 190°C for 24 h. The heterojunction photocatalyst was soon after centrifuged, washed, and dried at 120°C for 8 h.

The advantages of the hydrothermal method are as follows: (i) very cheap starting precursors; (ii) mild reaction conditions; (iii) simultaneous heating and the pressurizing of the system closes to the critical point of the solvent which makes most of the material soluble; (iv) easy synthesis of the products with the intermediate state, metastable state,

https://www.twirpx.org & http://chemistry-chemists.com

and specific phases; (v) low melting point, high vapor pressure, and pyrolysis-induced substances are obtained; (vi) the varying size, shape, and crystallinity of the end product are specifically regulated by varying parameters such as reaction temperature, solvent type, surfactant type, and precursor; and (vii) in solvothermal synthesis, the crystallization rate is very high.

The disadvantages of the hydrothermal methods are as follows: (i) problem related to safety during the reaction; (ii) the rate of aggregation is very high; (iii) chemical contamination arising from combustion; (iv) costly equipment is required; and (v) in solvothermal synthesis, there is a challenge in mass production since it is difficult to control the reaction condition.

2.1.5 Solid-state reactions

In solid-state reactions, initially, the precursor materials that we consider are the solid mix that does not react at room temperature. It is a mechanochemical reaction process, which occurs between the particles of the reactant powder in the presence of an external force [48]. However, when subjected to heat at a high temperature it yields a stable final product. At high temperatures, the atoms or ions undergo a process of diffusion within the interior of the precursor salts, resulting in the final products. Therefore, at elevated temperatures, the transfer of matter from one phase to another takes place, which initiates the nucleation process. Latterly this results in the formation of the final product. The rate of reaction is an important characteristic inspired by the simultaneous effect of both kinetic and thermodynamic aspects. The solid solution is a single phase where all the components are atomically hybridized [49]. This means that as the components change the structures and properties also change. Fabrication of some solid solutions has even narrower bandgaps than those of the individual components.

The factors that influence the reaction rate are: (a) contact area between the grains of the reacting solids; (b) diffusion rates of the ions; and (c) rate of nucleation of the final product.

Normally the protocol for the synthesis of the visible photocatalysts starts with the mixing of the small amount of the different precursor salt by the help of a mortar pestle. For homogeneous mixing of the initial salts, an organic solvent is used which vaporizes during the process of grinding and mixing. After ensuring the complete vaporization of the volatile liquid from precursor materials were then calcined through the furnace set at a high temperature kept under an inert or air atmosphere. The conventional way to prepare visible light photocatalyst through the solid-state reactions process is shown in Fig. 5.

The synthesis of $BaBiO_3$ perovskite structure was done through solid-state synthesis followed by the hydrothermal method [39]. First of all barium carbonate and bismuth oxide were ground and thermally agitated at 800°C for 24 h. For the preparation of Pr_6O_{11}/g-C_3N_4, particular amounts of Pr6O11 and melamine were taken and ground to obtain a homogeneous mixture using a mortar pestle [50]. The mixture was then transferred into an alumina crucible capped with a lid and annealed at 520°C to obtain the Pr_6O_{11}/g-C_3N_4 composite, which was then utilized as the visible photoactive catalyst for oxidation of AV7 dye.

https://www.twirpx.org & http://chemistry-chemists.com

FIG. 5 Solid-state reaction method. Stepwise preparation of solid-state reactions method.

An Ag_2CO_3-based photocatalyst was prepared by grinding Ag_2CO_3, $AgNO_3$, and Na_2CO_3 for 1 h in an agate mortar [51]. The yellow powder was thoroughly washed by deionized water three times, and then dried under natural conditions for 12 h. Further, by varying the ratio of $AgNO_3$ and Na_2CO_3, composite Ag_2O/Ag_2CO_3 products were prepared for visible light-driven photocatalytic decomposition of organic pollutants.

The advantages of the solid-state reaction methods are as follows [52]: (i) preparation conditions are mild; (ii) the process is low cost; (iii) easy to use; and (iv) simple to scale up.

The disadvantages of the solid-state reaction methods are as follows [53]: (i) inconsistency; (ii) nonuniformity in the grain morphology; (iii) since the product

https://www.twirpx.org & http://chemistry-chemists.com

FIG. 6 Combustion reaction method. Flowchart for the combustion process for the preparation of visible light photocatalysts.

formation does not take place at the atomic level, there is a lack of purity in the products; (iv) frequent grinding is required; and (v) inability to reproduce.

2.1.6 Combustion reactions

Apart from the solid-state reactions method, the combustion reactions are based upon fast oxidation which generates heat [54]. In other words, combustion is a series of exothermic chemical reactions, which take place between the oxidant and fuel to produce chemical products [55]. For the combustion reaction to proceed, two things are important: (i) presence of reactants or oxidizer; and (ii) fuel. Therefore, the exothermic reaction may be homogeneous if the fuel and the oxidizer are in the same state, or heterogeneous if the fuel and the oxidizer are in a different state.

The process of combustion was carried out either by a volume reaction mode or by a propagation mode. When the reaction starts locally through the ignition and then extends within the whole sample through the propagation of the combustion wave, it is termed a propagation mode. However, when there is simultaneous heating of the entire sample (to its ignition temperature) and an exothermic combustion reaction occurs, it is termed a volume reaction mode [56]. The protocol for the preparation of visible light photocatalysts through the combustion reactions method is shown in Fig. 6.

Depending upon the above modes, the combustion reactions methods may be further classified into two categories: (a) solid combustion method; and (b) solution combustion method.

In general, the solid combustion synthesis is also termed as the self-propagating high-temperature synthesis method. Merzhanov and coworkers discovered this method in 1967 [57]. The reactants initially blended properly to form a pallet. This pallet ignited in the presence of an ignition source. As soon as the pallet ignited, this generated a high

https://www.twirpx.org & http://chemistry-chemists.com

exothermic reaction within the sample, which is also termed as auto-ignition. Due to this rate of reaction, fast production of the products takes place [58].

Synthesis of the WO_3 was achieved by dropwise addition of an ammonium tungsten oxide hydrate solution to a stirred solution of oxalic acid [59]. Then the mixture solution was placed in a furnace for igniting the system in order to attain combustion. Finally, the powder was washed several times in ethanol and dried to obtain hexagonal WO_3 powders as a visible photocatalyst.

An equal ratio of yttrium nitrate: iron nitrate: glycine: water precursor solution was stirred and heated at 250°C [60]. Slowly water was vaporized during heating. The produced foam was then ignited to obtain a light brown yttrium iron oxide nanocrystalline structure as an end product which is used as a visible light photocatalyst.

The synthesis of Bi_2WO_6 was performed by selecting a precursor $Bi(NO_3)$ dissolved in nitric acid; Na_2WO_4 was then added to different ratios of glycine, which acts as fuel [61]. The solution was then vigorously stirred at 200°C. Gradually, due to the heating, complete vaporization of the liquid took place and as a result the solution became viscous. After reaching critical temperature, evolution of different gases took place, leaving only the product which was finally ground, washed, and dried at 60°C in an ambient atmosphere. The prepared powder was used as a visible light-driven photocatalyst.

The solution combustion method, on the other hand, starts with the generation of high temperature beyond the melting point of the starting precursor, because of which the reaction precursor can vaporize, resulting in high-purity products [62]. The synthesis of $Ag/Bi_5O_7NO_3$ composites was carried out by the solution combustion method. For this, bismuth nitrate and $C_4H_6O_6$ powder were dissolved in nitric acid, which was then put into the furnace that was set at 500°C for 0.5 h. Continued heating of the clear solution gradually transformed the solution into a viscous gel, leading to self-ignition, combustion, and flame that results in the formation of $Bi_5O_7NO_3$ powder. Finally, adding a certain amount of $AgNO_3$ in the above reaction system results in the formation of $Ag/Bi_5O_7NO_3$ which was then applied to photocatalytic activities with respect to pristine $Bi_5O_7NO_3$.

A $ZnFe_2O_4$-ZnS nanostructure photocatalyst was synthesized through raw materials such as zinc nitrate, iron nitrate, potassium chloride, and thiourea [63]. The mixture was subjected to stirring for 45 min at 80°C. Then the solution was stirred at 325°C and persistent heating resulted in a colorless viscous gel. Finally, the powder was washed in DI water and magnetic separation was followed by drying at 80°C.

The solution combustion method was used to prepare a $ZnO/CuO/g\text{-}C_3N_4$ composite [64]. Stepwise growth was initiated through the formation of a ZnO/CuO heterostructure followed by the coating of $g\text{-}C_3N_4$. The synthesis of ZnO/CuO heterojunction was prepared by stirring $Cu(NO_3)$ and $Zn(NO_3)_2$. After some time, sucrose was dissolved in the above solution and heated at 250°C. Soon after the solution was evaporated, ignited, and flamed to obtain a ZnO/CuO powder. In the second step, $g\text{-}C_3N_4$ powders were formed by calcinating urea at 550°C for 1.5 h. At the end, coating of $g\text{-}C_3N_4$ powders was done by making a solution of the powder $g\text{-}C_3N_4$ and previously made ZnO/CuO powder in ethanol and water. H_2SO_4 was mixed to the above solution for maintaining a pH of 6. The reaction mixture was properly sonicated and stirred for 24 h. The product was then

https://www.twirpx.org & http://chemistry-chemists.com

centrifuged followed by washing and drying at 120°C on a hot plate. The prepared powder was applied as a visible light photocatalyst.

Bi/BiOBr photocatalyst was synthesized by preparing an equimolar solution of bismuth nitrate pentahydrate, ammonium bromide, and citric acid [65]. The solution was kept at 300°C followed by ignition and combustion reaction.

Eu doping over $MgFe_2O_4$ was done by the combustion method [66]. Stoichiometric amounts of magnesium nitrate, ferric nitrate, and europium nitrate was stirred in DDW with an appropriate amount of oxalyl dihydrazide fuel. The mixture was heated at 350°C in a furnace. A brown-colored fluffy product was produced, suggesting the formation of $MeFe_2O_4$:Eu^{3+}. The doping of Eu^{+} in the host matrix enhanced the visible light photocatalytic performance of the system.

Ru-doped $LaFeO_3$ coupled with Fe_2O_3 was grown stepwise [67]. Initially, an aqueous solution of $Fe(NO_3)_3$ and citric acid was stirred at 60°C. After 5 min, ammonium hydroxide solution was added to the previous solution, increasing the pH to 12, and this was then heated at 130°C to form a gel. This gel was then calcined at 300°C. Ru-doped $LaFeO_3$ was formed by stirring $Fe(NO_3)_3$, $La(NO_3)_3$, and $RuCl_3$ in DI water for 5 h at 60°C. The pH of 7 of the above solution was maintained by adding an ammonia solution. The solution was dried and calcined at 300°C for 3 h to ignite to form a Ru-$LaFeO_3$ powder. A physical mixture of Ru-doped $LaFeO_3$ and Fe_2O_3 was dispersed uniformly through stirring in DI water. Then tetraethyl orthosilicate, ethanol, and ammonia solution were added sequentially to the above solution which was then stirred for 12 h and centrifuged at 5000 rpm. Lastly, the solution mixture was calcined at 450°C for 30 min. Ru-$LaFeO_3$ powder was applied to achieve hydrogen production through the degradation of glucose in water.

Some advantages of the combustion method are as follows [68]: (i) no sophisticated instruments are used; (ii) highly pure products with desirable size and shape can be prepared; (iii) the metastable phases are quite stable; (iv) synthesis will take place at an atomic level; and (v) uniform grain morphology is obtained.

Some disadvantages of the combustion method are as follows [69]: (i) high degree of atomic control is necessary; (ii) evolution of H_2S instead of SO_2 gas at higher temperatures may result in corrosion of the furnace; and (iii) formation of excess air during synthesis will reduce the quality of the products.

2.1.7 Spray pyrolysis

Spray pyrolysis is also called an aerosol method. The spray pyrolysis process involves the acceleration of a liquid phase solution from a specially designed atomizing nozzle after which the transportation and the evaporation of the solvent within the aerosol droplets lead to the formation of nanostructured powder. Formation of the photocatalyst through the spray pyrolysis depends upon the nature of atomizers such as liquid/gas (pneumatic acceleration) energy, mechanical energy, vibrational (ultrasonic) energy, and electrical (electrostatic) energy. Depending upon the type of atomizer, spray pyrolysis can be categorized as pressurized spray pyrolysis, ultrasonic spray pyrolysis, and electrostatic spray pyrolysis [70–72].

The other factor on which spray pyrolysis depends upon is the transportation of the precursor/aerosol droplets through a gradual high-temperature zone within the presence

https://www.twirpx.org & http://chemistry-chemists.com

of a gas carrier. Here aerosols can be defined as a suspension of solid and liquid particles. The formation of nanoparticles starts from the injection of the aerosol droplet through the atomizer which is directed toward the furnace. Filipovic et al. reported that the formation of the aerosol experiences four forces: gravitational, electrical, strokes, and thermophoretic [73]. Due to abovementioned forces aerosol undergoes the continuous vaporization which leads to solvent evaporation and component diffusion, which in turn results in solute precipitation followed by drying and breakdown of the molecules due to high temperature. Lastly, sintering of the precipitation forms dense particles. The particle size is controlled by the aerosol droplet size and the environment of atomization [74]. The optimization of the deposition temperature, concentration and composition of the reactants, carrier gas ratio, solution flow rate, and the distance between the nozzle and the powder collector are responsible for better-yield products [75]. Fig. 7 shows a typical flowchart for the preparation of a visible light photocatalyst through the spray pyrolysis process.

Synthesis of Au:CdS was done using an equimolar concentration of cadmium acetate and thiourea [76]. Then chloroauric acid was mixed. The mixed solution of Au:CdS was sprayed at a rate of 2 mL/min in the presence of nitrogen as the carrier gas. The reactor has three different zones: 400°C, 750°C, and 350°C, respectively. Finally, the nanoparticles were collected and vacuum dried at 60°C.

CNT was dispersed into the aqueous solution of $Cu(CH_3COO)_2$ [77]. This solution was sprayed by an ultrasonic nebulizer in the reactor with an airflow rate of 150 mL/min having three zones: preheating, calcining, and cooling. Finally, the CNT/Cu_2O-CuO nanoparticles were collected after cooling.

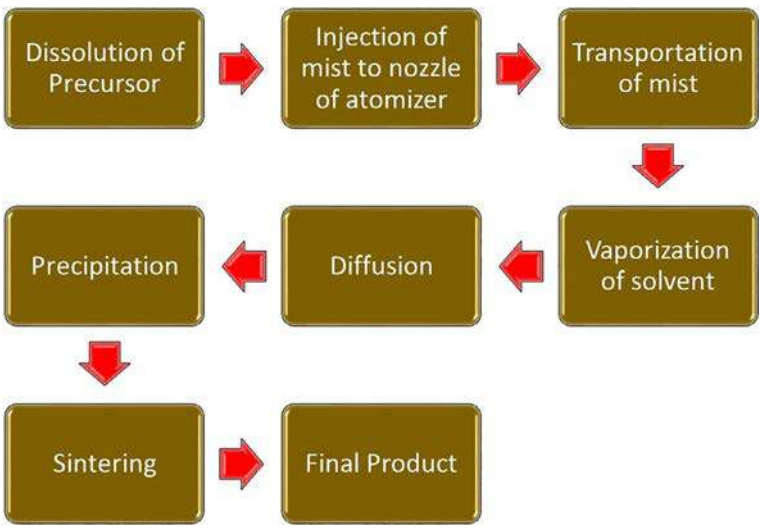

FIG. 7 Spray pyrolysis. A flowchart shows the elementary step of the spray pyrolysis process.

https://www.twirpx.org & http://chemistry-chemists.com

The mixed solution was prepared by adding (Zn $(NO_3)_2{\cdot}6H_2O$), (H_2WO_4), and ammonia solution in DDW [78]. The aerosol droplets were generated through an ultrasonic nebulizer and carried through the tube furnace at 700°C. The $ZnWO_4$ products were collected at the end of the tubular furnace. The obtained products were washed and dried at 70°C in an open atmosphere.

The advantages of spray pyrolysis are as follows [79]: (i) open atmosphere process; (ii) accessibility to observe the deposition procedure; (iii) low-cost and continuous operation; (iv) high-quality regents as precursors are not required; (v) high rate of production; (vi) crystal size is controllable with high surface area; and (vii) the products have compositional homogeneity.

The disadvantages of spray pyrolysis include [80]: (i) yield of the powder materials is very low; (ii) conversion of the sulfides into the oxide is required; and (iii) many complications toward the optimization regarding the growth temperature.

2.1.8 Flame synthesis

Apart from spray pyrolysis, flame synthesis is a direct approach to synthesize visible photocatalysts by directly applying high-temperature flame conditions. The formation of different materials through the flame synthesis process can be categorized into: (i) gas-to-particle conversion processes; and (ii) droplet-to-particle conversion processes. In the process of the gas-to-particle conversion process, the reactants get reacted at the gas phases, and coagulate to form the powders. In the droplet-to-particles conversion, the precursor in the solution phase is suspended into the medium through atomization and gets pyrolyzed at high temperatures to form powders [81–83]. The final products produced from the above methods are comprised of agglomerates or aggregates. The protocol to follow the synthesis of photocatalyst through flame synthesis is shown in Fig. 8.

Niobium pentaethanolate was stirred in ethanol and ignited by a flame [84]. Due to the application of the yellow part of the flame, black carbonaceous Nb_2O_5 was generated. A sufficient amount of the black powder was taken and washed and kept for calcination at 550°C for 2 h to convert into white powder of carbonaceous Nb_2O_5 microspheres; this was used in photocatalytic activity for hydrogen evolution.

Carbon nanoparticle powders were prepared through the flame soot method [85]. Naturally occurring products have been used as the precursor for carbon (i.e., almond, almond char, Indian ghee, mustard oil). Flame has been employed for all of these precursors to form soot which was collected and transferred for centrifugation and purification. Finally, the precipitate was dried. The preparation of the Au/carbon nanoparticles was reported by the self-reduction of the $AuCl_3$ dissolved in the organic solvent in the presence of carbon nanoparticles, which were applied for photocatalytic oxidation of methylene blue.

Low energy input and very good quality of the end product are the only advantages whereas the presence of carbon in the final product is the disadvantage of flame synthesis [86].

https://www.twirpx.org & http://chemistry-chemists.com

FIG. 8 Flame synthesis. Flowchart of the flame synthesis method.

2.1.9 Electrospinning method

The electrospinning method was firstly invented by the Formhals who has patented the apparatus for producing an artificial thread of polymer fibers by using electrostatic repulsion between the surface charges of the polymer [87]. The electrospinning method is a low-cost method to produce nanofibers within the range of a few micrometers to nanometers. The electrospinning method consists of: (i) a spinneret, which is an apparatus having a metal nozzle from which the spinning solution is forced to come out; (ii) a high-voltage power source, which is applied to the end of the needle—on increasing the electric field at the tip of the needle, the expansion of the liquid along the

https://www.twirpx.org & http://chemistry-chemists.com

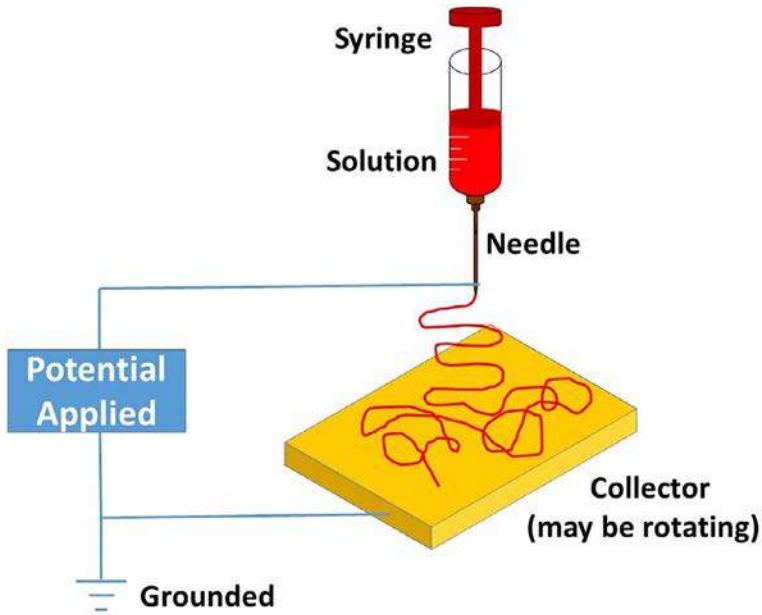

FIG. 9 Electrospinning process. Schematic of the electrospinning process.

hemispherical surface takes place, which creates a Taylor cone; and (iii) a conducting collector, which is helpful to collect the synthesized nanofibers.

The solution comes out from the nozzle of the spinneret due to the established high voltage at its tip. The solution becomes charged and ejected out from the jet; when this travels toward the collector, evaporation of the solvent takes place and the fibers accumulate on the oppositely charged conducting collector [88, 89]. In the end, the products formed by this technique are nonwoven fibers [90]. Electrospinning is basically categorized into: (a) static/vertical electrospinning mode; and (b) dynamic/horizontal electrospinning. A typical schematic of electrospinning is shown in Fig. 9.

Fabrication of the well-ordered nanofibers depends upon the different parameters such as: (a) solution viscosity; (b) surface tension; (c) porosity; (d) surface to volume ratio; (e) high applied voltage; (f) feed rate; (g) conductivity of the solution; and (h) the distance from the tip of the needle to the collector [91].

For the synthesis of α-Fe_2O_3, nanofibers are prepared by dissolving $Fe(NO_3)_3{\cdot}9H_2O$ in *N*, *N*-dimethylformamide (DMF); soon after polyvinylpyrrolidone is mixed to the solution, which is stirred at room temperature for 12 h, to form a sol [92]. Electrospinning was done at 20 kV at the nozzle tip, which is 15 cm away from the collector. Nanofibers were gathered from the collector and calcined at 650°C for 3 h. The α-Fe_2O_3 nanofibers have been utilized as a photocatalyst in water purification.

A $BiVO_4$ nanotube was synthesized by stirring of $Bi(NO_3)_35H_2O$ in DMF (*N*,*N*-dimethylformamide), followed by the addition of acetic acid [93]. After this,

https://www.twirpx.org & http://chemistry-chemists.com

vanadium(*IV*)oxy acetylacetonate was added to the solution. Formation of a sol was obtained by successively adding absolute ethanol and PVP slowly into the above solution, followed by overnight stirring. Electrospinning was done by applying 16 kV to the nozzle, which was placed 14 cm away from the collector. The collected powder was calcined at 500°C in air for 30 min. Within the same report, pristine $Bi_4V_2O_{11}$ nanofibers were synthesized by using $Bi(NO_3)_3$ and NH_4VO_3. $Ni_3V_2O_8$ nanotubes were fabricated by employing $Ni(NO_3)_2$ and $VO(acac)_2$. At the end, each of the parameters of the calcination step was kept the same. As an application, the synthesized $BiVO_4$ nanotubes were reported as the photocatalytic material. $Bi(NO_3)_3$ was added with the $Fe(NO_3)_3$ to make a solution in 2-methoxy ethanol [94]. Then ethanolamine and glacial acetic acid were added to the above solution and stirred well. Meanwhile, another solution was made where PVP was added to the particular ratio of DMF/acetone. Subsequently, this mixed solution was added to the above mixed solution. In the end, the complete solution was taken into the syringe which was applied to 13 kV potential. The as-prepared $BiFeO_3$ nanofibers which were collected from the collector were dried and annealed in air followed by the inert atmosphere. The as-prepared $BiFeO_3$ nanofibers demonstrated good photocatalytic activity.

The electrospinning method was employed to decorate CdS over the PET nanofibers, as reported by Ardona et al. [95]. First of all PET nanofibers were added to the ionic liquid to the mixed solution of cadmium acetate and sodium sulfide, respectively. The solution was sonicated well for a few hours and then transferred to the syringe through which the electrospinning was done. This composite was applied for the photooxidation of Rhodamine B under visible light.

$BiVO_4$/CdS nanofibers have been prepared by employing the electrospinning method [96]. Initially, $BiVO_4$ was synthesized by adding $Bi(NO_3)_3$, PVP, and $VO(acac)_2$ which was continuously stirred with the mixture of acetic acid (HAc), ethanol, and *N*, *N*-dimethylformamide (DMF). At the voltage of 9 V, the green color spinning solution was extruded out from the syringe with a feeding rate of 8 $\mu L min^{-1}$. The as-spun $BiVO_4$ nanofibers were collected and treated at 500°C which helped to remove PVP, leaving behind yellow powder of $BiVO_4$ nanofibers. This yellow powder was added to a $Cd(CH_3COO)_2$ aqueous solution and centrifuged, and then a thiourea solution was mixed into the above solution and incubated. Finally, this mixed solution was heated at 90°C. The separated powder of the $BiVO_4$/CdS was rinsed several times with DI water and dried. The fabricated heterojunction was used efficiently in visible light photodegradation.

The solution of citric acid was mixed with $(NH_4)_6Mo_7O_{24}$, $Bi(NO_3)_3$ and the concentrated nitric acid, and stirred for 1 h [97]. After that $Fe(NO_3)$ was added to the above solution. Meanwhile, another mixture was made by adding HNO_3 and ethanol. Intermixing of both solutions by maintaining the ratio of Bi^{3+} and Fe^{3+} was done and after that PVP was added and stirred to form a sol which was transferred to the syringe, to which was provided about 18 kV of potential. The electrospinning sol was injected with a speed of 2.27 mL/h. The α-Fe_2O_3/Bi_2MoO_6 heterojunction nanofibers were oven-dried followed by calcination at 500°C for 2 h. The prepared heterojunction showed photocatalytic activity.

https://www.twirpx.org & http://chemistry-chemists.com

The advantages of electrospinning are as follows: (i) low cost with large surface area; (ii) through controlled calcination, multifaceted hierarchical structures can be achieved; and (iii) long continuous nanofibers can be produced.

The disadvantages of electrospinning are as follows: (i) jet instability; (ii) precursor solvent used can be toxic; and (iii) limited control of pore structure due to the nozzle orifice.

2.1.10 Chemical vapor deposition

The term chemical vapor deposition (CVD) was first introduced by Dr. J. M. Blocher at the beginning of the 1960s [98]. The vapor deposition method was divided into physical vapor deposition (PVD) and chemical vapor deposition. In CVD, the powder precursor was converted into nanoparticles. The powder reactants were first thermally agitated so that they transform into vapors which are then reacted in their gaseous phases and transformed into solid powders within the presence of an inert gas atmosphere. These reactions are carried out in a controlled manner. The synthesis of oxides, nitrides, carbides, etc. was done through the CVD method.

The CVD method involves both homogeneous and heterogeneous chemical reactions of the gaseous reactants. The CVD method is also known as the solid-vapor reaction.

Tetragonal WO_3 nanobelts were fabricated through evaporation of $WO_{2.9}$ powder taken in an alumina boat kept at the pressure of 300 mTorr [99]. A tubular furnace was then heated at 500°C for 1.5 h and cooled down gradually till room temperature.

Melamine powder which was placed in an alumina crucible was vaporized and collected over the KIT-6 template [100]. Ramping in the applied temperature from 320°C to 550°C for 3 h forms g-C_3N_4. Flake-like g-C_3N_4 was also reported from direct pyrolysis of melamine at 550°C. Well-prepared g-C_3N_4 is an excellent photocatalyst for the reduction of CO_2 with water.

For the preparation of the $SrTiO_3$/graphene, APCVD method was utilized [101]. Initially, $SrTiO_3$ nanoparticles were taken into the quartz tube where they were set to vaporize at 1050°C; the same time H_2 and Ar were introduced in the same chamber. As soon as the surface of the $SrTiO_3$ was clean, CH_4 gas was introduced into the chamber in order to form $SrTiO_3$/graphene powder, which was then analyzed for the photocatalytic performance.

This process has the following advantages: (i) very simple; (ii) synthesis temperature is lower than the melting point of that material; (iii) high yield products; (iv) the products which are formed are highly dense—nearly 100%; and (v) a versatile method for the formation of materials.

Two disadvantages of the CVD method lie in the following points: (i) the apparatus is costlier; and (ii) the precursors which are used may be hazardous, which also creates more chances to get toxic products.

2.1.11 Microwave assisted

In the electromagnetic spectrum, microwaves lie between infrared and radio frequency (i.e., frequency of 0.3–300 GHz). Komarneni et al. were the first to introduce microwave-assisted inorganic synthesis in the liquid phase [102]. This is an energy conversion phenomenon

https://www.twirpx.org & http://chemistry-chemists.com

rather than heat transfer. The transfer of electromagnetic energy, which causes thermal energy, is called microwave heating. Microwave energies are not so high that they can break the chemical bonds [103]. There are two main mechanisms by which we can generate heat: (i) dipolar polarization mechanism; and (ii) conduction mechanism. In the dipolar mechanism, when the substance exposed to the microwaves possesses a dipole moment. Due to the presence of the external electric field, these dipoles get the energy to align themselves with the field of rotation [104]. During their alignment, these dipoles colloids with one another, and as a result, create heat within the sample. If we employ high-frequency radiation, the external electric field oscillates too quickly, which may result in the random motion of the molecules. Alternatively, if the frequency radiation is low then these dipole molecules do not experience randomness [105]. Therefore, the greater the polarity of the molecule of the solvent, higher will be the microwave effect, which in turns results in a high temperature [106].

Apart from the dipolar mechanism, in the conduction mechanism, the influence of the microwave electric field over the movement of any mobile charge carriers, such as electrons or ions, comes into existence. This movement of the charge carriers produces an induced electric field that creates heating in the sample due to resistances experienced within the movement of the charge carriers. As microwaves can propagate internally through the volume of the material and supply energy to it, this produces volumetric heating within the material [107].

Commonly, both of the above mechanisms were simultaneously applicable for the preparation of nanostructured materials. To carry out these reactions in a controlled manner, microwave reactors are used. Microwave-assisted growth has a smooth command over both nucleation and growth stages for the synthesis of nanomaterials. The factors, which are responsible for nucleation and growth, are synthesis temperature, way of adding reagents, and reaction yield [108]. Fig. 10 shows the growth of the bubble

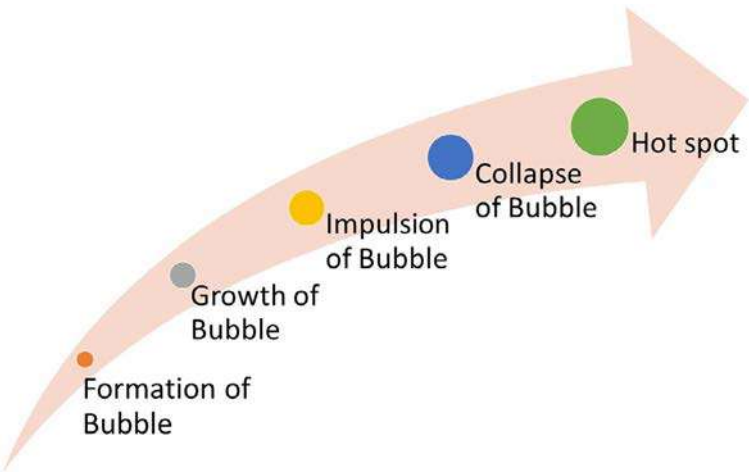

FIG. 10 Microwave-assisted. Representation of formation of a hot spot and overgrowth of the bubble in an acoustic cavitation.

https://www.twirpx.org & http://chemistry-chemists.com

which was formed during the acoustic cavitation to the synthesis of a visible light photocatalyst through the microwave method.

Star-shaped Bi_2S_3 was synthesized by microwave irradiation [109]. Prior to the formation of Bi_2S_3, the complex bismuth(III) tris(N-ethyl-*N*-phenyldithiocarbamate) was prepared. The preparation of the complex was done through dropwise addition of concentrated HCl into the solution of $Bi(NO_3)_3 \cdot 5H_2O$. This solution was stirred with ammonium N-ethyl-*N*-phenyldithiocarbamate for 1 h, followed by filtration, and the product was recrystallized from a chloroform solution. Then this complex powder was homogeneously dispersed into ethylene glycol and transferred into a microwave reactor which was kept at 180°C, 12 bar, for 5 min. Then the product was centrifuged, ethanol-washed, and air-dried. Finally the powder prepared showed photocatalytic degradation of Cr(VI).

$CuFeS_2$ powders were synthesized by dissolving copper chloride, ferric chloride, citric acid, and thiourea under continuous stirring; the final solution was placed in a microwave oven operated at 200°C with the power of 1400 W for 7 min [110]. The prepared powder was then applied for photo-Fenton oxidation of pollutants in water.

Dropwise addition of stannous chloride was dissolved in TEA with constant stirring into the solution of $ZnCl_2$ [111]. The pH was altered by adding NaOH which was then subjected to microwave irradiation. The precipitate was centrifuged, washed, and dried at 700°C for 5 h to form the powder of Zn_2SnO_4, which was used in photocatalytic oxidation of the organic dyes.

Synthesis of WO_{3-x} was reported by dissolving WCl_6 in the ethanol to form a yellow solution [112]. Afterward, the solution was moved to a Teflon-lined autoclave and was held in the microwave hydrothermal sensitizer at 150°C for 4 h. The resulting product was then centrifuged, washed, and dried in a vacuum at 50°C overnight; it was then used for photocatalytic bacterial inactivation.

The preparation of a W-doped $BiVO_4/WO_3$ heterojunction was reported by the microwave synthesis method [113]. First of all WO_3 was prepared by stirring $(NH_4)_6H_2W_{12}O_{40}.xH_2O$ and oxalic acid in ethylene glycol and kept in the microwave reactor. Then the powder was separated by centrifugation followed by calcination. The preparation of W:$BiVO_4$ was also reported by the same group. For the preparation of W:$BiVO_4$, two preliminary solutions were made with $Bi(NO_3)_3.5H_2O$ mixed with $(NH_4)_6H_2W_{12}O_{40}.xH_2O$ and NH_4VO_3 dissolved in ethylene glycol, which was then mixed. The pH of 1 of the reaction mixture was maintained by adding concentrated HNO_3 and the mixture was then transferred to a microwave oven. Finally, the powder was separated by centrifugation and calcination. The heterojunction was created by making a solvothermal solution of WO_3 through microwave irradiation. The solution of WO_3 was injected into the solution of W:$BiVO_4$ kept again for the microwave irradiation. At the end, the powder was separated by centrifugation followed by calcination. The prepared W-doped $BiVO_4/WO_3$ heterojunction powder was employed for photocatalytic activities.

For the formation of a VO_x/g-C_3N_4 heterojunction photocatalyst, the primary components which were required are melamine, ammonium metavanadate (NH_4VO_3), and oxalic acid ($C_2H_2O_4$) [114]. All the precursors were dissolved stepwise and impregnated for 2 h. The solution was then evaporated and the products were dried at 65°C for 24 h.

https://www.twirpx.org & http://chemistry-chemists.com

Then the products were grounded for 30 min and heated in a microwave for 40 min. Finally, the VO_x/g-C_3N_4 product was ground and applied for the oxidation of RhB under visible light.

Preparation of the $ZnFe_2O_4$@ methylcellulose nanostructure photocatalyst was done by mixing zinc nitrate and ferrous nitrate, followed by the addition of methylcellulose and sodium hydroxide for maintaining a pH of 13 [115]. The mixed solution was transferred into a microwave reactor from where the precipitate is obtained. Extraction of the required nanostructure composite was done by magnetic separation followed by washing with DI water. Finally, the composite was dried at 100°C in a vacuum for 24 h. The prepared powder was then reported in the photodegradation of metronidazole.

Stoichiometric quantities of nitrates of ferrous, cobalt, magnesium, and L-arginine precursors were homogeneously prepare to form Mg-doped cobalt ferrite spinel nanoparticles [116]. The mixed solution was poured into a silica crucible and kept inside a microwave oven with the irradiation frequency at 2.54 GHz, for 10 min at 900 W. As the solution reached its boiling point, spontaneous combustion and ignition occurred with a rapid flame leading to the gas evolution, leaving behind solid fluffy product. In the end, these nanoparticles were applied for photocatalytic oxidation of Rhodamine B.

The advantages of the microwave-assisted method of the preparation of different nanostructured materials are as follows [117]: (i) microwave heating technology provides excellent control over reaction mixing, enduring high temperature and pressures; (ii) this method exhibits reproducibility from reaction to reaction; (iii) microwave heating provides proper control over the nucleation and different growth steps in the fabrication of the nanomaterial; (iv) by the microwave, heating the possibility to heat either the solvent or the precursor molecules to produce homogeneity at a higher temperature for the synthesis of nanoparticles; and (v) there is no direct contact between the heating source and the reactants.

The disadvantages of the microwave-assisted method of the preparation of different nanostructured materials are as follows [118]: (i) microwave reactors are costlier; (ii) as microwaves have short penetration depth, the size of the reactors is kept small, which leads to a grave scaling-up problem; and (iii) in situ monitoring for the synthesis of the nanostructured materials is difficult.

2.1.12 Sonochemical method

The method in which chemical reactions were accelerated due to the application of the ultrasonic energy is termed as a sonochemical method. Moriguchi first introduced the use of ultrasound power in an electrochemical cell in 1934 [119]. The frequency ranges of the ultrasound go from 15 kHz to tens of megahertz. When this ultrasonic frequency passes through the liquid it causes acoustic cavitation, which can be divided into three stages as reported by Prince et al.: (i) formation and oscillation; (ii) growth and shrinking; and (iii) impulsive collapse of these liquid hollow bubbles within the liquid [120].

Furthermore, Suslick in 1988 reported that the cavitation process can be of two types: (a) stable cavitation, where the bubbles oscillate many times around the equilibrium; and

https://www.twirpx.org & http://chemistry-chemists.com

(b) transient cavitation, where the bubbles experience drastic volume changes which result in their fierce breakdown [121]. The formation of these bubbles takes place due to the superimposition of the expansion and compression of the alternating ultrasonic waves within the liquid. When the bubbles reach their critical size they collapse. From the formation to the collapse of the bubbles, there is the gradual absorption of sound energy, which undergoes an increase in the temperature inside these bubbles that is also termed as the "hot spot" as it reaches its critical stage. As per the hot spot theory at the critical stage, the temperature in this "hot spot" is around 5000 K, and the pressure of the hot spot is around 1000 atm [122]. This critical stage is known as the cavitation threshold. As the temperature and the pressure both exceed these hot spots they burst out and the synthesis of the different variety of materials takes place. Along with the hot spot theory, two more theories explain the concepts about cavitation: electrical theory and plasma theory. But the hot spot theory was found to be most popular.

Apart from this, the basic mechanism lies in the decomposition of water into hydroxyl radicals and hydrogen, which thereby initiates a series of chemical reactions under the influence of sound waves. The process of nucleation takes place at the gas-filled gaps or pores present over the particles, which were suspended in the solution. At the initial phase of low acoustic pressure, the bubbles start to grow due to the diffusion of gas molecules from the pores or gaps of the dissolved particles. The growth of these bubbles takes place at the expansion phase of the acoustic wave whereas at the compression phase the bubbles start contracting. Now as the acoustic pressure increases rapidly the bubble size expands until it reaches the critical size. The expansion and compression of the bubbles creates heat within the bubbles. The nature of heat generated inside the bubbles is adiabatic. Once the bubbles exceed the critical size, the compression cycle of the acoustic wave generates impulsive collapse of the bubbles, which is enough to trigger the chemical reaction. The formation of the cavity is influenced by many factors such as: (i) reaction temperature; (ii) hydrostatic pressure; (iii) irradiation frequency; (iv) ultrasonic intensity; and (v) nature of gases dissolved. For the fabrication of the metal nanoparticles, Gutierrez et al. first introduced the sonochemical method in 1987 [123].

$LaCl_3$ and $Fe(NO_3)_3$ were dissolved in DDW and then mixed with natural capping agents such as flour of starch, corn, and rice [124]. The reaction mixture was ultrasonicated, then tetraethylenepentamine (TEPA), ethylenediamine (en), or ammonia was added dropwise. Subsequently sonication was followed by centrifugation, washing, and drying to get $LaFeO_3$ perovskite nanostructure; the final product was applied for effective oxidation of organic pollutants in visible light.

The preparation of BiOI was done by dissolving $Bi(NO_3)_3$ with NaI in DDW [125]. NaOH was added slowly to adjust the pH of the solution which was then transferred to the ultrasonic bath kept at 35 kHz at 80°C for 5 h, followed by the collection and drying of the precipitate; it was reported to be used as a visible light photocatalyst.

Synthesis of CZTS nanoparticles was done by first of all preparing the sol with the gradual addition of precursor salts of Cu: Zn: Sn: S kept in a molar ratio of 2:1:1:8 for the different precursors [126]. The solution was then transferred to an ultrasonic bath for 1.5 h,

https://www.twirpx.org & http://chemistry-chemists.com

then the precipitate was separated by repeated washing in ethanol and then annealing for 2 h. The formed nanoparticles were employed for phthalic acid degradation.

For the preparation of the Cu_2O/CeO_2 nanocomposite, N_2H_2OH was dissolved and added to a solution containing $Ce(NO_3)_3.6H_2O$ and $Cu(NO_3)_3.3H_2O$ [127]. The mixture was then kept in an ultrasonic reactor. The precipitate was washed several times and dried for 12 h at 60°C. The synthesized nanostructured powder was used for photocatalytic oxidative desulfurization.

Ultrasonic treatment of 1 h of a stirred equimolar combination of NH_4VO_3 and $Bi(NO_3)_3$ solution results in the formation of yellow precipitate of $BiVO_4$ crystals, which was then centrifuged, washed, and dried for 10 h [128]. Synthesis of Bi_2WO_6 nano laminar was prepared by dissolving H_2WO_3 and $Bi(NO_3)$ in the presence of an NH_4OH solution to maintain the pH at 7 [129]. The complete solution was sonicated for 3 h. The precipitate was calcined at 500°C for 2 h. Finally, the precipitate was centrifuged, washed in ethanol: water, and dried at 50°C in an open atmosphere. Both $BiVO_4$ crystals and Bi_2WO_6 nano laminar were applied for visible light activity.

Equimolar solutions of $Yb(NO_3).6H_2O$ and NH_3VO_4 were stirred in DDW and the solutions were kept in the ultrasonic reactor and then collected, washed, dried, and calcined for 5 h at 500°C to get $YbVO_4$ powder [130]. For the preparation of $YbVO_4/CuWO_4$ the previously prepared $YbVO_4$ nanopowders were well mixed with the equimolar concentration of $Cu(NO_3)_2$ and Na_2WO_4 and transferred for sonication. The final precipitation was centrifuged, washed, dried, and calcined at 500°C for 1 h. Finally, prepared nanocomposites were applied for photocatalytic oxidation of organic dyes.

Precursors such as bismuth nitrate, concentrated nitric acid, titanium isopropoxide, and silver nitrate were used for the preparation of the Ag-modified $Bi_4Ti_3O_{12}$ nanoparticles [131]. An adequate amount of bismuth nitrate was dissolved in nitric acid, to which the aqueous suspension of titanium isopropoxide and the stoichiometric amount of silver nitrate was added, and the complete mixture was transferred to the ultrasonic reactor. The precipitate was then collected, washed, and dried at 700°C for 3 h to get the powder, which showed photocatalytic activity.

The advantages of the sonochemical method are as follows: (i) this method is relatively simple, quick, and easy; (ii) the synthesis of the visible light photocatalysts takes place at an ambient temperature; and (iii) the rate of reaction is very high, meaning that it takes less time to finish.

The disadvantages of the sonochemical method are as follows: (i) materials, which are prone to heat, cannot tolerate acoustic cavitation; (ii) it is difficult to scale up; (iii) this method is an energy-intensive process; and (iv) the nanoparticles harvested per unit energy supplied are very low.

2.1.13 Microemulsion method

In 1959, Schulman and coworkers [132] introduced the term "microemulsions" when they titrated a stable course emulsion (i.e., aliphatic or aromatic hydrocarbons, an anionic surfactant, cosurfactants, and an aqueous phase) by adding a proper amount of cosurfactant which led to the formation of the microdroplets with a diameter between 600 and

https://www.twirpx.org & http://chemistry-chemists.com

8000 nm. Therefore, because of these macroemulsion characteristics, micro-solutions were known as critical solutions and not real emulsions, but they behave as real solutions.

In addition, Schulman et al. suggested that when the optimum ratio of surfactant and cosurfactant is mixed together, this results in interfacial pressure at the interface of oil/water, which exceeds the initial interfacial tension, and as a result microemulsions are formed. Controlling the interfacial phase with the help of a proper amount of cosurfactant deprived of using mechanical agitation produces visible light photocatalysts at the nano level.

Microemulsions are isotropic, thermodynamically stable dispersions of two immiscible liquids in the presence of a surfactant [133]. Surfactant molecules have a crucial role since they form an interfacial layer separating the polar and nonpolar domains. Some properties of microemulsions are as follows: (i) ultra-low interfacial tension; (ii) large interfacial area high surface energies that control the aggregation of the particles; and (iii) high solubility with both oil and water components.

Two prominent theories exist which can give the idea for the synthesis of the nanoparticles. The first is the LaMer diagram (a plot that shows the concentration variation with time; reported by Sugimoto et al. [134]). As the concentration increases and reaches the critical or supersaturation state, nucleation (region between C_{min} and C_{max}) starts occurring. The phase of nucleation proceeds until the solution reaches its solubility limits; this then offers the direction of growth of the particles by diffusion, shown as a decrease in the concentration with time. The other model is based upon the thermodynamic stabilization of the nanoparticles by the surfactant. In this model, continuous occurrence of nucleation is taken into account.

Microemulsions can be classified into three categories [135]:

(a) oil-in-water (O/W) microemulsions;
(b) water-in-oil (W/O) microemulsions;
(c) supercritical CO_2 microemulsions.

(a) Oil-in-Water (O/W) Microemulsions

This kind of emulsion can be formed where the drops of water are dispersed homogeneously in the continuous phase of oil with the help of a surfactant. A mixture of ionic and nonionic surfactant is used which increases not only the range of temperature but also solubilization power. On increasing the pH, growth of O/W microemulsion becomes faster; this is due to the formation of the double layer at the interfacial boundary. The O/W system, also called micelles, was used to carry organic compounds of lipophilic solutes within the aqueous environment. During their motion, these micelles collide with each other which results in the interchange of these reactant precursors, which is then followed by the combination, hence resulting in the formation of the product.

(b) Water-in-Oil W/O Microemulsions

This emulsion can be achieved when the droplets of oil are dispersed in the continuous phase of water. For the synthesis of inorganic nanoparticles, W/O microemulsions are widely used. In the system of water-in-oil, when a surfactant molecule is added the

https://www.twirpx.org & http://chemistry-chemists.com

formation of the spheroidal aggregates takes place, which is termed as "reverse micelles," as suggested by Pileni et al. [136]. Another quantitative explanation given by Luisi et al. suggested that reverse micelles are the aggregates containing a small number of water molecules ($W^o < 15$; W^o = water/surfactant) [137]. However, if the aggregates contains a large number of water molecules ($W^o > 15$) then they are called "microemulsions." Further, Luisi et al. define reverse micelles as "The polar head groups of the surfactant molecules in this type of microemulsions directed inside by aqueous core while the hydrocarbon tail directed outwards."

(c) Supercritical CO_2 Microemulsions

These microemulsions are achieved by using supercritical CO_2 as a solvent. Within the conventional W/O emulsions, the main drawback is the removal of the solvent from the products. Switching to supercritical CO_2 as a solvent for the preparation of microemulsions has numerous benefits such as fast reaction speed, quick separation, and easy isolation of the solvent.

For the preparation of rare-earth-doped Bi_2O_3, a reverse microemulsion approach was reported [138]. Two phases were prepared separately in one of phase particular amount of bismuth nitrate pentahydrate [$Bi(NO_3)_3.5H_2O$] and lanthanum nitrate hexahydrate [$La(NO_3)_3.6H_2O$]/ceric nitrate hexahydrate [$Ce(NO_3)_3.6H_2O$] dissolved together in a nitric acid solution; ammonium hydroxide solution is the other phase of the microemulsion. Both the phases were dropwise added into the reaction mixture of cyclohexane, Triton X-100, and n-hexanol with a specified quantity. The complete solution was stirred for 3 h and the solid particles were separated through centrifugation, followed by washing and calcination.

WCl_6 microemulsion and NH_4OH microemulsion were prepared individually by adding CTAB and isooctane [139]. Both the microemulsions were added and the reaction time was maintained for 1 day. Finally, the microemulsions were centrifuged, dried, and calcined at 450°C for 4 h.

An equal ratio of cyclohexane and n-hexylalcohol/polyethylene glycoltertoctylphenylether (TX-100) microemulsion was formed [140]. The reverse microemulsion was formed by adding a $Bi(NO_3)_3{\cdot}5H_2O$ solution under continuous magnetic stirring at room temperature. Another reverse emulsion was prepared by adding an NH_4VO_3 aqueous solution to the above microemulsion. Then the second microemulsion was added to the first microemulsion and stirred to produce a yellow microemulsion, which was then centrifuged, washed, and dried in air at 60°C for 12 h to form $BiVO_4$ nanoparticles.

For the preparation of Bi_2MoO_6 the microemulsion was composed of the mixture cyclohexane and polyethylene glycoltertoctylphenylether (TX-100)/n-hexylalcohol [141]. The two aqueous phases was prepared by mixing $Bi(NO_3)_3$ dissolved in an HNO_3 solution whereas the other solution was of $(NH_4)_6Mo_7O_{24}.4H_2O$. This solution was then dropped into the above prepared microemulsion. Intense stirring and agitation for 24 h was followed by centrifugation, washing, and drying via calcination.

The advantages of the microemulsion are as follows [142] [143]: (i) use of simple techniques; (ii) the ability to prepare a wide variety of materials with the high degree of control

https://www.twirpx.org & http://chemistry-chemists.com

over composition and particle size; (iii) the products are crystalline structure with high surface area; (iv) the preparation conditions for the synthesis are quite close to the ambient temperature and pressure; (v) the microemulsions are thermodynamically stable which improves the stability of the system; (vi) the microemulsion method leaves a very small chance of the formation of agglomerates as the end products; and (vii) there is good biodegradability and biocompatibility of the synthesized material.

The disadvantages of the microemulsions are as follows: (i) relatively high concentration of surfactants and cosurfactants are necessary; (ii) the stability of the microemulsions is compromised by the pH and temperature; and (iii) suspension become thinner on pouring out the microemulsion into water.

The processes of formation of different nanostructures through the abovementioned methods are summarized in Table 1.

2.2 Fabrication of thin films

Apart from the preparation of nanopowders, the fabrication of thin films over fluorinated tin oxide coated glass substrate (FTO), indium tin oxide coated glass substrate (ITO), glass, etc. is also frequently applied for visible light photocatalysts. Some of them are described in this section.

2.2.1 Electrophoretic deposition

The electrophoretic deposition (EPD) process was first reported in the 19th century, whereas its practical applications were found when the thoria particles were deposited over the platinum electrodes mentioned in the reports presented by Besra et al. [144]. In general, electrophoretic deposition is a two-step process dealing with electrophoresis and deposition. In the electrophoresis step, the charged particles in the suspension migrate toward an oppositely charged substrate due to the applied electric field, whereas in the second step, coagulation of the charged particles takes place to create a coherent and homogeneous coating over the surface of the conducting electrode [145]. Depending upon the electrode, deposition needs to occur; therefore, electrophoretic deposition is divided into the following categories (i) anodic electrophoretic deposition; and (ii) cathodic electrophoretic deposition. Property-wise there is a basic difference between electroplating and electrophoretic deposition which can be understood as follows [146, 147]: (a) nature of the mobile species, i.e., ions for the electroplating and solid particles for the electrophoretic deposition; (b) conductance of the liquid medium is high for electroplating; and (c) low for the electrophoretic deposition and the preferred liquid is water for the electroplating and organic solvent for electrophoretic deposition.

The deposition of CuO over the ITO has been reported by Singh et al. for this first solution, which was prepared by dissolving the particular amount of nitrate salt of copper [148]. A three-terminal system was used in which ITO acted as a working electrode whereas platinum sheet and Ag/AgCl were termed as counter and reference electrodes, respectively. The deposition was carried for a specific time and soon after the films were annealed to get CuO nanostructured thin film, which was then used for nonenzymatic glucose sensing.

https://www.twirpx.org & http://chemistry-chemists.com

Table 1 Preparation of nanopowders. List of the nanostructured powders with their complete preparative parameters.

Sl. No.	Synthesis Method	Material used	Parameters	Product	Ref.
1	Precipitation	$Na_2WO_4.2H_2O$ (1 mmol) + aline + glycine + asparagine + $Mn(NO_3)_2.3H_2O$ (1 mmol)	Mixed the aqueous solution Heat up to 80°C for 10 min Brown ppt, centrifuged and washed in DI water + methanol Dried at 80°C for 10 min	$MnWO_4$ nanoparticles	[17]
		Bi $(NO_3)_3.5H_2O$ + KI + ethylene glycol + dropwise $MnWO_4$ NPs	Stirred for 4 h at RT Washed in DI water + ethanol Dried at 80°C for 24 h	$MnWO_4$/BiOI composite	
2	Precipitation	0.5 g $AgNO_3$ + DI + 40 mL of Na_2HPO_4 (0.03 M)	Stirred for 4 h under dark Centrifuged for 5000 rpm Washed with DI and ethyl alcohol Dried at 60°C for 12 h	Ag_3PO_4 nanoparticles	[18]
3	Precipitation	0.1 M Cu $(NO_3)_2$ + DI + curcumin + 3 mL 0.1 M NH_3	pH 11.7 Stirred for 1 h Stirred and heated in oil bath at 65°C for another 2 h Centrifugation and separation of precipitate Washed in DI water + ethanol Dried in vacuum at 50°C at the pressure 550 mmHg for 24 h	Curcumin-CuO nanoparticles	[19]
		Curcumin-CuO NP + 0.01 M $AgNO_3$	Agitated in a thermostatic water bath for 24 h (at 35°C) Addition of 0.5 mM of NaOH Mild heating with stirring at 40°C for 24 h Washed in DI water + ethanol Dried in vacuum at 50°C at the pressure 550 mmHg for 24 h	Curcumin-CuO/Ag nanoparticles	
4	Coprecipitation	5 g bamboo derived biochar + 5 mg CTAB + 100 mL DI water	Orbital shaker for 30 min Addition of 2.5 g of Fe_3O_4 Stirred vigorously for 1 h	Fe@BAB nanocomposite	[22]
		5 g Fe@BAB nanocomposite + 100 ethanol + 0.24 M $AgNO_3$	Mixture was agitated at RT for 12 h Dropwise addition 0.08 M of the $Na_2HPO_4 \bullet 12H_2O$ 1 h stirring Washing in DI water Drying in a vacuum oven	Ag-Fe@BAB nanocomposite	

https://www.twirpx.org & http://chemistry-chemists.com

5	Sol-gel	**Solution A**: 0.03 M ($Bi(NO_3)_3{\cdot}5H_2O$) + 50 mL of 4 M HNO_3 **Solution B**: 0.03 M (NH_4VO_3) + 50 mL of 4 M NH_4OH deionized water	Mixed Solution A and B for 30 min Addition of 100 mL of ethanol Stirred and heated at 70°C for 1 h Yellow sol is prepared Addition of 50 mL DI + 5 mL of 1 M acetic acid (CH_3COOH) Drying of gel at 100°C for 48 h Drying and calcination at 400°C for 2 h	$BiVO_4$ nanoparticles	[25]
6	Sol-gel	2.5 g of pluronic F-127 + 7 mL acetic acid + 0.8 mL HCl +50 mL CH_3CH_2OH + 0.1368 g $CdCl_2{\cdot}2.5H_2O$ + 20 mL Na_2SeSO_3 (0.02 M)	Heating 12 h at 40°C Materials were treated at 320°C for 4 h Rate of 1°C min^{-1} for heating Cooling processes to eliminate the F127 and to obtain highly crystalline CdSe	CdSe nanoparticles	[26]
7	Sol-gel	$Cu(NO_3)_2.3H_2O$ + $Cr(NO_3)_3.9H_2O$ + DI + sucrose	Stirred for 1 h Addition of NaOH (adjust pH) Washing several times with the various solvent Vacuum drying	$CuCr_2O_4$ nanoparticles	[27]
8	Sol-gel (pechini)	Manganese nitrate + lithium carbonate + DI water + EDTA solution	The ratio of M:EG:CA used was 1:1:1, that M is the sum of metal ions of Mn and Li Addition of NH_3 solution (adjust pH) Heating at 80°C Gel was placed in an oven at 100°C for 4 h Calcination at 700°C for 4 h	Li_2MnO_3 nanostructures	[28]
9	Sol-gel	0.1 M $La(NO_3)_3.6H_2O$ + 0.1 M $Fe(NO_3)_3.9H_2O$ + 0.2 mol citric acid	Stir to homogeneous Stir with heating 60–70°C pH 6–7 Nitrate-citrate sol Slow heating to 130°C $LaFeO_3$ dry gel Calcined at 500–900°C for 2 h	$LaFeO_3$ nanoparticles	[29]
10	Sol-gel (ultrasonic)	4.0399 g $Fe(NO_3)_3.9H_2O$ + 1.0582 g $Sr(NO_3)_2$ + 4.8035 g citric acid + DI water	Solution was stirred at 60–70°C Addition of ethylene glycol, to the mixture with a proportion (in mass) of citric acid/ethylene glycol = 60:40 pH 3 by using NH_3 solution Stirring for 30 min Addition of 0.4 g of thiourea Ultrasonic irradiation gel Calcination at 700°C for 8 h @ of 6°C min^{-1})	Rugby shaped—$SrFe_2O_4$	[30]

Continued

https://www.twirpx.org & http://chemistry-chemists.com

Table 1 Preparation of nanopowders. List of the nanostructured powders with their complete preparative parameters—cont'd

Sl. No.	Synthesis Method	Material used	Parameters	Product	Ref.
11	Sol-gel	**Solution A**: 3.843 g C6H8O7 was added to the 5.145 g $Bi(NO_3)_3$ solution+20 mL HNO_3(1 mol L-1) + 80 mL DI water	Both solution pH 7 Mixing of both solution Water bath for 6 h Drying Ashing	Molybdenum-doped $BiVO_4$	[31]
		Solution B: 1.182 g NH_4VO_3 and 3.843 g $C_6H_8O_7$ dissolved in 100 mL DI water to adjust the concentration to 0.1 molL-1	Grinding the powders $BiVO_4$ is impregnated in molybdic acid with different loading levels 0.64 wt% and 1.62 wt% Calcined at 375°C		
12	Sol-gel	2.1653 g $La(NO_3)_3{\cdot}6H_2O$ + 2.1467 g $Zr(NO_3)_4{\cdot}5H_2O$ + 2.5217 g citric acid	1.335 mL ethylene glycol was added dropwise pH 2.78 Heating at 70°C for 4 h in a water-bath to become collosol Dried at 125°C for 6 h Heating rate of 10°C·min^{-1} to 800°C for maintaining 1 h	$La_2Zr_2O_7$ white powder is obtained	[32]
13	Sol-gel	Solution A 0.2 g of $Bi(NO_3)_3.5H_2O$ + DI + few drops of nitric acid +5 mL of aqueous solution of tannic acid Solution B 0.1 g of $Cu(NO_3)_2.6H_2O$ + 0.05 g of NH_4VO_3 salt+ tannic acid	Solution A + Solution B Add a few drops of ethylenediamine pH 9 Aqueous Cu solution was added to the mixture Final solution was placed for heating at 100°C for 2 h Oven-dried for 4 h at 80°C Powder was calcined at 750°C for 2 h Desulfurization	Cube-like Cu/Cu_2O/ $BiVO_4$/Bi_7VO_{13}	[33]
14	Sol-gel	BCN (1 g) in 100 mL water+0.46 g of $NiCl_2$ + 1.62 g of $FeCl_3{\cdot}9H_2O$	Dispersion by stirring pH 13 using 3 M NaOH Stirring for 1 h at 80°C Dried at 90°C Calcination for 3 h at 450°C @ 5°C min^{-1}	Boron-doped C_3N_4/ $NiFeO_4$ nanocomposite	[34]

https://www.twirpx.org & http://chemistry-chemists.com

15	Hydrothermal	equimolar amounts of $Ba(NO_3)_2$ + $Bi(NO_3)_3.5H_2O$ + 15 mL DI water	Adding solution of ammonium hydroxide pH 8 Autoclave was maintained at 150°C for 6 h Centrifugation and washed with DI Dried at 80°C Annealing at 800°C during 24°C	$BaBiO_3$ perovskite powder	[39]
16	Hydrothermal	Na_2GeO_3 + $Zn(NO_3)_2{\cdot}6H_2O$ with a molar ratio of 1:1 + 25 mL of DI water	Stirring for 20 min Addition of 2.5 mM of HMT Stirring for 30 min at RT Autoclave was maintained at 100°C for 12 h Filtered and washed DI water+ethanol Drying at 60°C under reduced pressure overnight	Zn_2GeO_4 white powder	[40]
17	Hydrothermal	Solution A 3 mM of $Bi(NO_3)_3{\cdot}5H_2O$ (1.46 g) + 9 mL acetic acid Solution B 1 mM of niobium oxalate (0.54 g) + 40 mL methanol	Mixing Addition of 20 mL benzyl alcohol 1.68 g urea was added into the mixture pH 13 using KOH solution Autoclave was maintained at 180∘C for 24 h Washing in DI water+ethanol Drying at 60°C for 6 h	Bi_3NbO_7 porous nanosheets	[42]
18	Hydrothermal	0.4492 g $Bi(NO_3)_3{\cdot}5H_2O$ + 0.1083 g NH_4VO_3 by 1:1 M ratio + 20 mL and 10 mL 4.0 M HNO_3 two aqueous solutions were formed	Mixing of two solutions SDBS (0.1250 g) was added pH 6.0 using 2.0 M NaOH Stirring for 30 min Autoclave was maintained at 200°C for 4 h Centrifuged and washed Dried at 80°C for 12 h	2-D graphitic carbon nitride/bismuth vanadate	[44]
19	Hydrothermal	0.9 g of as-prepared g-CN + lanthanum nitrate hydrate +12 mL of ammonia solution (0.35 M)	Sonicated for 1 h Autoclave was maintained at 150°C for 6 h in an oven Washed in DI water+ethanol Dried in vacuum oven at 100°C for 3 h	La_2O_3-modified graphite carbon nitride (g-CN)	[45]
20	Hydrothermal	1 M of WCl_6 + 65 mM of C_2H_5NS + 50 mL of ethanol +25 mL DI water+5 mol/L HCl	pH 2–2.5 Stirred for 1 h at RT Autoclave was maintained at 190°C for 24 h Centrifuging, washed through DI water+ethanol Vacuum drying at 140°C for 6 h	Few-layer WS_2 and e-WS_2	[47]
		2 mM of Bi $(NO_3)_3{\cdot}5H_2O$ + 3 mM of $Na_2S{\cdot}9H_2O$ + 25 mL of DI water+20 mL of HCl	Stir Autoclave was maintained at 190°C for 24 h Centrifuging at 8000 rpm Washing DI water+ethanol Vacuum drying at 120°C for 8 h	1D Bi_2S_3 nanorod/2D e-WS_2 nanosheet	

Continued

https://www.twirpx.org & http://chemistry-chemists.com

Table 1 Preparation of nanopowders. List of the nanostructured powders with their complete preparative parameters—cont'd

Sl. No.	Synthesis Method	Material used	Parameters	Product	Ref.
21	Solid state	Pr_6O_{11} (weight %) + 5 g of melamine	30 min grinding Transferred into alumina crucible with lid Annealed at 520°C with heating rate of 20°C min^{-1} in air	Pr_6O_{11}/g-C_3N_4	[50]
22	Solid state	10 mM $AgNO_3$ + 5 mM Na_2CO_3	Grinding for 1 h Washed by DI water three times Dried under for 12 h	Ag_2O/Ag_2CO_3	[51]
23	Combustion	$C_2H_2O_4.2H_2O$ + DI water+$(NH_4)_6W_{12}O_{39}.xH_2O$ solution	Mixing to form the precursor solution Ignition+suspended powders Washing with ethanol	WO_3 powders	[59]
24	Combustion	$Y(NO_3)_3.6H_2O$ + $Fe(NO_3)_3.9H_2O$ + glycine+DI water to form the precursor solution with the ratio of 1:1:1–1.7:30	Crucible on hot plate for 250°C Stirring Ignition Light brown product	Nanocrystalline yttrium iron oxide	[60]
25	Combustion	Solution A 2 mM $Bi(NO_3)_3{\cdot}5H_2O$ + 2 mL 2 M nitric acid Solution B 1 mM $Na_2WO_4{\cdot}2H_2O$ + glycine+30 mL DI water	Mixing of solutions Stirring in hot plate for 200°C Ground in a mortar Washed with DI water Dried at 60°C in air for 12 h	Bi_2WO_6 nanoparticles	[61]
26	Combustion	0.005 M $Bi(NO_3)_3{\cdot}5H_2O$ + 0.0038 M $C_4H_6O_6$ + 30 mL nitric acid (4 mol/L)	Stirred and transferred to a muffle furnace and heated at 500°C for 30 min Transformation of solution into a viscous gel Heating, evaporation, self-ignition, combustion, and flame	Fine powder of $Bi_5O_7NO_3$	[62]
		0.005 M $Bi(NO_3)_3{\cdot}5H_2O$ + 0.0038 M $C_4H_6O_6$ + 30 mL nitric acid (4 mol/L) + $Ag(NO_3)$	Adding $AgNO_3$ into the above reaction system and following the similar synthesis procedure	$Ag/Bi_5O_7NO_3$	

https://www.twirpx.org & http://chemistry-chemists.com

27	Combustion	0.05 M (3.806 g) thiourea + 0.01 M (2.975 g) zinc nitrate hexahydrate + 0.02 M (8.080 g) Iron (III) nitrate nonahydrate + 0.02 M (1.491 g) KCl	Dissolved in acidic water (pH 4) adding HNO_3 to distilled water Stir at 80°C for 45 min Again stir at 325°C Heating until a viscous gel formed Boiling in about 400 mL of distilled water Magnetic separation and dried at 80°C	$ZnFe_2O_4$-ZnS nanostructure powders	[63]
28	Combustion	20 mg of the prepared g-C_3N_4 + 50 mL ethanol + 20 mL DI + H_2SO_4 + CuO/ZnO heterostructure	The ratio of Cu:Zn:C was 0.1:1:5 Sonication for 1 h Stirring for 24 h Centrifugation Washing with DI water Dried at 120°C on a hot plate	ZnO-CuO/g-C_3N_4 heterostructure	[64]
29	Combustion	$Eu(NO_3)_3$ was + stoichiometric amount of magnesium nitrate + ferric nitrate + DDW with required amount of ODH fuel	$MgFe_2O_4$: Eu^{3+} (0.1 mol%) The mixture was placed in a preheated furnace regulated at a temperature of 350 ± 10°C A brown fluffy product which on slight touch gets converted into brown powder	Eu-doped $MgFe_2O_4$ nanomaterials	[66]
30	Combustion	$Fe(NO_3)_3$ + $La(NO_3)_3$ + $RuCl_3$ + DI water	Stirred for 5 h at 60°C pH 7 of the above solution was maintained by adding ammonia solution Dried and calcined at 300°C for 3 h Addition of tetraethyl orthosilicate, ethanol, and ammonia solution Stirring of mixture for 12 h Centrifuged at 5000 rpm Calcined at 450°C for 30 min	Ru-doped $LaFeO_3$ photocatalyst (Ru-$LaFeO_3$)	[67]
31	Spray Pyrolysis	0.01 M ($Cd(CH_3CO_2)_2$) + 0.01 M ($SC(NH_2)_2$ + Molar concentration $HAuCl_4$ to form precursor solution	Au-CdS precursor solution was sprayed in the CoSP reactor at spray rate of 2.0 mL/min Nitrogen as carrier gas at a pressure of 2.0 kgf/cm^2 with flow rate of 6 l/min The temperature profile set as: first zone at 400°C, second zone at 750°C, and third zone at 350°C Nanoparticles were collected and dried in vacuum oven at 60°C overnight	Au-CdS hybrid nanoparticles	[76]
32	Spray pyrolysis	CNTs dispersion into the $Cu(CH_3COO)_2$ aqueous solutions (1.0 g/L)	Stirred at RT for 30 min Atomized to droplets by the ultrasonic nebulizer (25 W, 20 MHz) Flow rate (150 mL/min) into tubular reactor were solvent evaporation, solution precipitation, precursor decomposition, and calcining	CNTs/Cu_2O-CuO composite powder	[77]

Continued

https://www.twirpx.org & http://chemistry-chemists.com

Table 1 Preparation of nanopowders. List of the nanostructured powders with their complete preparative parameters—cont'd

Sl. No.	Synthesis Method	Material used	Parameters	Product	Ref.
33	Spray pyrolysis	10 mM zinc (II) nitrate hexahydrate ($Zn(NO_3)_2{\cdot}6H_2O$) + 10 mM tungstic acid (H_2WO_4) + ammonia solution +10 mL DI water	Mixing of solution Dilution to 100 mL with deionized water Solution was nebulized using an ultrasonic nebulizer at 1.7 MHz ± 10% Aerosol droplets generation at a tube furnace at 700°C by an air flow Washing with ethanol and DI water Drying at 70°C	$ZnWO_4$ microspheres	[78]
34	Flame synthesis	2.5 mL niobium pentaethanolate+17.5 mL ethanol is made to create the ratio of NPE/ethanol as 1:7	Stirring Ignited by a lighter Combustion with yellow flame for 20 min Ash was generated Annealed at 550°C for 2 h	Carbonaceous Nb_2O_5	[84]
35	Flame synthesis	Organic precursors of carbon (almond flames, mustard oil, Indian ghee, and burnt almond char)	Burning all precursors on neat and clean metallic surface Precursors soot deposited on metallic surface Collected by scratching Purification process in centrifuge tube Washing in ethanol Collection by centrifugation at 5500 rpm Drying at 50–55°C for 3–4 h	Carbon nanoparticles	[85]
36	Electrospinning method	Ratio is 1:10:5.4 $Fe(NO_3)_3{\cdot}9H_2O$ is+DMF + PVP (MW = 58,000) solution	Stirring at RT for 12 h Solution loading = 5 mL syringe Potential of the tip = 20 kV Tip-to-collector distance is 15 cm Calcined at 650°C for 3 h @ 1°C/min	Porous α-Fe_2O_3 hollow spheres	[92]
		Ratio is 1:10:1.8 $Fe(NO_3)_3{\cdot}9H_2O$ is+DMF + PVP (MW = 1,300,000) solution	Solution loading = 5 mL syringe Potential of the tip = 20 kV Tip-to-collector distance is 15 cm Calcined at 650°C for 3 h @ 1°C/min	α-Fe_2O_3 nanofibers	
37	Electrospinning method	0.485 g (1.0 mM) of $Bi(NO_3)_3{\cdot}5H_2O$ was dissolved in 8 mL of DMF + 6 mL acetic acid+0.265 g (1.0 mM) $VO(acac)_2$ + 8 mL absolute ethanol+2.0 g PVP (Mw ≈ 1,300,000)	Stirring overnight Solution loading in syringe Inner diameter of syringe needle = 0.901 mm Potential of the tip = 16 kV Tip-to-collector distance is 14 cm Feeding rate was controlled as 0.4 $mL{\cdot}h^{-1}$ Humidity level is 25% RH Calcinated at 500°C in air for 30 min @ 2°C min^{-1}	$BiVO_4$ nanofibers	[94]

https://www.twirpx.org & http://chemistry-chemists.com

		2 mM $Bi(NO_3)_3$ and 1 mM NH_4VO_3	Stirring overnight Solution loading in syringe Electrospun Calcinated at 500°C in air for 30 min @ 2°C min^{-1}	$Bi_4V_2O_{11}$ nanotubes	
		1.5 mM $Ni(NO_3)_2$ + 1 mM $VO(acac)_2$	Stirring overnight Solution loading in syringe Electrospun Calcinated at 500°C in air for 30 min @ 2°C min^{-1}	$Ni_3V_2O_8$ nanotubes	
38	Electrospinning method	PET pellets+DCMTFA-IL solvent system at a mass ratio 2:2:1. PET crystals	Collection with an Al foil on a steady plate collector Applied voltage of 50 kV Tip-to-collector distance = 18 cm Feed rate of 5 mL/h	PET fibers	[95]
		Methanolic solution+0.10 M cadmium acetate in 0.015 M IL + 0.03 M sodium sulfide in 0.015 M IL	Sonicated for 60 min at 60°C PET fibers in the precursor solution prior to sonication	CdS/PET	
39	Electrospinning method	1.21 g of $Bi(NO_3)_3.5H_2O$ + 0.7 g of PVP + 0.662 g of $VO(acac)_2$ + solvent of 2.0 g of acetic acid+2.5 g of ethanol+2.5 g of DMF	Stirred for 6 h to form a homogeneous solution Loading of solution in syringe Feeding rate of 8 μL min^{-1} (through syringe pump) Applied voltage of 9 kV Tip-to-collector distance = 15 cm High temperature of 500°C for 2 h @ 5°C min^{-1}	$BiVO_4$ nanofibers were formed with a yield of 39.1%	[96]
		60 mg of $BiVO_4$ nanofibers+40 mL of 1 mM $Cd(CH_3COO)_2$ aqueous solution	Centrifuge tube and slowly turned for 60 min by a rotary mixer 10 mL of thiourea (1 mM) solution was added Incubation for another 30 min Mixing and heating at 90°C for 2.5 h Dried at 70°C	$BiVO_4$/CdS hybrid nanofiber	
40	Electrospinning method	Solution 1 2.500 g (11.9 mM) citric acid was dissolved into 20 mL DI water+0.442 g (0.357 mM) $(NH_4)6Mo_7O_{24}{\cdot}4H_2O$ + 2.425 g (5 mM) $Bi(NO_3)_3{\cdot}5H_2O$ + 4 mL concentrated nitric acid (15 M)	Mixing 0.8 g PVP (K-90) in Solution 3 Sols were obtained after stirring for 10 h	1D α-Fe_2O_3/Bi_2MoO_6 nanofibers	[97]
		Solution 2 0.505 g (1.25 mM) $Fe(NO_3)_3{\cdot}9H_2O$ + *Solution 1* Solution 3 2 mL *Solution 2* + 1 mL conc. HNO_3 solution were + 10 mL absolute ethanol	Transferred into a 20-mL plastic syringe 1 mm inner diameter of syringe Potential applied 18 kV Propelled with the speed of 2.27 mL/h Tip-to-collector distance = 15 cm Dried in an oven at 70°C for 12 h Calcination at 500°C for 2 h		

Continued

https://www.twirpx.org & http://chemistry-chemists.com

Table 1 Preparation of nanopowders. List of the nanostructured powders with their complete preparative parameters—cont'd

Sl. No.	Synthesis Method	Material used	Parameters	Product	Ref.
41	Chemical vapor deposition	0.1 g $WO_{2.9}$ powder was taken in alumina boat	The furnace was 30 cm long uniform temperature zone of 10 cm Alumina boat was placed in the uniform temperature zone Silicon (100) wafer was placed at the low-temperature zone Pressure is 70 mTorr H_2 (10 sccm) System pressure = 300 mTorr The furnace was heated to 900°C @ 20°C min^{-1} After 1.5 h, the temperature decreased gradually to RT	WO_3 nanobelts	[99]
42	Chemical vapor deposition	6.0 g of melamine powder was placed in the bottom of the alumina crucible (50 mL) + 2.0 g of KIT-6 template	First heat treatment at 320°C for 4 h with a heating rate of 10 K/min Temperature increased to 550°C for 3 h @ 2 K/min Removal of silica by HF	Mesoporous g-C_3N_4	[100]
43	Chemical vapor deposition	1.0 g commercial $SrTiO_3$ nanoparticles (99.5%, Aladdin) were put into the quartz tube	Temperature was raised to 1050°C at a rate of 20°C min^{-1} 20 sccm H_2 diluted in 100 sccm Ar was introduced to the reactor Temperature was 1050°C for 20 min with the mixture gas flow of 5 sccm CH_4, 20 sccm H_2 and 100 sccm Ar Colling in the RT the flow of 100 sccm Ar and 20 sccm H_2	$SrTiO_3$/graphene	[101]
44	Microwave assisted	100 mg of the complex, in 30 mL ethylene glycol	Stirred for 1 h and transferred to microwave vessel Maintained at 180°C Pressure = 12 bar Time = 5 min under microwave irradiation Power = 50 W Addition of ethanol Centrifuged Washing thoroughly with ethanol Drying in air	Star-shaped Bi_2S_3	[109]

https://www.twirpx.org & http://chemistry-chemists.com

45	Microwave assisted	3 mM CuCl + 3 mM $FeCl_3 \cdot 6H_2O$ + 6 mM citric acid + 7.5 mM + 40 mL distilled water	Stirring for 1 h The solution was placed in a microwave oven heated at 200°C, 1400 W and 7 min Filtered and washed with hot distilled water Dried under vacuum	$CuFeS_2$ powders	[110]
46	Microwave assisted	20 mM $ZnCl_2$ solution + [ethanol + 20 mM stannous chloride + 5 mL TEA] + [160 mM NaOH + DDW]	Constant stirring Microwave radiation (600 W) for 15 min Centrifugation Washed in DI water + ethanol Drying in hot air oven at 60°C Post annealed at 700°C for 5 h	Zn_2SnO_4 nanorods	[111]
47	Microwave assisted	Solution A 0.79 g of $Bi(NO_3)_3.5H_2O$ + 10 mL of ethylene glycol Solution B 0.234 g of NH_4VO_3 + 10 mL of ethylene glycol	Mix Solution A + Solution B Stirred for 30 min pH was altered to 1 by HNO_3 Stirred for another 15 min Transferred to microwave reactor At 200°C for 12 min, for 300 W of irradiation Centrifugation Calcined at 500°C for 1 h	$BiVO_4$ powders	[113]
		Adding 1%, 3%, and 5% in wt of $(NH_4)_6H_2W_{12}O_{40}.xH_2O$ to the mixture of solutions A and B	Stirring for 30 min pH 1 using HNO_3 aqueous solution Stirring for 15 min Transferred to microwave reactor at 200°C for 12 min, using 300 W of irradiation Precipitate, centrifugation and calcined at 500°C for 1 h	W-doped-$BiVO_4$	
		0.142 g of $(NH_4)_6H_2W_{12}O_{40}.xH_2O$ + 3.24 g of oxalic acid in 9.6 g of ethylene glycol	200°C for 12 min, at 300 W of microwave irradiation Addition of 0.432 mL of the $BiVO_4$ precursor and W(X)-$BiVO_4$ Microwave irradiation for 12 min at 200°C, using 300 W Centrifugation and calcination at 500°C for 1 h	W-doped $BiVO_4/WO_3$ heterojunction	
48	Microwave assisted	10.0 g melamine + 0.01 g ammonium metavanadate NH_4VO_3 + 0.0216 g oxalic acid $C_2H_2O_4$ + 40 mL DI water	Stirred at 50°C to form a clear solution Evaporation to form solids Dried at 65°C for 24 h Ground and kept in the microwave for 40 min	VOx/g-C_3N_4 powder	[114]

Continued

https://www.twirpx.org & http://chemistry-chemists.com

Table 1 Preparation of nanopowders. List of the nanostructured powders with their complete preparative parameters—cont'd

Sl. No.	Synthesis Method	Material used	Parameters	Product	Ref.
49	Microwave assisted	8.06 g $Zn(NO_3)_2{\cdot}6H_2O$ + 2.97 g $Fe(NO_3)_3{\cdot}9H_2O$ + 50 mL of DI water for 1:2 ratio Addition of 1 g of MC (Methylcellulose)	Stirring pH 13 through addition of NaOH Stirring for 60 min at RT Transferred to microwave irradiation at 550 W External magnet was used to keep the magnetic solids Washing in DI water Drying at 100°C in a vacuum oven for 24 h	$ZnFe_2O_4$@MC nanostructures	[115]
50	Microwave assisted	Stoichiometric quantities of ferric nitrate + cobalt nitrate + magnesium nitrate + L-arginine + DDW	Stirring Poured into silica crucible and kept inside a microwave oven with microwave irradiation frequency at 2.54 GHz, for 10 min at 900 W Spontaneous combustion, ignition happened with a rapid flame and resulted in solid fluffy final products of $Co_{1-x}Mg_xFe_2O_4$ (x = 0 to 0.5) Calcined at 500°C for 2 h	$Co_{1-x}Mg_xFe_2O_4$ ($0 \leq x \leq 0.5$) spinel nanoparticles	[116]
51	Sonochemical method	0.2 g of $LaCl_3{\cdot}7H_2O$ and 0.21 g of $Fe(NO_3)_3{\cdot}9H_2O$ in 20 mL DDW separately	Mixed the solution Natural capping agents were added such as starch, corn, and rice; they were first ground and their flour was then dissolved in 20 mL hot DI water Ultrasonicated under condition, tetraethylenepentamin, ethylenediamine or ammonia added dropwise Washing by ethanol and water Dried at 70°C for 24 h Final calcination in different temperatures for 2 h	$LaFeO_3$ nanostructures	[124]
52	Sonochemical method	0.005 M of $Bi(NO_3)_36H_2O$ and NaI was dissolved in 100 mL deionized water	Mix well Slow addition of 3 M NaOH to maintain pH of 2–12 Ultrasonicated frequency = 35 kHz Bath temperature = 80°C for 5 h	BiOI nanoplates	[125]
53	Sonochemical method	Molar ratio taken as Cu: Zn: Sn: S (2:1:1:8) molar proportion	2 M of $CuCl_2$ added to 100 mL of 2-methoxyethanol for stirring for 30 min Addition of 1 M $ZnCl_2$ and stirring for 15 min 1 M $SnCl_2$ was added with stirring for next 15 min Addition of 8 M thiourea in monoethanolamine	CZTS nanoparticles	[126]

https://www.twirpx.org & http://chemistry-chemists.com

			Frequency = 40 kHz of sonication system Power = 40 W Transferred to ultrasonic bath for next 1.5 h Washed using absolute ethanol and then annealed at 160°C for 2 h		
54	Sonochemical method	**Solution A** 2 mL of N_2H_2OH + 20 mL of distilled water	Mix **Solution B** + **Solution A** Stirring and sonicated at 50 W/cm^3 for 15 min of solution A Final solution was put ultrasonic reactor for another 15 min	Cu_2O-CeO_2 nanocomposites	[127]
		Solution B 0.43 g of Ce $(NO_3)_3{\cdot}6H_2O$ and 0.3 g of $Cu(NO_3)_3{\cdot}_3H_2O$ were dissolved in 20 mL of distilled water	Precipitate was collected Washing in ethanol and distilled water Dried for 12 h at 60°C		
55	Sonochemical method	1 mM of $Yb(NO_3).6H_2O$ solution, namely, and 1 mM NH_3VO_4 solution	Stirred Exposed to ultrasonic radiation for 30 min For different ultrasonic power, and temperature Washed with distilled water three times Dried in vacuum at 60°C Centrifuged and dried Calcined in temperature 500°C for 5 h	$YbVO_4$ nanostructures	[130]
		1 mM $Cu(NO_3)_2.6H_2O$ + 1 mM $Na_2WO_4.2H_2O$ solution were made individually	Solution mix and added to dispersed $YbVO_4$ in 30 mL solvent Ultrasonic waves power = 320 W for 15 min Washed three times Drying and calcination at a temperature of 500°C for 1 h	$YbVO_4/CuWO_4$ nanocomposite	
56	Sonochemical method	**Solution A** $[Bi(NO_3)_3.5H_2O]$ + 5 mL HNO_3 + 20 mL nanopure water **Solution B** $[Ti(OPri)_4]$ + nanopure water	Mix **Solution A** and **Solution B** Fix pH 7 by adding ammonia solution Ultrasonic power = 100 W/cm^2 Operating frequency = 40 kHz For 90 min at RT Centrifugation and washing with DI water and ethanol Product was heated at 700°C for 3 h	$Bi_4Ti_3O_{12}$ nanostructures	[131]
		Solution A + **Solution B** + stoichiometric addition of silver nitrate Ag(x%) were x = 2 and 5	Complete parameters are kept same for the preparation of the Ag: $Bi_4Ti_3O_{12}$	Ag-modified $Bi_4Ti_3O_{12}$ nanostructures	

Continued

https://www.twirpx.org & http://chemistry-chemists.com

Table 1 Preparation of nanopowders. List of the nanostructured powders with their complete preparative parameters—cont'd

Sl. No.	Synthesis Method	Material used	Parameters	Product	Ref.
57	Microemulsion method	**Microemulsions** Cyclohexane, Triton X-100, and n-hexanol at a quality ratio of 15:6:4 as oil phase **Solution A** Bismuth nitrate pentahydrate + lanthanum nitrate hexahydrate + ceric nitrate hexahydrate with various molar ratios dissolved by appropriate amounts of 2.5 M nitric acid solution **Solution B** 7.0 M ammonia hydroxide solution	Stirring of **microemulsions** for 0.5 h **Solution A** and **Solution B** were dropped into the **microemulsion** individually to form **phase A** and **phase B microemulsion** Dropwise addition of **phase B microemulsion to phase A microemulsion** pH 10 Stirred for 3 h Centrifuge at 4000 rpm Washed with DI water and ethanol three times Oven dried for 80°C for 12 h Calcination for 3 h at 500°C Final products are ball milled	La-doped Bi_2O_3 and Ce-doped Bi_2O_3	[138]
58	Microemulsion method	**Microemulsion A** 0.16 M CTAB concentration and a given amount of isooctane + 0.48 mmol WCl_6 **Microemulsion B** 0.16 M CTAB concentration and a given amount of isooctane + 0.72 mmol NH_4OH	Mixing of **microemulsion B** and **microemulsion A** was maintained for 24 h with stirring at RT Methanol was added to the mixture Washed for 10 min three times Centrifuged Dried at 60°C Calcinated at 450°C for 4 h in air	WO_3 nanoparticles	[139]
59	Microemulsion method	**Microemulsion A** 6 g TX-100 and 6 g n-hexylalcohol into 12.0 g cyclohexane 5 mM of $Bi(NO_3)_3 \cdot 5H_2O$ + 10 mL of 4 M/dm^3 HNO_3 solution + 5 mM of NH_4VO_3 dissolved in 10 mL of 2 M/dm^3 NaOH solution	Mixing of **microemulsion B** and **microemulsion A** Stirring for 30 min under dry atmosphere Centrifuged	$BiVO_4$ nanoparticles	[140]

https://www.twirpx.org & http://chemistry-chemists.com

			Washing in DI water + ethanol		
		Microemulsion B	Dried in an oven at 60°C for 12 h		
		6 g TX-100 and 6 g n-hexylalcohol into 12.0 g cyclohexane + NH_4VO_3 aqueous solution	Calcination at 300°C, 400°C, 500°C, 600°C, and 700°C respectively for 1 h in air atmosphere		
60	Microemulsion method	Microemulsion A 5:3:2 weight ratios of cyclohexane: polyethylene glycoltertoctylphenylether(TX-100): n-hexylalcohol + 0.01 M of $Bi(NO_3)_3.5H_2O$ + 10.0 mL of 6.0 M/dm^3 HNO_3 solution	Mixing of microemulsion B and microemulsion A Stirring	Bi_2MoO_6 nanoparticles	[141]
		Microemulsion B 5:3:2 weight ratios of cyclohexane: polyethylene glycoltertoctylphenylether(TX-100): n-hexylalcohol + 0.714 mmol of $(NH_4)6Mo_7O_{24}.4H_2O$ dissolved in 10.0 mL H_2O solution	Aged for 24 h Centrifuged Washed with DI water + ethanol Dried at 100°C for about 2 h Calcination at 250°C, 350°C, 400°C, 450°C, 500°C, and 550°C respectively with a heating rate of 2°C min^{-1}		

https://www.twirpx.org & http://chemistry-chemists.com

$BiVO_4$ was also prepared by Wang et al., who used an acetone solution containing iodine and ground $BiVO_4$ powder [149]. The size of the FTO electrodes was 1.1 × 2 cm and these were immersed parallel with the Pt electrodes in the solution, keeping a distance of about 8 cm within the 20 V of bias condition for 1 min. A thickness of about 2 m with good reproducibility was achieved to analyze photocatalytic water oxidation.

The metal sulfides such as CdS nanoparticles were electrophoretically deposited on commercial aluminum plates with the dimensions 0.8 cm × 4 cm; they were separated by 1 cm [150]. Deposition was done for 24 h at the applied voltage of 600 mV. Soon after, the electrodes were removed from the colloidal suspension and kept at the same voltage for another 15 min. These coatings of CdS were used for the degradation of tetracycline antibiotics.

Zargazi et al. prepared Bi_2WO_6 films by anodic EPD on polished commercial stainless steel mesh substrates with specific dimensions [151]. Similar dimensions were used for the counter electrode, which was placed 15 mm in the electrophoretic cell where the EPD was performed at the DC power voltages from 30 to 70 V, which was then left to dry at room conditions. The films which were developed were then used for photocatalytic activity for oxidation of binary mixtures.

The preparation of $PbMoO_4$ coatings was done by dispersing 20 mg of the as-prepared nanoparticles in 20 mL of isopropyl alcohol and sonicated for 15 min [152]. The deposition was carried out by immersing two aluminum plates which were separated by 1 cm. About 12 V was applied for different time durations varying from 15 to 45 min. After deposition, the electrodes were kept for another 15 min standing time. The effect of variation of the applied voltages over photocatalytic performance was also reported by the authors, and the coatings were then applied for photocatalytic degradation of tetracycline.

The advantages of electrophoretic deposition are as follows: (i) EPD may deposit any particulate system (such as metals, polymers, ceramics, glasses, and biological entities combined) [153]; (ii) through the EPD process the possibility of easy control over the film thickness and morphology by simply adjusting depositing time and applied potential is high [154]; (iii) the thin film prepared by the EPD is very fast processing with high yield; (iv) EPD is a single-step process; and (v) no sophisticated instruments are required.

The disadvantages of electrophoretic deposition are as follows: (i) water as the liquid medium cannot be used since the application of voltage causes the evolution of hydrogen and oxygen gases at the electrodes that can severely affect the yield of the deposits formed; and (ii) in general, coatings of the electrophoretic technique have poor adhesion, which need posttreatment to improve adhesion [155].

2.2.2 Spin coating method

Spin coating is the method for preparing very thin film within the nanometer range [156]. The principle of the formation of thin film depends upon the centrifugal force. For synthesis, the glass substrates were mounted over apparatus called a spinner or chuck. The material solution was first dispensed over the substrate. When this chuck rotated, the excess precursor solution was flung off the substrate. Flat deposition of the film took place due to the viscous force and the surface tension of the liquid. The speed of spinning

https://www.twirpx.org & http://chemistry-chemists.com

and the viscosity of the solution are vital as they affect the thickness of the coated film [157]. For spin coating, four stages are essential: (a) deposition; (b) spin-up; (c) spin-off; and (d) evaporation.

Before the fabrication of Bi_2WO_6 thin films, the powder of Bi_2WO_6 was prepared in which particular amounts of diethylenetriaminepenta-acetic acid (H5DTPA) and ammonia water were added to hot distilled water [158]. The clear solution was then made by adding particular amounts of Bi_2O_3 powder and ammonium paratungstate powder. The colorless solution was then heated at 80°C. For spin coating, one drop of the above solution was dropped over the ITO glass while spinning at a high speed of 60 rps. Then curing was done for 48 h, and the leftover organic elements were eliminated by annealing at 500°C; The end products were used as visible light-active photocatalysts.

Particular stoichiometric amounts of the two different nitrate salts of Sr, and Ti were dissolved in separate beakers and mixed with stirring at 80°C for a specified time period, resulting in the formation of a viscous gel [159]. This gel was spin-coated over the substrate which was rotated at 2000 rpm for 0.5 h. Soon after, the films were dried for 10 min at 80°C. Finally, annealing was done 400°C for 4 h. Similarly, the group also doped barium by making $Ba(NO_3)_2$ as the starting solution to achieve a Ba-doped $SrTiO_3$ photocatalyst which was used for hydrogen generation.

The advantages of spin coating are as follows [160]: (i) very thin and uniform thickness of the film can be acquired; (ii) excellent technique on laboratory scale; and (iii) very quick and easy deposition of the thin film can be achieved.

The disadvantages of spin coating are as follows [161]: (i) limitation in the size of the substrates—substrates with large space spinning become difficult; (ii) the end product may have contaminants; (iii) thin film lower than 10 nm cannot be formed; and (iv) lower efficiency of the materials, as about 95%–98% of the materials gets flung off and the film deposition takes place with only 5%–2% of the material left.

2.2.3 Spray pyrolysis deposition

Spray pyrolysis deposition is an appropriate method of depositing both thick and thin films [162]. The atomizer, precursor solution, substrate heater, and temperature controller combine to form a spray pyrolysis unit. The atomizer is one of the key parts of this technique because it acts as the source of the liquid precursor in the chamber. Fundamentally, the atomizers are of three kinds: (a) air blast [163]; (b) ultrasonic [164]; and (c) electrostatic [165]. These atomizers have a spray nozzle from where the precursor solution is injected into the chamber. At a certain distance, the substrate is placed over the hot plate. The fine droplets of the injected precursor solution experience drying and decomposition as they reach the surface of the substrates. For even deposition of the film throughout the substrate, the nozzle keeps moving whereas the substrate is set firm. The precursor droplets, as soon as they are injected into the high-temperature chamber, undergo the following stages [166, 167]:

(1) solvent evaporation at the surface of the drop;
(2) drying of the solvent left with the precipitated solute;

https://www.twirpx.org & http://chemistry-chemists.com

(3) the precipitate which gathers over the surface of the substrate starts annealing (also called thermolysis);
(4) initialization of the formation of microporous particles with a particular phase composition;
(5) conversion of microporous particles into solid particles; and
(6) sintering of solid particles.

The quality and the characteristic properties, such as thickness, of the thin film grown through spray pyrolysis deposition depend upon three factors [168, 169]: (i) distance between nozzle and substrate; (ii) substrate temperature; and (iii) precursor concentration.

Initially, bismuth nitrate was added with ethylenediaminetetraacetic acid (EDTA) which was dissolved in an aqueous ammonia solution [170]. A suitable amount of NH_4VO_3 was dissolved in the ammonia aqueous solution under stirring and heating. Then the two solutions were mixed and stirred for 2 h, and the solution color was found to be yellowish. The substrate temperature was calibrated by fixing the surface temperature of the substrates. The other factors, such as the distance between hot plate and nozzle, the carrier gas (nitrogen, N_2) flow rate, the depth of the precursor solution, the velocity of the nozzle and the times of scanning motion, were all kept constant. In order to remove all organic solvents from the fabricated thin film, the substrates were kept at 500°C for 2 h. Soon after this, a hydrogen reducing treatment was carried out on the prepared $BiVO_4$ thin film substrates by annealing the substrates at 250°C in a hydrogen atmosphere. The thin film was used for photoelectrochemical studies.

The advantages of spray pyrolysis deposition are as follows [80]: (i) it is a cost-effective method; (ii) high-quality reagents are not required; and (iii) large-scale deposition with precise control of the film is possible.

The disadvantages of spray pyrolysis deposition are as follows [80]: (i) this process is low yield; (ii) difficulties in the determination of the growth temperature of the thin film; and (iii) not suitable for preparation of nonoxide-based materials such as chalcogenides.

2.2.4 Sputtering

Sputtering is a process whereby the thin film is deposited by the particle emission of the target which depends upon the collision of high-energy particles, which are mostly ions of the noble metals. Usually a sputtering system consists of a glow discharge where the plasma is created through the several hundred voltage into the vacuum chamber which is filled with noble gas maintaining a pressure of 1–10 mTorr. The deposition of the thin film takes place by applying the high voltage to the anode, which creates an electrostatic field inside the ion source. This results in the confining of electrons at the center of the source. As soon as the noble gas is injected into the chamber, it ionizes and creates plasma inside the source region. At the same time, the ions are accelerated from the anode to the cathode region. The generation of the ion beam results in the impingment over the target materials through the momentum transfer between the ion and target materials. As a result, the materials sputter over the sample.

https://www.twirpx.org & http://chemistry-chemists.com

Graphene was reported to grow over copper foil in a tubular furnace by Polat et al. [171]. The furnace was set at 1050°C with a heating rate of 25°C min^{-1}. The Cu surface was cleaned via annealing in the presence of hydrogen gas. As soon as the annealing was finished, methane gas was allowed to flow within the whole tube. The growth of graphene was done for 0.5 h and the system was cooled slowly without the presence of methane gas. Fe_2O_3 over graphene was prepared through magnetron sputtering, where the pressure inside the chamber was kept to around 6×10^{-6} mmHg. Then Ar was fed into the chamber. At the pressure level, 10^{-3} mmHg Fe_2O_3 coating was carried out with 70 W RF-power with a cooling rate of 0.2 Å per second. At the end of the sputtering, about 284.7 nm thickness of Fe_2O_3 was examined to obtain the graphene layer. The substrates were found to show activity at the visible region.

The advantages of sputtering are as follows: (i) thin film with defect coverage can be prepared; (ii) adhesion of the film is very good; (iii) wide variety of metals, alloys, and composites can be deposited; (iv) quality of the film with step coverage is better than the evaporation; (v) controlled reproducibility of the film is possible; and (vi) film deposition over the large substrate with a uniform thickness is possible.

The disadvantages of sputtering are as follows: (i) substrate damage due to ion bombardment; (ii) deposition rate of some materials is quite low; (iii) most of the incidents of the high-energy particles generate heat; and (iv) materials such as organic materials degrade due to ion bombardment.

2.2.5 Thermal evaporation

The thermal evaporation method can be classified as one of the forms of the physical vapor deposition technique. Thermal evaporation is the method by which we can fabricate thin films under a high vacuum environment at the typical pressure of 10^{-4} Pa. Principally, within this method the thin film formation is based upon the evaporation of the source material and then condensation and adhesion to the substrate surface. A typical thermal evaporation technique involves: (i) a vacuum chamber enclosed by a bell jar; (ii) a substrate holder; (iii) a hot filament which contains precursor powder; and (iv) a crystal monitor. Thin film deposition was carried out by passing a high voltage to the base. Since at the base the filament is connected with the boat, the source material gets evaporated due to heating. The substrate is kept at the opposite end of the source. Finally, adhesion of the source material over the substrate surface will take place.

In the report, tungsten wire was used as the filament which was hung by two copper electrodes at a height of 1 cm above the substrates [172]. Prior to the deposition, the substrate was exposed to hydrogen plasma with RF-power of 15 W for 10 min. Deposition took place at the fixed filament temperature of around 1000°C in the nitrogen atmosphere within the RF-power of 50 W at the pressure of 0.4 m bar and a temperature of 200°C to form as-deposited samples. The different heterojunction thin films such as InN/In_2O_3, WO_3/In_2O_3, and W_2N/In_2O_3 were synthesized by in situ thermal annealing of the as-deposited samples at the temperatures of 1300, 1400, and 1700°C, respectively, for 30 min to observe the different photoelectrochemical performances. The Cu_2CoSnS_4 thin

https://www.twirpx.org & http://chemistry-chemists.com

films were deposited by single-source thermal evaporation in a vacuum system at a pressure of 10^{-5} Torr [173]. The substrates were placed above the source at 15 cm. The as-grown samples were set for sulfurization in a quartz tube furnace held at 450°C for 2 h under a vacuum at the pressure of 10^{-3} Torr in a sulfur atmosphere to form a Cu_2CoSnS_4 thin film as the final product, which was prepared for photocatalytic applications.

The advantages of thermal evaporation are as follows: (i) it is simple and cheap; (ii) less substrate surface damage; (iii) excellent purity of films; (iv) the quartz crystal gives us the upper hand in terms of the extent of deposition; and (v) high deposition rates.

The disadvantages of thermal evaporation are as follows: (i) limited to low melting point metals; (ii) it is impossible to evaporate dielectric materials; and (iii) the filament limits the amount of material that is deposited.

2.2.6 Dip-coating method

Dip coating is an easy technique which involves the deposition of thin film via precise and controlled withdrawal of the substrate from the precursor solution at a constant speed [174, 175]. Dip coating is also known as impregnation and is commonly used to coat flat or cylindrical substrates as described by Joshi et al. [176]. Scriven elaborately described the five different stages of the dip-coating, as follows [177]: (i) immersion; (ii) startup; (iii) deposition; (iv) drainage; and (v) evaporation. To carry out fabrication of thin film through the dip-coating method, the precursor solution needs to be made in the organic solvent. As a result of this, the step-by-step process of draining and the evaporation of the solution lead to the formation of the thin film. At a glance, the complete process of the dip-coating method can be separated into basic three components:

(a) The substrates are immersed in the precursor solution where they get completely wetted.
(b) The substrate is withdrawn from the precursor solution. The speed of withdrawal of the substrate will affect the thickness of the film, as this results in the amount of the draining of the solvent solution.
(c) As the withdrawal happens, simultaneously the solvent gets evaporated, resulting in the film formation.

The physics behind the formation of thin film dip coating lies in the following forces [178]. As the substrate is lifted upward the viscous drag force appears on the liquid which results, due to the force of gravity, as a result of which the surface tension which occurs in a concave curved meniscus, at the same time due to the inertial force of the boundary layer liquid will start moving toward the deposition region, apart from this the surface tension gradient and disjoining or conjoining pressure as a whole leads to the formation of the thin film.

A γ-Bi_2MoO_6 film was deposited onto an indium tin oxide (ITO) substrate from an amorphous heteronuclear complex solution by the dip-coating method [179–181]. Ammonium molybdate was mixed with bismuth nitrate in DI water. Diethylenetriamine-pent acetic acid (DTPA) was added to the suspension so that the molar ratio was

https://www.twirpx.org & http://chemistry-chemists.com

maintained as 1:2. The solution was dried for the speculated time. For the dip coating, the ITO substrates were dipped into an aqueous solution and kept at 500°C in the air for 4 h. Before each experiment, the anode film was rinsed by Milli-Q water and the copper foil used as a cathode was rinsed by hydrochloric acid, cleaned with 800-grit sandpapers to remove any rust or solid deposits, and double rinsed with Milli-Q water; it was then applied for the degradation of diclofenac.

The advantages of dip coating are as follows [182, 183]: (i) low-cost method; (ii) the thickness of the film can be adjusted; (iii) Large-scale uniform deposition is possible; (iv) high-quality thin films can be fabricated; (v) unique advantages in the formation of the fibrous coatings; and (vi) thin film coated with this technique shows excellent adhesion and tribological performance.

The disadvantages of dip coating are as follows [184, 185]: (i) it is a very slow process; (ii) has characteristics to block the screen that effects in the final product; and (iii) high-temperature sintering over relatively thick films deteriorates the mechanical properties of the film.

2.2.7 Doctor blade method

The doctor blade method is a popular method which is employed to form a uniform thin film of liquid continuously into the moving webs [186]. In 1952, one patent was issued which emphasized the use of aqueous and nonaqueous slurries implemented to move plaster batts by the doctor blading technique [187]. To understand the preparation method for the formation of thin film, the synthesis of the precursor slurry is an important part [188]. The slurry is made by adding binders, dispersants, or plasticizers with the precursor salts. The precursor slurry was first dropped over the substrate and then a constant relative movement is made between the blade and the substrate. As a result, the spreading of slurry over the complete substrate surface will take place. Postdrying of the substrate leads to the formation of a gel layer. About 20 to several hundred microns of wet film thickness can be coated over the substrate and a speed of several meters per minute can be achieved. Many reports deal with the hybrid methods, which also include the formation of visible light photocatalysts in their powder form and then made thin films from the powder to address different further characterizations. The doctor blade method is a hybrid method.

Deepa et al. reported the formation of Cu_2ZnSnS_4 (CZTS) nanoparticles made through the solvothermal method [189]. Chloride salts of copper, zinc, and tin were dissolved in a mixture of oleic acid and 1-octadecane and heated to 170°C for 1 h until completely dissolved. Another solution of sulfur was added to a mixed solution of oleic acid and 1-octadecane, which was then kept for 150°C for a specific time. As the solution temperature became normal, the solution was added dropwise to the above metal precursor solution, which was kept at 170°C. The temperature of the above solution was raised to 240°C and maintained for 3 h. As the temperature of the solution was cooled, the particles were washed with ethanol, dried in air, and dispersed in toluene. Then for the thin film these CZTS particles were dispersed into the toluene at a ratio of 100 mg/mL and kept overnight. For the

https://www.twirpx.org & http://chemistry-chemists.com

formation of thin film over a glass slide, the doctor blade method was employed in which about 300 μL of the above solution was taken. Postannealing of the substrate was done at 100°C for 30 min with a definite heating rate. The authors reported the formation of film nearly 600 nm thick. The prepared thin film was applied as a reusable visible light photocatalyst.

Prior to the formation of the WO_3 thin film through the doctor blade method reported by Zhu et al. [190] which demonstrate the formation of the WO_3 nanopowder through the hydrothermal method which was already reported by Hong et al. [191]. The nanopowder which was procured was calcined at 500°C for 3 h. Some WO_3 nanopowder was added to an agate jar with terpineol as a solvent and ethylcellulose was used as the binder. Then a WO_3 paste was made through ball milling for 8 h. Soon after this, a WO_3 thin film was made through the doctor blade method and the samples were kept for 1 h at 450°C. The prepared film was applied for photoelectrochemical activity under visible light.

The advantages of the doctor blade method are as follows: (i) it is a very fast and easy process which is well suited for large-scale deposition; (ii) uniformity in the nature of the film can be possible at the nano level; (iii) scalability and flexibility of this process make this process unique; (iv) the setup is inexpensive and easy to organize, and produces a high throughput; and (v) much less precursor solution is wasted during the deposition of a film.

The disadvantages of the doctor blade method are as follows: (i) patterning is not possible; (ii) poor reproducibility; and (iii) any contamination may produce streaks in the wet film caused by the drag of the blade close to the substrate.

2.2.8 Drop-coating method

The drop-coating method involves the dropping of the precursor solution over a flat surface which is followed by the evaporation of the solution. The factors which are responsible for thin film preparation through this method include: (i) the mixing of the right concentration of the precursor particles in the proper solvent to form a solution; (ii) the substrate pull rate; and (iii) the surface tension between the substrate and the solution.

Bi_2O_3 films were prepared by the simple drop-coating method [192]. 0.2 M of a bismuth nitrate solution was made in ethylene glycol including 1 M nitric acid, and was mixed properly. For the preparation of the film about 20 μL of the precursor solution was pipetted over an FTO substrate and dried in a vacuum for 80°C. After this, the films were annealed at 500°C for 3 h. Heterojunction Bi_2O_3 films were formed and immersed for 6 h in the 0.2 M KI solution. After immersion, the obtained films were washed in DI water and dried at room temperature. These Bi_2O_3 films were applied for highly enhanced visible light photoelectrocatalytic activity.

The thin film preparation method as described by Elias et al. [193] deals with initial sol formation of $Zn_3(PO_4)_2$/CNT; for that, $Zn(CH_3COO)_2$ was dissolved in absolute ethanol soon after which H_3PO_4 and functionalized carbon nanotube (*f*-CNT) were added and a homogeneous mixture was made. A stabilizer, triethanaloamine, was added dropwise to the above solution and kept stirring at 60°C. After aging for 24 h the sol was then poured dropwise on the surface of the glass substrate, which was then heated at 80°C in an oven

https://www.twirpx.org & http://chemistry-chemists.com

for 20 min. Finally, the loosely bonded particles were removed by water vapor. Synthesis of $Zn_3(PO_4)_2$/carbon nanotubes nanocomposite thin film was applied for enhanced photocatalytic activity.

An advantage of the drop-coating method is that it is relatively fast to form a thin film, but a disadvantage is that the quality in terms of thickness is not uniform.

Formations of thin films through different techniques are listed in Table 2.

3 Hybrid methods

Synthesis of MoO_3 powder was done by first dissolving ammonium molybdate and urea powders; the solution was heated at 60°C for 10 min [194]. This solution was directly atomized through an ultrasonic nebulizer into a tubular furnace which was heated to a different temperature in advance. As the solution was subjected to enter in the tubular furnace. Due to the power generated by the atomizer moving fast within the furnace, this process is atomization. At the end of the furnace, the droplets cool down and attach at that part of the furnace; these were then collected soon after the inner temperature of the tube became equal to room temperature. The MoO_3 powder was applied as a visible light photocatalyst.

For the synthesis of the heterojunction photocatalyst, the combination of two preparation techniques is also reported. Some examples are included in this chapter. The combination of the solid-state method and the hydrothermal method was used for the preparation of N-doped g-C_3N_4/Bi_2WO_6 [195]. The starting materials required for the preparation of N-doped g-C_3N_4 were a mixture of urea powder and citric acid monohydrate. These were ground and calcinated at 550°C for 4 h and then repeatedly washed with DI water and ethanol. Formation of Bi_2WO_6 was done over N-doped g-C_3N_4 by sonicating a particular amount of previously made N-doped g-C_3N_4 with a solution of bismuth nitrate in acetic acid. The mixture was put into a hydrothermal reactor for 12 h at 180° C. The precipitates were centrifuged and washed with DI water and ethanol. Finally, the product was dried overnight. Degradation of phenol was reported as an application of the $BiWO_6$ modified by the N-doped g-C_3N_4.

Abhinandan et al. reported that the fabrication of codoping of oxygen and sulfur g-C_3N_4/Bi_2MoO_6 was done through the microwave-assisted method followed by the solvothermal method [147, 196]. Codoping of both oxygen and sulfur into the matrix of g-C_3N_4 was done by the microwave-assisted route. The precursors that were used were citric acid and thiourea, and these were stirred and transferred into the microwave reactor at 700 W for 5–7 min. The products were then kept for cooling and subsequently processed for centrifugation and filtered through a 0.45 μm membrane filter. The powder which was formed was dissolved into the mixed solution of $Bi(NO_3)_2.5H_2O$ and 0.06 g of $(NH_4)6Mo_7O_{24}$ in ethylene glycol. The solution was subsequently put into an autoclave for 160°C for 24 h. The composite powder that was synthesized was washed in DI water and ethanol a few times and kept for oven drying at 60°C. The prepared nanopowder was applied for phenol degradation.

https://www.twirpx.org & http://chemistry-chemists.com

Table 2 Fabrication of thin films for visible light photocatalysis. Summarizing the different parameters for the fabrication of thin film visible light photocatalysts.

Sl. No.	Synthesis method	Material used	Parameters	Product	Ref.
1	Electrodeposition	0.1 M $Cu(NO_3)_2$	Deposition time 5, 10, and 15 min Operating potential 1 V Post annealing at 400°C for 2 h	Cubic structure CuO thin film	[148]
2	Electrodeposition	20 mg of $BiVO_4$ powder + Acetone	WE and 8 CE cm apart Operating potential 20 V for 1 min (repeated four times) Post annealing at 673 K for 30 min	$BiVO_4$ thin film	[149]
3	Electrodeposition	CdS NP + acetone + water	Operating potential 600 mV for 24 h Post deposition kept same potential for 15 min	CdS thin film	[150]
4	Electrodeposition	0.1 g/L $BiVO_4$ NP + water + ethanol + acetone + isopropanol	WE and 15 CE cm apart Operating potential 30 V Drying at RT	Bi_2WO_6 thin film	[151]
5	Electrodeposition	20 mg $PbMoO_4$ + 20 mL of isopropanol	WE and 1 CE cm apart Operating potential 12 V Post deposition kept same potential for 15 min	$PbMoO_4$ nanoparticle thin film	[152]
6	Spin coating	30 mL of amorphous complex precursor of Bi_2WO_6	Drop and 60 rps Curing and kept in oven at 70°C for 2 days Post annealing at 500°C	Bi_2WO_6 porous thin film	[158]
7	Spin coating	$Sr(NO_3)_2$ + $Ti(NO_3)_4$ + $Ba(NO_3)_2$	Stirred for 6 h to form viscous sol Drop and 2000 rpm for 30 min Dried at 80°C for 10 min Post annealing at 400°C for 4 h	Ba-doped $SrTiO_3$ thin film	[159]
8	Spray pyrolysis	0.02 M $Bi(NO_3)_2$ + HNO_3 + EDTA + ammonia solution + NH_4VO_3	Stir and heat Flow rate = 0.16 m^3/h Precursor solution (depth) = 35 mm Heated at 500°C for 2 h Annealed in H_2 gas 1 h at 250°C	$BiVO_4$ thin film	[170]

https://www.twirpx.org & http://chemistry-chemists.com

9	Sputtering	Fe_2O_3 target	Pressure = 6×10^{-6} mmHg Ar is fed to the pressure of 10^{-3} mm 70 W RF power coating rate of 0.2 Å/s	Fe_2O_3/2D graphene/Cu	[171]
10	Thermal evaporation	W wire as the filament and In_2O_3 grown over *p*-Si substrate	T_f = 1000°C N_2 plasma 50 W 40 sccm 0.4 m bar 200°C In situ annealing at T_f of 1300°C, 1400°C, and 1700°C	Depending upon the value T_f InN/In_2O_3, WO_3/In_2O_3, W_2N/In_2O_3	[172]
11	Thermal evaporation	Cu, Co, Sn, and S were weighted as stoichiometric proportions of 2:1:1:4 and mixed in a quartz ampoule	CCTS ingot is formed by heating the mixture at 1000°C CCTS as a source for thin film T_s = 200°C Pressure = 10^{-5} Torr Source/substrate distance = 15 cm Sulfurization = 450°C, 2 h at 10^{-3} Torr	Cu_2CoSnS_4 thin film	[173]
12	Doctor blade	CZTS NP + toulene	300 μL Annealing at 100°C for 30 min with heating rate 0.8°C min^{-1}	Cu_2CoZnS_4 nanoparticle thin film	[189]
13	Doctor blade	WO_3 NP + terpineol + ethyl cellulose	Doctor blading Annealing at 450°C for 1 h	$NiWO_4$/WO_3 nanostructured thin film	[190]
14	Drop casting	0.2 M $Bi(NO_3)_3.5H_2O$ + 1 M HNO_3	20 μL drop over FTO Dried in vacuum at 80°C Annealing to 500°C for 3 h Dipped into 0.2 M of KI solution Immersion time 360 min	3D-Bi_2O_3/BiOI thin film	[192]
15	Drop casting	$Zn(CH_3COO)_2$ + ethanol + *f*-CNT + TEA	Stir for 60°C $Zn_3(PO_4)_2$/*f*-CNT sol is formed Drop coated Dried at 80°C in the oven for 20 min	$Zn_3(PO_4)_2$/CNT thin film	[193]

https://www.twirpx.org & http://chemistry-chemists.com

The combination of microwave and chemical bath deposition is used for the preparation of $BiVO_4$/CdS heterostructures [197]. First of all, a $BiVO_4$ solution was made by dissolving $Bi(NO_3)_3$ in concentrated HNO_3 uniformly and then the surfactants SDBS, PVP, and EDTA were added. Next, NH_4VO_3 was added and stirred for 1 h and transferred into the microwave reactor, then centrifuged, washed in acetone, and dried at 80°C. Further for the deposition of CdS over $BiVO_4$. The solution of Cd $(CH_3COO)_2{\cdot}2H_2O$ was prepared and then previously made $BiVO_4$ powder was added. Subsequently, CH_4N_2S was added to the above solution and thermal agitation was maintained at 80°C for 30 min. After that, the precipitate was washed with DI water several times, followed by drying in a vacuum oven. Furthermore, the group reported the photocatalytic nature of the above-synthesized heterojunction.

The deposition of Ag nanoparticles over $PbMoO_4$ was reported by Gyawali et al. [198]. Initially, $PbMoO_4$ was prepared by dissolving $Pb(NO_3)_2$ and H_2MoO_4. The extra addition of ammonia solution and HNO_3 acid was made to maintain a pH of 10 of the solution, which was then transferred to an ultrasonic reactor for 2 h. For the coating of Ag nanoparticles over $PbMoO_4$, photoreduction of Ag nanoparticles was done by using a mixed solution of $Ag(NO_3)$ and $PbMoO_4$ by keeping it in the photoreactor. The final product was obtained by consecutive washing and drying at 70°C for 24 h; it was then applied as a visible light photocatalyst.

An oxide heterojunction of $ZnFe_2O_4/CeO_2$ was prepared by mixed hydrothermal/sonochemical methods [150]. First of all, cerium nitrate was sonicated well and the solution agitated thermally for 2 h. Then NaOH was added to the above solution and dried at 100°C. The precipitates were washed in DDW and dried at 700°C for 5 h to obtain a highly crystalline powder of CeO_2. A small entity of the prepared powder was dissolved within the solution of zinc nitrate hexahydrate and iron nitrate nonahydrate to form suspensions of $ZnFe_2O_4$:CeO_2. Dropwise addition of NH_4OH solution was used for adjusting the pH and then the solution was ultrasonicated for 30 min. Finally, the solution was transferred into the hydrothermal reactor for 15 h at 180°C; this was followed by filtering and drying at 80°C for 24 h. Finally, the prepared powder was applied for as a visible light photocatalyst.

A combination of microwave irradiation and sonochemical methodology was adopted by Chachvalvutikul et al. for the formation of a $Bi_2S_3/ZnIn_2S_4$ composite [199]. They addressed the formation of $ZnIn_2S_4$ by using a 1:2:4 molecular ratio of $Zn(NO_3)_2$, $InCl_3$, and C_2H_5NS dissolved in ethylene glycol and transferred into a microwave reactor. After a specific time, the powder was separated through centrifugation and washed several times before being dried in the oven overnight. Simultaneously, Bi_2S_3 was prepared by dissolving $Bi(NO_3)_3.5H_2O$ and C_2H_5NS into the ethylene glycol and kept in the microwave reactor; it was then centrifuged, washed, and dried. Finally, the $ZnIn_2S_4$ powder was dissolved into methanol, followed by the addition of Bi_2S_3 powder to the above suspension, and was kept for sonochemical for 24 h. The powder of the $Bi_2S_3/ZnIn_2S_4$ composite was

https://www.twirpx.org & http://chemistry-chemists.com

gathered by centrifugation followed by washing and drying. The formed products were applied in the photocatalytic oxidation of methylene blue.

The hydrothermal and sonochemical methods were reported for the preparation of a V_2O_5-coated Zn_2SnO_4 nanocomposite [200]. For the preparation of V_2O_5, the hydrothermal method was employed in which NH_4VO_3 was dissolved in DI water, to which some drops of HCl were added and the solution was transferred into an autoclave for 20 h at 80°C. Soon after, the samples were centrifuged, washed, and dried at 60°C for 6 h. This powder was firstly sonicated and then stirred for 24 h with the precursors such as $ZnCl_2$ and $SnCl_4$, which were added to an equal ratio of water/ethylene glycol in an n-butylamine aqueous solution. The resultant powder was centrifuged, washed, and dried at 80°C for 24 h. The fabricated powder was used for the photocatalytic degradation of Eosin Yellow. Preparation of the $BiWO_6$ as a visible light photocatalyst was reported by combining the microemulsion and hydrothermal methods [201]. For the preparation of the oil, the phase is the mixture of n-heptane, n-butyl alcohol as the cosurfactant, and polysorbate 80 as the surfactant. One of the microemulsions was prepared by mixing $Bi(NO_3)_3$ in the continuous oil phase, whereas in the other micro-solution there was a mixture of Na_2WO_4 aqueous solution in the continuous oil phase. Both the microemulsions were added and stirred vigorously. After this, a particular amount of NH_3 solution was added, and the mixture was then transferred to a hydrothermal reactor for a set time. The samples were filtered by vacuum filtration and vacuum dried at 60°C for 6 h to obtain Bi_2WO_6 powders.

Ma et al. used the hydrothermal method for the preparation of polyethylene glycol (PEG)-modified $Ag/Ag_2O/Ag_3PO_4/Bi_2WO_6$ thin film by the combination of the hydrothermal and the dip-coating methods [202]. Firstly they prepared PEG_{MW}-AP-BWO photocatalysts by the two-step hydrothermal method. In this, 10 μmol Na_2WO_6 was dissolved in 45 mL water, and 20 μmol of $Bi(NO_3)_3$ was dissolved in 15 mL 1 M HNO_3 to which was then added a certain amount of PEG. Next the above Na_2WO_6 solution was added dropwise into the transparent $Bi(NO_3)_3$ solution with vigorous stirring. After 3 h of stirring, the NH_4OH solution was used to adjust the pH to 7. Soon after, the prepared solution was put into a Teflon-lined autoclave at a certain temperature and for a specific time. The precipitates obtained were washed and collected as powder and then the solution was made in 45 mL of ethanol. Another beaker was used for the preparation of 1 μmol of Ag^+ ($AgNO_3$ and Ag_3PO_4) dissolved in an HNO_3 solution and added into a previously made ethanoic suspension, which was then again placed in the Teflon-lined autoclave at a certain temperature and for a specific time. Finally, the precipitate was washed with water and dried at 80°C for 16 h. A PEG_{MW}-AP-BWO photocatalyst was successfully prepared. After the preparation of the (PEG)-modified $Ag/Ag_2O/Ag_3PO_4/Bi_2WO_6$ photocatalyst, the thin film was prepared by the dip-coating method. For that, about 0.5 g of the powder was mixed thoroughly with 50 mL of ethanol for 10 min to obtain the suspension, which was then ultrasonic. The glass tubes were coated by immersing for 3 min, then oven-dried at 60°C for 12 h.

https://www.twirpx.org & http://chemistry-chemists.com

4 Conclusion

Syntheses of various metal oxide, chalcogenide, and nitride nanostructures by using different techniques have been mentioned in this chapter. However, the important entity that requires care is the optimization condition for improving reproducibility and yield. Apart from the fabrication of single nanostructured compound materials, the heterojunction and the composite comprise the *Z*-scheme which leads to optimization of various steps during fabrication to achieve visible light photocatalytic properties. This chapter provided an outline of the synthesis of different fabrication processes for the preparation of nanoparticles and nanocomposites, along with their advantages and disadvantages.

References

[1] Israel B. How much water is on earth?; 2021.

[2] Catley-Carlson M. Water supply: the emptying well. Nature 2017;542:412–3. https://doi.org/10.1038/542412a.

[3] Patil SB, Bhojya Naik HS, Nagaraju G, Viswanath R, Rashmi SK. Synthesis of visible light active Gd3+−substituted ZnFe2O4 nanoparticles for photocatalytic and antibacterial activities. Eur Phys J Plus 2017;132:328. https://doi.org/10.1140/epjp/i2017-11602-x.

[4] Chowdhary P, Raj A, Bharagava RN. Environmental pollution and health hazards from distillery wastewater and treatment approaches to combat the environmental threats: a review. Chemosphere 2018;194:229–46. https://doi.org/10.1016/j.chemosphere.2017.11.163.

[5] Dharupaneedi SP, Nataraj SK, Nadagouda M, Reddy KR, Shukla SS, Aminabhavi TM. Membrane-based separation of potential emerging pollutants. Sep Purif Technol 2019;210:850–66. https://doi.org/10.1016/j.seppur.2018.09.003.

[6] Alharbi OML, Basheer AA, Khattab RA, Ali I. Health and environmental effects of persistent organic pollutants. J Mol Liq 2018;263:442–53. https://doi.org/10.1016/j.molliq.2018.05.029.

[7] Senthilvelan S, Chandraboss VL, Karthikeyan B, Natanapatham L, Murugavelu M. TiO2, ZnO and nanobimetallic silica catalyzed photodegradation of methyl green. Mater Sci Semicond Process 2013;16:185–92. https://doi.org/10.1016/j.mssp.2012.04.018.

[8] Zelmanov G, Semiat R. Phenol oxidation kinetics in water solution using iron(3)-oxide-based nanocatalysts. Water Res 2008;42:3848–56. https://doi.org/10.1016/j.watres.2008.05.009.

[9] Jing J, Li J, Feng J, Li W, Yu WW. Photodegradation of quinoline in water over magnetically separable Fe3O4/TiO2 composite photocatalysts. Chem Eng J 2013;219:355–60. https://doi.org/10.1016/j.cej.2012.12.058.

[10] Ju Y, Qiao J, Peng X, Xu Z, Fang J, Yang S, et al. Photodegradation of malachite green using UV–vis light from two microwave-powered electrodeless discharge lamps (MPEDL-2): further investigation on products, dominant routes and mechanism. Chem Eng J 2013;221:353–62. https://doi.org/10.1016/j.cej.2012.06.055.

[11] Li Y, Zhao H, Yang M. TiO2 nanoparticles supported on PMMA nanofibers for photocatalytic degradation of methyl orange. J Colloid Interface Sci 2017;508:500–7. https://doi.org/10.1016/j.jcis.2017.08.076.

[12] Alijani M, Kaleji BK, Rezaee S. Highly visible-light active with Co/Sn co-doping of TiO2 nanoparticles for degradation of methylene blue. J Mater Sci Mater Electron 2017;28:15345–53. https://doi.org/10.1007/s10854-017-7420-6.

https://www.twirpx.org & http://chemistry-chemists.com

[13] Wei Z, Liu D, Wei W, Chen X, Han Q, Yao W, et al. Ultrathin TiO2(B) nanosheets as the inductive agent for transfrering H2O2 into superoxide radicals. ACS Appl Mater Interfaces 2017;9:15533–40. https://doi.org/10.1021/acsami.7b03073.

[14] Marcilly C. Preparation of catalysts. Part I. Rev Inst Fr Pétrol 1984;39:189–208.

[15] Schwarz JA, Cristian C, Adriana C. Methods for preparation of catalytic materials. Chem Rev 1995;95:477–510. https://doi.org/10.1021/cr00035a002.

[16] Schüth F, Unger K. Precipitation and coprecipitation. Preparation of solid catalysts; 1999. p. 60–84. https://doi.org/10.1002/9783527619528.ch3d.

[17] Ramasamy Raja V, Karthika A, Suganthi A, Rajarajan M. Facile synthesis of MnWO4/BiOI nanocomposites and their efficient photocatalytic and photoelectrochemical activities under the visible-light irradiation. J Sci Adv Mat Dev 2018;3:331–41. https://doi.org/10.1016/j.jsamd.2018.07.003.

[18] Zhu C, Li Y, Yang Y, Chen Y, Yang Z, Wang P, et al. Influence of operational parameters on photocatalytic decolorization of a cationic azo dye under visible-light in aqueous Ag3PO4. Inorg Chem Commun 2020;115:107850. https://doi.org/10.1016/j.inoche.2020.107850.

[19] Kumar S, Pal S, Kuntail J, Sinha I. Curcumin functionalized CuO/Ag nanocomposite: efficient visible light Z-scheme photocatalyst for methyl orange degradation. Environ Nanotechnol Monit Manage 2019;12:100236. https://doi.org/10.1016/j.enmm.2019.100236.

[20] Rheingans B, Mittemeijer EJ. Modelling precipitation kinetics: evaluation of the thermodynamics of nucleation and growth. Calphad 2015;50:49–58. https://doi.org/10.1016/j.calphad.2015.04.013.

[21] Sun H, Qin P, Wu Z, Liao C, Guo J, Luo S, et al. Visible light-driven photocatalytic degradation of organic pollutants by a novel Ag3VO4/Ag2CO3 p–n heterojunction photocatalyst: mechanistic insight and degradation pathways. J Alloys Compd 2020;834:155211. https://doi.org/10.1016/j.jallcom.2020.155211.

[22] Talukdar K, Jun B-M, Yoon Y, Kim Y, Fayyaz A, Park CM. Novel Z-scheme Ag3PO4/Fe3O4-activated biochar photocatalyst with enhanced visible-light catalytic performance toward degradation of bisphenol A. J Hazard Mater 2020;123025. https://doi.org/10.1016/j.jhazmat.2020.123025.

[23] Dimitriev Y, Ivanova Y, Iordanova R. History of sol-gel science and technology. J Univ Chem Technol Metall 2008;43:181–92.

[24] Danks AE, Hall SR, Schnepp Z. The evolution of 'sol–gel' chemistry as a technique for materials synthesis. Mater Horiz 2016;3:91–112. https://doi.org/10.1039/c5mh00260e.

[25] Deebasree JP, Maheskumar V, Vidhya B. Investigation of the visible light photocatalytic activity of BiVO4 prepared by sol gel method assisted by ultrasonication. Ultrason Sonochem 2018;45:123–32. https://doi.org/10.1016/j.ultsonch.2018.02.002.

[26] Mkhalid IA, Shawky A. Visible light-active CdSe/rGO heterojunction photocatalyst for improved oxidative desulfurization of thiophene. Ceram Int 2020. https://doi.org/10.1016/j.ceramint.2020.05.033.

[27] Peymanfar R, Ramezanalizadeh H. Sol-gel assisted synthesis of CuCr2O4 nanoparticles: an efficient visible-light driven photocatalyst for the degradation of water pollutions. Optik 2018;169:424–31. https://doi.org/10.1016/j.ijleo.2018.05.072.

[28] Ranjeh M, Masjedi-Arani M, Salavati-Niasari M, Moayedi H. EDTA-modified sol-gel synthesis of monoclinic Li2MnO3 nanoparticles as an effective photocatalyst for degradation of organic dyes. J Mol Liq 2020;300:112292. https://doi.org/10.1016/j.molliq.2019.112292.

[29] Parida KM, Reddy KH, Martha S, Das DP, Biswal N. Fabrication of nanocrystalline LaFeO3: an efficient sol–gel auto-combustion assisted visible light responsive photocatalyst for water decomposition. Int J Hydrogen Energy 2010;35:12161–8. https://doi.org/10.1016/j.ijhydene.2010.08.029.

[30] Zhang D, Zhang L. Ultrasonic-assisted sol-gel synthesis of rugby-shaped SrFe2O4/reduced graphene oxide hybrid as versatile visible light photocatalyst. J Taiwan Inst Chem Eng 2016;69:156–62. https://doi.org/10.1016/j.jtice.2016.10.015.

https://www.twirpx.org & http://chemistry-chemists.com

[31] Wang G-L, Shan L-W, Wu Z, Dong L-M. Enhanced photocatalytic properties of molybdenum-doped BiVO4 prepared by sol–gel method. Rare Metals 2017;36:129–33. https://doi.org/10.1007/s12598-015-0669-0.

[32] Wang Z, Wang Y, Huang L, Liu X, Han Y, Wang L. La2Zr2O7/rGO synthesized by one-step sol-gel method for photocatalytic degradation of tetracycline under visible-light. Chem Eng J 2020;384:123380. https://doi.org/10.1016/j.cej.2019.123380.

[33] Mousavi-Kamazani M. Cube-like Cu/Cu2O/BiVO4/Bi7VO13 composite nanoparticles: facile sol-gel synthesis for photocatalytic desulfurization of thiophene under visible light. J Alloys Compd 2020;823:153786. https://doi.org/10.1016/j.jallcom.2020.153786.

[34] Kamal S, Balu S, Palanisamy S, Uma K, Velusamy V, Yang TCK. Synthesis of boron doped C3N4/NiFe2O4 nanocomposite: an enhanced visible light photocatalyst for the degradation of methylene blue. Results Phys 2019;12:1238–44. https://doi.org/10.1016/j.rinp.2019.01.004.

[35] Rane AV, Kanny K, Abitha VK, Thomas S. Chapter 5. Methods for synthesis of nanoparticles and fabrication of nanocomposites. In: Micro and nano technologies. Woodhead Publishing; 2018. p. 121–39. https://doi.org/10.1016/B978-0-08-101975-7.00005-1.

[36] Byrappa K. Novel hydrothermal solution routes of advanced high melting nanomaterials processing. J Cerma Soc Jpn 2009;117:236–44. https://doi.org/10.2109/jcersj2.117.236.

[37] Byrappa K, Yoshimura M. Handbook of hydrothermal technology. William Andrew; 2012.

[38] Adschiri T, Hakuta Y, Arai K. Hydrothermal synthesis of metal oxide fine particles at supercritical conditions. Ind Eng Chem Res 2000;39:4901–7. https://doi.org/10.1021/ie0003279.

[39] Huerta-Flores AM, Sánchez-Martínez D, del Rocío H-RM, Zarazúa-Morín ME, Torres-Martínez LM. Visible-light-driven BaBiO3 perovskite photocatalysts: effect of physicochemical properties on the photoactivity towards water splitting and the removal of rhodamine B from aqueous systems. J Photochem Photobiol A Chem 2019;368:70–7. https://doi.org/10.1016/j.jphotochem.2018.09.025.

[40] Wang J, Asakura Y, Yin S. Synthesis of zinc germanium oxynitride nanotube as a visible-light driven photocatalyst for NOx decomposition through ordered morphological transformation from Zn2GeO4 nanorod obtained by hydrothermal reaction. J Hazard Mater 2020;396:122709. https://doi.org/10.1016/j.jhazmat.2020.122709.

[41] Zhong H, Mirkovic T, Scholes GD. 5.06—Nanocrystal Synthesis. Amsterdam: Academic Press; 2011. p. 153–201. https://doi.org/10.1016/B978-0-12-374396-1.00051-9.

[42] Wang Q, Yuan L, Dun M, Yang X, Chen H, Li J, et al. Synthesis and characterization of visible light responsive Bi3NbO7 porous nanosheets photocatalyst. Appl Catal Environ 2016;196:127–34. https://doi.org/10.1016/j.apcatb.2016.05.026.

[43] Wang J, Zhang W, Zhang X, Wang F, Yang Y, Lv G. Enhanced photocatalytic ability and easy retrievable photocatalysts of Bi2WO6 quantum dots decorated magnetic carbon nano-onions. J Alloys Compd 2020;826:154217. https://doi.org/10.1016/j.jallcom.2020.154217.

[44] Liu Y, Yuan A, Xiao Y, Yu H, Dong X. Two-dimensional/two-dimensional Z-scheme photocatalyst of graphitic carbon nitride/bismuth vanadate for visible-light-driven photocatalytic synthesis of imines. Ceram Int 2020;46:16157–65. https://doi.org/10.1016/j.ceramint.2020.03.171.

[45] Xie Y, Wu J, Sun C, Ling Y, Li S, Li X, et al. La2O3-modified graphite carbon nitride achieving the enhanced photocatalytic degradation of different organic pollutants under visible light irradiation. Mater Chem Phys 2020;246:122846. https://doi.org/10.1016/j.matchemphys.2020.122846.

[46] Wang C, Fan H, Ren X, Ma J, Fang J, Wang W. Hydrothermally induced oxygen doping of graphitic carbon nitride with a highly ordered architecture and enhanced photocatalytic activity. ChemSusChem 2018;11:700–8. https://doi.org/10.1002/cssc.201702278.

[47] Vattikuti SVP, Shim J, Byon C. 1D Bi2S3 nanorod/2D e-WS2 nanosheet heterojunction photocatalyst for enhanced photocatalytic activity. J Solid State Chem 2018;258:526–35. https://doi.org/10.1016/j.jssc.2017.11.017.

https://www.twirpx.org & http://chemistry-chemists.com

[48] Bekri-Abbes I, Srasra E. Investigation of structure and conductivity properties of polyaniline synthesized by solid–solid reaction. J Polym Res 2011;18:659–65. https://doi.org/10.1007/s10965-010-9461-x.

[49] Maeda K, Teramura K, Lu D, Takata T, Saito N, Inoue Y, et al. Photocatalyst releasing hydrogen from water. Nature 2006;440:295. https://doi.org/10.1038/440295a.

[50] Shende AG, Ghugal SG, Vidyasagar D, Kokane SB, Jagannath, Umare SS, et al. Solvent free solid-state synthesis of Pr6O11/g-C3N4 visible light active photocatalyst for degradation of AV7 dye. Mater Res Bull 2018;107:154–63. https://doi.org/10.1016/j.materresbull.2018.07.022.

[51] Hu J, Xu H, Wang S, Jia W, Cao Y. In-situ solid-state synthesis and regulation of Ag2O/Ag2CO3 heterojunctions with promoted visible-light driven photocatalytic decomposition for organic pollutant. Sep Purif Technol 2019;226:95–108. https://doi.org/10.1016/j.seppur.2019.05.080.

[52] Li Y, Cao Y, Jia D. A general strategy for synthesis of metal nanoparticles by a solid-state redox route under ambient conditions. J Mater Chem A 2014;2:3761–5. https://doi.org/10.1039/C3TA14427E.

[53] Xu Z, Chu R, Hao J, Li G, Yin Q. Citrate-oxide method to prepare SrBi4Ti4O15 powders and ceramics. J Alloys Compd 2009;479:500–4. https://doi.org/10.1016/j.jallcom.2008.12.094.

[54] Turns SR, et al. Introduction to combustion. vol. 287. McGraw-Hill Companies; 1996.

[55] Lackner M, Palotás Á, Winter F. Combustion: from basics to applications. John Wiley & Sons; 2013.

[56] Varma A, Rogachev AS, Mukasyan AS, Hwang S. Combustion synthesis of advanced materials: principles and applications. vol. 24. Academic Press; 1998. p. 79–226. https://doi.org/10.1016/S0065-2377(08)60093-9.

[57] Merzhanov AG. Solid flames: discoveries, concepts, and horizons of cognition. Combust Sci Technol 1994;98:307–36. https://doi.org/10.1080/00102209408935417.

[58] Parkin IP. Solvent free reactions in the solid state: solid state metathesis. Transit Met Chem 2002;27:569–73. https://doi.org/10.1023/A:1019885916386.

[59] Kaplan SS, Sonmez MS. Single step solution combustion synthesis of hexagonal WO3 powders as visible light photocatalysts. Mater Chem Phys 2020;240:122152. https://doi.org/10.1016/j.matchemphys.2019.122152.

[60] Wu L, Yu JC, Zhang L, Wang X, Li S. Selective self-propagating combustion synthesis of hexagonal and orthorhombic nanocrystalline yttrium iron oxide. J Solid State Chem 2004;177:3666–74. https://doi.org/10.1016/j.jssc.2004.06.020.

[61] Zhang Z, Wang W, Shang M, Yin W. Low-temperature combustion synthesis of Bi2WO6 nanoparticles as a visible-light-driven photocatalyst. J Hazard Mater 2010;177:1013–8. https://doi.org/10.1016/j.jhazmat.2010.01.020.

[62] Du X, Wang X. Solution combustion synthesis of Ag-decorated Bi5O7NO3 composites with enhanced photocatalytic properties. Ceram Int 2019;45:1409–11. https://doi.org/10.1016/j.ceramint.2018.09.141.

[63] Abbasian AR, Rahmani M. Salt-assisted solution combustion synthesis of nanostructured ZnFe2O4-ZnS powders. Inorg Chem Commun 2020;111:107629. https://doi.org/10.1016/j.inoche.2019.107629.

[64] Bajiri MA, Hezam A, Namratha K, Viswanath R, Drmosh QA, Bhojya Naik HS, et al. CuO/ZnO/g-C3N4 heterostructures as efficient visible light-driven photocatalysts. J Environ Chem Eng 2019;7:103412. https://doi.org/10.1016/j.jece.2019.103412.

[65] Zhang D, Liu H, Su C, Li H, Geng Y. Combustion synthesis of highly efficient Bi/BiOBr visible light photocatalyst with synergetic effects of oxygen vacancies and surface plasma resonance. Sep Purif Technol 2019;218:1–7. https://doi.org/10.1016/j.seppur.2019.02.037.

[66] Patil S, Anantharaju KS, Rangappa D, Vidya YS, Sharma SC, Renuka L, et al. Magnetic Eu-doped MgFe2O4 nanomaterials: an investigation of their structural, optical and enhanced

https://www.twirpx.org & http://chemistry-chemists.com

visible-light-driven photocatalytic performance. Environ Nanotechnol Monit Manage 2020;13:100268. https://doi.org/10.1016/j.enmm.2019.100268.

[67] Iervolino G, Vaiano V, Sannino D, Rizzo L, Galluzzi A, Polichetti M, et al. Hydrogen production from glucose degradation in water and wastewater treated by Ru-LaFeO3/Fe2O3 magnetic particles photocatalysis and heterogeneous photo-Fenton. Int J Hydrogen Energy 2018;43:2184–96. https://doi.org/10.1016/j.ijhydene.2017.12.071.

[68] Kavitha V, Jose R, Wariar P, Koshy J. Combustion synthesis and characterization of Ba2NdSbO6 nanocrystals. Bull Mater Sci 2011;34:661–5. https://doi.org/10.1007/s12034-011-0178-1.

[69] Sarkar DK. Air pollution control. Elsevier; 2015. p. 479–522. https://doi.org/10.1016/B978-0-12-801575-9.00014-7. Chapter 14.

[70] Amani Hamedani H, Dahmen K, Peydaye-Saheli H, Garmestani H, Khaleel M. Fabrication of gradient porous LSM cathode by optimizing deposition parameters in ultrasonic spray pyrolysis. Mater Sci Eng, B 2008;153:1–9. https://doi.org/10.1016/j.mseb.2008.07.006.

[71] Wilhelm O, Pratsinis SE, Perednis D, Gauckler LJ. Electrospray and pressurized spray deposition of yttria-stabilized zirconia films. Thin Solid Films 2005;479:121–9. https://doi.org/10.1016/j.tsf.2004.11.206.

[72] Kim J, Park Y, Sung DJ, Moon S, Lee KB, Hong S-I. Preparation of thin film YSZ electrolyte by using electrostatic spray deposition. Int J Refract Met Hard Mater 2009;27:985–90. https://doi.org/10.1016/j.ijrmhm.2009.07.001.

[73] Filipovic L, Selberherr S, Mutinati GC, Brunet E, Steinhauer S, Köck A, et al. Modeling spray pyrolysis deposition. Proc World Cong Eng 2013;2:987–92.

[74] Bayvel L, Orzechowski Z. Liquid atomization. Taylor and Francis; 1993. Washington, DC.

[75] Rahemi Ardekani S, Sabour Rouh Aghdam A, Nazari M, Bayat A, Yazdani E, Saievar-Iranizad E. A comprehensive review on ultrasonic spray pyrolysis technique: mechanism, main parameters and applications in condensed matter. J Anal Appl Pyrolysis 2019;141:104631. https://doi.org/10.1016/j.jaap.2019.104631.

[76] Kumar N, Komarala VK, Dutta V. In-situ synthesis of Au–CdS plasmonic photocatalyst by continuous spray pyrolysis and its visible light photocatalysis. Chem Eng J 2014;236:66–74. https://doi.org/10.1016/j.cej.2013.09.052.

[77] Liu P, Bao R, Fang D, Yi J, Li L. A facile synthesis of CNTs/Cu2O-CuO heterostructure composites by spray pyrolysis and its visible light responding photocatalytic properties. Adv Powder Technol 2018;29:2027–34. https://doi.org/10.1016/j.apt.2018.05.009.

[78] Huang Y, Gao Y, Zhang Q, Cao J, Huang R, Ho W, et al. Hierarchical porous ZnWO4 microspheres synthesized by ultrasonic spray pyrolysis: characterization, mechanistic and photocatalytic NOx removal studies. Appl Catal Gen 2016;515:170–8. https://doi.org/10.1016/j.apcata.2016.02.007.

[79] Okuyama K, Wuled Lenggoro I. Preparation of nanoparticles via spray route. Chem Eng Sci 2003;58:537–47. https://doi.org/10.1016/S0009-2509(02)00578-X.

[80] Gavrilovic T, Jovanovic D, Dramicanin M. Chapter 2: synthesis of multifunctional inorganic materials: from micrometer to nanometer dimensions. In: Bhanvase BA, Pawade VB, Dhoble SJ, Sonawane SH, Ashokkumar M, editors. Nanomaterials for green energy. Elsevier; 2018. p. 20.

[81] Strobel R, Baiker A, Pratsinis SE. Aerosol flame synthesis of catalysts. Adv Powder Technol 2006;17:457–80. https://doi.org/10.1163/156855206778440525.

[82] Koirala R, Pratsinis SE, Baiker A. Synthesis of catalytic materials in flames: opportunities and challenges. Chem Soc Rev 2016;45:3053–68. https://doi.org/10.1039/C5CS00011D.

[83] Johannessen T, Jensen JR, Mosleh M, Johansen J, Quaade U, Livbjerg H. Flame synthesis of nanoparticles: applications in catalysis and product/process engineering. Chem Eng Res Des 2004;82:1444–52. https://doi.org/10.1205/cerd.82.11.1444.52025.

https://www.twirpx.org & http://chemistry-chemists.com

[84] Ma X, Chen Y, Li H, Cui X, Lin Y. Annealing-free synthesis of carbonaceous Nb2O5 microspheres by flame thermal method and enhanced photocatalytic activity for hydrogen evolution. Mater Res Bull 2015;66:51–8. https://doi.org/10.1016/j.materresbull.2015.02.005.

[85] Kshirsagar A, Khanna T, Khanna P, Dhanwe V, Khanna PK. Flame deposition method for carbon nanoparticles employing green precursors and its composite with Au nanoparticles for photocatalytic degradation of methylene blue. Vacuum 2017;146:633–40. https://doi.org/10.1016/j.vacuum.2017.07.039.

[86] Bensebaa F. Chapter 3—dry production methods. In: Nanoparticle technologies, vol. 19. Elsevier; 2013. p. 147–84. https://doi.org/10.1016/B978-0-12-369550-5.00003-3.

[87] Anton F. Process and apparatus for preparing artificial threads; 1934.

[88] Reneker DH, Chun I. Nanometre diameter fibres of polymer, produced by electrospinning. Nanotechnology 1996;7:216–23. https://doi.org/10.1088/0957-4484/7/3/009.

[89] Kim J-S, Reneker DH. Polybenzimidazole nanofiber produced by electrospinning. Polym Eng Sci 1999;39:849–54. https://doi.org/10.1002/pen.11473.

[90] Xing X. Subwavelength and nanometer diameter optical polymer fibers as building blocks for miniaturized photonics integration. Rijeka: IntechOpen; 2012. https://doi.org/10.5772/47822. p. Ch. 12-Ch. 12.

[91] Patil J, Mali S, Kalekar A, Hong C, Kim J, Patil P. Electrospinning: a versatile technique for making of 1D growth of nanostructured nanofibers and its applications: an experimental approach. Appl Surf Sci 2017;423. https://doi.org/10.1016/j.apsusc.2017.06.116.

[92] Huang J, Liu X, Chen G, Zhang N, Ma R, Qiu G. Selective fabrication of porous iron oxides hollow spheres and nanofibers by electrospinning for photocatalytic water purification. Solid State Sci 2018;82:24–8. https://doi.org/10.1016/j.solidstatesciences.2018.05.014.

[93] Lv C, Sun J, Chen G, Zhou Y, Li D, Wang Z, et al. Organic salt induced electrospinning gradient effect: achievement of BiVO4 nanotubes with promoted photocatalytic performance. Appl Catal Environ 2017;208:14–21. https://doi.org/10.1016/j.apcatb.2017.02.058.

[94] Wang W, Li N, Chi Y, Li Y, Yan W, Li X, et al. Electrospinning of magnetical bismuth ferrite nanofibers with photocatalytic activity. Ceram Int 2013;39:3511–8. https://doi.org/10.1016/j.ceramint.2012.10.175.

[95] Ardoña HAM, Paredes FU, Arellano IHJ, Arco SD. Electrospun PET supported-ionic liquid-stabilized CdS catalyst for the photodegradation of Rhodamine B under visible light. Mater Lett 2013;91:96–9. https://doi.org/10.1016/j.matlet.2012.09.069.

[96] Liu J, Qiu L, Chang M-J, Yuan B, Sun M, Fan S-M, et al. Fabrication of novel fibrous BiVO4/CdS heterostructures by electrospinning method for efficient visible light photodegradation. Mater Chem Phys 2020;247:122858. https://doi.org/10.1016/j.matchemphys.2020.122858.

[97] Zhao J, Lu Q, Wei M, Wang C. Synthesis of one-dimensional α-Fe2O3/Bi2MoO6 heterostructures by electrospinning process with enhanced photocatalytic activity. J Alloys Compd 2015;646:417–24. https://doi.org/10.1016/j.jallcom.2015.05.191.

[98] Powell CF, Oxley JH, Blocher JM. Chemically deposited nonmetals. In: Powell CF, Oxley JH, Blocher Jr JM, editors. Vapor deposition. New York: Wiley; 1966. p. 343–420.

[99] Wu W, Yu Q, Lian J, Bao J, Liu Z, Pei S-S. Tetragonal tungsten oxide nanobelts synthesized by chemical vapor deposition. J Cryst Growth 2010;312:3147–50. https://doi.org/10.1016/j.jcrysgro.2010.07.057.

[100] Wang Y, Wang F, Zuo Y, Zhang X, Cui L-F. Simple synthesis of ordered cubic mesoporous graphitic carbon nitride by chemical vapor deposition method using melamine. Mater Lett 2014;136:271–3. https://doi.org/10.1016/j.matlet.2014.08.078.

https://www.twirpx.org & http://chemistry-chemists.com

[101] He C, Bu X, Yang S, He P, Ding G, Xie X. Core-shell SrTiO3/graphene structure by chemical vapor deposition for enhanced photocatalytic performance. Appl Surf Sci 2018;436:373–81. https://doi.org/10.1016/j.apsusc.2017.12.063.

[102] Komarneni S, Roy R. Titania gel spheres by a new sol-gel process. Mater Lett 1985;3:165–7. https://doi.org/10.1016/0167-577X(85)90151-X.

[103] Kappe CO. Controlled microwave heating in modern organic synthesis. Angew Chem Int Ed 2004;43:6250–84. https://doi.org/10.1002/anie.200400655.

[104] Lidström P, Tierney J, Wathey B, Westman J. Microwave assisted organic synthesis—a review. Tetrahedron 2001;57:9225–83. https://doi.org/10.1016/S0040-4020(01)00906-1.

[105] Millos CJ, Whittaker AG, Brechin EK. Microwave heating—a new synthetic tool for cluster synthesis. Polyhedron 2007;26:1927–33.

[106] Gedye R, Rank W, Westaway K. The rapid synthesis of organic compounds in microwave ovens. II. Can J Chem 2011;69:706–11. https://doi.org/10.1139/v91-106.

[107] Das S, Mukhopadhyay A, Datta S, Basu D. Prospects of microwave processing: an overview. Bull Mater Sci 2009;32:1–13. https://doi.org/10.1007/s12034-009-0001-4.

[108] Blosi M, Albonetti S, Dondi M, Martelli C, Baldi G. Microwave-assisted polyol synthesis of Cu nanoparticles. J Nanopart Res 2011;13:127–38. https://doi.org/10.1007/s11051-010-0010-7.

[109] Onwudiwe DC, Oyewo OA, Atamtürk U, Ojelere O, Mathur S. Photocatalytic reduction of Cr(VI) using star-shaped Bi2S3 obtained from microwave irradiation of bismuth complex. J Environ Chem Eng 2020;8:103816. https://doi.org/10.1016/j.jece.2020.103816.

[110] da Silveira SJ, Dotto GL, Hotza D, Landers R, da Boit MK, Foletto EL. Enhanced catalytic performance of CuFeS2 chalcogenide prepared by microwave-assisted route for photo-Fenton oxidation of emerging pollutant in water. J Environ Chem Eng 2020;8:104077. https://doi.org/10.1016/j.jece.2020.104077.

[111] Jain S, Shah AP, Shimpi NG. An efficient photocatalytic degradation of organic dyes under visible light using zinc stannate (Zn2SnO4) nanorods prepared by microwave irradiation. Nano-Struct Nano-Obj 2020;21:100410. https://doi.org/10.1016/j.nanoso.2019.100410.

[112] Gu W, Wang W, Li G, Xie H, Wong PK, An T. Microwave-assisted synthesis of defective tungsten trioxide for photocatalytic bacterial inactivation: role of the oxygen vacancy. Chin J Catal 2020;41:1488–97. https://doi.org/10.1016/S1872-2067(19)63409-1.

[113] Claudino CH, Kuznetsova M, Rodrigues BS, Chen C, Wang Z, Sardela M, et al. Facile one-pot microwave-assisted synthesis of tungsten-doped BiVO4/WO3 heterojunctions with enhanced photocatalytic activity. Mater Res Bull 2020;125:110783. https://doi.org/10.1016/j.materresbull.2020.110783.

[114] Zhao C, Chen Y, Li C, Zhang Q, Chen P, Shi K, et al. One step and fast preparation of VOx/g-C3N4 photocatalyst via microwave heating for effective degradation of RhB under visible light. J Phys Chem Solid 2020;136:109122. https://doi.org/10.1016/j.jpcs.2019.109122.

[115] Tamaddon F, Mosslemin MH, Asadipour A, Gharaghani MA, Nasiri A. Microwave-assisted preparation of ZnFe2O4@methyl cellulose as a new nano-biomagnetic photocatalyst for photodegradation of metronidazole. Int J Biol Macromol 2020;154:1036–49. https://doi.org/10.1016/j.ijbiomac.2020.03.069.

[116] Sundararajan M, John Kennedy L, Nithya P, Judith Vijaya J, Bououdina M. Visible light driven photocatalytic degradation of rhodamine B using Mg doped cobalt ferrite spinel nanoparticles synthesized by microwave combustion method. J Phys Chem Solid 2017;108:61–75. https://doi.org/10.1016/j.jpcs.2017.04.002.

[117] Chikan V, McLaurin EJ. Rapid nanoparticle synthesis by magnetic and microwave heating. Nanomaterials (Basel, Switzerland) 2016;6:85. https://doi.org/10.3390/nano6050085.

https://www.twirpx.org & http://chemistry-chemists.com

[118] Tompsett GA, Panzarella B, Conner WC, Yngvesson KS, Lu F, Suib SL, et al. In situ small angle x-ray scattering, wide angle x-ray scattering, and Raman spectroscopy of microwave synthesis. Rev Sci Instrum 2006;77:124101. https://doi.org/10.1063/1.2390630.

[119] Moriguchi N. The influence of supersonic waves on chemical phenomena. III The influence on the concentration polarisation, Nippon Kagaku Kaishi 1934;55(8):749–50. https://doi.org/10.1246/nikkashi1921.55.8_749.

[120] Leeman S, Vaughan PW, Price GJ. In: Price GJ, editor. Current trends in sonochemistry. The Royal Society of Chemistry; 1992. p. 26.

[121] Ritenour ER. Ultrasound: its chemical, physical, and biological effects. Radiology 1989;173:136. https://doi.org/10.1148/radiology.173.1.136.

[122] Suslick KS. Sonochemistry. Science 1990;247:1439–45. https://doi.org/10.1126/science.247.4949.1439.

[123] Maritza G, Arnim H, Dohrmann JK. Hydrogen atom reactions in the sonolysis of aqueous solutions. J Phys Chem 1987;91:6687–90. https://doi.org/10.1021/j100311a026.

[124] Mehdizadeh P, Amiri O, Rashki S, Salavati-Niasari M, Salimian M, Foong LK. Effective removal of organic pollution by using sonochemical prepared LaFeO3 perovskite under visible light. Ultrason Sonochem 2020;61:104848. https://doi.org/10.1016/j.ultsonch.2019.104848.

[125] Intaphong P, Phuruangrat A, Thongtem S, Thongtem T. Sonochemical synthesis and characterization of BiOI nanoplates for using as visible-light-driven photocatalyst. Mater Lett 2018;213:88–91. https://doi.org/10.1016/j.matlet.2017.11.014.

[126] Hunge YM, Yadav AA, Liu S, Mathe VL. Sonochemical synthesis of CZTS photocatalyst for photocatalytic degradation of phthalic acid. Ultrason Sonochem 2019;56:284–9. https://doi.org/10.1016/j.ultsonch.2019.04.003.

[127] Mousavi-Kamazani M, Ashrafi S. Single-step sonochemical synthesis of Cu2O-CeO2 nanocomposites with enhanced photocatalytic oxidative desulfurization. Ultrason Sonochem 2020;63:104948. https://doi.org/10.1016/j.ultsonch.2019.104948.

[128] Zhou L, Wang W, Liu S, Zhang L, Xu H, Zhu W. A sonochemical route to visible-light-driven high-activity BiVO4 photocatalyst. J Mol Catal A Chem 2006;252:120–4. https://doi.org/10.1016/j.molcata.2006.01.052.

[129] Zhang F-J, Xie F-Z, Liu J, Zhao W, Zhang K. Rapid sonochemical synthesis of irregular nanolaminar-like Bi2WO6 as efficient visible-light-active photocatalysts. Ultrason Sonochem 2013;20:209–15. https://doi.org/10.1016/j.ultsonch.2012.07.019.

[130] Eghbali-Arani M, Sobhani-Nasab A, Rahimi-Nasrabadi M, Ahmadi F, Pourmasoud S. Ultrasound-assisted synthesis of YbVO4 nanostructure and YbVO4/CuWO4 nanocomposites for enhanced photocatalytic degradation of organic dyes under visible light. Ultrason Sonochem 2018;43:120–35. https://doi.org/10.1016/j.ultsonch.2017.11.040.

[131] Dutta DP, Tyagi AK. Facile sonochemical synthesis of Ag modified Bi4Ti3O12 nanoparticles with enhanced photocatalytic activity under visible light. Mater Res Bull 2016;74:397–407. https://doi.org/10.1016/j.materresbull.2015.11.005.

[132] Schulman JH, Stoeckenius W, Prince LM. Mechanism of formation and structure of micro emulsions by electron microscopy. J Phys Chem 1959;63:1677–80. https://doi.org/10.1021/j150580a027.

[133] Ganguli AK, Ganguly A, Vaidya S. Microemulsion-based synthesis of nanocrystalline materials. Chem Soc Rev 2010;39:474–85. https://doi.org/10.1039/B814613F.

[134] Sugimoto T. Underlying mechanisms in size control of uniform nanoparticles. J Colloid Interface Sci 2007;309:106–18. https://doi.org/10.1016/j.jcis.2007.01.036.

[135] Eastoe J, Hollamby MJ, Hudson L. Recent advances in nanoparticle synthesis with reversed micelles. Adv Colloid Interface Sci 2006;128–130:5–15. https://doi.org/10.1016/j.cis.2006.11.009.

[136] Anon. Structure and reactivity in reverse micelles. Netherlands: Elsevier; 1989.

https://www.twirpx.org & http://chemistry-chemists.com

[137] Luisi PL, Magid LJ, Fendler JH. Solubilization of enzymes and nucleic acids in hydrocarbon micellar solution. Crit Rev Biochem 1986;20:409–74. https://doi.org/10.3109/10409238609081999.

[138] Wu S, Fang J, Xu X, Liu Z, Zhu X, Xu W. Microemulsion synthesis, characterization of highly visible light responsive rare earth-doped Bi2O3. Photochem Photobiol 2012;88:1205–10. https://doi.org/10.1111/j.1751-1097.2012.01164.x.

[139] Abazari R, Mahjoub AR, Saghatforoush LA, Sanati S. Characterization and optical properties of spherical WO3 nanoparticles synthesized via the reverse microemulsion process and their photocatalytic behavior. Mater Lett 2014;133:208–11. https://doi.org/10.1016/j.matlet.2014.07.032.

[140] Liu W, Wang X, Cao L, Su G, Zhang L, Wang Y. Microemulsion synthesis and photocatalytic activity of visible light-active BiVO4 nanoparticles. Sci China Chem 2011;54:724–9. https://doi.org/10.1007/s11426-010-4156-z.

[141] Zhang L, Dai Z, Zheng G, Mu J, Yao Z. Synthesis and photocatalytic properties of Bi2MoO6 nanoparticles prepared via a water-in-oil microemulsion method. Ferroelectrics 2018;530:17–24. https://doi.org/10.1080/00150193.2018.1454051.

[142] Salager J-L. Emulsion properties and related know-how to attain them; 2000. p. 73–125. https://doi.org/10.1201/b14005-4.

[143] Djordjevic L, Primorac M, Stupar M, Krajisnik D. Characterization of caprylocaproyl macrogolglycerides based microemulsion drug delivery vehicles for an amphiphilic drug. Int J Pharm 2004;271:11–9. https://doi.org/10.1016/j.ijpharm.2003.10.037.

[144] Besra L, Liu M. A review on fundamentals and applications of electrophoretic deposition (EPD). Prog Mater Sci 2007;52:1–61. https://doi.org/10.1016/j.pmatsci.2006.07.001.

[145] Sarkar P, Nicholson PS. Electrophoretic deposition (EPD): mechanisms, kinetics, and application to ceramics. J Am Ceram Soc 1996;79:1987–2002. https://doi.org/10.1111/j.1151-2916.1996.tb08929.x.

[146] Binner J. Advanced ceramic processing and technology, http://proxy.library.carleton.ca/login?url=http://app.knovel.com/web/toc.v/cid:kpACPT0004; 1990.

[147] Zhitomirsky I. Cathodic electrodeposition of ceramic and organoceramic materials. Fundamental aspects. Adv Colloid Interface Sci 2002;97:279–317. https://doi.org/10.1016/S0001-8686(01)00068-9.

[148] Singh J, Manna AK, Soni RK. Sunlight driven photocatalysis and non-enzymatic glucose sensing performance of cubic structured CuO thin films. Appl Surf Sci 2020;530:147258. https://doi.org/10.1016/j.apsusc.2020.147258.

[149] Wang D, Li R, Zhu J, Shi J, Han J, Zong X, et al. Photocatalytic water oxidation on BiVO4 with the electrocatalyst as an oxidation cocatalyst: essential relations between electrocatalyst and Photocatalyst. J Phys Chem C 2012;116:5082–9. https://doi.org/10.1021/jp210584b.

[150] Vázquez A, Hernández-Uresti DB, Obregón S. Electrophoretic deposition of CdS coatings and their photocatalytic activities in the degradation of tetracycline antibiotic. Appl Surf Sci 2016;386:412–7. https://doi.org/10.1016/j.apsusc.2016.06.034.

[151] Zargazi M, Entezari MH. Anodic electrophoretic deposition of Bi2WO6 thin film: high photocatalytic activity for degradation of a binary mixture. Appl Catal Environ 2019;242:507–17. https://doi.org/10.1016/j.apcatb.2018.09.093.

[152] Obregón S, Hernández-Uresti DB, Vázquez A, Sánchez-Martínez D. Electrophoretic deposition of PbMoO4 nanoparticles for photocatalytic degradation of tetracycline. Appl Surf Sci 2018;457:501–7. https://doi.org/10.1016/j.apsusc.2018.06.203.

[153] Van der Biest OO, Vandeperre LJ. Electrophoretic deposition of materials. Annu Rev Mater Sci 1999;29:327–52. https://doi.org/10.1146/annurev.matsci.29.1.327.

[154] Marín-Suárez M, Medina-Rodríguez S, Ergeneman O, Pané S, Fernández-Sánchez JF, Nelson BJ, et al. Electrophoretic deposition as a new approach to produce optical sensing films adaptable to microdevices. Nanoscale 2014;6:263–71. https://doi.org/10.1039/C3NR03336H.

https://www.twirpx.org & http://chemistry-chemists.com

[155] Wei M, Ruys AJ, Swain MV, Kim SH, Milthorpe BK, Sorrell CC. Interfacial bond strength of electrophoretically deposited hydroxyapatite coatings on metals. J Mater Sci Mater Med 1999;10:401–9. https://doi.org/10.1023/A:1008923029945.

[156] Mishra A, Bhatt N, Bajpai AK, Nguyen Tri P, Rtimi S, Ouellet Plamondon CM. Chapter 12 - nanostructured superhydrophobic coatings for solar panel applications. In: Micro and nano technologies. Elsevier; 2019. p. 397–424. https://doi.org/10.1016/B978-0-12-815884-5.00012-0.

[157] Jeffrey BC, Scherer GW. Sol-gel science: the physics and chemistry of sol-gel processing. Saint Louis: Elsevier Science; 2014.

[158] Zhang L-W, Wang Y-J, Cheng H-Y, Yao W-Q, Zhu Y-F. Synthesis of porous Bi2WO6 thin films as efficient visible-light-active photocatalysts. Adv Mater 2009;21:1286–90. https://doi.org/10.1002/adma.200801354.

[159] Hussain T, Junaid M, Qayyum HA. Preparation of Ba-doped SrTiO3 photocatalyst by sol-gel method for hydrogen generation. Chem Phys Lett 2020;754:137741. https://doi.org/10.1016/j.cplett.2020.137741.

[160] Azzedine B, Chakaroun M, Fischer A. Organic Light-emitting Diodes. In: Organic lasers; 2017. p. 49–93. https://doi.org/10.1016/B978-1-78548-158-1.50002-X.

[161] Sahu N, Parija B, Panigrahi S. Fundamental understanding and modeling of spin coating process: a review. Indian J Phys 2009;83:493–502. https://doi.org/10.1007/s12648-009-0009-z.

[162] Perednis D, Gauckler LJ. Thin film deposition using spray pyrolysis. J Electroceram 2005;14:103–11. https://doi.org/10.1007/s10832-005-0870-x.

[163] Balkenende AR, Bogaerts AAMB, Scholtz JJ, Tijburg RRM, Willems HX. Thin MgO layers for effective hopping transport of electrons. Philips J Res 1996;50:365–73. https://doi.org/10.1016/S0165-5817(97)84680-3.

[164] Arya SPS, Hintermann HE. Growth of Y-Ba-Cu-O superconducting thin films by ultrasonic spray pyrolysis. Thin Solid Films 1990;193–194:841–6. https://doi.org/10.1016/0040-6090(90)90237-8.

[165] Chen C, Kelder EM, van der Put PJJM, Schoonman J. Morphology control of thin LiCoO2 films fabricated using the electrostatic spray deposition (ESD) technique. J Mater Chem 1996;6:765–71. https://doi.org/10.1039/JM9960600765.

[166] Gurav A, Kodas T, Pluym T, Xiong Y. Aerosol processing of materials. Null, 19; 1993. p. 411–52. https://doi.org/10.1080/02786829308959650.

[167] Mooney JB, Radding SB. Spray pyrolysis processing. Annu Rev Mater Sci 1982;12:81–101. https://doi.org/10.1146/annurev.ms.12.080182.000501.

[168] Saha JK, Bukke RN, Mude NN, Jang J. Significant improvement of spray pyrolyzed ZnO thin film by precursor optimization for high mobility thin film transistors. Sci Rep 2020;10:8999. https://doi.org/10.1038/s41598-020-65938-6.

[169] Wang F, Chemseddine A, Abdi FF, van de Krol R, Berglund SP. Spray pyrolysis of CuBi2O4 photocathodes: improved solution chemistry for highly homogeneous thin films. J Mater Chem A 2017;5:12838–47. https://doi.org/10.1039/C7TA03009F.

[170] Li M, Zhao L, Guo L. Preparation and photoelectrochemical study of BiVO4 thin films deposited by ultrasonic spray pyrolysis. Int J Hydrogen Energy 2010;35:7127–33. https://doi.org/10.1016/j.ijhydene.2010.02.026. 09.

[171] Polat K. Thin film photocatalyst made from Fe2O3/2D graphene/Cu working in the visible region of the solar spectrum. Solid State Commun 2020;319:113993. https://doi.org/10.1016/j.ssc.2020.113993.

[172] Saroni A, Alizadeh M, Rahman SA, Meevasana W, Goh BT. In-situ synthesis of In2O3-based heterojunction thin films for enhanced visible light photoelectrochemical performance. J Power Sources 2020;480:228829. https://doi.org/10.1016/j.jpowsour.2020.228829.

https://www.twirpx.org & http://chemistry-chemists.com

[173] Hammami H, Marzougui M, Oueslati H, Rabeh MB, Kanzari M. Synthesis, growth and characterization of Cu2CoSnS4 thin films via thermal evaporation method. Optik 2021;227:166054. https://doi.org/10.1016/j.ijleo.2020.166054.

[174] Jeffrey Brinker C, Hurd AJ. Fundamentals of sol-gel dip-coating. J Phys III France 1994;4:1231–42.

[175] Arendt E, Maione A, Klisinska A, Sanz O, Montes M, Suarez S, et al. Structuration of LaMnO3 perovskite catalysts on ceramic and metallic monoliths: physico-chemical characterisation and catalytic activity in methane combustion. Appl Catal Gen 2008;339:1–14. https://doi.org/10.1016/j.apcata.2008.01.016.

[176] Joshi M, Butola B. Application technologies for coating, lamination and finishing of technical textiles. In: Advances in the dyeing and finishing of technical textiles; 2013. p. 355–411. https://doi.org/10.1533/9780857097613.2.355.

[177] Scriven LE. Physics and applications of DIP coating and spin coating. MRS proceedings. 121; 1988. p. 717. https://doi.org/10.1557/PROC-121-717.

[178] Rahaman MN. Ceramic processing and sintering. 2nd ed; 2017. https://doi.org/10.1201/9781315274126.

[179] Liu S, Zhao X, Zeng H, Wang Y, Qiao M, Guan W. Enhancement of photoelectrocatalytic degradation of diclofenac with persulfate activated by Cu cathode. Chem Eng J 2017;320:168–77. https://doi.org/10.1016/j.cej.2017.03.047.

[180] Zhao X, Qu J, Liu H, Hu C. Photoelectrocatalytic degradation of triazine-containing azo dyes at γ-Bi2MoO6 film electrode under visible light irradiation ($\lambda > 420$ nm). Environ Sci Technol 2007;41:6802–7. https://doi.org/10.1021/es070598b.

[181] Zhao X, Wu Y, Yao W-Q. Photoelectrochemical properties of thin Bi2WO6 films. Thin Solid Films 2007;515:4753–7. https://doi.org/10.1016/j.tsf.2006.11.017.

[182] Tang X, Yan X. Dip-coating for fibrous materials: mechanism, methods and applications. J Sol-Gel Sci Technol 2017;81:378–404. https://doi.org/10.1007/s10971-016-4197-7.

[183] Chaki SH, Mahato KS, Malek TJ, Deshpande MP. CuAlS2 thin films—dip coating deposition and characterization. Journal of Science: Advanced Materials and Devices 2017;2:215–24. https://doi.org/10.1016/j.jsamd.2017.04.002.

[184] Sahoo SK, Manoharan B, Sivakumar N, Thomas S, Thankappan A. Introduction: why perovskite and perovskite solar cells? Academic Press; 2018. p. 1–24. https://doi.org/10.1016/B978-0-12-812915-9.00001-0. Chapter 1.

[185] Neacsu I, Nicoară A, Vasile O, Vasile B. Inorganic micro- and nanostructured implants for tissue engineering; 2016. p. 271–95. https://doi.org/10.1016/B978-0-323-42862-0.00009-2.

[186] Aidun CK, Triantafillopoulos NG. High-speed blade coating. Dordrecht: Springer Netherlands; 1997. p. 637–72. https://doi.org/10.1007/978-94-011-5342-3_18.

[187] Howatt GN. Method of producing high dielectric high insulation ceramic plates; 1952.

[188] Berni A, Mennig M, Schmidt H. Doctor blade. Boston, MA: Springer US; 2004. p. 89–92. https://doi.org/10.1007/978-0-387-88953-5_10.

[189] Deepa KG, Ramamurthy PC, Singha MK. Mesoporous Cu2ZnSnS4 nanoparticle film as a flexible and reusable visible light photocatalyst. Opt Mater 2019;98:109492. https://doi.org/10.1016/j.optmat.2019.109492.

[190] Zhu J, Li W, Li J, Li Y, Hu H, Yang Y. Photoelectrochemical activity of NiWO4/WO3 heterojunction photoanode under visible light irradiation. Electrochim Acta 2013;112:191–8. https://doi.org/10.1016/j.electacta.2013.08.146.

[191] Hong SJ, Jun H, Borse PH, Lee JS. Size effects of WO3 nanocrystals for photooxidation of water in particulate suspension and photoelectrochemical film systems. Int J Hydrogen Energy 2009;34:3234–42. https://doi.org/10.1016/j.ijhydene.2009.02.006.

https://www.twirpx.org & http://chemistry-chemists.com

[192] Cong Y, Ji Y, Ge Y, Jin H, Zhang Y, Wang Q. Fabrication of 3D Bi2O3-BiOI heterojunction by a simple dipping method: highly enhanced visible-light photoelectrocatalytic activity. Chem Eng J 2017;307:572–82. https://doi.org/10.1016/j.cej.2016.08.114.

[193] Md E, Akter S, Hossain MA, Suhag MH. Fabrication of Zn3(PO4)2/carbon nanotubes nanocomposite thin film via sol-gel drop coating method with enhanced photocatalytic activity. Thin Solid Films 2021;717:138472. https://doi.org/10.1016/j.tsf.2020.138472.

[194] Du X, Wang X, Liu Y, Feng P. Spray solution combustion synthesis of hollow porous MoO3 photocatalyst. Ceram Int 2019;45:12599–601. https://doi.org/10.1016/j.ceramint.2019.03.168.

[195] Zhu D, Zhou Q. Novel Bi2WO6 modified by N-doped graphitic carbon nitride photocatalyst for efficient photocatalytic degradation of phenol under visible light. Appl Catal Environ 2020;268:118426. https://doi.org/10.1016/j.apcatb.2019.118426.

[196] Kumar A, Raizada P, Singh P, Hosseini-Bandegharaei A, Thakur VK. Facile synthesis and extended visible light activity of oxygen and sulphur co-doped carbon nitride quantum dots modified Bi2MoO6 for phenol degradation. J Photochem Photobiol A Chem 2020;397:112588. https://doi.org/10.1016/j.jphotochem.2020.112588.

[197] Wu Z, Xue Y, He X, Li Y, Yang X, Wu Z, et al. Surfactants-assisted preparation of BiVO4 with novel morphologies via microwave method and CdS decoration for enhanced photocatalytic properties. J Hazard Mater 2020;387:122019. https://doi.org/10.1016/j.jhazmat.2020.122019.

[198] Gyawali G, Adhikari R, Joshi B, Kim T, Glez V, Lee S. Sonochemical synthesis of solar-light-driven Ag°-PbMoO4 photocatalyst; 2014.

[199] Chachvalvutikul A, Pudkon W, Luangwanta T, Thongtem T, Thongtem S, Kittiwachana S, et al. Enhanced photocatalytic degradation of methylene blue by a direct Z-scheme Bi2S3/ZnIn2S4 photocatalyst. Mater Res Bull 2019;111:53–60. https://doi.org/10.1016/j.materresbull.2018.10.034.

[200] Ramasamy Raja V, Rosaline DR, Suganthi A, Rajarajan M. Facile sonochemical synthesis of Zn2SnO4-V2O5 nanocomposite as an effective photocatalyst for degradation of Eosin Yellow. Ultrason Sonochem 2018;44:310–8. https://doi.org/10.1016/j.ultsonch.2018.02.043.

[201] Ge L, Zhang X, Liu J. Synthesis and photocatalytic performance of novel visible-light-driven Bi2WO6 photocatalyst via a reverse microemulsion process. Adv Mat Res 2010;105–106:837–40. https://doi.org/10.4028/www.scientific.net/AMR.105-106.837.

[202] Ma Q, Hu X, Liu N, Sharma A, Zhang C, Kawazoe N, et al. Polyethylene glycol (PEG)-modified Ag/Ag2O/Ag3PO4/Bi2WO6 photocatalyst film with enhanced efficiency and stability under solar light. J Colloid Interface Sci 2020;569:101–13. https://doi.org/10.1016/j.jcis.2020.02.064.

https://www.twirpx.org & http://chemistry-chemists.com

https://www.twirpx.org & http://chemistry-chemists.com

4

Carbon-based materials for visible light photocatalysis

Rajashree Sahoo[a] and Arpan Kumar Nayak[b]

[a]DEPARTMENT OF PHYSICS, SCHOOL OF APPLIED SCIENCES, KIIT DEEMED TO BE UNIVERSITY, ODISHA, INDIA [b]DEPARTMENT OF PHYSICS, SCHOOL OF ADVANCED SCIENCES, VELLORE INSTITUTE OF TECHNOLOGY, VELLORE, TAMIL NADU, INDIA

1 Introduction

Rapid industrialization and economic growth have created serious hazardous environmental pollution and lack of energy sources. These two have emerged as worldwide issues which have serious impacts on the sustainable development of the society. To overcome these problems, the industry should focus on clean energy sources and remedies for environmental pollution [1]. In this context, photocatalysis has been considered as a clean environmental remediation technology and has attracted researchers' attention due to its several advantages like low cost, abundant availability, and inexhaustible energy sources [2, 3]. Until now, various photocatalytic processes were developed for different applications such as water splitting [4, 5], self-cleaning surfaces [6], decomposition of organic contaminants [7, 8], bacteria disinfection [9, 10], and reduction of CO_2 [11, 12]. Mainly, the performance of photocatalysis depends on the photocatalyst's nature and properties. It has been seen that photocatalysts are mostly semiconductors, such as "TiO_2," which was first used by Fujishima and Honda in 1972 for H_2 generation, ZnO, SnO_2, etc. [13]. Subsequently metal oxide-based, metal sulfide-based, and metal nitride-based semiconductor photocatalysts were developed for photocatalysis application. However, several issues were found in the above photocatalysts such as low utilization efficiency of visible light from solar energy, wide energy bandgap, toxicity, high recombination rate of photogenerated electron-hole pairs, insufficient physicochemical stability, and limited storage in the earth of metal-based semiconductors [14–18]. Thus, there is a need for the development of metal-free catalysts with more efficiency in the visible region, low cost, and good stability [19–22]. Therefore, carbonaceous materials like activated carbons, carbon dots, graphene, fullerene, carbon nanotube, carbon nanofiber, etc. have been developed for this purpose. Carbon is abundantly available and can be used in large-scale applications. It not only increases the light absorption region but also enhances the absorption of reactants toward active sites. Thus, new opportunities using carbonaceous materials to achieve enhanced photocatalytic activity are welcomed. Five

Nanostructured Materials for Visible Light Photocatalysis. https://doi.org/10.1016/B978-0-12-823018-3.00006-3
Copyright © 2022 Elsevier Inc. All rights reserved.

https://www.twirpx.org & http://chemistry-chemists.com

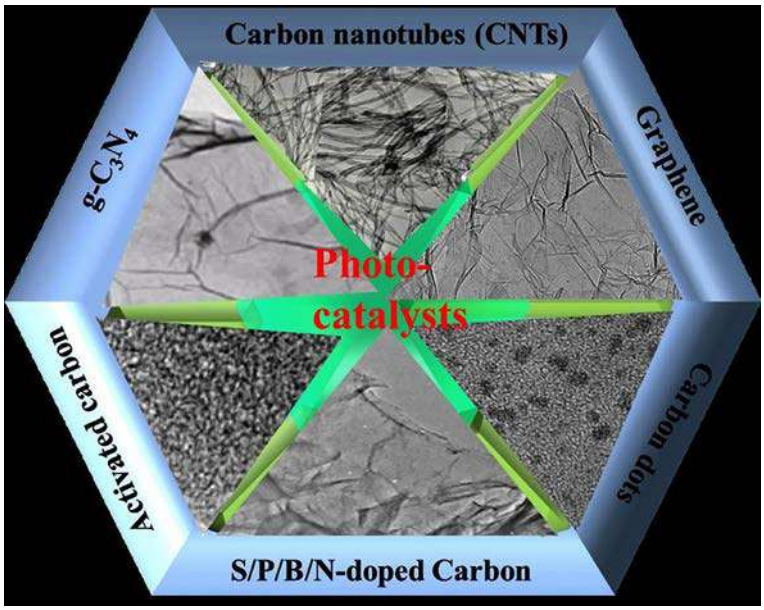

SCHEME 1 Schematic representation of carbon-based materials.

critical aspects play important roles in increasing the photocatalytic activity of materials in the visible region:

(1) reduction of the bandgap to increase visible light exposure efficiency;
(2) enhancement of light absorption capacity for the generation of more and more electron-hole pairs;
(3) prevention of electron-hole pair recombination to increase quantum efficiency;
(4) increment of surface area of the photocatalyst to increase more active sites;
(5) improvement in the physicochemical stability of the photocatalyst to ensure long-term performance during the reaction.

In this chapter, a comprehensive review on carbon-based materials in the presence of visible light is provided. This review covers the synthesis and application of carbon-based materials like CNTs, graphene, carbon-dots (C-dots), AC, C60, and g-C_3N_4, as shown in Scheme 1.

2 Carbon-based materials

2.1 Carbon nanotubes (CNTs)

Carbon nanotubes (CNTs) are 1D structures synthesized through graphite sheets with excellent mechanical, electrical, and thermal properties. CNTs can be synthesized using

https://www.twirpx.org & http://chemistry-chemists.com

various methods including laser ablation of graphite, chemical vapor deposition, plasma-enhanced CVD methods, arc discharge, etc. They are promising materials for cleanliness of the environment due to their large surface area, presence of pi bond electrons on the surface, and formation of more active sites on the hollow nanotubes.

2.2 Synthesis process of carbon nanotubes (CNTs)

2.2.1 Electric arc discharge

This technique requires high temperature, i.e., 1700°C for CNTs synthesis. In the arc discharge setup, two graphite rods having diameters of 7 and 20 mm are placed at a distance of 1–2 mm at a subatmospheric pressure. This chamber contains some evaporated gas molecules, some solid metal catalyst particles, and a graphite cathode and anode. When a current is passed through this arcing process, the chamber is heated up to 4000 K with the result that half of the solidified carbon forms a cylindrical hard cigar-like structure and the anode is consumed. Chamber soot forms near the walls of the chamber and cathode soot near the cathode. The inner core which forms cathode soot and chamber soot is soft and dark, and forms either single-walled or multiwalled carbon nanotubes [23].

2.2.2 Laser ablation method

In this method, a quartz tube containing pure graphite is heated in a furnace at 1200°C in an inert atmosphere using high power laser vaporization. The main aim is to vaporize the graphite inside the quartz. For generation of single-wall carbon nanotubes (SWNTs), using the metal particles as catalyst to the graphite target with the help of laser ablation technique is necessary. A previous report has shown that the diameter of the nanotube becomes thinner with the variation of laser power [24]. Studies have also shown that ultrafast laser pulses are able to produce large amount of SWNTs.

Several parameters are optimized like structural and chemical properties of the target material, the laser properties like the fluence, wavelength, and repetition rate, etc., as these are needed for the preparation of CNTs. This method carries a good property for the production for SWNTs. The main advantage is that it produces relatively high yield. However, the obtained nanotubes in this process are not uniform, which is the major disadvantage in this process.

2.2.3 Chemical vapor deposition (CVD)

This method is basically the catalytic decomposition of hydrocarbon using the metal as a catalyst [25]. Horizontal configuration and vertical configuration furnaces are used for this purpose. In the case of a horizontal configuration furnace, the catalyst is placed in a quartz tube. The hydrocarbon and an inert gas mixture cross over the catalyst at temperatures of 500–1100°C. CNTs are obtained by cooling the system to room temperature. In the case of a vertical configuration furnace, the catalyst and carbon source are placed at the top of the furnace for the formation of carbon fibers/nanotubes. Mainly the nanotube growth

https://www.twirpx.org & http://chemistry-chemists.com

mechanism in the CVD process helps in the separation of hydrocarbon molecules catalyzed by the transition metal and the saturation of carbon atoms occurs in the metal nanoparticle [25]. The formation of tubular carbon solids carries a sp^2 structure. There are different working conditions such as temperature, volume, concentration of hydrocarbon, etc. to be maintained for the formation of carbon nanotubes using the CVD method [26]. The length and diameter of the tube can be controlled by varying reaction time and active particles on the surface of the catalyst [27].

Different structures of carbon are formed like amorphous carbon layers on the catalyst, SWNTs and MWNTs prepared from filaments of amorphous carbon, and well-crystallized graphite layers. It allows selective CNT growth in various forms like powder form [28, 29] and aligned forrest of CNTs [30, 31]. The produced nanotubes have straight, curved, planar-spiral-like structures. In particular, CCVD (catalytic chemical vapor deposition) gives the possibility of growing CNTs using a catalyst on a desired substrate [32, 33]. It is used in some fields like field-emission displays [34], specific designing of nanotube devices [35], or probe tips of scanning probe microscopes (SPMs) [36, 37].

2.2.4 Electrolysis

Electrolysis is a common method for production of CNT and was developed by Hsu et al. in 1995 [38]. According to Abbasloo et al., production of CNTs through electrolysis involves molten alkali metal chlorides in a graphite crucible acting as the anode, and a graphite rod dipped in the melt behaves as the cathode [39]. However, some researchers also used alumina crucibles containing salt used for melting and two graphite rods act as the anode and cathode electrode [40–43]. During the process, the graphite cathode is destroyed and carbon constituents are released from the graphite surface with the result of formation of CNTs inside liquid phase. After this process, the molten salt cools down. The solidified salt is washed off with distilled water to retrieve the carbon product [39]. Similarly, Bai et al. have grown SWNTs and MWNTs using NaCl electrolysis [38, 39].

Novoselovaa et al. developed a new synthetic technique for the production of carbon nanotubes from CO_2 [44]. From a liquid salt phase a new condensed carbon phase is formed on the cathode. A ternary mixture of earth metal chloride was used as the base electrolyte. It was found that the obtained MWNTs are mostly in the curved form which agglomerates into bundles. The outer diameter of CNTs ranged from 5 to 250 nm, whereas the inner diameter ranges from 2 to 140 nm. Mostly CNTs are covered with electrolyte salt. It has been seen that with the increase of current density, the diameter of the nanotube decreases and at the same time carbon yield increases [44].

2.3 Carbon dots (CDs)

C-dots synthetization follows two methods: the top-down approach and the bottom-up approach, as shown in Fig. 1 [45, 46]. The top-down approach refers to breaking of bigger carbon structures through chemical oxidation, discharge, electrochemical oxidation, and ultrasonic methods [46]. On the other side, the bottom-up approach refers to construction

https://www.twirpx.org & http://chemistry-chemists.com

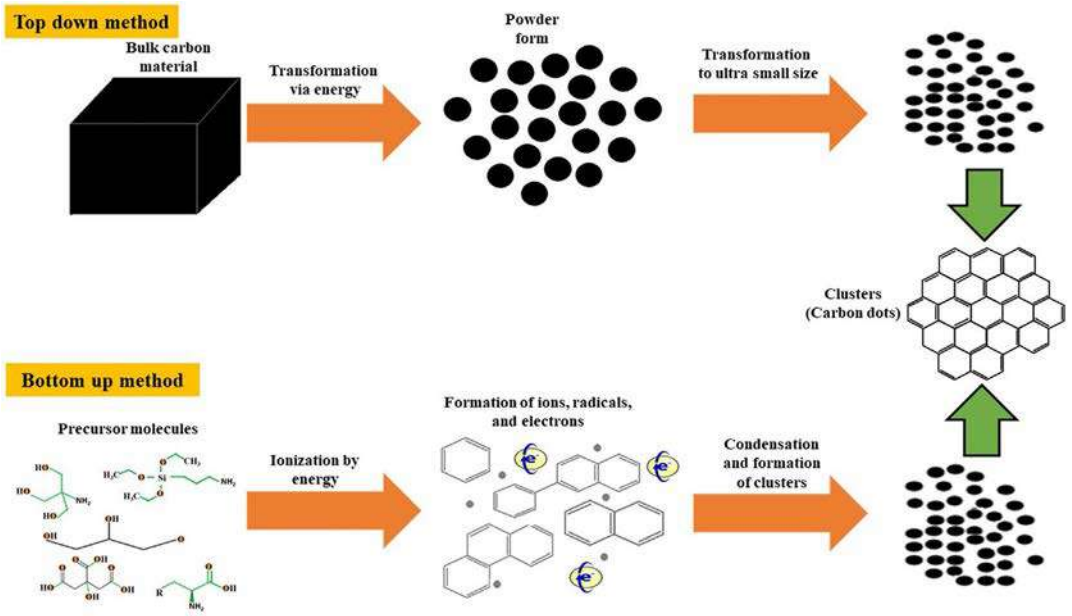

FIG. 1 Synthesis methods of CDs [45].

of bigger carbon structures through hydrothermal treatment, ultrasonic treatment, thermal decomposition, pyrolysis, and the solvothermal method [46].

Han et al. synthesized C-dots using the hydrothermal method where two precursors like citric acid (0.40 g) and L-histidine (0.14 g) were used. A colorless solution was made and sealed at temperature 200°C for 5 h. The solution was centrifuged at 4000 rpm for 15 min for the removal of precipitate. The C-dots were collected by washing with ultrapure water for 12 h at room temperature [47].

Similarly, Kapitonov et al. synthesized CDs using the hydrothermal method. The experiment was carried out in an autoclave within a drying cabinet having temperature 180°C for 10–18 min and 5 h. The soots were obtained from the composition of carbon black, NH_3, and DI water. The synthesis times were 1, 2, and 4 h. Another method is using berry juices. These juices were obtained by pressing cowberry and blueberry juices with the composition of juice (2 mL), of NH_3 (6 mL), and DI (15 mL) [48].

Carvalho et al. synthesized C-dots using the carbonization method [49]. In this method, an acerola fruit juice was made. From this, 20 g of juice was transferred into an autoclave chamber. The chamber was sealed and put into an oven and kept for 12, 18, 24, and 36 h with different temperatures 100°C, 130°C, 160°C, and 180°C to get the reaction product. The reaction product was centrifuged for the removal of black precipitates. Qu et al. also made CDs using the hydrothermal method where an aqueous solution was heated at 180°C temperature for 6 h in an autoclave. The obtained spherical CDs were purified via a centrifugation process having an average diameter of about 3.8 nm [50].

https://www.twirpx.org & http://chemistry-chemists.com

2.4 Graphitic carbon nitride (g-C_3N_4)

Covalent carbon nitride was discovered by Berzelius with two substructures heptazine and poly units [51]. It has seven different phases, namely α-C_3N_4, β-C_3N_4, cubic-C_3N_4, pseudocubic-C_3N_4, g-h-triazine, g-h-heptazine, and g-o-triazine, possessing bandgaps of 5.49, 4.85, 4.30, 4.13, 2.97, 2.88, and 0.93 eV respectively [52]. Here the pseudocubic-C_3N_4 and g-h-triazine-C_3N_4 possess a direct bandgap structure, whereas α-C_3N_4, β-C_3N_4, cubic-C_3N_4, g-h-heptazine, and g-o-triazine possess an indirect bandgap structure in bulk form [52]. g-C_3N_4 is a stable, highly ordered polymeric structure [53]. It can be prepared by adding precursors like melamine, urea, and/or uric acid through thermal polymerization at 400–600°C. It helps in the generation of H_2 and O_2 from water splitting reported by Wang et al. [54]. It has received researchers' attention due to its unique properties such as suitable bandgap energy (≈2.7 eV) which helps in photocatalytic H_2 generation and removal of pollutants in visible light exposure [55–57]. It constitutes 43% of the solar spectrum in electromagnetic radiation. Thus, it possesses better photocatalytic efficiency in the visible region. Using heteroatom doping and copolymerization in the electronic band structure of g-C_3N_4 helps in the enhancement of light absorption capacity and redox potential adjustment for necessary reactions.

To develop a metal-free photocatalyst, modification in g-C_3N_4 with other metalloid materials is required to improve its photocatalytic activity for H_2 evolution. Recently some researchers reported on metal-free catalysts on g-C_3N_4 modified with carbon nanodots. Kang's group was involved in the study of H_2 generation from water splitting using a metal-free carbon nanodot-carbon nitride (C_3N_4) nanocomposite as a catalyst in the presence of solar light exposure [20]. In the conversion of solar energy to hydrogen energy, the overall energy conversion was calculated to be 2% which is one order of magnitude higher than that previously reported regarding water splitting photocatalysts. Two electron processes were involved for the water splitting process. The CDs were prepared by a typical electrochemical method followed by a hydrothermal process using ammonia [48]. After that, ammonia-treated mixtures were heated at 550°C for 3 h and CDs-C_3N_4 composites were formed. The bandgap was found between 2.0 and 2.7 eV from the Tauc plot curve, which was helpful for absorption of light and increased the photocatalytic efficiency [20].

Subsequently, Gao et al. investigated a photocatalytic study for hydrogen generation by water splitting using C-dots with a g-C_3N_4 photocatalyst. The DFT calculation was done to understand the interactions occurring between g-C_3N_4 and trigonal/hexagonal shaped C-dots. It was found that hybrid C-dots/g-C_3N_4 form a type-II Van der Waals heterojunction, which leads to bandgap reduction and increases photogenerated electron-hole pairs [58].

Xia et al. also prepared g-C_3N_4 nanosheets (CNNS) with CQDs using a one-step hydrothermal method. H_2 generation was observed near the infrared region. The H_2 production rate was 6.76 μmol h^{-1} g^{-1} without any cocatalysts, with the wavelength 808 nm [59]. This was possible due to the special interaction and electronic coupling, which increases the absorption region into the NIR region.

https://www.twirpx.org & http://chemistry-chemists.com

Table 1 Photocatalytic H_2-evolution studies using metal-free photocatalysts.

Photocatalyst	Synthesis method	Light source	Bandgap	H_2 evol. (μmol h^{-1} g^{-1})	Reference
C-dots-C_3N_4 composites	Electrochemical method followed by hydrothermal treatment	300 W Xe-lamp $\lambda > 420$ nm	2.7 eV	105	[20]
C-dots-g-C_3N_4		Visible	1.45 eV		[58]
CQDs/g-C_3N_4 nanosheets	One-step hydrothermal method	808 nm laser		6.76	[59]
C-ZIF/g-C_3N_4 composite	Facile thermal condensation method	300 W Xe-lamp $\lambda > 420$ nm		326	[60]
MWCNTs/g-C_3N_4	Cyanamide (550C in air for 4 h)	300 W Xenon lamp			[61]
Boron carbide		300 W Xe-lamp $\lambda \geq 420$ nm		14.5	[62]

Another report by He et al. studied the carbon-based photocatalytic system for H_2 generation using C-ZIF (ZIF-8 derived carbon) as an electron acceptor and cocatalysts g-C_3N_4 through a facile thermal condensation process. The C-ZIF/g-C_3N_4 composite showed a better photocatalytic H_2 production rate compared to pure g-C_3N_4 under visible light irradiation. This may be due to C-ZIF/g-C_3N_4 promoting greater charge carrier separation and transfer [60]. The C-ZIF acts not only as an effective electron acceptor, but also as a good cocatalyst to promote photocatalytic H_2 generation. This study was one of the effective works for the metal-free H_2 generation using carbon-based materials.

Suryawanshi et al. studied the evolution of H_2 from water splitting using g-C_3N_4 with MWCNTs in the presence of visible light. The composite was synthesized by adding MWCNT in situ to a 1.5 M aqueous solution of cyanamide with the heat treatment of 550°C in air for 6 h. This showed 100% improvement in its photocatalytic activity [61]. Therefore, these types of studies have given great cause for optimism in terms of constructing metal-free photocatalysts for H_2 generation under visible light exposure. Table 1 shows photocatalytic H_2 generation using various metal-free photocatalysts.

2.5 Graphene

Graphene is one of the advanced carbon nano-materials used worldwide having unique properties like zero bandgap, large surface area, high thermal conductivity, and hydrophilic properties [57, 63–65]. It is an allotrope of carbon where the carbon atoms are arranged in a single layer. The carbon atoms are sp^2-hybridized in a two-dimensional arrangement having a honeycomb or hexagonal structure [57].

There are different derivatives of graphene like graphene oxide (GO) and reduced graphene oxide (RGO). These can be easily prepared via the reduction of graphene oxide (GO)

https://www.twirpx.org & http://chemistry-chemists.com

using a facile chemical exfoliation method [66]. Graphene oxide can be prepared through the Hummers method, which helps in the removal of pollutants from wastewater [63]. They can be also prepared through a low-cost chemical oxidation method followed by exfoliation in ultrasonication [67]. Graphene has gained researchers' attention in diverse field like electronics, photonics, capacitors, supercapacitors, biosensing, etc. It is used in several applications like photocatalysis, energy storage devices, drug delivery, etc. It is used as a good adsorbent, a good catalyst for H_2 evolution, and the removal of hazardous pollutants from wastewater [63].

2.5.1 N-doped carbon-based materials

Li et al. synthesized water-soluble N-doped CDs by taking ammonium citrate and ethylenediamine as two precursors and the aqueous solution was heated at 200°C for 5 h. The spherical shapes of N-doped CDs are obtained having an average diameter of 4.8 nm with a quantum yield of (QY) 66.8% [68].

Liu et al. developed N-CNT with mpg-C_3N_4 for the degradation of RhB, MO, and TC pollutants under visible light exposure. The material was prepared through a facile technique via thermal polycondensation. Photocatalytic degradation efficiency of 88% was achieved in the presence of the N-CNT/mpg-C_3N_4 sample but, in the case of the pure mpg-C_3N_4 sample, it showed poor photocatalytic activity. The N-CNT/mpg-C_3N_4 sample showed 4.9 times and 65.2 times higher photocatalytic activity than that of pure mpg-C_3N_4 and N-CNT samples for MO dye, respectively. The highest photocatalytic degradation efficiency was found to be 95% for decomposition of RhB dye [69]. Photocatalytic degradation efficiencies of tetracycline (TC) dye of 53.2% and 67.1% were achieved for pure mpg-C_3N_4 and N-CNT/mpg-C_3N_4 samples, respectively.

2.5.2 P, S-codoped carbon materials

Jiang et al. used phosphorus- and sulfur-codoped graphitic carbon nitride photocatalysts for the degradation of tetracycline and methyl orange dye under visible light exposure. These were prepared through in-situ thermal copolymerization of hexachlorocyclotriphosphazene and thiourea. They showed 5.9 times and 7.1 times better photocatalytic activity than that of individual g-C_3N_4 for the degradation of tetracycline (TC) and methyl orange (MO) dye, respectively [70]. This may be due to the doping of P and S which can broaden the visible light response and create defects in the samples. TOC removal of 70.33% and 55.37% was achieved for TC and MO dye, respectively [70].

Zheng et al. studied the dye degradation of Rhodamine B (RhB) and hexavalent chromium Cr(VI) using S-doped polymeric carbon nitride microrods as catalysts prepared through thermal polymerization under visible light exposure. The S-doped carbon nitride microrods prepared at a temperature of 650°C exhibited higher photocatalytic activity than that of bulk carbon nitride for degradation of RhB dye and less photocatalytic activity in the case of Cr(VI) dye [71].

Mathew et al. focused on methylene blue dye degradation using undoped carbon nanodots (CDs) and P-doped carbon nanodots (P-CDs) as catalysts under visible light exposure. They prepared the CDs and P-CDs using the hydrothermal method. Dye

https://www.twirpx.org & http://chemistry-chemists.com

degradation efficiency of 85% was achieved within 3 h in the case of P-CDs and in the case of CDs, 59% was achieved. This may be due to the P-doping which increases the electrostatic potential (V) at the surface and the holes from the valance band migrate to the surface [72].

Lv et al. synthesized sulfur-doped 2D graphitic carbon nitride nanosheets for the photodegradation of phenol and also hydrogen evolution. Degradation efficiency of 93% was achieved within 90 min of visible light exposure [73].

Duan and his group focused on catalytic oxidation reaction of phenol using S, N-codoped graphene. From the experimental and theoretical studies, it was demonstrated that codopants (S and N) enhance the PMS activation compared to the pristine and N- (or S-) sole-doped graphene [74]. This study showed the utilization of chemically modified graphene as a superior metal-free catalyst for sustainable environmental remediation.

Zhang et al. used phosphorus-doped carbon nitride materials synthesized through a one-pot green synthetic method for the degradation of Rhodamine B and methyl orange dye under visible light exposure. It was found that the P-doped carbon nitride material showed better photocatalytic activity than undoped g-C_3N_4. This may be due to high surface area and smaller structural size [75].

Zhou et al. prepared P-doped g-C_3N_4 synthesized through a thermally induced copolymerization method using hexachlorocyclotriphosphazene and guanidiniumhydrochloride as precursors. The photodegradation activity of P-doped g-C_3N_4 was three times higher than that of the pure g-C_3N_4 in the case of Rhodamine B dye. The P-doped g-C_3N_4 took only 10 min to decompose the dye, whereas pure g-C_3N_4 took 30 min for the decomposition of the dye [76].

Zheng et al. developed black phosphorus (BP) and polymeric carbon nitride (CN) through a one-step exfoliation method. When BP and CN are combined, they facilitate the charge separation and increase photocatalytic activity in the visible region. RhB degradation efficiency of 98% was achieved within 15 min of light exposure [77].

Xiao et al. developed S-doped porous g-C_3N_4 (C_3N_4-S) synthesized through a one-step calcination process. They used thiourea and melamine as precursors for the degradation of RhB dye under visible radiation. The degradation efficiency was found to be 96.13% within 18 min [78].

Liu et al. developed S-doped graphitic C_3N_4 for the degradation of phenol dye solution under visible light exposure. The surface area increased from 12 m^2/g of g-C_3N_4 to 63 m^2/g for S-doped g-C_3N_4, showing the photocatalytic oxidation of phenol [79].

2.5.3 B-doped carbon materials

Lu et al. developed boron-doped g-C_3N_4 for the photocatalytic reduction of UO_2^{2+} under visible light exposure. It has been observed that B-g-C_3N_4 has shown 2.54 times higher photocatalytic activity than g-C_3N_4. A narrow bandgap of the material leads to increase photogenerated electron-hole pairs under visible light irradiation [80].

Yan et al. also developed B-doped g-C_3N_4 nanosheets prepared through a facile one-pot strategy. They used H_3BO_3 and urea as the precursors during thermal polymerization for the degradation of MB dye under visible radiation. The B-doped g-C_3N_4 showed

https://www.twirpx.org & http://chemistry-chemists.com

17 times higher photocatalytic activity than g-C_3N_4 [81]. This may be due to the higher specific surface areas, narrow bandgap, and production of more active sites.

In addition, boron carbide ($B_{4.3}C$ and $B_{13}C_2$) and C-doped BN materials have shown promising photocatalytic activity for H_2 evolution under visible light [62, 82].

2.6 Photocatalytic reduction of CO_2

Global energy consumption is increasing day by day. Currently 80% of global energy consumption occurs due to fossil fuels. This not only creates harmful effects on the depletion layer but also increases CO_2 emissions in the atmosphere. Several technologies have been developed for the transformation of CO_2 into hydrocarbon fuels. In recent years, many semiconductor photocatalysts have been developed for the reduction of CO_2. However, nowadays researchers are focusing on metal-free photocatalysts for the photoreduction of CO_2.

Wang's group developed an ultrathin 2D/2D rGO/g-C_3N_4 nanocomposite using g-C_3N_4 nanosheets and graphene oxide (GO) followed by an $NaHSO_3$ reducing process. The enhanced photocatalytic activity of MO dye degradation and CO_2 reduction has been observed in the ultrathin 2D/2D rGO/g-C_3N_4 nanocomposite compared to pure g-C_3N_4 nanosheet in the visible region. This may be due to the strong interfacial interaction and fast charge carrier separation efficiency [83].

Ong et al. focused on sandwich-like graphene/g-C_3N_4 (GCN) nanocomposites using a facile one-pot impregnation-thermal reduction strategy. This sample showed slightly red shifting of absorption band edge which forms a covalent cross link between graphene and g-C_3N_4. It has high visible photocatalytic activity toward CO_2 reduction [84].

2.7 Photocatalytic removal of NO_x

Rapid industrialization releases hazardous gases like nitrogen monoxide and dioxide into the air. It creates air pollution. Due to this air pollution, NO_x emissions create acid rain and photochemical smog, which are harmful to human health. They cause heart disease, respiratory tract infection, stroke, lung cancer, and so on. Until now, several techniques have been developed for the removal of NO_x like a selective catalytic reduction system, an electrochemical reduction system, adsorption, chemical reaction, photocatalysis, and so on. Among them, metal-free photocatalysts during photocatalysis techniques play important roles for the removal of NO_x. The metal-free semiconductor of g-C_3N_4 has drawn the attention of researchers due to its good photocatalytic activity. Bulk-g-C_3N_4 has shown low photocatalytic activity because of its low specific surface area and fast recombination rate. Several approaches have been applied for increasing the efficiency of g-C_3N_4 by controlling the morphology of the sample and creating heterojunctions. Dong et al. constructed g-C_3N_4/g-C_3N_4 metal-free heterojunctions using an in-situ method for visible light photocatalysis. This heterojunction has shown an NO removal ratio of 47.6%, which is much higher than that of pure g-C_3N_4 [85]. Sano et al. synthesized g-C_3N_4 using an alkaline hydrothermal treatment. The specific surface area was increased from 7.7 to 65 m^2g^{-1} with an NaOH solution at 90–150°C. The oxidation rate of NO was increased by 8.6 times under visible light exposure [86]. Zhu et al. used g-C_3N_4 as the

https://www.twirpx.org & http://chemistry-chemists.com

polymeric material for NO decomposition. This g-C_3N_4 material is active at temperatures above 400°C for the decomposition of NO [87]. Its activity increased as the temperature rose. A discussion has also taken place on support for differentiating oxygen activation sites, a functional material for nanomaterial synthesis, and a good photocatalyst.

2.8 Photocatalytic degradation of organic pollutants

Rapid population growth and industrialization growth have brought hazardous organic pollutants into water. Different technologies like membrane filtration, chemical oxidation, and bioremediation using microorganisms have been developed. However, technologies that are robust and low cost are greatly needed. Thus, the degradation of organic pollutants via the photocatalysis technique is a green technique to decompose the pollutants and purify water. The basic mechanism of photocatalysis is shown in Scheme 2.

During the photocatalysis process, photoinduced electrons react with dissolved oxygen to form superoxide radicals ($^{\bullet}O_2^-$) and holes cannot directly oxidize the pollutants (Scheme 2). They react with water to form hydroxyl radicals ($^{\bullet}OH$). These superoxide radicals and hydroxyls react with the organic dyes, and the bigger molecules are reduced to smaller harmless molecules like CO_2 (Scheme 2).

Dong et al. developed a polymeric g-C_3N_4 layered material for RhB dye degradation under visible light exposure [88]. This material was synthesized by following a facile and efficient method using urea powder as the precursor. It was demonstrated from this experiment that the as-prepared g-C_3N_4 showed better photocatalytic activity than C-TiO_2. This may be due to the proper bandgap (2.7 eV), large surface area, and layered structure.

Zhu's group developed porous g-C_3N_4 synthesized by pyrolysis of dicyandiamide in air using urea as a bubble template. The nanostructures obtained showed efficient

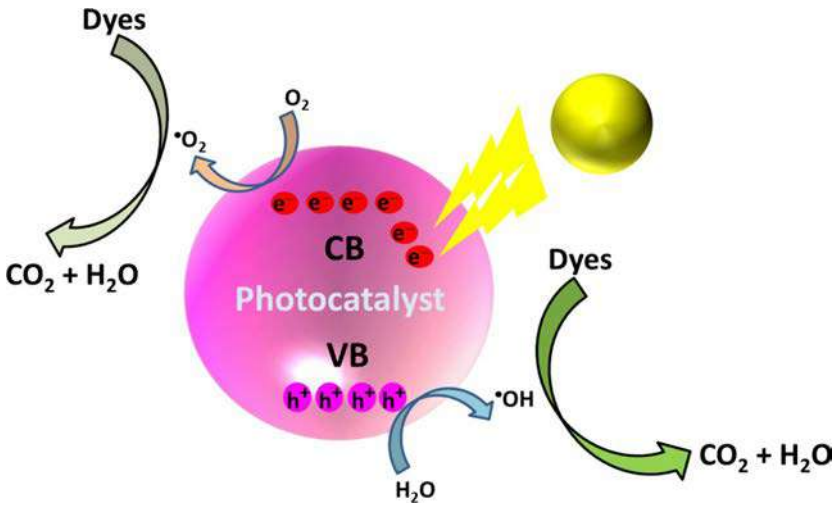

SCHEME 2 Photocatalytic degradation mechanism.

https://www.twirpx.org & http://chemistry-chemists.com

photocatalytic degradation of MB and phenol dye under visible light exposure. It was shown that the as-synthesized g-C_3N_4 had enhancement factors of 2.1 and 2.8 compared to the bulk g-C_3N_4 for MB and phenol dye, respectively. This may be due to the porous structure which changed the charge distribution of C_3N_4, making charge transfer easier. Zhu's group also developed a method to change the morphology of g-C_3N_4 from nanoplates to nanorods using a simple reflux method. It was found from the experiment that the g-C_3N_4 nanorod showed better photocatalytic activity for the degradation of MB dye under 500 W Xe lamp exposure than nanoplates. This may be due to the increment in the active lattice face [89]. Lin et al. developed a three-dimensionally ordered macroporous (3DOM) g-C_3N_4 photocatalyst synthesized through a thermal condensation-assisted colloidal crystal template method for the decomposition of RhB dye under visible light exposure. It was found that the 3DOM g-C_3N_4 showed 5.3 times better photocatalytic activity than the pure g-C_3N_4 samples [90]. Degradation efficiency of 100% was achieved within 40 min of light exposure. This is due to the large surface area and porosity, which increase the number of reaction active sites. The 3DOM active structure provides optical absorption active sites which help in photon trapping and energy bandgap narrowing.

Tahir et al. developed graphitic-C_3N_4nanofibers (GCNNFs) for supercapacitor and photocatalysis application. A facile chemical route was applied for the fabrication of this nanofiber. The photocatalytic dye degradation of RhB dye was performed using GCNNF and GCN. The GCNNF showed better photocatalytic activity due to large surface area, suitable bandgap, and less crystal defects. This sample has also high reproducibility [91]. Gong et al. developed a metal-free polyimide (PI)/g-C_3N_4 heterojunction synthesized through a sonochemical approach. It has shown high photocatalytic activity for degradation of 2,4-dichlorophenol (2,4-DCP) dye under visible light exposure. It has also shown 3.8 times higher photocatalytic activity than g-C_3N_4. This was due to the proper bandgap and different electronic structure of g-C_3N_4 and PI components in the heterojunction for efficient charge separation and transfer [92]. Luo et al. developed an urchin-like g-C_3N_4 prepared by a thermal-induced self-condensation method. It was found that the urchin-like g-C_3N_4 showed 12.3 times higher photocatalytic activity than the bulk g-C_3N_4 for degradation of RhB dye under visible light irradiation [93]. This may be due to the large surface area and reduced recombination of photogenerated electron-hole pairs.

Graphite oxide is another metal-free photocatalyst for the degradation of organic dyes. Zhang et al. developed graphene oxide (GO) and reduced graphene oxide (RGO) platelets were pillared with CNTs through CVD method [94]. The carbon source and nickel nanoparticles acted as two catalysts for the degradation of the dye. The CNT-pillared RGO composite showed better photocatalytic activity for the degradation of RhB dye under visible light exposure. This is due to the porous structure and exceptional electron transfer property of graphene.

Neelgund et al. prepared a graphene-polyaniline nanocomposite using an acid-less in-situ polymerization method. It has the quality of removal of toxic dyes like MO, MB, and RhB in the presence of solar light. This may be due to infrared absorption and heat generation [95]. Lin et al. developed a metal-free C60/CNTs/g-C_3N_4 nanoheterostructure

https://www.twirpx.org & http://chemistry-chemists.com

synthesized through a solution-phase method for the degradation of RhB dye under visible light exposure [96]. Excellent photocatalytic activity efficiency of 100% was found, due to the large surface area and adsorption efficiency.

Bhati et al. developed water-soluble graphitic hollow carbon nanorods (wsCNRs) prepared through a pyrolysis method from castor seed oil for the decomposition of methylene blue dye under sunlight exposure [97].

Xu et al. used g-C_3N_4 material derived from different precursors used for photocatalytic decomposition of MB dye under visible irradiation. It was found that g-C_3N_4 derived from melamine at 500°C showed better photocatalytic activity than from dicyandiamide at 500°C [98]. This was due to the larger surface area of CN-M500. Jian et al. developed carbon quantum dots/g-C_3N_4 through an electrostatic self-assembly strategy. It enhanced the photodegradation of MB dye under visible light irradiation [99].

Zhang et al. developed carbon dot-decorated g-C_3N_4 which was synthesized through an impregnation thermal method. It showed 3.7 times higher photocatalytic degradation of phenol under visible light exposure than pristine g-C_3N_4 [100]. This was due to the increment of photogenerated electron-hole pairs.

Chai et al. prepared fullerene-modified C_3N_4 (C60/C_3N_4) synthesized by using a simple adsorption approach for photocatalytic dye decomposition of RhB dye under visible light irradiation. The photocatalytic activity of 1 wt% C60/C_3N_4 composite proved to be 97%, which is the highest photocatalytic performance [101]. This was due to the narrow bandgap (2.85 eV), which helps in the generation of electrons and holes. Table 2 provides a summary of photocatalytic activity for decomposition of organic pollutants under visible light.

3 Conclusions and future scopes

In this chapter, a detailed explanation was given of metal-free carbon-based materials, their synthesis methods, and their applications in the field of photocatalytic H_2 generation, photocatalytic CO_2 reduction, photocatalytic removal of NO_x, and photodegradation of organic pollutants. Carbonaceous materials are used due to their availability, high efficiency, and low cost. Although these materials have shown remarkable performances on these applications, high scalability for large-scale production of the material is still required. The creation of defects, active sites production, and their interaction with the reactant, electronic structure of these carbon-based materials need to be analyzed. The proper experimental technique, theoretical calculations, and fine structural property study to be carried out. This needs practical usage of the materials in the industrial sector. Extensive studies are required for the sustainability of these carbon-based materials for large-scale production. Cost minimization and environmental safety should be maintained.

Although there are more challenges to face, metal-free carbon-based materials and their applications are well-recognized by the research community. It is hoped that this chapter will increase aspirations for further development and remarkable changes in metal-free carbon-based materials for practical applications in visible light exposure.

https://www.twirpx.org & http://chemistry-chemists.com

Table 2 The photocatalytic degradation of organic dyes under visible light using carbon-based materials.

Photocatalyst	Dye	Light source	Wavelength	Bandgap (eV)	Degradation rate	Reference
Polymeric g-C_3N_4	RhB 5 mg/L	Xenon lamp 500 W	$\lambda < 400$ nm	2.7	100%	[88]
Pg-C_3N_4	MB (0.03 mM)	Xenon lamp 500 W	$\lambda > 420$ nm	2.7		[89]
3D macroporous g-C_3N_4	RhB (10 mg/L)	Xenon lamp (300)	$\lambda \geq 420$ nm	2.65	100%	[90]
g-C_3N_4 nanofibers	RhB (0.01 M)	Xenon lamp (500)	Visible light	2.67	100%	[91]
Polyimide (PI)/g-C_3N_4	2,4-DCP (10 mg/L)	Xenon lamp (300)	Visible light	2.8	98%	[92]
Urchin-like g-C_3N_4	RhB (50 mg/L)	Xenon lamp (500)	$\lambda > 420$ nm	2.8		[93]
CNT-pillared RGO	RhB (5.3×10^{-3} mM)	Xenon lamp (350)	Visible light			[94]
Polyaniline conjugated graphene	MO MB RhB (10 mg/L)	Natural sunlight	Visible light			[95]
C_{60}/CNTs/g-C_3N	RhB	Xenon lamp (500)	Visible light		100%	[96]
wsCNRs	MB (20 mg/L)	Direct sunlight	Visible light			[97]
g-C_3N_4	MB	Xenon lamp	200–1000 nm	2.71		[98]
CQDs/g-C_3N_4	MB	Xenon lamp	Visible light	2.7		[99]
C_{60}/C_3N_4	RhB	Xenon lamp (500)	Visible light	2.85	97%	[101]

References

[1] Sueyoshi T, Goto M. Investment strategy for sustainable society by development of regional economies and prevention of industrial pollutions in Japanese manufacturing sectors. Energy Econ 2014;42:299–312.

[2] Yoon TP, Ischay MA, Du J. Visible light photocatalysis as a greener approach to photochemical synthesis. Nat Chem 2010;2:527–32.

[3] Yi Z, Ye J, Kikugawa N, Kako T, Ouyang S, Stuart-Williams H, et al. An orthophosphate semiconductor with photooxidation properties under visible-light irradiation. Nat Mater 2010;9:559–64.

[4] Kudo A, Miseki Y. Heterogeneous photocatalyst materials for water splitting. Chem Soc Rev 2009;38:253–78.

[5] Zou Z, Ye J, Sayama K, Arakawa H. Direct splitting of water under visible light irradiation with an oxide semiconductor photocatalyst. Nature 2001;414:625–7.

https://www.twirpx.org & http://chemistry-chemists.com

[6] Banerjee S, Dionysiou DD, Pillai SC. Self-cleaning applications of TiO_2 by photo-induced hydrophilicity and photocatalysis. Appl Catal Environ 2015;176:396–428.

[7] Pelaez M, Nolan NT, Pillai SC, Seery MK, Falaras P, Kontos AG, et al. A review on the visible light active titanium dioxide photocatalysts for environmental applications. Appl Catal Environ 2012;125:331–49.

[8] Lee SY, Park SJ. TiO_2 photocatalyst for water treatment applications. J Ind Eng Chem 2013;19:1761–9.

[9] Zhang LS, Wong KH, Yip HY, Hu C, Yu JC, Chan CY, et al. Effective photocatalytic disinfection of *E. coli* K-12 using AgBr-Ag-Bi_2WO_6 nanojunction system irradiated by visible light: the role of diffusing using hydroxyl radicals. Environ Sci Technol 2010;44:1392–8.

[10] Sunada K, Kikuchi Y, Hashimoto K, Fujishima A. Bactericidal and detoxification effects of TiO_2 thin film photocatalysts. Environ Sci Technol 1998;32:726–8.

[11] Liu L, Zhao H, Andino JM, Li Y. Photocatalytic CO_2 reduction with H_2O on TiO_2 nanocrystals: comparison of anatase, rutile, and brookite polymorphs and exploration of surface chemistry. ACS Catal 2012;2:1817–28.

[12] Sato S, Arai T, Morikawa T, Uemura K, Suzuki TM, Tanaka H, et al. Selective CO_2 conversion to formate conjugated with H_2O oxidation utilizing semiconductor/complex hybrid photocatalysts. J Am Chem Soc 2011;133:15240–3.

[13] Fujishima A, Honda K. Electrochemical photolysis of water at a semiconductor electrode. Nature 1972;238:37–8.

[14] Nayak AK, Seungwon L, Sohn Y, Pradhan D. Biomolecule-assisted synthesis of In $(OH)_3$ nanocubes and In_2O_3 nanoparticles: photocatalytic degradation of organic contaminants and CO oxidation. Nanotechnology 2015;26:485601.

[15] Nayak AK, Lee S, Sohn Y, Pradhan D. Synthesis of In_2S_3 microspheres using a template-free and surfactant-less hydrothermal process and their visible light photocatalysis. CrstEngComm 2014;16:8064–72.

[16] Puhan A, Bhushan B, Satpathy S, Meena S, Nayak AK, Rout D. Facile single phase synthesis of Sr, Co co-doped $BiFeO_3$ nanoparticles for boosting photocatalytic and magnetic properties. Appl Surf Sci 2019;493:593–604.

[17] Rani B, Thamizharasan G, Nayak AK, Sahu NK. Degradation mechanism of organic dyes by effective transition metal oxide. In: Photocatalysts in Advanced Oxidation Processes for Wastewater Treatment. Wiley Online Library; 2020. p. 197–228.

[18] Nayak AK, Lee S, Choi YI, Yoon HJ, Sohn Y, Pradhan D. Crystal phase and size-controlled synthesis of tungsten trioxide hydrate nanoplates at room temperature: enhanced Cr (VI) photoreduction and methylene blue adsorption properties. ACS Sustain Chem Eng 2017;5:2741–50.

[19] Zou X, Zhang Y. Noble metal-free hydrogen evolution catalysts for water splitting. Chem Soc Rev 2015;44:5148–80.

[20] Liu J, Liu Y, Liu N, Han Y, Zhang X, Huang H, et al. Metal-free efficient photocatalyst for stable visible water splitting via a two-electron pathway. Science 2015;347:970–4.

[21] Ge J, Zhang Y, Jin PS. Recent advances in carbonaceous photocatalysts with enhanced photocatalytic performances: a mini review. Materials 2019;12:1916.

[22] Yacaman MJ, Yoshida MM, Rendon L. Catalytic growth of carbon microtubules with fullerene structur. Appl Phys Lett 1993;62:202–4.

[23] Eatemadi A, Daraee H, Karimkhanloo H, Kouhi M, Zarghami N. Carbon nanotubes: properties, synthesis, purification, and medical applications. Nanoscale Res Lett 2014;9:393.

[24] Paradise M, Goswami T. Carbon nanotubes-production and industrial application. Mater Des 2007;28:1477–89.

https://www.twirpx.org & http://chemistry-chemists.com

[25] Szabó A, Perri C, Csató A, Giordano G, Vuono D, Nagy JB. Synthesis methods of carbon nanotubes and related materials. Materials 2010;3:3092–140.

[26] Journet C, Bernier P. Production of carbon nanotubes. Appl Phys A 1998;67:1–9.

[27] Flahaut E, Govindaraj A, Peigney A, Laurent C, Rousset A, Rao CNR. Synthesis of single-walled carbon nanotubes using binary (Fe, Co, Ni) alloy nanoparticles prepared in situ by the reduction of oxide solid solutions. Chem Phys Lett 1999;300:236–42.

[28] Couteau E, Hernadi K, Seo JW, Thien-Nga L, Cs M, Gaal R, et al. CVD synthesis of high-purity multiwalled carbon nanotubes using $CaCO_3$ catalyst support for large-scale production. Chem Phys Lett 2003;378:9–17.

[29] Ren ZF, Huang ZP, Xu J, Wang JH, Bush P, Siegal MP, et al. Synthesis of large arrays of well-aligned carbon nanotubes on glass. Science 1998;282:1105–7.

[30] Fan S, Chapline MG, Franklin NR, Tombler TW, Cassell AM, Dai H. Self-oriented regular arrays of carbon nanotubes and their field emission properties. Science 1999;283:512–4.

[31] Ren ZF, Huang ZP, Wang DZ, Wen JG. Growth of a single freestanding multiwall carbon nanotube on each nanonickel dot. Appl Phys Lett 1999;75:1086–8.

[32] Bonard JM, Kind H, Stockli T, Nilsson LA. Field emission from carbon nanotubes: the first five years. Solid State Electron 2001;45:893–914.

[33] Choi WB, Chung DS, Kang JH, Kim HY, Jin YW, Han IT, et al. Fully sealed, high-brightness carbon-nanotube field-emission display. Appl Phys Lett 1999;75:3129–31.

[34] Dai H, Kong J, Zhou C, Franklin N, Tombler T, Cassell A, et al. Controlled chemical routes to nanotube architectures, physics, and devices. J Phys Chem B 1999;103:11246–55.

[35] Hafner JH, Cheung CL, Lieber CM. Growth of nanotubes for probe microscopy tips. Nature 1999;398:761–2.

[36] Hafner JH, Cheung CL, Lieber CM. Direct growth of single-walled carbon nanotube scanning probe microscopy tips. J Am Chem Soc 1999;121:9750–1.

[37] Ismach A, Segev L, Wachtel E, Joselevich E. Atomic-step-templated formation of single wall carbon nanotube patterns. Angew Chem Int Ed 2004;43:6140–3.

[38] Bai JB, Hamon A-L, Marraud A, Jouffrey B, Zymla V. Synthesis of SWNTs and MWNTs by a molten salt (NaCl) method. Chem Phys Lett 2002;365:184–8.

[39] Abbasloo S, Ojaghi-Ilkhchi M, Mozammel M. Synthesis of carbon nanotubes by molten salt electrolysis: a review. In: 5th international biennial conference on ultrafine grained and nanostructured materials; 2015.

[40] Dimitrov AT, Tomova A, Grozdanov A, Paunović P. Production, purification, characterization, and application of CNTs. In: Nanotechnological basis for advanced sensors. Springer; 2011. p. 121–42.

[41] Dimitrov AT, Tomova A, Grozdanov A, Popovski O, Paunović P. Electrochemical production, characterization, and application of MWCNTs. J Solid State Electrochem 2013;17:399–407.

[42] Gupta RD, Schwandt C, Fray DJ. Preparation of tin-filled carbon nanotubes and nanoparticles by molten salt electrolysis. Carbon 2014;70:142–8.

[43] Schwandt C, Dimitrov AT, Fray D. High-yield synthesis of multi-walled carbon nanotubes from graphite by molten salt electrolysis. Carbon 2012;50:1311–5.

[44] Novoselova IA, Oliinyk NF, Volkov SV, Konchits AA, Yanchuk IB, Yefanov VS, et al. Electrolytic synthesis of carbon nanotubes from carbon dioxide in molten salts and their characterization. Physica E 2008;40:2231–7.

[45] Sharma A, Das J. Small molecules derived carbon dots: synthesis and applications in sensing, catalysis, imaging, and biomedicine. J Nanobiotechnol 2019;17. https://doi.org/10.1186/s12951-019-0525-8.

https://www.twirpx.org & http://chemistry-chemists.com

[46] Lim SY, Shen W, Gao Z. Carbon quantum dots and their applications. Chem Soc Rev 2015;44:362–81.

[47] Han Z, He L, Pan S, Liu H. Hydrothermal synthesis of carbon dots and their application for detection of chlorogenic acid. Luminescence 2020;1–9. https://doi.org/10.1002/bio.3803.

[48] Kapitonov AN, Egorova MN, Tomskaya AE, Smagulova SA. Hydrothermal synthesis of carbon dots and their luminescence. AIP Conf Proc 2018;2041. https://doi.org/10.1063/1.5079363.

[49] Carvalho J, Santos LR, Germino JC. Hydrothermal synthesis to water-stable luminescent carbon dots from acerola fruit for photoluminescent composites preparation and its application as sensors. Mater Res 2019;22. https://doi.org/10.1590/1980-5373-MR-2018-0920.

[50] Qu K, Wang J, Ren J, Qu X. Carbon dots prepared by hydrothermal treatment of dopamine as an effective fluorescent sensing platform for the label-free detection of iron(III) ions and dopamine. Chem A Eur J 2013;19:7243–349. https://doi.org/10.1002/chem.201300042.

[51] Wang X, Blechert S, Antonietti M. Polymeric graphitic carbon nitride for heterogeneous photocatalysis. ACS Catal 2012;2:1596–606. https://doi.org/10.1021/cs300240x.

[52] Wang X, Maeda K, Chen X, Takanabe K, Domen K, Hou Y, et al. Polymer semiconductors for artificial photosynthesis: hydrogen evolution by mesoporous graphitic carbon nitride with visible light. J Am Chem Soc 2009;131:1680–1. https://doi.org/10.1021/ja809307s.

[53] Wang Y, Wang X, Antonietti M. Polymeric graphitic carbon nitride as a heterogeneous organocatalyst: from photochemistry to multipurpose catalysis to sustainable chemistry. Angew Chem Int Ed 2012;51:68–89. https://doi.org/10.1002/anie.201101182.

[54] Wang X, Maeda K, Thomas A, Takanabe K, Xin G, Carlsson JM, et al. A metal-free polymeric photocatalyst for hydrogen production from water under visible light. Nat Mater 2008;8:76–80. https://doi.org/10.1038/nmat2317.

[55] Yang S, Gong Y, Zhang J, Zhan L, Ma L, Fang Z, et al. Exfoliated graphitic carbon nitride nanosheets as efficient catalysts for hydrogen evolution under visible light. Adv Mater 2013;25:2452–6. https://doi.org/10.1002/adma.201204453.

[56] Christoforidis KC, Melchionna M, Montini T, Papoulis D, Stathatos E, Zafeiratos S, et al. Solar and visible light photocatalytic enhancement of halloysite nanotubes/g-C_3N_4 heteroarchitectures. RSC Adv 2016;6:86617–26. https://doi.org/10.1039/C6RA15581B.

[57] Kumar S, Kumar A, Bahuguna A, Sharma V, Krishnan V. Two-dimensional carbon-based nanocomposites for photocatalytic energy generation and environmental remediation applications. Beilstein J Nanotechnol 2017;8:1571–600. https://doi.org/10.3762/bjnano.8.159.

[58] Gao G, Jiao Y, Ma F, Jiao Y. Carbon nanodot decorated graphitic carbon nitride: new insights on the enhanced photocatalytic water splitting from abinitio studies. Phys Chem Chem Phys 2015;17:31140–4. https://doi.org/10.1039/C5CP05512A.

[59] Xia X, Deng N, Cui G, Xie J, Shi X, Zhao Y, et al. NIR light induced H2 evolution by a metal-free photocatalyst. Chem Commun 2015;51:10899–902. https://doi.org/10.1039/C5CC02589C.

[60] He F, Chen G, Zhou YS, Yu YG, Li LQ, Hao S, et al. ZIF-8 derived carbon (C-ZIF) as a bifunctional electron acceptor and HER cocatalyst for g-C_3N_4: construction of a metal-free, all carbon-based photocatalytic system for efficient hydrogen evolution. J Mater Chem A 2016;4:3822–7.

[61] Suryawanshi A, Dhanasekaran P, Mhamane D, Kelkar S. Doubling of photocatalytic H_2 evolution from gC_3N_4 via its nanocomposite formation with multiwall carbon nanotubes: electronic and morphological effects. Int J Hydrogen Energy 2012;37:9584–9. https://doi.org/10.1016/j.ijhydene.2012.03.123.

[62] Liu J, Wen S, Hou Y, Zuo F, Beran GJO, Feng P. Boron carbides as efficient, metal-free, visible-light-responsive photocatalysts. Angew Chem 2013;125:3323–7. https://doi.org/10.1002/ange.201209363.

[63] Perreault F, Faria AFD, Elimelech M. Environmental applications of graphene-based nanomaterials. Chem Soc Rev 2015;44:5861–96. https://doi.org/10.1039/c5cs0 0021a.

https://www.twirpx.org & http://chemistry-chemists.com

[64] Xu L, Wang J. The application of graphene-based materials for the removal of heavy metals and radionuclides from water and wastewater. Crit Rev Environ Sci 2017;47:1024–105. https://doi.org/10.1080/10643 389.2017.13425 14.

[65] Jilani A, Hafiz M, Othman D. Graphene and its derivatives: synthesis, modifications, and applications in wastewater treatment. Environ Chem Lett 2018;16:1301–23. https://doi.org/10.1007/s1031 1-018-0755-2.

[66] Nayak AK, Swain AK. Facile room temperature synthesis of reduced graphene oxide as efficient metal-free electrocatalyst for oxygen reduction reaction. In: Surface engineering of graphene; 2019. p. 259–71. https://doi.org/10.1007/978-3-030-30207-8_10.

[67] Lü K, Zhao G, Wang X. A brief review of graphene-based material synthesis and its application in environmental pollution management. Chin Sci Bull 2012;57:1223–34. https://doi.org/10.1007/s1143 4-012-4986-5.

[68] Li Z, Yu H, Bian T, Zhao Y, Zhou C. Highly luminescent nitrogen-doped carbon quantum dots as effective fluorescent probes for mercuric and iodide ions. J Mater Chem C 2015;3:1922–8. https://doi.org/10.1039/c4tc02756f.

[69] Liu J, Song Y, Xu H, Zhu X, Lian J, Xu Y, et al. Non-metal photocatalyst nitrogen-doped carbon nanotubes modified mpg-C_3N_4: facile synthesis and the enhanced visible-light photocatalytic activity. J Colloid Interface Sci 2017;494:38–46. https://doi.org/10.1016/j.jcis.2017.01.010.

[70] Jiang L, Yuan X, Zeng G, Chen X, Wu Z, Liang J, et al. Phosphorus- and sulfur-codoped g-C_3N_4: facile preparation, mechanism insight, and application as efficient photocatalyst for tetracycline and methyl orange degradation under visible light irradiation. ACS Sustain Chem Eng 2017;5:5831–41. https://doi.org/10.1021/acssuschemeng.7b00559.

[71] Zheng Y, Yu Z, Lin F, Guo F, Alamry KA, Taib LA, et al. Sulfur-doped carbon nitride polymers for photocatalytic degradation of organic pollutant and reduction of Cr(VI). Molecules 2017;22:572. https://doi.org/10.3390/molecules22040572.

[72] Mathew RM, John J, Zachariah ES, Jose J, Titus T, Abraham R, et al. Metal free, phosphorus doped carbon nanodot mediated photocatalytic reduction of methylene blue. In: Reaction kinetics, mechanisms and catalysis; 2020. https://doi.org/10.1007/s11144-020-01724-9.

[73] Lv H, Huang Y, Koodali RT, Liu G, Zeng Y, Meng Q, et al. Synthesis of sulfur-doped 2D graphitic carbon nitride nanosheets for efficient photocatalytic degradation of phenol and hydrogen evolution. ACS Appl Mater Interfaces 2020;12:12656–67. https://doi.org/10.1021/acsami.9b19057.

[74] Duan X, Donnell KO, Sun H, Wang Y, Wang S. Sulfur and nitrogen co-doped graphene for metal-free catalytic oxidation reactions. Catalysis 2015;11:3036–44. https://doi.org/10.1002/smll.201403715.

[75] Zhang L, Chen X, Guan J, Jiang Y, Hou T, Mu X. Facile synthesis of phosphorus doped graphitic carbon nitride polymers with enhanced visible-light photocatalytic activity. Mater Res Bull 2013;48:3485–91. https://doi.org/10.1016/j.materresbull.2013.05.040.

[76] Zhou Y, Zhang L, Liu J, Fan X, Wang B, Wang M, et al. Brand new P-doped g-C_3N_4: enhanced photocatalytic activity for H_2 evolution and Rhodamine B degradation under visible light. J Mater Chem A 2015;3:3862. https://doi.org/10.1039/c4ta05292g.

[77] Zheng Y, Yu Z, Ou H, Asiri AM, Chen Y, Wang X. Black phosphorus and polymeric carbon nitride heterostructure for photoinduced molecular oxygen activation. Adv Funct Mater 2018;28:1705407. https://doi.org/10.1002/adfm.201705407.

[78] Xiao X, Wang Y, Bo Q, Xu X, Zhang D. One-step preparation of sulfur-doped porous g-C_3N_4 for enhanced visible light photocatalytic performance. Dalton Trans 2020. https://doi.org/10.1039/D0DT00299B.

[79] Liu G, Niu P, Sun C, Smith SC, Chen Z, Lu GQ, et al. Unique electronic structure induced high photoreactivity of sulfur-doped graphitic C_3N_4. J Am Chem Soc 2010;132:11642–8. https://doi.org/10.1021/ja103798k.

https://www.twirpx.org & http://chemistry-chemists.com

[80] Lu C, Chen R, Wu X, Fan M, Liu Y, Le Z, et al. Boron doped g-C_3N_4 with enhanced photocatalytic UO22+ reduction performance. Appl Surf Sci 2016;360:1016–22. https://doi.org/10.1016/j.apsusc.2015.11.112.

[81] Yan Q, Huang G, Li D, Zhang M, Pan A, Huang W. Facile synthesis and superior photocatalytic and electrocatalytic performances of porous B-doped g-C_3N_4 nanosheets. J Mater Sci Technol 2017. https://doi.org/10.1016/j.jmst.2017.06.018.

[82] Huang C, Chen C, Zhang M, Lin L, Ye X, Lin S, et al. Carbon-doped BN nanosheets for metal-free photoredox catalysis. Nat Commun 2015;6. https://doi.org/10.1038/ncomms8698.

[83] Yu K, Hu X, Yao K, Luo P, Wang X, Wang H. Preparation of an ultrathin 2D/2D rGO/g-C_3N_4 nanocomposite with enhanced visible-light-driven photocatalytic performance. RSC Adv 2017;7:36793. https://doi.org/10.1039/c7ra06210a.

[84] Ong WJ, Ling Tan L, Chai SP, Yong ST. Graphene oxide as a structure-directing agent for the two-dimensional interface engineering of sandwich-like graphene-g-C_3N_4 hybrid nanostructures with enhanced visible-light photoreduction of CO_2 to methane. Chem Commun 2015;51:858–61. https://doi.org/10.1039/C4CC08996K.

[85] Wang Z, Guan W, Sun Y, Dong F, Zhou Y, Ho W-K. Water-assisted production of honeycomb-like g-C_3N_4 with ultralong carrier lifetime and outstanding photocatalytic activity. Nanoscale 2015;7:2471–9.

[86] Sano T, Tsutsui S, Koike K, Hirakawa T, Teramoto Y, Negishi N, et al. Activation of graphitic carbon nitride (g-C_3N_4) by alkaline hydrothermal treatment for photocatalytic NO oxidation in gas phase. J Mater Chem A 2013;1:6489.

[87] Zhu J, Xiao P, Li H, Carabineiro SAC. Graphitic carbon nitride: synthesis, properties, and applications in catalysis. ACS Appl Mater Interfaces 2014;6:16449–65. https://doi.org/10.1021/am502925j.

[88] Dong F, Wu L, Sun Y, Fu M, Wu Z, Lee SC. Efficient synthesis of polymeric g-C_3N_4 layered materials as novel efficient visible light driven photocatalysts. J Mater Chem 2011;21:15171. https://doi.org/10.1039/C1JM12844B.

[89] Zhang M, Xu J, Zong R, Zhu Y. Enhancement of visible light photocatalytic activities via porous structure of g-C_3N_4. Appl Catal Environ 2014;147:229–35. https://doi.org/10.1016/j.apcatb.2013.09.002.

[90] Lin B, Yang G, Yang B, Zhao Y. Construction of novel three dimensionally ordered macroporous carbon nitride for highly efficient photocatalytic activity. Appl Catal B 2016;198:276–85. https://doi.org/10.1016/j.apcatb.2016.05.069.

[91] Tahir M, Cao C, Mahmood N, Butt FK, Mahmood A, Idrees F, et al. Multifunctional g-C_3N_4 nanofibers: a template-free fabrication and enhanced optical, electrochemical, and photocatalyst properties. ACS Appl Mater Interfaces 2014;6:1258–65. https://doi.org/10.1021/am405076b.

[92] Gong Y, Yu H, Chen S, Quan X. Constructing metal-free polyimide/g-C_3N_4 with high photocatalytic activity under visible light irradiation. RSC Adv 2015;5:83225–31. https://doi.org/10.1039/C5RA17146F.

[93] Luo L, Zhang A, Janik MJ, Song C, Guo X. Facile fabrication of metal-free urchin-like g-C_3N_4 with superior photocatalytic activity. RSC Adv 2013;6:94496–501. https://doi.org/10.1039/C6RA20940H.

[94] Zhang LL, Xiong Z, Zhao XS. Pillaring chemically exfoliated graphene oxide with carbon nanotubes for photocatalytic degradation of dyes under visible light irradiation. ACS Nano 2010;4:7030–6. https://doi.org/10.1021/nn102308r.

[95] Neelgund GM, Bliznyuk VN, Oki A. Photocatalytic activity and NIR laser response of polyaniline conjugated graphene nanocomposite prepared by a novel acid-less method. Appl Catal Environ 2016;187:357–66. https://doi.org/10.1016/j.apcatb.2016.01.009.

[96] Lin X, Zhao R, Xi Y, Li X, Shi J, Yan N. Metal-free C60/CNTs/g-C_3N_4 ternary heterostructures: synthesis and enhanced visible-light-driven photocatalytic performance. R Soc Open Sci 2018;5:172290. https://doi.org/10.1098/rsos.172290.

https://www.twirpx.org & http://chemistry-chemists.com

[97] Bhati A, Singh A, Tripathi KM, Sonkar SK. Sunlight-induced photochemical degradation of methylene blue by water-soluble carbon nanorods. Int J Photoenergy 2016;1–8. https://doi.org/10.1155/2016/2583821.

[98] Xu H, Wu L, Zhao H, Jin L, Qi S. Synergic effect between adsorption and photocatalysis of metal-free g-C_3N_4 derived from different precursors. PLoS ONE 2015;10. https://doi.org/10.1371/journal.pone.0142616, e0142616.

[99] Jian X, Liu X, Yang H, Li J, Song X, Dai H, et al. Construction of carbon quantum dots/proton-functionalized graphitic carbon nitride nanocomposite via electrostatic self-assembly strategy and its application. Appl Surf Sci 2016;370:514–21. https://doi.org/10.1016/j.apsusc.2016.02.119.

[100] Zhang H, Zhao L, Geng F, Guo L, Wan B, Yang Y. Carbon dots decorated graphitic carbon nitride as an efficient metal-free photocatalyst for phenol degradation. Appl Catal Environ 2016;180:656–62. https://doi.org/10.1016/j.apcatb.2015.06.056.

[101] Chai B, Liao X, Song F, Zhou H. Fullerene modified C_3N_4 composites with enhanced photocatalytic activity under visible light irradiation. Dalton Trans 2014;43:982. https://doi.org/10.1039/c3dt52454j.

https://www.twirpx.org & http://chemistry-chemists.com

5

Bismuth series photocatalytic materials for the treatment of environmental pollutants

Arpan Kumar Nayak

DEPARTMENT OF PHYSICS, SCHOOL OF ADVANCED SCIENCES, VELLORE INSTITUTE OF TECHNOLOGY, VELLORE, TAMIL NADU, INDIA

1 Introduction

Water pollution is one of the biggest environmental threats worldwide. It remains a significant challenge to researchers for the efficient removal of pollutants existing in water [1]. The primary source of water pollution is caused by the textile industry discharging untreated textile effluents into water bodies. The untreated textile effluent covers several types of organic dyes that are harmful not only for the environment but also for aquatic lives. Therefore, it is crucial to remove the organic hazardous dyes before discharging it into the earth's surface. These toxic dyes are not biodegradable and/or aerobic water treatment, and some dyes are entirely absorbed by mud in biological therapy. Several methods are available for the detoxification of textile effluents, including precipitation, ozonation, coagulation-flocculation, ion exchange method, activated carbon adsorption, and biological treatment [2–5]. However, these methods have limitations such as optimization of the process, expense, incompatibility for dispersed dyes, longer acclimatization, and selective for specific dye. On the other hand, many researchers have been following photocatalytic treatments to remove toxic dyes from wastewater and the synthesis of novel semiconducting compounds [6]. Current research is highly oriented on the photocatalysis treatment for the removal of dye industry effluent. In the photocatalysis process, harmful organic dyes break down to harmless water and CO_2. Oxide semiconductors such as TiO_2, SnO_2, and ZnO are well-known and widely used as photocatalysts for the degradation of organic dyes [7–9]. The photocatalysts absorb the appropriate wavelength of photons to gain high energy. This high energy is then used to excite the electrons from the valence band (VB) to the conduction band (CB), which causes redox reactions and is used for the degradation of organic dyes (Fig. 5.1).

The excitation of electrons can be made by doping, making composites, changing various morphologies, modifying crystal structures, and varying synthesis strategy. The electrons and holes existing in the catalysts show redox activities that lead to the formation of

Nanostructured Materials for Visible Light Photocatalysis. https://doi.org/10.1016/B978-0-12-823018-3.00005-1
Copyright © 2022 Elsevier Inc. All rights reserved.

https://www.twirpx.org & http://chemistry-chemists.com

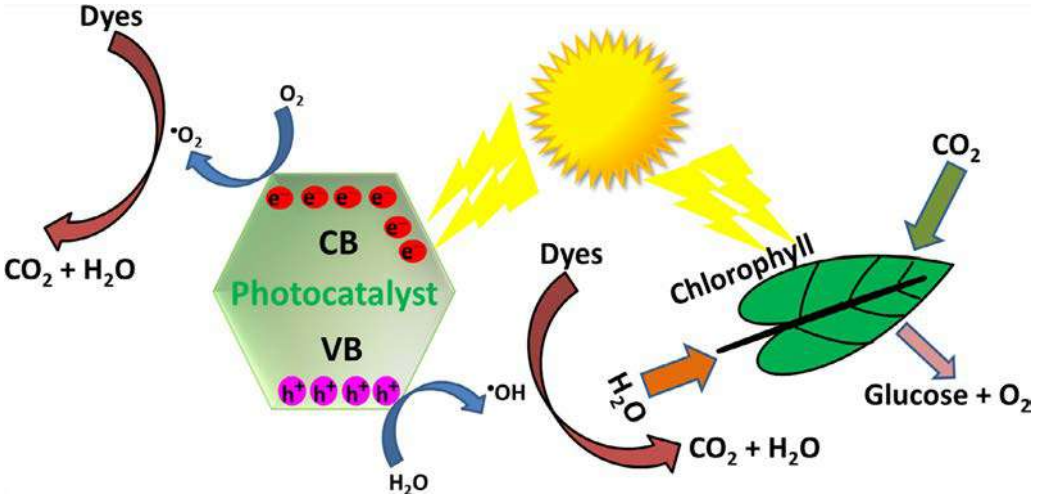

FIG. 5.1 Schematic representation of photocatalysis and its mechanism. No permission required.

•OH (hydroxyl) radicals and $\bullet O_2$ (superoxide) anion. Hydroxyl radicals are formed due to the neutralization of surface hydroxide (OH) via photo-hole (h^+) and superoxide anion by the dissolved oxygen and surface electron. The ·OH radical bonding energy is relatively higher than the C—C, N—H, C—H, C—N, O—H, and C—O bonding energies in the organic dyes. Thus ·OH radicals easily break these bonds from the dyes present in the contaminated water. Development of an active visible light photocatalyst is highly desirable and the light absorption of suitable energy is determined by the material's bandgap. Photocatalytic performance can be enhanced by doping metal on a catalyst's surface or making nanocomposites that lead to the charge transfer between them and could decrease the electron-hole pairs recombination. Variations in morphology and crystal structure also have impacts on photocatalysis, which can be observed by varying synthesis parameters. Fig. 5.2 represents the amount of solar energy including ultraviolet (UV), visible, and infrared (IR) spectra irradiated on the earth's surface at different wavelengths [10].

It can be seen that 46% of visible light is irradiated while only 5% UV light of the electromagnetic spectrum is irradiated on the earth's surface [10]. Meanwhile the photocatalytic activities of TiO_2, SnO_2, and ZnO are limited to the UV region, and better alternative materials are currently being investigated. In contrast, bismuth (Bi)-based catalysts have attracted attention due to their lower bandgap and are capable of splitting water under visible light irradiation. Various Bi^{3+}-based catalysts that work under visible light, such as Bi_2WO_6, $BiFeO_3$, Bi_2O_3, $BiVO_4$, $BiPO_4$, $Bi_4Ti_3O_{12}$, BiOX (X = Cl, Br, I), and $Bi_2O_2CO_3$, showed mainly layered structure with plate-like morphology. On the other hand, Bi^{5+}-based visible light catalysts such as $LiBiO_3$, $KBiO_3$, and $NaBiO_3$ were less reported in the literature due to the unstable nature of Bi^{5+}. In Bi-based catalysts the hybridization of O 2p and Bi $6s^2$ orbitals could cause an upshift of the VBs, indicating the reduction

https://www.twirpx.org & http://chemistry-chemists.com

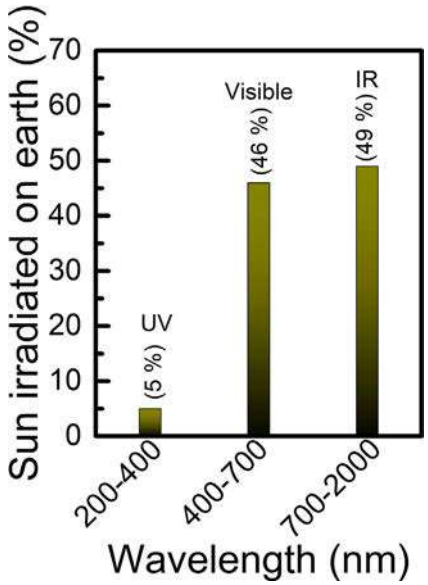

FIG. 5.2 The various wavelengths of solar radiation on the earth's surface. No permission required.

of bandgap to less than 3 eV and able to excited by visible light. This chapter addresses the synthesis methods of Bi-based materials and their photocatalytic activity over various dyes such as RhB, MB, MO, 4BS, phenol, and Cr(VI) under visible light irradiation.

2 Bi-based nanostructured materials synthesis

Bi-based nanostructured materials synthesis has been implemented by various methods. Herein, we present common synthesis strategies with controlled morphology and their applications in visible light-induced photocatalysis.

2.1 Synthesis of bismuth oxyhalide

The major synthesis methods for bismuth oxyhalide (BiOX) micro/nanostructures include precipitation, hydrothermal/solvothermal, template, microwave, calcination, and sonochemical methods [11–18]. The synthesis of bismuth oxyhalide photocatalysts (BiOX; X = Cl, Br, I) received great interest due to the cost-effective, easy process that involved simply stirring bismuth and halogen sources in an organic or aqueous solvent at room temperature or an appropriate temperature. The bismuth precursors most commonly used were $Bi(NO_3)_3{\cdot}5H_2O$, $NaBiO_3$, and Bi_2O_3, while CTAB (hexadecyltrimethylammonium bromide), CTAC (hexadecyltrimethylammonium chloride), halogen containing acids (HCl, HBr, HI, etc.), potassium halides (KCl, KBr, KI, etc.), and ionic liquid were usually used as halogen precursors. More importantly, the crystal phase, size, shape,

https://www.twirpx.org & http://chemistry-chemists.com

dimensionality and exposed facet of as-synthesized BiOX nanostructured materials could be controlled as the synthesis parameters, temperature, and duration. For example, Chen et al. reported room temperature synthesis of 3D bismuth oxyhalide (BiOX (X = Cl, Br, I)) hierarchical structures [11]. The bismuth ($Bi(NO_3)_3{\cdot}5H_2O$) and halogen (Cl, Br, I; HCl (36.5 wt%), HBr (40 wt%), and HI (57 wt%)) sources in the presence of L-lysine surfactant hydrolyzes and self-assembles to form a hierarchical flower-like architecture within 10 min [11]. Fig. 5.3 shows FESEM images of the 3D flower-like hierarchical structure of BiOX (X = Cl Br, I) [11]. The presence of nano- and macro-pores on the surface of nanoplates are favorable for light harvesting and separation of electron-hole pairs. Both factors are important for the enhancement of photocatalytic activity [11]. Long et al.

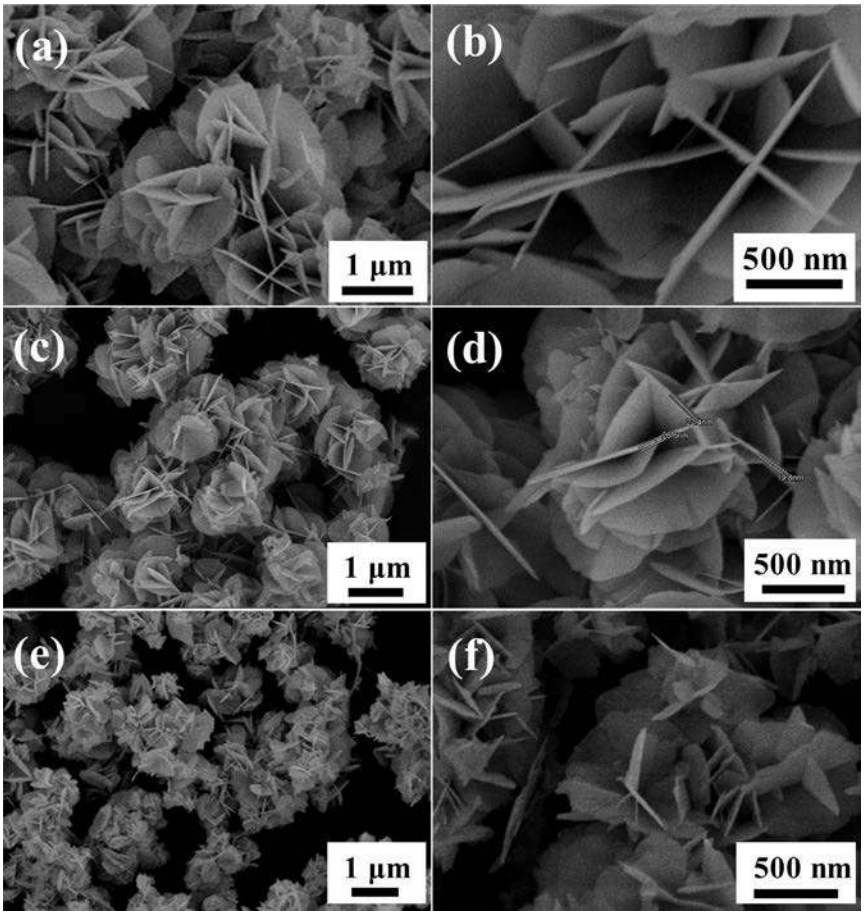

FIG. 5.3 FESEM images of (A, B) BiOCl, (C, D) BiOBr, and (E, F) BiOI. From Nayak A. Bismuth series photocatalytic materials for the treatment of environmental pollutants. In: Nayak A, Sahu N, editors. Nanostructured materials for visible-light-photocatalysis, vol. 52. 19th ed., American Chemical Society; 2013, p. 11118–11125. https://doi.org/10.1021/ic401349j. 11120. (Copyright © 2013, American Chemical Society.)

https://www.twirpx.org & http://chemistry-chemists.com

demonstrated a fast and simple solvent-free mechanical grinding method to synthesize BiOX (BioCl, ViOBr, and BiOI) flower-like hierarchical nanostructures for the first time by just grinding $Bi(NO_3)_3{\cdot}5H_2O$ and potassium halides for 5 min [12]. The as-synthesized BiOX-based materials were used as photocatalysts for the degradation of mixed dyes (RhB and MB) using simulated sunlight for 120 min. It was noted that BiOI (1.68 eV) showed poor photocatalytic performance compared to BiOCl (3.24 eV) and BiOBr (2.64 eV), due to its thick nanosheets morphology and lower surface area [12].

2.2 Synthesis of bismuth oxide

Bismuth oxide (Bi_2O_3) has proved to be an ideal photocatalyst under visible light due to its excellent properties such as narrow bandgap (2.0–3.96 eV), high refractive index, and high dielectric permittivity [19]. Bi_2O_3 exhibits five polymorphs: α-(monoclinic) known as stable phase at low temperature; β-(tetragonal), γ-(body-centered cubic), and ε-(triclinic) phases known as metastable phases; and δ-(face-centered cubic) phase known as stable phase at high temperature [19]. Bi_2O_3 can be synthesized using various methods including hydrothermal, precipitation, oxidative metal vapor transport, template-based heat treatment, sol-gel, and microwave methods for several applications [19–24]. In particular, Zhou et al. synthesized δ-Bi_2O_3 hierarchical structures by a template-free aqueous method at 60–80°C for 6 h. It should be noted that the as-synthesized δ-Bi_2O_3 hierarchical structures exhibited 6–10 times higher photocatalytic performance compared to commercial samples [20]. Qiu et al. synthesized α- and β-Bi_2O_3 nanowires of diameter 7–200 nm using an oxidative metal vapor transport deposition method [21]. They studied the photocatalytic activity of Orange-G and found that the α- and β-Bi_2O_3 nanowires showed higher activity than Degussa TiO_2 P25 under visible light. They observed that β-Bi_2O_3 nanowires exhibited the highest activity compared to others; this was because their lower bandgap, high specific surface area, and smaller size allowed more facile transfer of photogenerated electrons and holes to the nanowire surface and increased the photo-efficiency by improving the electron-hole separation [21].

2.3 Synthesis of other bismuth-based oxides (Bi_aAO_b; A = Fe, V, W, Mo)

Among various Bi-based semiconductors, Bi_aAO_b ($BiFeO_3$ (2.1–2.4 eV), $BiVO_4$ (2.4–2.4 eV), Bi_2WO_6 (2.6–2.7 eV), Bi_2MoO_6 (2.3–2.7 eV), etc. have attracted continuous research focus due to their exceptional visible light absorption, high stability, and suitable band potential [25–32]. Furthermore, the specific crystal structure of Bi_aAO_b promises a superior charge transfer capacity compared to other photocatalysts. Among the various factors, nanostructure modification is one of the important tools to promote the photocatalytic efficiency of Bi_aAO_b, which could be observed by modulating the synthesis methods and parameters. In general, Bi_aAO_b nanostructures can be modulated using solid-state reaction and hydrothermal methods [25, 33]. The advantages of the hydrothermal method over the solid-state reaction one are low cost, convenience, and the fact that it is controllable [34–36]. Consequently the hydrothermal synthesized products show high surface

https://www.twirpx.org & http://chemistry-chemists.com

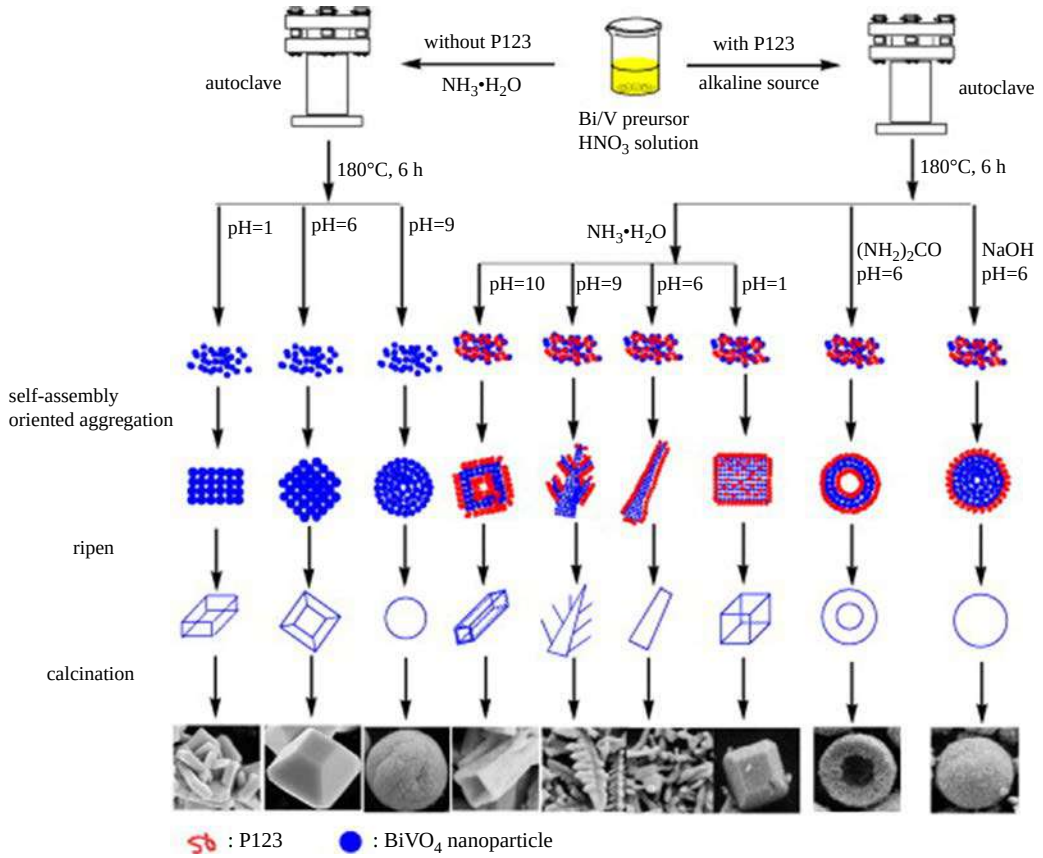

FIG. 5.4 Schematic representation of $BiVO_4$ with various morphology formation mechanisms at different hydrothermal conditions [33]. From Nayak A. Bismuth series photocatalytic materials for the treatment of environmental pollutants. In: Nayak A, Sahu N, editors. Nanostructured materials for visible-light-photocatalysis, vol. 125. 1-2nd ed., Elsevier; 2011, p. 59–66. https://doi.org/10.1016/j.matchemphys.2010.08.071. 63. (Copyright © 2011, Elsevier.)

area and high heterogeneity in shape and size [32, 33, 37, 38]. The variation in morphologies using the hydrothermal method depends on the nature of surfactants, metal precursors, alkaline source, the precursor solution's pH value, duration of reaction, and hydrothermal temperature [34, 35]. For example, Meng et al. reported the triblock copolymer P123-mediated hydrothermal synthesis of monoclinic $BiVO_4$ single crystallites with polyhedral, rod, tubular, leaf, and spherical morphologies (Fig. 5.4) using $Bi(NO_3)_3{\cdot}5H_2O$ and NH_3VO_3 as metal precursors and various bases for pH adjustor [33]. They further used the as-synthesized $BiVO_4$ nanostructures for the degradation of MB dye under visible light irradiation. Among the various morphologies, rod- and tubular-shaped $BiVO_4$ single crystallites showed excellent photocatalytic activity due their unique morphology, high surface area, and higher oxygen vacancies [33].

https://www.twirpx.org & http://chemistry-chemists.com

Sun et al. demonstrated $BiVO_4$ quantum tubes with 5 nm diameter, 1 nm thickness, and [020] exposed facets using $Bi(NO_3)_3{\cdot}5H_2O$ and $Na_3VO_4{\cdot}12H_2O$ by the hydrothermal method at 100°C [39]. The photocatalytic degradation of RhB dye using $BiVO_4$ quantum tubes was found to be 10 times higher than that of bulk $BiVO_4$ and roughly 3 times higher that of m-$BiVO_4$ nanoellipsoids under visible light irradiation. After 15 min irradiation, the photodecomposition of RhB dye reached 98.7% using $BiVO_4$ quantum tubes, whereas the standard TiO_2 (P-25) reached only 8%. The remarkable enhanced photocatalytic activity of as-synthesized $BiVO_4$ quantum tubes can be ascribed to their morphology, quantum size effect, and larger surface area [40].

Bi_2WO_6 micro/nanostructures are another important class of visible light photocatalyst and can be synthesized using sol-gel, combustion, hydro-/solvo-thermal, ultrasonic, and coprecipitation methods [29, 40–44]. Among the above methods the hydro-/solvothermal method is the most promising one used to synthesize Bi_2WO_6 micro/nanostructures. The precursor's solution pH value, surfactants, and/or template have a strong effect on the formation of different morphologies of Bi_2WO_6 micro/nanostructures, which directly affect the photocatalytic performance [45]. The pH value of 7 favors more Bi_2WO_6 phase formation. Various morphologies including plates, particles, flowers, helixes, and nanocage superstructures (Fig. 5.5) of Bi_2WO_6 were summarized by Zhang et al. [46] The bismuth precursors (e.g., $Bi(NO_3)_3{\cdot}5H_2O$) are less soluble in water, thus nitric acid is added to the solution in the hydrothermal method [47]. Furthermore, bismuth nitrate was found to be dissolved in various alcohols and most commonly ethylene glycol was used as a solvent to synthesize uniform Bi_2WO_6 nanostructures via the solvothermal method [48]. Hu et al. solvothermally synthesized ethylene glycol-assisted Bi_2WO_6 hollow microspheres composed of nanoparticles which exhibited excellent photodegradation of RhB dye up to 99% in 4o min under visible light and was found to be much higher than standard P-25-TiO_2 [48]. Moreover, in an effort to decrease the reaction duration, microwave heating by replacing normal oven heating was employed, resulting in a remarkable decrease of duration from 10–20 h to 5–10 min [49–51]. Nanosheets, nanoplates, and flower-like morphologies of Bi_2WO_6 were synthesized using a microwave-assisted hydro-/solvo-thermal method.

Similarly, Bi_2MoO_6 nanostructures have also been synthesized by hydrothermal/solvothermal, microwave, coprecipitation and solid-state reaction methods [31, 52–54]. The Aurivillius oxide family member Bi_2MoO_6 is composed of $[Bi_2O_2]^{2+}$ with a corner sharing of MoO_6 octahedra [55]. This interesting structure uses Bi_2MoO_6 as an alternative visible light photocatalyst. Various morphologies including hierarchical flower-like hollow spheres (solvothermal method), nanobelts (hydrothermal method), nanoplates (microwave-assisted hydrothermal method), and nanoparticles (coprecipitation method) of Bi_2MoO_6 have been reported [52–54, 56]. The major applications of Bi_2MoO_6 involve the photodegradation of organic hazardous pollutants from water and air. Hazardous pollutants including dyes, phenol, Cr(VI), and microorganisms such as *Escherichia coli* are detoxified using Bi_2MoO_6 nanostructures [52, 53, 57–59].

https://www.twirpx.org & http://chemistry-chemists.com

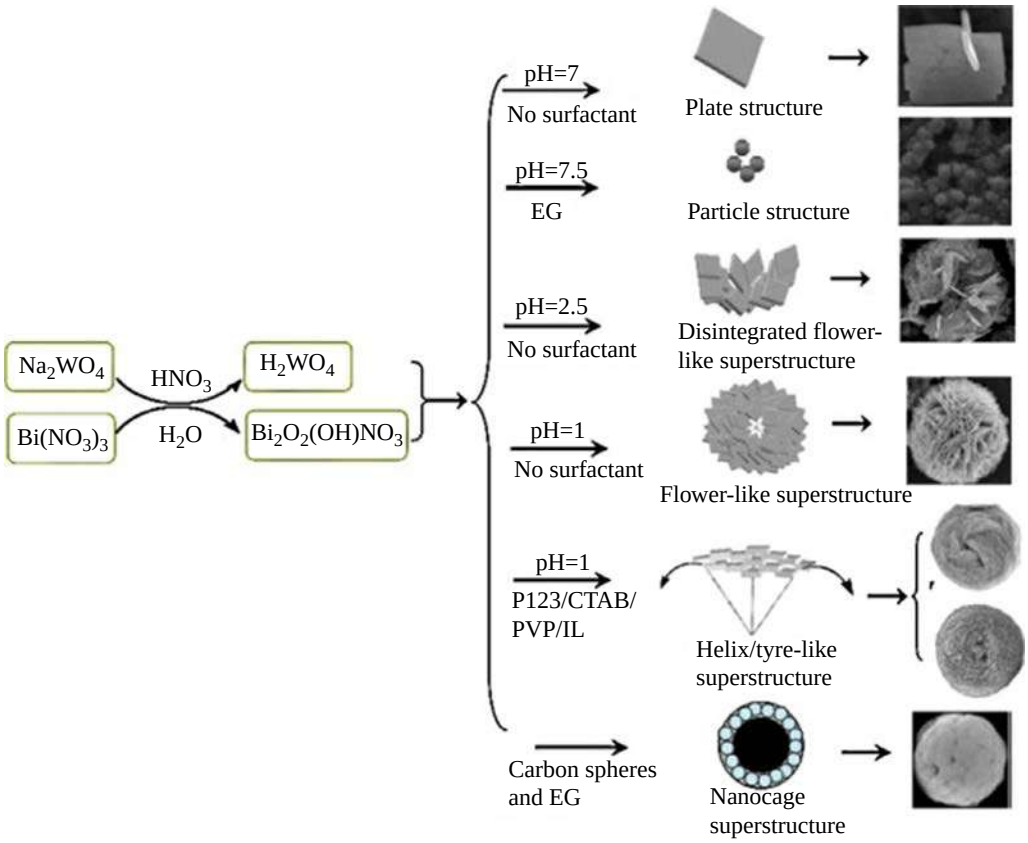

FIG. 5.5 Bi_2WO_6 micro/nanostructures of diverse shapes synthesized with different pH values and/or different surfactants. From Nayak A. Bismuth series photocatalytic materials for the treatment of environmental pollutants. In: Nayak A, Sahu N, editors. Nanostructured materials for visible-light-photocatalysis, vol. 106. 1-2nd ed., Elsevier; 2011, p. 1–13. https://doi.org/10.1016/j.apcatb.2011.05.008. 3. (Copyright © 2011, Elsevier.)

3 Bi-based nanostructured materials for environmental remediation

3.1 Photocatalytic degradation of organic pollutants using Bi-based nanostructured materials

In recent years, huge efforts have been dedicated to the remediation of organic hazardous dyes which comes from industrial, medical, and domestic effluents [11, 60–62]. In this context, Bi-based photocatalysts are highly active in the degradation of organic pollutants under visible light irradiation. Table 5.1 provides a list of Bi-assisted photocatalysts for the degradation of various dyes under visible light [17, 25, 26, 56, 60, 63–66].

https://www.twirpx.org & http://chemistry-chemists.com

Table 5.1 Bi-based nanostructured materials for the photodegradation of organic pollutants.

S. no	Photocatalyst	Method and experimental condition	Morphology (size)	Light wavelength (Bandgap)	% of degradation (Dye)	Ref.
1	(BiOX, (X = Cl, Br, and I)	Solvothermal crystallization and $Bi(NO_3)_3{\cdot}5H_2O$, ethylene glycol, Bi:X (I:1), KCl or KBr or KI; 120°C, 140°C, 160°C for 3, 24, and 48 h [Best BiOI; 120°C 3 h	Microspheres (2 μm)	≥400 nm (1.7 eV for BiOI)	86.2% in 2 h (RhB) for BiOI	[17]
2	α/β Bi_2O_3	Hydrothermal and $Bi(NO_3)_3{\cdot}5H_2O$, glycerol; 190°C for 6 h	Nanoparticles (113.8 nm (α), 71 nm (β))	Natural sun light (2.78 eV (α), 2.35 eV (β))	99.6% in 180 min (RhB)	[25]
3	$BiFeO_3$	Sol-gel and $Bi(NO_3)_3{\cdot}6H_2O$, $Fe(NO_3)_3{\cdot}9H_2O$, ethylene glycol; 400°C for 1 h, 500°C for 1 h	Nanoparticles (64 nm)	500 W halogen lamp (2.37 eV)	62.3% in 90 min (RhB)	[26]
4	BiOCl	Self-combustion synthesis and $Bi(NO_3)_3{\cdot}6H_2O$, NH_4Cl, H_2O, HNO_3; 300°C	Hierarchical flower-like structure (40.3 nm)	400 W halogen lamp (2.69 eV)	80% in 120 min (fluoroquinolone)	[60]
5	$BiFeO_3$	Ultrasound and $Bi(NO_3)_3{\cdot}6H_2O$, $Fe(NO_3)_3{\cdot}9H_2O$, ethylene glycol; 400°C for 0.5 h, 500°C for 0.5 h	Nanoparticles (60–80 nm)	Solar light (2 eV)	100% in 35 min (RhB)	[63]
6	$Bi_4V_2O_{11}$	Template growth and $Bi(NO_3)_3{\cdot}6H_2O$, ethylene glycol, NH_4VO_3; 550°C	Multishell hollow spheres	(300 W Xe lamp) > 420 nm (2.56)	100% in 80 min (MB)	[64]
7	$BiVO_4$	Hydrothermal and $Bi(NO_3)_3{\cdot}6H_2O$, HNO_3, NH_4VO_3, sodium dodecyl benzene sulfonate (SDBS), H_2O (DI);150°C for 24 h	Octahedral (200 nm–5 μm)	Fluorescent lamps (8 W × 10), 435 nm (2.25–2.29 eV)	100% in 10 h (RhB)	[65]
8	γ-Bi_2MoO_6	Hydrothermal and $Bi(NO_3)_3{\cdot}6H_2O$, HNO_3, H_2O, oleylamine, $NH_3{\cdot}H_2O$, $(NH_4)_6Mo_7O_{24}{\cdot}4H_2O$; 160°C for 10 h solvothermal and $Bi(NO_3)_3{\cdot}6H_2O$, ethylene glycol, ethanol $(NH_4)_6Mo_7O_{24}{\cdot}4H_2O$; 160°C for 24 h	Nanobelt (lengths 300–600 nm, widths 20–30 nm, and thicknesses 5–10 nm) nanorod-based microspheres	(300 W Xe lamp) > 420 nm (2.65 eV)	Completely degraded 120 min (RhB) 660 min (RhB)	[56]
9	Bi_2MoO_6	Hydrothermal and $Bi(NO_3)_3{\cdot}6H_2O$, HNO_3, $NH_3{\cdot}H_2O$, Na_2MoO_4; 180°C for 24 h	Microrod (1 μm diameter, 3 μm length)	(500 W Xe lamp) > 420 nm (2.81 eV)	99% in 120 min (MB)	[66]
10	Mg/Bi_2WO_6	Hydrothermal and Na_2WO_4, $Bi(NO_3)_3$, CTAB, $Mg(NO_3)_2$, H_2O; 160°C for 12 h		(300 W Xe light) > 420 nm (2.17 eV)	89.44% in 150 min (Norfloxacin) 99.11% (Ciprofloxacin)	[67]

https://www.twirpx.org & http://chemistry-chemists.com

3.2 Photocatalytic reduction of heavy metals using Bi-based nanostructured materials

Unlike organic hazardous dyes, various heavy metal ions are evidenced to be toxic or carcinogenic [67, 68]. Heavy metal ions detoxification can be observed using conventional technologies such as physical adsorption, ion exchange, precipitation, photocatalytic reduction, and biological treatment [69–71]. Among the above methods, photocatalytic reduction has attracted attention due to its low energy consumption and no secondary pollution. Photocatalytic reduction involves adsorption and reduction of heavy metals on the photocatalyst's surface. Finally the reduced metal ions can be removed by physical and/or chemical processes. Though Bi-based nanostructured materials are widely used as visible light photocatalysts for the degradation of organic pollutants (Table 5.1), they also have great potential for the photoreduction of heavy metals (Table 5.2) [71–76].

Table 5.2 Bi-based nanostructured materials for the photoreduction of heavy metals.

S. no	Photocatalyst	Method and experimental condition	Morphology	Light wavelength (Bandgap)	% of degradation (Cr(VI))	Ref.
1	BiOCl	Precipitation and $NaBiO_3{\cdot}2H_2O$, H_2O + ethanol, HCl		125 W medium pressure mercury lamp	95% in 30 min (Cr (VI))	[71]
2	BiOCl	Hydrothermal and $Bi(NO_3)_3{\cdot}5H_2O$, KCl, H_2O, sodium citrate; 160°C for 12 h	Microrods	Solar light, (2.24 eV)	100% in 4 min (acidic) in 10 min (neutral) (Cr (VI))	[72]
3	I doped Bi_2MoO_6	Solvothermal-calcination and $Bi(NO_3)_3{\cdot}6H_2O$, $(NH_4)_6Mo_7O_{24}{\cdot}4H_2O$, ethylene glycol, KI; 160°C for 10 h, 400°C for 2 h	Microspheres	350 W xenon lamp > 420 nm (2.71 eV)	3 h (Cr (VI)) 88.8% (TC), 90% (CPEX), 89.6% (OTTCH)	[73]
4	Bi_2S_3/Bi_2WO_6	Hydrothermal and $Bi(NO_3)_3{\cdot}6H_2O$, PVP, ethanol, acetic acid, sodium tungstate, thiourea; 180°C for 3 h	Hierarchical structure (1.5–3.5 μm)	>400 nm (≫2.6 eV)	95% in 60 min (Cr (VI))	[74]
5	$BiVO_4$/RGO	Hydrothermal and $Bi(NO_3)_3{\cdot}5H_2O$, ethanol, H_2O, NH_4VO_3, graphite oxide; 180°C for 6 h	Nanocomposite	500 W Xe lamp (1.99 eV)	84.7% in 150 min (Cr (VI)) For BiVO4 34.6% in 150 min	[75]
6	Bi_2WO_6	Hydrothermal and $Na_2WO_4{\cdot}2H_2O$, $Bi(NO_3)_3$, CTAB, H_2O; 120°C for 24 h	Porous nanosheets (18 nm thickness)	(300 W Xe light) > 420 nm (2.87 eV)	99.5% in 100 min (Cr (VI))	[76]

https://www.twirpx.org & http://chemistry-chemists.com

3.3 Photocatalytic oxidation of air contaminants using Bi-based nanostructured materials

The rapid growth of civilization and the increasing deterioration of atmospheric quality mean that air pollution must be controlled. Several methods have been used to purify the polluted air including catalysis redox, photocatalytic oxidation, and physical adsorption [77, 78]. Among these methods, photocatalytic oxidation is a promising method due to its highest efficiency with durability and without secondary pollution. Table 5.3 provides a list of Bi-based photocatalysts for the photocatalytic oxidation of air contaminants [77–81].

Table 5.3 Bi-based nanostructured materials for the photocatalytic oxidation of air pollutants.

S. no	Photocatalyst	Method and experimental condition	Morphology	Light wavelength (Bandgap)	% of degradation (air pollutant)	Ref.
1	BiOBr	Nonaqueous sol-gel and $Bi(NO_3)_3{\cdot}5H_2O$, ethylene glycol, CTAB; 180°C for 12 h	Microspheres	>420 nm	30% in 10 min (NO)	[77]
2	BiOI	pH-induced transformation method and $Bi(NO_3)_3{\cdot}5H_2O$, KI, H_2O, HNO_3/NaOH; room temperature for 2 h	Flower composed of nano plates (10–20 nm thickness)	300 W Xe lamp > 420 nm (1.75 eV)	75.6% in 1 h exposed (110) facet (Hg0)	[78]
3	BiOX (X = Cl, Br, I)	Precipitation and KX (X = Cl, Br, I), $Bi(NO_3)_3{\cdot}6H_2O$, H_2O, acetic acid; room temperature for 4 h	Nanoplates (72–108 nm thickness) BiOCl nanoplates (58 nm thickness) BiOBr nanoplates (158–216 nm thickness)	100 W tungsten halogen lamp (420 nm) 3.2 eV (BiOCl) 2.76 eV (BiOBr) 1.77 eV (BiOI)	BiOCl 11.8% in 40 min (NO) BiOI 2.5% in 40 min (NO)	[79]
4	Bi_2WO_6	Solvothermal and $Bi(NO_3)_3{\cdot}6H_2O$, ethylene glycol, $Na_2WO_4{\cdot}2H_2O$; 160°C for 6, 12, 18, and 24 h; 250°C, 350°C, 450°C, and 550°C for 4 h		150 W tungsten halogen lamp (420 nm) (2.48–2.74 eV)	47% in 30 min (NO)	[80]
5	Bi_2WO_6	Solvothermal and $Bi(NO_3)_3{\cdot}6H_2O$, ethylene glycol, ethanol, $Na_2WO_4{\cdot}2H_2O$; 180°C for 12 h, 400°C for 2 h	Mesoporous nanoplate	300 W xenon lamp (>420 nm)	89.8% in 120 min (NO)	[81]

https://www.twirpx.org & http://chemistry-chemists.com

4 Conclusions and perspectives

In past decades, Bi-series nanostructured photocatalysts have been developed to address energy demands and environmental challenges. The exceptional properties of Bi-series nanostructured materials have shown more possibilities to enhance their photocatalytic performance. In this chapter, we summarized the recent reported results in the field of environmental remediation under visible light including photodegradation of organic dyes, photoreduction of heavy metal ions, and photocatalytic oxidation of air contaminants based on Bi-series-based nanostructured materials. We briefly reported the recent studies on Bi-based photocatalysts, which will provide guidelines for future research. Though many efforts have been made in the development of Bi-series-based photocatalysts, they still cannot satisfy the demand for practical applications and are in an experimental stage. It remains a challenge in the development of Bi-series-based photocatalysts with high efficiency under visible light to control environmental pollution. We discussed the various synthesis methods and experimental conditions for bismuth oxyhalides (BiOX), bismuth oxides, and other bismuth-based oxides (Bi_aAO_b). Then we focused on the degradation of various organic pollutants, heavy metal ions (Cr(VI)), and air contaminants using Bi-series-based photocatalysts. However, complex organic pollutants, mixed dyes, other heavy metals, and air pollutants were not found. In addition, the efficiency and mechanism of Bi-series-based nanostructured materials toward visible light irradiated photocatalysis are not clear and need to be explored.

References

[1] Khin MM, Nair AS, Babu VJ, Murugan R, Ramakrishna S. A review on nanomaterials for environmental remediation. Energy Environ Sci 2012;5:8075–109. https://doi.org/10.1039/c2ee21818f.

[2] Holkar CR, Jadhav AJ, Pinjari DV, Mahamuni NM, Pandit AB. A critical review on textile wastewater treatments: possible approaches. J Environ Manage 2016;182:351–66. https://doi.org/10.1016/j.jenvman.2016.07.090.

[3] Bhatia D, Sharma NR, Singh J, Kanwar RS. Biological methods for textile dye removal from wastewater: a review. Crit Rev Environ Sci Technol 2017;47:1836–76. https://doi.org/10.1080/10643389.2017.1393263.

[4] Kiran S, Adeel S, Nosheen S, Hassan A, Usman M, Rafique MA. Recent trends in textile effluent treatments: a review. In: Advanced materials for waste water treatment. Pakistan: Wiley; 2017. p. 29–49. https://doi.org/10.1002/9781119407805.ch2.

[5] Verma AK, Dash RR, Bhunia P. A review on chemical coagulation/flocculation technologies for removal of colour from textile wastewaters. J Environ Manage 2012;93:154–68. https://doi.org/10.1016/j.jenvman.2011.09.012.

[6] Bahnemann D. Photocatalytic water treatment: solar energy applications. Sol Energy 2004;77:445–59. https://doi.org/10.1016/j.solener.2004.03.031.

[7] Gautam A, Kshirsagar A, Biswas R, Banerjee S, Khanna PK. Photodegradation of organic dyes based on anatase and rutile TiO2 nanoparticles. RSC Adv 2016;6:2746–59. https://doi.org/10.1039/c5ra20861k.

[8] Kumar R, Kumar G, Umar A. ZnO nano-mushrooms for photocatalytic degradation of methyl orange. Mater Lett 2013;97:100–3. https://doi.org/10.1016/j.matlet.2013.01.044.

https://www.twirpx.org & http://chemistry-chemists.com

[9] Gnanasekaran L, Hemamalini R, Saravanan R, Ravichandran K, Gracia F, Agarwal S, et al. Synthesis and characterization of metal oxides (CeO_2, CuO, NiO, Mn_3O_4, SnO_2 and ZnO) nanoparticles as photo catalysts for degradation of textile dyes. J Photochem Photobiol B Biol 2017;173:43–9. https://doi.org/10.1016/j.jphotobiol.2017.05.027.

[10] Erik C, Virender SK, Xiang-Zhong L. Synthesis and photocatalytic activity of ferrites under visible light: a review. Sep Purif Technol 2012;1–14. https://doi.org/10.1016/j.seppur.2011.11.034.

[11] Chen L, Huang R, Xiong M, Yuan Q, He J, Jia J, et al. Room-temperature synthesis of flower-like BiOX (X = Cl, Br, I) hierarchical structures and their visible-light photocatalytic activity. Inorg Chem 2013;52:11118–25. https://doi.org/10.1021/ic401349j.

[12] Yang L, Qiang H, Zhiqing Y, Yongjian A, Shaoai S, Yi W, et al. A novel solvent-free strategy for the synthesis of bismuth oxyhalides. J Mater Chem A 2018;13005–11. https://doi.org/10.1039/C8TA04529A.

[13] Ai L, Zeng Y, Jiang J. Hierarchical porous BiOI architectures: facile microwave nonaqueous synthesis, characterization and application in the removal of Congo red from aqueous solution. Chem Eng J 2014;235:331–9. https://doi.org/10.1016/j.cej.2013.09.046.

[14] Di J, Xia J, Li H, Guo S, Dai S. Bismuth oxyhalide layered materials for energy and environmental applications. Nano Energy 2017;41:172–92. https://doi.org/10.1016/j.nanoen.2017.09.008.

[15] Lei Y, Wang G, Song S, Fan W, Zhang H. Synthesis, characterization and assembly of BiOCl nanostructure and their photocatalytic properties. CrstEngComm 2009;11:1857–62. https://doi.org/10.1039/b909013b.

[16] Wang Y, Long Y, Zhang D. Facile in situ growth of high strong BiOI network films on metal wire meshes with photocatalytic activity. ACS Sustain Chem Eng 2017;5:2454–62. https://doi.org/10.1021/acssuschemeng.6b02810.

[17] Bárdos E, Király AK, Pap Z, Baia L, Garg S, Hernádi K. The effect of the synthesis temperature and duration on the morphology and photocatalytic activity of BiOX (X = Cl, Br, I) materials. Appl Surf Sci 2019;479:745–56. https://doi.org/10.1016/j.apsusc.2019.02.136.

[18] Ye L, Tian L, Peng T, Zan L. Synthesis of highly symmetrical BiOI single-crystal nanosheets and their {001} facet-dependent photoactivity. J Mater Chem 2011;21:12479–84. https://doi.org/10.1039/c1jm11005e.

[19] Lu Y, Zhao Y, Zhao J, Song Y, Huang Z, Gao F, et al. Induced aqueous synthesis of metastable β-Bi_2O_3 microcrystals for visible-light photocatalyst study. Cryst Growth Des 2015;15:1031–42. https://doi.org/10.1021/cg500792v.

[20] Zhou L, Wang W, Xu H, Sun S, Shang M. Bi_2O_3 hierarchical nanostructures: controllable synthesis, growth mechanism, and their application in photocatalysis. Chem A Eur J 2009;15:1776–82. https://doi.org/10.1002/chem.200801234.

[21] Qiu Y, Yang M, Fan H, Zuo Y, Shao Y, Xu Y, et al. Nanowires of α- and β-Bi_2O_3: phase-selective synthesis and application in photocatalysis. CrstEngComm 2011;13:1843–50. https://doi.org/10.1039/c0ce00508h.

[22] Schmidt S, Kubaski ET, Volanti DP, Sequinel T, Bezzon VDN, Beltrán A, et al. Effect of pressure-assisted heat treatment on photoluminescence emission of α-Bi_2O_3 needles. Inorg Chem 2015;54:10184–91. https://doi.org/10.1021/acs.inorgchem.5b01237.

[23] Sudrajat H, Sujaridworakun P. Low-temperature synthesis of δ-Bi_2O_3 hierarchical nanostructures composed of ultrathin nanosheets for efficient photocatalysis. Mater Des 2017;130:501–11. https://doi.org/10.1016/j.matdes.2017.05.087.

[24] Kanti BK, Rituparna M, Malay C, Kumar BS. Phase control synthesis of α, β and α/β Bi_2O_3 hetero-junction with enhanced and synergistic photocatalytic activity on degradation of toxic dye, rhodamine-B under natural sunlight. J Hazard Mater 2018;182–91. https://doi.org/10.1016/j.jhazmat.2018.03.029.

https://www.twirpx.org & http://chemistry-chemists.com

[25] Puhan A, Bhushan B, Satpathy S, Meena SS, Nayak AK, Rout D. Facile single phase synthesis of Sr, Co co-doped $BiFeO_3$ nanoparticles for boosting photocatalytic and magnetic properties. Appl Surf Sci 2019;493:593–604. https://doi.org/10.1016/j.apsusc.2019.07.002.

[26] Puhan A, Nayak AK, Bhushan B, Praharaj S, Meena SS, Rout D. Enhanced electrical, magnetic and optical behaviour of Cr doped $Bi_{0.98}Ho_{0.02}FeO_3$ nanoparticles. J Alloys Compd 2019;796:229–36. https://doi.org/10.1016/j.jallcom.2019.05.025.

[27] Malathi A, Madhavan J, Ashokkumar M, Arunachalam P. A review on $BiVO_4$ photocatalyst: activity enhancement methods for solar photocatalytic applications. Appl Catal Gen 2018;555:47–74. https://doi.org/10.1016/j.apcata.2018.02.010.

[28] Huang Y, Kang S, Yang Y, Qin H, Ni Z, Yang S, et al. Facile synthesis of Bi/Bi_2WO_6 nanocomposite with enhanced photocatalytic activity under visible light. Appl Catal Environ 2016;196:89–99. https://doi.org/10.1016/j.apcatb.2016.05.022.

[29] Zhang Z, Wang W, Shang M, Yin W. Low-temperature combustion synthesis of Bi_2WO_6 nanoparticles as a visible-light-driven photocatalyst. J Hazard Mater 2010;177:1013–8. https://doi.org/10.1016/j.jhazmat.2010.01.020.

[30] Yanjuan S, Hong W, Qian X, Wen C, Jieyuan L, Sujuan W, et al. The pivotal effects of oxygen vacancy on Bi_2MoO_6: promoted visible light photocatalytic activity and reaction mechanism. Chin J Catal 2019;647–55. https://doi.org/10.1016/s1872-2067(19)63277-8.

[31] Yu H, Jiang L, Wang H, Huang B, Yuan X, Huang J, et al. Modulation of Bi_2MoO_6-based materials for photocatalytic water splitting and environmental application: a critical review. Small 2019;15. https://doi.org/10.1002/smll.201901008.

[32] Liu X, Gu S, Zhao Y, Zhou G, Li W. $BiVO_4$, Bi_2WO_6 and Bi_2MoO_6 photocatalysis: a brief review. J Mater Sci Technol 2020. https://doi.org/10.1016/j.jmst.2020.04.023.

[33] Meng X, Zhang L, Dai H, Zhao Z, Zhang R, Liu Y. Surfactant-assisted hydrothermal fabrication and visible-light-driven photocatalytic degradation of methylene blue over multiple morphological $BiVO_4$ single-crystallites. Mater Chem Phys 2011;125:59–65. https://doi.org/10.1016/j.matchemphys.2010.08.071.

[34] Nayak AK, Sohn Y, Pradhan D. Facile green synthesis of $WO_3{\cdot}H_2O$ nanoplates and WO_3 nanowires with enhanced photoelectrochemical performance. Cryst Growth Des 2017;17:4949–57. https://doi.org/10.1021/acs.cgd.7b00886.

[35] Nayak AK, Lee S, Sohn Y, Pradhan D. Synthesis of In_2S_3 microspheres using a template-free and surfactant-less hydrothermal process and their visible light photocatalysis. CrstEngComm 2014;16:8064–72. https://doi.org/10.1039/c4ce00836g.

[36] Song J, Han W, Dong S, Fang C, Cheng Y, Liu D, et al. Constructing hydrothermal carbonization coatings on carbon fibers with controllable thickness for achieving tunable sorption of dyes and oils via a simple heat-treated route. J Colloid Interface Sci 2020;559:263–72. https://doi.org/10.1016/j.jcis.2019.10.047.

[37] Nayak AK, Lee S, Sohn Y, Pradhan D. Biomolecule-assisted synthesis of $In(OH)_3$ nanocubes and In_2O_3 nanoparticles: photocatalytic degradation of organic contaminants and CO oxidation. Nanotechnology 2015;26.

[38] Nayak AK, Ghosh R, Santra S, Guha PK, Pradhan D. Hierarchical nanostructured WO_3-SnO_2 for selective sensing of volatile organic compounds. Nanoscale 2015;7:12460–73. https://doi.org/10.1039/c5nr02571k.

[39] Sun Y, Xie Y, Wu C, Zhang S, Jiang S. Aqueous synthesis of mesostructured $BiVO_4$ quantum tubes with excellent dual response to visible light and temperature. Nano Res 2010;3:620–31. https://doi.org/10.1007/s12274-010-0022-8.

[40] Zhang G, Lü F, Li M, Yang J, Zhang X, Huang B. Synthesis of nanometer Bi_2WO_6 synthesized by sol-gel method and its visible-light photocatalytic activity for degradation of 4BS. J Phys Chem Solid 2010;71:579–82. https://doi.org/10.1016/j.jpcs.2009.12.041.

https://www.twirpx.org & http://chemistry-chemists.com

[41] Li Y, Liu J, Huang X, Li G. Hydrothermal synthesis of Bi_2WO_6 uniform hierarchical microspheres. Cryst Growth Des 2007;7:1350–5. https://doi.org/10.1021/cg070343+.

[42] Tian Y, Hua G, Xu W, Li N, Fang M, Zhang L. Bismuth tungstate nano/microstructures: controllable morphologies, growth mechanism and photocatalytic properties. J Alloys Compd 2011;509:724–30. https://doi.org/10.1016/j.jallcom.2010.09.010.

[43] Alfaro SO, Martínez-De La Cruz A. Synthesis, characterization and visible-light photocatalytic properties of Bi_2WO_6 and $Bi_2W_2O_9$ obtained by co-precipitation method. Appl Catal Gen 2010;383:128–33. https://doi.org/10.1016/j.apcata.2010.05.034.

[44] Zhou L, Wang W, Zhang L. Ultrasonic-assisted synthesis of visible-light-induced Bi_2MO_6 (M = W, Mo) photocatalysts. J Mol Catal A Chem 2007;268:195–200. https://doi.org/10.1016/j.molcata.2006.12.026.

[45] Zhang L, Wang W, Zhou L, Xu H. Bi_2WO_6 nano- and microstructures: shape control and associated visible-light-driven photocatalytic activities. Small 2007;3:1618–25. https://doi.org/10.1002/smll.200700043.

[46] Zhang L, Wang H, Chen Z, Wong PK, Liu J. Bi_2WO_6 micro/nano-structures: synthesis, modifications and visible-light-driven photocatalytic applications. Appl Catal Environ 2011;106:1–13. https://doi.org/10.1016/j.apcatb.2011.05.008.

[47] Saison T, Chemin N, Chaneéac C, Durupthy O, Ruaux V, Mariey L, et al. Bi_2O_3, $BiVO_4$, and Bi_2WO_6: impact of surface properties on photocatalytic activity under visible light. J Phys Chem C 2011;115:5657–66. https://doi.org/10.1021/jp109134z.

[48] Hu SP, Xu CY, Zhen L. Solvothermal synthesis of Bi_2WO_6 hollow structures with excellent visible-light photocatalytic properties. Mater Lett 2013;95:117–20. https://doi.org/10.1016/j.matlet.2012.12.058.

[49] Nayak AK, Pradhan D. Microwave-assisted greener synthesis of defect-rich tungsten oxide nanowires with enhanced photocatalytic and photoelectrochemical performance. J Phys Chem C 2018;122:3183–93. https://doi.org/10.1021/acs.jpcc.7b09479.

[50] Cao XF, Zhang L, Chen XT, Xue ZL. Microwave-assisted solution-phase preparation of flower-like Bi_2WO_6 and its visible-light-driven photocatalytic properties. CrstEngComm 2011;13:306–11. https://doi.org/10.1039/c0ce00031k.

[51] Xie H, Shen D, Wang X, Shen G. Microwave hydrothermal synthesis and visible-light photocatalytic activity of Bi_2WO_6 nanoplates. Mater Chem Phys 2007;103:334–9. https://doi.org/10.1016/j.matchemphys.2007.02.040.

[52] Tian G, Chen Y, Zhou W, Pan K, Dong Y, Tian C, et al. Facile solvothermal synthesis of hierarchical flower-like Bi_2MoO_6 hollow spheres as high performance visible-light driven photocatalysts. J Mater Chem 2011;21:887–92. https://doi.org/10.1039/c0jm03040f.

[53] Xie H, Shen D, Wang X, Shen G. Microwave hydrothermal synthesis and visible-light photocatalytic activity of γ-Bi_2MoO_6 nanoplates. Mater Chem Phys 2008;110:332–6. https://doi.org/10.1016/j.matchemphys.2008.02.008.

[54] la Cruz AM-d, Alfaro SO. Synthesis and characterization of γ-Bi2MoO6 prepared by co-precipitation: photoassisted degradation of organic dyes under vis-irradiation. J Mol Catal A Chem 2010;85–91. https://doi.org/10.1016/j.molcata.2010.01.008.

[55] Ma Y, Jia Y, Wang L, Yang M, Bi Y, Qi Y. Exfoliated thin Bi_2MoO_6 nanosheets supported on WO_3 electrode for enhanced photoelectrochemical water splitting. Appl Surf Sci 2016;390:399–405. https://doi.org/10.1016/j.apsusc.2016.08.116.

[56] Long J, Wang S, Chang H, Zhao B, Liu B, Zhou Y, et al. Bi_2MoO_6 nanobelts for crystal facet-enhanced photocatalysis. Small 2014;10:2791–5. https://doi.org/10.1002/smll.201302950.

[57] Yin W, Wang W, Sun S. Photocatalytic degradation of phenol over cage-like Bi_2MoO_6 hollow spheres under visible-light irradiation. Catal Commun 2010;11:647–50. https://doi.org/10.1016/j.catcom.2010.01.014.

https://www.twirpx.org & http://chemistry-chemists.com

[58] Xiao J, Zhang J, Liu W, Huang T, Qu Y, Chen H, et al. Construction of rGO/Bi_2MoO_6 2D/2D nanocomposites for enhancement visible light-driven photocatalytic reduction of Cr (VI). Mater Res Expr 2018;5. https://doi.org/10.1088/2053-1591/aade7a.

[59] Zhang Y, Zhu Y, Yu J, Yang D, Ng TW, Wong PK, et al. Enhanced photocatalytic water disinfection properties of Bi_2MoO_6-RGO nanocomposites under visible light irradiation. Nanoscale 2013;5:6307–10. https://doi.org/10.1039/c3nr01338c.

[60] Shabani M, Haghighi M, Kahforoushan D, Haghighi A. Mesoporous-mixed-phase of hierarchical bismuth oxychlorides nanophotocatalyst with enhanced photocatalytic application in treatment of antibiotic effluents. J Clean Prod 2019;207:444–57. https://doi.org/10.1016/j.jclepro.2018.10.042.

[61] Yin B, Fang Z, Luo B, Zhang G, Shi W. Facile preparation of $Bi_{24}O_{31}Cl_{10}$ nanosheets for visible-light-driven photocatalytic degradation of tetracycline hydrochloride. Catal Lett 2017;147:2167–72. https://doi.org/10.1007/s10562-017-2115-4.

[62] Zhu F, Lv Y, Li J, Ding J, Xia X, Wei L, et al. Enhanced visible light photocatalytic performance with metal-doped Bi_2WO_6 for typical fluoroquinolones degradation: efficiencies, pathways and mechanisms. Chemosphere 2020;252. https://doi.org/10.1016/j.chemosphere.2020.126577.

[63] Soltani T, Entezari MH. Sono-synthesis of bismuth ferrite nanoparticles with high photocatalytic activity in degradation of rhodamine B under solar light irradiation. Chem Eng J 2013;223:145–54. https://doi.org/10.1016/j.cej.2013.02.124.

[64] Zong L, Cui P, Qin F, Zhao K, Wang Z, Yu R. Heterostructured bismuth vanadate multi-shell hollow spheres with high visible-light-driven photocatalytic activity. Mater Res Bull 2017;86:44–50. https://doi.org/10.1016/j.materresbull.2016.09.031.

[65] Han M, Chen X, Sun T, Tan OK, Tse MS. Synthesis of mono-dispersed m-$BiVO_4$ octahedral nano-crystals with enhanced visible light photocatalytic properties. CrstEngComm 2011;13:6674–9. https://doi.org/10.1039/c1ce05539a.

[66] Zhang L, Xu T, Zhao X, Zhu Y. Controllable synthesis of Bi_2MoO_6 and effect of morphology and variation in local structure on photocatalytic activities. Appl Catal Environ 2010;98:138–46. https://doi.org/10.1016/j.apcatb.2010.05.022.

[67] Zeng G, Zhang C, Huang D, Lai C, Tang L, Zhou Y, et al. Practical and regenerable electrochemical aptasensor based on nanoporous gold and thymine-Hg^{2+}–thymine base pairs for Hg^{2+} detection. Biosens Bioelectron 2017;90:542–8. https://doi.org/10.1016/j.bios.2016.10.018.

[68] Kumar NA, Seungwon L, In CY, Jung YH, Youngku S, Debabrata P. Crystal phase and size-controlled synthesis of tungsten trioxide hydrate nanoplates at room temperature: enhanced Cr(VI) photoreduction and methylene blue adsorption properties. ACS Sustain Chem Eng 2017;2741–50. https://doi.org/10.1021/acssuschemeng.6b03084.

[69] Fan T, Liu Y, Feng B, Zeng G, Yang C, Zhou M, et al. Biosorption of cadmium(II), zinc(II) and lead(II) by Penicillium simplicissimum: isotherms, kinetics and thermodynamics. J Hazard Mater 2008;160:655–61. https://doi.org/10.1016/j.jhazmat.2008.03.038.

[70] Hu XJ, Wang JS, Liu YG, Li X, Zeng GM, Bao ZL, et al. Adsorption of chromium (VI) by ethylenediamine-modified cross-linked magnetic chitosan resin: Isotherms, kinetics and thermodynamics. J Hazard Mater 2011;185:306–14. https://doi.org/10.1016/j.jhazmat.2010.09.034.

[71] Liu Z, Liu X, Yu C, Wei L, Ji H. Fabrication and characterization of I doped Bi_2MoO_6 microspheres with distinct performance for removing antibiotics and Cr (VI) under visible light illumination. Sep Purif Technol 2020;247:116951. https://doi.org/10.1016/j.seppur.2020.116951.

[72] Peng Y, Mao YG, Kan PF, Liu JY, Fang Z. Controllable synthesis and photoreduction performance towards Cr(vi) of BiOCl microrods with exposed (110) crystal facets. New J Chem 2018;42:16911–8. https://doi.org/10.1039/c8nj03323d.

https://www.twirpx.org & http://chemistry-chemists.com

[73] Qamar M, Yamani ZH. Bismuth oxychloride-mediated and laser-induced efficient reduction of Cr(VI) in aqueous suspensions. Appl Catal Gen 2012;439–440:187–91. https://doi.org/10.1016/j.apcata.2012.07.004.

[74] Rauf A, Sher Shah MSA, Choi GH, Humayoun UB, Yoon DH, Bae JW, et al. Facile synthesis of hierarchically structured Bi_2S_3/Bi_2WO_6 photocatalysts for highly efficient reduction of Cr(VI). ACS Sustain Chem Eng 2015;3:2847–55. https://doi.org/10.1021/acssuschemeng.5b00783.

[75] Wang A, Shen S, Zhao Y, Wu W. Preparation and characterizations of $BiVO_4$/reduced graphene oxide nanocomposites with higher visible light reduction activities. J Colloid Interface Sci 2015;445:330–6. https://doi.org/10.1016/j.jcis.2015.01.017.

[76] Xu F, Chen H, Xu C, Wu D, Gao Z, Zhang Q, et al. Ultra-thin Bi_2WO_6 porous nanosheets with high lattice coherence for enhanced performance for photocatalytic reduction of Cr(VI). J Colloid Interface Sci 2018;525:97–106. https://doi.org/10.1016/j.jcis.2018.04.057.

[77] Ai Z, Ho W, Lee S, Zhang L. Efficient photocatalytic removal of NO in indoor air with hierarchical bismuth oxybromide nanoplate microspheres under visible light. Environ Sci Tech 2009;43:4143–50. https://doi.org/10.1021/es9004366.

[78] Sun X, Wu J, Liu Q, Tian F. Mechanism insights into the enhanced activity and stability of hierarchical bismuth oxyiodide microspheres with selectively exposed (0 0 1) or (1 1 0) facets for photocatalytic oxidation of gaseous mercury. Appl Surf Sci 2018;455:864–75. https://doi.org/10.1016/j.apsusc.2018.06.049.

[79] Huo WC, Dong X, Li JY, Liu M, Liu XY, Zhang YX, et al. Synthesis of Bi_2WO_6 with gradient oxygen vacancies for highly photocatalytic NO oxidation and mechanism study. Chem Eng J 2019;361:129–38. https://doi.org/10.1016/j.cej.2018.12.071.

[80] Wan J, Du X, Wang R, Liu E, Jia J, Bai X, et al. Mesoporous nanoplate multi-directional assembled Bi_2WO_6 for high efficient photocatalytic oxidation of NO. Chemosphere 2018;193:737–44. https://doi.org/10.1016/j.chemosphere.2017.11.048.

[81] Zhang W, Zhang Q, Dong F. Visible-light photocatalytic removal of NO in air over BiOX (X = Cl, Br, I) single-crystal nanoplates prepared at room temperature. Ind Eng Chem Res 2013;52:6740–6. https://doi.org/10.1021/ie400615f.

https://www.twirpx.org & http://chemistry-chemists.com

https://www.twirpx.org & http://chemistry-chemists.com

6

Transition metal oxide-based materials for visible-light-photocatalysis

S.R. Meher

DEPARTMENT OF PHYSICS, SCHOOL OF ADVANCED SCIENCES, VELLORE INSTITUTE OF TECHNOLOGY, VELLORE, INDIA

1 Introduction

Transition metal oxides (TMOs) are technologically significant materials and have potential applications in the field of optoelectronics, sensors, magnetic storage devices, and light-induced catalysis [1]. The main characteristics of TMOs are the partially filled $3d$-shells for the positive metallic cations. The well-known semiconductors TiO_2 and Cu_2O are the end points of the $3d$ transition metal oxide series having $3d^0$ and $3d^{10}$ electronic configurations for the respective cations [2]. These two end-point semiconductors exhibit *n*-type and *p*-type conductivity, respectively. The partially filled *d*-shells in TMOs result in various unique properties such as wide bandgap, high dielectric constant, ferromagnetic and ferrimagnetic states, etc. The origin of the wide bandgap for the TMOs can be successfully described by the on-site *d*-*d* Coulombic and exchange interaction. Owing to the above properties, TMOs are thoroughly studied materials resulting in various technological and environmental applications [3]. This chapter discusses the in-depth analysis of the different approaches adopted in the literature for visible light-driven photocatalysis employing TMOs. The different preparation techniques and their impacts on photocatalytic efficiency for the above approaches are also discussed in parallel.

2 Different approaches for visible light photocatalysis in TMOs

TMOs produce active oxygen species as well as electron-hole (*e*-*h*) pairs when their surface is exposed to ultraviolet (UV) or visible light. This unique property of TMOs is the basis for the heterogeneous photocatalytic reaction which is used in many applications such as self-cleaning windows [4], pollution degradation from wastewater [5, 6], photochemical water splitting [7], CO_2 reduction [8], bacterial disinfection [9], etc. (Fig. 1). In the basic photocatalytic reaction, the photons of energy ($h\nu$) greater than the bandgap of the TMO are absorbed in it, which results in the generation of *e*-*h* pairs. These photogenerated

Nanostructured Materials for Visible Light Photocatalysis. https://doi.org/10.1016/B978-0-12-823018-3.00021-X
Copyright © 2022 Elsevier Inc. All rights reserved.

https://www.twirpx.org & http://chemistry-chemists.com

FIG. 1 Application of TMO-based photocatalysts in various fields.

electrons (e^-) and holes (h^+) then react with the available oxidants and reductants, respectively (Fig. 2). The position of the conduction band edge (CBE) and valence band edge (VBE) of the TMO with respect to the redox potential of the adsorbate species decides the transfer of the photogenerated charge carriers to the adsorbate surface. The VBE should be located relatively at a positive potential with respect to the donor species. Similarly, the CBE of the TMO should be at a negative potential with respect to the acceptor species. The reaction of the charge carriers with the available oxidants and reductants produces the highly reactive hydroxyl (OH^*) and superoxide (O_2^{*-}) radicals which degrade the organic pollutants converting them to CO_2 and H_2O with a number of intermediate steps. However, one of the major drawbacks of heterogeneous photocatalysis is that the *e-h* pairs are prone to recombine and thereby the photocatalytic efficiency is reduced [10].

The important parameters which influence heterogeneous photocatalytic efficiency are the bandgap of the photocatalyst, intensity of light, concentration of pollutant, amount of catalyst loaded, etc. [10]. The UV light ($\lambda < 400$ nm) constitutes only 5% of the solar spectrum whereas the visible light ($\lambda = 400$–700 nm) constitutes ~47%. However, only a limited number of TMOs like Co_3O_4, MnO_2, and Cu_2O can be excited by visible light because of their narrower bandgap. On the other hand, the most studied photocatalysts

https://www.twirpx.org & http://chemistry-chemists.com

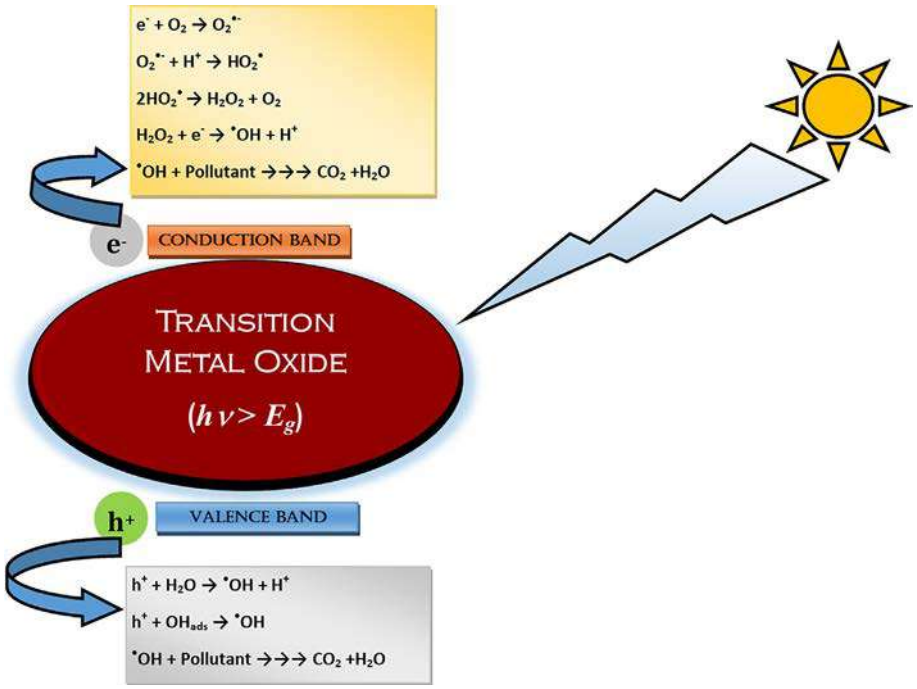

FIG. 2 Schematic illustration of heterogeneous photocatalysis by the TMOs.

like TiO_2 and ZnO are sensitive only to the UV light because of their wider bandgap (>3 eV). The rest of the solar spectrum is not efficiently utilized by these wider bandgap TMOs. Moreover, even for narrower bandgap TMOs, the position of the CBE or VBE with respect to the redox potential of the adsorbate species should also be favorable for good photocatalytic activity. Again, the band-to-band recombination rate in narrow bandgap semiconductors is more, which is not ideal for photocatalytic reaction. It is a challenging task to have a TMO with sufficiently negative CBE for H_2 production with the required narrow bandgap (<3 eV) for the absorption of visible light. It is because the VBE is mostly dominated by the O 2*p* orbitals which pulls it toward positive potential with respect to the normal hydrogen electrode (NHE) [6]. Therefore, in order to realize good visible light photocatalytic activity in wide bandgap TMOs several approaches such as doping [11], heterogeneous coupling with a narrow bandgap semiconductor [12], addition of noble metal nanoparticles [13], dye sensitization [14], etc. have been prescribed in the literature. The dopants may introduce shallow or deep level trap states in TMOs without altering the CBE or VBE and thereby allowing the absorption of longer wavelength visible photons. But, these trap states may also act as the recombination centers. On the other hand, some other dopants may shift the absorption edge toward lower energies and thereby increasing the visible light photocatalytic activity. The visible light can also be utilized by coupling the wide bandgap TMO with another narrow bandgap semiconductor. In this case, the visible photons are easily absorbed by the narrow bandgap semiconductor and depending upon the CB alignment of these two semiconductors, the electrons may be injected into the CB of

https://www.twirpx.org & http://chemistry-chemists.com

wide bandgap TMO. In the sensitization approach, the sensitizer, which may be an organic molecule, an inorganic complex, or a nanostructure, can absorb the visible light and transfer the electrons or holes to the CB or VB of the TMO, respectively. Another type of sensitization is achieved through the surface complexation of ligand to metal charge transfer. In this case, upon exposure to visible light the electron is photoexcited directly from the highest occupied molecular orbital (HOMO) level of the adsorbate to the CB of the *n*-type TMO semiconductor [8]. In the case of noble metal nanoparticle-loaded TMOs, the localized surface plasmon resonance (LSPR) is excited in the metal nanocrystals and this plasmonic energy is transferred to the TMO semiconductor, resulting in the creation of *e*-*h* pair.

2.1 Doping

For a typical semiconductor like TMO, cationic or anionic doping results in the shifting of the band edges or the creation of defect states in the bandgap. There are several reports on the metal or nonmetal doping of wider bandgap TMOs leading to increased visible light photocatalytic activity [15]. The common metal dopants for these wide bandgap photocatalysts such as TiO_2 and ZnO are Cu, Mg, Co, Fe, Cr, V, etc. The nonmetal dopants such as N, F, S, C, P, etc. also lead to improved visible light photocatalysis in these TMOs. An indicative list of various metal-doped TMOs along with their preparation methods and visible light photocatalytic activity is given in Table 1. The details of various nonmetal-doped TMOs used for visible light photocatalytic activity are provided in Table 2.

Table 1 Indicative list of various metal-doped TMOs as visible light photocatalysts.

Host photocatalyst	Metal dopant	Preparation method	Pollutant	Reference
TiO_2	V	Sol-gel route	Automobile exhaust	[16]
TiO_2	Mn	Hydrothermal method	Malachite green	[17]
TiO_2	Cr	Sol-gel spin coating	Methyl orange	[18]
TiO_2	Fe	Sol-gel route	Reactive red 198	[19]
TiO_2	Co	Multicomponent self-assembly process	CO_2	[20]
TiO_2	Ni	Microwave-assisted sol-gel route	Bisphenol A	[21]
TiO_2	Cu	Ammonia evaporation induced synthesis	Sunset yellow, Rhodamine B, and methylene blue	[22]
TiO_2	Zn	Sol-gel route	Methylene blue	[23]
ZnO	Co	Solvothermal method	Methyl orange	[24]
ZnO	Cu	Precipitation method	Arsenite	[25]
ZnO	Ni	Solvothermal method	Rhodamine B	[26]
ZnO	Fe	Sol-gel route	Rhodamine B	[27]
Fe_2O_3	Sn	Solution combustion synthesis	Methylene blue	[28]
Fe_2O_3	Cu/Ni/Co	Coprecipitation method	Acid red-27	[29]
Fe_2O_3	Ga	Coprecipitation method	Benzoquinone	[30]
NiO	Mn	Sol-gel route	Methylene blue	[31]

https://www.twirpx.org & http://chemistry-chemists.com

Table 2 Indicative list of various nonmetal-doped TMOs as visible light photocatalysts.

Host photocatalyst	Dopant	Preparation method	Pollutant	**References**
TiO_2	N	Flame aerosol method	Phenol	[32]
TiO_2	S	Metalorganic chemical vapor deposition (MOCVD)	Methyl orange	[33]
TiO_2	C	Reactive pulsed DC magnetron cosputtering	Methylene blue and stearic acid	[34]
TiO_2	F	Sol-gel method	Methylene blue	[35]
TiO_2	P	Hydrolysis	Phenol	[36]
ZnO	N	Ion implantation method	Photoelectrochemical water splitting	[37]
ZnO	C	Polymer-assisted pyrolysis	Methylene blue	[38]
WO_3	N	Electrochemical synthesis and drying in N_2 stream	Methyl orange	[39]
WO_3	C	Spray pyrolysis	Photoelectrochemical water splitting	[40]
Fe_2O_3	S	Hybrid hydrothermal-calcination treatment	Acid orange 7	[41]
Ta_2O_5	N	Sol-gel method	CO_2 reduction	[42]

2.1.1 Doping in TiO_2

TiO_2 is one of the most studied TMOs for photocatalysis. Owing to the position of the CBE and VBE, anatase TiO_2 is a natural choice for the redox transformation of organic pollutants. Over the past decades, several metal-doped TiO_2 photocatalysts have been thoroughly investigated for their visible light activity. Metal doping in TiO_2 favors the formation of the anatase phase over the rutile phase [43] and also suppresses the crystallite size. Umebayashi et al. [44] analyzed the electronic structure of 3*d* transition metal-doped TiO_2 through ab initio density functional theory calculations using the full potential linearized augmented plane wave method. Their calculations suggest the presence of a highly localized electron occupied mid-gap level for the V, Cr, Mn, Fe, and Co dopants. For Ni, the electrons are highly delocalized and contribute significantly to the VB. Inturi et al. [45] synthesized transition metal (V, Cr, Fe, Co, Mn, Ni, Cu)-doped TiO_2 nanoparticles through a one-step liquid flame aerosol synthesis technique. They have studied the degradation of acetonitrile in gas phase using these doped TiO_2 under visible light irradiation. They have observed that the Cr-doped titania exhibits the best photocatalytic activity, with the corresponding rate constant being ~18 times than the rest of the samples. Bhatia et al. [46] synthesized Bi- and Ni-doped titania nanoparticles by the sol-gel method and have studied their visible light photocatalytic activity for the degradation of the antiinflammatory drug Ibuprofen. They reported that Bi-doped TiO_2 have better photocatalytic activity than Ni-doped TiO_2 or Degussa TiO_2. They achieved 89% degradation of Ibuprofen with 0.25% Bi doped TiO_2 photocatalyst under 6 h illumination with solar light. Sood et al. [47] prepared Fe-doped TiO_2 nanoparticles through a facile ultrasonic assisted hydrothermal

https://www.twirpx.org & http://chemistry-chemists.com

method and studied their photocatalytic activity toward para-nitrophenol. They reported 92% degradation of para-nitorphenol for 0.05 mol% Fe-doped anatase TiO_2. Ni-doped TiO_2 thin films were prepared by the spray coating method on glazed ceramic tiles [48]. The optical bandgap of TiO_2 thin films was reduced to 2.48 eV with Ni doping. The prepared photocatalysts successfully decomposed the vegetable olive oil upon exposure to visible light. Visible light-activated Fe-doped TiO_2 thin films anchored to a wood surface showed successful degradation of gaseous formaldehyde [49]. In addition, the coated woods exhibited significant improvement in their flame resistance. The formation of CuO and Cu_2O secondary phases in Cu-doped TiO_2 thin films prepared by the sol-gel dip coating method was found to decrease photocatalytic activity [50]. These secondary phases were found to act as carrier recombination centers. Moreover, metal ion implantation is also an effective way to modify the TiO_2 powders as well as thin films for the absorption and proper utilization of visible light [51, 52]. There are reports on the successful implantation of Mn, Cr, V, Co, and Fe ions in TiO_2 for the enhancement of visible light photocatalytic activity of TiO_2. The absorption edge of anatase TiO_2 has been found to shift toward higher wavelengths with Cr and V implantation [53, 54]. Cr ion implanted TiO_2 powders were found to decompose toxic NO effectively into N_2 and O_2 under visible light illumination [55]. The degradation of formic acid to H_2O and CO_2 under visible light irradiation has been reported for V ion implanted TiO_2 thin films prepared by ionized cluster beam deposition method [56]. Similarly, Impellizzeri et al. [57] reported the Fe ion implanted TiO_2 thin films for efficient visible light photocatalytic degradation of methylene blue. They observed a local bandgap lowering of TiO_2 thin films from 3.2 eV to 1.6–1.9 eV with Fe implantation. However, metal doping suffers from a few drawbacks such as thermal instability, electron trapping by metal centers, and expensive ion implantation facilities.

Nonmetal doping in TiO_2 is another effective way to narrow down its bandgap for the absorption of visible light. N is a promising dopant in TiO_2 because of its comparable size with the O atoms, small ionization energy, and high stability. N-doping is believed to introduce energy levels above the valence band of TiO_2 due to the hybridization of N 2*p* orbitals with that of O 2*p* [58]. However, the exact mechanism of visible light photocatalysis in N-doped TiO_2 is still debatable. The first breakthrough work for the visible light photocatalysis using N-doped TiO_2 was reported by Asahi et al. [59] in 2001. They suggested that the N-atoms act as the substitutional impurity for O sites in TiO_2. N-doped TiO_2 was found to degrade methylene blue and gaseous acetaldehyde under visible light illumination. Zhang et al. [60] gave a detailed review on the development of N-doped TiO_2 as a visible light active photocatalyst. The incorporation of N into the TiO_2 lattice can be achieved by a number of physical and chemical techniques such as sputtering, the sol-gel method, hydrothermal synthesis, ball milling, etc. Significant milestones regarding the preparation of N-doped TiO_2 photocatalysts for the removal of organic pollutants from environmental media were reviewed by Ansari et al. [58]. C-doped TiO_2 is another promising visible light photocatalyst which shows higher activity compared to undoped TiO_2 and Degussa P25 under visible light irradiation [61]. C can exist in three different forms inside the TiO_2 lattice: as an interstitial impurity, as a substitutional impurity and as carbonate species. It has

https://www.twirpx.org & http://chemistry-chemists.com

been observed that most of the C exists in the elemental form in TiO_2 and the other forms are very small in quantity [62, 63]. It has also been reported that C has large electron storage capacity and hence can accept the photogenerated electrons, which suppresses the *e-h* pair recombination. Lu et al. [64] reported the visible light photocatalytic degradation of Rhodamine-B (RhB) dye with the help of mesoporous C-doped TiO_2 crystals containing O vacancies prepared by a modified sol-gel synthesis. They obtained the corresponding rate constant to be 0.3921 m^{-1}. They attributed this visible light activity to the structural modification of TiO_2 crystals because of C doping. The separation of *e-h* pair is conducive under C doping which provides a sensitized surface to visible light. The O vacancies induced by the C doping help in preventing *e-h* pair recombination. Moreover, the mesoporous surface of C-doped TiO_2 crystals results in more surface area for the efficient absorption of the organic pollutant. Zhang et al. [65] developed a viable method for industrial-scale development of C-doped TiO_2 nanoparticles for the mineralization of gaseous toluene under visible light irradiation. Lee et al. [66] demonstrated the C deposited inverse opal structure with better visible light photocatalytic activity toward organic dyes than the corresponding mesoporous TiO_2 structure. S and P doping in TiO_2 have also been studied by many researchers for their visible light photocatalytic activity. The ab initio DFT calculations performed by Yang et al. [67] showed that the anionic substitutional S and P doping in TiO_2 resulted in narrowing down of the bandgap and the creation of localized S 3*p* states in the bandgap. Gul et al. [68] synthesized P-doped TiO_2 nanocrystals by the hydrothermal method and investigated their visible light photocatalytic activity. They observed drastic improvement in the activity of P-doped samples compared to the undoped ones under visible light irradiation. Mendiola-Alvarez et al. [69] synthesized mesoporous P-doped TiO_2 with different wt% of P (0.5, 1.0, 1.5) by the microwave-assisted sol-gel method. They studied the visible light photocatalytic degradation of sulfamethazine using these samples. The enhanced activity of 1 wt% P doped TiO_2 was due to the increased surface area and shift of the absorption edge toward the visible region. Moreover, it was observed that the formation of the PO_4^{-3} ions at the surface and incorporation of P^{+5} by the substitution of Ti^{+4} ions to form Ti-O-P suppresses the carrier recombination. The S ions can act as cationic as well as anionic dopants in the TiO_2 lattice [70–72]. S-doped TiO_2 is thermally stable and has the absorption edge in the visible region. Lin et al. [73] reported the visible light-induced photocatalytic degradation of dimethyl sulfide using S-doped TiO_2 prepared by the sol-gel method. S-doped TiO_2 was prepared by the flame spray pyrolysis method by Boningari et al. [74]. The presence of S^{+4} and S^{+6} oxidation states in TiO_2 was confirmed from XPS. It was observed that the presence of S^{+6} plays an important role in enhancing the visible light photocatalytic degradation of acetaldehyde.

2.1.2 Doping in ZnO

ZnO is another promising material for the photocatalytic applications. In ZnO, the VBE is more positive than the redox potential of $\bullet OH/H_2O$ (+2.53 V vs. NHE), which eases the oxidation of water molecules by the photogenerated holes to form hydroxyl radicals.

https://www.twirpx.org & http://chemistry-chemists.com

Similarly, the CBE is more negative than the redox potential of $O_2/O_2^{-}\bullet$ (−0.33 V vs. NHE), leading to the production of superoxide anion radicals. Some reports suggest that ZnO is more efficient than TiO_2 for the photocatalytic degradation of few azo dyes, pulp wastewater, and phenols [75]. The optical bandgap of ZnO is 3.3 eV and therefore UV light is required for the photogeneration of *e-h* pairs. There have been many successful attempts to modify the electronic band structure of ZnO with the help of metal and nonmetal doping in order to convert it into a visible light photocatalyst. The metal doping in ZnO usually creates deep level donor and acceptor states shifting the absorption edge to the visible region. However, at the same time these mid-gap states can also act as charge recombination centers. On the other hand, nonmetal doping in ZnO generally pulls the valence band upwards and thereby enables visible light absorption. Therefore, nonmetal doping is less likely to create recombination centers. Samadi et al. [76] presented a complete review on the doped ZnO nanostructures for visible light photocatalysis.

Qi et al. [77] reported the synthesis of transition metal (3% Mn, Fe, Co, Ni or Cu)-doped hexagonal wurtzite ZnO through the solvothermal method. The cationic substitutional doping was confirmed from X-ray photoelectron spectroscopy. They observed a shift in the bandgap toward the longer wavelengths with transition metal doping. Cu-doped ZnO nanoparticles showed the best visible light photocatalytic performance among all other transition metal-doped ZnO. Ni-doped ZnO thin films were deposited by DC/RF cosputtering [78]. The bandgap of ZnO thin films was successfully tailored from 3.4 to 1.4 eV by changing the Ni concentration. The Ni-doped ZnO thin films exhibited enhanced visible light photocatalytic degradation of methyl green dye compared to the undoped ZnO thin films. Yildirim et al. [79] deposited Co-doped ZnO thin films using the sol-gel spin coating method. They varied the Co concentration from 0 to 5 at.%. XPS studies revealed that Co^{+2} ions substitute the Zn^{+2} ions in the ZnO lattice. They studied the photocatalytic degradation of methylene blue under visible light irradiation. The 3 at.% Co-doped ZnO films showed the highest activity with 92% decomposition of the methylene blue solution upon 60 min exposure to visible light. Saleh et al. [80] observed a decrease in photocatalytic activity under visible light for Mn- and Co-doped ZnO nanoparticles prepared by coprecipitation. Their study suggests that the bandgap narrowing is not always favorable for enhancing the visible light photocatalytic activity.

Nonmetal doping such as N, C, and S is expected to substitute the O anions in the ZnO lattice. These doped systems have shown promising results as visible light photocatalysts. N is claimed to be a suitable dopant for ZnO due to its similar ionic size with that of O; it is also less electronegative than O. The electronic structure calculations suggests the hybridization of O 2*p* states with the N 2*p* states which pulls the VBE upwards, resulting in the bandgap narrowing for substitutional occupation [76]. On the other hand, interstitial occupation of N in the tetrahedral or octahedral voids results in N—O bond formation with an intermediate state lying at 1.4 eV above the VBE. Hybrid density functional theory calculations suggest that N substitutional doping alone is not responsible for the bandgap narrowing of ZnO. N doping results in the creation of more number of O vacancies and Zn interstitials, leading to narrowing down of the ZnO bandgap. In the literature, different

https://www.twirpx.org & http://chemistry-chemists.com

methods such as sol-gel, reactive magnetron sputtering, chemical vapor deposition, hydrothermal synthesis, combustion reaction, wet chemical process, etc. have been suggested for effective doping of N into the ZnO lattice. XPS has been widely used to ascertain the chemical state of the N dopant in the host lattice. Wu et al. [81] synthesized N-doped ZnO micropolyhedrons for efficient visible light degradation of formaldehyde. They demonstrated that the N-doped ZnO system had better photocatalytic activity than N-doped P25 TiO_2. Visible light active N-doped ZnO was synthesized by Sudrajat et al. [82] through the combustion reaction method. They reported the substitutional as well as interstitial occupation of N in ZnO. They observed increased surface area and narrowing down of the bandgap as a result of N doping. This led to enhanced visible light activity of N-doped ZnO. Zinc oxynitride thin films were reported to be deposited by reactive high power magnetron sputtering of a pure Zn target in the presence of an $Ar/N_2/O_2$ gas mixture [83]. The N concentration in the films was found to be varying from 0% to 6.2% with a corresponding bandgap of 3.34–1.67 eV. The optimal N concentration was found to be 3.4 at.% for the highest visible light photocatalytic activity toward water splitting. The RF magnetron sputtered N-doped ZnO nanocrystalline thin films showed good sunlight photocatalytic degradation of 2-chlorophenol. Among other nonmetal dopants, C is also very popular for extending the photocatalytic activity of ZnO toward the visible region. Ab initio calculations have shown favorable formation energy for substitutional as well as interstitial occupation of C in ZnO. C is likely to substitute Zn as well as O. Moreover, the formation of CO/CO_2 species is favored at oxygen-rich conditions. The cationic substitutional C acts as a donor with the lowest formation energy whereas the defect complex $C_{Zn} + 2O_i$ acts as an acceptor with slightly higher formation energy [84]. Zhang et al. [85] synthesized large-scale C-doped ZnO nanostructures by a facile, one-pot morphology controlled technique through urea-assisted thermal decomposition of zinc acetate. The C incorporation resulted in a decrease of the optical bandgap, which led to the generation of the *e-h* pairs under visible light irradiation and the degradation of methylene blue. The C-doped ZnO nanorods were synthesized by the cost-effective precipitation method [86]. From the XPS analysis, it was suggested that the C is incorporated into the lattice by replacing Zn and is bonded to four O atoms. The photocatalytic activity under visible light was studied through the decomposition of p-aminobenzoic acid. The nanorods were found to be reusable and they retained good photodegradation efficiency with a rate constant of 0.028 min^{-1}. The degradation of orange-II dye was studied using C-doped ZnO nanostructures by [87]. They used vitamin C as the source of carbon. X-ray diffraction studies revealed a lattice expansion, suggesting anionic substitution of O^{-2} by C^{-4} even though the former has a larger ionic radius (260 pm) than the latter (140 pm). This is in contrast with the other reports where lattice expansion has been observed, suggesting the substitution of Zn^{+2} ions (ionic size: 74 pm) by C^{+4} ions (ionic size: 16 pm). S doping in ZnO has not been explored much and the results are debatable. A few studies have reported widening of the ZnO bandgap due to S doping because of Burstein-Moss shift, whereas a few other have reported a decrease in the bandgap. Zhang et al. [88] studied the optoelectronic properties of the S-doped ZnO system using DFT. For S substituting the O site, the

https://www.twirpx.org & http://chemistry-chemists.com

bandgap of S doped ZnO is found to be reduced due to the creation of additional levels above the VB arising out of the mixture of S 3*p* and O 2*p* states. The increase in the S concentration in the O sites has little effect on the bandgap. However, experimentally, S doping always results in the creation of a greater number of O and Zn vacancies in the lattice, leading to enhanced photocatalytic activity in the UV-visible region. Patil et al. [89] used a simple mechano-chemical method for the synthesis of S-doped ZnO powders by the thermal decomposition of bisthiourea zinc oxalate. The lattice expansion was observed with S doping. XPS studies confirmed the substitutional incorporation of S into the ZnO lattice. Solar photodegradation of resorcinol using S doped ZnO was found to be twice as great as that of undoped ZnO. The enhanced visible light photocatalytic activity was attributed to the increased number of O vacancies due to S doping. Poongodi et al. [90] prepared S-doped ZnO thin films by a combination of the sol-gel spin coating and hydrothermal methods. They observed a reduction in the optical bandgap due to S doping. The S-doped ZnO thin films were found to have enhanced photocatalytic activity compared to the undoped ones. They attributed the increased photocatalytic activity to the reactive oxygen species created by the S-induced defects which act as electron trapping centers, suppressing the *e-h* recombination. Chen et al. [75] studied the visible light photocatalytic behavior of N, S, and C codoped ZnO prepared by the coprecipitation method. Visible light photocatalysis was confirmed from the degradation of acid orange 7 and phenol.

2.2 Semiconductor heterojunction photocatalysts

One of the efficient approaches to inhibit the *e-h* pair recombination in semiconductor-based heterogeneous photocatalysis is to couple it to another semiconductor of different bandgap. A semiconductor coupled to another semiconductor with a different bandgap is termed as a heterojunction. If the band edges of these two semiconductors do not align with each other, then a band offset is developed at the heterojunction interface. The heterojunction interface gives rise to the "straddling" (type-I) or "staggered" (type-II) like band offset depending on the difference in the electron affinities of the two semiconductors (Fig. 3) [91]. If the CB and VB of one semiconductor (narrow bandgap) are lower and higher, respectively, than the other semiconductor (wider bandgap), then the band offset is referred to as type-I. In case of type-II band offset, both the CB and VB of one semiconductor is situated higher than the corresponding bands of the other semiconductor. In addition to this, there is another class of heterojunction interface where there is no overlap between the bandgaps of the two semiconductors and therefore is referred to as the broken gap (type-III) band offset. Out of these three different types of heterojunctions, the type-II interface is suitable for visible light photocatalysis and is widely engineered. In this case, the *e-h* pair is generated in the narrow bandgap semiconductor upon exposure to visible light. Due to the favorable staggered type band offset, the electron easily migrates to the CB of the wide bandgap semiconductor. This results in an effective charge separation.

https://www.twirpx.org & http://chemistry-chemists.com

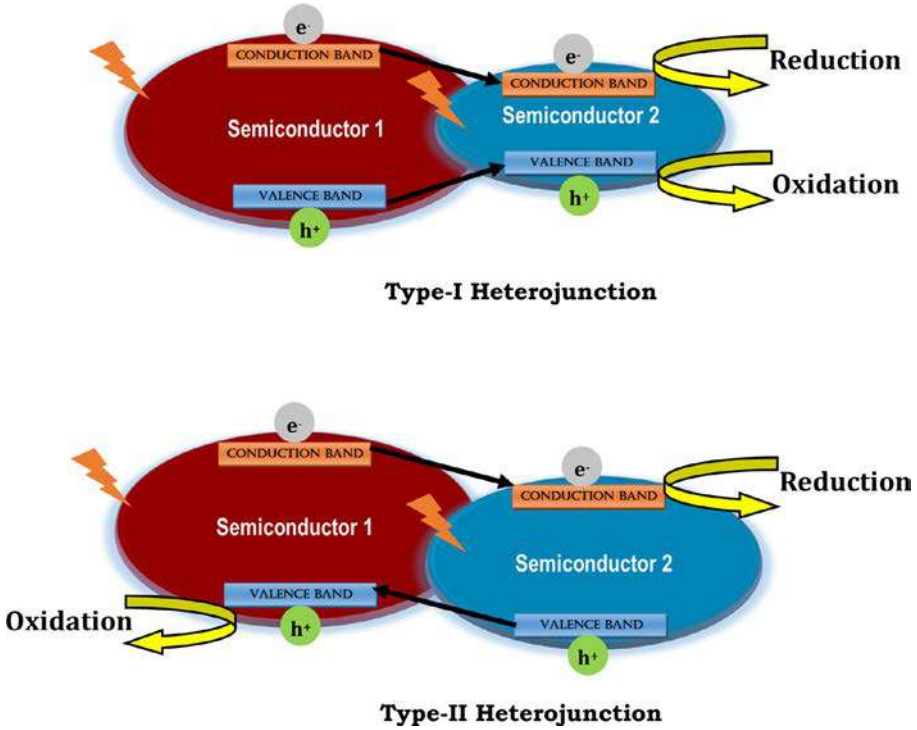

FIG. 3 Schematic illustration of the heterogeneous photocatalysis in type-I and type-II semiconductor heterojunctions.

Visible light active photocatalysts have been successfully engineered by the heterogeneous coupling of TiO_2 with Cu_2O, Fe_2O_3, and Ag_2O. Similarly, the ZnO/Fe_2O_3 and ZnO/Ag_2O heterojunction composites also exhibit good visible light photocatalytic activity. Wang et al. [12] have synthesized Cu_2O/TiO_2 nanocomposites through a simple solvothermal method. XRD results indicated the composite phase of tetragonal rutile TiO_2 and cubic Cu_2O. The composite was found to have hierarchical hollow microstructures with pretty rough surfaces. These nanocomposites were found to exhibit good visible light photodegradation of methylene blue. Nearly 100% decolorization of methylene blue was observed within 120 min of reaction time. The enhanced visible light activity is mainly attributed to the effective charge separation at the heterojunction interface as well as the increased surface area. Li et al. [92] reported the Cu_2O modified TiO_2 nanoparticles prepared by a facile ethanol reduction method followed by calcination. The *p-n* heterojunction between Cu_2O and TiO_2 was found to have better photocatalytic activity for H_2 evolution than that of pure P25. The enhanced visible light photocatalysis is due to the absorption of visible light in Cu_2O, effective charge separation at the interface, and plenty of reaction active sites on the surface of the photocatalyst. Similarly, the Fe_2O_3/TiO_2 nanocomposite heterostructures were reported to effectively degrade Cr(VI) under visible

https://www.twirpx.org & http://chemistry-chemists.com

light irradiation [93]. Nasirian et al. [94] synthesized Fe_2O_3/TiO_2 photocatalysts through a novel UV-assisted thermal method. These photocatalysts were evaluated for the degradation of textile dyes such as Congo red and methyl orange. They found that the calcination temperature of 300°C was optimum for which the degradation of these textile dyes is maximum. The synthesis of Ag_2O/TiO_2 heterojunction nanostructures by a simple precipitation method was reported by Duran-Alvarez et al. [95]. The photocatalytic activity was evaluated by the mineralization of iopromide in pure water under UV or visible light irradiation. The photocatalytic efficiency of the Ag_2O/TiO_2 composite was found to be outstanding compared to its pure counterparts.

The visible light activity of ZnO has also been successfully achieved by heterogeneous coupling with a narrow bandgap semiconductor such that type-II band offset is obtained at the junction interface. Rod-like composites of Fe_2O_3/ZnO were synthesized by a rapid thermal method using ferric nitrate, zinc nitrate, and sodium hydroxide as the reactants [96]. These nanostructured composites were used for the degradation of pentachlorophenol, which is a soil and water contaminant. Degradation was achieved under UV-visible irradiation because Fe_2O_3 was helpful in extending the optical absorption up to the visible region. The type-II band offset also is favorable for the inhibition of the recombination of photogenerated carriers. Liu et al. [97] synthesized Fe_2O_3/ZnO heterojunction nanotubes via photochemical deposition under UV light irradiation at room temperature. The nanosheets of Fe_2O_3/ZnO were reported to be prepared by a total reflux and hydrothermal method [98]. These nanosheets were found to be effective in the degradation of cefixime trihydrate under UV-visible irradiation. The degradation efficiency was found to be 99.1% within 127 min. Kadam et al. [99] reported a template-free synthesis of ZnO/Ag_2O nanocomposites as the effective visible light photocatalysts for the detoxification of methyl orange. The degradation efficiency of methyl orange over the ZnO/Ag_2O composites was found to be 22 times and 4 times more than that of the pure ZnO and Ag_2O, respectively. A detailed list of different visible light TMO-based photocatalysts engineered by heterogeneous coupling is provided in Table 3.

2.3 Modification by noble metal nanoparticles

Nanoparticles of noble metals (Au, Ag, Pt) can absorb strong visible light due to their localized surface plasmon resonance (LSPR). Plasmons are the collective excitation of the free charge carriers. The electromagnetic (EM) radiation having frequency less than the plasma frequency is reflected because the electric field of the radiation is screened by the electrons. Above this frequency, the EM radiation is transmitted because the electrons cannot respond fast enough to screen it. At the plasmon frequency, a resonance in the absorption occurs as the real part of the dielectric function goes to zero [13]. An intense electric field is generated at the surface of the metal nanoparticles when they are irradiated at the plasmon frequency. The plasmon frequency of a metal can be tuned by changing its shape, size, and the dielectric environment. For the noble metal nanoparticles, this

https://www.twirpx.org & http://chemistry-chemists.com

Table 3 Indicative list of visible light photocatalysts engineered by heterogeneous coupling.

Semiconductor I	Semiconductor II	Preparation method	Pollutant	**References**
TiO_2	g-C_3N_4	Calcination method	Rhodamine B	[100]
TiO_2	Bi_2O_3	Hydrothermal-Calcination method (TiO_2) and sol-gel method (Bi_2O_3)	Methylene blue	[101]
TiO_2	WO_3	Hydrothermal method (TiO_2) and sol-gel method (WO_3)	Methyl orange and 2, 4-dichlorophenol	[102]
ZnO	CuO	Wet chemical route (ZnO) and Thermal evaporation (CuO)	Methyl orange and Rhodamine B	[103]
ZnO	g-C_3N_4	Solution conversion method (ZnO) and heating of urea (g-C_3N_4)	4-chlorophenol	[104]
ZnO	Bi_2O_3	Hydrothermal method	Alizarin red	[105]
WO_3	TiO_2	Sol-gel method	Rhodamine B	[106]
MoO_3	TiO_2	Sol-gel method	Rhodamine B	[106]
Fe_2O_3	NiO	Hydrothermal method	Congo red	[107]
Fe_2O_3	Cu_2O	Wet chemical method	CO_2 reduction	[108]

frequency of resonance occurs in the visible or infrared region. The unique transfer of energy between the plasmonic metal nanoparticles and the conventional semiconductor photocatalysts like TiO_2 or ZnO results in the efficient utilization of solar energy for visible light photocatalysis (Fig. 4). The primary processes for the energy transfer are plasmon-induced hot electron injection and resonance energy transfer. Hot electrons are generated during the nonradiative relaxation of the collective oscillations at the plasmon frequency. This nonradiative relaxation is mainly through the *e-e* scattering. The hot electrons have enough energy to cross the Schottky barrier between the metal-semiconductor junction and get injected into the CB of the semiconductor. Quantum tunneling is another way for these hot electrons to enter the CB of the semiconductor if they cannot overcome the Schottky barrier. Another widely accepted mechanism is plasmon-induced resonance energy transfer. At the resonance frequency, the plasmons generate intense local electric fields near to the surface of the nanoparticles. These regions with intense electric fields are also referred to as "hot spots." In these hot spots, the *e-h* pair generation rate is 1000 times more than the incident EM radiation. Due to this local field, the photogeneration of charge carriers is enhanced considerably on the metal oxide surface. Ma et al. [109] discussed in detail the different probable mechanisms for the energy transfer between the plasmonic nanoparticles and the semiconductor. Different noble metal-loaded TMOs and their visible light photocatalytic features are listed in Table 4.

2.3.1 Au/TMO-based plasmonic photocatalysts

The Schottky barrier energy between the Au/TiO_2 is estimated to be ~1 eV from the Schottky-Mott theory. The energy of the hot electrons generated in Au typically ranges from 1 to 4 eV. Therefore, the hot electrons can easily be injected from the Au

https://www.twirpx.org & http://chemistry-chemists.com

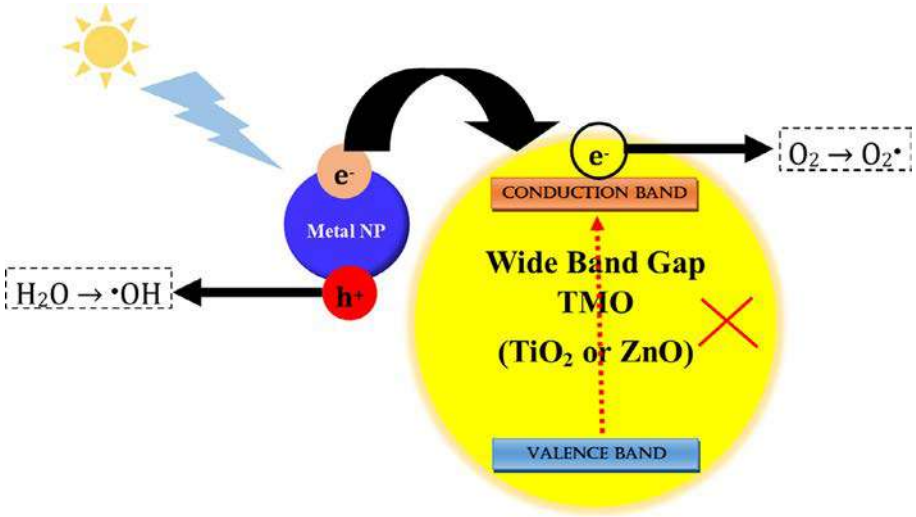

FIG. 4 Schematic illustration of the SPR-mediated visible light photocatalysis in TMOs.

Table 4 Noble metal loaded TMOs as visible light photocatalysts.

Host TMO	Noble metal	Preparation route	Pollutant	**References**
TiO_2	Au	Wet chemical route	Phenol	[110]
TiO_2	Au	Sputtering	Methylene blue	[111]
TiO_2	Ag	Sputtering	Methylene blue	[112]
TiO_2	Ag	Hydrothermal method	Rhodamine B	[113]
TiO_2	Pt	Electrospinning followed by photodeposition	Orange II	[114]
TiO_2	Pd	Photochemical deposition of Pd nanoparticles on TiO_2 nanorods	Rhodamine B	[115]
ZnO	Au	Photodeposition	Terephthalic acid	[116]
ZnO	Au	Wet chemical route	Rhodamine B	[117]
ZnO	Ag	Wet chemical route	Methane oxidation	[118]
ZnO	Ag	Wet chemical route	Methyl orange	[119]
ZnO	Pt	Flame spray pyrolysis	Methylene blue	[120]
ZnO	Pd	Wet chemical route	Methyl tert-butyl ether	[121]

nanoparticles to the CB of TiO_2 either by overcoming the Schottky barrier or by tunneling. Dozzi et al. [122] have studied the photocatalytic degradation of formic acid and azo dye acid red 1 by the Au-loaded TiO_2 under visible light irradiation. The Au-loaded samples exhibited the typical SPR peak at 550 nm and thereby induced visible light photocatalysis. The Au present on the TiO_2 surface facilitates the electron transfer to O_2 and the mineralization of formic acid. Commercial titania modified by the Au nanoparticles was investigated for its photocatalytic activity toward the degradation of acetic acid and 2-propanol

https://www.twirpx.org & http://chemistry-chemists.com

under visible light irradiation [123]. The LSPR absorption for the Au/TiO_2 structure was observed in the region 530–600 nm. The photocatalytic activity was found to be strongly dependent on the size and shape of the Au nanoparticle as well as the TiO_2 phase. The rutile phase loaded with Au nanoparticles of a wide range of sizes exhibited the highest activity. Chen et al. [124] modified the TiO_2 hollow nanoboxes by Au nanoparticles having different morphologies. The photocatalytic activity of these Au/TiO_2 modified nanostructures was evaluated through the degradation of Rhodamine B and NO under visible light illumination. The enhanced activity of Au/TiO_2 was attributed to the SPR effect of Au nanoparticles through the injection of hot electrons.

Au modified ZnO nanostructures were also investigated widely for their visible light photocatalytic activity. Au nanoparticles supported on ZnO nanowires were reported to have been fabricated through a simple wet chemical method by Yu et al. [125]. This Au/ZnO hybrid structure was evaluated for its visible light activity for the degradation of benzene. LSPR peaks for Au nanoparticles were observed between 500 and 600 nm. The degradation efficiency of the hybrid structure for benzene was found to be 35.8% under visible light irradiation. He et al. [126] reported Au/ZnO nanoparticles with enhanced visible light photocatalytic hydrogen production and degradation of Rhodamine B. They ascribed the improvement in visible light activity to the SPR-induced electron injection into the CB of the ZnO nanoparticles. Moreover, the Au nanoparticles act as the sink for the photogenerated electrons, which inhibits their recombination with the holes. Bora et al. [127] investigated the role of surface defects on the visible light-enabled plasmonic photocatalysis in Au-ZnO nanorods. The O vacancies present at the surface of the ZnO nanorods were found to reduce the plasmonic-assisted photocatalysis significantly.

2.3.2 Ag/TMO-based plasmonic photocatalysts

Ag nanoparticles are commonly used as plasmonic-assisted photocatalysts in TiO_2 and ZnO because of their strong localized surface plasmon resonance. Subrahmanyam et al. [128] sprinkled Ag nanoparticles on the surface of sol-gel spin coated TiO_2 thin films by magnetron sputtering. They checked the photocatalytic activity of Ag-loaded TiO_2 thin films by the degradation of Rhodamine B in the presence of UV as well as sunlight. The TiO_2 thin films sprinkled with Ag for 15 s through magnetron sputtering showed the highest photocatalytic activity under sunlight. The corresponding rate constant was found to be 2.45 times higher than that of pure TiO_2. Duan et al. [129] synthesized Ag-TiO_{2-x} nanocomposites via a photoreduction process followed by postannealing. The postannealing treatment was found to favor the formation of Schottky contact and O vacancies. The samples were found to have excellent visible light photocatalytic activity and good stability regarding the removal of NO. Singh et al. [130] reported nanocomposite thin films of Ag-TiO_2 with different Ag concentrations by the cosputtering of Ag and TiO_2 with 1.5 keV Ar atoms using the atom beam sputtering setup. The solar photocatalytic activity was tested for methylene blue. The LSPR-mediated visible light photocatalysis was found to be the maximum for Ag concentration of 5 at.%. The effects of plasmon excitation on

https://www.twirpx.org & http://chemistry-chemists.com

the photocatalytic activity of Ag/TiO_2 and Au/TiO_2 nanocomposites were investigated by Sellappan et al. [131]. They prepared these nanocomposites by magnetron sputtering followed by annealing. However, they could not observe any appreciable photocatalytic degradation of C_2H_4 and CH_3OH under visible light illumination. Photocatalytic activity was observed only under UV irradiation. They concluded that the plasmonic nanoparticle preparation method and the size and regime of irradiation must be carefully considered for LSPR-mediated hot electron injection from the metal nanoparticle to TiO_2.

The shape and the surface compositional effects of Ag in Ag/ZnO nanorods on their visible light photocatalytic activity were investigated by Lu et al. [132]. The nanorods were synthesized by photoreduction and hydrothermal methods. However, the LSPR effect was observed only in the samples grown by the hydrothermal method. The Ag nanoparticle-modified ZnO nanorods exhibited visible light photocatalytic activity toward methyl orange. But the same was not observed for Ag nanosheet-modified ZnO nanorods. The hierarchical ZnO nanostructure decorated with Ag nanoparticles was synthesized by Patil et al. [133] by a plant extract-mediated hydrothermal method. The photoresponse toward methylene blue was found to be enhanced significantly due to the LSPR effect of the Ag nanoparticles.

2.4 Dye sensitization

Dye sensitization provides a cost-effective approach toward the visible light photocatalytic activity of TMOs and can absorb a very wide range of the solar spectrum [8]. When a dye-sensitized metal oxide semiconductor is exposed to visible light, the dye absorbs the light and reaches an excited state. The excited state of the dye has a lower redox potential with respect to its ground state. If the redox potential is lower than the CBE of the metal oxide semiconductor, the electron gets transferred from the lowest unoccupied molecular orbital (LUMO) of the dye molecule to the CB of the *n*-type semiconductor and the dye itself becomes a cationic radical. This results in a greater number of CB electrons on the surface of the TMO semiconductor, giving rise to more number of active oxygen species which take part in the photocatalytic degradation process. Similarly, in the case of a *p*-type TMO semiconductor, the holes get injected into the VB if the highest occupied molecular orbital (HOMO) of the dye is sufficiently low. In the case of dye-sensitized photocatalysis, the semiconductor TMO only acts as a mediator to transfer the electrons or holes to the surface.

Youssef et al. [134] gave a good review for the use of dye-sensitized TiO_2 and ZnO nanoparticles for water purification. They found that dye sensitization by means of organic photosensitizers was a relevant alternative method to enhance photocatalytic efficiency and to extend the activity toward the visible region. The scientific literature is quite rich regarding the demonstration of visible light photocatalysis through the dye sensitization of TiO_2 and ZnO. Li et al. [135] reported the selective oxidation of alcohols to aldehydes or ketones in the presence of visible light with the help of alizarin red S dye anchored onto the TiO_2 surface. Alizarin red S-sensitized TiO_2 has also been reported for the selective aerobic

https://www.twirpx.org & http://chemistry-chemists.com

oxidation of amines to imines [136]. Similarly, alizarin red S dye with a concentration of 0.33 mol% on anatase TiO_2 surface was found to selectively improve the visible light photocatalytic aerobic oxidation of sulfides to sulfoxides. Lang et al. [137] found that the redox mediator TEMPO [(2, 2, 6, 6-tetramethyl-piperidin-1-yl)oxyl] ensured the stability of the anchored dye alizarin red S. Yang et al. [138] demonstrated that the dye-sensitized TiO_2-polyoxometalate system was effective for the visible light aerobic oxidation of alcohols. Photocatalytic removal of Cr (VI) from an aqueous solution using alizarin red S dye-sensitized ZnO under visible light irradiation was reported by Yang et al. [139]. The natural dye anthocyanin is found to effectively sensitize ZnO nanoparticles for the visible light photocatalytic degradation of *E. coli* bacteria and their organic contents [14]. Nanocomposites of polythiophene-sensitized ZnO nanoparticles were synthesized by an in-situ chemical oxidative polymerization method [140]. These photosensitized ZnO nanoparticles were studied for their photocatalytic activity through the degradation of methyl orange under visible light illumination. The photodegradation of methyl orange was found to be improved for higher percentages of polythiophene in ZnO.

3 Other TMOs for visible light photocatalysis

The visible light photocatalytic activities of some of the potential 4*d* and 5*d* TMOs such as Ta_2O_5, Nb_2O_5, and WO_3 modified with the approaches elucidated in section 2 are briefly discussed here.

Ta_2O_5 is an ultra-wide bandgap semiconductor ($E_g \sim 4$ eV) and intrinsically can absorb only UV light of the solar spectrum. But nitrogen doping has been used widely to shift the band edge of Ta_2O_5 toward the visible region. Murase et al. [141] synthesized N-doped Ta_2O_5 powders by annealing pure Ta_2O_5 under an NH_3 atmosphere. They evaluated their visible light photocatalytic activity toward the decomposition of isopropyl alcohol. N-doped Ta_2O_5 nanoflowers were reported by Shi et al. [142] for the efficient degradation of methylene blue under visible light. N-doped Ta_2O_5 samples were prepared by the nitridation reaction in NH_3 atmosphere and were tested for their visible light photocatalytic H_2 production [143]. The N doping introduced some oxygen vacancies in the lattice and induced bandgap narrowing. In addition, some of the O sites at the surface were occupied by N. The samples annealed at 650°C showed the highest H_2 evolution. For the rest of the samples, the activity was less because of the formation of the Ta_3N_5 secondary phase at the surface. Ismail et al. [144] synthesized S-doped Ta_2O_5 nanocomposites through the sol-gel reaction of tantalum chloride and thiourea. The gels were calcined at 700°C for 4 h to obtain mesoporous S-doped Ta_2O_5 nanocomposites. The 1.5 at.% S-doped samples exhibited excellent photocatalytic activity with 92% degradation of methylene blue. SPR-mediated visible light photocatalysis has also been reported for Au-loaded Ta_2O_5 obtained via a facile photodeposition method [145]. The Au-loaded samples exhibited enhanced visible light activity for the degradation of Rhodamine B dye. Parida et al. [146] fabricated NiO/Ta_2O_5 composites by the solid-state reaction method. They observed a red shift in the

https://www.twirpx.org & http://chemistry-chemists.com

absorption edge for the composites extended to the visible region. The composites photocatalyst prepared at the metal ratio (1:3) showed the highest result toward H_2 production under UV and visible light irradiation.

Nb_2O_5 is an *n*-type TMO and has been studied widely for its photocatalytic property because of its good chemical stability and nontoxicity. But its application is limited only to UV irradiation because of its wide bandgap ranging from 3.1 to 4 eV. In order to bring its bandgap to the visible region, Zn is a good candidate for cationic doping because of its similar ionic radius and electronegativity as that of Nb. Oliveira et al. [147] synthesized 0.1 and 0.2 mol% Zn-doped Nb_2O_5 by the oxidant peroxide method with crystallization under hydrothermal conditions. The 0.1 mol% Zn-doped samples were found to have a bandgap of 2.61 eV. The photocatalytic activities of the undoped and doped samples were evaluated by the degradation of Rhodamine B and caffeic acid under visible light. Both these pollutants were found to be degraded to ∼80% after three consecutive reuse cycles. A novel N-doped Nb_2O_5 nanobelt quasiarray has been prepared by the hydrothermal reaction followed by annealing in an NH_3 atmosphere on metal Nb foil [148]. The methylene blue was found to be completely degraded after 4 h by these samples in the presence of visible light. Nogueira et al. [149] fabricated an Nb_2O_5/CuO heterostructure by a solvothermal method. The weight ratio of 10% for CuO on Nb_2O_5 provided the best visible light photoreduction of Cr(IV) to Cr(III). The corresponding photoreduction efficiency was found to be 20 times higher than that of pure Nb_2O_5 under visible light irradiation. SPR-induced visible light photocatalysis for Pt-, Au-, and Cu-loaded mesoporous Nb_2O_5 was reported by Lin et al. [150]. The mesoporous Nb_2O_5 was prepared by an evaporation-induced self-assembly method on which the noble metals were loaded through photodeposition. The noble metal-loaded samples exhibited the characteristic SPR peaks in the visible region. But the samples were tested for photocatalytic H_2 production only under the UV light irradiation having a wavelength of 360 nm. The Pt-loaded Nb_2O_5 showed the highest photoactivity.

Even though the bandgap of WO_3 lies in the visible region (∼2.5–2.8 eV), pure WO_3 has much reduced visible light photocatalytic activity due to fast recombination of the charge carriers. The low photocatalytic activity is also due to the fact that the CB potential of WO_3 (+0.5 V vs. NHE) is more positive than the potential for single electron reduction of O_2 (−0.13 V vs. NHE). However, there are many reports where the Pt-loaded WO_3 shows very good photocatalytic activity. This is due to the promotion of a multielectron reduction of O_2 which results in the efficient consumption of CB electrons of WO_3 on the Pt nanoparticles [151]. Shiraishi et al. [151] carried out visible light photocatalytic degradation of cyclohexane with molecular oxygen using Pt-loaded WO_3 catalysts. They used H_2PtCl_6 as the Pt precursor, which was added to the WO_3 particles. Kim et al. [152] investigated the visible light photocatalytic activity of platinized WO_3 toward the degradation of aquatic pollutants. They confirmed the production of OH radicals on Pt/WO_3 in the presence of visible light by the fluorescence method as well as from a spin trap method. They also used chloroplatinic acid as the Pt source. These samples exhibited good photocatalytic degradation of dichloroacetate, 4-chlorophenol, tetramethylammonium, arsenite, and methylene blue acid orange 7 under visible light irradiation.

https://www.twirpx.org & http://chemistry-chemists.com

4 Unitary TMOs as visible light photocatalysts (MnO_2, Fe_2O_3, Cu_xO, WO_3)

This section is based on certain unitary narrow bandgap TMOs like MnO_2, Fe_2O_3, Cu_2O, and CuO, which are potential candidates to be used as visible light photocatalysts. The literature reviewed in this section is only indicative but not exhaustive.

With a narrow bandgap energy of 1–2 eV, MnO_2 is a potential visible light photocatalyst. Chiam et al. [153] gave a complete review of the significant findings related to MnO_2-based photocatalysts for the removal of organic pollutants. Unilamellar MnO_2 nanosheets were reported by Sakai et al. [154] with the generation of anodic photocurrent under visible light irradiation. They estimated the bandgap of these nanosheets to be 2.23 eV on the basis of photocurrent action spectrum. The nanosheet molecular thickness of ~0.5 nm was helpful in the efficient separation of *e*-*h* pairs, which is generally difficult for bulk MnO_2 due to strongly localized *d*-*d* transition. Baral et al. [155] studied the degradation of Rhodamine B dye using α-MnO_2 nanorods synthesized by a low-temperature, single-step precipitation route. They reported the complete decolorization of Rhodamine B in 10 min and its total mineralization in 25 min under visible light irradiation. The removal of methylene blue from water using the commercial γ-MnO_2 powders under visible light excitation was reported by Kuan et al. [156]. Chan et al. [157] fabricated β-MnO_2 nanotube coatings by sol-gel dip coating on flexible PET (polyethylene terephthalate) fibers. Their visible light photocatalytic activity toward Rhodamine B was investigated. The corresponding rate constant was found to be 1.23 h^{-1}. The photodegradation of Rose Bengal using commercial MnO_2 powder under visible light illumination was investigated by Mittal et al. [158].

α-Fe_2O_3 (hematite) is an *n*-type TMO with a bandgap of 2.1 eV and therefore is an ideal candidate for the absorption of visible light. It is highly cost-effective and is stable in most aqueous solutions having pH > 3. In spite of being a promising photoanode material for photoelectrochemical water splitting, the photocatalytic activity of α-Fe_2O_3 is limited by certain factors such as high recombination rate, low diffusion length of holes, and VB positioning. There are many attempts cited in the literature for lowering the recombination rate by forming suitable nanostructures. The morphology-based visible light photocatalysis exhibited by nanostructured materials is discussed in more detail in Chapter 14. Mishra et al. [159] gave a complete review of various approaches adopted in the literature to enhance the visible light activity of α-Fe_2O_3. Cauliflower-like α-Fe_2O_3 was synthesized by a biphasic toluene-water interfacial reaction route [160]. This unique hierarchical microstructure was found to exhibit enhanced visible light photocatalytic activity toward the degradation of Rhodamine B in the presence of H_2O_2 compared to commercial α-Fe_2O_3 powders. Yang et al. [161] synthesized α-Fe_2O_3 nanoparticles through a facile additive free hydrothermal method. They evaluated its photocatalytic activity through the degradation of Rhodamine B under visible light irradiation. They were able to degrade the Rhodamine B dye completely within a time span of 180 min. Katz et al. [162] envisioned α-Fe_2O_3 as the future candidate for the photochemical water splitting in the presence of sunlight and "rust."

https://www.twirpx.org & http://chemistry-chemists.com

Cu_2O and CuO are *p*-type semiconductors with their bandgap lying in the visible region of the EM spectrum. Because of its unique optoelectronic properties, copper oxide (Cu_2O as well as CuO) is a promising material with applications in the field of solar energy conversion, electrode for Li ion batteries, and also in photocatalytic degradation of organic pollutants under visible light. Xu et al. [163] performed a shape evolution and size controllable synthesis of Cu_2O octahedral nanostructures, and studied their photocatalytic response toward methyl orange in the presence of visible light. The octahedral Cu_2O particles were found to have improved adsorption and photodegradation ability compared to the cubic Cu_2O particles. The shape effects of Cu_2O polyhedral microcrystals on the photocatalytic degradation of methyl orange were also investigated by Zhang et al. [164]. Vaidehi et al. [165] synthesized CuO nanoparticles by a green synthesis method. These spherical nanoparticles exhibited good photocatalytic degradation of crystal violet dye in the presence of visible light. The degradation efficiency was found to be more than 97%. The CuO nanoparticles synthesized by the electrochemical method were investigated for their photocatalytic activity through the degradation of methylene blue, Congo red, and methyl red in the presence of sunlight [166]. These nanoparticles showed the highest photocatalytic efficiency of 93% for the degradation of methylene blue. The rate constants were found to be $\sim$0.02 min^{-1}. Graphene-like CuO nanofilms were grown by Lu et al. [167] through annealing of $Cu(OH)_2$ prepared by the anodic oxidation of Cu foam. These nanofilm photocatalysts were found to exhibit better decoloration of methylene blue dyes than the commercial CuO powders in the presence of visible light.

WO_3 is a 5*d* TMO which is an ideal candidate for the intrinsically driven visible light photocatalysis owing to its tunable stoichiometry, structure, and bandgap. It can absorb light up to 480 nm with several other advantages such as low cost, environmental friendliness, and stability in acidic and oxidative conditions. However, bare WO_3 exhibits comparatively very low photocatalytic efficiency due to the fast recombination rate of the photogenerated *e-h* pairs. Zhao et al. [168] reported the synthesis of WO_3 octahedra by the chemical etching of WO_3 nanoparticles. These WO_3 octahedra were found to exhibit good visible light activity toward the reducibility of Ag^+ ions from $AgNO_3$ solution. The amounts of Ag deposited on the WO_3 octahedra were found to be 11 and 74 times more than that on commercial WO_3 and Degussa 25, respectively. Ultrathin WO_3 nanowires with a diameter of 1.1 nm were fabricated through a simple oleylamine assisted nonhydrolytic process [169]. These ultrathin nanowires were found to exhibit high photocatalytic activity toward the degradation of Rhodamine B under visible light. This was attributed to their enhanced visible light absorption and the presence of oxygen vacancies. Dong et al. [170] gave a detailed review about the relationship between the morphology control and photocatalytic activity of WO_3.

5 Conclusion

This chapter provided a basic review of TMO-based visible light photocatalysts for the degradation of environmental organic pollutants. Different methods such as metal doping, nonmetal doping, heterogeneous coupling, noble metal loading, and dye

https://www.twirpx.org & http://chemistry-chemists.com

photosensitization to extend the activity of conventional photocatalysts like TiO_2 and ZnO toward the visible spectrum were discussed. The detailed mechanism for each approach was explained briefly. Even though the information provided herein is not exhaustive, it provides a bird's-eye view of these approaches.

The transition metal doping suitably shifts the absorption edge toward the visible region and also inhibits the *e-h* pair recombination by acting as electron traps. However, the metal doping requires sophisticated and expensive setups like sputtering or ion-implantation. Moreover, the thermal instability of the metal-doped systems also degrades photocatalytic efficiency. On the other hand, nonmetal doping introduces mid-gap states and thus lowers the bandgap into the visible regime. However, nonmetal doping into TMOs often results in the creation of oxygen vacancies which can act as recombination centers for the photogenerated charge carriers. For metal as well as nonmetal doping, the impurity/vacancies creates recombination centers which deteriorates the photocatalytic activity. Even though heterogeneous coupling with another semiconductor is an efficient approach for the creation and effective separation of charge carriers, it is limited only to a particular set of TMOs with proper type-II band alignment. The major advantage of noble metal-loaded TMOs is the effective *e-h* pair separation at the metal-semiconductor interface. Moreover, the absorption of visible light is facilitated through SPR exhibited by the metal nanoparticles. However, one major disadvantage of this approach is that it is not cost-effective due to the requirement of expensive noble metals like Au or Ag. Furthermore, Au nanoparticles have a tendency to agglomerate over time whereas Ag nanoparticles are prone to form Ag_2O. The dye-sensitized TMOs cover the entire solar spectrum and therefore they utilize the sunlight effectively. However, the stability of these sensitized TMOs is highly debatable. Finally, the visible light photocatalytic activity shown by a few intrinsically driven TMO-based photocatalysts was discussed.

References

[1] Kardona H-JQM, Fulde P, Klitzing K. Springer Series in Solid-State Sciences. Springer; 2004.

[2] Lany S. Semiconducting transition metal oxides. J Phys Condens Matter 2015;27. https://doi.org/10.1088/0953-8984/27/28/283203.

[3] Kung HH. Transition Metal Oxides. Amsterdam: Elsevier; 1989.

[4] Meher SR, Balakrishnan L. Sol-gel derived nanocrystalline TiO2 thin films: a promising candidate for self-cleaning smart window applications. Mater Sci Semicond Process 2014;26:251–8. https://doi.org/10.1016/j.mssp.2014.05.006.

[5] Søgaard EG. Chemistry of Advanced Environmental Purification Processes of Water: Fundamentals and Applications. Denmark: Elsevier Inc.; 2014. https://doi.org/10.1016/C2009-0-16598-4.

[6] Dong S, Feng J, Fan M, Pi Y, Hu L, Han X, et al. Recent developments in heterogeneous photocatalytic water treatment using visible light-responsive photocatalysts: A review. RSC Adv 2015;5:14610–30. https://doi.org/10.1039/c4ra13734e.

[7] Moniz SJA, Shevlin SA, Martin DJ, Guo ZX, Tang J. Visible-light driven heterojunction photocatalysts for water splitting-a critical review. Energ Environ Sci 2015;8:731–59. https://doi.org/10.1039/c4ee03271c.

[8] Medynsky AZ. Metal Oxide Based Photocatalysis. Elsevier; 2018.

https://www.twirpx.org & http://chemistry-chemists.com

[9] Qi K, Cheng B, Yu J, Ho W. Review on the improvement of the photocatalytic and antibacterial activities of ZnO. J Alloys Compd 2017;727:792–820. https://doi.org/10.1016/j.jallcom.2017.08.142.

[10] Bora LV, Mewada RK. Visible/solar light active photocatalysts for organic effluent treatment: fundamentals, mechanisms and parametric review. Renew Sustain Energy Rev 2017;76:1393–421. https://doi.org/10.1016/j.rser.2017.01.130.

[11] Siriwong C, Wetchakun N, Inceesungvorn B, Channei D, Samerjai T, Phanichphant S. Doped-metal oxide nanoparticles for use as photocatalysts. Prog Cryst Growth Charact Mater 2012;58:145–63. https://doi.org/10.1016/j.pcrysgrow.2012.02.004.

[12] Wang Y, Tao J, Wang X, Wang Z, Zhang M, He G, et al. A unique Cu2O/TiO2 nanocomposite with enhanced photocatalytic performance under visible light irradiation. Ceram Int 2017;43:4866–72. https://doi.org/10.1016/j.ceramint.2016.12.130.

[13] Hou W, Cronin SB. A review of surface plasmon resonance-enhanced photocatalysis. Adv Funct Mater 2013;23:1612–9. https://doi.org/10.1002/adfm.201202148.

[14] Zyoud A, Dwikat M, Al-Shakhshir S, Ateeq S, Shteiwi J, Zu'bi A, et al. Natural dye-sensitized ZnO nano-particles as photo-catalysts in complete degradation of E coli bacteria and their organic content. J Photochem Photobiol, A 2016;328:207–16. https://doi.org/10.1016/j.jphotochem.2016.05.020.

[15] Khaki MRD, Shafeeyan MS, Raman AAA, Daud WMAW. Application of doped photocatalysts for organic pollutant degradation—a review. J Environ Manage 2017;198:78–94. https://doi.org/10.1016/j.jenvman.2017.04.099.

[16] Wang T, Shen D, Xu T, Jiang R. Photocatalytic degradation properties of V-doped TiO2 to automobile exhaust. Sci Total Environ 2017;586:347–54. https://doi.org/10.1016/j.scitotenv.2017.02.021.

[17] Kamble R, Sabale S, Chikode P, Puri V, Mahajan S. Structural and photocatalytic studies of hydrothermally synthesized Mn2+-TiO2 nanoparticles under UV and visible light irradiation. Mater Res Express 2016;3. https://doi.org/10.1088/2053-1591/3/11/115005.

[18] Peng YH, Huang GF, Huang WQ. Visible-light absorption and photocatalytic activity of Cr-doped TiO 2 nanocrystal films. Adv Powder Technol 2012;23:8–12. https://doi.org/10.1016/j.apt.2010.11.006.

[19] Moradi H, Eshaghi A, Hosseini SR, Ghani K. Fabrication of Fe-doped TiO2 nanoparticles and investigation of photocatalytic decolorization of reactive red 198 under visible light irradiation. Ultrason Sonochem 2016;32:314–9. https://doi.org/10.1016/j.ultsonch.2016.03.025.

[20] Wang T, Meng X, Liu G, Chang K, Li P, Kang Q, et al. In situ synthesis of ordered mesoporous Co-doped TiO2 and its enhanced photocatalytic activity and selectivity for the reduction of CO2. J Mater Chem A 2015;3:9491–501. https://doi.org/10.1039/c4ta05892e.

[21] Blanco-Vega MP, Guzmán-Mar JL, Villanueva-Rodríguez M, Maya-Treviño L, Garza-Tovar LL, Hernández-Ramírez A, et al. Photocatalytic elimination of bisphenol A under visible light using Ni-doped TiO2 synthesized by microwave assisted sol-gel method. Mater Sci Semicond Process 2017;71:275–82. https://doi.org/10.1016/j.mssp.2017.08.013.

[22] Karunakaran C, Abiramasundari G, Gomathisankar P, Manikandan G, Anandi V. Cu-doped TiO2 nanoparticles for photocatalytic disinfection of bacteria under visible light. J Colloid Interface Sci 2010;352:68–74. https://doi.org/10.1016/j.jcis.2010.08.012.

[23] Nair RG, Mazumdar S, Modak B, Bapat R, Ayyub P, Bhattacharyya K. The role of surface O-vacancies in the photocatalytic oxidation of Methylene Blue by Zn-doped TiO2: a mechanistic approach. J Photochem Photobiol A Chem 2017;345:36–53. https://doi.org/10.1016/j.jphotochem.2017.05.016.

[24] Šutka A, Käämbre T, Pärna R, Juhnevica I, Maiorov M, Joost U, et al. Co doped ZnO nanowires as visible light photocatalysts. Solid State Sci 2016;56:54–62. https://doi.org/10.1016/j.solidstatesciences.2016.04.008.

https://www.twirpx.org & http://chemistry-chemists.com

[25] Vaiano V, Iervolino G, Rizzo L. Cu-doped ZnO as efficient photocatalyst for the oxidation of arsenite to arsenate under visible light. Appl Catal Environ 2018;238:471–9. https://doi.org/10.1016/j.apcatb.2018.07.026.

[26] Yin Q, Qiao R, Li Z, Zhang XL, Zhu L. Hierarchical nanostructures of nickel-doped zinc oxide: morphology controlled synthesis and enhanced visible-light photocatalytic activity. J Alloys Compd 2015;618:318–25. https://doi.org/10.1016/j.jallcom.2014.08.087.

[27] Bousslama W, Elhouichet H, Férid M. Enhanced photocatalytic activity of Fe doped ZnO nanocrystals under sunlight irradiation. Optik 2017;134:88–98. https://doi.org/10.1016/j.ijleo.2017.01.025.

[28] Cao Z, Qin M, Gu Y, Jia B, Chen P, Qu X. Synthesis and characterization of Sn-doped hematite as visible light photocatalyst. Mater Res Bull 2016;77:41–7. https://doi.org/10.1016/j.materresbull.2016.01.004.

[29] Satheesh R, Vignesh K, Suganthi A, Rajarajan M. Visible light responsive photocatalytic applications of transition metal (M = Cu, Ni and Co) doped α-Fe2O3 nanoparticles. J Environ Chem Eng 2014;2:1956–68. https://doi.org/10.1016/j.jece.2014.08.016.

[30] Zhenghua X, Jianzhang L, Junbo Z, Wei H, Jun Z, Shengtian H, et al. Enhanced photocatalytic decolorization of methyl orange by gallium-doped α-Fe2O3. Mater Sci Semicond Process 2014;104–9. https://doi.org/10.1016/j.mssp.2014.03.028.

[31] Sankar S, Sharma SK, An N, Lee H, Kim DY, Im YB, et al. Photocatalytic properties of Mn-doped NiO spherical nanoparticles synthesized from sol-gel method. Optik 2016;127:10727–34. https://doi.org/10.1016/j.ijleo.2016.08.126.

[32] Smirniotis PG, Boningari T, Damma D, Inturi SNR. Single-step rapid aerosol synthesis of N-doped TiO2 for enhanced visible light photocatalytic activity. Cat Com 2018;113:1–5. https://doi.org/10.1016/j.catcom.2018.04.019.

[33] Bento RT, Correa OV, Pillis MF. Photocatalytic activity of undoped and sulfur-doped TiO2 films grown by MOCVD for water treatment under visible light. J Eur Ceram Soc 2019;39:3498–504. https://doi.org/10.1016/j.jeurceramsoc.2019.02.046.

[34] Ratova M, Klaysri R, Praserthdam P, Kelly PJ. Visible light active photocatalytic C-doped titanium dioxide films deposited via reactive pulsed DC magnetron co-sputtering: properties and photocatalytic activity. Vacuum 2018;149:214–24. https://doi.org/10.1016/j.vacuum.2018.01.003.

[35] Liu D, Tian R, Wang J, Nie E, Piao X, Li X, et al. Photoelectrocatalytic degradation of methylene blue using F doped TiO2 photoelectrode under visible light irradiation. Chemosphere 2017;185:574–81. https://doi.org/10.1016/j.chemosphere.2017.07.071.

[36] Iwase M, Yamada K, Kurisaki T, Prieto-Mahaney OO, Ohtani B, Wakita H. Visible-light photocatalysis with phosphorus-doped titanium(IV) oxide particles prepared using a phosphide compound. Appl Catal Environ 2013;132–133:39–44. https://doi.org/10.1016/j.apcatb.2012.11.014.

[37] Wang M, Ren F, Zhou J, Cai G, Cai L, Hu Y, et al. N doping to ZnO nanorods for photoelectrochemical water splitting under visible light: engineered impurity distribution and terraced band structure. Sci Rep 2015;5. https://doi.org/10.1038/srep12925.

[38] Alshammari AS, Chi L, Chen X, Bagabas A, Kramer D, Alromaeh A, et al. Visible-light photocatalysis on C-doped ZnO derived from polymer-assisted pyrolysis. RSC Adv 2015;5:27690–8. https://doi.org/10.1039/c4ra17227b.

[39] Liu Y, Li Y, Li W, Han S, Liu C. Photoelectrochemical properties and photocatalytic activity of nitrogen-doped nanoporous WO 3 photoelectrodes under visible light. Appl Surf Sci 2012;258:5038–45. https://doi.org/10.1016/j.apsusc.2012.01.080.

[40] Sun Y, Murphy CJ, Reyes-Gil KR, Reyes-Garcia EA, Thornton JM, Morris NA, et al. Photoelectrochemical and structural characterization of carbon-doped WO3 films prepared via spray pyrolysis. Int J Hydrogen Energy 2009;34:8476–84. https://doi.org/10.1016/j.ijhydene.2009.08.015.

https://www.twirpx.org & http://chemistry-chemists.com

[41] Guo L, Chen F, Fan X, Cai W, Zhang J. S-doped α-Fe2O3 as a highly active heterogeneous Fenton-like catalyst towards the degradation of acid orange 7 and phenol. Appl Catal Environ 2010;96:162–8. https://doi.org/10.1016/j.apcatb.2010.02.015.

[42] Suzuki TM, Nakamura T, Saeki S, Matsuoka Y, Tanaka H, Yano K, et al. Visible light-sensitive mesoporous N-doped Ta2O5 spheres: synthesis and photocatalytic activity for hydrogen evolution and CO2 reduction. J Mater Chem 2012;22:24584–90. https://doi.org/10.1039/c2jm33980c.

[43] Wu JCS, Lin HM. Photo reduction of CO2 to methanol via TiO2 photocatalyst. Int J Photogr 2005;7:115–9. https://doi.org/10.1155/S1110662X05000176.

[44] Umebayashi T, Yamaki T, Itoh H, Asai K. Analysis of electronic structures of 3d transition metal-doped TiO2 based on band calculations. J Phys Chem Solid 2002;63:1909–20. https://doi.org/10.1016/S0022-3697(02)00177-4.

[45] Inturi SNR, Boningari T, Suidan M, Smirniotis PG. Visible-light-induced photodegradation of gas phase acetonitrile using aerosol-made transition metal (V, Cr, Fe, Co, Mn, Mo, Ni, Cu, Y, Ce, and Zr) doped TiO2. Appl Catal Environ 2014;144:333–42. https://doi.org/10.1016/j.apcatb.2013.07.032.

[46] Bhatia V, Dhir A. Transition metal doped TiO2 mediated photocatalytic degradation of anti-inflammatory drug under solar irradiations. J Environ Chem Eng 2016;4:1267–73. https://doi.org/10.1016/j.jece.2016.01.032.

[47] Sood S, Umar A, Mehta SK, Kansal SK. Highly effective Fe-doped TiO2 nanoparticles photocatalysts for visible-light driven photocatalytic degradation of toxic organic compounds. J Colloid Interface Sci 2015;450:213–23. https://doi.org/10.1016/j.jcis.2015.03.018.

[48] Barmeh A, Nilforoushan MR, Otroj S. Wetting and photocatalytic properties of Ni-doped TiO2 coating on glazed ceramic tiles under visible light. Thin Solid Films 2018;666:137–42. https://doi.org/10.1016/j.tsf.2018.09.007.

[49] Li J, Ren D, Wu Z, Xu J, Bao Y, He S, et al. Flame retardant and visible light-activated Fe-doped TiO2 thin films anchored to wood surfaces for the photocatalytic degradation of gaseous formaldehyde. J Colloid Interface Sci 2018;530:78–87. https://doi.org/10.1016/j.jcis.2018.06.066.

[50] Bensouici F, Bououdina M, Dakhel AA, Tala-Ighil R, Tounane M, Iratni A, et al. Optical, structural and photocatalysis properties of Cu-doped TiO 2 thin films. Appl Surf Sci 2017;395:110–6. https://doi.org/10.1016/j.apsusc.2016.07.034.

[51] Yamashita H, Li H. Nanostructured Photocatalysts; 2016. https://doi.org/10.1007/978-3-319-26079-2.

[52] Qin LZ, Liang H, Liao B, Liu AD, Wu XY, Sun J. Photocatalytic performance of Fe-, Ni-, or Cu-ion implanted TiO2 films under UV light, visible light and sunlight irradiation. Nucl Instrum Methods Phys Res, Sect B 2013;307:385–90. https://doi.org/10.1016/j.nimb.2012.12.082.

[53] Lam RCW, Leung MKH, Leung DYC, Vrijmoed LLP, Yam WC, Ng SP. Visible-light-assisted photocatalytic degradation of gaseous formaldehyde by parallel-plate reactor coated with Cr ion-implanted TiO2 thin film. Sol Energy Mater Sol Cells 2007;91:54–61. https://doi.org/10.1016/j.solmat.2006.07.004.

[54] Zhou J, Takeuchi M, Ray AK, Anpo M, Zhao XS. Enhancement of photocatalytic activity of P25 TiO2 by vanadium-ion implantation under visible light irradiation. J Colloid Interface Sci 2007;311:497–501. https://doi.org/10.1016/j.jcis.2007.03.007.

[55] Takeuchi M, Yamashita H, Matsuoka M, Anpo M, Hirao T, Itoh N, et al. Photocatalytic decomposition of NO under visible light irradiation on the Cr-ion-implanted TiO2 thin film photocatalyst. Catal Lett 2000;67:135–7.

[56] Zhou J, Takeuchi M, Zhao XS, Ray AK, Anpo M. Photocatalytic decomposition of formic acid under visible light irradiation over V-ion-implanted TiO2 thin film photocatalysts prepared on quartz substrate by ionized cluster beam (ICB) deposition method. Catal Lett 2006;106:67–70. https://doi.org/10.1007/s10562-005-9192-5.

https://www.twirpx.org & http://chemistry-chemists.com

[57] Impellizzeri G, Scuderi V, Romano L, Sberna PM, Arcadipane E, Sanz R, et al. Fe ion-implanted TiO2 thin film for efficient visible-light photocatalysis. J Appl Phys 2014;116. https://doi.org/10.1063/1.4901208.

[58] Ansari SA, Khan MM, Ansari MO, Cho MH. Nitrogen-doped titanium dioxide (N-doped TiO2) for visible light photocatalysis. New J Chem 2016;40:3000–9. https://doi.org/10.1039/c5nj03478g.

[59] Asahi R, Morikawa T, Ohwaki T, Aoki K, Taga Y. Visible-light photocatalysis in nitrogen-doped titanium oxides. Science 2001;293:269–71. https://doi.org/10.1126/science.1061051.

[60] Zhang J, Wu Y, Xing M, Leghari SAK, Sajjad S. Development of modified N doped TiO2 photocatalyst with metals, nonmetals and metal oxides. Energ Environ Sci 2010;3:715–26. https://doi.org/10.1039/b927575d.

[61] Ren W, Ai Z, Jia F, Zhang L, Fan X, Zou Z. Low temperature preparation and visible light photocatalytic activity of mesoporous carbon-doped crystalline TiO2. Appl Catal Environ 2007;69:138–44. https://doi.org/10.1016/j.apcatb.2006.06.015.

[62] Kim MS, Liu G, Nam WK, Kim BW. Preparation of porous carbon-doped TiO2 film by sol-gel method and its application for the removal of gaseous toluene in the optical fiber reactor. J Ind Eng Chem 2011;17:223–8. https://doi.org/10.1016/j.jiec.2011.02.010.

[63] Zhang Y, Zhao Z, Chen J, Cheng L, Chang J, Sheng W, et al. C-doped hollow TiO2 spheres: in situ synthesis, controlled shell thickness, and superior visible-light photocatalytic activity. Appl Catal Environ 2015;165:715–22. https://doi.org/10.1016/j.apcatb.2014.10.063.

[64] Lu J, Wang Y, Huang J, Fei J, Cao L, Li C. In situ synthesis of mesoporous C-doped TiO2 single crystal with oxygen vacancy and its enhanced sunlight photocatalytic properties. Dyes Pigments 2017;144:203–11. https://doi.org/10.1016/j.dyepig.2017.05.033.

[65] Zhang L, Tse MS, Tan OK, Wang YX, Han M. Facile fabrication and characterization of multi-type carbon-doped TiO 2 for visible light-activated photocatalytic mineralization of gaseous toluene. J Mater Chem A 2013;1:4497–507. https://doi.org/10.1039/c3ta01366a.

[66] Lee S, Lee Y, Kim DH, Moon JH. Carbon-deposited TiO2 3D inverse opal photocatalysts: visible-light photocatalytic activity and enhanced activity in a viscous solution. ACS Appl Mater Interfaces 2013;5:12526–32. https://doi.org/10.1021/am403820e.

[67] Yang K, Dai Y, Huang B. Understanding photocatalytic activity of S- And P-doped TiO2 under visible light from first-principles. J Phys Chem C 2007;111:18985–94. https://doi.org/10.1021/jp0756350.

[68] Gul SR, Khan M, Wu B, Yi Z. Combined experimental and theoretical study of visible light active P doped TiO2 photocatalyst. Mater Res Express 2017;4. https://doi.org/10.1088/2053-1591/aa75e8.

[69] Mendiola-Alvarez SY, Hernández-Ramírez MA, Guzmán-Mar JL, Garza-Tovar LL, Hinojosa-Reyes L. Phosphorous-doped TiO 2 nanoparticles: synthesis, characterization, and visible photocatalytic evaluation on sulfamethazine degradation. Environ Sci Pollut Res 2019;26:4180–91. https://doi.org/10.1007/s11356-018-2314-6.

[70] Umebayashi T, Yamaki T, Itoh H, Asai K. Band gap narrowing of titanium dioxide by sulfur doping. Appl Phys Lett 2002;81:454–6. https://doi.org/10.1063/1.1493647.

[71] Umebayashi T, Yamaki T, Tanaka S, Asai K. Visible light-induced degradation of methylene blue on S-doped TiO2. Chem Lett 2003;32:330–1. https://doi.org/10.1246/cl.2003.330.

[72] Ohno T, Mitsui T, Matsumura M. Photocatalytic activity of S-doped TiO2 photocatalyst under visible light. Chem Lett 2003;32:364–5. https://doi.org/10.1246/cl.2003.364.

[73] Lin YH, Hsueh HT, Chang CW, Chu H. The visible light-driven photodegradation of dimethyl sulfide on S-doped TiO2: characterization, kinetics, and reaction pathways. Appl Catal Environ 2016;199:1–10. https://doi.org/10.1016/j.apcatb.2016.06.024.

https://www.twirpx.org & http://chemistry-chemists.com

[74] Boningari T, Inturi SNR, Suidan M, Smirniotis PG. Novel one-step synthesis of sulfur doped-TiO2 by flame spray pyrolysis for visible light photocatalytic degradation of acetaldehyde. Chem Eng J 2018;339:249–58. https://doi.org/10.1016/j.cej.2018.01.063.

[75] Chen LC, Tu YJ, Wang YS, Kan RS, Huang CM. Characterization and photoreactivity of N-, S-, and C-doped ZnO under UV and visible light illumination. J Photochem Photobiol A Chem 2008;199:170–8. https://doi.org/10.1016/j.jphotochem.2008.05.022.

[76] Samadi M, Zirak M, Naseri A, Khorashadizade E, Moshfegh AZ. Recent progress on doped ZnO nanostructures for visible-light photocatalysis. Thin Solid Films 2016;605:2–19. https://doi.org/10.1016/j.tsf.2015.12.064.

[77] Qi K, Xing X, Zada A, Li M, Wang Q, Liu SY, et al. Transition metal doped ZnO nanoparticles with enhanced photocatalytic and antibacterial performances: experimental and DFT studies. Ceram Int 2020;46:1494–502. https://doi.org/10.1016/j.ceramint.2019.09.116.

[78] Abdel-Wahab MS, Jilani A, Yahia IS, Al-Ghamdi AA. Enhanced the photocatalytic activity of Ni-doped ZnO thin films: morphological, optical and XPS analysis. Superlattice Microst 2016;94:108–18. https://doi.org/10.1016/j.spmi.2016.03.043.

[79] Altintas Yildirim O, Arslan H, Sönmezoğlu S. Facile synthesis of cobalt-doped zinc oxide thin films for highly efficient visible light photocatalysts. Appl Surf Sci 2016;390:111–21. https://doi.org/10.1016/j.apsusc.2016.08.069.

[80] Saleh R, Djaja NF. Transition-metal-doped ZnO nanoparticles: synthesis, characterization and photocatalytic activity under UV light. Spectrochim Acta A Mol Biomol Spectrosc 2014;130:581–90. https://doi.org/10.1016/j.saa.2014.03.089.

[81] Wu C. Facile one-step synthesis of N-doped ZnO micropolyhedrons forefficient photocatalytic degradation of formaldehyde undervisible-light irradiation. Appl Surf Sci 2014;319:237–43. https://doi.org/10.1016/j.apsusc.2014.04.217.

[82] Sudrajat H, Babel S. A novel visible light active N-doped ZnO for photocatalytic degradation of dyes. J Water Proc Eng 2017;16:309–18. https://doi.org/10.1016/j.jwpe.2016.11.006.

[83] Tiron V, Velicu IL, Stanescu D, Magnan H, Sirghi L. High visible light photocatalytic activity of nitrogen-doped ZnO thin films deposited by HiPIMS. Surf Coat Technol 2017;324:594–600. https://doi.org/10.1016/j.surfcoat.2016.11.087.

[84] Tan ST, Sun XW, Yu ZG, Wu P, Lo GQ, Kwong DL. p-type conduction in unintentional carbon-doped ZnO thin films. Appl Phys Lett 2007;91. https://doi.org/10.1063/1.2768917.

[85] Zhang X, Qin J, Hao R, Wang L, Shen X, Yu R, et al. Carbon-doped ZnO nanostructures: facile synthesis and visible light photocatalytic applications. J Phys Chem C 2015;119:20544–54. https://doi.org/10.1021/acs.jpcc.5b07116.

[86] Perillo PM, Atia MN. C-doped ZnO nanorods for photocatalytic degradation of p-aminobenzoic acid under sunlight. Nano-Struct Nano-Obj 2017;10:125–30. https://doi.org/10.1016/j.nanoso.2017.04.001.

[87] Cho S, Jang JW, Lee JS, Lee KH. Carbon-doped ZnO nanostructures synthesized using vitamin C for visible light photocatalysis. CrstEngComm 2010;12:3929–35. https://doi.org/10.1039/c0ce00063a.

[88] Zhang H, Tao Z, Xu W, Lu S, Yuan F. First-principles study of dopants and defects in S-doped ZnO and its effect on photocatalytic activity. Comput Mater Sci 2012;58:119–24. https://doi.org/10.1016/j.commatsci.2012.01.016.

[89] Patil AB, Patil KR, Pardeshi SK. Ecofriendly synthesis and solar photocatalytic activity of S-doped ZnO. J Hazard Mater 2010;183:315–23. https://doi.org/10.1016/j.jhazmat.2010.07.026.

[90] Poongodi G, Mohan Kumar R, Jayavel R. Influence of S doping on structural, optical and visible light photocatalytic activity of ZnO thin films. Ceram Int 2014;40:14733–40. https://doi.org/10.1016/j.ceramint.2014.06.062.

https://www.twirpx.org & http://chemistry-chemists.com

[91] Low J, Yu J, Jaroniec M, Wageh S, Al-Ghamdi AA. Heterojunction photocatalysts. Adv Mater 2017;29. https://doi.org/10.1002/adma.201601694.

[92] Li Y, Wang B, Liu S, Duan X, Hu Z. Synthesis and characterization of Cu 2 O/TiO 2 photocatalysts for H 2 evolution from aqueous solution with different scavengers. Appl Surf Sci 2015;324:736–44. https://doi.org/10.1016/j.apsusc.2014.11.027.

[93] Mei Q, Zhang F, Wang N, Yang Y, Wu R, Wang W. TiO2/Fe2O3 heterostructures with enhanced photocatalytic reduction of Cr(vi) under visible light irradiation. RSC Adv 2019;9:22764–71. https://doi.org/10.1039/c9ra03531a.

[94] Nasirian M, Bustillo-Lecompte CF, Mehrvar M. Photocatalytic efficiency of Fe2O3/TiO2 for the degradation of typical dyes in textile industries: effects of calcination temperature and UV-assisted thermal synthesis. J Environ Manage 2017;196:487–98. https://doi.org/10.1016/j.jenvman.2017.03.030.

[95] Durán-Álvarez JC, Hernández-Morales VA, Rodríguez-Varela M, Guerrero-Araque D, Ramirez-Ortega D, Castillón F, et al. Ag2O/TiO2 nanostructures for the photocatalytic mineralization of the highly recalcitrant pollutant iopromide in pure and tap water. Catal Today 2020;341:71–81. https://doi.org/10.1016/j.cattod.2019.01.027.

[96] Xie J, Zhou Z, Lian Y, Hao Y, Li P, Wei Y. Synthesis of α-Fe2O3/ZnO composites for photocatalytic degradation of pentachlorophenol under UV-vis light irradiation. Ceram Int 2015;41:2622–5. https://doi.org/10.1016/j.ceramint.2014.10.043.

[97] Liu Y, Sun L, Wu J, Fang T, Cai R, Wei A. Preparation and photocatalytic activity of ZnO/Fe2O3 nanotube composites. Mater Sci Eng, B 2015;194:9–13. https://doi.org/10.1016/j.mseb.2014.12.021.

[98] Shooshtari NM, Ghazi MM. An investigation of the photocatalytic activity of nano A-Fe2O3/ZnO on the photodegradation of cefixime trihydrate. Chem Eng J 2017;315:527–36. https://doi.org/10.1016/j.cej.2017.01.058.

[99] Kadam A, Dhabbe R, Gophane A, Sathe T, Garadkar K. Template free synthesis of ZnO/Ag2O nanocomposites as a highly efficient visible active photocatalyst for detoxification of methyl orange. J Photochem Photobiol B Biol 2016;154:24–33. https://doi.org/10.1016/j.jphotobiol.2015.11.007.

[100] Hao R, Wang G, Tang H, Sun L, Xu C, Han D. Template-free preparation of macro/mesoporous g-C3N4/TiO2 heterojunction photocatalysts with enhanced visible light photocatalytic activity. Appl Catal Environ 2016;187:47–58. https://doi.org/10.1016/j.apcatb.2016.01.026.

[101] Huang Y, Wei Y, Wang J, Luo D, Fan L, Wu J. Controllable fabrication of Bi2O3/TiO2 heterojunction with excellent visible-light responsive photocatalytic performance. Appl Surf Sci 2017;423:119–30. https://doi.org/10.1016/j.apsusc.2017.06.158.

[102] Leghari SAK, Sajjad S, Chen F, Zhang J. WO3/TiO2 composite with morphology change via hydrothermal template-free route as an efficient visible light photocatalyst. Chem Eng J 2011;166:906–15. https://doi.org/10.1016/j.cej.2010.11.065.

[103] Pal S, Maiti S, Maiti UN, Chattopadhyay KK. Low temperature solution processed ZnO/CuO heterojunction photocatalyst for visible light induced photo-degradation of organic pollutants. CrstEngComm 2015;17:1464–76. https://doi.org/10.1039/c4ce02159b.

[104] Wang J, Xia Y, Zhao H, Wang G, Xiang L, Xu J, et al. Oxygen defects-mediated Z-scheme charge separation in g-C3N4/ZnO photocatalysts for enhanced visible-light degradation of 4-chlorophenol and hydrogen evolution. Appl Catal Environ 2017;206:406–16. https://doi.org/10.1016/j.apcatb.2017.01.067.

[105] Yi S, Yue X, Xu D, Liu Z, Zhao F, Wang D, et al. Study on photogenerated charge transfer properties and enhanced visible-light photocatalytic activity of p-type Bi2O3/n-type ZnO heterojunctions. New J Chem 2015;39:2917–24. https://doi.org/10.1039/c4nj01738b.

[106] Bai S, Liu H, Sun J, Tian Y, Chen S, Song J, et al. Improvement of TiO 2 photocatalytic properties under visible light by WO3/TiO2 and MoO3/TiO2 composites. Appl Surf Sci 2015;338:61–8. https://doi.org/10.1016/j.apsusc.2015.02.103.

https://www.twirpx.org & http://chemistry-chemists.com

[107] Jiao Y, Liu Y, Yin B, Zhang S, Qu F, Wu X. Hybrid α-Fe2O3@NiO heterostructures for flexible and high performance supercapacitor electrodes and visible light driven photocatalysts. Nano Energy 2014;10:90–8. https://doi.org/10.1016/j.nanoen.2014.09.002.

[108] Wang JC, Zhang L, Fang WX, Ren J, Li YY, Yao HC, et al. Enhanced photoreduction CO2 activity over direct Z-Scheme α-Fe2O3/Cu2O heterostructures under visible light irradiation. ACS Appl Mater Interfaces 2015;7:8631–9. https://doi.org/10.1021/acsami.5b00822.

[109] Ma XC, Dai Y, Yu L, Huang BB. Energy transfer in plasmonic photocatalytic composites. Light Sci Appl 2016;5. https://doi.org/10.1038/lsa.2016.17.

[110] Gołabiewska A, Malankowska A, Jarek M, Lisowski W, Nowaczyk G, Jurga S, et al. The effect of gold shape and size on the properties and visible light-induced photoactivity of Au-TiO2. Appl Catal Environ 2016;196:27–40. https://doi.org/10.1016/j.apcatb.2016.05.013.

[111] Zhou D, Liu Y, Zhang W, Liang W, Yang F. Au-TiO2 nanofilms for enhanced photocatalytic activity. Thin Solid Films 2017;636:490–8. https://doi.org/10.1016/j.tsf.2017.06.051.

[112] Sanzone G, Zimbone M, Cacciato G, Ruffino F, Carles R, Privitera V, et al. Ag/TiO2 nanocomposite for visible light-driven photocatalysis. Superlattice Microst 2018;123:394–402. https://doi.org/10.1016/j.spmi.2018.09.028.

[113] Zhang Y, Wang T, Zhou M, Wang Y, Zhang Z. Hydrothermal preparation of Ag-TiO2 nanostructures with exposed {001}/{101} facets for enhancing visible light photocatalytic activity. Ceram Int 2017;43:3118–26. https://doi.org/10.1016/j.ceramint.2016.11.127.

[114] Yang Z, Lu J, Ye W, Yu C, Chang Y. Preparation of Pt/TiO 2 hollow nanofibers with highly visible light photocatalytic activity. Appl Surf Sci 2017;392:472–80. https://doi.org/10.1016/j.apsusc.2016.09.065.

[115] Yilmaz P, Lacerda AM, Larrosa I, Dunn S. Photoelectrocatalysis of rhodamine B and solar hydrogen production by TiO2 and Pd/TiO2 catalyst systems. Electrochim Acta 2017;231:641–9. https://doi.org/10.1016/j.electacta.2017.02.035.

[116] Wang X, Wang W, Miao Y, Feng G, Zhang R. Facet-selective photodeposition of gold nanoparticles on faceted ZnO crystals for visible light photocatalysis. J Colloid Interface Sci 2016;475:112–8. https://doi.org/10.1016/j.jcis.2016.04.048.

[117] Zhang Y, Zhou J, Li Z, Feng Q. Photodegradation pathway of rhodamine B with novel Au nanorods @ ZnO microspheres driven by visible light irradiation. J Mater Sci 2018;53:3149–62. https://doi.org/10.1007/s10853-017-1779-x.

[118] Xuxing C, Yunpeng L, Xiaoyang P, David C, Xintang H, Zhiguo Y. Photocatalytic oxidation of methane over silver decorated zinc oxide nanocatalysts. Nat Commun 2016. https://doi.org/10.1038/ncomms12273.

[119] Kuriakose S, Choudhary V, Satpati B, Mohapatra S. Facile synthesis of Ag-ZnO hybrid nanospindles for highly efficient photocatalytic degradation of methyl orange. Phys Chem Chem Phys 2014;16:17560–8. https://doi.org/10.1039/c4cp02228a.

[120] Pawinrat P, Mekasuwandumrong O, Panpranot J. Synthesis of Au-ZnO and Pt-ZnO nanocomposites by one-step flame spray pyrolysis and its application for photocatalytic degradation of dyes. Cat Com 2009;10:1380–5. https://doi.org/10.1016/j.catcom.2009.03.002.

[121] Seddigi ZS, Ahmed SA, Bumajdad A, Danish EY, Shawky AM, Gondal MA, et al. The efficient photocatalytic degradation of methyl tert-butyl ether under Pd/ZnO and visible light irradiation. Photochem Photobiol 2015;91:265–71. https://doi.org/10.1111/php.12391.

[122] Dozzi MV, Prati L, Canton P, Selli E. Effects of gold nanoparticles deposition on the photocatalytic activity of titanium dioxide under visible light. Phys Chem Chem Phys 2009;11:7171–80. https://doi.org/10.1039/b907317e.

[123] Kowalska E, Mahaney OOP, Abe R, Ohtani B. Visible-light-induced photocatalysis through surface plasmon excitation of gold on titania surfaces. Phys Chem Chem Phys 2010;12:2344–55. https://doi.org/10.1039/b917399d.

https://www.twirpx.org & http://chemistry-chemists.com

[124] Chen L, Tian L, Zhao X, Hu Z, Fan J, Lv K. SPR effect of Au nanoparticles on the visible photocatalytic RhB degradation and NO oxidation over TiO2 hollow nanoboxes. Arab J Chem 2020;13:4404–16. https://doi.org/10.1016/j.arabjc.2019.08.011.

[125] Yu H, Ming H, Zhang H, Li H, Pan K, Liu Y, et al. Au/ZnO nanocomposites: facile fabrication and enhanced photocatalytic activity for degradation of benzene. Mater Chem Phys 2012;137:113–7. https://doi.org/10.1016/j.matchemphys.2012.02.076.

[126] He L, Li L, Wang T, Gao H, Li G, Wu X, et al. Fabrication of Au/ZnO nanoparticles derived from ZIF-8 with visible light photocatalytic hydrogen production and degradation dye activities. Dalton Trans 2014;43:16981–5. https://doi.org/10.1039/c4dt02557a.

[127] Bora T, Myint MTZ, Al-Harthi SH, Dutta J. Role of surface defects on visible light enabled plasmonic photocatalysis in Au-ZnO nanocatalysts. RSC Adv 2015;5:96670–80. https://doi.org/10.1039/c5ra16569e.

[128] Subrahmanyam A, Biju KP, Rajesh P, Jagadeesh Kumar K, Raveendra KM. Surface modification of sol gel TiO 2 surface with sputtered metallic silver for Sun light photocatalytic activity: initial studies. Sol Energy Mater Sol Cells 2012;101:241–8. https://doi.org/10.1016/j.solmat.2012.01.023.

[129] Duan Y, Zhang M, Wang L, Wang F, Yang L, Li X, et al. Plasmonic Ag-TiO2 − x nanocomposites for the photocatalytic removal of NO under visible light with high selectivity: the role of oxygen vacancies. Appl Catal Environ 2017;204:67–77. https://doi.org/10.1016/j.apcatb.2016.11.023.

[130] Singh J, Sahu K, Pandey A, Kumar M, Ghosh T, Satpati B, et al. Atom beam sputtered Ag-TiO 2 plasmonic nanocomposite thin films for photocatalytic applications. Appl Surf Sci 2017;411:347–54. https://doi.org/10.1016/j.apsusc.2017.03.152.

[131] Sellappan R, Nielsen MG, González-Posada F, Vesborg PCK, Chorkendorff I, Chakarov D. Effects of plasmon excitation on photocatalytic activity of Ag/TiO 2 and Au/TiO2 nanocomposites. J Catal 2013;307:214–21. https://doi.org/10.1016/j.jcat.2013.07.024.

[132] Lu J, Wang H, Dong S, Wang F, Dong Y. Effect of Ag shapes and surface compositions on the photocatalytic performance of Ag/ZnO nanorods. J Alloys Compd 2014;617:869–76. https://doi.org/10.1016/j.jallcom.2014.08.096.

[133] Kale BB, Mali MG, Tamboli MS, Patil DR, Kulkarni MV, Yoon H, et al. Green approach for hierarchical nanostructured Ag-ZnO and their photocatalytic performance under sunlight. Cat Today 2016;260:126–34. https://doi.org/10.1016/j.cattod.2015.06.004.

[134] Youssef Z, Colombeau L, Yesmurzayeva N, Baros F, Vanderesse R, Hamieh T, et al. Dye-sensitized nanoparticles for heterogeneous photocatalysis: cases studies with TiO2, ZnO, fullerene and graphene for water purification. Dyes Pigments 2018;159:49–71. https://doi.org/10.1016/j.dyepig.2018.06.002.

[135] Li X, Shi JL, Hao H, Lang X. Visible light-induced selective oxidation of alcohols with air by dye-sensitized TiO2 photocatalysis. Appl Catal Environ 2018;232:260–7. https://doi.org/10.1016/j.apcatb.2018.03.043.

[136] Wang Z, Lang X. Visible light photocatalysis of dye-sensitized TiO2: the selective aerobic oxidation of amines to imines. Appl Catal Environ 2018;224:404–9. https://doi.org/10.1016/j.apcatb.2017.10.002.

[137] Lang X, Zhao J, Chen X. Visible-light-induced photoredox catalysis of dye-sensitized titanium dioxide: selective aerobic oxidation of organic sulfides. Angew Chem Int Ed 2016;55:4697–700. https://doi.org/10.1002/anie.201600405.

[138] Yang X, Zhao H, Feng J, Chen Y, Gao S, Cao R. Visible-light-driven selective oxidation of alcohols using a dye-sensitized TiO2-polyoxometalate catalyst. J Catal 2017;351:59–66. https://doi.org/10.1016/j.jcat.2017.03.017.

[139] Yang GCC, Chan SW. Photocatalytic reduction of chromium(VI) in aqueous solution using dye-sensitized nanoscale ZnO under visible light irradiation. J Nanopart Res 2009;11:221–30. https://doi.org/10.1007/s11051-008-9423-y.

https://www.twirpx.org & http://chemistry-chemists.com

[140] Khatamian M, Fazayeli M, Divband B. Preparation, characterization and photocatalytic properties of polythiophene-sensitized zinc oxide hybrid nanocomposites. Mater Sci Semicond Process 2014;26:540–7. https://doi.org/10.1016/j.mssp.2014.04.038.

[141] Murase T, Irie H, Hashimoto K. Visible light sensitive photocatalysts, nitrogen-doped Ta2O 5 powders. J Phys Chem B 2004;108:15803–7. https://doi.org/10.1021/jp047874i.

[142] Shi X, Ma D, Ma Y, Hu A. N-doping Ta2O5 nanoflowers with strong adsorption and visible light photocatalytic activity for efficient removal of methylene blue. J Photochem Photobiol A Chem 2017;332:487–96. https://doi.org/10.1016/j.jphotochem.2016.09.014.

[143] Liu WS, Huang SH, Liu CF, Hu CW, Chen TY, Perng TP. Nitrogen doping in Ta 2 O 5 and its implication for photocatalytic H 2 production. Appl Surf Sci 2018;459:477–82. https://doi.org/10.1016/j.apsusc.2018.07.185.

[144] Ismail AA, Faisal M, Harraz FA, Al-Hajry A, Al-Sehemi AG. Synthesis of mesoporous sulfur-doped Ta2O5 nanocomposites and their photocatalytic activities. J Colloid Interface Sci 2016;471:145–54. https://doi.org/10.1016/j.jcis.2016.03.019.

[145] Zhou C, Shang L, Yu H, Bian T, Wu LZ, Tung CH, et al. Mesoporous plasmonic Au-loaded Ta2O5 nanocomposites for efficient visible light photocatalysis. Cat Today 2014;225:158–63. https://doi.org/10.1016/j.cattod.2013.10.085.

[146] Parida KM, Martha S, Nashim A. Fabrication of NiO/Ta 2 O 5 composite photocatalyst for hydrogen production under visible light. Int J Energy Res 2011;37:161–70. https://doi.org/10.1002/er.

[147] Oliveira JA, Reis MO, Pires MS, Ruotolo LAM, Ramalho TC, Oliveira CR, et al. Zn-doped Nb 2 O 5 photocatalysts driven by visible-light: an experimental and theoretical study. Mater Chem Phys 2019;228:160–7. https://doi.org/10.1016/j.matchemphys.2019.02.062.

[148] Hu B, Liu Y. Nitrogen-doped Nb2O5 nanobelt quasi-arrays for visible light photocatalysis. J Alloys Compd 2015;635:1–4. https://doi.org/10.1016/j.jallcom.2015.02.109.

[149] Nogueira AE, Lopes OF, Neto ABS, Ribeiro C. Enhanced Cr(VI) photoreduction in aqueous solution using Nb2O5/CuO heterostructures under UV and visible irradiation. Chem Eng J 2017;312:220–7. https://doi.org/10.1016/j.cej.2016.11.135.

[150] Lin HY, Yang HC, Wang WL. Synthesis of mesoporous Nb2O5 photocatalysts with Pt, Au, Cu and NiO cocatalyst for water splitting. Cat Today 2011;174:106–13. https://doi.org/10.1016/j.cattod.2011.01.052.

[151] Shiraishi Y, Sugano Y, Ichikawa S, Hirai T. Visible light-induced partial oxidation of cyclohexane on WO 3 loaded with Pt nanoparticles. Cat Sci Technol 2012;2:400–5. https://doi.org/10.1039/c1cy00331c.

[152] Kim J, Choi W. Platinized WO3 as an environmental photocatalyst that generates OH radicals under visible light. Environ Sci Tech 2011;45:3183–4. https://doi.org/10.1021/es200551x.

[153] Chiam SL, Pung SY, Yeoh FY. Recent developments in MnO2-based photocatalysts for organic dye removal: a review. Environ Sci Pollut Res 2020;27:5759–78. https://doi.org/10.1007/s11356-019-07568-8.

[154] Sakai N, Ebina Y, Takada K, Sasaki T. Photocurrent generation from semiconducting manganese oxide nanosheets in response to visible light. J Phys Chem B 2005;109:9651–5. https://doi.org/10.1021/jp0500485.

[155] Baral A, Das DP, Minakshi M, Ghosh MK, Padhi DK. Probing environmental remediation of RhB organic dye using α-MnO2 under visible- light irradiation: structural, photocatalytic and mineralization studies. ChemistrySelect 2016;1:4277–85. https://doi.org/10.1002/slct.201600867.

[156] Kuan WH, Chen CY, Hu CY. Removal of methylene blue from water by γ-MnO 2. Water Sci Technol 2011;64:899–903. https://doi.org/10.2166/wst.2011.262.

https://www.twirpx.org & http://chemistry-chemists.com

[157] Chan YL, Pung SY, Sreekantan S, Yeoh FY. Photocatalytic activity of β-MnO2 nanotubes grown on PET fibre under visible light irradiation. J Exp Nanosci 2016;11:603–18. https://doi.org/10.1080/17458080.2015.1102342.

[158] Mittal N, Shah A, Punjabi PB, Sharma VK. Photodegradation of rose bengal using MnO2 (manganese dioxide). Rasayan J Chem 2009;2:516–20.

[159] Mishra M, Chun DM. α-Fe2O3 as a photocatalytic material: a review. Appl Catal Gen 2015;498:126–41. https://doi.org/10.1016/j.apcata.2015.03.023.

[160] Cheng XL, Jiang JS, Jin CY, Lin CC, Zeng Y, Zhang QH. Cauliflower-like α-Fe2O3 microstructures: toluene-water interface-assisted synthesis, characterization, and applications in wastewater treatment and visible-light photocatalysis. Chem Eng J 2014;236:139–48. https://doi.org/10.1016/j.cej.2013.09.089.

[161] Yang S, Xu Y, Sun Y, Zhang G, Gao D. Size-controlled synthesis, magnetic property, and photocatalytic property of uniform α-Fe 2O 3 nanoparticles via a facile additive-free hydrothermal route. CrstEngComm 2012;14:7915–21. https://doi.org/10.1039/c2ce25929j.

[162] Katz MJ, Riha SC, Jeong NC, Martinson ABF, Farha OK, Hupp JT. Toward solar fuels: water splitting with sunlight and \rust\ ? Coord Chem Rev 2012;256:2521–9. https://doi.org/10.1016/j.ccr.2012.06.017.

[163] Xu H, Wang W, Zhu W. Shape evolution and size-controllable synthesis of Cu2O octahedra and their morphology-dependent photocatalytic properties. J Phys Chem B 2006;110:13829–34. https://doi.org/10.1021/jp061934y.

[164] Zhang Y, Deng B, Zhang T, Gao D, Xu AW. Shape effects of Cu2O polyhedral microcrystals on photocatalytic activity. J Phys Chem C 2010;114:5073–9. https://doi.org/10.1021/jp9110037.

[165] Vaidehi D, Bhuvaneshwari V, Bharathi D, Sheetal BP. Antibacterial and photocatalytic activity of copper oxide nanoparticles synthesized using Solanum lycopersicum leaf extract. Mater Res Express 2018;5. https://doi.org/10.1088/2053-1591/aad426.

[166] Katwal R, Kaur H, Sharma G, Naushad M, Pathania D. Electrochemical synthesized copper oxide nanoparticles for enhanced photocatalytic and antimicrobial activity. J Ind Eng Chem 2015;31:173–84. https://doi.org/10.1016/j.jiec.2015.06.021.

[167] Lu Y, Liu X, Qiu K, Cheng J, Wang W, Yan H, et al. Facile synthesis of graphene-like copper oxide nanofilms with enhanced electrochemical and photocatalytic properties in energy and environmental applications. ACS Appl Mater Interfaces 2015;7:9682–90. https://doi.org/10.1021/acsami.5b01451.

[168] Zhao ZG, Liu ZF, Miyauchi M. Nature-inspired construction, characterization, and photocatalytic properties of single-crystalline tungsten oxide octahedra. Chem Commun 2010;46:3321–3. https://doi.org/10.1039/c001928c.

[169] Liu F, Chen X, Xia Q, Tian L, Chen X. Ultrathin tungsten oxide nanowires: oleylamine assisted nonhydrolytic growth, oxygen vacancies and good photocatalytic properties. RSC Adv 2015;5:77423–8. https://doi.org/10.1039/c5ra12993a.

[170] Dong P, Hou G, Xi X, Shao R, Dong F. WO3-based photocatalysts: morphology control, activity enhancement and multifunctional applications. Environ Sci Nano 2017;4:539–57. https://doi.org/10.1039/c6en00478d.

https://www.twirpx.org & http://chemistry-chemists.com

https://www.twirpx.org & http://chemistry-chemists.com

7

Chalcogenides for visible light-induced photocatalysis

Mohammad Mansoob Khan

CHEMICAL SCIENCES, FACULTY OF SCIENCE, UNIVERSITI BRUNEI DARUSSALAM, BRUNEI DARUSSALAM

1 Introduction

A chalcogenide is a chemical compound consisting of at least one chalcogen anion (S^{2-}, Se^{2-}, and Te^{2-}) and at least one electropositive element. In other words, a chalcogenide is a semiconductor other than oxide. All group 16 elements of the periodic table are defined as chalcogens; the word chalcogenide is more commonly used for sulfides, selenides, and tellurides other than oxides [1, 2]. Although all elements in group 16 (Group VI) are considered as chalcogens, the term "chalcogenide" is only addressed to sulfides, selenides, and tellurides. Chalcogenides are all the elements of group 16 in the periodic table and are also known as the oxygen family. Since oxygen has very different chemical behavior compared to other chalcogens, it is often viewed separately and most of the time is totally excluded from the term "chalcogen." Oxide is excluded from the chalcogenides as oxygen has very different chemical behavior and polonium is a radioactive element [1–5].

Over the past decades, UV- and visible light-responsive photocatalysts have been extensively studied. Some photocatalyst systems with outstanding photocatalytic activities have been developed such as CdS, ZnS, TiO_2, ZnO, Bi_2WO_6, etc. Basically, the applications of most photocatalysts, such as ZnO, SnO_2, etc., are limited by the low quantum yield because of charge-carrier (e/h) recombination and large bandgap energy, which decides the optical absorption energy. Therefore, the improvement of photocatalysts by extending the light absorption is of great significance. At the same time it has been found that most chalcogenides are light active because of their narrow bandgap which allows them to harvest sunlight [1–5].

2 Classification of chalcogenides

Chalcogenides can be classified in several ways based on type of metals, number of metals, number of chalcogen anions, etc. There are several classifications of chalcogenides that are alkali metal and alkaline earth metal chalcogenides, transition metal chalcogenides (TMCs), and main group chalcogenides which are based on type of metals and

Nanostructured Materials for Visible Light Photocatalysis. https://doi.org/10.1016/B978-0-12-823018-3.00019-1
Copyright © 2022 Elsevier Inc. All rights reserved.

https://www.twirpx.org & http://chemistry-chemists.com

number of metals and anions. Another classification of chalcogenides is based on the number of elements involved such as binary, ternary, and quaternary chalcogenides [2–6].

2.1 Classification of chalcogenides based on metals

This class of chalcogenides is further classified into various kinds based on the type of metals.

2.1.1 Alkali metal and alkaline earth metal chalcogenides

Alkali metal and alkaline earth mono-chalcogenides are compounds that are colorless and look like salt. They are often soluble in water. Derivatives that contain disulfide anions are formed when the sulfides undergo hydrolysis. The antifluorite structure and the alkaline earth metal salts found in the sodium chloride motif are often crystallized with the alkali metal chalcogenides. Examples of alkali metal chalcogenides are KLiX (X = S, Se, and Te), whereas alkaline-earth metal chalcogenides are MX (M = Ca, Sr, and Ba and X = S, Se, and Te).

2.1.2 Transition metal chalcogenides

Transition metal chalcogenides are found with many stoichiometries and structures such that the most important stoichiometries are the simpler ones which are 1:1 and 1:2. The most widely explored TMCs are zinc, cadmium, and mercury chalcogenides. Due to their wurtzite or zinc-blende structure, TMCs display highly covalent behavior. Transition metal chalcogenides are further divided into different types based on the number of chalcogen ions as follows.

Monochalcogenides

Monochalcogenides are composed of an MX structure, where M is a transition metal and X is a single chalcogenide anion such as S^{2-}, Se^{2-}, or Te^{2-}. These solid compounds have low friction and high wear resistance to slide surfaces. This is due to their lamellar structure where strongly bonded atoms form extensive rigid sheets. Monochalcogenides such as GaS or GaSe exhibit a crystal structure in which a double layer of Ga is sandwiched between S or Se ions [3].

Dichalcogenides

Metal dichalcogenides are composed of the formula MX_2, where M is a transition metal and X is a chalcogen anion such as S^{2-}, Se^{2-}, or Te^{2-}. They have a precise 1:2 stoichiometry and are crystallized in 2D structures. The 2D layered structures consist of X-M-X sandwiched sheets which are separated by Van der Waals forces [2]. The coordination of the metal ions inside the sheets is sixfold which is either octahedral or a body-centered trigonal prism. Examples of dichalcogenides are MoS_2, $TiSe_2$, $MoSe_2$, and WSe_2.

Tri- and tetrachalcogenides

Transition metal trichalcogenides are described as $M^{4+}(X_2^{2-})(X^{2-})$, where M is a transition metal and X is sulfide, selenide, or telluride. These chalcogenides are bonded by Van der Waals forces and have attracted attention ever since the discovery of magnetism in its

https://www.twirpx.org & http://chemistry-chemists.com

few-layer forms [2–5]. However, exploration for 4d and 5d transition metals are much less studied extensively compared to the 3d transition metal elements. An example of trichalcogenide is MoS_3 produced by treatment of MoS_4^{2-} with the addition of acid and the chemical reaction as follows:

$$MoS_4{}^{2-} + 2H^+ \rightarrow MoS_3 + H_2S$$

Metal-rich chalcogenides

Most of the transition metals in these metal-rich chalcogenides exhibit oxidation states of II or greater. These compounds generally have extensive metal-to-metal bonding which exhibits various structures and physical properties. Siegmund et al. reported that metal-rich chalcogenides that are made from high-abundant elements are favorable catalysts for electrocatalytic hydrogen formation. Example of the structure of a metal-rich sulfide is $Nb_{21}S_8$ [7].

2.1.3 Main group chalcogenides

Main group metal chalcogenides have developed an important class of semiconducting materials with applications and potential for applications in many areas of modern technology. The availability of materials often depends on the processing methodologies available. Main group chalcogenides such as SiS_2, B_2S_3, and Sb_2S_3 have covalent bonded structures. One of the main group chalcogenides that has received great interest in photovoltaics is tin monosulfide (SnS). The main reason is its low bandgap energy of 1.1–1.4 eV, which is compatible with solar absorption. As main group chalcogenides are composed of covalent bonding, SnS has a layer structure of Van der Waals force. Matthews et al. reported that the band gap energy of SnS can be controlled by thinning it to a 2D structure. This shows that band gap energy also depends on morphology and layers [5]. Chalcogen derivatives are known for all of the main group elements except the noble gases. Generally, their stoichiometries follow the classical valence trends, e.g., SiS_2, B_2S_3, Sb_2S_3. Many exceptions exist, however, e.g., P_4S_3 and S_4N_4. The structures of many main group materials are dictated by directional covalent bonding, rather than by close packing [3].

2.2 Classification of chalcogenides based on number of elements

2.2.1 Binary chalcogenide

Cadmium sulfide (CdS) is one of many binary chalcogenides that hold important properties in photoelectric applications. CdS has a functionality of particle-size dependent electronic band structure [8]. This influences the size quantization effects. According to Bajpai et al., CdS can be synthesized more efficiently by thermal decomposition where CdS can be made to the desired size by heating a cadmium thiolate powder [9]. The desired size is achieved by controlled reaction of the precursors. CdS nanoparticles (NPs) can also be synthesized by the use of solution of trioctylphosphine, trioctylphosphineoxide, hexadecylamine, tetradecylamine, trioctylamine, or dodecylamine, where any of the solution reacts with cadmium metal ions and a molecule that contains sulfur [3].

https://www.twirpx.org & http://chemistry-chemists.com

2.2.2 Ternary chalcogenide

Ternary chalcogenide is made up of three different elements including a chalcogen anion. Previously, ZnCdX (X = S, Se) has received high interest because of the possibility of fine-tuning of electronic properties just by changing the Zn:Cd atomic ratio. Focusing on the ZnCdS compound, the bandgap energy of this ternary chalcogenide semiconductor can be varied from 2.4 to 3.7 eV just by changing the ratio of Zn:Cd [10]. Due to its variability, ZnCdS has a magnificent range of uses such as wide bandgap window material in heterojunction solar cells, low-voltage cathodoluminescence, high-density optical recording, and blue as well as UV laser diodes [3]. ZnCdS has also been synthesized through the thermochemical method using commercial CdS and ZnS powders as the precursors. It provides a promising route for the syntheses of numerous ternary nanostructured semiconductors. It has wide potential applications in various nanodevices, and various materials have been shaped into nanotubes, nanowires, nanobelts, and nanocables. Due to their core-shell structures, an assembly of a nanowire and a nanotube as well as nanocables may possess intriguing properties that lead to new applications in nanoelectronics and photonics [11].

2.2.3 Quaternary chalcogenide

The study of chalcogen was first carried out in glasses where chalcogen elements such as S, Se, and Te were usually paired up with Ge and As, which improves the formation of stable glasses [12, 13]. The study of the quaternary chalcogenides, for example, the addition of Te in GeAsSe, increased the infrared transparent region compared to when only an Se atom was added in the glasses [14]. The transparent range of the infrared fiber is 3–12 μm where it is necessary to have low optical loss in the infrared region [15]. Thus, the addition of Te improves the transmission of wavelength with low optical losses [15, 16]. However, excess addition of Te will increase crystallization and decrease the glass transition [16]. Nonetheless, the addition of chalcogen in the quaternary compound increases the infrared transmission to a longer wavelength as it provides better stabilization in the atmospheric moisture and has low optical losses in the chalcogenides glasses [13, 15].

3 Chemistry of metal chalcogenides

Researchers have shown significant interest in the field of nanomaterials and nanotechnology. As the particle size decreases, nanomaterials exhibit several advantages over their bulk materials, such as a larger surface to volume ratio and higher porosity which changes the properties of the material [17]. Likewise, metal chalcogenides in nanoscale range have also been widely studied and utilized for various applications such as photodetectors, photovoltaics, catalysts, batteries, and glasses, as metal chalcogenide-based nanomaterials have good electrical and optical properties [18]. The term chalcogenide refers to a chemical compound that consists of at least one chalcogen anion of sulfur (S), selenium (Se), and tellurium (Te) from group 16 (group VI), and at least one electropositive element.

https://www.twirpx.org & http://chemistry-chemists.com

As a result, chalcogenide has very distinct properties compared to oxides as the d-orbitals of chalcogen offer more metal-metal bonds. Among these, sulfur-based chalcogenide compounds are the most studied chalcogenide materials owing to their carrier mobility, tuned bandgap, and good photovoltaic properties [19].

The most significant attribute of chalcogen-based materials is that they can exist in different forms, arrangements, and structures which are the crystalline, amorphous, and nanocrystalline forms. The primary difference between an amorphous solid and the other two forms in terms of structure is the absence of long-range order (LRO) in the amorphous form. Owing to this absence, the band structure of the amorphous materials can be easily tuned. However, the energy distribution of the electronic levels of the amorphous materials is not affected by the absence of LRO. The amorphous form exhibits disorders such as topological, substitutional, and vibrational disorders.

When the amorphous phase is heated at room temperature, the potential barrier to convert a semiconductor from amorphous to crystalline state is not overcome. This shows that the amorphous phase is stable. If the amorphous material is heated with sufficient thermal energy and it cannot contain the excitation energy of the electrons, a phase change to a crystalline phase may take place. A reasonable amount of energy is released during the process. However, it takes a very short time to crystallize an amorphous material.

Solar energy is one of the most promising renewable energies because of its associated amount of energy density incoming to the earth's surface, which is about 36,000 TW. It should be borne in mind that the population is predicted to reach approximately 9 billion by 2050 with an expected energy demand of 28 TW. Hence, harvesting and storing solar energy is regarded as a suitable solution. Photocatalysis is a state-of-the-art technology that can harvest solar energy and undergo chemical transformations to generate solar fuels, especially H_2 gas, which is a key factor for the predicted low-carbon economy due to its high energetic density ~142 MJ/kg [1–5]. The photocatalyst is the most important factor in the photocatalysis process. Nevertheless, at the time of writing, the photoconversion of most efficient catalysts for photocatalytic H_2 evolution is still far behind the level of significant applications [3, 7, 18].

4 Light-active chalcogenide materials

Photocatalysis is currently rapidly growing and can contribute in solving many environmental and energy-related issues. The use of chalcogenides, in general, is mostly for the ecological purification of industrial wastewaters, industrial gas waste, H_2 production from different raw materials, CO production in the methanol industry, etc. In terms of producing or synthesizing chalcogenides as a photocatalyst, there are many ways to synthesize it. Examples are the sol-gel, hydrothermal, solvothermal, and microwave-assisted methods. These methods produce different kinds of chalcogenides. Choosing different methods of synthesizing chalcogenides is mainly dependent on the application of the chalcogenides.

https://www.twirpx.org & http://chemistry-chemists.com

The use of chalcogenides suggests a favorable future due to their novel acquired properties whereby an improved method can produce a different level of chalcogenide [1–4]. From this, chalcogenides can be used in different types of the industries, not mainly focused on the applications specified above. The following discussion will focus on the general properties of different types of chalcogens and the photocatalytic activities of the metal sulfides, selenides, and tellurides.

4.1 Photocatalytic activity of sulfide, selenide, and telluride

In the last few decades, several chalcogenides have been investigated by researchers regarding their photocatalytic activities [1, 2]. Among them, metal sulfides are the most extensively studied semiconducting materials owing to their low bandgap energy of 1.3–2.4 eV that is suitable for solar energy applications [3–5]. Furthermore, different sulfide-based semiconductor materials such as CdS, ZnS, Sb_2S_3, Bi_2S_3, and MoS have favorable characteristics to be used in various photocatalytic processes, in which CdS and ZnS have attracted the attention of researchers. The valence band of metal sulfides normally consists of 3p orbitals of S, which results in a more occupied valence band and narrower bandgap energy compared to metal oxides which consist of 2p orbitals of O [2].

In spite of the characteristics of the narrow bandgap, metal sulfides are very sensitive to photocorrosion. However, metal sulfides continue to gain interest as photocatalysts because of their response toward visible light. CdS has a suitable bandgap of ~2.4 eV and good band positions for visible light harvesting and water splitting [2]. However, it is toxic in aqueous media as S^{2-} in CdS is easily oxidized by photogenerated holes and releases toxic metal ions (Cd^{2+}) into the reaction mixture. Hence, this limits practical application of CdS in an aqueous medium. In some cases, this photocorrosion can be considerably suppressed in the presence of sacrificial reagents. Furthermore, ZnS is the only metal sulfide that has a wide bandgap of 3.5 eV. Despite this, it is nontoxic and shows good photocatalytic activity for the removal of hazardous pollutants from air and water.

Cadmium selenide (CdSe) and telluride (CdTe) have the ability to reduce water for H_2 production because of the negative conduction band (CB) position versus the NHE (normal hydrogen electrode). These chalcogenides are unable to oxidize water as they have valence band (VB) redox potential lower than 1.23 V at 20°C. Therefore, they exhibit poor photocatalytic activity for oxidation of organic pollutants [13–15].

4.1.1 Metal sulfides as photocatalyst chalcogenides

Among different type of chalcogenides, metal sulfides are considered the most common chalcogenides to be used as semiconducting materials owing to their low bandgap energy, 1.3–2.4 eV, which allows them to harvest solar energy efficiently. The chalcogenides that possess narrow bandgap energies are CdS, ZnS, Bi_2S_3, etc., making them suitable to be utilized for different photocatalytic applications under visible light or solar spectrum. The reason behind their narrow bandgap stems from the VBs of sulfide semiconductors

https://www.twirpx.org & http://chemistry-chemists.com

consisting of S 3p orbitals which are in a more negative position than O 2p. However, despite the appropriate bandgap, chalcogenides suffer from photocorrosion. In order to reduce the process of photocorrosion, sacrificial agents are frequently used [2]. Although the majority of chalcogenides have a narrow bandgap, ZnS is the exception with a wide bandgap of 3.5 eV. Regardless of this large bandgap, ZnS is known to be nontoxic and has good photocatalytic activity for the removal of hazardous pollutants [2].

Sulfide-based chalcogenides are widely studied due to their desired properties of having narrow bandgap, high electron mobility, and suitable morphology with high surface area and stability. Sulfur-based quaternary chalcogenide semiconductors also appear to have an ideal photovoltaic application due to their optoelectronic properties, environmentally friendly nature, and earth-abundant composition. In addition, with suitable band engineering, rapid recombination of electron-hole (e^--h^+) pairs can be prevented, as well as backward reactions, which makes them highly efficient [20, 21].

Two of the most commonly studied sulfide-based chalcogenides are ZnS and CdS. These chalcogenides possess high photocatalytic activity which gives rise to the energetic feasibility for overall water splitting [22]. As a result, water is reduced to hydrogen, in a reaction involving hydrogen evolution from aqueous solutions that contains sacrificial reagents such as SO_3^{2-} and S^{2-}, without the presence of a cocatalyst.

As ZnS has a large bandgap, it minimizes its photocatalytic applications within the visible light regions. Thus, a visible light-responsive photocatalyst with high photocatalytic activity is required to utilize the solar light energy completely [23]. Hence, doping and codoping of ZnS can be performed to increase the light absorption ability to the visible light region while maintaining its high CB level. By implementing this method, photocorrosion can be prevented and recombination rate of e^--h^+ pairs can be minimized [23, 24].

Chalcogenides like monochalcogenides such as CdS and ZnS have received a lot of interest for their good photocatalytic properties. In the case of CdS, it has a suitable bandgap energy of 2.4 eV compared to ZnS at 3.5 eV. However, ZnS is nontoxic unlike CdS, which requires a sacrificial reagent to neutralize Cd^{2+} during the photocatalysis. Nevertheless, ZnS is still the more popular choice because of its superior photocatalytic abilities due to having high specific surface area, porous structures, and high hydrophilicity.

Additionally, ZnS NPs have good chemical stability against oxidation and hydrolysis which could be used for photocatalytic water splitting as they are environmental friendly, stable, and inexpensive. In addition, sensitizing ZnS can lower the bandgap considerably to the point where it shows higher photocatalytic activity than TiO_2 under visible light irradiation [2, 4, 5].

4.1.2 Metal selenides as photocatalyst chalcogenides

Properties of selenide-based chalcogenide: Cadmium selenide

Cadmium selenide (CdSe) is a binary chalcogenide compound that has both ionic and covalent characters. There are three phases of CdSe: hexagonal wurtzite, zinc blende sphalerite and cubic rock salt, with the hexagonal wurtzite phase being the most

https://www.twirpx.org & http://chemistry-chemists.com

commonly found and used. The wurtzite phase can be formed by heating sphalerite from a start temperature of 130–700°C for completion. CdSe has a low bandgap energy of ~1.7 eV. Nanocrystals of CdSe can be prepared using various techniques including solvothermal methods, colloidal methods, chemical vapor deposition (CVD) processes, and many more.

Application of cadmium selenide: Although reduction of water using CdSe for the process of H_2 production is reasonable owing to its lower (negative) conduction band (CB) position *vs* the NHE (normal hydrogen electrode), due to this chalcogenide having a lower valence band (VB) gap of 1.7 eV (*vs* NHE) than anticipated, CdSe cannot undergo oxidation of water. Hence, CdSe is not considered a viable option for the photocatalytic process [2]. In addition, CdSe nanostructures are used for implementation of nanotransistors, coupling devices of charges, and chromophores. Fabricated CdSe nanotubes and nanowires are utilized by applying techniques such as chemical and electrochemical for use in optoelectronic applications. For example, they are used in solar panels.

Properties of selenide-based chalcogenides: Nickel selenide

Anantharaj et al. reported a nonstoichiometric selenide-based chalcogenide such as $Ni_{1-x}Se$ $(0 < x < 0.15)$. Generally, nickel selenides (NiSe and $NiSe_2$) are found as black color and are insoluble in all solvents except for strong oxidizing agents, e.g., HNO_3. This property of its solubility is important for its application in electrocatalytic water splitting [25]. In addition, in water and other electrolytes, these selenide-based chalcogenides are stable. During the reduction reaction at the cathode, the acidic cadmium selenides are stable. This is in contrast with the oxidation reaction at the anode, which has high solubility when interacted with the electrolyte.

Moreover, the formation of surface layers of oxides or hydroxides can be attained in an alkaline medium. This formation resulted in a highly efficient catalyst for the oxygen evolution reaction (OER). Generally, all forms of nickel selenides (NiSe, $NiSe_2$, etc.) are semiconductors in nature, and with that, the electrodes are the main material which highly affects the activity of the electrocatalyst.

Application of nickel selenide: Sivanantham et al. reported the efficiency and durability of nickel selenide (Ni_3Se_2) hybridized with nickel foam as an electrode (anode) in an alkaline medium electrolysis. Ni foam has an ability to increase the capacity of the electrode and enhance the life span of such electrodes. Furthermore, the impedance of the electrode showed that it is considerably lower, which results in expansion of its volume [26].

Evidently, in alkaline water electrolysis, implementation of Ni foam on the Ni_3Se_2 produces a very stable OER value of 285 h. At 100 mA/cm^2, the value of over potential is 315 mV along with a small amount of 5.5% potential loss. Furthermore, Sivanantham et al. also conducted an experiment between Ni_3Se_2/NF as the anode and $NiCo_2S_4$/NF as the cathode. The overall results exhibit an excellent reaction where in a current density of 10 mA/cm^2, it demands 1.58 V as well as in 1 mold/m^3 KOH solution, showing a stability of about 500 h [26].

Hence, when demonstrated for H_2 production using solar energy, nickel selenide has shown significant values where solar cells are being utilized for production of current at

https://www.twirpx.org & http://chemistry-chemists.com

the required voltage. It has shown constant evolution of O_2 and H_2 which results in an inexpensive method having efficient production and high durability for hybridized nickel selenide with nickel foam in 1 mold/m^3 KOH alkaline electrolysis. Hence, H_2 production utilizing solar energy using Ni_3Se_2/NF and $NiCo_2S_4$/NF in 1 mold/m^3 KOH solution proves efficient and successful.

4.1.3 Metal tellurides as photocatalyst chalcogenides

Cadmium telluride (CdTe) forms a dark-colored stable chalcogenide crystal compound which is a nonflammable powder, and is a semiconductor which belongs to the II–VI family in the periodic table. Owing to the structure and properties of CdTe, it is mainly used for various semiconducting applications, and more commonly used for photovoltaic (PV) cells and infrared optical windows [27–29].

Bandgap energy of cadmium telluride

CdTe has a bandgap energy of about 1.4–1.5 eV [28]. This bandgap energy accounts for its suitability to harvest and absorb light in the solar spectrum. Furthermore, the range of bandgap energy between 1.4 and 1.5 eV is optimal as a semiconducting material used for solar cells. Moreover, CdTe has a direct bandgap transition which enhances its advantages of using CdTe in an application for solar cells. It was found that the direct and indirect bandgap and depth of light penetration can affect the efficiency of light absorption as well as the thickness of material for efficient light absorption [28].

For an indirect bandgap

The light has to penetrate deep into the material before it gets absorbed by the material. Hence, this type of bandgap transition exhibits weak light absorption which then requires several thicknesses to absorb light [29].

For a direct bandgap

The light only needs to penetrate on or close to the surface of the material before it gets absorbed by the material. Hence, this type of bandgap transition exhibits strong light absorption which then requires far fewer thicknesses to absorb light [29]. CdTe has a direct bandgap, which leads to a high absorption coefficient roughly greater than 10^5 cm^{-1} [28]. Hence, this results in the requirement of a very thin layer, roughly a few μm thick, to absorb light more than 90% above the bandgap energy. According to Bonnet et al., 1 mm thickness of the film could harvest and absorb light up to 90% [28].

5 Conclusion

Chalcogens such as sulfur, selenium, and tellurium are the fundamental elements of most chalcogenide-based compounds. Several classifications of chalcogenides such as alkali metal and alkaline earth chalcogenides, transition metal chalcogenides, and main group chalcogenides have been discussed based on the type of bonding and structure, for example, CdSe, GaS, GaSe, MoS_2, MoS_3, and SnS. In addition, metal sulfides such as CdS and

https://www.twirpx.org & http://chemistry-chemists.com

ZnS have attracted great attention from researchers due to their low bandgap energy and various applications including solar energy utilization, photocatalytic activity for the visible light response, visible light-assisted water splitting, and removal of hazardous pollutants. Sulfide-, selenide-, and telluride-based chalcogenides have unique characteristics, structure, and physical as well as chemical properties, making them one of the most studied nanostructures. Numerous chalcogenides have been reported and studied extensively, hence, chalcogenides related applications can be further explored.

References

[1] Bouroushian M. Chalcogens and metal chalcogenides. In: Electrochemistry of metal chalcogenrides. Berlin, Heidelberg: Springer; 2010.

[2] Hernandez-Ramirez A. Semiconducting, materials. In: Photocatalytic semiconductors: synthesis, characterization, and environmental applications. Switzerland: Springer International Publishing; 2015.

[3] Ahluwalia. Chalcogenides ons of, Se, Te; 2017. https://doi.org/10.1007/978-3-319-41190-3. https://link.springer.com/chapter/10.1007/978-3-319-41190-3_1.

[4] Jensen WB. A note on the term\chalcogen\. J Chem Educ 1997;1063. https://doi.org/10.1021/ed074p1063.

[5] Matthews PD, McNaughter PD, Lewis DJ, O'Brien P. Shining a light on transition metal chalcogenides for sustainable photovoltaics. Chem Sci 2017;8:4177–87. https://doi.org/10.1039/c7sc00642j.

[6] Khan MM. Chalcogenide-based nanomaterials as photocatalysts. Elsevier; 2021. eBook ISBN: 9780128209172. Paperback ISBN: 9780128204986.

[7] Siegmund D, Blanc N, Smialkowski M, Tschulik K, Apfel U-P, et al. Rich chalcogenides for electrocatalytic hydrogen evolution: activity of electrodes and bulk materials. ChemElectroChem 2020;7.

[8] Yang Y, Chen H, Bao X. Synthesis and optical properties of cds semiconductor nanocrystallites encapsulated in a poly (ethylene oxide) matrix. J Cryst Growth 2003;252:251–6. https://doi.org/10.1016/S0022-0248(03)00870-4.

[9] Bajpai PK, Yadav S, Tiwari A, Virk HS. Recent advances in the synthesis and characterization of chalcogenide nanoparticles. Solid State Phenom 2015;222:187–223. https://doi.org/10.4028/www.scientific.net/SSP.222.187.

[10] Salem AM. Structure, refractive-index dispersion and the optical absorption edge of chemically deposited ZnxCd(1-x)S thin films. Appl Phys Mater Sci Process 2002;74:205–11. https://doi.org/10.1007/s003390100877.

[11] Liu HJ, Zhu YC. Synthesis and characterization of ternary chalcogenide ZnCdS 1D nanostructures. Mater Lett 2008;62:255–7. https://doi.org/10.1016/j.matlet.2007.05.011.

[12] Benson TM, Pan WJ, Furniss D, Miller CA, Rowe H, Zhang D, et al. Fine embossing of chalcogenide glasses—a new fabrication route for photonic integrated circuits. J Non Cryst Solids 2006;352:2515–20. https://doi.org/10.1016/j.jnoncrysol.2006.03.025.

[13] Talley D, Roselle D, Miklos R, Nguyen VQ, Pureza PC, Cole BC, et al. Development and infrared applications of chalcogenide glass optical fibers. Fiber Integr Opt 2000;19:251–74. https://doi.org/10.1080/01468030050058811.

[14] Xu J, Yang R, Chen Q, Jiang W, Ye H. The effects of Te, I atoms on the properties and structure of Ge-As-Se system glasses. J Non Cryst Solids 1995;184:302–8. https://doi.org/10.1016/0022-3093(94)00629-6.

https://www.twirpx.org & http://chemistry-chemists.com

[15] Shiryaev VS, Adam JL, Zhang XH, Boussard-Plédel C, Lucas J, Churbanov MF. Infrared fibers based on Te-As-Se glass system with low optical losses. J Non Cryst Solids 2004;336:113–9. https://doi.org/10.1016/j.jnoncrysol.2004.01.006.

[16] Shiryaev VS, Adam JL, Zhang XH, Churbanov MF. Study of characteristic temperatures and non-isothermal crystallization kinetics in As-Se-Te glass system. Solid State Sci 2005;7:209–15. https://doi.org/10.1016/j.solidstatesciences.2004.10.027.

[17] Kattan PI. Ratio of surface area to volume in nanotechnology and nanoscience. In: Basic nanomechanics series. Petra Books; 2011.

[18] Wu JJ, Lee GJ. Advanced nanomaterials for water splitting and hydrogen generation. In: Nanomaterials for green energy. Taiwan: Elsevier; 2018. p. 145–67. https://doi.org/10.1016/B978-0-12-813731-4.00005-9.

[19] Cho DH, Lee WJ, Park SW, Wi JH, Han WS, Kim J, et al. Non-toxically enhanced sulfur reaction for formation of chalcogenide thin films using a thermal cracker. J Mater Chem A 2014;2:14593–9. https://doi.org/10.1039/c4ta02507e.

[20] Khan ME, Khan MM, Cho MH. CdS-graphene nanocomposite for efficient visible-light-driven photocatalytic and Photoelectrochemical applications. J Colloid Interface Sci 2016;482:221–32. https://doi.org/10.1016/j.jcis.2016.07.070.

[21] Sanad MMS, Elseman AM, Elsenety MM, Rashad MM, Elsayed BA. Facile synthesis of sulfide-based chalcogenide as hole-transporting materials for cost-effective efficient perovskite solar cells. J Mater Sci Mater Electron 2019;30:6868–75. https://doi.org/10.1007/s10854-019-01001-z.

[22] Moroz P, Boddy A, Zamkov M. Challenges and prospects of photocatalytic applications utilizing semiconductor nanocrystals. Front Chem 2018;6. https://doi.org/10.3389/fchem.2018.00353.

[23] Melody K, Leny Y, Mustaffa S. Preparation of high activity Ga and Cu doped ZnS by hydrothermal method for hydrogen production under visible light irradiation. J Nanomater 2015;1–9. https://doi.org/10.1155/2015/195024.

[24] Mei Z, Ouyang S, Zhang Y, Kako T. Ultrafine Zn1-xCuxS ($0 \leq x \leq 0.066$) nanocrystallites for photocatalytic H2 evolution under visible light irradiation. RSC Adv 2013;3:10654–7. https://doi.org/10.1039/c3ra41076e.

[25] Anantharaj S, Subrata K, Suguru N. Progress in nickel chalcogenide electrocatalyzed hydrogen evolution reaction. J Mater Chem A 2020;4174–92. https://doi.org/10.1039/c9ta14037a.

[26] Sivanantham A, Shanmugam S. Nickel selenide supported on nickel foam as an efficient and durable non-precious electrocatalyst for the alkaline water electrolysis. Appl Catal Environ 2017;203:485–93. https://doi.org/10.1016/j.apcatb.2016.10.050.

[27] Bang JH, Kamat PV. Quantum dot sensitized solar cells. A tale of two semiconductor nanocrystals: CdSe and CdTe. ACS Nano 2009;3:1467–76. https://doi.org/10.1021/nn900324q.

[28] Bonnet D. Cadmium telluride thin-film PV modules. In: Solar cells. Germany: Elsevier Ltd; 2005. p. 269–302. https://doi.org/10.1016/B978-185617457-2/50012-3.

[29] Jiajia Y, NMB C, Rebeckah B, Zhentao H, Sowers KL, Krauss TD. Size dependence of photocatalytic hydrogen generation for CdTe quantum dots. J Chem Phys 2019;174707. https://doi.org/10.1063/1.5125000.

https://www.twirpx.org & http://chemistry-chemists.com

https://www.twirpx.org & http://chemistry-chemists.com

8

Phosphides and nitrides for visible light photocatalysis

Rishika Chakraborty[a] and Mukul Pradhan[b]

[a]DEPARTMENT OF CHEMISTRY, NATIONAL INSTITUTE OF TECHNOLOGY MEGHALAYA, SHILLONG, MEGHALAYA, INDIA [b]DEPARTMENT OF CHEMISTRY, NATIONAL INSTITUTE OF TECHNOLOGY WARANGAL, WARANGAL, TELANGANA, INDIA

1 Introduction

1.1 Background

The rapid expansion of global population and industrialization has resulted in a concomitant increase of environmental pollution and energy issues in the new century. This crisis has caused severe contamination to the essential elements of nature such as water and air that are vital for sustenance of life on earth. In addition, worldwide manifestation of energy dearth and upsurge of greenhouse gas (GHG) emission levels have resulted in a conscious shift from utilization of fossil fuels to alternative green sources of energy. In the past decade, several mainstream techniques have emerged in order to remove anthropogenic organic pollutants from water and atmosphere as well as projects exclusively designed to address the future depletion of fossil fuel reserves [1, 2]. For example, energy-systems established on hydrogen have been observed as a promising option due to its role as the ultimate clean energy resource. At present, hydrogen is mostly generated using hydrocarbon feedstock from fossil fuel reserves in a steam reforming method [3].

However, the downside is in the bulk production of CO_2 [3]. An ideal renewable technology requires abundant, inexpensive, and nontoxic chemical reagents, energy source, and catalysts with no secondary pollution. Therefore, viable development of high efficiency and green energy sources using organic strategies for environmental reformation and desired energy generation has become an imperative task.

Solar energy is the richest energy asset on earth, which have enormous potential for the fulfillment of total energy requirement. Even though solar energy transformation by the solar thermal method [4] and photovoltaics [5] have been extensively studied, the controlled usage of this perpetual energy yet encounters relentless challenges within modern science. In view of this, photocatalysis has materialized as the best-advanced and most positive technology concerning easy utilization of natural solar energy with the aid of rationally designed photocatalysts. Its promising applications are chiefly found in four

Nanostructured Materials for Visible Light Photocatalysis. https://doi.org/10.1016/B978-0-12-823018-3.00020-8
Copyright © 2022 Elsevier Inc. All rights reserved.

https://www.twirpx.org & http://chemistry-chemists.com

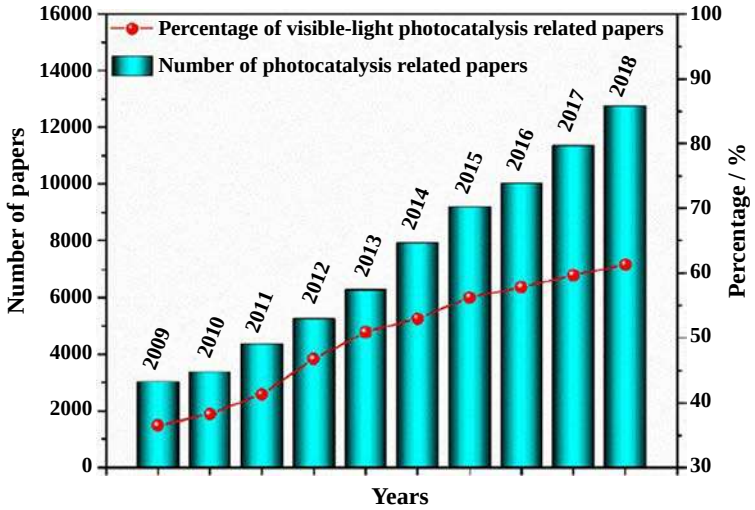

FIG. 1 Progress in photocatalysis. Papers linked to photocatalysis published during the last decade. *From Zhang Z, Bai L, Li Z, Qu Y, Jing L. Review on constructed strategies of heterojunctional nanocomposites as efficient visible-light catalysts by modulating excited electrons with appropriate thermodynamic energy. J Mater Chem A 2019;7:10879–97. https://doi.org/10.1039/C9TA02373A. 10,880.*

outlooks: (i) photocatalytic water splitting for H_2 and O_2 evolution [6, 7]; (ii) photocatalytic degradation of environmental organic pollutants [8]; (iii) photocatalytic reduction process of CO_2 to solar fuels [9]; and (iv) photocatalytic synthesis of organic substances [10]. According to statistics available in the Web of Science, almost 60,000 papers were published from 2009 to 2018 (confirmed January 29, 2019), with "photocatalytic" as the keyword in the search engine, as shown in Fig. 1. Remarkably, practically half of the publications are identified with "visible light photocatalysis." The major advancements achieved in the expansion of visible light-active photocatalysts are due to visible light and the infrared irradiation accounting for nearly 95% of total solar energy while ultraviolet (UV) proportion is attributed to only 5%. Therefore, from scientific and engineering viewpoints, development of such photocatalysts is currently an ongoing significant trend in photocatalysis.

1.2 Basic fundamentals of photocatalysis

In principle, photocatalysis is an intricate technique of photophysical and photochemical processes [11]. A semiconductor or otherwise known as a photocatalyst behaves like a photoactive material because of its band profile. The highest energy band occupied by electrons is called the valence band (VB) and the empty or partially occupied lowest energy band is the conduction band (CB), separated across by a region of forbidden energy commonly known as the bandgap. The key aspects of this process are shown in Fig. 2. It is now readily accepted that photocatalytic performance is influenced by efficient optical absorption, charge separation, and carrier-induced catalytic reactions. Clearly, it is the

https://www.twirpx.org & http://chemistry-chemists.com

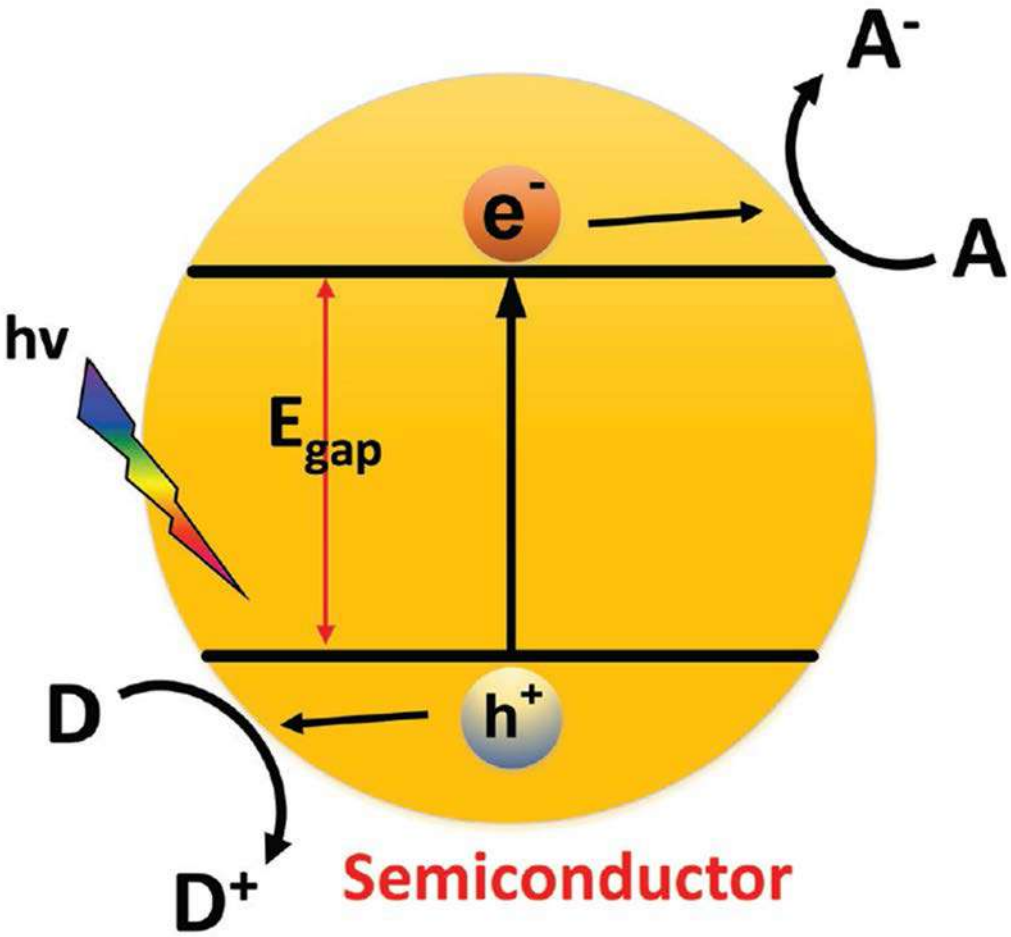

FIG. 2 Primary steps in a photocatalytic mechanism. Schematic illustration of photocatalysis on a semiconductor. *From Vu N, Kaliaguine S, Do T. Critical aspects and recent advances in structural engineering of photocatalysts for sunlight-driven photocatalytic reduction of CO2 into fuels. Adv Functional Materials 2019;29:1901825–69. https://doi.org/10.1002/adfm.201901825.*

thermodynamic energy of photoelectrons that play the determinant role in monitoring the efficiencies in H_2 production, water-treatment, and CO_2 reduction processes.

For instance, a system of heterogeneous semiconductor photocatalyst includes a light harvesting antenna and various active species to facilitate the degradation processes of pollutants and dyes. The sequence of oxidative-reductive photoreactions that take place at the photon-activated catalyst surface have been generally proposed as follows [12]:

$$\text{Photocatalyst} + h\upsilon \rightarrow \mathrm{h^{+}_{vb}} + \mathrm{e^{-}_{cb}} \quad (1)$$

$$\mathrm{h^{+}_{vb}} + \mathrm{e^{-}_{cb}} \rightarrow \text{Heat energy} \quad (2)$$

https://www.twirpx.org & http://chemistry-chemists.com

$$h^{+}_{vb} + H_2O \rightarrow {}^{\bullet}OH + H^{+} \quad (3)$$

$$h^{+}_{vb} + OH^{-} \rightarrow {}^{\bullet}OH \quad (4)$$

$$h^{+}_{vb} + \text{pollutant/dye} \rightarrow (\text{pollutant})^{+}/(\text{dye})^{+} \quad (5)$$

$$e^{-}_{cb} + O_2 \rightarrow {}^{\bullet}O_2^{-} \quad (6)$$

$${}^{\bullet}O_2^{-} + H^{+} \rightarrow {}^{\bullet}OOH \quad (7)$$

$$2{}^{\bullet}OOH \rightarrow O_2 + H_2O_2 \quad (8)$$

$$H_2O_2 + {}^{\bullet}O_2^{-} \rightarrow {}^{\bullet}OH + OH^{-} + O_2 \quad (9)$$

$$H_2O_2 + h\upsilon \rightarrow 2{}^{\bullet}OH \quad (10)$$

$$\text{Pollutant/dye} + ({}^{\bullet}OH, h^{+}_{vb}, {}^{\bullet}OOH \text{ or } {}^{\bullet}O_2^{-}) \rightarrow \text{degraded product} + H_2O + CO_2 \quad (11)$$

Since the surface-interface properties of a photocatalyst influence the crucial steps in photocatalysis, accordingly it is important to carry out investigations upon surface-controlled properties of a semiconductor photocatalyst.

The surfacing of nanoscience in the 21st century revealed itself as a promising choice against monolithics and microcomposites in the matter of isolated physio-chemical properties wherein the matter exhibits intermediary sizes between 1 nm and 100 nm. The importance of nanoscale in photocatalysis is evident since all the elementary steps involved with photocatalytic process takes place on a nanosize-scale level. This causes nanostructured photocatalysts to acquire increased surface area and high aspect ratio compared to bulk materials with improved photocatalytic activity [13]. However, nanosized semiconductor particles usually exhibit numerous surface defects and are generally hostile to effective photogenerated charge separation and limit photocatalytic activity to a great extent [14]. Because of this fact, diverse nano unit-surface tuning strategies have been successfully developed based on appropriate functional molecules. Therefore, design and fabrication of nanostructures based on up-to-date concepts can create entirely new paradigms in photocatalytic applications.

In conclusion, harvesting the majority of the total solar energy (46%), i.e., visible light by renewable technology such as photocatalysis, is critical not only to mitigate environmental pollution but also to contribute substantially to the easing of the energy predicament. Furthermore, to ensure the optimal performance of a photocatalyst, it is vital to integrate successfully the bandgap energy with nanoscale crystallite size of a semiconductor.

2 Semiconductor materials for photocatalysis

2.1 The past and present of photocatalysis

In 1972, Honda and Fujishima reported for the first time about the UV-driven photo-assisted decomposition of water by the photoelectrochemical (PEC) method [15]. As shown in Fig. 3, TiO_2, upon irradiation with UV light, generates electrons and holes.

https://www.twirpx.org & http://chemistry-chemists.com

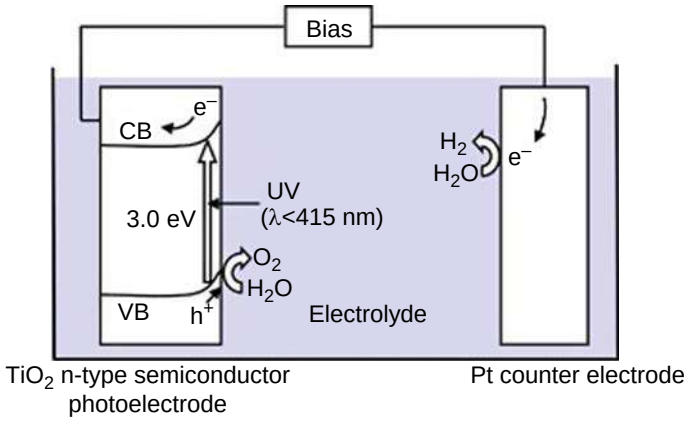

FIG. 3 Sketch map of Honda-Fujishima effect. Water-splitting reaction using titanium oxide as a photocatalyst in the photoelectrochemical method. *From Kudo A, Miseki Y. Heterogeneous photocatalyst materials for water splitting. Chem Soc Rev 2009;38:253–78. https://doi.org/10.1039/B800489G.*

The photoelectrons will reduce H_2O to produce H_2 on Pt-based counter electrode while the holes will oxidize water to produce O_2.

By 1979, powder TiO_2 was reported to split water under sunlight by means of sacrificial reagents without external bias voltage unlike in the PEC method [16]. Since then, enormous progress has been made on the advancement of photocatalytic reaction as a result of widespread attention in the scientific community. Presently, the efficiency of solar energy conversion from water splitting by TiO_2 is yet to be satisfactory because of the following reasons:

(i) Rapid recombination ability of photogenerated carriers results in energy loss.
(ii) The backward reaction of H_2 and O_2 advances readily due to absorption of energy in the forward reaction of H_2O production.
(iii) TiO_2 does not have sufficient bandgap energy (3.2 eV) to absorb visible light energy of the solar spectrum.

In order to resolve the above-listed issues, several approaches have been undertaken to modify the bandgap of TiO_2 like doping and the codeposition method [17, 18], dye-sensitization [19], forming composites having heterojunction with other visible light-active photocatalysts [20], incorporating oxygen vacancies [21], high-pressure densification [22], chemical functionalization [2], surface modification or hybridization [23], defect-engineering [24–26], fundamental theoretical studies [27], and coupling with other technology [28, 29]. Following the extensive research dedicated to TiO_2 photocatalyst, extraordinary efforts have been directed to the design of novel and proficient photocatalysts such as Fe_2O_3 [30], Bi_2S_3 [31], ZnO, WO_3, $SrTiO_3$, CdS, CdSe, etc [32]. In addition, the emergence of 2D nanomaterials progressively promoted the performance of photocatalysis [33–37].

https://www.twirpx.org & http://chemistry-chemists.com

2.2 Evolution of phosphides and nitrides for visible light photocatalysis

Thermodynamically, the water-splitting reaction (Eq. 12) is an energetically unfavorable, uphill process having positive Gibbs free energy.

$$2H_2O\,(l) \rightarrow 2H_2\,(g) + O_2\,(g) \tag{12}$$

For water dissociation, the standard Gibbs free energy change (ΔG^0) is 1.23 eV (Δ238 kJ/molar). The half-cell reactions are represented as follows:

$$\text{Oxidation}: 2H_2O \rightarrow O_2 + 4H^+ + 4e^- \tag{13}$$

$$\text{Reduction}: 4H^+ + 4e^- \rightarrow 2H_2 \tag{14}$$

The oxidation potential for O_2/H_2O is 1.23 V vs. standard hydrogen electrode (SHE) and the reduction potential for H^+/H_2 is 0 V vs. SHE [38].

The change in redox potential at different conditions is given by the Nernst equation as follows:

$$E^e = E^o - \frac{RT}{zF}\ln\frac{\text{oxidized}}{\text{reduced}} \tag{15}$$

where E^e refers to the potential of electrode, E^o refers to the standard potential, R refers to the universal gas constant, F is known as the Faraday constant, z indicates the number of moles of electrons transferred, and T is the temperature.

High performance efficiency of photocatalysts for practical applications depends on:

- **(i)** short bulk-to-surface carrier distance for good mobility of excited charge carriers [39].
- **(ii)** abundant active surface area for adsorption of water and to provide rapid charge and energy exchange rates with extra charged species [40].
- **(iii)** Effective charge carrier separation dynamics for low recombination rate [41].
- **(iv)** desirable CB and VB edge shift to enhance the thermodynamic driving energy force for reactions under illumination [42] and
- **(v)** suitable materials which are thermodynamically capable of forming •OH radicals from water [43].

Therefore, a suitable photocatalyst will be one where the potential of CB energy level must be negatively higher than the H^+/H_2 redox potential, i.e., water reduction, while the VB needs to be positively higher than the OH^-/O_2 redox potential, i.e., water oxidation. Thus the appropriate bandgap energy for photocatalysis should correspond to the lowest potential difference of 1.23 eV to straddle the redox potentials of water-splitting reaction [44]. Another significant parameter in a competent photocatalyst is rational stability in aqueous media under prolonged irradiation [45, 46]. As mentioned in the preceding section, although various semiconductors have emerged with admirable visible light response, achieving maximum photocurrent density is nevertheless below the approximate theoretical value because of an inherent photochemical stability issue. In general,

https://www.twirpx.org & http://chemistry-chemists.com

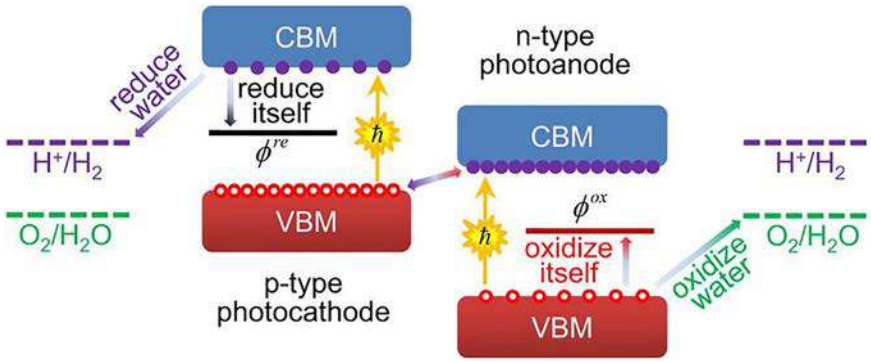

FIG. 4 Appropriate band alignment in photocatalytic semiconductor system for absorption of visible light. Schematic illustration of band alignment in p-type and n-type semiconductors relative to water redox potentials in *Z*-scheme pathway. *From Chen S, Wang L. Thermodynamic oxidation and reduction potentials of photocatalytic semiconductors in aqueous solution. Chem Mater 2012;24:3659–66. https://doi.org/10.1021/cm302533s.*

the stability of a semiconductor in the aqueous medium depends on the band alignment positions of thermodynamic reduction potential (ϕ_{re}) with respect to conduction band minimum (CBM) and thermodynamic oxidation potential (ϕ_{ox}) with respect to valance band maximum (VBM). As presented in Fig. 4, if ϕ_{ox} (O_2/H_2O) is higher than the VBM of a semiconductor such as in CdS, ZnO, ZnS, TiO_2, etc., then the semiconductor will suffer self-oxidization from unconsumed holes. Similarly, if the semiconductor exhibits CBM higher than ϕ_{re} (H^+/H_2), it will undergo self-reduction from unconsumed electrons like in Cu_2O, WO_3, etc [47]. At the same time, the bandgap of such metal oxides becomes too enlarged and in consequence the materials only respond to UV light irradiation. In addition, metal sulfides are prone to oxidation by photoexcited holes which results in the formation of either sulfate (SO_4^{2-}) in the presence of molecular oxygen or sulfur (S^0) in the absence of oxygen receiving light irradiation. This results in decreased photocatalytic performance.

With regard to this photoreaction, stability can be improved by using sacrificial agents and by expanding the adsorption ability of the material or loading appropriate cocatalyst on semiconductor surface to prevent photocorrosion. Among the various known cocatalysts, explicitly the platinum-series elements (Pt, Au, Pd, Rh, etc.) [48–54], have generally been used as effective sinks for electrons and proton reduction sites. However, the high costs have tightened their corresponding bulk-scale application to a great extent and significant efforts are being made to find novel materials with increased effectiveness to rival the activity of Pt.

In this perspective, phosphides and nitrides have emerged as robust and resourceful low-cost catalysts as well as cocatalysts with configured band profile for promoting photocatalytic applications especially when a "*Z*-scheme" heterogeneous nanostructure is constituted. In the next section, we shall discuss in detail about phosphides and nitrides and their role in visible light photocatalysis.

https://www.twirpx.org & http://chemistry-chemists.com

3 Phosphides and nitrides

3.1 A brief introduction

3.1.1 Phosphides

Phosphides (mainly transition metal phosphides; TMPs), despite having been initially reported in 1792, largely continued to be unexploited for decades, until in the 1960s, the implementation had steadily expanded in the fields of metallurgy and pesticides [55] and finally in photocatalysis. Metal phosphides can demonstrate various properties as per the nature of the metal, M/P ratio, and crystallographic structure. Mostly metal-rich phosphides exhibit properties close to metals and ceramics. In addition, they demonstrate exceptional heat and electrical conductivity as well as possessing good thermal and chemical stability. Methodical test systems have revealed that the extent of electron delocalization existing in the metal sublattice depends strongly on the P atom in the phosphides [56]. Moreover, since P belongs to the same series as the N group, it is expected to exhibit more advanced chemical properties due to the presence of multielectron orbitals compared to N_2 atoms.

Metal phosphides like Ni_2P, CoP, and Cu_3P have exhibited impressive H_2 evolution by visible light irradiation and photocatalytic CO_2 reduction [57, 58]. InP and GaP nanomaterials also have been successfully exploited for water splitting. An interesting result on degradation of phenol using P-doped TiO_2 [59] showed that with increased P content, the absorbed band alignment increases to the visible light domain, which is probably due to increased density of oxygen vacancies [60]. Phosphide photocatalysts have also been evaluated for overall treatment of water such as BN-Zn_3P_2 nanowire [61]. The photocatalyst was successful in disinfecting water contaminated with *E. coli* by hydroxyl radical generation that damaged the bacterial cell. As cocatalysts, TMPs are complementary to zero-valent metals in terms of stability property in photocatalytic water reduction despite the pH conditions. In this respect, CdS loaded with TMPs nanoparticle cocatalysts (CoP, Ni_2P, and Cu_3P) for H_2 generation presented interesting results. Out of the composites, the CoP/CdS nanocomposite displayed the best result. The durability test demonstrated that after irradiation duration of 50 h, a slight decrease in H_2 production was noticed [62]. The result suggested that CoP cocatalysts successfully improved the photoreaction stability of CdS, which otherwise is prone to photocorrosion and photooxidative dissolution in low pH even without light irradiation. An important metal-free phosphide worth mentioning is boron phosphide (BP). BP, which has an indirect bandgap energy 2.0 eV, is known to exhibit good chemical and thermal stability as well as high charge mobility and mechanical strength [63]. In addition, it can be doped with excess boron to give rise to p-type conductivity while excess phosphorus doping will cause n-type conductivity in BP [64]. Studies have shown that n-type BP demonstrates higher mobility of carriers and poorer resistivity compared to the p-type BP, an attribute that might be more conducive for application in photocatalysis [64]. In view of this, the n-type BP photocatalyst has demonstrated excellent performance for visible light-driven H_2 evolution without loading any

https://www.twirpx.org & http://chemistry-chemists.com

noble metals as cocatalyst. In addition, the metal-free BP exhibited high stability and resistance to corrosion in strong acid and alkali reaction media [65]. TMPs are also employed for effective removal of dyes from wastewater. Visible light-driven CoP/Fe_2P@mC photocatalysts have shown successful photodegradation of water-soluble organic Rhodamine B (RhB) dye. The catalyst with 100 mg L^{-1} dosage showed that 94% RhB is photodegraded toward 20 mg L^{-1} RhB [66].

3.1.2 Nitrides

Metal nitrides (MNs) of late have surfaced as new active materials. MNs are often referred as "interstitial alloys," [67] prepared by incorporating N atoms in the parent metal interstitial sites wherein the host lattice structure is altered upon intercalation. The formation of interstitial metal nitrides results in an expanded metal structure with a broadened d-band. The metal d-band contraction gives rise to pronounced density of states (DOS) close to the Fermi energy level compared to the host metal [68]. The redistribution of the states is useful for enhancing the properties of the noble metals. Transition metals like Fe, Co, and Ni are highly capable of forming nitrides [69–71]. MNs differ substantially from transition metal dichalcogenides and metal oxides. Furthermore, some of the noble metals are not economical, such as the Pt-group metals. The advantages of using MNs is in their cost, natural abundance, excellent thermal-mechanical stability, and steady tolerance to common catalyst poisons [72]. In particular, MNs have promising applications in photocatalytic reactions because of their unique electronic structures, great corrosion resistance, and high electrical conductivity [73].

From 2005 onward, there was a radical shift from the development of metal oxide-based photocatalysts to nitrides. This is attributed to the higher potential energy of the N 2p orbital compared to the O 2p orbital that creates narrow bandgap semiconductors [74]. The first positive example of a water-splitting reaction receiving UV irradiation is β-Ge_3N_4/RuO_2 [75]. However, the performance was affected largely from the crystallinity and defect densities of the materials [76]. Among all the known MNs, GaN is the most studied semiconductor with a bandgap energy of nearly 3.4 eV [77–80]. Furthermore, theoretical analysis has revealed that GaN or AlN can combine with MoS_2 due to their similar lattice parameters, and this leads to the formation of Van der Waals heterostructures. Such a design facilitates separate H_2 and O_2 evolution sites at separate monolayers [81]. Another currently well-known MN is InGaN, whose bandgap energy can range over approximately the full solar spectrum through tuning the elemental ratio between In and Ga [81, 82]. For instance, a multiband InGaN/GaN heterostructure enriched with Rh/Cr_2O_3 nanoparticles [83] and p-type Mg-dopant [84] achieved stable H_2 generation. Ta_3N_5 has long been examined as a photocatalyst because of its appropriate bandgap of almost 2.1 eV and was found to split water, receiving visible light radiation using sacrificial agents [85]. Ta_3N_5 has long been examined as a photocatalyst due to its appropriate bandgap of 2.1 eV and was found to split water under visible light radiation in the company of sacrificial electron donors and acceptors. However, in order to improve its limited quantum efficiency, Ta_3N_5/Ta_2O_5 exhibited a six-fold enhancement of photocatalytic activity for O_2 production under visible

https://www.twirpx.org & http://chemistry-chemists.com

light [85]. In terms of photocatalytic dye degradation, urea@Ta_3N_5 provided enhanced catalytic activity for methylene blue dye degradation, which was credited to its nanocrystalline particle size [86]. Another notable example is of multiband GaN nanowires, which exhibited high photocatalytic decay of 89% in visible irradiation toward methylene blue [87]. InGaN as mentioned earlier can also readily photoreduce CO_2 into CO and hydrocarbons [88]. p-InGaN/GaN nanowires have successfully exhibited the reduction of CO_2 under visible light [89].

Similar to MNs, there is also oxynitrides of transition metal cations that are widely used in photocatalytic applications [90–93]. Generally, oxynitrides have better aerial stability than pure nitrides, but with narrower bandgaps compared to analogous oxides (1.6–3.3 eV). Tantalum oxynitride (TaON) is also a well-recognized visible light-active semiconductor [94]. The CB has empty Ta 5d states and the VB has hybridized N 2p and O 2p orbitals. It is the hybridized orbital state which results in a higher potential in comparison to the metal oxide O 2p states and results in reduced bandgap energy [95]. Titanium-based oxynitride ($Ti_3O_3N_2$) with a bandgap of 2.37 eV was predicted both experimentally and theoretically to be suitable for the water redox process [96, 97]. Gallium oxynitride (GaON) has also been reported in the literature for photocatalytic reactions [98–100]. The bandgaps of Ga_2O_3 and GaN are 4.7 and 3.4 eV, respectively. Under such a set of conditions, the introduction of O_2 into the GaN lattice results in the formation of GaON with notable reduction in bandgap energy [98]. Perovskite-based oxynitrides like $LaTiO_2N$, alkaline-Ta based oxynitride perovskites, and Nb-based perovskite were reported to drive various photocatalytic applications under visible light irradiation [101–103].

Apart from inorganic semiconductors, an important polymeric material belonging to the class of nitride is graphitic carbon nitride (g-C_3N_4). The CB and VB potentials are −1.09 and +1.56 eV, respectively, with tunable bandgap energy of ∼2.7 eV that entitles it to initiate photocatalytic reactions on absorption of visible light [104]. A review by Xu et al. regarding the recent advances in noble metal-free doped graphitic carbon nitride-based nanohybrids for photocatalysis of organic contaminants in water reveals that porous g-C_3N_4 nanosheets could completely destroy *E. coli* cells under visible light within 4 h [105]. The improved activities were credited to higher specific surface area with more quantities of surface reactive sites. Even so, g-C_3N_4 still suffers from shortcomings like restricted optical absorption spectrum, poor electronic conductivity, and inherently fast recombination rate of charge carriers [106]. Several strategies, such as element doping [107], coupling with organic/inorganic semiconductors [108], and depositing with quantum metals dots [109], have been conducted to modify g-C_3N_4. Among these modifications, integration of functionalized cocatalyts with g-C_3N_4 can entrap photogenerated charge carriers from adjacent semiconductor through the Schottky junction at the metal-semiconductor interface [110]. Consequently, noble and plasmon metals can act as efficient cocatalysts [111, 112]. Among earth-abundant transition metal compounds, TMPs have appeared as the most appealing cocatalysts. A few recent photocatalytic examples under visible light irradiation include MoP/g-C_3N_4 [113], Ni_2P-CdS/g-C_3N_4 [114], Fe_2P-Co_2P/g-C_3N_4 [115], etc. for H_2 evolution. CoP as a cocatalyst in high-crystalline

https://www.twirpx.org & http://chemistry-chemists.com

g-C_3N_4 (HCCN) demonstrated impressive photocatalytic performance toward tetracycline degradation in wastewater. In particular, 5 wt% CoP/HCCN revealed optimum photocatalytic efficiency (96.7%, 120 min) with 10.2 times of degradation rate constant than HCCN [116].

Thus, we can conclude from the above studies that phosphides and nitrides exhibit promising results in the field of photocatalysis. In our further discussion, we will cover the synthetic methodologies citing recent examples and mechanism behind their catalytic activity.

4 Synthetic routes for preparation of phosphides and nitrides

4.1 Synthesis of phosphides

The elements of metals in transition metal phosphides (TMPs) primarily consist of Fe, Co, Ni, and Mo. Other elements like W, Mn, Cu, etc. have also gathered more and more research attention. These metal elements are used for the synthesis for a wide variety of phosphides. In photocatalysis, more research attention has been paid to single TMPs (CoP, Ni_2P, FeP, etc.), which act as cocatalysts compared to bimetallic phosphides (Co-Fe-P, NiFe-P). Among these, the activity of Co- and Ni-based phosphides is more notable. TMPs are generally synthesized from diverse methods and in varied forms (Fig. 5) such as single crystals [117, 118], bulk polycrystalline powders [119], films [120], and nanostructured solids [121–123].

Over the years, bulk metal phosphides have been synthesized using a conventional solid-state method. By means of this, many metal phosphide phases may be regularly prepared to a high level of purity and on a large scale. As is observed in solid-state reactions, elevated temperatures and time-consuming reaction duration are commonly required. In an illustrative synthesis of bulk FeP, stoichiometric quantities of Fe and red P were vacuum-sealed in a silica tube and subsequently heated to 900°C for nearly 8 days [124]. Red P is mostly employed, though white P is also utilized, as are some specific metal phosphides [125]. However, solid-state reactions mostly produce highly toxic byproducts (P_4 and PH_3), hence, reactions and isolation of products must proceed rigorously under inert conditions.

To overcome the drawbacks, phosphidation is mostly preferred [126, 127]. Here, the temperature condition and molar ratio of the reactant species could be modified to reform the performance of TMPs. The process is achieved either by direct contact with phosphine gas [126] or interrelated compounds produced in situ from reduction of phosphate-based salts by either hydrogen [128] or carbon [129]. For example, TiP [60, 130] and MoP can be obtained easily by temperature-programmed reduction (TPR) process using corresponding salts. In a representative example of TPR synthesis for MoP, a stoichiometric amount of ammonium molybdate tetrahydrate and diammonium phosphate was kept in an oil bath at 90°C overnight and annealed at 500°C for 10 h. Chains of MoP/CdS hybrid structures were subsequently prepared that led to a 20 times higher H_2 rate over CdS [57].

https://www.twirpx.org & http://chemistry-chemists.com

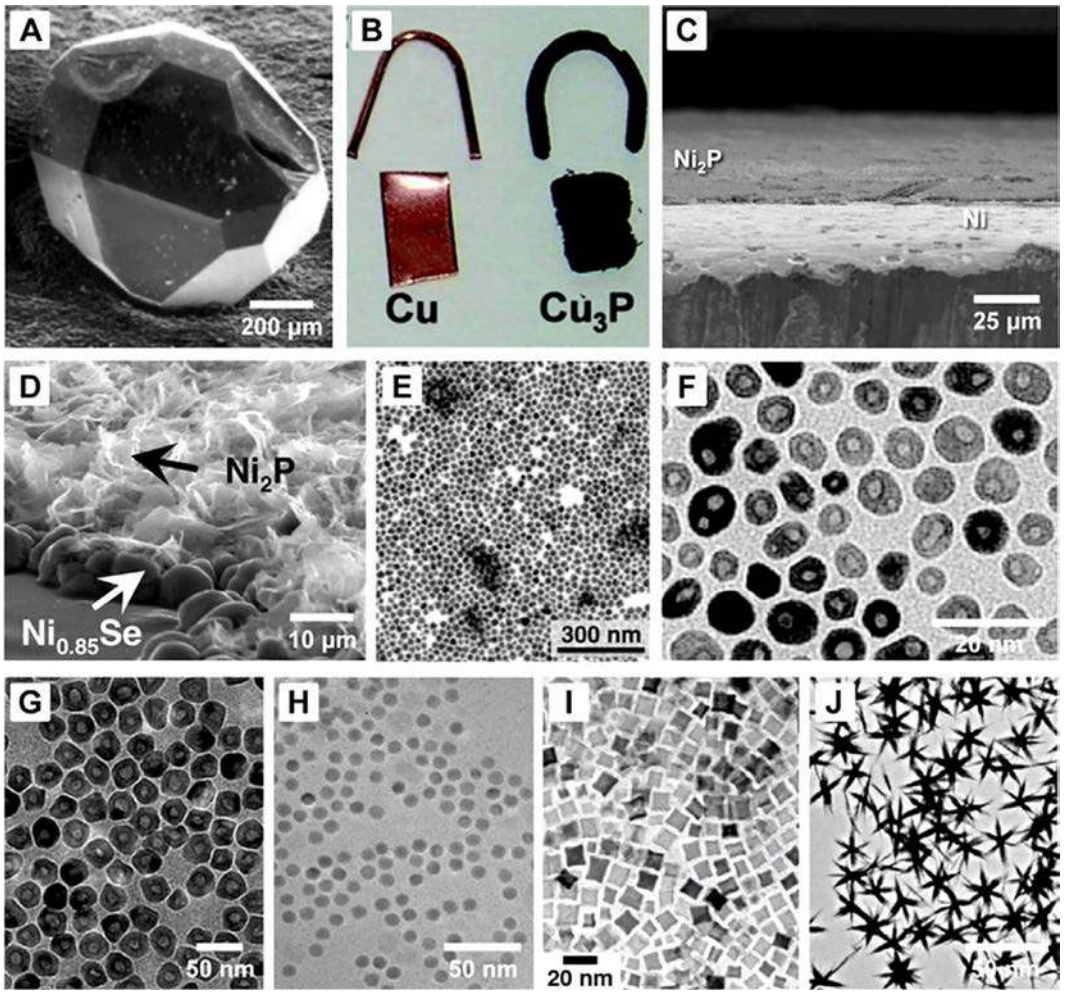

FIG. 5 Types of metal phosphide crystals, films, and nanoparticles. (A) Crystal of $NdFe_4P_{12}$, (B) Cu_3P made by refluxing in trioctylphosphine, SEM images of (C) Ni_2P film, (D) Ni_2P and $Ni_{0.85}Se$ thin films, TEM image of (E) Zn_3P_2, (F,G) Ni_2P, (H) $Fe_xNi_{2-x}P$, (I) Rh_2P and (J) CoP nanoparticles. *From Callejas JF, Read CG, Roske CW, Lewis NS, Schaak RE. Synthesis, characterization, and properties of metal phosphide catalysts for the hydrogen-evolution reaction. Chem Mater 2016;28:6017–44. https://doi.org/10.1021/acs.chemmater.6b02148.*

The requirement for high specific surface area and crystalline materials gradually led to revived interest in employing alternate approaches. For instance, solvothermal/hydrothermal reactions, reactions [131–133], thermal dissociation of single-sourced organometallic parent precursors [134], and reaction of organometallic composites and metal nanomaterials with organophosphine reagents [135] use milder reaction conditions than those in direct reaction approaches. Furthermore, these methods typically give rise to dispersible nanocrystals that can directly be used by either drop-casting or even spin-coating on the electrode surfaces. Reagents like white P, tri-n-octylphosphine (TOP), $P(SiMe_3)_3$,

https://www.twirpx.org & http://chemistry-chemists.com

and trioctylphosphine oxide (TOPO) are commonly used for the conversion of metals to metal phosphides at low temperatures [136, 137]. Nonetheless, in such conditions, the temperature range is generally restricted. Moreover, the abovementioned reagents are highly toxic and do not satisfactorily meet the present requirements for green chemistry.

Flower-like PbS/Ni_2P composites have been synthesized using surfactants like CTAB and SDS as templates. The photocatalyst showed improved degradation activity toward methylene blue (75%) which is higher than PbS (16.6%) and Ni_2P nanoparticles (44.8%) [138]. Surfactants not only modify the nanoscale morphology of TMPs by preventing aggregation but also increase their dispersity in aqueous solutions [139]. However, they can also suppress the unmasking of active sites. Yang et al. prepared GaP on a large scale from $Ga(C_2H_5)_3$ and $C_9H_{27}PSi_3$ precursors along with a noncoordinating squalane solvent. This approach was carried out by the solution-liquid-solid (SLS) method. As shown in Fig. 6, the Ga droplets formed as a precursor in the solvent had a vital part in the generation of spherical Ga particle. Additionally, the SLS process facilitated growth of GaP nanowires [140].

Likewise, other examples include $Ni_xP/g\text{-}C_3N_4$ [141], $g\text{-}C_3N_4/Cu_3P$ heterojunctions [142], and $Ni_{12}P_5$ [143]. These examples demonstrated excellent photocatalytic activity for H_2 generation.

CoP nanowires (CoP NWs) prepared in low-temperature phosphidation reaction for photocatalytic H_2 production displayed increased photocatalytic activity. This enhanced activity was attributed to electronic coupling effect, suitable band structure, and facile

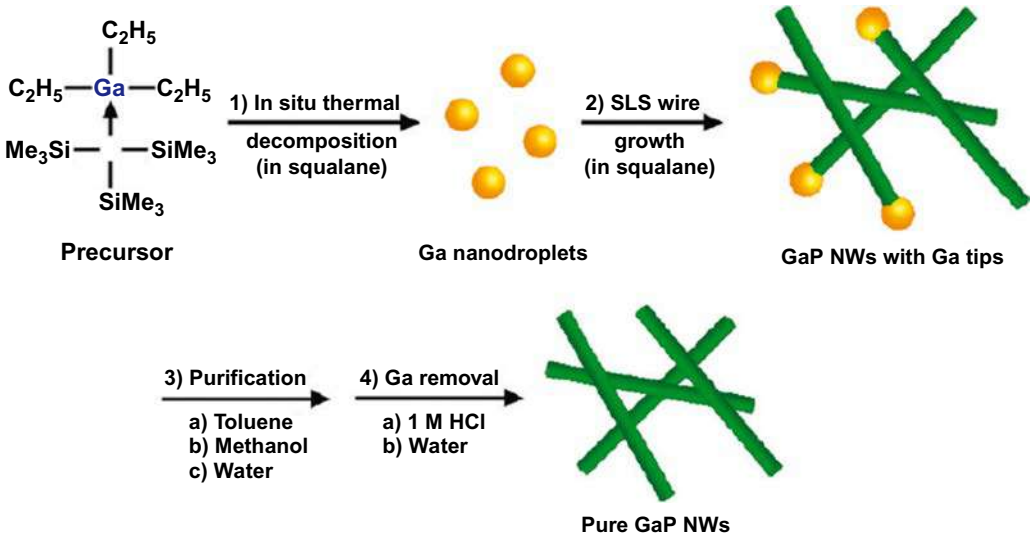

FIG. 6 Representative example of the solution-liquid-solid method. Schematic illustration for synthesis and purification of colloidal GaP nanowires using triethylgallium and tris(trimethylsilyl) phosphine as precursors and squalane solvent. *From Sun J, Liu C, Yang P. Surfactant-free, large-scale, solution-liquid-solid growth of gallium phosphide nanowires and their use for visible-light-driven hydrogen production from water reduction. J Am Chem Soc 2011;133:19306–09. https://doi.org/10.1021/ja2083398.*

https://www.twirpx.org & http://chemistry-chemists.com

charge carrier separation and migration [144]. Similarly, NiCoP/g-C_3N_4 was prepared using a humble one-pot method by directly heating melamine. This study aims to provide an easy scheme for the fabrication of such phosphides as effective cocatalysts [145].

Several thin-film growth techniques like chemical vapor deposition (CVD) [146], metal–organic chemical vapor deposition (MOCVD) [120], pulsed laser deposition (PLD) [147], and physical vapor deposition (PVD) [148, 149] like sputtering techniques have also been applied for the synthesis of thin films of TMPs on varying substrates.

Ingenious nanocomposite formation of carbon-based substrates in conjunction with TMPs was found to be beneficial for efficient electron transfer and inhibition of e-h recombination at the same time [150]. Especially, graphene is mostly used as a valued support or substrate for catalyst confinement. It not only prevents aggregation of the catalyst but also helps in the exposure of more active sites for catalyst-induced reactions [151]. Kim and his group fabricated a hierarchical CoP-modified CdS/rGO-MoS_2 nanocomposite by sonication (Fig. 7). Under optimized experimental conditions, the photocatalyst hybrid could reach a rate of up to 83,907 μmol g^{-1} h^{-1} toward H_2 evolution that exceeded that of Pt/CdS [152].

Similarly, CoP/CNTs and CoP/rGO prepared by hydrothermal method demonstrated excellent catalytic activities for CO_2 reduction [153]. In another work, Cu_3P-CNT synthesized by direct phosphatization resulted in the highest apparent quantum efficiency (AQE) of nearly 10.23%, achieved at 500 nm [154].

Currently, H_2 evolution is mostly conducted in model deionized water. The rate of photocatalytic H_2 generation in ordinary seawater is nearly half in comparison to pure water, mostly due to the complex cations and microorganisms that are present in seawater. In view of this, recently, Liu and his coworker designed an organic polymer having a carbon-encapsulated Ni_2P photocatalyst (COP-TF@CNi_2P) via solution-phase synthesis. It was suggested in their work that the carbon layers can strengthen the carrier mobility and protect Ni_2P from photocorrosion. Therefore the visible light-active hybrid system achieved 92% efficiency even after 15 days [155].

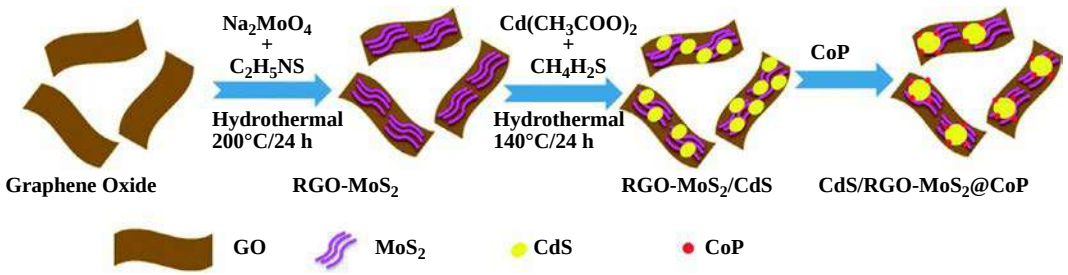

FIG. 7 Multicomponent nanocomposite construction between carbon-based material and transition metal phosphide. Schematic illustration of CoP-modified CdS/rGO-MoS_2 nanocomposite using the hydrothermal method. *From Reddy DA, Choi J, Lee S, Kim Y, Hong S, Praveen Kumar D, et al. Hierarchical dandelion-flower-like cobalt-phosphide modified CdS/reduced graphene oxide-MoS2 nanocomposites as a noble-metal-free catalyst for efficient hydrogen evolution from water. Catal Sci Technol 2016;6:6197–206. https://doi.org/10.1039/C6CY00768F.*

https://www.twirpx.org & http://chemistry-chemists.com

FIG. 8 Representative example of metal-organic framework template-engaged strategy. Schematic illustration of synthesis of multicomponent transition metal phosphide-CdS nanorod. *From Amaranatha Reddy D, Kim HK, Kim Y, Lee S, Choi J, Jahurul Islam M. Multicomponent transition metal phosphides derived from layered double hydroxide double-shelled nanocages as an efficient non-precious co-catalyst for hydrogen production. J Mater Chem A 2016;4:13890–98. https://doi.org/10.1039/C6TA05741A.*

Suitable nanocomposite formation of TMPs with metal-organic frameworks (MOF) has been reported to overcome the limitations of TMPs in terms of low surface area and conductivity. For example, a multicomponent TMP (Co, Ni, and Mo)-CdS nanorod was prepared from a MOF template-engaged strategy as shown in Fig. 8. The photocatalyst exhibited exceptionally high stability and high hydrogen evolution capability under visible light [156].

Keeping in mind the synthetic routes described above, a few more recent examples of TMPs as photocatalysts are listed in Table 1.

4.2 Synthesis of nitrides

Synthesis of transition metal nitrides (TMNs) is more complex than that of corresponding metal oxides, requiring much higher temperatures and implementation of inert and anhydrous conditions. The stringent reaction conditions generally lead to grain growth, thereby strongly impacting the nanoscale properties. The most convenient and conventional applied technique to prepare TMNs is direct heat-treatment of metal precursors by ammonolysis or nitridation in NH_3 or N_2 [157].

https://www.twirpx.org & http://chemistry-chemists.com

Table 1 Summary of phosphide-based visible light-active catalysts for photocatalytic applications. Recent examples of visible light-responsive phosphide photocatalysts.

Photocatalyst	Synthetic Method	Photocatalytic Performance	Reference
g-C_3N_4/Fe_xP	Hydrothermal and phosphidation	H_2 production (166.4 μmol g^{-1} h^{-1})	Zhao H, Wang J, Dong Y, Jiang P. Noble-metal-free iron phosphide cocatalyst loaded graphitic carbon nitride as an efficient and robust photocatalyst for hydrogen evolution under visible light irradiation. ACS Sustainable Chemistry & Engineering 2017; 5:8053–60. https://doi.org/10.1021/acssuschemeng.7b01665
CdS/O-Co_2P	Solvothermal and phosphidation	H_2 production (184.8 μmmol g^{-1} h^{-1})	Chao Y, Zheng J, Zhang H, Li F, Yan F, Tan Y, Zhu, Z. Oxygen-incorporation in Co_2P as a non-noble metal cocatalyst to enhance photocatalysis for reducing water to H_2 under visible light. Chemical Engineering Journal 2018; 346:281–88. https://doi.org/10.1016/j.cej.2018.04.025
Co_1P/PCN	Phosphidation	H_2 production (410.3 μmmol g^{-1} h^{-1})	Liu W, Cao L, Cheng W, Cao Y, Liu X, Zhang W, Mou X, Jin L, Zheng X, Che W, Liu Q, Yao T, Wei, S. Single-site active cobalt-based photocatalyst with long carriers lifetime for spontaneous overall water splitting. Angewandte Chemie International Edition 2017; 56: 9312–17. https://doi.org/10.1002/anie.201704358.
Cu_3P/CdS	Solvothermal	H_2 production (200 μmol g^{-1} h^{-1})	Sun Z, Yue Q, Li J, Xu J, Zheng H, Du P. Copper phosphide modified cadmium sulfide nanorods as a novel p-n heterojunction for highly efficient visible-light-driven hydrogen production in water. Journal of Material Chemistry A 2015; 3:10243–47. https://doi.org/10.1039/C5TA02105G
MoP-Cu_3P	Metal-organic frameworks (MOFs)-assisted	H_2 production (855 μmol g^{-1} h^{-1})	Song Y, Xin X, Guo S, Zhang Y, Yang L, Wang B, Li X. One-step MOFs-assisted synthesis of intimate contact MoP-Cu3P hybrids for photocatalytic water splitting. Chemical Engineering Journal. 2020; 384:123337–59. https://doi.org/10.1016/j.cej.2019.123337
Cu_3P/$ZnIn_2S_4$	Solution-phase	H_2 production (2561.1 μmol g^{-1} $h^{-1)}$	Yang Z, Shao L, Wang L, Xia X, LiuY, Cheng S, Yang C, Li S. Boosted photogenerated carriers separation in *Z*-scheme Cu_3P/$ZnIn_2S_4$ heterojunction photocatalyst for highly efficient H_2 evolution under visible light. International Journal of Hydrogen Energy 2020; 45: 14334–46. https://doi.org/10.1016/j.ijhydene.2020.03.139

https://www.twirpx.org & http://chemistry-chemists.com

Table 1 Summary of phosphide-based visible light-active catalysts for photocatalytic applications. Recent examples of visible light-responsive phosphide photocatalysts—cont'd

Photocatalyst	Synthetic Method	Photocatalytic Performance	Reference
Fe/GTiP	Solution-phase	Degradation of berberine chloride and tetracycline hydrochloride (79%; 89%)	Nahyoon NA, Liu L, Rabé K, Yuan L, Nahyoon SA, Yang, F. An ideal visible nanocomposite (Fe/GTiP) photoanode catalyst for treatment of antibiotics in water and simultaneous electricity generation in the photocatalytic fuel cell panel. International Journal of Hydrogen Energy 2019; 44: 21703–15. https://doi.org/10.1016/j.ijhydene.2019.06.131
Ni_2P	Low-temperature precipitation	Degradation of 4-nitrophenol (25.5%)	Liu X, Zhao L, Wang H, Lai H, Peng G, Li J, Yi Z, Chen, K. Visible-light-driven H_2 production and decomposition of 4-nitrophenol over nickel phosphides. RSC Advances 2018; 8:34259–65. https://doi.org/10.1039/C8RA06770H
Zn:ZnO/Ni_2P	Electrochemical	Degradation of auramine O (95.47%)	Barzegar MH, Ghaedi M, Avargani VM, Sabzehmeidani MM, Sadeghfar F, Jannesar R. Electrochemical synthesis of Zn:ZnO/Ni_2P and efficient photocatalytic degradation of Auramine O in aqueous solution under multi-variable experimental design optimization. Polyhedron 2019; 165:1–8. https://doi.org/10.1016/j.poly.2019.02.003
Co_2P/TiO_2	Hydrothermal	Degradation of methylene blue (88.73%)	Zhang X, Fan X, Wang X, Deng T, Liu E, Chen B. Facile fabrication of Co_2P/TiO_2 nanotube arrays photoelectrode for efficient methylene blue degradation. Colloids and Surfaces A: Physicochemical and Engineering Aspects 2020; 599:124875–901. https://doi.org/10.1016/j.colsurfa.2020.124875
Ni_2P/BCN	Hydrothermal	N_2 reduction (0.010%)	Shiraishi Y, Chishiro K, Tanaka S, Hirai T. Photocatalytic dinitrogen reduction with water on boron-doped carbon nitride loaded with nickel phosphide particles. Langmuir 2020; 36:734–41. https://doi.org/10.1021/acs.langmuir.9b03445.
NiCoOP-NPs@MHCFs	Electrospinning, phosphidation, and carbonization	CO_2 reduction (CO evolution rate (16.6 μmol g^{-1} h^{-1})	Wang Y, Wang S, Lou XWD. Dispersed nickel cobalt oxyphosphide nanoparticles confined in multichannel hollow carbon fibers for photocatalytic CO_2 reduction. Angewandte Chemie International Edition 2019; 58:17236–40. https://doi.org/10.1002/anie.201909707

Continued

https://www.twirpx.org & http://chemistry-chemists.com

Table 1 Summary of phosphide-based visible light-active catalysts for photocatalytic applications. Recent examples of visible light-responsive phosphide photocatalysts—cont'd

Photocatalyst	Synthetic Method	Photocatalytic Performance	Reference
Ni_5P_4/g-C_3N_4	Phosphorization	H_2 production (1157.5 μmol g^{-1} h^{-1})	Liu X, Zhao Y, Yang X, Liu Q, Yu X, Li Y, Tang H, Zhang T. Porous Ni_5P_4 as a promising cocatalyst for boosting the photocatalytic hydrogen evolution reaction performance. Applied Catalysis B: Environmental 2020; 275:119144–78. https://doi.org/10.1016/j.apcatb.2020.119144

A novel MOCVD technique was employed by Jung et al. where GaN was grown in situ on sapphire substrates by e-beam evaporation to synthesize single-crystalline GaN nanowires directly. The photocatalyst exhibited higher activity for photodegradation of organic dye (Orange II) at various pH due to a high surface-to-volume ratio [158]. GaN:ZnO is an example of a stable visible light photocatalyst. The synthetic procedure mostly followed is a solid-phase solution process where the Ga_2O_3 and ZnO mixture is nitrided at elevated temperatures under NH_3 flow [159]. Even though the photocatalyst can catalyze the half-reaction, it is unable to produce H_2 in methanol solution [160]. In view of this, Maeda et al. functionalized GaN:ZnO with a suitable proton reduction cocatalyst like oxygen-insensitive $Rh_{2-y}Cr_yO_3$ and achieved at 410 nm an apparent quantum yield (AQY) of almost 5.1%.

TMNs such as Co_3N [161], Ni_3N [162], and Fe_4N [163] have been reported to be promising cocatalyts for H_2 generation in visible light. Even so, pure-phase TMNs in nanoscale-regime are difficult to synthesize because of the harsh reaction conditions. Meng et al. designed a face-centered cubic chromium titanium nitride ($Cr_{0.5}Ti_{0.5}N$) nanomaterial as an alternative to the Pt cocatalyst via a solid-solid phase separation method under NH_3 flow at high temperature (Fig. 9) [164]. Similarly, a titanium nitride (TN) nanocluster

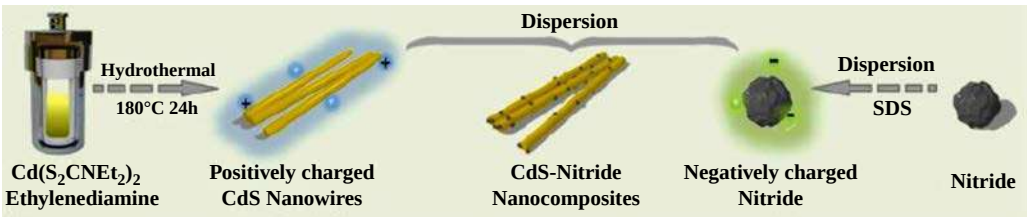

FIG. 9 Representative example of the solid-solid phase separation method. Schematic illustration of synthesis of a one-dimensional $Cr_{0.5}Ti_{0.5}N$-CdS nanocomposite by hydrothermal and nitridation methods. *From Meng X, Qi W, Kuang W, Adimi S, Guo H, Thomas T, et al. Chromium-titanium nitride as an efficient co-catalyst for photocatalytic hydrogen production. J Mater Chem A 2020:Advanced Article. https://doi.org/10.1039/D0TA00488J.*

https://www.twirpx.org & http://chemistry-chemists.com

synthesized through NH_3 nitrification of titania nanotubes at 900°C demonstrated high H_2 yield in a visible light-driven water-splitting reaction [165].

Conventional routes to synthesize Ta_3N_5 include thermal dissociation of tantalum precursors [166] and ammonolysis for $TaCl_5$ and TaS_2 [167, 168]. Reaction between Ta_2O_5 and NH_3 at 750–850°C and for 8–15 h has been reported to prepare pure Ta_3N_5 [169, 170]. However, compared to other visible light-active photocatalysts [171–173], Ta_3N_5 has a comparatively simple structural composition. In view of this, a Ta_3N_5 nanocrystal was prepared by nitridation of oxide powder in the presence of NH_3 at 700°C for 5 h. The semiconductor showed enhanced activity for degradation of methylene blue compared to nitrogen-doped titania nanomaterials [174]. In order to upgrade the performance of Ta_3N_5 along with tailored morphology, flux and alkaline metal (AM) ions were utilized for the synthesis of Ta_3N_5 [175]. In addition, by doping AM ions, Ta_3N_5 performance for water oxidation was improved [176]. Nonetheless, such positive effects are often met by unfavorable flux and dopants residues which result in poor crystallinity and more trap site densities, specifically in photocatalytic O_2 evolution reactions where reduction and oxidation reactions both occur on the semiconductor surface, unlike in photoelectrochemical reactions. Ma et al. developed highly crystallized Ta_3N_5 nanomaterials, nitrided from an AM salt-modified Ta_2O_5 precursor with ammonolysis process (Fig. 10). The photocatalyst yielded six times more improvement in O_2 evolution activity under visible light irradiation [177].

Instead of calcination of metal oxides or metal salts precursors under NH_3 or N_2 for synthesis of TMPs, which unavoidably require demanding reaction conditions, a nitrogen-doped carbon matrix@Mo_2N was developed from heating MoO_3 and melamine pre-treated with HNO_3 at 600°C for 4 h. Subsequently, it was mixed with modified CdS nanorods for an H_2 evolution reaction. In another work, an Mo_2N cocatalyst was prepared by TPR process for 4 h at temperature range 650–850°C [178]. Ternary metal nitrides like

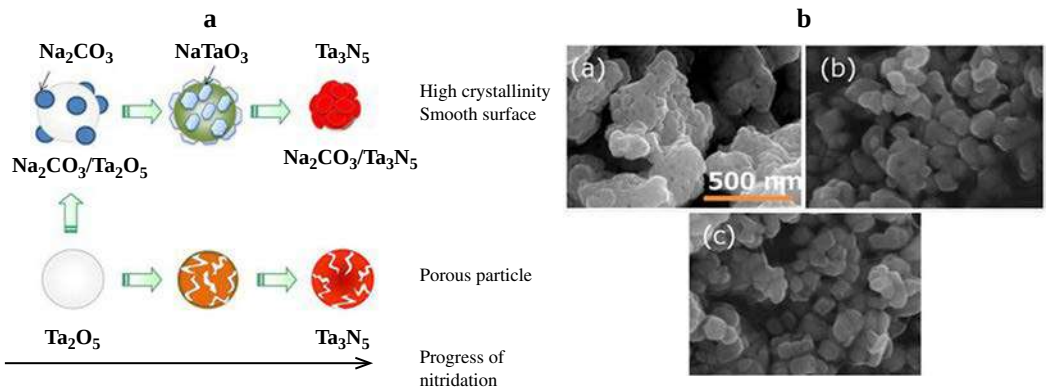

FIG. 10 Representative example of the nitridation process under ammonia flow with SEM images of obtained samples. (A). Illustrative synthesis of conventional Ta_3N_5 and Na_2CO_3/Ta_3N_5. (B). SEM images of Ta_3N_5 (a) unmodified and modified with (b) NaCl and (c) Na_2CO_3. *From Su Khine Ma S, Hisatomi T, Maeda K, Moriya Y, Domen K. Enhanced water oxidation on Ta3N5 photocatalysts by modification with alkaline metal salts. J Am Chem Soc 2012;134:19993–96. https://doi.org/10.1021/ja3095747.*

https://www.twirpx.org & http://chemistry-chemists.com

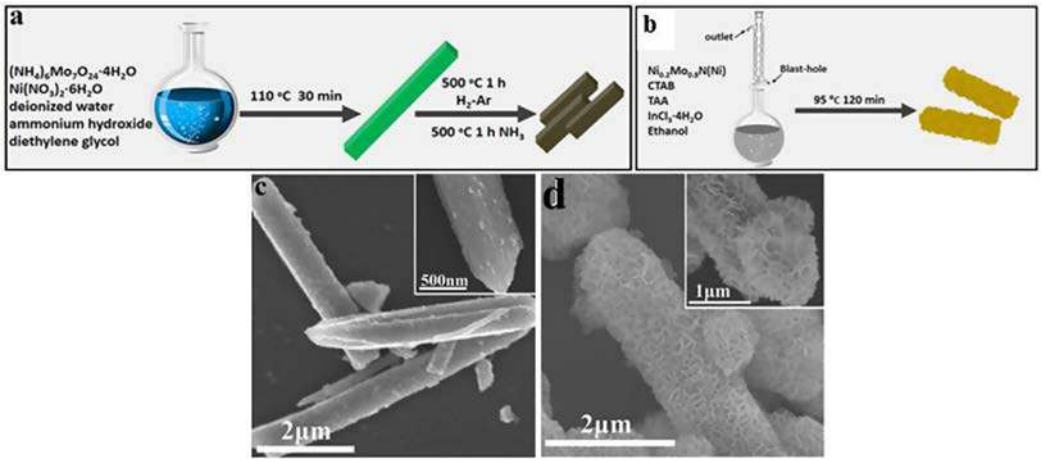

FIG. 11 Representative example of solution-phase synthesis with SEM images of obtained samples. Synthesis of (A) $Ni_{0.2}Mo_{0.8}N$(Ni) material and (B) synthesis of In_2S_3-$Ni_{0.2}Mo_{0.8}N$(Ni) composite, SEM images of (C) $Ni_{0.2}Mo_{0.8}N$(Ni) and (D) In_2S_3-$Ni_{0.2}Mo_{0.8}N$(Ni). *From Wang C, Qi W, Zhou Y, Kuang W, Azhagan T, Thomas T, et al. Ni-Mo ternary nitrides based one-dimensional hierarchical structures for efficient hydrogen evolution. Chemical Engineering Journal 2020;381:122611–20. https://doi.org/10.1016/j.cej.2019.122611.*

Ni-Mo-based one-dimensional hierarchical nanohybrid structures (In_2S_3-$Ni_{0.2}Mo_{0.8}N$(Ni)) have been successfully fabricated by Wang and coworkers to boost H_2 evolution efficiency over a blank In_2S_3 photocatalyst. $Ni_{0.2}Mo_{0.8}N$(Ni) as a primary cocatalyst was designed for the first time using solution-phase synthesis and nitridation under NH_3 flow for 1 h at 500°C, as illustrated in Fig. 11 [179].

One of the rarely reported TMN for visible light-responsive photocatalyst is tungsten nitride (WN). Wang et al. established that black metallic WN served as an overall water-spitting photocatalyst at wavelengths of up to 765 nm. The photocatalyst was synthesized via a two-step process (Fig. 12). The intermediate H_2WO_4 was formed by drying the reaction mixture of ammonium tungstate and concentrated hydrochloric acid aqueous solution, followed by treatment in an NH_3 atmosphere at 600°C for 2 h. Theoretical calculations and experimental results showed that WN displays metallic characteristics, which have a significant role in overall water splitting in red-light illumination. More importantly, PtO_x/WN (50 mg) exhibited 1.08 μmol H_2 and 0.58 μmol O_2 evolution rates after 24 h [180].

Generally, solid-gas reactions have limitations, both thermodynamically and kinetically, due to the severe requirement of high temperature. In order to relatively moderate the reaction parameters, Kachina et al. in his work demonstrated that addition of gaseous oxophilic acceptors, like carbon tetrachloride, to the treatment gas flow may change the reaction pathways for the preparation of highly divided metal nitrides. Traditionally, nitrogen-doped TiO_2 is prepared by oxide nitridation with NH_3 at temperatures above 600°C [181]. However, the "pseudo CVD" [182] regime allowed the nitridation temperature to decrease by about 200°C and at the same time significantly increased the amount of

https://www.twirpx.org & http://chemistry-chemists.com

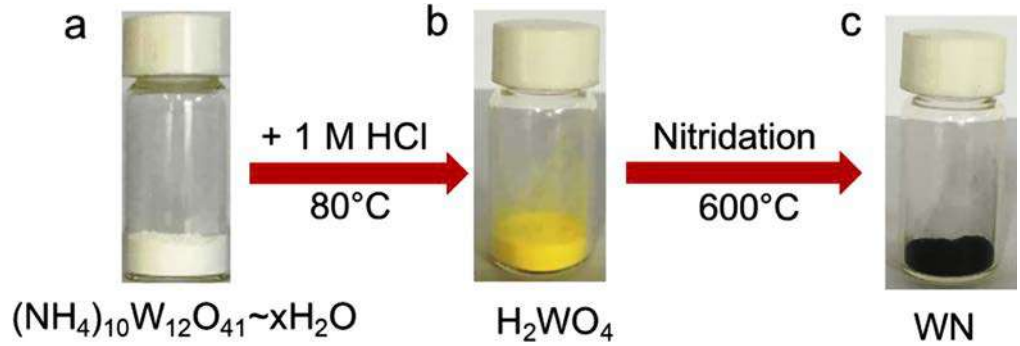

FIG. 12 Representative example of acid- and heat-treatment processes. Photographs of (A) $(NH_4)_{10}W_{12}O_{41\sim x}H_2O$ precursor, (B) intermediate H_2WO_4 and (C) tungsten nitride (WN). *From Lei Wang Y, Nie T, Li YH, Lu Wang X, Zheng LR, Chen AP, et al. Black tungsten nitride as a metallic photocatalyst for overall water splitting operable at up to 765 nm. Angew Chem 2017;129:7538–42. https://doi.org/10.1002/ange.201702943 (Supporting information).*

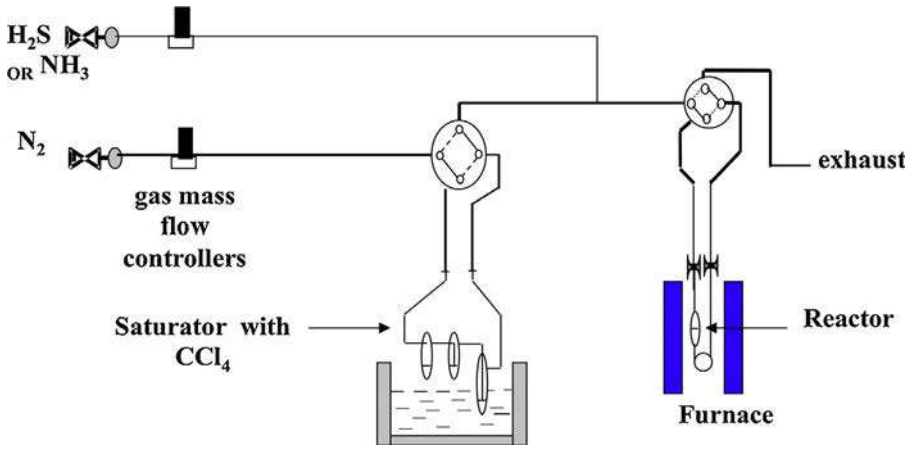

FIG. 13 Representative example of an experimental design using oxophilic molecules under gas flow treatment. Modified standard solid-gas sulfidation/nitridation setup. *From Afanasiev P. New approach to the preparation of highly dispersed transition metals sulfides and nitrides. Catal Today 2015;250:134–44. https://doi.org/10.1016/j.cattod.2014.03.046.*

introduced N_2 for enhanced catalytic activity. The semiconductor obtained by CCl_4-assisted nitridation demonstrates improved visible light activity for H_2 production along with enhanced specific surface area [183], as presented in Fig. 13.

Similar to metal nitrides, synthesis of oxynitrides follow the general approach of heat treatment of reactants in NH_3 and N_2 such as TaON [184]. Ammonolysis involve precursor sources like oxides, binary metal oxides, metal nitrides, or carbonates. As illustrated in Fig. 14, single crystal zinc gallium oxynitride (ZnGaNO) prepared from nitriding a mixture of ZnO and Ga_2O_3 at 800°C for 5 h achieved an enhanced CO_2 reduction [185]. Similarly, Qi and his group designed Ba-modified Ta_3N_5 as a visible light-responsive photocatalyst.

https://www.twirpx.org & http://chemistry-chemists.com

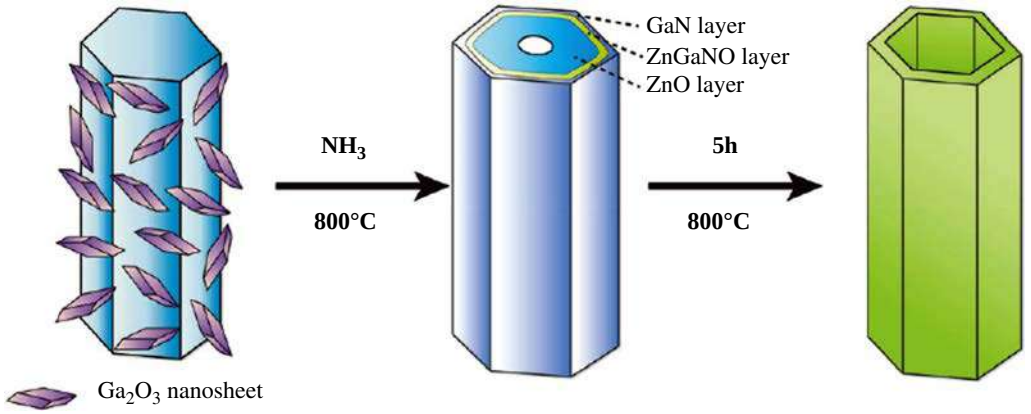

FIG. 14 Representative example of synthesis of oxynitride by heat-treatment method (Kirkendall effect). Schematic illustration showing the preparation of ZnGaNO nanotubes. *From Zhou P, Gao HL, Yan SC, Zou ZG. The Kirkendall effect toward oxynitride nanotubes with improved visible light driven conversion of CO2 into CH4. Dalton Trans 2016;45:3480–3485. https://doi.org/10.1039/C5DT04124D.*

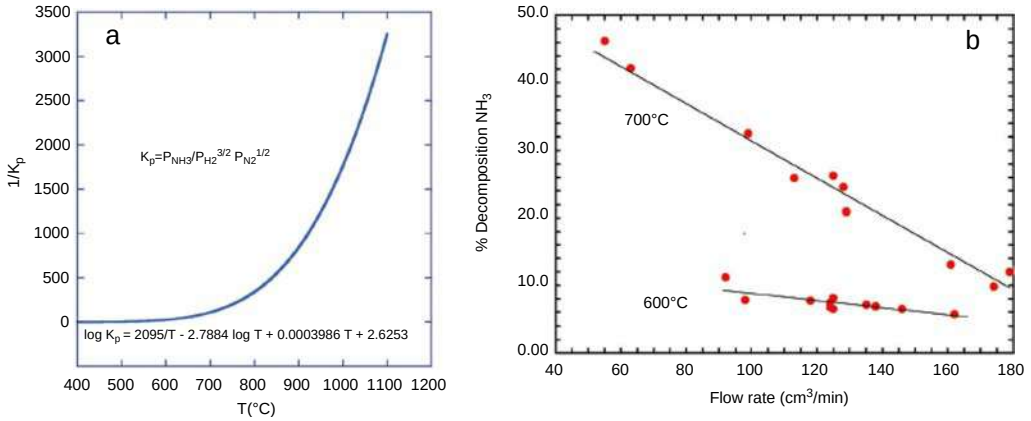

FIG. 15 Kinetics of ammonia decomposition during ammonolysis. (A) Equilibrium constant as temperature function and (B) percent dissociation as a flow rate function at various temperatures. *From Fuertes A. Metal oxynitrides as emerging materials with photocatalytic and electronic properties. Mater Horiz 2015;2:453–61. https://doi.org/10.1039/c5mh00046g.*

$Ta_3N_5/BaTaO_2N$ was synthesized by a simple one-pot nitridation method at 950°C for 20 h [186]. In another example, TaON and Pt-TaON oxynitrides prepared by heat treatment were investigated for photodegradation under visible light irradiation of five polycyclic aromatic hydrocarbons including phenanthrene, anthracene, acenaphthene, benzoanthracene, and pyrene [187].

Ammonia is known to dissociate substantially into corresponding N_2 and H_2 gases at above 500°C (Fig. 15A). The dissociation kinetics is slow and is monitored by the flow rate (Fig. 15B). The key reaction conditions of temperature, flow rate, duration, and sample position govern the gas about the sample and must be reflected to improve the purity

https://www.twirpx.org & http://chemistry-chemists.com

of the oxynitride [188]. The reducing ability of NH_3 and H_2 makes it challenging for stabilization of the oxynitrides of the late transition metals, which results in interstitial nitrides having cations with low oxidation states [189]. However, few cations may get oxidized. For instance, vanadium oxynitrides [$(RVO_{3x}N_x$ (R = La, Pr, Nd)] synthesized under NH_3 in between 650°C and 800°C with monazite or zircon (RVO_4) precursors proceeds over initial reduction of the precursors to RVO_3 which are gradually nitrided and reoxidized into $RVO_{3x}N_x$ with variable V^{4+}/V^{3+} proportions [190].

Because the preparation process of oxynitrides using NH_3 require moderate temperatures, the sintering is testing. High pressure has been utilized for generating 85% above densities [191]. Homogeneity of samples with regard to N stoichiometry is crucial, and in the majority of circumstances numerous treatments are therefore required. Better homogeneous and sintered materials are achieved under N_2 flow, which is implemented at elevated temperatures (1300–1500°C). This requires severe governance of H_2O and O_2 impurities to prevent any undesirable formation of oxides. Usage of carbonate reactants is usual, and they also provide an extra source of O_2. Again, CO_2 decays to CO and O_2 at elevated temperatures (>1300°C) which may react at lower temperatures with nitrides and oxidize N^{3-} to N_2, giving rise to oxides [192]. Common nitrogen sources are amides, imides, urea, and azides [193].

High-pressure techniques have been employed in a few cases for stabilization of quaternary oxynitrides with small cations. For instance, the perovskite $LnZrO_2N$ is synthesized at room pressure for Ln = La and rare earth metals (Pr, Sm, or Nd) are synthesized at 2–3 GPa and 1200–1500°C [194]. Lately, $MnTaO_2N$ has been prepared at 6 GPa and at 1400°C [195]. The benefits of this high-pressure high temperature treatment include improved crystallinity and compensation of N vacancies. In other cases, acid treatments are carried out to chemically remove the surface layers, which could be reasonably nitrided compared to the exterior. Another sought-after posttreatment process is a solution technique known as the flux method [196]. Herein, metals and inorganic compounds having high melting temperatures are taken as solvents, called flux. The expected advantages are that high-quality crystals can be obtained with few defects and the crystals are not affected by the precursors. Over the years, films of oxynitrides have been prepared by techniques like pulsed laser deposition (PLD) [197] (e.g., $LaTiO_2N$) and radio frequency magnetron sputtering [198] (e.g., $LaTiO_2N$).

Ida et al. in their inspirational work designed for the first time calcium tantalum oxynitride by exfoliating parent layered $CsCa_2Ta_3O_{9.7}N_{0.2}$ by a proton-exchange method, a two-step process intercalation of ethylamine and tetrabutylammonium, and subsequent exfoliation. The synthesized nanosheets (mono-, bi-, and trilayers) were about 2.8–3.1 nm thick, nearly 1.3 nm thicker than the precursor perovskite blocks materials due to absorption of water and amine [199]. Recently, a hybrid nanostructure photocatalyst of GaZnON and RGO was fabricated for the first time by Adeli and his coworker. The synthesis of GaZnON was carried out by microwave irradiation, Ga^{3+}/Zn^{2+} layered double hydroxide as the parent material and urea as the soft-template, and finally integrated wholly by a facile electrostatic self-assembly approach. Studies have concluded that by utilizing structural

https://www.twirpx.org & http://chemistry-chemists.com

nanopores and graphene for the redox active sites, the activity was enhanced 7.5-fold in comparison to a 1 wt% Rh-loaded oxynitride semiconductor [200].

A polymeric carbon-based semiconductor, graphitic carbon nitride is generally prepared by polymerization [201, 202], the solvent method [203], a template-directed solid-state reaction [204], soft-templating [205], and sonochemical [206] processes. However, pure g-C_3N_4 cannot produce H_2 or O_2 in water-splitting reactions [207]. Suitable structural optimization is therefore required to overcome this drawback by surface regulation, functionalization, and assembly construction, as illustrated in Fig. 16 [208].

Detailed discussion on the synthetic procedures and surface modification techniques of g-C_3N_4 toward photocatalytic applications is beyond the scope of the current chapter. However, a few recent examples of TMPs and TMNs coupled with g-C_3N_4 have been presented.

Wen and his group reported $Ni_{12}P_5$ modified g-C_3N_4 by a simple and facile grinding method using commercial $Ni_{12}P_5$ nanopowder and g-C_3N_4 [209]. Meso-g-C_3N_4/WP/meso-g-C_3N_4 nanosheets were synthesized by Yang et al. from a solid-phase in-situ reduction reaction combined with the high temperature calcination method (Fig. 17). The unique 3D interbed heterojunction nanosheet structure resulted in 10-fold higher photocatalytic activity compared to g-C_3N_4 [210].

Xia et al. designed a Schottky photocatalyst MoN/2D g-C_3N_4 by a self-assembly and annealing process, as presented in Fig. 18. The photocatalyst demonstrated a high H_2 production rate and 95.5% RhB removal after 1 h. The higher efficiencies than pristine g-C_3N_4 were credited to enhanced charge separation and transportation [211].

A few recent research reports on photocatalysis using nitrides, oxynitrides, and graphitic carbon nitrides photocatalysts are listed in Tables 2 and 3.

In summary, the design and fabrication of materials with improved efficacy is the key for successful implementation of photocatalysis for real-world applications. In this context, various synthesis methods have been discussed together with substantial and recent examples. The next part of the chapter focuses on the in-depth mechanism behind the different photocatalytic applications.

5 Mechanistic pathway proposal

5.1 Role of phosphide

As mentioned earlier, TMPs exhibit different characteristics depending on the type of metal, M/P ratios, and crystal structure. According to the principle by Sabatier, robust metal-hydrogen bonds on transition metal surfaces impede the release of H_2 from the active sites. Remarkably, TMPs exhibit a weak "ligand effect" [212] due to the presence of phosphorus in M-P bonds along with decreased number of sites due to an "ensemble effect." [213] Thus structural alignment of TMPs can expedite H_2 release from such sites. As discussed previously, metal-rich TMPs like Ni_2P, $Ni_{12}P_5$, Co_2P, CoP, and Cu_3P mostly have been used as water-splitting photocatalysts. The elemental chemical states

https://www.twirpx.org & http://chemistry-chemists.com

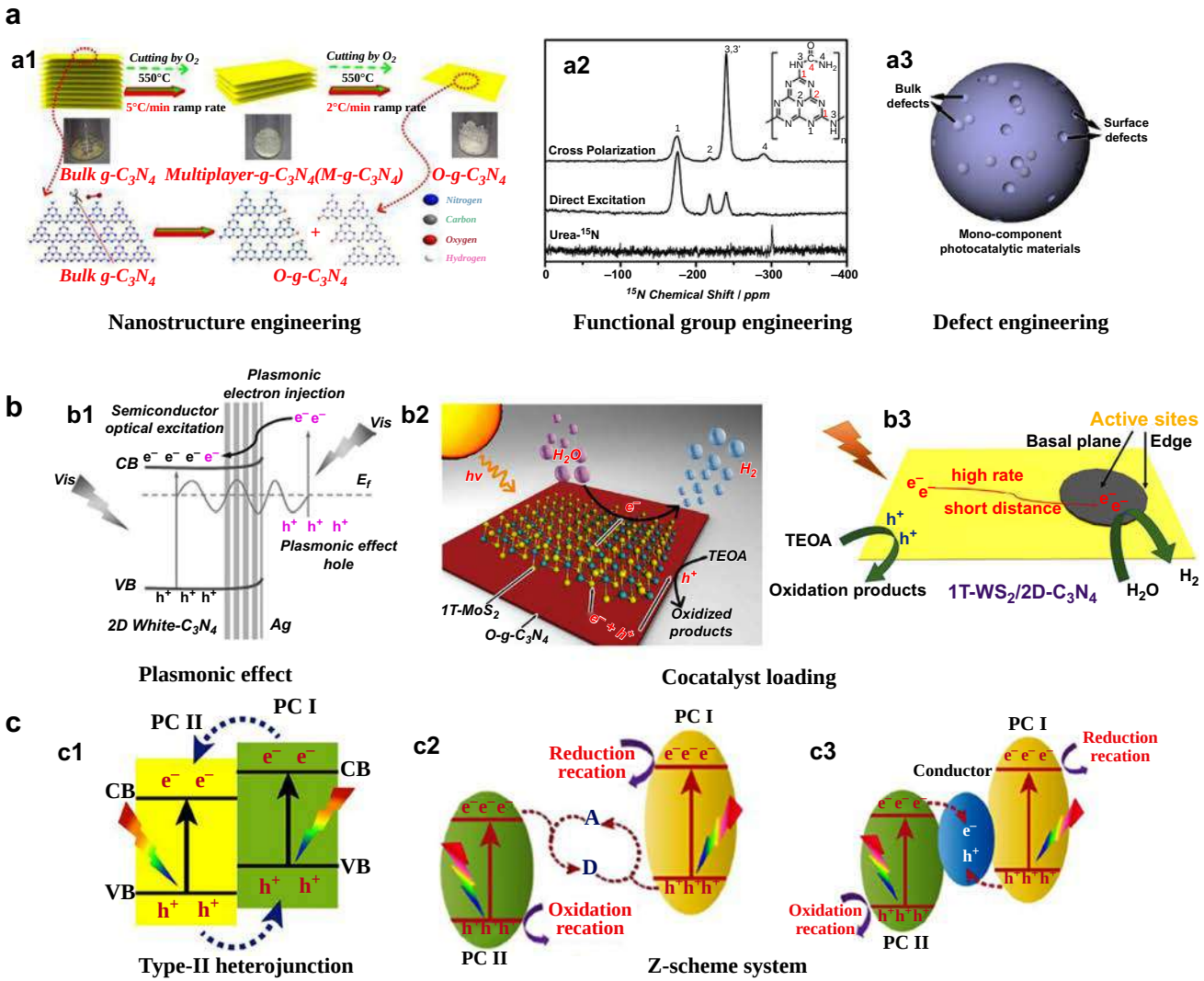

FIG. 16 Different approaches for structural modification of g-C_3N_4. Schematic demonstration of surface strategies. (A) Surface modifications (A1–A3), (B) surface functionalizations (B1–B3) and (C) surface assemblies (C1–C3). *From Yi J, El-Alami W, Song Y, Li H, M. Ajayan P, Xu H. Emerging surface strategies on graphitic carbon nitride for solar driven water splitting. Chem Eng J 2020;382:122812–64. https://doi.org/10.1016/j.cej.2019.122812.*

https://www.twirpx.org & http://chemistry-chemists.com

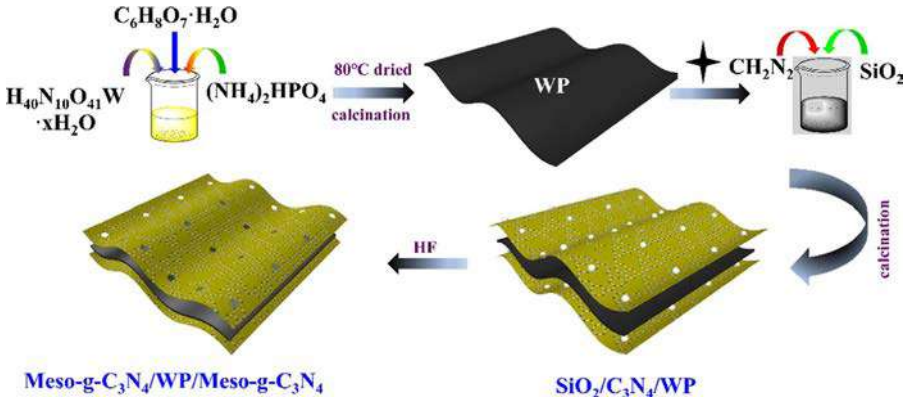

FIG. 17 Representative example of the high temperature calcination method in combination with in-situ solid phase controlled reaction. Preparation process of meso-g-C_3N_4/WP/meso-g-C_3N_4 laminated heterojunction nanosheets. *From Yang Z, Xing Z, Feng Q, Jiang H, Zhang J, Xiao Y, et al. Sandwich-like mesoporous graphite-like carbon nitride (Meso-g-C3N4)/WP/Meso-g-C3N4 laminated heterojunctions solar-driven photocatalysts. J Colloid Interface Sci 2020;568:255–63. https://doi.org/10.1016/j.jcis.2020.02.060.*

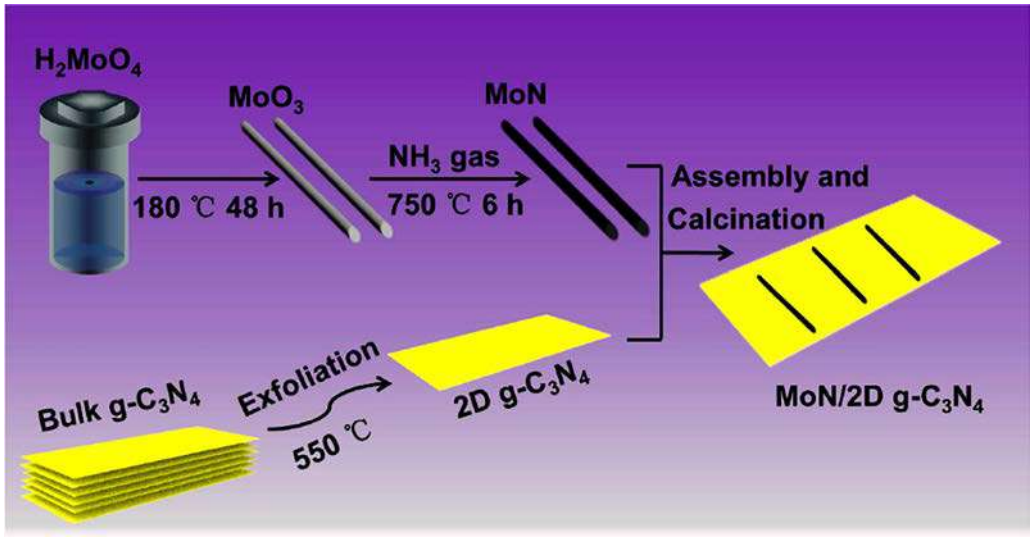

FIG. 18 Representative example of self-assembly method. Scheme for preparation of MoN/2D g-C_3N_4 Schottky catalyst. *From Xia K, Chen Z, Yi J, Xu H, Yu Y, She X, et al. Highly efficient visible-light-driven Schottky catalyst MoN/2D g-C3N4 for hydrogen production and organic pollutants degradation. Indus Eng Chem Res 2018;57:8863–70. https://doi.org/10.1021/acs.iecr.8b01268.*

are usually determined by X-ray photon spectroscopy (XPS). Based on this, almost all the metals and phosphorus exhibit binding energy (BE) values approximately near to zero-valent states. For example, as shown in Fig. 19, the BE of Ni in $Ni_{12}P_5$ was 853.1 eV, almost comparable to Ni^0 (852.8 eV) but with a small positive charge ($Ni^{\delta+}$, $0 < \delta < 2$). The position at 129.7 eV was allotted to P in $Ni_{12}P_5$, having a marginally negative charge in

https://www.twirpx.org & http://chemistry-chemists.com

Table 2 List of nitride- and oxynitride-based visible light-active catalysts for photocatalytic applications. Numerous recent examples of nitride and oxynitride photocatalysts summarized with common synthetic methodologies and corresponding photocatalytic performances.

Photocatalyst	Synthetic method	Photocatalytic performance	Reference
$Mo_2N/Mo_2C/GR/CdS$	Heat-treatment	H_2 production (4520 μmol g^{-1} h^{-1})	Ma B, Wang X, Lin K, Li J, Liu Y, Zhan H, Liu W. A novel ultraefficient non-noble metal composite cocatalyst Mo_2N/Mo_2C/graphene for enhanced photocatalytic H_2 evolution. International Journal of Hydrogen Energy 2017; 42:18977–84. https://doi.org/10.1016/j.ijhydene.2017.05.212
La/Zr codoped $SrTaO_2N$	Thermal ammonolysis	H_2 production (AQE 0.84%)	Wang R, Lin G, Xu X. $SrTaO_2N$ co-doped with La/Zr as promising photocatalysts for water reduction under visible light illumination. Inorganic Chemistry Frontiers 2020; Advance Article. https://doi.org/10.1039/D0QI00361A
ZnGaON ZnGaInON	Urea glass route	H_2 production (12 μmol h^{-1}) H_2 production (16 μmol h^{-1})	Rao T, Saladino ML, Fang Y, Wang X, Giordano C. Multimetallic oxynitrides nanoparticles for a new generation of photocatalysts. Chemistry-A European Journal 2019; 25:16676–82. https://doi.org/10.1002/chem.201904033
IrO_x(1 wt%)-$LaHfO_2N$	Solid-state reaction	O_2 evolution rate (9 μmol h^{-1})	Black AP, Suzuki H, Higashi M, Frontera C, Ritter C, De C, Sundaresan A, Abeb R, Fuertes A. New rare earth hafnium oxynitride perovskites with photocatalytic activity in water oxidation and reduction. Chemical Communications 2018; 54:1525–28. https://doi.org/10.1039/C7CC08965A
$SrTaO_2N$-$CaTaO_2N$	Ammonolysis	O_2 evolution (AQE 1.67%)	Wang Y, Wei S, Xu X. $SrTaO_2N$-$CaTaO_2N$ solid solutions as efficient visible light active photocatalysts for water oxidation and reduction. Applied Catalysis B: Environmental 2020; 263:118315–25. https://doi.org/10.1016/j.apcatb.2019.118315
V-Ta_3N_5	Heat-treatment	CO_2 reduction (H_2 evolution rate 56 mmol g_{cat}^{-1} h^{-1})	Nguyen TDC, Nguyen TPLC, Mai HTT, Dao VD, Nguyen MP, Nguyen VN. Novel photocatalytic conversion of CO_2 by vanadium-doped tantalum nitride for valuable solar fuel production. Journal of Catalysis 2017; 352:67–74. https://doi.org/10.1016/j.jcat.2017.04.020
TaON	Nitridation and hydrothermal	CO_2 reduction (C_2H_5OH evolution rate 2.03 μmol g_{cat}^{-1} h^{-1})	Han Q, Zhou Y, Tang L, Li P, Tu W, Li L, Li H, Zou Z. Synthesis of single-crystalline, porous TaON microspheres toward visible light photocatalytic conversion of CO_2 into liquid hydrocarbon fuels. RSC Advances 2016; 6:90792–96. https://doi.org/10.1039/C6RA19368D

Continued

https://www.twirpx.org & http://chemistry-chemists.com

Table 2 List of nitride- and oxynitride-based visible light-active catalysts for photocatalytic applications. Numerous recent examples of nitride and oxynitride photocatalysts summarized with common synthetic methodologies and corresponding photocatalytic performances—cont'd

Photocatalyst	Synthetic method	Photocatalytic performance	Reference
CuO-$TiO_{2x}N_x$	Thermal decomposition and annealing	CO_2 reduction (CH_4 evolution rate 41.3 ppm g^{-1} h^{-1})	In SI, Vaughn DD, Schaak RE. Hybrid CuO-$TiO_{(2-x)}N_{(x)}$ hollow nanocubes for photocatalytic conversion of CO_2 into methane under solar irradiation. Angewandte Chemie International Edition 2012; 51:3915–18. doi.org/1002/anie.201108936
$(Zn_{1+x}Ge)(N_2O_x)$	Nitridation	CO_2 reduction (CH_4 evolution rate (0.098 μmol h^{-1})	Liu Q, Xu M, Zhou B, Liu R, Tao F, Mao G. Unique zinc germanium oxynitride hyperbranched nanostructures with enhanced visible light photocatalystic activity for CO_2 reduction. European Journal of Inorganic Chemistry 2017; 2017:2195–200. https://doi.org/10.1002/ejic.201700044
TiO_2@$TiO_{1-x}N_x$	Nitridation	Degradation of methylene blue (60%)	Yoo JB, Yoo HJ, Jung HJ, Kim HS, Bang S, Choi J, Suh H, Lee JH, Kimb JG, Hur NH. Titanium oxynitride microspheres with the rock-salt structure for use as visible light photocatalysts. Journal of Materials Chemistry A 2016; 4:869–76. https://doi.org/10.1039/C5TA06758H
CoO_x-ABO_2N (A = Ca, Sr, Ba, La; B = Nb, Ta)	Hydrothermal ammonolysis	Degradation of methyl orange	Oehler F, Ebbinghaus SG. Photocatalytic properties of CoO_x-loaded nano-crystalline perovskite oxynitrides ABO_2N (A = Ca, Sr, Ba, La; B = Nb, Ta). Solid State Sciences 2016; 54:43–48. https://doi.org/10.1016/j.solidstatesciences.2015.09.003
t-ZrO_2/SiOC(N)	Cross-linking polymerization	Degradation of methylene blue (72%)	Bhaskar S, Awin EW, Kumar KCH, Abhijeet Lale, Bernard S, Kumar R. Design of nanoscaled heterojunctions in precursor-derived t-ZrO_2/SiOC(N) nanocomposites: Transgressing the boundaries of catalytic activity from UV to visible light. Scientific Reports 2020; 10:430–443. https://doi.org/10.1038/s41598-019-57,394-8
MoS_2/TaON	Heat-treatment	Degradation of Rhodamine B (75%)	Chen Y, Tan L, Sun M, Lu C, Kou J, Xu Z. Enhancement of photocatalytic performance of TaON by combining it with noble-metal-free MoS_2 cocatalysts. Journal of Materials Science 2019; 54:5321–30. https://doi.org/10.1007/s10853-018-03214-9

Note: *AQE*, apparent quantum efficiency.

https://www.twirpx.org & http://chemistry-chemists.com

Table 3 List of graphitic carbon nitride composites as visible light-active catalysts for photocatalytic applications. Recently developed graphitic carbon nitride based photocatalysts prepared from different types of strategy and their photodisinfection, photodegradation, and water-splitting performances.

Photocatalyst	Synthetic method	Photocatalytic performance	Reference
Bacteria-treated g-C_3N_4nanosheets	Thermal polymerization	Photodisinfection efficiency to *E. coli* (1×10^7 CFU mL^{-1}) 100%	Kang S, Huang W, Zhang L, He M, Xu S, Sun D, Jiang X. Moderate bacterial etching allows scalable and clean delamination of g-C_3N_4 with enriched unpaired electrons for highly improved photocatalytic water disinfection. ACS Applied Materials & Interfaces 2018; 10:13796–804. https://doi.org/10.1021/acsami.8b00007
g-C_3N_4 nanosheets	Heat-treatment	Photodisinfection efficiency to bacteriophage MS2 (1×10^8 PFU mL^{-1}) 100%	Zhang C, Li Y, Zhang W, Wang P, Wang C. Metal-free virucidal effects induced by g-C3N4 under visible light irradiation: statistical analysis and parameter optimization. Chemosphere 2018; 195:551–58. https://doi.org/10.1016/j.chemosphere.2017.12.122
g-C_3N_4/EP	Thermal method	Photodisinfection efficiency to *E. coli* (1×10^8 CFU mL^{-1}) 100%	Zhang C, Li Y, Shuai D, Zhang W, Niu L, Wang L, Zhang H. Visible light driven, water-surface-floating antimicrobials developed from graphitic carbon nitride and expanded perlite for water disinfection. Chemosphere 2018; 208: 84–92. https://doi.org/10.1016/j.chemosphere.2018.05.163
Porous g-C_3N_4 nanosheets	Hydrothermal etching	Photodegradation efficiency on methylene blue (100%)	Xu J, Wang Z, Zhu Y. Enhanced visible light-driven photocatalytic disinfection performance and organic pollutants degradation activity of porous g-C_3N_4 nanosheets. ACS Applied Materials & Interfaces 2017; 9: 27727–35. https://doi.org/10.1021/acsami.7b07657
UiO-66/g-C_3N_4	Annealing	Photodegradation efficiency on methylene blue (100%)	Zhang Y, Zhou J, Feng Q, Chen X, Hu Z. Visible light photocatalytic degradation of MB using UiO-66/g-C_3N_4 heterojunction nanocatalyst. Chemosphere 2018; 212:523–32. https://doi.org/10.1016/j.chemosphere.2018.08.117
S-doped g-C_3N_4	Thermal method	H_2 and O_2 production (24.6 and 14.5 μmol h^{-1})	Lin YR, Dizon GVC, Yamada K, Liu CY, Venault A, Lin HY, Yoshida M, Hu C. Sulfur-doped g-C_3N_4 nanosheets for photocatalysis: *Z*-scheme water splitting and decreased biofouling. Journal of Colloid and Interface Science 2020; 567:202–12. https://doi.org/10.1016/j.jcis.2020.02.017

Continued

https://www.twirpx.org & http://chemistry-chemists.com

Table 3 List of graphitic carbon nitride composites as visible light-active catalysts for photocatalytic applications. Recently developed graphitic carbon nitride based photocatalysts prepared from different types of strategy and their photodisinfection, photodegradation, and water-splitting performances—cont'd

Photocatalyst	Synthetic method	Photocatalytic performance	Reference
g-C_3N_4/Fe_xP	Hydrothermal and phosphidation	H_2 production (166.4 μmol g^{-1} h^{-1})	Zhao H, Wang J, Dong Y, Jiang P. Noble-metal-free iron phosphide cocatalyst loaded graphitic carbon nitride as an efficient and robust photocatalyst for hydrogen evolution under visible light irradiation. ACS Sustainable Chemistry & Engineering 2017; 5:8053–60. https://doi.org/10.1021/acssuschemeng.7b01665
Cu_3P/g-C_3N_4	Phosphorization	H_2 production (277.2 μmol g^{-1} h^{-1})	Wang W, Zhao X, Cao Y, Yan Z, Zhu R, Tao Y, Chen X, Zhang D, Li G, Phillips DL. Copper phosphide-enhanced lower charge trapping occurrence in graphitic-C_3N_4 for efficient noble-metal-free photocatalytic H_2 evolution. ACS Applied Materials & Interfaces 2019; 11:16527–37. https://doi.org/10.1021/acsami.9b01421
NiFeP/g-C_3N_4	Phosphatization	H_2 production (3.549 mmol g^{-1} h^{-1})	Zhu Q, Qiu B, Duan H, Gong Y, Qin Z, Shen B, Xing M, Zhang J. Electron directed migration cooperated with thermodynamic regulation over bimetallic NiFeP/g-C_3N_4 for enhanced photocatalytic hydrogen evolution. Applied Catalysis B: Environmental 2019; 259:118078–87. https://doi.org/10.1016/j.apcatb.2019.118078
CdS/Boron-CN	Photodeposition	Photoreduction of CO_2 (CO production rate 12.5 μmol h^{-1})	Zhou M, Wang S, Yang P, Huang C, Wang X. Boron carbon nitride semiconductors decorated with CdS nanoparticles for photocatalytic reduction of CO_2. ACS Catalysis 2018; 8:4928–36. https://doi.org/10.1021/acscatal.8b00104

Note: *CFU*, colony-forming unit; *PFU*, plaque-forming unit.

comparison to P ($P^{\delta-}$, $0 < \delta < 1$). The peak positions at 856.0, 860.9, and 132.8 eV corresponded to the oxidized states of Ni and P, owing to air exposure. Hence, XPS study revealed that the metal-rich TMPs possessed properties analogous to zero-valent metals. Simultaneously, the M-P bonds have charge-transfer characteristics. Viewing this from another perspective, electron delocalization inside the metal sublattice might be regarded as somewhat similar to the [NiFe] hydrogenase catalytic reaction [214].

Several theoretical studies based on density functional theory (DFT) have been successful to provide insight on TMPs. Liu and Rodriguez concluded in their inspirational

https://www.twirpx.org & http://chemistry-chemists.com

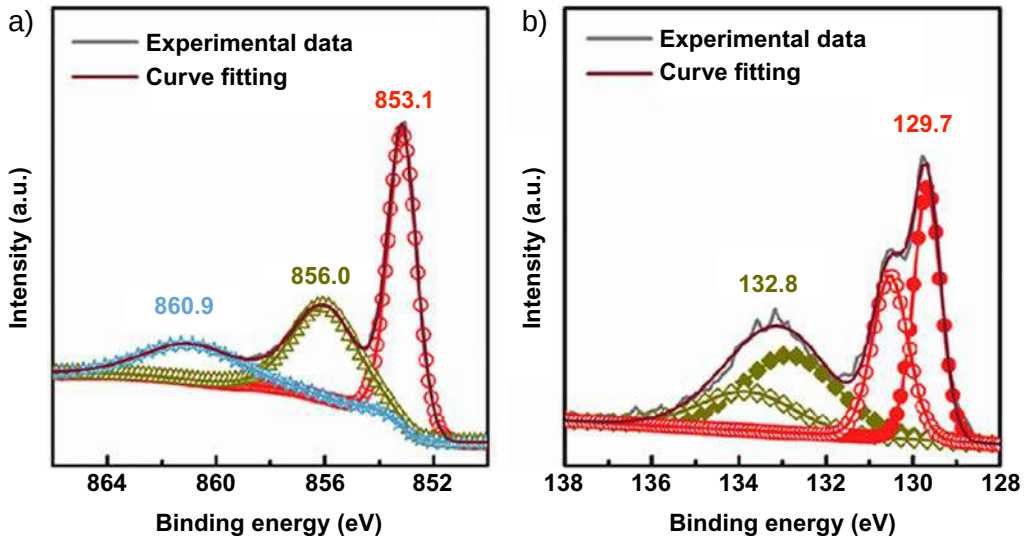

FIG. 19 Determination of chemical states of Ni and P in $Ni_{12}P_5$ nanoparticles. XPS spectra of (A) Ni 2p 3/2 and (B) P 2p of $Ni_{12}P_5$ nanoparticles. *From Huang Z, Chen Z, Chen Z, Lv C, Meng H, Zhang C. Ni12P5 Nanoparticles as an efficient catalyst for hydrogen generation via electrolysis and photoelectrolysis. ACS Nano 2014;8:8121–29. https://doi.org/10.1021/nn5022204.*

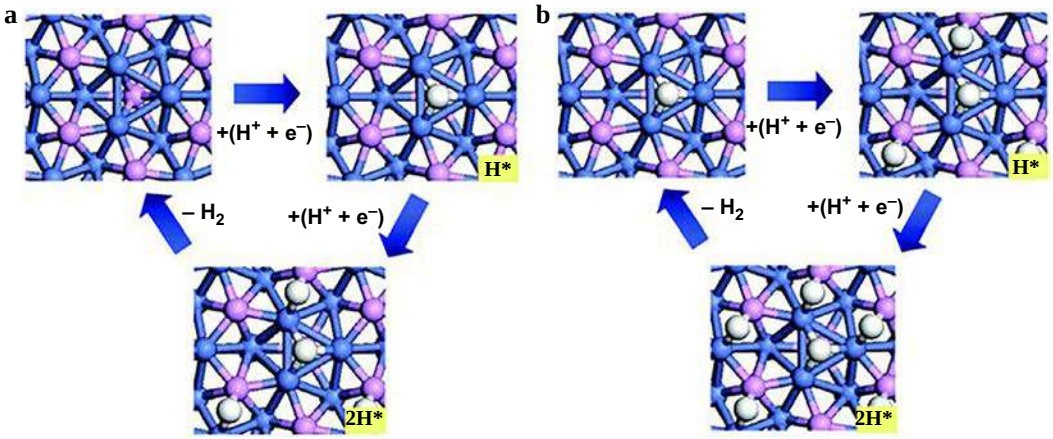

FIG. 20 Density functional theory studies on nickel phosphide. Optimized structures in a HER catalytic cycle on (A) Ni_2P (001) and (B) H-poisoned Ni_2P(001) surfaces. *From Liu P, Rodriguez JA. Catalysts for hydrogen evolution from the [NiFe] hydrogenase to the Ni2P(001) surface: the importance of ensemble effect. J Am Chem Soc 2005;127:14871–14,878. https://doi.org/10.1021/ja0540019.*

work from DFT calculations that Ni_2P could act like a water reduction catalyst. In particular, the H-poisoned Ni_2P (001) surface might drastically advocate the activity of the Ni-P bridge sites, as illustrated in Fig. 20 [215]. Furthermore, the ensemble effect between Ni and P, along with hollow Ni sites, was considered a milestone for the hydrogen evolution reaction. Again in 2008, the electronic structural profile for a series of TMPs were

https://www.twirpx.org & http://chemistry-chemists.com

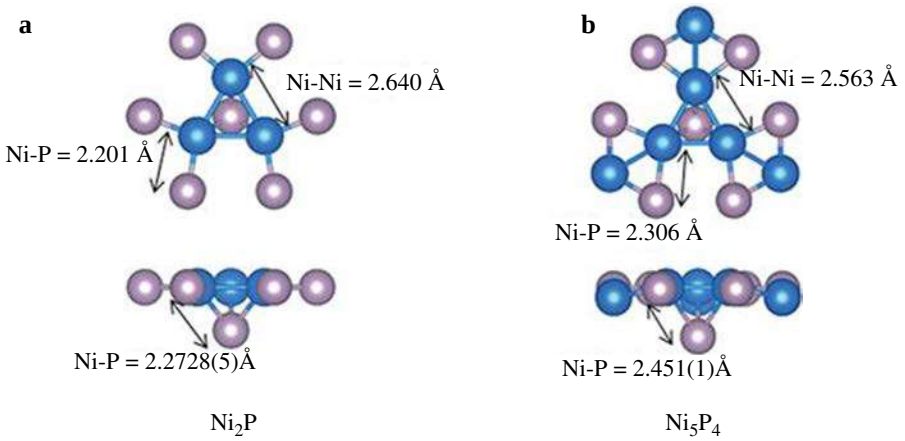

FIG. 21 Comparative density functional theory studies on nickel phosphides. Proposed active sites on (A) Ni_2P (001) and (B) Ni_5P_4 (001) surfaces. *From Laursen AB, Patraju KR, Whitaker MJ, Retuerto M, Sarkar T, Yao N, et al. Nanocrystalline Ni5P4: a hydrogen evolution electrocatalyst of exceptional efficiency in both alkaline and acidic media. Energy Environ Sci 2015;8:1027–1034. https://doi.org/10.1039/C4EE02940B.*

computed using different DFT codes [55]. Considering Ni_2P as an example, the computed DOS indicated a metallic situation along with plausible electron localization at the CB level [216].

Laursen et al. in 2015 proposed that Ni_5P_4 had a structure similar to that of the Ni_2P (001) surface. Additionally, the H_2 evolution rate was credited to the heightened BE of the first hydrogenic intermediate that in turn accelerated the second proton affinity (Fig. 21) [56]. Besides this, it was also pointed out that the d electron density states between the Ni atom and the P atom were parallel to Pt. This indicated that Ni_2P may possibly behave like noble metals [217]. In addition, DFT studies have shown that P atoms being more electronegative can attract a higher number of electrons from metal atoms, and the P atoms being negatively charged can act as trapping sites for H^+ ions, thus boosting catalytic activity. Furthermore, the TMPs tend to adopt triangular prismatic structures owing to the larger size of P atoms (0.109 nm). This possibly results in increased quantities of coordinatively unsaturated atoms that fundamentally display high catalytic activity [131].

TMPs in hybrid heterojunction configuration can behave like a potential interfacial bridge to bring about enhanced charge separation and high photoactivity. A recent example to illustrate this point is g-C_3N_4 enriched with CoP nanodots with distinctive P(δ^-)-Co(δ^+)-N(δ^-) bonding states. Results based on X-ray absorption near edge structure (XANES) and Fourier transform (FT) of extended X-ray absorption fine structure (EXAFS) spectrum demonstrate that the formation of the bonding states on CoP/g-C_3N_4 is due to charge transfer between the atoms, as presented in Fig. 22A and B [218]. Furthermore, the proposed mechanism for the H_2 evolution is based on a dual synergistic molecular reaction mechanism, as illustrated in Fig. 22C.

https://www.twirpx.org & http://chemistry-chemists.com

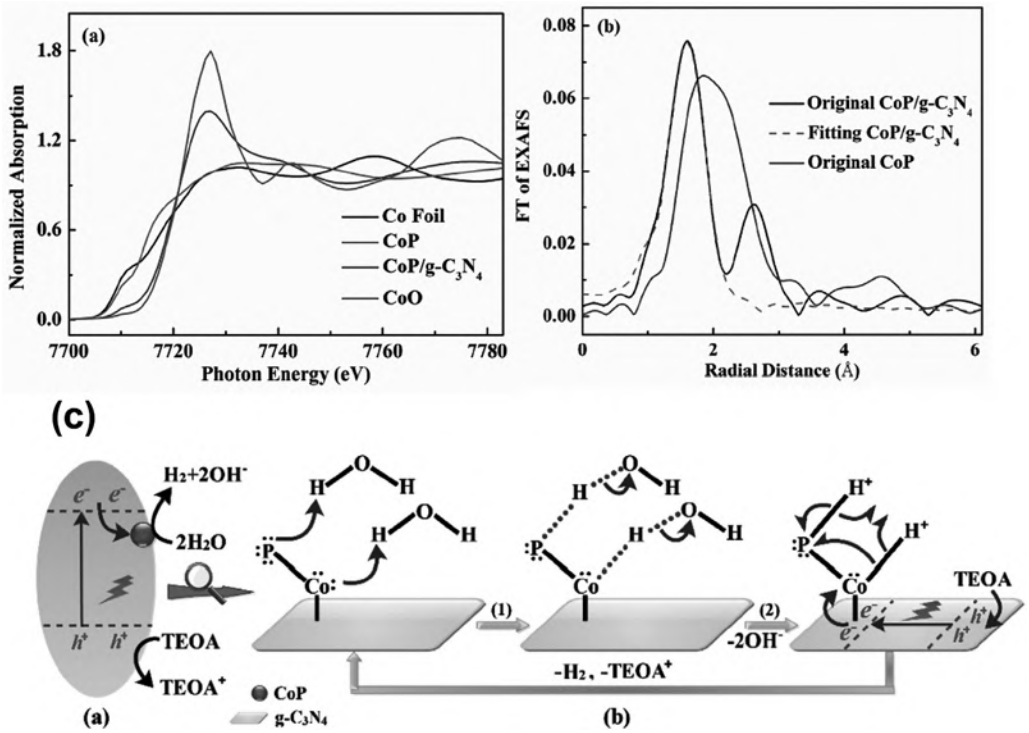

FIG. 22 Investigation of surface bonding states in CoP/g-C_3N_4. (A) Co K-edge XANES spectra, (B) FT of EXAFS spectra (CoP and CoP/g-C_3N_4), and (C) proposed photocatalytic mechanism of CoP/g-C_3N_4. *From Li C, Du Y, Wang D, Yin S, Tu W, Chen Z, et al. Unique P-Co-N surface bonding states constructed on g-C3N4 nanosheets for drastically enhanced photocatalytic activity of H2 evolution. Adv Funct Mater 2017;27:1604328–36. https://doi.org/10.1002/adfm.201604328.*

Another notable example with regard to RhB degradation using visible light irradiation is CoP/Fe_2P@mC photocatalyst designed by Hu et al. [66]. A probable mechanism was presented from radical trapping and electron spin resonance results (Fig. 23).

The main reaction steps are outlined as follows:

$$\mathrm{RhB} + h\upsilon \rightarrow \mathrm{RhB}^{*} \tag{16}$$

$$\mathrm{CoP/Fe_2P@mC} + h\upsilon \rightarrow \mathrm{CoP/Fe_2P@mC}\,(\mathrm{h}^{+} + \mathrm{e}^{-}) \tag{17}$$

$$\mathrm{RhB}^{*} + \mathrm{CoP/Fe_2P@mC} \rightarrow \mathrm{RhB} + + \mathrm{CoP/Fe_2P@mC}\,(\mathrm{e}^{-}) \tag{18}$$

$$\mathrm{O_2} + \mathrm{e}^{-} \rightarrow {}^{\bullet}\mathrm{O_2}^{-} \tag{19}$$

$${}^{\bullet}\mathrm{O_2}^{-} + \mathrm{H_2O} \rightarrow {}^{\bullet}\mathrm{OH} + \mathrm{OH}^{-} \tag{20}$$

$$\mathrm{RhB} + \text{active species}\,({}^{\bullet}\mathrm{O_2}^{-}\mathrm{h}^{+} \text{ and } {}^{\bullet}\mathrm{OH}) \rightarrow \text{degraded dye} \tag{21}$$

https://www.twirpx.org & http://chemistry-chemists.com

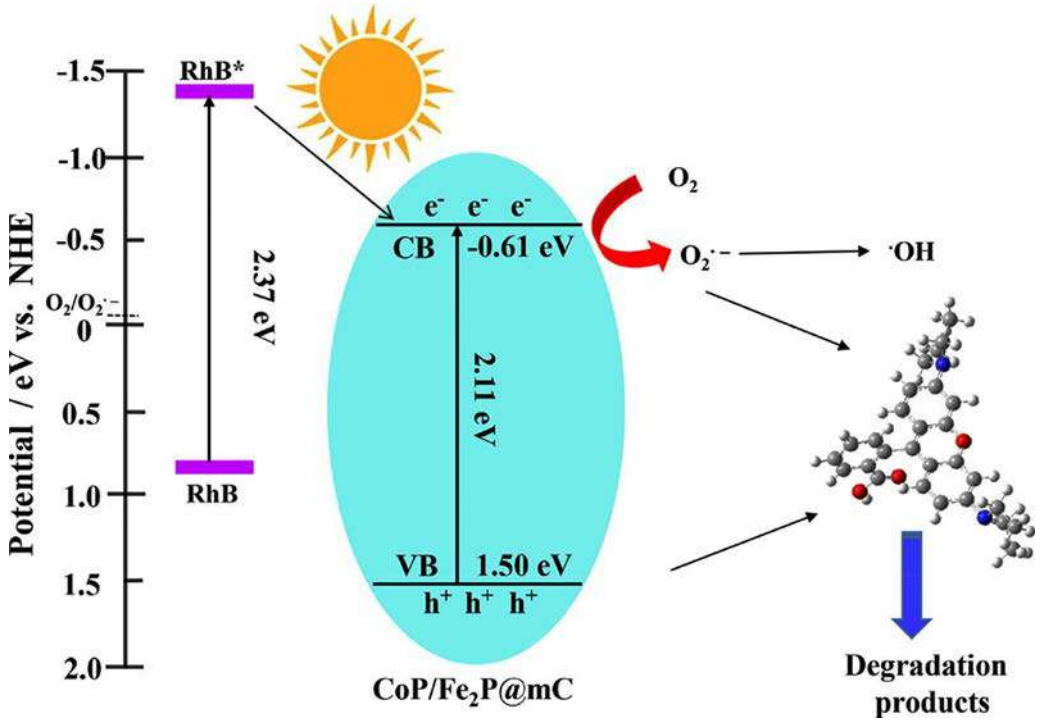

FIG. 23 Proposed mechanism of RhB degradation at visible light illumination. Photodegradation mechanism of RhB by CoP/Fe_2P@mC nanocomposite. *From Hu B, Yuan J, Tian J, Wang M, Wang X, He L, et al. Co/Fe-bimetallic organic framework-derived carbon-incorporated cobalt-ferric mixed metal phosphide as a highly efficient photocatalyst under visible light. J Colloid Interface Sci 2018;531:148–59. https://doi.org/10.1016/j.jcis.2018.07.037.*

5.2 Role of nitride and oxynitride

Nitrides and oxynitrides have been recognized as promising new materials for high-performing photocatalytic applications. The presence of nitrogen even at doping level expands the opportunities of tuning band-alignment properties of semiconductors. It is well-known that nitrogen, being less electronegative and having more polarizability than oxygen, displays a better bonding covalency with metals. This results in decreased inter-electronic repulsion with increased nephelauxetic effect. Again, due to the higher charge present in nitrides, the crystal field splitting is larger. The (−)3 charge on the nitride anion could permit the development of new compounds. Thus the VB of (oxy)nitrides consist of hybridized N 2p and O 2p orbitals, where the larger contribution comes from the N 2p orbitals. The higher VB edge results in a lower bandgap compared to oxides [94]. For example, the VBM of TaON shifts from +2.0 to 1.5 V vs. NHE in Ta_3N_5. Similarly, the CBM also shows a shift. As a consequence, the absorption bands of TaON and Ta_3N_5 lie at 500 and 600 nm, respectively, and thus become suitable for photocatalytic applications. Similarly, in (oxy)nitrides (MoN), the N atoms mostly inhabit the largest interstitial sites in a metal sublattice [219].

https://www.twirpx.org & http://chemistry-chemists.com

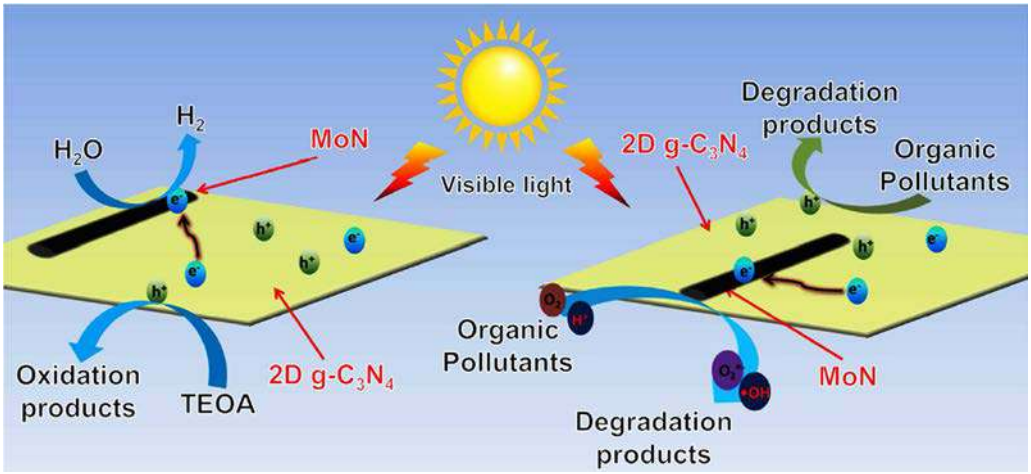

FIG. 24 Elucidating the photocatalytic activity of MoN/2D g-C_3N_4 based on metal-semiconductor junction principles. Scheme of proposed mechanism for MoN/2D g-C_3N_4. *From Xia K, Chen Z, Yi J, Xu H, Yu Y, She X, et al. Highly efficient visible-light-driven Schottky catalyst MoN/2D g-C3N4 for hydrogen production and organic pollutants degradation. Indus Eng Chem Res 2018;57:8863–70. https://doi.org/10.1021/acs.iecr.8b01268.*

As an illustrative example, a photocatalytic mechanism of MoN/2D g-C_3N_4 toward H_2 evolution and RhB degradation has been proposed (Fig. 24) [211]. The Schottky junction present in the photocatalyst promotes electron mobility from 2D g-C_3N_4 to MoN. The excellent conductivity of MoN facilitates the rapid transfer of electrons to its surface, which are subsequently captured by H^+, accomplishing the reduction process and finally the generation of H_2. During the photocatalytic dye degradation reaction, the holes and the $\bullet O_2^-$ radicals produced on the CB of g-C_3N_4 oxidize RhB. Moreover, MoN improves the surface charge carrier density to a great extent and generates •OH radicals, which further improve the oxidation ability.

Generally, the metastable nature of TMNs frequently leads to unavoidable formation of impurities throughout the fabrication process. Qi et al. studied the effects of oxidized impurity in Ni_3N and found that in fact, heterojunctions created during the calcination process clearly result in enhanced efficiency through a *Z*-scheme pathway over NiO-Ni_3N/g-C_3N_4, as presented in Fig. 25 [211].

Oxynitride and perovskite oxynitrides were reported by experimental studies to produce N_2 in the premature period of a photocatalytic reaction, as evidenced by self-oxidation of N^{3-} anions by holes [220–222]. The evolution rate of N_2 was found to be associated with a drop in O_2 evolution (OER) activity with increasing reaction time, the emergence of the second effect still being unspecified. Ouhbi and his coworker by means of DFT calculations investigated the repercussion of anionic vacancies on the OER activity using $SrTaO_2N$ (001) as a prototype [223]. According to Fig. 26 I and II, an energetic inclination exists for both the vacancies to occupy the catalyst surface layers, automatically healed by *O and *OH adsorbates during the OER conditions. Self-healing of the nitrogen vacancies causes a change in the stoichiometry ($Ta_4O_{8+x}N_{4-x}$), along with

https://www.twirpx.org & http://chemistry-chemists.com

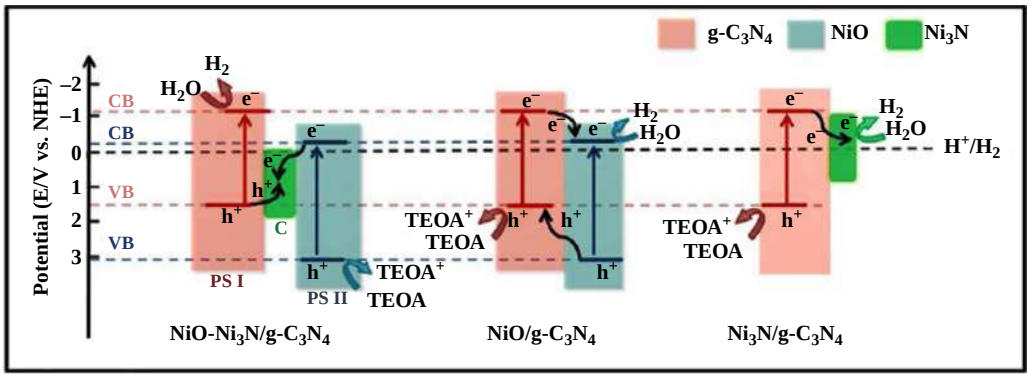

FIG. 25 Formation of Z-scheme pathway from metal oxide-metal nitride heterojunction. Proposed schematic illustration of charge separation process in NiO-Ni_3N/g-C_3N_4, NiO/g-C_3N_4, and Ni_3N/g-C_3N_4 composites. *From Qi W, Zhou Y, Liu S, Liu H, Shu Hui L, Turak A, et al. Oxidized impurity in transition metal nitride for improving the hydrogen evolution efficiency of transition metal nitride-based catalyst. Appl Mater Today 2020;18:100476–85. https://doi.org/10.1016/j.apmt.2019.100476.*

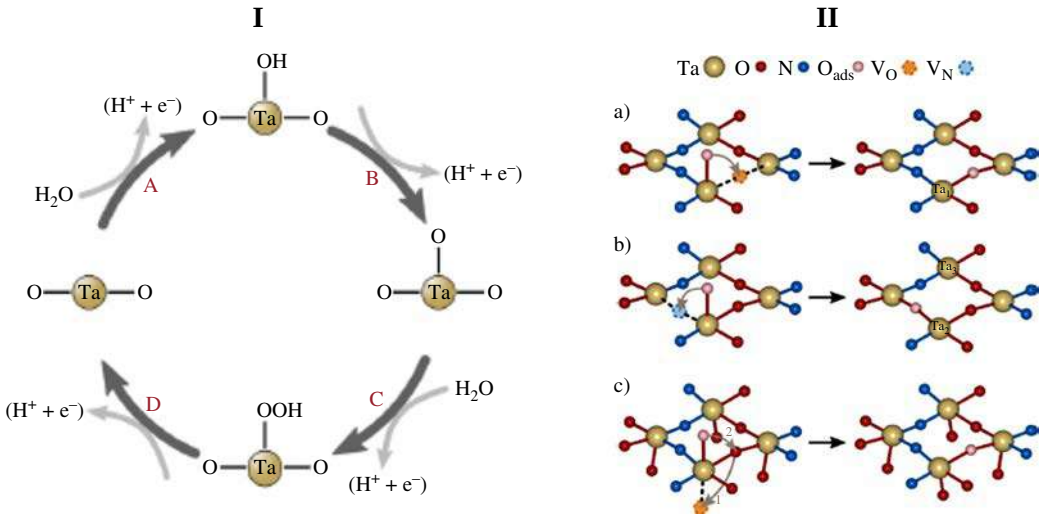

FIG. 26 Investigation of anionic vacancies on oxygen evolution reaction activity of perovskite oxynitride by DFT calculations. (I) Schematic illustration of OER mechanism and (II) self-healing of anion vacancies on TaON-terminated (001) surface in $SrTaO_2N$ (A) surface oxygen vacancy (VO1), (B) surface nitrogen vacancy (VN1), and (C) subsurface oxygen vacancy VO2. *From Ouhbi H, Aschauer U. Nitrogen loss and oxygen evolution reaction activity of perovskite oxynitrides. ACS Mater Lett 2019;1:52–57. https://doi.org/10.1021/acsmaterialslett.9b00088.*

electron doping. The decreased N content gives rise to tensile strain, which borders the surplus charge onto the surface, thus governing the BE of the intermediates and substantially escalating the OER overpotential. Hence, the changes in the electronic structure provide an atomic-scale rational clarification on the decreased OER activity in oxynitride photocatalysts. The result also emphasizes the importance of using protective coatings, cocatalysts, or codoping to halt the self-oxidation process of nitrogen.

https://www.twirpx.org & http://chemistry-chemists.com

Jia et al. studied the synergistic effect of nitride and oxynitride semiconductors coupled together by constructing a unique type II heterostructured photocatalyst system (Ta_3N_5/STON) composed of 1D Ta_3N_5 nanorods and 0D $SrTaO_2N$ (STON) nanoparticles toward hydrogen evolution. It is well-known that the type II heterojunction system is very effective for supporting interfacial carrier separation due to the harmonized band alignments of each component. As shown in Fig. 27, both Ta_3N_5 and STON could be excited directly

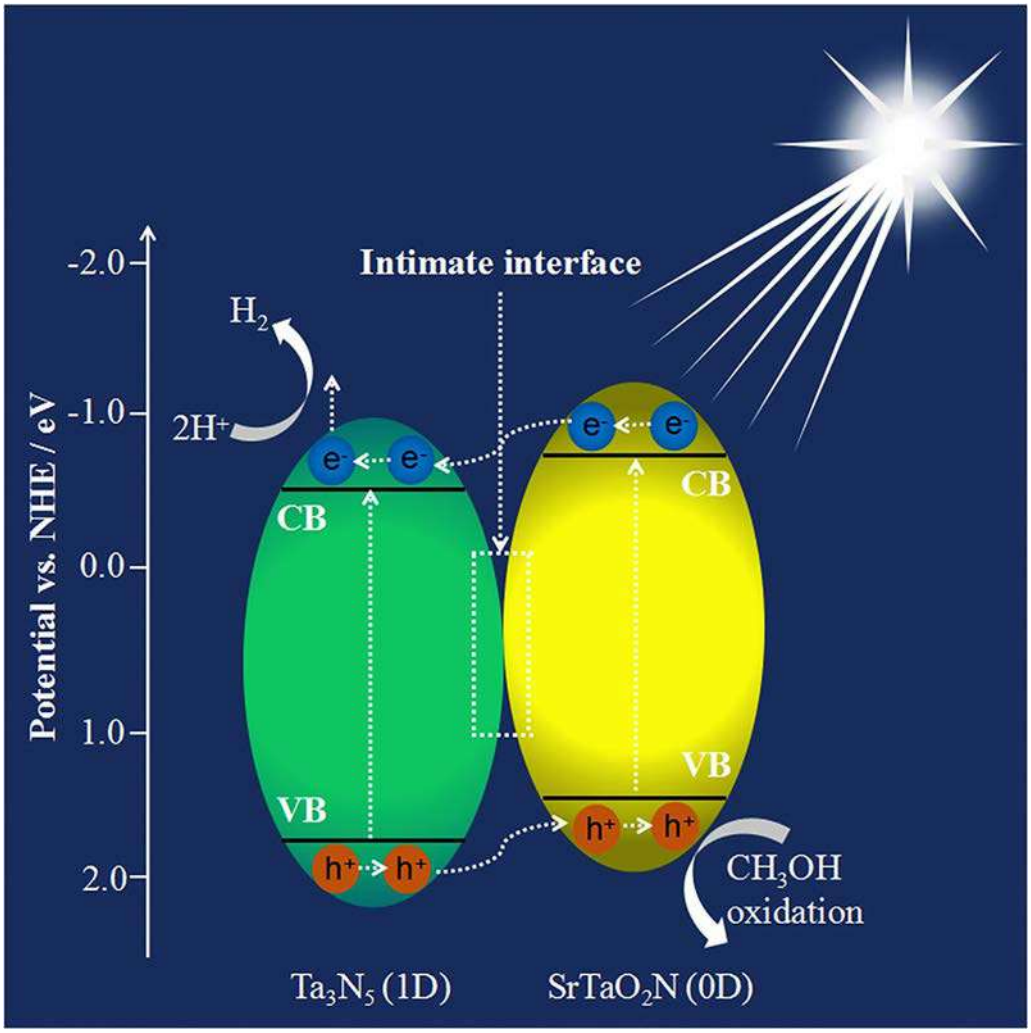

FIG. 27 Illustrative example of unique type II heterostructured photocatalyst. Schematic representation of visible light-active type II Ta_3N_5/STON heterojunction for hydrogen evolution reaction from methanol. *From Jia X, Chen W, Li Y, Zhou X, Yu X, Xing Y. Enhanced photoexcited carrier separation in Ta3N5/SrTaO2N (1D/0D) heterojunctions for highly efficient visible light-driven hydrogen evolution. Appl Surface Sci 2020;514:145915–50. https://doi.org/10.1016/j.apsusc.2020.145915.*

https://www.twirpx.org & http://chemistry-chemists.com

under visible light illumination. Due to the staggered gap, the excited electrons get relocated from the CB of STON (−0.48 eV) to the CB of Ta_3N_5 (−0.41 eV) followed by migration along the orientation direction of Ta_3N_5 nanorod. Simultaneously, the holes will get transferred from the VB of Ta_3N_5 to the VB of STON. Thus, well-defined heterojunctions and intimate interface contact accelerate the charge separation and migration processes synergistically, leading to enhanced performance [224].

Another notable work on *Z*-scheme heterojunction system is the $LaTiO_2N/Bi_2S_3$@RGO photocatalyst designed for degradation of tetracycline (TC). The proposed pathway of Z-scheme transfer is $Bi_2S_3 \rightarrow RGO \rightarrow LaTiO_2N$. The system provides benefits like enhanced charge flow, generation of active oxygen species, reduced recombination, and diminished photocorrosion [225].

In addition to the role portrayed by phosphide and nitride materials in device fabrication of photocatalysts, metal (or electrolyte)-semiconductor interfaces based on Schottky junction and Ohmic contact also account for the transport properties in heterojunction devices, as seen in the above few examples. The detailed mechanisms on the junction theory have already been discussed by our group elsewhere [226].

In conclusion, the selected few mechanisms mentioned above aim to highlight the key aspects of photocatalysis on phosphide and nitride systems based on experimental and theoretical viewpoints.

6 Challenges and future perspective

Despite the great progress made by phosphides and nitrides in the field of photocatalysis, there are still a few essential drawbacks restraining their practical applications. In this, we will aim to spotlight a few ongoing challenges and time ahead directions.

- The first and foremost challenge lies in the large-scale and reproducible synthesis of semiconductors with a tunable bandgap between 1.6 and 3 eV. Assembly of metal phosphides and nitrides with optimized structure, specific crystal planes and precise composition generally involves multistep and elevated temperature treatment. This makes the synthesis route expensive, complicated, and even uneconomical (e.g., template synthesis). Hence, novel, green techniques and cost-effective schemes are still required for the synthesis of desirable TMPs and TMNs. Additionally, there is still very little knowledge about the intermediates and impurities formed during the synthesis procedures. Hence, it is essential to choose wisely metal precursors along with rational reaction parameters.
- The stability of TMPs and TMNs based semiconductors in aqueous electrolyte under illumination and air remains a critical challenge, particularly in water oxidation and overall solar water-splitting reactions. Different techniques have been utilized to prevail over the stability issues like adjusting the solution compositions, addition of additives to stabilize semiconductor/electrolyte interface, and protective coating by the atomic layer deposition (ALD) technique. Even so, it is imperative to probe the

https://www.twirpx.org & http://chemistry-chemists.com

atomic structure and electronic profile of a photocatalyst surface right down to the atomic-level interfacial structure. This can be brought about by designing favorable type-II staggered band alignment heterojunctions based on Schottky contact and surface state modifications. Additionally, recognition and investigation of loss mechanisms in electrodes by operando or in situ spectroscopic measurements may be used during the actual photochemical reactions and in turn improve the performance efficiency.

- Although several reports based on theoretical and computational studies have kept pouring in over the years, detailed fundamental understandings of electrochemical reactions in TMPs and TMNs are less understood in comparison to carbon materials and metal oxides from thermodynamic and kinetic viewpoints. Moreover, the mechanisms, identification of reactive sites, and the influence of defect density with structure-property relationship remain the primary challenges. Therefore, it is vital to take full advantage of computer simulations like DFT calculations, which are becoming more powerful, in order to predict the in-depth kinetics and performance of these photocatalysts.
- One of the central problems to note is the dynamics associated with the charge carriers where fast recombination is the dominating factor. A few viable strategies to increase the photocatalytic efficiency in TMPs and TMNs include optimized nanostructuring, suitable bandgap engineering with thermodynamically feasible charge transfer process, ingenious construction of 2D/3D conductive carbon templates for better anchoring of pollutants, and cocatalyst loading.

Given the large family of phosphides and nitrides available with their distinctive chemical, physical, and electrochemical properties, there is still a large area to explore. Future challenges mostly center on value-added reflection of the benign, facile, supportable, and bulk-scale synthetic methodologies, conducive to advance toward better practical applications. Furthermore, severing the traditional concepts and constructing superior systems may bring surprising outcomes.

7 Conclusion

The rapid exhaustion of environmental assets and long-lasting feasibility of the ecosystem are the prime obstacles for human permanence and growth in the current century. In this regard, undoubtedly, energy conversion photocatalysis technology and material nanochemistry are the present-day research hot spots and have consequently motivated extensive interests in evolving better and more refined resourceful materials. With the remarkable advancement in earth-rich transition phosphide and nitride materials, an overall analysis of TMPs and TMNs in energy-related applications for profound perception and ideal usage is particularly of the essence. To this end, the first segment of the chapter endeavored to convey to readers the significance of integrated photocatalysis and nanoscience in the current scenario and the elementary concepts associated with solar-

https://www.twirpx.org & http://chemistry-chemists.com

to-hydrogen conversion and environmental remediation applications. In this context, we observed that scientific investigation has been expanding in every dimension while keeping intact the fundamental objective for delivering green and sustainable energy. In the library of photocatalyst materials, metal oxides like TiO_2 have marked their distinguished presence in photocatalysis due to their effectiveness, stability, and robustness, among several other advantages. However, TiO_2 is mostly responsive for UV light, which encompasses only about 5% of the entire solar spectrum, while visible light settles for 25%. Similarly, metal sulfide-based semiconductors such as CdS can be easily oxidized by photoexcited holes and undergo photocorrosion under light irradiation, thus exhibiting inadequate photocatalytic performance. Keeping this in mind, we brought about our discussions on phosphides and nitrides including polymeric graphitic nitride as low-cost catalysts and cocatalysts in the field of photocatalysis.

TMPs and TMNs are arising as a new era of electro-active materials especially in visible light-active water-splitting reaction and photocatalytic dye degradation processes owing to tunable band structure, high reactivity, and impressive electrical conductivity. Currently, various synthetic approaches for the fabrication of TMPs and TMNs have been introduced and summarized with relevant examples. For example, TMPs have mostly been prepared by a gas-solid reaction route using sodium hypophosphite as the phosphorus precursor. In addition, hydrothermal and solvothermal methods have been employed to obtain high-surface-area and crystalline nanocomposites. Similarly, in TMNs, postammonia treatment or nitrogen annealing is the primary course to convert metal precursors to TMNs. The central advantage lies in improved crystallinity and well-preserved morphology of the preformed precursors. In addition, thin-film growth techniques and ingenious use of carbon-based materials (graphene, MOF, etc.) have also been discussed. Based on the diversity of the synthesis methods and the excellent performances reported toward photocatalytic applications, in-depth mechanisms behind the photoactivity of TMPs and TMNs were reviewed and discussed in terms of both experimental results and computational simulations. For instance, Li et al. established unique bonding states for CoP/g-C_3N_4 photocatalyst surfaces using XANES and FT studies. Similarly, Ouhbi and his coworker by means of DFT calculations investigated the effect of anionic vacancies on the OER activity in $SrTaO_2N$ (001). Even then, more attention should be given to the mechanistic and core fundamental aspects of TMPs and TMNs in a photocatalytic process, as highlighted in the final section. Although the material provided herein is not exhaustive with regard to the extensive scope of photocatalysis, we have made our best efforts to discuss significant points from the theoretical context, potent and recognized mechanistic point of view, and vital parameters. Hence, photocatalysis can be considered a simple yet challenging phenomenon. It is simple with reference to its operation and utilization, but challenging concerning validation of the results in a technically logical form. Phosphide- and nitride-based photocatalysts are anticipated to address a broad spectrum of photo-applications with earnest understanding, further research, and appropriate material engineering.

https://www.twirpx.org & http://chemistry-chemists.com

References

[1] Kemp KC, Seema H, Saleh M, Le NH, Mahesh K, Chandra V, et al. Environmental applications using graphene composites: water remediation and gas adsorption. Nanoscale 2013;5:3149–71. https://doi.org/10.1039/c3nr33708a.

[2] Chen X, Shen S, Guo L, Mao SS. Semiconductor-based photocatalytic hydrogen generation. Chem Rev 2010;110:6503–70. https://doi.org/10.1021/cr1001645.

[3] Rostrup-Nielsen JR, Sehested J, Nørskov JK. Hydrogen and synthesis gas by steam- and CO2 reforming. Adv Catal 2002;47:65–139. https://doi.org/10.1016/S0360-0564(02)47006-X.

[4] Ahmed SF, Khalid M, Rashmi W, Chan A, Shahbaz K. Recent progress in solar thermal energy storage using nanomaterials. Renew Sustain Energy Rev 2017;67:450–60. https://doi.org/10.1016/j.rser.2016.09.034.

[5] Li Y, Xu G, Cui C, Li Y. Flexible and Semitransparent organic solar cells. Adv Energy Mater 2018;8:1701791–819. https://doi.org/10.1002/aenm.201701791.

[6] Chen HM, Chen CK, Liu RS, Zhang L, Zhang J, Wilkinson DP. Nano-architecture and material designs for water splitting photoelectrodes. Chem Soc Rev 2012;41:5654–71. https://doi.org/10.1039/c2cs35019j.

[7] Shimura K, Yoshida H. Heterogeneous photocatalytic hydrogen production from water and biomass derivatives. Energ Environ Sci 2011;4:2467–81. https://doi.org/10.1039/C1EE01120K.

[8] Koodali RT, Zhao D. Photocatalytic degradation of aqueous organic pollutants using titania supported periodic mesoporous silica. Energ Environ Sci 2010;3:608–14. https://doi.org/10.1039/b927247j.

[9] Schneider J, Jia H, Muckerman JT, Fujita E. Thermodynamics and kinetics of CO 2, CO, and H + binding to the metal centre of CO 2 reduction catalysts. Chem Soc Rev 2012;41:2036–51. https://doi.org/10.1039/c1cs15278e.

[10] Narayanam JMR, Stephenson CRJ. Visible light photoredox catalysis: applications in organic synthesis. Chem Soc Rev 2011;40:102–13. https://doi.org/10.1039/b913880n.

[11] Li L, Salvador PA, Rohrer GS. Photocatalysts with internal electric fields. Nanoscale 2014;6:24–42. https://doi.org/10.1039/c3nr03998f.

[12] Dong S, Feng J, Fan M, Pi Y, Hu L, Han X, et al. Recent developments in heterogeneous photocatalytic water treatment using visible lightresponsive photocatalysts: a review. RSC Adv 2015;5:14610–30. https://doi.org/10.1039/C4RA13734E.

[13] Wohlfahrt-Mehrens M, Hormann U, Kubiak P, Kucerova G, Pfanzelt M, Weiss CK, et al. High surface area crystalline titanium dioxide: potential and limits in electrochemical energy storage and catalysis. Chem Soc Rev 2012;41:5313–60. https://doi.org/10.1039/C2CS35013K.

[14] Vericat C, Vela ME, Salvarezza RC. Self-assembled monolayers of alkanethiols on au(111): surface structures, defects and dynamics. Phys Chem Chem Phys 2005;7:3258–68. https://doi.org/10.1039/b505903h.

[15] Fujishima A, Honda K. Electrochemical photolysis of water at a semiconductor electrode. Nature 1972;238:37–8. https://doi.org/10.1038/238037a0.

[16] J. BA. Photoelectrochemistry. Science 1980;139–44. https://doi.org/10.1126/science.207.4427.139.

[17] Dhakshinamoorthy A, Navalon S, Corma A, Garcia H. Photocatalytic CO2 reduction by TiO2 and related titanium containing solids. Energ Environ Sci 2012;5:9217–33. https://doi.org/10.1039/c2ee21948d.

[18] Kamat PV. Photoinduced transformations in semiconductor-metal nanocomposite assemblies. Pure Appl Chem 2002;74:1693–706. https://doi.org/10.1351/pac200274091693.

https://www.twirpx.org & http://chemistry-chemists.com

[19] Habisreutinger SN, Schmidt-Mende L, Stolarczyk JK. Photocatalytic reduction of CO2 on TiO2 and other semiconductors. Angew Chem Int Ed 2013;52:7372–408. https://doi.org/10.1002/anie.201207199.

[20] Yan Y, Wang C, Yan X, Xiao L, He J, Gu W, et al. Graphene acting as surface phase junction in anatase–graphene–rutile heterojunction photocatalysts for H2 production from water splitting. J Phys Chem C 2014;118:23519–26. https://doi.org/10.1021/jp507087k.

[21] Hu YH. A highly efficient photocatalyst-hydrogenated black TiO2 for the photocatalytic splitting of water. Angew Chem Int Ed 2012;51:12410–2. https://doi.org/10.1002/anie.201206375.

[22] Chen X, Mao SS. Titanium dioxide nanomaterials: synthesis, properties, modifications, and applications. Chem Rev 2007;107:2891–959. https://doi.org/10.1021/cr0500535.

[23] Warren CS, Thimsen E. Plasmonic solar water splitting. Energ Environ Sci 2011;5:5133–46. https://doi.org/10.1039/C1EE02875H.

[24] Pan H, Zhang YW, Shenoy VB, Gao H. Effects of H-, N-, and (*H*,N)-doping on the photocatalytic activity of TiO2. J Phys Chem C 2011;115:12224–31. https://doi.org/10.1021/jp202385q.

[25] Wendt S, Sprunger TP, Lira E, KHG M, Li Z, et al. The role of interstitial sites in the Ti3d defect state in the band gap of Titania. Science 2008;320:1755–9. https://doi.org/10.1126/science.1159846.

[26] Wang J, Mao B, Gole LJ, Burda C. Visible-light-driven reversible and switchable hydrophobic to hydrophilic nitrogen-doped titania surfaces: correlation with photocatalysis. Nanoscale 2010;2:2257–61. https://doi.org/10.1039/C0NR00313A.

[27] Su J, Vayssieres L. A place in the sun for artificial photosynthesis? ACS Energy Lett 2016;1:121–35. https://doi.org/10.1021/acsenergylett.6b00059.

[28] Wang Y, Lin J, Zong R, He J, Zhu Y. Enhanced photoelectric catalytic degradation of methylene blue via TiO 2 nanotube arrays hybridized with graphite-like carbon. J Mol Catal A Chem 2011;349:13–9. https://doi.org/10.1016/j.molcata.2011.08.020.

[29] Warren SC, Thimsen E. Plasmonic solar watersplitting. Energ Environ Sci 2012;5:5133–46. https://doi.org/10.1039/C1EE02875H.

[30] Barroso M, Pendlebury SR, Cowan AJ, Durrant JR. Charge carrier trapping, recombination and transfer in hematite (α-Fe2O3) water splitting photoanodes. Chem Sci 2013;4:2724–34. https://doi.org/10.1039/c3sc50496d.

[31] Cademartiri L, Guerin G, Bishop KJM, Winnik MA, Ozin GA. Polymer-like conformation and growth kinetics of Bi 2S 3 nanowires. J Am Chem Soc 2012;134:9327–34. https://doi.org/10.1021/ja301855z.

[32] Townsend TK. Inorganic Metal Oxide Nanocrystal Photocatalysts for Solar Fuel Generation From Water. Berlin: Springer Science & Business Media; 2014.

[33] Denk M, Kuhness D, Wagner M, Surnev S, Negreiros FR, Sementa L, et al. Metal tungstates at the ultimate two-dimensional limit: fabrication of a CuWO4 nanophase. ACS Nano 2014;8:3947–54. https://doi.org/10.1021/nn500867y.

[34] Yu J, Xu CY, Ma FX, Hu SP, Zhang YW, Zhen L. Monodisperse SnS2 nanosheets for high-performance photocatalytic hydrogen generation. ACS Appl Mater Interfaces 2014;6:22370–7. https://doi.org/10.1021/am506396z.

[35] Mahler B, Hoepfner V, Liao K, Ozin GA. Colloidal synthesis of 1T-WS2 and 2H-WS2 nanosheets: applications for photocatalytic hydrogen evolution. J Am Chem Soc 2014;136:14121–7. https://doi.org/10.1021/ja506261t.

[36] Chen J, Wu XJ, Yin L, Li B, Hong X, Fan Z, et al. One-pot synthesis of CdS nanocrystals hybridized with single-layer transition-metal dichalcogenide nanosheets for efficient photocatalytic hydrogen evolution. Angew Chem Int Ed 2015;54:1210–4. https://doi.org/10.1002/anie.201410172.

https://www.twirpx.org & http://chemistry-chemists.com

[37] Jia L, Wang DH, Huang YX, Xu AW, Yu HQ. Highly durable N-doped graphene/CdS nanocomposites with enhanced photocatalytic hydrogen evolution from water under visible light irradiation. J Phys Chem C 2011;115:11466–73. https://doi.org/10.1021/jp2023617.

[38] Linsebigler AL, Lu G, Yates JT. Photocatalysis on TiO2 surfaces: principles, mechanisms, and selected results. Chem Rev 1995;95:735–58. https://doi.org/10.1021/cr00035a013.

[39] Baxter JB, Richter C, Schmuttenmaer CA. Ultrafast carrier dynamics in nanostructures for solar fuels. Annu Rev Phys Chem 2014;65:423–47. https://doi.org/10.1146/annurev-physchem-040513-103742.

[40] Yan S, Wan L, Li Z, Zou Z. Facile temperature-controlled synthesis of hexagonal Zn2GeO4nanorods with different aspect ratios toward improved photocatalytic activity for overall water splitting and photoreduction of CO2. Chem Commun 2011;47:5632–4. https://doi.org/10.1039/c1cc10513b.

[41] Marschall R. Semiconductor composites: strategies for enhancing charge carrier separation to improve photocatalytic activity. Adv Funct Mater 2014;24:2421–40. https://doi.org/10.1002/adfm.201303214.

[42] Sun S, Wang W, Li D, Zhang L, Jiang D. Solar light driven pure water splitting on quantum sized BiVO4 without any cocatalyst. ACS Catal 2014;4:3498–503. https://doi.org/10.1021/cs501076a.

[43] Pasternak S, Paz Y. On the similarity and dissimilarity between photocatalytic water splitting and photocatalytic degradation of pollutants. ChemPhysChem 2013;14:2059–70. https://doi.org/10.1002/cphc.201300247.

[44] Ager J, Shaner M, Walczak K, Sharp I, Ardo S. Experimental demonstrations of spontaneous, solar-driven photoelectrochemical water splitting. Energ Environ Sci 2015;8:2811–24. https://doi.org/10.1039/C5EE00457H.

[45] Bard AJ, Fox MA. Artificial photosynthesis: solar splitting of water to hydrogen and oxygen. Acc Chem Res 1995;28:141–5. https://doi.org/10.1021/ar00051a007.

[46] Chen S, Huang D, Zeng G, Xue W, Lei L, Xu P, et al. In-situ synthesis of facet-dependent BiVO4/Ag3PO4/PANI photocatalyst with enhanced visible-light-induced photocatalytic degradation performance: synergism of interfacial coupling and hole-transfer. Chem Eng J 2020;382:122840–55. https://doi.org/10.1016/j.cej.2019.122840.

[47] Chen S, Wang LW. Thermodynamic oxidation and reduction potentials of photocatalytic semiconductors in aqueous solution. Chem Mater 2012;24:3659–66. https://doi.org/10.1021/cm302533s.

[48] Kalisman P, Nakibli Y, Amirav L. Perfect photon-to-hydrogen conversion efficiency. Nano Lett 2016;16:1776–81. https://doi.org/10.1021/acs.nanolett.5b04813.

[49] Li Y, Sharp ID, Kudo A, Yamada T, Domen K, Wang C, et al. Scalable water splitting on particulate photocatalyst sheets with a solar-to-hydrogen energy conversion efficiency exceeding 1%. Nat Mater 2016;15:611–5. https://doi.org/10.1038/nmat4589.

[50] Jensen HH, Wendt S, Catlow CRA, Kiely CJ, Hutchings GJ, Besenbacher F, et al. Designer titania-supported Au-Pd nanoparticles for efficient photocatalytic hydrogen production. ACS Nano 2014;8:3490–7. https://doi.org/10.1021/nn500963m.

[51] Wang X, Peng WC, Li XY. Photocatalytic hydrogen generation with simultaneous organic degradation by composite CdS-ZnS nanoparticles under visible light. Int J Hydrogen Energy 2014;39:13454–61. https://doi.org/10.1016/j.ijhydene.2014.04.034.

[52] Shi L, Liang L, Ma J, Wang F, Sun J. Enhanced photocatalytic activity over the Ag2O-g-C 3N4 composite under visible light. Cat Sci Technol 2014;4:758–65. https://doi.org/10.1039/c3cy00871a.

[53] Liu S, Xu YJ. Efficient electrostatic self-assembly of one-dimensional CdS-Au nanocomposites with enhanced photoactivity, not the surface plasmon resonance effect. Nanoscale 2013;5:9330–9. https://doi.org/10.1039/c3nr02682e.

https://www.twirpx.org & http://chemistry-chemists.com

[54] Fukuzumi S, Hong D, Yamada Y. Bioinspired photocatalytic water reduction and oxidation with earth-abundant metal catalysts. J Phys Chem Lett 2013;4:3458–67. https://doi.org/10.1021/jz401560x.

[55] Carenco S, Portehault D, Boissière C, Mézailles N, Sanchez C. Nanoscaled metal borides and phosphides: recent developments and perspectives. Chem Rev 2013;113:7981–8065. https://doi.org/10.1021/cr400020d.

[56] Laursen AB, Patraju KR, Whitaker MJ, Retuerto M, Sarkar T, Yao N, et al. Nanocrystalline Ni5P4: a hydrogen evolution electrocatalyst of exceptional efficiency in both alkaline and acidic media. Energ Environ Sci 2015;8:1027–34. https://doi.org/10.1039/c4ee02940b.

[57] Yue Q, Wan Y, Sun Z, Wu X, Yuan Y, Du P. MoP is a novel, noble-metal-free cocatalyst for enhanced photocatalytic hydrogen production from water under visible light. J Mater Chem A 2015;3:16941–7. https://doi.org/10.1039/C5TA03949E.

[58] Marschall R, Wang L. Non-metal doping of transition metal oxides for visible-light photocatalysis. Catal Today 2014;225:111–35. https://doi.org/10.1016/j.cattod.2013.10.088.

[59] Kaneco S, Ueno Y, Katsumata H, Suzuki T, Ohta K. Photoelectrochemical reduction of CO2 at p-InP electrode in copper particle-suspended methanol. Chem Eng J 2009;148:57–62. https://doi.org/10.1016/j.cej.2008.07.038.

[60] Iwase M, Yamada K, Kurisaki T, Prieto-Mahaney OO, Ohtani B, Wakita H. Visible-light photocatalysis with phosphorus-doped titanium(IV) oxide particles prepared using a phosphide compound. Appl Catal Environ 2013;132–133:39–44. https://doi.org/10.1016/j.apcatb.2012.11.014.

[61] Vance CC, Vaddiraju S, Karthikeyan R. Water disinfection using zinc phosphide nanowires under visible light conditions. J Environ Chem Eng 2018;6:568–73. https://doi.org/10.1016/j.jece.2017.12.052.

[62] Cao S, Chen Y, Wang C-J, Lv X-J, Fu W-F. Spectacular photocatalytic hydrogen evolution using metal-phosphide/CdS hybrid catalysts under sunlight irradiation. Chem Commun 2015;51:8708–11. https://doi.org/10.1039/C5CC01799H.

[63] Archer RJ, Koyama RY, Loebner EE, Lucas RC. Optical absorption, electroluminescence, and the band gap of BP. Phys Rev Lett 1964;12:538–40. https://doi.org/10.1103/PhysRevLett.12.538.

[64] Kumashiro Y. Refractory semiconductor of boron phosphide. J Mater Res 1990;5:2933–47. https://doi.org/10.1557/JMR.1990.2933.

[65] Shi L, Li P, Zhou W, Wang T, Chang K, Zhang H, et al. N-type boron phosphide as a highly stable, metal-free, visible-light-active photocatalyst for hydrogen evolution. Nano Energy 2016;28:158–63. https://doi.org/10.1016/j.nanoen.2016.08.041.

[66] Hu B, Yun Yuan J, Yue Tian J, Wang M, Wang X, He L, et al. Co/Fe-bimetallic organic framework-derived carbon-incorporated cobalt–ferric mixed metal phosphide as a highly efficient photocatalyst under visible light. J Colloid Interface Sci 2018;531:148–59. https://doi.org/10.1016/j.jcis.2018.07.037.

[67] Ramanathan S, Oyama S. New catalysts for hydroprocessing: transition metal carbides and nitrides. J Phys Chem 1995;99:16365–72. https://doi.org/10.1021/j100044a025.

[68] Dong S, Chen X, Zhang X, Cui G. Nanostructured transition metal nitrides for energy storage and fuel cells. Coord Chem Rev 2013;257:1946–56. https://doi.org/10.1016/j.ccr.2012.12.012.

[69] Lee JS. Metal carbides. In: Encyclopedia of Catalysis; 2010. https://doi.org/10.1002/0471227617.eoc136.pub2.

[70] Fu ZW, Wang Y, Yue XL, Zhao SL, Qin QZ. Electrochemical reactions of lithium with transition metal nitride electrodes. J Phys Chem B 2004;108:2236–44. https://doi.org/10.1021/jp030530s.

[71] Li X, Hasan MM, Hector AL, Owen JR. Performance of nanocrystalline Ni3N as a negative electrode for sodium-ion batteries. J Mater Chem A 2013;1:6441–5. https://doi.org/10.1039/C3TA00184A.

https://www.twirpx.org & http://chemistry-chemists.com

[72] Lengauer W. Handbook of Ceramic Hard Materials. New York: Weinheim ; New York: Wiley-VCH, ©2000; 2000.

[73] Cao B, Veith GM, Neuefeind JC, Adzic RR, Khalifah PG. Mixed close-packed cobalt molybdenum nitrides as non-noble metal electrocatalysts for the hydrogen evolution reaction. J Am Chem Soc 2013;135:19186–92. https://doi.org/10.1021/ja4081056.

[74] Arai N, Saito N, Nishiyama H, Domen K, Kobayashi H, Sato K, et al. Effects of divalent metal ion (Mg2+, Zn2+ and Be2+) doping on photocatalytic activity of ruthenium oxide-loaded gallium nitride for water splitting. Catal Today 2007;407–13. https://doi.org/10.1016/j.cattod.2006.08.072.

[75] Sato J, Saito N, Yamada Y, Maeda K, Takata T, Kondo JN, et al. RuO2-loaded β-Ge3N4 as a non-oxide photocatalyst for overall water splitting. J Am Chem Soc 2005;127:4150–1. https://doi.org/10.1021/ja042973v.

[76] Maeda K, Saitoh N, Inoue Y, Domen K. Dependence of activity and stability of germanium nitride powder for photocatalytic overall water splitting on structural properties. Chem Mater 2007;19:4092–7. https://doi.org/10.1021/cm0709828.

[77] Maeda K, Teramura K, Saito N, Inoue Y, Domen K. Photocatalytic overall water splitting on gallium nitride powder. Bull Chem Soc Jpn 2007;80:1004–10. https://doi.org/10.1246/bcsj.80.1004.

[78] Arai N, Saito N, Nishiyama H, Inoue Y, Domen K, Sato K. Overall water splitting by RuO 2-dispersed divalent-ion-doped GaN photocatalysts with d 10 electronic configuration. Chem Lett 2006;35:796–7. https://doi.org/10.1246/cl.2006.796.

[79] Wang D, Pierre A, Kibria MG, Cui K, Han X, Bevan KH, et al. Wafer-level photocatalytic water splitting on Gan nanowire arrays grown by molecular beam epitaxy. Nano Lett 2011;11:2353–7. https://doi.org/10.1021/nl2006802.

[80] Toshiharu T, Kazunari D, Taizo Y, Takahiro I, Naoyuki S, Takashi H, et al. Photocatalytic overall water splitting promoted by two different Cocatalysts for hydrogen and oxygen evolution under visible light. Angew Chem 2010;4190–3. https://doi.org/10.1002/ange.201001259.

[81] Liao J, Sa B, Zhou J, Ahuja R, Sun Z. Design of high-efficiency visible-light photocatalysts for water splitting: MoS2/AlN(GaN) heterostructures. J Phys Chem C 2014;118:17594–9. https://doi.org/10.1021/jp5038014.

[82] Li J, Lin J, Jiang HX. Direct hydrogen gas generation by using InGaN epilayers as working electrodes. Appl Phys Lett 2008;93:162107–9. https://doi.org/10.1063/1.3006332.

[83] Kibria MG, Nguyen HPT, Cui K, Zhao S, Liu D, Guo H, et al. One-step overall water splitting under visible light using multiband InGaN/GaN nanowire heterostructures. ACS Nano 2013;7:7886–93. https://doi.org/10.1021/nn4028823.

[84] Kibria M, Chowdhury F, Zhao S, AlOtaibi B, Trudeau M, Guo H, et al. Visible light-driven efficient overall water splitting using p-type metal-nitride nanowire arrays. Nat Commun 2015;6:6797–805. https://doi.org/10.1038/ncomms7797.

[85] Hitoki G, Ishikawa A, Takata T, Kondo JN, Hara M, Domen K. Ta3N5 as a novel visible light-driven photocatalyst ($\lambda < 600$nm). Chem Lett 2002;736–7. https://doi.org/10.1246/cl.2002.736.

[86] Young Kim J, Hee Lee M, Hyuk Kim J, Woo Kim C, Hyun YD. Facile nanocrystalline Ta3N5 synthesis for photocatalytic dye degradation under visible light. Chem Phys Lett 2020;738:136900–21. https://doi.org/10.1016/j.cplett.2019.136900.

[87] Varadhan P, Saravanan P, Kandhasamy J, Shanmugam P, Kwon YJ, Kulandaivel J. Photocatalytic dye degradation properties of wafer level GaN nanowires by catalytic and self-catalytic approach using chemical vapor deposition. RSC Adv 2014;4:25569–75. https://doi.org/10.1039/C4RA03642E.

[88] Moses PG, Van De Walle CG. Band bowing and band alignment in InGaN alloys. Appl Phys Lett 2010;96. https://doi.org/10.1063/1.3291055.

https://www.twirpx.org & http://chemistry-chemists.com

[89] Guo H, Mi Z, Vanka S, Woo SY, Pofelski A, Oudjedi F, et al. Photochemical carbon dioxide reduction on mg-doped Ga(in)N nanowire arrays under visible light irradiation. ACS Energy Lett 2016;1:246–52. https://doi.org/10.1021/acsenergylett.6b00119.

[90] Maeda K, Lu D, Domen K. Direct water splitting into hydrogen and oxygen under visible light by using modified TaON Photocatalysts with d0 electronic configuration. Chem 2013;19:4986–91. https://doi.org/10.1002/chem.201300158.

[91] Du Y, Zhao L, Zhang Y. Roles of TaON and Ta3N5 in the visible-Fenton-like degradation of atrazine. J Hazard Mater 2014;267:55–61. https://doi.org/10.1016/j.jhazmat.2013.12.042.

[92] Huang J, Cui Y, Wang X. Visible light-sensitive ZnGe oxynitride catalysts for the decomposition of organic pollutants in water. Environ Sci Technol 2010;44:3500–4. https://doi.org/10.1021/es1001264.

[93] Phuong LCNT, Thanh TMH, Cao VH, Dieu CNT, Minh TNT, Thu PTT, et al. Synthesis of tantalum oxynitride with enhanced visible light efficiency in photoreduction of carbon dioxide. Vietnam J Chem 2018;504–8. https://doi.org/10.1002/vjch.201800038.

[94] Fuertes A. Metal oxynitrides as emerging materials with photocatalytic and electronic properties. Mater Horiz 2015;2:453–61. https://doi.org/10.1039/C5MH00046G.

[95] Maeda K, Lu D, Domen K. Oxidation of water under visible-light irradiation over modified BaTaO2N photocatalysts promoted by tungsten species. Angew Chem Int Ed 2013;52:6488–91. https://doi.org/10.1002/anie.201301357.

[96] Wu Y, Lazic P, Hautier G, Persson K, Ceder G. First principles high throughput screening of oxynitrides for water-splitting photocatalysts. Energ Environ Sci 2013;6:157–68. https://doi.org/10.1039/C2EE23482C.

[97] Martınez-Ferrero E, Sakatani Y, Boissière C, Grosso D, Fuertes A, Fraxedas J, et al. Nanostructured titanium oxynitride porous thin films as efficient visible-active photocatalysts. Adv Funct Mater 2007;17:3348–54. https://doi.org/10.1002/adfm.200700396.

[98] Hu C, Teng H. Gallium oxynitride photocatalysts synthesized from Ga(OH)3 for water splitting under visible light irradiation. J Phys Chem C 2010;114:20100–6. https://doi.org/10.1021/jp1070083.

[99] Tsuneoka H, Teramura K, Shishido T, Tanaka T. Adsorbed species of CO2 and H2 on Ga2O3 for the photocatalytic reduction of CO2. J Phys Chem C 2010;114:8892–8. https://doi.org/10.1021/jp910835k.

[100] Lu J, Xing J, Chen D, Xu H, Han X, Li D. Enhanced photocatalytic activity of β-Ga2O3 nanowires by au nanoparticles decoration. J Mater Sci 2019;54:6530–41. https://doi.org/10.1007/s10853-019-03359-1.

[101] Kasahara A, Nukumizu K, Hitoki G, Takata T, Kondo J, Hara M, et al. Photoreactions on LaTiO2N under visible light irradiation. Chem A Eur J 2002;106:6750–3. https://doi.org/10.1021/jp025961.

[102] Balaz S, Porter S, Woodward P, Brillson L. Electronic structure of tantalum oxynitride perovskite photocatalysts. Chem Mater 2013;25:3337–43. https://doi.org/10.1021/cm401815w.

[103] Bhavin S, Kazuhiko M, Takashi H, Kazunari D. Synthesis and photocatalytic activity of perovskite niobium oxynitrides with wide visible-light absorption bands. ChemSusChem 2011;74–8. https://doi.org/10.1002/cssc.201000207.

[104] Sun Z, Wang H, Wu Z, Wang L. G-C3N4 based composite photocatalysts for photocatalytic CO2 reduction. Catal Today 2018;300:160–72. https://doi.org/10.1016/j.cattod.2017.05.033.

[105] Jing X, Zhouping W, Yongfa Z. Enhanced visible-light-driven photocatalytic disinfection performance and organic pollutant degradation activity of porous g-C 3 N 4 nanosheets. ACS Appl Mater Interfaces 2017;27727–35. https://doi.org/10.1021/acsami.7b07657.

[106] Yang Y, Wang S, Li Y, Wang J, Wang L. Strategies for efficient solar water splitting using carbon nitride. Chem Asian J 2017;12:1421–34. https://doi.org/10.1002/asia.201700540.

https://www.twirpx.org & http://chemistry-chemists.com

[107] Li Y, Xu H, Ouyang S, Lu D, Wang X, Wang D, et al. In situ surface alkalinized g-C3N4 toward enhancement of photocatalytic H2 evolution under visible-light irradiation. J Mater Chem A 2016;4:2943–50. https://doi.org/10.1039/C5TA05128B.

[108] Liu J, Cheng B, Yu J. A new understanding of the photocatalytic mechanism of the direct Z-scheme g-C3N4/TiO2 heterostructure. Phys Chem Chem Phys 2016;18:31175–83. https://doi.org/10.1039/C6CP06147H.

[109] Liu J, Liu Y, Liu N, Han Y, Zhang X, Huang H, et al. Metal-free efficient photocatalyst for stable visible water splitting via a two-electron pathway. Science 2015;347:970. https://doi.org/10.1126/science.aaa3145.

[110] Bai S, Jiang J, Zhang Q, Xiong Y. Steering charge kinetics in photocatalysis: intersection of materials syntheses, characterization techniques and theoretical simulations. Chem Soc Rev 2015;44:2893–939. https://doi.org/10.1039/C5CS00064E.

[111] Cao S, Low J, Yu J, Jaroniec M. Polymeric photocatalysts based on graphitic carbon nitride. Adv Mater 2015;2:2150–76. https://doi.org/10.1002/adma.201500033.

[112] Lang SM, Bernhardt TM. Gas phase metal cluster model systems for heterogeneous catalysis. Phys Chem Chem Phys 2012;14:9255–69. https://doi.org/10.1039/C2CP40660H.

[113] Cheng C, Zong S, Shi J, Xue F, Guan X, Zheng B, et al. Facile preparation of nanosized MoP as cocatalyst coupled with g-C3N4 by surface bonding state for enhanced photocatalytic hydrogen production. Appl Catal Environ 2020;265:118620–8. https://doi.org/10.1016/j.apcatb.2020.118620.

[114] Tengfei W, Peifang W, Jin Q, Yanhui A, Chao W, Jun H. Noble-metal-free nickel phosphide modified CdS/C 3 N 4 nanorods for dramatically enhanced photocatalytic hydrogen evolution under visible light irradiation. Dalton Trans 2017;46:13793–801. https://doi.org/10.1039/C7DT02929B.

[115] Cheng L, Xie S, Zou Y, Ma D, Sun D, Li Z, et al. Noble-metal-free Fe2PeCo2P co-catalyst boosting visible-light-driven photocatalytic hydrogen production over graphitic carbon nitride: the synergistic effects between the metal phosphides. Int J Hydrogen Energy 2019;44:4133–42. https://doi.org/10.1016/j.ijhydene.2018.12.159.

[116] Guo F, Huang X, Chen Z, Sun H, Chen L. Prominent co-catalytic effect of CoP nanoparticles anchored on high-crystalline g-C3N4 nanosheets for enhanced visible-light photocatalytic degradation of tetracycline in wastewater. Chem Eng J 2020;395:125118–45. https://doi.org/10.1016/j.cej.2020.125118.

[117] Kanatzidis MG, Pöttgen R, Jeitschko W. The metal flux: a preparative tool for the exploration of intermetallic compounds. Angew Chem Int Ed 2005;44:6996–7023. https://doi.org/10.1002/anie.200462170.

[118] Otani S, Ohashi N. Preparation of Ni2P and Fe2P single crystals by the floating-zone method. J Cerma Soc Jpn 2013;121:331–2. https://doi.org/10.2109/jcersj2.121.331.

[119] Henkes AE, Schaak RE. Trioctylphosphine: a general phosphorus source for the low-temperature conversion of metals into metal phosphides. Chem Mater 2007;19:4234–42. https://doi.org/10.1021/cm071021w.

[120] Panneerselvam A, Malik MA, Afzaal M, O'Brien P, Helliwell M. The chemical vapor deposition of nickel phosphide or selenide thin films from a single precursor. J Am Chem Soc 2008;130:2420–1. https://doi.org/10.1021/ja078202j.

[121] Wang J, Johnston-Peck AC, Tracy JB. Nickel phosphide nanoparticles with hollow, solid, and amorphous structures. Chem Mater 2009;21:4462–7. https://doi.org/10.1021/cm901073k.

[122] Hitihami-Mudiyanselage A, Arachchige MP, Seda T, Lawes G, Brock SL. Synthesis and characterization of discrete FexNi2-xP nanocrystals ($0 < x < 2$): compositional effects on magnetic properties. Chem Mater 2015;27:6592–600. https://doi.org/10.1021/acs.chemmater.5b02149.

https://www.twirpx.org & http://chemistry-chemists.com

[123] Zhang H, Ha DH, Hovden R, Kourkoutis LF, Robinson RD. Controlled synthesis of uniform cobalt phosphide hyperbranched nanocrystals using tri-n-octylphosphine oxide as a phosphorus source. Nano Lett 2011;11:188–97. https://doi.org/10.1021/nl103400a.

[124] Stein BF, Walmsley RH. Magnetic susceptibility and nuclear magnetic resonance in transition-metal monophosphides. Phys Rev 1966;148:933–9. https://doi.org/10.1103/PhysRev.148.933.

[125] Ripley RL. The preparation and properties of some transition phosphides. J Less-Common Met 1962;4:496–503. https://doi.org/10.1016/0022-5088(62)90037-1.

[126] Yang S, Liang C, Prins R. A novel approach to synthesizing highly active Ni2P/SiO2 hydrotreating catalysts. J Catal 2006;118–30. https://doi.org/10.1016/j.jcat.2005.10.021.

[127] Dong Y, Tian T, Xu C, Ma K, Sun W, Ding Y. Cubic co-co prussian blue MOF-based transition metal phosphide as an efficient catalyst for visible light-driven water oxidation. J Catal 2020;382:13–21. https://doi.org/10.1016/j.jcat.2019.12.009.

[128] Oyama ST. Novel catalysts for advanced hydroprocessing: transition metal phosphides. J Catal 2003;216:343–52. https://doi.org/10.1016/S0021-9517(02)00069-6.

[129] Yang X, Lu AY, Zhu Y, Hedhili MN, Min S, Huang KW, et al. CoP nanosheet assembly grown on carbon cloth: a highly efficient electrocatalyst for hydrogen generation. Nano Energy 2015;15:634–41. https://doi.org/10.1016/j.nanoen.2015.05.026.

[130] Iwase M, Yamada K, Kurisaki T, Ohtani B, Wakita H. A study on the active sites for visible-light photocatalytic activity of phosphorus-doped titanium(IV) oxide particles prepared using a phosphide compound. Appl Catal Environ 2013;140–141:327–32. https://doi.org/10.1016/j.apcatb.2013.04.018.

[131] Shi Y, Zhang B. Recent advances in transition metal phosphide nanomaterials: synthesis and applications in hydrogen evolution reaction. Chem Soc Rev 2016;45:1529–41. https://doi.org/10.1039/c5cs00434a.

[132] Wang J, Yang Q, Zhang Z, Sun S. Phase-controlled synthesis of transition-metal phosphide nanowires by ullmann-type reactions. Chem A Eur J 2010;16:7916–24. https://doi.org/10.1002/chem.200902151.

[133] Xie Y, Su HL, Qian XF, Liu XM, Qian YT. A mild one-step solvothermal route to metal phosphides (metal = co, Ni, cu). J Solid State Chem 2000;149:88–91. https://doi.org/10.1006/jssc.1999.8499.

[134] Lukehart CM, Milne SB, Stock SR. Formation of crystalline nanoclusters of Fe2P, RuP, Co2P, Rh2P, Ni2P, Pd5P2, or PtP2 in a silica Xerogel matrix from single-source molecular precursors. Chem Mater 1998;10:903–8. https://doi.org/10.1021/cm970673p.

[135] Henkes AE, Vasquez Y, Schaak RE. Converting metals into phosphides: a general strategy for the synthesis of metal phosphide nanocrystals. J Am Chem Soc 2007;129:1896–7. https://doi.org/10.1021/ja068502l.

[136] Anirban D, Dutta SK, Mehetor SK, Indranil M, Ujjwal P, Narayan P. Oriented attachments and formation of ring-on-disk heterostructure Au–Cu3P photocatalysts. Chem Mater 2016;28:1872–8. https://doi.org/10.1021/acs.chemmater.6b00050.

[137] Man H-W, Tsang C-S, Li MM-J, Mo J, Huang B, Lee LYS, et al. Transition metal-doped nickel phosphide nanoparticles as electro- and photocatalysts for hydrogen generation reactions. Appl Catal Environ 2019;242:186–93. https://doi.org/10.1016/j.apcatb.2018.09.103.

[138] Liu S, Han L, Liu H. Synthesis, characterization and photocatalytic performance of PbS/Ni2P flowers. Appl Surf Sci 2016;387:393–8. https://doi.org/10.1016/j.apsusc.2016.06.123.

[139] Cao S, Wang CJ, Lv XJ, Chen Y, Fu WF. A highly efficient photocatalytic H2 evolution system using colloidal CdS nanorods and nickel nanoparticles in water under visible light irradiation. Appl Catal Environ 2015;162:381–91. https://doi.org/10.1016/j.apcatb.2014.07.014.

[140] Sun J, Liu C, Yang P. Surfactant-free, large-scale, solution–liquid–solid growth of gallium phosphide nanowires and their use for visible-light-driven hydrogen production from water reduction. J Am Chem Soc 2011;133:19306–9. https://doi.org/10.1021/ja2083398.

https://www.twirpx.org & http://chemistry-chemists.com

[141] Dong Y, Kong L, Jiang P, Wang G, Zhao N, Zhang H, et al. A general strategy to fabricate NixP as highly efficient Cocatalyst via Photoreduction deposition for hydrogen evolution. ACS Sustain Chem Eng 2017;5:6845–53. https://doi.org/10.1021/acssuschemeng.7b01079.

[142] Shen R, Xie J, Lu X, Chen X, Li X. Bifunctional Cu3P decorated g-C3N4 Nanosheets as a highly active and robust visible-light Photocatalyst for H2 production. ACS Sustain Chem Eng 2018;6:4026–36. https://doi.org/10.1021/acssuschemeng.7b04403.

[143] Wu W, Yue X, Wu XY, Lu CZ. Efficient visible-light-induced hydrogen evolution from water splitting using a nanocrystalline nickel phosphide catalyst. RSC Adv 2016;6:24361–5. https://doi.org/10.1039/c5ra25286e.

[144] Wang P, Zhan S, Wang H, Xia Y, Hou Q, Zhou Q, et al. Cobalt phosphide nanowires as efficient co-catalyst for photocatalytic hydrogen evolution over Zn0.5Cd0.5S. Appl Catal Environ 2018;230:210–9. https://doi.org/10.1016/j.apcatb.2018.02.043.

[145] Bi L, Gao X, Zhang L, Wang D, Zou X, Xie T. Enhanced photocatalytic hydrogen evolution of NiCoP/g-C3N4 with improved separation efficiency and charge transfer efficiency. ChemSusChem 2018;11:276–84. https://doi.org/10.1002/cssc.201701574.

[146] Motojima S, Haguri K, Takahashi Y, Sugiyama K. Chemical vapor deposition of nickel phosphide Ni2P. J Less-Common Met 1979;64:101–6. https://doi.org/10.1016/0022-5088(79)90137-1.

[147] Iribarren A, Castro-Rodríguez R, Ponce-Cabrera L, Peñab JL. Growth of polycrystalline InP thin films by the pulsed laser deposition technique. Thin Solid Films 2006;134–7. https://doi.org/10.1016/j.tsf.2005.12.302.

[148] Schrey F, Boone T, Nakahara S, Robbins M, Appelbaum A. Structure of sputtered Ni2P films. Thin Solid Films 1987;149:303–11. https://doi.org/10.1016/0040-6090(87)90393-2.

[149] Yoon JS, Doerr HJ, Deshpandey CV, Bunshah RF. Amorphous nickel phosphide alloy coatings obtained by magnetron sputtering methods for magnetic recording disk. J Electrochem Soc 1989;136:3513–7. https://doi.org/10.1149/1.2096496.

[150] Kuang P, Sayed M, Fan J, Cheng B, Yu J. 3D graphene-based H2-production photocatalyst and electrocatalyst. Adv Energy Mater 2020;10:1903802–53. https://doi.org/10.1002/aenm.201903802.

[151] Tan H, Tang J, Henzie J, Li Y, Xu X, Chen T, et al. Assembly of hollow carbon nanospheres on graphene nanosheets and creation of iron-nitrogen-doped porous carbon for oxygen reduction. ACS Nano 2018;12:5674–83. https://doi.org/10.1021/acsnano.8b01502.

[152] Reddy DA, Choi J, Lee S, Kim Y, Hong S, Kumar DP, et al. Hierarchical dandelion-flower-like cobalt-phosphide modified CdS/reduced graphene oxide-MoS2 nanocomposites as a noble-metal-free catalyst for efficient hydrogen evolution from water. Cat Sci Technol 2016;6:6197–206. https://doi.org/10.1039/c6cy00768f.

[153] Lin ZS, Fu WF, Moore JT, Liang F, Nie XC, Mi C, et al. Highly efficient photocatalytic system constructed from CoP/carbon nanotubes or graphene for visible-light-driven CO2 reduction. Chem A Eur J 2018;24:4273–8. https://doi.org/10.1002/chem.201800335.

[154] Shen R, Xie J, Ding Y, Liu S, Adamski A, Chen X, et al. Carbon nanotube-supported Cu3P as high-efficiency and Low-cost Cocatalysts for exceptional semiconductor-free photocatalytic H2 evolution. ACS Sustain Chem Eng 2019;7:3243–50. https://doi.org/10.1021/acssuschemeng.8b05185.

[155] Liu Y, Xiang Z. Fully conjugated covalent organic polymer with carbon-encapsulated Ni2P for highly sustained photocatalytic H2 production from seawater. ACS Appl Mater Interfaces 2019;11:41313–20. https://doi.org/10.1021/acsami.9b13540.

[156] Amaranatha RD, Kook KH, Yujin K, Seunghee L, Jiha C, Jahurul IM, et al. Multicomponent transition metal phosphides derived from layered double hydroxide double-shelled nanocages as an efficient non-precious co-catalyst for hydrogen production. J Mater Chem A 2016;13890–8. https://doi.org/10.1039/C6TA05741A.

https://www.twirpx.org & http://chemistry-chemists.com

[157] Yang M, MacLeod MJ, Tessier F, Disalvo FJ. Mesoporous metal nitride materials prepared from bulk oxides. J Am Ceram Soc 2012;95:3084–9. https://doi.org/10.1111/j.1551-2916.2012.05351.x.

[158] Jung HS, Hong YJ, Li Y, Cho J, Kim YJ, Yi GC. Photocatalysis using GaN nanowires. ACS Nano 2008;2:637–42. https://doi.org/10.1021/nn700320y.

[159] Maeda K, Takata T, Hara M, Saito N, Inoue Y, Kobayashi H, et al. GaN:ZnO solid solution as a photocatalyst for visible-light-driven overall water splitting. J Am Chem Soc 2005;127:8286–7. https://doi.org/10.1021/ja0518777.

[160] Maeda K, Teramura K, Masuda H, Takata T, Saito N, Inoue Y, et al. Efficient overall water splitting under visible-light irradiation on (Ga1-xZnx)(N1-xOx) dispersed with Rh-Cr mixed-oxide nanoparticles: effect of reaction conditions on photocatalytic activity. J Phys Chem B 2006;110:13107–12. https://doi.org/10.1021/jp0616563.

[161] Chen H, Jiang D, Sun Z, Irfan RM, Zhang L, Du P. Cobalt nitride as an efficient cocatalyst on CdS nanorods for enhanced photocatalytic hydrogen production in water. Cat Sci Technol 2017;7:1515–22. https://doi.org/10.1039/c7cy00046d.

[162] Sun Z, Chen H, Zhang L, Lu D, Du P. Enhanced photocatalytic H2 production on cadmium sulfide photocatalysts using nickel nitride as a novel cocatalyst. J Mater Chem A 2016;4:13289–95. https://doi.org/10.1039/c6ta04696g.

[163] Dhanasekaran P, Salunke HG, Gupta NM. Visible-light-induced photosplitting of water over γ′-Fe 4N and γ′-Fe 4N/α-Fe 2O 3 nanocatalysts. J Phys Chem C 2012;116:12156–64. https://doi.org/10.1021/jp303255f.

[164] Meng X, Qi W, Kuang W, Adimi S, Guo H, Thomas T, et al. Chromium-titanium nitride as efficient co-catalyst for photocatalytic hydrogen production. J Mater Chem A 2020. https://doi.org/10.1039/D0TA00488J. Advance Article.

[165] Wang X, Wu L, Li J, Wang G, Wen J, Li X, et al. Titania nanotube derived titanium nitride nano-cluster for visible light driven water splitting. Catal Lett 2019;149:61–8. https://doi.org/10.1007/s10562-018-2614-y.

[166] Winter CH, Jayaratne KC, Proscia JW. Single-source precursors to niobium nitride and tantalum nitride films. MRS Proc 1994;327:103–8. https://doi.org/10.1557/PROC-327-103.

[167] Ritala M, Kalsi P, Riihelä D, Kukli K, Leskelä M, Jokinen. Controlled growth of TaN, Ta3N5, and TaOxNy thin films by atomic layer deposition. Chem Mater 1999;11:1712–8. https://doi.org/10.1021/cm980760x.

[168] Marchand R, Tessier F, Disalvo FJ. New routes to transition metal nitrides: and characterization of new phases. J Mater Chem 1999;9:297–304. https://doi.org/10.1039/A805315D.

[169] Hitoki G, Ishikawa A, Takata T, Kondo JN, Hara M, Domen K. Ta3N5 as a novel visible light-driven Photocatalyst ($\lambda < 600$ nm). Chem Lett 2002;31:736–7. https://doi.org/10.1246/cl.2002.736.

[170] Jiang Y, Liu P, Chen YC, Zhou Z, Yang H, Hong Y, et al. Construction of stable Ta3N5/g-C3N4 metal/non-metal nitride hybrids with enhanced visible-light photocatalysis. Appl Surf Sci 2017;391:392–403. https://doi.org/10.1016/j.apsusc.2016.04.094.

[171] Anpo M, Takeuchi MJ. The design and development of highly reactive titanium oxide photocatalysts operating under visible light irradiation. J Catal 2003;216:505–16. https://doi.org/10.1016/S0021-9517(02)00104-5.

[172] Zou Z, Ye J, Sayama K, Arakawa H. Direct splitting of water under visible light irradiation with an oxide semiconductor photocatalyst. Nature 2001;414:625–7. https://doi.org/10.1038/414625a.

[173] Ishikawa A, Takata T, Kondo JN, Hara M, Kobayashi H, Domen K. Oxysulfide Sm2Ti2S2O5 as a stable photocatalyst for water oxidation and reduction under visible light irradiation ($\lambda \leq 650$ nm). J Am Chem Soc 2002;124:13547–53. https://doi.org/10.1021/ja0269643.

https://www.twirpx.org & http://chemistry-chemists.com

[174] Zhang Q, Gao L. Ta3N5 nanoparticles with enhanced photocatalytic efficiency under visible light irradiation. Langmuir 2004;20:9821–7. https://doi.org/10.1021/la048807i.

[175] Takata T, Lu D, Domen K. Synthesis of structurally defined Ta3N5 particles by flux-assisted nitridation. Cryst Growth Des 2011;11:33–8. https://doi.org/10.1021/cg901025e.

[176] Kado Y, Lee CY, Lee K, Müller J, Moll M, Spiecker E, et al. Enhanced water splitting activity of M-doped Ta3N5 (M = Na, K, Rb, Cs). Chem Commun 2012;48:8685–7. https://doi.org/10.1039/C2CC33822J.

[177] Ma SSK, Hisatomi T, Maeda K, Moriya Y, Domen K. Enhanced water oxidation on Ta3N5 photocatalysts by modification with alkaline metal salts. J Am Chem Soc 2012;134:19993–6. https://doi.org/10.1021/ja3095747.

[178] Ma B, Liu Y, Li J, Lin K, Liu W, Zhan H. Mo2N: an efficient non-noble metal cocatalyst on CdS for enhanced photocatalytic H2 evolution under visible light irradiation. Int J Hydrogen Energy 2016;41:22009–16. https://doi.org/10.1016/j.ijhydene.2016.08.133.

[179] Wang C, Qi W, Zhou Y, Kuang W, Azhagan T, Thomas T, et al. Ni-Mo ternary nitrides based one-dimensional hierarchical structures for efficient hydrogen evolution. Chem Eng J 2020;381:122611–20. https://doi.org/10.1016/j.cej.2019.122611.

[180] Wang YL, Nie T, Li YH, Wang XL, Zheng LR, Chen AP, et al. Black tungsten nitride as a metallic photocatalyst for overall water splitting operable at up to 765 nm. Angew Chem Int Ed 2017;56:7430–4. https://doi.org/10.1002/anie.201702943.

[181] Asahi R, Morikawa T, Ohwaki T, Aoki K, Taga Y. Visible-light photocatalysis in nitrogen-doped titanium oxides. Science 2001;293:269–71. https://doi.org/10.1126/science.1061051.

[182] Afanasiev P. New approach to the preparation of highly dispersed transition metals sulfides and nitrides. Catal Today 2015;250:134–44. https://doi.org/10.1016/j.cattod.2014.03.046.

[183] Kachina A, Puzenat E, Ould-Chikh S, Geantet C, Delichere P, Afanasiev P. A new approach to the preparation of nitrogen-doped titania visible light photocatalyst. Chem Mater 2012;24:636–42. https://doi.org/10.1021/cm203848f.

[184] Orhan E, Tessier F, Marchand R. Synthesis and energetics of yellow TaON. Solid State Sci 2002;4:1071–6. https://doi.org/10.1016/S1293-2558(02)01369-9.

[185] Zhou P, Gao HL, Yan SC, Zou ZG. The Kirkendall effect towards oxynitride nanotubes with improved visible light driven conversion of CO2 into CH4. Dalton Trans 2016;45:3480–5. https://doi.org/10.1039/c5dt04124d.

[186] Qi Y, Chen S, Li M, Ding Q, Li Z, Cui J, et al. Achievement of visible-light-driven Z-scheme overall water splitting using barium-modified Ta3N5 as a H2-evolving photocatalyst. Chem Sci 2017;8:437–43. https://doi.org/10.1039/C6SC02750D.

[187] Kou J, Li Z, Yuan Y, Zhang H, Wang Y, Zou. Visible-light-induced photocatalytic oxidation of polycyclic aromatic hydrocarbons over tantalum oxynitride photocatalysts. Environ Sci Technol 2009;43:2919–24. https://doi.org/10.1021/es802940a.

[188] Brophy MR, Pilgrim SM, Schulze WA. Synthesis of BaTaO2N powders utilizing NH3 decomposition. J Am Ceram Soc 2011;94:4263–8. https://doi.org/10.1111/j.1551-2916.2011.04826.x.

[189] Gregory DH. Structural families in nitride chemistry. Dalton Trans 1999;3:259–70. https://doi.org/10.1039/A807732K.

[190] Oró-Solé J, Clark L, Kumar N, Bonin W, Sundaresan A, Attfield JP, et al. Synthesis, anion order and magnetic properties of RVO3 − xNx perovskites (R = La, Pr, Nd; 0 ≤ x ≤ 1). J Mater Chem C 2014;2:2212–20. https://doi.org/10.1039/C3TC32362E.

[191] Masubuchi Y, Kawamura F, Taniguchi T, Kikkawa S. High pressure densification and dielectric properties of perovskite-type oxynitride SrTaO2N. J Eur Ceram Soc 2015;35:1191–7. https://doi.org/10.1016/j.jeurceramsoc.2014.10.028.

https://www.twirpx.org & http://chemistry-chemists.com

[192] Sun SK, Motohashi T, Masubuchi Y, Kikkawa S. Direct synthesis of SrTaO2N from SrCO3/Ta3N5 involving CO evolution. J Eur Ceram Soc 2014;34:4451–5. https://doi.org/10.1016/j.jeurceramsoc.2014.07.003.

[193] Gomathi A, Reshma S, Rao CNR. A simple urea-based route to ternary metal oxynitride nanoparticles. J Solid State Chem 2009;182:72–6. https://doi.org/10.1016/j.jssc.2008.10.004.

[194] Yang M, Rodgers JA, Middler LC, Oró-Solé J, Jorge AB, Fuertes A, et al. Direct solid-state synthesis at high pressures of new mixed-metal oxynitrides: RZrO2N (R = Pr, Nd, and Sm). Inorg Chem 2009;48:11498–500. https://doi.org/10.1021/ic902020r.

[195] Tassel C, Kuno Y, Goto Y, Yamamoto T, Brown CM, Hester J, et al. MnTaO2N: polar LiNbO3-type Oxynitride with a helical spin order. Angew Chem 2015;54:516–21. https://doi.org/10.1002/anie.201408483.

[196] Mori Y, Imade M, Murakami K, Takazawa H, Imabayashi H, Todoroki Y, et al. Growth of bulk GaN crystal by Na flux method under various conditions. J Cryst Growth 2012;350:72–4. https://doi.org/10.1016/j.jcrysgro.2011.12.026.

[197] Kim YI, Si W, Woodward PM, Sutter E, Park S, Vogt T. Epitaxial thin-film deposition and dielectric properties of the perovskite oxynitride BaTaO2N. Chem Mater 2007;19:618–23. https://doi.org/10.1021/cm062480k.

[198] Paven-Thivet CL, Ishikawa A, Ziani A, Gendre LL, Yoshida M, Kubota J, et al. Photoelectrochemical properties of crystalline perovskite lanthanum titanium oxynitride films under visible light. J Phys Chem C 2009;113:6156–62. https://doi.org/10.1021/jp811100r.

[199] Ida S, Okamoto Y, Matsuka M, Hagiwara H, Ishihara T. Preparation of tantalum-based oxynitride nanosheets by exfoliation of a layered oxynitride, CsCa2Ta3O10–xNy, and their photocatalytic activity. J Am Chem Soc 2012;134:15773–82. https://doi.org/10.1021/ja3043678.

[200] Adeli B, Taghipour F. Atomic-scale synthesis of nanoporous gallium-zinc oxynitride-reduced graphene oxide photocatalyst with tailored carrier transport mechanism. RSC Adv 2020;10:14906–14. https://doi.org/10.1039/d0ra01725f.

[201] Zheng Y, Liu J, Liang J, Jaroniec M, Qiao SZ. Graphitic carbon nitride materials: controllable synthesis and applications in fuel cells and photocatalysis. Energ Environ Sci 2012;5:6717–31. https://doi.org/10.1039/c2ee03479d.

[202] Thomas A, Fischer A, Goettmann F, Antonietti M, Müller JO, Schlögl R, et al. Graphitic carbon nitride materials: variation of structure and morphology and their use as metal-free catalysts. J Mater Chem 2008;18:4893–908. https://doi.org/10.1039/b800274f.

[203] Guo Q, Xie Y, Wang X, Lv S, Hou T, Liu X. Characterization of well-crystallized graphitic carbon nitride nanocrystallites via a benzene-thermal route at low temperatures. Chem Phys Lett 2003;380:84–7. https://doi.org/10.1016/j.cplett.2003.09.009.

[204] Aleksandr S, Peng CZ, Dariya D. Baking 'crumbly' carbon nitrides with improved photocatalytic properties using ammonium chloride. RSC Adv 2016;2910–3. https://doi.org/10.1039/C5RA22167F.

[205] Yan H. Soft-templating synthesis of mesoporous graphitic carbon nitride with enhanced photocatalytic H2 evolution under visible light. Chem Commun 2012;48:3430–2. https://doi.org/10.1039/c2cc00001f.

[206] Huang Y, Wang Y, Bi Y, Jin J, Ehsan MF, Fu M, et al. Preparation of 2D hydroxyl-rich carbon nitride nanosheets for photocatalytic reduction of CO2. RSC Adv 2015;5:33254–61. https://doi.org/10.1039/c5ra04227e.

[207] Teixeira IF, Barbosa ECM, Tsang SCE, Camargo PHC. Carbon nitrides and metal nanoparticles: from controlled synthesis to design principles for improved photocatalysis. Chem Soc Rev 2018;47:7783–817. https://doi.org/10.1039/c8cs00479j.

https://www.twirpx.org & http://chemistry-chemists.com

[208] Yi J, El-Alami W, Song Y, Li H, Ajayan PM, Xu H. Emerging surface strategies on graphitic carbon nitride for solar driven water splitting. Chem Eng J 2020;382:122812–75. https://doi.org/10.1016/j.cej.2019.122812.

[209] Wen J, Xie J, Shen R, Li X, Luo XY, Zhang H, et al. Markedly enhanced visible-light photocatalytic H2 generation over g-C3N4 nanosheets decorated by robust nickel phosphide (Ni12P5) cocatalysts. Dalton Trans 2017;46:1794–802. https://doi.org/10.1039/c6dt04575h.

[210] Yang Z, Xing Z, Feng Q, Jiang H, Zhang J, Xiao Y, et al. Sandwich-like mesoporous graphite-like carbon nitride (Meso-g-C3N4)/WP/Meso-g-C3N4 laminated heterojunctions solar-driven photocatalysts. J Colloid Interface Sci 2020;568:255–63. https://doi.org/10.1016/j.jcis.2020.02.060.

[211] Kaixiang X, Zhigang C, Jianjian Y, Hui X, Yahui Y, Xiaojie S, et al. Highly efficient visible-light-driven Schottky catalyst MoN/2D g-C 3 N 4 for hydrogen production and organic pollutants degradation. Ind Eng Chem Res 2018;8863–70. https://doi.org/10.1021/acs.iecr.8b01268.

[212] Liu P, Rodriguez JA. Catalytic properties of molybdenum carbide, nitride and phosphide: a theoretical study. Catal Lett 2003;91:247–52. https://doi.org/10.1023/B:CATL.0000007163.01772.19.

[213] Liu P, Rodriguez JA, Asakura T, Gomes J, Nakamura K. Desulfurization reactions on Ni 2P(001) and α-Mo 2(001) surfaces: complex role of P and C sites. J Phys Chem B 2005;109:4575–83. https://doi.org/10.1021/jp044301x.

[214] Huang Z, Chen Z, Chen Z, Lv C, Meng H, Zhang C. Ni12P5 nanoparticles as an efficient catalyst for hydrogen generation via electrolysis and photoelectrolysis. ACS Nano 2014;8:8121–9. https://doi.org/10.1021/nn5022204.

[215] Liu P, Rodriguez JA. Catalysts for hydrogen evolution from the [NiFe] hydrogenase to the Ni 2P(001) surface: the importance of ensemble effect. J Am Chem Soc 2005;127:14871–8. https://doi.org/10.1021/ja0540019.

[216] Bekaert E, Bernardi J, Boyanov S, Monconduit L, Doublet ML, Ménétrier M. Direct correlation between the 31P MAS NMR response and the electronic structure of some transition metal phosphides. J Phys Chem C 2008;112:20481–90. https://doi.org/10.1021/jp808122q.

[217] Diplas S, Løvvik OM. Electronic structure studies of Ni–X (X: B, S, P) alloys using x-ray photoelectron spectroscopy, x-ray induced auger electron spectroscopy and density functional theory calculations. J Phys Condens Matter 2009;21:245503–11. https://doi.org/10.1088/0953-8984/21/24/245503.

[218] Li C, Du Y, Wang D, Yin S, Tu W, Chen Z, et al. Unique P-co-N surface bonding states constructed on g-C3N4 Nanosheets for drastically enhanced photocatalytic activity of H2 evolution. Adv Funct Mater 2017;27:1604328–36. https://doi.org/10.1002/adfm.201604328.

[219] Mazumder B, Hector AL. Synthesis and applications of nanocrystalline nitride materials. J Mater Chem 2009;19:4673–86. https://doi.org/10.1039/b817407e.

[220] Rachel A, Ebbinghaus SG, Güngerich M, Klar PJ, Hanss J, Weidenkaff A, et al. Tantalum and niobium perovskite oxynitrides: synthesis and analysis of the thermal behaviour. Thermochim Acta 2005;438:134–43. https://doi.org/10.1016/j.tca.2005.08.010.

[221] Higashi M, Domen K, Abe R. Fabrication of efficient TaON and ta 3N 5 photoanodes for water splitting under visible light irradiation. Energ Environ Sci 2011;4:4138–47. https://doi.org/10.1039/c1ee01878g.

[222] Tsutomu M, Naoyuki N, Jun K, Kazunari D. Photoelectrochemical properties of LaTiO2N electrodes prepared by particle transfer for sunlight-driven water splitting. Chem Sci 2013;1120. https://doi.org/10.1039/c2sc21845c.

[223] Ouhbi H, Aschauer U. Nitrogen loss and oxygen evolution reaction activity of perovskite oxynitrides. ACS Mater Lett 2019;1:52–7. https://doi.org/10.1021/acsmaterialslett.9b00088.

[224] Jia X, Chen W, Li Y, Zhou X, Yu X, Xing Y. Enhanced photoexcited carrier separation in Ta3N5/SrTaO2N (1D/0D) heterojunctions for highly efficient visible light-driven hydrogen evolution. Appl Surf Sci 2020;514:145915–50. https://doi.org/10.1016/j.apsusc.2020.145915.

https://www.twirpx.org & http://chemistry-chemists.com

[225] Kumar SS, Amit K, Gaurav S, Stadler JF, Mu N, Ghfar AA, et al. LaTiO2N/Bi2S3 Z-scheme nano heterostructures modified by rGO with high interfacial contact for rapid photocatalytic degradation of tetracycline. J Mol Liq 2020;113300. https://doi.org/10.1016/j.molliq.2020.113300.

[226] Chakraborty R, Pradhan M, Debnath K, Goh KL, Aswathi MK, De Silva RT, Thomas S. Band-gap engineering using metal-semiconductor interfaces for photocatalysis and supercapacitor application: a nanoparticle reinforced ceramic composite perspective. In: Interfaces in Particle and Fibre Reinforced Composites. Woodhead Publishing Series in Composites Science and Engineering. Elsevier; 2020. p. 391–451. https://doi.org/10.1016/B978-0-08-102665-6.00015-7.

https://www.twirpx.org & http://chemistry-chemists.com

9

Rare earth doped nanomaterials for visible-light-driven photocatalytic degradation of organic dyes

Dipti Bidwai, Niroj Kumar Sahu, and G. Swati

CENTRE FOR NANOTECHNOLOGY RESEARCH, VELLORE INSTITUTE OF TECHNOLOGY, VELLORE, TAMIL NADU, INDIA

1 Introduction

Rapidly growing demand in textile industries has resulted in the development of more than one lakh of synthetically derived organic dyes across the globe [1, 2]. Consumption of dyes is not only restricted to textile industries; they are also being extensively used by paper, leather, cosmetics, pharmaceuticals, and printing industries across the globe [3, 4]. Heavy consumption of organic dyes not only poses a severe threat to aquatic bodies but also disrupts the ecological balance of nature. Due to the long-lived perseverance of dyes, they enter the ecological food cycle resulting in carcinogenic disease, mutagenesis, skin allergies, and hormonal imbalance, thereby severely affecting humankind and aquatic species [5, 6]. Dyes, being nonbiodegradable, stable, and complex organic molecular entities, in turn block the penetration of sunlight and thereby hinder the re-oxygenation of water bodies. To deal with this problem, many methods have been established so far, for instance, physical adsorption using activated materials, electrochemical coagulation, reverse osmosis, membrane filtration, ozonation, ultrafiltration, biochemical process, etc. [7, 8] However, these are unable to oxidize completely synthetically stable dyes up to the permissible limits, and may also result in harmful by-products and intermediates that need further chemical purification. Photocatalysis is an innovative method because of its capability to mineralize intractable organic dyes thoroughly by using a renewable source of energy, e.g., sunlight [9–13]. Advanced oxidation processes involving semiconductor-based photocatalysts such as TiO_2, ZnO [14], SnO_2 [15], ZnS [16], MoS_2, $BiVO_4$ [17], MgO, $La_2Ti_2O_7$, $SrTiO_3$ [18], and CdS [19] are gaining importance. The year 1911 marked the study of degradation of Prussian blue dye upon excitation of ZnO with photons of suitable energy by A. Eibner [20]. Fujishima and Honda reported a major breakthrough in this field in 1972, explaining the electrochemical photolysis of water at a TiO_2 electrode [21]. Later, in 1984, Serpone et al. stated that the heterostructure of TiO_2 with CdS showed enhanced efficiency due to proper spatial separation of the excited

Nanostructured Materials for Visible Light Photocatalysis. https://doi.org/10.1016/B978-0-12-823018-3.00011-7
Copyright © 2022 Elsevier Inc. All rights reserved.

https://www.twirpx.org & http://chemistry-chemists.com

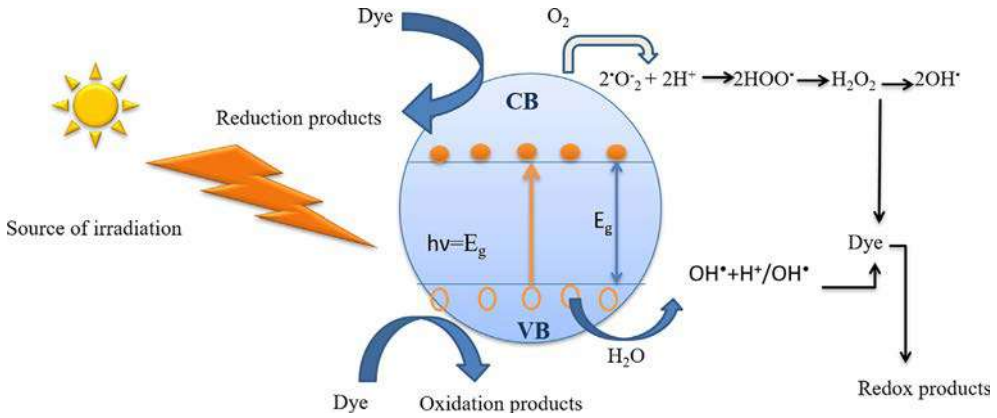

FIG. 1 Indirect photocatalytic degradation of complex organic dye in semiconductor photocatalyst.

charge carriers in different semiconductors [22]. In year 1996, Grätzel et al. [23] have reported the dye sensitisation of semiconductors to assist the process of photocatalysis, since then quest for novel semiconducting materials have gained importance. Research toward advanced materials such as graphene, fullerenes, noon metals, and nobel metals have gained huge importance.

Photocatalytic reactions occur at the interface of the semiconductor and dye in solution or gaseous form. The semiconductor acts as a photocatalyst by generating electron-hole pairs upon exciting semiconductor with photon energy equivalent or more than its forbidden energy gap energy, as schematically shown in Fig. 1 [24]. Charge carriers thereby result in creation of reactive oxygen species (ROS). More precisely, the electron and hole react with the molecular oxygen and water molecules to produce highly reactive radicals such as $O_2^{\cdot -}$ and $^{\cdot}OH$. Active radicals chemically interact with dye molecules, thereby converting them into similar compounds, CO_2 and H_2O. A series of photocatalytic chemical reactions which take place between the semiconductor and dye interface are as shown in Fig. 1.

At the same time, dye molecules may directly get excited to a higher energy triplet state. It is reported that the excited triplet state of dye molecules loses its electron to the conduction band (CB) of TiO_2, converting itself into semioxidized radical cation ($dye^{\cdot +}$) [24–27]. The electron present in the CB of semiconductor chemically reacts with O_2, resulting in the formation of hydroxide radicals ($OH^{\cdot}$), which leads to direct photooxidation of dye molecules, as represented schematically in Fig. 2. However, the direct oxidation process is not an efficient mode of oxidation of dyes due to the rate-limiting kinetics of the reactions involved.

https://www.twirpx.org & http://chemistry-chemists.com

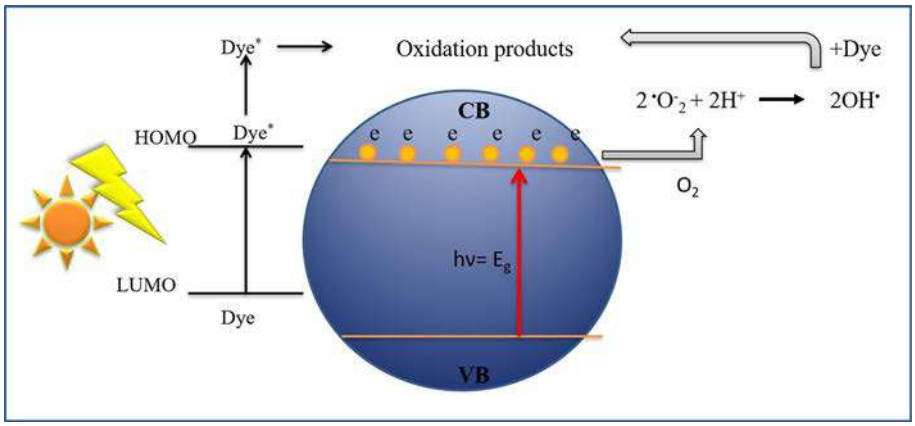

FIG. 2 Direct photocatalytic degradation of complex organic dyes mechanism.

2 Modifications to conventional semiconductors

Because of the rapid recombination rate of photogenerated electron-hole pairs and spectral mismatch between the solar spectrum and bandgap of the existing semiconductors, only 3%–4% of the solar spectrum is being utilized, thus their UV activity is not high enough from the viewpoint of practical applications [28]. Additionally, self-corrosion, poor photochemical stability, low separation efficiency, and high recombination rate are also key limiting factors which need to be addressed. To move beyond these limits, researchers are adapting novel strategies to engineer the bandgap of semiconductors. Some of the significant modifications to the semiconductors are explained in detail.

2.1 Nonmetal doping

Tailoring bandgap of semiconductor photocatalysts with nonmetal creates electronic states above the valence band (VB) of oxide semiconductors, which in turn make the visible catalyst light-responsive. Various nonmetal dopants such as boron, carbon, nitrogen, and fluorine have been widely reported for photocatalytic application, However, the mechanism of doping nonmetals is still uncertain whether nonmetallic ions are substitutes at the host site or merely occupies interstitial and vacancy sites. According to the literature, doping may reduce the bandgap of the TiO_2 by up to 2.5 eV, thereby extending the absorption of TiO_2 in visible light [29–31]. Doping of nonmetals like carbon and nitrogen reduces the crystalline size of the particle, thereby decreasing the recombination of electrons and holes, and increasing the surface area, which enriches the photocatalytic activity of catalysts. Salarian et al. reported N-doped TiO_2 synthesized via the hydrothermal method for the degradation of diazinon. They made a comparative study of bare TiO_2

https://www.twirpx.org & http://chemistry-chemists.com

and nitrogen-doped TiO_2 [28]. The sizes of bare TiO_2 and N-TiO_2 were 44 nm and 27 nm, respectively, indicating the successful doping of N. The results showed the extended absorption region of N-TiO_2. The degradation percentage of diazinon dye under solar light using N-TiO_2 was 86% while the bare TiO_2 experiment revealed no degradation of diazinon. Dong et al. made C-doped TiO_2 by the hydrothermal method with postthermal treatments at different temperature of 100°C, 200°C, and 300°C. The degradation of gaseous toluene was carried out under visible light [32]. Li et al. prepared C-TiO_2 by the hydrothermal method and tested the catalyst by the degradation of methyl orange. C-TiO_2 at 130°C showed a degradation effectiveness of 99% in 4 min under visible light [33].

2.2 Transition metal doping

Transition metal ions doping in semiconductor oxide catalysts tunes the bandgap of these photocatalysts toward visible light-responsive. Transition metal ions doping enhances morphology and optical properties, and reduces the crystallite size of particles. The transition metals Fe, Ag, Au, Mn, Co, Ni, V, Cr, and Cu have been used as dopants [34–39]. Among all these, Cu is the most suitable because of its availability and low cost; in addition, the ionic radius of Cu^{2+} (0.73 Å) is nearly comparable to that of Zn^{2+} (0.83 Å) and Ti^{4+} (0.64 Å) which helps to incorporate Cu^{2+} ions in TiO_2 (or ZnO) crystal structures. A transition metal creates impurity levels below the conduction band (CB) which can act as electron traps and thus increases the recombination time, resulting in improved photo-reactivity. Yang et al. reported enhanced photocatalytic decomposition of organic methyl orange (MO) dye by Copper doped TiO_2 than bare TiO_2. The enhanced degradation rate was attributed to doping carbon in TiO_2 which increases the absorbance ability of the catalyst toward the visible light spectrum [40].

2.3 Multiatom doped TiO_2

It is anticipated that the addition of nonmetallic ions such as carbon, sulfur, and nitrogen restricts the growth of semiconductor nanoparticles, thereby enhancing the active surface area. In addition, doping with nonmetals broadens the sufficient bandgaps of the semiconductors [41]. Szkoda et al. incorporated nonmetal N, B, and I in TiO_2 catalysts. BTiO_2 degraded methyl blue dye more efficiently than I and N, with efficiency of 38%. The incorporation of nonmetals effectively suppressed the recombination of charge species and increased generation of highly unstable OH radicals [41]. Yang et al. doped carbon, sulfur, and nitrogen in TiO_2 via the solgel method. The results showed that the surface area of doped TiO_2 was more than that of the pristine one, and the crystalline size was smaller than the undoped one [42]. Liu et al. reported codoped TiO_2 with La and N along with activated carbon prepared by the solgel technique for degradation of naphthalene [43]. This multiatom doped composite exhibited 93.5% decomposition efficiency of naphthalene under visible light treatment.

https://www.twirpx.org & http://chemistry-chemists.com

2.4 Doping with iron

Injection of iron (Fe^{3+}) in TiO_2 or ZnO creates the electronic energy levels above the VB which traps the photogenerated holes. But the higher concentration of metal ions such as Fe can act as the recombination center, decreasing photocatalytic action. In a study, Moradi et al. reported that various doping concentrations (0.5, 1, 5, and 10 wt%) of Fe in TiO_2 were utilized for removal of reactive red 198 (RR 198) dye. The samples were produced by the solgel technique [44]. The optimum doping of 1 wt% of Fe displayed the highest degradation efficiency of RR 198 dye compared to the undoped titania under visible light. Yu et al. synthesized Fe-doped ZnO via the solgel method with 0–4 mol% doping concentration. Pure ZnO did not exhibit absorption in visible light while Fe-doped ZnO allowed the absorption edge in the visible light spectrum (400–600 nm). The redshift was a result of the transition of electrons between the CB of ZnO and *d*-electrons of Fe. Among the different concentrations, 1% doping showed 96% efficiency MO degradation after 120 min [45].

2.5 Coupling with other narrow bandgap semiconductors

Investigations have also been carried out by combining two semiconductors. Combining a narrow bandgap semiconductor with a broad bandgap semiconductor shifts the absorption edge of the photocatalyst in the visible light region. Coupling of these semiconductors allows the transmission of an electron from one semiconductor to another, resulting in better charge separation, thereby minimizing the recombination rates. Pérez-González et al. reported the heterostructures ZnO-TiO_2 and Ag-doped ZnO-TiO_2 synthesized via a simple solgel method [46]. The composite of ZnO-TiO_2 decomposed the methyl blue dye with 70% efficiency in 2 h. The addition of Ag increased the photocatalytic activity to 80% in 2 h. It was reported that a Bi_2MoO_6/TiO_2 heterostructure results in a redshift of absorption spectra than that of the bare TiO_2 and Bi_2MoO_6 [47]. The obtained bandgap for the pure Bi_2MoO_6 and TiO_2 is 2.66 eV and 3.11 eV, respectively. However, for heterostructure of Bi_2MoO_6/TiO_2 the bandgap is found to vary in a range of 2.77 to 2.93 eV. The RhB dye was successfully degraded with 92% in 5 h with heterostructure while it was negligible in the case of pure TiO_2 and Bi_2MoO_6. Dammala et al. reported improved photocatalytic activity of Zn_2SnO_4/SnO_2 and ZnO/SnO_2 biphasic nanocatalysts for the degradation of acid red-183 (AR-183) dye compared to bare SnO_2 and ZnO nanoparticles [48].

2.6 Dye sensitization in photocatalysis

Dye sensitization-assisted photocatalysis causes dye adsorption on the surface of TiO_2 and the excited state electron of dye transfers to the CB of TiO_2 and then reacts with the oxygen to form superoxide radicals, which in turn forms $^{\cdot}OH$ radicals. There should be fast injection of electrons from dye to CB of TiO_2 for better charge separation. In the study, Bakar et al. presented the immobilized system of TiO_2 with PVA and PEG as binders along with reactive red-4 dye as a sensitizer [49]. The results showed complete

https://www.twirpx.org & http://chemistry-chemists.com

decomposition of MO in the presence of reactive red-4 dye in 1 h while in the absence of reactive red-4, the degradation required more than 1 h. Jing et al. prepared the perylene tetracarboxylic diimide (PTCDI) (organic dye having absorption in visible light) and copper phthalocyanine tetra sulfonic acid (CuPcTs) (can absorb radiation in blue-green region of visible light region) cosensitized and single-sensitized TiO_2 composites. Among all composites, a cosensitized composite of TiO_2/PTCDI/CuPcTs showed strong absorption in the 400–800 nm range with better electron transfer and degradation of RhB [50].

2.7 Rare earth ions doping

Two major concerns which limit the application of semiconductor oxide-based photocatalysts are wide forbidden energy gap (>3.0 eV), as a result of which only 4%–5% of solar spectrum received on Earth's surface is utilized by conventional semiconductors, and rapid recombination rate of photo-generated charge species. One of the progressive studies toward development of more efficient photocatalyst which can utilize UV-Vis-NIR radiations received in Earth's atmosphere is via doping rare earth ions in conventionally used semiconductors. Carefully incorporating optimum rare earth ions results in the creation of additional energy levels within the energy bandgap of the semiconductors and insulators which ranges the light absorption to the visible or IR light region. In addition, to improve the efficiency of the photocatalytic process driven by semiconductors, it is obligatory to enhance the separation efficiency of photogenerated charge carriers. By incorporating rare earth metal doping in semiconductor oxides material, dopants also facilitate the retardation of the electron-hole pair recombination upon excitation. Rare earth also may act as Lewis base, which is responsible for distillating the organic dye contaminants dissolved in an aqueous medium over the surface of the semiconductor, thereby improving the electron transfer for the direct degradation of the organic dye or increasing the probability of interaction between the molecules and the radicals formed [24]. Another possible mechanism for enhanced photocatalytic degradation is attributed to the adsorption of these rare earth ions on the surface of the semiconductors, which causes surface charge imbalance; this in turn can yield surface defects and vacancies of oxygen as well as metal [51]. Thus, these rare earth ions lead to surface states that act as electron scavengers and decrease the recombination of photogenerated charges, increasing the possibility of •OH formation.

A generic model explaining the photocatalysis process in presence of rare earth ions can be understood on the basis of Fig. 3. *4f* energy states of the rare earth ions, being close to the CB of the semiconductors, form energy levels in the vicinity of CB edge of semiconductors. Upon excitation with photons of suitable energy, electrons are excited from the VB to *4f* energy states of rare earth ions. Electron trapping at the rare earth energy levels suppresses electron-hole recombination. Thus, the lanthanide ions may act as electron scavengers. These trapped electrons further react with the molecular oxygen to form ROS, which causes degradation of organic dye molecules. Simultaneously, the direct dye degradation mechanism (see Fig. 2) may also continue to exist [24]. Free electrons

https://www.twirpx.org & http://chemistry-chemists.com

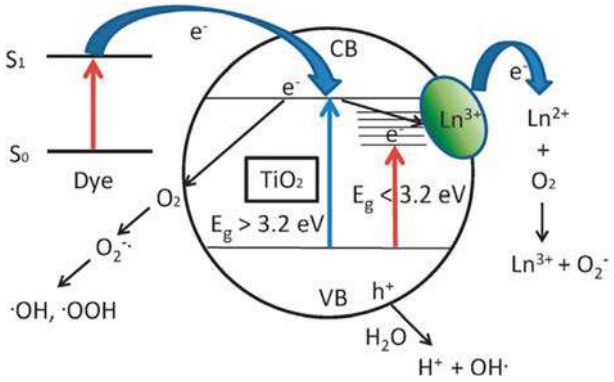

FIG. 3 Illustration of mechanism for lanthanide-assisted photocatalytic degradation of organic dyes. *(Adapted from Amanda S. Weber et al., Lanthanide modified semiconductor photocatalysts, Cat Sci Technol 2012;20:683–93.)*

produced in the excited state of dye molecules subsequently get transferred to the *4f* energy levels of the rare earth ions. Considering the advantages, researchers are working toward rare earth-doped upconversion, downconversion, and persistent luminescent materials. Furthermore, a detailed review of rare earth doped downconversion, upconversion, and persistent phosphors have been discussed in detail.

3 Fluorescence and phosphorescence mechanism

Derived from the Latin word *lumen*, meaning light, luminescence is a cold body radiation phenomenon in which spontaneously high energy electromagnetic radiations are converted into visible or near-visible light. Luminescent materials, which are also known as phosphors, consist of an inorganic host lattice doped with impurities. Impurities may include uninventable point defects such as vacancies, cation deficiencies, etc. Impurities which are responsible for imparting emission color in the visible light to the host lattice are also known as activators. Transition metals such as Cr^{3+}, Ti^{4+}, and Sb^{3+} are responsible for imparting emissions in visible spectra due to their partly filled d-orbital ($d \rightarrow d$), whereas rare earth ions show transitions among the *5d* shell and the *4f* shell of rare-earth ions ($d \rightarrow f$ transitions) [52].

Two common manifestations of luminescence are fluorescence and phosphorescence. Upon excitation of atoms in a material by suitable energy, electrons reach a higher energy state (S_1). From this higher energy state, the electrons relax back to a lower energy (S_0) state spontaneously, with release of photons in $\sim 10^{-8}$ s. Such a spontaneous phenomenon results in emission of light photons of equivalent energy, whereas phosphorescence is a temperature-dependent phenomenon. Electrons get trapped in meta-stable energy levels (T_1 and T_2) within the forbidden gap before reaching ground state, resulting in delayed luminescence, ranging from 10^{-4} s to a few minutes. A radiationless transition occurring between the first excited singlet state (S_1) and the triplet (T_1) state is called intersystem

https://www.twirpx.org & http://chemistry-chemists.com

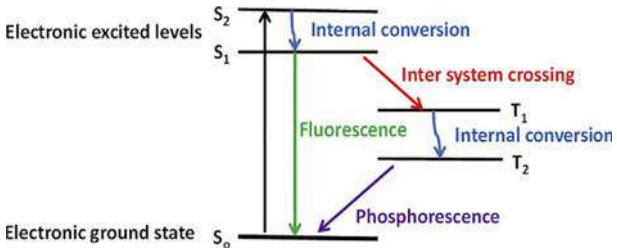

FIG. 4 Energy level diagram for fluorescence and phosphorescence phenomenon. *(Adapted from Swati G et al. Rare-earth doping in afterglow oxide phosphors: Materials, persistence mechanisms, and dark vision display applications. In Spectroscopy of Lanthanide Doped Oxide Materials, Woodhead Publishing, 2020, p. 393–425.)*

crossing. A spin change occurs with inter-system crossing, which is against Pauli's exclusive principle, as shown in Fig. 4 [53].

In conventional florescence phenomena, high energy radiations such as UV and X-rays are spectrally downconverted into low energy radiations in the visible range. Phosphors which exhibit such a phenomenon of spectrally downconverting the absorbed energy are known as downconversion phosphors. Since the energy of emitted photons is less than that of the excitation photon, downconversion phosphors obey the energy conservation rule; thus this is considered to be a Stokes process [53]. On the other hand, an interesting optical nonlinear phenomenon exhibited by phosphor which involves consecutive absorption of two or more photons results in the emission of shorter wavelength light than the excitation wavelength, known as upconversion phosphors. Since the emitted photons has a greater energy than that of the individual excitation photons, the process comes under the category of anti-Stokes luminescence. Long afterglow phosphors or persistent phosphors are a special class of photon energy storage materials in which charge carriers are trapped at defect centers. Charge carriers are thermally detrapped from these trap levels, thereby causing electron-hole recombination resulting in delayed luminescence or afterglow phenomena ranging from minutes to hours. Defect centers are mostly created intentionally via codoping, multicenter doping, and defect-related trapping centers. We present a concise review of a variety of downconversion, upconversion, and long afterglow phosphors which are being studied for effective visible light-driven photocatalysis.

3.1 Upconversion luminescent materials

Solar radiation received on Earth constitutes more than 48% of infrared radiations. Utilization of this infrared radiation plays a significant role in improving the efficiency of photocatalytic reactions. Upconversion is a nonlinear optical method which spectrally converts low energy photons into higher energy photons via a two-photon or/and multi-photon mechanism [54]. Upconverting luminescent materials converts infrared or visible radiation into UV radiation, which is responsible for exciting the semiconductor. Apart from the upconverting phenomenon, reduced electron-hole recombination rate and

https://www.twirpx.org & http://chemistry-chemists.com

enhanced absorption are additional benefits of using hybrids of semiconductors and upconverting luminescent material or phosphors.

In early 2005, Wang et al. [55] established a visible light-driven photocatalyst, based on a combination of Er-containing upconversion materials with TiO_2. In research work by Wu et al., blue color emitting Yb, Tm-doped $NaYF_4$, green emitting Yb, Er-doped $NaYF_4$, and red emitting Yb, Er-doped Y_2O_3/YOF UCP were coupled with carbon-doped TiO_2 [56]. A composite was found to be excitable by UV, visible, and NIR light. Absorbed NIR light was upconverted by the phosphors into visible light radiation via a nonlinear multiphoton mechanism which was utilized by carbon-doped TiO_2, thereby generating electron-hole pairs for degradation of Rhodamine dye and for NO gas destruction. In 2015, Feng et al. reported tungstate-based upconversion phosphor $ZnWO_4$:Yb^{3+}, Tm^{3+} on TiO_2 for the degradation of complex methyl orange dye. Dye degradation of 55.6% was observed under sun-like irradiation for 210 min [57]. Wang et al. reported the enhanced photocatalytic activity of TiO_2 with the upconversion luminescent material $Y_3Al_5O_{12}$:Er^{3+} [58]. $Y_3Al_5O_{12}$:Er^{3+} was excited with 488 nm visible light radiation and the emission peaks obtained in the UV region. Photocatalytic activity was carried out for Congo red dye. In 5 h, the complete degradation of the dye with TiO_2/$Y_3Al_5O_{12}$:Er^{3+} was observed. Yin et al. synthesized Er^{3+}:$Y_3Al_5O_{12}$/TiO_2–ZrO_2 via ultrasonic dispersion plus liquid boiling process for degradation of Azo fuchsine dye [59]. Photocatalytic degradation of Azo fuchsine in the case of Er^{3+}:$Y_3Al_5O_{12}$/TiO_2–ZrO_2 was found to be 90.39% in 60 min whereas for Er^{3+}:$Y_3Al_5O_{12}$/TiO_2 and Er^{3+}:$Y_3Al_5O_{12}$/ZrO_2 composite, it was 77.99% and 5.74%, respectively. Table 1 lists the upconversion phosphors reported for degradation of various organic dyes.

In an interesting study by Gao et al., hierarchical core-shell microspheres of $NaYF_4$:Yb^{3+}, Er^{3+}, and Tm^{3+}@TiO_2–Ag have been utilized for photodegradation of methylene orange dye [68]. In addition to the benefits of upconversion, the advantage of noble metal silver because of its property of surface plasmon resonance has also been exploited in the study. Upon excitation at 980 nm, $NaYF_4$: Yb^{3+}, Er^{3+}, and Tm^{3+} emit at 345, 360, 452, 474, 521, and 544 nm; these results are ascribed to the transitions of Er^{3+} and Tm^{3+}. Upon coating with TiO_2 shell and loading of silver nanoparticles, emissions intensity was drastically reduced in the composite, confirming the efficient energy transfer from $NaYF_4$: Yb^{3+}, Er^{3+}, and Tm^{3+} phosphor to TiO_2; thereby charge carriers recombination in the composite was largely suppressed.

Fig. 5A and B shows the MO dye degradation mechanism using $NaYF_4$: Yb^{3+}, Er^{3+}, and Tm^{3+}@TiO_2-Ag under visible and UV light. Ag nanoparticles behave as trapping centers for photogenerated electrons. On irradiation of UV light, there is a formation of electrons and holes in the CB and VB of TiO_2. The electrons in the CB transferred to the Ag nanoparticles. These trapped electrons react with the O_2 molecules and hence superoxide radicals are formed. Concurrently, the holes in valence bands of semiconductors react with water molecules to generate the •OH radicals, as shown in Fig. 5D. The existence of Ag nanoparticles

https://www.twirpx.org & http://chemistry-chemists.com

Table 1 List of upconversion phosphors for degradation of organic dyes.

Sr. no.	Host lattice	Activator	Codopant/ composite	Organic compounds	Synthesis methodology adapted	Excitation wavelength	Degradation efficiency and time	Reference
1.	$Y_3Al_5O_{12}$	Er^{3+}	Bi_2WO_6	Phenol	Hydrothermal	488 nm	51% in 120 min	[60]
2.	$Y_3Al_5O_{12}$	Er^{3+}	TiO_2	MB	–	450–500 nm	–	[58]
3.	$Y_3Al_5O_{12}$	Er^{3+}	TiO_2/ZrO_2	Azo fuchsine	Ultrasonic dispersion and liquid boiling	–	90.39% in 60 min	[59]
4.	$YAlO_3$	Er^{3+}	ZnO	Acid red B	Ultrasonic dispersion and liquid boiling	486.5 nm and 542.4 nm:675 nm	86% in 60 min	[61]
5.	$YFeO_3$	Er^{3+}	TiO_2/SAC	MO	Solgel	>400 nm	90.8% in 120 min	[62]
6.	YF_3	Yb^{3+}, Tm^{3+}	TiO_2(P25)/ graphene	MO	Hydrothermal	98 nm laser	78% in 60 min	[63]
7.	$NaYF_4$	Si^{4+}	Gd^{3+}/ TiO_2	MB	Combustion and solgel	200–400 nm	~87.5% in 240 min	[64]
8.	Bi_2WO_6	Tm^{3+}	Yb^{3+}	RhB	Coprecipitation	~498 nm	97.6% in 25 min	[65]
9.	TiO_2	–	Carbon quantum dots (CQDs)	MB	Solgel	>400 nm	90% in 120 min	[66]
10.	TiO_2	–	Graphene quantum dots (GQDs)	RhB	Hydrothermal and ultrasound	550–600 nm	100% in 30 min	[67]

https://www.twirpx.org & http://chemistry-chemists.com

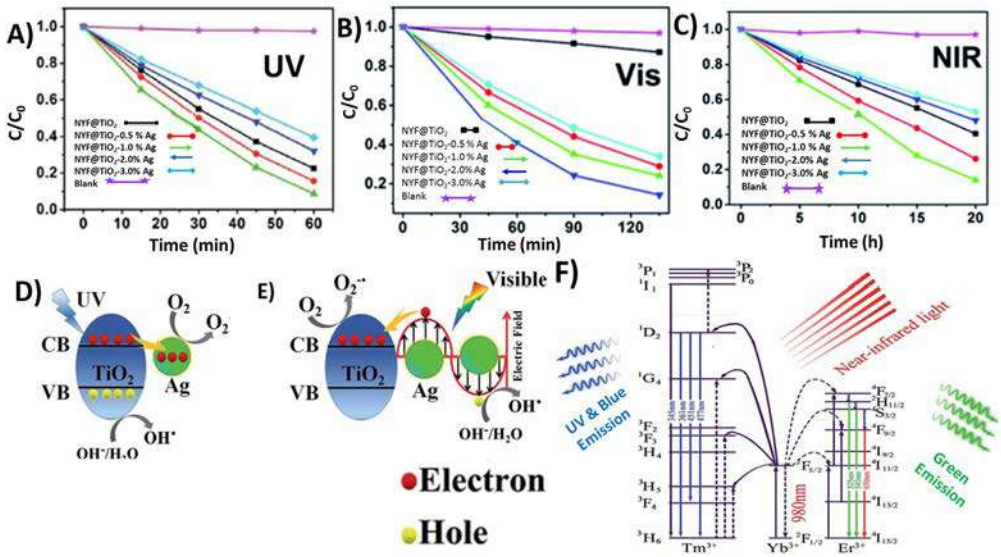

FIG. 5 Decomposition of methyl orange dye under (A) UV, (B) visible, and (C) NIR illumination and mechanism of NYF@TiO2–Ag catalyst under (D) ultraviolet excitation and (E) visible light excitation, (F) energy level representation, upconversion excitation showing UV and visible light radiations under the NIR light irradiation source using 980 nm laser. *(Adapted from Yu Gao et al., Synergistic effect of upconversion and plasmons in NaYF4: Yb 3+, Er 3+, Tm3+@ TiO2–Ag composites for MO photodegradation. RSC Adv 2017;7:54555–54561.)*

enhances the visible light absorption of $NaYF_4$: Yb^{3+}, Er^{3+}, and the Tm^{3+}@TiO_2-Ag catalyst because of the localized surface plasmon resonance (LSPR) effect. Due to irradiation of visible light, the LSPR effect on the interface of TiO_2-Ag enhances the charge carriers as shown in Fig. 5E. The generated electrons move to the TiO_2 CB from the interface of TiO_2-Ag, hence generating the $\cdot O_2^-$ radicals, and simultaneously the holes form $^{\cdot}OH$ radicals. The ·OH and $^{\cdot}O_2^-$ are important species in the photodegradation process. But on visible light excitation, the dye molecules get excited to form dye* and electrons. These electrons are then injected to the CB of TiO_2, which helps to generate the superoxide radicals. Fig. 5F shows the energy level diagram of NIR exciting upconversion photocatalysis. The NIR light (980 nm) is absorbed by the Yb^{3+} and it transfers the energy to Er^{3+} and Tm^{3+} because of the spectral overlapping. The emission of blue light from Tm^{3+} results from upconversion at 345, 360, 452, and 474 nm, and green light emission (521 and 544 nm) from Er^{3+} is due to the LSPR effect. This emission appears from Tm^{3+} and Er^{3+} as these are not excitable by 980 nm large wavelengths. The photocatalytic degradation of organic compound MO dye is carried out in UV, visible, and NIR light. Fig. 5A, B, and C shows the degradation of dye with varying concentrations of Ag. Under UV light radiation, the degradation of methyl orange dye was 91% with optimum loading of Ag nanoparticles of 1%, while under visible and NIR light the degradation percentage was seen as 82% in the presence of 2% Ag nanoparticles and 86% with 1% Ag loading, respectively.

https://www.twirpx.org & http://chemistry-chemists.com

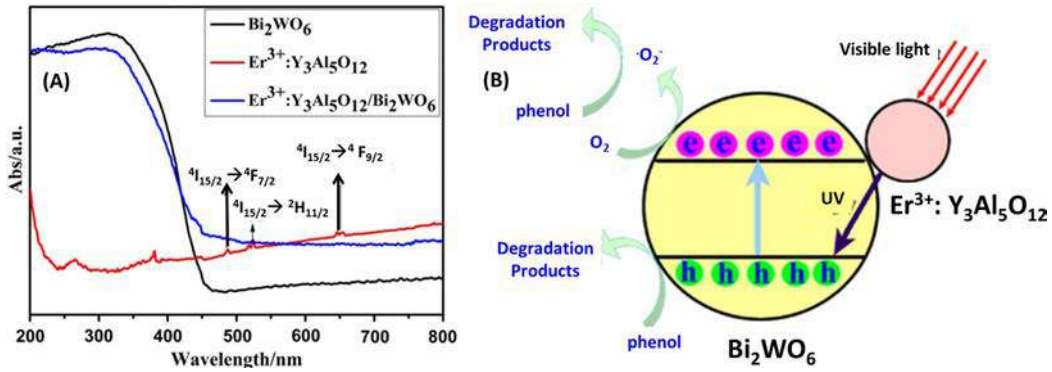

FIG. 6 (A) UV-vis spectra of Bi_2WO_6, $Y_3Al_5O_{12}:Er^{3+}/Bi_2WO_6$ and $Y_3Al_5O_{12}:Er^{3+}$. (B) Photocatalytic degradation of phenol mechanism by $Y_3Al_5O_{12}:Er^{3+}/Bi_2WO_6$ photocatalyst in visible light. *(Adapted from Zhijie Zhang et al. Enhanced photocatalytic activity of Bi2WO6 doped with upconversion luminescence agent. Cat Com 2011;13:31–34.)*

Apart from fluorides, oxides and sulfides, tungstates are also potential materials for visible light-driven photocatalysis. In early 1999, Kudo and Hijii reported Bi_2WO_6, which presents photoabsorption properties from UV light to the visible light region due to its energy bandgap in the range of ~2.8 eV [69]. Later compounds such as WO_3, Bi_2WO_6, and $BiWO_4$ are being extensively studied by researchers globally [52–59, 68–73]. With the intention of widening the range of visible light photo-responses, various strategies are being adapted such as doping, surface modifications, reducing particle size, coupling with order semiconductors, etc.

In a recent work by Zhang et al., novel downconverting phosphor Er^{3+}-doped $Y_3Al_5O_{12}$ was coupled with a Bi_2WO_6 photocatalyst [60]. A composite of $Y_3Al_5O_{12}:Er^{3+}/Bi_2WO_6$ was found to be effective in the degradation of phenol. Of the initial concentration of phenol, 51% was found to be degraded within 120 min, whereas only 31.5% was degraded by using bare Bi_2WO_6. According to UV-visible studies, it was found that in comparison to bare Bi_2WO_6, the Er^{3+}-$Y_3Al_5O_{12}$ -Er^{3+}/Bi_2WO_6 sample showed an increased absorption ability in the visible light region, which was ascribed to the visible light absorption ability of $Y_3Al_5O_{12}:Er^{3+}$, as shown in Fig. 6A. As seen from Fig. 6B, upconverting luminescence $Y_3Al_5O_{12}:Er^{3+}$ excited Bi_2WO_6. Charge carriers produced in Bi_2WO_6 result in the formation of active chemical radicals, which degrade phenol.

Particular attention is also being diverted toward carbon-based novel materials such as graphene, carbon nanotubes, carbon dots, and g-C_3N_4 owing to their exceptionally high surface area, excellent electronic properties, adsorption properties, and chemical inertness [74–78]. They are found to be efficient due to their ability of electron transfer, and separation of photogenerated charge. Owing to the excellent electrical conductivity for storing and transporting electrons, graphene in particularly is considered an ideal 2D material for scavenging photogenerated electrons [79, 80]. In a recent work by Ren et al., a nanocomposite comprising of UC phosphor ($YF_3:Yb^{3+},Tm^{3+}$), wide band semiconductor TiO_2 (P25), and graphene (GR) has been reported as an effective sunlight-activated

https://www.twirpx.org & http://chemistry-chemists.com

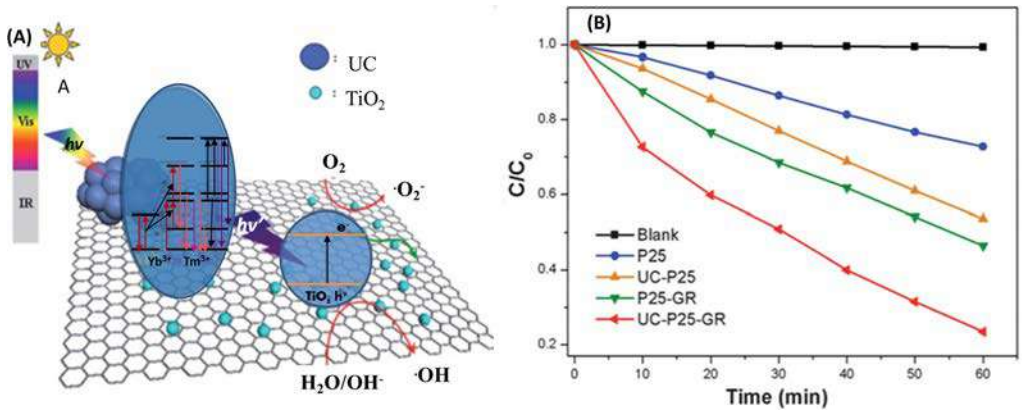

FIG. 7 (A) Schematic structure of nanocomposites of YF_3:Yb^{3+},Tm^{3+}–TiO_2–graphene showing photocatalysis mechanism. (B) Photodegradation of MO by TiO_2, YF_3:Yb^{3+}, Tm^{3+}–TiO_2, TiO_2–graphene combinations and YF_3:Yb^{3+}, Tm^{3+}–TiO_2–graphene for 60 min under sunlight irradiation. *(Adapted from Long Ren et al., Upconversion-P25-graphene composite as an advanced sunlight driven photocatalytic hybrid material. J Mater Chem 2012;22: 11765–11771.)*

photocatalyst for mineralization of methyl orange dye. The composite utilizes benefits of upconversion luminescence of phosphor and the excellent electrical properties of graphene. Due to the upconversion process in YF_3:Yb^{3+}, Tm^{3+} exhibit emission at 347 and 362 nm under the NIR excitation (980 nm) . Additional blue emission peaks at 452 nm and 476 nm are assigned to transitions of Tm^{3+} ions. As explained in Fig. 7A, YF_3:Yb^{3+}, Tm^{3+} spectrally upconverts the absorbed NIR light into UV light. Emitted light from the upconverting phosphor activates TiO_2, generating photogenerated electron-hole pairs. Graphene functions as an acceptor of the photogenerated electrons by TiO_2 and guarantees fast charge transportation. Graphene facilitates charge separation of electron-hole pairs and also enhances the capacity of the photocatalyst. Photodegradation studies revealed that a composite of YF_3:Yb^{3+}, Tm^{3+} TiO_2 (P25), and graphene degraded 30% of MO dye within the first 10 min. Upon 60 min of sunlight illumination, more than 78% of the initial dyes were decomposed, as shown in Fig. 7B. [63]

3.2 Downconversion phosphors photocatalysis

Photon conversion/spectral conversion is a budding method to improve the light harnessing property of wide bandgap semiconductors. Spectral conversion as an emerging technology is being utilized in various optoelectronic devices, photovoltaic solar cells, and light-emitting diodes. Downconversion phosphors have attracted attention because of their spectral downconverting property of converting high-energy photons into low-energy photons. A downconverting phosphor can convert the partial or entire UV region (200–400 nm) of the solar spectrum into visible light photons. Incorporating downconversion phosphor in conventional semiconductors has proved to improve the light absorbance capacity of wide bandgap catalysts by increasing the visible light absorbing

https://www.twirpx.org & http://chemistry-chemists.com

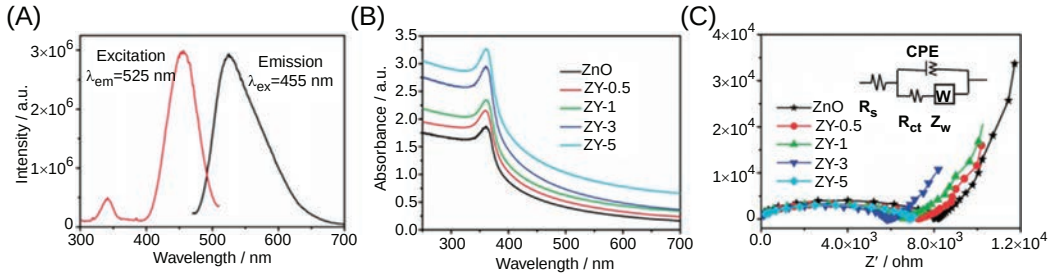

FIG. 8 (A) Photoluminescence spectra of excitation and emission of $Y_2Al_5O_{12}:Ce^{3+}$. (B) UV-vis spectra of ZnO and its composite with $Y_2Al_5O_{12}:Ce^{3+}$ at different wt%. (C) Nyquist plots of ZnO and its composite with $Y_2Al_5O_{12}:Ce^{3+}$ at different wt%. Inset figure is equivalent circuit. *(Adapted from Xinjuan Liu et al. Microwave-assisted synthesis of ZnO–Y3Al5O12: Ce3+ composites with enhanced visible light photocatalysis. J Mater Chem 2012;22:16293–16298.)*

ability. Additionally, a heterojunction is formed due to the different band structure of LAP, and phosphors suppress the recombination of photo-induced carriers which further improves the photocatalytic property. Different rare earth ions (Eu^{3+}, Pr^{3+}, Ce^{3+}, Tb^{3+}, Er^{3+}) are incorporated in the host lattice to give emission at different wavelength. Recently Liu et al. have studied the influence of downconverting phosphor $Y_2Al_5O_{12}:Ce^{3+}$ in a pristine ZnO semiconductor via the microwave-assisted method [81]. Since $Y_2Al_5O_{12}:Ce^{3+}$ phosphor exhibits a wide emission spectrum centered at 525 nm with an excitation wavelength of 455 nm (as shown in Fig. 8A), which falls in the absorption region of the dye methylene blue, photocatalytic performance was tested by degradation of methyl blue dye under visible light using a 400 W halogen lamp (390–800 nm). Systematic incorporation of $Y_2Al_5O_{12}:Ce^{3+}$ phosphor in the amounts of 0.5, 1, 3, and 5 wt% in ZnO was reported. UV-visible absorption studies revealed that a composite of $Y_2Al_5O_{12}:Ce^{3+}$ and ZnO exhibited higher absorbance in the visible light spectrum compared to the pristine ZnO as shown in Fig. 8B. Augmentation of light absorption intensity and range can increase the number of photo-generated charge carriers to participate in the photocatalytic reaction, thereby increasing the photocatalytic performance. It was found that charge transfer impedance at the photocatalyst/electrolyte interface decreases with an optimum concentration of downconverting $Y_2Al_5O_{12}:Ce^{3+}$ phosphor, as shown in Fig. 8C. An increase in the charge transfer impedance was attributed to the $Y_2Al_5O_{12}:Ce^{3+}$ phosphors in pristine ZnO, causing electron transfer and suppressing charge recombination in ZnO. Upon visible light illumination, the degradation rate of methylene blue dye was found to be a maximum value of 93% for a composite of $Y_2Al_5O_{12}:Ce^{3+}$ and ZnO after 2 h.

In a similar study by Zammouri et al., YAG:Ce/ZnO core/shell NPs were used for removal of sulfathiazole (STZ) dye [82]. The YAG:Ce/ZnO shows a broad visible light absorption from 400 to 550 nm. The degradation of STZ was found to be 98% in 90 min, whereas the degradation of STZ was only 70% in the presence of pure ZnO. Liu et al. also studied the role of spectrally downconverting rare earth-doped $NaSrBO_3:Tb^{3+}$ phosphor incorporated in ZnO via the microwave-assisted method [83]. The photocatalytic performance of the composite catalyst was analyzed for degradation of methyl blue (MB), methyl orange (MO), and Rhodamine blue (RhB) dyes in visible irradiation.

https://www.twirpx.org & http://chemistry-chemists.com

Rare earth-based perovskites are also gaining importance due to their exceptional structural stability, biocompatible nature, and piezoelectric and multiferroic properties. These compounds are reported to have optimum reduction and oxidation potentials toward water splitting reaction, photocatalytic conversion of carbon dioxide into useful fuels, and visible light photocatalysis [84–90]. Recently Abdel-Latif et al. reported strontium-doped neodymium manganites $Nd_{1-x}Sr_xMnO_3$ perovskite for photocatalytic degradation of acridine orange dye (AO) in visible light illumination [87]. An optimized bandgap energy and flexible crystal structure make rare earth-based perovskite an ideal candidate for visible light-driven photocatalysis. At optimum doping concentration ($x = 0.7$ mol) of strontium in $NdMnO_3$ perovskite, a blue shift in the optical absorption edge was detected as shown in Fig. 9A. Thus, the bandgap of pristine $NdMnO_3$ was found to shift from 3.05 eV to 2.92 eV by incorporation of strontium. From the dye degradation studies it was found that 95% of the AO dye was successfully degraded after 3 hour of visible light illumination, and the reaction rate constant of strontium-doped perovskite $Nd_{0.3}Sr_{0.7}MnO_3$ was found to be two times greater than the pristine $NdMnO_3$.

Table 2 presents a list of reported downconversion phosphors and their composites with large bandgap semiconductors. Though scanty work has been reported in the field of visible light-active semiconductors and photocatalysts doped with downconverting phosphor, the mechanism prevailing at the semiconductor and phosphor interface is still not clearly understood. Hence, this limits the practical applications of this technology on a larger scale.

3.3 Long afterglow phosphors (LAPs) Photocatalysis

A special category of photon energy storage luminescent materials is known by various terminologies such as LAPs, persistent phosphors, and long decay phosphors; these are successfully utilized for sunlight-driven photocatalysis. A major breakthrough in this field

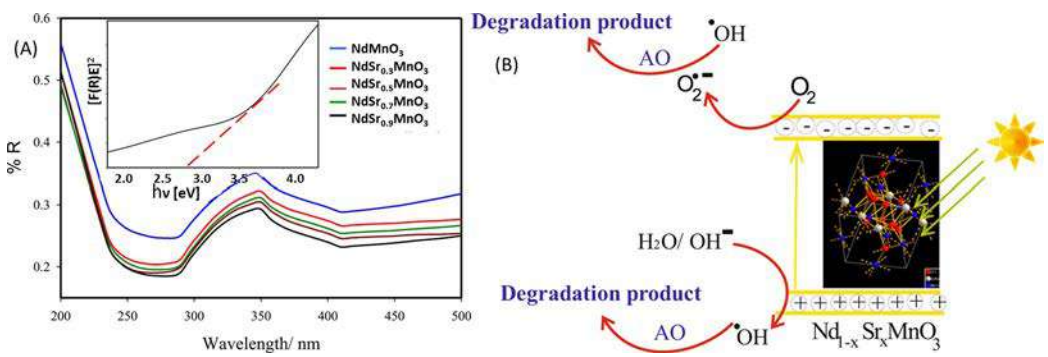

FIG. 9 (A) UV-visible spectra of doped and undoped neodymium manganites; inset figure of Kubelka-Munk versus energy of $Nd_{0.3}Sr_{0.7}MnO_3$ compound. (B) Acridine orange dye degradation mechanism of using $Nd_{1-x}Sr_xMnO_3$ photocatalysts in visible light irradiation. *(Adapted from Abdel-Latif IA, et al. Doping strontium into neodymium Manganites nanocomposites for enhanced visible light driven photocatalysis. Sci Rep 2019;9:1–11.)*

https://www.twirpx.org & http://chemistry-chemists.com

Table 2 Visible light-active downconversion phosphors and their composite photocatalysts.

Sr. no.	Host lattice	Activator	Codopant/ composite	Synthesis methodology adapted	Organic compounds	Excitation wavelength	Degradation efficiency and time	Reference
1.	Y_3AlO_{12}	Ce^{3+}	ZnO	Microwave	MB	455 nm	93% in 240 min	[81, 82]
2.	Y_2O_2S	Eu^{3+}	ZnO	Microwave	MB, MO, RhB	Visible light	95% in 240 min; larger for MB than RhB and MO	[91]
3.	$NaSrBO_3$	Tb^{3+}	ZnO	Microwave	MB	544 nm	97% in 240 min	[83]
4.	$Lu_3Al_5O_{12}$	Ce^{3+}	α-Si_3N_4	Microwave-assisted	MB.	Visible light	91% in 240 min	[92]
5.	$CaTiO_3$	Eu^{3+}	Ni	Solgel	toluene	410 nm	–	[93]
6.	BiOBr	–	Cu_2O quantum dots	Simple reductive chemistry route	MB	Visible light	95% in 60 min	[94]

was development of green-emitting alkaline earth aluminate phosphors by Matsuzawa et al. [95]. Even after decades of discovery of such materials, only a handful of stable sunlight excitable long afterglow phosphors have been reported so far due to their complicated trapping-detrapping mechanism. LAPs have been used for various dark vision display applications such as disaster management and consumer goods due to their glow-in-the-dark property. However, with advancements, these phosphors are being used for in-vivo and in-vitro biological staining, latent fingerprint development, photovoltaic cells, impact sensors, etc. [95–97]. Due to their exceptional properties of energy storage, they are known to emit visible light from minutes to hours even after the excitation source has been removed, which makes them potential candidates regarding the development of "round the clock" photocatalysts. Such a self-assisted luminescence system would provide a solution to existing glitches associated with conventional photocatalysts. Apart from the round-the-clock working system, photocatalytic efficiency can also be enhanced owing to spatial separation between these defects/codopant-related trap centers and the activator centers (or more precisely, because of the deficiency of their orbital overlap), thereby reducing the probability of direct recombination. Induced energy band bending in LAPs and semiconductors due to the formation of a heterojunction between two dissimilar semiconductors further boosts the photocatalytic efficiency of the suggested composite.

In 2004, Zhang et al. reported TiO_2 coated with sunlight-activated long afterglow phosphor for decomposition of Rhodamine B (RhB) in the dark. Long afterglow phosphor was found to have potential in terms of energy saving by supplying irradiation intermittently to TiO_2 [98]. Li et al. reported a metal-free, visible light-activated photocatalyst graphitic-C_3N_4(g-C_3N_4) coupled with long afterglow phosphor $Sr_4Al_{14}O_{25}$:Eu, Dy for the photodegradation of methylene blue (MB) dye in the dark [99]. Yoon et al. synthesized the TiO_2- $CaAl_2O_4$:Eu^{2+}, Nd^{3+} photocatalyst by the solgel process for degradation of methylene

https://www.twirpx.org & http://chemistry-chemists.com

blue [100]. Coupling of $CaAl_2O_4$:Eu^{2+}, Nd^{3+} phosphor with TiO_2 has red-shifted the absorption edge of TiO_2 in the visible light region. Li et al. prepared a composite of $TiO_{2-x}N_y$-$CaAl_2O_4$:Eu^{2+}, Nd^{3+} for decomposition of acetaldehyde [101]. The comparative study of $CaAl_2O_4$:Eu^{2+},Nd^{3+} with other phosphors ($Sr_2Mg(Si_2O_7)$:Eu, $Sr_4Al_{14}O_{25}$:(Eu, Dy), $SrAl_2O_4$:(Eu, Dy), and $SrAl_2O_4$:Eu) was carried out. The results revealed that $CaAl_2O_4$:Eu^{2+}, Nd^{3+} with emission centered at 440 nm was the best light source for photocatalysis. The degradation of acetaldehyde was estimated by releasing of CO_2 gas which increased in 360 min for the $CaAl_2O_4$:Eu^{2+}-Nd^{3+}-$TiO_{2-x}N_y$ photocatalyst, while in the case of the other catalyst it was constant in 60 min. Hence CO_2 generation was very high for $CaAl_2O_4$:Eu^{2+}-Nd^{3+}-$TiO_{2-x}N_y$ compared to the others. Li et al. reported green phosphorescence in $Sr_4Al_{14}O_{25}$:Eu, Dy coupled with $AgPO_4$ which was examined for degradation of Rhodamine B (RhB) [102]. The LAP $Sr_4Al_{14}O_{25}$-Eu-Dy has emission at 490 nm (green light) which falls under the absorption edge of $AgPO_4$ (500 nm). Hence the combination phosphor with $AgPO_4$ can work in the dark in decomposing organic dye pollutants. The composite was synthesized through a precipitation process with an optimum amount of $Sr_4Al_{14}O_{25}$:Eu, Dy (50 wt%). The degradation efficiency was 100% in 10.5 h. The degradation was carried out in the dark (without light) as well as in visible light illumination. Table 3 lists of UV and visible light-driven long afterglow phosphors for photocatalysis and their composites for degradation of dyes and gaseous pollutants.

Zhou et al. carried out a thought-provoking study on round-the-clock and visible light-driven photocatalysts by combining $Sr_2MgSi_2O_7$:Eu^{2+}, Dy^{3+} with g-C_3N_4 for the photocatalytic degradation of Rhodamine B and methyl orange [109]. The composite was found to remain active for 6 h in the dark. The mechanism of a round-the-clock working photocatalyst is illustrated in Fig. 10. Upon sunlight excitation, Eu^{2+} from its ground state $4f^7$ is excited to $4f^65d$ state positioned in the CB. This creates a free electron and Eu^{3+} ion. The generated electron is caught in Dy^{3+} which forms Dy^{2+} below the CB. Once the source of excitation is removed, trapped electrons return to CB, recombining with Eu^{3+} to form Eu^{2+}. This transition from *5d-4f* leads to emission of luminescence. The emitted light from phosphor is sufficient to excite g-C_3N_4 as the absorption band of g-C_3N_4 overlaps with the emission band of $Sr_2MgSi_2O_7$:Eu^{2+}, Dy^{3+}. Excitation of g-C_3N_4 leads to generation of electrons and holes. The electrons transfer to the catalyst surface and react with water and oxygen to form OH and O_2 radicals. These radicals, being reactive, decompose the pollutants into by-products.

In a recent work by Yin et al., an Ag/BiOBr composite coupled with long afterglow phosphor emitting at 488 nm was used for the degradation of Rhodamine [112]. Higher photocatalytic performance due to enhanced visible light harvesting and lower recombination rate of the photoinduced charges was reported. To improve the light harnessing property, a novel disk-type rotating hollow reactor was used in which a novel photocatalysis reactor was coated with a film of Ag-BiOBr. Inside the reactor was filled with a long afterglow phosphor coating, as shown in Fig. 11C. Due to the continuous rotation, a light blocking effect due to the colored water solution was avoided. Fig. 11A shows the photocatalytic degradation of RhB dye on the reactor coated with BiOBr or Ag/BiOBr film. With LAP, the

https://www.twirpx.org & http://chemistry-chemists.com

Table 3 List of visible light-driven long afterglow phosphors and their composites.

Sr. no.	Photocatalyst	Excitation λ (nm); emission λ (nm)	Organic compound	Degradation efficiency and time	Reference
1.	N-TiO_2/ $Sr_{2.90}Eu_{0.03}$ $Dy_{0.07}Al_4SiO_{11}$	365 nm; 440 nm	Crystal violet	90% in 180 min	[103]
2.	SAED/g-C_3N_4	Visible light (450–700 nm); 464 nm and 485 nm	Methyl blue, methyl orange, Rhodamine B	92%, 50% and 72%	[104]
3.	$BaAl_2O_4$ and $MgAl_2O_4$	254 nm; 423 nm ($MgAl_2O_4$) 533 nm ($BaAl_2O_4$)	Methyl blue	59% in 90 min ($MgAl_2O_4$) 100% in 90 min ($BaAl_2O_4$)	[105]
4.	$Sr_4Al_{14}O_{25}$:Eu, Dy/ZnO:Co + Ag	Violet and blue; 450–500 nm	Methyl orange	–	[106]
5.	Cu_2O NCs/M-TiO_2/LAP	>420 nm (visible light); 430–520 nm	Rhodamine B, bisphenol	–	[107]
6.	NP-TiO_2/(3ZnO: Ga_2O_3:2GeO_2):Cr^{3+}	Visible light	Methyl blue Ofloxacin	89% in 50 min; (>95%) in 30 min	[108]
7.	$Sr_4Al_{14}O_{25}$:(Eu,Dy)/$AgPO_4$	490 nm (solar light); 600 nm	Rhodamine B	–	[102]
8.	$Sr_2MgSi_2O_7$: (Eu, Dy)@ g-C_3N_4	>420 nm (visible light); 420–550 nm	Rhodamine B, methyl orange	–	[109]
9.	$CaAl_2O_4$:Eu,Nd/TiO_2	350 nm; 450 nm	Methyl blue	–	[110]
10.	$CaAl_2O_4$:Eu,Nd/ $TiO_{(2-x)}N_y$	Visible light 400–700 nm; 440 nm	Gaseous Acetaldehyde	100%	[101]
11.	$BaZrO_3$:Mg/ TiO_2	350–550 nm; 400 nm	Methyl blue	–	[111]
12	BiOBr/Ag	420 nm; 488 nm	Rhodamine B	~80% in 75 min	[112]
13.	$CaAl_2O_4$:(Eu, Nd)/$TiO_{2-x}N_y$	325–700 nm; 440 nm	NO gas	80%	[113]
14.	$CaAl_2O_4$:(Eu,Nd)/$TiO_{2-x}N_y$ and Sr4Al14O25:(Eu,Dy)/ $TiO_{2-x}N_y$	325 nm; 440 nm and 490 nm	NO gas and acetaldehyde	–	[110]
15.	$CaAl_2O_4$:(Eu, Nd)/$TiO_{2-x}N_y$	445, 390 nm; 440 nm	NO gas	55%–60%	[114]

https://www.twirpx.org & http://chemistry-chemists.com

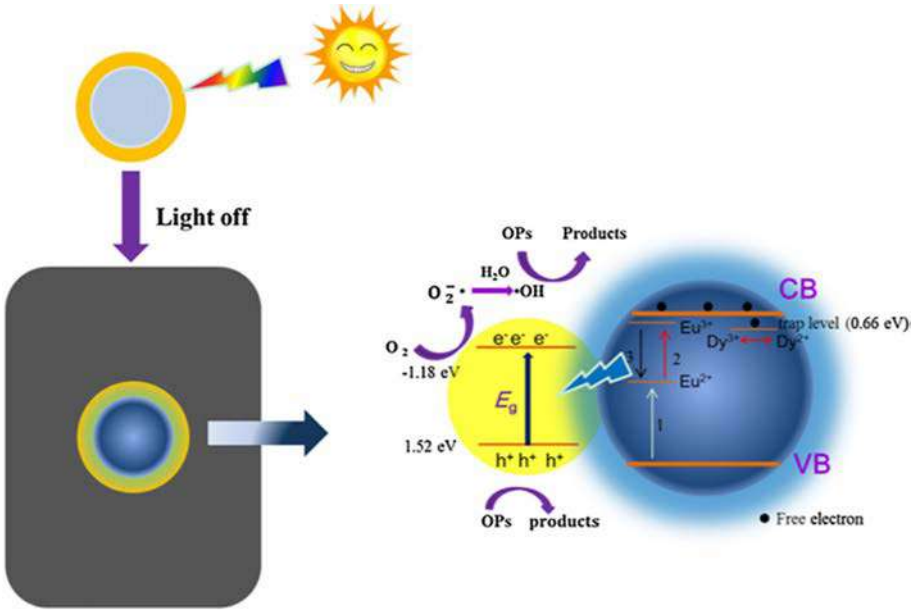

FIG. 10 Photocatalytic mechanism in composite of $Sr_2MgSi_2O_7:Eu^{2+}$, $Dy^{3+}$and g-C_3N_4. *(Adapted from Qiang Zhou et al. Long afterglow phosphor driven round-the-clock g-C3N4 photocatalyst. J Photochem Photobil A 2016;328: 182–188.)*

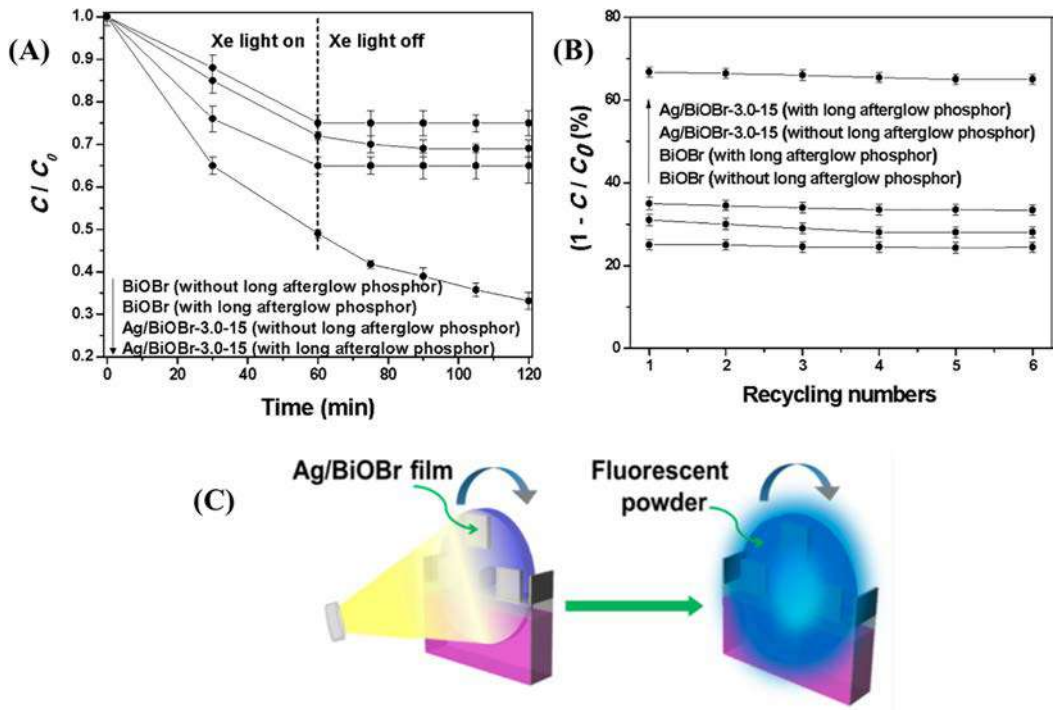

FIG. 11 (A) Photodegradation of RhB dye on rotating disk reactor with different films with or without long afterglow phosphor. (B) Recycling test of different films with or without long afterglow phosphor. (C) Schematic illustration of mechanism of rotating disk reactor with LAP [112].

https://www.twirpx.org & http://chemistry-chemists.com

degradation continued even after turning off the Xe light in the dark. Upon UV-visible irradiation, BiOBr showed greater removing activity in the presence of light-storing phosphor, and after recycling six times there was no significant reduction of the photoactivity, as shown in Fig. 11B. The coupled silver nanoparticles result in higher light absorption ability of BiOBr up to ~500 nm via the surface plasmon resonance effect. As a consequence of this, light emitted from long afterglow phosphor (~488 nm) activated the Ag/BiOBr film.

4 Conclusion

Rare doped luminescent materials coupled with semiconductors demonstrate exceptional photocatalytic activity compared to traditional semiconductor photocatalysts. Utilizing rare earth-doped upconversion phosphors is an effective approach to capture the unutilized infrared light which constitutes 44% of the solar spectrum reaching the Earth's surface. Upconverting phosphors can absorb the readily available infrared radiation, converting them to higher energy photons which can be effectively used to excite the semiconductor. This excited semiconductor results in generation of electrons and holes, which react with H_2O and atmospheric O_2 to form active radicals, resulting in photodegradation of organic pollutants. On the other hand, downconverting phosphors absorbs the high-energy photons in the UV range and converts it to near-UV or visible range photons which can excite the wide bandgap semiconductors. Apart from widening the absorption spectra, rare earth doping may delay the process of recombination. In addition to all these advantages, long afterglow phosphors can be employed to develop round-the-clock working photocatalysts. A heterojunction is formed due to the different band structures of LAP and semiconductor, which suppresses the recombination of photo-induced electrons and holes and boosts the photocatalytic property. Such a self-fluorescence-assisted system can be used to develop round-the-clock working photocatalytic systems even at night, on cloudy days, and even in nontransparent water. Though the degradation efficiency is low using long afterglow phosphors, critical understanding of LAP-assisted photocatalytic mechanism at the semiconducting surface can result in a substantial breakthrough in this area. Thus, the encouraging idea of LAP for photocatalysis is in its early stages, which need to be explored fully.

References

[1] Yusuf M, et al. Natural colorants: Historical, processing and sustainable prospects. Nat Prod Bioprospect 2017;7:123–45.

[2] El H, et al. Classifications, properties and applications of textile dyes: A review. Appl J Envir Eng Sci 2017;3. 00000-3.

[3] Venil CK, et al. Bacterial pigments and their applications. Process Biochem 2013;48:1065–79.

[4] Gürses A, et al. Dyes and pigments: their structure and properties. Dyes and Pigm 2016;13–29.

[5] Pattnaik P, et al. A review on the sustainability of textile industries wastewater with and without treatment methodologies. Rev Environ Health 2018;33:163–203.

https://www.twirpx.org & http://chemistry-chemists.com

[6] Lellis B, et al. Effects of textile dyes on health and the environment and bioremediation potential of living organisms. Biotech Res Innov 2019.

[7] Ahmad A, et al. Recent advances in new generation dye removal technologies: novel search for approaches to reprocess wastewater. RSC Adv 2015;5:30801–18.

[8] Natarajan S, et al. Recent advances based on the synergetic effect of adsorption for removal of dyes from waste water using photocatalytic process. J Environ Sci 2018;65:201–22.

[9] Kabra K, et al. Treatment of hazardous organic and inorganic compounds through aqueous-phase photocatalysis: a review. Ind Eng Chem Res 2004;43:7683–96.

[10] Kim SP, et al. Photocatalytic activity of SnO_2 nanoparticles in methylene blue degradation. Mater Res Bull 2016;74:85–9.

[11] Ahmad K, et al. Photocatalytic Technology: A review of environmental protection and renewable energy application for sustainable development. Environ Technol Innov 2020;, 100893.

[12] Akerdi AG, et al. Application of heterogeneous nano-semiconductors for photocatalytic advanced oxidation of organic compounds: a review. J Environ Chem Eng 2019;7:103283.

[13] Cai Z, et al. An overview of nanomaterials applied for removing dyes from wastewater. Environ Sci Pollut Res 2017;24:15882–904.

[14] Thongam DD, et al. Investigating the role of different reducing agents, molar ratios, and synthesis medium over the formation of ZnO nanostructures and their photo-catalytic activity. J Mater Sci 2018;53:1110–22.

[15] Rani B, et al. Polyol asserted hydrothermal synthesis of SnO_2 nanoparticles for the fast adsorption and photocatalytic degradation of methylene blue cationic dye. New J Chem 2018;42:943–54.

[16] Sharma M, et al. Photocatalytic degradation of organic dyes under UV–Visible light using capped ZnS nanoparticles. Sol Energy 2012;86:626–33.

[17] Shang M, et al. Nanosized $BiVO_4$ with high visible-light-induced photocatalytic activity: ultrasonic-assisted synthesis and protective effect of surfactant. J Hazard Mater 2009;172:338–44.

[18] Xian T, et al. Photocatalytic properties of $SrTiO_3$ nanoparticles prepared by a polyacrylamide gel route. Mater Lett 2011;65:3254–7.

[19] Li X, et al. Photocatalytic activity of CdS nanoparticles synthesized by a facile composite molten salt method. Appl Surf Sci 2012;258:4370–6.

[20] Serpone N, et al. On the genesis of heterogeneous photocatalysis: a brief historical perspective in the period 1910 to the mid-1980s. Photochem Photobiol Sci 2012;11:1121–50.

[21] Fujishima A, Honda K. Electrochemical photolysis of water at a semiconductor electrode. Nature 1972;238:37–8.

[22] Serpone N, et al. Visible light induced generation of hydrogen from H_2S in mixed semiconductor dispersions; improved efficiency through inter-particle electron transfer. J Chem Soc Chem Commun 1984;6:342–4.

[23] Grätzel M. Femtosecond electron-transfer dynamics at a sensitizing dye-semiconductor (TiO_2) interface. J Phys Chem 1996;100:9577–8.

[24] Ajmal A, et al. Principles and mechanisms of photocatalytic dye degradation on TiO_2 based photocatalysts: a comparative overview. RSC Adv 2014;4:37003–26.

[25] Belver C, et al. Semiconductor Photocatalysis for water purification. In: Nanoscale Materials in Water Purification. Elsevier; 2019. p. 581–651.

[26] Konstantinou IK, et al. TiO_2-assisted photocatalytic degradation of azo dyes in aqueous solution: kinetic and mechanistic investigations: a review. Appl Catal Environ 2004;49:1–14.

[27] Han F, et al. Tailored titanium dioxide photocatalysts for the degradation of organic dyes in wastewater treatment: a review. Appl Catal A Gen 2009;359:25–40.

https://www.twirpx.org & http://chemistry-chemists.com

[28] Salarian A-A, et al. N-doped TiO_2 nanosheets for photocatalytic degradation and mineralization of diazinon under simulated solar irradiation: optimization and modeling using a response surface methodology. J Mol Li 2016;220:183–91.

[29] Pirhashemi M, et al. Review on the criteria anticipated for the fabrication of highly efficient ZnO-based visible-light-driven photocatalysts. J Ind Eng Chem 2018;62:1–25.

[30] Basavarajappa PS, et al. Recent progress in metal-doped TiO2, non-metal doped/codoped TiO2 and TiO2 nanostructured hybrids for enhanced photocatalysis. Int J Hydrogen Energy 2020;45:7764–78.

[31] Samadi M, et al. Recent progress on doped ZnO nanostructures for visible-light photocatalysis. Thin Solid Films 2016;605:2–19.

[32] Dong F, et al. Enhancement of the visible light photocatalytic activity of C-doped TiO_2 nanomaterials prepared by a green synthetic approach. J Phys Chem C 2011;115:13285–92.

[33] Li H, et al. Synthesis of highly efficient C-doped TiO_2 photocatalyst and its photo-generated charge-transfer properties. J Colloid Interface Sci 2011;354:175–80.

[34] Ebrahimi R, et al. Effects of doping zinc oxide nanoparticles with transition metals (Ag, Cu, Mn) on photocatalytic degradation of Direct Blue 15 dye under UV and visible light irradiation. J Environ Health Sci 2019;17:479–92.

[35] Barick KC, et al. Porosity and photocatalytic studies of transition metal doped ZnO nanoclusters. Micropor Mesopor Mat 2010;134:195–202.

[36] Di Paola A, et al. Photocatalytic degradation of organic compounds in aqueous systems by transition metal doped polycrystalline TiO_2. Catal Today 2002;75:87–93.

[37] Ekambaram S, et al. Combustion synthesis and photocatalytic properties of transition metal-incorporated ZnO. J Alloys Compd 2007;433:237–40.

[38] Saleh R, et al. Transition-metal-doped ZnO nanoparticles: synthesis, characterization and photocatalytic activity under UV light. Spectrochim Acta A 2014;130:581–90.

[39] Chang S-m, et al. The roles of surface-doped metal ions (V, Mn, Fe, Cu, Ce, and W) in the interfacial behavior of TiO_2 photocatalysts. Appl Catal B 2014;156:466–75.

[40] Yang X-j, et al. Preparation and photocatalytic performance of Cu-doped TiO_2 nanoparticles. Trans Nonferrous Met Soc 2015;25:504–9.

[41] Szkoda M, et al. Non-metal doped TiO_2 nanotube arrays for high efficiency photocatalytic decomposition of organic species in water. Physica E Low Dimen Syst Nanostruct 2016;84:141–5.

[42] Yang X, et al. Photo-catalytic degradation of rhodamine B on C-, S-, N-, and Fe-doped TiO_2 under visible-light irradiation. Appl Catal Environ 2009;91:657–62.

[43] Liu D, et al. Synthesis of N and La co-doped TiO_2/AC photocatalyst by microwave irradiation for the photocatalytic degradation of naphthalene. J Alloys Compd 2016;676:489–98.

[44] Moradi H, et al. Fabrication of Fe-doped TiO_2 nanoparticles and investigation of photocatalytic decolorization of reactive red 198 under visible light irradiation. Ultrason Sonochem 2016;32:314–9.

[45] Yu X, et al. Enhanced photocatalytic activity of Fe-doped ZnO nanoparticles synthesized via a two-step sol–gel method. J Mater Sci Mater Electron 2014;25:3920–3.

[46] Pérez-González M, et al. Sol-gel synthesis of Ag-loaded TiO_2-ZnO thin films with enhanced photocatalytic activity. J Alloys Compd 2019;779:908–17.

[47] Zhang M, et al. One-dimensional Bi_2MoO_6/TiO_2 hierarchical heterostructures with enhanced photocatalytic activity. CrstEngComm 2012;14:605–12.

[48] Dammala P, et al. Synthesis of biphasic nanomaterials based on ZnO and SnO_2: Application towards photocatalytic degradation of acid red dye. Nano-Struct Nano-Obj 2019;18:100292.

[49] Bakar F, et al. The effect of reactive red 4 dye as a sensitizer in enhancing photocatalytic activity of TiO_2 for degradation of methyl orange. Appl Mech Mater 2016;835:366–71. Trans Tech Publications Ltd.

https://www.twirpx.org & http://chemistry-chemists.com

[50] Shang J, et al. Photocatalytic degradation of rhodamine B by dye-sensitized TiO_2 under visible-light irradiation. Sci China Chem 2011;54:167–72.

[51] Bingham S, et al. Recent advances in making nano-sized TiO 2 visible-light active through rare-earth metal doping. J Mater Chem 2011;21:2041–50.

[52] Ronda CR. Luminescence: from theory to applications. Weinheim: Wiley-VCH Verlag GmbH & Co. KGaA; 2007.

[53] Swati G, et al. Rare-earth doping in afterglow oxide phosphors: Materials, persistence mechanisms, and dark vision display applications. In: Spectroscopy of Lanthanide Doped Oxide Materials. Woodhead Publishing; 2020. p. 393–425.

[54] Liu Q, et al. Upconversion luminescence imaging of cells and small animals. Nat Protoc 2013;8:2033.

[55] Wang J, et al. Degradation of dyestuff wastewater using visible light in the presence of a novel nano TiO_2 catalyst doped with upconversion luminescence agent. J Environ Sci 2005;17:727–30.

[56] Wu X, et al. Blue/green/red colour emitting up-conversion phosphors coupled C-TiO_2 composites with UV, visible and NIR responsive photocatalytic performance. Appl Catal Environ 2014;156:257–64.

[57] Feng K, et al. Enhanced photocatalytic activities of the heterostructured upconversion photocatalysts with cotton mediated on $TiO_2/ZnWO_4$: Yb^{3+}, Tm^{3+}. Dalton Trans 2015;44:13681–7.

[58] Wang J, et al. Efficient photocatalytic degradation of organic dyes over titanium dioxide coating upconversion luminescence agent under visible and sunlight irradiation. Appl Catal Gen 2008;334:227–33.

[59] Yin L, et al. Synthesis of Er $^{3+}$: $Y_3Al_5O_{12}$ and its effects on the solar light photocatalytic activity of TiO_2–ZrO_2 composite. Res Chem Intermediat 2012;38:523–36.

[60] Zhang Z, et al. Enhanced photocatalytic activity of Bi_2WO_6 doped with upconversion luminescence agent. Cat Com 2011;13:31–4.

[61] Wang J, et al. Photocatalytic degradation of organic dyes with Er^{3+}: $YAlO_3$/ZnO composite under solar light. Sol Energy Mater Sol Cells 2009;93:355–61.

[62] Hou D, et al. Preparation, characterization and performance of a novel visible light responsive spherical activated carbon-supported and Er^{3+}:$YFeO_3$-doped TiO_2 photocatalyst. J Hazard Mater 2012;199:301–8.

[63] Ren L, et al. Upconversion-P25-graphene composite as an advanced sunlight driven photocatalytic hybrid material. J Mater Chem 2012;22:11765–71.

[64] Mavengere S, et al. UV–visible light photocatalytic properties of $NaYF_4$:(Gd, Si)/TiO_2 composites. Appl Surf Sci 2018;444:491–6.

[65] Shen Z, et al. Novel Tm^{3+} and Yb^{3+} co-doped bismuth tungstate up-conversion photocatalyst with greatly improved photocatalytic properties. J Photochem Photobiol A 2019;380:111864.

[66] Ke J, et al. Upconversion carbon quantum dots as visible light responsive component for efficient enhancement of photocatalytic performance. J Colloid Interface Sci 2017;496:425–33.

[67] Shafaee M, et al. TiO_2 nanoparticles and TiO_2@ graphene quantum dots nancomposites as effective visible/solar light photocatalysts. J Photochem Photobiol A 2018;357:90–102.

[68] Yu G, et al. Synergistic effect of upconversion and plasmons in $NaYF_4$: Yb $^{3+}$, Er $^{3+}$, Tm^{3+}@ TiO_2–Ag composites for MO photodegradation. RSC Adv 2017;7:54555–61.

[69] Kudo A, et al. H_2 or O_2 evolution from aqueous solutions on layered oxide photocatalysts consisting of Bi^{3+} with $6s^2$ configuration and d^0 transition metal ions. Chem Lett 1999;28:1103–4.

[70] Huang C, et al. Synthesis and application of Bi $_2WO_6$ for the photocatalytic degradation of two typical fluoroquinolones under visible light irradiation. RSC Adv 2019;9:27768–79.

https://www.twirpx.org & http://chemistry-chemists.com

[71] Zhang L, et al. A review of controllable synthesis and enhancement of performances of bismuth tungstate visible-light-driven photocatalysts. Catal Sci Tech 2012;2:694–706.

[72] Zhong S, et al. Synthesis of modified bismuth tungstate and the photocatalytic properties on tetracycline degradation and pathways. J Mater Res Technol 2019;8:1849–58.

[73] Li G, et al. An efficient bismuth tungstate visible-light-driven photocatalyst for breaking down nitric oxide. Environ Sci Technol 2010;44:4276–81.

[74] Djokic VR, et al. Preparation of TiO_2/carbon nanotubes photocatalysts: The influence of the method of oxidation of the carbon nanotubes on the photocatalytic activity of the nanocomposites. Ceram Int 2012;38:6123–9.

[75] Das GS, et al. Biomass-derived carbon quantum dots for visible-light-induced photocatalysis and Label-free Detection of Fe (iii) and ascorbic acid. Sci Rep 2019;9:1–9.

[76] Xu Q, et al. Making co-condensed amorphous carbon/g-C_3N_4 composites with improved visible-light photocatalytic H_2-production performance using Pt as cocatalyst. Carbon 2017;118:241–9.

[77] Tian J, et al. Carbon quantum dots/hydrogenated TiO_2 nanobelt heterostructures and their broad-spectrum photocatalytic properties under UV, visible, and near-infrared irradiation. Nano Energy 2015;11:419–27.

[78] Chai Y-Y, et al. Carbon quantum dots/Zn^{2+} ions doped-CdS nanowires with enhanced photocatalytic activity for reduction of 4-nitroaniline to p-phenylenediamine. Appl Surf Sci 2018;450:1–8.

[79] Williams G, et al. TiO_2-graphene nanocomposites. UV-assisted photocatalytic reduction of graphene oxide. ACS Nano 2008;2:1487–91.

[80] Bell NJ, et al. Understanding the enhancement in photoelectrochemical properties of photocatalytically prepared TiO_2-reduced graphene oxide composite. J Phys Chem C 2011;115:6004–9.

[81] Liu X, et al. Microwave-assisted synthesis of ZnO–$Y_3Al_5O_{12}$: Ce^{3+} composites with enhanced visible light photocatalysis. J Mater Chem 2012;22:16293–8.

[82] Zammouri L, et al. Synthesis of YAG: Ce/ZnO core/shell nanoparticles with enhanced UV-visible and visible light photocatalytic activity and application for the antibiotic removal from aqueous media. J Mater Res 2019;34:1318–30.

[83] Liu X, et al. Enhanced visible light photocatalytic activity of ZnO doped with down-conversion $NaSrBO_3$: Tb^{3+} phosphors. Dalton Trans 2015;44:97–103.

[84] Mierwaldt D, et al. In situ XANES/XPS investigation of doped manganese perovskite catalysts. Catalysts 2014;4:129–45.

[85] Black AP, et al. New rare earth hafnium oxynitride perovskites with photocatalytic activity in water oxidation and reduction. Chemcomm 2018;54:1525–8.

[86] Kaviyarasu K, et al. High performance of pyrochlore like $Sm_2Ti_2O_7$ heterojunction photocatalyst for efficient degradation of rhodamine-B dye with waste water under visible light irradiation. J King Saud Univ Sci 2020;32:1516–22.

[87] Abdel-Latif IA, et al. Doping strontium into neodymium Manganites nanocomposites for enhanced visible light driven photocatalysis. Sci Rep 2019;9:1–11.

[88] Anandan S, et al. Highly active rare-earth-metal La-doped photocatalysts: fabrication, characterization, and their photocatalytic activity. Int J Photoenergy 2011;2012:1–10.

[89] Kanhere P, et al. A review on visible light active perovskite-based photocatalysts. Molecules 2014;19:19995–20022.

[90] Gupta P, et al. Using Raman and dielectric spectroscopy to elucidate the spin phonon and magnetoelectric coupling in $DyCrO_3$ nanoplatelets. RSC Adv 2015;5:10094–101.

[91] Liu X, et al. Light down-converting characteristics of ZnO–Y_2O_2S:Eu^{3+} for visible light photocatalysis. J Colloid Interface Sci 2013;404:150–4.

https://www.twirpx.org & http://chemistry-chemists.com

[92] Chu H, et al. Down-conversion phosphors as noble-metal-free co-catalyst in ZnO for efficient visible light photocatalysis. Appl Surf Sci 2017;391:468–75.

[93] Park B-G. Photoluminescence of Eu^{3+}-doped $CaTiO_3$ perovskites and their photocatalytic properties with a metal ion loading. Chem Phys Lett 2019;722:44–9.

[94] Cui W, et al. Novel Cu_2O quantum dots coupled flower-like BiOBr for enhanced photocatalytic degradation of organic contaminant. J Hazard Mater 2014;280:417–27.

[95] Matsuzawa, et al. A New Long Phosphorescent Phosphor with High Brightness, $SrAl_2O_4$: Eu^{2+}, Dy^{3+}. J Electrochem Soc 1996;143:2670.

[96] Sun H, et al. Long afterglow $SrAl_2O_4$: Eu, Dy phosphors for CdS quantum dot-sensitized solar cells with enhanced photovoltaic performance. J Mater Chem A 2013;1:6388–92.

[97] Swati G, et al. Chemistry of extracting high-contrast invisible fingerprints from transparent and colored substrates using a novel phosphorescent label. Anal Methods 2018;10:308–13.

[98] Zhang J, et al. Light-storing photocatalyst. Appl Phys Lett 2004;85:5778–80.

[99] Li H, et al. Enhanced photocatalytic performance of luminescent g-C_3N_4 photocatalyst in darkroom. Nanoscale Res Lett 2016;11:1–9.

[100] Yoon J-H, et al. Investigation of photocatalytic reaction for the titanium dioxide-phosphor composite. Ionics 2010;16:131–5.

[101] Li H, et al. Persistent fluorescence-assisted $TiO_{2-x}N_y$-based photocatalyst for gaseous acetaldehyde degradation. Environ Sci Technol 2012;46:7741–5.

[102] Li H, et al. Green phosphorescence-assisted degradation of rhodamine B dyes by Ag_3PO_4. J Mater Chem A 2013;1:1123–6.

[103] Vaiano V, et al. Electric energy saving in photocatalytic removal of crystal violet dye through the simultaneous use of long-persistent blue phosphors, nitrogen-doped TiO_2 and UV-light emitting diodes. J Clean Prod 2019;210:1015–21.

[104] Hong K, et al. Long lifetime g-C3N4 photocatalyst coupled with phosphorescent material working under dark condition. J Photochem Photobiol A 2020;112520.

[105] Mumanga TJ, et al. MAl_2O_4 (M = Ba, Mg) photocatalytic activity dependence on annealing atmosphere. Appl Optics 2020;59:D246–52.

[106] Havasi V, et al. Photocatalytic performance of $Sr_4Al_{14}O_{25}$: Eu, Dy phosphor assisted ZnO: Co+ Ag nanocomposite under continuous and pulsed illumination. Catal Today 2017;284:107–13.

[107] Lu Y, et al. Cu_2O nanocrystals/TiO_2 microspheres film on a rotating disk containing long-afterglow phosphor for enhanced round-the-clock photocatalysis. Appl Catal Environ 2018;224:239–48.

[108] Alberti S, et al. Photocatalysis in darkness: optimization of Sol–Gel synthesis of NP-TiO_2 supported on a persistent luminescence material and its application for the removal of ofloxacin from water. J Nanomed Nanotechnol 2018;9:501.

[109] Zhou Q, et al. Long afterglow phosphor driven round-the-clock g-C3N4 photocatalyst. J Photochem Photobil A 2016;328:182–8.

[110] Li H, et al. Novel luminescent photocatalytic deNO_x activity of $CaAl_2O_4$:(Eu, Nd)/$TiO_{2-x}N_y$ composite. Appl Catal Environ 2011;106:586–91.

[111] Ma X, et al. Violet blue long-lasting phosphorescence properties of Mg-doped $BaZrO_3$ and its ability to assist photocatalysis. J Alloys Compd 2013;580:564–9.

[112] Yin H, et al. Ag/BiOBr film in a rotating-disk reactor containing long-afterglow phosphor for round-the-clock photocatalysis. ACS Appl Mater Interfaces 2015;7:20076–82.

[113] Huihui Li et al., Photocatalysis enhancement of $CaAl_2O_4$: Eu^{2+}, Nd^{3+}@ TiO_2 composite powders." Res Chem Intermediat 36, (2010), 51–59.

[114] Li H, et al. Persistent luminescence assisted photocatalytic properties of $CaAl_2O_4$:(Eu, Nd)/$TiO_{2-x}N_y$ and $Sr_4Al_{14}O_{25}$:(Eu, Dy)/$TiO_{2-x}N_y$. J Mol Catal A Chem 2012;363:129–33.

https://www.twirpx.org & http://chemistry-chemists.com

https://www.twirpx.org & http://chemistry-chemists.com

10

Doped ceramics for visible light photocatalysis

Ankur Rastogi[a,b]

[a]DEPARTMENT OF PHYSICS, VELLORE INSTITUTE TECHNOLOGY, VELLORE, INDIA [b]CENTER FOR FUNCTIONAL MATERIALS, VELLORE INSTITUTE TECHNOLOGY, VELLORE, INDIA

1 Introduction

Considering the present energy scenario, and the excessive use of fossil fuel, the need for clean energy is greater than ever before to meet our future energy requirements. The use of abundant solar energy is one of the many ways to reduce our dependence on fossil fuel. Recent advancements in technology have potentially paved the way for overcoming the present challenges and opened new avenues to produce sustainable clean energy [1–6].

One such research field is photocatalysis, which has proven a strong candidate for an alternative energy source and attracted much attention. Photocatalysis is an excellent way to utilize cheap solar power and transfer it into high-value clean energy. Ceramics are mainly used for many aspects of photocatalysis, which has the potential to solve the energy crises not only by using photocatalytic water splitting for hydrogen production but also by enabling room temperature photodegradation of organic pollutants and their photoreduction into hydrocarbons/salt. Normally to treat organic pollutants, advance oxidation processes such as hydrogen peroxide/UV, ozone/UV sonolysis, etc. are used. These techniques have a few drawbacks such as transportation, handling, slow reaction, and complex process. Ceramics, due to their stability (physical and chemical), low cost, nontoxicity, and ease to access, became an appealing candidate for water splitting and photodegradation of organic pollutants.

Photocatalysis was first realized with the use of semiconductor material when Fujishima and Honda [7] reached a milestone and were the first to demonstrate electrochemical photolysis of water. The role of photocatalysis involves starting or speeding up specific reduction and oxidation reactions (redox reactions) in the presence of photo illumination. Ceramics-based semiconductor photocatalysis drew enormous attention as it has promising potential, and most of the research was concentrated around the wide bandgap semiconductors like TiO_2 [8–11], ZnO [12], etc. and limited to use in the ultraviolet radiation range. Since the majority of the solar spectrum is in the visible and infrared region, tailoring the bandgaps of materials is one of the feasible solutions and an efficient method to convert solar energy into electrical energy. Secondly, the recombination of the

Nanostructured Materials for Visible Light Photocatalysis. https://doi.org/10.1016/B978-0-12-823018-3.00014-2
Copyright © 2022 Elsevier Inc. All rights reserved.

https://www.twirpx.org & http://chemistry-chemists.com

charge carriers posed a further challenge [13–15]. The key to success lay in the designing of material, which helps to expedite the reaction, reduce recombination, and thus improve the efficiency of the conversion, making it a crucial aspect of the current research. To enhance the photocatalytic reaction during the process, the used catalyst should increase (i) generation, (ii) transfer, and (iii) reaction of photogenerated charge carriers. The idea is adapted from the role of a catalyst in a chemical reaction, which accelerates the chemical reaction by lowering the activation energies by creating different transition states.

Once the condition is met, the electrons from the valence band (VB) are activated to the conduction band (CB), producing a hole (positively charged) in the VB. The generated electron-hole pairs in this process migrate to the surface and undergo bulk/surface recombination, and then react with the reactants on the surface. The redox potential of the carriers is determined by the position of the VB and CB. A limited absorption of visible spectrum and fast charge recombination in semiconductor photocatalysts, elemental doping is useful for tuning the electronic structure of the material, thereby lowering the activation energy or bandgap [16, 17]. Elemental doping is one of various ways to achieve this goal. The doping not only changes the bandgap that affects the absorption of incident radiation range, but also creates intermediate trap sites that hinder the recombination of the charge carriers.

Fig. 1 represents the influence of doping in semiconductors which can tune by (i) efficient light absorption for energizing electrons from the VB to CB, (ii) alter the band positions, and (iii) recombination rate of the carriers to avoid dissipation of energy in the form of emission. Controlled doping will create few defects in the crystalline lattice and provide trap sites, which will make recombination harder, thereby increasing the efficiency. This chapter will provide a comprehensive overview of elemental doping and its impact on photocatalysis for visible radiation. There is a variety of ceramics that can be used for photocatalysis in their pristine and/or doped form. Metal-based ceramics is one type; these can be complex metal oxides or metal-sulfides or nitrides. Examples include TiO_2 [7], ZnO [18], $SrTiO_3$ [19, 20], MoS_2 [21], CdS [22], etc. A metal-free or nonmetal photocatalyst, it contains the nonmetal, earth-abundant elements, like carbon,

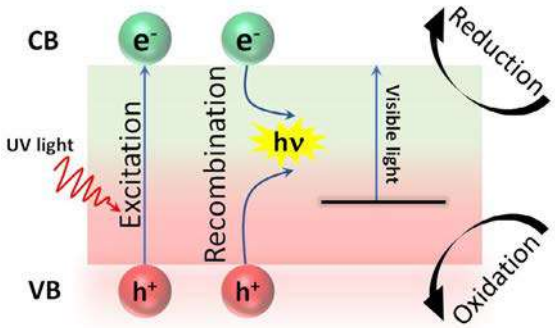

FIG. 1 Schematic representation of various effects of elemental doping which can alter the radiation absorption, carrier recombination, and the chemical activity of the material. *No permission required.*

https://www.twirpx.org & http://chemistry-chemists.com

nitrogen, for example, graphitic carbon nitride (C_3N_4) [23–28], has also been projected as a promising candidate.

2 Doping in ceramics and its influence

The bandgap of the widely used semiconductor photocatalyst, TiO_2 (3.2 eV), and ZnO (3.3 eV), lies in the UV region, which is only ~4% in the solar spectrum and usually faces the issue of relatively easy recombination of photogenerated carriers. In contrast, pure WO_3 has the ability to absorb radiation in the visible region, but the lower light energy conversion efficiency makes it less favorable [29, 30]. To improve the performance and extend the utilization of these materials, a variety of strategies have been adopted for using visible incident photon energies. This can be achieved by tailoring the bandgap absorption through foreign metal/nonmetal doping/implantation. The doping creates lattice modification, which leads to change in the crystal field and thus the electron bonding and influences band structure. This in turn results in significant changes in the behavior of photogenerated charge carriers, including excitation, transfer, and redox reaction, in a photocatalytic process. The doping route can be executed using metals like Fe, V, Cr, Mo, Ni, etc., or nonmetallic elements such as C, N, S, F [31, 32], etc. However, doping with transition metal or rare-earth ions sometimes encounters poor thermal stability [33, 34]; in a few cases, doping of nonmetallic elements was able to overcome such shortcomings [31]. The presence of bimetallic doping benefits the photocatalytic process as it hinders carrier recombination and enhances photocatalytic activity. Oxygen doping or oxygen vacancy, which are similar to intrinsic defects, have also received attention in order to enhance the underlying properties of metal oxides.

2.1 Modifications in light absorption

It is well-known that the energy gap between the conduction band and valence band can determine the absorption of particular radiation and strongly affects the photocatalytic activity. Many of the widely used ceramics generate the photo carriers in the presence of UV radiation and limit their efficiency. Many current approaches, such as metal/nonmetal ion doping, noble metal deposition, codoping, and self-doping, are dedicated to overcoming this issue by tuning the electronic structure of the ceramic-based photocatalysis so that a significant part of the solar spectrum can be utilized. The widely used ceramic TiO_2 suffers from limited light absorption and results in an insufficient photocatalyst performance. Brookite, anatase, and rutile are three crystalline structures of TiO_2; among them, anatase shows the largest efficiency and is well-studied. Elemental doping of metal/nonmetal ions is found to be a controlled modification in the energy bandgap, and thus the optical property of TiO_2, thereby enhancing efficiency for visible radiation absorption [35, 36].

Enhancement in the visible light absorption in Fe-doped TiO_2 (prepared by the hydrothermal synthesis) was reported by Zhu et al. [37]. They observed a shift in the absorption

https://www.twirpx.org & http://chemistry-chemists.com

spectra to longer wavelengths toward the visible region. Furthermore, their findings showed that the light toward the visible region was almost absorbed for all the metal ion-doped samples, compared to the nondoped sample. The result also indicates that the red shift in the spectra was associated with the charge transfer between the Fe-3d and TiO_2 conduction/valence bands. As the energy of Fe^{3+} lies just above the valence band of TiO_2, it acts like a mid-energy level. George et al. also demonstrated the tuning of the bandgap of the TiO_2 upon Fe doping, which decreases as the Fe doping increases in the TiO_2 matrix [38] (Fig. 2). The doping of Fe concentration governs the formation of trap levels between the CB and VB of TiO_2 and the bandgap energy toward visible wavelengths. A few ceramics with different metal/nonmetal doping are listed in Table 1 [31, 39–49].

Similarly, doping in the form of implantation can also impact absorbance by altering the electronic properties of the ceramic semiconductors. The implantation of vanadium and chromium metal ions in TiO_2 for altering the optical property was studied by Masakazu [50]. Their results indicate that the pure TiO_2 mostly absorbs the UV radiation from the solar spectrum (~4%), as shown in Fig. 3. However, the absorption spectra of the Cr

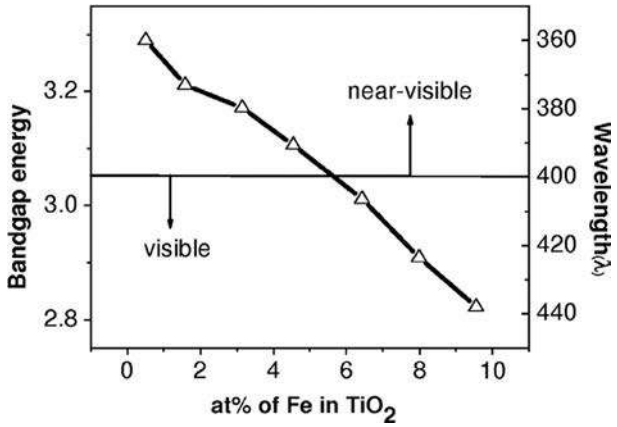

FIG. 2 The increasing concentration of Fe leads to the lowering in the bandgap of TiO_2 from 3.3 to 2.8 eV. *Reproduced from George S, Pokhrel S, Ji Z, Henderson BL, Xia T, Li L, et al. Role of Fe doping in tuning the band gap of TiO2 for the photo-oxidation-induced cytotoxicity paradigm. J Am Chem Soc 2011;133:11270–11278. doi:10.1021/ja202836s.*

Table 1 Doped/heterostructured ceramics for photoelectrochemical water splitting with their bandgap and photocurrent density.

Material	Bandgap (eV)	Photocurrent density (mA/cm^2)
N-TiO_2	2.5	3.6
C-In_2O_3	2.6	0.8
S-TiO_2	2.8–2.9	2.92
B-TiO_2	2.9–3.1	2.38
Mo-$BiVO_4$	2.6	1.62
α-Fe_2O_3/TiO_2	2.2	0.68
$WO_3/BiVO_4$	2.4	2.3
Ni-Bi_2O_3	2.7	0.75

https://www.twirpx.org & http://chemistry-chemists.com

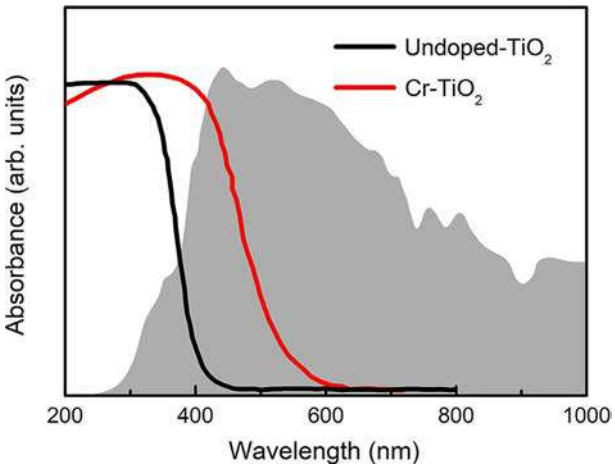

FIG. 3 Solar spectrum *(gray area)* and the diffuse reflectance UV-vis absorption spectra of TiO_2 *(black solid line)* and Cr ion-implanted TiO_2 photocatalysts *(red solid line). Modified from Masakazu A. Use of visible light. Second-generation titanium oxide photocatalysts prepared by the application of an advanced metal ion-implantation method. Pure Appl Chem 2000;72:1787–1792. https://doi.org/10.1351/pac200072091787.*

ion-implanted TiO_2 is shifted toward the visible region. This was the first successful demonstration which clearly showed enhancement in visible light absorption in TiO_2 after ion implantation. Furthermore, the study suggested implantation is capable of enabling the design of a unique doped TiO_2 base photocatalyst which operates expeditiously in both UV and visible region irradiation.

Sato was the first to explore nonmetal doping to modify visible light photocatalysis in TiO_2 [51]. When a nonmetal with a higher energy level than that of oxygen such as nitrogen is introduced in the TiO_2 lattice, it generates an additional energy level, thereby creating a mid-energy gap [31]. It enables the photoexcitation process of 2p electrons in nitrogen to occur at visible radiation, which was not allowed in the case of 2p oxygen electrons for the same radiation range. Theoretical calculations have also supported the abovementioned statement, and as a result N-doping into TiO_2 causes bandgap narrowing by mixing with O-2p [52].

One of the wide bandgap semiconductors is indium oxide (In_2O_3), with a bandgap of 3.5 eV; this can be tuned to favor the photoelectrochemical water splitting [53]. The bandgap of In_2O_3 can be reduced to 2.9 eV with carbon doping [39], as shown in Fig. 4. Furthermore, the morphology gives an added benefit by increasing the photoelectrochemical performance [54].

Moreover, there are many nonmetallic photocatalysts as the next generation; graphitic carbon nitride (C_3N_4) is one of these and excited the research communities due to its promising electronic band structure, high stability, and earth-abundant nature [23, 24, 26–28]. As shown in Fig. 5A and B, undoped C_3N_4 has a bandgap suitable for visible light absorption, while it has been found that the doping of noble metals like Au further increases the excitation efficiency [24].

https://www.twirpx.org & http://chemistry-chemists.com

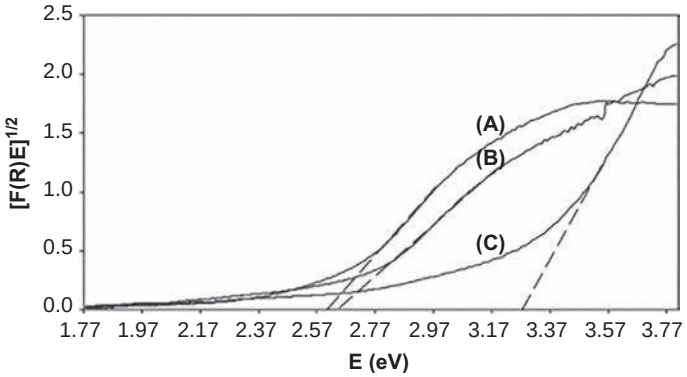

FIG. 4 Transformed diffuse reflectance spectra (deduced from UV-vis absorption spectra) of (A) C-doped (doping source: octanoic acid), (B) C-doped (doping source: glucose), and (C) undoped In_2O_3, respectively. *Modified from Sun Y, Murphy CJ, Reyes-Gil KR, Reyes-Garcia EA, Lilly JP, Raftery D. Carbon-doped In_2O_3 films for photoelectrochemical hydrogen production. Int J Hydro. Energy 2008;33:5967–5974.* https://doi.org/10.1016/j.ijhydene.2008.07.100.

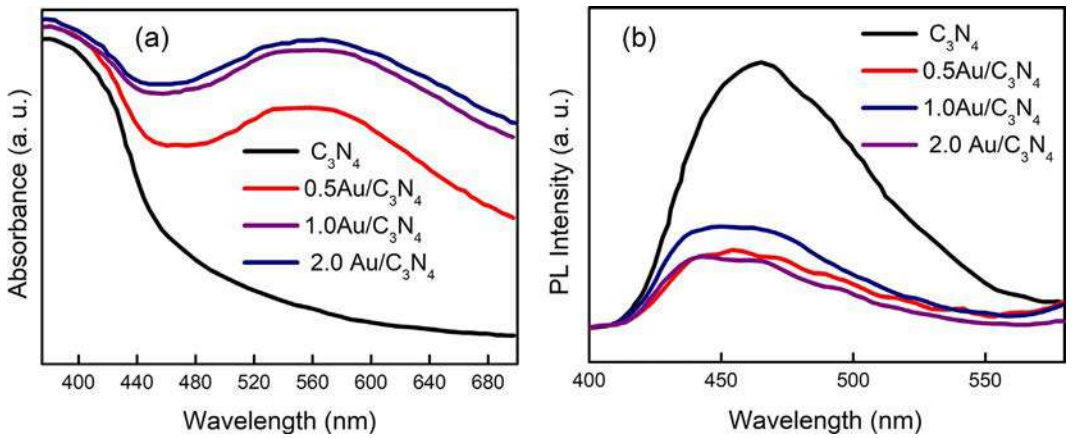

FIG. 5 (A) UV-visible absorption spectra of g-C_3N_4 and Au/g-C_3N_4. (B) Photo illuminance spectra of different Au doped C_3N_4. *Reproduced from Samanta S., Martha S., Parida K. Facile synthesis of Au/g-C_3N_4 nanocomposites: an inorganic/organic hybrid plasmonic photocatalyst with enhanced hydrogen gas evolution under visible-light irradiation. ChemCatChem 2014;6:1453–1462. doi:10.1002/cctc.201300949.*

2.2 Modifications in the band position

Doping will help to customize the electronic structures by constituting new energy bands or localized defects levels within the bandgap, and enables the radiation range to be extended. To facilitate the use of visible radiation, the material bandgap must be lower than 3.0 eV, and to ease the redox ability by photo-excited electrons and holes, the band-gap should match the redox potential. However, upon doping to achieve excitation under visible light irradiation, the redox ability of the photogenerated charge carriers may also

https://www.twirpx.org & http://chemistry-chemists.com

decrease, and therefore most photocatalysts prepared by the doping strategy may fail in overall water splitting [19, 55]. As a result, the desired modification is needed to maintain the compatibility between the use of visible radiation by preserving the driving force for redox reactions. In general, for a water-splitting application, the favorable position of the CB and VB of the ceramic should lie above the reduction potential of H^+/H_2 and below the oxidation potential of O_2/H_2O, respectively.

Niishiro et al. looked into the photocatalytic activities of doped $SrTiO_3$ (STO) under UV and visible light radiation, and showed that doping alone is not sufficient for obtaining the desired result. Their observations indicate that Ni doping actually reduces the bandgap to 1.6 eV, while no redox activity was observed; this was overcome with the codoping of Ta along with reduction under an H_2 atmosphere (Table 1). The authors found when doping with Ni, and Ni/Ta-doped STO is subjected to UV light, the activity is decreased by one order of magnitude, and a huge difference was observed in O_2 evolution upon Ni doping and Ni/Ta dopin; there were no changes for H_2 evolution. O_2 evolution activity was found to quadruple with the insertion of Ta in Ni:STO compared to bare Ni:STO (Table 2).

When both the singly Ni-doped and codoped STO were illuminated with visible light, they recorded activities for H_2 but not for O_2 evolution, while activity of codoped STO STO was found to be higher than that of only Ni-doped STO. The H_2 reduction treatment of both the samples further enhanced the activities of H_2 as well as O_2 evolution. As a consequence of codoping of Ta^{5+}, the impurity energy levels were formed below the conduction band of STO, which consists of Ti-3d bands and is more localized. Doped Ni^{3+} ions formed electron acceptor and donor levels within the bandgap, thereby greatly impacting the absorption in the visible range. Codoped Ta^{5+} ions also played a vital role in charge compensation and resulted in the suppression of the formation of Ni^{3+} ions.

Wang et al. performed a theoretical study on different metal doped WO_3 ceramics [56]. Their findings also showed that doping can increase in efficiency of excitation of electrons to the valence band but does not necessarily enhance the photochemical activity. For example, W substitution by Mo can reduce the bandgap of WO_3, which favors visible light absorption. However, as shown in Fig. 6, Mo doping causes a shift of conductance minimum to the lower energy, which determines the photoelectrochemical (PEC) water splitting, regulating the photocatalytic activity.

Table 2 Photocatalytic activities of doped $SrTiO_3$.

		Activity (mmol/h)			
		UV radiation (λ > 300 nm)		Visible radiation (λ > 420 nm)	
Dopant (mol % to Ti) in STO	Energy gap (eV)	H_2	O_2	H_2	O_2
Undoped	3.2	74	35	–	–
Ni(1.0)	1.6	7.3	0.3	0.7	0
Ni(1.0)/Ta(2.0)	1.7	5.3	1.3	1.4	–
$Ni(1.0)/Ta(2.0)_t$	2.8	3.3	2.4	2.4	0.5

Ni(1.0)/Ta(2.0)t is for the treated with H_2 [21].

https://www.twirpx.org & http://chemistry-chemists.com

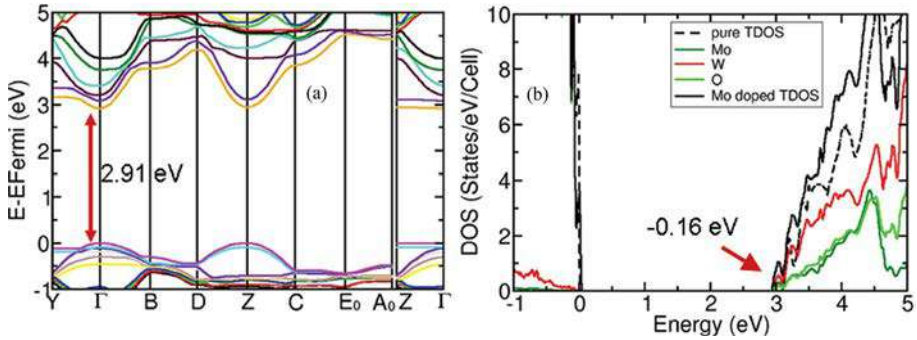

FIG. 6 (A) Band structure and (B) DOS of substitutional Mo-doped WO_3. *From Wang F, Di Valentin C, Pacchioni G. Doping of WO_3 for photocatalytic water splitting: hints from density functional theory. J Phys Chem C 2012;116:8901–8909. https://doi.org/10.1021/jp300867j.*

Very recently, Kalanur et al. reported a systematic study of 3d transition metal doped WO_3 thin films [57]. They found that doping can improve or degrade the photo conversion efficiency (PCE) and will depend on the dopant. Their experimental observations showed that all dopants except V and Cr were found to enhance the PEC and PCE. Among 3d-element dopants, Co- was found to be favorable for PEC compared with other dopants. Table 3 shows the effect of the 3d transition metal on the WO_3 bandgap and position of the bands [57].

2.3 Modification in carrier recombination

Under a suitable irradiation range, all ceramic-based photocatalysts will generate electron-hole pairs. Many of the photogenerated carriers recombine within the crystal before reaching the photocatalyst surface to contribute to the redox reaction. This is

Table 3 Various parameters like bandgap, CB band position, VB band position, and the energy difference between the Fermi level and valence band of undoped and doped WO_3 thin films with different 3d transition metal ions [57].

Dopant	Bandgap (eV)	CB edge position vs RHE (V)	VB edge position vs RHE (V)	Energy difference between Fermi level and VB position (eV) ± 0.01 eV
Undoped WO_3	2.62	0.44	3.06	2.07
V	2.49	0.91	3.4	1.76
Cr	2.34	0.16	2.5	1.95
Mn	2.55	0.44	2.99	1.83
Fe	2.45	0.46	2.91	1.81
Co	2.51	0.08	2.43	2.25
Ni	2.41	1.15	3.56	1.51
Cu	2.45	0.2	2.65	1.77
Zn	2.57	0.31	2.88	1.75

https://www.twirpx.org & http://chemistry-chemists.com

one of the main reasons for the poor performance of ceramic-based photocatalysts. Normally, it is found that redox energy levels of transition metal ions mostly occupy inside the bandgap. For example, energies of metals such as Fe, Cr, V, Au, and Pt lie close to the VB or CB edge within the bandgap of TiO_2. This facilitates visible radiation absorption at mid-bandgap energies. Moreover, metal doping provides an additional benefit as metal ions also act as a carrier trap and reduce carrier recombination (electron-hole pair), resulting in improved photoactivity under radiation. Yi et al. reported enhanced photocatalytic activity under visible light irradiation for iron-doped zinc oxide nanoflowers. The metal dopant increases the electron capturing capacity of semiconductors [58].

Since the efficiency depends significantly upon the metal ion charge transfer, it is found that under the low intensity of radiation, the metal dopant performs well to trap photogenerated carriers and affects the electron-hole pair recombination rates. In contrast, these metal ions can also act as recombination centers as the intensity of incident radiation is increased, which heavily reduces photoactivity. For example, Choi et al. showed that photoactivity of metal ion-doped TiO_2 greatly depends on the dopant concentration, its energy within the level, distribution, electron configuration, and the intensity of the radiation [33]. A few reports demonstrated that metal dopants can also favor the recombination centers due to the localized d-states in the TiO_2 bandgap [31].

The effective spatial separation of photogenerated charge carriers plays a vital role in minimizing recombination rates. To compensate the recombination of electron-hole pairs, Asahi et al. proposed to dope the TiO_2 with nonmetallic elements such as N, C, and S, whose energy bands significantly overlap with that of TiO_2, and within the photoexcited carriers' lifetimes, doping effectively channelizes these carriers to reactive sites at the catalyst surface [31]. The recombination rates were slowed down via a few routes such as directional migration, and trapping of certain photoinduced species has been employed [59, 60]. This can be done using specific structural factors, like surface vacancies, lattice distortions, and dopants, by trapping the charge carriers into the defect-mediated states, and would be favorable for charge separation. Wang et al. showed that the oxygen-deficient TiO_2 provided a base for visible excitation while codoping with nitrogen helped to reduce the recombination rate of photogenerated carriers by creating single electron trapped oxygen vacancies (SETOVs) [61, 62]. These trapped states formed a mid-energy band just below the conduction band, and apart from slowing the relaxation dynamics, they also contributed to the visible light excitation. Fig. 7 shows a schematic of the band diagram of N-doped and undoped TiO_2; both of these show the enhanced photoexcitation under the visible radiation, while undoped TiO_2 with only oxygen vacancies does not show any photoactivity due to the recombination of the carriers.

The intensity of the photoluminescence (PL) is one indication of how well the material can hold the charge separation as it arises from indirect bandgap transition and surface recombination processes. As shown in Fig. 5, the intensity of the PL signal for doped and undoped C_3N_4 indicates that the photogenerated carrier recombination rate is significantly higher in the case of undoped C_3N_4. Under the same test conditions, lower PL intensity denotes a lower recombination rate and higher separation efficiency.

https://www.twirpx.org & http://chemistry-chemists.com

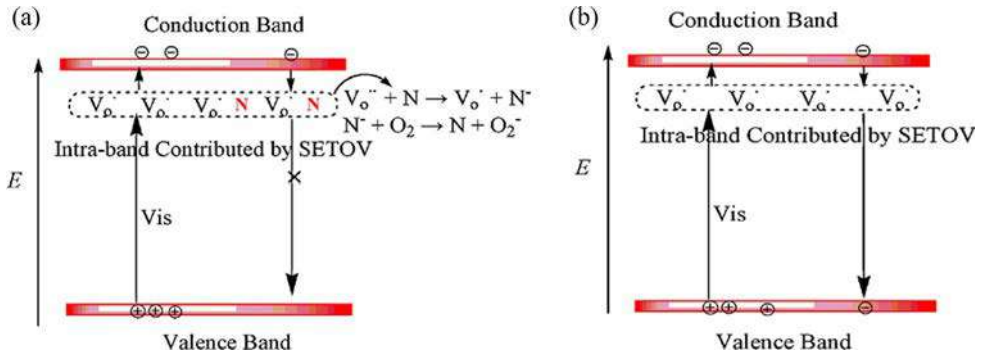

FIG. 7 Schematic illustrations of the role of nitrogen dopant in preventing photoinduced electrons and holes from recombination for (A) N-doped TiO_2 and (B) undoped TiO_2. *From Wang Y, Feng C, Zhang M, Yang J, Zhang Z. Enhanced visible light photocatalytic activity of N-doped TiO_2 in relation to single-electron-trapped oxygen vacancy and doped-nitrogen. Appl Catal Environ 2010;100:84–90. https://doi.org/10.1016/j.apcatb.2010.07.015.*

Jiang et al. investigated doped TiO_2 with different dopants and codopants like Yb, N, and P, and found that these have better photoactivity compared to that of undoped TiO_2. From their photoluminescence observation, they showed that Yb-doping could undergo indirect recombination, while P doping restricts the recombination of photogenerated electron-hole pairs. To assess the effects of Yb, N, and P dopants on photoactivity, the authors tested the degradation of methylene blue (MB) in aqueous solutions under visible light and UV irradiation, and found that the P^{5+}, as an electron trap center, reduced the recombination rate of photogenerated charge carriers and enhanced the photon efficiency (Fig. 8) [63]. The P-doping concentration is 5 wt%, showing the highest photoactivity; any deviation from 5 wt% of the P-doping dose suppresses the photoactivity of TiO_2.

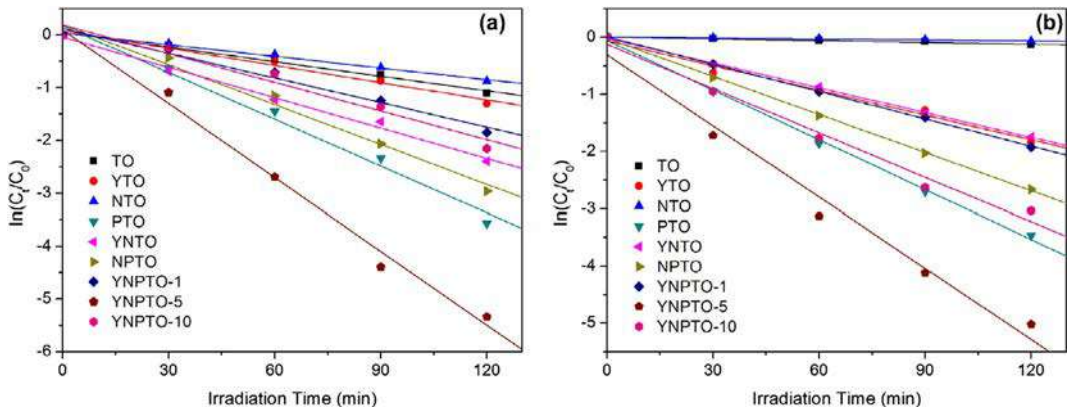

FIG. 8 Kinetic curves for (A) visible light photodegradation and (B) UV photodegradation of methylene blue over different doped TiO_2 samples. Here TO represents TiO_2 and MTO (M = Y, N, P)-doped TiO_2, while the number shows the doping in wt%. *Reproduced from Jiang H., Yan P., Wang Q., Zang S., Li J., Wang Q. High-performance Yb, N, P-tridoped anatase-TiO_2 nano-photocatalyst with visible light response by sol-solvothermal method. Chem Eng J 2013;215–216:348–357. doi:10.1016/j.cej.2012.10.082..*

https://www.twirpx.org & http://chemistry-chemists.com

Bismuth vanadate ($BiVO_4$) is a low-cost, highly active, and stable ceramic. Due to these features, some researchers have used it for visible light-driven photocatalytic and photoelectrochemical water oxidation. However, the low mobility of charge carriers and speedy recombination rates makes $BiVO_4$ (BVO) ineffective for photocatalytic activity. It was experimentally found that the efficiency of $BiVO_4$ (BVO) for oxygen evolution could be considerably increased by Mo doping (Fig. 9). It was established that the water oxidation rate under simulated solar light can be further improved by W-doping [64].

3 Degradation of organic pollutants

Availability of clean water is one of the future challenges; it is also a prime focus of current research and photocatalysis may play a part in overcoming this challenge. Various doping attempts have been made to check the recombination of the photogenerated electron-hole pairs in the photocatalysis process. In general, compared to their pure form, doped ceramics demonstrated better performance in the degradation process of organic pollutants. As it was established favored doping can reduce the bandgap of ceramic materials, resulting in a shift in the optical absorption (toward the visible light region). It enables easy electron migration from the VB to the CB even under visible light illumination. The electrons that reach the conduction band and holes in the valence band act as powerful oxidizing and reducing agents. The electron on the CB is removed by an oxygen molecule to make highly reactive superoxide radical anions, while the hole reacts with a surface-bound water molecule to produce hydroxyl radicals. These radicals can help to degrade

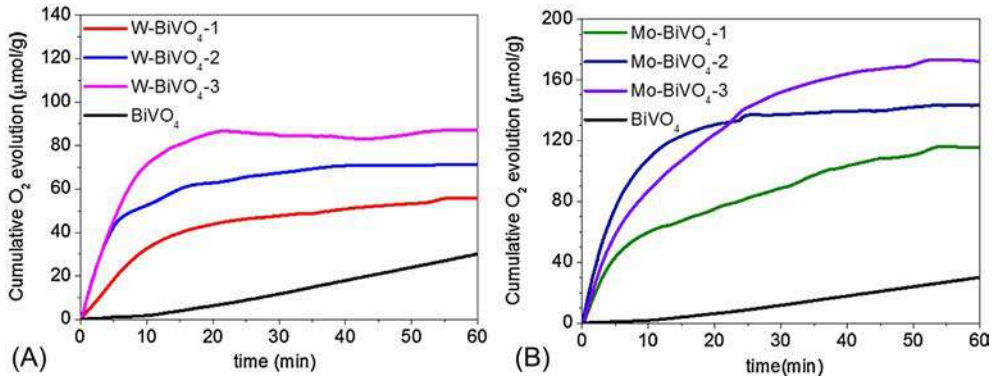

FIG. 9 Time course of O_2 evolution: (A) W-doped and (B) Mo-doped $BiVO_4$ samples under simulated sunlight illumination (100 mW/cm^2). *From Thalluri SM, Hussain M, Saracco G, Barber J, Russo N. Green-synthesized $BiVO_4$ oriented along {040} facets for visible-light-driven ethylene degradation. Ind Eng Chem Res 2014;53:2640–2646. https://doi.org/10.1021/ie403999g.*

https://www.twirpx.org & http://chemistry-chemists.com

Table 4 Effect of initial organic pollutant concentration on photocatalytic activity.

Material	Organic pollutant	Range of pollutant concentration (mg/L)	Light source	Degradation efficiency (%)	Irradiation time (h)
C-TiO_2 [65]	Methylene blue	5–50	Solar light	100	2–3
N-TiO_2 [66]	Phenol	10–200	UV	–	–
P-TiO_2 [67]	Rhodamine B	5–50	Solar light	85	–
Fe-TiO_2 [68]	Methyl orange	20	UV-vis	99.7	3
Fe-ZnO [69]	Reactive black 5	30	Vis	90	3
La-Bi_2O_3 [70]	CBBG-250	–	Vis	96	2

the organic pollutants in the form of salts, water, or carbon dioxide. Table 4 provides a list of a few doped ceramics used for photodegradation of pollutants, along with their efficiency [65–70].

4 Conclusion and future prospects

In this chapter, we discussed the influence of doping on the different types of ceramic materials from metal oxides to nonmetal and perovskite oxides. In a photoexcitation process, charge transfer, trapping, and recombination play significant roles. Different dopants counter differently with each step in the photocatalysis process under extended light radiation. A successful doping scheme takes account of all aspects: efficient response to visible light absorption, modification in the band's position, and high charge carriers' generation and their separation. We see from the various studies that metal/nonmetal dopants certainly increase the visible light excitation efficiency of electrons in the valence band of the parent (undoped) ceramic semiconductor. However, sometimes as a consequence of doping, the created mid-energy gaps also act as recombination centers, which must be avoided to achieve better photocatalytic activity. For example, there are a few strategies to make use of low dimensional materials as in bulk dopants distribute themselves inside the crystal, resulting in higher recombination centers. The other possibility is to use the codopant; for example, in perovskite $SrTiO_3$, one of the dopants helps to reduce the bandgap, and a different dopant positions the bands for favorable redox reaction and carrier separation. Moreover, the use of narrow-bandgap ceramics can be promising when coupled with 2D materials or composites. Defect engineering, such as inducing oxygen vacancies, leads to significantly improved performances in charge carrier-involved photocatalytic reactions. Recent works on optimizing the interactions between photogenerated carriers to tune the photocatalytic processes of semiconductors by confining them between layered structures have gained a lot of attention.

https://www.twirpx.org & http://chemistry-chemists.com

A dopant should not only enhance the efficiency in the visible region but also positively contribute to lift the energy band positions suitable for redox reaction and minimize the photogenerated electron-hole pairs. Careful designing, fabrication, and choice of dopants will help to tune the electronic band structure for a suitable photocatalyst. Metal oxides' stability, easy fabrication, and tunable photochemical properties make them suitable next-generation materials for photocatalysis and pollutant degradation.

References

[1] Granqvist CG. Solar energy materials. Adv Mater 2003;15:1789–803. https://doi.org/10.1002/adma.200300378.

[2] Mekhilef S, Saidur R, Safari A. A review on solar energy use in industries. Renew Sustain Energy Rev 2011;15:1777–90. https://doi.org/10.1016/j.rser.2010.12.018.

[3] Solangi KH, Islam MR, Saidur R, Rahim NA, Fayaz H. A review on global solar energy policy. Renew Sustain Energy Rev 2011;15:2149–63. https://doi.org/10.1016/j.rser.2011.01.007.

[4] Sun H, Wang S. Research advances in the synthesis of nanocarbon-based photocatalysts and their applications for photocatalytic conversion of carbon dioxide to hydrocarbon fuels. Energy Fuel 2014;28:22–36. https://doi.org/10.1021/ef401426x.

[5] Tiba S, Omri A. Literature survey on the relationships between energy, environment and economic growth. Renew Sustain Energy Rev 2017;69:1129–46. https://doi.org/10.1016/j.rser.2016.09.113.

[6] Landman A, Dotan H, Shter GE, Wullenkord M, Houaijia A, Maljusch A, et al. Photoelectrochemical water splitting in separate oxygen and hydrogen cells. Nat Mater 2017;16:646–51. https://doi.org/10.1038/nmat4876.

[7] Fujishima A, Honda K. Electrochemical photolysis of water at a semiconductor electrode. Nature 1972;238:37–8. https://doi.org/10.1038/238037a0.

[8] Linsebigler AL, Lu G, Yates JT. Photocatalysis on TiO_2 surfaces: principles, mechanisms, and selected results. Chem Rev 1995;95:735–58. https://doi.org/10.1021/cr00035a013.

[9] Hadjiivanov KI, Klissurski DG. Surface chemistry of titania (anatase) and titania-supported catalysts. Chem Soc Rev 1996;25:61–9. https://doi.org/10.1039/cs9962500061.

[10] Heller A. Chemistry and applications of photocatalytic oxidation of thin organic films. Acc Chem Res 1995;28:503–8. https://doi.org/10.1021/ar00060a006.

[11] Hoffmann MR, Martin ST, Choi W, Bahnemann DW. Environmental applications of semiconductor photocatalysis. Chem Rev 1995;95:69–96. https://doi.org/10.1021/cr00033a004.

[12] Scott Bohle D, Spina CJ. Cationic and anionic surface binding sites on nanocrystalline zinc oxide: surface influence on photoluminescence and photocatalysis. J Am Chem Soc 2009;131:4397–404. https://doi.org/10.1021/ja808663b.

[13] Fox MA, Dulay MT. Heterogeneous photocatalysis. Chem Rev 1993;93:341–57. https://doi.org/10.1021/cr00017a016.

[14] Kapilashrami M, Zhang Y, Liu YS, Hagfeldt A, Guo J. Probing the optical property and electronic structure of TiO_2 nanomaterials for renewable energy applications. Chem Rev 2014;114:9662–707. https://doi.org/10.1021/cr5000893.

[15] Liu G, Wang L, Yang HG, Cheng HM, Lu GQ. Titania-based photocatalysts—crystal growth, doping and heterostructuring. J Mater Chem 2010;20:831–43. https://doi.org/10.1039/b909930a.

[16] Wang H, Zhang X, Xie Y. Recent progress in ultrathin two-dimensional semiconductors for photocatalysis. Mater Sci Eng R Rep 2018;130:1–39. https://doi.org/10.1016/j.mser.2018.04.002.

https://www.twirpx.org & http://chemistry-chemists.com

[17] Yu Z, Chen X-Q, Kang X, Xie Y, Zhu H, Wang S, et al. Noninvasively modifying band structures of wide-bandgap metal oxides to boost photocatalytic activity. Adv Mater 2018;30:1706259. https://doi.org/10.1002/adma.201706259.

[18] Height MJ, Pratsinis SE, Mekasuwandumrong O, Praserthdam P. Ag-ZnO catalysts for UV-photodegradation of methylene blue. Appl Catal Environ 2006;63:305–12. https://doi.org/10.1016/j.apcatb.2005.10.018.

[19] Niishiro R, Kato H, Kudo A. Nickel and either tantalum or niobium-codoped TiO_2 and $SrTiO_3$ photocatalysts with visible-light response for H_2 or O_2 evolution from aqueous solutions. Phys Chem Chem Phys 2005;7:2241–5. https://doi.org/10.1039/b502147b.

[20] Shi J, Shen S, Chen Y, Guo L, Mao SS. Visible light-driven photocatalysis of doped $SrTiO_3$ tubular structure. Opt Express 2012;20:A351–9. https://doi.org/10.1364/OE.20.00A351.

[21] Li Y, Li YL, Araujo CM, Luo W, Ahuja R. Single-layer MoS_2 as an efficient photocatalyst. Cat Sci Technol 2013;3:2214–20. https://doi.org/10.1039/c3cy00207a.

[22] Yu Z, Yin B, Qu F, Wu X. Synthesis of self-assembled CdS nanospheres and their photocatalytic activities by photodegradation of organic dye molecules. Chem Eng J 2014;258:203–9. https://doi.org/10.1016/j.cej.2014.07.041.

[23] Ho W, Zhang Z, Xu M, Zhang X, Wang X, Huang Y. Enhanced visible-light-driven photocatalytic removal of NO: effect on layer distortion on g-C3N4 by H2 heating. Appl Catal Environ 2015;179:106–12. https://doi.org/10.1016/j.apcatb.2015.05.010.

[24] Samanta S, Martha S, Parida K. Facile synthesis of Au/g-C_3N_4 nanocomposites: an inorganic/organic hybrid plasmonic photocatalyst with enhanced hydrogen gas evolution under visible-light irradiation. ChemCatChem 2014;6:1453–62. https://doi.org/10.1002/cctc.201300949.

[25] Wang X, Blechert S, Antonietti M. Polymeric graphitic carbon nitride for heterogeneous photocatalysis. ACS Catal 2012;2:1596–606. https://doi.org/10.1021/cs300240x.

[26] Xiong T, Cen W, Zhang Y, Dong F. Bridging the g-C_3N_4 interlayers for enhanced photocatalysis. ACS Catal 2016;6:2462–72. https://doi.org/10.1021/acscatal.5b02922.

[27] Zhang L, Jin Z, Lu H, Lin T, Ruan S, Zhao XS, et al. Improving the visible-light photocatalytic activity of graphitic carbon nitride by carbon black doping. ACS Omega 2018;3:15009–17. https://doi.org/10.1021/acsomega.8b01933.

[28] Zhu M, Zhai C, Sun M, Hu Y, Yan B, Du Y. Ultrathin graphitic C_3N_4 nanosheet as a promising visible-light-activated support for boosting photoelectrocatalytic methanol oxidation. Appl Catal Environ 2017;203:108–15. https://doi.org/10.1016/j.apcatb.2016.10.012.

[29] Xu Z, Tabata I, Hirogaki K, Hisada K, Wang T, Wang S, et al. Preparation of platinum-loaded cubic tungsten oxide: a highly efficient visible light-driven photocatalyst. Mater Lett 2011;65:1252–6. https://doi.org/10.1016/j.matlet.2010.12.011.

[30] Zhao ZG, Miyauchi M. Nanoporous-walled tungsten oxide nanotubes as highly active visible-light-driven photocatalysts. Angew Chem Int Ed 2008;47:7051–5. https://doi.org/10.1002/anie.200802207.

[31] Asahi R, Morikawa T, Ohwaki T, Aoki K, Taga Y. Visible-light photocatalysis in nitrogen-doped titanium oxides. Science 2001;293:269–71. https://doi.org/10.1126/science.1061051.

[32] Chen X, Burda C. The electronic origin of the visible-light absorption properties of C-, N- and S-doped TiO2 nanomaterials. J Am Chem Soc 2008;130:5018–9. https://doi.org/10.1021/ja711023z.

[33] Choi W, Termin A, Hoffmann MR. Effects of metal-ion dopants on the photocatalytic reactivity of quantum-sized TiO2 particles. Angew Chem Int Ed Engl 1994;33:1091–2. https://doi.org/10.1002/anie.199410911.

[34] Xu AW, Gao Y, Liu HQ. The preparation, characterization, and their photocatalytic activities of rare-earth-doped TiO2 nanoparticles. J Catal 2002;207:151–7. https://doi.org/10.1006/jcat.2002.3539.

https://www.twirpx.org & http://chemistry-chemists.com

[35] Sun H, Bai Y, Cheng Y, Jin W, Xu N. Preparation and characterization of visible-light-driven carbon—sulfur-codoped TiO2 photocatalysts. Ind Eng Chem Res 2006;45:4971–6. https://doi.org/10.1021/ie060350f.

[36] Sun H, Bai Y, Jin W, Xu N. Visible-light-driven TiO_2 catalysts doped with low-concentration nitrogen species. Sol Energy Mater Sol Cells 2008;92:76–83. https://doi.org/10.1016/j.solmat.2007.09.003.

[37] Zhu J, Zheng W, He B, Zhang J, Anpo M. Characterization of Fe-TiO_2 photocatalysts synthesized by hydrothermal method and their photocatalytic reactivity for photodegradation of XRG dye diluted in water. J Mol Catal A Chem 2004;216:35–43. https://doi.org/10.1016/j.molcata.2004.01.008.

[38] George S, Pokhrel S, Ji Z, Henderson BL, Xia T, Li L, et al. Role of Fe doping in tuning the band gap of TiO_2 for the photo-oxidation-induced cytotoxicity paradigm. J Am Chem Soc 2011;133:11270–8. https://doi.org/10.1021/ja202836s.

[39] Sun Y, Murphy CJ, Reyes-Gil KR, Reyes-Garcia EA, Lilly JP, Raftery D. Carbon-doped In_2O_3 films for photoelectrochemical hydrogen production. Int J Hydrogen Energy 2008;33:5967–74. https://doi.org/10.1016/j.ijhydene.2008.07.100.

[40] Khan SUM, Al-Shahry M, Ingler WB. Efficient photochemical water splitting by a chemically modified n-TiO. Science 2002;297:2243. https://doi.org/10.1126/science.1075035.

[41] Bilgin Simsek E. Solvothermal synthesized boron doped TiO_2 catalysts: photocatalytic degradation of endocrine disrupting compounds and pharmaceuticals under visible light irradiation. Appl Catal Environ 2017;200:309–22. https://doi.org/10.1016/j.apcatb.2016.07.016.

[42] Chen Y-S, Lin L-Y, Ma J-S. Synthesizing molybdenum-doped bismuth vanadate nanoneedle array as photocatalyst for water oxidation using bifunctional molybdenum as dopant and structure directing agent. Electrochim Acta 2020;329:135171. https://doi.org/10.1016/j.electacta.2019.135171.

[43] Li H, Zhang X, Huo Y, Zhu J. Supercritical preparation of a highly active S-doped TiO_2 photocatalyst for methylene blue mineralization. Environ Sci Technol 2007;41:4410–4. https://doi.org/10.1021/es062680x.

[44] Malathy P, Vignesh K, Rajarajan M, Suganthi A. Enhanced photocatalytic performance of transition metal doped Bi_2O_3 nanoparticles under visible light irradiation. Ceram Int 2014;40:101–7. https://doi.org/10.1016/j.ceramint.2013.05.109.

[45] Pihosh Y, Turkevych I, Mawatari K, Asai T, Hisatomi T, Uemura J, et al. Nanostructured WO_3/$BiVO_4$ photoanodes for efficient photoelectrochemical water splitting. Small 2014;10:3692–9. https://doi.org/10.1002/smll.201400276.

[46] Shin SW, Lee JY, Ahn K-S, Kang SH, Kim JH. Visible light absorbing TiO_2 nanotube arrays by sulfur treatment for photoelectrochemical water splitting. J Phys Chem C 2015;119:13375–83. https://doi.org/10.1021/acs.jpcc.5b01104.

[47] Singh S, Sharma R. Bi_2O_3/Ni-Bi_2O_3 system obtained via Ni-doping for enhanced PEC and photocatalytic activity supported by DFT and experimental study. Sol Energy Mater Sol Cells 2018;186:208–16. https://doi.org/10.1016/j.solmat.2018.06.049.

[48] Su J, Guo L, Bao N, Grimes CA. Nanostructured WO_3/$BiVO_4$ heterojunction films for efficient photoelectrochemical water splitting. Nano Lett 2011;11:1928–33. https://doi.org/10.1021/nl2000743.

[49] Zhang C, Wu Q, Ke X, Wang J, Jin X, Xue S. Ultrathin hematite films deposited layer-by-layer on a TiO_2 underlayer for efficient water splitting under visible light. Int J Hydrogen Energy 2014;39:14604–12. https://doi.org/10.1016/j.ijhydene.2014.07.120.

[50] Masakazu A. Use of visible light. Second-generation titanium oxide photocatalysts prepared by the application of an advanced metal ion-implantation method. Pure Appl Chem 2000;72:1787–92.

[51] Sato S. Photocatalytic activity of NOx-doped TiO_2 in the visible light region. Chem Phys Lett 1986;123:126–8. https://doi.org/10.1016/0009-2614(86)87026-9.

https://www.twirpx.org & http://chemistry-chemists.com

[52] Takeshi M, Ryoji A, Takeshi O, Koyu A, Yasunori T. Band-gap narrowing of titanium dioxide by nitrogen doping. Jpn J Appl Phys 2001;L561–3. https://doi.org/10.1143/JJAP.40.L561.

[53] Mu J, Chen B, Zhang M, Guo Z, Zhang P, Zhang Z, et al. Enhancement of the visible-light photocatalytic activity of In_2O_3–TiO_2 nanofiber heteroarchitectures. ACS Appl Mater Interfaces 2012;4:424–30. https://doi.org/10.1021/am201499r.

[54] Chen C, Moir J, Soheilnia N, Mahler B, Hoch L, Liao K, et al. Morphology-controlled In_2O_3 nanostructures enhance the performance of photoelectrochemical water oxidation. Nanoscale 2015;7:3683–93. https://doi.org/10.1039/C4NR07394K.

[55] Irie H, Maruyama Y, Hashimoto K. Ag+- and Pb2+-doped SrTiO3 photocatalysts. A correlation between band structure and photocatalytic activity. J Phys Chem C 2007;111:1847–52. https://doi.org/10.1021/jp066591i.

[56] Wang F, Di Valentin C, Pacchioni G. Doping of WO_3 for photocatalytic water splitting: hints from density functional theory. J Phys Chem C 2012;116:8901–9. https://doi.org/10.1021/jp300867j.

[57] Kalanur SS, Noh YG, Seo H. Engineering band edge properties of WO_3 with respect to photoelectrochemical water splitting potentials via a generalized doping protocol of first-row transition metal ions. Appl Surf Sci 2020;509. https://doi.org/10.1016/j.apsusc.2020.145253.

[58] Yi S, Cui J, Li S, Zhang L, Wang D, Lin Y. Enhanced visible-light photocatalytic activity of Fe/ZnO for rhodamineB degradation and its photogenerated charge transfer properties. Appl Surf Sci 2014;319:230–6. https://doi.org/10.1016/j.apsusc.2014.06.151.

[59] Pan X, Yang MQ, Fu X, Zhang N, Xu YJ. Defective TiO_2 with oxygen vacancies: synthesis, properties and photocatalytic applications. Nanoscale 2013;5:3601–14. https://doi.org/10.1039/c3nr00476g.

[60] Wang H, Zhang L, Chen Z, Hu J, Li S, Wang Z, et al. Semiconductor heterojunction photocatalysts: design, construction, and photocatalytic performances. Chem Soc Rev 2014;43:5234–44. https://doi.org/10.1039/c4cs00126e.

[61] Wang Y, Feng C, Zhang M, Yang J, Zhang Z. Enhanced visible light photocatalytic activity of N-doped TiO_2 in relation to single-electron-trapped oxygen vacancy and doped-nitrogen. Appl Catal Environ 2010;100:84–90. https://doi.org/10.1016/j.apcatb.2010.07.015.

[62] Wang Y, Feng C, Zhang M, Yang J, Zhang Z. Visible light active N-doped TiO_2 prepared from different precursors: origin of the visible light absorption and photoactivity. Appl Catal Environ 2011;104:268–74. https://doi.org/10.1016/j.apcatb.2011.03.020.

[63] Jiang H, Yan P, Wang Q, Zang S, Li J, Wang Q. High-performance Yb, N, P-tridoped anatase-TiO_2 nanophotocatalyst with visible light response by sol-solvothermal method. Chem Eng J 2013;215–216:348–57. https://doi.org/10.1016/j.cej.2012.10.082.

[64] Thalluri SM, Hussain M, Saracco G, Barber J, Russo N. Green-synthesized W- and Mo-doped $BiVO_4$ oriented along the {0 4 0} facet with enhanced activity for the sun-driven water oxidation. Appl Catal B Environ 2016;180:630–6. https://doi.org/10.1016/j.apcatb.2015.07.029.

[65] Devi LG, Rajashekhar KE. A kinetic model based on non-linear regression analysis is proposed for the degradation of phenol under UV/solar light using nitrogen doped TiO2. J Mol Catal A Chem 2011;334:65–76. https://doi.org/10.1016/j.molcata.2010.10.025.

[66] Xiao Q, Zhang J, Xiao C, Si Z, Tan X. Solar photocatalytic degradation of methylene blue in carbon-doped TiO_2 nanoparticles suspension. Sol Energy 2008;82:706–13. https://doi.org/10.1016/j.solener.2008.02.006.

[67] Deng L, Wang S, Liu D, Zhu B, Huang W, Wu S, et al. Synthesis, characterization of Fe-doped TiO_2 nanotubes with high photocatalytic activity. Catal Lett 2009;129:513–8. https://doi.org/10.1007/s10562-008-9834-5.

[68] Lv Y, Yu L, Huang H, Liu H, Feng Y. Preparation, characterization of P-doped TiO_2 nanoparticles and their excellent photocatalystic properties under the solar light irradiation. J Alloys Compd 2009;488:314–9. https://doi.org/10.1016/j.jallcom.2009.08.116.

https://www.twirpx.org & http://chemistry-chemists.com

[69] Mohsin M, Bhatti IA, Ashar A, Mahmood A, Maryam, ul Hassan Q, et al. Fe/ZnO@ceramic fabrication for the enhanced photocatalytic performance under solar light irradiation for dye degradation. J Mater Res Technol 2020;9:4218–29. https://doi.org/10.1016/j.jmrt.2020.02.048.

[70] Raza W, Bahnemann D, Muneer M. A green approach for degradation of organic pollutants using rare earth metal doped bismuth oxide. Catal Today 2018;300:89–98. https://doi.org/10.1016/j.cattod.2017.07.029.

https://www.twirpx.org & http://chemistry-chemists.com

https://www.twirpx.org & http://chemistry-chemists.com

11

Nanocomposites for visible light photocatalysis

Abhijit N. Kadam[a], Jinhyeok Lee[a], Sandip V. Nipane[b], and Sang-Wha Lee[a]

[a]DEPARTMENT OF CHEMICAL AND BIOLOGICAL ENGINEERING, GACHON UNIVERSITY, SEONGNAM-SI, SOUTH KOREA [b]DEPARTMENT OF CHEMISTRY, SMT. KASTURBAI WALCHAND COLLEGE, SANGLI, MS, INDIA

1 Introduction

Environmental pollution and the scarcity of sustainable energy are caused by continuous increases in population and industrialization [1]. The numerous pollutants released from the pharmaceutical, leathering manufacturing, and textile industries are serious threats to human beings and aquatic biota [2]. For instance, organic pollutants including phenol, dyes, pesticides, pharmaceutical drugs, and inorganic pollutant Cr VII are leading sources of water pollution [3–5]. At present, several conventional methods are available for the abatement of pollutants (such as chemical oxidation, physical adsorption, biodegradation, and membrane filtration). However, these methods are found to be less effective for removing completely contaminants at trace level [6, 7]. In addition, the conventional treatments involve transferring the contaminants from one phase to another phase, leading to secondary pollution and hampering their practical applications. In this regard, photocatalysis has emerged as a promising green technology to treat pollutants at trace level under sustainable solar light [8]. Photocatalysis operating at ambient conditions offers many advantages. It is cost-effective, efficient, and environmentally friendly, as well as offering complete mineralization with diminished toxicity [9]. Among photocatalysts, TiO_2 has been frequently considered as a gold-standard photocatalyst because of its nontoxic nature, relatively low cost, and good stability [10]. However, it has a wide bandgap of 3.2 eV, limiting its application under UV light (solar light consisting of 4% UV, 46% visible, and rest of NIR) and has high recombination of charge carriers [11]. However, visible light-responsive photocatalysts can be utilized in various applications such as cleaning wastewater and renewable energy to generate hydrogen, and CO_2 reduction into valuable products and solar fuel [12–14]. Thus, narrowing the bandgaps of conventional semiconductors (ZrO_2, SnO_2, TiO_2 and ZnO) has been considered an efficient way to harvest maximum solar light [15, 16].

On the other hand, there are narrow bandgap semiconductors such as Fe_2O_3 (2.1 eV), CuO (1.5 eV), CdS (2.4 eV), and $BiVO_4$ (2.4 eV) that can absorb visible light [17–20]. Nevertheless, the high recombination rate of charge carriers and inadequate valence band or conduction band cause them to generate superoxide radical anions and hydroxyl radicals

Nanostructured Materials for Visible Light Photocatalysis. https://doi.org/10.1016/B978-0-12-823018-3.00017-8
Copyright © 2022 Elsevier Inc. All rights reserved.

https://www.twirpx.org & http://chemistry-chemists.com

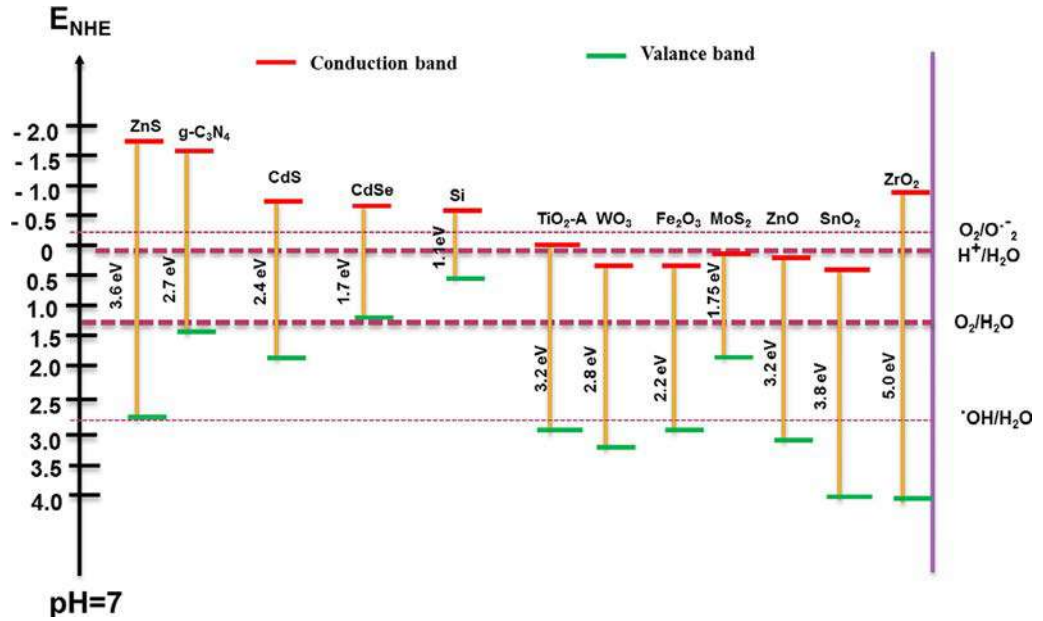

FIG. 1 Bandgap energy, VB and CB positions of several common semiconductors on a potential scale (V) vs. NHE.

efficiently [21]. To accomplish maximum efficiency, the required properties for the photocatalysts are profound absorption of solar light in the visible light range, efficient separation of charge carrier, suitable band edge potential for redox reactions, and prolonged photostability [22, 23]. Various strategies are available to modify photocatalysts to achieve high photocatalytic activity by increasing the separation of charge carriers and tuning the bandgap with desirable band edge by employing doping of metal or nonmetal, decoration of noble metals, heterojunction with low bandgap semiconductor, dye sensitization, surface modification, and defect engineering [24–27]. Among these strategies, heterostructure nanocomposites have been the most efficient way to achieve excellent activity under visible light irradiation [28]. The well-defined band edge potential can deliberately improve the separation of photogenerated charge carriers (electrons (e^-) and holes (h^+)) due to the synergistic effect of individual semiconductors [29, 30]. However, careful selection of semiconductor material is required with respect to band edge positions. Fig. 1 shows the position of the band edge potential of widely used semiconductors.

In this chapter, we will focus on types of heterostructure nanocomposites based on band alignment and dimensions. The various synthetic methods for semiconductor nanocomposites will be discussed. Application of visible light-active nanocomposites will be discussed in the aspects of photocatalytic degradation of dye, emerging pollutant and photoreduction of heavy metal ions. The mechanism of the photocatalytic process will be discussed in detail. The current status, challenges, and future prospects of visible light-active nanocomposites for photocatalytic applications will also be discussed. This

https://www.twirpx.org & http://chemistry-chemists.com

chapter can provide useful understanding for the further development of highly active visible light-driven heterojunctions for the photocatalytic elimination of pollutants.

2 The critical conditions to design heterostructure

The following factors are very important to design heterostructure nanocomposites:

(1) The choice of the band edge potential of two semiconductors is a crucial parameter in order to accomplish maximum separation of charge carriers and desired potential for active radical formation [21].
(2) The low bandgap of the material can act as a sensitizer to harvest visible light [27].
(3) Conductivity also plays an important role in efficient transfer of the charge carrier on the surface of semiconductors for photocatalytic process [28].
(4) The high surface area is an important criterion for selecting a semiconductor that can provide copious active sites for practical photocatalytic application [31].
(5) A strong junction between two semiconductors is required for an efficient transfer of the charge carrier [30].

3 Types of heterojunction nanocomposites based on band alignment

Not only boosting the absorption of light into the visible light region but also suppressing the rate of recombination can be achieved by coupling narrow bandgap semiconductors with suitable band alignment by forming semiconductor-semiconductor heterostructure [27]. Compared to semiconductor-metal composite systems, semiconductor-semiconductor coupling can independently absorb the light radiation corresponding to each semiconductor [21]. As a result, the heterostructure can harvest more photonic energy with efficient separation of charge carrier. Fig. 2 shows the Web of Science statistics on visible light-active nanocomposites for photocatalysis, indicating the rapid increases of publication numbers between 2009 and 2020.

Hence, the exploration of visible light-active nanocomposites of photocatalysis is of great significance. Furthermore, in the view of band alignment energy, heterostructure photocatalysts can be classified into three types: type-I (straddling gap), type-II (staggered gap), and type-III (broken gap) (Fig. 3).

A type-I heterojunction is formed when the conduction band and valence band of semiconductor I are lower and higher than those of semiconductor II, respectively. Therefore, both electrons and holes will be transferred and accumulate on the semiconductor I. Hence, the electron and hole pairs cannot be efficiently separated in the type-I heterojunction. An example of a type-I heterojunction is TiO_2-Fe_2O_3 [32]. In addition, a type-II heterojunction is formed when the valence band and conduction band of the semiconductor II are higher than the valence band and conduction band of semiconductor I, respectively. Holes transfer

https://www.twirpx.org & http://chemistry-chemists.com

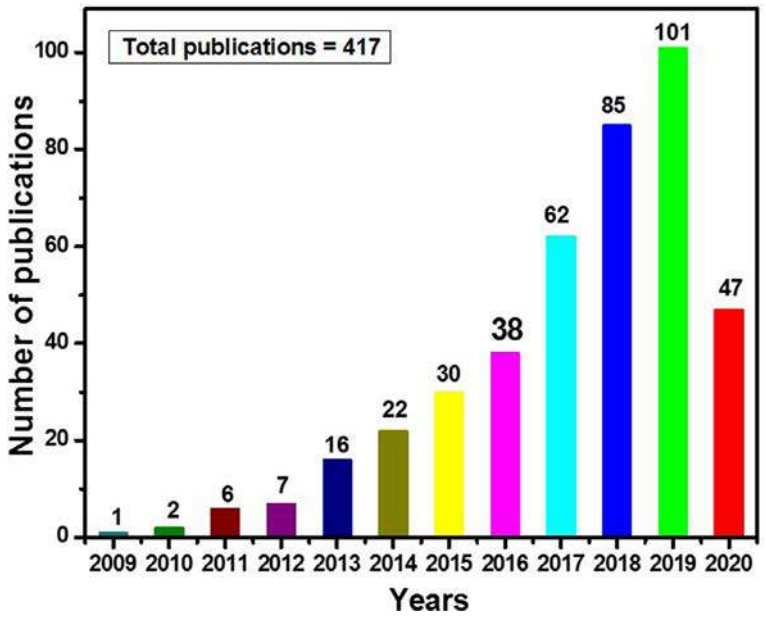

FIG. 2 Web of science statistics on visible light-active nanocomposites for photocatalysis from 2009 to 2020.

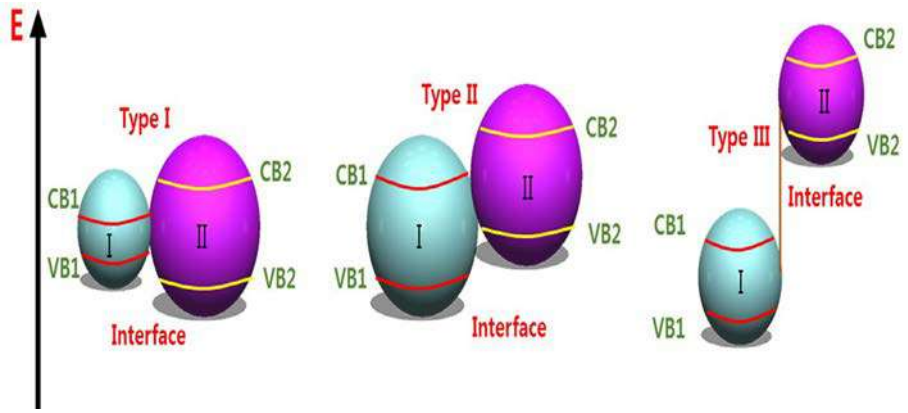

FIG. 3 Schematic representation of energy gap of three types of SC-SC heterojunctions.

from semiconductor I to semiconductor II, while electrons transfer from the conduction band of semiconductor II to conduction band of semiconductor I. For example, SnS_2-gC_3N_4 is a type-II heterojunction [29]. A type-III heterojunction is similar to a type-II heterojunction. However, the most significant difference in the conduction and valence band edges aligned with higher driving force to transfer the charges [29]. This is known to be misaligned configuration. However, it increases photocatalytic performance due to a higher driving

https://www.twirpx.org & http://chemistry-chemists.com

force for charge transfer. The photogenerated electrons from material I combine with the hole of material II, and the electron from material II and the hole from material I participate in the reduction and oxidation of water, respectively. The SnS_2-WSe_2 system represents the type-III heterojunction [33]. Thus, among the three types of heterojunctions, the type-II heterojunction system is the most favorable for photocatalysis because band bending of the semiconductor was caused by the difference in the chemical potential at the interface of the semiconductors [29]. The band bending phenomenon induces an electric field, which transfers the electrons and holes of semiconductors under light irradiation. As a result, the spatial separation of photoexcited charge carriers can enhance their photocatalytic activity [30]. Most importantly, type-II heterojunctions are designed for enhancing light absorption and efficient charge separation. In order to get an enhanced visible light absorption, heterojunction composite materials are generally composed of one semiconductor with wide bandgap, i.e., active under the UV light (TiO_2 or ZnO), whereas the other semiconductor with narrow bandgap, i.e., active under the visible light (CdS, CdSe, etc.). Under UV light radiation, type-II composite materials are excited simultaneously. That is, electrons migrate from CB2 to CB1, and holes migrate from VB1 to VB2, leading to efficient separation of photogenerated electrons and holes (Fig. 4A).

When type-II heterojunctions are excited under visible light, only the narrow bandgap material is excited, and the electrons from CB2 migrate to CB1 and holes remain within VB2, resulting in efficient charge separation (see Fig. 4B). Above all, in these SC–SC nanocomposites systems with type-II heterojunction, two crucial conditions are fulfilled: improved light absorption and proficient charge separation and migration. However, type-II has limitation in its practical photocatalytic application because the redox ability of the type-II was reduced like type-I. The reduction reaction takes places on the semiconductor I with lower reduction potential and oxidation reaction takes place on the semiconductor II with lower oxidation potential. Thus, it is highly demanding to increase redox property of photocatalytic materials for efficient performance. Type-II also shows a new Z-scheme when electrons from the CB of semiconductor I combine with the holes from the VB of semiconductor II (Fig. 5). For example, $BiVO_4$-g-C_3N_4 represents this type of Z-scheme heterojunction [34]. Wide absorption in the visible region, the stability of the photocatalyst, efficient separation of the charge carrier, and strong redox ability can be achieved by fabricating Z-scheme heterojunction nanocomposites.

4 Classifications of nanocomposites based on morphology

The morphology of the photocatalytic systems is a crucial factor that can modulate photocatalytic performance. The photocatalytic heterostructure can be classified based on the composite dimensions like 0D-0D (point contact), 0D-1D (point contact), 0D-2D (point contact), 1D-1D (line contact), 1D-2D (line contact), and 2D-2D (face contact), as shown in Fig. 6. Among all configurations, novel two-dimensional (2D-2D)-based nanocomposites are highly anticipated for efficient photocatalysis because 2D structures provide

https://www.twirpx.org & http://chemistry-chemists.com

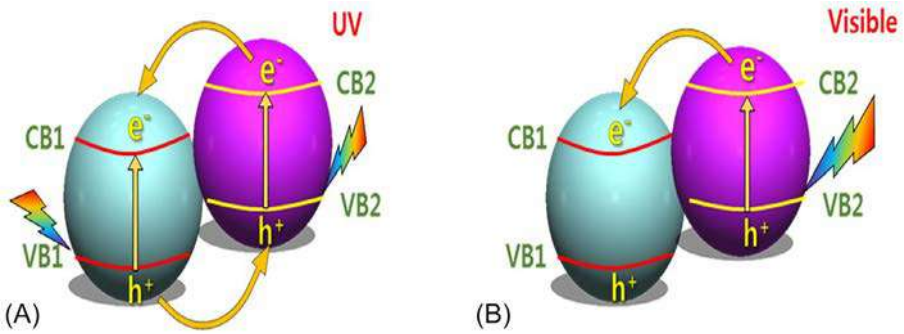

FIG. 4 Bandgap diagram of type-II heterojunctions illustrating the photogeneration of charge carriers and efficient separation of them upon (A) UV excitation and (B) visible light excitation.

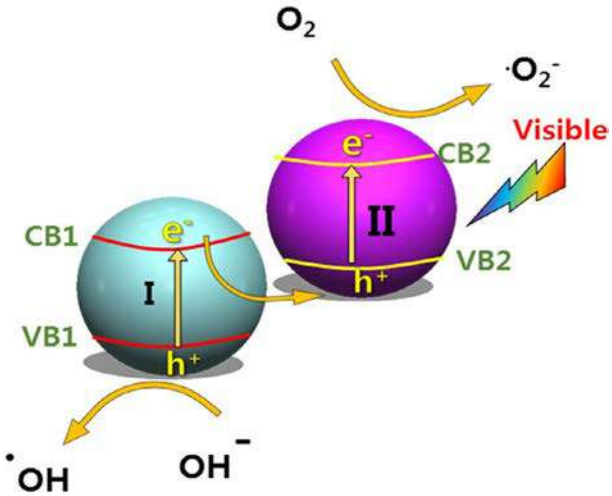

FIG. 5 New Z-scheme photocatalytic mechanism under visible light.

copious amounts of interfacial contact area, which is favorable for charge transfer and shortening the charge diffusion distance from the interface to the surface [35]. For instance, Sun et al. [36] synthesized $BiVO_4$-RGO nanocomposites via a solvothermal method with different dimension (0D-2D, 1D-2D, and 2D-2D) and compared their visible light-active photocatalytic activity toward degradation of acetaminophen. Among different dimensions, the 2D-2D interface showed the highest photocatalytic activity and prolonged lifetime because of large interfacial contact and stronger electronic and physical coupling effect between $BiVO_4$ nanosheets and graphene nanosheets, which is beneficial for an efficient separation and transfer of the charge carrier.

https://www.twirpx.org & http://chemistry-chemists.com

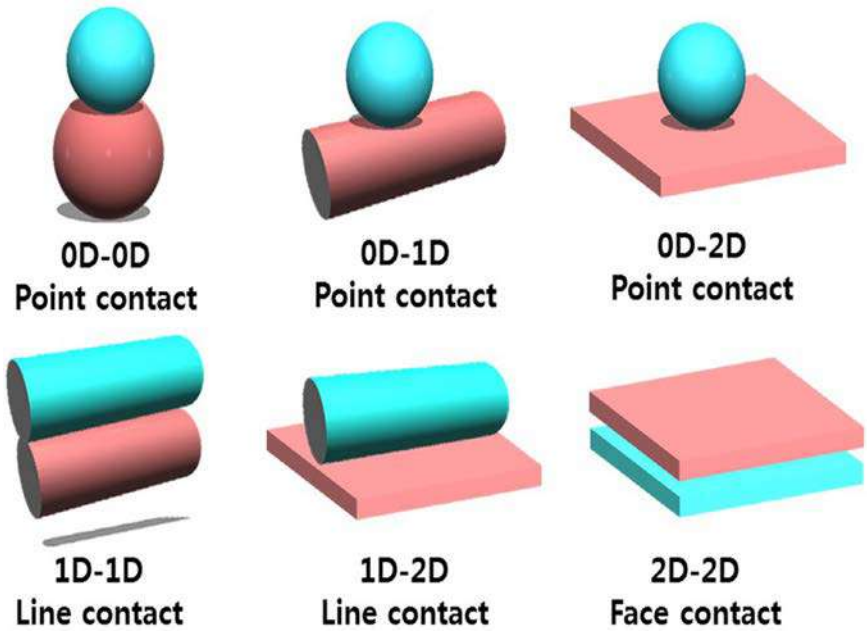

FIG. 6 Schematic illustration of 2D layered composites in comparison with other kinds of composites.

5 Synthesis strategies of nanocomposites

The nanocomposites can be synthesized by taking into account of many aspects:

(1) The band edge potentials should be matched between two semiconductors selected for heterojunction composites.
(2) Various aspects such as morphology, exposed facets, surface states, and interfacial properties should be considered.
(3) Intimate contact between two semiconductors should be designed for efficient separation of charge carrier while reducing interfacial resistance.

There are various strategies available for the synthesis of nanocomposites.

5.1 Deposition-precipitation method

The deposition-precipitation method has been used as a promising and versatile strategy for the synthesis of visible light-active nanocomposites [36]. Typically, the deposition-precipitation experiment is performed by depositing one semiconductor on the surface of a different semiconductor at a relatively low temperature. For example, the surface of ZnO nanorods with wide bandgap was decorated with Ag_2O nanoparticles with narrow bandgap by precipitation of Ag_2O on the surface of ZnO nanorods at room temperature [36]. Particularly, when an $AgNO_3$ solution was added to an aqueous solution of ZnO, Ag^+ ions were adsorbed from the solution onto the surface of ZnO nanorods in the dark

https://www.twirpx.org & http://chemistry-chemists.com

condition. Subsequently, after dropwise introducing of NaOH solution into the mixture solution, the Ag^+ adsorbed on the ZnO nanorods resulted in the formation of an Ag_2O/ZnO composite. The intimate contact and matched band edge potential caused high separation of charge carrier and boosted the absorption toward visible region. As a result, Ag_2O-ZnO nanocomposites showed enhanced photocatalytic activity compared to those of bare ZnO and Ag_2O. For a deposition-precipitation method employed to construct heterojunction nanocomposites, the as-synthesized component acts as a substrate to deliver sufficient surface active sites for in-situ nucleation as well as growth of the deposited component, which bestows intimate contact and thereby prevents aggregation, enabling the efficient separation of charge carrier and transfer between two components. Sometime a further postcalcination treatment is required to improve its crystallinity, which hampers recombination of the charge carrier and enhances the photocatalytic activity under visible light irradiation.

5.2 Hydrothermal and solvothermal method

Typically, the hydrothermal process is conducted in a closed autoclave under high pressure and high temperature, thus bestowing the fabrication of semiconductor nanocomposites with improved crystallinity and narrow size distribution without postheat treatment. For instance, a hydrothermal method was employed to fabricate an $InVO_4$/β-$AgVO_3$ composite through in-situ growth by Yang et al. [37]. In this work, $InVO_4$ NPs were dispersed evenly upon the surface of β-$AgVO_3$ nanoribbons, which intensely restrain the aggregation of $InVO_4$ nanoparticles. The intimate contact at interface and matched energy-band edges of $InVO_4$ nanocrystals and β-$AgVO_3$ nanoribbons produce superior photocatalytic activity through the Z-scheme. This method is also used for hydrothermal-assisted precipitation and in-situ deposition of semiconductors with close contact with other presynthesized material. For example, Zhang et al. [38] fabricated a TiO_2/g-C_3N_4 2D-2D heterostructure via an in situ strategy. Here g-C_3N_4 ultrathin nanosheets provided sufficient surface sites for anchoring TiO_2 sheets under hydrothermal condition and took advantage of strong interactions between g-C_3N_4-TiO_2 2D-2D nanosheets. The strong bonded g-C_3N_4-TiO_2 2D-2D underwent efficient separation of charge carrier and exhibited superior photocatalytic activity to that of mechanically assisted synthesis of g-C_3N_4-TiO_2 2D-2D. Notably, the hydrothermal method causes strong intimate contact between two components because of the in-situ growth and nucleation process, which offers efficient separation and transfer of the charge carrier. The solvothermal process is very similar to that of the hydrothermal process except that the solvothermal process uses an organic solvent.

5.3 Ion exchange method

The ion exchange method can be divided into two parts: cation exchange and anion exchange. This process has become the most popular method over the past few decades. The ion exchange process involves rapid replacement of ions in an ionic crystal whereas

https://www.twirpx.org & http://chemistry-chemists.com

the framework remains preserved while exposing the parent ionic crystal to new ions. The ion exchange is more favorable at nanocrystals than that of the bulk material, which can be accomplished speedily owing to lower activation barriers to the diffusing ions and enhanced surface access. For instance, Yu et al. [39] successfully synthesized CuS/ZnS monodispersed nanocomposite hollow spheres with about 255 nm and shells formed by nanoparticles by an ion exchange method using monodispersed ZnS solid spheres as a precursor. Thus, the ion exchange strategy will provide new understanding into the construction of hollow sphere composites and other new visible light-active photocatalysts. Notably, ion exchange provides a useful strategy for the fabrication of excellent interfacial contact between two semiconductors. In addition, the ion exchange strategy is straightforward to operate by simply adjusting the experimental conditions. As a result, ion exchange has speedily emerged as an effective approach for postsynthetic alteration of nanocrystals.

5.4 Self-assembly method

The electrostatic self-assembly approach is a general and facile strategy for preparation of heterostructures. In this approach, the electrostatic force between two components is mainly responsible for the formation of heterostructures with robust interfacial contact. Li et al. successfully described CdS-$Ti_3C_2T_x$ MXene composites as a fascinating example of 1D/2D photocatalysts [40]. More specifically, the addition of the negatively charged Ti_3C_2Tx MXene to positively charged CdS nanowires under vigorous stirring resulted in the electrostatic attraction between negatively charged Ti_3C_2Tx MXene nanosheet and positively charged CdS nanowire to give a CdS-$Ti_3C_2T_x$ MXene composite. The self-assembly approach is very useful for narrow size distribution and better control of morphology under mild operation conditions.

5.5 Wet impregnation method

This is one of the facile and commonly used methods that operate at easy condition for the fabrication of nanocomposites of more than one presynthesized component. One component is sonochemically dispersed into another semiconductor and further stirred to disperse materials uniformly for 24–48 h by evaporating the solvent. Sometimes solvent is evaporated at 80°C with constant stirring. Ethanol, methanol, and water or a mixture of solvents are used in the wet impregnation method. After that the powder was dried, and this was subsequently calcined to get more intimate contact between two components. Good intimate interface contact results in efficient separation and transfer of the charge carrier, leading to better photocatalytic activity. For instance, Malathi et al. [41] prepared a robust visible light-responsive $BiFeWO_6$/BiOI photocatalyst by the wet impregnation method. Typically, different weight percentages of $BiFeWO_6$ were added into BiOI dispersed in methanol solution with the aid of sonication for 30 min and then stirred at 80°C to evaporate the solvent. The dried powder was further annealed in an oven to obtain strong intimate contact at interface. The resultant nanocomposites showed higher photocatalytic activity due to narrow bandgap and efficient separation of charge carriers.

https://www.twirpx.org & http://chemistry-chemists.com

5.6 Mechanical agitation method

Typically, the mechanical agitation method underwent the attachment of more than one presynthesized semiconductor component through physical methods, including grinding and high energy ball-milling. Nevertheless, the components attached by employing these strategies have no strong intimate interface, and the components are detached during the photocatalytic reaction, which causes comparatively little charge carrier separation and transfer efficiency, resulting in only moderate photocatalytic activity. Devi et al. [42] fabricated composites of SnO_2 and Fe_2O_3 nanocomposites simply by mechanical grinding of calculated amounts of SnO_2 and Fe_2O_3 for 2 h using a volatile organic solvent to get a homogeneous mixture. However, the photocatalytic activity was stable for just three cycles. Zhou and coworkers prepared g-C_3N_4-TiO_2 composites using a high-energy ball-milling method [43]. It is noteworthy that TiO_2 loaded on the g-C_3N_4 sheet was highly dispersed on the surface of pulverized g-C_3N_4 particles, contributing to the enlarged specific surface area and improved MB degradation under UV and visible light irradiations. Among numerous synthesis strategies, the in-situ growth approaches were used, such as ion exchange, deposition-precipitation, hydrothermal, and solvothermal, which provide robust contact as well as closed interface at the junction of the two components, promoting efficient charge carrier transfer. Accordingly, chemical bonds are formed between these two semiconductors, acting as channels and aiding efficient charge transfer. Exclusively, the ion exchange process is in favor for the fabrication of excellent interface, as well as the protection of the original morphology. The wet impregnation method is facile and efficient to construct nanocomposites with uniform distribution of nanoparticles on the interface of nanoparticles. Self-assembly method is suitable for distribution of narrow size and superior morphology. The self-assembly approach can provide moderate binding contact between two components. Conversely, the physical mechanical agitation strategy leads to poor intimate contact at interface between semiconductors in visible light-active nanocomposites photocatalysts, which weakens the efficiency of the charge carrier transfer.

6 Visible light-driven photocatalytic applications of nanocomposites

The ideal photocatalyst possesses characteristic properties such as absorbing maximum solar light, high surface area, stable, low cost, easily available, nontoxic, easy to separate, high quantum efficiency, and maximum separation and fast transfer of photogenerated charge carriers [43]. The solar light was comprised of 4% UV light, 46% visible light, and rest of the NIR light [11]. Although single narrow bandgap semiconductors can harvest visible light, they suffer unsatisfactory photocatalytic activity

https://www.twirpx.org & http://chemistry-chemists.com

due to fast recombination of charge carriers and either not oxidative or reductive photocatalysts. Doping can modify marginal band edge potential but not enough to reach the desired potential [44]. In view of utilizing abundant amounts of solar light and efficient separation of charge carriers, coupling of narrow bandgap semiconductors with well-matched band edge potential to form a heterojunction is a promising approach which can enhance light absorption into the visible region and increase efficient separation of charge carriers. Nanocomposites are mainly classified as metal free nanocomposites, metal oxide-based nanocomposites, and metal chalcogenide-based photocatalysts. The visible light-active nanocomposites have been used for photocatalytic degradation of various pollutants including dye, emerging pollutants, and photocatalytic reduction of heavy metal ions.

6.1 Common organic pollutants in wastewater

6.1.1 Photocatalytic dye removal

Dye contaminants released into industrial wastewater often give rise much attention due to their color and toxicity problems. Their processing has caused significant pollution in many countries around the world. Only a limited volume of dyes (<1 ppm for certain dyes) are known to be significant class of wastewater pollutants since they can be clearly detected in water by human eyes [45]. Dyes may cause serious contamination as in excess of 10,000 commercially accessible dyes are unavoidably utilized in numerous industrial fields, such as textiles, dyestuffs, plastics, paper, rubber, tanneries, paints, cosmetics, and leathers [46]. In excess of 700,000 tons of dyes are generated every year around the world. It has been noted that the roughly 12% of the total world invention of dyes wasted during processing. Moreover, 20% of these waste dyes enter into water bodies and cause serious pollution [47]. Different sorts of dyes from various industries pose serious hazards to aquatic living organisms. Dyes also contribute to negative impacts on human beings, such as nausea, vomiting, diarrhea, abdominal discomfort, and irritation [48]. Hence, treatment of these dye pollutants from the effluents is of extreme importance. Kadam et al. [36] fabricated ZnO/Ag_2O by the deposition-precipitation method at room temperature for detoxification of methyl orange under visible light. The optimal ratio of ZnO to Ag_2O was found to be 4:2 to achieve highest photodegradation of MO. The rate constants of ZnO/Ag_2O (4:2) for the photodegradation of MO were 22 and 4 times higher than those of pure ZnO and Ag_2O, respectively (Fig. 7). The enhanced photocatalytic activity was mainly attributed to formation of heterostructures with strong intimate contact, leading to increased separation and transfer of charge carriers and absorption of more visible light. Moreover, genotoxicity of MO before and after photodegradation was tested by comet assay. The results indicated that toxicity of MO is reduced significantly after degradation. The various nanocomposites for photocatalytic degradation of organic dyes under visible or solar light are summarized in Table 1.

https://www.twirpx.org & http://chemistry-chemists.com

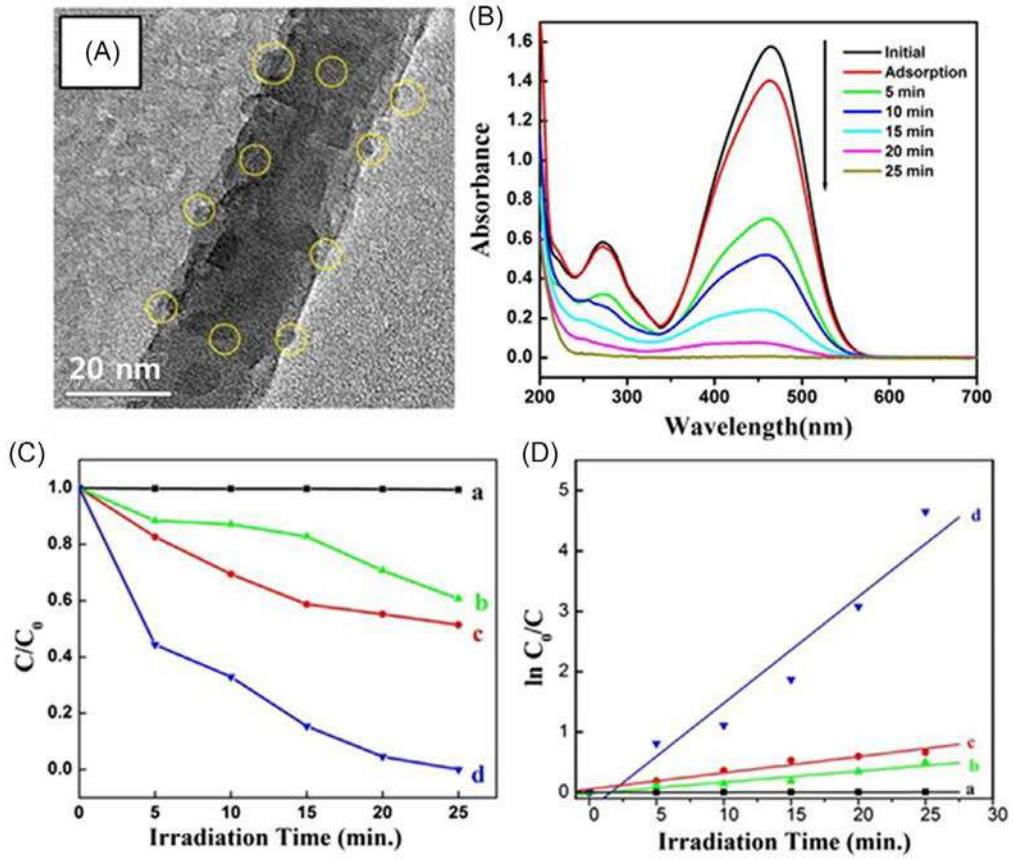

FIG. 7 TEM image of 4:2 ZnO/Ag_2O nanocomposite (A), UV-visible absorption spectra of degradation of MO under visible light (B), photocatalytic activity (C) and kinetics (D) of MO degradation under visible light irradiation (A) photolysis, (B) ZnO nanorods, (C) Ag_2O, and (D) 4:2 ZnO/Ag_2O nanocomposites. *Reproduced with permission fromKadam A., Dhabbe R., Gophane A., Sathe T., Garadkar K. Template free synthesis of ZnO/Ag_2O nanocomposites as a highly efficient visible active photocatalyst for detoxification of methyl orange. J Photochem Photobiol B Biol 2016;154:24–33. https://doi.org/10.1016/j.jphotobiol.2015.11.007.*

6.1.2 Emerging pollutants

Apart from dye industrial effluents, recently phenols, pharmaceuticals, personal care products, pesticides, and herbicides have been considered as emerging pollutants. Although emerging pollutants are generally spotted at low concentrations (ng/L–μg/L) in receiving water bodies and urban wastewater, they can cause chronic toxicity and/or subchronic toxicity with potential security effect on aquatic biota and human health through the food

https://www.twirpx.org & http://chemistry-chemists.com

Table 1 The representative nanocomposites for photocatalytic dye degradation under visible or solar light [36, 49–57].

Nanocomposite	Synthesis	Dye degradation (mg/L)	Catalyst amount	Light source	Time	% degradation	Ref
Fe_2O_3/g-C_3N_4	Hydrothermal	RhB (10 mg/L)	1 g/L	300 W Xe arc lamp ($\lambda \geq$420 nm	4 h	96.7%	[50]
ZnO/Ag_2O	Precipitation deposition	MO (20 mg/L)	1.5 g/L	9 W white lamp 520 nm	1.5 h	96%	[37]
β-$AgVO_3$/TiO_2	Hydrothermal	RhB (10 mg/L)	0.25 g/L	85 W Oreva CFL bulb λ = 450–650 nm)	2 h	93%	[51]
Bi_2WO_6/MoO_3	Wet impregnation and calcination	Acid blue 92 (10 mg/L)	0.1 g/L	Xenon lamp (300 W, with a cutoff filter $\lambda < 420$ nm	15 min	99%	[52]
Metal-free h-BN/ g-C_3N_4	Calcination strategy	RhB 20 mg/L	0.5 g/L	Xenon lamp (300 W, with a cutoff filter $\lambda < 420$ nm)	40 min	99.5%	[53]
Ag_3PO_4/RGO/Ag	Photoreduction	RhB 20 mg/L	1 g/L	250 W tungsten halogen ($\lambda \geq$400 nm)	30 min	99.5%	[54]
Ag_3PO_4/ $MnFe_2O_4$	Hydrothermal	MB (15 mg/L)	0.50 g/L	Natural sunlight	82 min	98%	[55]
SnO_2-SnS_2	Hydrothermal	MO (10 mg/L)	1 g/L	300 W Xenon lamp, >420 nm	60 min	99%	[56]
Mn_3O_4-MnO_2	Hydrothermal	MB (10 mg/L)	0.5 g/L	300 W Xe lamp (400 nm)	60 min	93.5%	[57]
Ag@CuxO/ZnO	Biogenic	MO (20 mg/L)	1.5 g/dm^3	Sunlight	60 min	79%	[58]

chain. It has been noted that wastewater treatment plants cannot eliminate emerging contaminants completely, resulting in their discharge to water bodies. Even trace amounts of these pollutants drained in water bodies can harmfully affect aquatic organisms. Regrettably, chemical and biological methods applied in contemporary sewage management plants are ineffective to remove these emerging pollutants when discharged in trace amounts. Recently, photocatalytic degradation under visible light irradiation has been considered as a favorable approach for the environmentally friendly degradation of emerging pollutants, offering high efficiency, ease of operation, and cost-effectiveness. For instance, Hong et al. [58] synthesized an in-situ direct Z-scheme V_2O_5/g-C_3N_4 system for the degradation of tetracycline (TC) emerging pollutant under visible light. The results show that V_2O_5 nanoparticles uniformly dispersed onto g-C_3N_4 nanosheet with good intimate contact between V_2O_5 and gC_3N_4. Enhanced photocatalytic activity was observed for the composite photocatalyst, which exhibited 75.5% photodegradation of TC, whereas pure g-C_3N_4 (30.3%) and bare V_2O_5 (19.0%) exhibited low photocatalytic performance. The enhanced photocatalytic activity was ascribed to an efficient separation of charge carriers through Z-scheme,

https://www.twirpx.org & http://chemistry-chemists.com

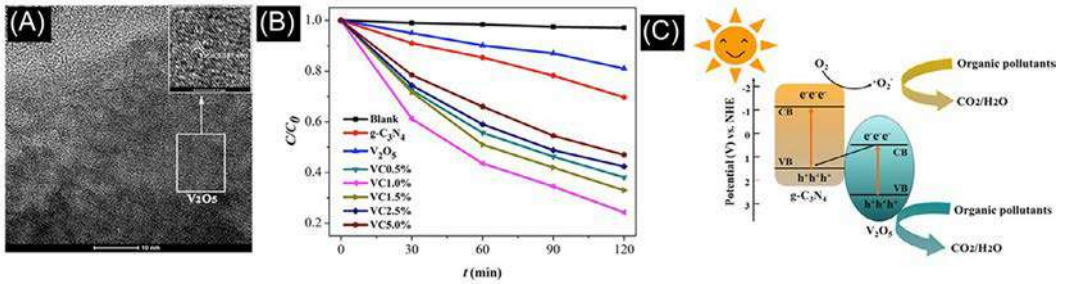

FIG. 8 TEM image of VC1.0% sample (A). The photocatalytic activities of as-prepared samples for the degradation of TC under visible light irradiation (B). The possible photocatalytic mechanism of V_2O_5/g-C_3N_4 heterojunction photocatalysts for degradation of organic pollutants under visible light irradiation (C). *Reproduced with permission from Hong Y., Jiang Y., Li C., Fan W., Yan X., Yan M., et al. In-situ synthesis of direct solid-state Z-scheme V_2O_5/g-C_3N_4 heterojunctions with enhanced visible light efficiency in photocatalytic degradation of pollutants. Appl Catal Environ 2016;180:663–673. https://doi.org/10.1016/j.apcatb.2015.06.057.*

Table 2 The representative nanocomposites for photocatalytic degradation of emerging pollutants under visible or solar light.

Nanocomposites	Synthesis	Emerging pollutant degradation	Catalyst amount	Light source	Time	% degradation	Ref
Bi_2WO_6-N doped g-C_3N_4	Hydrothermal	Phenol (10 mg/L)	1 g/L	300 W xenon lamp	5 h	93.1	[59]
$ZnFe_2O_4/TiO_2$	Refluxed	Bisphenol A (10 mgL^{-1})	1 g/L	8 W (BLB lamp (465 ± 40 nm)	30 min	94%	[60]
MoS_2/ Cd0.9Zn0.1S	Hydrothermal	Diclofenac (20 uM)	0.5 g/L	350 W xenon lamp (420 nm)	30 min	90%	[61]
V_2O_5/g-C_3N_4	In-situ calcination	Tetracycline (TC) (10 mg/L)	0.5 g/L	250 W xenon lamp (420 nm)	120 min		
CuS/$BiFeO_3$	Hydrothermal	Alachlor (5 mg/L)	0.25 g/L	150 W xenon lamp ($\lambda > 400$ nm)	60 min	95%	[62]

maximum absorption of visible light, and increased surface area (Fig. 8). The representative nanocomposites for photocatalytic degradation of emerging pollutants under visible (or solar) light are summarized in Table 2 [58–61, 63].

6.1.3 Photocatalytic degradation of inorganic pollutants

Among heavy metal ions, Cr(VI) is a common pollutant in the effluents produced from pigments, chromate, and electroplating industries [62]. It causes excessive harm to the

https://www.twirpx.org & http://chemistry-chemists.com

Table 3 The representative nanocomposites for photocatalytic reduction of Cr(VI) to Cr(III) under visible or solar light [65–69].

Nanocomposites	Synthesis	Emerging pollutant degradation	Catalyst amount	Light source	Time	% degradation	Ref
Bi_2MoO_6/ZnO	Solvothermal	Reduction of Cr(VI) (50 mg/L)	2 g/L	Xenon lamp (300 W, $\lambda > 400$ nm)	150 min	99.9%	[67]
SnS_2/SnO_2	Hydrothermal	Reduction of Cr(VI) (50 mg/L)	2 g/L	Xenon lamp (300 W, $\lambda > 420$ nm)	40 min	99% Cr(VI) u	[68]
Bi_2O_3/BiOI	Precipitation method	Reduction of Cr(VI) (20 mg/L)	0.1 g/L	Xenon lamp (300 W, $\lambda > 420$ nm)	100 min	94.5%	[69]
CoFe-LDH/g-C_3N_4	Coprecipitation and calcination	Reduction of Cr(VI) (50 mg/L)	1 g/L	Xenon lamp (300 W, $\lambda > 420$ nm)	120 min	99%	[70]
CuS-RGO aerogel	Chemical reduction	Cr(VI) (20 mgL^{-1})	1.5 g/L	Xenon lamp (500 W, $\lambda > 420$ nm)	80 min	98.9%	[71]

environment, aquatic biota, and human health because of its high toxicity and fast mobility in water. Due to toxicity of chromium, it causes pulmonary, cancer, and even liver damage because of its multiple toxicity. Semiconductor mediator photocatalytic reduction is a favorable strategy to treat aqueous Cr(VI) under visible light due to its outstanding properties such as low cost, direct use of abundant solar energy, and no toxic undesirable product [64]. The reduction of Cr(VI) turns into Cr(III), which is far less toxic than Cr(VI). In addition, Cr(III) can be easily precipitated in neutral and alkaline conditions and removed as solid waste. Moreover, Cr(III) plays an essential role in humans and plant metabolism. The design and fabrication of heterojunctions have been considered as efficient strategies to deal with toxic Cr(VI). The use of representative nanocomposites for photocatalytic reduction of Cr(VI) under visible or solar light are summarized in Table 3. For example, Zhang et al. [65] synthesized core-shell Bi_2MoO_6/ZnO hierarchical heterostructures via the solvothermal method for enhanced visible light photoreduction of Cr(VI) to Cr(III) up to 100%. The enhanced photocatalytic performance was mainly due to the heterojunction formation between Bi_2MoO_6 and ZnO, which increased the visible light absorption, surface area, and separation and transfer of electrons and holes, as shown in Fig. 9.

https://www.twirpx.org & http://chemistry-chemists.com

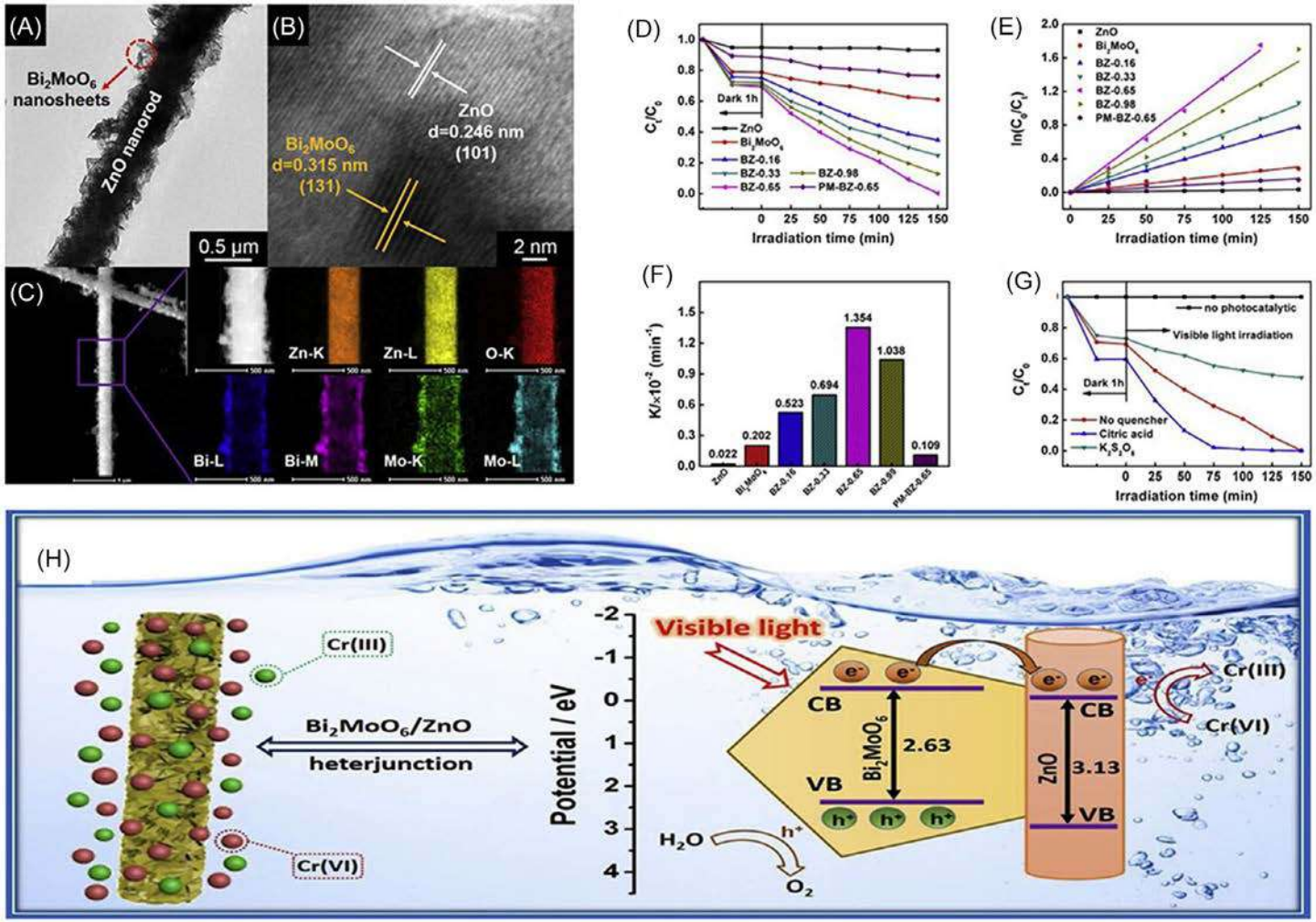

FIG. 9 Typical TEM image of the BZ-0.65 sample (A), HRTEM image taken at the interface between Bi_2MoO_6 and ZnO (B), and HAADF-STEM/EDX mapping images of the BZ-0.65 sample (C). Photocatalytic reduction of Cr(VI) over different catalysts under visible-light irradiation (D). Corresponding pseudo-first-order kinetics fitting curves and apparent rate constants over different catalysts (E, F). Photocatalytic reduction of Cr(VI) by BZ-0.65 sample in the presence of an electron scavenger ($K_2S_2O_8$) and hole scavenger (citric acid). The dosages of $K_2S_2O_8$ and citric acid were 100μL of 50mg/mL aqueous solutions of $K_2S_2O_8$ and citric acid, respectively (G). Schematic illustration of the proposed mechanism of reduction of Cr(VI) over the 3D Bi_2MoO_6/ZnO composite under visible-light irradiation (D). *Reproduced with permission from Guping Z., Dongyun C., Najun L., Qingfeng X., Hua L., Jinghui H., et al. Fabrication of Bi_2MoO_6/ZnO hierarchical heterostructures with enhanced visible-light photocatalytic activity. Appl Catal Environ 2019;313–324.* https://doi:10.1016/j.apcatb.2019.03.055.

https://www.twirpx.org & http://chemistry-chemists.com

7 Photocatalytic mechanism

7.1 Determination of valence band and conduction band position

The matching of the conduction and valence bands is a crucial criterion for making high-performance nanocomposites for photocatalytic applications. First, the band edge position of the valence band (VB) and conduction band (CB) determination is a critical step of the photocatalytic mechanism. For example, for semiconductors, the VB and CB can be calculated according to the empirical equations of (1) and (2) [70]:

where E_e is the energy of free electrons on the hydrogen scale ($E_e = 4.5$ eV), X is the value of electronegativity of the semiconductor, and E_g is the bandgap energy. In addition, VB potential can also be calculated from the XPS valence band spectra and the value of the CB can be calculated by Mott-Schottky plots.

7.2 Determination of charge carrier separation and transfer

7.2.1 Photoluminescence (PL) spectra, PL study, and lifetime

Photoluminescence (PL) is used to investigate the separation of photogenerated charge carriers because the PL signal generally resulted from recombination of photogenerated electron-hole pairs. Thus, high PL intensity indicates more recombination of charge carriers, whereas lower PL intensity suggests the maximum separation of charge carriers, which is very useful for efficient photocatalytic performance [36]. In the case of an optimal heterojunction, the PL intensity is quenched due to maximum separation of charge carriers. The lifetime is also used to evaluate the rate of recombination of charge carriers. The longer lifetime plays a vital role in terms of efficient photocatalytic activity.

7.2.2 Transient photocurrent

The transient photocurrent is also used for the determination of photogenerated charge carriers separation. More specifically, transient photocurrents of the photocatalyst deposited on the conducting substrate is generally executed for a certain time with an on-and-off cycle under the illumination of visible light. It is generally accepted that a stronger photocurrent intensity is associated with higher efficiency of electron-hole pairs. Generally, optimized nanocomposites show the highest photocurrent intensity than that of the pure counterpart, demonstrating superior photocatalytic performance [66].

7.2.3 Electrochemical impedance spectroscopy (EIS)

Electrochemical impedance spectroscopy (EIS) is used for the determination of charge carrier separation and transfer across the junction of nanocomposites. Generally, a smaller arc radius of the EIS plot indicates more separation of photogenerated electron-hole pairs and rapid interfacial charge transfer [58]. The arc radius is smaller for the heterojunction than that of its pure counterpart, which is beneficial for superior photocatalysis.

https://www.twirpx.org & http://chemistry-chemists.com

7.3 Determination of reactive species in Photocatalysis

7.3.1 Scavenger study

The photocatalytic reaction is strongly influenced by various free radicals which are generated during the course of the photocatalytic reactions, such as holes (h^+), superoxide radicals ($^{\bullet}O_2^-$), and hydroxyl radicals ($^{\bullet}OH$). Such holes, superoxide radicals, and hydroxyl radicals can be determined using scavengers of triethanolamine (TEA), 1,4-benzoquinone (BQ), and isopropanol (IPA), respectively [44]. For example, if photocatalytic activity is significantly reduced by the addition of an IPA scavenger, this indicates that $^{\bullet}OH$ is the main reactive species responsible for photodegradation of the corresponding pollutant.

7.3.2 Electron spin resonance study (ESR)

Free radicals can also be determined by using ESR techniques. Typically, DMPO (5,5-dimethyl-1-dimethyl *N*-oxide) is generally used as a radical scavenger due to the generation of stable free radicals, e.g., DMPO-$^{\bullet}O_2^-$ or DMPO-$^{\cdot}OH^-$. Under visible light irradiation, significant evolution of ESR signals in H_2O and DMSO can be observed, suggesting the generation of hydroxyl radicals ($^{\bullet}OH$) and superoxide radicals ($^{\bullet}O_2^-$) [71].

8 Conclusion, current challenges, and future prospects

Visible light-driven nanocomposites can be considered as a promising candidate for the photocatalytic treatment of organic dyes, emerging pollutants, and heavy metal ions. In view of utilizing renewable solar light, coupling of narrow bandgap semiconductor with well-matched band edge potential to form heterojunctions is a promising approach which can enhance light absorption into the visible region and increase efficient separation of charge carriers. The nanocomposite Z-scheme structure shows efficient photocatalytic performance compared to other structures, because of effective separation of charge carriers and increased redox potential. The nanocomposite heterostructure depends on various morphologies classified as 1D-1D, 0D-1D, 0D-2D, 1D-2D, and 2D-2D. Among them, 2D-2D nanocomposites show superior photocatalytic performance because of their large interfacial contact, contributing a stronger electronic and physical coupling effect, which is beneficial for an efficient separation and transfer of the charge carrier with a prolonged lifetime. Among numerous synthesis strategies, the in-situ growth approaches, such as the ion exchange, deposition-precipitation, hydrothermal, and solvothermal methods, are providing robust contact, closed interface at the junction of the two components, and promoting efficient charge carrier transfer. Accordingly, chemical bonds formed between these two semiconductors act as channels that can aid efficient charge transfer. This chapter provides an understanding of the photocatalytic mechanism.

However, there are still challenges in the photocatalysis for the industrial applications. The main challenges are the recovery and separation of the photocatalyst, in order to reduce the electricity cost, and the design of optimal reactors for the full utilization of solar energy. It is vital to increase the stability of photocatalysts by preventing aggregation during

https://www.twirpx.org & http://chemistry-chemists.com

the photodegradation process. It should be noted that the biggest issues with practical applications of photocatalysis are cost-effective and time-effective scaling up to an industrial process. Although sound development in heterojunction photocatalysis for wastewater treatment under visible light irradiation has been accomplished, works in this field are still incomplete and further improvements are urgently required. Design of controlled active sites of the nanocomposites for selective photocatalytic degradation is highly challenging and yet demanding. The exploration of plenty of theoretical and modeling work is also useful and imperative to gain a deeper insight into the mechanism and charge-migration kinetics in heterojunction photocatalysts. A flawless material for engineering nanocomposite photocatalysts should satisfy numerous necessities, including high solar-conversion efficiency, visible light activity, proper bandgap structure for redox reactions, high photostability, cost-effectiveness, nontoxicity, and scalability for commercialization. We anticipate that this chapter will provide guidelines for the next decade of research in the fields of visible light-active nanocomposites for environmental remediation and clean energy generation.

Acknowledgments

This research work was also supported by the Korea Institute of Energy Technology Evaluation and Planning (KETEP) and the Ministry of Trade, Industry and Energy (MOTIE) of the Republic of Korea (20194030202440). This research was also supported by the Basic Science Research Capacity Enhancement Project through Korea Basic Science Institute (National Research Facilities and Equipment Center) grant funded by the Ministry of Education [2019R1A6C1010016].

References

[1] Kadam AN, Bhopate DP, Kondalkar VV, Majhi SM, Bathula CD, Tran AV, et al. Facile synthesis of Ag-ZnO core–shell nanostructures with enhanced photocatalytic activity. J Ind Eng Chem 2018;61:78–86. https://doi.org/10.1016/j.jiec.2017.12.003.

[2] Kadam A, Dhabbe R, Shin DS, Garadkar K, Park J. Sunlight driven high photocatalytic activity of Sn doped N-TiO2 nanoparticles synthesized by a microwave assisted method. Ceram Int 2017;43:5164–72. https://doi.org/10.1016/j.ceramint.2017.01.039.

[3] Kite SV, Sathe DJ, Kadam AN, Chavan SS, Garadkar KM. Highly efficient photodegradation of 4-nitrophenol over the nano-TiO_2 obtained from chemical bath deposition technique. Res Chem Intermed 2020;46:1255–82. https://doi.org/10.1007/s11164-019-04032-7.

[4] Patil CS, Gunjal DB, Naik VM, Harale NS, Jagadale SD, Kadam AN, et al. Waste tea residue as a low cost adsorbent for removal of hydralazine hydrochloride pharmaceutical pollutant from aqueous media: an environmental remediation. J Clean Prod 2019;206:407–18. https://doi.org/10.1016/j.jclepro.2018.09.140.

[5] Kadam AN, Moniruzzaman M, Lee SW. Dual functional S-doped g-C_3N_4 pinhole porous nanosheets for selective fluorescence sensing of Ag+ and visible-light photocatalysis of dyes. Molecules 2019;24. https://doi.org/10.3390/molecules24030450.

[6] Patil CS, Kadam AN, Gunjal DB, Naik VM, Lee SW, Kolekar GB, et al. Sugarcane molasses derived carbon sheet@sea sand composite for direct removal of methylene blue from textile wastewater: industrial wastewater remediation through sustainable, greener, and scalable methodology. Sep Purif Technol 2020;247. https://doi.org/10.1016/j.seppur.2020.116997.

https://www.twirpx.org & http://chemistry-chemists.com

[7] Tran VA, Kadam AN, Lee SW. Adsorption-assisted photocatalytic degradation of methyl orange dye by zeolite-imidazole-framework-derived nanoparticles. J Alloys Compd 2020;835. https://doi.org/10.1016/j.jallcom.2020.155414.

[8] Jung WS, Park SH, Kadam AN, Kim H, Lee SW. Direct hydrothermal synthesis of amine-functionalized cubic hematite (C-Fe_2O_3) and sonochemical deposition of nanosized Au for its application as a visible-light photocatalyst. Dalton Trans 2020;49:2924–32. https://doi.org/10.1039/c9dt04611a.

[9] Kadam AN, Dhabbe RS, Kokate MR, Gaikwad YB, Garadkar KM. Preparation of N doped TiO_2 via microwave-assisted method and its photocatalytic activity for degradation of Malathion. Spectrochim Acta A Mol Biomol Spectrosc 2014;133:669–76. https://doi.org/10.1016/j.saa.2014.06.020.

[10] Suwarnkar MB, Dhabbe RS, Kadam AN, Garadkar KM. Enhanced photocatalytic activity of Ag doped TiO_2 nanoparticles synthesized by a microwave assisted method. Ceram Int 2014;40:5489–96. https://doi.org/10.1016/j.ceramint.2013.10.137.

[11] Babu B, Kadam AN, Ravikumar RVSSN, Byon C. Enhanced visible light photocatalytic activity of Cu-doped SnO_2 quantum dots by solution combustion synthesis. J Alloys Compd 2017;703:330–6. https://doi.org/10.1016/j.jallcom.2017.01.311.

[12] Dhabbe RS, Kadam AN, Suwarnkar MB, Kokate MR, Garadkar KM. Enhancement in the photocatalytic activity of Ag loaded N-doped TiO_2 nanocomposite under sunlight. J Mater Sci Mater Electron 2014;25:3179–89. https://doi.org/10.1007/s10854-014-2001-4.

[13] Di T, Cheng B, Ho W, Yu J, Tang H. Hierarchically CdS–Ag_2S nanocomposites for efficient photocatalytic H_2 production. Appl Surf Sci 2019;470:196–204. https://doi.org/10.1016/j.apsusc.2018.11.010.

[14] Zhou L, Kamyab H, Surendar A, Maseleno A, Ibatova AZ, Chelliapan S, et al. Novel Z-scheme composite Ag_2CrO_4/NG/polyimide as high performance nano catalyst for photoreduction of CO_2: design, fabrication, characterization and mechanism. J Photochem Photobiol A Chem 2019;368:30–40. https://doi.org/10.1016/j.jphotochem.2018.09.006.

[15] Babu B, Kadam AN, Rao GT, Lee SW, Byon C, Shim J. Enhancement of visible-light-driven photoresponse of Mn-doped SnO_2 quantum dots obtained by rapid and energy efficient synthesis. JOL 2018;195:283–9. https://doi.org/10.1016/j.jlumin.2017.11.040.

[16] Kadam AN, Salunkhe TT, Kim H, Lee SW. Biogenic synthesis of mesoporous N–S–C tri-doped TiO_2 photocatalyst via ultrasonic-assisted derivatization of biotemplate from expired egg white protein. Appl Surf Sci 2020;518. https://doi.org/10.1016/j.apsusc.2020.146194.

[17] Ganeshbabu M, Kannan N, Venkatesh PS, Paulraj G, Jeganathan K, MubarakAli D. Synthesis and characterization of $BiVO_4$ nanoparticles for environmental applications. RSC Adv 2020;10:18315–22. https://doi.org/10.1039/d0ra01065k.

[18] Sheikholeslami Z, Kebria DY, Qaderi F. Application of γ-Fe_2O_3 nanoparticles for pollution removal from water with visible light. J Mol Liq 2020;299. https://doi.org/10.1016/j.molliq.2019.112118.

[19] Kadam AN, Dhabbe RS, Kokate MR, Garadkar KM. Room temperature synthesis of CdS nanoflakes for photocatalytic properties. J Mater Sci Mater Electron 2014;25:1887–92. https://doi.org/10.1007/s10854-014-1816-3.

[20] Katal R, Masudy-panah S, Kong EYJ, Dasineh Khiavi N, Abadi Farahani MHD, Gong X. Nanocrystal-engineered thin CuO film photocatalyst for visible-light-driven photocatalytic degradation of organic pollutant in aqueous solution. Catal Today 2020;340:236–44. https://doi.org/10.1016/j.cattod.2018.12.019.

[21] Su W, Liu X, Tan L, Cui Z, Liang Y, Li Z, et al. Rapid sterilization by photocatalytic Ag_3PO_4/α-Fe_2O_3 composites using visible light. ACS Sustain Chem Eng 2020;8:2577–85. https://doi.org/10.1021/acssuschemeng.9b07615.

[22] Nipane SV, Lee SW, Gokavi GS, Kadam AN. In situ one pot synthesis of nanoscale TiO_2-anchored reduced graphene oxide (RGO) for improved photodegradation of 5-fluorouracil drug. J Mater Sci Mater Electron 2018;29:16553–64. https://doi.org/10.1007/s10854-018-9749-x.

https://www.twirpx.org & http://chemistry-chemists.com

[23] Abhijit K, Rohant D, Kalyanrao G. Microwave assisted synthesis and enhanced photocatalytic activity of solar-light-active N-doped TiO_2–ZnO nanoparticles. J Nanosci Nanotechnol 2015;176–85. https://doi.org/10.1166/jnan.2015.1231.

[24] Babar SB, Gavade NL, Bhopate DP, Kadam AN, Kokane SB, Sartale SD, et al. An efficient fabrication of ZnO–carbon nanocomposites with enhanced photocatalytic activity and superior photostability. J Mater Sci Mater Electron 2019;30:1133–47. https://doi.org/10.1007/s10854-018-0382-5.

[25] Babu B, Shim J, Kadam AN, Yoo K. Modification of porous g-C_3N_4 nanosheets for enhanced photocatalytic activity: in-situ synthesis and optimization of NH_4Cl quantity. Catal Commun 2019;124:123–7. https://doi.org/10.1016/j.catcom.2019.01.009.

[26] Gavade NL, Kadam AN, Babar SB, Gophane AD, Garadkar KM, Lee SW. Biogenic synthesis of gold-anchored ZnO nanorods as photocatalyst for sunlight-induced degradation of dye effluent and its toxicity assessment. Ceram Int 2020;46:11317–27. https://doi.org/10.1016/j.ceramint.2020.01.161.

[27] Sahu K, Bisht A, Kuriakose S, Mohapatra S. Two-dimensional CuO-ZnO nanohybrids with enhanced photocatalytic performance for removal of pollutants. J Phys Chem Solid 2020;137. https://doi.org/10.1016/j.jpcs.2019.109223.

[28] Zhang M, Yao J, Arif M, Qiu B, Yin H, Liu X, et al. 0D/2D CeO_2/$ZnIn_2S_4$ Z-scheme heterojunction for visible-light-driven photocatalytic H_2 evolution. Appl Surf Sci 2020;526. https://doi.org/10.1016/j.apsusc.2020.145749.

[29] Zhang R, Bi L, Wang D, Lin Y, Zou X, Xie T, et al. Investigation on various photo-generated carrier transfer processes of SnS_2/g-C_3N_4 heterojunction photocatalysts for hydrogen evolution. J Colloid Interface Sci 2020;578:431–40. https://doi.org/10.1016/j.jcis.2020.04.033.

[30] Zhou J, Zhang Z, Kong X, He F, Zhao R, Wu R, et al. A novel P-N heterojunction with staggered energy level based on $ZnFe_2O_4$ decorating SnS_2 nanosheet for efficient photocatalytic degradation. Appl Surf Sci 2020;510:145442–52.

[31] Zhao W, Liu C. Mesoporous cu-Cu_2O@TiO_2 heterojunction photocatalysts derived from metal-organic frameworks. RSC Adv 2020;10:14550–5. https://doi.org/10.1039/d0ra01327g.

[32] Mohamed RM, Kadi MW, Ismail AA. A facile synthesis of mesoporous α-Fe_2O_3/TiO_2 nanocomposites for hydrogen evolution under visible light. Ceram Int 2020;46:15604–12. https://doi.org/10.1016/j.ceramint.2020.03.107.

[33] Ouerghi A, Khalil L, Zheng B, Avila J, Pierucci D, Brule T, et al. Strong interlayer hybridization in the aligned SnS_2/WSe_2 hetero-bilayer structure. NPJ 2D Mater Appl 2019;3. https://doi.org/10.1038/s41699-019-0109-3.

[34] Tian N, Huang H, He Y, Guo Y, Zhang T, Zhang Y. Mediator-free direct Z-scheme photocatalytic system: $BiVO_4$/g-C_3N_4 organic-inorganic hybrid photocatalyst with highly efficient visible-light-induced photocatalytic activity. Dalton Trans 2015;44:4297–307. https://doi.org/10.1039/c4dt03905j.

[35] Wang K, Li Y, Li J, Zhang G. Boosting interfacial charge separation of $Ba_5Nb_4O_{15}$/g-C_3N_4 photocatalysts by 2D/2D nanojunction towards efficient visible-light driven H_2 generation. Appl Catal Environ 2020;263. https://doi.org/10.1016/j.apcatb.2019.05.032.

[36] Kadam A, Dhabbe R, Gophane A, Sathe T, Garadkar K. Template free synthesis of ZnO/Ag_2O nanocomposites as a highly efficient visible active photocatalyst for detoxification of methyl orange. J Photochem Photobiol B Biol 2016;154:24–33. https://doi.org/10.1016/j.jphotobiol.2015.11.007.

[37] Yang J, Hao J, Xu S, Wang Q, Dai J, Zhang A, et al. $InVO_4$/β-$AgVO_3$ nanocomposite as a direct Z-scheme photocatalyst toward efficient and selective visible-light-driven CO_2 reduction. ACS Appl Mater Interfaces 2019;11:32025–37. https://doi.org/10.1021/acsami.9b10758.

[38] Zhang Y, Xu J, Mei J, Sarina S, Wu Z, Liao T, et al. Strongly interfacial-coupled 2D-2D TiO_2/g-C_3N_4 heterostructure for enhanced visible-light induced synthesis and conversion. J Hazard Mater 2020;394. https://doi.org/10.1016/j.jhazmat.2020.122529.

[39] Yu J, Zhang J, Liu S. Ion-exchange synthesis and enhanced visible-light photoactivity of CuS/ZnS nanocomposite hollow spheres. J Phys Chem C 2010;114:13642–9. https://doi.org/10.1021/jp101816c.

https://www.twirpx.org & http://chemistry-chemists.com

[40] Li JY, Li YH, Zhang F, Tang ZR, Xu YJ. Visible-light-driven integrated organic synthesis and hydrogen evolution over 1D/2D CdS-Ti_3C_2Tx MXene composites. Appl Catal Environ 2020;269. https://doi.org/10.1016/j.apcatb.2020.118783.

[41] Malathi A, Arunachalam P, Grace AN, Madhavan J, Al-Mayouf AM. A robust visible-light driven $BiFeWO_6$/BiOI nanohybrid with efficient photocatalytic and photoelectrochemical performance. Appl Surf Sci 2017;412:85–95. https://doi.org/10.1016/j.apsusc.2017.03.199.

[42] Devi LG, Shyamala R. Photocatalytic activity of SnO_{2-a}-Fe_2O_3 composite mixtures: exploration of number of active sites, turnover number and turnover frequency. Mater Chem Front 2018;2:796–806. https://doi.org/10.1039/c7qm00536a.

[43] Zhou J, Zhang M, Zhu Y. Photocatalytic enhancement of hybrid C_3N_4/TiO_2 prepared via ball milling method. Phys Chem Chem Phys 2015;17:3647–52. https://doi.org/10.1039/c4cp05173d.

[44] Kadam AN, Kim TG, Shin DS, Garadkar KM, Park J. Morphological evolution of Cu doped ZnO for enhancement of photocatalytic activity. J Alloys Compd 2017;710:102–13. https://doi.org/10.1016/j.jallcom.2017.03.150.

[45] Gawade VV, Gavade NL, Shinde HM, Babar SB, Kadam AN, Garadkar KM. Green synthesis of ZnO nanoparticles by using *Calotropis procera* leaves for the photodegradation of methyl orange. J Mater Sci Mater Electron 2017;28:14033–9. https://doi.org/10.1007/s10854-017-7254-2.

[46] Gavade NL, Kadam AN, Gaikwad YB, Dhanavade MJ, Garadkar KM. Decoration of biogenic AgNPs on template free ZnO nanorods for sunlight driven photocatalytic detoxification of dyes and inhibition of bacteria. J Mater Sci Mater Electron 2016;27:11080–91. https://doi.org/10.1007/s10854-016-5225-7.

[47] Suwarnkar MB, Kadam AN, Khade GV, Gavade NL, Garadkar KM. Modification of TiO_2 nanoparticles by HZSM-5 for the enhancement in photodegradation of Acid Green 25. J Mater Sci Mater Electron 2016;27:843–51. https://doi.org/10.1007/s10854-015-3825-2.

[48] Dhabbe R, Kadam A, Korake P, Kokate M, Waghmare P, Garadkar K. Synthesis and enhanced photocatalytic activity of Zr-doped N-TiO_2 nanostructures. J Mater Sci Mater Electron 2014;26:554–63. https://doi.org/10.1007/s10854-014-2434-9.

[49] Abroshan E, Farhadi S, Zabardasti A. Novel magnetically separable Ag_3PO_4/$MnFe_2O_4$ nanocomposite and its high photocatalytic degradation performance for organic dyes under solar-light irradiation. Sol Energy Mater Sol Cells 2018;178:154–63. https://doi.org/10.1016/j.solmat.2018.01.026.

[50] Cui C, Wang Y, Liang D, Cui W, Hu H, Lu B, et al. Photo-assisted synthesis of Ag_3PO_4/reduced graphene oxide/Ag heterostructure photocatalyst with enhanced photocatalytic activity and stability under visible light. Appl Catal Environ 2014;158–159:150–60. https://doi.org/10.1016/j.apcatb.2014.04.007.

[51] Gavade NL, Babar SB, Kadam AN, Gophane AD, Garadkar KM. Fabrication of M@CuxO/ZnO (M = Ag, Au) Heterostructured nanocomposite with enhanced photocatalytic performance under sunlight. Ind Eng Chem Res 2017;56:14489–501. https://doi.org/10.1021/acs.iecr.7b03168.

[52] Jiang L, Yuan X, Zeng G, Wu Z, Liang J, Chen X, et al. Metal-free efficient photocatalyst for stable visible-light photocatalytic degradation of refractory pollutant. Appl Catal Environ 2018;221:715–25. https://doi.org/10.1016/j.apcatb.2017.09.059.

[53] Jyotsna KA, Kansal SK, Umar A. β-$AgVO_3$ nanowires/TiO_2 nanoparticles heterojunction assembly with improved visible light driven photocatalytic decomposition of hazardous pollutants and mechanism insight. Sep Purif Technol 2020;251. https://doi.org/10.1016/j.seppur.2020.117271.

[54] Salari H. Facile template-free synthesis of 3D flower-like Bi2WO6/MoO3 nanocomposites with ultrathin sheets and their associated photocatalytic properties under visible light irradiation. J Photochem Photobiol A Chem 2019;385. https://doi.org/10.1016/j.jphotochem.2019.112069.

[55] Sunaina YKK, Ankush GSK, Sood K, Mehta SK, et al. Mechanistic insights of enhanced photocatalytic efficiency of SnO_2-SnS_2 heterostructures derived from partial sulphurization of SnO_2. Sep Purif Technol 2020;242. https://doi.org/10.1016/j.seppur.2020.116835.

https://www.twirpx.org & http://chemistry-chemists.com

[56] Xu Y, Huang S, Xie M, Li Y, Xu H, Huang L, et al. Magnetically separable Fe_2O_3/g-C_3N_4 catalyst with enhanced photocatalytic activity. RSC Adv 2015;5:95727–35. https://doi.org/10.1039/c5ra18009k.

[57] Zhao J, Nan J, Zhao Z, Li N, Liu J, Cui F. Energy-efficient fabrication of a novel multivalence Mn_3O_4-MnO_2 heterojunction for dye degradation under visible light irradiation. Appl Catal Environ 2017;202:509–17. https://doi.org/10.1016/j.apcatb.2016.09.065.

[58] Hong Y, Jiang Y, Li C, Fan W, Yan X, Yan M, et al. In-situ synthesis of direct solid-state Z-scheme V_2O_5/g-C_3N_4 heterojunctions with enhanced visible light efficiency in photocatalytic degradation of pollutants. Appl Catal Environ 2016;180:663–73. https://doi.org/10.1016/j.apcatb.2015.06.057.

[59] Cai M, Li R, Xie Z, Huang J, Zeng Y, Zhang Q, et al. Synthesis of a core-shell heterostructured MoS_2/$Cd_{0.9}Zn_{0.1}S$ photocatalyst for the degradation of diclofenac under visible light. Appl Catal Environ 2019;259. https://doi.org/10.1016/j.apcatb.2019.118033.

[60] Nguyen TB, Huang CP, Doong RA. Photocatalytic degradation of bisphenol A over a $ZnFe_2O_4$/TiO_2 nanocomposite under visible light. Sci Total Environ 2019;646:745–56. https://doi.org/10.1016/j.scitotenv.2018.07.352.

[61] Zhu D, Zhou Q. Novel Bi_2WO_6 modified by N-doped graphitic carbon nitride photocatalyst for efficient photocatalytic degradation of phenol under visible light. Appl Catal Environ 2020;268. https://doi.org/10.1016/j.apcatb.2019.118426.

[62] Li Y, Zhang J, Zhan C, Kong F, Li W, Yang C, et al. Facile synthesis of TiO_2/CNC nanocomposites for enhanced Cr(VI) photoreduction: synergistic roles of cellulose nanocrystals. Carbohydr Polym 2020;233. https://doi.org/10.1016/j.carbpol.2020.115838.

[63] Bhoi YP, Mishra BG. Photocatalytic degradation of alachlor using type-II CuS/$BiFeO_3$ heterojunctions as novel photocatalyst under visible light irradiation. Chem Eng J 2018;344:391–401. https://doi.org/10.1016/j.cej.2018.03.094.

[64] Geioushy RA, El-Sheikh SM, Azzam AB, Salah BA, El-Dars FM. One-pot fabrication of BiPO4/Bi2S3 hybrid structures for visible-light driven reduction of hazardous Cr(VI). J Hazard Mater 2020;381. https://doi.org/10.1016/j.jhazmat.2019.120955.

[65] Zhang YC, Yao L, Zhang G, Dionysiou DD, Li J, Du X. One-step hydrothermal synthesis of high-performance visible-light-driven SnS_2/SnO_2 nanoheterojunction photocatalyst for the reduction of aqueous Cr(VI). Appl Catal Environ 2014;144:730–8. https://doi.org/10.1016/j.apcatb.2013.08.006.

[66] Guping Z, Dongyun C, Najun L, Qingfeng X, Hua L, Jinghui H, et al. Fabrication of Bi_2MoO_6/ZnO hierarchical heterostructures with enhanced visible-light photocatalytic activity. Appl Catal Environ 2019;313–24. https://doi.org/10.1016/j.apcatb.2019.03.055.

[67] Bano Z, Saeed RMY, Zhu S, Xia MZ, Mao S, Lei W, et al. Mesoporous CuS nanospheres decorated rGO aerogel for high photocatalytic activity towards Cr(VI) and organic pollutants. Chemosphere 2020;246. https://doi.org/10.1016/j.chemosphere.2020.125846.

[68] Ou B, Wang J, Wu Y, Zhao S, Wang Z. Efficient removal of Cr (VI) by magnetic and recyclable calcined CoFe-LDH/g-C_3N_4 via the synergy of adsorption and photocatalysis under visible light. Chem Eng J 2020;380. https://doi.org/10.1016/j.cej.2019.122600.

[69] Wei Z, Zheng N, Dong X, Zhang X, Ma H, Zhang X, et al. Green and controllable synthesis of one-dimensional Bi_2O_3/BiOI heterojunction for highly efficient visible-light-driven photocatalytic reduction of Cr(VI). Chemosphere 2020;257. https://doi.org/10.1016/j.chemosphere.2020.127210.

[70] Babar S, Gavade N, Shinde H, Gore A, Mahajan P, Lee KH, et al. An innovative transformation of waste toner powder into magnetic g-C_3N_4-Fe_2O_3 photocatalyst: sustainable e-waste management. J Environ Chem Eng 2019;7. https://doi.org/10.1016/j.jece.2019.103041.

[71] Pirzada BM, Pushpendra KRK, Naidu BS. Synthesis of $LaFeO_3$/Ag_2CO_3 nanocomposites for photocatalytic degradation of rhodamine B and p-chlorophenol under natural sunlight. ACS Omega 2019;4:2618–29. https://doi.org/10.1021/acsomega.8b02829.

https://www.twirpx.org & http://chemistry-chemists.com

https://www.twirpx.org & http://chemistry-chemists.com

12

Defects in nanomaterials for visible light photocatalysis

Jagriti Gupta[a], P.A. Hassan[a,b], and K.C. Barick[a,b]

[a]CHEMISTRY DIVISION, BHABHA ATOMIC RESEARCH CENTRE, TROMBAY, MUMBAI, INDIA
[b]HOMI BHABHA NATIONAL INSTITUTE, ANUSHAKTINAGAR, MUMBAI, INDIA

1 Introduction

Photocatalysis is a promising approach to convert solar light into chemical energy and has been considered as one of the most effective solutions to improve and resolve environmental and energy issues [1–5]. Numerous highly efficient and attractive visible light photocatalyst nanomaterials have been extensively studied and explored. However, the photocatalytic performance of photocatalysts has some limitations and faces several challenges such as limited or/and the poor light-absorption, poor photo-stability, low photocatalytic efficiency, and a higher recombination rate which greatly diminishes the efficiency of photocatalysts [4, 6–8]. The performance of photocatalyst nanomaterials depends on light harvesting to produce photogenerated electron-hole pairs (charge carriers), their separation efficiency and transfer to surface, as well as interfacial redox reaction on the active site of photocatalysts' surfaces. Several modifications were applied to enhance the photocatalytic performance of photocatalyst nanomaterials, such as morphological and structural changes, crystal facet exposure, defects engineering, doping, heterojunctions, etc. [3, 4, 9–12]. Among them, "defect engineering" is an efficient and economical tactic to narrow the bandgap of semiconductor nanomaterials to boost light absorption in visible light, charge separation, and energy transfer efficiency, and create abundant active sites to stimulate the interfacial redox reactions and reduce the recombination rate of photogenerated charge carriers [3, 7, 13].

In past decades, semiconductors have been extensively used as efficient photocatalysts and gained considerable attention in various applications including electronic, energy storage, sensing, photocatalysis, and biomedical applications [14–17]. Various semiconductors, especially oxides, sulfides, and nitrides, have been investigated as potential photocatalysts for visible light photocatalytic applications [6, 7, 18–22]. Among them, metal oxides as photocatalysts have been the most broadly deliberated owing to their unique physicochemical properties, chemical stability, photostability, corrosion-resistant, economic, safe, and biocompatible behavior for photocatalytic applications [6, 18, 19]. Furthermore, various types of nanostructured photocatalysts have been

Nanostructured Materials for Visible Light Photocatalysis. https://doi.org/10.1016/B978-0-12-823018-3.00002-6
Copyright © 2022 Elsevier Inc. All rights reserved.

https://www.twirpx.org & http://chemistry-chemists.com

developed in different shapes and sizes in nanometer such as nanoparticles, porous nanoassembly, nanotubes, nanorods, nanowires, flowers, spindles, hexagonal plates, etc. [3–5, 8–10, 17, 23–26]. These nanostructured photocatalysts demonstrate extraordinary features such as higher surface area, and shape- and size-dependent properties including amplified absorption coefficient, improved bandgap, reduced recombination rate, and more reactive sites that extend their use in the solar spectrum as efficient visible light-sensitive photocatalysts. However, metal oxide nanostructured photocatalysts are highly stable, but still suffer from low or restricted visible light absorption due to a wide bandgap and fast rate of recombination of electron-hole pairs and low charge separation efficiency, which greatly restricts their real-world applications.

Defect engineering is revealed as a potent approach for developing an efficient and stable photocatalyst by utilizing a visible portion of solar energy through narrowing the bandgap. Defect engineering is a vital process and still the biggest challenge specially to generate controlled defects. Therefore, defects have been widely explored and found to be able to tune the physical and chemical properties of semiconductor photocatalyst nanomaterials proficiently [1, 3, 4, 7, 9, 18, 19]. The defects are defined as the disturbance or displacement of atoms and molecules from their periodic arrangement in the crystal structures and they greatly affect the photocatalytic performance of semiconductor photocatalyst nanomaterials. The existence of defects in semiconductors plays a vital role to modify the electronic structures and conductivity, optical absorption ability, as well as serving as recombination centers or active sites to reduce the recombination rate of photogenerated charge carriers and absorbing sites for various molecules during photocatalysis. The numerous types of crystal defects have been described in crystalline nanomaterials and classified as point defects, line defects, surface defects, and volume defects. The most common observed point defects in semiconductors are oxygen and metal vacancies, which could be either substitution or interstitial, precipitate impurity atoms, and vacancy cluster [4, 8, 25, 27, 28]. Density functional theory (DFT) has predicted that oxygen vacancies serve as shallow donors and contribute to an n-type conductivity, while metal vacancies serve shallow acceptors and are answerable for p-type conductivity [27, 29]. Furthermore, the type of defects as well as their concentration, distribution, and mobility play a significant role in promoting photocatalytic performance [18, 25, 29–35]. To date, the role of oxygen vacancy defects has been well explored in the performance of photocatalysts compared to metal vacancies due to the unavailability of a facile, stable, and reliable approach to engineer and manipulate metal defects. Furthermore, it is very essential to investigate and understand the role of various types of defects and their ratio at surface/interface or in bulk and bulk-to-surface ratio for developing efficient and high-performance photocatalysts [36–39].

The most widely applied strategies for defect engineering in semiconductor photocatalyst nanomaterials are the substitution of metals and nonmetals, thermal- and photoinduction, and aerodynamic levitated laser annealing, etc. [13, 40]. In addition to these techniques, other methods have also been applied for the formation of controlled oxygen vacancy including annealing under vacuum and/or reducing environment, high energy

https://www.twirpx.org & http://chemistry-chemists.com

particle bombardment, pressurized hydrogen conditions, aluminum or magnesium reduction, chemical reduction, chemical vapor deposition, etc. [11, 41–49]. As a result of the generation of oxygen vacancy, unbalanced charge states or nonstoichiometry in the lattice structure are responsible for the formation of the electric field that favors the separation of photogenerated charge carriers. After the defect engineering in the semiconductor photocatalysts, it is very important to recognize them by the more reliable techniques either by experimentally or theoretical methods. In the past decade, the most common experimental techniques used for detection of defects are spectroscopic techniques such as X-ray photoelectron spectroscopy (XPS), electron paramagnetic resonance (EPR), and photoluminescence spectroscopy (PL), and microscopic techniques such as transmission electron microscopy (TEM) and high-resolution scanning tunneling microscopy (STM), etc. [50–54].

Furthermore, the crystalline nature and surface area of the nanomaterials also play crucial roles in the enhancement of photocatalytic performance. It was reported that highly crystalline nanomaterials possess fewer crystal defects, showing improved photocatalytic performance [6, 55]. The formation of higher crystalline nanomaterials requires high-temperature annealing, which leads to many issues like phase transformations and aggregations which reduce the photocatalytic performance of nanomaterials. Tian et al. synthesized a highly stable porous TiO_2 photocatalyst with high crystallinity and large specific surface area by a hydrothermal process and posttreatment in the presence of ethylenediamine (EN). EN treatment at a higher temperature stabilizes the anatase crystalline phase, reduces the crystal defects, and improves the photocatalytic efficiency by reducing the recombination of photogenerated electron-hole pairs by modifying the electronic properties of TiO_2 [6]. Similarly, Zhou et al. also successfully synthesized highly crystalline and ordered mesoporous anatase TiO_2 with large surface area, large pore size, and thermally-stable over 700°C through an evaporation-induced self-assembly technique in combination with encircling ethylenediamine (EN) followed by higher temperature calcination [55]. Here EN protects to maintain the mesoporous ordering and framework against collapsing and inhibits the undesirable transformation of grain growth and phase during the calcination process showing the improvement of crystallization. Zhou et al. reported that the ordered mesoporous structure facilitated the mass transport and the high crystallinity of anatase TiO_2 favored the separation of photogenerated charge carriers that made it an excellent photocatalytic nanomaterial.

Ultimately, this chapter contains state-of-the-art exciting findings of defective photocatalyst nanomaterials and their potential approach toward visible light-responsive photocatalysis. Here, the main emphasis is given to understand the effect of defects on the photocatalytic behaviors of semiconductor photocatalysts. The recent development of photocatalysts showing defects mediated enhancement in their performance has been summarized and the importance of various types of defects, namely anion vacancies, cation vacancies, surface defects, interface defects, and vacancy associated are discussed in semiconductor photocatalyst nanomaterials.

https://www.twirpx.org & http://chemistry-chemists.com

2 Classification and type of defects in nanomaterials

Generally, the defects in semiconductor photocatalyst nanomaterials can be categorized based on their existence in atomic arrangements/dimensions or by their locations. According to the arrangement of atoms in the dimensions of the crystal lattice, defects are appropriately divided into four main divisions: zero-, one-, two-, and three-dimensional defects (0, 1, 2, and 3D defects). The zero-, one-, two-, and three-dimensional defects are envisaged as point defects (vacancies, interstitial defects, and substitution defects), line (screw dislocation and edge dislocation), sheet (lattice disorder and void), and volume defects (grain boundary and twin boundary). All four types of defects are well-known and intimately related to each other. For instance, volume defects are 3D and may be considered as clusters of point defects, whereas sheet defects are 1D and are confined by line defects, and in other cases networks of line defects and point defects involve to make sheet defects. Furthermore, these defects can also be categorized according to their existence in various locations in nanomaterials such as bulk phase, surface, or interfaces of photocatalysts. Generally, point defects can work as both bulk and surface defects in which vacancies and dopants are present. On the other hand, line defects including dislocations and boundaries also work as bulk defects, while their terminations act the surface defects. Volume defects (grain boundary and twin boundary) are more parallel to point defects and could be present either in the bulk or on the surface of photocatalyst nanomaterials. Moreover, the heterostructure nanomaterials are composed of more than one component and possess bulk, surface, and interface defects, and form mutual interfaces where charge generation, transfer, and consumption simultaneously take place between each other through their interface. These interface defects may come under point defects, volume defects, line defects, and sheet defects [56–64]. Fig. 1 shows the different types of defects and their systematic pictorial representation in photocatalyst nanomaterials.

2.1 Bulk defects

The defects in various semiconductor photocatalysts are well-recognized and revealed as active sites for charge carriers that play a critical role in the application point of view in photocatalyst nanomaterials. The intrinsic physical properties of photocatalysts can be modulated by introducing various types of defects. The missing atoms from their respective position in the crystal lattice are known as vacancies whereas positions taken by atoms at interstitial sites of the crystal lattice are recognized as interstitial defects. Generally, the defects affect the bond length, bond formation energy, energy band structure, atom coordination number, Fermi level, charge carrier concentration, and so on. The formation of different kinds of defects depends mainly on the ionization energies. The various types of surface defects in photocatalysts and their encouraging effects have been concisely discussed.

https://www.twirpx.org & http://chemistry-chemists.com

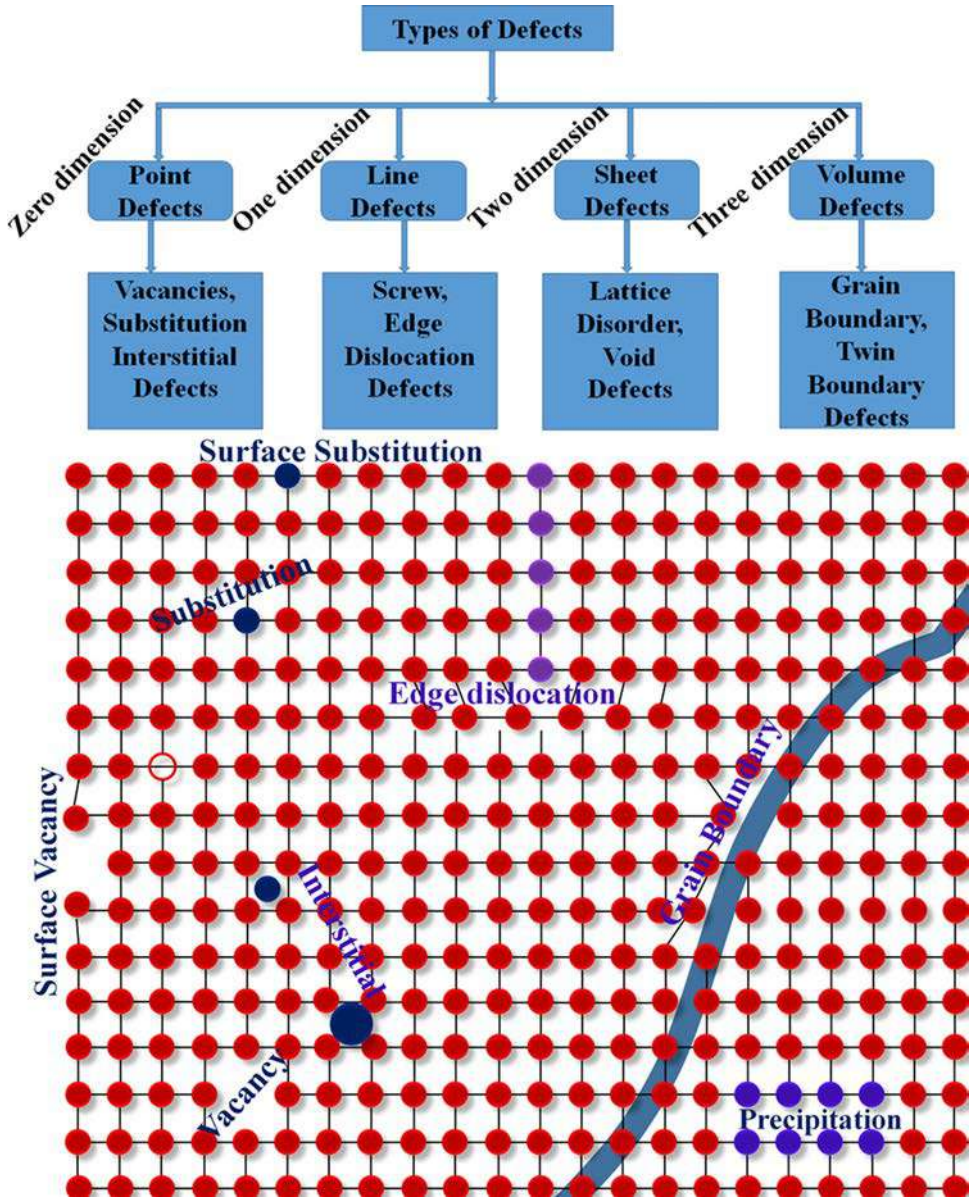

FIG. 1 Systematic illustration of various types of defects in photocatalyst nanomaterials and their pictorial representation.

https://www.twirpx.org & http://chemistry-chemists.com

2.1.1 Anion vacancy or oxygen vacancy defects

The most common anion vacancy is the oxygen vacancy defect, which is widely observed in oxides having a low formation energy. Generally, oxygen vacancy defect is a loss of oxygen atom from their respective position in the crystal lattice and mainly exist both in the bulk and on the surface or subsurface of the nanomaterials. The presence of oxygen vacancies in semiconductor oxides can effectively alter their electronic and physicochemical properties, and thus significantly affect the photocatalytic performance of the photocatalyst. The introduction of a controlled amount of oxygen vacancy is very important to obtain enhanced photocatalytic performance of semiconductor nanomaterials. TiO_2 and ZnO are the most extensively studied photocatalysts due to being cost-effective, stable, eco-friendly, and biocompatible [6, 15, 18]. Hypothetically, the oxygen vacancies in TiO_2 lead to the formation of unpaired electrons or Ti^{3+} centers, which could create the donor level in the electronic structure of TiO_2 [4, 5, 29]. In addition, the oxygen vacancies affect the recombination of photogenerated charge carriers (electron-hole recombination process) due to the presence of additional energy states and changing the chemical rates that depend on the transfer of charge either from electrons or holes. Theoretical and experimental results predict that the oxygen vacancy affects surface reactivity and adsorption of oxygen and water molecules on TiO_2 [65, 66]. Moreover, the most important parameters responsible for the improved photocatalytic performance are photo-response or optical absorption and efficient charge separation and transfer efficiency of photogenerated charge carriers, as shown in Fig. 2. Many reports demonstrated that crystal defects in TiO_2 could introduce new energy levels below the conduction band which expand the optical absorption of TiO_2 into the visible region. Dong et al. synthesized defective TiO_{2-x} via a facile anodization technique having an oxygen-deficient environment and investigated the existence of oxygen vacancies by various techniques [34]. High-resolution

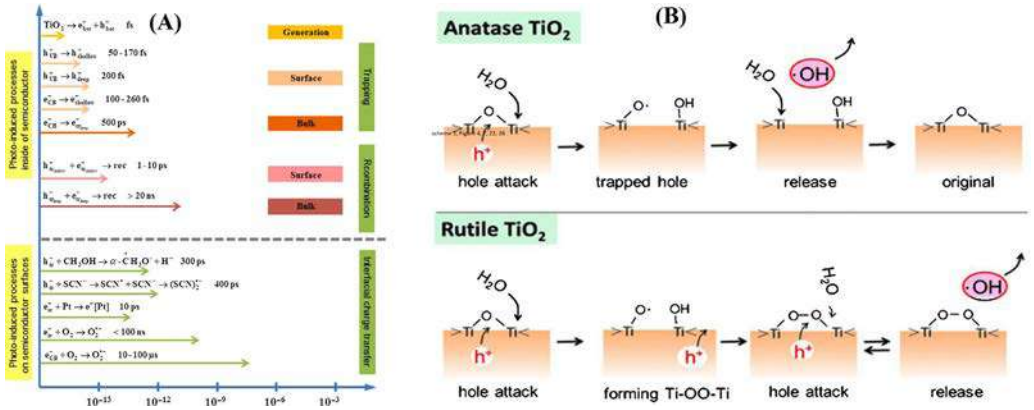

FIG. 2 (A) Various photocatalysis processes involved in photocatalyst. (B) Pictorial representation showing the mechanism of OH radical production with anatase and rutile. *From Visible-light activation of TiO_2 photocatalysts: Advances in theory and experiments. J Photochem Photobiol C: Photochem Rev 2015;25:1–29. https://doi.org/10.1016/j.jphotochemrev.2015.08.003.*

https://www.twirpx.org & http://chemistry-chemists.com

transmission electron micrograph (HRTEM) and X-ray diffraction reveal the formation of a nanocrystal of pure anatase having a disorder surface layer. Electron paramagnetic resonance (EPR) analysis shows a strong and sharp signal at $g = 2.004$ induced by electrons trapped on V_o, confirming the existence of oxygen vacancies. The higher photon-absorbance of defective TiO_{2-x} in the visible light region (400–800 nm) was suggested for the enhanced photocatalytic activity. In another case, Han et al. prepared oxygen vacancy-rich black TiO_2 (B-TiO_2) by thermal treatment amorphous $Ti(OH)_x$ in a vacuum [67]. The oxygen-rich black TiO_2 consists of compactly and densely stacked nanoparticle aggregation which gives large specific areas having plentiful pores. The large amounts of oxygen vacancies and the special structure expand the visible light scope and high charge separation efficiency of photogenerated electron-holes which enhanced the photocatalytic performance of B-TiO_2 drastically.

Furthermore, the concentration of oxygen vacancy is equally important to improve the photocatalytic performance of the photocatalyst. The low concentration of oxygen vacancy possesses fewer active sites and hence exhibits limited photocatalytic performance. Conversely, the higher concentration of oxygen vacancy serves as recombination centers and prevents the rapid migration for photogenerated charge carrier due to the excessive distortion crystal structure. The amount of oxygen vacancy defects is different depending upon the route of synthesis and morphology of nanomaterials. The quantitative analysis of the oxygen vacancy defect is still unclear so far. Chen et al. reported the regulation of defect distribution on TiO_2 nanosheets by annealing the pristine TiO_2 in oxygen and hydrogen atmospheres sequentially [65]. The surface oxygen vacancy (V_{Os}) performed as a positive charged and easily adsorbed molecular oxygen (O_2). Moreover, the photogenerated electrons are easily trapped in oxygen vacancy, leading to the generation of reactive oxygen species (ROS), which was confirmed by EPR. The results revealed that the combination of a surface-active site with a suitable ratio of surface to bulk defects promotes both generation ROS and the charge separation of electron-hole pairs which improves the photocatalytic performance. Cao et al. reported the effect of the different concentrations of oxygen vacancy defect and different shapes of nanosphere, nanocube, and nanopyramid on the photocatalytic degradation under visible light irradiation [68]. The nanopyramidal shape TiO_2 having oxygen vacancy defect exhibits the highest photocatalytic activity compared to nanospherical shape TiO_2 coating without oxygen vacancy defect. The sharp edges and corners of the nanopyramid decrease the recombination rate of photogenerated electron-hole pairs and oxygen vacancy defect expand the photo-absorption in the visible region via narrowing the bandgap energy and enhance the charge separation of the electron-hole pairs. Similarly, the distribution of oxygen vacancy and their concentration have equal importance to improve the photocatalytic performance by improving charge separation and optical absorption.

Furthermore, the oxygen vacancy is equally potential in other semiconductor oxides and improves photocatalytic performance [25, 33, 62, 69–74]. Likewise, TiO_2, ZnO also exhibits the oxygen vacancy-dependent photocatalytic performance in the visible region.

https://www.twirpx.org & http://chemistry-chemists.com

Wang et al. fabricated ZnO nanosheets with tunable BET surface area and rich oxygen vacancy defects via a facile ultra-rapid solution method [3]. Raman scattering, room-temperature photoluminescence (PL), XPS, and ESR revealed the oxygen-vacancies rich ZnO nanosheets. BET surface area of ZnO nanosheet increases from 6.7 to 34.5 m^2/g, through an electrostatic-controlled growth and self-assembly mechanism which further increases the concentration of surface oxygen vacancy. The oxygen-vacancies-rich ZnO nanosheets showed high photocurrent response and photocatalytic performance toward the degradation of Rhodamine B under the visible region due to the expansion in the visible region. Fig. 3 shows (A and B) SEM, (C and D) TEM micrographs of the ZnO nanosheets, (E) N_2 adsorption-desorption isotherms, (F) pore size distributions, (G) high-resolution O1s XPS spectra, and (H) ESR spectra of the ZnO samples. Similar to nanosheet, defect enriched ZnO nanorods were reported by Singh et al. using a low-temperature hydrothermal synthesis route [26]. They revealed that by controlling pH, oxygen defects can be easily controlled and confirmed by XPS and Raman spectroscopy. These oxygen defects narrow the bandgap and improve ROS generation, hence significantly enhance photocatalytic behavior. Lastly, different morphologies of ZnO nanostructures such as nanorods, tetrapod, nanoassembly, flowers, spindles, microspheres, and so on have been developed which also possess varying amounts of oxygen vacancy defects [3, 8, 17, 23, 26, 75, 76]. These oxygen vacancy defects improve visible light absorption and facilitate the charge generation. Correspondingly, other photocatalyst nanomaterials including CeO_2, WO_3, Al_2O_3, Ga_2O_3, BiOBr/Cl, etc. were also reported for visible light photocatalysis having various amount of oxygen defects [19, 70–72] [77–79]. In summary, the oxygen vacancy defects with controlled fashion, optimum concentration, and abundant

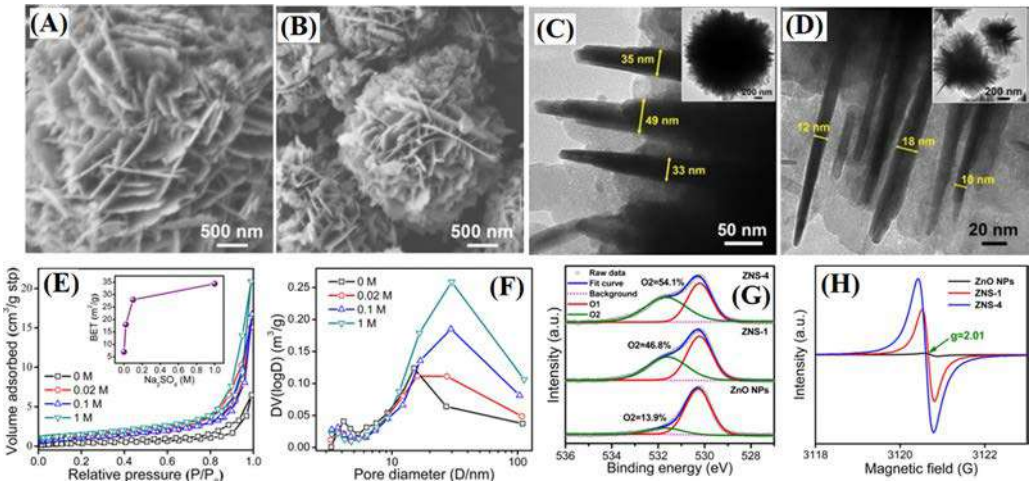

FIG. 3 (A and B) SEM, (C and D) TEM micrographs of the ZnO nanosheets, (E) N_2 adsorption-desorption isotherms, (F) pore size distributions, (G) high-resolution O1s XPS spectra, and (H) ESR spectra of ZnO samples. *From Wang J, Xia Y, Dong Y, Chen R, Komarneni S. Defect-rich ZnO nanosheets of high surface area as an efficient visible-light photocatalyst. Appl Catal B: Environ 2016;192:8–16. https://doi.org/10.1016/j.apcatb.2016.03.040.*

https://www.twirpx.org & http://chemistry-chemists.com

localized electrons have a positive impact in terms of improving the absorption in visible region by narrowing the bandgap and activation of O_2 to ROS, which improves the charge separation of photogenerated charge carriers.

2.1.2 Cation vacancy or metal (M^{n+}) vacancy defects

In the past decades, oxygen vacancy defects are believed to be very important, and have been extensively studied. However, very few reports are available in the literature focusing on the existence of the metal vacancy. Similar to anion vacancies, cation vacancies or metal vacancies (M^{n+}) also judiciously improve the electronic structure and physicochemical properties due to electron configuration and orbital distributions. However, the engineering and manipulation of cation vacancies or metal vacancies (M^{n+}) are more difficult due to the large formation of energy, and hence are still a major challenge. The cation vacancy or metal vacancy (M^{n+}) is usually created by the doping of metal ions especially transitional metals showing multiple vacancies such as Ti^{n+}, Fe^{n+}, Ta^{n+}, W^{n+}, Zn^{n+}, Ce^{n+}, Mo^{n+}, etc. [80–85]. In some cases, self-doping by a low valence cation and heteroatoms doping have also been applied as an effective approach to improve the photocatalytic performance of semiconductor photocatalyst nanomaterials [86–90]. Wang et al. reported the introduction of the metal vacancies (V_{Ti}) in undoped oxides via solvothermal treatment in an ethanol-glycerol mixture followed by thermal calcination [29]. DFT calculations on the cell structure predict that the existence of abundant V_{Ti} makes the c axis shrink heavily with the slightly elongated a and b axes and gives a strong EPR peak at $g = 1.998$ at room temperature. The nonstoichiometric defective TiO_2 is attributed more to the presence of Ti vacancies than oxygen interstitials in the lattice, which changes the charge density and valence band edge and conductivity from n-type to p-type with higher charge mobility. Ti-defected TiO_2 shows extraordinarily higher photocatalytic performance compared to normal TiO_2, as shown in Fig. 4. The higher photocatalytic performance is attributed to efficient charge separation of photogenerated electron-hole pairs and transfer in bulk and at the semiconductor/electrolyte interface. The existence of Ti^{3+} and oxygen vacancy introduces a new energy level below the conduction band level and could narrow the bandgap. The new energy level can significantly extend the lifetime of photogenerated electrons and hamper the recombination of electron-hole pairs [86]. Consequently, the synergistic effect of crystal surface and self-doped Ti^{3+} in the TiO_2 nanostructured materials could result in enhanced photocatalytic performance. To date, extensive works have been reported for the careful introduction of Ti^{3+} and/or V_o defects into the bulk lattice of TiO_2 by applying various methods such as oxidation/reduction, hydrogenation, etc. [48, 91]. Recently, self-doping Ti^{3+} in TiO_2 was observed as an efficient approach is not only extending the absorption spectra of TiO_2, but also simultaneously helps to eliminate the side effect of extrinsic dopants like introducing extra carriers recombination centers. Consequently, self-doped TiO_2 nanostructures reveal good stability and considerable photocatalytic activity for hydrogen production under visible light. Furthermore, hydrogenation is another most recent and very promising approach to introduce surface disorders within TiO_2 to improve photocatalytic performance. The hydrogenation

https://www.twirpx.org & http://chemistry-chemists.com

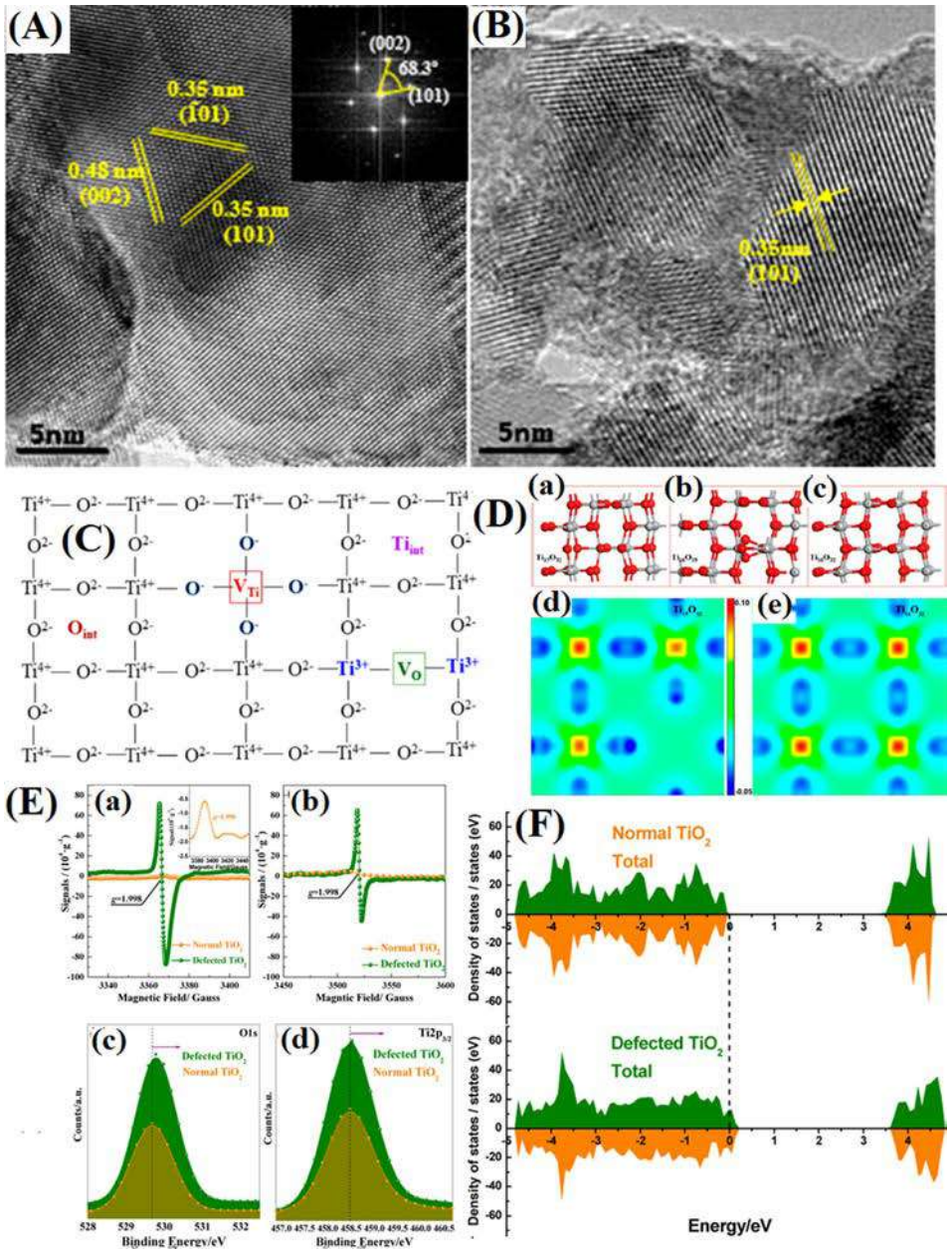

FIG. 4 TEM images of (A) defected and (B) normal TiO_2, (C) representation of different types of defects in undoped TiO_2, (D-(a–c)) Optimized cell structures of Ti-defected and normal anatase TiO_2, (D-(d and e)) charge density difference of Ti-defected and normal TiO_2, respectively, (E) EPR spectra of Ti-defected and normal TiO_2 (a) low temperature (120*K*) and (b) room temperature (298 K), inset in (*E*-(a) enlarged EPR spectrum of normal TiO_2, (F) XPS spectra of defected and normal TiO_2 (c) O 1 s and (d) Ti $2p^{3/2}$, (F) density of states of normal TiO_2 and defected TiO_2. *From Wang S, Pan L, Song J, Mi W, Zou J, Wang L, et al. Titanium-defected undoped anatase TiO_2 with p-type conductivity, room-temperature ferromagnetism, and remarkable photocatalytic performance. J Am Chem Soc 2015;137:2975–2983.* https://doi.org/10.1021/ja512047k.

https://www.twirpx.org & http://chemistry-chemists.com

process introduces the newly created oxygen vacancies which prevent the recombination of charge carriers and defect states in TiO_2 lattice by oxygen subtraction by the partial reduction of Ti^{4+} to Ti^{3+}. As a consequence, the Fermi level of TiO_2 is moved toward the conduction band, which leads to a significant enhancement of optical absorption and photo-activity [91].

Furthermore, self-doping is also observed in other semiconductor oxides which improves the charge separation of electron-hole pairs and photocatalytic performance of nanomaterials. Takata et al. demonstrated that a low valence cation doping in the parent cation efficiently enhanced photocatalytic activity compared to a higher valence cation showing the suppression on photocatalytic performance [83]. The lower valence cation doping introduces oxygen vacancies and Ti^{3+} defects that effectively boost the charge separation of charge carriers. Shang et al. also demonstrated Ti^{3+} dual-doping on both $SrTiO_3$ and TiO_2. The self-doping improves the charge transport and separation, and enhances visible light photo-response between $SrTiO_{3-x}$ and TiO_{2-x}, and special heterostructures [92]. In contrast to this, Chen et al. reported that the surface Ti^{3+} defects exhibit a negative impact on the photocatalytic hydrogen evolution activity of $SrTiO_3$ [93]. Similar to $SrTiO_3$, self-doping with lower valency state is also observed in Ta_2O_5 [73, 89]. Ta^{4+} self-doping in Ta_2O_5 nanoparticles enhances optical absorption in the visible range that significantly improves the photocatalytic performance of Ta_2O_5 nanoparticles. In addition, Hoa et al. reported the hydrothermal synthesis approach for the successful creation of different amounts of zinc vacancies in the defective ZnS and demonstrated vacancy-dependent visible light-responsive photocatalytic hydrogen evolution [35]. The existence of abundant zinc vacancies and their remarkable effects on the electronic structure of ZnS which was confirmed by fluorescence emission spectra, XPS analysis, UV-visible absorption spectra, and Mott-Schottky plots, respectively. Zinc vacancies raise the valence band (VB) position by weakening the oxidative capacity of the holes and improve the antiphotocorrosion property of ZnS. The electro-chemical and photo-electrochemical results demonstrated the charge separation and the electrons transfer that enhance the photostability and visible light photocatalytic activity of ZnS for H_2 production due to more efficient Zn vacancies in ZnS. Moreover, Zn vacancy defects showed significant importance to modify the electronic structure by introducing additional energy levels and hence improved the properties of photogenerated charge carriers and consequently enhanced the photocatalytic performance of various hierarchical heterojunctions with n-type wide-bandgap semiconductor photocatalysts [94, 95].

Apart from the self-doping and intrinsic defects, doping of other metal ions (heterometal cation doping) creates bulk defects in the crystal lattice of semiconductor nanomaterials [96]. Doping of metal ions having different charges could generate a charge imbalance between the dopants and host nanomaterials, which significantly stimulates the charge separation of photogenerated electron-hole pairs. Transition metal ions have been widely reported as efficient dopants for improving the photocatalytic performance of various semiconductor nanomaterials in the visible region [82, 84, 85, 97–99]. Recently, Qi et al. successfully prepared transition metal-doped ZnO (TM-ZnO) nanoparticles via a

https://www.twirpx.org & http://chemistry-chemists.com

simple solvothermal route [84]. They revealed a significant advance in the absorption in visible light and photocatalytic performance of transition metal doping ZnO nanomaterials. Furthermore, transition metal ions doping has also been reported with other nanomaterials such as CeO_2, TiO_2, ZnS, etc. [85, 97–99]. In addition to transition metal ion doping, some other metal ions such as Ce have also been reported for improving the photo-response in the visible region with enhanced charge separation efficiency and photocatalytic performance of nanomaterials [100, 101]. Jiang et al. reported a one-spot facile solvothermal method for doped monoclinic $BiVO_4$ by varying Ce concentrations and investigated the photocatalytic performance for oxygen evolution [100]. The doping of Ce^{3+} ions into the host structure of monoclinic $BiVO_4$ at Bi^{3+} sites without any distortion was confirmed by Raman, XPS, electrochemical impedance spectroscopy (EIS), and the density of states calculation, as shown in Fig. 5. Ce^{3+} ions trap the photogenerated holes and reduce the recombination of photogenerated charge carriers, and hence enhance the photocatalytic performance for water oxidation of Ce-$BiVO_4$. Dai et al. also developed a Ce^{3+} dopant by varying content which mediated the crystal defects lattice in the host Bi_2MoO_6 [101]. The defect engineering in crystal structures expressively influenced the electron dynamics and band structure by facilitating the one-electron and two-electron reactions by introducing the Ce^{3+}/Ce^{4+} and Mo^{4+}/Mo^{6+} redox couples that significantly improved the charge separation and enhanced ROS generation, resulting in the improved photocatalytic degradation of highly toxic nerve agent simulants (NAS), organic dyes, and photo-inactivation of bacterial. Conclusively, certain types of M^+ defects show an encouraging effect on the photocatalytic performance of nanomaterials by improving the charge

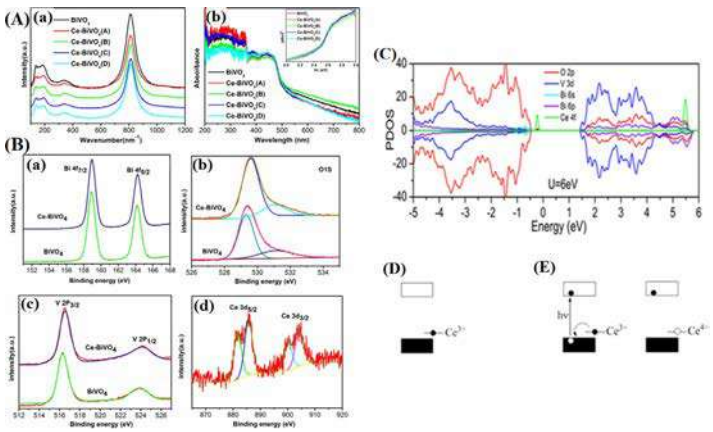

FIG. 5 (A-(a and b)) Raman spectra and UV-vis absorption spectra of pristine $BiVO_4$ and Ce-$BiVO_4$. Inset of (b): plots of $(ah\nu)^2$ vs. hv of $BiVO_4$ and Ce-$BiVO_4$ (B). High-resolution XPS spectra of Ce-$BiVO_4$ and pristine $BiVO_4$ (a) Bi 4f, (b) O 1 s, (c) V 2p, and (d) Ce 3d. (C) PDOS plots of Ce-$BiVO_4$ calculated using U(Ce) = 6 eV. (D) Schematic view of the essential electronic structure of Ce-$BiVO_4$. The filled and empty boxes represent the VB and CB. The up-spin f1 level of a Ce^{3+} dopant ion lies above, The role of a dopant Ce^{3+} ion as a hole trap in Ce-$BiVO_4$. *From Jiang Z, Liu Y, Jing T, Huang B, Zhang X, Qin X, et al. Enhancing the photocatalytic activity of $BiVO_4$ for oxygen evolution by Ce doping: Ce^{3+} ions as hole traps. J Phys Chem C 2016;120:2058–2063. https://doi.org/10.1021/acs.jpcc.5b10856.*

https://www.twirpx.org & http://chemistry-chemists.com

separation efficiency. In some cases, the negative impact of the metal defect on the photocatalytic activity of nanomaterials has also been observed. Nevertheless, several crystal defects in semiconductors greatly influence their physico-chemical properties of nanomaterials along with their photocatalytic performance.

2.2 Surface defects

Intrinsic surface defects and subsurface defects in semiconductors serve as recombination centers and active sites to trap photogenerated charge carriers that control the electron-hole recombination process [3, 4, 11, 19, 74, 102], while bulk defects only work as recombination centers for photogenerated charge carriers. Principally, bulk, surface, and subsurface defects are important for the activation of the photocatalysis process. However, during photocatalysis, most of the photogenerated electrons and holes recombine, resulting in moderate photocatalytic efficiency of photocatalyst nanomaterials. The photocatalyst nanomaterials exhibit several unique properties such as higher surface area, surface reactivity, surface energy, and the presence of paramount surface atoms having a dangling bond. Therefore, the presence of surface defects is predictable in the photocatalyst nanomaterials. The most common examples of surface defects are oxygen defects and Ti^{3+} defects. They play an important role to boost photocatalytic performance by facilitating the activation and interaction of molecules with surface oxygen vacancy defects. Wang et al. reported the positive impact of surface oxygen vacancies on the photocatalytic performance of hydrogenated $BiFeO_3$ (BFO) nanoparticles, synthesized by a high-pressure hydrogenation process [74]. The surface oxygen vacancies improved the optical absorption, the charge separation, and transfer that suppress the recombination of photogenerated electron-hole pairs of hydrogenated BFO compared to the pristine BFO. Therefore, the hydrogenated BFO exhibited enhanced photocatalytic degradation of methyl orange under visible light irradiation. Based on the existing literature, it was observed that surface oxygen vacancies showed a positive effect on the photocatalytic performance of nanomaterials by improving the charge separation efficiency of electron-hole pairs, narrowing the bandgap with improved optical absorption ability in the visible region.

Besides surface oxygen vacancies, other vacancies such as carbon (C), nitrogen (N), and sulfur (S) have also been observed and studied in various photocatalyst nanomaterials [103–114]. For instance, C vacancy has been recognized as the most common defect in carbon-based photocatalytic nanomaterials, especially in graphitic carbon nitride [103, 104]. Carbon nanomaterials with the suitable bandgap as a metal-free photocatalyst have gained increasing attention due to their easy availability, absorption ability in the visible light, low cost, and good stability. These C vacancy defects are important to improve the adsorption and activation of gaseous molecular due to the presence of abundant localized electrons, which is advantageous for photocatalysis for reducing the recombination of charge carriers with the enhanced charge separation efficiency. Di et al. synthesized the ultrathin porous graphite carbon nitride (g-C_3N_4) of the average thickness of ~0.9 nm and higher surface area of about 165 m^2g^{-1} with confined surface carbon defects via the twice thermal

https://www.twirpx.org & http://chemistry-chemists.com

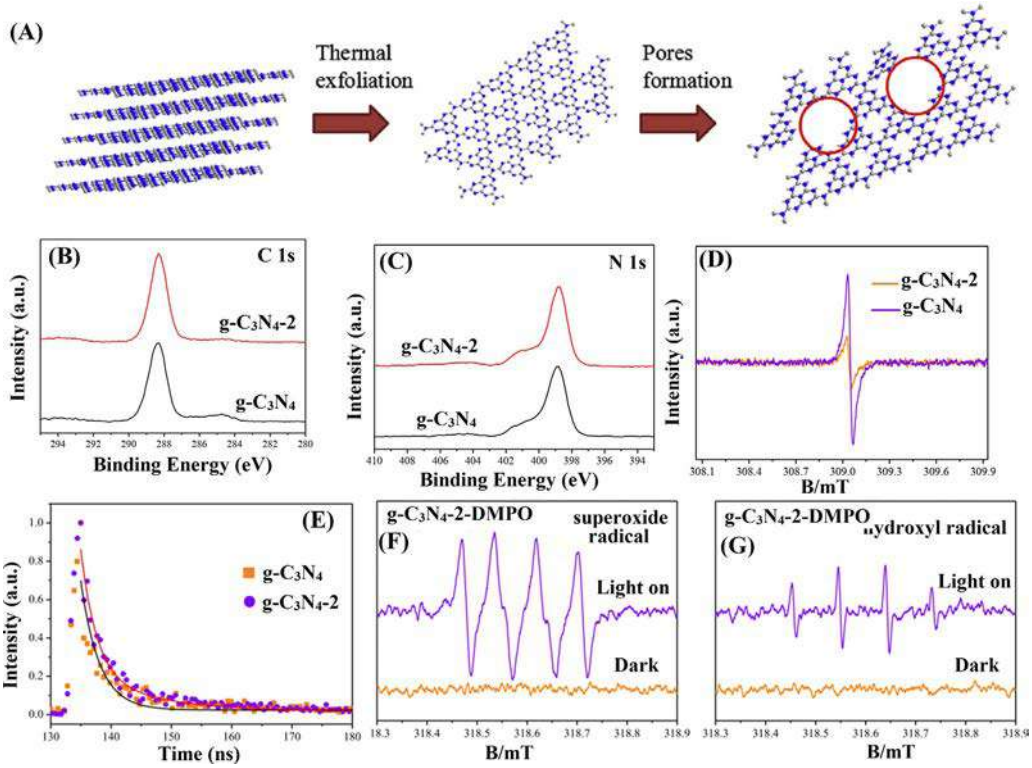

FIG. 6 (A) Systemic illustration of the formation process for porous ultrathin g-C_3N_4-2 nanosheets. (B and C) High-resolution XPS spectra of C 1 s and N 1s, respectively. (D) EPR spectra of g-C_3N_4 and g-C_3N_4-2. (E) Time-resolved transient PL decay. (F and G) DMPO spin-trapping ESR spectra of porous ultrathin g-C_3N_4-2 material under visible light irradiation. *From Constructing confined surface carbon defects in ultrathin graphitic carbon nitride for photocatalytic free radical manipulation. Carbon 2016;107:1–10. https://doi.org/10.1016/j.carbon.2016.05.028.*

treatment of bulk g-C_3N_4 [103]. The confined surface carbon defects in porous ultrathin g-C_3N_4 accelerated bidirectional carrier separation for both bulk and the surface. ESR and XPS studies confirmed the change of the main free radical by changing the bulk g-C_3N_4 to porous ultrathin g-C_3N_4 with the confined surface C defects, shown in Fig. 6. The porous ultrathin g-C_3N_4 reduced the distance between the charge transfer carriers and the surface and lowered the probability of recombination of charge carriers by empowering the higher charge separation efficiency effectively enhancing the photocatalytic activity under visible light. Similarly, graphitic carbon nitride (HGCN) nanosheets have also been reported with plentiful in-plane holes with carbon vacancy by thermally treated bulk GCN (BGCN) under an NH_3 atmosphere having a higher specific surface area of 196 m^2/g with an enlarged bandgap of 2.95 eV [104]. The HGCN with in-plane holes has more exposed active edges and cross-plane diffusion channels that significantly accelerated mass and photogenerated charge transfer. Additionally, the self-modified carbon vacancies in HGCN made them the potential for extending light absorption in the near-infrared region, higher donor density, and remarkably

https://www.twirpx.org & http://chemistry-chemists.com

longer lifetime of charge carriers. Therefore, HGCN possessed enhanced photocatalytic activity for hydrogen production compared to BGCN.

Furthermore, accompanied by the carbon vacancy, graphite carbon nitride is also well-known for the existence of the nitrogen vacancy [105–112]. Nitrogen vacancy not only broadened the absorption in the visible region and charge separation but also served as reactive/active sites to facilitate the interactions and charge transfer between absorbed molecules and graphite carbon nitride, which improved the photocatalytic performance of the carbon nitride nanomaterials. Niu et al. introduced nitrogen vacancies (V_N) in the framework of g-C_3N_4 by controlling the polycondensation temperature of a dicyandiamide precursor [106]. The narrowed bandgap extended visible light absorbance (between 450 and 600 nm) and restrained intrinsic radiative recombination of electrons and holes were observed in g-C_3N_4 due to the existence of abundant nitrogen vacancies which were analyzed by UV-visible absorption, valence band, and steady and time-resolved fluorescence emission spectra spectroscopy. Subsequently, the nitrogen-deficient g-C_3N_4 displayed enhanced photocatalytic activity and hydrogen evolution from water splitting. Hong et al. also reported a hydrothermal approach for the synthesis of nitrogen-deficient graphic carbon nitride (g-C_3N_{4-x}) using ammonium thiosulfate as a weak oxidant [108]. The study demonstrated that the deficiency of terminal amino species on g-C_3N_4 introduced the new defect-induced interband levels and expanded the visible light absorption spectrum and charge separation efficiency, which is responsible for the enhanced photocatalytic performance of nitrogen-deficient g-C_3N_4. The nitrogen-deficient g-C_3N_4 catalyst exhibited a stable photocatalytic H_2-evolution rate up to 31.6 μmol h^{-1}, which is three times higher compared to g-C_3N_4. It was also observed that the surface nitrogen vacancy defects in g-C_3N_4 could be present in many forms including nitrogen defects, primary amine species at the surface, and/or cyanamide moiety (—NCN—). The cyanamide moiety (—NCN—) and oxygen-bearing functional groups (—O—, —OH, —COOH) were recognized by Lau et al. as the nitrogen defects which were responsible for the improved photocatalytic activity of g-C_3N_4 [109]. Ding et al. reported that the nitrogen vacancies positioned at the uncondensed terminal NH_x lattice sites and improved the optical absorption, and the charge separation efficiency of the photogenerated charge carrier which are responsible for the improved photocatalytic oxidation activity [105]. Recently, Wu et al. reported a novel, template-free, cost-effective hydrothermal copolymerization process for the synthesis of nitrogen-deficient nanocage-like 3D porous graphitic carbon nitride (g-C_3N_4) with a high surface area for enhanced photocatalytic H_2 activity [110]. The nitrogen vacancies with a nanocage-like structure exhibited a synergetic effect to endow the visible-responsive and efficient separation of the photogenerated charge carrier due to more exposed active lateral edges, and catalytically active sites.

In addition, nitrogen vacancies not only modulate the electronic properties but also offer more sites for adsorbing molecular nitrogen, thereby facilitating the transfer of electrons from carbon nitride to the surface adsorbed molecules. The nitrogen vacancy is an effective approach to accomplish selectively and strong absorption and activation of nitrogen due to the same shape and size of nitrogen for the photocatalytic nitrogen

https://www.twirpx.org & http://chemistry-chemists.com

fixation. The N-vacancy defected g-C_3N_4 with improved separation efficiency and the electron transfer of photogenerated carriers was developed by Dong et al. in the presence of nitrogen gas by heat treatment. The N vacancy easily traps the photogenerated electrons at the surface of g-C_3N_4, which is immediately transferred to the adsorbed N_2 to activate the photocatalytic N_2 fixation [111]. Recently, Huang et al. also developed the nitrogen vacancies and oxygen doping (N_v&O_d-CN) hollow porous prismatic g-C_3N_4 with a high specific surface area of 220.16 $m^2\ g^{-1}$ via a facile low-temperature hydrothermal method followed by a subsequent calcination process [107]. Nitrogen vacancy and oxygen doping in hollow porous prismatic structure of N_v&O_d-CN were reported to be beneficial for the adsorption and activation of nitrogen molecules. The enhanced photocatalytic performance of nitrogen fixation of the as-obtained hollow porous prismatic N_v&O_d-CN under visible light irradiation was ascribed to its unique surface morphology and characteristic such as hollow and porous prismatic structure with highly exposed active nitrogen vacancies sites, changes in the electronic structure with suitable band structure and absorption in visible region, and efficient charge separation. Similarly, the porous structure of graphitic carbon nitride (g-C_3N_4) with nitrogen defects and oxygen dopants was also reported through a simple copyrolysis of dicyandiamide and ammonium persulfate ($(NH_4)_2S_2O_8$) [112]. The nitrogen defects and oxygen dopants changed the electron transition by electrons state of π band and lone pair (LP) in the modified g-C_3N_4, and therefore the modified g-C_3N_4 demonstrated six times higher photocatalytic hydrogen evolution activity than pristine g-C_3N_4 under visible light illumination due to improving the charge separation efficiency of photogenerated electron-hole pairs.

2.3 Interface defects

Interface defects are more complex which exist between the interfaces of two or more components. The interface is formed in multicomponents through face-to-face interaction of the individual component. Therefore, surface defects can be present on the interface of the photocatalyst nanomaterials and influence numerous processes occurring during photocatalysis such as charge transfer, separation, and stabilization of photogenerated charge carriers [115–119]. Generally, the photocatalytic performance of a heterostructure photocatalyst strongly depends on the interfacial charge transfer at the interface, which is usually determined by the electronic structure of the individual component. Furthermore, the engineered interfacial defects can efficiently improve the charge carrier density with an extended lifetime of electrons. The inherent phenomenon of defective electronic structures in different heterostructures creates a significant impact on their photocatalytic performance. Many heterostructures have been reported for their enhanced photocatalytic performance under visible light, including heterostructures of TiO_2, ZnO, CeO_2, MoS_2, and so on [116–118, 120–124].

TiO_2/graphene heterostructures have been taken as an example, they possess interface detects at their surface of the individual components. Tang et al. developed the nanohybrids by decorating graphene quantum dot on self-doped Ti^{3+}-TiO_2/nanosheets

https://www.twirpx.org & http://chemistry-chemists.com

(Ti^{3+}-TiO_2/GQD NSs) via a facile calcination method [116]. The carbothermal reduction reaction created Ti^{3+} sites on the surface of TiO_2 nanosheets. The experimental results with the support of theoretical calculations demonstrated the synergistic effect on the enhanced photocatalytic performance due to the existence of both Ti^{3+}/O_v defect sites. A strong and sharp ESR signal at $g = 2.03$ and the large and broad signal at $g = 1.98$ are attributed to the oxygen vacancies and Ti^{3+} sites on the surface of Ti^{3+}-TiO_2/GQDs hybrid composites. Ti^{3+} ions/oxygen vacancies introduced the defect energy barriers to prompt the efficient carrier separation with the reduction recombination of electron-holes, and thereby Ti^{3+}-TiO_2/GQDs showed excellent photocatalytic performance under visible light compared to pure TiO_2. Similarly, a facile hydrothermal-calcination method was reported for the creation of Ti^{3+} and oxygen defects by coupling with Ti^{3+} self-doped TiO_2 and reduced graphite oxide (TiO_{2-x}/rGO)in TiO_{2-x}/rGO by Yang et al. for the rapid removal of organic pollutants [117]. The average lifetime of photoluminescence decay in TiO_{2-x}/rGO was observed to be only 3.43 ns, which is much shorter than that of pristine TiO_2 (5.70 ns) and TiO_{2-x} (4.81 ns), indicating the faster electron transfer from TiO_{2-x} to rGO that enhanced the charge separation of photo-induced charge carriers in TiO_{2-x}/rGO. Consequently, the enhanced visible light harvesting with the efficient charge separation exhibited a synergistic effect on the photocatalytic performance of the TiO_{2-x}/rGO nanocomposite under visible light, as shown in Fig. 7.

Additionally, similar to graphene as a supporting material, C_3N_4 nanosheets (NSs) have also been used as supporting materials to improve interfacial charge transfer. For instance, Tan et al. demonstrated the formation of 3D/2D DTMC/g-C_3N_4 heterostructure through the in-situ growth of defective anatase TiO_{2-x} nanosized mesocrystals (DTMCs) on g-C_3N_4 NSs by the formation of strong interfaces contact between chemical bonds [118]. A strong ESR peak at $g \approx 1.991$ and XPS spectra confirmed the presence of a paramagnetic defective Ti^{3+} center in the bulk. However, these defective Ti^{3+} sites on the surface are usually found to be unstable in the air. The energy levels of the defective sites (Ti^{3+} or Ov) are extremely shallow in DTMCs and the excess electrons are lean toward to be delocalized over these sites, and a mini-band which is formed right below the conduction band (CB) of TiO_2, the narrowing of the bandgap (ca. 0.29 eV) and visible-light response of DTMCs. Tan et al. also demonstrated that both DTMCs and g-C_3N_4 NSs produced photogenerated charge carriers under visible light and subsequently the photo-excited electrons confined in the mini-band of the DTMCs while the photo-induced holes in the valence band (VB) of the g-C_3N_4 NSs effectively enhance the charge transfer across the interface between the two components, thereby promoting the spatial separation of photogenerated charge carriers, leading to the enhancement of the overall photocatalytic activity of the material. Likewise, Xue et al. also reported the role of defects on the interfacial electron transfer (IET) of the g-C_3N_4/MoS_2 heterojunction photocatalyst [119]. The theoretical simulations and experimental studies suggested that N vacancy states in C_3N_4 work as shallow trap states for photogenerated electrons and thereby enhanced the interfacial electron transfer process due to a large energy difference between shallow trap

https://www.twirpx.org & http://chemistry-chemists.com

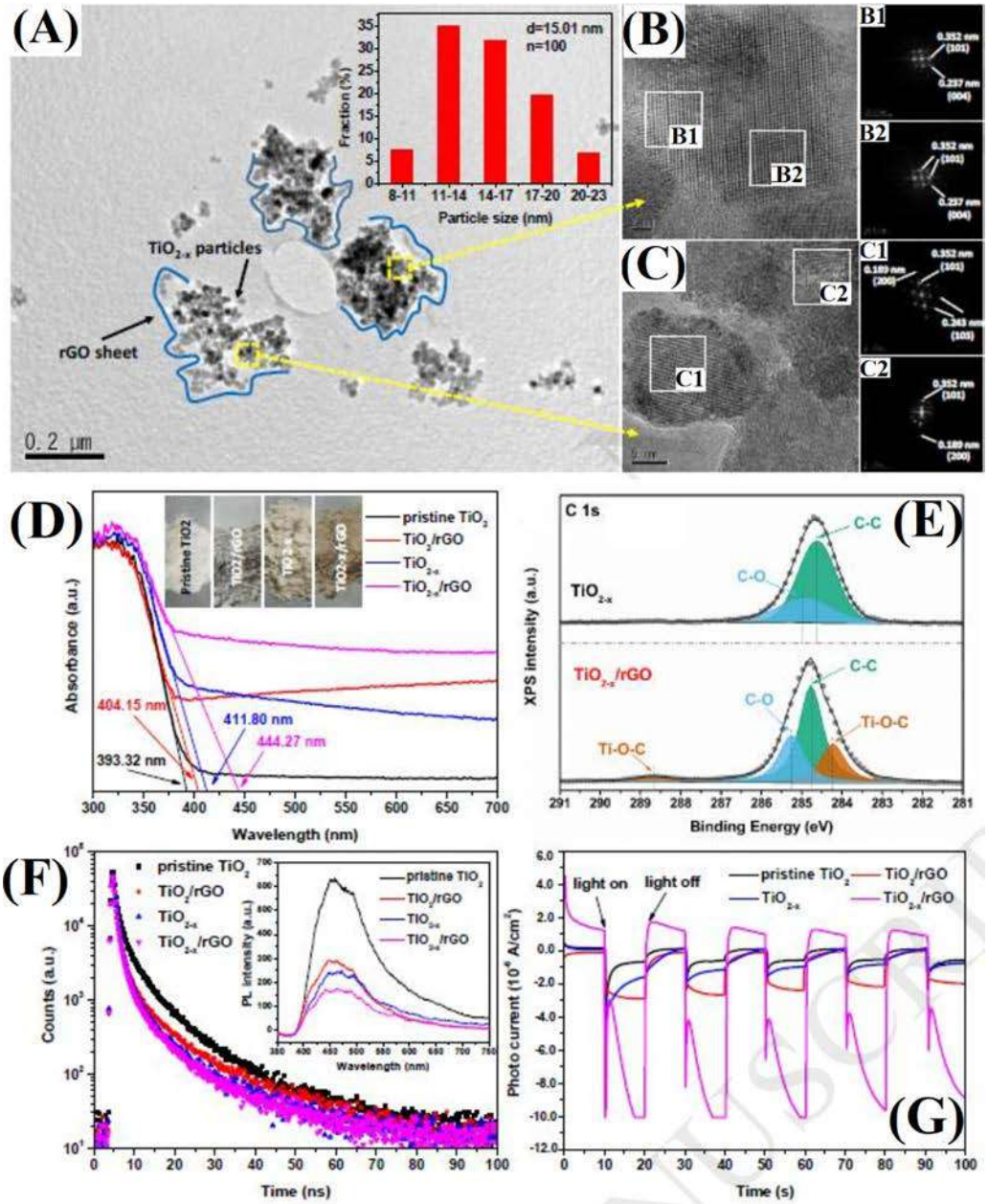

FIG. 7 (A) Low-resolution and (B and C) high-resolution TEM image of TiO_{2-x}/rGO. Inset of (A): particle size distributions of TiO_{2-x} in the TiO_{2-x}/rGO nanocomposite. (D) UV-vis DRS spectra. Inset of (D) photographs. (E) C1s XPS spectra. (F) Time-resolved PL spectra. Inset of (F) steady-state PL spectra. (G) Transient photo-current responses under visible light of TiO_{2-x}/rGO photocatalysts. *From Enhanced visible-light activation of persulfate by Ti^{3+} self-doped TiO_2/graphene nanocomposite for the rapid and efficient degradation of micropollutants in water. J Hazard Mater 2019;365:107–117. https://doi.org/10.1016/j.jhazmat.2018.10.090.*

https://www.twirpx.org & http://chemistry-chemists.com

states and charge separation states. Additionally, the excess electrons producing N vacancies could partially transfer to MoS_2 to generate shallow trap states in the forbidden band of MoS_2. This study suggested that nitrogen vacancy defects induced electronic modifications in C_3N_4 by altering the IET kinetics by making heterojunction photocatalysts for attaining highly efficient photocatalytic reactions.

2.4 Vacancy associates

Similar to the various types of vacancies, the existence of vacancy associates was also observed in various photocatalyst nanomaterials and could tune the electronic structures. Various types of vacancy associates such as single, triple and large vacancy associates ($V_{Bi'''}V_{O}^{\bullet\bullet}V_{Bi'''}$) have been predominant observed in BiOCl [79, 125]. Gaun et al. revealed the existence of the triple vacancy associates predominantly ($V_{Bi'''}V_{O}^{\bullet\bullet}V_{Bi'''}$) with the reduction of the thickness of BiOCl nanosheets at the atomic level while single Bi vacancy defects in BiOCl nanoplates ($V_{Bi'''}$) ([79], These vacancy associates ($V_{Bi'''}V_{O}^{\bullet\bullet}V_{Bi'''}$) create more negatively charged (001) facets that enhance the adsorption and photosensitization process of cationic dye molecules onto the photocatalysts and narrow the bandgap by shifting the valence band upward to the maximum and the conduction band to the minimum. Here, the observed advantages by the change of defects from isolated or single $V_{Bi'''}$ to ($V_{Bi'''}V_{O}^{\bullet\bullet}V_{Bi'''}$) vacancy associates not only affect significantly the adsorption proficiency and electronic structure but also effectively improve the charge separation efficiency of the ultrathin BiOCl nanosheets, as shown in Fig. 8. Therefore, the ultrathin BiOCl nanosheets exhibit significantly enhanced solar-driven photocatalytic performance with an extremely low photocatalyst. Recently Goa et al. developed two nanosheets-assembled hierarchical 3D BiOCl mesoporous nanostructures of similar morphology and exposed facets having different thicknesses and the stable large vacancies associates [79]. The existence of both large vacancy associates ($V_{Bi'''}V_{O}^{\bullet\bullet}V_{Bi'''}V_{O}^{\bullet\bullet}V_{Bi'''}$) and triple vacancy associates ($V_{Bi'''}V_{O}^{\bullet\bullet}V_{Bi'''}$) have been perceived in BiOCl assembled nanosheets with thicknesses of 3–6 nm while BiOCl assembled nanosheets with thicknesses of 10–20 nm have only triple vacancy associates ($V_{Bi'''}V_{O}^{\bullet\bullet}V_{Bi'''}$), which was proven by positron annihilation spectroscopy (PAS) analysis. The formation energy calculations of isolated Bi vacancy by the density functional theory demonstrated the significance of mesopores for the formation of large and stable vacancy associates by counter balancing the thermodynamic instability associated with the incomplete association of Bi and O atoms accompanied by mesopores edges. The extraordinarily large vacancy associates ($V_{Bi'''}V_{O}^{\bullet\bullet}V_{Bi'''}V_{O}^{\bullet\bullet}V_{Bi'''}$) enhanced the generation of photoexcitation electrons in company with prevention the recombination of charge carriers, and thereby exhibited the rapid and complete degradation of bisphenol A (BPA; 10^{-5} M) with low concentration of photocatalyst (1 g L^{-1}), $N\bar{O}_3$ reduction, and bacterial inhibition.

Furthermore, it has also been reported that the exposure of high-energy facets facilitates the formation of surface vacancy associates defects [126–128]. Zhang et al. reported the formation of the high density of high-energy facets in Bi_2WO_6 nanobipyramids [126].

https://www.twirpx.org & http://chemistry-chemists.com

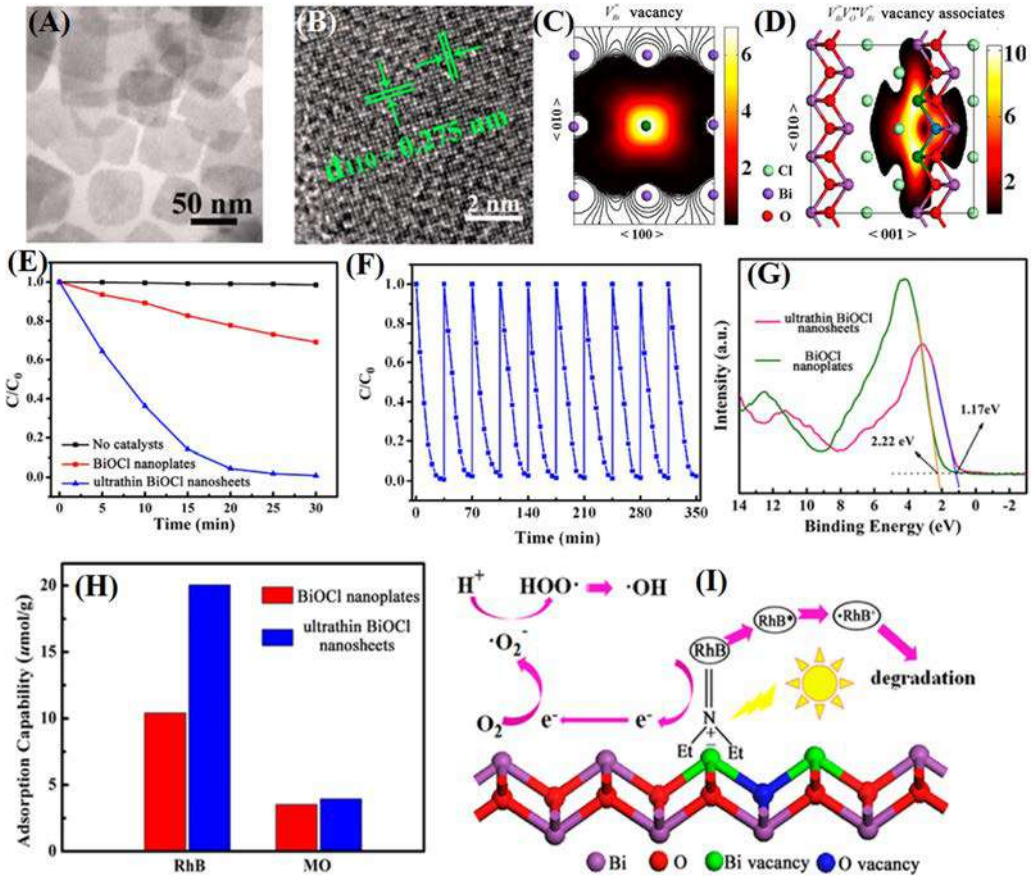

FIG. 8 (A) TEM and (B) HRTEM micrographs of the ultrathin BiOCl nanosheets. (C) Schematic representations of trapped positrons V_{Bi}''' defect and (D) $V_{Bi}'''V_{O}^{\bullet\bullet}V_{Bi}'''$ vacancy associates. (E) Photo-decomposition of Rhodamine B with ultrathin BiOCl nanosheets and BiOCl nanoplates under simulated solar irradiation. (F) Cycling curve of photocatalytic degradation of Rhodamine B for ultrathin BiOCl nanosheets with near fully exposed {001} facets. (G) Valence-band XPS spectra. (H) Adsorption amounts of RhB and MO over the ultrathin BiOCl nanosheets and BiOCl nanoplates. (I) Schematic diagram illustrating photo-sensitization process under visible light irradiation. *From Guan M, Xiao C, Zhang J, Fan S, An R. Vacancy associates promoting solar-driven photocatalytic activity of ultrathin bismuth oxychloride nanosheets. J Am Chem Soc 2013;135:10411–10,417. https://doi.org/10.1021/ja402956f.*

PAS, XPS, and theoretical calculations confirmed the presence of "Bi-O" vacancy associates having (100) high-energy facets exposed to Bi_2WO_6 nanobipyramids. These vacancy associates ("Bi-O") support reducing the bandgap with the enhancement of charge separation efficiency, which significantly enhances the photocatalytic activity of Bi_2WO_6 nanobipyramids for the degradation of pollutants. Recently, the formation of highly exposed facets "Bi-O" vacancy associates has been demonstrated in porous β-Bi_2O_3 experimentally and theoretically [127]. These multiple vacancy associates (Bi-O) significantly improve the electronic structure by the polarization of the related atoms and orbitals and thereby enhance the outstanding photocatalytic performances due to the improved

https://www.twirpx.org & http://chemistry-chemists.com

charge separation efficiency and transfer by producing more surface-active species that simultaneously accelerate the transfer of the electron from pollutants to the catalyst [9, 127]. Li et al. also engineered the vacancy associates "Bi-O" into BiO_{2-x} monolayers [129]. UV-vis NIR diffuse reflectance spectra (DRS) and photocurrent measurements show the increment of the density of states at the conduction band (CB) minimum in the monolayer BiO_{2-x}, which cause enhanced photon responsibility and photo-absorption, Theoretical and experimental results confirmed that the monolayer BiO_{2-x} exhibit the improved photocatalytic performance for Rhodamine B and phenol removal under UV, visible and near-infrared light (NIR) irradiation due to the presence of the vacancy associates $V_{Bi\text{-}O''}$. These "Bi-O" vacancy associates act as trapping centers for charge carriers and improve the charge separation efficiency of photogenerated electron-hole pairs effectively.

2.5 Voids or pits and lattice dislocations

Voids (or pits) and lattice dislocations have also been observed and reported in many semiconductor photocatalysts [56–63, 76]. Voids are a small region where there is an absence of atoms and can be considered as clusters of vacancies in bulk which also have a substantial consequence on the electronic structures and photocatalytic performance of the photocatalyst nanomaterials. Hypothetically, they introduce defect states near the Fermi level by the enhancement surface charge separation efficiency and carrier concentration as well as serving as more specific surface sites for the redox reaction between photocatalysts and pollutants. For instance, pit-structured ZnO nanorods have been successfully synthesized at low temperatures (60°C) via a simple chemical approach in the presence of ammonia using water as the solvent. The decomposition of a trace amount of $ZnO(NH_3)n$ complex was observed into ZnO crystals and formed the pit-structured ZnO nanorods [76]. Besides various vacancy-related defects, other types of lattice defects including lattice dislocations, distortion, and disorders have also been observed and their significant effects on the electron structure and physicochemical properties of photocatalyst nanomaterials reported [59–63]. Generally, nanocrystals attempt to sustain the thermodynamically stable state by reducing their surface energy. The generated surface distortions during synthesis in nanocrystals reduce the surface energy and alleviate the crystal structure. The surface alteration affects the local arrangement of atoms such as bond length, bond angle, interatomic distance, and coordination numbers, and thereby influences the electronic structure and further modifies photocatalytic performance. Fan et al. created lattice disordering/distortion engineering in metal oxide semiconductor nanocrystals by applying ultrasonic irradiation to assist the hydrolysis reaction and hydroxyls addition. The structural modification on nanocrystals shows the modification of the electronic structure with band tails and taper bandgap [62]. These disordered lattices serve as effective active sites for the photogenerated electron-hole pairs and provide a larger surface area to afford more adsorbents to take part in reactions like dissolved oxygen reduction and organic molecules oxidization, respectively. Moreover, the lattice disordering and bandgap narrowing

https://www.twirpx.org & http://chemistry-chemists.com

enhance the photocatalytic performance of photocatalysts by suppression of the recombination of photogenerated charge carriers, higher optical absorption in the visible region, and increased surface area.

3 Characterization techniques of defects

Various types of defects are observed in photocatalytic nanomaterials which possess numerous advantages during photocatalysis. Therefore, it is very important to identify and characterize these defects for the evaluation of the consequence of defect engineering in photocatalytic performance. To characterize these defects, various characterization techniques are developed to confirm the presence of the defects in nanomaterials. Herein, advanced characterization techniques used for defect study in photocatalytic nanomaterials are summarized.

3.1 Spectroscopic techniques

3.1.1 Electron paramagnetic resonance

Electron paramagnetic resonance (EPR) spectroscopy has been widely used to identify defects such as oxygen vacancy, metal vacancy, and nitrogen vacancy that have unpaired electrons both on the surface and in the bulk of nanomaterials. ESR spectra are also used to obtain qualitative information between vacancies and excess electrons by the double integration of vacancy peaks. Therefore, the concentration of vacancies can easily be estimated by ESR. ESR spectra provide the different g values and signal intensities which are directly related to types of defects and their relative concentrations. For instance, the EPR spectrum shows a strong signal at $g = 2.003$ due to oxygen vacancy (V_o), while a g-value of 1.960–1.990 is attributed to the existence of Ti^{3+} cations in TiO_2 [29].

3.1.2 X-ray photoelectron spectroscopy

X-ray photoelectron spectroscopy (XPS) is a very sensitive technique to determine the chemical state of the elements and composition of materials. XPS can resolve surface vacancies of materials to only a few nanometers due to the limited penetration testing depth profile analysis. For example, a symmetrical XPS peak with a shoulder band appearing at 456.9 eV for Ti 2p was reported for the Ti^{3+} defect in defective TiO_2 [29]. Moreover, XPS analysis also gives useful information for the existence of surface defects such as lattice and absorbed oxygen species. XPS O 1s spectra show multiple peaks which provide information for the presence of different forms of surface oxygen defects. The XPS peak located at ~530 eV is allocated to lattice oxygen while the shoulder peak at ~532 eV is ascribed to adsorbed oxygen, and is observed as surface defects [37].

3.1.3 Positron annihilation spectroscopy

Positron annihilation spectroscopy (PAS) is an important, powerful, and sensitive technique to investigate the types of vacancy defects (both intrinsic and extrinsic defects)

https://www.twirpx.org & http://chemistry-chemists.com

in semiconductors. It provides important information about the types, sizes of vacancies, and their concentrations at ppm level by measuring the lifetime of positrons. When a bulk material is treated with positrons and thermalized and annihilated with electrons, consequently γ rays emission is generated, which provides information on the lifetime of positrons and types of defects. Positrons tend to be distributed in the regions of low electron density, e.g., defects including vacancy, vacancy clusters, and microvoids compared to the bulk material. Based on the different positron lifetimes, types of vacancy and their relative concentrations can be determined. For instance, in the case of a defected system, small vacancies or shallow positron traps reduce the surrounding electron density and consequently increase the lifetime (τ_1) of the positron compared to normal or defect-free crystals. The lifetime for defective TiO_2 is recorded as 287 ps compared to 264 and 178 ps for normal and defect-free TiO_2 crystal, respectively, demonstrating the presence of monovacancies or point defects in TiO_2 [29]. Similarly, a higher lifetime (τ_3, 550–590 ps) was observed for BiOCl ultrathin nanosheets and (τ_4, 2.2–2.5 ns) for BiOCl nanoplates, suggesting the presence of large defect clusters and the interface present in the material. The observed shortest positron lifetime (τ_1, around 250 ps) was observed for the presence of the single isolated bismuth vacancies, whereas a higher positron lifetime (τ_2, around 325 ps) was recorded for ($V_{Bi}'''V_O^{\bullet\bullet}V_{Bi}'''$) Bi^{3+}-oxygen vacancy associates [125].

3.1.4 Photoluminescence (PL) spectroscopy

Photoluminescence (PL) spectroscopy is a nondestructive technique used to supply information about lattice defects and oxygen vacancies, charge trapping and diffusion, and recombination of photogenerated charge carriers. For instance, ZnO gives two emission peaks: one in the ultraviolet region and the other in the visible region. The ultraviolet (UV) emission peak is attributed to the band-to-band transitions, i.e., recombination of the holes with the valence band (VB) and the electrons with the conduction band (CB), which provide useful information about the recombination of photogenerated electron-hole pairs and charge separation. While a broad visible emission peak in the range of 400–700 nm is known as a defect emission peak, it is ascribed to the radiative recombination of photogenerated holes with defects such as singly ionized oxygen vacancy and Zn interstitials in ZnO [3, 13]. Wang et al. observed a very weak green emission centered at ∼500 nm for ZnO NPs, and an intensive green-yellow emission centered at 550 nm, which could be deconvoluted peaks into two peaks, one green emission peak centered at ∼520 nm originated due to singly charged oxygen vacancies$^{\bullet}$ and the yellow one at ∼580 nm due to doubly charged oxygen vacancies$^{\bullet}$ [3].

3.2 Microscopic techniques

Electron microscopy reveals the atomic structure of materials. Among the others, transmission electron microscopy (TEM) is generally used to analyze defects, especially the properties of dislocations and stacking faults. Recently, scanning transmission electron microscope (STEM) such as high-angle annular dark-field STEM (HAADF-STEM),

https://www.twirpx.org & http://chemistry-chemists.com

high-angle annular dark-field (HAADF), and annual bright-field (ABF)-STEM, have been used for studying the structural characterization of defective photocatalysts. STEM has advantages over TEM as STEM can be performed on thicker TEM samples. Thus, STEM can be used to differentiate surface and bulk defects [63]. In addition, high-resolution noncontact atomic force microscopy (NC-AFM) and scanning tunneling microscopy (STM) also provide information about structural defects. For instance, STM directly established the interaction between oxygen-deficient sites and hydroxyl groups formed after water splitting [54]. STM also provides information about the interaction of water and oxygen molecules with oxygen vacancies [130].

4 Conclusion

This chapter coveresrecent progress of different types of defects in engineered photocatalyst nanomaterials showing importance in visible light-mediated photocatalysis. Defects were classified based on dimensions and their existence. The different defect types including bulk defects (anion vacancies and cation vacancies), surface defects, interface defects, and vacancy associates were discussed. These defects show a great effect on their physicochemical properties and effectively modify the electronic structure, charge carrier concentration, and atom coordination number in the various photocatalyst nanomaterials, and cause a further improvement in the photocatalytic performance. Several strategies have been employed to engineer the defects in photocatalyst nanomaterials such as the substitution of metal and nonmetal, thermal annealing in various environments, pressurized hydrogen conditions, chemical reduction using aluminum or magnesium, $NaBH_4$, and chemical vapor deposition. Furthermore, both microscopic and spectroscopic techniques have been used to study the different types of defects. The most widely used various sophisticated characterization techniques such as ESR, XPS, Raman, PAS, and STEM have been used to identify and quantify various kinds of defects in photocatalyst nanomaterials. Moreover, these defects not only show promising effects on the narrowing bandgap, improving light absorption and carrier concentration, but also work as the surface active sites to trap the charge carrier to improve surface charge separation efficiency along with chemisorption sites for oxygen, water molecules, and organic species, and thereby improve photocatalytic performance.

References

[1] Pan X, Yang MQ, Fu X, Zhang N, Xu YJ. Defective TiO_2 with oxygen vacancies: synthesis, properties and photocatalytic applications. Nanoscale 2013;5:3601–14. https://doi.org/10.1039/c3nr00476g.

[2] Gupta J, Barick KC, Bahadur D. Defect mediated photocatalytic activity in shape-controlled ZnO nanostructures. J Alloys Compd 2011;509:6725–30. https://doi.org/10.1016/j.jallcom.2011.03.157.

[3] Wang J, Xia Y, Dong Y, Chen R, Xiang L, Komarneni S. Defect-rich ZnO nanosheets of high surface area as an efficient visible-light photocatalyst. Appl Catal Environ 2016;192:8–16. https://doi.org/10.1016/j.apcatb.2016.03.040.

https://www.twirpx.org & http://chemistry-chemists.com

[4] Muhammad WS, Yunqing Z, Xiaoyun F, Jie Z, Yingxuan L, Sumreen A, et al. Facile synthesis of defective TiO_{2-x} nanocrystals with high surface area and tailoring bandgap for visible-light photocatalysis. Sci Rep 2015. https://doi.org/10.1038/srep15804.

[5] Li L, Yan J, Wang T, Zhao ZJ, Zhang J, Gong J, et al. Sub-10 nm rutile titanium dioxide nanoparticles for efficient visible-light-driven photocatalytic hydrogen production. Nat Commun 2015;6. https://doi.org/10.1038/ncomms6881.

[6] Guohui T, Honggang F, Liqiang J, Baifu X, Kai P. Preparation and characterization of stable biphase TiO_2 photocatalyst with high crystallinity, large surface area, and enhanced photoactivity. J Phys Chem C 2008;112:3083–9. https://doi.org/10.1021/jp710283p.

[7] Fang Z, Weng S, Ye X, Feng W, Zheng Z, Lu M, et al. Defect engineering and phase junction architecture of wide-bandgap ZnS for conflicting visible light activity in photocatalytic H_2 evolution. ACS Appl Mater Interfaces 2015;7:13915–24. https://doi.org/10.1021/acsami.5b02641.

[8] Baruah S, Sinha SS, Ghosh B, Pal SK, Raychaudhuri AK, Dutta J. Photoreactivity of ZnO nanoparticles in visible light: effect of surface states on electron transfer reaction. J Appl Phys 2009;105. https://doi.org/10.1063/1.3100221.

[9] Chen S, Li D, Liu Y, Huang W. Morphology-dependent defect structures and photocatalytic performance of hydrogenated anatase TiO_2 nanocrystals. J Catal 2016;341:126–35. https://doi.org/10.1016/j.jcat.2016.06.016.

[10] Kaushik R, Vineeth Daniel P, Mondal P, Halder A. Transformation of 2-D TiO_2 to mesoporous hollow 3-D TiO_2 spheres-comparative studies on morphology-dependent photocatalytic and anti-bacterial activity. Microporous Mesoporous Mater 2019;285:32–42. https://doi.org/10.1016/j.micromeso.2019.04.068.

[11] Li T, Shen Z, Shu Y, Li X, Jiang C, Chen W. Facet-dependent evolution of surface defects in anatase TiO_2 by thermal treatment: implications for environmental applications of photocatalysis. Environ Sci Nano 2019;6:1740–53. https://doi.org/10.1039/c9en00264b.

[12] Gupta J, Bahadur D. Visible light sensitive mesoporous Cu-substituted ZnO nanoassembly for enhanced photocatalysis, bacterial inhibition, and noninvasive tumor regression. ACS Sustain Chem Eng 2017;5:8702–9. https://doi.org/10.1021/acssuschemeng.7b01433.

[13] Gupta J, Bahadur D. Modulation in band gap and efficient charge separation in Cd substituted ZnO quantum dots with enhanced photocatalytic and antibacterial activity. Mater Res Express 2019;6. https://doi.org/10.1088/2053-1591/aafd4b.

[14] Madhu R, Veeramani V, Chen SM, Veerakumar P, Liu SB, Miyamoto N. Functional porous carbon-ZnO nanocomposites for high-performance biosensors and energy storage applications. Phys Chem Chem Phys 2016;18:16466–75. https://doi.org/10.1039/c6cp01285j.

[15] Gupta J, Bahadur D. Defect-mediated reactive oxygen species generation in Mg-substituted ZnO nanoparticles: efficient nanomaterials for bacterial inhibition and Cancer therapy. ACS Omega 2018;3:2956–65. https://doi.org/10.1021/acsomega.7b01953.

[16] Lah NAC, Zubir MNM, Samykano MA. Engineered nanomaterial in electronics and electrical industries. In: Handbook of Nanomaterials for Industrial Applications. Malaysia: Elsevier; 2018. p. 324–64. https://doi.org/10.1016/B978-0-12-813351-4.00021-3.

[17] Adelung R, Modi G, Cretu V, Postica V, Lupan O, Reimer T, et al. Direct growth of free standing ZnO tetrapod networks for multifunctional applications in photocatalysis, UV photodetection, and gas sensing. ACS Appl Mater Interfaces 2015;7:14303–16. https://doi.org/10.1021/acsami.5b02816.

[18] Wang J, Chen R, Xia Y, Wang G, Zhao H, Xiang L, et al. Cost-effective large-scale synthesis of oxygen-defective ZnO photocatalyst with superior activities under UV and visible light. Ceram Int 2017;43:1870–9. https://doi.org/10.1016/j.ceramint.2016.10.146.

[19] Aslam M, Qamar MT, Soomro MT, Ismail IMI, Salah N, Almeelbi T, et al. The effect of sunlight induced surface defects on the photocatalytic activity of nanosized CeO_2 for the degradation of

https://www.twirpx.org & http://chemistry-chemists.com

phenol and its derivatives. Appl Catal Environ 2016;180:391–402. https://doi.org/10.1016/j.apcatb.2015.06.050.

[20] Soltani N, Saion E, Mahmood Mat Yunus W, Navasery M, Bahmanrokh G, Erfani M, et al. Photocatalytic degradation of methylene blue under visible light using PVP-capped ZnS and CdS nanoparticles. Solar Energy 2013;97:147–54. https://doi.org/10.1016/j.solener.2013.08.023.

[21] Kang Y, Yang Y, Yin LC, Kang X, Wang L, Liu G, et al. Selective breaking of hydrogen bonds of layered carbon nitride for visible light Photocatalysis. Adv Mater 2016;28:6471–7. https://doi.org/10.1002/adma.201601567.

[22] Kibria MG, Chowdhury FA, Zhao S, AlOtaibi B, Trudeau ML, Guo H, et al. Visible light-driven efficient overall water splitting using p-type metal-nitride nanowire arrays. Nat Commun 2015;6. https://doi.org/10.1038/ncomms7797.

[23] Thongam DD, Gupta J, Sahu NK, Bahadur D. Investigating the role of different reducing agents, molar ratios, and synthesis medium over the formation of ZnO nanostructures and their photocatalytic activity. J Mater Sci 2018;53:1110–22. https://doi.org/10.1007/s10853-017-1587-3.

[24] Gupta J, Bhargava P, Bahadur D. Morphology dependent photocatalytic and magnetic properties of ZnO nanostructures. Phys B Condens Matter 2014;448:16–9. https://doi.org/10.1016/j.physb.2014.03.081.

[25] Xu Y, Li H, Sun B, Qiao P, Ren L, Tian G, et al. Surface oxygen vacancy defect-promoted electron-hole separation for porous defective ZnO hexagonal plates and enhanced solar-driven photocatalytic performance. Chem Eng J 2020;379. https://doi.org/10.1016/j.cej.2019.122295.

[26] Singh J, Juneja S, Palsaniya S, Manna AK, Soni RK, Bhattacharya J. Evidence of oxygen defects mediated enhanced photocatalytic and antibacterial performance of ZnO nanorods. Colloids Surf B Biointerfaces 2019;184. https://doi.org/10.1016/j.colsurfb.2019.110541.

[27] Morgan BJ, Watson GW. Polaronic trapping of electrons and holes by native defects in anatase TiO_2. Phys Rev B: Condens Matter Mater Phys 2009;80. https://doi.org/10.1103/PhysRevB.80.233102.

[28] Pei Z, Weng S, Liu P. Enhanced photocatalytic activity by bulk trapping and spatial separation of charge carriers: a case study of defect and facet mediated TiO_2. Appl Catal Environ 2016;180:463–70. https://doi.org/10.1016/j.apcatb.2015.06.045.

[29] Wang S, Pan L, Song JJ, Mi W, Zou JJ, Wang L, et al. Titanium-defected undoped anatase TiO_2 with p-type conductivity, room-temperature ferromagnetism, and remarkable photocatalytic performance. J Am Chem Soc 2015;137:2975–83. https://doi.org/10.1021/ja512047k.

[30] Bai X, Sun B, Wang X, Zhang T, Hao Q, Ni BJ, et al. Defective crystal plane-oriented induced lattice polarization for the photocatalytic enhancement of ZnO. CrstEngComm 2020;22:2709–17. https://doi.org/10.1039/c9ce01966a.

[31] Chen J, Wu G, Wang T, Li X, Li M, Sang Y, et al. Carrier step-by-step transport initiated by precise defect distribution engineering for efficient photocatalytic hydrogen generation. ACS Appl Mater Interfaces 2017;9:4634–42. https://doi.org/10.1021/acsami.6b14700.

[32] Gurylev V, Su CY, Perng TP. Surface reconstruction, oxygen vacancy distribution and photocatalytic activity of hydrogenated titanium oxide thin film. J Catal 2015;330:177–86. https://doi.org/10.1016/j.jcat.2015.07.016.

[33] Choudhury B, Chetri P, Choudhury A. Oxygen defects and formation of Ce^{3+} affecting the photocatalytic performance of CeO_2 nanoparticles. RSC Adv 2014;4:4663–71. https://doi.org/10.1039/c3ra44603d.

[34] Dong J, Han J, Liu Y, Nakajima A, Matsushita S, Wei S, et al. Defective black TiO_2 synthesized via anodization for visible-light photocatalysis. ACS Appl Mater Interfaces 2014;6:1385–8. https://doi.org/10.1021/am405549p.

[35] Hao X, Wang Y, Zhou J, Cui Z, Wang Y, Zou Z. Zinc vacancy-promoted photocatalytic activity and photostability of ZnS for efficient visible-light-driven hydrogen evolution. Appl Catal Environ 2018;221:302–11. https://doi.org/10.1016/j.apcatb.2017.09.006.

https://www.twirpx.org & http://chemistry-chemists.com

[36] Aggelopoulos CA, Dimitropoulos M, Govatsi A, Sygellou L, Tsakiroglou CD, Yannopoulos SN. Influence of the surface-to-bulk defects ratio of ZnO and TiO_2 on their UV-mediated photocatalytic activity. Appl Catal Environ 2017;205:292–301. https://doi.org/10.1016/j.apcatb.2016.12.023.

[37] Wu Z, Cao S, Zhang C, Piao L. Effects of bulk and surface defects on the photocatalytic performance of size-controlled TiO_2 nanoparticles. Nanotechnology 2017;28. https://doi.org/10.1088/1361-6528/aa7374.

[38] Kong M, Li Y, Chen X, Tian T, Fang P, Zheng F, et al. Tuning the relative concentration ratio of bulk defects to surface defects in TiO_2 nanocrystals leads to high photocatalytic efficiency. J Am Chem Soc 2011;133:16414–7. https://doi.org/10.1021/ja207826q.

[39] Xin X, Xu T, Yin J, Wang L, Wang C. Management on the location and concentration of Ti^{3+} in anatase TiO_2 for defects-induced visible-light photocatalysis. Appl Catal Environ 2015;176–177:354–62. https://doi.org/10.1016/j.apcatb.2015.04.016.

[40] Basavarajappa PS, Patil SB, Ganganagappa N, Reddy KR, Raghu AV, Reddy CV. Recent progress in metal-doped TiO_2, non-metal doped/codoped TiO_2 and TiO_2 nanostructured hybrids for enhanced photocatalysis. Int J Hydrogen Energy 2020;45:7764–78. https://doi.org/10.1016/j.ijhydene.2019.07.241.

[41] Das A, Sahoo RK, Kumar Mishra D, Singh SK, Mane RS, Kim KH. Thermal plasma-inspired synthesis of $ZnO_{1-X}Mn_x$ dilute magnetic semiconductors for enhanced visible light photocatalysis. Appl Surf Sci 2019;467–468:1059–69. https://doi.org/10.1016/j.apsusc.2018.10.235.

[42] Peng Z, Wu H, Gu L, Li J, Si W, Ou G, et al. Aerodynamic levitated laser annealing method to defective titanium dioxide with enhanced photocatalytic performance. Nano Res 2016;9:3839–47. https://doi.org/10.1007/s12274-016-1253-0.

[43] Ning D, Wei H, Ou G, Zhang R, Wu H. Copper reduced defective TiO_2 nanoparticles with enhanced visible light photocatalytic activity. J Am Ceram Soc 2018;101:4857–63. https://doi.org/10.1111/jace.15808.

[44] Sun S, Wu H, Zhang A, Wang H, Wei H, Ou G, et al. Room temperature Mg reduction of TiO_2: formation mechanism and application in photocatalysis. Chem Commun 2019;55:7675–8. https://doi.org/10.1039/c9cc03396c.

[45] Jiang M, Yang C, Lin T, Yin H, Chen P, Wan D, et al. Visible-light photocatalytic, solar thermal and photoelectrochemical properties of aluminium-reduced black titania. Energy Environ Sci 2013;6:3007–14. https://doi.org/10.1039/c3ee41817k.

[46] Gondal MA, Ilyas AM, Baig U. Pulsed laser ablation in liquid synthesis of ZnO/TiO_2 nanocomposite catalyst with enhanced photovoltaic and photocatalytic performance. Ceram Int 2016;42:13151–60. https://doi.org/10.1016/j.ceramint.2016.05.104.

[47] Wang C, Yang J, Li T, Shen Z, Guo T, Zhang H, et al. In situ tuning of defects and phase transition in titanium dioxide by Lithiothermic reduction. ACS Appl Mater Interfaces 2020;12:5750–8. https://doi.org/10.1021/acsami.9b18359.

[48] Ariyanti D, Mills L, Dong J, Yao Y, Gao W. $NaBH_4$ modified TiO_2: defect site enhancement related to its photocatalytic activity. Mater Chem Phys 2017;199:571–6. https://doi.org/10.1016/j.matchemphys.2017.07.054.

[49] Yu Y, Ma K, Zhuang R, Wu K, Liao Q, Zhong S, et al. Hydroxyl-mediated formation of highly dispersed SnO_2/TiO_2 heterojunction via pulsed chemical vapor deposition to enhance photocatalytic activity. Ind Eng Chem Res 2019;58:14655–63. https://doi.org/10.1021/acs.iecr.9b02360.

[50] Ye K, Li K, Lu Y, Guo Z, Ni N, Liu H, et al. An overview of advanced methods for the characterization of oxygen vacancies in materials. TrAC - Trends Anal Chem 2019;116:102–8. https://doi.org/10.1016/j.trac.2019.05.002.

[51] Lu B, Wang X, Li L, Du Y, Chen W, Liu Y. Direct spectroscopic evidence on the photocatalytic activities of different ZnO crystal facets toward photo-induced decomposition of CH_2O. Appl Surf Sci 2019;478:62–7. https://doi.org/10.1016/j.apsusc.2019.01.152.

https://www.twirpx.org & http://chemistry-chemists.com

[52] Sarkar A, Khan GG. The formation and detection techniques of oxygen vacancies in titanium oxide-based nanostructures. Nanoscale 2019;11:3414–44. https://doi.org/10.1039/c8nr09666j.

[53] Nellist PD. Electron-optical sectioning for three-dimensional imaging of crystal defect structures. Mater Sci Semicond Process 2017;65:18–23. https://doi.org/10.1016/j.mssp.2016.09.041.

[54] Schaub R, Thostrup P, Lopez N, Lagsgaard E, Stensgaard I, Nurskov JK, et al. Oxygen vacancies as active sites for water dissociation on rutile TiO2(110). Phys Rev Lett 2001;87:2661041–4.

[55] Zhou W, Sun F, Pan K, Tian G, Jiang B, Ren Z, et al. Well-ordered large-pore mesoporous anatase TiO_2 with remarkably high thermal stability and improved crystallinity: preparation, characterization, and photocatalytic performance. Adv Funct Mater 2011;21:1922–30. https://doi.org/10.1002/adfm.201002535.

[56] Banerjee B, Amoli V, Maurya A, Sinha AK, Bhaumik A. Green synthesis of Pt-doped TiO_2 nanocrystals with exposed (001) facets and mesoscopic void space for photo-splitting of water under solar irradiation. Nanoscale 2015;7:10504–12. https://doi.org/10.1039/c5nr02097b.

[57] Kumari V, Patra AK, Bhaumik A. Self-assembled ultra-small zinc stannate nanocrystals with mesoscopic voids via a salicylate templating pathway and their photocatalytic properties. RSC Adv 2014;4:13626–34. https://doi.org/10.1039/c4ra00251b.

[58] Dong G, Chen D, Luo J, Zhu Y, Zeng Y, Wang C. Voids padding induced further enhancement in photocatalytic performance of porous graphene-like carbon nitride. J Hazard Mater 2017;335:66–74. https://doi.org/10.1016/j.jhazmat.2017.04.033.

[59] Ren P, Song M, Lee J, Zheng J, Lu Z, Engelhard M, et al. Edge dislocations induce improved photocatalytic efficiency of colored TiO_2. Adv Mater Interfaces 2019;6. https://doi.org/10.1002/admi.201901121.

[60] Nishikawa M, Yuto S, Nakajima T, Tsuchiya T, Saito N. Effect of lattice distortion on photocatalytic performance of TiO_2. Catal Lett 2017;147:292–300. https://doi.org/10.1007/s10562-016-1928-x.

[61] Lin L, Huang J, Li X, Abass MA, Zhang S. Effective surface disorder engineering of metal oxide nanocrystals for improved photocatalysis. Appl Catal Environ 2017;203:615–24. https://doi.org/10.1016/j.apcatb.2016.10.054.

[62] Fan C, Yu S, Qian G, Wang Z. Ultrasonic-induced disorder engineering on ZnO, ZrO_2, Fe_2O_3 and SnO_2 nanocrystals. RSC Adv 2017;7:18785–92. https://doi.org/10.1039/c7ra01209h.

[63] Folger A, Ebbinghaus P, Erbe A, Scheu C. Role of vacancy condensation in the formation of voids in rutile TiO_2 nanowires. ACS Appl Mater Interfaces 2017;9:13471–9. https://doi.org/10.1021/acsami.7b01160.

[64] Jiao S, Fu X, Zhang L, Zeng YJ, Huang H. Point-defect-optimized electron distribution for enhanced electrocatalysis: towards the perfection of the imperfections. Nano Today 2020;31. https://doi.org/10.1016/j.nantod.2019.100833.

[65] Chen Q, Wang H, Wang C, Guan R, Duan R, Fang Y, et al. Activation of molecular oxygen in selectively photocatalytic organic conversion upon defective TiO_2 nanosheets with boosted separation of charge carriers. Appl Catal Environ 2020;262. https://doi.org/10.1016/j.apcatb.2019.118258.

[66] Etacheri V, Di Valentin C, Schneider J, Bahnemann D, Pillai SC. Visible-light activation of TiO_2 photocatalysts: advances in theory and experiments. J Photochem Photobiol C Photchem Rev 2015;25:1–29. https://doi.org/10.1016/j.jphotochemrev.2015.08.003.

[67] Han L, Su B, Liu G, Ma Z, An X. Synthesis of oxygen vacancy-rich black TiO_2 nanoparticles and the visible light photocatalytic performance. Mol Catal 2018;456:96–101. https://doi.org/10.1016/j.mcat.2018.07.006.

[68] Cao Y, Huang L, Bai Y, Jermsittiparsert K, Hosseinzadeh R, Rasoulnezhad H, et al. Synergic effect of oxygen vacancy defect and shape on the photocatalytic performance of nanostructured TiO_2 coating. Polyhedron 2020;175. https://doi.org/10.1016/j.poly.2019.114214.

https://www.twirpx.org & http://chemistry-chemists.com

[69] Hezam A, Namratha K, Drmosh QA, Ponnamma D, Wang J, Prasad S, et al. CeO_2 nanostructures enriched with oxygen vacancies for photocatalytic CO_2 reduction. ACS Appl Nano Mater 2020;3:138–48. https://doi.org/10.1021/acsanm.9b01833.

[70] Li Y, Tang Z, Zhang J, Zhang Z. Defect engineering of air-treated WO_3 and its enhanced visible-light-driven photocatalytic and electrochemical performance. J Phys Chem C 2016;120:9750–63. https://doi.org/10.1021/acs.jpcc.6b00457.

[71] Zarubica A, Ljupković R, Papan J, Vukoje I, Porobić S, Ahrenkiel SP, et al. Visible-light-responsive Al_2O_3 powder: photocatalytic study. Opt Mater 2020;106. https://doi.org/10.1016/j.optmat.2020.110013.

[72] Zhao ZC, Yang CL, Meng QT, Wang MS, Ma XG. Photocatalytic hydrogen production from water splitting with N-doped β-Ga_2O_3 and visible light. Spectrochim Acta A Mol Biomol Spectrosc 2019;211:71–8. https://doi.org/10.1016/j.saa.2018.11.039.

[73] Yu X, Li W, Li Z, Liu J, Hu P. Defect engineered Ta_2O_5 nanorod: one-pot synthesis, visible-light driven hydrogen generation and mechanism. Appl Catal Environ 2017;217:48–56. https://doi.org/10.1016/j.apcatb.2017.05.024.

[74] Wang S, Chen D, Niu F, Zhang N, Qin L, Huang Y. Hydrogenation-induced surface oxygen vacancies in $BiFeO_3$ nanoparticles for enhanced visible light photocatalytic performance. J Alloys Compd 2016;688:399–406. https://doi.org/10.1016/j.jallcom.2016.07.076.

[75] Xia W, Wang Y, Wang Q, Yan Y, Jiang Y. Tubular acceptor-rich ZnO hierarchical heterostructure as an efficient photocatalyst for organic degradation. Appl Surf Sci 2020;506. https://doi.org/10.1016/j.apsusc.2019.145008.

[76] Wu D, Wang W, Tan F, Sun F, Lu H, Qiao X. Fabrication of pit-structured ZnO nanorods and their enhanced photocatalytic performance. RSC Adv 2013;3:20054–9. https://doi.org/10.1039/c3ra42874e.

[77] Wang X, Zhao Y, Li F, Dou L, Li Y, Zhao J, et al. A Chelation Strategy for In-situ Constructing Surface Oxygen Vacancy on {001} Facets Exposed BiOBr Nanosheets. Sci Rep 2016;6.

[78] Tong X, Cao X, Han T, Cheong WC, Lin R, Chen Z, et al. Convenient fabrication of BiOBr ultrathin nanosheets with rich oxygen vacancies for photocatalytic selective oxidation of secondary amines. Nano Res 2019;12:1625–30. https://doi.org/10.1007/s12274-018-2404-x.

[79] Guo SQ, Zhu XH, Zhang HJ, Gu BC, Chen W, Liu L, et al. Improving photocatalytic water treatment through nanocrystal engineering: mesoporous Nanosheet-assembled 3D BiOCl hierarchical nanostructures that induce unprecedented large vacancies. Environ Sci Tech 2018;52:6872–80. https://doi.org/10.1021/acs.est.8b00352.

[80] Motola M, Čaplovičová M, Krbal M, Sopha H, Thirunavukkarasu GK, Gregor M, et al. Ti^{3+} doped anodic single-wall TiO_2 nanotubes as highly efficient photocatalyst. Electrochim Acta 2020;331. https://doi.org/10.1016/j.electacta.2019.135374.

[81] Fang W, Dappozze F, Guillard C, Zhou Y, Xing M, Mishra S, et al. Zn-assisted TiO_{2-x} Photocatalyst with efficient charge separation for enhanced photocatalytic activities. J Phys Chem C 2017;121:17068–76. https://doi.org/10.1021/acs.jpcc.7b03724.

[82] Yang K, Li D-F, Huang W-Q, Xu L, Huang G-F, Wen S. Origin of enhanced visible-light photocatalytic activity of transition-metal (Fe, Cr and Co)-doped CeO_2: effect of 3d orbital splitting. Appl Phys A 2016;123.

[83] Takata T, Domen K. Defect engineering of photocatalysts by doping of aliovalent metal cations for efficient water splitting. J Phys Chem C 2009;113:19386–8. https://doi.org/10.1021/jp908621e.

[84] Qi K, Xing X, Zada A, Li M, Wang Q, Liu Sy, et al. Transition metal doped ZnO nanoparticles with enhanced photocatalytic and antibacterial performances: experimental and DFT studies. Ceram Int 2020;46:1494–502. https://doi.org/10.1016/j.ceramint.2019.09.116.

https://www.twirpx.org & http://chemistry-chemists.com

[85] Zhang D, Chen J, Xiang Q, Li Y, Liu M, Liao Y. Transition-metal-ion (Fe, Co, Cr, Mn, Etc.) doping of TiO_2 nanotubes: a general approach. Inorg Chem 2019;58:12511–5. https://doi.org/10.1021/acs.inorgchem.9b01889.

[86] Li J, Niu L, He X. Enhanced visible-light activity of Ti_{3+} self-doped TiO_2 with co-exposed (001) and (101) facets. Micro Nano Lett 2018;13:514–7. https://doi.org/10.1049/mnl.2017.0642.

[87] Zhang Y, Xing Z, Liu X, Li Z, Wu X, Jiang J, et al. Ti^{3+} self-doped blue TiO_2(B) single-crystalline nanorods for efficient solar-driven photocatalytic performance. ACS Appl Mater Interfaces 2016;8:26851–9. https://doi.org/10.1021/acsami.6b09061.

[88] Xiu Z, Guo M, Zhao T, Pan K, Xing Z, Li Z, et al. Recent advances in Ti^{3+} self-doped nanostructured TiO_2 visible light photocatalysts for environmental and energy applications. Chem Eng J 2020;382. https://doi.org/10.1016/j.cej.2019.123011.

[89] Gomes LE, Da Silva MF, Gonçalves RV, MacHado G, Alcantara GB, Caires ARL, et al. Synthesis and visible-light-driven photocatalytic activity of Ta^{4+} self-doped gray Ta_2O_5 nanoparticles. J Phys Chem C 2018;122:6014–25. https://doi.org/10.1021/acs.jpcc.7b11822.

[90] Liu S, Yuan S, Zhang Q, Xu B, Wang C, Zhang M, et al. Fabrication and characterization of black TiO_2 with different Ti^{3+} concentrations under atmospheric conditions. J Catal 2018;366:282–8. https://doi.org/10.1016/j.jcat.2018.07.018.

[91] Tian J, Leng Y, Cui H, Liu H. Hydrogenated TiO_2 nanobelts as highly efficient photocatalytic organic dye degradation and hydrogen evolution photocatalyst. J Hazard Mater 2015;299:165–73. https://doi.org/10.1016/j.jhazmat.2015.06.019.

[92] Shang M, Hu H, Lu G, Bi Y. Synergistic effects of $SrTiO_3$ nanocubes and Ti^{3+} dual-doping for highly improved photoelectrochemical performance of TiO_2 nanotube arrays under visible light. J Mater Chem A 2016;4:5849–53. https://doi.org/10.1039/c6ta00033a.

[93] Chen H, Zhang F, Zhang W, Du Y, Li G. Negative impact of surface Ti^{3+} defects on the photocatalytic hydrogen evolution activity of $SrTiO_3$. Appl Phys Lett 2018;112. https://doi.org/10.1063/1.5009321.

[94] Zhu S, Zhang Y, Qian X, Wang X, Su W. Zn defect-mediated Z-scheme electron-hole separation in $AgIn_5S_8$/ZnS heterojunction for enhanced visible-light photocatalytic hydrogen evolution. Appl Surf Sci 2020;504. https://doi.org/10.1016/j.apsusc.2019.144396.

[95] Hao X, Zhou J, Cui Z, Wang Y, Wang Y, Zou Z. Zn-vacancy mediated electron-hole separation in ZnS/g-C_3N_4 heterojunction for efficient visible-light photocatalytic hydrogen production. Appl Catal Environ 2018;229:41–51. https://doi.org/10.1016/j.apcatb.2018.02.006.

[96] Khan H, Swati IK. Fe^{3+}−doped Anatase TiO_2 with d-d transition, oxygen vacancies and Ti^{3+} centers: synthesis, characterization, UV-vis photocatalytic and mechanistic studies. Ind Eng Chem Res 2016;55:6619–33. https://doi.org/10.1021/acs.iecr.6b01104.

[97] Suganthi N, Pushpanathan K. Photocatalytic degradation and antimicrobial activity of transition metal doped mesoporous ZnS nanoparticles. Int J Environ Sci Technol 2019;16:3375–88. https://doi.org/10.1007/s13762-018-1811-y.

[98] Qi Y, Ye J, Zhang S, Tian Q, Xu N, Tian P, et al. Controllable synthesis of transition metal ion-doped CeO_2 micro/nanostructures for improving photocatalytic performance. J Alloys Compd 2019;782:780–8. https://doi.org/10.1016/j.jallcom.2018.12.111.

[99] Man HW, Tsang CS, Li MMJ, Mo J, Huang B, Lee LYS, et al. Transition metal-doped nickel phosphide nanoparticles as electro- and photocatalysts for hydrogen generation reactions. Appl Catal Environ 2019;242:186–93. https://doi.org/10.1016/j.apcatb.2018.09.103.

[100] Jiang Z, Liu Y, Jing T, Huang B, Zhang X, Qin X, et al. Enhancing the photocatalytic activity of $BiVO_4$ for oxygen evolution by Ce doping: Ce^{3+} ions as hole traps. J Phys Chem C 2016;120:2058–63. https://doi.org/10.1021/acs.jpcc.5b10856.

[101] Dai Z, Qin F, Zhao H, Ding J, Liu Y, Chen R. Crystal defect engineering of Aurivillius Bi_2MoO_6 by Ce doping for increased reactive species production in Photocatalysis. ACS Catal 2016;6:3180–92. https://doi.org/10.1021/acscatal.6b00490.

https://www.twirpx.org & http://chemistry-chemists.com

[102] Du M, Chen Q, Wang Y, Hu J, Meng X. Synchronous construction of oxygen vacancies and phase junction in TiO_2 hierarchical structure for enhancement of visible light photocatalytic activity. J Alloys Compd 2020;830. https://doi.org/10.1016/j.jallcom.2020.154649.

[103] Di J, Xia J, Li X, Ji M, Xu H, Chen Z, et al. Constructing confined surface carbon defects in ultrathin graphitic carbon nitride for photocatalytic free radical manipulation. Carbon 2016;107:1–10. https://doi.org/10.1016/j.carbon.2016.05.028.

[104] Liang Q, Li Z, Huang ZH, Kang F, Yang QH. Holey graphitic carbon nitride Nanosheets with carbon vacancies for highly improved photocatalytic hydrogen production. Adv Funct Mater 2015;25:6885–92. https://doi.org/10.1002/adfm.201503221.

[105] Ding J, Xu W, Wan H, Yuan D, Chen C, Wang L, et al. Nitrogen vacancy engineered graphitic C_3N_4-based polymers for photocatalytic oxidation of aromatic alcohols to aldehydes. Appl Catal Environ 2018;221:626–34. https://doi.org/10.1016/j.apcatb.2017.09.048.

[106] Niu P, Liu G, Cheng HM. Nitrogen vacancy-promoted photocatalytic activity of graphitic carbon nitride. J Phys Chem C 2012;116:11013–8. https://doi.org/10.1021/jp301026y.

[107] Huang T, Pan S, Shi L, Yu A, Wang X, Fu Y. Hollow porous prismatic graphitic carbon nitride with nitrogen vacancies and oxygen doping: a high-performance visible light-driven catalyst for nitrogen fixation. Nanoscale 2020;12:1833–41. https://doi.org/10.1039/c9nr08705b.

[108] Hong Z, Shen B, Chen Y, Lin B, Gao B. Enhancement of photocatalytic H_2 evolution over nitrogen-deficient graphitic carbon nitride. J Mater Chem A 2013;1:11754–61. https://doi.org/10.1039/c3ta12332d.

[109] Blum V, Lotsch BV, Ehrat F, Botari T, Moudrakovski I, Simon T, et al. Urea-modified carbon nitrides: enhancing photocatalytic hydrogen evolution by rational defect engineering. Adv Energy Mater 2017;7. https://doi.org/10.1002/aenm.201602251.

[110] Wu M, Gong Y, Nie T, Zhang J, Wang R, Wang H, et al. Template-free synthesis of nanocage-like g-C_3N_4 with high surface area and nitrogen defects for enhanced photocatalytic H_2 activity. J Mater Chem A 2019;7:5324–32. https://doi.org/10.1039/c8ta12076e.

[111] Dong G, Ho W, Wang C. Selective photocatalytic N_2 fixation dependent on g-C_3N_4 induced by nitrogen vacancies. J Mater Chem A 2015;3:23435–41. https://doi.org/10.1039/c5ta06540b.

[112] Jiang Y, Sun Z, Tang C, Zhou Y, Zeng L, Huang L. Enhancement of photocatalytic hydrogen evolution activity of porous oxygen doped g-C_3N_4 with nitrogen defects induced by changing electron transition. Appl Catal Environ 2019;240:30–8. https://doi.org/10.1016/j.apcatb.2018.08.059.

[113] Zhang J, Zhang M, Yang C, Wang X. Nanospherical carbon nitride frameworks with sharp edges accelerating charge collection and separation at a soft photocatalytic interface. Adv Mater 2014;26:4121–6. https://doi.org/10.1002/adma.201400573.

[114] Wang Y, Chen D, Qin L, Liang J, Huang Y. Hydrogenated $ZnIn_2S_4$ microspheres: boosting photocatalytic hydrogen evolution by sulfur vacancy engineering and mechanism insight. Phys Chem Chem Phys 2019;21:25484–94. https://doi.org/10.1039/c9cp04709c.

[115] An X, Li T, Wen B, Tang J, Hu Z, Liu L-M, et al. New insights into defect-mediated heterostructures for photoelectrochemical water splitting. Adv Energy Mater 2016;6.

[116] Tang J, Liu Y, Hu Y, Lv G, Yang C, Yang G. Carbothermal reduction induced Ti^{3+} self-doped TiO_2/GQD nanohybrids for high-performance visible light photocatalysis. Chem A Eur J 2018;24:4390–8. https://doi.org/10.1002/chem.201705637.

[117] Yang L, Xu L, Bai X, Jin P. Enhanced visible-light activation of persulfate by Ti^{3+} self-doped TiO_2/graphene nanocomposite for the rapid and efficient degradation of micropollutants in water. J Hazard Mater 2019;365:107–17. https://doi.org/10.1016/j.jhazmat.2018.10.090.

[118] Tan B, Ye X, Li Y, Ma X, Wang Y, Ye J. Defective anatase TiO_{2-x} mesocrystal growth in situ on g-C_3N_4 nanosheets: construction of 3D/2D Z-scheme heterostructures for highly efficient visible-light photocatalysis. Chem A Eur J 2018;24:13311–21. https://doi.org/10.1002/chem.201802366.

https://www.twirpx.org & http://chemistry-chemists.com

[119] Xue J, Fujitsuka M, Majima T. Shallow trap state-induced efficient Electron transfer at the Interface of heterojunction Photocatalysts: the crucial role of vacancy defects. ACS Appl Mater Interfaces 2019;11:40860–7. https://doi.org/10.1021/acsami.9b14128.

[120] Khan ME, Khan MM, Cho MH. Ce^{3+}−ion, surface oxygen vacancy, and visible light-induced photocatalytic dye degradation and photocapacitive performance of CeO_2-graphene nanostructures. Sci Rep 2017;7. https://doi.org/10.1038/s41598-017-06139-6.

[121] Tang L, Chen R, Meng X, Lv B, Fan F, Ye J, et al. Unique homo-heterojunction synergistic system consisting of stacked BiOCl nanoplate/Zn-Cr layered double hydroxide nanosheets promoting photocatalytic conversion of CO_2 into solar fuels. Chem Commun 2018;54:5126–9. https://doi.org/10.1039/c8cc01873a.

[122] Prakash A, Singh S, Gupta J, Bahadur D. Highly efficient zinc oxide-reduced graphene oxide nanohybrids for photocatalytic degradation of dye under dark and UV light. Mater Res Express 2020;6.

[123] Ahmed G, Hanif M, Zhao L, Hussain M, Khan J, Liu Z. Defect engineering of ZnO nanoparticles by graphene oxide leading to enhanced visible light photocatalysis. J Mol Catal A Chem 2016;425:310–21. https://doi.org/10.1016/j.molcata.2016.10.026.

[124] Lu D, Wang H, Zhao X, Kondamareddy KK, Ding J, Li C, et al. Highly efficient visible-light-induced photoactivity of Z-scheme g-C_3N_4/Ag/MoS_2 ternary photocatalysts for organic pollutant degradation and production of hydrogen. ACS Sustain Chem Eng 2017;5:1436–45. https://doi.org/10.1021/acssuschemeng.6b02010.

[125] Guan M, Xiao C, Zhang J, Fan S, An R, Cheng Q, et al. Vacancy associates promoting solar-driven photocatalytic activity of ultrathin bismuth oxychloride nanosheets. J Am Chem Soc 2013;135:10411–7. https://doi.org/10.1021/ja402956f.

[126] Zhang G, Hu Z, Sun M, Liu Y, Liu L, Liu H, et al. Formation of Bi_2WO_6 bipyramids with vacancy pairs for enhanced solar-driven photoactivity. Adv Funct Mater 2015;25:3726–34. https://doi.org/10.1002/adfm.201501009.

[127] Zhang L, Shi Y, Wang Z, Hu C, Shi B, Cao X. Porous β-Bi_2O_3 with multiple vacancy associates on highly exposed active {220} facets for enhanced photocatalytic activity. Appl Catal Environ 2020;265. https://doi.org/10.1016/j.apcatb.2019.118563.

[128] Loh KP, Pennycook SJ, Li H, Liu Z, Xia J, Xiong J, et al. Atomically-thin Bi_2MoO_6 nanosheets with vacancy pairs for improved photocatalytic CO_2 reduction. Nano Energy 2019;61:54–9. https://doi.org/10.1016/j.nanoen.2019.04.029.

[129] Li J, Wu X, Pan W, Zhang G, Chen H. Vacancy-rich monolayer BiO_{2-x} as a highly efficient UV, visible, and near-infrared responsive Photocatalyst. Angew Chem Int Ed 2018;57:491–5. https://doi.org/10.1002/anie.201708709.

[130] Hammer B, Besenbacher F, Matthiesen J, Vestergaard EK, Wahlström E, Rasmussen MD, et al. Oxygen vacancies on TiO_2(110) and their interaction with H_2O and O_2: a combined high-resolution STM and DFT study. Surf Sci 2005;598:226–45. https://doi.org/10.1016/j.susc.2005.08.041.

https://www.twirpx.org & http://chemistry-chemists.com

13

Facet-dependent nanostructures for visible light photocatalysis

Abhaya Kumar Mishra[a] and Arpan Kumar Nayak[b]

[a]MATERIALS SCIENCE CENTRE, INDIAN INSTITUTE OF TECHNOLOGY, KHARAGPUR, WEST BENGAL, INDIA [b]DEPARTMENT OF PHYSICS, SCHOOL OF ADVANCED SCIENCES, VELLORE INSTITUTE OF TECHNOLOGY, VELLORE, TAMIL NADU, INDIA

1 Introduction

Clean and sustainable renewable technologies must be explored to deal with the rapid increase in the global energy crisis and severe environmental pollution. The development of various photoinduced reaction techniques have been focused on the efficient uses of inexhaustible solar energy in the environmental and energy-related fields [1–3]. The first demonstration of water splitting using TiO_2 as a photoanode under ultraviolet illumination by Fujishima and Honda in 1972, allowed photocatalysis research [4]. Nowadays, semiconductor photocatalysis has gained significant attention for its potential applications in water splitting, CO_2 reduction, nitrogen fixation, and pollutant degradation [5–9]. Semiconductor photocatalysis is a heterogeneous surface phenomenon that involves both catalyst and light to initiate or accelerate the redox reaction [10]. Progress in nanomaterials and nanotechnology has contributed excessively to the field of photocatalysis. The nanostructured photocatalyst has unique properties compared to its bulk form [11], namely: (a) high surface area, which means that more number of active sites will be available for physical and chemical interactions; (b) reduced chance of recombination of photogenerated excitons in bulk because the increase in the surface active sites can efficiently extract the charge carrier to the surface for a later redox reaction; (c) quantum confinement effect influences electronic band structure and optical properties; and (d) anisotropic surface structure that controls both selectivity and reaction kinetics.

In principle, semiconductor photocatalysis involves three major elementary steps, [12] as shown in Fig. 1: (i) light absorption to produce excitation (electrons, holes); (ii) excition (electron-holes), which doesn't trap at a defect in the bulk or recombine transfer to the surface; and (iii) the consumption of the photogenerated electrons and holes in the redox reaction on the catalyst surface.

Thus the efficiency of each step determines the overall solar-to-chemical energy conversion performance of the photocatalyst. More importantly, light sources having energy greater than equal to the semiconductor material bandgap are harvested to induce the photogenerated charge carriers [13]. Titanium dioxides (TiO_2) and zinc oxides (ZnO)

Nanostructured Materials for Visible Light Photocatalysis. https://doi.org/10.1016/B978-0-12-823018-3.00003-8
Copyright © 2022 Elsevier Inc. All rights reserved.

https://www.twirpx.org & http://chemistry-chemists.com

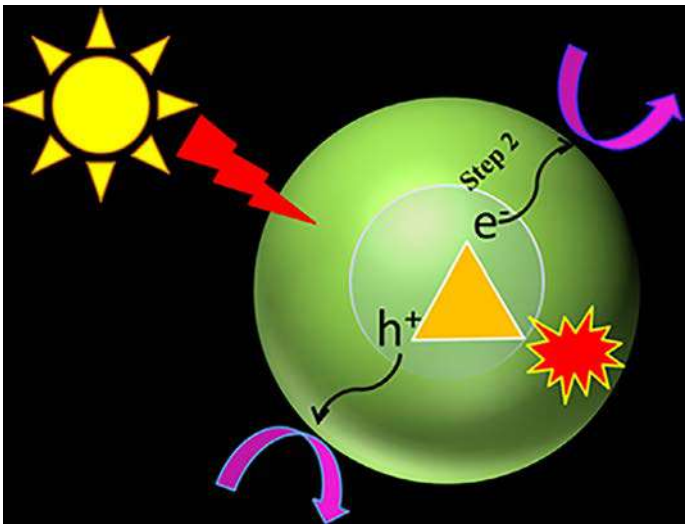

FIG. 1 Schematic representation of the photocatalytic process.

are known as benchmark photocatalysts due to their intrinsic high activity [14, 15]. However, the wide bandgap (E_g) natures of TiO_2 and ZnO (3.2 and 3.4 eV, respectively), and the massive recombination of photoinduced charge carriers hinders their practical application [16]. These materials utilize only ultraviolet (UV) light, which is only 3%–5% of the solar spectrum available for photocatalytic reaction [17]. Hence, it is necessary to explore and develop a new active visible light-induced photocatalytic system for efficient utilization of maximal portions, i.e., 45% of the solar spectrum. Recently, visible light-harvesting semiconductor nanomaterials with well-defined crystal shapes, i.e., exposed facets, have been found to offer greater versatility in enhancing photoactivity and have become a hot topic of research interest. The faceted activities of semiconductor nanomaterials are explained based on the following mechanisms:

- **(i)** The facets exhibit different atomic arrangements and coordination, thus the adsorption and activation energy varies for the reacting molecule, and hence influences catalytic activity and selectivity (Fig. 2A) [18, 19].
- **(ii)** The crystal facets manifest different electronic band structures (i.e., bandgap width and the relative location of the valence band and conduction band (CB)), and therefore furnish different redox abilities of photogenerated charge carrier for catalytic reaction (Fig. 2B) [20].
- **(iii)** Moreover, multifaceted semiconductors show the spatial separation of photogenerated charge carriers. Thus, certain facets of the same nanocrystals prefer oxidation, while other facets favor reduction (Fig. 2C) [21–23].

Roy et al. demonstrated that photogenerated electrons and holes prefer to be accumulated on {101}and {001} exposed crystal facets of TiO_2, respectively [24]. Thus, the variation in

https://www.twirpx.org & http://chemistry-chemists.com

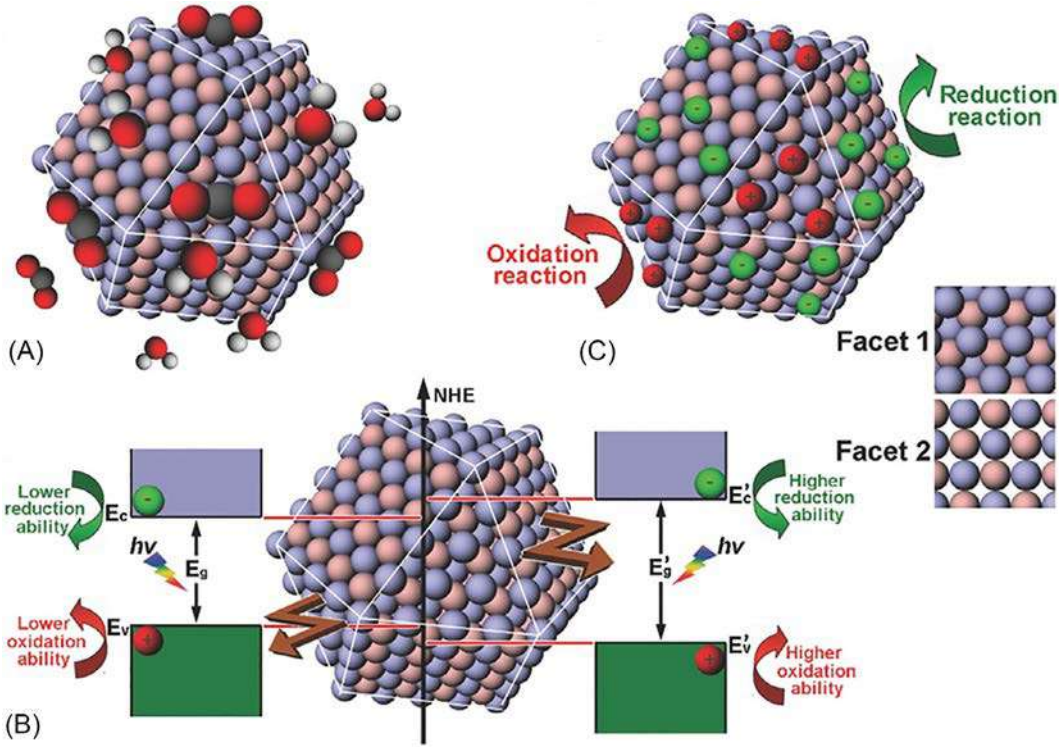

FIG. 2 Schemes show the important roles of the exposed facets in the surface design of photocatalytic materials. (A) Adsorption and activation of reactant molecule on different facets. (B) Redox abilities of photogenerated charge carriers tuned by the surface electronic band structures of different facets. (C) Accumulations of photoinduced charge carriers on different facets. *From Song B, Lili W, Zhengquan L, Yujie X. Facet-engineered surface and interface design of photocatalytic materials. Adv Sci 2017:1600216. https://doi.org/10.1002/advs.201600216.*

photocatalytic activity with different exposed facets of the same material is worth noting and becomes a broad research area for developing better material.

Both bottom-up and top-down strategies have been employed to control the exposed facets of the nanocrystal. The bottom-up approach generally proceeds through solution-based synthesis in which atom-by-atom and/or molecule-by-molecule assembly forms a nanostructure. This process involves two stages: nucleation and the growth of seeds into nanocrystals. In the nucleation stage, building blocks (atoms, ions, or molecules) aggregate into nuclei/cluster through homogeneous nucleation [25]. Then, those nuclei further grow to form larger structures of a particular shape and size. In fact, the final morphology and exposed facets of nanocrystals are influenced by the interplay between the thermodynamic and kinetic factors [26]. When the reaction is under thermodynamic control, the product will be bounded by low-index facets, and the Wulff construction theoretically decides the final equilibrium shape of the crystals [27, 28]. According to this theorem, surface energy minimization is the driving force for the evolution of the crystals' equilibrium facets. Due to anisotropic surface energy, the lower energy facets are usually exposed on

https://www.twirpx.org & http://chemistry-chemists.com

the surface of the natural growth crystals, and facets with high surface energy grow much faster and disappear in the final crystals [18]. However, selective adsorption of a capping agent or stabilizing reagent changes the crystals' growth from the originally favored thermodynamics, and ultimate exposed facets thus can be controlled effectively [29, 30]. On the other hand, the kinetic control condition provides the formation of a metastable nanocrystal shape by tuning the growth rate of various facets during nucleation and growth before the reaction reaches equilibrium. It is also worth noting that kinetic control is an important step for the formation of the high-index facet in which at least one of the Miller indices {*hkl*} is larger than unity [31, 32]. The presence of additives/impurities also controls the growth rate under nonequilibrium conditions, hence bringing out desired exposed facets. The high-index faceted nanocrystals possess a high density of low-coordinated atoms as for example steps, edges, and kinks, becoming a virtual arena in expanding facet-dependent photocatalyst application. For example, Zhang et al. reported that high-index faceted AgCl polyhedrals exhibited much higher photocatalytic activity for organic degradation than octahedral AgCl NCs whose facets mainly exposed {111} [33]. Fig. 3 presents the roles of solvent and impurities/additives on controlling the growth of the crystal facets [19].

This chapter focuses on the facets dependence on visible light-driven photocatalytic activity of metal oxides nanocrystals, i.e., Cu_2O, Fe_2O_3, $BiVO_4$. The role of individual facets and the synergy effect of exposed facets of the nanomaterial toward various photocatalysis reactions are compared and discussed. The dramatic difference in photoactivity of the different distinct facets is correlated with various factors such as surface energy, surface atomic arrangement, and configuration associated with terraces, steps, kinks, and vacancies. Furthermore, we also highlight important points to take into consideration in future research work.

2 Cuprous oxide photocatalysts

Copper(I) oxides (Cu_2O, cuprous oxides) are one of the first known p-type semiconductors, and have recently received great attention as visible light photocatalysts [34, 35]. Besides their well-known merits such as low cost, abundance, nontoxicity, and easy synthesis, the advantageous bandgap energy (1.8–2.2 eV) of Cu_2O crystals has attracted potential as a solar-driven photocatalyst material [36]. Their good visible light absorption coefficient, suitable theoretical conduction, and valence band positions are appropriate for exploring water-splitting reaction, CO_2 reduction, organic dye degradation, and organic molecule transformation [37–40]. The unique physicochemical properties of Cu_2O crystals is influenced by not only crystal size but also the surface geometry (atomic arrangement and coordination), and thus exposed facets of the Cu_2O crystal. So far, Cu_2O crystals with low-index facets such as {110}, {111}, and {100} and high-index facet includes ({211}, {311}, {522}, {332}, {544}, {104}, and {744}) have been reported [41–46]. Cubic, octahedral, and rhombic are the three basic shapes of Cu_2O crystal enclosed by {100}, {111}, and {110} low-index facets, respectively. For example, Mishra et al. reported a simple

https://www.twirpx.org & http://chemistry-chemists.com

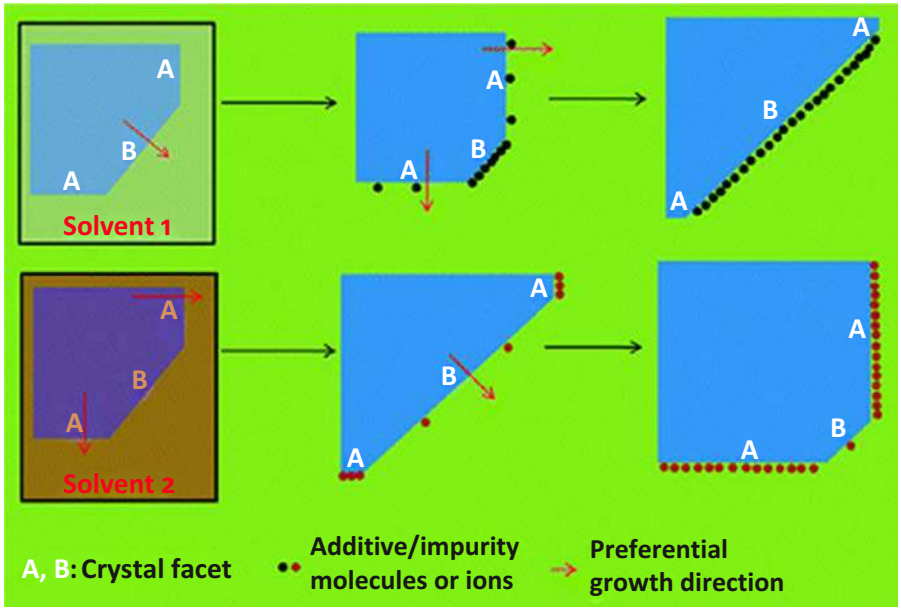

FIG. 3 Schematic of the effect of solvent and additive/impurity molecules or ions on controlling the growth of crystal facets. *From Liu G, Yu J, Lu G, Cheng H. Crystal facet engineering of semiconductor photocatalysts: motivations, advances and unique properties. Chem Commun 2011;47:6763–83. https://doi.org/10.1039/c1cc10665a.*

solution-based synthesis of three different Cu_2O morphology such as octahedra, truncated octahedra, and cubes by varying the reaction temperature to 40°C, 60°C, and 100°C, respectively, while keeping the rest of the experimental parameters fixed (Fig. 4) [47]. It was noted that the octahedron shape of Cu_2O crystals enclosed by eight (111) facets, whereas the truncated octahedra contained six (100) facets and eight (111) facets, and the exposed surfaces of cubes contained six (100) facets.

Fig. 5 presents the unit cell model of cuprous oxides (Cu_2O) cubic crystal structure. In the unit cell, each copper ion is coordinated by two neighboring oxygen ions, and each oxygen ion is located at the center of an ideal tetrahedron encircled by four copper ions [48]. Fig. 6 shows the arrangements of Cu^+ and O^{2-} along the three low-index planes such as {110}, {111}, and {100} [49]. As shown in Fig. 6A, the {110} facets of Cu_2O are constituted by both Cu, and O atoms; however, the Cu atoms are coordinated with unsaturated, forming the positive plane charge. These imply that in the {110} facet Cu atoms are present in two different types of arrangement: (i) a row of two-fold-coordinated; and (ii) one-fold-coordinated with one dangling bond perpendicular to the surface. Similarly, the {111} facet has the same terminated Cu atoms with dangling bonds (Fig. 6B); at the same time, the {111} facets have a lower number of Cu dangling bonds than the {110} facets. The {100} facet (Fig. 6C and D) is predominated with oxygen atoms only, leading to the surface

https://www.twirpx.org & http://chemistry-chemists.com

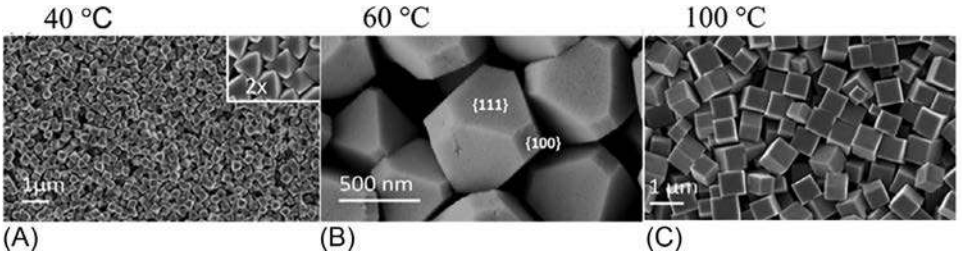

FIG. 4 FESEM images with various shapes of Cu_2O crystals obtained at (A) 40°C, (B) 60°C, and (C) 100°C. *From Kumar MA, Debabrata P. Morphology controlled solution-based synthesis of Cu_2O crystals for the facets-dependent catalytic reduction of highly toxic aqueous Cr(VI). Cryst Growth Design 2016;16:3688–98. https://doi.org/10.1021/acs.cgd.6b00186.*

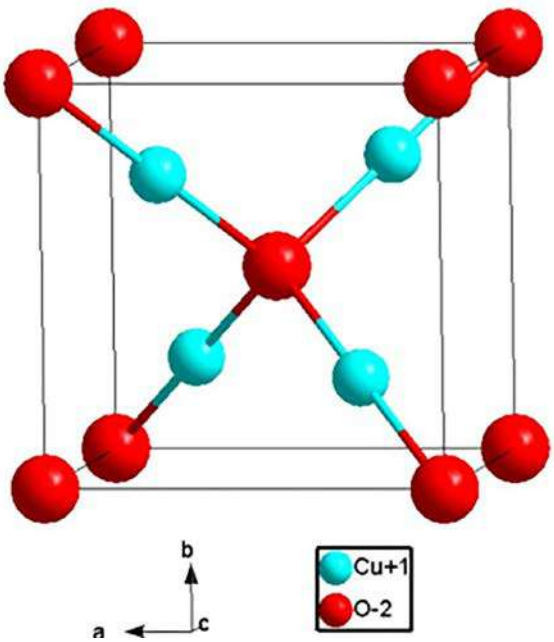

FIG. 5 Unit cell model of Cu_2O crystal. *From Jiasheng X, Dongfeng X. Five branching growth patterns in the cubic crystal system: A direct observation of cuprous oxide microcrystals. Acta Mater 2007;55:2397–406. https://doi.org/10.1016/j.actamat.2006.11.032.*

having a slightly negative or electric neutral state. Thus the relative surface energies of low-index exposed facets of Cu_2O crystals are in the following order: $\gamma\{100\} < \gamma\{111\} < \gamma\{110\}$. Therefore, cuprous oxide with well-defined facets makes it a suitable material to examine structure-function relationships in various photocatalysis reactions [50].

Facet-dependent visible light photocatalytic responses of cuprous oxide (Cu_2O) crystals will be discussed in terms of the photodegradation of major industrial pollutants such as negatively charged methyl orange (MO) and positively charged methyl blue (MB).

https://www.twirpx.org & http://chemistry-chemists.com

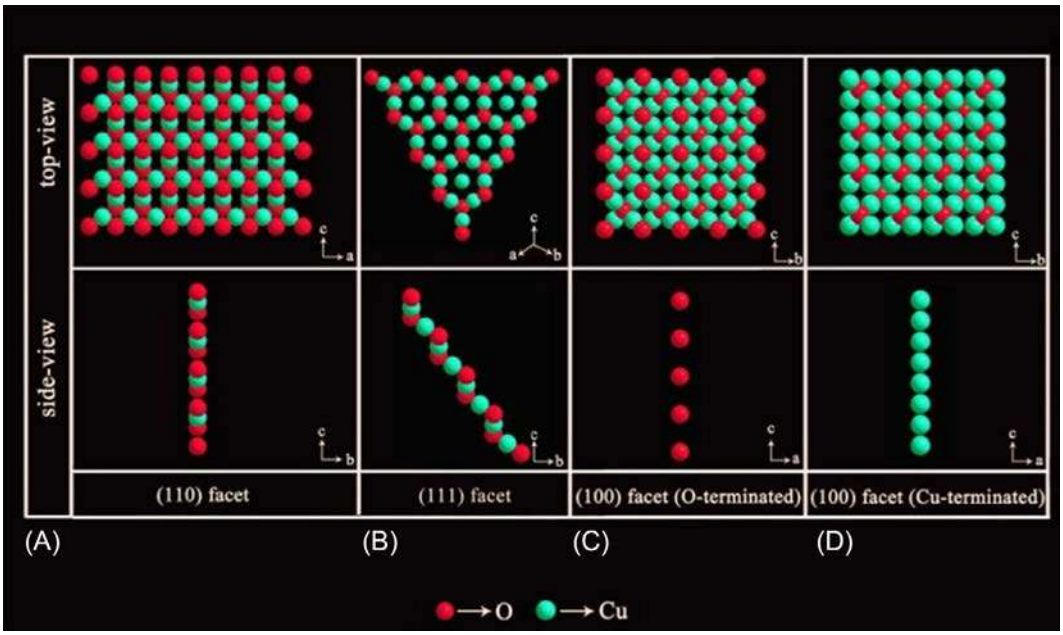

FIG. 6 Illustration of atomic structures of different facets of Cu_2O. (A) {110} facet, (B) {111} facet, and (C, D) {100} facet. *From Shaodong S, Xiaojing Z, Qing Y, Shuhua L, Xiaozhe Z, Zhimao Y. Cuprous oxide (Cu_2O) crystals with tailored architectures: a comprehensive review on synthesis, fundamental properties, functional modifications and applications. Progr Mater Sci 2018;96:111–73. https://doi.org/10.1016/j.pmatsci.2018.03.006.*

Xu et al. synthesized spheres, octahedra, cubes, and shapes of Cu_2O nanocrystals, and demonstrated their facet-dependent photodegradation of negatively charged methyl orange [51]. The exposed {111} facets with octahedral shape show higher activity than Cu_2O cubes with {100} exposed facets. Kuo et al. reported similar results, i.e., octahedral Cu_2O crystals consisting of {111} facets are photocatalytically more active for methyl orange degradation than truncated cubic crystals abundant {100} facets [52]. Ho et al. demonstrated that the extended hexapods Cu_2O with more {111} crystal surface were more effective, even than octahedral shapes (Fig. 7A) [54]. Subsequently, they reported exceptionally high photocatalytic activity of rhombic dodecahedral Cu_2O structures exposing only the {110} facets [55]. The results demonstrated that exposed surface facets were involved in the reaction and influenced the rate of photocatalysis reaction. These effects have been attributed to the electrostatic interaction between the anionic methyl orange molecule and different facet of Cu_2O crystal. As discussed earlier, the {110} crystal facets possess a positive charge. Therefore, the negative MO is easily adsorbed on the surface, and as a result higher photocatalytic activity is observed.

The above discussion clearly demonstrates that the visible light photodegradation activity of Cu_2O for MO depends on the exposed surface facets. On the other hand, all the distinct surface structures of Cu_2O crystal, such as cubes {100}, octahedra {111}, and rhombic dodecahedra {110}, are found to be inactive toward photodegradation of

https://www.twirpx.org & http://chemistry-chemists.com

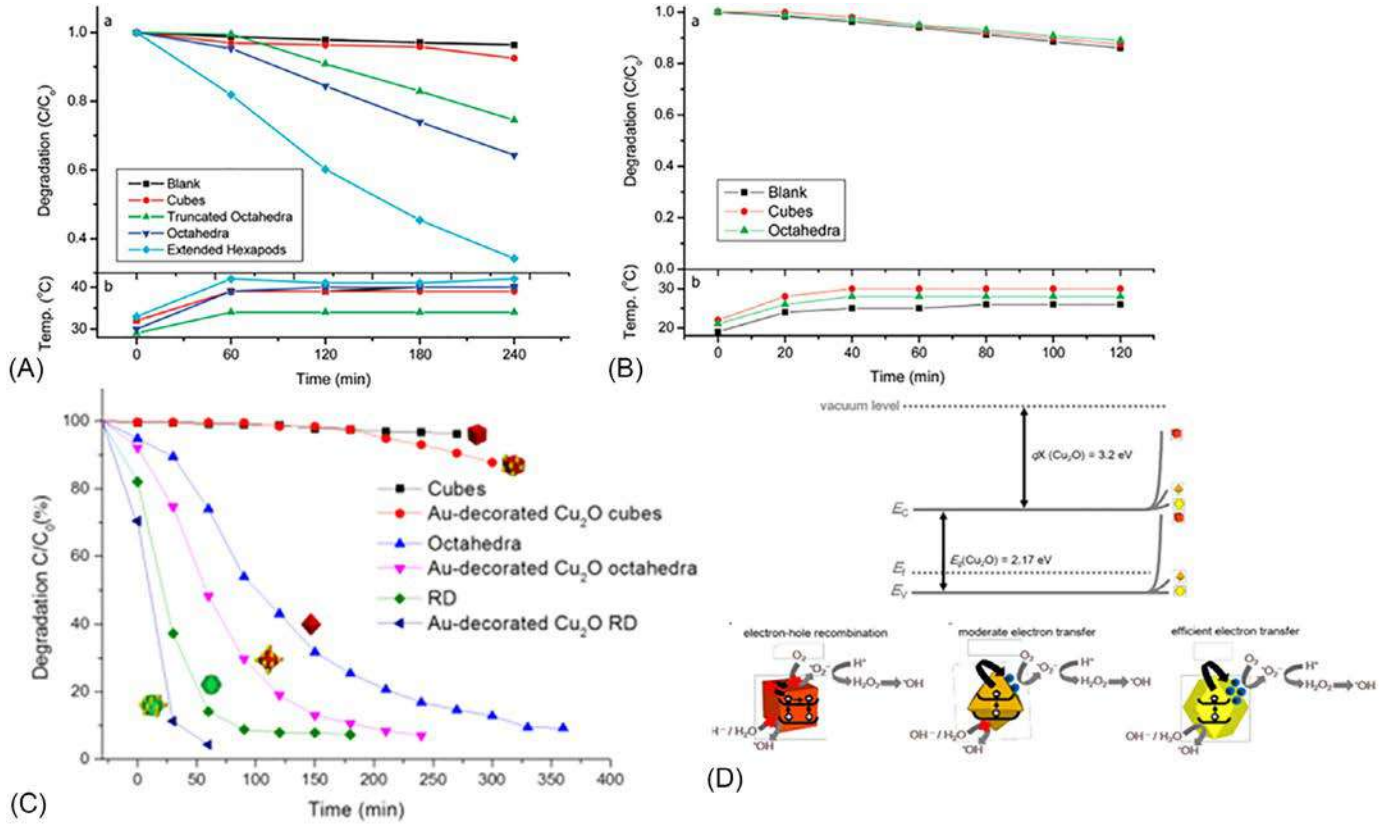

FIG. 7 (A, B) Plots show Cu_2O shape-dependent photodegradation vs. time for (A) methyl orange (B) methyl blue respectively. (C) The extent of photoinduced degradation of MO as a function of time for the various shapes of Cu_2O crystals and Au-decorated Cu_2O heterostructures. (D) Band diagram of Cu_2O with consideration of different degrees of band bending for different crystal surfaces and the picture shows different photocatalytic responses for Cu_2O cubes, octahedra, and rhombic dodecahedra [53]. *Reprinted with permission from (A, B) Jin-Yi H., Michael H.H. Synthesis of submicrometer-sized Cu_2O crystals with morphological evolution from cubic to hexapod structures and their comparative photocatalytic activity. J Phys Chem C 2009;113:14159–14164. doi:10.1021/jp903928p. (C) Michael H.H. Facet-dependent optical properties of semiconductor nanocrystals. Small 2019;1804726. doi:10.1002/smll.201804726. (D) Chieh-Yu C., Michael H.H. Facet-dependent photocatalytic properties of Cu_2O crystals probed by using electron, hole and radical scavengers. J Mater Chem A 2017;15116–15123. doi:10.1039/C7TA03848H.*

https://www.twirpx.org & http://chemistry-chemists.com

positively charged methyl blue. However, {100} facets with negative surface charge are believed to show higher activity (Fig. 7B) [54]. A comprehensive review by Kuo et al. mentioned that neither the cubes nor the octahedral facets of the Cu_2O caused any photodegradation of methyl blue [34]. The electrostatic force of repulsion was assumed to be the reason for the inactivity of octahedron and hexapod shapes, whereas cubic-shaped Cu_2O crystals are insensitive due to the surface barrier height, as discussed later. Fig. 7C shows that decorating gold particles over the surface of Cu_2O octahedra and rhombic dodecahedra improves photocatalytic decomposition of methyl orange, because of migration of photogenerated electrons to the Au particles, leading to more efficient charge separation and reduction in the charge recombination. While Au decorated, Cu_2O cubes remained inactive. This result shows that cubes having {100} facets cannot benefit from this effect because no photoinduced charge carrier is generated from the {100} facets [56].

We can understand crystal facets dependent on different wavelengths of light absorption through distinct band structures and varying degrees of band bending of the exposed surface. Chu et al. introduced electron-holes and radical scavengers in the photodegradation of methyl orange to understand nanocubes' inactivity and the superior activity of rhombic dodecahedra compared with octahedral shapes of Cu_2O crystal [57]. Scavenger experiment outcomes show that photogenerated electrons and holes experience considerable barrier heights at the {100} exposed facets of cubes, preventing charge migration to the particle surfaces, leading to photo inactivity. A modified band diagram displayed in Fig. 7D shows that the charge carriers experience the highest bend bending for the cubic shapes with {100} facets representing its largest energy barrier for charge carriers to transport across the surface and lower photocatalytic activity. The least bend bending barrier for the rhombic dodecahedra with {110} face than octahedron with {111} exposed the surface of Cu_2O nanocrystals, showing the comparably excellent photocatalytic activity of the former. Recently, Wu et al. demonstrated that the {110} facet of Cu_2O crystal is photoactive for CO_2 reduction to methanol while the {100} facet is inert [58]. However, numerous studies show the moderate photocatalytic activity of Cu_2O cubes, which may be due to the presence of a small percentage of the other facets or the presence of surface CuO [56].

Especially in recent years, it has been established that high-index faceted C_2O micro-/nanostructure manifests higher photocatalytic activity than that of the low-index facet. Therefore, the concept of high-index facet of Cu_2O crystal has also been considered to figure out the relationship between high-index exposed surface and activity. Liang et al. demonstrated the shape-controlled synthesis of 50-facet Cu_2O microcrystals with exposed high-index {211}, {522}, or {311} facets via the reduction of copper salts using glucose in alkali media under very mild reaction conditions (Fig. 8) [41].

The photoactivity of Cu_2O microcrystals for the degradation of methyl orange follows the resultant order: {311} $\approx$ 50-facet polyhedra with {522}} $\approx$ 50-facet polyhedra with {211} $>$ octahedron with {111} $>$ cubes with {100}, respectively [41]. Sun et al. also reported that the novel 50-facet Cu_2O crystal shows superior photocatalytic activity, which could be due to surface oxygen vacancies, and unsaturated "Cu" dangling bonds. As a result, the highly oxidative OH radicals are produced in large amounts, leading to the

https://www.twirpx.org & http://chemistry-chemists.com

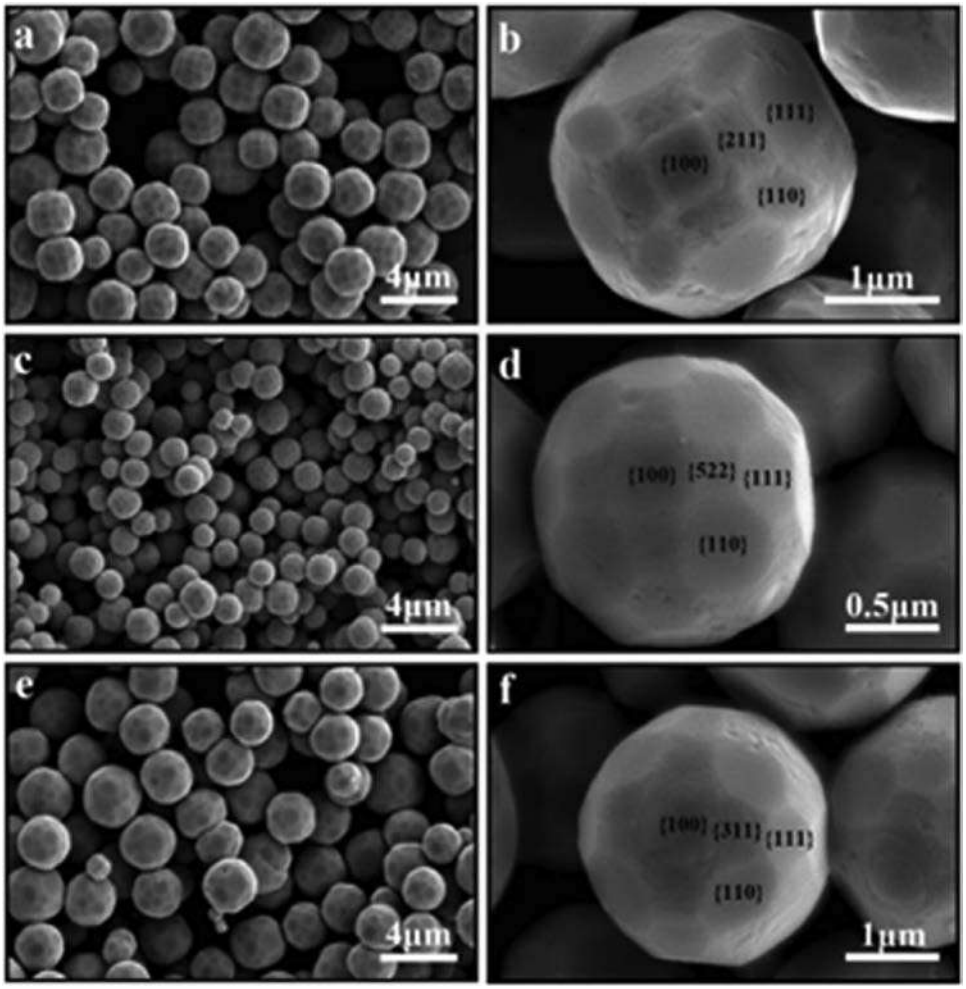

FIG. 8 SEM images of the 50-facet Cu_2O polyhedral with different high-index facets: (A, B) {211}; (C, D) {522}; (E, F) {311}. *From Liang Y, Shang L, Bian T, Zhou C, Zhang D, Yu H, et al. Shape-controlled synthesis of polyhedral 50-facet Cu_2O microcrystals with high-index facets. CrystEngComm 2012;14:4431–6. https://doi.org/10.1039/c2ce25218j.*

enhancement of MO dyes decomposition [44]. Yang et al. prepared Cu_2O microcrystals with {332} high-index facets by a facile wet chemical method and using Zn^{2+} structure-directing agents. They reported that concave trisoctahedra showed better photodecomposition of MO under visible light than other structures such as octahedra and convex [53]. Zhan et al. synthesized multifaced Cu_2O crystal via a facile one-step method [46]. It was noted that photoinduced electrons tended to accumulate on high-index facets, while holes were on {100} facets of a Cu_2O polyhedron, resulting in efficient charge separation and hence enhanced photocatalytic reforming of glucose. Fig. 9 shows the typical

https://www.twirpx.org & http://chemistry-chemists.com

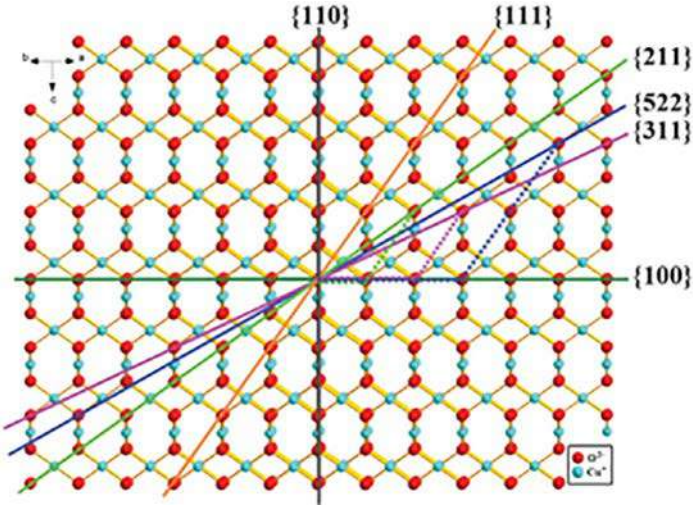

FIG. 9 The surface atomic arrangement of Cu_2O crystal observed from the direction parallel to the {110} facets. *From Shang Y, Guo L. Facet-controlled synthetic strategy of Cu_2O-based crystals for catalysis and sensing. Adv Sci 2015;2. https://doi.org/10.1002/advs.201500140.*

crystallographic facets model of Cu_2O with different atomic structures. It was observed that the high-index facets have significantly more atomic steps and kinks than the low-index {111}, {110}, and {100} facets. Therefore, multifaceted Cu_2O polyhedra with high-index facets exhibit higher activity than those of the cubes and octahedra [50].

Based on the atomic arrangements of Fe^{3+}, Fe^{2+}, and O^{2-} ions in the crystal, iron oxides exist in nature with a variety of polymorphs [59]. Hematite (α-Fe_2O_3), maghemite (γ-Fe_2O_3), and Fe_3O_4 (magnetite) are more common, while, γ-, ε-Fe_2O_3, and $Fe_{1-x}O$ (wüstite) are less common [60]. Among these polymorphs, thermodynamically more stable hematite (α-Fe_2O_3) is isostructural with corundum (α-Al_2O_3) [59]. The trigonal-hexagonal and the primitive rhombohedral unit cells are two formula units of the trigonal (hexagonal scalenohedral) crystallographic phase of α-Fe_2O_3 (Fig. 10) [61, 62]. In the hematite crystal structure, the anions O^{2-} are arranged in a hexagonal close-packed lattice (hcp) along the [001] direction, and the cations (Fe^{3+}) occupy two-thirds of the octahedral sites.

Numerous properties make hematite a promising photocatalytic material [63, 64]. It is one of the most stable and ecofriendly visible light n-type semiconductors with a narrow bandgap (2.0–2.2 eV), which can absorb a greater fraction of solar radiation [65]. Moreover, hematite is the most stable, nontoxic, environmentally friendly, corrosion-resistant metal oxide, and is stable in an aqueous medium (pH $>$ 3) [66]. The photocatalytic properties of hematite (α-Fe_2O_3) depend not only on various morphologies, such as nanowires, nanotubes, nanorings, spindles, spheres, and nanoflowers, but also on well-defined crystal facets [67–70]. However, few studies have reported the facet-controlled synthesis of α-Fe_2O_3 and their shape effect on photocatalysis. The exposed face of α-Fe_2O_3

https://www.twirpx.org & http://chemistry-chemists.com

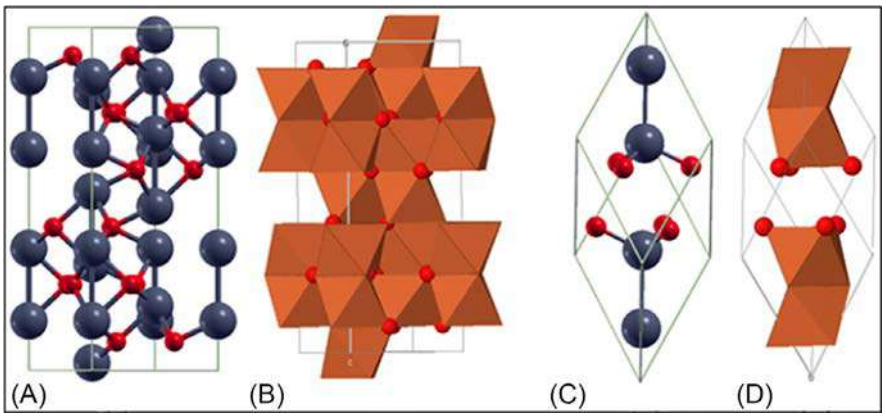

FIG. 10 Schematic diagram of the (A) hexagonal unit cell and (C) the rhombohedral primitive cell of α-Fe_2O_3. The face-sharing octahedra in (A) and (C) are presented in (B) and (D), respectively. Color: Fe = gray and O = red. *From Dzade N, Roldan A, de Leeuw N. A density functional theory study of the adsorption of benzene on hematite (α-Fe_2O_3) surfaces. Minerals 2014;4:89–115. https://doi.org/10.3390/min4010089.*

nanostructures was controlled by introducing capping agents or inorganic metal ions with different adsorption properties into the reaction system. The photoactivity of distinct individual facets and exposed high-index facets of Fe_2O_3 are briefly reviewed to provide a new approach to the design of highly effective hematite visible light photocatalysts by the exposed facets of crystals.

Wu et al. reported that truncated nanocubes with the {012} and {104} exposed plane showed higher photoresponse toward photodegradation of Rhodamine B dyes than that of oblique nanocubes with {012} exposed facets [71]. However, the observed photocatalytic activity is not per the BET surface area value of truncated nanocubes (20.25 $m^2\ g^{-1}$) and oblique nanocubes (32.57 $m^2\ g^{-1}$). Numerous literature reviews reported that the higher the surface area, the more active sites for the reaction and the photocatalytic activity. Therefore, this implies a certain role of crystal facets exposed by Fe_2O_3 nanostructures on the visible photodegradation of Rhodamine B. The higher photodegradation performance ascribed to the formation of hydroxyl radicals ($^{\bullet}OH$), which is a key step for photocatalytic degradation. The surface Fe^{3+} ions undergo the redox reaction to generate the hydroxyl radicals ($^{\bullet}OH$), which take part in the heterogeneous photo-Fenton reaction. Therefore, exposed Fe^{3+} ion density is often considered the most effective reactant for photocatalytic degradation. The {104} and {012} crystal planes of hematite have approximately 10.3 and 7.33 of exposed Fe^{3+}, respectively. This shows that the {104} facet is more reactive, and provides more catalytic active sites for RhB adsorption, corresponding to higher activity. Patra et al. synthesized different-shaped Fe_2O_3 nanocrystals by varying the hydrothermal reaction temperatures and holding times as shown in Fig. 11 [72]. Visible

https://www.twirpx.org & http://chemistry-chemists.com

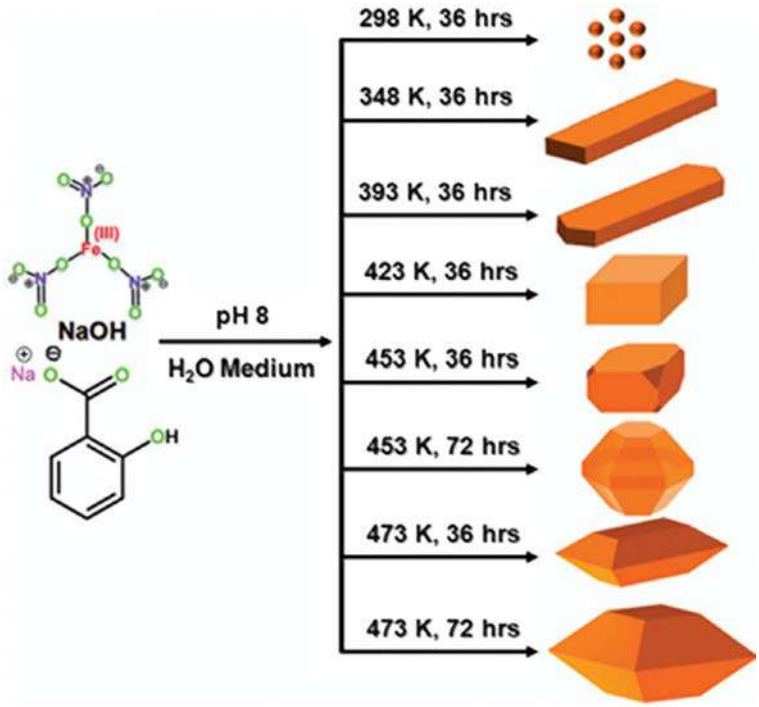

FIG. 11 *Schematic presentation for the hydrothermal synthesis of various shapes Fe_2O_3 nanocrystals. From K. PA, K. KS, Asim B, Dukjoon K. Morphology evolution of single-crystalline hematite nanocrystals: magnetically recoverable nanocatalysts for enhanced facet-driven photoredox activity. Nanoscale 2016;8:365–77. https://doi.org/10.1039/C5NR06509G.*

light-induced MO degradation on hematite nanocrystals with different exposed facets was in the order of {104} + {100} + {001} (bitruncated-dodecahedron) > {101} + {001} (bitruncated-octahedron) > {001} + {110} (nanorods) > {012} (nanocuboid). This also implies greater photoinduced activity of the {104} exposed facet.

Rahman et al. also confirmed that the exposed {104} facets in Fe_2O_3 enhance the photodegradation of methylene blue (MB) along with {110} and {102} facets [73]. Wang et al. reported the hydrothermal synthesis of different morphology α-Fe_2O_3 nanocrystals such as polyhedra with exposed {101} and {001} facets, rods with predominant {001} facets, ellipses, and cylinders [74].. However, due to the higher surface energy of {101} facets, the polyhedron manifested much higher photocatalytic activity than the other shapes toward the degradation of organic contaminants. Zhao et al. demonstrated a similar reaction condition for the synthesis of rhombohedron-shaped of α-Fe_2O_3 nanocrystals exposed with {1010} and {0001} planes and truncated-dodecahedron-like particles with predominant {1012} facets [75]. These particles exhibit similar crystal sizes and BET surface area, ideal for studying facet-dependent activity. Zhao et al.'s observations revealed that α-Fe_2O_3 with {1012} facet exhibited much higher photoactivity toward the

https://www.twirpx.org & http://chemistry-chemists.com

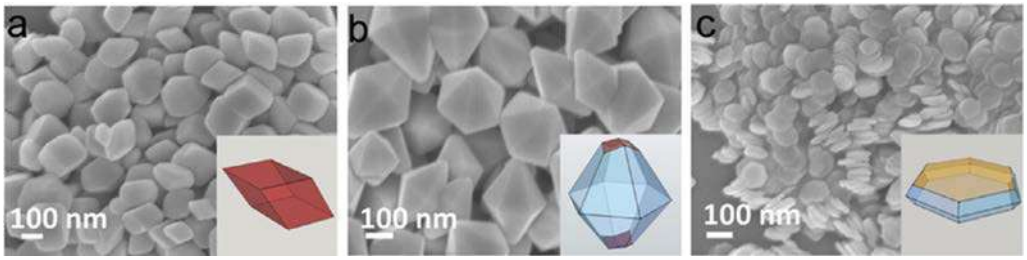

FIG. 12 SEM images of different shapes of a-Fe_2O_3 nanoparticles after 400°C calcination: (A) rhombohedron; (B) hexagonal bipyramid; (C) hexagonal nanoplate. The inset on the right corner shows the schematic diagram of the corresponding particles. *From Chan J, Ang S, Ye E, Sullivan M, Zhang J, Lin M. Heterogeneous photo-Fenton reaction on hematite (α-Fe_2O_3) {104}, {113} and {001} surface facets. Phys Chem Chem Phys 2015;17:25333–41. https://doi.org/10.1039/c5cp03332b.*

degradation of organic dye compared to the rhombohedron-shaped with {0001} and {1010} facets. This was due to the presence of a higher density of Fe^{3+} ions on the {1012} facet of the truncated-dodecahedron-shaped a-Fe_2O_3. Chan et al. reported the solvent dependent surfactant-free hydrothermal synthesis of α-Fe_2O_3 nanocrystals exposed with three types of crystal facets, including {104} rhombohedron, {113}) hexagonal bipyramid, and {001} hexagonal nanoplates, as shown in Fig. 12 [76]. The visible light-induced Rhodamine B degradation over the as-synthesized hematite surface follows the order {113} > {104} > {001}, respectively.

Xiang et al. used the solvothermal method technique to fabricate four different morphologies of α-Fe_2O_3 catalysts with specific exposed facets [77]. The physicochemical properties and catalytic water oxidation activities of α-Fe_2O_3 catalysts are presented in Table 1 [77]. The visible light-induced water oxidation activity of the as-synthesized catalysts follows the order nanocubes > nanoparticles > nanoplates > nanoflakes. This shows that cubes with exposed {012} facets are more active for water oxidation among the four samples. Wang et al. demonstrated that the O_2 evolution activity of the α-Fe_2O_3 photocatalyst surrounded by {012} and {104} facets is 84 times higher than that of α-Fe_2O_3 mostly with {101} and {111} planes [78].

Table 1 Physicochemical properties and photocatalytic water oxidation activities of α-Fe_2O_3 samples.

Samples	Morphology	Size (nm) (length × diameter × height)	Dominant facets	Specific surface area ($m^2\ g^{-1}$)	O_2 [μmol]	% Yield
1	Nanocubes	50 × 60 × 65	{012}	53.2	2.15	13.4
2	Nanoplates	200 × 200 × 20	{001}	32.8	0.72	4.5
3	Nanoflakes	250 × 250 × 15	{001}	48.3	0.48	3.0
4	Nanoparticles	35 × 40 × 50	–	86.4	2.83	17.7

From Quanjun X, Gui C, Tai-Chu L. Effects of morphology and exposed facets of α-Fe_2O_3 nanocrystals on photocatalytic water oxidation. RSC Adv 2015:52210–6. https://doi.org/10.1039/C5RA09354F.

https://www.twirpx.org & http://chemistry-chemists.com

3 Bismuth vanadates ($BiVO_4$) photocatalyst

Bismuth vanadate ($BiVO_4$), a bright yellow n-type inorganic semiconductor, has received intense attention as an active visible light photocatalyst. Therefore, studies of $BiVO_4$ are mainly focused on photodegradation of organic compounds or oxygen evolution under sunlight irradiation, both of which are the most significant photocatalysis applications for environmental remediation and energy production [79–81]. It is noted that $BiVO_4$ exists in three primary crystalline structures: monoclinic scheelite, tetragonal scheelite, and tetragonal zircon type structure [82]. Among these, monoclinic scheelite is more important from a photocatalysis point of view. Therefore, more emphasis has been given to this structure, in which the basic structural unit is built up by a VO_4 tetrahedron and a BiO_8 dodecahedron, respectively. The V and Bi sites are coordinated by four and eight oxygen atoms, respectively (Fig. 13) [83].

The significant advantages found in $BiVO_4$ are: (i) nontoxicity; (ii) suitable bandgap energy of ca. 2.4 eV (for monoclinic scheelite), implying the absorption in the visible region; (iii) its valence band edge position is ca. 2.4 V vs. RHE (reversible hydrogen

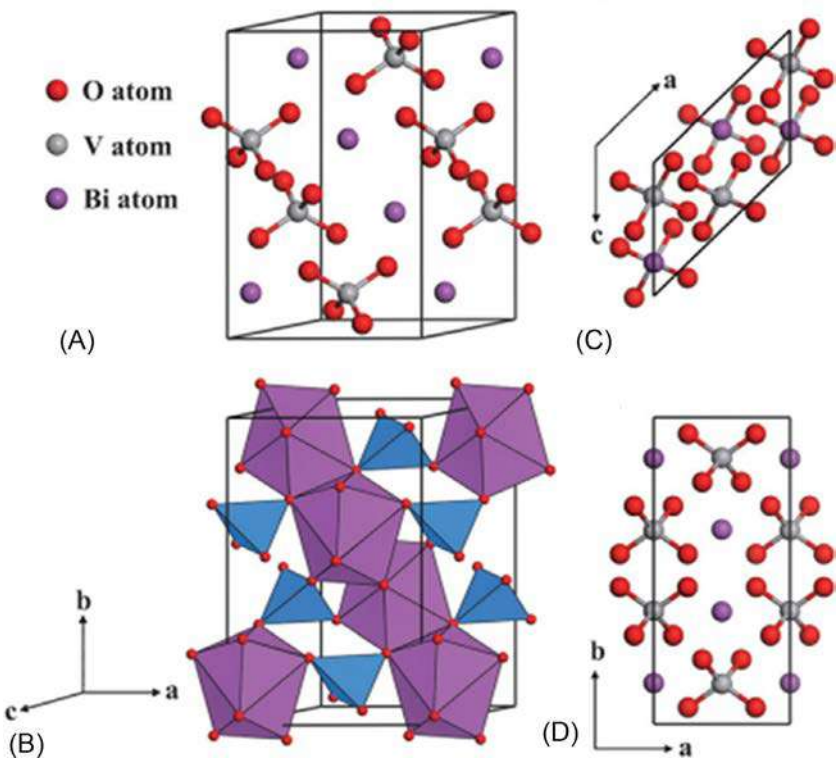

FIG. 13 (A) Crystal structure of monoclinic clinobisvanite $BiVO_4$; (B) polyhedron structure illustration; (C) top view and (D) side view respectively. *From Zongyan Z, Zhaosheng L, Zhigang Z. Electronic structure and optical properties of monoclinic clinobisvanite $BiVO_4$. Phys Chem Chem Phys 2011:4746. https://doi.org/10.1039/c0cp01871f.*

https://www.twirpx.org & http://chemistry-chemists.com

electrode), which provides sufficient overpotential for water oxidation, while the conduction band edge position is lower than the thermodynamic potential for H_2 evolution; and (iv) improved separation and extraction of the photoinduced charge carrier compared to the other binary metal oxides such as TiO_2, In_2O_3, and WO_3 [83, 84]. However, the solar conversation efficiency of $BiVO_4$ material is still far below the theoretical value. The low photocatalytic activity of $BiVO_4$ is due to the poor adsorption, sluggish water oxidation kinetics, and difficulty in migration and separation of charge carrier [85–89].

In light of this, so far, various novel ideas and techniques have been devoted to improving the photoresponses of $BiVO_4$. One of the most suitable approaches is the synthesis of nanostructured $BiVO_4$ with well-defined exposed facets. Up to now, numerous synthesis techniques have been reported to control the morphologies of $BiVO_4$, such as the hydrothermal method [90], solid-state reaction [91], coprecipitation [92], solution combustion method [93], sol-gel method [94], and metal-organic decomposition [95]. For example, Zhang et al. reported synthesized $BiVO_4$ nanosheets with well-defined {010} facets by a hydrothermal method by using sodium dodecyl benzene sulfonate (SDBS) as the morphology-directing template. The as-synthesized nanosheets exhibited faster photodegradation of *N*,*N*,*N*′,*N*′-tetraethylated Rhodamine (RB) than bulk $BiVO_4$ [96]. In another study, Xi et al. demonstrated the hydrothermal synthesis of well-defined $BiVO_4$ nanoplates without any template or organic surfactant [97]. Interestingly, the visible light photocatalytic activity toward the degradation of organic dyes and O_2 generation from water using nanoplate with {001} exposed facets is found to be higher than for $BiVO_4$ nanorods and microcrystal. Furthermore, Wang et al. utilized the hydrothermal technique to synthesize different growth extents of (040)/(110) facets of $BiVO_4$ by using a trace amount of $TiCl_3$ as the directing agent and correlated the photocatalytic oxygen evolution rate of as-synthesized $BiVO_4$ [98].

The description and survey collected from the recent literature demonstrate that photoinduced charge carriers may be drifted to different exposed facets present in a polyhedron [19, 99]. Consequently, oxidation and reduction may occur at different facets of the distinct polyhedron [100, 101]. Ohno et al. initially demonstrated such a phenomenon with the benchmark titanium dioxide (TiO_2) photocatalyst [102]. The synergistic redox functional facets property is also seen on monoclinic bismuth vanadate (m-$BiVO_4$), demonstrating that facet modification could be a significant strategy to improve quantum efficiency. In particular, Li et al. reported that the photoinduced electrons-driven reduction of Au, Pt^{+4}, and Ag^{+1} ions to metal and photoinduced holes-driven oxidation of Pb^{+2}, Mn^{+2} ions to metal oxide takes place on the {010} and {110} facets of $BiVO_4$ crystal, respectively. The theoretical DFT calculation revealed that the conduction and valence band energy of the {010} facets is relatively lower than that of the {110} facets. This means that thermodynamically feasible electron transfer occurs from the {110} to the {010} facets, leading to the separation of electrons and holes on the {010} and {110} facets, respectively. Additionally, the photocatalytic selective deposition of Pt on the {010} facets and MnO_X on the {010} facets of $BiVO_4$ show much high photocatalytic water oxidation reaction compared with

https://www.twirpx.org & http://chemistry-chemists.com

randomly distributed Pt and MO_X. They also demonstrate that the preferential deposition of cocatalysts on the designed semiconductor facets further enhances their photocatalytic activity. Li et al. further reported different energy of {110} and {010} exposed facets through photocatalytic degradation of both Rhodamine B and 4-nonylphenol. The results show better activity of the $BiVO_4$-110-TiO_2 compared to the $BiVO_4$-010-TiO_2 heterojunction under visible light ($\geq$422 nm) irradiation. The above observation is due to different energy barriers between TiO_2 and the two different facets of $BiVO_4$.

The metal/metal oxide deposition, DFT study, and in-situ microscopic techniques collectively confirmed the preferential accumulation of photogenerated holes on the {110} facets of $BiVO_4$, allowing the {110} facet to act as active oxidation sites. However, the exposed {010} dominated facets of $BiVO_4$, which act as reduction sites, show higher photooxidation of water and dye degradation performance. The contradicting observation may be due to the following reason: (i) faster charge mobility, better water absorption, and lower energy barrier of {010} facets than that of {110} facets in water photooxidation, as proposed by Yang et al. [103]; and (ii) multiple morphological distinctions, i.e., nanoparticle size, surface area, and types of exposed crystal planes. Tan et al. fabricated two dual faceted forms of $BiVO_4$ with comparable size and surface area, but one was {010} dominant and the other {110} dominant. The former m-$BiVO_4$ exhibited superior photoinduced activities compared to the {110}-dominant $BiVO_4$, as demonstrated by photocatalytic water oxidation and also 2,4-dichlorophenoxyacetic acid photodegradation. Steady-state photoluminescence (PL) measurements in the presence of charge scavengers analysis and flat band potential estimation from Mott-Schottky relationship spectra revealed that more electron-hole pair charge separation occurs in {110} dominant m-$BiVO_4$ facets, favoring the photocatalysis process. In contrast, faster electron-hole pair charge recombination in {110} dominant m-$BiVO_4$ deteriorated its photoactivity.

The $BiVO_4$ photocatalyst with high-index facets has attracted significant attention due to its higher performance in water oxidation. The high-index faceted $BiVO_4$ has shown a decrease in the overpotential (0.7–1.0 V) compared to the low-index faceted $BiVO_4$ for photoinduced oxygen evolution reaction [104]. Using Au nanoparticles as a structure-directing agent in a mixture of NH_4VO_3/$Bi(NO_3)_3$/nitric acid solution/ammonia, Li et al. demonstrated the controlled growth of unprecedented 30-faceted polyhedral $BiVO_4$ predominantly surrounded by high-index {132}, {321}, and {121} facets [105]. They reported that the exposed high-index facets exhibited a 3–5-fold increment of photocatalytic O_2 evolution reaction relative to the low-index counterpart. Furthermore, Hu et al. also fabricated a highly symmetrical 24 faceted concave $BiVO_4$ polyhedron exposed with multiple high index {012}, {210}, {115}, and {511} facets [106]. The visible light O_2 evolution properties of this high-index facet in the absence of any cocatalyst were observed to be two orders of magnitude higher than those of the bulk material. The high-index facets of $BiVO_4$ were ascertained to be energetically more favorable for the photoinduced water-splitting reaction, which opens a new door for other metal oxides to study the effect of an exposed new type of high-index facet on their photocatalytic activity.

https://www.twirpx.org & http://chemistry-chemists.com

4 Conclusions

The light-harvesting property of metal oxide semiconductors is found to be a promising avenue to solve various environmental problems and energy demand issues in future. Undoubtedly, the exposed facets are the critical factor for a photocatalytic redox reaction. Therefore, most significant research directions have focused on the semiconductors' facet engineering to enhance the visible light-driven reaction. This chapter provides a comprehensive review of the growth rate of different facets and effects of exposed facets on the visible light absorption property, and photoinduced charges separation efficiency. The various exposed facets of the same metal oxide show different properties such as photosensitivity, charge separation, kinetics of the reaction, and stability. Generally, metal oxides exposed with high-index facets manifest higher photocatalytic activity than low-index facets because of low coordinate atoms (edges, steps, and kinks), and surface dangling bond. Although some encouraging progress has been achieved to enhance visible light performance, nevertheless, significant challenges remain, including the following.

(i) Selection of material that is low-cost, nontoxic, with charge separation and transfer, bandgap position, and optical absorption in the visible region of solar spectrum region.
(ii) Facet-controlled synthesis of photocatalysts is a challenging issue, as facet with high energy grows faster and finally vanishes.
(iii) The long-term photostability of the photocatalyst is a major obstacle for industrial applications.

It is hoped that this chapter will stimulate more attention in the engineering of facets of noble metal oxides with desirable photoinduced properties to overcome the current issues.

References

[1] Maneesha M, Doo-Man C. α-Fe 2 O 3 as a photocatalytic material: a review. Appl Catal Gen 2015;126–41. https://doi.org/10.1016/j.apcata.2015.03.023.

[2] Nosaka Y, Nosaka AY. Generation and detection of reactive oxygen species in photocatalysis. Chem Rev 2017;117:11302–36. https://doi.org/10.1021/acs.chemrev.7b00161.

[3] Park Y, Mc Donald KJ, Choi KS. Progress in bismuth vanadate photoanodes for use in solar water oxidation. Chem Soc Rev 2013;42:2321–37. https://doi.org/10.1039/c2cs35260e.

[4] Akira F, Kenichi H. Electrochemical photolysis of water at a semiconductor electrode. Nature 1972;37–8. https://doi.org/10.1038/238037a0.

[5] Anise A, Aziz H-Y, Masoud A, Shima RP. Review on photocatalytic conversion of carbon dioxide to value-added compounds and renewable fuels by graphitic carbon nitride-based photocatalysts. Catal Rev 2019;595–628. https://doi.org/10.1080/01614940.2019.1654224.

[6] Ma Y, Wang X, Jia Y, Chen X, Han H, Li C. Titanium dioxide-based nanomaterials for photocatalytic fuel generations. Chem Rev 2014;114:9987–10043. https://doi.org/10.1021/cr500008u.

https://www.twirpx.org & http://chemistry-chemists.com

[7] Nayak AK, Lee S, Sohn Y, Pradhan D. Synthesis of In2S3 microspheres using a template-free and surfactant-less hydrothermal process and their visible light photocatalysis. CrstEngComm 2014;16:8064–72. https://doi.org/10.1039/c4ce00836g.

[8] Tong H, Ouyang S, Bi Y, Umezawa N, Oshikiri M, Ye J. Nano-photocatalytic materials: possibilities and challenges. Adv Mater 2012;24:229–51. https://doi.org/10.1002/adma.201102752.

[9] Wee-Jun O, Lling-Lling T, Siang-Piao C, Siek-Ting Y, Rahman MA. Facet-dependent photocatalytic properties of TiO2-based composites for energy conversion and environmental remediation. ChemSusChem 2014;690–719. https://doi.org/10.1002/cssc.201300924.

[10] Peng YK, Tsang SCE. Facet-dependent photocatalysis of nanosize semiconductive metal oxides and progress of their characterization. Nano Today 2018;18:15–34. https://doi.org/10.1016/j.nantod.2017.12.011.

[11] Zheng H, Ou JZ, Strano MS, Kaner RB, Mitchell A, Kalantar-Zadeh K. Nanostructured tungsten oxide—properties, synthesis, and applications. Adv Funct Mater 2011;21:2175–96. https://doi.org/10.1002/adfm.201002477.

[12] Bai S, Gao C, Low J, Xiong Y. Crystal phase engineering on photocatalytic materials for energy and environmental applications. Nano Res 2019;12:2031–54. https://doi.org/10.1007/s12274-018-2267-6.

[13] Abe R. Recent progress on photocatalytic and photoelectrochemical water splitting under visible light irradiation. J Photochem Photobiol C Photchem Rev 2010;11:179–209. https://doi.org/10.1016/j.jphotochemrev.2011.02.003.

[14] Landong L, Junqing Y, Tuo W, Zhi-Jian Z, Jian Z, Jinlong G, et al. Sub-10 nm rutile titanium dioxide nanoparticles for efficient visible-light-driven photocatalytic hydrogen production. Nat Commun 2015. https://doi.org/10.1038/ncomms6881.

[15] Mohd Adnan MA, Julkapli NM, Abd Hamid SB. Review on ZnO hybrid photocatalyst: impact on photocatalytic activities of water pollutant degradation. Rev Inorg Chem 2016;36:77–104. https://doi.org/10.1515/revic-2015-0015.

[16] Liu B, Fang Y, Li Z, Xu S. Visible-light nanostructured photocatalysts—a review. J Nanosci Nanotechnol 2015;15:889–920. https://doi.org/10.1166/jnn.2015.9784.

[17] Dong P, Xi X, Hou G. Typical non-TiO_2-based visible-light photocatalysts. In: Semiconductor Photocatalysis-Materials, Mechanisms and Applications. IntechOpen; 2016.

[18] Kebin Z, Yadong L. Catalysis based on nanocrystals with well-defined facets. Angew Chem Int Ed 2012;602–13. https://doi.org/10.1002/anie.201102619.

[19] Liu G, Yu JC, Lu GQ, Cheng HM. Crystal facet engineering of semiconductor photocatalysts: motivations, advances and unique properties. Chem Commun 2011;47:6763–83. https://doi.org/10.1039/c1cc10665a.

[20] Xu H, Reunchan P, Ouyang S, Tong H, Umezawa N, Kako T, et al. Anatase TiO_2 single crystals exposed with high-reactive {111} facets toward efficient H_2 evolution. Chem Mater 2013;25:405–11. https://doi.org/10.1021/cm303502b.

[21] Jiang J, Zhao K, Xiao X, Zhang L. Synthesis and facet-dependent photoreactivity of BiOCl single-crystalline nanosheets. J Am Chem Soc 2012;134:4473–6. https://doi.org/10.1021/ja210484t.

[22] Nianqiang W, Jin W, Nyago TD, Hong W, Jian-Guo Z, Lj P, et al. Shape-enhanced photocatalytic activity of single-crystalline anatase TiO_2 (101) nanobelts. J Am Chem Soc 2010;6679–85. https://doi.org/10.1021/ja909456f.

[23] Song B, Lili W, Zhengquan L, Yujie X. Facet-engineered surface and interface design of photocatalytic materials. Adv Sci 2017;1600216. https://doi.org/10.1002/advs.201600216.

https://www.twirpx.org & http://chemistry-chemists.com

[24] Nitish R, Youngku S, Debabrata P. Synergy of Low-energy {101} and high-energy {001} TiO_2 crystal facets for enhanced photocatalysis. ACS Nano 2013;2532–40. https://doi.org/10.1021/nn305877v.

[25] Xia Y, Yang P, Sun Y, Wu Y, Mayers B, Gates B, et al. One-dimensional nanostructures: synthesis, characterization, and applications. Adv Mater 2003;15:353–89. https://doi.org/10.1002/adma.200390087.

[26] Jiang D, Wang W. Fundamental studies on photocatalytic structures with well-defined crystal facets. Stud Surf Sci Catal 2017;177:409–38. https://doi.org/10.1016/B978-0-12-805090-3.00011-5. China: Elsevier Inc.

[27] Dobrushin R, Lvovich R, Kotecký R, Shlosman S. Wulff construction: a global shape from local interaction. vol. 104. American Mathematical Society; 1992.

[28] Jaya P, Tarasankar P. Faceted metal and metal oxide nanoparticles: design, fabrication and catalysis. Nanoscale 2015;14159–90. https://doi.org/10.1039/C5NR03395K.

[29] Gui YH, Hua SC, Zhang QS, Jin Z, Gang L, Campbell SS, et al. Anatase TiO_2 single crystals with a large percentage of reactive facets. Nature 2008;638–41. https://doi.org/10.1038/nature06964.

[30] Javed R, Usman M, Tabassum S, Zia M. Effect of capping agents: structural, optical and biological properties of ZnO nanoparticles. Appl Surf Sci 2016;386:319–26. https://doi.org/10.1016/j.apsusc.2016.06.042.

[31] Hui Z, Mingshang J, Younan X. Noble-metal nanocrystals with concave surfaces: synthesis and applications. Angew Chem Int Ed 2012;7656–73. https://doi.org/10.1002/anie.201201557.

[32] Kousik B, Moumita C, Debabrata P. Exposed facets-dependent catalytic properties of nanocrystals: noble metals (Pd, Pt, and Au) and oxides of first row d-block elements. J Nanosci Nanotechnol 2019;332–55. https://doi.org/10.1166/jnn.2019.15782.

[33] Haibin Z, Yonggang L, Hong L, Jingzhong F. One-pot synthesis of high-index faceted AgCl nanocrystals with trapezohedral, concave hexoctahedral structures and their photocatalytic activity. Nanoscale 2015;11591–601. https://doi.org/10.1039/C5NR02049B.

[34] Kuo CH, Huang MH. Morphologically controlled synthesis of Cu_2O nanocrystals and their properties. Nano Today 2010;5:106–16. https://doi.org/10.1016/j.nantod.2010.02.001.

[35] Zoolfakar AS, Rani RA, Morfa AJ, O'Mullane AP, Kalantar-Zadeh K. Nanostructured copper oxide semiconductors: a perspective on materials, synthesis methods and applications. J Mater Chem C 2014;2:5247–70. https://doi.org/10.1039/c4tc00345d.

[36] Kunfeng C, Congting S, Shuyan S, Dongfeng X. Polymorphic crystallization of Cu_2O compound. CrstEngComm 2014;5257–67. https://doi.org/10.1039/c4ce00339j.

[37] Li H, Zhang X, MacFarlane DR. Carbon quantum dots/Cu_2O heterostructures for solar-light-driven conversion of CO_2 to methanol. Adv Energy Mater 2015;5. https://doi.org/10.1002/aenm.201401077.

[38] Michikazu H, Takeshi K, Mutsuko K, Sigeru I, N KJ, Kazunari D, et al. Cu_2O as a photocatalyst for overall water splitting under visible light irradiation. Chem Commun 1998;357–8. https://doi.org/10.1039/a707440i.

[39] Santosh K, Christopher MAP, Mark IA, Danielle VJ, Richard ED, Martin CRS, et al. Facile synthesis of hierarchical Cu_2O nanocubes as visible light photocatalysts. Appl Catal Environ 2016;226–32. https://doi.org/10.1016/j.apcatb.2016.02.038.

[40] Sushma Y, Arti J, Priti M. A review on the sustainable routes for the synthesis and applications of cuprous oxide nanoparticles and their nanocomposites. Green Chem 2019;937–55. https://doi.org/10.1039/c8gc03303j.

[41] Liang Y, Shang L, Bian T, Zhou C, Zhang D, Yu H, et al. Shape-controlled synthesis of polyhedral 50-facet Cu_2O microcrystals with high-index facets. CrstEngComm 2012;14:4431–6. https://doi.org/10.1039/c2ce25218j.

https://www.twirpx.org & http://chemistry-chemists.com

[42] Sun S, Deng D, Kong C, Gao Y, Yang S, Song X, et al. Seed-mediated synthesis of polyhedral 50-facet Cu_2O architectures. CrstEngComm 2011;13:5993–7. https://doi.org/10.1039/c1ce05243h.

[43] Sun S, Kong C, Yang S, Wang L, Song X, Ding B, et al. Highly symmetric polyhedral Cu_2O crystals with controllable-index planes. CrstEngComm 2011;13:2217–21. https://doi.org/10.1039/c0ce00679c.

[44] Sun S, Song X, Sun Y, Deng D, Yang Z. The crystal-facet-dependent effect of polyhedral Cu_2O microcrystals on photocatalytic activity. Cat Sci Technol 2012;2:925–30. https://doi.org/10.1039/c2cy00530a.

[45] Wang X, Jiao S, Wu D, Li Q, Zhou J, Jiang K, et al. A facile strategy for crystal engineering of Cu_2O polyhedrons with high-index facets. CrstEngComm 2013;15:1849–52. https://doi.org/10.1039/c3ce26881k.

[46] Zhang L, Shi J, Liu M, Jing D, Guo L. Photocatalytic reforming of glucose under visible light over morphology controlled Cu_2O: efficient charge separation by crystal facet engineering. Chem Commun 2014;50:192–4. https://doi.org/10.1039/c3cc46423g.

[47] Kumar MA, Debabrata P. Morphology controlled solution-based synthesis of Cu_2O crystals for the facets-dependent catalytic reduction of highly toxic aqueous Cr(VI). Cryst Growth Des 2016;16:3688–98. https://doi.org/10.1021/acs.cgd.6b00186.

[48] Jiasheng X, Dongfeng X. Five branching growth patterns in the cubic crystal system: a direct observation of cuprous oxide microcrystals. Acta Mater 2007;55:2397–406. https://doi.org/10.1016/j.actamat.2006.11.032.

[49] Shaodong S, Xiaojing Z, Qing Y, Shuhua L, Xiaozhe Z, Zhimao Y. Cuprous oxide (Cu_2O) crystals with tailored architectures: a comprehensive review on synthesis, fundamental properties, functional modifications and applications. Prog Mater Sci 2018;96:111–73. https://doi.org/10.1016/j.pmatsci.2018.03.006.

[50] Shang Y, Guo L. Facet-controlled synthetic strategy of Cu_2O-based crystals for catalysis and sensing. Adv Sci 2015;2. https://doi.org/10.1002/advs.201500140.

[51] Xu H, Wang W, Zhu W. Shape evolution and size-controllable synthesis of Cu_2O octahedra and their morphology-dependent photocatalytic properties. J Phys Chem B 2006;110:13829–34. https://doi.org/10.1021/jp061934y.

[52] Kuo CH, Huang MH. Facile synthesis of Cu_2O nanocrystals with systematic shape evolution from cubic to octahedral structures. J Phys Chem C 2008;112:18355–60. https://doi.org/10.1021/jp8060027.

[53] Renchun Y, Fengyun M, Tingxian T, Dingxing T, Yiming R, Zhiming C, et al. Zn^{2+}-assisted synthesis of concave Cu_2O crystals and enhanced photocatalytic properties. Catal Commun 2013;109–12. https://doi.org/10.1016/j.catcom.2013.08.010.

[54] Jin-Yi H, Michael HH. Synthesis of submicrometer-sized Cu_2O crystals with morphological evolution from cubic to hexapod structures and their comparative photocatalytic activity. J Phys Chem C 2009;113:14159–64. https://doi.org/10.1021/jp903928p.

[55] Huang WC, Lyu LM, Yang YC, Huang MH. Synthesis of Cu_2O nanocrystals from cubic to rhombic dodecahedral structures and their comparative photocatalytic activity. J Am Chem Soc 2012;134:1261–7. https://doi.org/10.1021/ja209662v.

[56] Michael HH. Facet-dependent optical properties of semiconductor nanocrystals. Small 2019;1804726. https://doi.org/10.1002/smll.201804726.

[57] Chieh-Yu C, Michael HH. Facet-dependent photocatalytic properties of Cu_2O crystals probed by using electron, hole and radical scavengers. J Mater Chem A 2017;15116–23. https://doi.org/10.1039/C7TA03848H.

[58] Yimin AW, Ian M, Cong L, Chun LK, Qi L, Arvydas PP, et al. Facet-dependent active sites of a single Cu_2O particle photocatalyst for CO_2 reduction to methanol. Nat Energy 2019;957–68. https://doi.org/10.1038/s41560-019-0490-3.

https://www.twirpx.org & http://chemistry-chemists.com

[59] Cornell RM, Schwertmann U. The iron oxides: structure, properties, reactions, occurrences and uses. John Wiley & Sons; 2003.

[60] Shinde M, Qureshi N, Rane S, Kim JA, Kim T, Amalnerkar D. Instantaneous synthesis of faceted iron oxide nanostructures using microwave solvothermal assisted combustion technique. J Nanosci Nanotechnol 2017;17:5024–30. https://doi.org/10.1166/jnn.2017.13453.

[61] Gedamu TA, John R, Aregahegn DA, Wei-Nien S, Bing-Joe H. Using hematite for photoelectrochemical water splitting: a review of current progress and challenges. Nanoscale Horiz 2016;243–67. https://doi.org/10.1039/C5NH00098J.

[62] Nelson D, Alberto R, de Nora L. A density functional theory study of the adsorption of benzene on hematite (α-Fe_2O_3) surfaces. Minerals 2014;89–115. https://doi.org/10.3390/min4010089.

[63] Maneesha M, Doo-Man C. α-Fe_2O_3 as a photocatalytic material: a review. Appl Catal Gen 2015;126–41. https://doi.org/10.1016/j.apcata.2015.03.023.

[64] Saurabh BP, Helena WL, James B. Iron based photoanodes for solar fuel production. Phys Chem Chem Phys 2014;11834. https://doi.org/10.1039/c3cp55174a.

[65] Kusior A, Michalec K, Jelen P, Radecka M. Shaped Fe_2O_3 nanoparticles—synthesis and enhanced photocatalytic degradation towards RhB. Appl Surf Sci 2019;476:342–52. https://doi.org/10.1016/j.apsusc.2018.12.113.

[66] Hitam CNC, Jalil AA. A review on exploration of Fe_2O_3 photocatalyst towards degradation of dyes and organic contaminants. J Environ Manage 2020;258.

[67] Kinjal G, Jeotikanta M, Kabir HM, Kevin E, Narayan P, Krishnan R, et al. Mesoporous iron oxide nanowires: synthesis, magnetic and photocatalytic properties. RSC Adv 2016;90537–46. https://doi.org/10.1039/C6RA18530D.

[68] Yudong X, Yunting W. A review of the α-Fe_2O_3 (hematite) nanotube structure: recent advances in synthesis, characterization, and applications. Nanoscale 2020;10912–32. https://doi.org/10.1039/d0nr02705g.

[69] Mushove T, Breault TM, Thompson LT. Synthesis and characterization of hematite nanotube arrays for photocatalysis. Ind Eng Chem Res 2015;54:4285–92. https://doi.org/10.1021/ie504585q.

[70] Suyuan Z, Kaibin T, Tanwei L, Zhenhua L, Dong W, Yongkun W, et al. Hematite hollow spindles and microspheres: selective synthesis, growth mechanisms, and application in lithium ion battery and water treatment. J Phys Chem C 2007;10217–25. https://doi.org/10.1021/jp0719661.

[71] Wu W, Hao R, Liu F, Su X, Hou Y. Single-crystalline α-Fe_2O_3 nanostructures: controlled synthesis and high-index plane-enhanced photodegradation by visible light. J Mater Chem A 2013;1:6888–94. https://doi.org/10.1039/c3ta10886d.

[72] Astam KP, Sudipta KK, Asim B, Dukjoon K. Morphology evolution of single-crystalline hematite nanocrystals: magnetically recoverable nanocatalysts for enhanced facet-driven photoredox activity. Nanoscale 2016;8:365–77. https://doi.org/10.1039/C5NR06509G.

[73] Sarish R, Wenglong Y, Fei L, Yu H, Ting W, Yanglong H. Facile synthesis of anisotropic single crystalline α-Fe_2O_3 nanoplates and their facet-dependent catalytic performance. Inorg Chem Front 2015;576–83. https://doi.org/10.1039/C5QI00042D.

[74] Wang X, Wang J, Cui Z, Wang S, Cao M. Facet effect of α-Fe_2O_3 crystals on photocatalytic performance in the photo-Fenton reaction. RSC Adv 2014;4:34387–94. https://doi.org/10.1039/c4ra03866e.

[75] Yubao Z, Feng P, Hui L, Tianchao N, Guoqin X, Wei C. Facile synthesis of uniform α-Fe_2O_3 crystals and their facet-dependent catalytic performance in the photo-Fenton reaction. J Mater Chem A 2013;7242. https://doi.org/10.1039/c3ta10966f.

[76] Chan JYT, Ang SY, Ye EY, Sullivan M, Zhang J, Lin M. Heterogeneous photo-Fenton reaction on hematite (α-Fe_2O_3){104}, {113} and {001} surface facets. Phys Chem Chem Phys 2015;17:25333–41. https://doi.org/10.1039/c5cp03332b.

https://www.twirpx.org & http://chemistry-chemists.com

[77] Quanjun X, Gui C, Tai-Chu L. Effects of morphology and exposed facets of α-Fe_2O_3 nanocrystals on photocatalytic water oxidation. RSC Adv 2015;52210–6. https://doi.org/10.1039/C5RA09354F.

[78] Lei WY, Hang LY, Lu WX, Yu H, Ping CA, Gui YH. Effects of redox mediators on α-Fe_2O_3 exposed by {012} and {104} facets for photocatalytic water oxidation. Appl Catal Environ 2017;216–20. https://doi.org/10.1016/j.apcatb.2016.11.028.

[79] Kanlaya P, Jun C, Wiyong K, Gordon WG, Sukon P, Andrew N. Composite photocatalysts containing $BiVO_4$ for degradation of cationic dyes. Sci Rep 2017. https://doi.org/10.1038/s41598-017-09514-5.

[80] Kudo A, Miseki Y. Heterogeneous photocatalyst materials for water splitting. Chem Soc Rev 2009;38:253–78. https://doi.org/10.1039/b800489g.

[81] Zhang X, Ai Z, Jia F, Zhang L, Fan X, Zou Z. Selective synthesis and visible-light photocatalytic activities of $BiVO_4$ with different crystalline phases. Mater Chem Phys 2007;103:162–7. https://doi.org/10.1016/j.matchemphys.2007.02.008.

[82] Conrado MS, Simelys H, Nunzio R. $BiVO_4$ as photocatalyst for solar fuels production through water splitting: a short review. Appl Catal Gen 2015;158–70. https://doi.org/10.1016/j.apcata.2014.11.044.

[83] Zongyan Z, Zhaosheng L, Zhigang Z. Electronic structure and optical properties of monoclinic clinobisvanite $BiVO_4$. Phys Chem Chem Phys 2011;4746. https://doi.org/10.1039/c0cp01871f.

[84] Xie B, Zhang H, Cai P, Qiu R, Xiong Y. Simultaneous photocatalytic reduction of Cr(VI) and oxidation of phenol over monoclinic $BiVO_4$ under visible light irradiation. Chemosphere 2006;63:956–63. https://doi.org/10.1016/j.chemosphere.2005.08.064.

[85] Fatwa AF, Tom JS, Matthias MM, Bernard D, van de Roel K. The origin of slow carrier transport in $BiVO_4$ thin film photoanodes: a time-resolved microwave conductivity study. J Phys Chem Lett 2013;2752–7. https://doi.org/10.1021/jz4013257.

[86] Ling TH, Rose A, Hau NY. Alternative strategies in improving the photocatalytic and photoelectrochemical activities of visible light-driven $BiVO_4$: a review. J Mater Chem A 2017;16498–521. https://doi.org/10.1039/C7TA04441K.

[87] Zou L, Wang H, Wang X. High efficient photodegradation and photocatalytic hydrogen production of CdS/$BiVO_4$ Heterostructure through Z-scheme process. ACS Sustain Chem Eng 2017;5:303–9. https://doi.org/10.1021/acssuschemeng.6b01628.

[88] Kim TW, Choi KS. Nanoporous $BiVO_4$ photoanodes with dual-layer oxygen evolution catalysts for solar water splitting. Science 2014;343:990–4. https://doi.org/10.1126/science.1246913.

[89] Tamar S, Nicolas C, Corinne C, Olivier D, Valérie R, Laurence M, et al. Bi_2O_3, $BiVO_4$, and Bi_2WO_6: impact of surface properties on photocatalytic activity under visible light. J Phys Chem C 2011;5657–66. https://doi.org/10.1021/jp109134z.

[90] Sun S, Wang W, Zhou L, Xu H. Efficient methylene blue removal over hydrothermally synthesized starlike $BiVO_4$. Ind Eng Chem Res 2009;48:1735–9. https://doi.org/10.1021/ie801516u.

[91] Gotić M, Musić S, Ivanda M, Šoufek M, Popović S. Synthesis and characterisation of bismuth(III) vanadate. J Mol Struct 2005;744–747:535–40. https://doi.org/10.1016/j.molstruc.2004.10.075.

[92] Jianqiang Y, Yan Z, Akihiko K. Synthesis and photocatalytic performances of $BiVO_4$ by ammonia co-precipitation process. J Solid State Chem 2009;223–8. https://doi.org/10.1016/j.jssc.2008.10.021.

[93] Somashekar MA, Siddagangamma PN, Shivanna M, Adarakatti PS, Ganganagappa N. Green synthesis of flower-like $BiVO_4$ nanoparticles by solution combustion method using lemon (*Citrus limon*) juice as a fuel: photocatalytic and electrochemical study. ChemistrySelect 2018;13456–63. https://doi.org/10.1002/slct.201801853.

[94] Lingyun Z, Zhenxiang D, Ganhong Z, Zifeng Y, Jingjing M. Superior visible light photocatalytic performance of reticular $BiVO_4$ synthesized via a modified sol–gel method. RSC Adv 2018;10654–64. https://doi.org/10.1039/C8RA00554K.

[95] Galembeck A, Alves OL. BiVO4 thin film preparation by metalorganic decomposition. Thin Solid Films 2000;365:90–3. https://doi.org/10.1016/S0040-6090(99)01079-2.

https://www.twirpx.org & http://chemistry-chemists.com

[96] Li Z, Dairong C, Xiuling J. Monoclinic structured $BiVO_4$ nanosheets: hydrothermal preparation, formation mechanism, and coloristic and photocatalytic properties. J Phys Chem B 2006;2668–73. https://doi.org/10.1021/jp056367d.

[97] Guangcheng X, Jinhua Y. Synthesis of bismuth vanadate nanoplates with exposed {001} facets and enhanced visible-light photocatalytic properties. Chem Commun 2010;1893. https://doi.org/10.1039/b923435g.

[98] Wang D, Jiang H, Zong X, Xu Q, Ma Y, Li G, et al. Crystal facet dependence of water oxidation on $BiVO_4$ sheets under visible light irradiation. Chem A Eur J 2011;17:1275–82. https://doi.org/10.1002/chem.201001636.

[99] Li R, Han H, Zhang F, Wang D, Li C. Highly efficient photocatalysts constructed by rational assembly of dual-cocatalysts separately on different facets of $BiVO_4$. Energ Environ Sci 2014;7:1369–76. https://doi.org/10.1039/c3ee43304h.

[100] Pan J, Liu G, Lu GQ, Cheng HM. On the true photoreactivity order of {001}, {010}, and {101} facets of anatase TiO_2 crystals. Angew Chem Int Ed 2011;50:2133–7. https://doi.org/10.1002/anie.201006057.

[101] Li L, Wang M. Advanced catalytic materials-photocatalysis and other current trends. IntechOpen; 2016.

[102] Teruhisa O, Koji S, Michio M. Crystal faces of rutile and anatase TiO_2 particles and their roles in photocatalytic reactions. New J Chem 2002;1167–70. https://doi.org/10.1039/b202140d.

[103] Yang J, Wang D, Zhou X, Li C. A theoretical study on the mechanism of photocatalytic oxygen evolution on $BiVO_4$ in aqueous solution. Chem A Eur J 2013;19:1320–6. https://doi.org/10.1002/chem.201202365.

[104] Sha C, Danlian H, Piao X, Xiaomin G, Wenjing X, Lei L, et al. Facet-engineered surface and interface design of monoclinic scheelite bismuth vanadate for enhanced photocatalytic performance. ACS Catal 2019;1024–59. https://doi.org/10.1021/acscatal.9b03411.

[105] Li P, Chen X, He H, Zhou X, Zhou Y, Zou Z. Polyhedral 30-faceted $BiVO_4$ microcrystals predominantly enclosed by high-index planes promoting photocatalytic water-splitting activity. Adv Mater 2018;30. https://doi.org/10.1002/adma.201703119.

[106] Jianqiang H, Huichao H, Liang L, Xin Z, Zhaosheng L, Qing S, et al. Highly symmetrical, 24-faceted, concave $BiVO_4$ polyhedron bounded by multiple high-index facets for prominent photocatalytic O_2 evolution under visible light. Chem Commun 2019;4777–80. https://doi.org/10.1039/c9cc01366k.

https://www.twirpx.org & http://chemistry-chemists.com

14

Morphology-dependent visible light photocatalysis

Tridib Kumar Sinha

DEPARTMENT OF MATERIALS ENGINEERING AND CONVERGENCE TECHNOLOGY, GYEONGSANG NATIONAL UNIVERSITY, JINJU, SOUTH KOREA

1 Introduction

Acceleration of the photoreaction (i.e., mainly oxidation and reduction) in presence of a catalyst is known as photocatalysis [1, 2]. In this process, light, after being absorbed by the catalyst, creates electron (e−)/hole (h+) pairs on the catalyst surface, resulting in generation of free radicals capable of undergoing a secondary reaction. Broadly, photocatalysis is classified into two types: homogeneous and heterogeneous. In the case of homogeneous catalysis, reactants and the photocatalysts exist in the same phase, whereas these are in different phases for heterogeneous catalysis. Because of the robustness, lower operational cost, and particularly easier recovery/separation, heterogeneous catalysis is widely preferred over homogeneous catalysis. In addition, reproduction of starting materials due to the possibility of back-electron transfer reaction is considered to be a major disadvantage of homogeneous catalysis [3–6]. Heterogeneous photocatalysis includes a large variety of reactions, e.g., mild or total oxidations, dehydrogenation, hydrogen transfer reaction, metal deposition, water detoxification, gaseous pollutant removal, etc. [8] As a consequence, heterogeneous photocatalysis is considered as an emerging green technology particularly in the areas of energy, environment, materials, and chemistry.

Generally, nanosized transition metal oxides and other semiconductors are well-known catalyst materials for heterogeneous photocatalysis [9]. A photon of energy equal to or greater than the bandgap of the photocatalyst, after being absorbed, excites an electron from the valence band (VB) to the conduction band (CB), generating a positive hole (h^+) in the valence band. This photogenerated electron (e^-)/hole (h^+) pair is known as an exciton. When the excited electrons (e^-) react with the oxidants they produce reduced products, whereas the reactions between the holes and reductants produce oxidized products [10]. Large-scale photocatalysis during pilot-scale paper production [11], conversion of water to hydrogen gas by photocatalytic water splitting [12, 13], production of self-cleaning glass [14, 15], solar water disinfection [16, 17], self-sterilizing photocatalytic coatings (particularly for food packaging) [18], oxidation of organic contaminants [19–22], conversion of carbon dioxide into gaseous hydrocarbons [22–25], sterilization of surgical

Nanostructured Materials for Visible Light Photocatalysis. https://doi.org/10.1016/B978-0-12-823018-3.00012-9
Copyright © 2022 Elsevier Inc. All rights reserved.

https://www.twirpx.org & http://chemistry-chemists.com

instruments and removal of unwanted fingerprints from sensitive electrical and optical components [26, 27], formulation of less toxic alternatives to tin- and copper-based antifouling marine paints [28], development of antifouling coatings for filtration membranes (performing as both the separation layer and photocatalyst to degrade the contaminants) [29], decomposition of crude oil (especially polyaromatic hydrocarbons (PAHs)) [30–33], developing adsorbents impregnated with active photocatalyst for decontamination of surface/ground water [34–36], performing photocatalyzed organic reactions [37–39], and moreover artificial photosynthesis [40, 41] are emerging and widely used photocatalysis processes to resolve the current energy and environmental issues in a time resolved and cost-effective manner.

At the time of writing, most of the used materials are metal oxide semiconductors, mainly zinc oxide (ZnO) and titania (TiO_2), which can perform photocatalysis only under UV irradiation. For large-scale and reasonable application of photocatalysis, apart from the catalyst materials, the source of photon (i.e., light) should be instantaneous. In this regard, use of sunlight is considered the most reliable and zero-cost light source for effective photocatalysis. Out of the total broadband solar radiation, 5%, 43%, and 52% fall in the UV region, visible region, and near infrared region, respectively [2]. As mentioned above, it can be said that the traditional photocatalysts are mainly effective in the presence of UV light which accounts for only 5% of the total solar spectrum. In addition, as UV light is harmful to the human body, it is not advisable to perform even lab-scale photocatalysis experimentation [42, 43]. Thus, there is a huge demand for developing suitable materials for efficient visible light photocatalysis.

Many attempts are being made to modify existing materials, and/or develop new materials. Although various new semiconductors including oxides, sulfides, nitrides (or oxy nitrides) of various metals mainly having d^0 and d^{10} configuration, metal-free semiconductors, plasmonic metals, and other elemental photocatalysts are currently reported for their multifaceted applications, most of these materials remain unable to completely satisfy the practical requirements, e.g., long lifetime of the excitons, low bandgap energy enable to fully utilize the broadband solar spectrum, safety, low cost, high efficiency and reproducibility, all of which greatly hinders their practical usability [44]. In this scenario, development of efficient and stable photocatalysts capable of performing under visible light quickly becomes crucial. Optimization of the synthesis strategies toward varying the morphologies (i.e., shape, appearance, texture, topography, etc.) of the existing or new photocatalyst materials, coupling with different nanomaterials (e.g., nanocarbons, plasmonic nanometals, etc.), adding the cocatalysts, developing efficient heterojunctions and all-solid-state *Z*-schemes are being attempted to enable efficient visible light photocatalysis. In this regard, the modification of heterogeneous photocatalysts for improving their activity is being achieved mainly by two ways: structural and compositional.[45–48] In the case of heterojunction photocatalysts developed through making the junction of two or multiple photoactive materials, the morphologies of the component materials should be well-matched. In addition, it has been observed that the photocatalytic performance of the semiconductors is strongly dependent on their crystal morphologies and structural

https://www.twirpx.org & http://chemistry-chemists.com

features at the nanometer level to ensure the possible maximum absorption of the light and presence of active sites to be reacted with the reactants [3, 44–49]. Thus, optimization and control over the structural properties of the photocatalysts become important to realize their enhanced performance.

Various synthesis and structure-engineering strategies have been found promising to develop efficient photocatalysts having desirable structures and morphologies [44, 45, 47, 49–51]. Photocatalysts having modified surface area, preferred planar orientation, and enhanced active sites to ensure their efficiency are being realized through alteration of their nanostructured morphologies. By varying the morphology, the rate of photocatalytic activity can be controlled through controlling the number of photons striking on the surface of the catalyst by controlling its effective surface area and tuning the bandgap [10]. Based on the type of confinement, the nanomaterials are classified into zero- (0D), one- (1D), two- (2D), and three-dimensional (3D). For 0D materials, the electron is confined in all three dimensions, whereas it is confined in two and one dimensions for 1D and 2D nanomaterials, respectively. 0D materials are spherical nanoparticles/quantum dots, etc. 1D and 2D materials are wires/rods and nanosheets, respectively [45, 50].

Among various methods, the hydro-/solvothermal method, being ecofriendly, cost-effective, and facile, has been recognized as the most common and widely accepted way to develop a large variety of morphology (microstructure) [45]. During synthesis of nanomaterials, the choice of reducing agents, ligands, and templates, in addition to the precursor materials and solvent, plays a vital role to develop the various morphologies of the nanomaterials [44, 45, 47, 50, 52–54]. Other than these liquid phase synthesis, physical methods (e.g., mechanical grinding, ultrasonication, physical vapor deposition (e.g., glancing angle deposition)) are found effective to develop photocatalysts of varying morphologies [55, 56]. Considering all these factors, although various approaches have been proposed to develop efficient visible light photocatalysts having desired structures and morphologies, among them, preparation of self-assembled 3D hierarchical nanostructures is being considered the most promising and feasible strategy [44, 50, 51]. This kind of synthesis approach not only facilitates the prevention of aggregation but also enhances the quantum efficiency of the photocatalysts because of their special hierarchical architecture. After pioneering the formation of hierarchical 3D ordered structures of different oxide materials (by Yang et al. in 1998) [57], significant research works have been accomplished for designing and synthesis of high-performance photocatalysts of various hierarchical functional nanomaterials of controlled morphology, nanocrystallinity, composition, facets, dimensionality, porous microstructure, etc. Hierarchical nanomaterials assembled with interconnected porous structures and active surface of large area enhance light harvesting efficacy, as well as promoting the adsorption and transportation of higher amounts of reactants to the active sites, resulting in significantly enhanced photocatalytic performance.

Instead of using UV or visible light, attempts to use nondestructive far infrared light (which accounts for 52% of total solar spectrum) are currently being made for photocatalysis [58]. It has been noticed that the tunable use of different light source by a single material can be achieved by varying its morphology. Further, scientists are attempting to improve

https://www.twirpx.org & http://chemistry-chemists.com

the photocatalysis performance by introducing different external forces (e.g., piezo-/triboelectric power) which may enable fast and high-yield photocatalysis output [59–62].

In this chapter, morphology-dependent visible light photocatalysis (i.e., heterogeneous) has been attempted for thorough discussion. Accordingly, the basic idea about the morphology including the synthesis procedures to enable nanostructured materials having varied morphologies, types of photocatalysts, brief discussion on morphology-dependent visible light photocatalysis by exemplifying the reported materials of various morphologies, and future scope of high yield broadband solar light (ranging from UV to visible to near infrared) photocatalysis have been included in this chapter.

2 General mechanism of photocatalysis

During photocatalysis, photons or light energy, after being absorbed by the catalysts, generate electron (e^-)/hole (h^+) pairs to initiate redox reactions with the surface adsorbed molecule(s) to yield the final products (as shown in Fig. 1).

Broadly, when light energy that is equivalent/higher compared to the bandgap energy (Eg) of the photocatalyst material is irradiated, valence band (VB) electrons are excited to the conduction band (CB) with subsequent formation of holes (h^+) in the VB of the photocatalyst. These photogenerated electrons (e^-) and holes (h^+), also known as excitons, undergo subsequent oxidation or reduction of the surface adsorbed test materials to generate the final products [45]. Efficient photocatalysis could be enabled if the bandgap energy between e^- and h^+ were higher than that needed for the desired redox reaction, and the rate of this redox reaction is faster than that of the electron (e^-)/hole (h^+) recombination. In short, photocatalysis consists of five fundamental processes: (1) light absorption, (2) excitation, (3) charge separation, (4) migration or transportation of charge carriers, and (5) photocatalysis on the catalyst surface (surface reaction). Another competitive happening to the surface reaction, i.e., recombination of charge carriers, may also be possible if the bandgap energy is low, which is considered a major

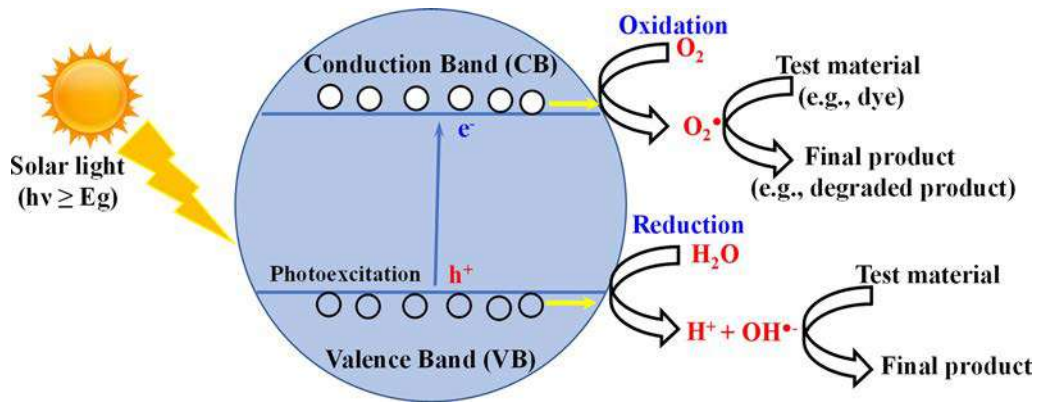

FIG. 1 Basic principle of heterogeneous photocatalysis.

https://www.twirpx.org & http://chemistry-chemists.com

disadvantage of photocatalysis [51]. Because of shorter wavelength or higher energy, UV irradiation can promote photoexcitation, followed by generation of electron/hole pairs for maximum semiconductor photocatalysis, especially TiO_2 and ZnO. In contrast, visible light, being lower-energy solar radiation, can promote photocatalysis with difficulties, or visible light photocatalysis results in very poor yield. Considering that the solar spectrum consists of 43% nonhazardous visible light compared to the 5% hazardous UV light, tremendous research efforts are being carried out to utilize visible light for sustainable and potential green photocatalysis. However, photocatalysis, particularly in terms of visible light, suffers from various requirements, e.g.:

(1) availability of suitable materials capable to harvest maximum solar energy for subsequent generation of sufficiently energetic excitons having high mobility and long diffusion length enabling suppression of the bulk recombination;
(2) generation of excitons having strong redox power sufficiently effective to promote the redox reactions, such as water oxidation, which needs four electrons; and.
(3) presence of abundant active sites on the catalyst surface to ensure forward reactions and suppression backward reactions [44, 63].

In this regard, apart from developing new materials to be highly active under visible light illumination, featuring various morphologies on these new materials or existing materials are being afforded to realize and accomplish visible light photocatalysis [64–89]. As the photocatalytic reaction takes place in the adsorbed phase of the photocatalyst, and the number of photons striking the catalyst surface controls the rate of photocatalysis, the tunability of surface morphology toward developing the nanostructured materials accompanied with a larger active surface area may show better photocatalytic performance than that containing a smaller active surface area. Thus, tunability of catalyst morphology can be of immense importance to enable the photocatalytic reaction in a desired manner. Although broadband light (particularly visible light) absorption efficacy can be accomplished by tuning the materials morphology or by developing new materials, an increase of light absorption range (i.e., from UV to visible) by the materials having reduced bandgaps usually results in lowering the efficacy of electrons and holes for efficient reduction and oxidation, respectively. Thus, there are different underlying conflicts associated with photocatalysis, particularly for visible light irradiation [3, 10, 44–51, 86–90]. Other than this morphology dependency, many more factors regulate the photocatalysis, e.g., catalyst loading and its crystal structure, crystallinity, crystal size, surface structure, cocatalyst concentration and nature of the test materials (e.g., dye), pH of the solution, temperature, irradiation of time and intensity of light, presence of inorganic ions, external stimuli (e.g., mechanical stimuli: ultrasonication), etc. [45]

Before detailing photocatalysts and the impacts of their morphologies on visible light photocatalysis, it is useful to understand properly the morphology of the catalyst materials, and related electronic properties toward promoting efficient photocatalysis reactions. In the following section, we provide a brief discussion about the morphology of different nanostructured materials.

https://www.twirpx.org & http://chemistry-chemists.com

3 Morphology

Herein, we have attempted to summarize the different types of morphology, their electronic properties, and the morphology dependency on the photocatalysis. As per the International Union of Pure and Applied Chemistry (IUPAC), morphology of a material can be defined by its shape, appearance, texture, and phase domain types [50]. Although the morphology and shape of nanomaterials seem to be synonymous, the morphology means the specific dimensions including size, uniformity, roundedness, sphericalness, aspect ratio, etc. while the shape considers appearance (i.e., the projection) only (as presented in Fig. 2).

The shape of nanomaterials may be regular or irregular. The shape may be similar while having different morphology. The concept of morphology needs an appropriate classification to describe the morphology of various materials on the basis of different advanced microscopic imaging techniques (e.g., SEM, TEM). Pokropivny and Skorokhod developed a modified classification system depending on the geometrical dimension (e.g., 0D, 1D, 2D) of the nanomaterials [91]. In Fig. 3, nanostructures of various morphology and corresponding plots of energy versus density of states (DOS) have been represented. For various nanostructures, the DOS is determined by its degree of confinement [50, 86, 90].

From Fig. 3, it can be seen that by decreasing the dimensionality, the DOS becomes discrete, which increases the confinement of electron and hole mobility and decreases the delocalization of the electron. For 0D materials, the electron is confined in a 3D space and no electron delocalization occurs. In the case of 1D materials, electron confinement occurs in 2D, and its delocalization takes place along the long axis of the material (e.g., nanowire, rod, tube). For 2D materials, the electron is confined in 1D (i.e., across the

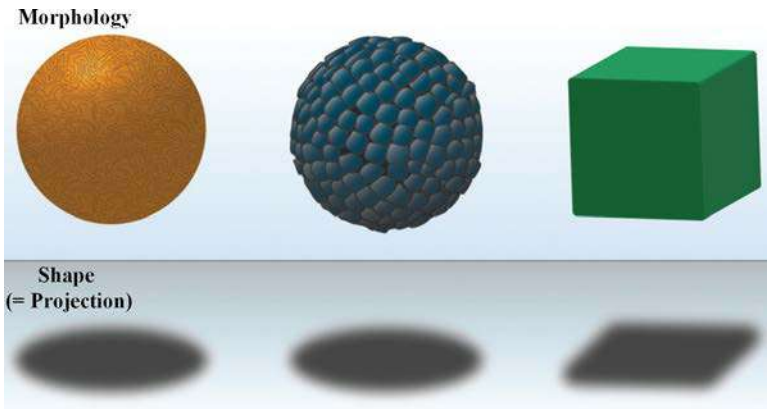

FIG. 2 Pictorial representation of morphology and shape of nanomaterials. *Top*: morphology (left to right: sphere of smooth surface, sphere of rough surface, and cube of smooth surface); *bottom*: shape or projection (left to right: spherical, spherical, and square).

https://www.twirpx.org & http://chemistry-chemists.com

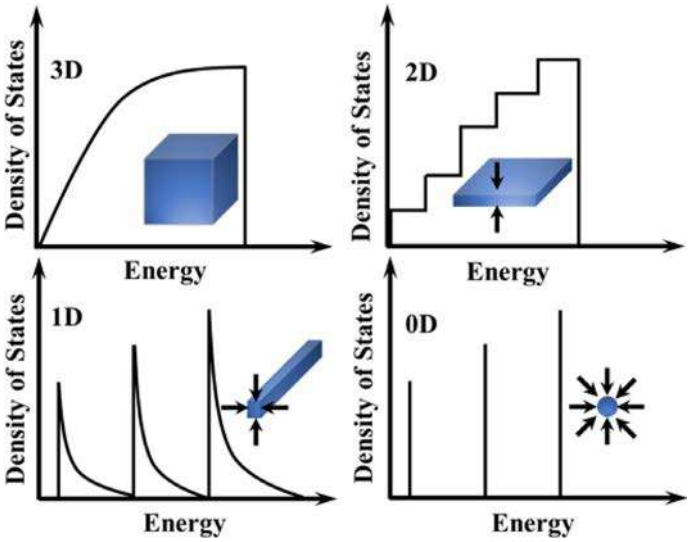

FIG. 3 Electronic density of states of the nanomaterials having various dimensional morphologies (3D, 2D, 1D, and 0D).

thickness), and delocalized in 2D (i.e., the plane of the sheet). Electrons are fully delocalized in the case of 3D nanomaterials. According to the "particle-in-a-box" model, the degree of quantization along the confined direction increases with the reduction of dimension. In general, it can be said that the higher the DOS is, the sparser the band structure is.

Again from Fig. 3, it can be seen that with reducing the dimension, for instance, from 3D to 2D, the DOS is changed from continuous square-root to a step-like. Considering the particle-in-a-box approximations, because of the confinement effect and changed dimensionality, some interesting features can be noted as follows [86, 90].

(1) As the degree of confinement increases, the electron-hole binding energy also increases, suggesting the enhanced possibility of exciton formation for the materials of lower dimension having a higher degree of confinement.
(2) With reduction of dimension, bandgaps are enlarged.
(3) The stronger the confinement is, the larger the bandgap is, and consequently the larger the emission energy is during recombination of excitons. Thus, according to the strength of confinement and bandgap energy (ΔE_g), the materials of different dimensionality can be expressed as $0D > 1D > 2D > 3D$.

The increasing bandgap is also associated with decreasing the size [86, 90]. The enlarged bandgap, due to the large driving force of photogenerated charge carriers (or excitons), causes low recombination and favors redox reactions. However, by increasing the bandgap energy, absorption of light of higher wavelength or lower energy decreases which limits the feasibility of high bandgap energy materials to be effective under irradiation

https://www.twirpx.org & http://chemistry-chemists.com

of low-energy visible light. Thus, to enable visible light photocatalysis, band engineering through structural or morphological modification is highly important. We shall now consider the outlook and facts of the different nanomaterials having various morphologies.

3.1 Zero-dimensional (0D) nanostructures

0D nanostructures, e.g., quantum dots [92], spheres, ellipsoids [93], and polyhedra [94], having nanoscale dimensions of a few to several nanometers (Fig. 4), can be amorphous or crystalline, consisting of single or more chemical elements [50]. Quantum dots (QDs) having diameter of 2–10 nm are shapeless, irregular polyhedra, and because of the high surface-to-volume ratio, they exhibit unique electronic properties. Although facets (i.e., flat faces on particular geometric shapes) are not well developed in QDs, they are efficient to interact with the surroundings because of their high surface energy and presence of undercoordinated atoms [95].

Various nanomaterials are transformed to spheres by reducing their surface energy, which is known to be most stable morphology in nature. Nanosphere materials exhibit a high surface-to-volume ratio and good mechanical performance. In addition, they show a better dispersion property due to the plausibility of existing the electrostatic charges in their surface. When the spheres are elongated in one direction, ellipsoids are formed which are generally unstable under extreme conditions and tend to transform the most stable spherical geometry again by minimizing the surface energy. Nanomaterials having cubic crystal symmetry and (100) facets exhibit cubical morphology. In this case, the high surface energy caused by the undercoordinated atoms is minimized by rounding their edges and vertices. Well-oriented 1D superstructures exhibiting controlled electromagnetic properties are often made of the cubes as building blocks. Octahedra (having eight (111) facets) and cubes are the most studied nanostructures for their interesting physicochemical properties. Depending on the orientation, octahedron morphologies can be viewed under a microscope as rectangles, rhombuses, hexagons, etc. Among all the aforementioned 0D morphologies, the precise synthesis of octahedra is quite difficult, and octahedra are often considered as classical models for examining various surface properties.

Different plasmonic nanomaterials are generally found to possess 0D morphologies [66, 72]. Because of their low bandgap, they are mostly capable of capturing low-energy visible light. However, because of the low confinement effect, there is always a chance of charge carrier recombination, which reduces the photocatalytic performance of 0D materials. Thus, the visible light harvesting efficacy especially of different 0D plasmonic nanomaterials is being utilized for efficient visible light photocatalysis through different surface engineering approaches. As, 0D nanomaterials are more susceptible to interact with the surrounding molecules (especially due to their spherical shape and smaller size) compared to the bulk materials, herein, because of the plausible interaction with the surrounding, the different composite nanostructures of 0D plasmonic materials are being proposed for development of efficient photocatalytic system [47, 66, 72]. On the other hand, the formation of heat due to the charge carrier recombination may speed up the catalysis reactions.

https://www.twirpx.org & http://chemistry-chemists.com

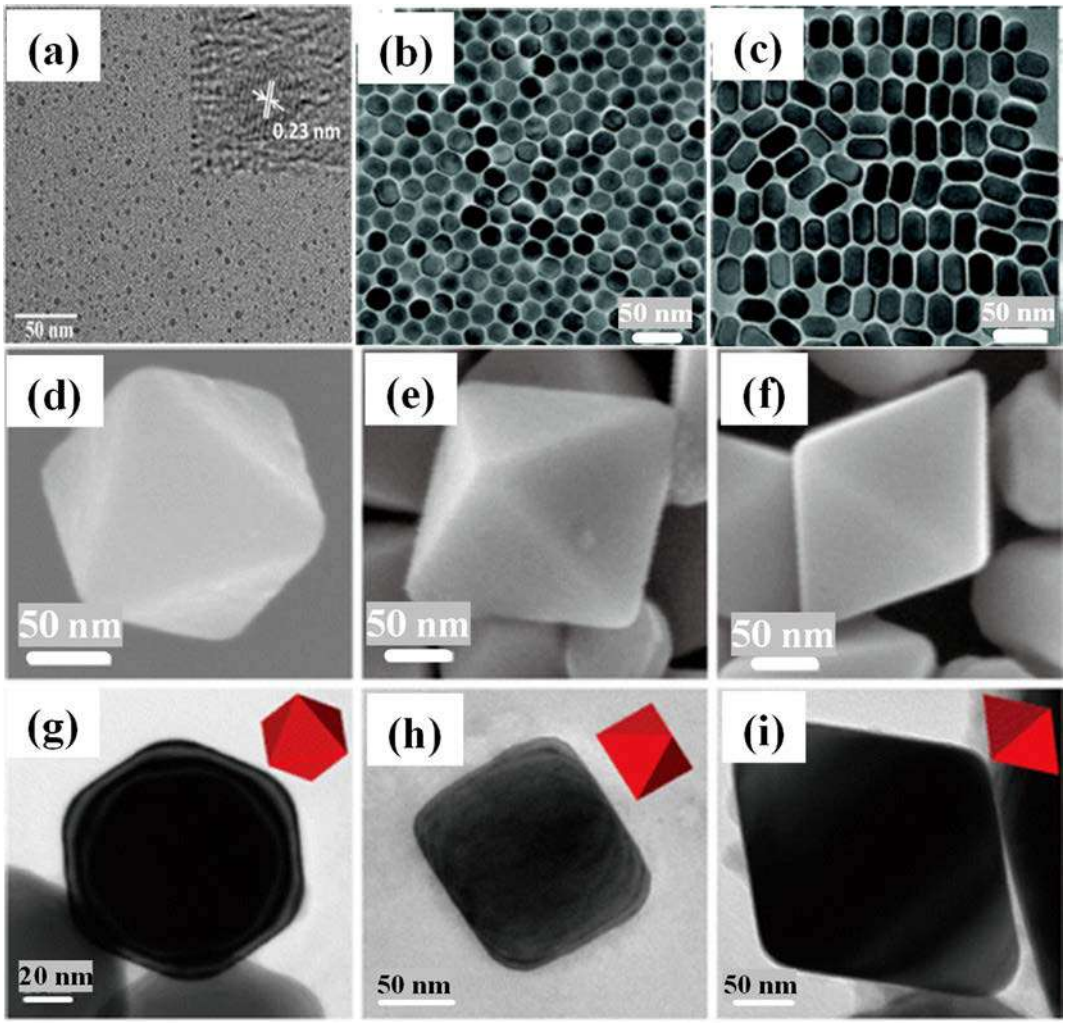

FIG. 4 Microscopic (A–C and G–I—TEM; D–F—SEM) images of 0D nanostructures: (A) quantum dots; (B) spheres; and (C) elongated nanocrystals. Octahedron viewed from (111) axis (D and G), (112) axis (E and H), and (110) axis (F and I) *Panel (A) adapted with permission from Yu, Chunhe, Xiaohua Jiang, Dongmiao Qin, Guichun Mo, Xiangfei Zheng, and Biyang Deng. Facile syntheses of s, n-codoped carbon quantum dots and their applications to a novel off–on nanoprobe for detection of 6-thioguanine and its bioimaging. ACS Sustain Chem Eng 7.19 (2019): 16112–16120. Copyright (2019), American Chemical Society. Panel (C) adapted with permission from Li, Peng, Caiyun Nan, Zhe Wei, Jun Lu, Qing Peng, and Yadong Li. Mn3O4 nanocrystals: facile synthesis, controlled assembly, and application. Chem Mater 22.14 (2010): 4232–4236. (Copyright 2010), American Chemical Society. Panels (F) and (I) adapted with permission from Lu, Shu-Chen, Ming-Cheng Hsiao, Mustafa Yorulmaz, Lin-Yung Wang, Po-Yuan Yang, Stephan Link, Wei-Shun Chang, and Hsing-Yu Tuan. Single-crystalline copper nano-octahedra. Chem Mater 27.24 (2015): 8185–8188. Copyright (2015), American Chemical Society.*

https://www.twirpx.org & http://chemistry-chemists.com

3.2 One-dimensional (1D) nanostructures

1D nanostructure includes different shapes, e.g., rods [96], wires [97], tubes [98], belts [99], hooks, ribbons, needles [100], helices (or spirals) [101], fibers [102], zigzags [103, 104], etc. (Fig. 5). 1D material shows a high ratio of any one dimension (e.g., X-direction) over the two others (Y- and *Z*-directions) (e.g., length≫width or diameter) [95]. In many cases, any of the dimensions can reach even the millimeter range. Rods exhibiting aspect ratios

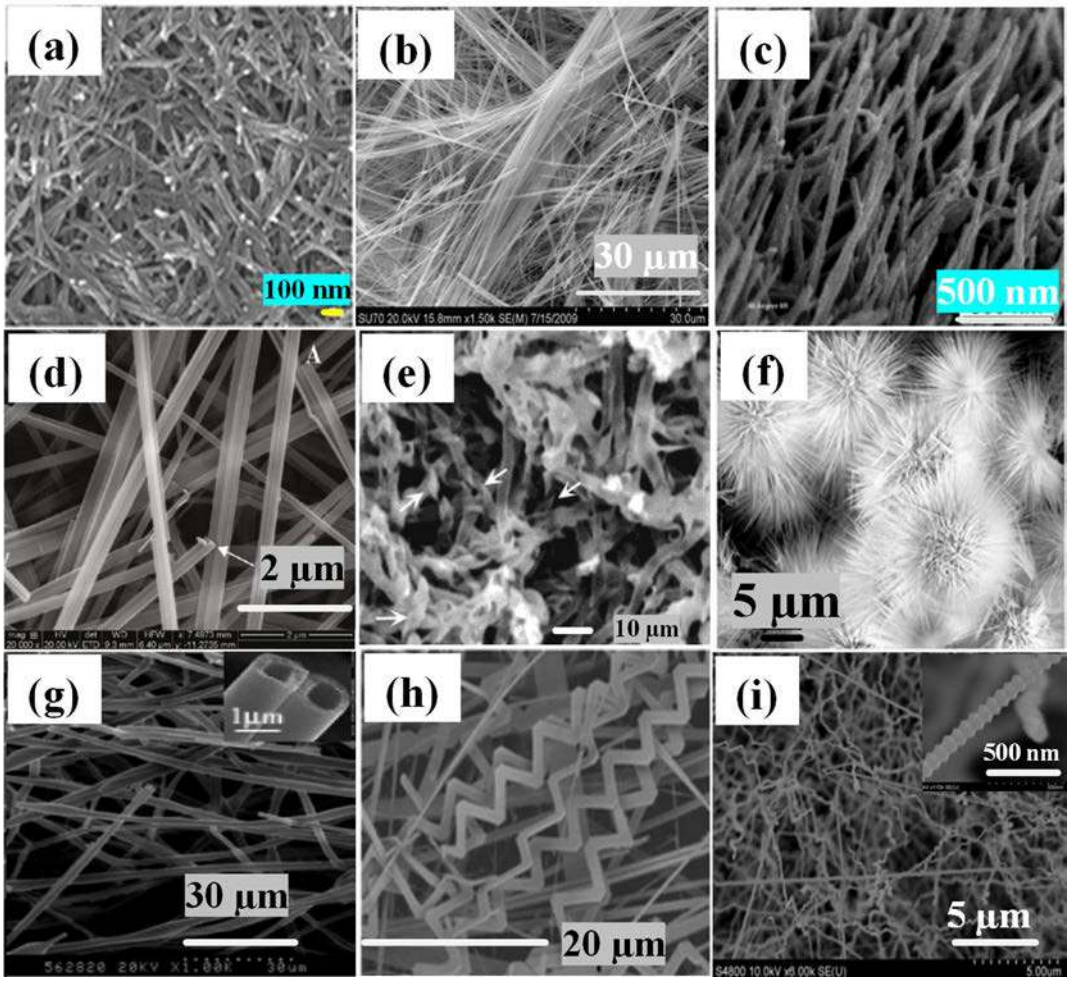

FIG. 5 Microscopic (SEM) images of 1D nanostructure materials: (A) rod shape; (B) wires; (C) arrays of nanotubes; (D) belt-like; (E) ribbons of helical structure, and layered nanotubes; (F) needles; (G) hollow fiber structures; (H) belt of zigzag structure; and (I) zigzag. *Panel (A) adapted with permission from Zhang, Xiong, Peng Yu, Dacheng Zhang, Haitao Zhang, Xianzhong Sun, and Yanwei Ma. Room temperature synthesis of Mn3O4 nanoparticles: characterization, electrochemical properties and hydrothermal transformation to γ-MnO2 nanorods. Mater Lett 92 (2013): 401–404. (Copyright 2013), Elsevier. Panel (B) adapted with permission from Patridge, Christopher J., Tai-Lung Wu, Cherno Jaye, Bruce Ravel, Esther S. Takeuchi, Daniel A. Fischer, G. Sambandamurthy, and Sarbajit Banerjee. Synthesis, spectroscopic characterization, and*

(Continued)

https://www.twirpx.org & http://chemistry-chemists.com

(i.e., the ratio of longer side (length) to the shorter side (width or diameter)) of 3–5 may appear as aggregates with different building blocks, e.g., dots, polyhedral, platelets, etc. In contrast, the wires are thinner and more flexible, and exhibit an aspect ratio greater than 1000. Generally, the structure of wires is defectless and simple, facilitating the passing of electrons without any obstacle. Tubes are single- or multiwalled, and hollow. Based on the wall structure (i.e., how they are rolled up), the properties of tubes are varied. Belts are ribbon-shaped with a rectangular cross-section. They are thin and flat. Because of high specific surface areas, the nanomaterials having 1D belt morphology are often used in photocatalysis [85, 105]. The ease in developing phase pure and dimensionally controlled 1D nanomaterials via different advanced synthesis strategies has widened its applications in different areas, especially photocatalysis. Due to the presence of highly anisotropic bonding in 1D nanocrystal, many materials of 1D morphology are found to be naturally grown. 1D nanomaterials, because of their large aspect ratio, not only facilitate charge transportation and charge carrier collection, but also cause lower recombination loss [10, 45, 47, 50, 85, 86, 105]. Thus, the nanomaterials of 1D architecture have huge potential to be applied in photocatalytic solar energy conversion. In addition, the feasibility of 1D materials to be integrated into higher-order 2D and 3D architectures (including biomimetic hierarchical nanomaterials) of enhanced optical, electrical, and mechanical properties makes it more interesting in the area of photocatalysis. Other advantages associated with 1D materials are ease in processability and tailorability in selective functionalization (toward various special architectures, e.g., self-assembly, core-shell).

Two kinds of approaches, top-down and bottom-up, are mainly considered to develop the nanomaterials of 1D morphology. The details of fabricating 1D nanomaterials have been well described in various reports [50, 85].

FIG. 5, cont'd observation of massive metal insulator transitions in nanowires of a nonstoichiometric vanadium oxide bronze. Nano Lett 10, 7 (2010): 2448–2453. Copyright (2010), American Chemical Society. Panel (C) adapted with permission from Tian, Zhengrong R., James A. Voigt, Jun Liu, Bonnie Mckenzie, and Huifang Xu. Large oriented arrays and continuous films of TiO2-based nanotubes. J Am Chem Soc 125, no. 41 (2003): 12384–12385. Copyright (2003), American Chemical Society. Panel (D) adapted with permission from Chandrappa, Gujjarahalli Thimmanna, Pallellappa Chithaiah, Siddaramanna Ashoka, and Jacques Livage. Morphological evolution of (NH4) 0.5 V2O5· m H2O fibers into belts, triangles, and rings. Inorg Chem 50, 16 (2011): 7421–7428. Copyright (2011), American Chemical Society. Panel (E) adapted with permission from Jung, Jong Hwa, Hideki Kobayashi, Kjeld JC Van Bommel, Seiji Shinkai, and Toshimi Shimizu. Creation of novel helical ribbon and double-layered nanotube TiO2 structures using an organogel template. Chem Mater 14, 4 (2002): 1445–1447. Copyright (2002), American Chemical Society. Panel (F) adapted with permission from Guan, Qun, Jianli Cheng, Bin Wang, Wei Ni, Guifang Gu, Xiaodong Li, Ling Huang, Guangcheng Yang, and Fude Nie. Needle-like Co3O4 anchored on the graphene with enhanced electrochemical performance for aqueous supercapacitors. ACS Appl Mater Interfaces 6, 10 (2014): 7626–7632. Copyright (2014), American Chemical Society. Panel (G) adapted with permission from Zhan, Sihui, Dairong Chen, Xiuling Jiao, and Caihong Tao. Long TiO2 hollow fibers with mesoporous walls: sol – gel combined electrospun fabrication and photocatalytic properties. J Phys Chem B 110, 23 (2006): 11199–11204. Copyright (2006), American Chemical Society. Panel (H) adapted with permission from Butt, Faheem K., Chuanbao Cao, Waheed S. Khan, Muhammad Safdar, Xuewen Fu, Muhammad Tahir, Faryal Idrees, Zulfiqar Ali, Ghulam Nabi, and Dapeng Yu. Electrical and optical properties of single zigzag SnO 2 nanobelts. CrstEngComm 15, 11 (2013): 2106–2112. Copyright (2013), Royal Society of Chemistry. Panel (I) adapted with permission from Suo, Guoquan, and Jianye Li. One dimensional polar surface dominated GaN nanostructures with zigzag morphology. J Alloys Compd 674 (2016): 16–20. Copyright (2016), Elsevier.

https://www.twirpx.org & http://chemistry-chemists.com

3.3 Two-dimensional (2D) nanostructures

2D nanomaterials including plates [106], membranes [7, 107], discs [108], walls [109], flakes [110], films [111], diskettes [112], rings [113], etc. possess thickness of a few to tens of nanometers, lateral dimension of a few nanometers to many centimeters, and show a very high surface-to-volume ratio (because of their possible extremely large surface area) (Fig. 6) [50, 86, 87]. In the last few years, immense research interest has been paid to 2D materials for use in different advanced applications. In general, 2D materials having single- or multilayered nanostructures are known to exhibit strong covalent bonds in the basal plane and weak Van

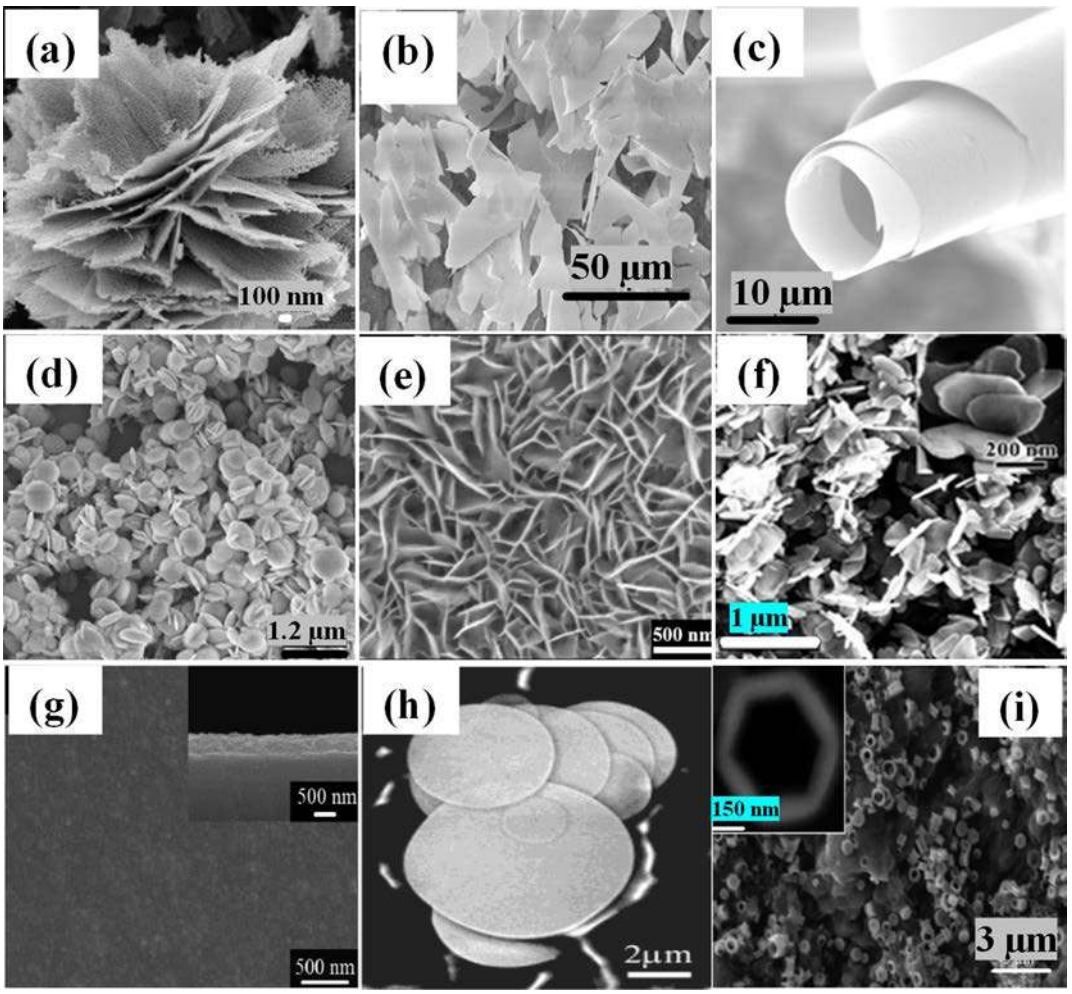

FIG. 6 Microscopic (SEM) images of 2D nanostructure materials: (A) plates; (B) membranes (licensed under CC-BY [7]); (C) membranes (licensed under CC-BY [107]); (D) discs; (E) arrays of wall; (F) flakes; (G) thick films; (H) diskettes; and (I) ring-like. *Panel (A) adapted with permission from Jing, Zhihong, and Jinhua Zhan. Fabrication and gas-sensing*

(Continued)

https://www.twirpx.org & http://chemistry-chemists.com

der Waals interactions among the layers. Because of the ease in surface functionalization and processability, presence of active sites, and possibility to assemble into 3D structures, various 2D materials, e.g., graphene, metal oxides/hydroxides/chalcogenides, polymers, boron nitride, phosphorene, MXenes, metal organic frameworks (MOFs), etc. are being enormously used in different areas (e.g., photocatalysis) with or without other supporting substrates [114]. These nanomaterials with 2D morphology have been synthesized using various top-down and bottom-up approaches including solvent extraction, exfoliation, vapor deposition, and other wet chemical methods [86, 87]. Among the different nanostructures, platelets, based on the crystal structure and growth direction, under 2D microscopy may appear like flat triangles, rectangles, rhombuses, or hexagons. Discs and discoids on the other hand possess circular or irregular shape. Film and sheet exhibit very high aspect ratios (although not well-defined), and generally have superior mechanical properties. During the formation of film over the substrate, the film-substrate and film-film (i.e., layer-layer) interactions determine the initial nucleation and growth of the nanostructured materials. The ease in processing of 2D materials of different functionalities enables their wide applications in different areas, e.g., sensors, electronic devices, photocatalysts, etc.

High aspect ratio, larger surface area, possibility in separating the charge carriers between the edges and basal plane, ease in modification of the properties through enabling easy incorporation of different host materials within the 2D structure, possibility of strain-modulated band structure toward lowering the bandgap for efficient visible light absorption, etc. make 2D materials very promising in the area of photocatalysis [44–46, 86, 87].

3.4 Three-dimensional (3D) nanostructures

3D nanostructures having three random dimensions $\geq$100 nm are generally assembled of 0D, 1D, 2D, or multiscale nanocomponents [50, 51]. The examples are spheres [93, 115], polyhedra [116] (e.g., tetrahedra, cubes, octahedra), multipods [116, 117] (e.g., eightpod cubes, six-armed starlike), and hierarchical structures [44, 118–123] (e.g., doughnuts,

FIG. 6, cont'd properties of porous ZnO nanoplates. Adv Mater 20, 23 (2008): 4547–4551. Copyright (2008), John Wiley and Sons. Panel (D) adapted with permission from Chen, Chao, Hong Jian, Kaiguang Mai, Zhimin Ren, Jia Wang, Xinxin Fu, Chenyao Fan, Chunxiao Sun, Guodong Qian, and Zhiyu Wang. Shape-and size-controlled synthesis of Mn3O4 nanocrystals at room temperature. Eur J Inorg Chem 2014, 19 (2014): 3023–3029. Copyright (2014), John Wiley and Sons. Panel (E) adapted with permission from Chiu, I-Ting, Chun-Ting Li, Chuan-Pei Lee, Pei-Yu Chen, Yu-Hao Tseng, R. Vittal, and Kuo-Chuan Ho. Nanoclimbing-wall-like CoSe2/carbon composite film for the counter electrode of a highly efficient dye-sensitized solar cell: a study on the morphology control. Nano Energy 22 (2016): 594–606. Copyright (2016), Elsevier. Panel (F) adapted with permission from Han, Xi-Guang, Hui-Zhong He, Qin Kuang, Xi Zhou, Xian-Hua Zhang, Tao Xu, Zhao-Xiong Xie, and Lan-Sun Zheng. Controlling morphologies and tuning the related properties of nano/microstructured ZnO crystallites. J Phys Chem C 113, no. 2 (2009): 584–589. Copyright (2009), American Chemical Society. Panel (G) adapted with permission from Yuan, Y. F., X. H. Xia, J. B. Wu, J. L. Yang, Y. B. Chen, and S. Y. Guo. Hierarchically ordered porous nickel oxide array film with enhanced electrochemical properties for lithium ion batteries. Electrochem Commun 12, no. 7 (2010): 890–893. Copyright (2010), Elsevier. Panel (H) adapted with permission from Dai Zu Rong, Zheng Wei Pan, and Zhong L. Wang. Growth and structure evolution of novel tin oxide diskettes. J Am Chem Soc 124, 29 (2002): 8673–8680. Copyright (2002), American Chemical Society. Panel (I) adapted with permission from Peng, Yin, An-Wu Xu, Bin Deng, Markus Antonietti, and Helmut Cölfen. Polymer-controlled crystallization of zinc oxide hexagonal nanorings and disks. J Phys Chem B 110, no. 7 (2006): 2988–2993. Copyright (2006), American Chemical Society.

https://www.twirpx.org & http://chemistry-chemists.com

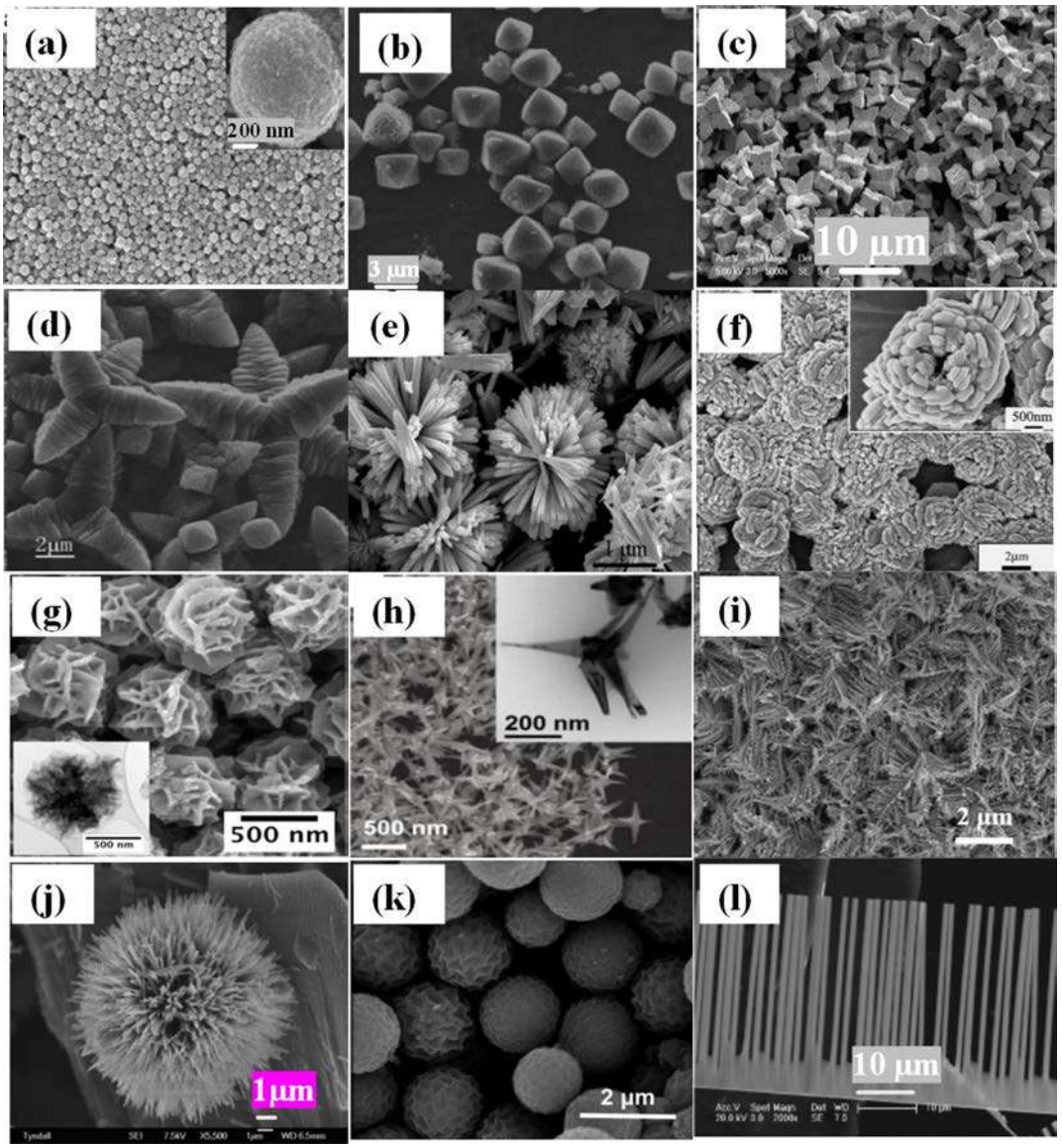

FIG. 7 Microscopic (SEM) images of 3D nanostructure materials: (A) spheres; (B) octahedra; (C) cubes having eight pods; (D) six-armed stars (); (E) microspheres made of nanorods; (F) doughnut-like; (G) flower-like; (H) multipods; (I) dendritic; (J) urchin-like; (K) balls; and (L) branches. *Panel (A) adapted with permission from Li, Peng, Caiyun Nan, Zhe Wei, Jun Lu, Qing Peng, and Yadong Li. Mn3O4 nanocrystals: facile synthesis, controlled assembly, and application. Chem Mater 22.14 (2010): 4232–4236. Copyright (2010), American Chemical Society. Panel (D) adapted with permission from Liu, Huarong, Weifeng Miao, Song Yang, Zengming Zhang, and Jiafu Chen. Controlled synthesis of different shapes of Cu2O via γ-irradiation. Cryst Growth Des 9, 4 (2009): 1733–1740. Copyright (2009), American Chemical Society. Panel (E) adapted with permission from Zhang, Yuan, Jiaqiang Xu, Qun Xiang, Hui Li, Qingyi Pan, and Pengcheng Xu. Brush-like hierarchical ZnO nanostructures: synthesis, photoluminescence and gas sensor properties. J Phys Chem C 113, 9 (2009): 3430–3435. Copyright (2009), American Chemical Society. Panel*

(Continued)

https://www.twirpx.org & http://chemistry-chemists.com

flowers, dendritic, urchins, balls, branches). (Fig. 7). The 3D spheres and polyhedra are basically polycrystalline in nature, and made of various low-dimensional (0D/1D) building blocks, e.g., dot, rod, platelet. In comparison to the 0D, the 3D spheres and polyhedra are larger and often exhibit porous, hollow, or multilayered structure. They are found with different surface properties (smooth or rough). 3D nanostructure with a spherical core and long arms (4–8) of uniform width and rounded ends is known as a multipod. It exhibits a high aspect ratio. In the case of cones, the height and diameter are the same in order of magnitude. The cones are mostly made of carbon. For example, the cone morphology can be found on the graphite surface. Balls are well-ordered spheres having dendritic exteriors and rough surfaces. Hierarchical nanostructures are made of low-dimensional subunits, and possess nature-inspired well-organized structures, e.g., trees, flowers, and sea urchins. Consequently, most hierarchical structures are porous in nature. Because of the availability of the various synthesis strategies, the physicochemical properties of the hierarchical nanomaterials can be precisely tuned for specific applications.

For instance, the flowerlike structures, made of several layers having interconnected petals of different shapes and thickness, exhibit a very good surface-to-volume ratio, abundant adsorption sites, and quite good charge transfer propertes. Generally, the sizes of flower-like nanomaterials are in the range 100–500 nm. This type of architecture can be used in designing different novel catalysts, solar cells, biosensors, etc. Among the other 3D nanostructures, branches made of long arms radially grown from the main frame have been widely studied due to their facile synthetic strategies from different types of chemical compounds and ease in modification. The properties of branches are varied with their length and morphology. The branches are considered as fractal for a tree-like structure. Urchins are made of a sphere covered with highly dense interconnected needles. Compared to the multipods, urchins are spherical cores attached with a greater number of

FIG. 7, cont'd (F) adapted with permission from Liang, Jianbo, Jianwei Liu, Qin Xie, Sha Bai, Weichao Yu, and Yitai Qian. Hydrothermal growth and optical properties of doughnut-shaped ZnO microparticles. J Phys Chem B 109, 19 (2005): 9463–9467. Copyright (2005), American Chemical Society. Panel (G) adapted with permission from Chen, Shucheng, David Mathai Koshy, Yuchi Tsao, Raphael Pfattner, Xuzhou Yan, Dawei Feng, and Zhenan Bao. Highly tunable and facile synthesis of uniform carbon flower particles. J Am Chem Soc 140, 32 (2018): 10297–10304. Copyright (2018), American Chemical Society. Panel (H) adapted with permission from Vakil, Parth N., David A. Hardy, and Geoffrey F. Strouse. Synthesis of highly uniform nickel multipods with tunable aspect ratio by microwave power control. ACS Nano 12, 7 (2018): 6784–6793. Copyright (2018), American Chemical Society. Panel (I) adapted with permission from Zhang, Gaixia, Shuhui Sun, Mohammad Norouzi Banis, Ruying Li, Mei Cai, and Xueliang Sun. Morphology-controlled green synthesis of single crystalline silver dendrites, dendritic flowers, and rods, and their growth mechanism. Cryst Growth Des 11, 6 (2011): 2493–2499. Copyright (2011), American Chemical Society. Panel (J) adapted with permission from O'Dwyer, Colm, D. Navas, Vladimir Lavayen, Eglantina Benavente, María Angélica Santa Ana, Guillermo Gonzalez, Simon B. Newcomb, and Clivia M. Sotomayor Torres. Nano-urchin: the formation and structure of high-density spherical clusters of vanadium oxide nanotubes. Chem Mater 18, 13 (2006): 3016–3022. Copyright (2006), American Chemical Society. Panel (K) adapted with permission from Yang, Huayu, Xin Lu, and Zhong Xin. One-step synthesis of nonspherical organosilica particles with tunable morphology. Langmuir 34, 39 (2018): 11723–11728. Copyright (2018), American Chemical Society. Panel (L) adapted with permission from Li, Chun, Guojia Fang, Fuhai Su, Guohua Li, Xiaoguang Wu, and Xingzhong Zhao. Self-organized ZnO microcombs with cuboid nanobranches by simple thermal evaporation. Cryst Growth Des 6, 11 (2006): 2588–2591. Copyright (2006), American Chemical Society.

https://www.twirpx.org & http://chemistry-chemists.com

arms. Thus, in the case of 3D nanomaterials, there is an opportunity to use all the prospective features of other dimensionalities. In addition to the strong confinement effect, 3D photocatalysts (especially hierarchical structures), because of their high structural stability, high specific surface area, porous structure, high adsorptive capacity, presence of larger number of active sites, etc., are being recognized as promising candidates for solar energy conversion or remediation of environmental pollution issues thorough their efficient photocatalytic performances [50, 51]. The corresponding physical and wet chemical approaches to formulate nanomaterials of various morphologies, can be well understood from the recent review articles of Hwang et al. and Xu et al. [50, 51] We shall next look at the types of photocatalysts, and their basic principles, to realize how photocatalyst materials of various morphologies may enable visible light to promote efficient visible light photocatalysis.

4 Types of photocatalysts

In general, photocatalysts (represented in Fig. 8) are either single materials or heterojunctions [45, 47]. These are mainly metal-based different nanostructured semiconductor materials (e.g., metal oxides/chalcogenides, metal-organic framework (MOF)), and very much emerging metal-free semiconductors (e.g., carbon nitride (g-C3N4), conducting

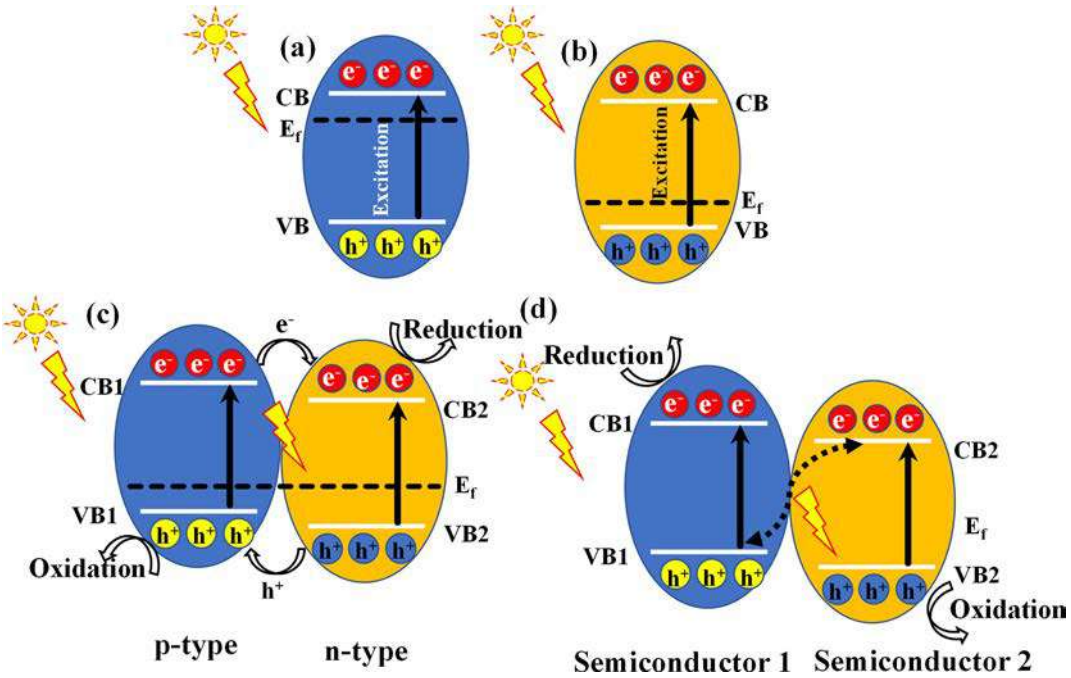

FIG. 8 Schematic representations illustrating the photocatalyst types: (A) and (B) single material; (C) heterojunction; and (D) *Z*-scheme.

https://www.twirpx.org & http://chemistry-chemists.com

polymers) [124, 125]. Broadly, the nanostructured semiconductor materials used in photocatalysis can be classified in four different categories.

These are pure semiconductor photocatalysts (binary and ternary), solid solution photocatalysts, nanocomposites or heterojunctions (type I, II, and III), and Z-scheme materials [10, 45, 47, 49–51].

4.1 Single-material photocatalysts

These are generally metal or metal-free n- or p-type semiconductor materials (Fig. 8A and B) [45]. Although the synthesis strategies of these single molecule photocatalysts are facile and very cost-effective, nowadays their importance has declined due to their wide bandgap [45]. Common strategies to improve their performance especially for visible light photocatalysis are surface engineering (or morphology control), manipulation of defect sites, and introducing dopants and sensitizers.

Since the photoreaction is a surface reaction, its efficiency can be tuned through controlling the morphology (shape, appearance, texture, etc.) of the nanostructured materials. The number of active sites toward yielding higher photocatalytic performance can be increased by increasing the catalyst surface area and its proportion of crystal facets. In general, the variation in morphology of a same material (such as nanocrystals vs nanowires) on its photocatalytic performance is described as structural sensitivity or facet-dependent reactivity. As the facet of high surface energy is thermodynamically unfavorable, it can be accomplished by controlling the reaction conditions during the synthesis.

4.2 Heterojunction photocatalysts

Visible light photocatalysis without the drawback of recombination can be efficiently extended by deploying the advantages of heterojunctions (Fig. 8C and D).

4.2.1 Common heterojunction photocatalysts

Heterojunction photocatalysts (p-n heterojunctions, semiconductor-semiconductor heterojunctions, metal-semiconductor heterojunctions), on the basis of their energy band alignment, are classified as type I (showing straddling bandgap), type II (showing staggered bad gap), or type III (showing broken bad gap) (as illustrated in Fig. 9A) [45, 47]. This classification is made mainly on the basis of the contact morphology of the materials during the design of the heterojunction photocatalysts. These photocatalysts can be partial contact or core-shell type. Herein, the most important factor to consider when designing an efficient heterojunction photocatalyst is the band edge alignment at the interface of the contacting materials. This alignment is affected by the interface properties of the contacting materials (e.g., surface dipoles, interfacial defects) and the resulting trapped charges, which in turn manipulate the band bending of the contacting materials. This band edge alignment and related phenomenon are very common for developing semiconductor devices to be used in different areas, especially electronics and optoelectronics. Compared to these electronic devices, some different features, e.g., interfacial charge transportation,

https://www.twirpx.org & http://chemistry-chemists.com

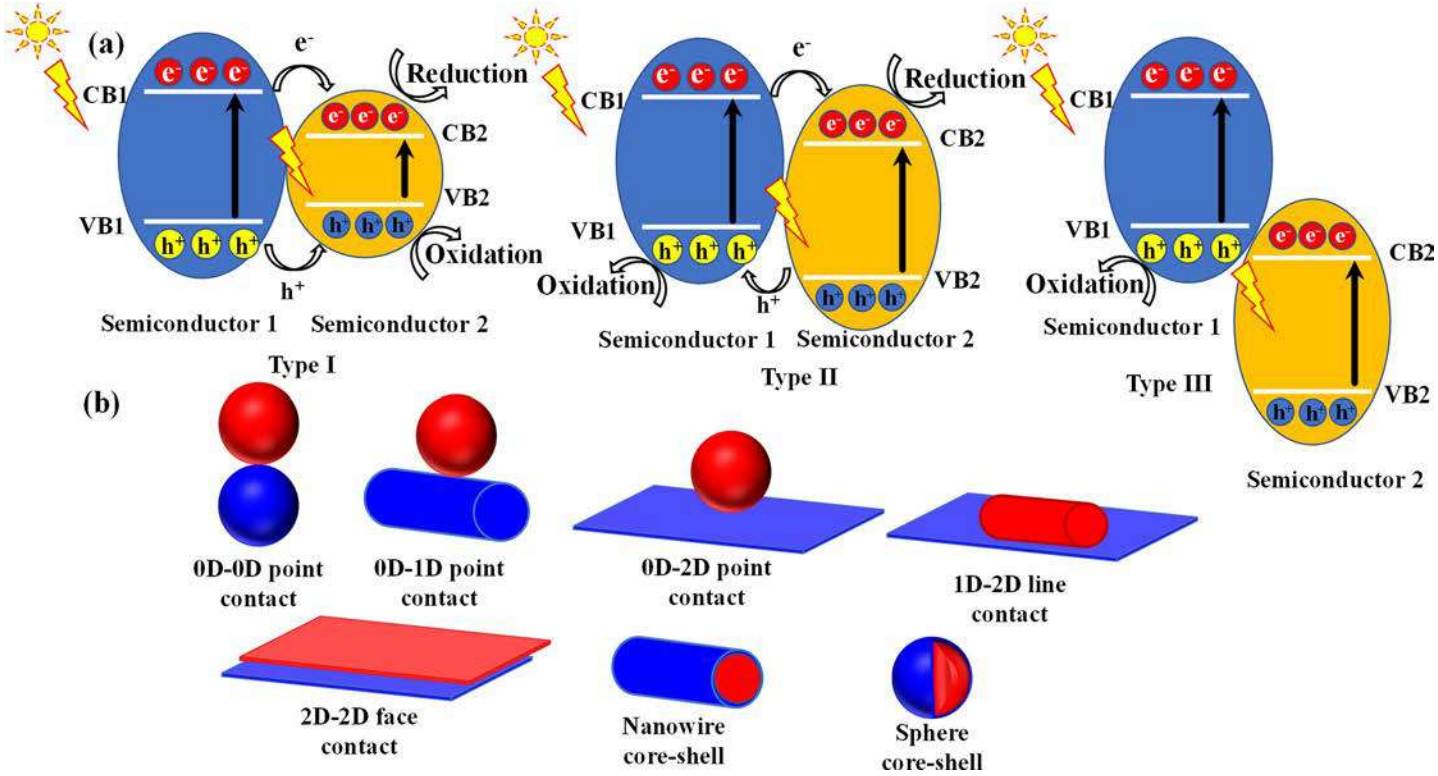

FIG. 9 Schematic representation of different heterojunction photocatalysts: (A) type I, II, and III; (B) partial contact and core-shell.

https://www.twirpx.org & http://chemistry-chemists.com

are also important for photocatalysts. The alignment and bending of band are strongly dependent on the sizes, arrangements, and facets of the nanomaterials to be used for developing the heterojunction [45, 86–90]. The facet regulates the photocatalytic activity by also affecting the interfacial charge transportation at the contact plane of different materials. In addition to the junction of different materials or same materials having different crystal phases, band bending may occur in the junction of the same materials of similar crystal structure.

The electric field generated due to this band bending (particularly in the surface) acts as a driving force during the charge carrier separation [45]. Depending on the morphology, the contact between two materials can be point contact (in the case of nanoparticles), line contact (in the case of nanowires/ribbons/sheet)s, face contact (when both materials are 2D), and the core-shell type (as illustrated in Fig. 9B). Apart from band bending and morphology, lattice mismatch is considered as another factor to choose the materials to use in the heterojunction. Instead of higher lattice mismatch causing higher strain and increased interfacial defects responsible for increasing the recombination losses, materials of low lattice mismatch are prioritized for developing the heterojunction photocatalysts. At the time of writing, many heterojunctions, e.g., CeO_2-AgI [126], g-C_3N_4/Bi_2WO_6 [127], Ag_2O/Bi_5O_7I [128], In_2S_3/$CdIn_2S_4$ nanotubes [129], CdS/MoS_2 [130], amorphous NiO/g-C_3N_4 [131], ZnS/g-C_3N_4 [132], g-C_3N_4/$ZnIn_2S_4$ [133], g-C_3N_4/phosphorene [134], and $ZnIn_2S_4$-In_2O_3 [135], have been reported for efficient visible light photocatalysis. Nowadays, instead of these inorganic semiconductors, polymer or carbon-based various nanomaterials, e.g., polyaniline (PANI), polypyrrole, carbon nanotubes (CNTs), and graphene or graphene oxide (GO), are being investigated for visible light photocatalysis [45, 64, 65, 136–140]. In addition, various active materials coated with different metal organic frameworks (MOFs) (e.g., molybdenum oxide/zeolitic imidazolate framework core-shell) have been investigated for synergistic application of active materials as photocatalysts and the MOF as an adsorbent [45, 50, 141, 142]. Nanomaterials having surfaces of two or more distinct physical properties, known as Janus particles, are another recently reported type of heterojunction material, being used in attempts to achieve efficient visible light photocatalysis [143]. Generally, the heterojunctions are known to exhibit better performance than the single-material photocatalysts. Still, further improvements on design of materials and their surface engineering are needed to improve the light absorption (particularly visible light) and charge carrier separation efficacy of the photocatalyst materials. In this regard, attempts are being made to develop some special types of heterojunctions based on *Z*-scheme and plasmonic materials, aiming at the reduction of recombination losses and enhanced visible light absorption [45].

4.2.2 Z-scheme photocatalysts

In the case of heterojunction photocatalysts, compared to single-material photocatalysts, improved carrier separation along with reduction of charge recombination losses has been reported. However, these kinds of surface engineering cannot meet the desired charge separation and sufficient redox power to promote broadband (particularly visible

https://www.twirpx.org & http://chemistry-chemists.com

light) photocatalysis [3, 5, 6, 45–47, 51]. For *Z*-scheme (as shown in Fig. 8D), an electron mediator is used to promote the transfer of electron from the CB of one material to the VB of the other material, ensuring a larger potential difference compared to that of the common heterojunction materials (as shown in Fig. 8C). Because of this large potential difference (i.e., strong redox capability), immense attention has been paid to Z-scheme photocatalysis, particularly in the area of photocatalytic water splitting and hydrogen fuel generation. The Z-scheme system may be liquid or solid. Due to the possibility of backward reactions, low pH tolerance, additional requirement of electron mediator, and low light harvesting efficacy of liquid-based Z-scheme materials, solid-state Z-scheme photocatalysts have received growing interest. In this system, metal- or nonmetal-based conductors (e.g., metal nanoparticles, graphene, CNT) act as electron mediators.

Another type of this photocatalyst system is direct *Z*-scheme photocatalysts having a type-II-like band alignment but herein, the charge carrier is transferred in a different pathway [49]. In the case of type-II heterojunctions, the excited electron moves from the higher conduction band minimum (CBM) of one material to the lower CBM of another material, and the hole moves in the reverse direction, causing minimum electron-hole recombination. For direct Z-scheme, the recombination occurs between the lower CBM electron and the higher valence band maximum (VBM) hole, causing a large potential difference between the lower VBM and higher CBM, which ensures high redox power of the Z-scheme photocatalyst. Other advantages of the direct Z-scheme system are its simpler structure and higher light absorption efficacy laid by the additional light absorption by the mediator. At the time of writing, various compositions, e.g., graphene bridged Ag_3PO_4/Ag/$BiVO_4$ [144], $Ag_2Mo_2O_7/MoS_2$ [145], WO_3/g-C_3N_4 [146], g-C_3N_4/SnS_2 [147], $TiO_2/CuInS_2$, and [148] TiO_2/CdS [149], exist as efficient Z-scheme photocatalysts for different applications, especially in the areas of energy and environment (e.g., degrading pollutants, water splitting, and CO_2 reduction).

4.2.3 Plasmonic photocatalysts

The photocatalytic performance (especially visible light photocatalysis) of the catalyst systems, as mentioned above, can be achieved by exploiting the visible light harvesting efficacy of the plasmonic nanoparticles (NPs) [72, 89]. It is worth mentioning that plasmonic nanoparticles are reported mostly as zero-dimensional [150]. Considering the effect of size and morphology of the plasmonic NPs toward harvesting the light of particular wavelength, tunable photon absorption of any kind of photocatalyst system can be accomplished via incorporation of the plasmonic nanoparticles, particularly of different morphology and sizes [72, 89, 151]. Because of their additional light harvesting capability, plasmonic effects are promising in terms of improving photocatalytic performance (or increasing the reaction yield) of various catalyst systems, e.g., MOF-based, Z-scheme. The plasmonic effect, by means of various mechanisms, e.g., hot electron injection, localized electromagnetic field enhancement, and plasmon resonance energy transfer (PIRET), causes the improvement of photocatalytic performance of different catalyst systems [45]. Because of a strong localized surface plasmonic resonance (LSPR) effect, noble

https://www.twirpx.org & http://chemistry-chemists.com

metal NPs (e.g., AgNP, AuNP) are used as common plasmonic NPs in different catalyst systems [72]. Instead of noble metal NPs, more abundant and low-cost nonnoble metal NPs (e.g., Bi, Al, Cu) are also reported as wavelength tunable plasmonic materials for efficient solar light photocatalysis [151]. In contrast to metal materials, nonmetallic materials, e.g., MoS_2, have also been reported for pursuing the same purpose [116, 152, 153]. Further tuning of the properties and achieving the increased enhancement can be made via choosing the component materials of different photocatalyst systems [154, 155]. It is noteworthy to mention that compared to the isolated NPs, the connected NPs (e.g., plasmonic dimer), because of their stronger electromagnetic field, increase photocatalytic performance. There are three main steps involved in plasmonic visible light photocatalysis: charge or electron transfer, energy transfer, and thermal activation. Since visible light promotes electron/energy transfer, the occurrence of the first two steps is termed "plasmon-assisted photocatalysis," while the thermal activation is known as "plasmon-assisted catalysis," as LSPR may thermally activate the catalytic reaction [156, 157].

5 Challenges in visible light photocatalysis and advantages of hierarchical photocatalysts

In point of visible light photocatalysis, the tunability in morphologies (particularly for the metal oxide semiconductors) are being afforded firstly to minimize the bandgap to promote photon absorption under the visible range, and secondly to increase the surface area to enhance the amount of both absorbed photon and reactive sites to be interacted with the test materials. Narrowing the bandgap is possible through introducing crystal/lattice defects via enabling different morphological features. However, excessive defects may cause additional charge recombination, resulting in suppression of photocatalytic performance. Again, the alteration in donor or acceptor levels by means of a heterojunction could also reduce the redox ability of the photocatalysts and diminish the overall photocatalytic performance [46]. Thus, it can be said that the redox power, defined by CB/VB level, and the light harvesting efficacy, defined by the bandgap value, contradict each other, which needs careful optimization for developing efficient visible light photocatalysts. Other problems associated with the robustness of visible light photocatalyst materials are choice of facile synthetic routes and less hazardous chemicals.

Again, suitable bandgaps and redox power do not always guarantee good photoreactions. In the case of heterogeneous photocatalysis, the efficiency is considered as cumulative of four steps involved herein—i.e., light harvesting, exciton formation, migration, transportation and recombination of charge—and finally the redox reaction in the catalyst surface [46, 86, 87]. Partial loss in any of these factors may decrease overall performance. If the catalyst surface is flat and smooth, it will favor light reflection rather than light harvesting or absorption. In this regard, hierarchical porous photocatalysts, due to the possibility of multiple scattering of absorbed light inside the pores, exhibit enhanced light harvesting efficacy in terms of producing a greater number of excitons [44]. Another important

https://www.twirpx.org & http://chemistry-chemists.com

limitation associated with photocatalysis is the recombination loss. A decrease in surface area and agglomeration of various nanomaterials greatly decreases the redox kinetics, and increases the reagents' diffusion barriers, which can again be counted as a limiting factor for efficient photocatalysis. In the case of water splitting and CO_2 reduction, the excitons, because of the slow reaction kinetics, accumulate on the catalyst surface and favor charge carrier recombination (known as photocorrosion of the catalyst), resulting in poor photocatalytic performance. The hierarchical porous photocatalysts, because of their high surface area, greater number of active sites, enhanced light harvesting efficacy, and good diffusion kinetics, can promote fast reaction kinetics. For the photodegradation of various organic impurities, the improved adsorption and diffusion by the porous catalysts materials greatly enhance photocatalytic performance. Thus, immense attention should be paid to developing heterogeneous photocatalysts to improve their catalytic efficacy. In this regard, because of their unique morphology-driven enhanced light harvesting efficacy, increased active surface area, and improved molecular diffusion/transport property, the hierarchical photocatalysts should be prioritized over the others.

6 Morphology-dependent visible light photocatalysis for environmental and energy issues

Depending on the pros and cons of different morphologies—as it has been noticed that the hierarchical nanomaterials are promising over the others—in this section, for morphology-dependent visible light photocatalysis on the basis of their performances in various application areas, hierarchical photocatalysts are highlighted. The applications of photocatalysis can be broadly divided into three main categories: photodegradation (i.e., pollutant degradation or solar disinfection), fuel generation (i.e., water splitting or photocatalytic H_2 fuel generation, and reduction of CO_2), and synthetic chemistry. Below, a brief description is provided to highlight how the change in morphology can regulate the efficiency of visible light photocatalysis. In this regard, there are few interesting studies in the literature available to realize the effect of morphology or the synthesis route enabling different morphological or crystal features to be determinant for efficient visible light photocatalysis, which might be useful for the reader to conceptualize an easy and cost-effective formulation of efficient multipurpose photocatalysts [44, 45, 47, 50, 51].

6.1 Photodegradation

This particular application enables the use of solar light to purify the environment (especially water) by degrading the hazardous contaminants (e.g., dye). Because of wide bandgaps, most of the semiconductors, especially TiO_2 and ZnO, face significant limitation to absorb the visible light. These materials are low-cost and known to be robust under the photocatalytic environment. Thus, much attention is being paid to use these materials for efficient visible light photocatalysis. In this regard, various efforts have been made to design efficient visible light photocatalytic systems based on these metal oxide

https://www.twirpx.org & http://chemistry-chemists.com

semiconductors through their morphological alteration/modification, particularly via formulation of composite structures or heterojunctions. For example, doping of various elements into the wide-bandgap TiO_2 has been checked to enable its visible light activity. Fe-doped porous TiO_2 microspheres have shown excellent photodegradation of methylene blue (MB) under visible light. The morphological alteration from microsphere to nanosheet-type building blocks improves the photocatalytic performance of Fe-doped TiO_2 and enhances MB degradation efficacy. When commercial ZnO was compared with a C-doped ZnO superstructure (having a flower-like morphology) as obtained by annealing only of $Zn_5(CO_3)_2(OH)_6$ in air, it was found that the porous ZnO flower shows enhanced broadband light absorption (ranging from UV to the visible region) [158]. The synergistic influence of enhanced broadband light absorption and the porous morphology enable these ZnO flowers (obtained at 500°C annealing temperature) to degrade the Rhodamine B (RhB) dye efficiently in aqueous solutions under solar light illumination (Fig. 10).

Other hierarchical semiconductors, e.g., urchin-like CdS nanoflower made of self-assembled CdS nanorods, exhibit high-performance photocatalytic degradation of acid fuchsin under visible light [44, 159]. Because of the narrow bandgap and ease in processibility of various nanostructure hierarchical semiconductors based on In, e.g., $CuInS_2$, $ZnIn_2S_4$, CdS, In_2S_3, $CdIn_2S_4$, $SnIn_4S_8$, $InVO_4$, etc. and Bi, e.g., Bi_2MoO_6, $BiVO_4$, sensitized BiOCl, Bi_2WO_6, $BiOCl_xBr_{1-x}$,90 BiOI, BiOBr, $BiVO_4/Bi_2O_2CO_3$, etc. are attracting significant attention in the field of photocatalytic degradation [44, 124, 160, 161]. Again, these hierarchical photocatalysts (particularly the bismuth-based ones) are supposed to exhibit enhanced activity if the heterojunctions are made with other conductor or semiconductor materials.

6.2 Photocatalytic water splitting for H_2 fuel generation

As H_2 is a clean and green alternative to mitigate the issue srelated to the shortage of fossil fuels and related environmental pollution due to cracking/pyrolysis of the traditional fuels, sustainable and clean production of H_2 through photocatalytic water splitting is very promising. Among the various photocatalysts, chalcogenides show the highest performance for visible light water splitting [44, 70, 162–164]. In this regard, hierarchical sulfide materials (single component or heterojunctions) are considered promising particularly for visible light H_2 evolution reactions [124]. For instance, CdS nanoporous sheets and hollow nanorods loaded with crystalline Pt nanoparticles showed an apparent quantum yield of about 60% under 420 nm visible light irradiation [165]. It has been recently demonstrated that compared to pure CdS, the CdS-ZnS core-shell can exhibit a 56-fold enhanced rate of H_2 evolution under exposure to visible light (Fig. 11) [68].

Hierarchical CdS flowers were found to exhibit three times higher H_2 production (468.7 μmol h^{-1}) with an apparent quantum efficiency (QE) of 24.7% at 420 nm, compared to that of the pure CdS nanoparticles [166]. Hierarchical self-assembled porous structure and high surface area facilitate the separation of photogenerated electron-hole pairs and

https://www.twirpx.org & http://chemistry-chemists.com

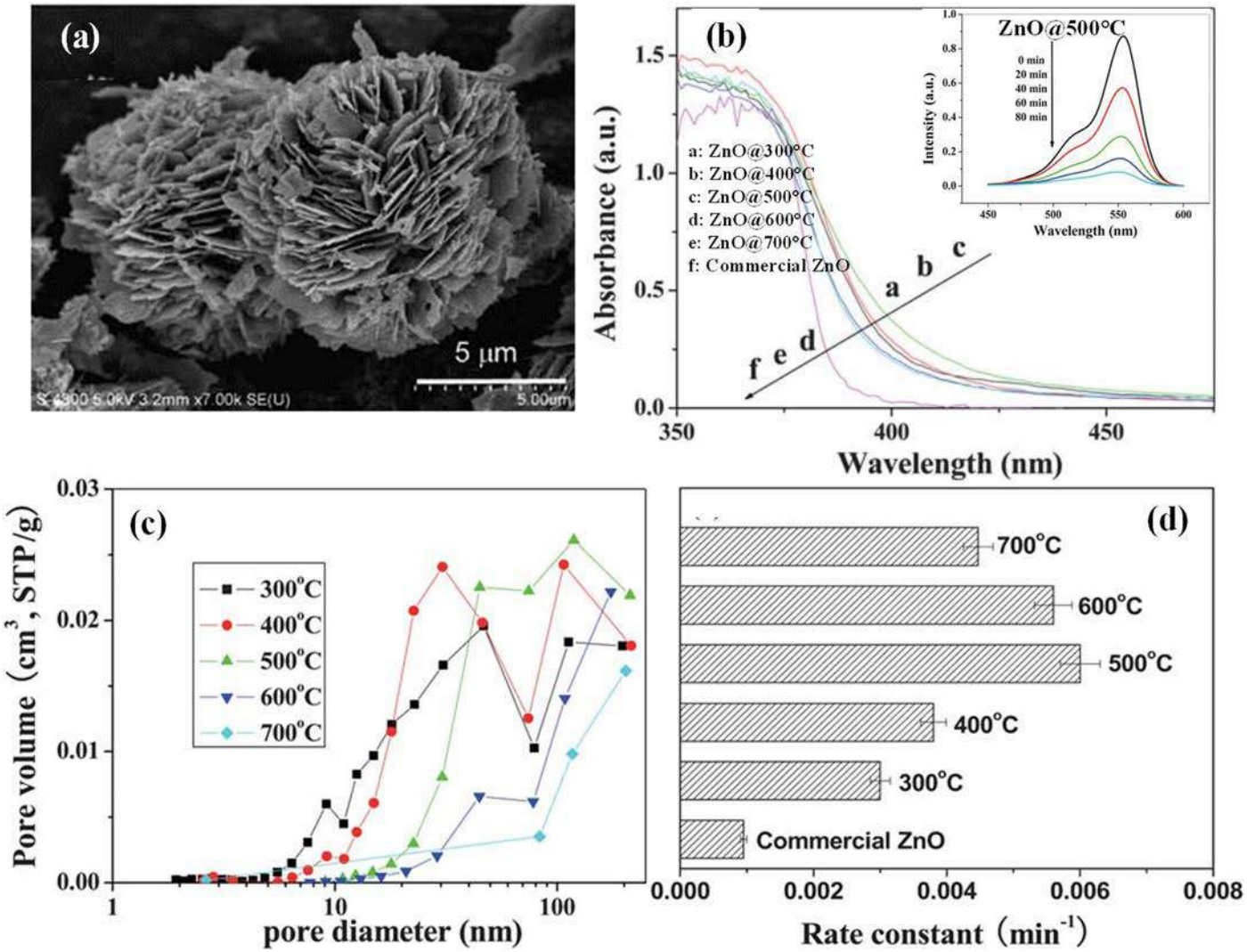

FIG. 10 (A) SEM images of ZnO flowers prepared at 500°C; (B) UV-vis absorption spectra of ZnO prepared at different calcination temperatures (inset: changes in adsorption of aqueous RhB in the presence of 500°C-calcined ZnO flowers under exposure of visible light); (C) pore size distribution for ZnO obtained at different temperatures; (D) comparison of the apparent rate constants (k) for ZnO obtained at different temperatures under exposure of visible light. *Panel (D) adapted with permission from Liu, Shengwei, et al. Improved visible-light photocatalytic activity of porous carbon self-doped ZnO nanosheet-assembled flowers. CrstEngComm 13.7 (2011): 2533–2541. Copyright (2011), Royal Society of Chemistry.*

https://www.twirpx.org & http://chemistry-chemists.com

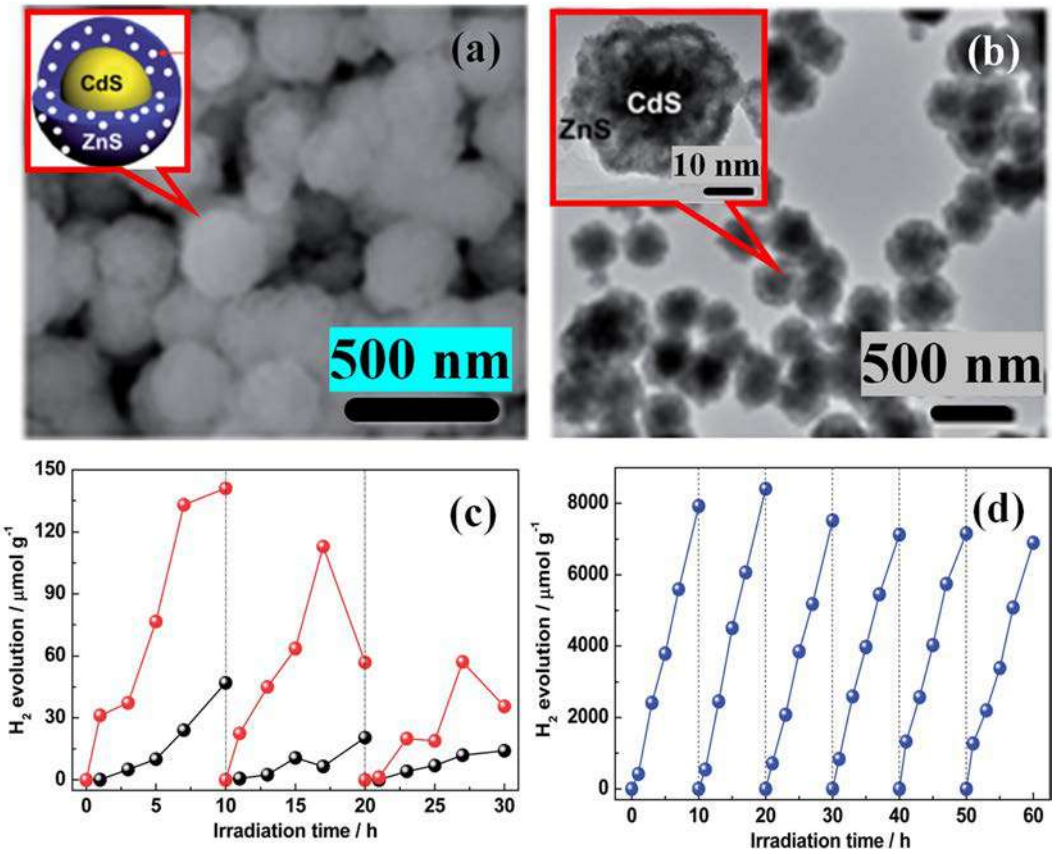

FIG. 11 (A) SEM and (B) TEM images of core shell type CdS-ZnS; irradiation time dependent hydrogen evolution by (C) ZnS (black line), CdS (red line), and (D) CdS-ZnS core-shell. *Panel (D) adapted with permission from Xie, Ying Peng, et al. CdS–mesoporous ZnS core–shell particles for efficient and stable photocatalytic hydrogen evolution under visible light. Energ Environ Sci 7.6 (2014): 1895–1901. Copyright (2014), Royal Society of Chemistry.*

enhance light absorption and the adsorption of the test materials on the active sites. The other CdS-based hierarchical composite photocatalysts, e.g., CdS quantum dots-TiO_2/titanate nanosheets, CdS/graphene nanosheet-type composites, and CdS-decorated 1D ZnO nanorods-2D graphene hybrids, showed very good visible light H_2 evolution because of the promoted charge separation and greater number of active sites. Considering all these efficient performance of hierarchical sulfide-based catalyst systems, their hybrid structure still deserves more attention. $Cd_xZn_{1-x}S$-like sulfide-based hierarchical solid-solution semiconductors of nanosheets morphology exhibited high-performance H_2 evolution reaction due to improved light harvesting efficacy, abundant active sites, and faster exciton formation. CuS/ZnS porous nanosheet-type photocatalysts showed H_2 production at a rate of 4147 μmol h^{-1} g^{-1}, and quantum efficiency of 20%. Photoinduced interfacial charge transfer is the cause of such high performance. Various kinds of hierarchical $ZnIn_2S_4$ microspheres and their heterojunctions (e.g., carbon quantum and Pt-decorated

https://www.twirpx.org & http://chemistry-chemists.com

$ZnIn_2S_4$), because of their improved light harvesting and charge separation abilities, showed very high visible light H_2 evolution. The efficacy of sulfide-based hierarchical solid-solution semiconductors can be enhanced further through narrowing the bandgap (by different engineering strategies), doping, and adding cocatalysts. Apart from the chalcogenides, different traditional metal oxide semiconductors, because of their hierarchical morphology (e.g., brush-like RGO-TiO_2 composite), increased active surface area, and improved charge separation, showed enhanced H_2 evolution performance. Hierarchical "forest-like" TiO_2 nanofiber/ZnO nanorod/CuO nanoparticles, because of their improved light harvesting efficacy (due to CuO), enhanced active surface area, and suppressed recombination of excitons, exhibited higher photocatalytic hydrogen generation rates [167]. Template-free synthesis of hierarchical nanostructure, having more branches and porosity, designing of efficient nanojunctions, etc. is still needed to give more attention to sustainable and cost-effective generation of H_2 through visible light photocatalytic water splitting.

6.3 Photocatalytic CO_2 reduction

Increases in environmental pollution caused by enhanced atmospheric CO_2 levels have attracted enormous research interest to capture and utilize CO_2 for its sustainable transformation. Reduction of CO_2 toward generation of fuels like methane or other essential chemicals can be a sustainable route to mitigate both the aforementioned energy and environmental issues. In this regard, the photocatalytic reduction in the presence of solar light is being considered as the most promising green technique to utilize hazardous CO_2 in the circular economy toward developing a sustainable society [41]. The efficient photocatalytic conversion of CO_2 is dependent on multiple factors, i.e., availability of a catalyst capable of efficiently harvesting visible light, charge transfer/separation efficiency, photostability, adsorption of CO_2, good surface reaction kinetics and suppression of undesirable reactions. Hierarchical photocatalysts, because of their fascinating characteristics, have attracted great attention in terms of superior photocatalytic performance for conversion of CO_2 into carbon fuels [44]. Various 3D microspheres of hierarchical morphology, e.g., $CdIn_2S_4$, Bi_2S_3, Bi_2WO_6, TiO_2, ZnTe, because of their spherical and macro/mesoporous structures, are known to exhibit superior catalytic performance and selectivity toward the photoreduction of CO_2 [44]. Currently, various alkaline tantalates $MTaO_3$ (M = Li, Na, K) having hierarchical morphology were observed to exhibit enhanced performance for CO_2 photoreduction [44, 168, 169]. Apart from these single molecule-based photocatalysts, hierarchical heterostructured photocatalysts, especially the nanocarbon-supported semiconducting materials (e.g., graphene/CdS nanorods, graphene/C_3N_4, graphitic carbon/TiO_2), because of their improved CO_2 adsorption and efficient charge transfer/separation, showed enhanced CO_2 photoconversion efficiency [44].

Considering the advantages of hierarchical heterostructured photocatalysts, other varieties of heterostructures, e.g., hollow and yolk shell structures, have been investigated for photocatalytic CO_2 reduction. Compared to the Degussa P25 TiO_2, the CuO-TiO_2-xNx

https://www.twirpx.org & http://chemistry-chemists.com

hollow nanocubes, because of enhanced visible light absorbance and efficient p-n junction formation, were found to exhibit 2.5 times higher CH_4 production [170]. In another report, compared to the unfunctionalized or commercial P25, amine functionalized titanate nanosheet-based yolk shell microspheres synthesized via one-pot organic amine mediated anhydrous alcoholysis of titanium (IV) butoxide at 200°C operating temperature (i.e., TN200), because of their strong visible light absorption, high CO_2 adsorption capacity, and excellent light-harvesting performance, showed high selectivity for production of CH_3OH through photoreduction of CO_2 under visible light irradiation (Fig. 12) [69]. This study opens a new way to develop a low-cost photocatalyst for CO_2 reduction only by introducing additional adsorptive groups onto the porous hierarchical semiconductor surface. Developing a cost-effective, less complicated, high-performing solid-state photocatalytic system, optimization and integration of light harvesting centers, charge transportation channels, and active sites for adsorption and catalysis in a single material becomes important especially in the area of photocatalytic CO_2 reduction. Sol-gel method derived core-shell TiO_2@insulating SiO_2 composites were applied for selective photoreduction of CO_2 in the presence of water vapor under simulated solar light irradiation. This catalyst system selectively produces CO from CO_2. A SiO_2 layer greatly inhibits the competitive H_2 formation on the TiO_2 surface. The improved performance may arise due to the enhanced CO_2 adsorption capacity and better charge carrier separation [171]. From this observation, it is anticipated that the CO_2 reduction efficiency of the semiconductors can be tuned by coating the hierarchical silica layer.

In another recent report, an efficient direct *Z*-scheme photocatalyst made of CdS nanoparticles embedded with hierarchical WO_3 hollow spheres showed higher selectivity of CH_4 production from photoreduced CO_2 under irradiation of 420 nm visible light than that of single-phase CdS or WO_3 photocatalysts [172]. In this case, 5 mol% CdS-hierarchical WO_3 exhibited the highest CH_4 production with a rate of 1.02 $\mu mol\ h^{-1}\ g^{-1}$, which was 100 and 10 times higher than that of individual WO_3 and CdS, respectively. The enhanced photocatalytic activity is attributed to the Z-scheme photocatalysis including hierarchical heterostructure, which can be considered promising in future, especially for photocatalytic CO_2 reduction.

7 Future scope

Although plenty of research articles explain the formulation of different nanostructured materials of varying morphology via various wet chemical synthesis techniques, and physical methods with or without the use of reducing agents, ligands, and/or templates, facile synthetic methods not including multiple processing steps and excluding the reducing agents, templates, or ligands still need to be studied to enable this area to become more facile and familiar. In this regard, only solvent-mediated synthesis of nanostructured materials (without the use of any reducing agent or stabilizer) and their composites can be considered facile, less hazardous, and cost-effective. The work done by Sinha and coworkers, particularly synthesis of porous calcium cobaltate from the in-house

https://www.twirpx.org & http://chemistry-chemists.com

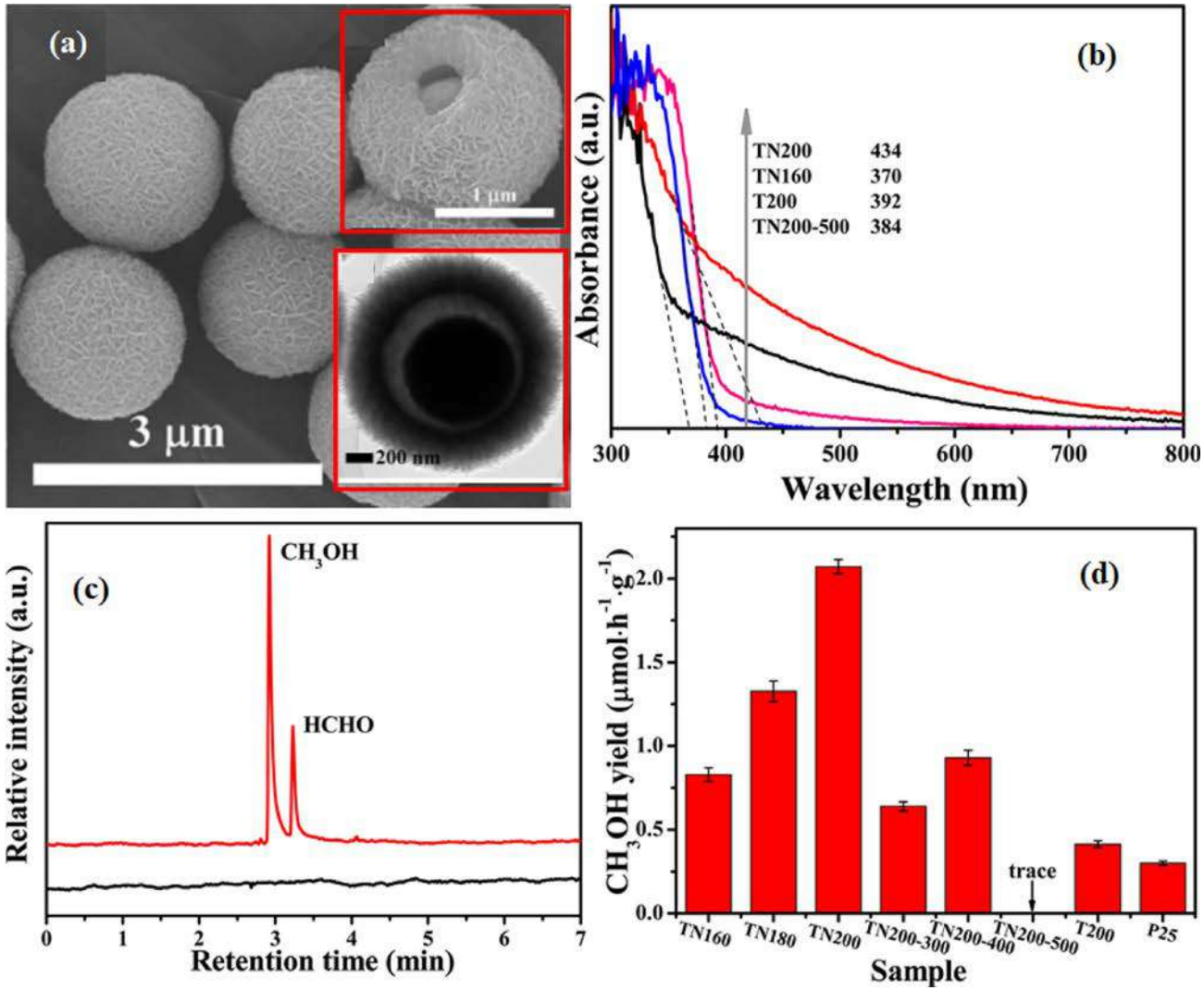

FIG. 12 (A) SEM (inset enlarged SEM and TEM); (B) absorbance spectra to highlight improved visible light absorption; (C) chromatograph to highlight the selectivity toward producing CH_3OH; and (D) high-performance CH_3OH productivity of the TN200. *Panel (D) adapted with permission from Liu, Shengwei, Jiaqiu Xia, and Jiaguo Yu. Amine-functionalized titanate nanosheet-assembled yolk@ shell microspheres for efficient cocatalyst-free visible-light photocatalytic CO2 reduction. ACS Appl Mater Interfaces 7.15 (2015): 8166–8175. Copyright (2015), American Chemical Society.*

https://www.twirpx.org & http://chemistry-chemists.com

synthesized corresponding metal-DMF complexes, in-situ formulation of plasmonic Ag incorporated 2D graphene, or MoS_2 are easy ways to develop various heterogeneous photocatalysts [173–176].

Other prospective approaches including development of black TiO_2, variation of glancing angle to enable the production of visible light active nanostructured semiconductor catalysts, etc. are promising toward sophisticated development of low-cost visible light photocatalysts [56, 177, 178].

In addition to the satisfactory development of different efficient photocatalysts of various morphologies in the area of photodegradation, CO_2 reduction, and water splitting for H_2 fuel generation, although numerous attempts have been made to use solar energy for different organic transformation by different UV active semiconductors, visible light active MOF, etc., more study is needed to exploit the morphological features to enable the design of sophisticated synthetic routes of various organic transformation and synthesis of fine chemicals (particularly from waste materials). In this case, *Z*-scheme photocatalysis employing hierarchical photocatalysts is very attractive [179].

As some external forces are supposed to improve the photocatalytic redox reaction [180], more investigation of exploiting the piezo-/tribo-electric phenomena during the photocatalysis needs to be carried out [61, 62].

Apart from visible light photocatalysis, if the morphology of nanomaterials can tune for their efficient light harvesting beyond visible light, i.e., near infrared (which is more than 50% of the total solar spectrum), broadband green solar photocatalysis can be realized. In this regard, although significant attempts are being made to use near infrared (NIR) light for efficient broadband photocatalysis, it suffers from low yield mainly due to lower availability of NIR active photocatalyst materials, low charge separation/transportation efficiency under NIR light, etc., which can be resolved by tuning the morphology/size of different visible light-active materials, and developing suitable heterojunctions (p-n, Z-scheme, etc.) [58].

8 Conclusion

In this chapter, the effect of morphology on the visible light photocatalysis was discussed. The basics of photocatalysis and nanostructured morphology and the types of photocatalysis were introduced. The importance and usage of visible light photocatalysts, based on their morphology, were extended further. It was observed that by tuning the required morphology, the photocatalytic activity of a given material can be altered/improved. Although the area of photocatalysis has been broadened to address different issues related with energy and the environment, it is still in its infancy, and its large-scale industrialization can be made feasible by establishing an easy strategy. Instead of developing new materials, modifying the existing materials to be broadband photoactive (through either surface engineering or tuning their morphology) and easy developing effective heterojunctions to take the commutative advantages of these materials can contribute to a better roadmap to enable large-scale application of photocatalysis and its proper industrialization.

https://www.twirpx.org & http://chemistry-chemists.com

References

[1] Pandikumar A, Jothivenkatachalam K, editors. Photocatalytic functional materials for environmental remediation. Incorporated: John Wiley & Sons; 2019.

[2] Naushad M, Rajendran S, Lichtfouse E, editors. Green photocatalysts. Springer International Publishing; 2020.

[3] Ibhadon AO, Fitzpatrick P. Heterogeneous photocatalysis: recent advances and applications. Catalysts 2013;3(1):189–218.

[4] Balzani V, et al. Solar-driven chemistry: towards new catalytic solutions for a sustainable world. Rendiconti Lincei Scienze Fisiche e Naturali 2019;30:443–52. 3.

[5] Pritchard J, et al. Heterogeneous and homogeneous catalysis for the hydrogenation of carboxylic acid derivatives: history, advances and future directions. Chem Soc Rev 2015;44(11):3808–33.

[6] Fox MA, Dulay MT. Heterogeneous photocatalysis. Chem Rev 1993;93(1):341–57.

[7] 6b. Liu X, Si W, Zhang J, Sun X, Deng J, Baunack S, Oswald S, Liu L, Yan C, Schmidt OG. Free-standing Fe 2 O 3 nanomembranes enabling ultra-long cycling life and high rate capability for Li-ion batteries. Sci Rep 2014;4(1):1–8.

[8] Herrmann J-M. Photocatalysis. Kirk-Othmer Encycl Chem Technol 2000;1–44.

[9] Riente P, Noël T. Application of metal oxide semiconductors in light-driven organic transformations. Cat Sci Technol 2019;9(19):5186–232.

[10] Zhu S, Wang D. Photocatalysis: basic principles, diverse forms of implementations and emerging scientific opportunities. Adv Energy Mater 2017;7(23):1700841.

[11] Sandberg M, Håkansson K, Granberg H. Paper machine manufactured photocatalysts-lateral variations. J Environ Chem Eng 2020;104075.

[12] Ni M, et al. A review and recent developments in photocatalytic water-splitting using TiO2 for hydrogen production. Renew Sustain Energy Rev 2007;11(3):401–25.

[13] Ashouri R, et al. The effect of ZnO-based carbonaceous materials for degradation of benzoic pollutants: a review. Int J Environ Sci Technol 2019;16(3):1729–40.

[14] Cedillo-González EI, et al. Self-cleaning glass prepared from a commercial TiO2 nano-dispersion and its photocatalytic performance under common anthropogenic and atmospheric factors. Build Environ 2014;71:7–14.

[15] Kahn JA, et al. Self-cleaning substrates and methods for making the same. U.S. Patent No. 8,617,665. 31 Dec; 2013.

[16] McCullagh C, et al. The application of TiO 2 photocatalysis for disinfection of water contaminated with pathogenic micro-organisms: a review. Res Chem Intermed 2007;33(375):359. 3–5.

[17] Hanaor DAH, Sorrell CC. Sand supported mixed-P hase ti O 2 Photocatalysts for water decontamination applications. Adv Eng Mater 2014;16(2):248–54.

[18] Cushnie TPT, et al. Photobactericidal effects of TiO2 thin films at low temperatures—a preliminary study. J Photochem Photobiol A Chem 2010;216(2–3):290–4.

[19] Perez M, et al. Removal of organic contaminants in paper pulp treatment effluents by TiO2 photocatalyzed oxidation. J Photochem Photobiol A Chem 1997;109(3):281–6.

[20] Pelizzetti E, Minero C. Mechanism of the photo-oxidative degradation of organic pollutants over TiO2 particles. Electrochim Acta 1993;38(1):47–55.

[21] Hariharan C. Photocatalytic degradation of organic contaminants in water by ZnO nanoparticles: revisited. Appl Catal Gen 2006;304:55–61.

[22] William IV L, et al. Magnetically agitated photocatalytic reactor for photocatalytic oxidation of aqueous phase organic pollutants. Environ Sci Technol 2005;39(20):8052–6.

https://www.twirpx.org & http://chemistry-chemists.com

[23] Mahmodi G, et al. Photocatalytic conversion of CO2 and CH4 using ZnO coated mesh: effect of operational parameters and optimization. Sol Energy Mater Sol Cells 2013;111:31–40.

[24] Tan SS, Zou L, Eric H. Photocatalytic reduction of carbon dioxide into gaseous hydrocarbon using TiO2 pellets. Catal Today 2006;115(1–4):269–73.

[25] Shehzad N, et al. A critical review on TiO2 based photocatalytic CO2 reduction system: Strategies to improve efficiency. J CO_2 Util 2018;26:98–122.

[26] Maan DM, Goswami M. Coating materials: nano-materials. In: Advanced surface coating techniques for modern industrial applications. IGI Global; 2021. p. 1–30.

[27] Shiraishi K, et al. Antibacterial metal implant with a TiO2-conferred photocatalytic bactericidal effect against *Staphylococcus aureus*. Surf Interface Anal 2009;41:17–22. 1.

[28] Scandura G, et al. Nanoflower-like Bi2WO6 encapsulated in ORMOSIL as a novel photocatalytic antifouling and foul-release coating. Chem A Eur J 2016;22(21):7063–7.

[29] Zhang X, et al. High-performance multifunctional TiO2 nanowire ultrafiltration membrane with a hierarchical layer structure for water treatment. Adv Funct Mater 2009;19(23):3731–6.

[30] Zhang L, et al. Photocatalytic degradation of polycyclic aromatic hydrocarbons on soil surfaces using TiO2 under UV light. J Hazard Mater 2008;158(2–3):478–84.

[31] Li Y, et al. Long-acting photocatalytic degradation of crude oil in seawater via combination of TiO2 and N-doped TiO2/reduced graphene oxide. Environ Technol 2019;1–11.

[32] Lu S-y, et al. Photocatalytic decomposition on nano-TiO2: destruction of chloroaromatic compounds. Chemosphere 2011;82(9):1215–24.

[33] Singh P, Mondal K, Sharma A. Reusable electrospun mesoporous ZnO nanofiber mats for photocatalytic degradation of polycyclic aromatic hydrocarbon dyes in wastewater. J Colloid Interface Sci 2013;394:208–15.

[34] Ishchenko OM, et al. TiO2-and ZnO-based materials for photocatalysis: material properties, device architecture and emerging concepts. In: Semiconductor photocatalysis-materials, mechanisms and applications; 2016. p. 3–30.

[35] Poudel BR, et al. Agro-waste derived biomass impregnated with TiO2 as a potential adsorbent for removal of as (III) from water. Catalysts 2020;10(10):1125.

[36] Cruz GJF, et al. Agrowaste derived biochars impregnated with ZnO for removal of arsenic and lead in water. J Environ Chem Eng 2020;8(3):103800.

[37] Matthews RW. Kinetics of photocatalytic oxidation of organic solutes over titanium dioxide. J Catal 1988;111(2):264–72.

[38] Minero C, et al. Photocatalytic transformation of organic compounds in the presence of inorganic ions. 2. Competitive reactions of phenol and alcohols on a titanium dioxide—fluoride system. Langmuir 2000;16(23):8964–72.

[39] Fujishima A, Zhang X, Tryk DA. TiO2 photocatalysis and related surface phenomena. Surf Sci Rep 2008;63(12):515–82.

[40] Kay A, Humphry-Baker R, Graetzel M. Artificial photosynthesis. 2. Investigations on the mechanism of photosensitization of nanocrystalline TiO2 solar cells by chlorophyll derivatives. J Phys Chem 1994;98(3):952–9.

[41] Ong W-J, Lin Z, Domen K. Artificial photosynthesis: taking a big leap for powering the earth by harnessing solar energy. Part Part Syst Charact 2018;35(1):1700451.

[42] Klein RC. Ultraviolet light hazards from transilluminators. Health Phys 2000;78.5(Suppl):S48–50.

[43] Ham William Jr T. Ocular hazards of light sources: review of current knowledge. J Occup Med 1983;25(2):101–3.

[44] Li X, Yu J, Jaroniec M. Hierarchical photocatalysts. Chem Soc Rev 2016;45(9):2603–36.

https://www.twirpx.org & http://chemistry-chemists.com

[45] Djurišić AB, He Y, Ng AMC. Visible-light photocatalysts: prospects and challenges. APL Mater 2020;8 (3), 030903.

[46] Qu Y, Duan X. Progress, challenge and perspective of heterogeneous photocatalysts. Chem Soc Rev 2013;42(7):2568–80.

[47] Xu C, et al. Nanostructured materials for photocatalysis. Chem Soc Rev 2019;48(14):3868–902.

[48] Moniz SJA, et al. Visible-light driven heterojunction photocatalysts for water splitting–a critical review. Energ Environ Sci 2015;8(3):731–59.

[49] Wang Y, et al. Visible light driven type II heterostructures and their enhanced photocatalysis properties: a review. Nanoscale 2013;5(18):8326–39.

[50] Hwang J, et al. Controlling the morphology of metal–organic frameworks and porous carbon materials: metal oxides as primary architecture-directing agents. Chem Soc Rev 2020;49(11):3348–422.

[51] Jiang W, et al. Three-dimensional photocatalysts with a network structure. J Mater Chem A 2017;5 (12):5661–79.

[52] Heuer-Jungemann A, et al. The role of ligands in the chemical synthesis and applications of inorganic nanoparticles. Chem Rev 2019;119(8):4819–80.

[53] Pérez-Page M, et al. Template-based syntheses for shape controlled nanostructures. Adv Colloid Interface Sci 2016;234:51–79.

[54] Butun S, et al. 0D, 1D, 2D, and 3D soft and hard templates for catalysis. Stud Surf Sci Catal 2017;177:317–57. Elsevier.

[55] Waseda Y, Muramatsu A, editors. Morphology control of materials and nanoparticles: advanced materials processing and characterization, vol. 64. Springer Science & Business Media; 2003.

[56] Shuang S, Zheng X, Zhang Z. Enhanced visible light photocatalytic performance by nanostructured semiconductors with glancing angle deposition method. In: Semiconductor photocatalysis: materials, mechanisms and applications; 2016. p. 163.

[57] Yang P, et al. Hierarchically ordered oxides. Science 1998;282(5397):2244–6.

[58] Wang L, et al. Near-infrared-driven photocatalysts: design, construction, and applications. Small 2019;, 1904107.

[59] Tu S, et al. Piezocatalysis and piezo-photocatalysis: catalysts classification and modification strategy, reaction mechanism, and practical application. Adv Funct Mater 2020;2005158.

[60] Qifeng L, et al. Photocatalytic, piezocatalytic, and piezo-photocatalytic effects in ferroelectric (Ba0. 875Ca0. 125)(Ti0. 95Sn0. 05) O3 ceramics. J Am Ceram Soc 2019;102(10):5807–17.

[61] Liang Z, et al. Piezoelectric materials for catalytic/photocatalytic removal of pollutants: recent advances and outlook. Appl Catal Environ 2019;241:256–69.

[62] Liu H, et al. Self-cleaning triboelectric nanogenerator based on TiO2 photocatalysis. Nano Energy 2020;70:104499.

[63] Li J, Nianqiang W. Semiconductor-based photocatalysts and photoelectrochemical cells for solar fuel generation: a review. Cat Sci Technol 2015;5(3):1360–84.

[64] Ghosh S, et al. Conducting polymer nanostructures for photocatalysis under visible light. Nat Mater 2015;14(5):505–11.

[65] Liras M, Barawi M, Víctor A. Hybrid materials based on conjugated polymers and inorganic semiconductors as photocatalysts: from environmental to energy applications. Chem Soc Rev 2019;48 (22):5454–87.

[66] Li W, et al. Single-molecular catalysis identifying activation energy of the intermediate product and rate-limiting step in plasmonic photocatalysis. Nano Lett 2020;20(4):2507–13.

[67] Sambandam B, et al. Rapid synthesis of C-TiO2: tuning the shape from spherical to rice grain morphology for visible light photocatalytic application. ACS Sustain Chem Eng 2015;3(7):1321–9.

https://www.twirpx.org & http://chemistry-chemists.com

[68] Xie YP, et al. CdS–mesoporous ZnS core–shell particles for efficient and stable photocatalytic hydrogen evolution under visible light. Energ Environ Sci 2014;7(6):1895–901.

[69] Liu S, Xia J, Jiaguo Y. Amine-functionalized titanate nanosheet-assembled yolk@ shell microspheres for efficient cocatalyst-free visible-light photocatalytic CO2 reduction. ACS Appl Mater Interfaces 2015;7(15):8166–75.

[70] Ravelli D, et al. Photocatalysis. A multi-faceted concept for green chemistry. Chem Soc Rev 2009;38 (7):1999–2011.

[71] Lang X, Chen X, Zhao J. Heterogeneous visible light photocatalysis for selective organic transformations. Chem Soc Rev 2014;43(1):473–86.

[72] Wang C, Astruc D. Nanogold plasmonic photocatalysis for organic synthesis and clean energy conversion. Chem Soc Rev 2014;43(20):7188–216.

[73] Zhang P, Zhang J, Gong J. Tantalum-based semiconductors for solar water splitting. Chem Soc Rev 2014;43(13):4395–422.

[74] Jing L, et al. Surface tuning for oxide-based nanomaterials as efficient photocatalysts. Chem Soc Rev 2013;42(24):9509–49.

[75] Dong P, et al. WO 3-based photocatalysts: morphology control, activity enhancement and multifunctional applications. Environ Sci Nano 2017;4(3):539–57.

[76] Ghosh S, editor. Visible-light-active photocatalysis: nanostructured catalyst design, mechanisms, and applications. John Wiley & Sons; 2018.

[77] Liu B, et al. Visible-light nanostructured photocatalysts—a review. J Nanosci Nanotechnol 2015;15 (2):889–920.

[78] Boddu S, Nishanthi ST, Kailasam K. Visible-light heterogeneous catalysts for photocatalytic CO2 reduction. In: Visible light-active photocatalysis: nanostructured catalyst design, mechanisms, and applications; 2018. p. 421–46.

[79] Rao H, et al. Visible light-driven photocatalytic degradation performance for methylene blue with different multi-morphological features of ZnS. RSC Adv 2016;6(52):46299–307.

[80] Mondal C, et al. Morphology controlled synthesis of SnS2 nanomaterial for promoting photocatalytic reduction of aqueous Cr (VI) under visible light. Langmuir 2014;30(14):4157–64.

[81] Chen L, et al. Morphology-controlled preparation and enhanced simulated sunlight and visible-light photocatalytic activity of Pt/Bi 5 Nb 3 O 15 heterostructures. Phys Chem Chem Phys 2013;15 (21):8342–51.

[82] Zhong Y, et al. Morphology-controlled self-assembly and synthesis of photocatalytic nanocrystals. Nano Lett 2014;14(12):7175–9.

[83] Menezes PW, et al. Morphology-dependent activities of silver phosphates: visible-light water oxidation and dye degradation. ChemPlusChem 2016;81(10):1068.

[84] Liu T-J, Wang Q, Jiang P. Morphology-dependent photo-catalysis of bare zinc oxide nanocrystals. RSC Adv 2013;3(31):12662–70.

[85] Liu S, et al. One-dimension-based spatially ordered architectures for solar energy conversion. Chem Soc Rev 2015;44(15):5053–75.

[86] Liu G, et al. Unique physicochemical properties of two-dimensional light absorbers facilitating photocatalysis. Chem Soc Rev 2018;47(16):6410–44.

[87] Zhao Y, et al. Two-dimensional-related catalytic materials for solar-driven conversion of CO x into valuable chemical feedstocks. Chem Soc Rev 2019;48(7):1972–2010.

[88] Xu Y, et al. Recent progress in two-dimensional inorganic quantum dots. Chem Soc Rev 2018;47 (2):586–625.

[89] Li X, Zhu J, Wei B. Hybrid nanostructures of metal/two-dimensional nanomaterials for plasmon-enhanced applications. Chem Soc Rev 2016;45(11):3145–87.

https://www.twirpx.org & http://chemistry-chemists.com

[90] Kumar DS, Kumar BJ, Mahesh HM. Quantum nanostructures (QDs): an overview. In: Synthesis of inorganic nanomaterials. Woodhead Publishing; 2018. p. 59–88.

[91] Pokropivny VV, Skorokhod VV. Classification of nanostructures by dimensionality and concept of surface forms engineering in nanomaterial science. Mater Sci Eng C 2007;27(5–8):990–3.

[92] Yu C, Jiang X, Qin D, Mo G, Zheng X, Deng B. Facile syntheses of s, n-codoped carbon quantum dots and their applications to a novel off–on nanoprobe for detection of 6-thioguanine and its bioimaging. ACS Sustain Chem Eng 2019;7(19):16112–20.

[93] Li P, Nan C, Wei Z, Lu J, Peng Q, Li Y. Mn3O4 nanocrystals: facile synthesis, controlled assembly, and application. Chem Mater 2010;22(14):4232–6.

[94] Lu S-C, Hsiao M-C, Yorulmaz M, Wang L-Y, Yang P-Y, Link S, Chang W-S, Tuan H-Y. Single-crystalline copper nano-octahedra. Chem Mater 2015;27(24):8185–8.

[95] Nunes D, et al. Metal oxide nanostructures: synthesis, properties and applications. Elsevier; 2018.

[96] Zhang X, Yu P, Zhang D, Zhang H, Sun X, Ma Y. Room temperature synthesis of Mn3O4 nanoparticles: characterization, electrochemical properties and hydrothermal transformation to γ-MnO2 nanorods. Mater Lett 2013;92:401–4.

[97] Patridge CJ, Wu T-L, Jaye C, Ravel B, Takeuchi ES, Fischer DA, Sambandamurthy G, Banerjee S. Synthesis, spectroscopic characterization, and observation of massive metal insulator transitions in nanowires of a nonstoichiometric vanadium oxide bronze. Nano Lett 2010;10(7):2448–53.

[98] Tian ZR, Voigt JA, Liu J, Mckenzie B, Huifang X. Large oriented arrays and continuous films of TiO2-based nanotubes. J Am Chem Soc 2003;125(41):12384–5.

[99] Chandrappa GT, Chithaiah P, Ashoka S, Livage J. Morphological evolution of (NH4) 0.5 V2O5· m H2O fibers into belts, triangles, and rings. Inorg Chem 2011;50(16):7421–8.

[100] Jung JH, Kobayashi H, Van Bommel KJC, Shinkai S, Shimizu T. Creation of novel helical ribbon and double-layered nanotube TiO2 structures using an organogel template. Chem Mater 2002;14 (4):1445–7.

[101] Guan Q, Cheng J, Wang B, Ni W, Guifang G, Li X, Huang L, Yang G, Nie F. Needle-like Co3O4 anchored on the graphene with enhanced electrochemical performance for aqueous supercapacitors. ACS Appl Mater Interfaces 2014;6(10):7626–32.

[102] Zhan S, Chen D, Jiao X, Tao C. Long TiO2 hollow fibers with mesoporous walls: sol – gel combined electrospun fabrication and photocatalytic properties. J Phys Chem B 2006;110 (23):11199–204.

[103] Butt FK, Cao C, Khan WS, Safdar M, Xuewen F, Tahir M, Idrees F, Ali Z, Nabi G, Dapeng Y. Electrical and optical properties of single zigzag SnO 2 nanobelts. CrstEngComm 2013;15(11):2106–12.

[104] Suo G, Li J. One dimensional polar surface dominated GaN nanostructures with zigzag morphology. J Alloys Compd 2016;674:16–20.

[105] Kaczmarek AM, Van Deun R. Rare earth tungstate and molybdate compounds–from 0D to 3D architectures. Chem Soc Rev 2013;42(23):8835–48.

[106] Jing Z, Zhan J. Fabrication and gas-sensing properties of porous ZnO nanoplates. Adv Mater 2008;20 (23):4547–51.

[107] Lu X, Deng J, Si W, Sun X, Liu X, Liu B, Liu L, et al. High-performance Li-O2 batteries with trilayered Pd/MnOx/Pd nanomembranes. Adv Sci 2015;2(9):1500113.

[108] Chen C, Jian H, Mai K, Ren Z, Wang J, Xinxin F, Fan C, Sun C, Qian G, Wang Z. Shape-and size-controlled synthesis of Mn3O4 nanocrystals at room temperature. Eur J Inorg Chem 2014;2014 (19):3023–9.

[109] Chiu I-T, Li C-T, Lee C-P, Chen P-Y, Yu-Hao T, Vittal R, Ho K-C. Nanoclimbing-wall-like CoSe2/carbon composite film for the counter electrode of a highly efficient dye-sensitized solar cell: a study on the morphology control. Nano Energy 2016;22:594–606.

https://www.twirpx.org & http://chemistry-chemists.com

[110] Han X-G, He H-Z, Kuang Q, Zhou X, Zhang X-H, Xu T, Xie Z-X, Zheng L-S. Controlling morphologies and tuning the related properties of nano/microstructured ZnO crystallites. J Phys Chem C 2009;113(2):584–9.

[111] Yuan YF, Xia XH, Wu JB, Yang JL, Chen YB, Guo SY. Hierarchically ordered porous nickel oxide array film with enhanced electrochemical properties for lithium ion batteries. Electrochem Commun 2010;12(7):890–3.

[112] Rong DZ, Pan ZW, Wang ZL. Growth and structure evolution of novel tin oxide diskettes. J Am Chem Soc 2002;124(29):8673–80.

[113] Peng Y, Xu A-W, Deng B, Antonietti M, Cölfen H. Polymer-controlled crystallization of zinc oxide hexagonal nanorings and disks. J Phys Chem B 2006;110(7):2988–93.

[114] Viswanath B, et al. Predicting the growth of two-dimensional nanostructures. Nanotechnology 2008;19(19):195603.

[115] Zhang Y, Xu J, Xiang Q, Li H, Pan Q, Pengcheng X. Brush-like hierarchical ZnO nanostructures: synthesis, photoluminescence and gas sensor properties. J Phys Chem C 2009;113(9):3430–5.

[116] Liu H, Miao W, Yang S, Zhang Z, Chen J. Controlled synthesis of different shapes of Cu2O via γ-irradiation. Cryst Growth Des 2009;9(4):1733–40.

[117] Vakil PN, Hardy DA, Strouse GF. Synthesis of highly uniform nickel multipods with tunable aspect ratio by microwave power control. ACS Nano 2018;12(7):6784–93.

[118] Liang J, Liu J, Xie Q, Bai S, Yu W, Qian Y. Hydrothermal growth and optical properties of doughnut-shaped ZnO microparticles. J Phys Chem B 2005;109(19):9463–7.

[119] Chen S, Koshy DM, Tsao Y, Pfattner R, Yan X, Feng D, Bao Z. Highly tunable and facile synthesis of uniform carbon flower particles. J Am Chem Soc 2018;140(32):10297–304.

[120] Zhang G, Sun S, Banis MN, Li R, Cai M, Sun X. Morphology-controlled green synthesis of single crystalline silver dendrites, dendritic flowers, and rods, and their growth mechanism. Cryst Growth Des 2011;11(6):2493–9.

[121] O'Dwyer C, Navas D, Lavayen V, Benavente E, Ana MAS, Gonzalez G, Newcomb SB, Sotomayor Torres CM. Nano-urchin: the formation and structure of high-density spherical clusters of vanadium oxide nanotubes. Chem Mater 2006;18(13):3016–22.

[122] Yang H, Lu X, Xin Z. One-step synthesis of nonspherical organosilica particles with tunable morphology. Langmuir 2018;34(39):11723–8.

[123] Li C, Fang G, Fuhai S, Li G, Wu X, Zhao X. Self-organized ZnO microcombs with cuboid nanobranches by simple thermal evaporation. Cryst Growth Des 2006;6(11):2588–91.

[124] Teixeira IF, et al. Carbon nitrides and metal nanoparticles: from controlled synthesis to design principles for improved photocatalysis. Chem Soc Rev 2018;47(20):7783–817.

[125] Nishanthi ST, Rao BV, Kailasam K. Metal-free organic semiconductors for visible-light-active photocatalytic water splitting. In: Visible light-active photocatalysis: nanostructured catalyst design, mechanisms, and applications; 2018. p. 329–63.

[126] Li M, et al. Different mechanisms for E. coli disinfection and BPA degradation by CeO2-AgI under visible light irradiation. Chem Eng J 2019;371:750–8.

[127] Wang J, et al. Atomic scale g-C3N4/Bi2WO6 2D/2D heterojunction with enhanced photocatalytic degradation of ibuprofen under visible light irradiation. Appl Catal Environ 2017;209:285–94.

[128] Chen Y, et al. Three-dimensional Ag2O/Bi5O7I p–n heterojunction photocatalyst harnessing UV–vis–NIR broad spectrum for photodegradation of organic pollutants. J Hazard Mater 2018;344:42–54.

[129] Wang S, et al. Formation of hierarchical In2S3–CdIn2S4 heterostructured nanotubes for efficient and stable visible light CO2 reduction. J Am Chem Soc 2017;139(48):17305–8.

https://www.twirpx.org & http://chemistry-chemists.com

[130] Han B, et al. One-dimensional CdS@ MoS2 core-shell nanowires for boosted photocatalytic hydrogen evolution under visible light. Appl Catal Environ 2017;202:298–304.

[131] Liu J, et al. Amorphous NiO as co-catalyst for enhanced visible-light-driven hydrogen generation over g-C3N4 photocatalyst. Appl Catal Environ 2018;222:35–43.

[132] Hao X, et al. Zn-vacancy mediated electron-hole separation in ZnS/g-C3N4 heterojunction for efficient visible-light photocatalytic hydrogen production. Appl Catal Environ 2018;229:41–51.

[133] Lin B, et al. Preparation of 2D/2D g-C3N4 nanosheet@ ZnIn2S4 nanoleaf heterojunctions with well-designed high-speed charge transfer nanochannels towards high-efficiency photocatalytic hydrogen evolution. Appl Catal Environ 2018;220:542–52.

[134] Ran J, et al. Metal-free 2D/2D phosphorene/g-C3N4 Van der Waals heterojunction for highly enhanced visible-light photocatalytic H2 production. Adv Mater 2018;30(25):1800128.

[135] Wang S, Guan BY, Lou XWD. Construction of ZnIn2S4–In2O3 hierarchical tubular heterostructures for efficient CO2 photoreduction. J Am Chem Soc 2018;140(15):5037–40.

[136] Xu Y-F, et al. A CsPbBr3 perovskite quantum dot/graphene oxide composite for photocatalytic CO2 reduction. J Am Chem Soc 2017;139(16):5660–3.

[137] Zhang F, et al. Exceptional synergistic enhancement of the photocatalytic activity of SnS2 by coupling with polyaniline and N-doped reduced graphene oxide. Appl Catal Environ 2018;236:53–63.

[138] Bellamkonda S, et al. Highly active and stable multi-walled carbon nanotubes-graphene-TiO2 nanohybrid: an efficient non-noble metal photocatalyst for water splitting. Catal Today 2019;321:120–7.

[139] Das KK, et al. Enhanced photocatalytic activities of polypyrrole sensitized zinc ferrite/graphitic carbon nitride nn heterojunction towards ciprofloxacin degradation, hydrogen evolution and antibacterial studies. J Colloid Interface Sci 2020;561:551–67.

[140] Patnaik S, et al. Enhanced photo catalytic reduction of Cr (VI) over polymer-sensitized g-C3N4/ZnFe2O4 and its synergism with phenol oxidation under visible light irradiation. Catal Today 2018;315:52–66.

[141] Liu S, et al. Enhanced photocatalytic conversion of greenhouse gas CO2 into solar fuels over g-C3N4 nanotubes with decorated transparent ZIF-8 nanoclusters. Appl Catal Environ 2017;211:1–10.

[142] Zhang Y, Park S-J. Facile construction of MoO3@ ZIF-8 core-shell nanorods for efficient photoreduction of aqueous Cr (VI). Appl Catal Environ 2019;240:92–101.

[143] Chauhan A, et al. Janus nanostructures for heterogeneous photocatalysis. Appl Phys Rev 2018;5(4), 041111.

[144] Chen F, et al. Hierarchical assembly of graphene-bridged Ag3PO4/Ag/BiVO4 (040) Z-scheme photocatalyst: an efficient, sustainable and heterogeneous catalyst with enhanced visible-light photoactivity towards tetracycline degradation under visible light irradiation. Appl Catal Environ 2017;200:330–42.

[145] Adhikari S, Mandal S, Kim D-H. Z-scheme 2D/1D MoS2 nanosheet-decorated Ag2Mo2O7 microrods for efficient catalytic oxidation of levofloxacin. Chem Eng J 2019;373:31–43.

[146] Xiao T, et al. In situ construction of hierarchical WO3/g-C3N4 composite hollow microspheres as a Z-scheme photocatalyst for the degradation of antibiotics. Appl Catal Environ 2018;220:417–28.

[147] Di T, et al. A direct Z-scheme g-C3N4/SnS2 photocatalyst with superior visible-light CO2 reduction performance. J Catal 2017;352:532–41.

[148] Xu F, et al. CuInS2 sensitized TiO2 hybrid nanofibers for improved photocatalytic CO2 reduction. Appl Catal Environ 2018;230:194–202.

[149] Meng A, et al. Direct Z-scheme TiO2/CdS hierarchical photocatalyst for enhanced photocatalytic H2-production activity. Appl Surf Sci 2017;422:518–27.

https://www.twirpx.org & http://chemistry-chemists.com

[150] Wang Z, et al. Application of zero-dimensional nanomaterials in biosensing. Front Chem 2020;8:320.

[151] Jiang Q, et al. Boosting the efficiency of photoelectrolysis by the addition of non-noble plasmonic metals: Al & Cu. Nanomaterials 2019;9(1):1.

[152] Guo L, et al. MoS 2/TiO 2 heterostructures as nonmetal plasmonic photocatalysts for highly efficient hydrogen evolution. Energ Environ Sci 2018;11(1):106–14.

[153] Stroyuk O, Raevskaya A, Gaponik N. Solar light harvesting with multinary metal chalcogenide nanocrystals. Chem Soc Rev 2018;47(14):5354–422.

[154] Hu Z, et al. Multiplasmon modes for enhancing the photocatalytic activity of Au/Ag/Cu 2 O core–shell nanorods. Nanoscale 2019;11(35):16445–54.

[155] Ma L, et al. Pt decorated (Au nanosphere)/(CuSe ultrathin nanoplate) Tangential hybrids for efficient photocatalytic hydrogen generation via dual-plasmon-induced strong VIS–NIR light absorption and interfacial electric field coupling. Solar RRL 2020;4(1), 1900376.

[156] Zhou L, et al. Quantifying hot carrier and thermal contributions in plasmonic photocatalysis. Science 2018;362(6410):69–72.

[157] Un IW, Sivan Y. Parametric study of temperature distribution in plasmon-assisted photocatalysis. Nanoscale 2020;12(34):17821–32.

[158] Liu S, et al. Improved visible-light photocatalytic activity of porous carbon self-doped ZnO nanosheet-assembled flowers. CrstEngComm 2011;13(7):2533–41.

[159] Yao W-T, et al. Architectural control syntheses of CdS and CdSe nanoflowers, branched nanowires, and nanotrees via a solvothermal approach in a mixed solution and their photocatalytic property. J Phys Chem B 2006;110(24):11704–10.

[160] Zhang J, et al. Tailored indium sulfide-based materials for solar-energy conversion and utilization. J Photochem Photobiol C Photchem Rev 2019;38:1–26.

[161] Ye L, et al. Bismuth-based photocatalysts for solar photocatalytic carbon dioxide conversion. ChemSusChem 2019;12(16):3671–701.

[162] Joy J, Mathew J, George SC. Nanomaterials for photoelectrochemical water splitting–review. Int J Hydrogen Energy 2018;43(10):4804–17.

[163] Ye S, et al. A review on g-C3N4 for photocatalytic water splitting and CO2 reduction. Appl Surf Sci 2015;358:15–27.

[164] Ran J, et al. Earth-abundant cocatalysts for semiconductor-based photocatalytic water splitting. Chem Soc Rev 2014;43(22):7787–812.

[165] Li Y, Zhou X, Xing Y. In situ thermal-assisted loading of monodispersed Pt nanoclusters on CdS nanoflowers for efficient photocatalytic hydrogen evolution. Appl Surf Sci 2020;506:144933.

[166] Xiang Q, Cheng B, Jiaguo Y. Hierarchical porous CdS nanosheet-assembled flowers with enhanced visible-light photocatalytic H2-production performance. Appl Catal Environ 2013;138:299–303.

[167] Bai H, Liu Z, Sun DD. The design of a hierarchical photocatalyst inspired by natural forest and its usage on hydrogen generation. Int J Hydrogen Energy 2012;37(19):13998–4008.

[168] Maeda K, Sekizawa K, Ishitani O. A polymeric-semiconductor–metal-complex hybrid photocatalyst for visible-light CO 2 reduction. Chem Commun 2013;49(86):10127–9.

[169] Zhou H, et al. Artificial photosynthesis on tree trunk derived alkaline tantalates with hierarchical anatomy: towards CO 2 photo-fixation into CO and CH 4. Nanoscale 2015;7(1):113–20.

[170] In S-I, Vaughn DD, Schaak RE. Hybrid CuO-TiO2 − xNx hollow nanocubes for photocatalytic conversion of CO2 into methane under solar irradiation. Angew Chem Int Ed 2012;51(16):3915–8.

[171] Yuan L, et al. Origin of enhancing the photocatalytic performance of TiO2 for artificial photoreduction of CO2 through a SiO2 coating strategy. J Phys Chem C 2016;120(1):265–73.

https://www.twirpx.org & http://chemistry-chemists.com

[172] Jin J, et al. A hierarchical Z-scheme CdS–WO3 photocatalyst with enhanced CO2 reduction activity. Small 2015;11(39):5262–71.

[173] Sinha TK, et al. Rapid growth of fully-inorganic flexible Ca x CoO 2 thin films from a ligand free aqueous precursor ink for thermoelectric applications. Chem Commun 2019;55(54):7784–7.

[174] Maiti R, et al. Enhanced and selective photodetection using graphene-stabilized hybrid plasmonic silver nanoparticles. Plasmonics 2016;11(5):1297–304.

[175] Sinha TK, et al. Graphene-silver-induced self-polarized PVDF-based flexible plasmonic nanogenerator toward the realization for new class of self powered optical sensor. ACS Appl Mater Interfaces 2016;8(24):14986–93.

[176] Chowdhury RK, et al. Synergistic effect of polymer encapsulated silver nanoparticle doped WS 2 sheets for plasmon enhanced 2D/3D heterojunction photodetectors. Nanoscale 2017;9(40):15591–7.

[177] Hu YH. A highly efficient photocatalyst—hydrogenated black TiO2 for the photocatalytic splitting of water. Angew Chem Int Ed 2012;51(50):12410–2.

[178] Dong J, et al. Defective black TiO2 synthesized via anodization for visible-light photocatalysis. ACS Appl Mater Interfaces 2014;6(3):1385–8.

[179] Friedmann D, et al. Heterogeneous photocatalytic organic synthesis: state-of-the-art and future perspectives. Green Chem 2016;18(20):5391–411.

[180] Bai S, et al. Steering charge kinetics in photocatalysis: intersection of materials syntheses, characterization techniques and theoretical simulations. Chem Soc Rev 2015;44(10):2893–939.

https://www.twirpx.org & http://chemistry-chemists.com

15

Green technology for environmental hazard remediation

Ajit Behera[a] and Ranjan K. Mohapatra[b]

[a]DEPARTMENT OF METALLURGICAL AND MATERIALS ENGINEERING, NATIONAL INSTITUTE OF TECHNOLOGY, ROURKELA, INDIA [b]DEPARTMENT OF CHEMISTRY, GOVERNMENT COLLEGE OF ENGINEERING, KEONJHAR, ODISHA, INDIA

1 What is green technology?

Green technology is a new concept that relates to science and engineering in the condition to protect nature from the adverse impacts of human activities. Much emphasis has been placed on green technology since the 1990s. Many of the techniques explored in green technology, also known by other terms such as green engineering, green chemistry, clean technology, environmental technology, and many more [1, 2]. The definition of green technology is "the process adopted and the final product, both should be maintained towards environmentally-friendly condition [1–4]." All these technologies are intended to ensure that nature remains protected. For example, microorganisms like microalgae and cyanobacteria consume solar energy to produce solar fuel. Some green plants uses the enzyme RuBisCO as a photocatalytic agent to reduce carbon dioxide to contribute to a pollution-free environment. Human beings need Earth to remain in a good environmental state for their own well-being. Green technology ensures that the planet remains healthy so that life may continue to exist. This is all about sustainability. This technology has risen rapidly as people have realized various harmful effects on the environment, including the greenhouse effect and the global warming.

Types of green technology range from very simple applications that can be used in the home to highly specialized systems [3, 4]. The world has a limited amount of natural resources, some of which have already been depleted or destroyed. For example, batteries and household electronics in many instances contain dangerous chemicals that contaminate soil and groundwater with chemicals that cannot be eliminated from the drinking water supply and end up in food crops and farm animals. The health risks alone are astonishing. Plastic pollutants are another unsustainable resource that destroys marine habitats worldwide, killing fish, birds, and many other species, reaching the bottom of the food chain. Green technology gives us the opportunity to neutralize the effects of climate change and pollution [5].

Among various technology, photocatalysis is a field of green chemistry as light is freely available and does not pollute the environment. Photocatalysis involves chemical reactions

Nanostructured Materials for Visible Light Photocatalysis. https://doi.org/10.1016/B978-0-12-823018-3.00022-1
Copyright © 2022 Elsevier Inc. All rights reserved.

https://www.twirpx.org & http://chemistry-chemists.com

that occur in the presence of light. The substrate that absorbs light and changes the rate of a chemical reaction is termed a photocatalyst. Keeping this in mind, Liu et al. [6] have reported a feasible and effective solution to construct bio-inspired hierarchical systems by using aquatic leaves for high-efficiency photocatalysis. This work should make a significant contribution to the future construction of light harvesting structures. The rust-induced photocatalytic activity of ZnO nanoparticles obtained from leaf extracts of *Prosopis juliflora* by biosynthesis has been studied by Mydeen et al. [7]. Here, the proposed mechanism was explored in photodegradation of methylene blue. Moreover, Lee et al. [8] reported ecofriendly biologically synthesized copper nanoparticles by using magnolia leaf extract as a reducing agent. Silver-based topical dressings are typically sought after as a treatment for open wounds, infection in burns, chronic ulcers, etc. With regard to this, Krithiga et al. [9] reported a simple, rapid, and economical synthesis of silver nanoparticles by employing *Solanum nigrum* and *Clitoria ternatea* leaf extracts. Furthermore, the nanoparticles were evaluated for their antibacterial activities at different concentrations against various nosocomial pathogens. The study will be effective in medicine as it has many applications.

Das et al. [10] reported a convenient and green deoximation pathway by using iodine in the aqueous extract of shikakai. In this work, the authors described the regeneration of various carbonyl compounds under microwave radiation. This proposed unique methodology is a novel green technique, which may be a suitable replacement of the reported hazardous chemicals in any other organic reactions. In another work, Das et al. [11] also reported similar reactions by taking aqueous extract of *Sapindus laurifolia* in place of *Acacia concinna*.

Due to rapid human and technological advances, harmful pollutants are continuously released to the environment. The expeditious detection of such toxic wastes and its control are common challenges for researchers nowadays. Biosensors are sensitive tools for this detection [12]. Luo et al. [13] reported pollution monitoring using sensor networks to protect the environment. The authors also discussed the challenges regarding pollution monitoring network systems using sensors. Vaseashta et al. [14] employed remote sensing technologies to predict urban pollution by using image processing to support public awareness in polluted areas.

Several regulations, policies, and technologies have been adopted for remediation of air pollution, but the air quality has still not changed appreciably. Currently, environmental pollution detection and control are usually done by utilizing plants and microorganisms. This process should be reliable, reproducible and cost-effective. Wei et al. [15] discussed leaf-based remediation technologies (phylloremediation) as plant leaves are able to absorb (or adsorb) air pollutants.

2 Principles of sustainability

There are three principles that determine sustainability in any kind of material, as described by the American ecologist and economist Herman Daly [16]: (1) nonrenewable

https://www.twirpx.org & http://chemistry-chemists.com

energies should not be consumed at rates more than the growing speed of renewable substitution; (2) renewable energies should not be utilized at a rate faster than their reclamation amount; and (3) the ability to absorb and regenerate the natural environment may not be exceeded. Nonrenewable energy resources include nuclear energy, fossil fuels, wind and geothermal, natural gas, oil, hydroelectric power, biomass energy, etc. At present, all of these sources are unsuccessful in terms of establishing sustainability in a direct or indirect way, but the most painful are the ability of the environment to absorb and regenerate the costs associated with various extraction or production processes. Nevertheless, these resources are not currently sufficiently utilized to replace the nonrenewables. In the current position, some members of the energy industry are determined not to be green, while other industries see it as a challenge and opportunity. The overall conclusion is that although nonrenewable energy sources now account for 80% of the world's energy needs, which is simply not be sustainable [17]. If we wish to preserve life on our planet, emerging green energy technology should be used in conjunction with existing methods to transform from the unsustainable to the sustainable.

3 Benefits from green technologies

Various environmentally friendly activities by green technologies are discussed in this section.

- *Recycling*: It is more beneficial to recycle glass, metal, paper, and plastic when compared to landfills. In addition, a large amount of recyclable material has allowed people to create fertilizers for plants, sculptures, fuels, and furniture. Green technology helps in terms of waste management, waste reduction, and waste utilization [18, 19].
- *Purifying of water*: Green technology purifies water. The lack of clean drinking water is an important concern. Using various green technologies, many campaigns have been able to provide people with drinking water [18, 19].
- *Purifying the air*: Tackling carbon emissions is an important aspect of environmental care. Cars, factories, etc. emit large amounts of carbon that are harmful to the atmosphere. Green technology helps reduce carbon emissions and enhances the cleanness of the air. It does not emit anything harmful to the air like SOx, NOx, etc. This helps creatures in the environment to breathe properly. It may also reduce the effects of global warming by reducing carbon emissions [19, 20].
- *Conserving energy*: Energy is maintained through the use of green technology. Renewable sources of energy can be generated with the help of natural sources such as sunlight and wind energy. Therefore, technologies such as solar cells, wind turbines, and geothermal sources provide replacements for fossil fuels. Alternatives are awaited for all the devices that use a lot of electricity or fuel. The uses of environmentally friendly appliances, like electric cars, are encouraged.
- *Rejuvenating ecosystems*: Clean technology is also used to benefit life in healthy ecosystems that have been severely damaged by human activity. According to the

https://www.twirpx.org & http://chemistry-chemists.com

concept of this technology, planting of trees is encouraged, and waste is minimized and recycled. These practices result in the transformation of affected ecosystems. This leads to the sustainability of many species of plants and animals that do not die out [19, 20].
- *Less maintenance, and economic benefits*: This technology does not require a lot of money to use the unlimited source, which indicates it will never run out. It may bring economic benefits to specific technology in various area.

4 Disadvantages of green technologies

In addition to the vast benefits, there are some limitations which need to be solved in the near future. These are given below [10, 15].

- *High cost of implementation*: The total cost of the initial investment is quite high.
- *No known alternative chemical or raw material inputs*: In some specific processes, it is very difficult to alter the requirement of chemicals.
- *Uncertainty about the impact of performance*: Under research/forcefully induced technology will give less impact on performance.
- *Lack of human resources and skills*: Alternative parameters may engage more human resource and skill.

5 Exploring the goals of green technology

These green technologies are means of safeguarding nature and its human denizens. This is why business owners and homeowners are making the choice to move toward more sustainable and environmentally friendly products. However, once these products reach marketing, installing them properly and benefiting in a timely manner requires professional experience that only a few have. The objectives in several areas are presented below:

- *Solar power*: Photovoltaic solar panels are a by-product of green technology. These panels convert solar energy to electrical energy. According to requirements, the panel size can be increased from small (for home) to large (for aircraft, spacecraft). Renowned industries like Google, Microsoft, and even Facebook's head offices account for most of their electricity needs using solar energy. It is an economic and ecological direction to generate huge amounts of electricity at a reasonable price [21, 22].
- *Wind turbines*: This is another way to generate kinetic energy from wind energy and finally convert the electric energy. The only real objection to wind turbines is that their presence can spoil the landscape. However, it is undebatable that these wind farms are a very eco-friendly and sustainable form of everlasting renewable energy source. Above all, they represent an extremely economical solution for meeting domestic, industrial,

https://www.twirpx.org & http://chemistry-chemists.com

and commercial energy needs. The only significant resource required for a wind farm is large areas of land. However, the number of commercial wind farms is on the rise. Residents have the option to purchase this wind renewable energy as per the need on the site. Additionally, all the energy needs of a domestic household can be met with a single [23].

- *Geothermal power*: Geothermal energy is based on the thermal energy produced by the Earth's core. While this power needs to account for the various soils and other regional fluctuations estimate the thermal energy available. Presently, Earth has the ability consistently to produce enough energy to meet various requirements and benefit from the geothermal potential around the world. It is a passive way of generating electricity worldwide. Recently, people have tried to harvest geothermal energy by different ways and also found out how to store the energy [24].
- *Smart power bars*: Electronic devices in your residence or work station continue to consume electric energy even when turned off. Loss of electricity from wired or standby electronic systems is known as "phantom loss" [25]. Smart lines can control a fully connected electronic device. These devices can also turn off the secondary electronics that can be connected to the bar (e.g., a TV or Xbox). It might seem as if smart power bars or strips have a superpower [26].

Another category of sustainable energies is the energy generated through photocatalysts, which is described in the next section.

6 Green technology using photocatalysts

In recent years, researchers have been focusing on innovative materials and advanced technology that can make photocatalysis practical. Photocatalysis is the process that occurs when light energy comes into contact with the surface of a semiconductor material. During photocatalysis, two simultaneous reactions occur: the oxidation of the power bores and the reduction of the electrodes produced by photogenic energy. Photocatalysis has received significant attention due to the ease of transformation of solar energy to provide energy, which is renewable and sustainable as a solution to the serious demand of energy. These applications also focus on hydrogen evolution from the splitting of water, conversion of CO_2 into hydrocarbon fuels, disinfecting water, and the degradation of pollutants via photocatalysis. Moreover, the use of TiO_2 as a photocatalyst has increased as it is low cost, nontoxic, and possesses high UV efficiency [27].

Lin et al. [28] reported indoor acetaldehyde extraction utilizing an N-doped TiO_2 photocatalyst irradiated with visible light. The mesoporous N-TiO_2 was highly capable of absorbing acetaldehyde, which was consequently photooxidized with irradiation from visible light. A decrease in the rate of adsorption of the internal acetaldehyde is observed when the temperature increases. Rebleanu et al. [29] described the sol-gel composition of Cu^{2+}-TiO_2 and Ag/TiO_2, which is useful for microbial disinfection with a nanostructured

https://www.twirpx.org & http://chemistry-chemists.com

photocatalyst. Ag-TiO_2 was more active than Cu^{2+}-TiO_2, whereas *E. coli* displayed higher sensitivity to Ag/TiO_2 than *S. cerevisiae*. The effect of photocatalysts developed on plants was assessed by exposure of the *Arabidopsis thaliana* Col-0 strain to these materials under diverse conditions and intensities. Harmful impacts on *A. thaliana* were observed due to silver-based materials' exposure to longer durations and higher photocatalyst concentrations. Yao [30] explored the preparation of amorphous TiO_2/alopecia areata encoded in C and N (C, N-TiO_2/HNT) using melamine as a source of C and N. Prepared C, N-TiO_2/HNT showed more powerful photocatalytic activity for C of methylene blue than that of TiO_2/HNT. Chen et al. [31] synthesized a beneficial CuO/Co_3O_4 compound on Cu wire meshes using an easy hydrothermal method. These CuO/Co_3O_4 coaxial heterodimers were simple to recycle and displayed improved photocatalytic activity for the degeneration of methylene blue from the single matrix CuO nanoparticles.

Ismail et al. [32] developed a novel method to immobilize TiO_2 by coating the TiO_2 solution on a double-sided adhesive film as a thin-layer binder in the absence of any organic additive. The immobilized TiO_2/DSAT exhibited a range from the lower end to the higher end of photocatalytic activity for the degradation of reactive red 4 and the methylene blue compared to the suspended TiO_2 powder, respectively. DSAT produced a clear interaction between the glass and the TiO_2 layers, and therefore repetitive use of immobilized TiO_2/DSAT can take up to 30 cycles. Wei et al. [33] reported a hydrophobic ZnO-TiO_2 nanocomposite, which featured a self-cleaning surface that elevated photocatalytic activity. The prepared membranes exhibited superior hydrophobicity and self-cleaning properties for organic materials under UV irradiation. Fan et al. [34] have studied the photocatalytic property of Cu added to $NaNbO_3$. Compared to the virgin $NaNbO_3$, Cu-$NaNbO_3$ as prepared showed improved photocatalytic activity for the evolution of H_2 from an aqueous methanol solution and the degradation of rhodamine under visible light irradiation. Cu doping reportedly improved the adsorption capacity of $NaNbO_3$ and accelerated the mineralization process.

7 Green nanostructured photocatalysts

Nanomaterials are the major constituents of solar energy conversion devices and have been implemented in the following three ways: (a) molecular assembly and donor acceptors that mimic photosynthesis; (b) solar photocatalytic fuel generation using semiconductors; and (c) the use of nanostructured semiconductor materials in solar cells. Among solar energy conversion systems and devices, binary and tripartite metal oxides are the most widely used and have a promising future in this field. Very few publications have been published on green photoactive nanomaterials and their main applications. Most books cover a wide range of photocatalysts, including metal oxides and nonmetallic oxides.

Certain binary and ternary metal oxides are photoactive and are used for photocatalytic activities in solar cells, water splitting, and other sun-induced reactions. Synthetic

https://www.twirpx.org & http://chemistry-chemists.com

methods for binary and trimetric metal oxide photocatalysts highlight the green reaction processes. The emergence of green, easy, and benign methods for the production of these nanomaterials is essential to address contemporary environmental concerns. Important aspects of such ecological methods are low temperature, rapid reaction rate, and reduction of toxic agents. There are some new techniques that produce photoactive nanomaterials to minimize the use and production of hazardous substances during the manufacturing process. Such techniques include hydrothermal approaches together with the polymer gel method, the chemical precipitation technique, the solvothermal method, ultrasonication, and the hybrid synthesis method [35–37]. For example, although there are currently several methods available, such as solid-state reactions, polymerizable composite and hydrothermal methods, titanium dioxide (TiO_2) is generally synthesized by colloidal methods [38].

Zirconium dioxide (ZrO_2) with a bandwidth of 5.0 eV is a photocatalyst that can divide the water without cocatalyst under UV irradiation due to the position of its high conductivity band. The photocatalytic activity of $ZrO_2$was reduced when loaded with cocatalysts such as Pt, copper (Cu), gold (Au), and ruthenium oxide (RuO_2) [39]. It is possible that the height of the electronic barrier of the semiconductor metal bar prevented the transfer of electrons and stopped other molecular water-sharing reactions. However, the photocatalytic activity was improved by the addition of Na_2CO_3. Niobium pentoxide (Nb_2O_5) with a bandwidth of 3.4 eV is inactive without any UV modification [40]. Effectively break down the water in "water-methanol mixture" after loading with a Pt cocatalyst is observed. Its higher photocatalytic activity under UV irradiation was observed as the assembled Nb_2O_5 intermediate.

Tantalum pentoxide (Ta_2O_5) with a bandwidth of 4.0 eV is also a known photocatalyst. It can produce a small amount of hydrogen without oxygen without any modification. Ta_2O_5 loaded with nickel oxide (NiO) and RuO_2 exhibits high photocatalytic activity to generate hydrogen and oxygen. The addition of Na_2CO_3 and intermediate structure of the catalyst showed improved photocatalytic activity. Nanostructured vanadium dioxide (VO_2) with a BCC structure and a large 2.7 eV optical band has shown excellent photocatalytic activity in the production of hydrogen from a solution of water and ethanol under UV irradiation. Strontium titanate ($SrTiO_3$) with a bandwidth of 3.2 eV and potassium tantalite ($KTaO_3$) with a bandwidth of 3.6 eV can be photoactive without external bias due to their high conductivity bands. These materials can be used as powder photocatalysts for solar cells and water separation. The enhanced photocatalytic activity of $SrTi0_3$was also reported using a new modified preparation or doping method with suitable metal cations (e.g., La31, Ga31, and Na1). Turmeric modified titanium is effective photocatalysts for splitting water under ultraviolet radiation. H_2 release from photocatalysts of sodium titanate $Na_2Ti_3O_7$ (stratified crystalline structure), potassium titanate $K_2Ti_2O_5$ (stratified crystalline structure) and potassium titanate $K_2Ti_4O_9$ (stratified crystalline structure) [41, 42].

Barium titanate ($BaTiO_3$) with a 3.22 eV film separation energy and crystalline structure of perovskite prepared using a polymerized complex method has high photocatalytic

https://www.twirpx.org & http://chemistry-chemists.com

activity compared to materials prepared by the traditional method due to its smaller size and larger surface area. Calcium titanate ($CaTiO_3$) with 3.5 eV film separation energy and Pt-loaded perovskite crystalline structure showed good photocatalytic activity under ultraviolet radiation. The activity of $CaTiO_3$ subjected to a solid zirconium ion solution (Zr41) was further increased. A series of titanium lanthanum (La_2TiO_5, $La_2Ti_3O_9$, and $La_2Ti_2O_7$) introduction to green nanostructured photocatalysts with stratified structures shows higher photocatalytic activities under UV irradiation. The photoreactive properties of barium (Ba), strontium (Sr), and calcium (Ca) in $La_2Ti_2O_7$ improved [43, 44].

8 Principles and mechanisms of green photocatalysis

8.1 Sunlight-driven photocatalysts

One of the essential works in this field is finding metal oxide semiconductors engaged as photocatalysts to eliminate or treat polluted water by solar energy. An ideal photocatalytic material must possess the required properties in its bandgap to receive a wide array of the solar spectrum, disperse water molecules, and maintain stability in the aquatic environment in the course of the reaction. It should also be a relatively simple, economical process with nontoxic parts that are readily available. In recent decades, different metal oxide nano-assemblies based on semiconductors have been invented and exhibited as catalytic materials for water purification purposes in sunlight [40].

The following are influencing factors for the photocatalyst process [41–45].

- *Dye concentration*: The rationale of the dye in photocatalytic reaction is the principal parameter. The catalyst can reduce the color on average. The dye is absorbed by the catalyst's surface, which subsequently undergoes a reaction as it is excited in light conditions. The absorption of color on the surface of the photocatalyst is directly associated to the actual density of the color. The actual concentration of color is an important characteristic that must be carefully considered. Generally, with an increase in the concentration of the dye, there is a reduction in the percentage of degradation, although the photocatalysts involved in the exchange must be maintained.
- *Catalyst amount*: The quantity of the catalyst also influences the reactions during the photocatalysis process. In the heterogeneous photocatalytic process, there is an increase in the photodegradation rate of the dye to increase the amount of photocatalyst. Increasing the number of catalysts can yield more active sites in the photocatalytic reaction, which promotes the creation of more reactive radicals in the photodegradation.
- *pH*: The pH of the solution also plays a crucial part in the degradation process. The entire photocatalytic processes can either be triggered or suppressed depending on the material properties and the nature of the contaminant. The catalyst's (metal oxide nanoparticles) surface potential can be modified by adjusting the solution's pH.

https://www.twirpx.org & http://chemistry-chemists.com

Consequently, the absorption of pollutants on the photocatalyst's surface is altered, resulting in a change in the rate of photodegradation.

- *Surface morphology of the photocatalyst*: Surface morphology has essential properties to be estimated for photodegradation. The phenomenon also comprises of activities such as particle size and shape. The number of photons incident on the surface of the photocatalyst is a way to measure the photocatalytic activity rate. Therefore, varying the number of photons assists in controlling the rate of photocatalytic activity. If photocatalysts have different forms, the reaction is more rapid.
- *Surface area*: Photocatalytic reactions favor materials with larger surface areas for higher performance. Additionally, the presence of active sites on the surface contributes to the efficiency of the photocatalytic reaction. Materials with larger surface area have the potential to create many active sites on the surface of the photocatalyst. Consequently, creating radical reactive species is effective for photodegradation activities.
- *Temperature-dependent reaction*: An optimum temperature of 0–80°C should be maintained for an effective photocatalytic reaction. When the temperature rises above 80°C, the photocatalytic reaction is suppressed as the catalyst promotes the recombination of electron-hole pairs. Therefore, photocatalytic reactions depend significantly on the reaction temperature.
- *Nature of the pollutants and their concentrations*: The extent of photodegradation can be estimated with the help of the concentration of the water matrix and the nature of certain pollutants. Some photocatalysts, such as TiO_2, are incapable of disinfection when the concentration of pollutants is high. Retardation in the formation of active radicals on the surface of the photocatalyst reduces photocatalytic efficiency.
- *Intensity and irradiation period of the light*: The intensity and radiation period of incoming light are the main factors influencing the photodegradation of pollutants. At high light intensity, the percentage of photodegradation and the intensity of light are inversely associated, due to the production of excitons being dominant at low light intensities and therefore able to slow down the reunification of electron-hole pairs. In contrast, when increasing the radiation light intensity, the electron-hole pairs' recoupling occurs on the surface of the photocatalyst, thus reducing the activity of the catalyst in the reaction.
- *Dopants on dye degradation*: There are different methods available for making various nanoparticles, which have the capacity to absorb photons with very low energy. Additionally, the techniques involve band engineering, which is prohibited by continuously transforming and modifying the valence and conduction bands with the introduction of various metallic and nonmetallic materials into photocatalytic materials. Moreover, surface modification can also be obtained by mixing with organic materials and semiconductors.

https://www.twirpx.org & http://chemistry-chemists.com

8.2 Metal oxide-driven photocatalysts

Nanostructured semiconductor metal oxide is also used for photocatalytic action to purify the contaminated water and dissociate hydrogen and oxygen. The sufficient photocatalytic action criteria are band edge position, bandgap, relatively larger surface area, precise morphology, chemical stability, and reuse. Different semiconductor metal oxides like ZnO, TiO_2, SnO_2, WO_3, and Cu_2O have important photocatalytic properties, such as absorption of light [45]. The light activates the charge carriers by creating pores which oxidize the organic matter. Lights from various sources and wavelengths such as visible, sunlight, UV, or a combination of both visible and UV can activate the nanostructured semiconductor metal oxide. From the valence band to the conduction band, creating electron/hole pairs, the charge carriers are created. The electron-hole pairs facilitate reactions to reduce the organic pollutants' molecular chains. The photocatalytic activity produces: (i) generation of hydroxyl radicals with the oxidation of OH anions; and (ii) reduction of the produced superoxide radicals by O^2. These radical reactive members can inhibit organic pollutants into a disinfectant or nonmineral by-products. Therefore, this photocatalytic activity has great scientific importance in the fields of environment, hydrogen fuel, and fuel production. Photocatalytic materials generally find applications in treating contaminated water with the removal of pathogens and other harmful pollutants. Fig. 1 illustrates the bandgap and the location of the band edge of some of the most commonly used photocatalytic semiconductor materials [46, 47]. Some alternative materials have sufficient bandgap energies to function in the visible light region, but there are some downsides to their performance, such as less stability and toxic effects. There is a possibility of photo-corrosion. Nevertheless, metal oxide semiconductors, SnO_2, WO_3, and Fe_2O_3 compared to the standard hydrogen electrode possess lower conduction band edges, and therefore display higher stability and photo-corrosive properties when used

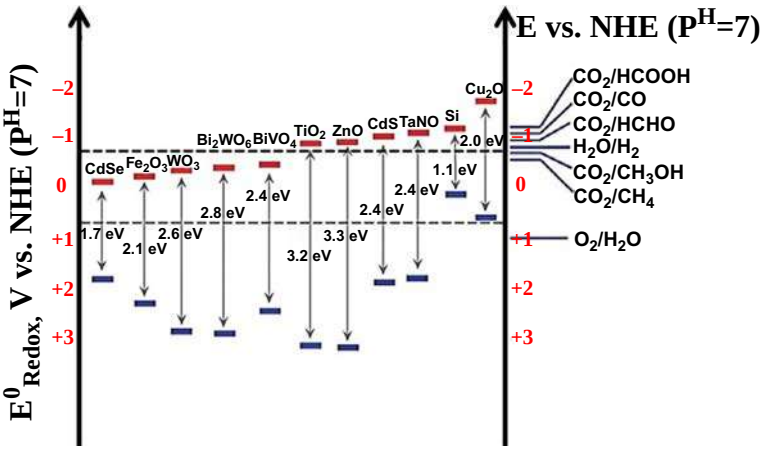

FIG. 1 The position of the strip edge of some metal oxide semiconductors relative to the common hydrogen electrode.

https://www.twirpx.org & http://chemistry-chemists.com

in aqueous solutions. The TiO_2 microstructure is resistant to corrosion and has excellent stability in an aqueous medium.

8.3 Metal-doped metal oxide photocatalysts

By doping, desired properties like absorption efficiency and the electronic properties of the semiconductor photocatalyst can be improved. The doping component in a semiconductor can modify the properties of the host material. Any foreign nucleus or molecule substituted in the host molecule network's sites is called substitution/alternative doping. This particular variance of doping is possible under the following criteria: (i) the host and doping metals have the same crystal structure, electronegativity, and the same solubility; and (ii) the variance in the radii of doping molecules does not exceed 15%. The condition of interstitial doping prevails when the foreign molecules are sandwiched between the normal positions of the network. The generation of voids occurs as the molecules are removed from the lattice between the host molecules. The probability of molecules entering the interstitial site is determined by measuring the radius of the interstitial molecule and the host. Variations in the molecular radius reveal where the doping molecules are in the intermediate space. Cations residing at defined intermediate sites are estimated by the ratio of the values of the cation/anion radius (r^+/r^-). TiO_2, SnO_2, ZnO, etc. are the semiconductor photocatalysts, generally active in UV light due to the wide bandgap energy [48]. By doping with suitable metallic/nonmetallic ions, the absorption range is raised in the semiconductor's visible area, which causes a beneficial change in the electronic structure of the semiconductor and the position of the strip edges. This doped semiconductor displays exceptional performance under irradiation from visible light.

8.4 Plasmonic photocatalysis

Plasmonic photocatalysts help to increase the photodegradation ability under visible light radiation by enhancing the broad range of the absorption from the sun and charge transport properties. This type of material, manufactured by dispersing nanoparticles of noble metal onto semiconductors, results in two distinct properties: (i) localized surface plasmon resonance; and (ii) shotgun barrier. These features assist in the efficient transfer of charge carriers under irradiation with visible light. The most essential characteristic of plasmonic photocatalysis is the localized surface plasmon resonance that represents the presence of significant oscillation on the surface of metallic nanoparticles and semiconductor photocatalysts. Fig. 2 shows the activities that occur with the help of the photocatalytic activity of plasmonic metal nanoparticles [50]. The metal-semiconductor junction in plasmon photocatalysts assists the efficient separation of electron-holes and has the ability to transfer charge carriers quickly as the diffusion lengths are short and it affect on the charge transfer at the interface. Heterojunction plasmonic metal nanoparticles such as Ag, Au, and Pt have resonant oscillations at particular wavelengths, which can alter the absorption range of active photocatalysts of UV light (TiO_2), accounting for the morphology, shape, and size of the noble metal nanoparticles [51]. The effect of

https://www.twirpx.org & http://chemistry-chemists.com

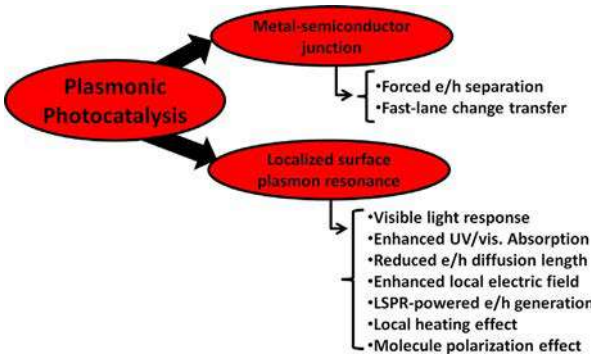

FIG. 2 Flowchart of plasmonic photocatalysis and its major effects [49].

plasmon resonance on the surface of metal nanoparticles can significantly improve the efficiency of light absorption in low bandgap semiconductor photocatalysts such as Fe_2O_3. The properties of electron transfer in a semiconductor can be enhanced by the high absorption capacity for the entire light incident on a very small layer of metallic nanoparticles. The length of the electron/photogenerated hole and the surface of the noble metal nanoparticles is small; the diffusion length is also short. Therefore, the photons are excited to facilitate the transport of charge carriers. Gold nanomaterials are partially enclosed on the surface of a TiO_2 photocatalyst. In general, TiO_2 nanoparticles have n-type properties of the local oxygen defects and excess electron present in material properties. The photocatalytic efficiency of Au-TiO_2 nanostructures facilitates the reduction and oxidation reaction of photodegradation of dangerous pollutants in aqueous media. In the process where charge transfer on the interface occurs, the recombination of electrons and pores is significantly repressed when compared to conventional TiO_2 photocatalysts. Recombination of electrons and paired holes is a crucial parameter affecting the performance of a semiconductor. The primary features of Au in plasmonic photocatalysts are the ability to absorb light in the visible light region and to hinder the rate of recombination of electron-hole pairs. Therefore, the material has a better photocatalytic performance than traditional TiO_2 photocatalysts [49].

8.5 Carbon family photocatalysts

In recent years, carbon nanomaterials have been the focus of many studies due to their uncommon physicochemical, structural, optical, and electronic properties. Carbon-based nanomaterials such as fullerenes, graphene, and carbon nanotubes are now employed as Co catalysts to produce rapid catalysis with traditional materials capable of photocatalysis such as TiO_2, ZnO, and SnO_2, for their quick photodegradation and the properties. Additionally, nanostructures based on carbon can generate a robust reduction capability with the capacity to break down complex and harmful contaminants in water resources.

https://www.twirpx.org & http://chemistry-chemists.com

Nanomaterials in various forms are used for applications like disinfecting water, oil adsorbent, and the elimination of contaminants from water. In this category, carbon nanostructures display exceptional physicochemical properties, which facilitate the removal of organic, inorganic, and additional heavy metals from water sources. Kamath et al. reported that TiO_2 nanocomposites decorated with graphene show outstanding photocatalysis with irradiation from a UV source [52]. The progress of this nanocomposite has been demonstrated in depth with a variety of materials for improved functionality. In different carbon nanostructures, graphene and its derivatives exhibit brilliant catalytic performance against a variety of pollutants due to their excellent physicochemical properties, high ability to accept electrons, modulation of work performance, and their electronic properties. This combination of properties makes graphene-based nanocomposites a suitable candidate for photocatalytic applications by altering appropriate properties to impact the semiconductor's activity under irradiation. Different approaches with a plethora of photocatalysts are designed to assimilate the various morphologies and graphene, either by electrostatic interaction or by chemical bonding for photocatalytic applications [53]. Carbon nanotubes (CNTs) are now more prominently seen as effective catalyst materials with superior characteristics in comparison to the catalytic activity in conventional systems such as graphite, activated carbon, and soot [54]. It has recently been found that CNTs can efficiently absorb certain active materials because CNTs have a greater number of active sites and a much larger area of contact. The incorporation of TiO_2 into the CNT matrix has proven to be a reliable means for photocatalysis with increased activity in contrast to virgin TiO_2 and virgin CNTs. These nanocomposites can significantly decrease the rate at which the recombination occurs by entrapping electrons in the valence band and absorption of broad light. The absorption of visible light from the nanocomposite is achieved with the reduction in the energy interval of the composite nanostructures. On this basis, metallic structures, graphitic carbon nitride, and other organic dyes are commonly employed as photocatalysts by combining graphene or CNT nanostructures [55–57].

8.6 *Z*-scheme in photocatalysis

In the development of a correctly assembled metal oxide semiconductor catalyst, the scope of nanomaterials is promoted as a solution to environmental problems because the capacity to capture light from the visible range of electromagnetic spectrum causes many photodegradation reactions. In particular, the advancement in the Z-scheme in photocatalysis supports many benefits, like a significant improvement in the ability to absorb sunlight, rapid separation of charges, creation and reduction of active species for oxidation, and a good mastery of redox, which enables good photocatalysis. The use or absorption of sunlight is much more efficient when compared to the conventional photocatalyst process. The energy involved in activating Z-scheme is also low. Tada et al. developed a strategy for photocatalytic performance affected by CdS-Au-TiO_2 nanocomposites and charge transfer processes. In particular, CdS-Au-TiO_2 nanocomposites are designed in such way that nanoparticles fill the space between CdS and TiO_2

https://www.twirpx.org & http://chemistry-chemists.com

nanoparticles, which affect the strong transfer of photoinduced electrons by TiO_2 and the transfer of photoinduced pores by CdS nanoparticles [58]. Then, as a consequence, photoinduced electrons possessing powerful reduction capability on CdS and the holes have the ability to oxidize the TiO_2 nanoparticles. This mechanism for the transfer of electrons is known as a shuttle redox mediator system. The mentioned mechanism is unique to Z-scheme photocatalysts. Additionally, the Z-shaped path of the charge transfer processes gives rise to the term "Z-scheme photocatalysts" [59].

8.7 Leaf-driven photocatalysis for nanoparticles

Plant-mediated nanoparticle synthesis has opened up a new genre in the realm of nanotechnology and gained considerable attention due to its economic and eco-friendly nature. A typical process of ZnO nanoparticles is provided in Fig. 3. Aritonang et al. [60] synthesized Ag nanoparticles with the help of aqueous extracts of *Lantana camara* and *Impatiens balsamina* plant leaves as bioreducing agents. Raj et al. [61] reported the biosynthesis of Ag nanoparticles with the assistance of *Terminalia arjuna* leaf extract and noted its efficacy as a catalyst in the degradation of organic dyes such as methylene blue, methyl orange, 4- nitrophenol, and Congo red. Moreover, a simple and rapid route was reported by Ahmed et al. [62] for the synthesis of Ag nanoparticles by using aqueous leaf extracts of *Azadirachta indica*. Devatha et al. [63] reported the green synthesis of Fe nanoparticles by using leaf extracts of *Azadirachta indica*, *Mangifera indica*, *Magnolia*

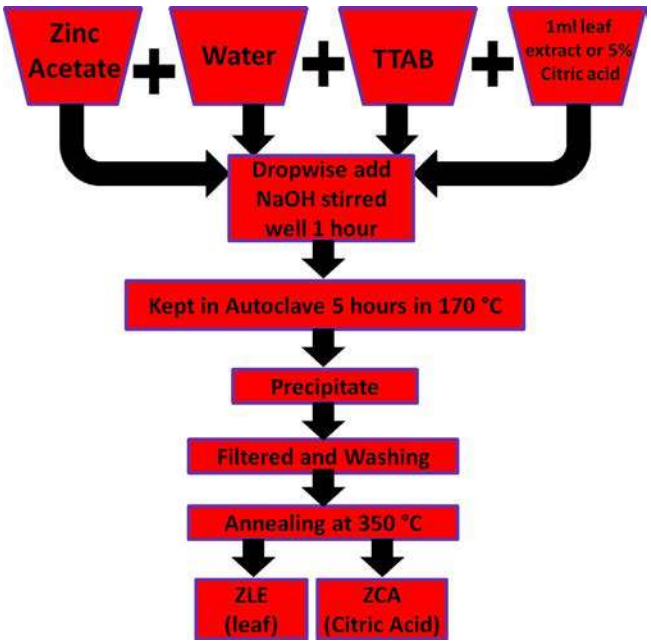

FIG. 3 Flow diagrams of ZnO nanoparticles synthesis.

https://www.twirpx.org & http://chemistry-chemists.com

champaca, and *Murraya koenigii*, and observed its efficacy for treating domestic waste water. In addition, Elemike et al. [64] reported the biosynthesis of Ag nanoparticles by employing leaf extract of *Lasienthra africanum*.

9 Summary

All green technologies are considered as medicine for the environment. These technologies have played a significant part in determining the direction of future environmental sustainability. In this chapter, most of the forms of renewable energy and nonrenewable energy were discussed. Various benefit of the green technology has been discussed in relation to air, water, soil. Solar power, wind turbines, geothermal power, and smart power bars were discussed along with the various conversions of photocatalytic energy. The mechanism of various green photocatalysis and its underlying principles was also briefly discussed. Nanotechnology also enables significant development of photosynthesis systems used in artificially storing solar energy. In order to decrease the quantity of organic contaminants in a location, solar energy is useful due to the exclusive properties of nanomaterials. The growth of eco-friendly, available, and safe techniques of manufacturing these nanomaterials is essential in tackling the modern concerns relating to the environment. Earth essentially requires protection and more eco-friendly technology to provide exactly what the planet needs in order to ensure the survival of the coming generations, and this depends on the actions of the current inhabitants of the planet.

References

[1] Gałuszka A, Migaszewski Z, Namieśnik J. The 12 principles of green analytical chemistry and the significance mnemonic of green analytical practices. TrAC Trends Anal Chem 2013;50:78–84. https://doi.org/10.1016/j.trac.2013.04.010.

[2] Mercer SM, Andraos J, Jessop PG. Choosing the greenest synthesis: a multivariate metric green chemistry exercise. J Chem Educ 2012;89(2):215–20. https://doi.org/10.1021/ed200249v.

[3] Çelik D, Yıldız M. Investigation of hydrogen production methods in accordance with green chemistry principles. Int J Hydrogen Energy 2017;42(36):23395–401.

[4] Anastas PT, Kirchhoff MM. Origins, current status, and future challenges of green chemistry. Acc Chem Res 2002;35(9):686–94. https://doi.org/10.1021/ar010065m.

[5] Balint T, Lamperti F, Mandel A, Napoletano M, Roventini A, Sapio A. Complexity and the economics of climate change: a survey and a look forward. Ecol Econ 2017;138:252–65. https://doi.org/10.1016/j.ecolecon.2017.03.032.

[6] Liu J, Yang Q, Yang W, Li M, Song Y. Aquatic plant inspired hierarchical artificial leaves for highly efficient photocatalysis. J Mater Chem A 2013;1:7760–6. https://doi.org/10.1039/c3ta11355h.

[7] Mydeen SS, Kumar RR, Kottaisamy M, Vasantha VS. Biosynthesis of ZnO nanoparticles through extract from Prosopis juliflora plant leaf: antibacterial activities and a new approach by rust-induced photocatalysis. J Saudi Chem Soc 2020;24:393–406. https://doi.org/10.1016/j.jscs.2020.03.003.

[8] H. J. Lee, G. Lee, N. R. Jang, J. H. Yun, J. Y. Song, B. S. Kim, Biological synthesis of copper nanoparticles using plant extract, NSTI-Nanotech 2011, 1, 2011, 371–374. ISBN 978-1-4398-7142-3.

https://www.twirpx.org & http://chemistry-chemists.com

[9] Krithiga N, Rajalakshmi A, Jayachitra A. Green synthesis of silver nanoparticles using leaf extracts of *Clitoria ternatea* and *Solanum nigrum* and study of its antibacterial effect against common nosocomial pathogens. J Nanosci 2015;928204. https://doi.org/10.1155/2015/928204.

[10] Das D, Sarangi AK, Mohapatra RK, Parhi PK, Mahal A, Sahu R, Kudrat-E-Zahan M. Aqueous extract of Shikakai: a green solvent for deoximation reaction: mechanistic approach from experimental to theoretical. J Mol Liq 2020;309:113133. https://doi.org/10.1016/j.molliq.2020.113133.

[11] Das D, Mohapatra RK, Parhi PK, Sarangi AK, Sahu R, Barik SR. Sustainable and efficient route for the regeneration of carbonyl compounds from oximes using aqueous extract of Sapindus laurifolia under microwave radiation. ACS Omega 2020;5:7716–21. https://doi.org/10.1021/acsomega.0c00774.

[12] Goradel NH, Mirzaei H, Sahebkar A, Poursadeghiyan M, Masoudifar A, Malekshahi ZV, Negahdari B. Biosensors for the detection of environmental and urban pollutions. J Cell Biochem 2017. https://doi.org/10.1002/jcb.26030.

[13] Luo X, Yang J. A survey on pollution monitoring using sensor networks in environment protection. J Sensors 2019. https://doi.org/10.1155/2019/6271206. Article ID 6271206.

[14] Vaseashta A, Vaclavikova M, Vaseashta S, Gallios G, Roy P, Pummakarnchana O. Nanostructures in environmental pollution detection, monitoring, and remediation. Sci Technol Adv Mater 2007;8:47–59. https://doi.org/10.1016/j.stam.2006.11.003.

[15] Wei X, Lyu S, Yu Y, Wang Z, Liu H, Pan D, Chen J. Phylloremediation of air pollutants: exploiting the potential of plant leaves and leaf-associated microbes. Front Plant Sci 2017;8:1318. https://doi.org/10.3389/fpls.2017.01318.

[16] Costanza R. Building a sustainable and desirable economy-in-society-in-nature. In: Worldwatch Institute (eds) State of the World. Washington, DC: Island Press; 2013. https://doi.org/10.5822/978-1-61091-458-1_11.

[17] Goldemberg J. The promise of clean energy. Energy Policy 2006;34(15):2185–90. https://doi.org/10.1016/j.enpol.2005.03.009.

[18] Banerjee S, Akuli RK. Advantages of green technology. Res Sci Technol 2014;6(1):97–100.

[19] Ge B, Yang Y, Jiang D, Gao Y, Du X, Zhou T. An empirical study on green innovation strategy and sustainable competitive advantages: path and boundary. Sustainability 2018;10:3631. https://doi.org/10.3390/su10103631.

[20] Singh N, Park YH, Tolmie CR, Bartikowski B. Green firm specific advantages for enhancing environmental and economic performance. Global Business Organ Excell 2014;34(1):6–17.

[21] Olson EL. Green innovation value chain analysis of PV solar power. J Clean Prod 2014;64:73–80. https://doi.org/10.1016/j.jclepro.2013.07.050.

[22] Devabhaktuni V, Alam M, Depuru SSSR, Green II RC, Nims D, Near C. Solar energy: Trends and enabling technologies. Renew Sustain Energy Rev 2013;19:555–64. https://doi.org/10.1016/j.rser.2012.11.024.

[23] Pao LY, Johnson KE. A tutorial on the dynamics and control of wind turbines and wind farms. In: 2009 American Control Conference, St. Louis, MO; 2009. p. 2076–89. https://doi.org/10.1109/ACC.2009.5160195.

[24] Bertani R. Geothermal power generation in the world 2010–2014 update report. Geothermics 2016;60:31–43. https://doi.org/10.1016/j.geothermics.2015.11.003.

[25] Tatomirescu A, Pedersen GF. Body-loss for popular thin smart phones. In: 7th European Conference on Antennas and Propagation (EuCAP), Gothenburg; 2013. p. 3754–7.

[26] Cottrell T. Three phantom budget cuts and how to avoid them. The Bottom Line 2012;25(1):16–20. https://doi.org/10.1108/08880451211229171.

[27] Tu W, Zhou Y, Zou Z. Photocatalytic conversion of CO2 into renewable hydrocarbon fuels: state-of-the-art accomplishment, challenges, and prospects. Adv Mater 2014;26(27):4607–26. https://doi.org/10.1002/adma.201400087.

https://www.twirpx.org & http://chemistry-chemists.com

[28] Lin YH, Weng C-H, Tzeng J-H, Lin Y-T. Adsorption and photocatalytic kinetics of visible-light response n-doped TiO2 nanocatalyst for indoor acetaldehyde removal under dark and light conditions. Photocatal Environ Energy Sustain 2016;2016:9. https://doi.org/10.1155/2016/3058429. Article ID 3058429.

[29] Rebleanu D, Gaidau C, Voicu G, Constantinescu CA, Sánchez CM, Rojas TC, Carvalho S, Calin M. The impact of photocatalytic Ag/TiO2 and Ag/N-TiO2 nanoparticles on human keratinocytes and epithelial lung cells. Toxicology 2019;416:30–43. https://doi.org/10.1016/j.tox.2019.01.013.

[30] Yao CA. Serum vitamin D level and disease severity of alopecia areata: a meta-regression analysis. J Am Acad Dermatol 2018;79(3):e49–50. https://doi.org/10.1016/j.jaad.2018.05.009.

[31] Long M, Cai W, Cai J, Zhou B, Chai X, Wu Y. Efficient photocatalytic degradation of phenol over Co3O4/BiVO4 composite under visible light irradiation. J Phys Chem B 2006;110(41):20211–6. https://doi.org/10.1021/jp063441z.

[32] Ismail WINW, Ain SK, Zaharudin R, Jawad AH, Ishak MAM, Ismail K, Sahid S. New TiO_2/DSAT immobilization system for photodegradation of anionic and cationic dyes. Photocatal Environ Energy Sustain 2015;6. https://doi.org/10.1155/2015/232741. Article ID 232741.

[33] Wei Q, Wang S, Li W, Yuan X, Bai Y. Hydrophobic ZnO-TiO_2 nanocomposite with photocatalytic promoting self-cleaning surface. Photocatal Environ Energy Sustain 2015. https://doi.org/10.1155/2015/925638. Article ID 925638, 6 pages.

[34] Fan M, Hu B, Yan X, Song C, Chen T, Feng Y, Shi W. Excellent visible-light-driven photocatalytic performance of Cu2O sensitized $NaNbO_3$ heterostructures. New J Chem 2015;39:6171–7. https://doi.org/10.1039/C5NJ00751H.

[35] Asmatulu R, Nuraje N, Mul G. Green photo-active nanomaterials: sustainable energy and environmental remediation. Royal Society of Chemistry; 2015. ISBN: 1782622640, 9781782622642.

[36] Xu L, Hu Y-L, Pelligra C, Chen C-H, Jin L, Huang H, Sithambaram S, Aindow M, Joesten R, Suibb SL. ZnO with different morphologies synthesized by solvothermal methods for enhanced photocatalytic activity. Chem Mater 2009;21(13):2875–85. https://doi.org/10.1021/cm900608d.

[37] Khan I, Mansha SAM, Qurashi A. Sonochemical assisted hydrothermal synthesis of pseudo-flower shaped Bismuth vanadate (BiVO4) and their solar-driven water splitting application. Ultrason Sonochem 2017;36:86–392. https://doi.org/10.1016/j.ultsonch.2016.12.014.

[38] Fu X, Clark LA, Yang Q, Anderson MA. Enhanced photocatalytic performance of titania-based binary metal oxides: TiO2/SiO2 and TiO2/ZrO2. Environ Sci Technol 1996;30(2):647–53. https://doi.org/10.1021/es950391v.

[39] H. Kato, H. Kobayashi, A. Kudo, Role of Ag^+ in the band structures and photocatalytic properties of AgMO3 (M: Ta and Nb) with the Perovskite structure, J Phys Chem B, 2002, 106, 48, 12441–12447, doi: https://doi.org/10.1021/jp025974n.

[40] A. M. Rabaa, J. Bautista-Ruíza, M. R. Joya, Synthesis and structural properties of niobium pentoxide powders: a comparative study of the growth process, Mater Res, DOI:https://doi.org/10.1590/1980-5373-MR-2015-0733.

[41] Kiatkittipong K. Synthesis of Titania/Titanate nanostructures for photocatalytic applications. A thesis submitted to The University of New South Wales in partial fulfilment of the degree of Doctor of Philosophy, School of Chemical Engineering, The University of New South Wales; July 2012.

[42] F. Amano, Yasumoto, Taikei; Shibayama, Tamaki; Uchida, Satoshi; Ohtani, Bunsho, Nanowire-structured titanate with anatase titania: Characterization and photocatalytic activity, Appl Catal Environ, 89(3–4), 583-589, doi:https://doi.org/10.1016/j.apcatb.2009.01.013.

[43] Gindelberger DE, Arnold J. Preparation and properties of magnesium, calcium, strontium, and barium selenolates and tellurolates. Inorg Chem 1994;33(26):6293–9. https://doi.org/10.1021/ic00104a045.

[44] Asmatulu R, Nuraje N, Mul G. Chapter 1: Introduction to green nanostructured photocatalysts, RSC Green Chemistry No. 42, Green photo-active nanomaterials: sustainable energy and environmental

https://www.twirpx.org & http://chemistry-chemists.com

remediation. In: Nuraje N, Asmatulu R, Mulr G, editors. The Royal Society of Chemistry. Published by the Royal Society of Chemistry; 2016.

[45] Yang L, Luo S, Li Y, Xiao Y, Kang Q, Cai Q. High efficient photocatalytic degradation of p-nitrophenol on a unique Cu2O/TiO2 p-n heterojunction network catalyst. Environ Sci Technol 2010;44 (19):7641–6. https://doi.org/10.1021/es101711k.

[46] Rawal SB, Bera S, Lee D, Jang D-J, Lee WI. Design of visible-light photocatalysts by coupling of narrow bandgap semiconductors and TiO_2: effect of their relative energy band positions on the photocatalytic efficiency. Cat Sci Technol 2013;3:1822–30. https://doi.org/10.1039/C3CY00004D.

[47] Bowker M. Sustainable hydrogen production by the application of ambient temperature photocatalysis. Green Chem 2011;13:2235–46. https://doi.org/10.1039/C1GC00022E.

[48] Thiruvenkatachari R, Vigneswaran S, Moon IS. A review on UV/TiO2 photocatalytic oxidation process (Journal Review). J Chem Eng 2008;25:64. https://doi.org/10.1007/s11814-008-0011-8.

[49] Wen L, Xu R, Cui C, Tang W, Mi Y, Lu X, Zeng Z, Suib SL, Gao P-X, Lei Y. Template-guided programmable Janus heteronanostructure arrays for efficient plasmonic photocatalysis. Nano Lett 2018;18 (8):4914–21. https://doi.org/10.1021/acs.nanolett.8b01675.

[50] Liu L, Ouyang S, Ye J. Gold nanorod photosensitized titanium dioxide with wide range visible light harvesting based on localized surface plasmon resonance. Angew Chem Int Ed Engl 2013;52 (26):6689–93. https://doi.org/10.1002/anie.201300239.

[51] Nakata K, Ochiaia T, Murakami T, Fujishima A. Photoenergy conversion with TiO2 photocatalysis: new materials and recent applications. Electrochim Acta 2012;84:103–11. https://doi.org/10.1016/j.electacta.2012.03.035.

[52] Luo Y, Li M, Hu G, Tang T, Wen J, Li X, Wang L. Enhanced photocatalytic activity of sulfur-doped graphene quantum dots decorated with TiO_2 nanocomposites. Mater Res Bull 2018;97:428–35. https://doi.org/10.1016/j.materresbull.2017.09.038.

[53] Li X, Yu J, Wageh S, Al-Ghamdi AA, Xie J. Graphene in photocatalysis: a review. Small 2016;12 (48):6640–96. https://doi.org/10.1002/smll.201600382.

[54] Wang D-Y, Gong M, Chou H-L, Pan C-J, Chen H-A, Wu Y, Lin M-C, Guan M, Yang J, Chen C-W, Wang Y-L, Hwang B-J, Chen C-C, Dai H. Highly active and stable hybrid catalyst of cobalt-doped FeS2 nanosheets-carbon nanotubes for hydrogen evolution reaction. J Am Chem Soc 2015;137 (4):1587–92. https://doi.org/10.1021/ja511572q.

[55] Pawar RC, Khare V, Lee CS. Hybrid photocatalysts using graphitic carbon nitride/cadmium sulfide/reduced graphene oxide (g-C3N4/CdS/RGO) for superior photodegradation of organic pollutants under UV and visible light. Dalton Trans 2014;43:12514–27. https://doi.org/10.1039/C4DT01278J.

[56] Verbruggen SW, Keulemans M, Filippousi M, Flahaut D, Tendeloo GV, Johan SL, Martens A, Lenaerts S. Plasmonic gold–silver alloy on TiO2 photocatalysts with tunable visible light activity. Appl Catal Environ 2014;156–157:116–21. https://doi.org/10.1016/j.apcatb.2014.03.027.

[57] Liu Q, Zhang J. Graphene supported Co-g-C3N4 as a novel metal-macrocyclic electrocatalyst for the oxygen reduction reaction in fuel cells. Langmuir 2013;29(11):3821–8. https://doi.org/10.1021/la400003h.

[58] Li J, Cushing SK, Bright J, Meng F, Senty TR, Zheng P, Bristow AD, Wu N. Ag@Cu_2O core-shell nanoparticles as visible-light plasmonic photocatalysts. ACS Catal 2013;3(1):47–51. https://doi.org/10.1021/cs300672f.

[59] Xu Q, Zhang L, Yu J, Wageh S, Al-Ghamdi AA, Jaroniec M. Direct Z-scheme photocatalysts: principles, synthesis, and applications. Mater Today 2018;21(10):1042–63. https://doi.org/10.1016/j.mattod.2018.04.008.

[60] Aritonang HF, Koleangan H, Wuntu AD. Synthesis of silver nanoparticles using aqueous extract of medicinal plants' (impatiens balsamina and *Lantana camara*) fresh leaves and analysis of antimicrobial activity. Int J Microbiol 2019. https://doi.org/10.1155/2019/8642303. Article ID 8642303.

https://www.twirpx.org & http://chemistry-chemists.com

[61] Raj S, Singh H, Trivedi R, Soni V. Biogenic synthesis of AgNPs employing Terminalia arjuna leaf extract and its efficacy towards catalytic degradation of organic dyes. Sci Rep 2020;10:9616. https://doi.org/10.1038/s41598-020-66851-8.

[62] Ahmed S, Saifullah, Ahmad M, Swami BL, Ikram S. Green synthesis of silver nanoparticles using *Azadirachta indica* aqueous leaf extract. J Radiat Res Appl Sci 2016;9:1–7. https://doi.org/10.1016/j.jrras.2015.06.006.

[63] Devatha CP, Thalla AK, Katte SY. Green synthesis of iron nanoparticles using different leaf extracts for treatment of domestic waste water. J Clean Prod 2016. https://doi.org/10.1016/j.jclepro.2016.09.019.

[64] Elemike EE, Onwudiwe DC, Arijeh O, Nwankwo HU. Plant-mediated biosynthesis of silver nanoparticles by leaf extracts of Lasienthra africanum and a study of the influence of kinetic parameters. Bull Mater Sci 2017;40(1):129–37. https://doi.org/10.1007/s12034-017-1362-8.

https://www.twirpx.org & http://chemistry-chemists.com

https://www.twirpx.org & http://chemistry-chemists.com

16

Degradation of emergent pollutants using visible light-triggered photocatalysts

Susanta Kumar Bhunia, Varsha UshaVipinachandran*, and Sathish Rajendran*

DEPARTMENT OF CHEMISTRY, SCHOOL OF ADVANCED SCIENCES, VELLORE INSTITUTE OF TECHNOLOGY, VELLORE, INDIA

1 Introduction

Environmental contamination caused by emerging pollutants has received significant research attention due to increased population growth and industrialization [1]. Exposure and accumulation of the pollutants in ecosystems, humans, and animals provoke potential risks such as increased drug resistance, causing allergic or toxic reactions among some hypersensitive individuals, and bone growth inhibition upon exposure to lower concentrations [2]. Although some biological and chemical treatment methods including coagulation, absorption, ultrafiltration, etc. are applied to decontaminate the pollutants, their frequent usage is limited due to the high costs of starting materials, insufficient separation, time consumption, and lack of recyclability. One simple technique named "photocatalysis" can separate and degrade pollutants effectively into nonhazardous compounds [1]. This process is considered green, cost-effective, and environmentally friendly, with no secondary pollution produced. It acts as a hanging bridge between physics, chemistry, materials science, and chemical engineering altogether [3]. From a chemistry point of view, it accelerates the chemical reaction through effective photon/light utilization in the presence of a catalyst. When light is absorbed by an adsorbed substrate, the catalyst accelerates electron-hole pair generation from the substrate. Next, the electron-hole pairs generate reactive oxygen species such as hydroxyl radicals ($^{\cdot}OH$) and superoxide ions ($O_2^{\cdot-}$), which further undergo secondary reactions with pollutants to convert them into nontoxic compounds, as shown in Fig. 1.

Photocatalysis can be classified in two categories: homogeneous and heterogeneous. The second type is more preferable and acceptable because of easy products separation and the high stability and recyclability of the photocatalyst [3]. Visible light-induced

*These authors contributed equally in this work.

Nanostructured Materials for Visible Light Photocatalysis. https://doi.org/10.1016/B978-0-12-823018-3.00004-X
Copyright © 2022 Elsevier Inc. All rights reserved.

https://www.twirpx.org & http://chemistry-chemists.com

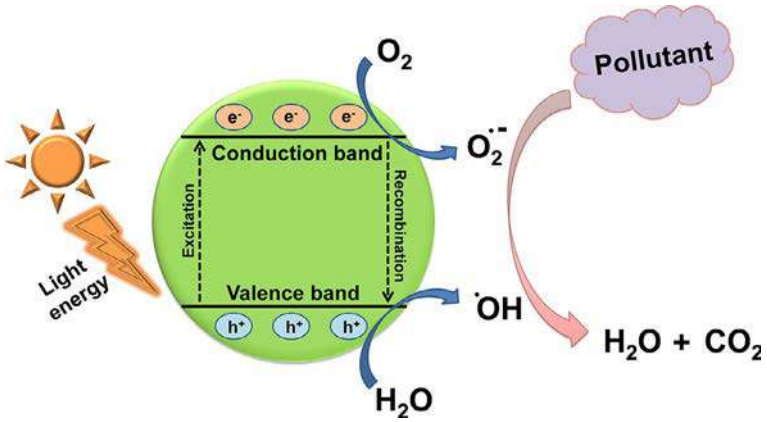

FIG. 1 Schematic of materials excitation by light illumination leading to electron-hole pair generation in the conduction band and valence band, respectively, followed by free radicals production which degrades pollutants.

photocatalysis is a much more promising approach than ultraviolet (UV) light because it is a clean, safe, abundant, and economical resource in nature [1, 4]. Although much progress has been achieved through the utilization of solar energy as visible light, the solar energy input in the UV region has been considered by most of the scientific community for materials bandgap excitation [5, 6], whereas solar light consists of UV, visible, and infrared components at 5%, 43%, and 52%, respectively [7]. So, the challenging issue will be to deal with visible light or near-infrared active photocatalytic materials which should possess highly efficient, stable, and easy synthetic method characteristics. Degradation of colored dyes (one type of pollutant regularly used in the textile industry) is comparatively easier and perfectly visible to the naked eye under visible light irradiation because of the dyes' absorbance in the visible wavelength region and gets excited by light to promote their degradation by forming active radical species from photocatalytic materials. A problem arises in the case of colorless pollutants because they possess UV-region absorbance. Thus, a UV light source is required to degrade them and this type of light (high energy) is not recommendable and applicable from a human health point of view. Therefore, visible light-induced degradation is a challenging task for these types of pollutants.

2 Emerging pollutants

Emerging pollutants are not considered as regular contaminants, but their presence causes adverse effects upon release in the environment. Enormous numbers of such pollutants are released daily in the environment due to unrestrained misuse [8]. This class of compounds includes plasticizers, pesticides (herbicides and insecticides), pharmaceuticals and personal care products (PPCPs), food additives, and veterinary compounds. A few examples of plasticizers and agrochemicals are shown in Figs. 2 and 3, respectively, and

https://www.twirpx.org & http://chemistry-chemists.com

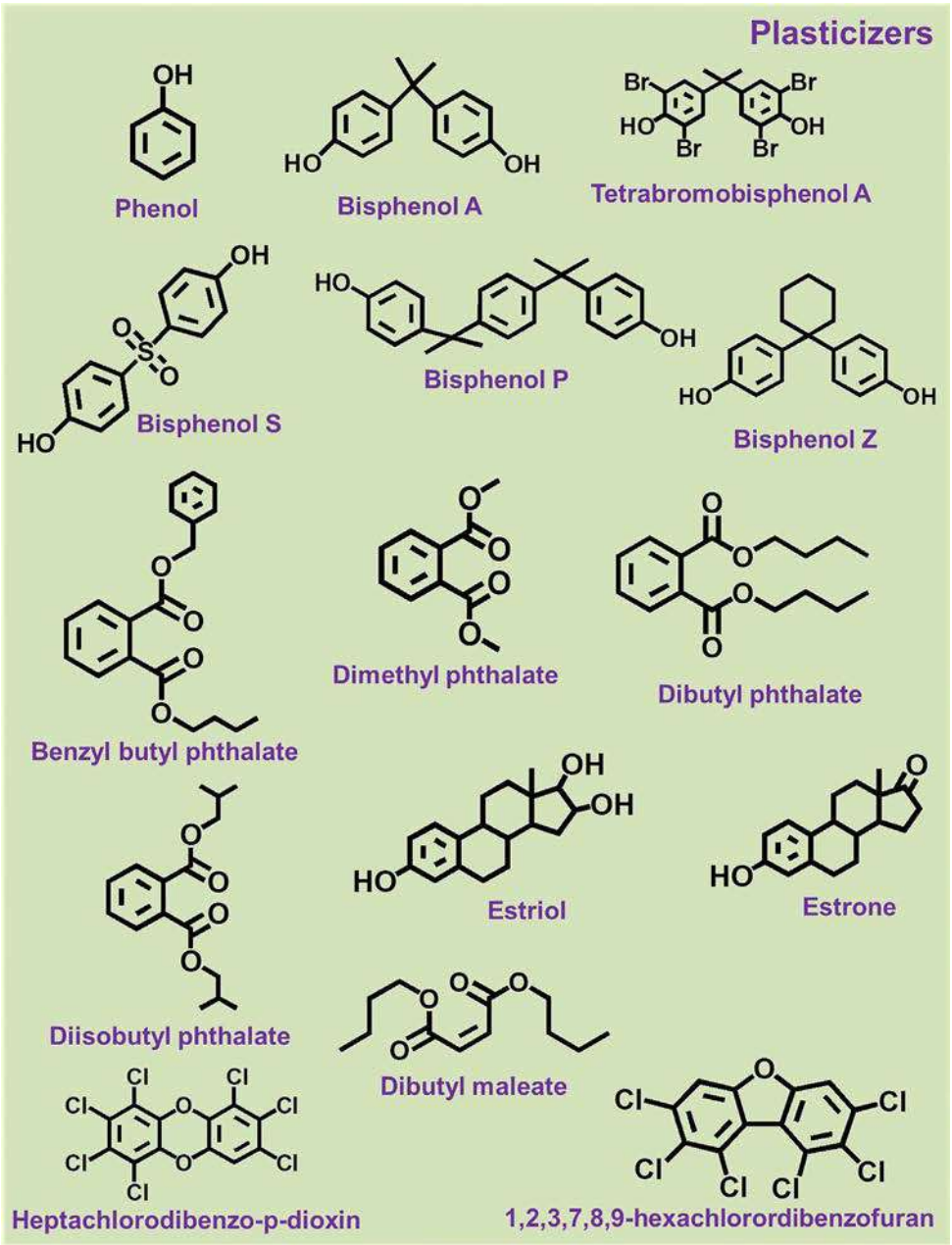

FIG. 2 Representative examples of plasticizers.

https://www.twirpx.org & http://chemistry-chemists.com

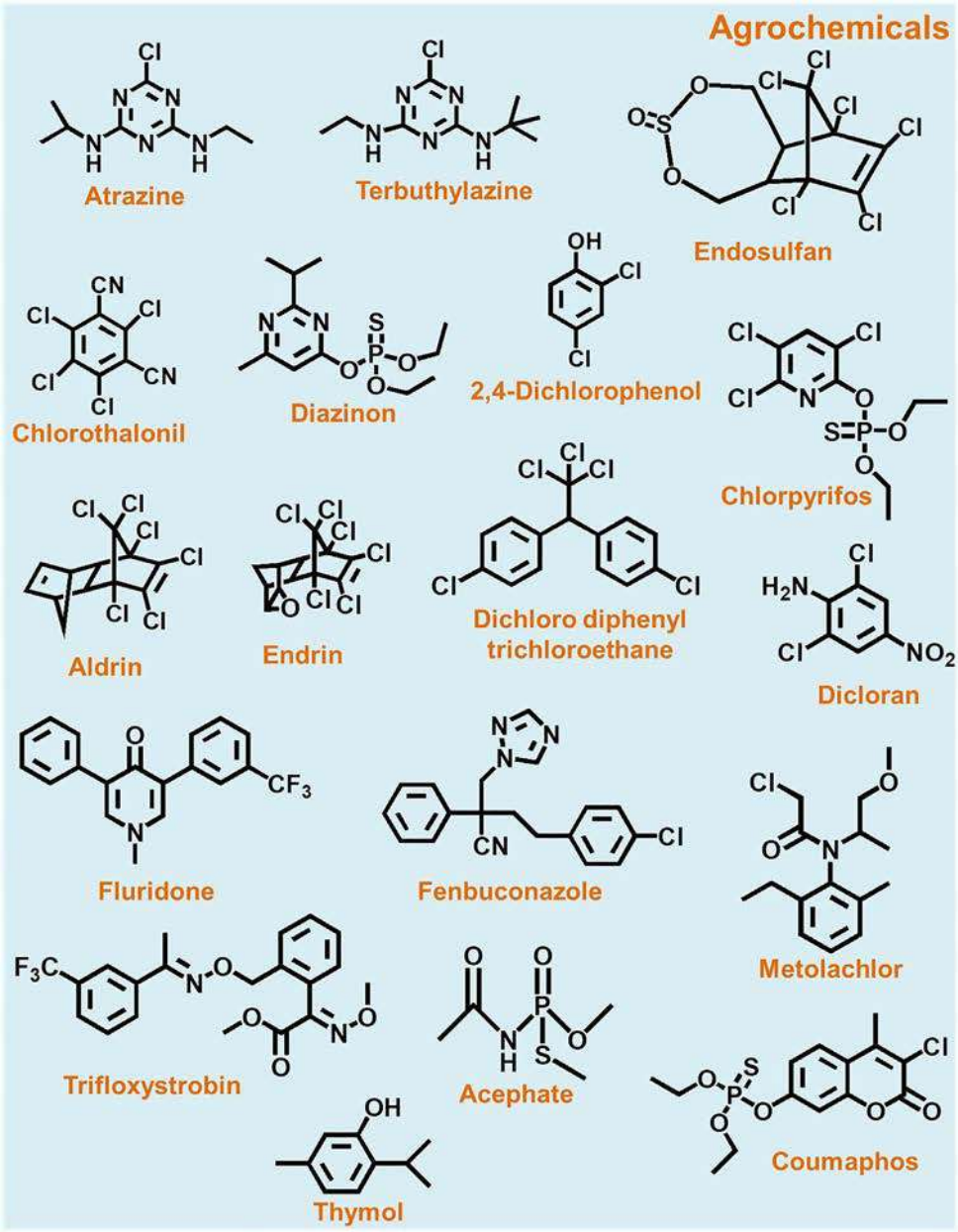

FIG. 3 Representative examples of agrochemicals.

https://www.twirpx.org & http://chemistry-chemists.com

PPCPs and food additives are shown in Fig. 4. Most of the compounds are frequently used in several essential aspects such as household materials fabrication, disease cures, agricultural applications, and industrial applications. For example, around 2.5 million tons of pesticides are used for agricultural purposes, out of which 0.5 million tons are used in the U.S. alone [9, 10]. Wood preservation in the U.S. consumes more than 4.0 million tons of pesticides. Significant amounts of persistent organic compounds and polychlorinated biphenyls are dispersed and stored in the environment from deposition of 20–50 million tons/year of electronic waste in the world [11, 12]. The major threat is that they are released into the aquatic ecosystem such as ponds, lakes, rivers, and oceans as well as underground water and drinking water because of improper disposal, and cause lethal health complications [13, 14].

It has already been reported that such types of compounds can create reproductive problem, cancer, hypospadias, miscarriages, endometriosis, and infertility even at ng/L to μg/L concentrations [15–18]. Therefore, it is essential to design materials to minimize the propagation of these compounds.

3 Visible light-triggered degradation of emerging pollutants

Varied types of visible light-active photocatalytic materials have been reported to degrade pollutants. These materials capture visible light which induces the separation of photoexcited electron-hole pairs from the materials. Next, the photogenerated charges generate active free radicals to achieve the breakdown of the contaminants. Different types of pollutant degradation under visible light illumination will be discussed in the following sections.

3.1 Plasticizers

Phenolic and steroidal estrogenic compounds, dioxins, and furans are commonly used in plastic appliances such as synthesis of plastic products, bottles, food packaging, and containers [8, 19–22]. For example, bisphenol A (BPA) is routinely used in plastic containers (including baby feed milk bottles) to prevent thermal stress and improve hardness [8]. The amount of BPA production is more than 2 billion pounds worldwide in a year [23, 24]. Environmental persistence and exposure of these plastics and plasticizer pollutants in aquatic ecosystem cause potential risk to aquatic organisms and human health, resulting in menstruation affection, reproductive problems, liver and kidney damage, diarrhea, hepatic damage, cardiovascular disease, cancer, etc. [25–28]. They can also bind to DNA and break the strands, consequently damaging DNA by promoting mutagenic effects [19, 29, 30]. Thus, their efficient degradation from wastewater has raised a considerable voice. A lot of research studies have been devoted to this topic and various types of visible light-active materials have been reported for the same [18, 31–37].

https://www.twirpx.org & http://chemistry-chemists.com

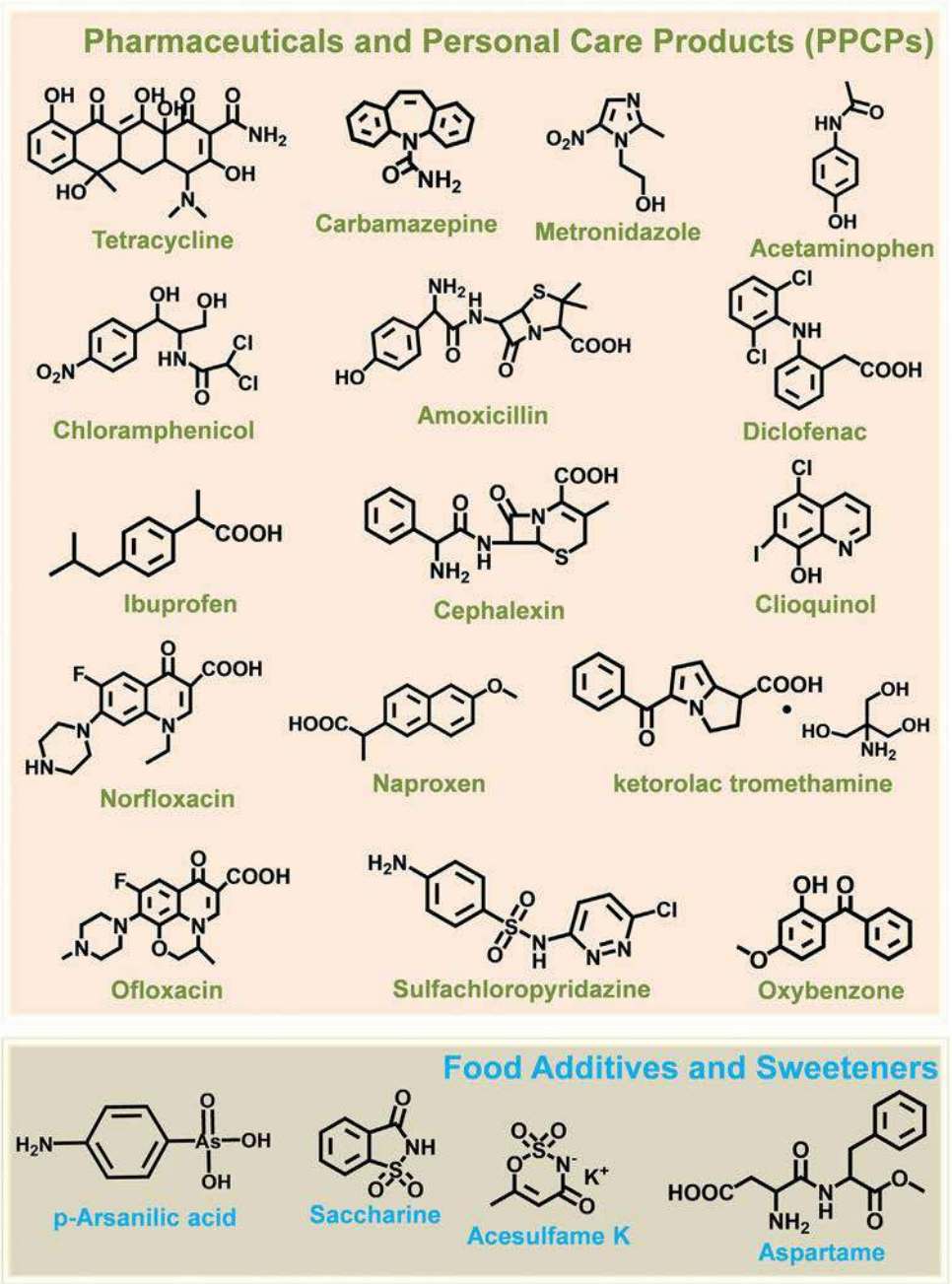

FIG. 4 Representative examples of PPCPs and food additives.

https://www.twirpx.org & http://chemistry-chemists.com

Phenol has been photocatalytically degraded by varied nanostructures. A common photocatalytic material, bare TiO_2 semiconductor, contains a wide bandgap and strong absorption in the UV light region. The wavelength can be extended at the visible region by doping with various metallic and nonmetallic elements, which can reduce the bandgap of TiO_2 and take part in visible light photocatalysis. Chen et al. synthesized a platinum-deposited, iodine-doped titanium dioxide (Pt/I-TiO_2) photocatalyst for the degradation of para-substituted phenols (phenol, *p*-methylphenol, *p*-chlorophenol, and *p*-nitrophenol) under visible light irradiation [31]. Pt/I-TiO_2 showed superior photoactivity over I-TiO_2 because of electron-hole separation enhancement by platinum modification. The degradation occurred in the order of *p*-methylphenol > phenol > *p*-chlorophenol > *p*-nitrophenol, and it depends on the activation ability of phenolic compounds to form a Ti-OH-Ph structure after getting adsorbed on the photocatalyst surface. Electron-donating molecules (*p*-methylphenol) accelerated such a type of structure formation resulting in the highest degradation, whereas p-nitrophenol showed nearly invariant due to electron withdrawing nature of the nitro group. One of the metal-free photocatalysts named graphitic carbon nitride (g-C_3N_4), has been actively used for pollutant degradation over the past few years. Different strategies including structural modification, heteroatom doping (metal or nonmetal), combining with other components, etc. were adopted to optimize its photocatalytic efficiency.

A comparison between bulk g-C_3N_4 and exfoliated g-C_3N_4 nanosheets was demonstrated for photocatalytic phenol degradation by Guo et al. [38]. The exfoliated nanosheet displayed higher photocatalytic efficiency compared to bulk g-C_3N_4. The overall phenol degradation efficiency was described by molecular oxygen activation processes on their surface. Oxygen was reduced to $O_2^{\cdot-}$ by one-electron transfer in the case of bulk g-C_3N_4, whereas surface-stabilized 1,4-endoperoxide was formed from the nanosheet by a two-electron transfer process. Therefore, efficient electron-hole pair separation and reactive oxygen species generation led to high photocatalytic efficiency in the case of the exfoliated g-C_3N_4 nanosheet. Wang et al. demonstrated the formation of carbon nanospheres on g-C_3N_4 (CN-CS) which showed significant phenol photodegradation activities [39]. Carbon nanospheres were synthesized at various temperatures, and results indicated that higher efficiency was obtained from nanospheres synthesized at high temperatures. Significant amounts of carbon spheres were formed at high temperatures especially 180°C on g-C_3N_4 (product abbreviated as CN-CS-180-3 h) led bandgap energy in a lower position and charge carrier separation enhancement resulting in higher photocatalytic activity (Fig. 5A and B). Han et al. synthesized a silver oxide nanoparticle/graphitic carbon nitride (Ag_2O/g-C_3N_4) composite for photocatalytic degradation of phenol [40]. Ag_2O and g-C_3N_4 behave as p-type and n-type semiconductors, respectively. Both Ag_2O and g-C_3N_4 could absorb light energy to generate electrons and holes. The photogenerated electrons transferred from Ag_2O and accumulated on g-C_3N_4 whereas the inner electric field insisted the holes for opposite transfer [32]. This caused an efficient electron-hole separation and enhanced photocatalytic activity. A novel Ag@AgCl/g-C_3N_4 plasmonic photocatalyst was synthesized for phenol degradation. Improved photocatalytic efficiency has been

https://www.twirpx.org & http://chemistry-chemists.com

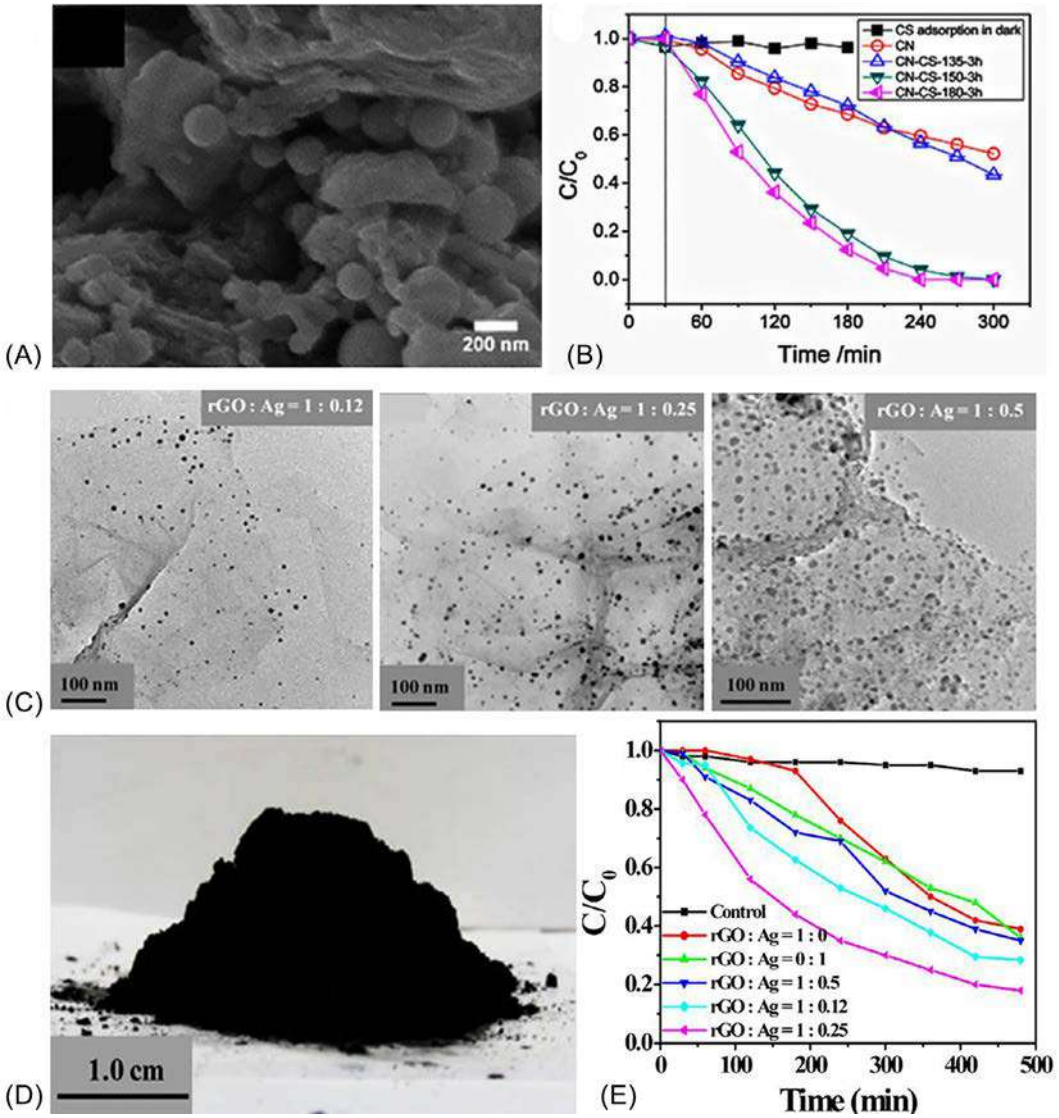

FIG. 5 (A) High-resolution scanning electron microscopy (HRSEM) image of CN-CS-180-3h. (B) Photodegradation of phenol solution by the materials synthesized at different temperatures. (C) Transmission electron microscopy (TEM) images of rGO-Ag composites with varied amount of Ag. (D) Digital image of synthesized large-scale solid materials. (E) Photocatalytic degradation of phenol with rGO-Ag composite by various amounts of Ag. *Panel B: Reprinted with permission from Sun H, Zhou G, Wang Y, Suvorova A, Wang S. A new metal-free carbon hybrid for enhanced photocatalysis. ACS Appl Mater Interfaces 2014;6:16745–54. https://doi.org/10.1021/am503820h. Copyright 2014 American Chemical Society; Panel E: Reprinted with permission from Bhunia SK, Jana NR. Reduced graphene oxide-silver nanoparticle composite as visible light photocatalyst for degradation of colorless endocrine disruptors. ACS Appl Mater Interfaces 2014;6:20085–92. https://doi.org/10.1021/am505677x. Copyright 2014 American Chemical Society.*

https://www.twirpx.org & http://chemistry-chemists.com

explained by the synergetic effect of plasmonic Ag@AgCl's suitable size and strong coupling between nanoparticles and nanosheets as well as fast separation of charge carriers. Wang et al. reported a direct solid-state nano-*Z*-scheme $BiVO_4$/pyridine-doped g-C_3N_4 photocatalytic system (BDCN) for phenol degradation [41]. Both pyridine-doped g-C_3N_4 (DCN) and $BiVO_4$ could absorb visible light and generate electron-hole pairs. The photoexcited electrons transferred to the valence band (VB) of $BiVO_4$ from the conduction band (CB) of DCN and became neutralized. Consequently, most negative electrons in the CB of DCN generate $O_2^{\cdot-}$ and most positive holes in the VB of $BiVO_4$ generate OH radicals. One Z-scheme was proposed where CB electrons of DCN and VB holes of BiVO4 produced $O_2^{\cdot-}$ and OH reactive species, which led to efficient separation of photoexcited electron-hole pairs and boosted the catalytic performance. Moreover, bare $BiVO_4$ of an ordered macroporous structure was employed for phenol degradation under visible light by Au et al. [42]. The photocatalytic activity was enhanced in the presence of hydrogen peroxide (H_2O_2). The presence of the high surface area and surface oxygen vacancy density of $BiVO_4$ could promote efficient capturing of light, whereas H_2O_2 acts as an electron scavenger and could trap photogenerated electrons from $BiVO_4$ to suppress the electron-hole recombination. On the other hand, graphene-based photocatalytic materials have drawn considerable attention owing to their high surface area, high adsorption capacity, and good conductivity of graphene.

Several efforts have been reported for the effective degradation of pollutants. Reduced graphene oxide (rGO) inhibits the photoexcited electron-hole recombination and shuttles the electrons from their excited state of photoactive materials to enhance the photochemical reaction. It also acts as a solid platform to decorate metal/metal oxide nanoparticles for wastewater treatment. A reduced graphene oxide-silver nanoparticle composite (rGO-Ag) was reported as an efficient visible light photocatalyst for phenol and bisphenol A (BPA) degradation by Jana et al. [18]. The pollutants get adsorbed first on the rGO surface through a hydrophobic-hydrophobic interaction. Ag nanoparticles offered visible light-induced excitation of silver plasmons, and conductive rGO as an efficient charge separator and thus induced oxidative degradation of the organic pollutants, as shown in Fig. 5C–E. Controlled loading of plasmonic nanoparticles on RGO led to effective utilization of visible light. The photocatalytic performance was completely dependent on the amount of Ag loading. It showed lower efficiency when the loading was too low or too high. A lower concentration of active species was formed in the case of low loading, whereas most of the RGO surface was covered by Ag in the case of high loading, so that adsorption of pollutants was less on the RGO surface and showed lower efficiency. It reached a maximum value when an optimum amount of Ag was loaded on the RGO surface. A high concentration of energetic electrons was produced at the Ag nanoparticles' surface by visible light excitation and the conductive rGO surface adjacent to Ag nanoparticles surface quickly transported electrons via an extended -conjugation structure. This resulted in efficient electron-hole pairs separation and produced reactive oxygen species responsible for pollutant degradation. Photocatalytic degradation was slow at low Ag loading because of

https://www.twirpx.org & http://chemistry-chemists.com

insufficient reactive oxygen species generation. Degradation was also low with excess Ag loading due to the contact area reduction of pollutants' absorption on the graphene's surface because most of the surface gets blocked by Ag.

Later on, Parida et al. synthesized an Fe_3O_4/RGO nanocomposite for phenol degradation [43]. The development of synergism between RGO and Fe_3O_4 could result in better charge separation followed by excellent photodegradation. The presence of RGO also enabled a degree of separation. A nanocomposite consisting of a reduced graphene oxide nanosheet decorated with Au-Pd bimetallic alloy nanoparticles (Au-Pd/rGO) has been fabricated for phenol and phenolic compounds degradation under direct natural sunlight exposure [44]. Pd synergistically enhanced the efficient degradation ability of Au together with rGO. Interband transition of Au 5d electrons to 6sp band occurs upon UV light absorption whereas the 6sp electrons involve intra-band excitation during visible light absorption. Pd nanoparticles help to increase the UV-visible light absorption capacity. The excited electrons were transferred from 5d to 6sp of Au under sunlight illumination, thereby leaving positively charged holes in the 5d orbital which resulted in the degradation of the phenolic group.

Effective mineralization of BPA and its derivatives has been carried out with various nanostructures. C_{60} fullerene and C_{60} derivatives can be photoexcited under UV and visible light irradiation. However, extremely hydrophobic C_{60} fullerene derivatives need to be transferred in an aqueous phase by functionalization with hydrophilic surface functional groups. Tetrakis C_{60} aminofullerene immobilized onto silica beads (aminoC_{60}/silica) was reported for BPA degradation [45]. This was attributed to kinetically enhanced singlet oxygen ($^1O_2$) generation (responsible for degradation) after immobilization, which could reduce aggregation of the catalyst, and adsorption of BPA on the silica support, which increased exposure to $^1O_2$ near photocatalytic sites. BPA could be degraded by using direct g-C_3N_4 and its nanocomposites. A mesoporous g-C_3N_4 nanosheet was found to active participation rather than the bulk g-C_3N_4 photocatalyst [46]. A greater number of surface reactive sites of nanosheets could improve the charge transfer efficiency and accelerate separation of photogenerated electron-hole pairs, leading to higher efficiency compared to bulk g-C_3N_4. Later on, Zhang et al. reported that carbon-vacancy-modified g-C_3N_4 (V_C-C_3N_4) demonstrated high photocatalytic removal efficiency of BPA compared to pristine g-C_3N_4 [47]. Firstly, carbon vacancies acted as photogenerated electron trappers to prevent electron-hole recombination. Secondly, those vacancies transferred the trapped electrons to the surface absorbed O_2 for abundant $O_2^{\cdot-}$ generation. A photocatalysis-Fenton system consisting of Fe-doped g-C_3N_4 (Fe-g-C_3N_4) was proposed by Cui et al. for phenol and bisphenol A mineralization [48]. Heptazine structures of g-C_3N_4 form σ-π coordinate bonds and caused Fe^{3+} to be firmly fixed to the g-C_3N_4 skeleton. The photogenerated charge could be rapidly transferred to Fe^{3+} from g-C_3N_4, so that Fe^{3+} reduced to Fe^{2+} and this Fe^{2+} generated OH in the presence of H_2O_2. A mesoporous g-C_3N_4/BiOI (MCN/BiOI) heterojunction photocatalyst was employed where the photogenerated carriers were separated by the internal electric field formed at the interface and generated active oxygen radicals such as $O_2^{\cdot-}$ and $HO_2^{\cdot-}$ under visible light excitation with energy

https://www.twirpx.org & http://chemistry-chemists.com

of 2.33–3.10 eV (531 nm $> \lambda >$ 400 nm) from oxygen [36]. These superoxide radicals could cleave the BPA ring.

Silver phosphate (Ag_3PO_4) is also known as an efficient photocatalyst. However, its small surface area, narrow energy gap, and easy photocorrosion without any sacrificial agent restrict it from consistent use. Structural modification of Ag_3PO_4 with other components can overcome the abovementioned problems. Silver phosphate/graphene oxide aerogel microspheres (SGAMs) were applied for BPA degradation by Yu et al. [49]. Silver phosphate as a photocatalyst generates electron-hole pairs by light absorption. Electron separation occurred through graphene oxide's surface and different ROS formed followed by BPA degradation. Honeycomb-shaped SGAMs led to better photocatalytic performance because:

- the channeled honeycomb-like structure shortened the diffusion pathway of pollutants and allowed rapid adsorption equilibrium to be achieved;
- there was photocorrosion reduction of Ag_3PO_4 due to fast electron hopping from Ag_3PO_4 to the GO sheet.

SGAMs showed a diameter of ∼250 μm with an open channel dimension of ∼4 μm and demonstrated high degradation activity as shown in Fig. 6A–D. The BPA mineralization pathway assisted by ROS was also discussed. The photocatalytic activity of Ag_3PO_4 was accelerated by coupling with Ag_2WO_4 which is a wide bandgap semiconductor and has strong redox potential [24]. The degradation of BPA was explained by the separation of electron-hole pairs, where Ag_2WO_4 transfer photoexcited electrons from Ag_3PO_4 under Xe light irradiation and generate ROS. Bismuth oxyhalides, a series of ternary oxide semiconductors, can generate photogenerated charge carriers through an internal static electric field perpendicular to each layer of their layered structures. A novel bismuth oxychloride ($Bi_{12}O_{15}Cl_6$) nanosheet was designed as a superior photocatalyst because of its favorable bandgap structure [37]. BPA and O_2 first get adsorbed onto the photocatalyst surface. $O_2^{\cdot-}$ was generated from CB excited electrons of $Bi_{12}O_{15}Cl_6$ and finally converted into OH as the main reactive species. Facet-dependent nanosheet-assembled bismuth oxyiodide (BiOI) microspheres were applied for BPA degradation by Gao et al. [50]. Visible light exposure to the (110) facet of BiOI led to absorption of greater amounts of O_2, resulting in more $O_2^{\cdot-}$ and OH formation compared to the (001) facet and efficient BPA degradation. On the other hand, bismuth tungstate (Bi_2WO_6) possesses a Bi_2O_2 layered structure with a perovskite-like slab of WO_6 and has photodegradation capability. Mesoporous Bi_2WO_6 could mineralize BPA even without OH formation [51]. The photogenerated hole on the Bi_2WO_6 surface could not produce OH because of the higher redox potential of $OH/^{-}OH$ (1.99 eV) compared to the standard oxidation potential of Bi_2WO_6 (1.59 eV). Thus the degradation of BPA was stated due to the direct oxidation by the photogenerated holes. Tetrabromobisphenol A (TBBPA), a derivative of BPA, was removed by a magnetic CoO@graphene nanocomposite photocatalyst [52]. The p-type CoO acted as a photocatalyst and photocatalytic efficiency was enhanced by the synergistic effect of CoO and graphene combination. Conductive graphene

https://www.twirpx.org & http://chemistry-chemists.com

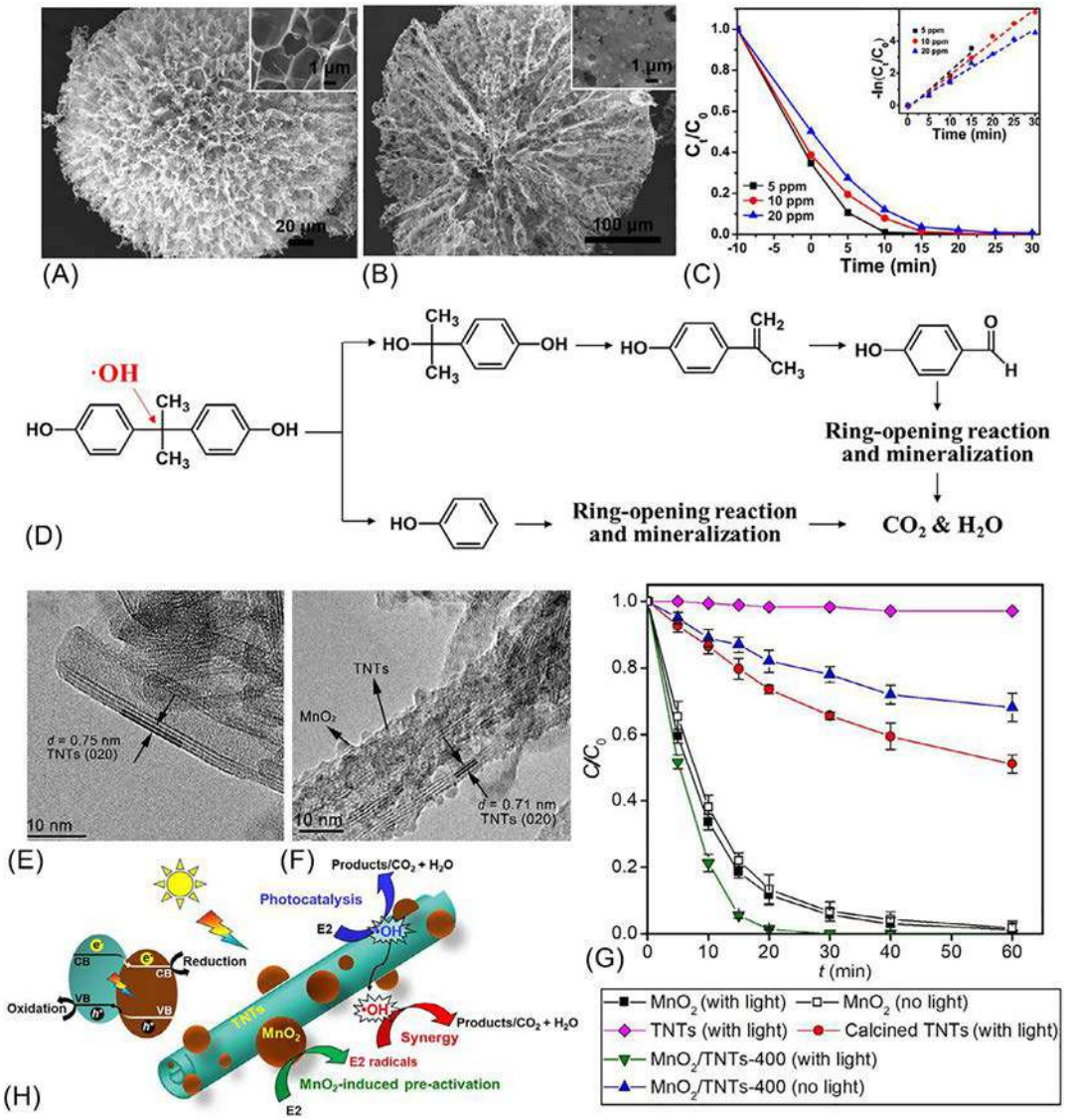

FIG. 6 SEM images of (A) SGAMs and (B) cross-section of SGAMs. (C) BPA degradation at different concentrations by SGAMs. Insets represent high-magnification SEM images of corresponding SGAMs. (D) Proposed degradation pathway BPA by the photocatalyst. HRTEM images of (E) TNTs and (F) MnO_2/TNTs. (G) Degradation of 17β-estradiol by various materials. (H) Representation of possible degradation mechanism over MnO_2/TNTs. *Panel D: Reprinted with permission from Liu Y, Yang D, Shi Y, Song L, Yu R, Qu J, et al. Silver phosphate/graphene oxide aerogel microspheres with radially oriented microchannels for highly efficient and continuous removal of pollutants from wastewaters. ACS Sustain Chem Eng 2019;7:11228–40. https://doi.org/10.1021/acssuschemeng.9b00561. Copyright 2019 American Chemical Society; Panel H: Reprinted with permission from Du P, Chang J, Zhao H, Liu W, Dang C, Tong M, et al. Sea-buckthorn-like MnO2 decorated Titanate nanotubes with oxidation property and photocatalytic activity for enhanced degradation of 17β-estradiol under solar light. ACS Appl Energ Mater 2018;1:2123–33. https://doi.org/10.1021/acsaem.8b00197. Copyright 2018 American Chemical Society.*

https://www.twirpx.org & http://chemistry-chemists.com

separated the photoexcited charges from recombination in CoO and charged species degraded absorbed TBBPA molecules via active radicals.

Estrogenic compounds, e.g., 17β-estradiol (E2), estrone, estrogen, were photocatalytically degraded by various composites. One-dimensional pure titanate nanotubes (TNTs) possess lower photodegradation activity because of the very fast recombination rate of photogenerated charge carriers. However, their efficiency can be improved by combining them with other materials. Sea-buckthorn-like MnO_2 decorated TNTs (MnO_2/TNTs) showed higher E2 degradation ability compared to bare TNTs [53]. MnO_2 could peroxidize E2 to an active form, E2*, via a one-electron oxidation pathway, and TNTs acted as a primary photocatalysis center. The long axis and short radial distance of TNTs promote absorption of incident sunlight and separation of photogenerated charge carriers, respectively [54, 55]. The photogenerated electrons transfer occurred to decorated MnO_2 from the CB of TNTs and led to spatial separation of electron-hole pairs. $O_2^{\cdot-}$ formed on the CB of MnO_2 from O_2 through the transferred electrons and induced a radical chain reaction for OH production. On the other hand, OH also formed from water oxidation through h^+. Dual-enhanced photocatalytic E2 degradation was thus explained by a synergetic effect: the decorated MnO_2 on TNTs surface preactivated E2 to active E2*, and generated OH from the VB and CB to further attack the activated E2*, leading to dramatic enhanced E2 degradation. The structural morphology, degradation behavior, and a schematic illustration of mechanism are shown in Fig. 6E–H.

Burning polyvinyl chloride (PVC)-produced dioxin congeners were photocatalytically degraded on TiO_2 films under solar light irradiation by Choi et al. [56]. The OH radicals were mentioned as the initiator to attack the aromatic ring structure.

3.2 Agrochemicals

Exponential increases in the global population results in huge food demands to sustain human life. Therefore, usage of pesticides, herbicides, bactericides, and wood preservatives has become commonplace to increase crop production and quality [57]. As a consequence, living systems face severe health issues when these pesticides and herbicides finally reach underground water. Exposure to these pollutants affects the nervous systems, cognitive functions, visual systems, and sensory functions of humans and animals. Many efforts have been made to decompose these pollutants, therefore.

Atrazine, one of the potent herbicides, has been degraded using various TiO_2- and g-C_3N_4-based heterostructures and many others [57–63]. Fu et al. designed thin carbon layer-coated Ti^{3+}-TiO_2 nanocrystallites for effective photocatalytic degradation [58]. The Ti^{3+} states/oxygen vacancies on the TiO_2 surface increased the charge separation and extended visible region absorbance, whereas the carbon layer and Ti^{3+} states/oxygen vacancies jointly enhanced O_2 adsorption on the photocatalyst's surface for efficient active species generation. Sulfate radical producing peroxymonosulfate addition on NF-TiO_2 films showed high photocatalytic efficiency, as proposed by Dionysiou et al. [57]. A certain and optimum concentration of carbon (with barbituric acid as the source)

https://www.twirpx.org & http://chemistry-chemists.com

doping on g-C_3N_4 led to improved charge separation [59]. In addition, a significant amount of atrazine degradation was attributed to the generation of active singlet oxygen ($^1O_2$) species. A three-component *Z*-scheme CdS-RGO-g-C_3N_4 hybrid showed efficient charge separation and generated enormous amounts of ROS. Both CdS and g-C_3N_4 acted as photocatalysts. The photogenerated electrons from the CB of CdS transferred and combined with the VB of g-C_3N_4 through a conductive RGO surface via the Z-scheme pathway [60], whereas the photoexcited electrons on the more negative (−1.13 eV vs. SHE) CB potential of g-C_3N_4 and holes on the positive (+1.86 eV vs. SHE) VB potential of CdS produced ROS, which helps to degrade atrazine.

Highly carcinogenic chlorophenols face difficulties in terms of biodegrading because of their high stability. The synergetic effect of MoS_2 and graphene on Ag_3PO_4 was investigated for 2,4-dichlorophenol decomposition by Li et al. [64]. The photocatalytic efficiency of Ag_3PO_4 was boosted by the addition of layered MoS_2/graphene. The MoS_2/graphene nanosheets behaved as an electron sink and transferred electrons at the interface to enhance the electron-hole pairs separation, and provided more active adsorption sites for pollutant degradation. Later on, Jing et al. succeeded in generating more $O_2^{\cdot-}$ by regulating photogenerated electrons from a g-C_3N_4/active carbon filter photocatalyst [65]. A ZnO-ZnS heterojunction nanocomposite was found to be active for 2,4-dichlorophenol and endosulfan photocatalytic degradation [66]. The bandgap of UV light-active ZnS was modified to the visible region by forming a heterojunction with ZnO. A zinc precursor was used along with urea and thiourea as fuels to prepare the composite. The particle morphology was tuned from a one-dimensional needle to a porous two-dimensional V-shaped one with increasing thiourea concentration (Fig. 7A and B). Distinct d-spacings have been observed for individual ZnO and ZnS. The porous structure and high surface area helped the charge carriers to diffuse first to the photocatalyst's surface for adsorbed pollutants oxidation.

Gas chromatography-mass spectrometry (GC-MS) analysis was performed to ensure the endosulfan degradation. The two prominent isomeric peaks of endosulfan α and β at retention times of 16.4 and 17.6 min were diminished after the photocatalytic reaction (Fig. 7C). In addition, various decomposition products (such as α-methylbenzyl alcohol, acetophenon, and 2-phenyl-2-propenol) of endosulfan were recorded from the peaks that appeared. Nanogold-doped TiO_2 nanoparticles [67], iron molybdate [68], and many other substances [69] were employed for endosulfan decomposition.

Among organophosphorous pesticides, fenitrothion is used for the treatment of chewing and sucking by pests on agricultural crops and to control cockroaches and mosquitoes [70]. It could be successfully decomposed by a GO/Fe_3O_4-TiO_2 mesoporous system [71]. The doped Fe_3O_4 and GO hindered fast electron-hole pair recombination whereas the anatase and rutile forms of TiO_2 increased the photocatalytic degradation. In addition, the authors utilized the same photocatalytic material for chlorpyrifos (another organophosphorous pesticide) degradation [72].

https://www.twirpx.org & http://chemistry-chemists.com

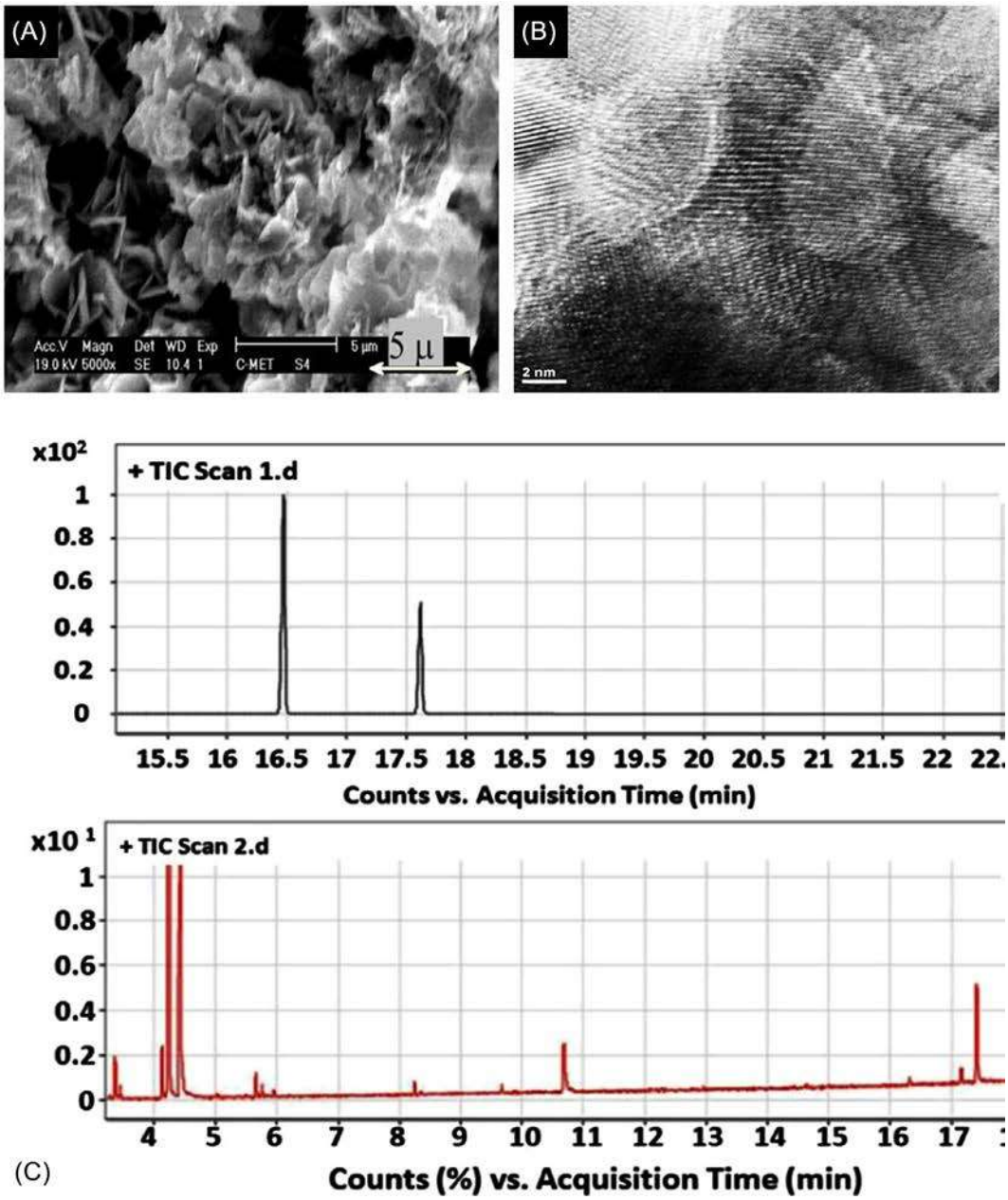

FIG. 7 (A) SEM and (B) HRTEM images of ZnO-ZnS composite. (C) GC-MS analysis of endosulfan *(top)* and endosulfan fragments *(bottom)* after sunlight irradiation with the composite. *Reprinted with permission from Devaraji P, Mapa M, Hakkeem, Sudhakar V, Krishnamoorthy K, Gopinath CS. ZnO–ZnS heterojunctions: a potential candidate for optoelectronics applications and mineralization of endocrine disruptors in direct sunlight. ACS Omega 2017;6768–81. Copyright 2017 American Chemical Society.*

https://www.twirpx.org & http://chemistry-chemists.com

Chlorpyrifos is used in agricultural fields to control pests such as rootworms, forage insects, and subterranean termites. Bare TiO_2 nanomaterials were employed by several researchers for this pesticide degradation [73, 74]. Bismuth subcarbonates (BSC) with a typical bandgap of 2.8–3.5 eV have potentiality in UV light-assisted photodegradation. But heteroatom doping and other constituents' combination with BSC showed significant visible light photocatalysis for chlorpyrifos decomposition. One heterojunction system comprising of CuS nanorods anchored $Bi_2O_2CO_3$ nanoplates (CuS/BSC) was reported for efficient generation of OH radicals from both the VB and CB of the material [75]. H_2O_2 was induced to react with CB electrons of CuS and transformation into active OH radicals. The photoexcited holes could not generate OH due to the high $OH^-/{}^{\cdot}OH$ potential; instead, CB electrons of BSC transferred into the VB of CuS and were neutralized. The photogenerated holes in the VB of BSC oxidized H_2O to OH radicals. The structural morphology of the material and proposed photocatalytic degradation mechanism are represented in Fig. 8. The probable degradation route of chlorpyrifos was proposed and is shown in Fig. 8C. The reaction end products were recorded are CO_2, H_2O, Cl^-, NH_4^+, NO_3^-, and PO_4^{3-} species.

Diazinon, a class II hazardous organophosphorous pesticide as categorized by the World Health Organization (WHO), has been degraded by a TiO_2/Fe_2O_3 nanocomposite [76]. The impregnation of Fe_2O_3 extended absorption spectra in the visible region of the composite and utilized visible light to effectively separate electron-hole pairs.

Fragmentation of another organophosphorous pesticide named imidacloprid was achieved from a GO/Fe_3O_4/TiO_2-NiO composite under visible light irradiation [77]. The OH radicals were formed as active species. Different ions such as Cl^-, NO_3^-, NO_2^-, and CO_2 were formed as the final degradation products. There was no record of organic intermediates formation during imidacloprid degradation. In addition, other nanostructures such as $H_3PW_{12}O_{40}$/La-TiO_2, GO@TiO_2, and $TiO_2/Na_2S_2O_8$ have been actively used for this pesticide decomposition.

Chlorothalonil, one of the organochlorine pesticides, is used for the treatment of foliar diseases in vegetable and ornamental crops in agricultural lands. Its degradation was performed through OH radicals generation from ferrioxalate photocatalyst by reacting with H_2O_2 [78]. Highly photosensitive ferrioxalate was converted into short lifetime oxyl radicals ($C_2O_4^{\cdot-}$), followed by $CO_2^{\cdot-}$ and CO_2 generation under light irradiation. The $CO_2^{\cdot-}$ radicals again react with another ferrioxalate with the formation of Fe^{2+}. Once Fe^{2+} is formed, present H_2O_2 in the solution reacts with it and forms OH radicals for chlorothalonil decomposition.

3.3 Pharmaceuticals and personal care products (PPCPs)

PPCPs are considered a major water pollution contributor. Various types of medicinal products including antibiotics, antimicrobials, antiinflammatories, etc. are included in pharmaceutical products [79]. It is reported that approximately 1500 tons of pharmaceutical

https://www.twirpx.org & http://chemistry-chemists.com

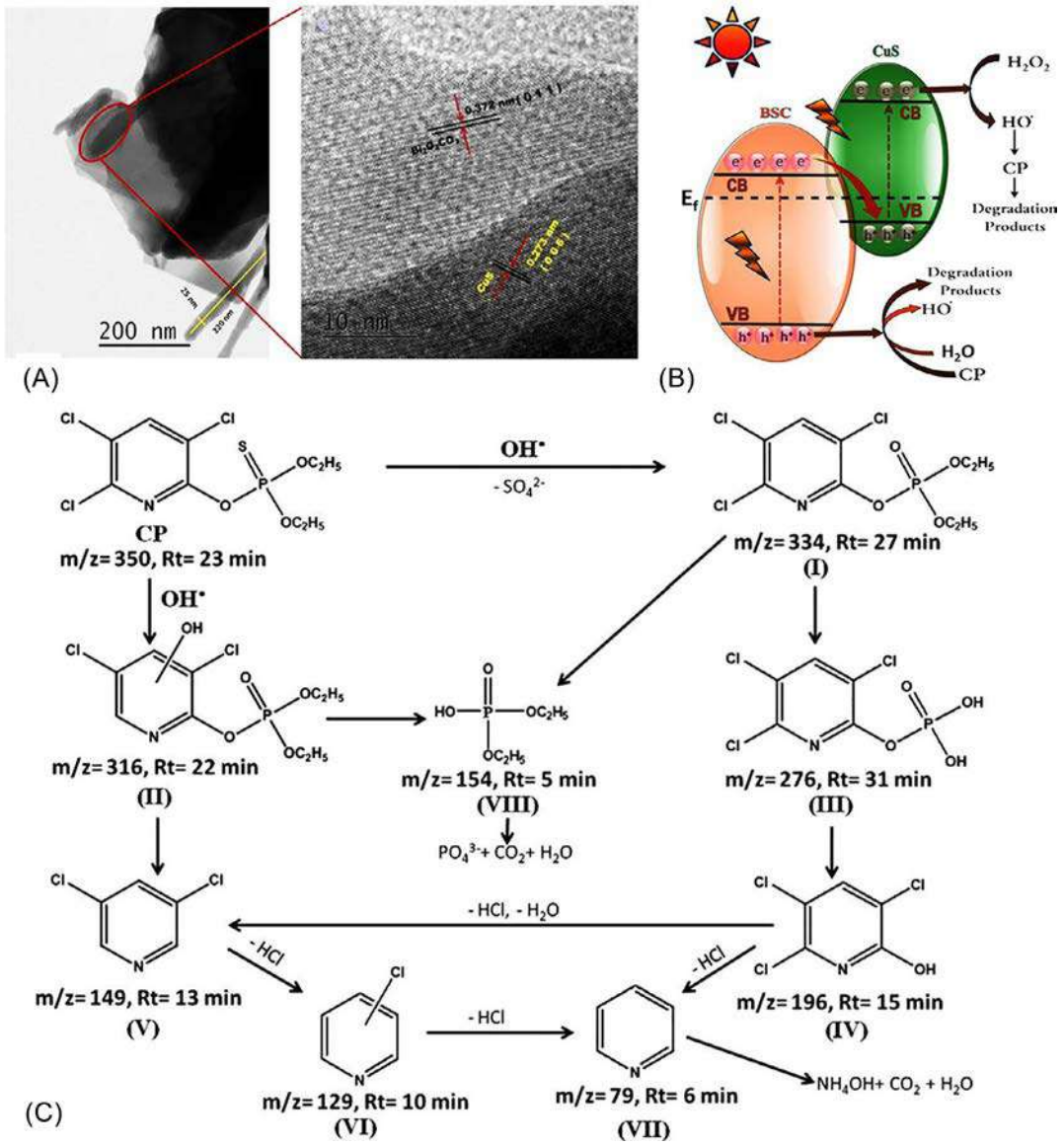

FIG. 8 (A) TEM image of CuS/BSC heterojunction photocatalyst. The right panel shows individual d-spacing in the composite. (B) Working principle of the photocatalyst for chlorpyrifos degradation. (C) Degradation pathway of chlorpyrifos with several intermediate products. *Reprinted with permission from Majhi D, Bhoi YP, Samal PK, Mishra BG. Morphology controlled synthesis and photocatalytic study of novel CuS-Bi 2 O 2 CO 3 heterojunction system for chlorpyrifos degradation under visible light illumination. Appl Surf Sci 2018;455:891–902. https://doi.org/10.1016/j.apsusc.2018.06.051. Copyright 2018 Elsevier B.V.*

https://www.twirpx.org & http://chemistry-chemists.com

products were consumed in 2003 and 95% of the doses were separated and expelled as waste through urine and stools after therapeutic use [80]. Finally they ended up in the water ecosystem. Humans consume many different antibiotics; more than 250 are available for therapeutic treatments [81]. The usage of antibiotics is increasing gradually but exponentially all over the world and even already increased by 30% in last few years as reported [79]. Therefore, it can be predicted that antibiotic consumption and their production rate will only worsen with increases in population and industrialization. The release of antibiotics into water are a cause for major concern as water contaminants. Gradual accumulation of pharmaceutical products in the water system will mainly affect humans' immune systems, and as a consequence around 25,000 and 500,000 people will die in the European Union and worldwide, respectively [79]. Different types of deodorants, perfumes, shaving cream, moisturizer, lip glows, lipstick, nail files, talcum powder, etc. are included in personal care products. They are used commonly in daily life. Carcinogens such as formaldehyde, phenacetin, butylated hydroxyanisole, benzene, coal tar, ethylene oxide, methylene glycol, etc. are used as major constituents to synthesize these personal care products. Exposure to these compounds can cause cancer, infertility in males, reproductive toxicity in females, abnormal growth development, mental confusion, mild depression, headache, acute and chronic toxicity, etc. Thus, their efficient degradation and removal is a matter of worldwide concern. Numerous photocatalytic materials such as tungstate oxide, bismuth vanadate, TiO_2, g-C_3N_4, CdS, Sn_2O_3-based nanohybrids, and many others have been reported for their effective mineralization. Some remarkable photocatalysts among these are presented here.

Tetracycline is commonly used as an antibacterial agent. Shi et al. synthesized Pt-modified WO_3 nanosheets for tetracycline degradation [82]. The VB position of pure WO_3 is lower than OH/OH^- potential, indicating that it can produce OH radicals. However, lower photoactivity of WO_3 limits its practical application. The photoexcited electrons from the WO_3 nanosheet photocatalyst produced OH radicals in the presence of the Pt cocatalyst and resulted in an enhancement of photocatalytic activity from the Pt-loaded WO_3. Bismuth vanadate (BVO) faces a difficulty in the passage of photogenerated charge carriers, resulting in lower efficiency. However, it was increased by doping of dysprosium in $Bi_4V_2O_{11}$ nanoparticles (Dy/BVO) [83]. Hydroxyl and superoxide radicals were formed as the active species from VB and CB of Dy/BVO, respectively, under light irradiation. In addition, superoxide could transform to OOH and finally H_2O_2 by reacting with a proton. Next, H_2O_2 could dissociate into OH radicals that can further attack tetracycline and enhance the degradation performance. A tetracycline degradation comparison study has been observed between undoped TiO_2 (P25) and nitrogen-doped TiO_2 (N-TiO_2) [84]. After the complex formation between tetracycline and nitrogen-doped TiO_2 (N-TiO_2), tetracycline absorbed visible light because of its small energy gap (1.97 eV) between HOMO and LUMO, and transferred electrons to the CB of N-TiO_2. The transferred electrons then reacted with adsorbed O_2 to form $O_2^{\cdot-}$, which degrades tetracycline. On the other hand, an unstable 1-electron oxidation product of tetracycline transformed to more stable products. Doped nitrogen atoms helped to generate more electron-hole pairs because of high absorbance in the visible region, resulting in acceleration of degradation

https://www.twirpx.org & http://chemistry-chemists.com

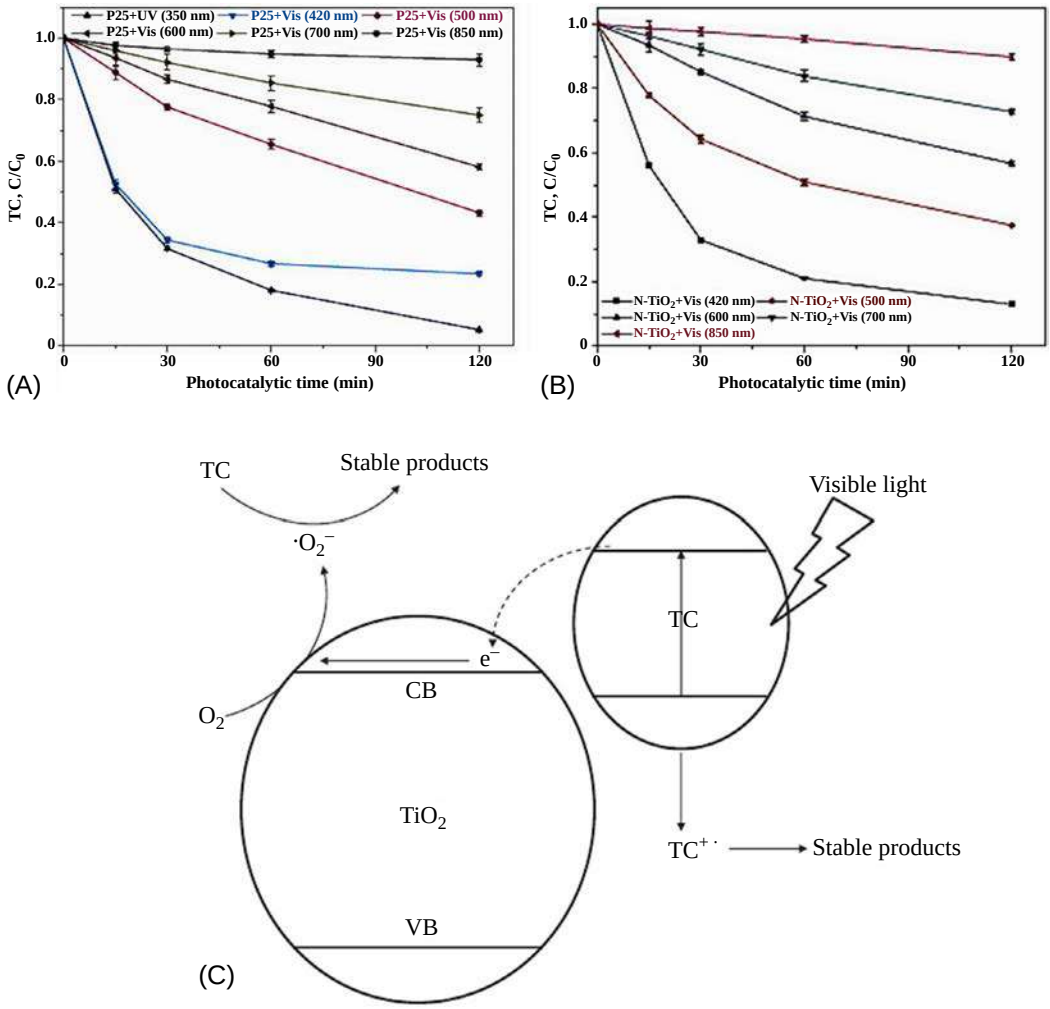

FIG. 9 Tetracycline degradation performance over (A) TiO_2-P25 and (B) N-TiO_2 under various light irradiation. (C) Proposed mechanism for tetracycline decomposition over the photocatalyst. *Reprinted with permission from Wu S, Hu H, Lin Y, Zhang J, Hu YH. Visible light photocatalytic degradation of tetracycline over TiO2. Chem Eng J 2020;382. https://doi.org/10.1016/j.cej.2019.122842. Copyright 2019 Elsevier B.V.*

rate over only TiO_2 (P25), as shown in Fig. 9. The photocatalytic degradation mechanism is also represented.

Although Au-TiO_2 nanostructures possess significant photoactivity compared to Au nanoparticles and TiO_2, they need a stable support to avoid aggregation, which can reduce the activity. For this reason, Au-TiO_2 has been attached on a polydopamine (pDA)-coated poly(vinylidene fluoride) (PVDF) membrane to prepare an Au-TiO_2/pDA/PVDF nanocomposite for tetracycline removal, as explained by Huo et al. [85]. The pDA acted as a photosensitizer to broaden the wavelength response range of TiO_2 in addition to serving

https://www.twirpx.org & http://chemistry-chemists.com

as a bioadhesion interface for bonding force improvement between the catalyst and the membrane substrate. The composite enhanced the photogenerated electrons transfer rate and Au improved the photocatalytic activity by its surface plasmon resonance effect. A meghemite (γ-Fe_2O_3)-based heterojunction with other photocatalysts also has potential activity. A *Z*-scheme heterostructure comprising of γ-Fe_2O_3 nanospheres decorated on a g-C_3N_4 nanosheet surface (γ-Fe_2O_3/g-C_3N_4) sped up the photoinduced charge carrier separation to boost tetracycline degradation activity [86]. The photoexcited electrons on the CB of γ-Fe_2O_3 neutralize with the photoexcited holes on the VB of g-C_3N_4 in the Z-scheme γ-Fe_2O_3/g-C_3N_4 heterojunction. Therefore, CB electrons of g-C_3N_4 and VB holes of γ-Fe_2O_3 produced different ROS, which showed significant tetracycline degradation. Later on, a different and interesting Z-scheme photocatalytic system was proposed by Huang et al. [87]. A ternary g-C_3N_4/Ag_2CO_3/graphene oxide (CN/AC/GO) composite showed tetracycline mineralization in a different mechanism. The photogenerated electrons and holes were generated from CN, AC, and GO under light exposure. The electrons on the CB of the catalysts generated Ag^0 to a lower extent from Ag^+ and that Ag^0 acted as a bridge between two indirect Z-scheme systems including CN/Ag/AC and AC/Ag/GO. The photoexcited electrons from the CB of AC migrated to Ag NPs and combined with the incoming holes from the VB of CN in the case of the CN/Ag/AC system. Meanwhile, the CB electrons of AC could also neutralize with the holes of Ag NPs that came from the VB of GO for the AC/Ag/GO system. Therefore, an electron-rich area is formed and accumulated on the CB of CN and GO, and thereby produces $O_2^{\cdot-}$ from O_2. On the other hand, accumulated holes on VB of AC could generate OH. As a result, tetracycline was decomposed by these OH, h^+, and $O_2^{\cdot-}$. The nanostructure morphology, photocatalytic performance, and proposed mechanism are shown in Fig. 10A–E.

A nonsteroidal antiinflammatory drug, ketorolac tromethamine (KTC), has been decomposed using a CdS-MOF composite noted as CdS/MIL-53(Fe) [13]. Molecular organic framework (MOF)-based photocatalysts, particularly iron-containing MOFs, have raised intriguing areas in photocatalysis due to the excitation of Fe μ_3-oxo clusters. In addition, functionalization promotes the removal efficiency of the pollutants via the LMCT process. This was due to the electron-hole recombination reduction because of the increase in the lifetime of electron-hole pairs. More negative CB electrons of CdS (−0.42 eV) would transfer into the CB of MIL-53(Fe) (−0.36 eV). Fewer holes migrated to the VB of CdS from the VB of MIL-53(Fe) and others reacted with H_2O to form OH radicals. Photogenerated electrons, holes, and OH radicals all took part in the degradation.

One persistent organic pollutant, 2-naphthol, causes serious health hazards upon its ingestion. Recently photocatalytic decomposition of this compound has been varied using g-C_3N_4 synthesized at different temperatures [88]. The bandgap of g-C_3N_4 was tuned during synthesis at variant temperature (450°C, 500°C, 550°C, 600°C, and 650°C), and the authors observed that synthetic g-C_3N_4 at 600°C (narrowest bandgap) has the high photocatalytic performance among the series. Significant amounts of different oxygen species radicals $O_2^{\cdot-}$, OH, HO_2, H_2O_2, and holes were formed from the narrowest bandgap g-C_3N_4 and showed high efficiency.

https://www.twirpx.org & http://chemistry-chemists.com

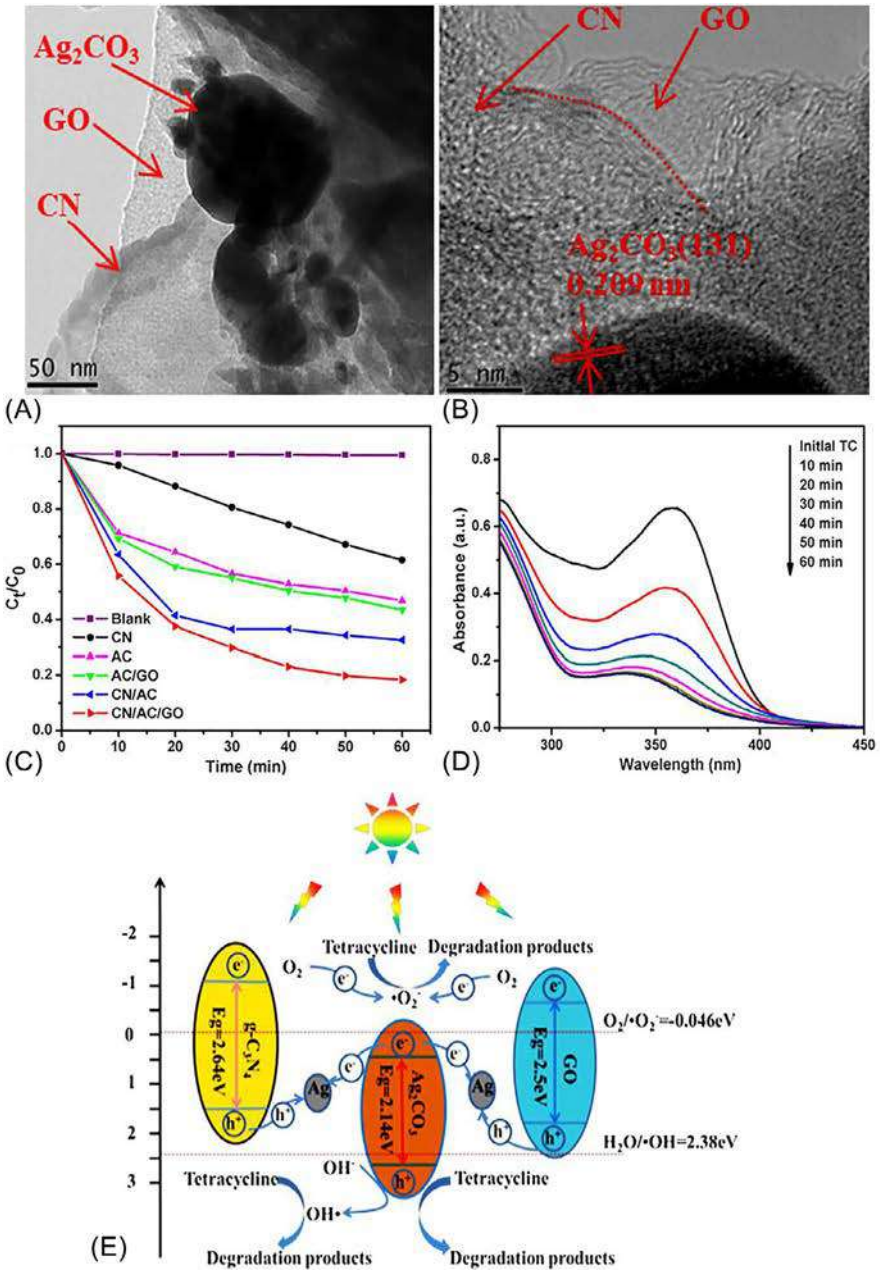

FIG. 10 (A) TEM and (B) HRTEM images of CN/AC/GO. (C) Photocatalytic degradation of tetracycline and (D) UV-vis absorption change of tetracycline by CN/AC/GO. (E) Representation of dual Z-scheme degradation pathway by the composite. *Reprinted with permission from Liu HY, Liang C, Niu CG, Huang DW, Du YB, Guo H, et al. Facile assembly of g-C3N4/Ag2CO3/graphene oxide with a novel dual Z-scheme system for enhanced photocatalytic pollutant degradation. Appl Surf Sci 2019;475:421–34. https://doi.org/10.1016/j.apsusc.2019.01.018. Copyright 2019 Elsevier B.V.*

https://www.twirpx.org & http://chemistry-chemists.com

Acetaminophen, an active pharmaceutical component, is applied in flu and cold medicines. UV-active ZnO is an n-type semiconductor and has native defects due to the presence of Zn interstitials and oxygen vacancies. Heteroatom doping can reduce the bandgap of ZnO and the material will be visible light-active. Nitrogen (N) ion implantation in a vertically aligned ZnO nanorod array (N-ZnO_4) exhibited high photocatalytic efficiency for acetaminophen decomposition through the formation of zinc interstitial levels and high amounts of ROS production [89]. Tetrakis C_{60} aminofullerene derivatized silica (aminoC_{60}/silica) has also been used for acetaminophen and carbamazepine degradation by a similar mechanism to that already described in BPA degradation [45].

One antiepileptic drug, carbamazepine, has been degraded using various shaped carbon-loaded anatase TiO_2 (C-TiO_2) because of its large surface area, lower energy, and thermodynamical stability [90]. The authors synthesized spherical, distorted spherical, hexagonal, and rice grain structured C-TiO_2. Among them, rice grain C-TiO_2 showed higher efficiency because of the coexposure of low energy/high energy (101)/(001) facets due to competition between F^- and H_2O_2 and high surface area. A sol-gel nitrogen-doped TiO_2 was also investigated for this drug degradation [91].

The β-lactum antibiotic, amoxicillin, has high levels of toxicity, slower biodegradation rate, and affects algal species growth. Significant numbers of electron-hole pairs were generated from a MOF@Sm_2O_3-ZnO photocatalyst to produce OH and $O_2^{\cdot-}$ which helped in amoxicillin oxidation [92]. Multivalent elements are known as electron trappers and suppliers in heterojunctions to promote photocatalytic activity. In particular, lanthanides are included as active materials for their unique 4f electrons [93]. The n-type semiconductor, Sm_2O_3, formed a Fermi energy level upon incorporation in the heterojunction. The transferred electrons from ZnO took part in reduction of Sm^{3+} to Sm^{2+}. As the Sm^{2+} reduction potential is more negative than $O_2/O_2^{\cdot-}$ potential, it will form $O_2^{\cdot-}$ radicals. MOF also played a leading role in the degradation reaction. Amoxicillin molecules were adsorbed through - interaction with the MOF scaffold. In addition, MOF, as an electron acceptor, can transfer electrons from ZnO through the high conductivity and planar structure of MOF, resulting in efficient photogenerated charge carriers separation.

One antimicrobial agent, chloramphenicol, is applied in infections coming from fungi and bacteria. It has been photodegraded using a $Ce(MoO_4)_2$ nanocubes/graphene oxide (CeM/GO) composite by Muthuraj et al. [94]. Transition metal-based catalysts are known to be photoactive. However, photocatalysts made of rare earth molybdates can be considered as effective due to high photostability, corrosion inhibition, and good photocatalytic conversion. Conductive GO could prevent the electron-hole pair recombination process in CeM/GO nanostructures, resulting in higher degradation of chloramphenicol compared to bare CeM. Conjugated polyene-modified TiO_2 was also involved in chloramphenicol photodegradation [95]. The lower bandgap of the composite and multiple bonds of the polymer synergistically could provide significant charge separation and improved photocatalytic efficiency.

Ciprofloxacin, a fluoroquinolone antibiotic, is used in the treatment of bacteria, skin, respiratory, bone, joint, and urinary tract infections. The combined action of nitrogen

https://www.twirpx.org & http://chemistry-chemists.com

defects and carbon dots (C-dots) loading could help in high degradation of this drug in C-dot@nitrogen-deficient g-C_3N_4 (C-dot@ND-g-C_3N_4) [96]. C-dots increased the visible light absorption capacity and accelerated charge transfer in C-dot@ND-g-C_3N_4, leading to enhanced degradation compared to pure g-C_3N_4. The structural morphology and degradation mechanism are displayed in Fig. 11A–C. The decoration of C-dots on the g-C_3N_4 nanosheet can clearly be observed (Fig. 11A–B). The photoexcited CB electrons of ND-g-C_3N_4 were captured by attached C-dots and transferred to the pollutant surface for mineralization via active oxygen radicals generation (Fig. 11C).

Another fluoroquinolone antibiotic, norfloxacin, is applied in the treatment of mainly bacterial and respiratory infections. Almost 70% of this drug is excreted in the environment and one significant problem is its poor biodegradability. Various photocatalysts such as TiO_2, CeO_2, Bi_2WO_6, and ZnS-based nanostructures have been actively involved for the removal of this drug [97–101]. Norfloxacin gets adsorbed on reduced TiO_2 through N, F, and O atoms, and the catalyst possesses photoactivity due to the high surface area, oxygen vacancy density, and high amount of Ti^{3+} concentration [100]. The active species (h^+ and OH radicals) could cleave the piperazine ring and hydroxylate the quinolone ring of norfloxacin during degradation. A Ti mesh supporting N-S-C-tridoped TiO_2 nanosheets (N-S-C/TiO_2/TMs) was investigated for this drug degradation by Yu et al. [101]. New impurity levels were formed in TiO_2 upon insertion of N, S, and C. The N 2p gap level could be formed on the top of the O 2p VB, whereas S 2p and C 1 s levels were in the bottom of Ti 3d CB. The S 2p and C 1 s levels acted as electron trappers and generated $O_2^{\cdot-}$ radicals from the adsorbed O_2 in addition with Ti 3d CB. The excited holes of N 2p generated OH radicals. An Fe-doped ZnS photocatalyst ($Zn_{0.9}Fe_{0.1}S$) supported on Ni-foam showed its photocatalytic ability [97]. Ni-foam could supply more active sites for reaction and act as an electron acceptor. The photocatalyst produced $O_2^{\cdot-}$, OH, and h^+ responsible for norfloxacin degradation.

Highly water-soluble metronidazole and cephalexin are used in the treatment of infectious diseases. Increases of active sites, photocatalytic centers, and OH radicals in N-TiO_2:$ZnFe_2O_4$ nanocomposites supported on zeolite boosted metronidazole and cephalexin degradation by Farhadian et al. [102]. Spinel $ZnFe_2O_4$ has free catalytic sites for its crystal lattice structure and extends the absorption of TiO_2 toward the visible region. Similar ionic size and lower ionization energy of nitrogen can tune the TiO_2 characteristic properties and prevent electron-hole pairs recombination. The synergistic effect between photocatalysis and ozonation led to significantly improved ROS generation and efficient antibiotics mineralization (Fig. 11D).

Propranolol, one of the β-blockers, is usually considered for the treatment of cardiovascular diseases. Spinel ferrites, in particular copper ferrites ($CuFe_2O_4$) with a bandgap of 1.4 eV, have catalytic potential ability due to their environmental compatibility and stability. A copper ferrite-modified g-C_3N_4 ($CuFe_2O_4$/g-C_3N_4) nanocomposite combined with peroxydisulfate (PDS) demonstrated photocatalytic propranolol decomposition [103]. The g-C_3N_4 VB level is more positive than the VB of $CuFe_2O_4$, and the CB level of $CuFe_2O_4$ is more negative compared to g-C_3N_4. Therefore, the photoexcited electrons and holes

https://www.twirpx.org & http://chemistry-chemists.com

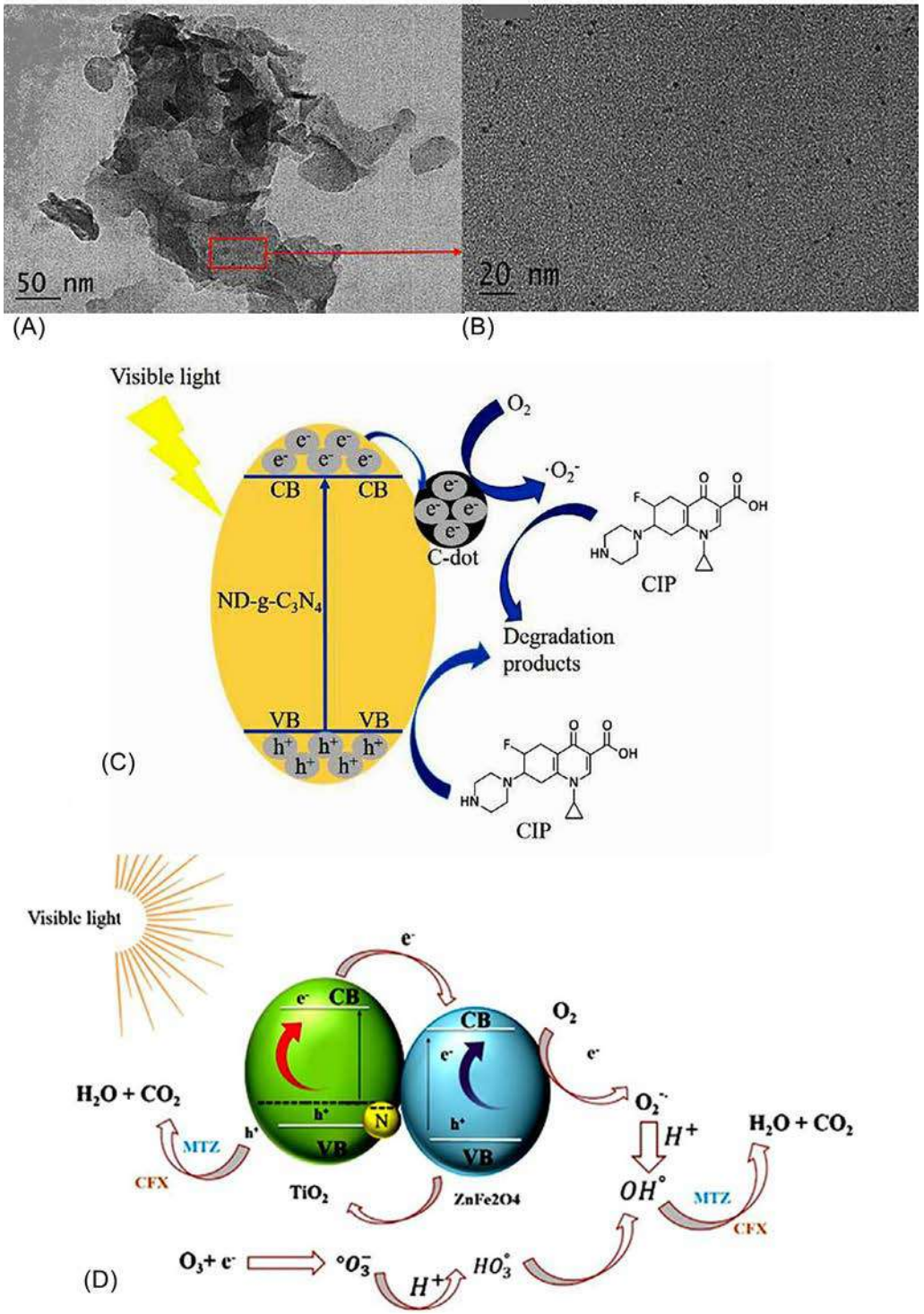

FIG. 11 (A) TEM and (B) HRTEM images of C-dot@ND-g-C_3N_4. (C) Photocatalytic ciprofloxacin degradation mechanism by C-dot@ND-g-C_3N_4. (D) Tentative photocatalytic ozonation mechanism of N-TiO_2:$ZnFe_2O_4$ nanostructures

(Continued)

https://www.twirpx.org & http://chemistry-chemists.com

were accumulated on the CB of g-C_3N_4 and the VB of $CuFe_2O_4$, respectively. However, the holes could not generate OH radicals from H_2O because of the more negative VB potential of $CuFe_2O_4$ compared to the OH/H_2O redox potential. The accumulated CB electrons of g-C_3N_4 activated PDS to produce $SO_4^{\cdot-}$ radicals. In addition, Fe (II) and Cu (I) of $CuFe_2O_4$ helped to generate $SO_4^{\cdot-}$ from PDS. These $SO_4^{\cdot-}$ radicals converted H_2O to OH, which further attacked propranolol to decompose it.

3.4 Food additives and sweeteners

In recent years, food additives and artificial sweeteners have been identified as emerging pollutants. Their presence in water sources is a deep concern in terms of water pollution. Veterinary food additives include *p*-arsanilic acid, roxarsone, phenylarsonic acid, etc. For example, *p*-arsanilic acid releases high toxic inorganic arsenic species (such as arsenate) after degradation, which leads to severe arsenic pollution in soil and groundwater [104]. On the other hand, the European Union approved the use of six types of artificial sweeteners: acesulfame, saccharin, aspartame, sucralose, cyclamate, and neohesperidin dihydrochalcone [105]. Most of the compounds do not metabolize easily and are excreted as a parent compound, causing water pollution worldwide. It is reported that high amounts of acesulfame (60–80 μg/L) are present in several wastewater treatment plants in Israel, Switzerland, Canada, and Germany [106]. Aquatic life will be affected by the presence of such additives during long-term exposure, and this exposure can cause mutagenic transformation in bone structure.

Acesulfame is commonly used in artificial sweeteners and is available on the market as potassium salt. This is why it is sometimes called acesulfame K. Several reports have been published for their effective mineralization [106, 107]. One of the photocatalysts, cerium-doped ZnO, has been reported as a photocatalyst for acesulfame K degradation by Paganini et al. [107]. The composite showed enhanced photocatalytic activity compared to bare ZnO and TiO_2 P25, as shown in Fig. 12. The efficiency showed variation upon changing the dopant salt (namely $CeCl_3$, labeled Ce1Cl and Ce05Cl) and a Ce (IV) salt (namely $Ce(SO_4)_2$, labeled Ce1S and Ce05S). Ce1Cl and Ce05Cl denote 1% and 0.5% $CeCl_3$ doping, respectively. The same will be effective for $Ce(SO_4)_2$. The results showed that the presence of $CeCl_3$ induced promising efficiency, and it was also inferred that the cerium initial oxidation state played a crucial role in degradation. An increase in the photocatalytic degradation rate of the doped composite was ascribed to the presence of intra-bandgap states which could permit visible photons to absorb via a step-by-step mechanism (vide infra). Later on, Ray et al. approached the solar photocatalytic degradation of acesulfame K by

FIG. 11, cont'd supported on zeolite for metronidazole and cephalexin degradation. *Panel C: Reprinted with permission from Zhang H, Wu W, Li Y, Wang Y, Zhang C, Zhang W, et al. Enhanced photocatalytic degradation of ciprofloxacin using novel C-dot@nitrogen deficient g-C3N4: synergistic effect of nitrogen defects and C-dots. Appl Surf Sci 2019;465:450–8. https://doi.org/10.1016/j.apsusc.2018.09.183. Copyright 2018 Elsevier BV; Panel D: Reprinted with permission from Aram M, Farhadian M, Solaimany Nazar AR, Tangestaninejad S, Eskandari P, Jeon BH. Metronidazole and cephalexin degradation by using of urea/TiO2/ZnFe2O4/clinoptiloite catalyst under visible-light irradiation and ozone injection. J Mol Liq 2020;304. https://doi.org/10.1016/j.molliq.2020.112764. Copyright 2020 Elsevier BV.*

https://www.twirpx.org & http://chemistry-chemists.com

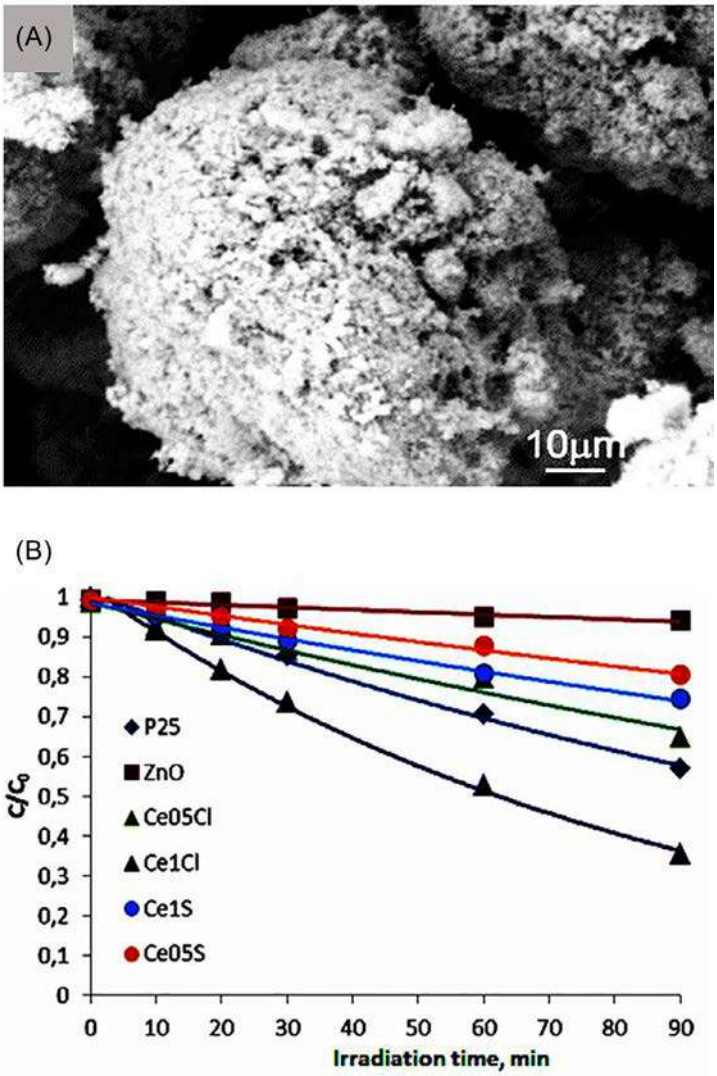

FIG. 12 (A) SEM image of cerium-doped ZnO. (B) Acesulfame K photocatalytic degradation performance study of cerium-doped ZnO over other nanomaterials. *Reprinted with permission from Calza P, Gionco C, Giletta M, Kalaboka M, Sakkas VA, Albanis T, et al. Assessment of the abatement of acelsulfame K using cerium doped ZnO as photocatalyst. J Hazard Mater 2017;323:471–7. https://doi.org/10.1016/j.jhazmat.2016.03.093. Copyright 2016 Elsevier BV.*

choosing TiO_2 [106]. The degradation of acesulfame K was initiated by OH radicals formation at the TiO_2 interface. Carbon dioxide and water were recorded as the final products after the photocatalytic reaction.

4 Summary and future outlook

The persistence accretion of emerging pollutants in aquatic resources and their exposure is associated with adverse health effects on living beings and negative environmental

https://www.twirpx.org & http://chemistry-chemists.com

impacts. Many of these pollutants take a long time (up to a couple of decades) to be degraded and gone from the environment. Photocatalysis undoubtedly is a major area for their degradation. Successful research on the design of novel visible light-active photocatalytic materials has flourished over time to cloister these environmental pollutants with an increase in our awareness. In addition, continuing reports on sophisticated and cost-effective materials will not only add to the list of photocatalytic materials resources, but boost the scientific community to increase the interest and future developments of this field as well as materials science. These materials can also be considered as a stepping stone for highly toxic inorganic ions (e.g., Cr and As) decontamination present in drinking water. This will be highly appreciable in terms of infrared active photocatalytic material synthesis for water purification, as sunlight contains 52% of infrared components. Not only new photocatalytic material but also some innovative concepts are required to utilize them effectively. In summary, all these aspects will open a new window for visible light or sunlight-triggered emergent pollutants photocatalysis.

References

[1] Chen C, Ma W, Zhao J. Semiconductor-mediated photodegradation of pollutants under visible-light irradiation. Chem Soc Rev 2010;39:4206–19. https://doi.org/10.1039/b921692h.

[2] Yong L, Kai Y, Jingdong Z. Graphitic carbon nitride sensitized with CdS quantum dots for visible-light-driven photoelectrochemical aptasensing of tetracycline. ACS Appl Mater Interfaces 2016;28255–64. https://doi.org/10.1021/acsami.5b08275.

[3] Xu C, Ravi Anusuyadevi P, Aymonier C, Luque R, Marre S. Nanostructured materials for photocatalysis. Chem Soc Rev 2019;48:3868–902. https://doi.org/10.1039/c9cs00102f.

[4] Linic S, Christopher P, Ingram DB. Plasmonic-metal nanostructures for efficient conversion of solar to chemical energy. Nat Mater 2011;10:911–21. https://doi.org/10.1038/nmat3151.

[5] Tong H, Ouyang S, Bi Y, Umezawa N, Oshikiri M, Ye J. Nano-photocatalytic materials: possibilities and challenges. Adv Mater 2012;24:229–51. https://doi.org/10.1002/adma.201102752.

[6] Liu G, Wang L, Yang HG, Cheng HM, Lu GQ. Titania-based photocatalysts—crystal growth, doping and heterostructuring. J Mater Chem 2010;20:831–43. https://doi.org/10.1039/b909930a.

[7] Peiris S, McMurtrie J, Zhu HY. Metal nanoparticle photocatalysts: emerging processes for green organic synthesis. Catal Sci Technol 2016;6:320–38. https://doi.org/10.1039/c5cy02048d.

[8] Manzetti S, Van Der Spoel ER, Van Der Spoel D. Chemical properties, environmental fate, and degradation of seven classes of pollutants. Chem Res Toxicol 2014;27:713–37. https://doi.org/10.1021/tx500014w.

[9] Fenner K, Canonica S, Wackett LP, Elsner M. Evaluating pesticide degradation in the environment: blind spots and emerging opportunities. Science 2013;341:752–8. https://doi.org/10.1126/science.1236281.

[10] Grube A, Donaldson D, Kiely T, Wu L. Pesticides industry sales and usage. US EPA; 2011.

[11] Robinson BH. E-waste: an assessment of global production and environmental impacts. Sci Total Environ 2009;408:183–91. https://doi.org/10.1016/j.scitotenv.2009.09.044.

[12] Wong CSC, Wu SC, Duzgoren-Aydin NS, Aydin A, Wong MH. Trace metal contamination of sediments in an e-waste processing village in China. Environ Pollut 2007;145:434–42. https://doi.org/10.1016/j.envpol.2006.05.017.

https://www.twirpx.org & http://chemistry-chemists.com

[13] Chaturvedi G, Kaur A, Kansal SK. CdS-decorated MIL-53 (Fe) microrods with enhanced visible light photocatalytic performance for the degradation of ketorolac tromethamine and mechanism insight. J Phys Chem C 2019;16857–67.

[14] Rajasulochana P, Preethy V. Comparison on efficiency of various techniques in treatment of waste and sewage water—a comprehensive review. Resour-Eff Technol 2016;175–84. https://doi.org/10.1016/j.reffit.2016.09.004.

[15] Choi J, Lee H, Choi Y, Kim S, Lee S, Lee S, et al. Heterogeneous photocatalytic treatment of pharmaceutical micropollutants: effects of wastewater effluent matrix and catalyst modifications. Appl Catal Environ 2014;147:8–16. https://doi.org/10.1016/j.apcatb.2013.08.032.

[16] Xiong W, Yang Y, Duan A, Zeng G, Huang D, Lai C, et al. Adsorption behavior of engineered carbons and carbon nanomaterials for metal endocrine disruptors: experiments and theoretical calculation. Chemosphere 2019;222:184–94. https://doi.org/10.1016/j.chemosphere.2019.01.128.

[17] Vaiano V, Sacco O, Sannino D, Ciambelli P. Photocatalytic removal of spiramycin from wastewater under visible light with N-doped TiO2 photocatalysts. Chem Eng J 2015;261:3–8. https://doi.org/10.1016/j.cej.2014.02.071.

[18] Bhunia SK, Jana NR. Reduced graphene oxide-silver nanoparticle composite as visible light photocatalyst for degradation of colorless endocrine disruptors. ACS Appl Mater Interfaces 2014;6:20085–92. https://doi.org/10.1021/am505677x.

[19] Fic A, Žegura B, Sollner Dolenc M, Filipič M, Peterlin ML. Mutagenicity and DNA damage of bisphenol a and its structural analogues in HepG2 cells. Arh Hig Rada Toksikol 2013;64:189–200. https://doi.org/10.2478/10004-1254-64-2013-2319.

[20] Howdeshell KL, Hotchkiss AK, Thayer KA, Vandenbergh JG, Saal FSV. Exposure to bisphenol A advances puberty. Nature 1999;763–4. https://doi.org/10.1038/44517.

[21] Nagel SC, Vom Saal FS, Thayer KA, Dhar MG, Boechler M, Welshons WV. Relative binding affinity-serum modified access (RBA-SMA) assay predicts the relative in vivo bioactivity of the xenoestrogens bisphenol A and octylphenol. Environ Health Perspect 1997;105:70–6. https://doi.org/10.1289/ehp.9710570.

[22] Staples CA, Dorn PB, Klecka GM, O'Block ST, Harris LR. A review of the environmental fate, effects, and exposures of bisphenol A. Chemosphere 1998;36:2149–73. https://doi.org/10.1016/S0045-6535(97)10133-3.

[23] Sharma RP, Schuhmacher M, Kumar V. The development of a pregnancy PBPK model for bisphenol A and its evaluation with the available biomonitoring data. Sci Total Environ 2018;624:55–68. https://doi.org/10.1016/j.scitotenv.2017.12.023.

[24] Li T, Wei H, Jia H, Xia T, Guo X, Wang T, et al. Mechanisms for highly efficient mineralization of bisphenol A by heterostructured Ag2WO4/Ag3PO4 under simulated solar light. ACS Sustain Chem Eng 2019;7:4177–85. https://doi.org/10.1021/acssuschemeng.8b05794.

[25] Kang JH, Aasi D, Katayama Y. Bisphenol A in the aquatic environment and its endocrine-disruptive effects on aquatic organisms. Crit Rev Toxicol 2007;37:607–25. https://doi.org/10.1080/10408440701493103.

[26] Oehlmann J, Schulte-Oehlmann U, Tillmann M, Markert B. Effects of endocrine disruptors on prosobranch snails (mollusca: Gastropoda) in the laboratory. Part I: bisphenol A and octylphenol as xeno-estrogens. Ecotoxicology 2000;9:383–97. https://doi.org/10.1023/A:1008972518019.

[27] Tallova J, Tomandl J, Bicikova M, Hill M. Changes of plasma total homocysteine levels during the menstrual cycle. Eur J Clin Invest 1999;29:1041–4. https://doi.org/10.1046/j.1365-2362.1999.00572.x.

[28] Leffers H, McLachlan JA, Meyer O, Müller J, Rajpert-De Meyts E, Scheike T, et al. Male reproductive health and environmental xenoestrogens. Environ Health Perspect 1996;104:741–803. https://doi.org/10.1289/ehp.96104s4741.

https://www.twirpx.org & http://chemistry-chemists.com

[29] Mobley JA, Bhat AS, Brueggemeier RW. Measurement of oxidative DNA damage by catechol estrogens and analogues in vitro. Chem Res Toxicol 1999;12:270–7. https://doi.org/10.1021/tx980128i.

[30] Gould JC, Leonard LS, Maness SC, Wagner BL, Conner K, Zacharewski T, et al. Bisphenol A interacts with the estrogen receptor α in a distinct manner from estradiol. Mol Cell Endocrinol 1998;142:203–14. https://doi.org/10.1016/S0303-7207(98)00084-7.

[31] He Z, Xie L, Tu J, Song S, Liu W, Liu Z, et al. Visible light-induced degradation of phenol over iodine-doped titanium dioxide modified with platinum: role of platinum and the reaction mechanism. J Phys Chem C 2010;114:526–32. https://doi.org/10.1021/jp908946c.

[32] Xu M, Han L, Dong S. Facile fabrication of highly efficient g-C3N4/Ag2O heterostructured photocatalysts with enhanced visible-light photocatalytic activity. ACS Appl Mater Interfaces 2013;5:12533–40. https://doi.org/10.1021/am4038307.

[33] Sheng J, Li X, Xu Y. Generation of H2O2 and OH radicals on Bi 2WO6 for phenol degradation under visible light. ACS Catal 2014;4:732–7. https://doi.org/10.1021/cs400927w.

[34] Long M, Cai W, Cai J, Zhou B, Chai X, Wu Y. Efficient photocatalytic degradation of phenol over Co3O 4/BiVO4 composite under visible light irradiation. J Phys Chem B 2006;110:20211–6. https://doi.org/10.1021/jp063441z.

[35] Shang M, Wang W, Sun S, Ren J, Zhou L, Zhang L. Efficient visible light-induced photocatalytic degradation of contaminant by spindle-like PANI/BiVO4. J Phys Chem C 2009;113:20228–33. https://doi.org/10.1021/jp9067729.

[36] Chang C, Zhu L, Wang S, Chu X, Yue L. Novel mesoporous graphite carbon nitride/BiOI heterojunction for enhancing photocatalytic performance under visible-light irradiation. ACS Appl Mater Interfaces 2014;6:5083–93. https://doi.org/10.1021/am5002597.

[37] Wang CY, Zhang X, Song XN, Wang WK, Yu HQ. Novel Bi12O15Cl6 Photocatalyst for the degradation of bisphenol A under visible-light irradiation. ACS Appl Mater Interfaces 2016;8:5320–6. https://doi.org/10.1021/acsami.5b12092.

[38] Zhang H, Guo LH, Zhao L, Wan B, Yang Y. Switching oxygen reduction pathway by exfoliating graphitic carbon nitride for enhanced photocatalytic phenol degradation. J Phys Chem Lett 2015;6:958–63. https://doi.org/10.1021/acs.jpclett.5b00149.

[39] Sun H, Zhou G, Wang Y, Suvorova A, Wang S. A new metal-free carbon hybrid for enhanced photocatalysis. ACS Appl Mater Interfaces 2014;6:16745–54. https://doi.org/10.1021/am503820h.

[40] Ren HT, Jia SY, Wu Y, Wu SH, Zhang TH, Han X. Improved photochemical reactivities of Ag2O/g-C3N4 in phenol degradation under UV and visible light. Ind Eng Chem Res 2014;53:17645–53. https://doi.org/10.1021/ie503312x.

[41] Meng Q, Lv H, Yuan M, Chen Z, Chen Z, Wang X. In situ hydrothermal construction of direct solid-state nano-Z-scheme BiVO4/pyridine-doped g-C3N4 photocatalyst with efficient visible-light-induced photocatalytic degradation of phenol and dyes. ACS Omega 2017;2728–39.

[42] Liu Y, Dai H, Deng J, Zhang L, Au CT. Three-dimensional ordered macroporous bismuth vanadates: PMMA-templating fabrication and excellent visible light-driven photocatalytic performance for phenol degradation. Nanoscale 2012;4:2317–25. https://doi.org/10.1039/c2nr12046a.

[43] Padhi DK, Panigrahi TK, Parida K, Singh SK, Mishra PM. Green synthesis of Fe3O4/RGO nanocomposite with enhanced photocatalytic performance for Cr(VI) reduction, phenol degradation, and antibacterial activity. ACS Sustain Chem Eng 2017;5:10551–62. https://doi.org/10.1021/acssuschemeng.7b02548.

[44] Darabdhara G, Boruah PK, Borthakur P, Hussain N, Das MR, Ahamad T, et al. Reduced graphene oxide nanosheets decorated with Au-Pd bimetallic alloy nanoparticles towards efficient photocatalytic degradation of phenolic compounds in water. Nanoscale 2016;8:8276–87. https://doi.org/10.1039/c6nr00231e.

https://www.twirpx.org & http://chemistry-chemists.com

[45] Lee J, Hong S, MacKeyev Y, Lee C, Chung E, Wilson LJ, et al. Photosensitized oxidation of emerging organic pollutants by tetrakis C 60 aminofullerene-derivatized silica under visible light irradiation. Environ Sci Tech 2011;45:10598–604. https://doi.org/10.1021/es2029944.

[46] Xu J, Wang Z, Zhu Y. Enhanced visible-light-driven photocatalytic disinfection performance and organic pollutant degradation activity of porous g-C3N4 nanosheets. ACS Appl Mater Interfaces 2017;9:27727–35. https://doi.org/10.1021/acsami.7b07657.

[47] Liang X, Wang G, Dong X, Wang G, Ma H, Zhang X. Graphitic carbon nitride with carbon vacancies for photocatalytic degradation of bisphenol A. ACS Appl Nano Mater 2019;2:517–24. https://doi.org/10.1021/acsanm.8b02089.

[48] Hu J, Zhang P, An W, Liu L, Liang Y, Cui W. In-situ Fe-doped g-C3N4 heterogeneous catalyst via photocatalysis-Fenton reaction with enriched photocatalytic performance for removal of complex wastewater. Appl Catal Environ 2019;245:130–42. https://doi.org/10.1016/j.apcatb.2018.12.029.

[49] Liu Y, Yang D, Shi Y, Song L, Yu R, Qu J, et al. Silver phosphate/graphene oxide aerogel microspheres with radially oriented microchannels for highly efficient and continuous removal of pollutants from wastewaters. ACS Sustain Chem Eng 2019;7:11228–40. https://doi.org/10.1021/acssuschemeng.9b00561.

[50] Pan M, Zhang H, Gao G, Liu L, Chen W. Facet-dependent catalytic activity of nanosheet-assembled bismuth oxyiodide microspheres in degradation of bisphenol a. Environ Sci Tech 2015;49:6240–8. https://doi.org/10.1021/acs.est.5b00626.

[51] Wang C, Zhang H, Li F, Zhu L. Degradation and mineralization of bisphenol A by mesoporous Bi 2WO6 under simulated solar light irradiation. Environ Sci Tech 2010;44:6843–8. https://doi.org/10.1021/es101890w.

[52] Tang Y, Dong L, Mao S, Gu H, Malkoske T, Chen B. Enhanced photocatalytic removal of Tetrabromobisphenol A by magnetic CoO@graphene nanocomposites under visible-light irradiation. ACS Appl Energ Mater 2018;1:2698–708. https://doi.org/10.1021/acsaem.8b00379.

[53] Du P, Chang J, Zhao H, Liu W, Dang C, Tong M, et al. Sea-buckthorn-like MnO2 decorated Titanate nanotubes with oxidation property and photocatalytic activity for enhanced degradation of 17β-estradiol under solar light. ACS Appl Energ Mater 2018;1:2123–33. https://doi.org/10.1021/acsaem.8b00197.

[54] Liu S, Tang ZR, Sun Y, Colmenares JC, Xu YJ. One-dimension-based spatially ordered architectures for solar energy conversion. Chem Soc Rev 2015;44:5053–75. https://doi.org/10.1039/c4cs00408f.

[55] Tang ZR, Yin X, Zhang Y, Xu YJ. Synthesis of titanate nanotube-CdS nanocomposites with enhanced visible light photocatalytic activity. Inorg Chem 2013;52:11758–66. https://doi.org/10.1021/ic4010483.

[56] Choi W, Hong SJ, Chang YS, Cho Y. Photocatalytic degradation of polychlorinated dibenzo-p-dioxins on TiO2 film under UV or solar light irradiation. Environ Sci Tech 2000;34:4810–5. https://doi.org/10.1021/es0011461.

[57] Andersen J, Pelaez M, Guay L, Zhang Z, O'Shea K, Dionysiou DD. NF-TiO2 photocatalysis of amitrole and atrazine with addition of oxidants under simulated solar light: emerging synergies, degradation intermediates, and reusable attributes. J Hazard Mater 2013;260:569–75. https://doi.org/10.1016/j.jhazmat.2013.05.056.

[58] Jiang B, Tang Y, Qu Y, Wang JQ, Xie Y, Tian C, et al. Thin carbon layer coated Ti3+-TiO2 nanocrystallites for visible-light driven photocatalysis. Nanoscale 2015;7:5035–45. https://doi.org/10.1039/c5nr00032g.

[59] Zheng Q, Durkin DP, Elenewski JE, Sun Y, Banek NA, Hua L, et al. Visible-light-responsive graphitic carbon nitride: rational design and photocatalytic applications for water treatment. Environ Sci Tech 2016;50:12938–48. https://doi.org/10.1021/acs.est.6b02579.

https://www.twirpx.org & http://chemistry-chemists.com

[60] Jo WK, Selvam NCS. Z-scheme CdS/g-C3N4 composites with RGO as an electron mediator for efficient photocatalytic H2 production and pollutant degradation. Chem Eng J 2017;317:913–24. https://doi.org/10.1016/j.cej.2017.02.129.

[61] Alkayal NS, Hussein MA. Photocatalytic degradation of atrazine under visible light using novel Ag@Mg4Ta2O9 nanocomposites. Sci Rep 2019;1–10.

[62] Malkhasian AYS. Synthesis and characterization of Pt/AgVO3 nanowires for degradation of atrazine using visible light irradiation. J Alloys Compd 2015;649:394–9. https://doi.org/10.1016/j.jallcom.2015.07.167.

[63] Xue Y, Wang P, Wang C, Ao Y. Efficient degradation of atrazine by BiOBr/UiO-66 composite photocatalyst under visible light irradiation: environmental factors, mechanisms and degradation pathways. Chemosphere 2018;203:497–505. https://doi.org/10.1016/j.chemosphere.2018.04.017.

[64] Peng WC, Wang X, Li XY. The synergetic effect of MoS2 and graphene on Ag 3PO4 for its ultra-enhanced photocatalytic activity in phenol degradation under visible light. Nanoscale 2014;6:8311–7. https://doi.org/10.1039/c4nr01654h.

[65] Chu M, Hu K, Wang J, Liu Y, Ali S, Qin C, et al. Synthesis of g-C3N4-based photocatalysts with recyclable feature for efficient 2,4-dichlorophenol degradation and mechanisms. Appl Catal Environ 2019;243:57–65. https://doi.org/10.1016/j.apcatb.2018.10.008.

[66] Devaraji P, Mapa M, Hakkeem SV, Krishnamoorthy K, Gopinath CS. ZnO–ZnS heterojunctions: a potential candidate for optoelectronics applications and mineralization of endocrine disruptors in direct sunlight. ACS Omega 2017;6768–81.

[67] Thomas J, Chitra KR. Nano gold doped nano TiO2 - An efficient solar photocatalyst for the degradation of persistent organic pollutants. Adv Mat Res 2014;938:292–6. https://doi.org/10.4028/www.scientific.net/AMR.938.292.

[68] Parveen S, Bhatti I, Ashar A, Javed T, Mohsin M, Hussain MT, et al. Synthesis, characterization and photocatalytic performance of iron molybdate (Fe2 (MoO4) 3) for the degradation of endosulfan pesticide. Mater Res Express 2020.

[69] Mudhoo A, Bhatnagar A, Rantalankila M, Srivastava V, Sillanpää M. Endosulfan removal through bioremediation, photocatalytic degradation, adsorption and membrane separation processes: a review. Chem Eng J 2019;360:912–28. https://doi.org/10.1016/j.cej.2018.12.055.

[70] Vinoth Kumar J, Karthik R, Chen SM, Natarajan K, Karuppiah C, Yang CC, et al. 3D flower-like gadolinium molybdate catalyst for efficient detection and degradation of organophosphate pesticide (Fenitrothion). ACS Appl Mater Interfaces 2018;10:15652–64. https://doi.org/10.1021/acsami.8b00625.

[71] Zangiabadi M, Saljooqi A, Shamspur T, Mostafavi A, Mehrabi F, Mohamadi M. Efficient degradation of Fenitrothion pesticide and reaction mechanism with GO-Fe3O4/TiO2 mesoporous photocatalyst under visible light irradiation. Pistachio Health J 2019;10–21.

[72] Zangiabadi M, Shamspur T, Saljooqi A, Mostafavi A. Evaluating the efficiency of the GO-Fe3O4/TiO2 mesoporous photocatalyst for degradation of chlorpyrifos pesticide under visible light irradiation. Appl Organomet Chem 2019.

[73] Amiri H, Nabizadeh R, Silva Martinez S, Jamaleddin Shahtaheri S, Yaghmaeian K, Badiei A, et al. Response surface methodology modeling to improve degradation of chlorpyrifos in agriculture runoff using TiO2 solar photocatalytic in a raceway pond reactor. Ecotoxicol Environ Saf 2018;147:919–25. https://doi.org/10.1016/j.ecoenv.2017.09.062.

[74] Kanmoni VGG, Daniel S, Raj GAG. Photocatalytic degradation of chlorpyrifos in aqueous suspensions using nanocrystals of ZnO and TiO 2. React Kinet Mech Catal 2012;106:325–39. https://doi.org/10.1007/s11144-012-0433-5.

[75] Majhi D, Bhoi YP, Samal PK, Mishra BG. Morphology controlled synthesis and photocatalytic study of novel CuS-Bi 2 O 2 CO 3 heterojunction system for chlorpyrifos degradation under visible light illumination. Appl Surf Sci 2018;455:891–902. https://doi.org/10.1016/j.apsusc.2018.06.051.

https://www.twirpx.org & http://chemistry-chemists.com

[76] Mirmasoomi SR, Mehdipour Ghazi M, Galedari M. Photocatalytic degradation of diazinon under visible light using TiO2/Fe2O3nanocomposite synthesized by ultrasonic-assisted impregnation method. Sep Purif Technol 2017;175:418–27. https://doi.org/10.1016/j.seppur.2016.11.021.

[77] Soltani-nezhad F, Saljooqi A, Shamspur T, Mostafavi A. Photocatalytic degradation of imidacloprid using GO/Fe3O4/TiO2-NiO under visible radiation: optimization by response level method. Polyhedron 2019;165:188–96. https://doi.org/10.1016/j.poly.2019.02.012.

[78] Chaudhuri M, Zuhali H, Affam AC. Degradation of pesticide chlorothalonil by visible light-responsive photocatalyst ferrioxalate and H2O2 under solar irradiation. Int J Photoenergy 2013;2013. https://doi.org/10.1155/2013/435017.

[79] Samanta P, Desai AV, Let S, Ghosh SK. Advanced porous materials for sensing, capture and detoxification of organic pollutants toward water remediation. ACS Sustain Chem Eng 2019;7:7456–78. https://doi.org/10.1021/acssuschemeng.9b00155.

[80] Castiglioni S, Bagnati R, Fanelli R, Pomati F, Calamari D, Zuccato E. Removal of pharmaceuticals in sewage treatment plants in Italy. Environ Sci Tech 2006;40:357–63. https://doi.org/10.1021/es050991m.

[81] Ahmed MB, Zhou JL, Ngo HH, Guo W. Adsorptive removal of antibiotics from water and wastewater: progress and challenges. Sci Total Environ 2015;532:112–26. https://doi.org/10.1016/j.scitotenv.2015.05.130.

[82] Zhang G, Guan W, Shen H, Zhang X, Fan W, Lu C, et al. Organic additives-free hydrothermal synthesis and visible-light-driven photodegradation of tetracycline of WO3 nanosheets. Ind Eng Chem Res 2014;53:5443–50. https://doi.org/10.1021/ie4036687.

[83] Naqvi FK, Faraz M, Beg S, Khare N. Synthesis and phase transformation studies of dysprosium-doped Bi4V2O11 nanoparticles and their application in visible light photocatalytic degradation of tetracycline drug. ACS Omega 2018;3:11300–6. https://doi.org/10.1021/acsomega.8b01012.

[84] Wu S, Hu H, Lin Y, Zhang J, Hu YH. Visible light photocatalytic degradation of tetracycline over TiO2. Chem Eng J 2020;382. https://doi.org/10.1016/j.cej.2019.122842.

[85] Wang C, Wu Y, Lu J, Zhao J, Cui J, Wu X, et al. Bioinspired synthesis of photocatalytic nanocomposite membranes based on synergy of Au-TiO2 and polydopamine for degradation of tetracycline under visible light. ACS Appl Mater Interfaces 2017;9:23687–97. https://doi.org/10.1021/acsami.7b04902.

[86] Li C, Yu S, Che H, Zhang X, Han J, Mao Y, et al. Fabrication of Z-scheme heterojunction by anchoring mesoporous γ-Fe2O3 nanospheres on g-C3N4 for degrading tetracycline hydrochloride in water. ACS Sustain Chem Eng 2018;6:16437–47. https://doi.org/10.1021/acssuschemeng.8b03500.

[87] Liu HY, Liang C, Niu CG, Huang DW, Du YB, Guo H, et al. Facile assembly of g-C3N4/Ag2CO3/graphene oxide with a novel dual Z-scheme system for enhanced photocatalytic pollutant degradation. Appl Surf Sci 2019;475:421–34. https://doi.org/10.1016/j.apsusc.2019.01.018.

[88] Lan Y, Li Z, Li D, Yan G, Yang Z, Guo S. Graphitic carbon nitride synthesized at different temperatures for enhanced visible-light photodegradation of 2-naphthol. Appl Surf Sci 2019;467–468:411–22. https://doi.org/10.1016/j.apsusc.2018.10.152.

[89] Kumar R, Ranjith D, Haldorai KS, Kandasami Y, Kumar, Rajendra TR. Nitrogen-implanted ZnO nanorod arrays for visible light photocatalytic degradation of a pharmaceutical drug acetaminophen. ACS Omega 2019;11973–9.

[90] Sambandam B, Surenjan A, Philip L, Pradeep T. Rapid synthesis of C-TiO2: tuning the shape from spherical to Rice grain morphology for visible light photocatalytic application. ACS Sustain Chem Eng 2015;3:1321–9. https://doi.org/10.1021/acssuschemeng.5b00044.

[91] Avisar D, Horovitz I, Lozzi L, Ruggieri F, Baker M, Abel ML, et al. Impact of water quality on removal of carbamazepine in natural waters by N-doped TiO2 photo-catalytic thin film surfaces. J Hazard Mater 2013;244–245:463–71. https://doi.org/10.1016/j.jhazmat.2012.09.058.

https://www.twirpx.org & http://chemistry-chemists.com

[92] Abazari R, Mahjoub AR. Amine-functionalized Al-MOF#@ yxSm2O3-ZnO: a visible light-driven nanocomposite with excellent photocatalytic activity for the photo-degradation of amoxicillin. Inorg Chem 2018;57:2529–45. https://doi.org/10.1021/acs.inorgchem.7b02880.

[93] Gu S, Li W, Bian Y, Wang F, Li H, Liu X. Highly-visible-light photocatalytic performance derived from a lanthanide self-redox cycle in Ln2O3/BiVO4 (ln: Sm, Eu, Tb) redox heterojunction. J Phys Chem C 2016;120:19242–51. https://doi.org/10.1021/acs.jpcc.6b06436.

[94] Karthik R, Kumar CS-M, Karuppiah C, Cheng Y-H, Muthuraj V. A study of electrocatalytic and photocatalytic activity of cerium molybdate nanocubes decorated graphene oxide for the sensing and degradation of antibiotic drug chloramphenicol. ACS Appl Mater Interfaces 2017;6547–59.

[95] Awofiranye OS, Modise SJ, Naidoo EB. Design and synthesis of polyvinyl alcohol derived conjugated polyene modified TiO2 for visible-light degradation of chloramphenicol. J Environ Chem Eng 2020.

[96] Zhang H, Wu W, Li Y, Wang Y, Zhang C, Zhang W, et al. Enhanced photocatalytic degradation of ciprofloxacin using novel C-dot@nitrogen deficient g-C3N4: synergistic effect of nitrogen defects and C-dots. Appl Surf Sci 2019;465:450–8. https://doi.org/10.1016/j.apsusc.2018.09.183.

[97] Zhang G, Xue Y, Wang Q, Wang P, Yao H, Zhang W, et al. Photocatalytic oxidation of norfloxacin by Zn0.9Fe0.1S supported on Ni-foam under visible light irradiation. Chemosphere 2019;230:406–15. https://doi.org/10.1016/j.chemosphere.2019.05.015.

[98] Remani KC, Binitha NN. Photocatalytic degradation of norfloxacin under UV, visible and solar light using ceria nanoparticles. Mater Today Proc 2020;246–51. https://doi.org/10.1016/j.matpr.2020.01.212.

[99] Chen M, Chu W. Efficient degradation of an antibiotic norfloxacin in aqueous solution via a simulated solar-light-mediated Bi 2WO 6 process. Ind Eng Chem Res 2012;51:4887–93. https://doi.org/10.1021/ie300146h.

[100] Yang H, Mei L, Wang P, Genereux J, Wang Y, Yi B, et al. Photocatalytic degradation of norfloxacin on different TiO2-:X polymorphs under visible light in water. RSC Adv 2017;7:45721–32. https://doi.org/10.1039/c7ra09022f.

[101] Zhang X, Li D, Wan J, Yu X. Preparation of Ti mesh supported N-S-C-tridoped TiO2 nanosheets to achieve high utilization of optical energy for photocatalytic degradation of norfloxacin. RSC Adv 2016;6:17906–12. https://doi.org/10.1039/c5ra27639j.

[102] Aram M, Farhadian M, Solaimany Nazar AR, Tangestaninejad S, Eskandari P, Jeon BH. Metronidazole and cephalexin degradation by using of urea/TiO2/ZnFe2O4/clinoptiloite catalyst under visible-light irradiation and ozone injection. J Mol Liq 2020;304. https://doi.org/10.1016/j.molliq.2020.112764.

[103] Li R, Cai M, Xie Z, Zhang Q, Zeng Y, Liu H, et al. Construction of heterostructured CuFe2O4/g-C3N4 nanocomposite as an efficient visible light photocatalyst with peroxydisulfate for the organic oxidation. Appl Catal Environ 2019;244:974–82. https://doi.org/10.1016/j.apcatb.2018.12.043.

[104] Wang L, Cheng H. Birnessite (γ-MnO2) mediated degradation of organoarsenic feed additive p-arsanilic acid. Environ Sci Tech 2015;49:3473–81. https://doi.org/10.1021/es505358c.

[105] Ordóñez EY, Quintana JB, Rodil R, Cela R. Determination of artificial sweeteners in water samples by solid-phase extraction and liquid chromatography-tandem mass spectrometry. J Chromatogr A 2012;1256:197–205. https://doi.org/10.1016/j.chroma.2012.07.073.

[106] Ghosh M, Chowdhury P, Ray AK. Study of solar photocatalytic degradation of Acesulfame K to limit the outpouring of artificial sweeteners. Sep Purif Technol 2018;207:51–7. https://doi.org/10.1016/j.seppur.2018.05.062.

[107] Calza P, Gionco C, Giletta M, Kalaboka M, Sakkas VA, Albanis T, et al. Assessment of the abatement of acelsulfame K using cerium doped ZnO as photocatalyst. J Hazard Mater 2017;323:471–7. https://doi.org/10.1016/j.jhazmat.2016.03.093.

https://www.twirpx.org & http://chemistry-chemists.com

https://www.twirpx.org & http://chemistry-chemists.com

17

Agricultural application of visible light photocatalyst

Jih-Hsing Chang, Mohanraj Kumar, and Shan-Yi Shen

DEPARTMENT OF ENVIRONMENTAL ENGINEERING AND MANAGEMENT, CHAOYANG UNIVERSITY OF TECHNOLOGY, TAICHUNG, TAIWAN

1 Introduction

Based on the US Environmental Protection Agency (USEPA) definition, pesticides refer to any substance or mixture that can prevent, destroy, repel, or mitigate pests. Pesticides can be chemicals, organisms (such as viruses or bacteria), fungicides, antiinfectives, or any means to fight pests. Humans use pesticides to kill harmful substances (e.g., pests) in order to protect agricultural products [1]. For the targeted pests, most of the pesticides used are insecticides and herbicides, but others include fungicides, acaricides, molluscicides, and so on [2]. The pesticides can be classified as organochlorines (OCs), carbamates, organophosphates, and substituted urea according to their chemical properties. Among them, OCs are harmful and belong to persistent organic pollutants (POPs), which can cause significant harm to the environment. Organochlorine pesticides are mainly insecticides and have been widely used in agriculture and mosquito control from the 1940s to the 1980s [3]. The OCs' representative compounds are dichlorodiphenyltrichloroethane (DDT), chlordane, dieldrin, methoxychlor, lindane, and benzene hexachloride. These belong to endocrine disruptors (EDCs) containing high chronic; i.e., about 1 million poisoning cases occur every year [4, 5].

Pesticides are more likely to cause health hazards in the fabrication and formulation process due to the high persistence and bioaccumulation of pesticides. Thus agricultural lands and in coastal environments [6], marine mammals [7], seafood, birds, and humans [8] are affected. In addition, pesticides also have long-distance transport characteristics, meaning they can be moved through air or water [9]; for example, hexachlorocyclohexane and endosulfan were transported from farmland to estuaries in tropical conditions, eventually posing serious risks to aquatic biota [10]. Fig. 1 shows the current main OC pesticides.

At present, the by-products of pesticides have received much attention due to their higher concentrations and toxicities than those of the parent. DDD and DDE are the more toxic by-products of DDT; dieldrin is a poisonous by-product of aldrin. Therefore, European regulations (91/414/EEC) stipulated that it must provide environmental data

Nanostructured Materials for Visible Light Photocatalysis. https://doi.org/10.1016/B978-0-12-823018-3.00010-5
Copyright © 2022 Elsevier Inc. All rights reserved.

https://www.twirpx.org & http://chemistry-chemists.com

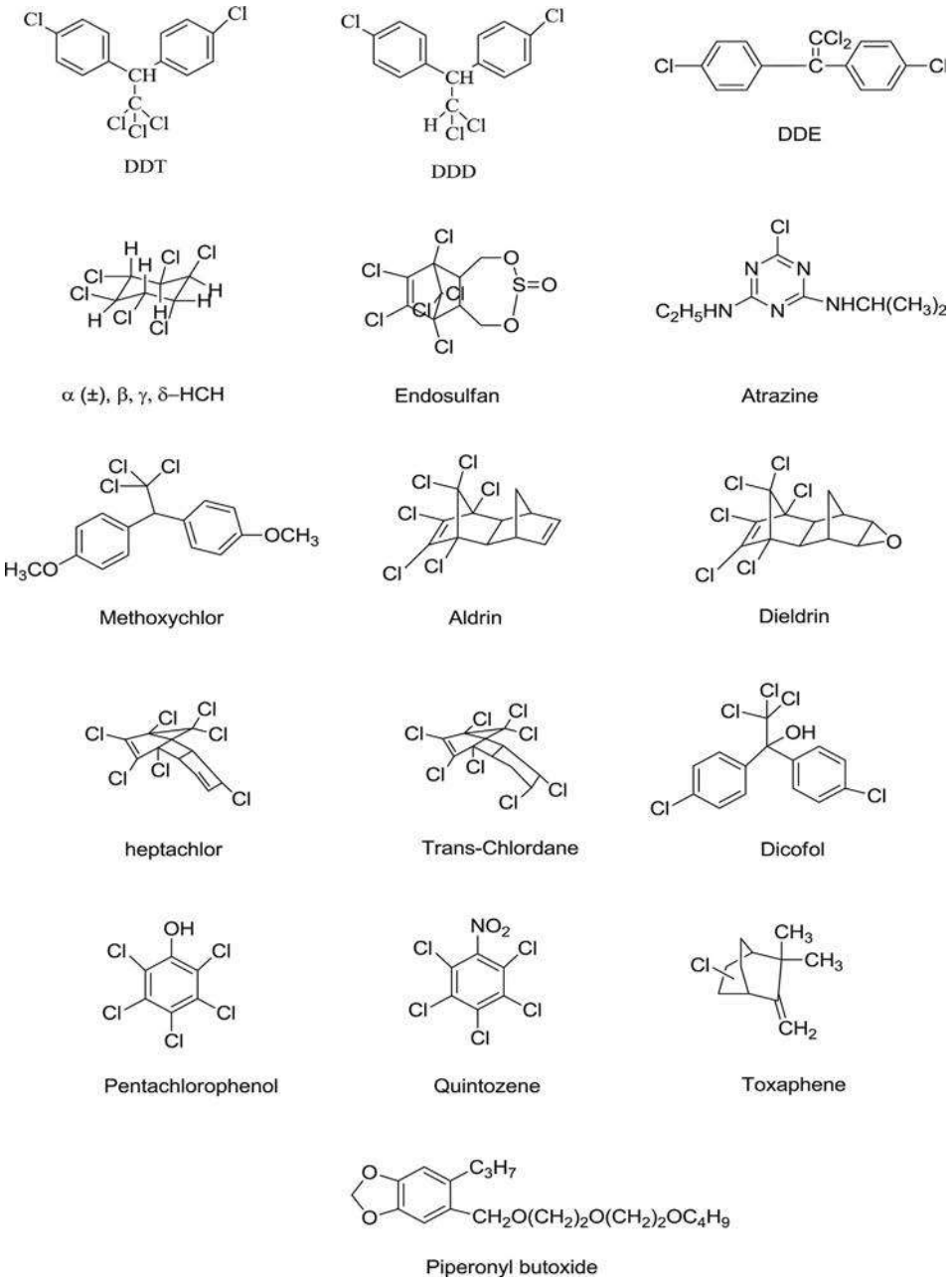

FIG. 1 Chemical structures of common organochlorine pesticides [11].

https://www.twirpx.org & http://chemistry-chemists.com

on complete metabolites and the amount of degradation and reaction products before new pesticides are launched on the market.

1.1 Consumption and production of pesticides

The largest consumer of pesticides in the world is Europe, followed by Asia. In addition, China, America, Brazil, France, and Japan are the largest pesticide producers/traders in the world [12]. In 2007, 44.75% of total pesticide sales were contributed by the United States. Atrazine is a widely used pesticide, especially in the developed countries. And its consumption reached 57.39 million pounds in 2005 [12]. The worldwide consumption of pesticides is shown in Table 1 [11]. India's pesticide production began in 1952; the country is the second-largest pesticide producer in Asia after China, and ranks 12th in the world [13]. Moreover, industrial-grade pesticides' production has been increasing steadily from 5000 tons in 1958 to 102,240 tons in 1998 in India. From 1996 to 1997, the demand for pesticides was estimated to be about US$500 million, accounting for about 2% of the global market.

1.2 Pernicious effects of pesticides

The harmful effects caused by the use of pesticides are far-reaching and have a life-threatening effect on nontarget species, including animals, plant biodiversity, aquatic and terrestrial ecosystems. According to data, about 80%–90% of the pesticides will be volatilized within a few days after pesticide application [14]. The volatilized pesticides will vaporize quickly, which causes danger to nontarget organisms. The waste pesticides will be harmful to the existence of bald eagles, peregrine falcons, and ospreys [15]. Moreover, air, water, and soil are also polluted to harmful levels by these chemicals. Depending on the solubility of pesticides, there are two different ways to enter the ecosystem. Water-soluble pesticides are dissolved in water and transported to watercourses, rivers, and lakes, causing damage to nontarget species; fat-soluble pesticides enter the animal body through the bio-amplification process.

Table 1 Consumption of pesticides worldwide [11].

Order	Nation	Consumption (kg/ha)
1	Taiwan	17
2	China	13
3	Japan	12
4	United States	7
5	Korea	7
6	France	5
7	United Kingdom	5
8	India	102,240 metric tons in 1998

https://www.twirpx.org & http://chemistry-chemists.com

1.2.1 Impact on humans

The long-term or random use of pesticides has caused serious health problems. In the past few decades, these chemical exposures have increased significantly, with increasing use of pesticides. According to a WHO report, there have been approximately 3,000,000 pesticide poisoning cases and 220,000 deaths in developing countries [16], and 2.2 million people face the threat of pesticide exposure [17]. Pesticides can enter the human body through ingestion, inhalation, or contact with the skin's upper layer. Although the human body has a mechanism to remove toxins, in some cases, it is still absorbed through the circulatory system and remains in the body. Studies have shown that pesticides are closely related to the development of cancer. Long-term exposure to pesticides has a higher risk of various malignant tumors, such as leukemia, neuroblastoma, sarcoma, ovarian cancer, lung cancer, stomach cancer, colon cancer, bladder cancer, and rectal cancer [18].

1.2.2 Impact on biodiversity

Water contaminated by pesticides can cause harm to aquatic organisms. It will affect aquatic plants, reduce dissolved oxygen in the water system, and cause changes in fish groups' physiology and behavior. About 80% of the dissolved oxygen is provided by aquatic plants, which is essential for aquatic organisms' survival. Aquatic animals are killed by herbicides leading to lower dissolved oxygen levels, which ultimately results in suffocation and decreased fish productivity. Due to the pollution caused by surface runoff and spray drift of farmland, the pesticide content in surface water is much higher than in groundwater. Pesticides enter the ground through the leakage of contaminated surface water, improper dumping, and accidental overflow, not only causing the death of nontarget plants, but also having lethal effects on terrestrial plants. In addition, despite the low-dose herbicides, sulfonylureas, sulfonamides, or imidazolinones will also have harmful effects on the productivity of nontarget crops, natural plants, and wildlife [19].

1.2.3 Soil pollution

The pesticides and pesticide transformation products will be moved from the soil through runoff and leaching, thereby causing health problems for people drinking water. The retention degree of pesticides and transformation products in the soil depends on the interaction between soil and pesticide characteristics. The most influential soil characteristic is the content of organic matter (OM). The pesticides and conversion product's adsorption increases with the organic content. In addition, soil pH is also an essential factor, and the adsorption of pesticides increases as the soil pH decreases [20].

2 Kind and decomposition of pesticides

Organochlorines (OCs) are a significantly dangerous category of pesticides, and their use has been prohibited or restricted in some countries. The main sources of OCs include the food industry, agriculture, and sewage waste. When high concentrations of OCs in wastewater are discharged into water bodies, this leads to environmental problems. Due to their

https://www.twirpx.org & http://chemistry-chemists.com

high toxicity, persistence, and bioaccumulation, OCs must be removed from wastewater. Organochlorine insecticides are organic compounds with the basic structure of hydrocarbons, and the chlorine atoms are connected to the carbon atoms, which have insecticidal effects. Most organochlorine pesticides have the properties of low production cost and long-term residue in animals, plants, and the environment. Such compounds have excellent insecticidal effects and were in some of the most common environmental pollutants in the world. The following section introduces common organochlorine pesticides.

2.1 Dichlorodiphenyltrichloroethane

DDT was widely used as an insecticide in the 1940s and 1970s and used in agriculture and public health to examine malaria and other mosquito diseases (such as yellow fever and encephalitis). The pesticides have properties of persistence and biomagnification in the food chain [21]; DDT can still be found in soils [22] and continues to pose significant risks to humans and the environment [23]. In order to effectively degrade DDT in the environment, bioremediation treatment [24], soil excavation, incineration or thermal degradation [25], photocatalytic technology, soil washing [26], and metal-catalyzed reactions [27] were studied. However, these methods are affected by the slow degradation ability and toxic by-products formation, resulting in limited treatment efficiency.

To solve these problems, nanoparticles that are highly efficient, cost-effective, and environmentally friendly have been used worldwide, which can degrade DDT by about 100% in a short period of time [28]. Fenton oxidation under acidic conditions has proven to be an effective and economical technology for degrading DDT [29]. Gautam and Suresh [30] used the Mg/Pd system to carry out the dechlorination reaction of DDT in an aqueous phase containing surfactants, in which 100 ppm of DDT was successfully degraded in 1 h. In addition, Ni/Fe nanoparticles can effectively degrade DDT in aqueous solutions under mild acid/alkalescent conditions.

2.2 Endosulfan

This pesticide can be used on various vegetables, fruits, grains, and cotton [31]. It has two stereoisomers, *a* (half-life = 60 days) and *b* (half-life = 800 days), formed in a ratio of 7:3 [32]. The two isomers undergo photolysis when exposed to light and produce endosulfan diol (half-life = 7 years). In the soil, endosulfan sulfate was formed after the biodegradation process, which had the same toxicity as the parent compound and is more durable in the environment [33]. Therefore, endosulfan was widely found in surface water and groundwater around the world [34]. Although the *a* and *b* types of endosulfan are highly stable, the silver-doped TiO_2 nano-photocatalyst can effectively degrade endosulfan [35] and completely mineralize the toxic metabolite endosulfan sulfate.

2.3 Chlordane

In 1948, chlordane was first registered for use in the United States. It was also used widely to control household termites in Japan in the early 1980s [36]. Chlordane and related

https://www.twirpx.org & http://chemistry-chemists.com

compounds have high partition coefficients (log $K_{ow} = 6.0$), which are still ubiquitous in the biosphere, humans, and the environment, and have caused concern about their unfavorable effects [37]. Due to chlordane's high persistence and toxicity, it is listed as a persistent organic pollutants (POP). Chlordane is a composite of more than 50 chemical substances; the trans-chlordane of 13.2% and cis-chlordane of 11.3% have the highest contents in the mixture. Chlordane can be degraded by microbial methods [38].

2.4 Endrin

Endrin is widely used in agriculture against rice insects and has caused environmental hazards, resulting in restricted use in several countries/regions. It has persistent in the soil with about 6 years of half-life [39]. Studies have shown that endrin can be degraded by microbial treatment [40]. Butler et al. [41] used acidified zinc to dechlorinate endrin completely reductively.

2.5 Heptachlor

Heptachlor is widely used in developing countries, mainly targeting termites and soil insects in the 1960s and 1970s. This pesticide is carcinogenic with a half-life of 250 days [42]. Up to 14 and 16 years after pesticides' use, trace amounts of heptachlor and the more persistent by-product heptachlor epoxide were still detected in the soil. Therefore, developing countries banned its use or restricted production and use in the 1970s [43]. However, due to its low production cost and wide range of uses, some developing countries continue to use this pesticide. The degradation of heptachlor by microorganisms or bacterial fungi has been extensively explored [44]. Several white-rot fungi (Phlebia genus) can degrade the heptachlor by 71%–90% [38] and also degrade the toxic metabolites (about 16%) of heptachlor epoxide.

3 Factors in the photocatalytic activities

Due to the rapid development of industry, the number of pollutants has also increased significantly. Pollutants include chemicals such as cosmetics, soaps, insect repellents and painkillers, antibiotics, and stimulants [45]. To deal with these emerging pollutants, new treatment technologies are urgently needed. The advanced oxidation process (AOP) has been verified as a feasible method for reducing pollutants; it includes O_3/UV, H_2O_2/UV, O_3/H_2O_2/UV, Fenton oxidation, and photocatalysis. Among these, heterogeneous photocatalysis has proved to mineralize pollutants completely in the gas or liquid phase [46].

Heterogeneous photocatalysis technology has the potential for environmental remediation. The world has been committed to improving the treatment efficiency of photocatalytic technology for more than 10 years. However, there are still many problems to overcome for large-scale applications under photocatalytic reaction systems. At present, photocatalytic efficiency improvement has attracted attention because it is more economical and robust for environmental remediation. Photocatalysis is an effective method

https://www.twirpx.org & http://chemistry-chemists.com

of removing pollutants, and has high potential. Therefore, researchers are committed to overcoming light intensity distribution, metal doping, visible photocatalytic range, fixed catalyst preparation, catalyst recovery, and large-scale application of the photocatalytic system.

The hydroxyl radicals produced by the photocatalytic reaction process have a high oxidizing capacity (2.80 V) [47], and the degradation of pollutants will not produce harmful disinfection by-products. Nano-scale TiO_2 with strong oxidizing ability has been widely used as a photocatalyst, which can decompose pollutants or organic compounds under ultraviolet light [48, 49]. Under ultraviolet light irradiation, the electron in the valence band of titanium dioxide was excited to the conduction band, forming an electron-hole pair. The holes react with water or hydroxide to produce hydroxyl radicals [50, 51]. However, the main limitation of the photocatalytic system is that the electron-hole pair is easy to recombine, which affects the yield of hydroxyl radicals and makes the application difficult [52].

The literature indicates that the coupling of doped graphene composites and a nano-scale crystal could facilitate the separation of electron-hole pairs, to reduce recombination and improve photocatalytic activity [53]. In addition, combining photocatalysis and membrane separation technology can also produce synergistic effects, which has high potential for producing clean water [54]. However, the photocatalytic system used on a large scale still has many problems, such as configuration design, quantum efficiency, influence of operating parameters, catalyst deactivation, combination of photocatalysis, and other technologies that need to be overcome.

The mechanism of photocatalysis is the reaction of a semiconductor catalyst with an appropriate light wavelength. For photocatalysts, electrons are located in the valence band under normal room temperature conditions. When an appropriate wavelength and energy larger than the material energy gap are provided, the electrons will be excited to rise from the valence band (VB) to the conduction band (CB) and thus produce electron-hole pairs (e/h^+), as shown in Fig. 2 [55–57]. The energy gap of a semiconductor material extends from the top of the filled VB to the empty CB's bottom. The energy gap level can also be used to evaluate the ability of oxidation-reduction [58]. Fig. 3 shows the energy gap level [59–61].

In the photocatalytic system where semiconductors exist, when the incident photon energy ($h\nu$) is greater than the energy gap of the semiconductor, the electrons of the VB (e^-) will jump to the CB and leave positive holes in the VB (h^+), which excites electrons from the VB to the CB [55]. The main reaction is shown in Eq. (1). For anatase crystals of titanium dioxide semiconductors, due to the energy gap being 3.2 eV, a UV light source less than 390 nm is required for effective excitation. Due to the continuous input of incident photon energy, electron-hole pairs can continue to be generated. Ti^{3+} may capture the charge, and O^- defects in the titanium dioxide or electron-hole pairs undergo a recombination reaction and consume energy. In addition, charge carriers can be transferred to titanium dioxide and carry out a redox reaction with the surface adsorbate; the hole can oxidize the hydroxide or water on the titanium dioxide catalyst's surface to produce hydroxyl radicals. The reactions are shown below.

https://www.twirpx.org & http://chemistry-chemists.com

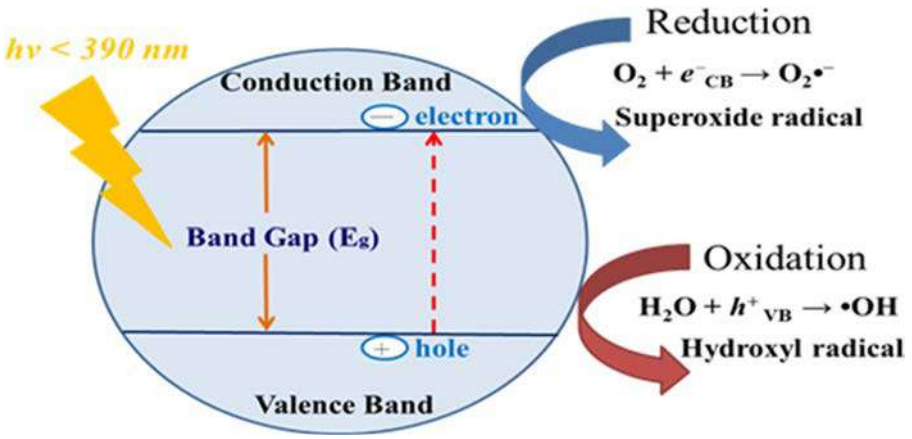

FIG. 2 Schematic diagram of electron-hole pair generation and interface reaction after titanium dioxide is excited by light.

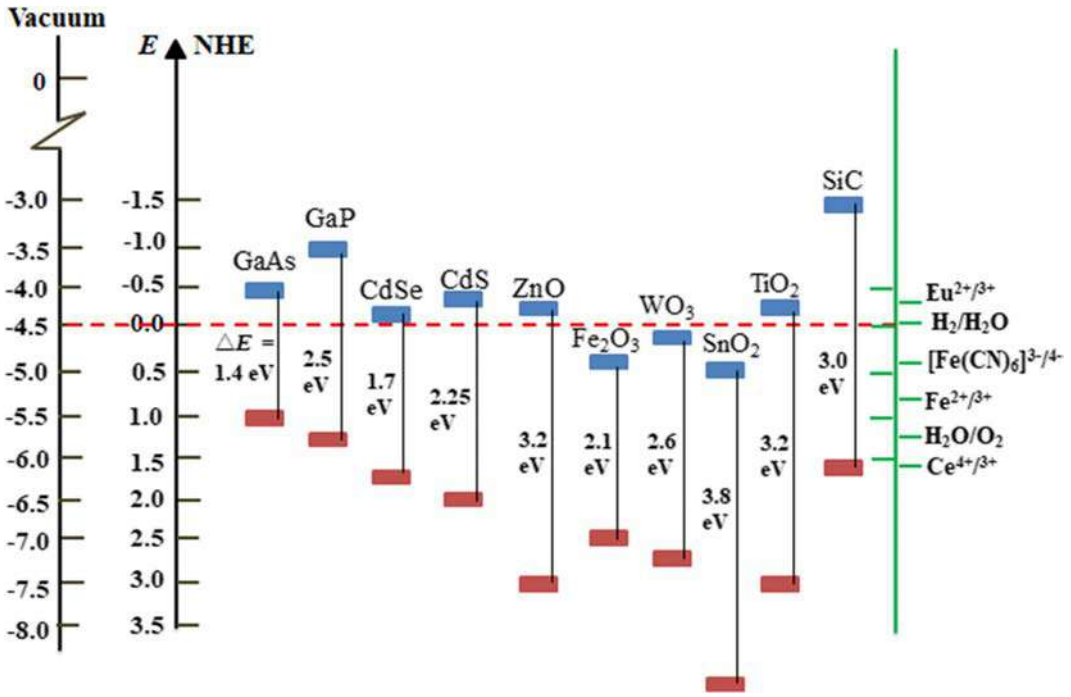

FIG. 3 The energy gap of different semiconductor materials.

https://www.twirpx.org & http://chemistry-chemists.com

$$TiO_2 + h\nu \rightarrow h^+{}_{VB} + e^-{}_{CB} \quad (1)$$

$$e^-{}_{CB} + h^+{}_{VB} \rightarrow \text{energy} \quad (2)$$

$$H_2O + h^+{}_{VB} \rightarrow \bullet OH + H^+ \quad (3)$$

Hydroxyl radicals are very strong oxidants, which can quickly oxidize organic substances to achieve mineralization reaction and produce inorganic salts, water, and carbon dioxide (Eq. (4)). In addition, the electrons will quickly react with the oxygen molecules adsorbed on the titanium dioxide to form superoxide anion radicals (Eq. (5)); at the same time, they can further react with H^+ to form hydrogen peroxide radicals ($\bullet OOH/HO_2\bullet$) form Eq. (6). Through electrochemical reduction to produce hydrogen peroxide, the above active oxygen species will contribute to the oxidative degradation of pollutants.

$$\bullet OH + \text{pollutant} \rightarrow H_2O + CO_2 \quad (4)$$

$$O_2 + e^-{}_{CB} \rightarrow O_2\bullet^- \quad (5)$$

$$O_2\bullet^- + H^+ \rightarrow \bullet OOH \quad (6)$$

$$\bullet OOH + \bullet OOH \rightarrow H_2O_2 + O_2 \quad (7)$$

$$O_2\bullet^- + \text{pollutant} \rightarrow CO_2 + H_2O \quad (8)$$

$$\bullet OOH + \text{pollutant} \rightarrow CO_2 + H_2O \quad (9)$$

3.1 pH influence

The essential operational parameter of organic mediate in photocatalytic degradation is the pH, which is one of the decisive factors for the catalyst's surface charge characteristics and hydroxyl radicals' formation mechanism. The reaction between light-generated holes and hydroxide ions produces the hydroxide radicals on the nano-TiO_2 surface. In neutral or high pH values, hydroxide radicals are considered the most important species [62, 63], and positively charged holes are considered to be the main substance causing oxidation reactions under lower pH. At high pH, the electrons of VB become more conductive, while at lower pH, the hole gradually becomes invalid. Hydroxyl radicals are the main oxidation substance in the photocatalytic nano-TiO_2. Higher pH values are considered to be more beneficial to water treatment. The size of the aggregate formed by TiO_2 particles is also affected by pH. When the pH is close to pH_{zpc}, the photocatalyst particles tend to agglomerate [64], resulting in a decrease in surface area and active sites, thereby reducing the photodegradation rate. The media's pH value will affect the ionization or formation of organic compounds, affecting the electrostatic interaction between the photocatalyst and the pollutant molecules; also, the adsorption reaction is faster than the photocatalysis, the surface blockage may occur, and the degradation efficiency may be reduced significantly.

The pH value affects the interaction between solvent molecules and catalysts and the free radicals or intermediates formed during the photocatalytic reaction. pH plays an important role in the adsorption of the TiO_2 surface, thereby affecting the removal efficiency. TiO_2 is an amphotericin aqueous solution, and depending on the preparation

https://www.twirpx.org & http://chemistry-chemists.com

method, the zero charge point (pH_{zpc}) of nano-TiO_2 is between 4.5 and 7 [65]. In acidic and alkaline conditions, nano-TiO_2 can be protonated and deprotonation according to the following equation (Eqs. 10, 11) [66]. Under acidic conditions (i.e., $pH < pH_{zpc}$), the surface of nano-TiO_2 remains positively charged, and the attraction of negatively charged pollutants was increased and easy to adsorb to the activated surface, thus increasing the subsequent photocatalytic reaction [65, 67]. Under alkaline (i.e., $pH > pH_{zpc}$), the surface of nano-titanium dioxide is negatively charged. The adsorption of positively charged pollutants is effective.

$$pH < pH_{zpc} \rightarrow TiOH + H^+ \leftrightarrow TiOH_2^+ \tag{10}$$

$$pH > pH_{zpc} \rightarrow TiOH + OH^- \leftrightarrow TiO^- + H_2O \tag{11}$$

Hydroxyl radicals generated by a reaction between hydroxide ions and holes are also affected by the medium's pH. In an alkaline solution, there are more hydroxide ions on the surface of titanium dioxide; it is easier to form hydroxide radicals to improve photodegradation efficiency [68]. Liu et al. [69] reported that the degradation efficiency of methamidophos under alkaline conditions was two times that of acidic conditions. However, one study still indicates that compared with neutral or alkaline pH, TiO_2 photocatalytic degradation of certain organic pollutants under acidic pH conditions is effective [70]. Fernández et al. [71] found that azo-dye orange II has the most obvious effect under pH 3 conditions. It can be understood that pH has a significant effect on the photocatalytic reaction, and it is necessary to point out from the literature or further experimental research that the most suitable pH value should be selected.

3.2 Intensity of light

Selecting an appropriate light intensity can effectively improve the efficiency of the catalytic reaction. The degradation rate increased linearly under a low-intensity light source (0–20 mW/cm^2), showing that increasing light intensity can increase the photocatalytic treatment efficiency of nano-TiO_2 [54]. Under a medium-intensity light source (e.g., 25 mW/cm^2), photocatalysis's reaction rate depends on the square root of the light intensity. Under high-intensity light sources, the reaction rate has no significant variation with the light intensity. Because the reaction rate depended on the mass transfer and the transfer of the adsorption and desorption of saturated solids on the catalyst surface [72], and reports show that the light intensity is increased by 1.5 times, nano-TiO_2 photocatalysis can increase phenol's degradation efficiency to 100%.

3.3 Flow rate of feed

The flow rate of feed is related to the detention time, which will affect the operating system's treatment efficiency. Increasing the flow rate can reduce the boundary layer's external mass transport and resistance in the liquid phase [73]. Reducing the hydraulic detention time may result in a decrease in reaction efficiency. Studies from Behnajady

https://www.twirpx.org & http://chemistry-chemists.com

et al. have shown that the decolorization of the dye is decreased when increasing the flow rate. In addition, the removal efficiency increases as the light intensity increases. When the flow rate is increased for degrading other pollutants, this will affect the photocatalytic activity and adsorption on the surface of TiO_2 [74], resulting in a significant decrease in degradation efficiency from 93% to 58%. Although increasing the flow rate will enhance turbulence and thus overcome the limitations of mass transport, the flow rate exceeding the optimal value will adversely affect photocatalytic activity. Therefore, it is necessary to consider simultaneously the correlation between the flow rate and the photocatalytic efficiency to obtain the maximum photocatalytic efficiency.

3.4 Concentration of pollutants

In general, there is a suitable range for pollutants concentration. An increase in the concentration of pollutants in a water body can improve photocatalytic efficiency, and it follows a first-order kinetic reaction. When the concentration exceeds the most suitable range, it has an adverse effect on photocatalytic efficiency [75]. Under the same photocatalyst dosage, light intensity, and irradiation time, the catalyst surface's active sites are constant. Photocatalytic degradation will be decreased when a high concentration of pollutants is present; a possible reason is insufficient production of reactive oxide species. At the same time, the high concentration will also cause ultraviolet light to scatter and reduce the light permeability of the solution. Under the condition of a high concentration of pollutants, the pollutant molecules that were adsorbed may also occupy all active sites on the catalyst, causing a zero-order kinetic reaction. In addition, when the photons reach the surface of the catalyst and undergo photocatalysis, the photons may be intercepted and then attenuate the photon energy [76].

3.5 Number of catalyst loading layers

The multilayer coating of the catalyst can increase the available number of catalysts and increase the photocatalytic reaction. High loading may still reduce the efficiency of the treatment process. In addition, the inner layer of the catalyst material is blocked by the outer surface, thereby increasing the probability of electron-hole pair recombination and reducing the photocatalytic efficiency. Studies have indicated that when the number of the coating is increased to five layers, the photodegradation efficiency has a significant improvement trend. When the number of the coating exceeds five layers, it slowly increases. To achieve effective photocatalytic degradation, an optimal number of coatings is required.

3.6 Immobilization temperature of the catalyst layer

The physical and chemical properties of the film were significantly influenced by the temperature of the photocatalyst immobilization process. Lowering the calcined temperature will reduce the critical load and adversely affect the coated film's mechanical stability.

https://www.twirpx.org & http://chemistry-chemists.com

The diffusion will be significantly increased from carrier molecules into the nano-TiO_2 thin film under higher calcination temperatures. Temperature also plays a key role in the adhesion of the film. The calcined temperature was a remarkable effect on the crystalline type of TiO_2. For instance, the calcined temperature of 450°C is the anatase type, while the rutile type is above 500°C. Under different temperatures, the photocatalysis efficiency of methyl orange was obviously improved at 500°C but decreased for temperatures of 600°C [77]. Therefore, finding an appropriate calcination temperature is still a basic requirement for improving photocatalytic activity and enhancing a substrate's adhesion.

3.7 Species of ions

Photocatalytic degradation will be affected by species of ions present in the water. Ionic matter can affect photogenerated electrons' number, inhibit the recombination of electron-hole pairs, and scavenge hydroxyl radicals. Inorganic anions (such as Cl^-, SO_4^{2-}, NO_3^-, NO_2^-, PO_4^{3-}, and HCO_3^-) in water will reduce photocatalytic activity [78]. The interaction of hole and hydroxide radicals with inorganic ions produces inorganic free radicals. These inorganic free radicals will be adsorbed on the nano-TiO_2 surface and reduce the photocatalytic activity [65]. Studies have shown that the reaction between carbonate (CO_3^{2-}), chloride (Cl^-), and bicarbonate (HCO_3^-) ions with hydroxide radicals will inhibit the photocatalytic performance, as presented in Eqs. (12)–(14):

$$CO_3{}^{2-} + \bullet OH \rightarrow OH^- + CO_3{}^- \tag{12}$$

$$Cl^- + \bullet OH \rightarrow \bullet Cl + OH^- \tag{13}$$

$$HCO_3{}^- + \bullet OH \rightarrow H_2O + CO_3{}^- \tag{14}$$

Ions (Cl^-) may adversely affect photocatalytic degradation by removing holes and hydroxide radicals, and subsequently generate the less reactive chlorine radicals ($Cl\bullet$) and dichloride radicals ($Cl_2\bullet$) [79]. The literature shows that chloride ions' presence is an unfavorable condition on photocatalytic degradation under acidic pH [80, 81].

4 Development of photocatalyst under visible light irradiation

With the rapid growth of population and industrial development, water resources available for human life are being greatly affected. Water contains toxic inorganic components of pathogens, trace metal components, and harmful components such as pesticides and herbicides, which seriously endanger human life. Although trace metals or ions are at low concentrations, they can still cause health issues for humans. Based on research, photocatalytic technology can convert metals into nontoxic ion states and recover them at the same time [82]. In fact, photocatalysis has three different treating mechanisms that can treat trace metal ions or neutral metals in water: when photons were excited, the direct reduction of electrons in the valence band; the indirection reduction of electron donors; and the oxidation process of holes or hydroxyl radicals.

https://www.twirpx.org & http://chemistry-chemists.com

Heterogeneous photocatalysis has the potential to treat water-containing metals or metalloids. Nano-titanium dioxide photocatalysis has been proven to effectively kill various bacteria and viruses in water [83, 84]. The main oxidation contribution is from hydroxide radicals and superoxide O_2•, which have the ability to destroy microbial cells and inhibit their growth. Meanwhile, many studies have used ultraviolet light sources for water disinfection [85, 86]. Textile industry wastewater is dangerous to humans and aquatic organisms. Many studies by nano-titanium dioxide photocatalytic treatment for such wastewater and well degradation efficiency have also been obtained [87–89]. In addition, a special mixing design of the reactor was carried out. For example, the nano-titanium dioxide was coated on the glass beads, and the boron-modified glass beads were designed in the reactor. The special structure can improve the UV radiation exposure and achieve the continuous operation of the reaction tank. Studies have shown that this nano-photocatalytic reaction tank can degrade more than 98% of dyes.

Due to the potential harm of human exposure to pesticide residues, some countries have implemented strict supervision. When pesticides are used, part of the dose is supplied to the soil and enters the environmental area, and the air, groundwater, and surface water are thus polluted. Different pesticides are stored in the soil, and the water leach pollutes the groundwater. Some studies have shown that nano-TiO_2 photocatalytic technology is an effective method for degrading organic and inorganic pesticides. For example, endosulphon, quinolphos, imidacloprid, and chloropyrifos have been degraded successfully by nano-TiO_2 photocatalytic systems [90–92]. These studies have confirmed that nano-TiO_2 is a highly efficient and feasible photocatalyst for degrading and mineralizing different organic pollutants. This is a green technology that can be applied to agriculture and protect crops from diseases. The combination of photocatalysis and membrane separation technology, the composite catalyst of titanium dioxide and graphene, and doping with nano-TiO_2 have shown great application potential and can expand the widespread use of nano-TiO_2 photocatalysis.

4.1 Hybrid photocatalysts

4.1.1 Graphene-based photocatalytic composites

Due to the high specific surface area and efficacious electron mobility of carbon-based, the combination of graphene and nano-TiO_2 photocatalysts has caused broad discussion [93]. So the photocatalyst composed of carbon-based has become an innovative photocatalyst [94]. For the photocatalyst reaction of TiO_2 containing graphene, it is expected that the electrons excited by the light from TiO_2 will be transferred to graphene, thereby inhibiting the recombination phenomenon [95]. In addition, the interface charge transfer from TiO_2 can extend the time for light to excite the electron-hole pairs. A schematic diagram of the reaction mechanism combining graphene and titanium dioxide is shown in Fig. 4. For TiO_2, the valence band and conduction band's energy levels relative to the normal hydrogen electrode (NHE) are 0.39 and 2.81 V, respectively [97]. The Fermi energy level of graphene is 0.08 vs NHE, which can transfer electrons generated after excitation

https://www.twirpx.org & http://chemistry-chemists.com

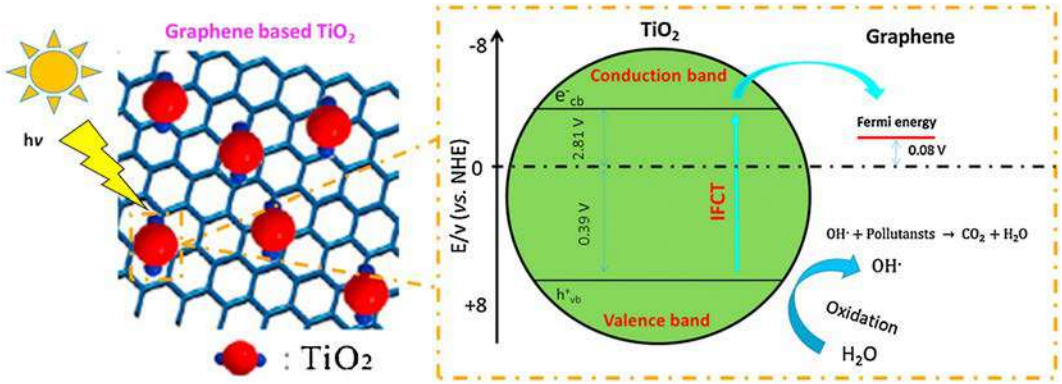

FIG. 4 Mechanism schematic of graphene-based TiO_2 photocatalysis [96].

by titanium dioxide as a trap for electrons. Graphene improves the characteristics of charge transportation, thereby enhancing the photocatalytic effect.

The graphene and nano-titanium dioxide can be synthesized through the chemical bond of the composite or mechanically mixed [98, 99], in which the chemically bonded composite material can obtain the mutually closely bonded nano-TiO_2 and graphene sheets [100]. This interaction promotes the transfer of electrons and achieves the smallest probability of electron-hole pair recombination, thereby ensuring higher photocatalytic activity. Due to the nano-TiO_2, charge transfer to graphene has well photogenerated electrons, and the photocatalytic activity is improved [95]. The combined graphene/TiO_2 composite material's energy gap was decreased from about 3.2 eV (anatase type) to 2.95 eV [101]. The change in this energy gap allowed the photocatalyst to be used in the visible light range, further expanding the wide application of graphene/TiO_2 composite catalyst materials [101, 102]. Since the composite catalyst can be used under visible light conditions, using solar application becomes a cost-effective method.

4.1.2 TiO_2-supported activated carbon composites

The composite material of TiO_2 loaded on activated carbon (AC) can have both adsorption and catalysis, significantly reducing the limitation of mass transmission [103, 104] and improving photocatalyst application. The improvement of the degradation performance of the composite catalyst is mainly due to the fact that the hydroxyl radicals can react closely with the concentrated pollutants and enhance the photon effect of the catalyst [105], which can also enable the recovery of titanium dioxide powder after water treatment. Studies in the literature have pointed out that AC/TiO_2 composite material's performance has easy recovery, is difficult to deactivate, and can be more effectively used than traditional pure titanium dioxide. The composite material AC/TiO_2 shows significant improvements in treatment time and efficiency [106, 107]. In addition, to improve the photocatalyst's light usability, the combination of titanium dioxide and activated carbon is a potential material. Many studies have applied the photocatalytic reaction of AC/TiO_2

https://www.twirpx.org & http://chemistry-chemists.com

under sunlight conditions [108, 109]. To use these composite materials on a large scale, AC/TiO_2 still has problems such as light stability, ultraviolet attenuation, scaling, mechanical stability, and regeneration that need to be overcome. In future, continuing research is needed to improve the adsorption and treatment efficiency of composite materials.

4.1.3 Doped-photocatalyst nanoparticles

In the past 10 years, researchers have focused on expanding the visible light utilization of catalysts in the solar spectrum. Nonmetal doping such as C, N, and S can achieve the absorption of photocatalysts under visible light and has shown great potential. The high stability of nitrogen, the similar size of oxygen atoms, and small ionization energy can easily introduce nitrogen into the nano-titanium dioxide structure. Therefore, nano-TiO_2 photocatalysis can achieve visible light activity through nitrogen doping [110, 111] and effectively degrade organic dyes [112, 113]. The most common method for synthesizing nitrogen-doped photocatalysis is the sol-gel method, which uses a titanium precursor to combine with the nitrogen in the surfactant. Most of the titanium dioxide crystal forms are anatase, but some studies indicate that the composite form of anatase-rutile has a unique performance. This heterogeneous photocatalyst can effectively transfer electrons from anatase to rutile, which promotes the separation of electron-hole pairs and enhances visible light activity [114, 115]. In addition to focusing on improving the absorption of visible light, researchers have also paid special attention to the modification of the microstructure of titanium dioxide and changed the morphology of TiO_2 to adjust its characteristics.

N-doped TiO_2 has photocatalytic activity and can decompose 2-propanol in an aqueous solution under visible light irradiation [116]. To expand the nitrogen-doped use, the codoping of nitrogen with other nonmetals has also been studied to enhance the advantages of nitrogen doping, such as S [117], C [118], and F [119]. Compared with single element-doped TiO_2, codoped TiO_2 of two elements may lead to a higher visible light response and be an effective method to improve photocatalytic efficiency [120, 121]. The literature contains studies observing that TiO_2 codoped with N and C is used to degrade BPA pollutants under visible light irradiation. The results show that higher BPA adsorption and photocatalysis were obtained [122]. Recently, three-element-doped photocatalysts have been widely studied. Reports in the literature point out that it can improve the surface thermal performance, increase the surface hydroxide content, reduce the recombination probability of the electrical carrier, and enhance the absorption of ultraviolet and visible light [123]. Similarly, tri-doping has higher treatment efficiency compared to the codoped two elements.

Metal deposition provides another possibility to shorten the energy gap and extend the photoresponse of visible light, while the introduction of the transition element can expand the photoresponse. Precious metal deposition such as gold or silver can increase the photocatalytic activity, and the combination of coupled semiconductors can also significantly improve the photocatalytic activity, such as CdS/TiO_2. These are all feasible methods for developing visible light photocatalysts. Doped cations or cation pairs can also

https://www.twirpx.org & http://chemistry-chemists.com

modify the photocatalyst material. The doped material will be inserted between the conduction band and the valence band. Ionic doping can improve charge separation and interface charge transfer. Nevertheless, charge recombination may still occur and cause the doped catalyst's quantum efficiency to be decreased in some cases.

4.1.4 Other photocatalytic-hybrid materials

According to the literature, surface modification of the most widely used catalysts has been deeply studied. Titanium dioxide's low quantum efficiency is still a problem as a photocatalyst [124, 125] and has attracted attention. Other composite photocatalyst materials have recently been used to treat dyes, bisphenol A [126], and dairy wastewater [127]. Special materials such as CQDs/$BiWO_6$ composite materials greatly enhance photocatalytic activity and exhibit high stability against pollutant degradation. Although the synthesis of composite photocatalytic materials has been extensively studied, composite materials' preparation is still relatively complicated and expensive. In addition, it is necessary to continue to research materials with high light absorption efficiency, effective migration, and low recombination probability of charge carrier in the future.

5 Summary

The challenge of nano-scale photocatalysis is the application of transferring ultraviolet light to the visible light range. As described in this chapter, many methods have been identified that can meet the photocatalytic reactions with visible light. With the wide application of photocatalysis, hybrid/composite catalyst systems have also been thoroughly discussed. Although photocatalysis has been significantly improved, the photocatalytic reactor integration with other reactors can be used to optimize the performance of nano-photocatalysis for large-scale design and application in the future. Meanwhile, using modified material to maximize functions, increasing light quantum efficiency, controlling operating parameters, innovative designs/combining other systems, and developing composite catalysts can further improve photocatalytic performance.

Among advanced oxidation processes, heterogeneous titanium dioxide photocatalysis technology can deal with pesticide pollution problems. For pollutants in trace concentrations, the high efficiency and long-lasting effects of photocatalysts are very important. At the same time, the oxidation reaction must be controlled to avoid the production of toxic by-products and ultimately achieve pollutants' mineralization. Biodegradation of pesticides in water is a common method, while photocatalysis is a nonbiological treatment method. The photocatalytic degradation of pesticides produces hydroxyl radicals and peroxygen anion radicals by absorbing sunlight to generate molecular excitations, which further attack the functional groups existing in the pesticides. There have been many studies on the removal of pesticides, and it is necessary to continue to study the extent and scope of the impact of pesticides on the environment.

https://www.twirpx.org & http://chemistry-chemists.com

6 Present and future scope

Most of the research in this area focuses on degrading pesticides by microorganisms, which requires a long time to operate and involves a high cost, meaning that it cannot be used on a large scale. Nano-scale photocatalyst materials have the potential for pesticide degradation. They can effectively mineralize pollutants to form nontoxic by-products, and degradation efficiency was significantly increased. For the degradation of organochlorine pesticides and transformation products, the applications of nano-scale materials still need more study, and cost-effective and ecologically friendly treatment technologies should be confirmed in the future.

References

[1] EPA. What is a pesticide? http://www.epa.gov/opp00001/about/; 2009.

[2] London, Meyers. General patterns of agricultural chemical usage in the southern regions of South Africa. S Afr J Sci 1995;91:508.

[3] Choi M, Lee IS, Jung RH. Rapid determination of organochlorine pesticides in fish using selective pressurized liquid extraction and gas chromatography-mass spectrometry. Food Chem 2016;205:1–8.

[4] Igbedioh SO. Effects of agricultural pesticides on humans, animals and higher plants in developing countries. Arch Environ Health 1991;46:218–26.

[5] WHO. Public health impact of pesticides used in agriculture. Geneva: World Health Organization; 1990. p. 88.

[6] Arienzo M, Masuccio AA, Ferrara L. Evaluation of sediment contamination by heavy metals, organochlorinated pesticides, and polyaromatic hydrocarbons in the Berre Coastal Lagoon (Southeast France). Arch Environ Contam Toxicol 2013;65:396e406.

[7] Robinson EM, Jia M, Trumble SJ, Usenko S. Selective pressurized liquid extraction technique for halogenated organic pollutants in marine mammal blubber: a lipid-rich matrix. J Chromatogr 2015;1385:111–5.

[8] Moon HB, Lee DH, Lee YS, Choi M, Choi HG, Kannan K. Polybrominateddiphenyl ethers, polychlorinated biphenyls, and organochlorine pesticides in adipose tissues of Korean women. Arch Environ Contam Toxicol 2012;62:176–84.

[9] Cortes DR, Hites RA. Detection of statistically significant trends in atmospheric concentrations of semivolatile compounds. Environ Sci Technol 2000;34:2826–9.

[10] Leadprathom N, Parkpian P, Satayavivad J, Delaune RD, Jugsujinda A. Transport and deposition of organochlorine pesticides from farmland to estuary under tropical regime and their potential risk to aquatic biota. J Environ Sci Health B 2009;44:249–61.

[11] Rani M, Shanker U, Jassal V. Recent strategies for removal and degradation of persistent & toxic organochlorine pesticides using nanoparticles: a review. J Environ Manag 2017;190:208–22.

[12] Zhang WJ, Jiang FB, Ou JF. Global pesticide consumption and pollution: with China as a focus. Pro Int Acad Ecol Environ Sci 2011;1:125–44.

[13] Mathur SC. Future of Indian pesticides industry in next millennium. Pestic Inf 1999;24:9–23.

[14] Majewski MS, Capel PD. Pesticides in the atmosphere: distribution, trends, and governing factors. CRC Press; 1996.

https://www.twirpx.org & http://chemistry-chemists.com

[15] Helfrich CD, Li YF, Sharp ND, Sales AE. Organizational readiness to change assessment (ORCA): development of an instrument based on the promoting action on research in health services (PARIHS) framework. Implement Sci 2009;4:38.

[16] Haakstad LA, Bø K. Exercise in pregnant women and birth weight: a randomized controlled trial. BMC Pregnancy Childbirth 2011;11:66.

[17] Hicks JK, Swen JJ, Thorn CF, Sangkuhl K, Kharasch ED, Ellingrod VL, et al. Clinical pharmacogenetics implementation consortium guideline for CYP2D6 and CYP2C19 genotypes and dosing of tricyclic antidepressants. J Clin Pharm Ther 2013;93:402–8.

[18] Bonner WM, Laskey RA. A film detection method for tritium-labelled proteins and nucleic acids inpolyacrylamide gels. Eur J Biochem 1974;46:83–8.

[19] Fletcher JS, Pfleeger TG, Ratsch HC. Potential environmental risks associated with the new sulfonylurea herbicides. Environ Sci Technol 1993;27:2250–2.

[20] Andreu V, Pico Y. Determination of pesticides and their degradation products in soil: critical review and comparison of methods. Trends Anal Chem 2004;23:772–89.

[21] Yang XL, Wang SS, Bian YR, Chen F, Yu GF, Gu CG, Jiang X. Dicofol application resulted in high DDTs residue in cotton fields from northern Jiangsu province. China J Hazard Mater 2008;150:92–8.

[22] Daly GL, Lei YD, Teixeira C, Muir DCG, Castillo LE, Jantunen LMM, Wania F. Organochlorine pesticides in the soils and atmosphere of Costa Rica. Environ Sci Technol 2007;41:1124–30.

[23] Longnecker PM, Rogan WJ, Lucier G. The human health effects of DDT (dichlorodiphenyltrichloroethane) and PCBs (polychlorinated biphenyls) and an overview of organochlorines in public health. Annu Rev Public Health 1997;18:211–44.

[24] Li FB, Li XM, Zhou SG, Zhuang L, Cao F, Huang DY, Xu W, Liu TX, Feng CH. Enhanced reductive dechlorination of DDT in an anaerobic system of dissimilatory iron-reducing bacteria and iron oxide. Environ Pollut 2010;158:1733–40.

[25] Rodante F, Marrosu G, Catalani G. Thermal-analysis and kinetic-study of decomposition processes of some pesticides. J Therm Anal Calorim 1992;38:2669–82.

[26] Smith E, Smith J, Naidu R, Juhasz AL. Desorption of DDT from a contaminated soil using cosolvent and surfactant washing in batch experiments. Water Air Soil Pollut 2004;151:71–86.

[27] Zinovyev SS, Shinkova NA, Perosa A, Tundo P. Liquid phase hydrodechlorination of dieldrin and DDT over Pd/C and Raney-Ni. Appl Catal Environ 2005;55:39–48.

[28] Tian H, Li J, Mu Z, Li L, Hao Z. Effect of pH on DDT degradation in aqueous solution using bimetallic Ni/Fe nanoparticles. Sep Purif Technol 2009;66:84–9.

[29] Boussahel R, Harik D, Mammar M, Lamara-Mohamed S. Degradation of obsolete DDT by Fenton oxidation with zero-valent iron. Desalination 2007;206:369–72.

[30] Gautam SK, Suresh S. Studies on dechlorination of DDT (1,1,1-trichloro-2,2-bis(4-chlorophenyl) ethane) using magnesium/palladium bimetallic system. J Hazard Mater 2007;139:146–53.

[31] Jayashree R, Vasudevan N, Chandrasekaran S. Surfactants enhanced recovery of endosulfan from contaminated soils. Int J Environ Sci Technol 2006;3:251–9.

[32] Jayaprabha KN, Suresh KK. Endosulfan contamination in water: a review on to an efficient method for its removal. J Chem Chem Sci 2016;6:182–91.

[33] Bhalerao TS, Puranik PR. Biodegradation of organochlorine pesticide, endosulfan, by a fungal soil isolate, Aspergillus niger. Int Biodeterior Biodegrad 2007;59:315–21.

[34] Quinete N, Castro J, Fernandez A, Zamora-Ley IM, Rand GM, Gardinali PR. Occurrence and distribution of endosulfan in water, sediment, and fish tissue: an ecological assessment of protected lands in South Florida. J Agric Food Chem 2013;61:11881–92.

[35] Thomas J, Kumar KP, Chitra KR. Synthesis of Ag doped nano TiO_2 as efficient solar photocatalyst for the degradation of endosulfan. Adv Sci Lett 2011;4:108–14.

https://www.twirpx.org & http://chemistry-chemists.com

[36] Taguchi S, Yakushiji T. Influence of termite treatment in the home on the chlordane concentration in human milk. Arch Environ Contam Toxicol 1988;17:65–71.

[37] Hirai Y, Tomokuni K. Human pollution by chlordane and life of subjects. Bull Environ Contam Toxicol 1995;54:135–41.

[38] Xiao P, Mori T, Kondo R. Biotransformation of the organochlorine pesticide trans-chlordane by wood-rot fungi. N Biotechnol 2011;29:107–15.

[39] Freeman HP, Taylor WW, Edwards WM. Heptachlor and dieldrin disappearance from a field soils measured by annual residue determinations. J Agric Food Chem 1975;23:1101–5.

[40] Patil KC, Matsumura F, Boush GM. Degradation of endrin, aldrin, and DDT by soil microorganisms. Appl Microbiol 1970;19:879–81.

[41] Butler LC, Staiff DC, Sovocool GW, Wilson NK, Magnuson JA. Reductive degradation of dieldrim and endrin in the field using acidified zinc. J Environ Sci Health B 1981;16:395–408.

[42] Augustijn-Beckers PWM, Hornsby AG, Wauchope RD. SCS/ARS/CES Pesticide properties database for environmental decision making. II. Additional compounds. Rev Environ Contam Toxicol 1994;137:1–82.

[43] Huber W. Ecotoxicological relevance of atrazine in aquatic systems. Environ Toxicol Chem 1993;12:1865–81.

[44] Miles JRW, Tu CM, Harris CR. Metabolism of heptachlor and its degradation products by soil microorganisms. J Econ Entomol 1969;62:1334–48.

[45] Thacker PD. Pharmaceutical data elude researchers. Environ Sci Technol 2005;39:193A–4A.

[46] Ajmal A, Majeed I, Malik RN, Iqbal M, Nadeem MA, Hussain I, Yousaf S, Zeshan G, Mustafa MI, Zafar MA. Photocatalytic degradation of textile dyes on Cu_2O-CuO/TiO_2 anatase powders. J Environ Chem Eng 2016;4:2138–46.

[47] Muruganandham M, Swaminathan M. Photochemical oxidation of reactive azo dye with UV–H_2O_2 process. Dyes Pigments 2004;62:269–75.

[48] Muhamad SG. Kinetic studies of catalytic photodegradation of chlorpyrifos insecticide in various natural waters. Arab J Chem 2010;3:127–33.

[49] Mokhtar Mohamed M, Osman G, Khairou KS. Fabrication of Ag nanoparticles modified TiO_2–CNT heterostructures for enhanced visible light photocatalytic degradation of organic pollutants and bacteria. J Environ Chem Eng 2015;3:1847–59.

[50] Fatimah I, Wijaya K, Narsito. Microwave assisted preparation of TiO_2/Al-pillared saponite for photocatalytic phenol photo-oxidation in aqueous solution. Arab J Chem 2015;8:228–32.

[51] Gar Alalm M, Tawfik A, Ookawara S. Enhancement of photocatalytic activity of TiO_2 by immobilization on activated carbon for degradation of pharmaceuticals. J Environ Chem Eng 2016;4:1929–37.

[52] Shen L, Liang R, Wu L. Strategies for engineering metal-organic frameworks as efficient photocatalysts. Chin J Catal 2015;36:2071–88.

[53] Engweiler J, Harf J, Baiker A. WOx/TiO_2 catalysts prepared by grafting of tungsten alkoxides: morphological properties and catalytic behavior in the selective reduction of NO by NH_3. J Catal 1996;159:259–69.

[54] Mozia S. Photocatalytic membrane reactors (PMRs) in water and wastewater treatment. A review. Sep Purif Technol 2010;73:71–91.

[55] Pelaez M, Nolan NT, Pillai SC, Seery MK, Falaras P, Kontos AG, Dunlop PSM, Hamilton JWJ, Jeremy WJ, Byrne JA, O'Shea K, Entezari MH, Dionysiou DD. A review on the visible light active titanium dioxide photocatalysts for environmental applications. Appl Catal Environ 2012;125 (21):331–49.

[56] Sajjad S. Synthesis, characterization and applications of nanomaterials in the field of photocatalysis. GRIN Verlag; 2011.

https://www.twirpx.org & http://chemistry-chemists.com

[57] Zhang L, Mohamed HH, Dillert R, Bahnemann D. Kinetics and mechanisms of charge transfer processes in photocatalytic systems: a review. J Photochem Photobiol C Photchem Rev 2012;13:263–76.

[58] Andreozzi R, Caprio V, Insola A, Marotta R. Advanced oxidation processes (AOPs) for water purification and recovery. Catal Today 1999;53(1):51–9.

[59] Hoffmann MR, Martin ST, Choi W, Bahnemann DW. Environmental applications of semiconductor photocatalysis. Chem Rev 1995;95(1):69–96.

[60] Karunakaran C, Anilkumar P. Photooxidation of iodide ion on immobilized semiconductor powders. Sol Energy Mater Sol Cells 2008;92(4):490–4.

[61] Mills A, Le Hunte S. An overview of semiconductor photocatalysis. J Photochem Photobiol A Chem 1997;108(1):1–35.

[62] Jallouli N, Elghniji K, Trabelsi H, Ksibi M. Photocatalytic degradation of paracetamol on TiO_2 nanoparticles and TiO_2/cellulosic fiber under UV and sunlight irradiation. Arab J Chem 2014. https://doi.org/10.1016/j.arabjc.2014.03.014.

[63] Shifu C, Gengyu C. Photocatalytic degradation of organophosphorus pesticides using floating photocatalyst TiO_2_SiO_2/beads by sunlight. Sol Energy 2005;79:1–9.

[64] Malato S, Fernández-Ibáñez P, Maldonado MI, Blanco J, Gernjak W. Decontamination and disinfection of water by solar photocatalysis: recent overview and trends. Catal Today 2009;147:1–59.

[65] Ahmed S, Rasul MG, Brown R, Hashib MA. Influence of parameters on the heterogeneous photocatalytic degradation of pesticides and phenolic contaminants in wastewater: a short review. J Environ Manage 2011;92:311–30.

[66] Umar M, Aziz HA. Photocatalytic degradation of organic pollutants in water. INTECH Open Access Publisher; 2013.

[67] Chong MN, Jin B, Chow CW, Saint C. Recent developments in photocatalytic water treatment technology: a review. Water Res 2010;44:2997–3027.

[68] Akpan UG, Hameed BH. Parameters affecting the photocatalytic degradation of dyes using TiO_2-based photocatalysts: a review. J Hazard Mater 2009;170:520–9.

[69] Liu W, Chen S, Zhao W, Zhang S. Titanium dioxide mediated photocatalytic degradation of methamidophos in aqueous phase. J Hazard Mater 2009;164:154–60.

[70] Shao C, Zhou G, Li Z, Wu Y, Xu D, Sun B. Fabrication of large-diameter tube-like mesoporous TiO_2 via homogeneous precipitation and photocatalytic decomposition of papermaking wastewater. Chem Eng J 2013;230:227–35.

[71] Fernández J, Kiwi J, Baeza J, Freer J, Lizama C, Mansilla HD. Orange II photocatalysis on immobilised TiO_2. Appl Catal Environ 2004;48:205–11.

[72] Lee KM, Lai CW, Ngai KS, Juan JC. Recent developments of zinc oxide based photocatalyst in water treatment technology: a review. Water Res 2016;88:428–48.

[73] Lin H, Valsaraj KT. Development of an optical fiber monolith reactor for photocatalytic wastewater treatment. J Appl Electrochem 2005;35:699–708.

[74] Behnajady MA, Modirshahla N, Daneshvar N, Rabbani M. Photocatalytic degradation of an azo dye in a tubular continuous-flow photoreactor with immobilized TiO2 on glass plates. Chem Eng J 2007;127:167–76.

[75] Merabet S, Bouzaza A, Wolbert D. Photocatalytic degradation of indole in a circulating upflow reactor by UV/TiO_2 process—influence of some operating parameters. J Hazard Mater 2009;166:1244–9.

[76] Konstantinou IK, Albanis TA. TiO_2-assisted photocatalytic degradation of azo dyes in aqueous solution: kinetic and mechanistic investigations. Appl Catal Environ 2004;49:1–14.

[77] Feng D, Xu S, Liu G. Application of immobilized TiO photocatalysis to improve the inactivation of Heterosigma akashiwo in ballast water by intense pulsed light. Chemosphere 2014;125:102–7.

https://www.twirpx.org & http://chemistry-chemists.com

[78] Hassan M, Zhao Y, Xie B. Employing TiO_2 photocatalysis to deal with landfill leachate: current status and development. Chem Eng J 2016;285:264–75.

[79] Sirtori C, Agüera A, Gernjak W, Malato S. Effect of water-matrix composition on trimethoprim solar photodegradation kinetics and pathways. Water Res 2010;44:2735–44.

[80] Yap P-S, Lim T-T. Effect of aqueous matrix species on synergistic removal of bisphenol—a under solar irradiation using nitrogen-doped TiO_2/AC composite. Appl Catal Environ 2011;101:709–17.

[81] Yap P-S, Lim T-T. Solar regeneration of powdered activated carbon impregnated with visible-light responsive photocatalyst: factors affecting performances and predictive model. Water Res 2012;46:3054–64.

[82] Hernández-Ramírez A, Medina-Ramírez I. Photocatalytic semiconductors: synthesis, characterization, and environmental applications. Springer; 2014.

[83] McCullagh C, Robertson JC, Bahnemann D, Robertson PJ. The application of TiO_2 photocatalysis for disinfection of water contaminated with pathogenic micro-organisms: a review. Res Chem Intermed 2007;33:359–75.

[84] Robertson PKJ, Robertson JMC, Bahnemann DW. Removal of microorganisms and their chemical metabolites from water using semiconductor photocatalysis. J Hazard Mater 2012;211–212:161–71.

[85] Nelson KY, McMartin DW, Yost CK, Runtz KJ, Ono T. Point-of-use water disinfection using UV light-emitting diodes to reduce bacterial contamination. Environ Sci Pollut Res 2013;20:5441–8.

[86] Wang X, Hu X, Wang H, Hu C. Synergistic effect of the sequential use of UV irradiation and chlorine to disinfect reclaimed water. Water Res 2012;46:1225–32.

[87] Agustina TE, Ang HM, Vareek VK. A review of synergistic effect of photocatalysis and ozonation on wastewater treatment. J Photochem Photobiol C Photchem Rev 2005;6:264–73.

[88] Alinsafi A, Evenou F, Abdulkarim EM, Pons MN, Zahraa O, Benhammou A, Yaacoubi A, Nejmeddine A. Treatment of textile industry wastewater by supported photocatalysis. Dyes Pigments 2007;74:439–45.

[89] Han F, Kambala VSR, Srinivasan M, Rajarathnam D, Naidu R. Tailored titanium dioxide photocatalysts for the degradation of organic dyes in wastewater treatment: a review. Appl Catal Gen 2009;359:25–40.

[90] Cruz M, Gomez C, Duran-Valle CJ, Pastrana-Martínez LM, Faria JL, Silva AMT, Faraldos M, Bahamonde A. Bare TiO_2 and graphene oxide TiO_2 photocatalysts on the degradation of selected pesticides and influence of the water matrix. Appl Surf Sci 2015. https://doi.org/10.1016/j.apsusc.2015.09.268.

[91] Carbajo J, García-Muñoz P, Tolosana-Moranchel A, Faraldos M, Bahamonde A. Effect of water composition on the photocatalytic removal of pesticides with different TiO_2 catalysts. Environ Sci Pollut Res Int 2014;21:12233–40.

[92] De Lasa HI, Lasa H, Serrano B, Salaices M. Photocatalytic reaction engineering. Springer; 2005.

[93] Chang K, Chen W. In situ synthesis of MoS_2/graphene nanosheet composites with extraordinarily high electrochemical performance for lithium ion batteries. Chem Commun 2011;47:4252–4.

[94] Sun L, Zhao Z, Zhou Y, Liu L. Anatase TiO_2 nanocrystals with exposed {001} facets on graphene sheets via molecular grafting for enhanced photocatalytic activity. Nanoscale 2012;4:613–20.

[95] Huang Q, Tian S, Zeng D, Wang X, Song W, Li Y, Xiao W, Xie C. Enhanced photocatalytic activity of chemically bonded TiO_2/graphene composites based on the effective interfacial charge transfer through the C–Ti bond. ACS Catal 2013;3:1477–85.

[96] Ahmad R, Ahmad Z, Khan AU, Mastoi NR, Aslam M, Kim J. Photocatalytic systems as an advanced environmental remediation: Recent developments, limitations and new avenues for applications. J Environ Chem Eng 2016;4:4143–64.

https://www.twirpx.org & http://chemistry-chemists.com

[97] Zhou J, Gu Y, Hu Y, Mai W, Yeh P-H, Bao G, Sood AK, Polla DL, Wang ZL. Gigantic enhancement in response and reset time of ZnO UV nanosensor by utilizing Schottky contact and surface functionalization. Appl Phys Lett 2009;94:191103.

[98] Athanasekou CP, Morales-Torres S, Likodimos V, Romanos GE, Pastrana-Martinez LM, Falaras P, Dionysiou DD, Faria JL, Figueiredo JL, Silva AMT. Prototype composite membranes of partially reduced graphene oxide/TiO_2 for photocatalytic ultrafiltration water treatment under visible light. Appl Catal Environ 2014;158–159:361–72.

[99] Rao G, Zhang Q, Zhao H, Chen J, Li Y. Novel titanium dioxide/iron (III) oxide/graphene oxide photocatalytic membrane for enhanced humic acid removal from water. Chem Eng J 2016;302:633–40.

[100] Cao A, Liu Z, Chu S, Wu M, Ye Z, Cai Z, Chang Y, Wang S, Gong Q, Liu Y. A facile one-step method to produce graphene–CdS quantum dot nanocomposites as promising optoelectronic materials. Adv Mater 2010;22:103–6.

[101] Pastrana-Martínez LM, Morales-Torres S, Kontos AG, Moustakas NG, Faria JL, Doña-Rodríguez JM, Falaras P, Silva AMT. TiO_2, surface modified TiO_2 and graphene oxide-TiO_2 photocatalysts for degradation of water pollutants under near-UV/vis and visible light. Chem Eng J 2013;224:17–23.

[102] Julkapli NM, Bagheri S. Graphene supported heterogeneous catalysts: an overview. Int J Hydrogen Energy 2015;40:948–79.

[103] Hou D, Feng L, Zhang J, Dong S, Zhou D, Lim TT. Preparation, characterization and performance of a novel visible light responsive spherical activated carbon-supported and Er^{3+}:$YFeO_3$-doped TiO_2 photocatalyst. J Hazard Mater 2012;199–200:301–8.

[104] Yap P-S, Lim T-T, Lim M, Srinivasan M. Synthesis and characterization of nitrogen-doped TiO_2/AC composite for the adsorption–photocatalytic degradation of aqueous bisphenol—a using solar light. Catal Today 2010;151:8–13.

[105] Lim T-T, Yap P-S, Srinivasan M, Fane AG. TiO_2/AC composites for synergistic adsorption-photocatalysis processes: present challenges and further developments for water treatment and reclamation. Crit Rev Environ Sci Technol 2011;41:1173–230.

[106] Asiltürk M, Şener Ş, Şener E. Preparation, characterization and photocatalytic activities of TiO_2-coated activated carbon catalysts for rhodamine B photodegradation. Bull Korean Chem Soc 2015;36:455–63.

[107] Liu J-H, Rong Y, Li S-M. Preparation and application of efficient TiO_2/ACFs photocatalyst. J Environ Sci 2006;18:979–82.

[108] Dong S, Zhang X, He F, Dong S, Zhou D, Wang B. Visible-light photocatalytic degradation of methyl orange over spherical activated carbon-supported and Er^{3+}: $YAlO_3$-doped TiO_2 in a fluidized bed. J Chem Technol Biotechnol 2015;90:880–7.

[109] Yap P-S, Lim T-T, Srinivasan M. Nitrogen-doped TiO_2/AC bi-functional composite prepared by two-stage calcination for enhanced synergistic removal of hydrophobic pollutant using solar irradiation. Catal Today 2011;161:46–52.

[110] Abdullah AM, Al-Thani NJ, Tawbi K, Al-Kandari H. Carbon/nitrogen-doped TiO_2: new synthesis route, characterization and application for phenol degradation. Arab J Chem 2015;9:229–37.

[111] Emeline AV, Kuznetsov VN, Rybchuk VK, Serpone N. Visible-light-active titania photocatalysts: the case of N-doped s—properties and some fundamental issues. Int J Photoenergy 2008;2007:19.

[112] Di Valentin C, Finazzi E, Pacchioni G, Selloni A, Livraghi S, Paganini MC, Giamello E. N-doped TiO_2: theory and experiment. Chem Phys 2007;339:44–56.

[113] Khan SUM, Al-Shahry M, Ingler WB. Efficient photochemical water splitting by a chemically modified n-TiO_2. Science 2002;297:2243–5.

[114] Etacheri V, Seery MK, Hinder SJ, Pillai SC. Highly visible light active TiO_2-xNx heterojunction photocatalysts. Chem Mater 2010;22:3843–53.

https://www.twirpx.org & http://chemistry-chemists.com

[115] Li Q, Shang JK. Heavily nitrogen-doped dual-phase titanium oxide thin films by reactive sputtering and rapid thermal annealing. J Am Ceram Soc 2008;91:3167–72.

[116] Nosaka Y, Matsushita M, Nishino J, Nosaka AY. Nitrogen-doped titanium dioxide photocatalysts for visible response prepared by using organic compounds. Sci Technol Adv Mater 2005;6:143–8.

[117] Zhang G, Zhang YC, Nadagouda M, Han C, O'Shea K, El-Sheikh SM, Ismail AA, Dionysiou DD. Visible light-sensitized S, N and C co-doped polymorphic TiO_2 for photocatalytic destruction of microcystin-LR. Appl Catal Environ 2014;144:614–21.

[118] Wu Y-C, Ju L-S. Annealing-free synthesis of CN co-doped TiO_2 hierarchical spheres by using amine agents via microwave-assisted solvothermal method and their photocatalytic activities. J Alloys Compd 2014;604:164–70.

[119] Giannakas AE, Seristatidou E, Deligiannakis Y, Konstantinou I. Photocatalytic activity of N-doped and N–F co-doped TiO_2 and reduction of chromium(VI) in aqueous solution: an EPR study. Appl Catal Environ 2013;132–133:460–8.

[120] Huo YN, Zhang XY, Jin Y, Zhu J, Li HX. Highly active La_2O_3/Ti1-xBxO_2 visible light photocatalysts prepared under supercritical conditions. Appl Catal Environ 2008;83:78–84.

[121] Pelaez M, de la Cruz AA, Stathatos E, Falaras P, Dionysiou DD. Visible light-activated N-F-codoped TiO_2 nanoparticles for the photocatalytic degradation of microcystin-LR in water. Catal Today 2009;144:19–25.

[122] Wang X, Lim T-T. Solvothermal synthesis of CN codoped TiO_2 and photocatalytic evaluation for bisphenol A degradation using a visible-light irradiated LED photoreactor. Appl Catal Environ 2010;100:355–64.

[123] Jiang H, Wang Q, Li S, Li J, Wang Q. Pr, N, and P tri-doped anatase TiO_2 nanosheets with enhanced photocatalytic activity under sunlight. Chin J Catal 2014;35:1068–77.

[124] Shankar H, Saravanan R, Suresh V, Narayanan V, Rossi F, Stephen A. Synthesis and characterization of nano-titania photocatalyst loaded on Mo-MCM-41 support. Adv Sci Lett 2011;4:89–95.

[125] Zhou X, Lan J, Liu G, Deng K, Yang Y, Nie G, Yu J, Zhi L. Facet-mediated photodegradation of organic dye over hematite architectures by visible light. Angew Chem Int Ed 2012;51:178–82.

[126] Di J, Xia J, Ge Y, Li H, Ji H, Xu H, Zhang Q, Li H, Li M. Novel visible-light-driven CQDs/Bi_2WO_6 hybrid materials with enhanced photocatalytic activity toward organic pollutants degradation and mechanism insight. Appl Catal Environ 2015;168–169:51–61.

[127] Kanjwal MA, Shawabkeh AQ, Alm M, Thomsen P, Barakat NAM, Chronakis IS. Hybrid matrices of ZnO nanofibers with silicone for high water flux photocatalytic degradation of dairy effluent. Mater Chem Phys 2016;181:495–500.

https://www.twirpx.org & http://chemistry-chemists.com

https://www.twirpx.org & http://chemistry-chemists.com

18

Polymer-based materials for visible light photocatalysis

Saralasrita Mohanty

SCHOOL OF PHYSICAL SCIENCES, NATIONAL INSTITUTE OF SCIENCE EDUCATION AND RESEARCH, HBNI, JATNI, INDIA

For more efficient use of sunlight energy, visible spectrum-induced photocatalysts have gained interest in recent years owing to their most promising solutions for renewable energy and many environmental-related issues at lower cost [1–12]. One important reason for this rising tendency for visible spectrum-sensitive photocatalysts is their potentiality for directly harvesting energy from sunlight energy, which will eventually become superior and indispensable in many areas of photonics and electronics [13–19]. It has been documented possibility of using new nanofeatures materials in photocatalysis with unforeseen potential for photocatalytic conversion of sunlight energy [20–24]. It should be noted that the electronic structure of the materials monitors the optical characteristics and band structure of the photocatalysts [25]. The mechanism of a visible spectrum-induced photocatalytic system involves three steps, as shown in Fig. 1. The first step is the absorption of light followed by formation of photogenerated charge carriers [26]. The second step is the transfer of photogenerated charge carriers; the charge carriers either reunite or reach at the surface [8]. The final step involves the surface chemical reactions by photogenerated holes and electrons [8]. Thus, the new designed material must have the potential to absorb the visible spectrum and possess a narrow bandwidth that facilitates excitation of visible spectrum photons and migration of charge carriers to the surface followed by surface redox reaction. For an optimized photocatalytic performance (especially optimized in morphology) from sunlight energy, in particular, under visible spectrum illumination, an efficient and stable photocatalyst which facilitates absorption of maximum visible radiation and maximum chemical reaction at the surface is essential. Furthermore, this optimized photocatalyst enhances the photogenerated charge carriers (e^-/h^+) separation and minimizes the charge recombination losses [27, 28]. Moreover, one of the important aspects of a photocatalyst is that it should be precisely reprocessed even after frequent chemical decomposition. It is also necessary to make improvements in various electronic characteristics of photocatalysts including atomic configuration, electronic energy band

Nanostructured Materials for Visible Light Photocatalysis. https://doi.org/10.1016/B978-0-12-823018-3.00013-0
Copyright © 2022 Elsevier Inc. All rights reserved.

https://www.twirpx.org & http://chemistry-chemists.com

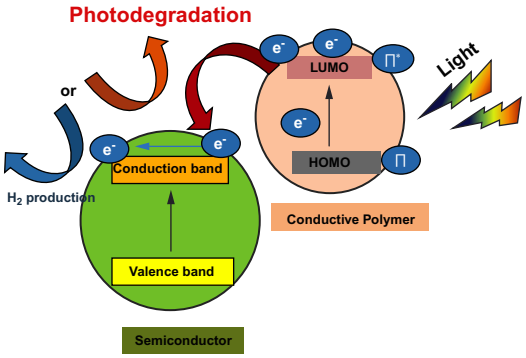

FIG. 1 The photocatalytic mechanism of a visible light-induced photocatalyst.

width, position of energy band, existence of electrons and holes, etc. to increase the photocatalytic activity of these materials under visible spectrum irradiation [1, 2, 22].

1 Introduction

In this context, considerable interest has been shown in the synthesis of various kinds of photocatalysts that would synergistically combine an ability to perform visible light-driven photo-redox reactions and remain stable in the water environment. In fact, over recent years, different photocatalyst materials have gained a prominent role under visible light photocatalysis. Furthermore, increasing attention is being drawn to the synthesis of photocatalyst materials to enhance energy at maximum level. The main focus of the material development strategies is to develop an efficient photocatalysts by facilitating chemical reactions from the solar energy.

1.1 An overview of recent developed UV- and visible light-induced photocatalysts

Different photocatalyst materials have been employed for photocatalysis either in the form of a lone material photocatalysts or as elements of heterojunctions. In the last few years, semiconducting-based metal oxide nanoparticles have received considerable attention as a photoactive material as they carry out better photocatalytic performance under UV illumination. In addition, conventional photocatalysts such as TiO_2 [3–7], ZnO [3, 5], carbon nitride g-C_3N_4 [8], metal-organic framework (MOF) compounds [9], graphene-based photocatalysts [10], etc. have confirmed an efficient photocatalysts for visible spectrum-sensitive photocatalyst [11]. Among the intensively examined different photocatalyst materials, oxide-based semiconductors, in particular the oxygen-rich layered TiO_2, have been considered benchmark photocatalysts due to their excellent photodecomposition power, high chemical resistance, high redox ability, superior photocatalytic efficiency, high stability, nontoxic nature, and inexpensiveness. The fundamental

https://www.twirpx.org & http://chemistry-chemists.com

process of photocatalytic activity of TiO_2 associated with the presence of Ti-O-O coordination bonds reduces the bandwidth energy and thus promotes the absorption of near UV light by TiO_2. The absorbed UV spectrum in TiO_2 induces charge splitting to produce electron-hole pairs and this is followed by their separation in the redox reaction [12–15].

Despite various efficient properties, some of the significant shortcomings associated with TiO_2 in terms of being used as an efficient photocatalyst are its low quantum yield and inactiveness under visible spectrum illumination. Owing to its intrinsic broad range of energy bandwidth (e.g., ∼3.2 eV for the anatase phase), TiO_2 limits its ability to absorb only UV radiation (narrow light response range), which prohibits extensive use of energy from sunlight for harvesting photocatalysis. Further, owing to a greater probability of reunification of photogenerated charge carriers in TiO_2, photocatalytic activity is hindered significantly [16–18]. To overcome such vital deficiencies, modifications toward the structure of TiO_2 or a search for suitable materials as photocatalysts are important tasks to lower their bandwidth and facilitate the usage of solar energy under visible spectrum illumination with good efficiency.

To solve the abovementioned issues of TiO_2, a number of methods, including the use of dopants such as metal ions or nonmetal atoms, have been employed to reduce the bandwidth. Furthermore, reducing the bandwidth structure of TiO_2 arises by novel metal depositing, semiconductor coupling, photosensitization of large-bandwidth semiconductors, and adsorbed modifiers (surface modification) through ion implantation, etc. [19–22]. Nowadays, black hydrogenated TiO_2 nanocrystals with high photocatalytic performance under sunlight have been established [23]. In addition, plasmonic photocatalysts have been formed by combining nanostructured plasmonic metals with TiO_2, which significantly increases the photocatalytic activity of TiO_2 in visible light due to the local surface plasmon resonance (LSPR) effect [24, 25]. Furthermore, surface modification of TiO_2 doping with S, C, or N or its modification with noble metal nanoparticles has improved solar absorption and significantly enhanced photocatalytic activity under UV and visible light. However, the abovementioned process is complex and expensive. Furthermore, the low stability with frequent cycling heavily limits its extensive usage [26–28]. Therefore, surviving photocatalysts have not yet been achieved for commercial usage [29]. To overcome these drawbacks, substitute materials are anticipated.

2 Polymer-based photocatalytic materials as efficient photocatalysts

The fundamental subject of recent investigation is to consider the expansion of the light absorption spectrum to the visible zone, thus facilitating the utilization of sunlight as an inexpensive and renewable energy source for photocatalytic processes. In this context, conducting polymer-based materials are emerging as a new energy material and have been widely investigated in different optical and electronic applications, including light-emitting diodes, supercapacitors, transistor, solar cells, etc. [29, 30].

https://www.twirpx.org & http://chemistry-chemists.com

In this respect, varieties of nanostructures conducting polymers including polypyrrole (PPy) [31–33] polyaniline (PANI) [34–37], poly(diacetylenes) and its derivatives including poly(diphenylbutadiyne) (PDPB) [38], polythiophene (PTh) and its derivatives including poly(3,4-ethylenedioxythiophene) (PEDOT) [39–42], polyisoprene [43], etc. have been studied for photocatalytic applications under visible radiation, and these are shown in Table 1 [45]. These nanostructures conducting polymers possess electrical and optical properties. Moreover, the conjugate polymer associated with a specially extended Π-bonding system is now becoming a hot research area owing to its unique high photon absorption coefficient under visible light, larger specific surface areas, high charge mobility, and better stability. The conducting form of PPy and PANI induces easy protonation transition from insulators to conductors and exhibits relatively lesser semiconducting performance, whereas PPy and PANI in their salt forms effectively demonstrate key conducting polymers for electronic usages where high conductivity is needed. Further, the conducting form of PEDOT, which is fabricated by incorporating semiconducting PEDOT with sulfonated polystyrene, is also more significant compared to its parent pristine semiconductor. The conducting polymers, PTh, and its derivatives are emerging as new energy second-generation polymeric semiconductors. They demonstrate outstanding optical and electrical characteristics, and retain suitable mechanical characteristics as well. Furthermore, PTh, and its derivatives are generally employed in their semiconducting forms for different usages including solar cells, fuel cells and rechargeable batteries. Indeed, PTh has revealed relatively lesser bandwidth by permitting greater adsorption of sunlight in the visible zone. Consequently, considerable research has been carried out into enhancing the decomposition rate of impurities by mingling inorganic materials by means of PTh to attain synergetic and complementary behaviors among PTh and other organic or inorganic materials. The nanofiber form of conjugated polymer, poly(diphenylbutadiyne)

Table 1 Existing polymer-based photocatalyst under visible light irradiation [44].

Photocatalyst	Synthesis method	Structure	Bandgap (eV)
Polyaniline (PANI)	Polymerization	Bulk PANI	3.2
PANI/gray-TiO_2	In situ polymerization	Nanocomposites	<3.2
PANI/MS-TiO_2	Solution evaporation and chemisorption	Mesoporous crystal microsphere	<3.2
PANI-TiO_2	Polymerization	Nanotube-nanoparticles	3.18
Polypyrrole (PPy)	Radiolysis/polymerization	Bulk PPy	3.1
PPy-TiO_2	Polymerization	Nanocomposites	2.22–2.23
Polythiophene (PTh)	Polymerization	Bulk PTh	2.1
Poly(3,4-ethylenedioxythiophene) (PEDOT)	Soft templates via electrochemical oxidative polymerization	Nanospindle	1.69
Poly(diphenyl butadiyne) (PDPB)	Photo-polymerization using soft templating approach	Nanofiber	2.0

https://www.twirpx.org & http://chemistry-chemists.com

(PDPB) has significantly improved the photocatalytic activity compared to its bare form for water decontamination under visible spectrum illumination [38].

When these conducting polymers nanostructure materials synergistically loaded with the different semiconducting materials and fabricate into conducting polymer-based composite photocatalysts [46, 47]. These composite conducting polymers are providing appropriate band structures and reducing the rejoining of photogenerated charge carriers that exhibited better performance of photocatalytic activities through directly harvesting energy from solar energy compared to their individual form. In addition, the synergic effect between conductive polymers and semiconductor nanomaterials dramatically improved the visible spectrum-driven catalyzed photolysis performance. The band structures of these polymer-based composite photocatalysts can be analyzed to describe the methods of their increased activities of catalyzed photolysis. Integration of conductive polymers leads to a significant enhanced in visible spectrum-driven catalyzed photolysis by increasing the splitting of photoexcited charge carriers, broadening the light absorption range, improving the adsorption of reactants, preventing photocorrosion, and lowering the formation of considerable agglomerates [48, 49].

Recently, researchers have explored polymeric-based nanostructures devices including conducting polymer-based nanocomposites as effective visible spectrum-sensitive photocatalysts because of their higher charge carrier mobility, high stability, ability to reuse catalysts even after repeated cycling, architectural diversity, chemical inertness, multifunctional surface chemistry, possibility of creating large area devices, good flexibility and processability, low-cost, and abundant availability [45, 50]. In addition, conducting polymeric-based nanostructure has excellent electrical, physical, mechanical, and electrochemical activities and has the ability to demonstrate catalyzed photolysis without use of any sacrificial substances under the visible spectrum. Moreover, the polymer-based nanostructure materials improve the activities of catalyzed photolysis of the materials by facilitating the surface adsorption of the target organic molecules [51, 52]. Conjugated polymer nanocomposites has experienced flexibility along with catalytic, electrical and optical characteristics. These materials have potential in areas of environmental protection, energy conversion, and storage usage including fuel cells, solar cells, and rechargeable lithium batteries [53–56].

In the past, TiO_2 nanoparticles modified by conducting polymer were investigated for development of TiO_2-based visible-spectrum-sensitive photocatalysts. For example, TiO_2/polyisoprene nanocomposites have been synthesized by modifying TiO_2 nanoparticles with conjugated derivatives of polyisoprene (CDPIP) by the bromine addition reaction of polyisoprene and dehydrobromination reaction of the brominated polyisoprene. Without changing the crystalline structure of TiO_2, CDPIP has significantly enhanced the absorbance of the nanocomposites in the whole range of the visible spectrum, and noticeably lowered the rejoining probability of photogenerated electrons and holes. In the photocatalytic experiments, the CDPIP-modified/TiO_2 nanocomposites demonstrated substantially higher performance in catalyzed photolysis than the bare TiO_2 [43]. Further, polypyrrole films associated with TiO_2 nanoparticles revealed superior performance in

https://www.twirpx.org & http://chemistry-chemists.com

catalyzed photolysis to bare TiO_2 for the decomposition of dyes under ultraviolet illumination [49]. Instead, TiO_2 tailored by conjugated derivatives of polyisoprene exhibited photocatalytic performance under the visible spectrum. Two conjugated polymers, poly (3-hexylthiophene) and poly(2-methoxy-5-)2-ethylhexyloxy-1,4-phenylene vinylene, were noticed to be very efficient in the decomposition of several textile dyes under ultraviolet illumination, instead of under the visible spectrum. A probable use of conjugated polymer photocatalysts in synthetic usages was demonstrated by the visible spectrum-driven pinacol pairing of benzaldehyde employing poly(*p*-phenylene) as a photo redox catalyst.

3 Synthesis and characterization of polymer-based photocatalytic materials

Polymer-based photocatalytic materials are prepared by different optimized novel techniques including photochemical, mechanical, chemical, and sono-chemical processes. The main problem associated with the fabrication of polymer nanocomposites is the uniform incorporation of the polymer nanostructure. Several innovative methods have been used to fabricate uniform and homogenate polymer nanocomposites-based photocatalyst for several applications.

3.1 Poly(diacetylene)-based photocatalyst

Poly(diacetylene), a Π-conjugated polymer, has been investigated as a novel visible light-induced photocatalyst. As an evidence of recent experimental findings, poly(diphenylbutadiyne) (PDPB) produced by photo polymerization by means of a soft templating approach has high photocatalytic activity under the visible spectrum without the assistance of sacrificial elements or expensive metal cocatalysts. In this context, Ghosh et al. fabricated nanofiber-based Π-conjugated, poly(diphenylbutadiyne) (PDPB) associated with an energy bandgap of 2.0 eV (as shown in Table 1), and the nanofiber exhibited a much higher performance in catalyzed photolysis than bulk PDPB under the visible spectrum [38]. Owing to its bigger size and occurrence of relatively more defects, bulk PDPB supports higher electron-hole rejoining, leading to lesser activity in catalyzed photolysis. PDPB nanofibers with swollen hexagonal mesophases structures consists of oil-swollen surfactant tubes. The swollen hexagonal mesophases structure of nanofiber contains 1,4-diphenylbutadiyne (DPB) monomers with concentrations of up to 20 wt%, which are polymerized through a 1,4-addition reaction by UV light radiation. The as-synthesized PDPB structure is translucent and removed from the mesophases through rinsing with ethanol and centrifuged, followed by drying.

3.1.1 Characterization of the material

The dried solid powders of PDPB were characterized using transmission electron microscopy (TEM). The TEM image revealed a uniform PDPB diameter of ∼19 nm. A photocatalytic degradation study under the presence of isopropanol showed a decrease

https://www.twirpx.org & http://chemistry-chemists.com

in electron-hole recombination rate which led to an excess number of electrons available for oxidative radicals-mediated degradation. After 240 min illumination of visible light, 64% of phenol was degraded with PDPB. To analyze the electronic structure of as-prepared PDPB, cyclic voltammetry (CV) calculation and density functional theory (DFT) measurements were performed; the results indicated that nano PDPB revealed bandwidths of 1.81 and 1.95 eV, respectively.

Photocatalytic activity measurements

To understand the procedures accountable for a photocatalytic performance of a material for a certain reaction and assess useful applicability of that material, thorough experimental characterizations are essential. The experimental characterization of the material is necessary to comprise its optical characteristics. The photocatalytic activity of PDPB nanofiber was performed under UV-visible illumination by photo-decomposition of organic pollutants including methyl orange (MO) and phenol, both of which are highly detrimental to the ecosystem. The photocatalytic performance of PDPB was influenced by the nature of light illuminated. For instance, when the PDPB nanofiber was irradiated with the photon energy band width energy 1.81 eV (or wavelength of 685 nm) more electron-hole pairs formed in the polymer chain which facilitated better activity in catalyzed photolysis in the visible range. It was observed that photocatalytic activities of PDPB nanofiber do not decrease even after repeated cycles, and this shows the high environmental stability and reusability of the nanofiber, indicating that it can be used for industrial applications.

3.2 Polyaniline-based photocatalyst

Polyaniline (PANI) has been the subject of considerable interest for photocatalysts owing to its concomitant energy bandwidth, linear polymer chains with a spatially extended Õ-bonding systems, and broad range of usages in many domains. PANI is a promising conducting polymer of energy bandgap of 3.2 eV (as shown in Table 1) having novel electrical and optical characteristics. PANI, when loaded with various semiconductor nanomaterials, such as titanium oxide, zinc oxide and bismuth-based nanomaterials, form the conducting polymer composite photocatalysts associated and provides a strong light-harvesting ability [57]. For example, Lin et al. effectively fabricated polyaniline (PANI)/TiO_2 nanocomposites by embedding TiO_2 in PANI [34].

The outcomes of the as-prepared PANI/TiO_2 nanocomposites demonstrate unprecedented photocatalytic performance and very high stability with cycling in photocatalytic decomposition of methyl orange and 4-chlorophenol compared to bare TiO_2 as a benchmark catalyst under UV-visible illumination. Furthermore, the structural and morphological characteristics of TiO_2/PANI nanocomposites are analyzed by transmission electron microscopy (TEM), X-ray diffraction (XRD), and Fourier transform infrared spectroscopy (FTIR), respectively. The photocatalytic exercise of the as-prepared PANI/-TiO_2 nanocomposites have been estimated by the photo-decomposition of Rhodamine B (RhB), methylene blue (MB), and phenol (C_6H_5OH) (as model pollutants) in the

https://www.twirpx.org & http://chemistry-chemists.com

existence of UV-light illumination. The nanocomposite catalysts demonstrated greater photocatalytic activity for the decomposition of organic pollutants than unmodified TiO_2 nanoparticles, which is due to the sensitizing effect of PANI. Moreover, Vanja et al. reported the stability and photocatalytic exercise of PANI/TiO_2 nanocomposites synthesized through an in situ chemical oxidation method [58]. Furthermore, another example is the study performed by Deng et al. which reported loading of PANI with unique mesoporous single crystal TiO_2; the results revealed that the photocatalytic performance of MS-TiO_2 increased drastically up to 99.8% in 120 min for Rhodamine B and 99.5% for methyl blue, which is three times higher than only MS-TiO_2 [59]. The advanced photocatalytic performance of PANI/MS-TiO_2 was due to loading of more PANI on the surface of MS-TiO_2, having a high specific surface area mesoporous structure that led to multiple light reflection in the catalyst. On the other hand, the incorporation of PANI on bismuth oxyhalide (BiOI) photocatalysts formed a synergistic effect among defective BiOI and PANI. For instance, the research done by Xu et al. reported that the integration of PANI on BiOI has considerably improved the splitting of photoexcited charge transporters and broadened the light absorption zone.

3.3 Polythiophene-based photocatalyst

Among the conjugated polymer composites, large portions of the research carried out were focused on polythiophene (PTh)-based composite photocatalysts because of their ease of synthesis, good thermal and chemical stability, and exceptional electrical and optical characteristics [60]. Compared to PANI and PPy, PTh exhibited a substantial increase in photocatalytic performance as the occurrence of PTh facilitates an increase in adsorption of light toward the visible range [61]. Recently, the effect of PTh presence in a copper-doped TiO_2 photocatalyst was studied by Chandra et al.; the photocatalytic activity study exhibited Cu-TiO_2/PTh nanorods degraded the Rhodamine B (RhB) at a higher rate (99.4% of RhB degraded after 75 min) compared to pure Cu-TiO_2 (only 70.5% RhB degraded after 75 min) under visible light illumination [62]. Generally, the incorporation of metal oxides with PTh formed a novel composite photocatalyst which showed that effectively a lower bandgap (energy bandgap of 2.1 eV, as shown in Table 1) associated with greater absorption of light in the visible region, leading to higher photocatalytic activities under the visible spectrum or UV illumination.

Furthermore, alkyl substituted PTh improves the electron mobility of the PTh, thereby offering wide potential applications in photocatalytic degradation. Alkyl substituted PTh, when loaded with semiconductor metal oxide nanoparticles, sensitized the surface of the semiconductor metal oxide and contributed to excellent photocatalytic performance. For instance, Zhu et al. synthesized PTh/TiO_2 nanocomposites by the conventional in situ polymerization technique for a visible light-responsive photocatalyst [63]. The synthesized procedure resulted in a nanocomposite with PTh coated on the surface of TiO_2 and the surface property of the nanocomposites, which is an important factor for the photocatalytic activity, extended the high absorption of solar spectrum in the UV-visible range. In addition, Liang et al. reported the synthesis of PTh/TiO_2

https://www.twirpx.org & http://chemistry-chemists.com

nanocomposites by coating of PTh on the surface of TiO_2 films using the electropolymerization technique [64]. Furthermore, Song et al. studied the photodegradation of phenol with derivative of PTh, PFTh, combined with TiO_2, and the result demonstrated the performance of the enhanced catalytic degradation properties of the model pollutants [65].

On the other hand, the Π-conjugated polymer, poly(3,4-ethylenedioxythiophene) (PEDOT), evolved as one of the most promising conducting polymers when assessing their photocatalytic properties for the depollution of water under visible light irradiation without use of any sacrificial reagents or cocatalysts. The PEDOT nanostructure illustrated a narrow bandgap ($E = 1.69$ eV) with excellent ability to harvest solar energy in the visible and near infrared regions. This novel conjugated polymer has unique stability, and is efficiently recycled and reused without substantial loss of activity. In addition, owing to its unique chemical stability, high conductivity, low cost, and biocompatible nature, PEDOT is potentially useful for many applications including biosensors, solar cells, light emitting devices, etc. For instance, Ghosh et al. fabricated PEDOT nanostructures with a bandgap of 1.69 eV (as shown in Table 1) associated with tunable morphology in a controlled soft-template-meditated method via chemical oxidative polymerization of 3,4-ethylenedioxythiophene (EDOT) monomers using an oxidizing agent (ferric chloride, $FeCl_3$) [39]. The as-prepared conjugate polymer PEDOT was associated with hexagonal mesophases nanostructure and turned into blue gel after polymerization. The results were demonstrated through polarized light microscopy and X-ray scattering measurements. The chemical structure of the PEDOT conjugate polymer was confirmed by Fourier transform infrared spectroscopy (FTIR) after extraction from hexagonal mesophases [66]. In addition, the morphology of PEDOT was evaluated by transmission and scanning electron microscopies. To identify the local chemical composition of PEDOT nanostructures, high resolution atomic force microscopy combined with infrared nano-spectroscopy was used. The photocatalytic activity of the nanopolymer was evaluated for degradation in the presence of the model pollutants in a water medium such as methyl orange (MO) and phenol under a UV-visible spectrophotometer. The results indicated that after 240 min illumination of visible light, 100% of phenol was degraded with PEDOT whereas 64% of phenol was degraded in the case of PDPB nanopolymers. Furthermore, PEDOT was analyzed for thermal stability up to 200°C and had a high conductivity value up to 0.4 S cm^{-1} as evaluated by thermogravimetric analysis (TGA) and four probe measurements, respectively.

However, there are some limitations associated with the fabrication procedure of PTh-based conjugated polymers. As the PTh is mostly synthesized by the chemical or electrochemical oxidative polymerization process, the photocatalytic efficiency of the PTh polymer is influenced by many factors such as reaction temperature, reaction time, type and concentration of monomer/oxidizing agent, ratio of monomer and oxidizing agent, etc. [60].

3.4 Polypyrrole-based photocatalysts

In recent years, polypyrrole (PPy) has been one of the most promising Π-conjugated polymers and has been studied widely for the fabrication of polymer-based photocatalysts.

https://www.twirpx.org & http://chemistry-chemists.com

Conventional semiconductor nanomaterials including TiO_2, ZnO, bismuth oxyhalide (BiOI), etc., when coupled with the pristine PPy, proved to be superior photocatalysts for visible light-responsive photocatalytic activity due to their unique electronic and energy band structure [45]. The energy bandgap is narrow enough (bandgap energy 3.1 eV, as shown in Table 1) to be excited under visible light irradiation. The PPy-based nanocomposite photocatalysts were used for photodegradation of organic pollutants such as phenol and methyl orange (MO) and photocatalytic H_2 production. For instance, Yuan et al. studied the photocatalytic activity of PPy nanostructures (PPy-NS) on photodegradation of organic pollutants, including phenol and methyl orange (MO) [67]. As the structure changes the surface area and the energy bandgap of the material, thus the photocatalytic performance of a material was influenced by the fabrication procedure and type of light illuminated. PPy-NS-c synthesized through chemical oxidation improved the photodegradation efficiency to about 100% within 4.5 h of UV light irradiation for phenol compared to PPy-NS-γ and PPy-bulk. On the other hand, PPy-NS-γ showed photodegradation efficiency of about 20% within 5 h of visible light irradiation, which is two times higher in terms of phenol than PPy-NS-c, and four times higher than that of PPy-bulk.

Furthermore, Baig et al. reported the coupling of PPy with TiO_2 and the nanocomposite, PPy-TiO_2, minimized the energy bandgap of TiO_2 that facilitated the visible light-driven photocatalytic activity [68]. PPy loaded with TiO_2 showed significantly enhanced photocatalytic performance under visible light as its Π-conjugated electron system was able to transfer sufficient charge carriers between PPy and TiO_2. The photocatalytic degradation study of PPy-TiO_2 nanocomposites evidenced that the relatively higher adsorption capacity of methyl orange (MO) in PPy-TiO_2 in comparison with pure TiO_2. The photodegradation efficiency of about 100% MO by PPy-TiO_2 was achieved within 60 min of visible light irradiation, whereas pure TiO_2 only reached about 55% of MO degradation efficiency. Thus, the result demonstrated that PPy/TiO_2 heterostructure nanocomposites enhanced the transfer of electron-hole pairs and were beneficial for lowering the e^--h^- recombination rate, and hence forming a stable and efficient visible light-responsive photocatalyst. Further, Gao et al. studied the reaction pathway of photodegradation a similar trend where Rhodamine B was used as the organic pollutant to observe the photocatalytic activity of PPy/TiO_2 nanocomposites [69].

4 Application of polymer-based materials in visible light-induced photocatalysis

In the last few decades, increasing attention has been paid to the applications of polymer-based materials for photocatalysis under visible light irradiation [70]. The conducting polymers embedded with semiconductor nanocomposite-based photocatalyst have offered a desirable way to resolve various environmental and energy issues including water purification, hydrogen production, antibacterial applications, etc. at relatively lower cost (as shown in Fig. 2). As the conductive polymer provides exact band structures with

https://www.twirpx.org & http://chemistry-chemists.com

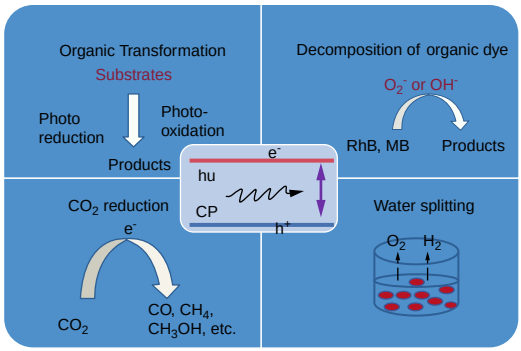

FIG. 2 Overview of various applications of polymer-based materials in visible light-induced photocatalysis.

respect to other semiconductor materials, the recombination rate of photogenerated charge carriers can be reduced for these nanocomposite photocatalysts. Therefore, conducting polymer-supported photocatalysts are mostly involved in organic synthesis, artificial photosynthesis, water purification, etc. [31, 71].

4.1 Hydrogen production from water under visible light

To produce clean and recyclable hydrogen by direct separation of water by means of a photocatalyst is a noble approach for an ideal future energy source. Conjugated polymer-based materials are used as energy transducers toward production of hydrogen from water. A conducting polymer-like semiconductor, prepared with carbon and nitrogen, i.e., polymeric carbon nitride, was observed to be an effective photocatalyst that generated hydrogen from water under visible spectrum illumination without use of any sacrificial reagent. Furthermore, the decomposition of H_2O for the distinct advancement of pure H_2 and O_2 is also being developed by means of visible spectrum-sensitive titanium oxide thin film photocatalysts under light illumination. Additionally, it was observed that Ti-oxide single-site photocatalysts made within zeolite frameworks can stimulate the reduction of CO_2 with H_2O to form hydrocarbons and O_2. Recently, researchers have been exploring how to promote the efficacy of these photocatalytic reactions [72–75].

4.2 Degradation of organic pollutants

Very recently, organic compound-contaminated wastewater has caused severe water pollution problems. The residual organic dyes (e.g., Alizarin S, Orange G, Remazol brilliant blue, etc.), phenols, polychlorinated biphenyls, etc. coming out from different industries (including textile, tannery, printing, and photographic industries, etc.) introduced wide varieties of organic pollutants into the natural water resources [76, 77]. A very low concentrated dye-containing effluent into the water environment seriously affects the nature of water, as many dyes are carcinogens and remain in the water for a long period of time. It is very difficult to oxidize or biodegrade these dyes without the help of chemicals. Recently, effective removal of different toxic organic pollutants from wastewater remains a huge

https://www.twirpx.org & http://chemistry-chemists.com

challenge. Therefore, an efficient and environmentally benign approach should be developed to degrade dyes in water or wastewater under visible light [11].

For removal of the toxic pollutants from water systems, different methodologies have been extensively exploited, including ion exchange, adsorption, coagulation, chemical oxidation process, photocatalysis, etc. Among these methodologies, photocatalysis is considered as an emerging economically viable technology and environmentally friendly process for current environmental pollution on a large scale due to the mechanism of photocatalysis relying on abundant light absorption for conversion of toxic pollutants to nontoxic ones [11]. Generally, the mechanism of photocatalysis is to convert photon energy into chemical energy. In the process, the photocatalyst plays a key role which produce a temporary state by using light absorption (photon energy) and discharging the charge carriers to fabricate the chemicals (chemical energy) in the form of products. For photo-assisted organic pollutant degradation of large organic molecules in water treatment, using polymer-based materials is a promising approach toward an alternative technology for wastewater treatment. In this context, TiO_2 has been widely investigated as an efficient photocatalyst for water splitting and removal of persistent organic pollutants from water or wastewater systems. Among different methods reported for the treatment of organic pollutants in wastewater, the heterogeneous photocatalytic method is one of the most promising technologies for the photocatalytic removal of organic pollutants using visible spectrum-active conducting polymers/semiconductors [70, 78].

In addition, different conducting polymers, including polyaniline, polypyrrole, PEDOT, and polythiophene, by means of semiconductor nanomaterials-based photocatalysts are considered as efficient and stable photocatalyst that can have the potential to resolve these problems by oxidizing a broad range of organic pollutants present in water environment, quickly and nonselectively [57, 58]. For instance, PPy nanostructures (i.e., PPy-NS-c, PPy-NS-γ, and PPy-bulk) synthesized with various approaches including chemical polymerization, radiolysis, and chemical method acting as an extremely promising photocatalyst for water depollution. PPy conjugated polymer-based nanostructures demonstrated relatively higher photocatalytic activity than bulk PPy (PPy-bulk) under both visible light and UV. PPy-NS-γ presents the best photocatalytic efficiency under visible light irradiation for photo-decomposition of organic pollutants (phenol), whereas PPy-NS-c exhibits the highest photocatalytic efficiency under UV light illumination [45].

Furthermore, PPy/TiO_2 composite film was observed to catalyze the decomposition of colors including methylene blue and methyl orange, and underwent separation of charges that caused oxidation of organic pollutants at the boundary under photoexcitation. The PPy/TiO_2 composite film was observed to increase the decomposition reactions better than pure TiO_2 nanoparticles owing to their speedy rejoining of photoexcited charge transporters and light absorption in a wide range. In a similar context, TiO_2/conjugated derivatives of polyisoprene (TiO_2/CDPIP) nanocomposites were evaluated as a novel photocatalyst by photodegrading of methyl orange under visible spectrum illumination [43, 44, 79, 80]. Table 2 lists the photodegradation efficiency of various polymer-based photocatalysts under visible spectrum illumination [45].

https://www.twirpx.org & http://chemistry-chemists.com

Table 2 Photocatalyst for model pollutant degradation under visible light irradiation [44].

Photocatalyst	Light source	Model pollutants	Degradation efficiency/time
PANI/gray-TiO_2	300 W Xe lamp (vis) ($\lambda = 420$ nm)	Rhodamine B	100%/180 min
PANI/MS-TiO_2	300 W Xe lamp (vis) ($\lambda > 420$ nm)	Rhodamine B (RhB) and methylene blue (MB)	RhB:99.8%/120 min and MB:99.5%/150 min
PANI-TiO_2	($\lambda > 420$ nm) (vis)	Methylene blue	85%/300 min
PPy	300 W Xe lamp (vis) ($\lambda < 420$ nm)	Phenol and methyl orange (MO)	Phenol: 20%/300 min and MO: 80%/300 min
PPy-TiO_2	500 W Xe lamp (vis)	Methyl orange (MO) and Rhodamine B (RhB)	MO: 100%/60 min and RhB: 97%/480 min
Poly(3,4-ethylenedioxythiophene) (PEDOT)	300 W Xe lamp (vis) ($\lambda > 420$ nm)	Phenol and methyl orange (MO)	Phenol: 100%/240 min and MO: 100%/180 min
Poly(diphenylbutadiyne) (PDPB)	Xenon lamp (vis) ($\lambda > 450$ nm)	Phenol and methyl orange (MO)	Phenol: 70%/270 min and methyl orange (MO): 75%/240 min

4.3 Degradation of inorganic pollutants

Various inorganic pollutants present in the water system such as iron, chromium, magnesium, zinc, residual ions and acids, etc. significantly affect the water environment because of their toxicity and nonbiodegradability. Most of the inorganic impurities having concentrations higher than a certain value are highly toxic and carcinogenic in nature, and affect living organisms severely. Among various toxic inorganic elements present in water and wastewater, chromium in an oxidative state Cr(vi) is one of the emerging inorganic pollutants. For example, hexavalent chromium (Cr(vi)), which is generally present in wastewater (mostly coming from pigment production and leather tanning industries), is highly toxic and carcinogenic in nature. For reduction of most toxic aquatic pollutants, viz Cr(VI) and bisphenol A (BPA), aqueous Cr(vi), a visible light-induced TiO_2 nanocomposite-based photocatalyst, was used [81, 82]. The conducting polymers/semiconductors-based photocatalyst associated with enormous surface area for facilitating strong absorption light and outstanding charge separation characteristics is essential for effective removal of inorganic pollutants present in water systems [77].

4.4 Degradation of biological pollutants

The presence of various kinds of microbes, including bacteria, viruses, algae, etc. in aquatic ecosystems is harmful to human health and also affects other living organism legitimate uses of water [77, 83]. Currently, photocatalytic disinfection of biological polluted water under visible light has received significant consideration [84–86]. For instance, a dye-sensitized TiO_2 thin film was employed in the photocatalytic disinfection of phytopathogenic bacteria under visible spectrum illumination. The visible spectrum-activated color-sensitized TiO_2 thin film associated with excellent visible light adsorption has the promising potential for direct cleaning of water systems [84]. Similarly, palladium-

https://www.twirpx.org & http://chemistry-chemists.com

modified nitrogen-doped titanium oxide (TiON/PdO) has been established as a promising visible spectrum-sensitive photocatalyst and has a better photocatalytic disinfection effect on fungi [85].

5 Conclusions and future perspectives

This chapter critically demonstrated recent advancements in visible spectrum-driven polymeric photocatalysts for directly harvested energy from solar light. Further, the fundamentals and regulatory mechanism of polymer-based photocatalysis of visible spectrum-driven photocatalysis were briefly discussed. Among different photocatalyst materials, the polymer-based visible spectrum-sensitive photocatalyst facilitates enhanced use of solar energy owing to its inherent characteristics and has pushed scientists to find sustainable solutions to diverse energy conversion usages. As already discussed, conducting polymer-based materials possess unique photo-decomposition power, molecularly tunable optoelectronic characteristics, high chemical stability, greater surface area, low cost, superior electrical conductivity, and the possibility of a unique hybridization feature associated with additional classes of nanostructures (e.g., semiconductors) to produce unique hybrid nanocomposites-based photocatalyst including multifunctional characteristics which make them exceptional candidates for applications in future. Polymer nanostructure, a state-of-the-art example of exhibiting relatively high visible spectrum activity, is environmentally friendly and sustainable compared to the traditional inorganic semiconducting catalytic materials such as TiO_2. To extend the optical response of photocatalysts into the visible zone, several studies have been carried out regarding synthesis of different conducting polymers. The conducing polymers including PPy, PTh, PDPB nanofibers, PEDOT, PANI, etc. are regarded as a new generation of visible spectrum-induced photocatalysts, demonstrating unprecedented photocatalytic activity without help of any sacrificial reagent for environmental protection. These conducting polymers are combined with benchmark semiconductor nanomaterials such as TiO_2 in different methods including soft template via chemical oxidative to synthesize the composite photocatalysts. The photocatalytic performance of these polymer-based catalysts was assessed by a UV-visible absorption spectrophotometer and the results demonstrated a new vista for occurrence of an effective and low-cost visible spectrum-sensitive photocatalyst for solving many environmental issues.

These visible spectrum-sensitive photocatalysis are gaining momentum globally and providing a wide range of applications in water and discarded water management, CO_2 reduction, and water splitting due to their unique features. These photocatalysts are broadly employed for the decomposition of inorganic and organic contaminants, and for photocatalytic decontamination. Thus, these outcomes exhibit possibilities for the additional progress of maintainable eco-friendly remediation know-how based on photocatalytic redox reactions induced by the visible spectrum as a renewable source of energy.

https://www.twirpx.org & http://chemistry-chemists.com

Future challenges lie ahead in tailoring the polymer hybrid nanocomposites and sensitization of semiconductor oxide catalysts under visible light irradiation. One question relates to the changes in polymer structure that influence their physicochemical properties and photocatalytic activities. More investigations should be carried out in the field of visible spectrum-driven polymer-based photocatalysts for enhancing photocatalytic performance. In addition, it is recognized that more structure-activity relationship analysis of visible light-driven conducting polymer-based multicomponent oxides and nanocomposites is needed for designing of novel polymeric materials. Novel polymeric-based visible light-driven photocatalyst and its applicability should continue to be explored. However, the photocatalytic performance of the tailored polymeric devices under visible spectrum irradiation are researched only in laboratory environments and are not yet fully explored for extensive applications. Thus, these new-generation polymeric materials need to be thoroughly investigated for large-scale usage. To promote a feasible "platform" for future visible spectrum-sensitive polymer-based photocatalyst devices, numerous important scientific limitations, including designing, improvement, and method optimization of polymer-based catalysts, need to be addressed.

References

[1] Linsebigler AL, Lu G, Yates JT. Photocatalysis on TiO_2 surfaces: principles, mechanisms, and selected results. Chem Rev 1995;95:735–58. https://doi.org/10.1021/cr00035a013.

[2] Honda K, Fujishima A. Electrochemical photolysis of water at a semiconductor electrode. Nature 1972;238:37–8.

[3] Farhadian N, Akbarzadeh R, Pirsaheb M, Jen TC, Fakhri Y, Asadi A. Chitosan modified N, S-doped TiO_2 and N, S-doped ZnO for visible light photocatalytic degradation of tetracycline. Int J Biol Macromol 2019;132:360–73. https://doi.org/10.1016/j.ijbiomac.2019.03.217.

[4] Li S, Hu J. Transformation products formation of ciprofloxacin in UVA/LED and UVA/LED/TiO_2 systems: impact of natural organic matter characteristics. Water Res 2018;132:320–30. https://doi.org/10.1016/j.watres.2017.12.065.

[5] Wetchakun K, Wetchakun N, Sakulsermsuk S. An overview of solar/visible light-driven heterogeneous photocatalysis for water purification: TiO_2- and ZnO-based photocatalysts used in suspension photoreactors. J Ind Eng Chem 2019;71:19–49. https://doi.org/10.1016/j.jiec.2018.11.025.

[6] Sedlak DL, David Waite T, Westerhoff P, Kim JH, Choi W, Crittenden J, et al. The technology horizon for photocatalytic water treatment: sunrise or sunset? Environ Sci Tech 2019;53:2937–47. https://doi.org/10.1021/acs.est.8b05041.

[7] Ge M, Cao C, Huang J, Li S, Chen Z, Zhang KQ, et al. A review of one-dimensional TiO_2 nanostructured materials for environmental and energy applications. J Mater Chem A 2016;4:6772–801. https://doi.org/10.1039/c5ta09323f.

[8] Jiang L, Yuan X, Zeng G, Liang J, Wu Z, Wang H. Construction of an all-solid-state Z-scheme photocatalyst based on graphite carbon nitride and its enhancement to catalytic activity. Environ Sci Nano 2018;5:599–615. https://doi.org/10.1039/c7en01031a.

[9] Dhakshinamoorthy A, Asiri AM, García H. Metal-organic framework (MOF) compounds: photocatalysts for redox reactions and solar fuel production. Angew Chem Int Ed 2016;55:5414–45. https://doi.org/10.1002/anie.201505581.

https://www.twirpx.org & http://chemistry-chemists.com

[10] Xiang Q, Cheng B, Yu J. Graphene-based photocatalysts for solar-fuel generation. Angew Chem Int Ed 2015;54:11350–66. https://doi.org/10.1002/anie.201411096.

[11] Djurišić AB, He Y, Ng AM. Visible-light photocatalysts: prospects and challenges. APL Mater 2020. https://doi.org/10.1063/1.5140497, 030903.

[12] Chen X, Mao SS. Titanium dioxide nanomaterials: synthesis, properties, modifications and applications. Chem Rev 2007;107:2891–959. https://doi.org/10.1021/cr0500535.

[13] Kim J, Lee J, Choi W. Synergic effect of simultaneous fluorination and platinization of TiO_2 surface on anoxic photocatalytic degradation of organic compounds. Chem Commun 2008;756–8. https://doi.org/10.1039/b715868h.

[14] Zeng J, Liu S, Cai J, Zhang L. TiO_2 immobilized in cellulose matrix for photocatalytic degradation of phenol under weak UV light irradiation. J Phys Chem C 2010;114:7806–11.

[15] Fujishima A, Zhang X, Tryk DA. TiO_2 photocatalysis and related surface phenomena. Surf Sci Rep 2008;63:515–82. https://doi.org/10.1016/j.surfrep.2008.10.001.

[16] Asahi R, Morikawa T, Ohwaki T, Aoki K, Taga Y. Visible-light photocatalysis in nitrogen-doped titanium oxides. Science 2001;293:269–71. https://doi.org/10.1126/science.1061051.

[17] Schneider J. Understanding TiO_2 photocatalysis: mechanisms and materials. Chem Rev 2014; 114:9919–86.

[18] Xu X, Randorn C, Efstathiou P, Irvine JTS. A red metallic oxide photocatalyst. Nat Mater 2012;11:595–8. https://doi.org/10.1038/nmat3312.

[19] Liu L, Ouyang S, Ye J. Gold-nanorod-photosensitized titanium dioxide with wide-range visible-light harvesting based on localized surface plasmon resonance. Angew Chem Int Ed 2013;52:6689–93. https://doi.org/10.1002/anie.201300239.

[20] Zhang N, Zhang Y, Xu YJ. Recent progress on graphene-based photocatalysts: current status and future perspectives. Nanoscale 2012;4:5792–813. https://doi.org/10.1039/c2nr31480k.

[21] Li L, Yan J, Wang T, Zhao ZJ, Zhang J, Gong J, et al. Sub-10 nm rutile titanium dioxide nanoparticles for efficient visible-light-driven photocatalytic hydrogen production. Nat Commun 2015;6. https://doi.org/10.1038/ncomms6881.

[22] Tao J, Luttrell T, Batzill M. A two-dimensional phase of TiO_2 with a reduced bandgap. Nat Chem 2011;3:296–300. https://doi.org/10.1038/nchem.1006.

[23] Chen X, Liu L, Peter YY, Mao SS. Increasing solar absorption for photocatalysis with black hydrogenated titanium dioxide nanocrystals. Science 2011;746–50. https://doi.org/10.1126/science.1200448.

[24] Linic S, Christopher P, Ingram DB. Plasmonic-metal nanostructures for efficient conversion of solar to chemical energy. Nat Mater 2011;10:911–21. https://doi.org/10.1038/nmat3151.

[25] Weng L, Zhang H, Govorov AO. Hierarchical synthesis of non-centrosymmetric hybrid nanostructures and enabled plasmon-driven photocatalysis. Nat Commun 2014;5:4792–802.

[26] Grabowska E, Zaleska A, Sorgues S, Kunst M, Etcheberry A, Colbeau-Justin C, et al. Modification of titanium(IV) dioxide with small silver nanoparticles: application in photocatalysis. J Phys Chem C 2013;117:1955–62. https://doi.org/10.1021/jp3112183.

[27] Remita H, El Kolli N, Uribe DB, Beaunier P, José-Yacaman M, Vigneron J, et al. Modification of TiO_2 by bimetallic Au-Cu nanoparticles for wastewater treatment. J Mater Chem A 2013;1:10829–35. https://doi.org/10.1039/c3ta11684k.

[28] Kowalska E, Yoshiiri K, Wei Z, Zheng S, Kastl E, Remita H, et al. Hybrid photocatalysts composed of titania modified with plasmonic nanoparticles and ruthenium complexes for decomposition of organic compounds. Appl Catal Environ 2015;178:133–43. https://doi.org/10.1016/j.apcatb.2014.10.003.

[29] Lang X, Chen X, Zhao J. Heterogeneous visible light photocatalysis for selective organic transformations. Chem Soc Rev 2014;43:473–86. https://doi.org/10.1039/c3cs60188a.

https://www.twirpx.org & http://chemistry-chemists.com

[30] Long YZ, Li MM, Gu C, Wan M, Duvail JL, Liu Z, et al. Recent advances in synthesis, physical properties and applications of conducting polymer nanotubes and nanofibers. Prog Polym Sci 2011;36:1415–42. https://doi.org/10.1016/j.progpolymsci.2011.04.001.

[31] Yin Z, Zheng Q. Controlled synthesis and energy applications of one-dimensional conducting polymer nanostructures: an overview. Adv Energy Mater 2012;2:179–218. https://doi.org/10.1002/aenm.201100560.

[32] Wang D, Wang Y, Li X, Luo Q, An J, Yue J. Sunlight photocatalytic activity of polypyrrole-TiO_2 nanocomposites prepared by "in situ" method. Catal Commun 2008;9:1162–6. https://doi.org/10.1016/j.catcom.2007.10.027.

[33] Chowdhury D, Paul A, Chattopadhyay A. Photocatalytic polypyrrole-TiO_2-nanoparticles composite thin film generated at the air-water interface. Langmuir 2005;21:4123–8. https://doi.org/10.1021/la0475425.

[34] Lin Y, Li D, Hu J, Xiao G, Wang J, Li W, et al. Highly efficient photocatalytic degradation of organic pollutants by PANI-modified TiO_2 composite. J Phys Chem C 2012;116:5764–72. https://doi.org/10.1021/jp211222w.

[35] Wang YH, Zhang LQ, Li JY, Wang JH, Wang HM. The quorum-sensing system AvsR-AvsI regulates both long-chain and short-chain acyl-homoserine lactones in agrobacterium vitis E26. Antonie van Leeuwenhoek 2008;93:267–73. https://doi.org/10.1007/s10482-007-9201-3.

[36] Zhang H, Zong R, Zhao J, Zhu Y. Dramatic visible photocatalytic degradation performances due to synergetic effect of TiO_2 with PANI. Environ Sci Tech 2008;42:3803–7. https://doi.org/10.1021/es703037x.

[37] Khanam Z, Sa'Don NA, Adam F. Synthesis and characterization of a novel paramagnetic polyaniline composite with uniformly distributed metallic nanoparticles sandwiched between polymer matrices. Synth Met 2014;192:1–9. https://doi.org/10.1016/j.synthmet.2014.03.001.

[38] Ghosh S, Kouamé NA, Ramos L, Remita S, Dazzi A, Deniset-Besseau A, et al. Conducting polymer nanostructures for photocatalysis under visible light. Nat Mater 2015;14:505–11. https://doi.org/10.1038/nmat4220.

[39] Srabanti G, Amoin KN, Samy R, Laurence R, Fabrice G, Pierre-Henri A, et al. Visible-light active conducting polymer nanostructures with superior photocatalytic activity. Sci Rep 2016. https://doi.org/10.1038/srep18002.

[40] Zhu Y, Xu S, Yi D. Photocatalytic degradation of methyl orange using polythiophene/titanium dioxide composites. React Funct Polym 2010;70:282–7. https://doi.org/10.1016/j.reactfunctpolym.2010.01.007.

[41] Wang D, Zhang J, Luo Q, Li X, Duan Y, An J. Characterization and photocatalytic activity of poly(3-hexylthiophene)-modified TiO_2 for degradation of methyl orange under visible light. J Hazard Mater 2009;169:546–50. https://doi.org/10.1016/j.jhazmat.2009.03.135.

[42] Liao G, Chen S, Quan X, Chen H, Zhang Y. Photonic crystal coupled TiO_2/polymer hybrid for efficient photocatalysis under visible light irradiation. Environ Sci Tech 2010;44:3481–5. https://doi.org/10.1021/es903833f.

[43] Luo Q, Bao L, Wang D, Li X, An J. Preparation and strongly enhanced visible light photocatalytic activity of TiO_2 nanoparticles modified by conjugated derivatives of polyisoprene. J Phys Chem C 2012;116:25806–15. https://doi.org/10.1021/jp308150j.

[44] Wang F, Min S, Han Y, Feng L. Visible-light-induced photocatalytic degradation of methylene blue with polyaniline-sensitized TiO2 composite photocatalysts. Superlattices Microstruct 2010;48:170–80. https://doi.org/10.1016/j.spmi.2010.06.009.

[45] Lee SL, Chang CJ. Recent developments about conductive polymer based composite photocatalysts. Polymers 2019;11. https://doi.org/10.3390/polym11020206.

[46] Muktha B, Madras G, Guru Row TN, Scherf U, Patil S. Conjugated polymers for photocatalysis. J Phys Chem B 2007;111:7994–8. https://doi.org/10.1021/jp071096n.

https://www.twirpx.org & http://chemistry-chemists.com

[47] Zhang M, Rouch WD, McCulla RD. Conjugated polymers as photoredox catalysts: visible-light-driven reduction of aryl aldehydes by poly(p-phenylene). Eur J Org Chem 2012;6187–96. https://doi.org/10.1002/ejoc.201200437.

[48] Gu L, Wang J, Qi R, Wang X, Xu P, Han X. A novel incorporating style of polyaniline/TiO_2 composites as effective visible photocatalysts. J Mol Catal A Chem 2012;357:19–25. https://doi.org/10.1016/j.molcata.2012.01.012.

[49] Wang J, Ni X. Photoresponsive polypyrrole-TiO_2 nanoparticles film fabricated by a novel surface initiated polymerization. Solid State Commun 2008;146:239–44. https://doi.org/10.1016/j.ssc.2008.02.022.

[50] Wang F, Min SX. TiO_2/polyaniline composites: an efficient photocatalyst for the degradation of methylene blue under natural light. Chin Chem Lett 2007;18:1273–7. https://doi.org/10.1016/j.cclet.2007.08.010.

[51] Riaz U, Ashraf SM, Kashyap J. Role of conducting polymers in enhancing TiO_2-based photocatalytic dye degradation: a short review. Polym-Plast Technol Eng 2015;54:1850–70. https://doi.org/10.1080/03602559.2015.1021485.

[52] Reddy KR, Karthik KV, Prasad SBB, Soni SK, Jeong HM, Raghu AV. Enhanced photocatalytic activity of nanostructured titanium dioxide/polyaniline hybrid photocatalysts. Polyhedron 2016;120:169–74. https://doi.org/10.1016/j.poly.2016.08.029.

[53] Zhao J, Biswas MRUD, Oh WC. A novel $BiVO_4$-GO-TiO_2-PANI composite for upgraded photocatalytic performance under visible light and its non-toxicity. Environ Sci Pollut Res 2019;26:11888–904. https://doi.org/10.1007/s11356-019-04441-6.

[54] Murugan S, Mariappan MS. Development of efficiency improved polymer-modified TiO_2 for the photocatalytic degradation of an organic dye from wastewater environment. Appl Water Sci 2017;1781–90. https://doi.org/10.1007/s13201-015-0351-6.

[55] Kratofil Krehula L, Stjepanović J, Perlog M, Krehula S, Gilja V, Travas-Sejdic J, et al. Conducting polymer polypyrrole and titanium dioxide nanocomposites for photocatalysis of RR45 dye under visible light. Polym Bull 2019;76:1697–715. https://doi.org/10.1007/s00289-018-2463-2.

[56] Moniz SJA, Shevlin SA, Martin DJ, Guo ZX, Tang J. Visible-light driven heterojunction photocatalysts for water splitting—a critical review. Energ Environ Sci 2015;8:731–59. https://doi.org/10.1039/c4ee03271c.

[57] Čomor MI, Abramović BF, Banić ND, Armaković SJ, Finčur NL, Lazarević MJ, et al. Photocatalytic decomposition of selected biologically active compounds in environmental waters using TiO_2/polyaniline nanocomposites: kinetics, toxicity and intermediates assessment. Environ Pollut 2018;457–65. https://doi.org/10.1016/j.envpol.2018.04.039.

[58] Vanja G, Katarina N, Jadranka T-S, Zlata H-M, Marijana KR, Mark Ž. Stability and synergistic effect of polyaniline/TiO_2 photocatalysts in degradation of azo dye in wastewater. Nanomaterials 2017;412. https://doi.org/10.3390/nano7120412.

[59] Deng Y, Tang L, Zeng G, Dong H, Yan M, Wang J, et al. Enhanced visible light photocatalytic performance of polyaniline modified mesoporous single crystal TiO_2 microsphere. Appl Surf Sci 2016;387:882–93. https://doi.org/10.1016/j.apsusc.2016.07.026.

[60] Ansari MO, Khan MM, Ansari SA, Cho MH. Polythiophene nanocomposites for photodegradation applications: past, present and future. J Saudi Chem Soc 2015;19:494–504. https://doi.org/10.1016/j.jscs.2015.06.004.

[61] Gonçalves VC, Balogh DT. Optical chemical sensors using polythiophene derivatives as active layer for detection of volatile organic compounds. Sens Actuators B 2012;307–12. https://doi.org/10.1016/j.snb.2011.12.084.

[62] Chandra MR, Rao TS, Kim HS, Pammi SVN, Prabhakarrao N, Manga RI. Hybrid copper doped titania/polythiophene nanorods as efficient visible light-driven photocatalyst for degradation of organic pollutants. J Asian Ceramic Soc 2017;5:436–43. https://doi.org/10.1016/j.jascer.2017.09.007.

https://www.twirpx.org & http://chemistry-chemists.com

[63] Zhu Y, Xu S, Jiang L, Pan K, Dan Y. Synthesis and characterization of polythiophene/titanium dioxide composites. React Funct Polym 2008;68:1492–8. https://doi.org/10.1016/j.reactfunctpolym.2008.07.008.

[64] Liang Hc, Li Xz. Visible-induced photocatalytic reactivity of polymer-sensitized titania nanotube films. Appl Catal Environ 2009;86:8–17. https://doi.org/10.1016/j.apcatb.2008.07.015.

[65] Song L, Qiu R, Mo Y, Zhang D, Wei H, Xiong Y. Photodegradation of phenol in a polymer-modified TiO_2 semiconductor particulate system under the irradiation of visible light. Catal Commun 2007;8:429–33. https://doi.org/10.1016/j.catcom.2006.07.001.

[66] Ghosh S, Remita H, Ramos L, Dazzi A, Deniset-Besseau A, Beaunier P, et al. PEDOT nanostructures synthesized in hexagonal mesophases. New J Chem 2014;38:1106–15. https://doi.org/10.1039/c3nj01349a.

[67] Yuan X, Floresyona D, Aubert PH, Bui TT, Remita S, Ghosh S, et al. Photocatalytic degradation of organic pollutant with polypyrrole nanostructures under UV and visible light. Appl Catal Environ 2019;242:284–92. https://doi.org/10.1016/j.apcatb.2018.10.002.

[68] Baig U, Gondal MA, Ilyas AM, Sanagi MM. Band gap engineered polymeric-inorganic nanocomposite catalysts: synthesis, isothermal stability, photocatalytic activity and photovoltaic performance. J Mater Sci Technol 2017;33:547–57. https://doi.org/10.1016/j.jmst.2016.11.031.

[69] Gao F, Hou X, Wang A, Chu G, Wu W, Chen J, et al. Preparation of polypyrrole/TiO_2 nanocomposites with enhanced photocatalytic performance. Particuology 2016;26:73–8. https://doi.org/10.1016/j.partic.2015.07.003.

[70] Filipe V, Kai Z, Markus A. Conjugated porous polymers for energy applications. Energ Environ Sci 2012;7819. https://doi.org/10.1039/c2ee22002d.

[71] Wang X, Maeda K, Thomas A, Takanabe K, Xin G, Carlsson JM, et al. A metal-free polymeric photocatalyst for hydrogen production from water under visible light. Nat Mater 2009;8:76–80. https://doi.org/10.1038/nmat2317.

[72] Zuo F, Wang L, Wu T, Zhang Z, Borchardt D, Feng P. Self-doped Ti3+ enhanced photocatalyst for hydrogen production under visible light. J Am Chem Soc 2010;132:11856–7. https://doi.org/10.1021/ja103843d.

[73] Ou H, Chen X, Lin L, Fang Y, Wang X. Biomimetic donor–acceptor motifs in conjugated polymers for promoting exciton splitting and charge separation. Angew Chem Int Ed 2018;57:8729–33. https://doi.org/10.1002/anie.201803863.

[74] Fang Y, Xu Y, Li X, Ma Y, Wang X. Coating polymeric carbon nitride photoanodes on conductive Y:ZnO nanorod arrays for overall water splitting. Angew Chem Int Ed 2018;57:9749–53. https://doi.org/10.1002/anie.201804530.

[75] Maeda K, Teramura K, Lu D, Takata T, Saito N, Inoue Y, et al. Photocatalyst releasing hydrogen from water. Nature 2006;440:295. https://doi.org/10.1038/440295a.

[76] Mamba G, Mishra AK. Graphitic carbon nitride (g-C_3N_4) nanocomposites: a new and exciting generation of visible light driven photocatalysts for environmental pollution remediation. Appl Catal Environ 2016;198:347–77. https://doi.org/10.1016/j.apcatb.2016.05.052.

[77] Ghosh S, Remita H, Basu RN. Visible-light-induced reduction of Cr(VI) by PDPB-ZnO nanohybrids and its photo-electrochemical response. Appl Catal Environ 2018;239:362–72. https://doi.org/10.1016/j.apcatb.2018.08.034.

[78] Shang M, Wang W, Sun S, Ren J, Zhou L, Zhang L. Efficient visible light-induced photocatalytic degradation of contaminant by spindle-like PANI/$BiVO_4$. J Phys Chem C 2009;113:20228–33. https://doi.org/10.1021/jp9067729.

[79] Dimitrijevic NM, Tepavcevic S, Liu Y, Rajh T, Silver SC, Tiede DM. Nanostructured TiO_2/polypyrrole for visible light photocatalysis. J Phys Chem C 2013;117:15540–4. https://doi.org/10.1021/jp405562b.

https://www.twirpx.org & http://chemistry-chemists.com

[80] Wang Q, Hui J, Li J, Cai Y, Yin S, Wang F, et al. Photodegradation of methyl orange with PANI-modified BiOCl photocatalyst under visible light irradiation. Appl Surf Sci 2013;283:577–83. https://doi.org/10.1016/j.apsusc.2013.06.149.

[81] Wang L, Li X, Teng W, Zhao Q, Shi Y, Yue R, et al. Efficient photocatalytic reduction of aqueous Cr(VI) over flower-like $SnIn_4S_8$ microspheres under visible light illumination. J Hazard Mater 2013;244–245:681–8. https://doi.org/10.1016/j.jhazmat.2012.10.062.

[82] Juan Y, Jun D, Jiantong L. Visible-light-induced photocatalytic reduction of Cr(VI) with coupled Bi_2O_3/TiO_2 photocatalyst and the synergistic bisphenol A oxidation. Environ Sci Pollut Res 2013;2435–47. https://doi.org/10.1007/s11356-012-1131-6.

[83] Chen H, Zheng X, Chen Y, Mu H. Long-term performance of enhanced biological phosphorus removal with increasing concentrations of silver nanoparticles and ions. RSC Adv 2013;3:9835–42. https://doi.org/10.1039/c3ra40989a.

[84] Yao KS, Wang DY, Chang CY, Weng KW, Yang LY, Lee SJ, et al. Photocatalytic disinfection of phytopathogenic bacteria by dye-sensitized TiO_2 thin film activated by visible light. Surf Coat Technol 2007;202:1329–32. https://doi.org/10.1016/j.surfcoat.2007.07.102.

[85] Zhang J, Liu Y, Li Q, Zhang X, Shang JK. Antifungal activity and mechanism of palladium-modified nitrogen-doped titanium oxide photocatalyst on agricultural pathogenic fungi *Fusarium graminearum*. ACS Appl Mater Interfaces 2013;5:10953–9. https://doi.org/10.1021/am4031196.

[86] Joanne G, Zisheng Z. Applications of photocatalytic disinfection. Int J Photoenergy 2010;1–11. https://doi.org/10.1155/2010/764870.

https://www.twirpx.org & http://chemistry-chemists.com

19

Large-scale materials for visible light photocatalysis

Manoj Patowary[a] and Himani Kalita[b]

[a]SCHOOL OF ENGINEERING, MIT-ADT UNIVERSITY, PUNE, MAHARASHTRA, INDIA
[b]DEPARTMENT OF CHEMISTRY, SAVITRIBAI PHULE PUNE UNIVERSITY, PUNE, MAHARASHTRA, INDIA

1 Introduction

Photocatalysis that harnesses solar energy, has emerged as an efficient, inexpensive, green, and eco-friendly approach for accelerating chemical transformations, in contrast to thermal catalytic methods. The term "photocatalysis" has been defined by the IUPAC as "variation in a chemical reaction's rate or its commencement upon irradiation with ultra-violet, visible, or infra-red light in presence of light absorbing material, viz. the photocatalyst, which is entailed in reaction partners' chemical transformations," while a "photocatalyst" has been described as "a material that could absorb ultra-violet, visible or infra-red light and produce reaction partners' chemical transformations, while repetitively emerging with the reactants in intermediate chemical interaction and restoring its chemical constituent after each series of such interaction" [1]. Whereas catalysts require heat (for its activation) to reduce or accelerate the temperature of a particular chemical reaction, photocatalysts use ultraviolet or visible light to carry out the chemical reactions at room temperature [2]. Thus, photocatalysis is a synergic process that involves both light radiation and the photocatalyst to accelerate chemical transformations.

Ever-growing modernization and industrialization have imposed a significant burden on the environment with enormous amount of pollutants, toxicants, and toxic gases such as organic pollutants, dyes, metal ions, heavy metals, pharmaceutical and personal care products, CH_4, N_2O, NO_x, CFCs, CO_2, etc., that are eventually dumped on land surfaces or released into the atmosphere and water bodies. These pose a great threat to the entire ecosystem, along with causing serious land, air, and water pollution. To tackle these serious environmental concerns, the combating measures require production in bulk amounts so as to remove these pollutants effectively from the environment on a large scale. Additionally, the growing industrialization currently relies on the limited nonrenewable fossil fuels as the energy source that has resulted in both energy crisis issues and environmental pollution. Hence, alternative clean energy sources (such as hydrogen fuel) are much desired in response to this growing industrialization. In this context, photocatalysis is a promising effective, environmentally friendly, and economical approach to cope with these issues,

Nanostructured Materials for Visible Light Photocatalysis. https://doi.org/10.1016/B978-0-12-823018-3.00007-5
Copyright © 2022 Elsevier Inc. All rights reserved.

https://www.twirpx.org & http://chemistry-chemists.com

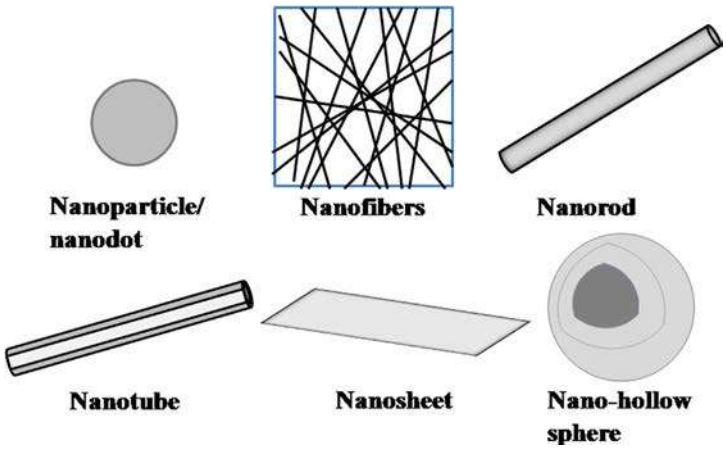

FIG. 1 A few nanostructured morphologies. *No permission required.*

as it utilizes a major renewable source of energy, viz. solar energy, that can be scaled up sufficiently to meet all these requirements under ambient conditions. Photocatalysis has also been considered a potential approach in some significant areas of application such as CO_2 reduction to value-added chemicals, organic reaction transformations, sterilization of biological pollutants such as microbes, etc. Up to the time of writing, numerous photocatalysts have been synthesized on a large scale and studied for mitigating these aforementioned issues. These photocatalysts have been synthesized in different morphologies such as nanoparticles, nanodots, nanocomposites, nanofibers, nanorods, nanotubes, nanosheets, nanodiscs, hollow spheres, etc. (Fig. 1). These photocatalysts were reported to exhibit efficient photocatalytic activity under ambient conditions and their production could be scaled up for extensive application. The photocatalysts have been synthesized on a large scale via common fabrication techniques such as hydrothermal, solvothermal, thermal, wet chemical, ion-exchange, microwave-assisted heating, refluxing, electrochemical anodization, sol-gel, spark plasma sintering, ball milling, etc. either alone or in combination with other techniques (Fig. 2).

In the following section, some of the important fabrication techniques employed for developing photocatalysts on a large scale for various photocatalytic applications will be discussed.

2 Strategies for fabrication of photocatalysts on a large scale

2.1 Hydrothermal method

The hydrothermal method is a very attractive technique to synthesize photocatalysts in nano-dimensions. The term “hydrothermal” is of geological origin, and was first coined to explain the action of water at elevated pressures and temperatures to bring changes

https://www.twirpx.org & http://chemistry-chemists.com

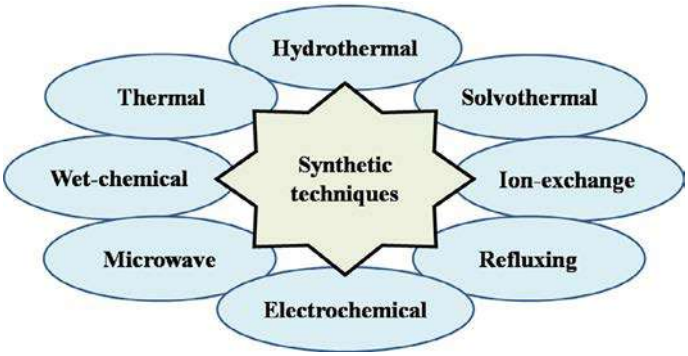

FIG. 2 Some common synthetic techniques used to synthesize photocatalysts on a large scale. *No permission required.*

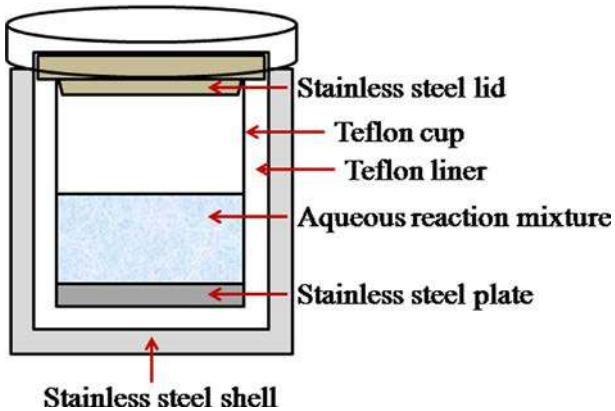

FIG. 3 Schematic diagram of an autoclave used in the hydrothermal technique. *No permission required.*

in the earth's crust that led to the formation of various rocks and minerals. Hydrothermal, in general, is a solution reaction-based approach, where a heterogeneous solution mixture (comprising of water, precursor, and a reagent capable of regulating the crystal growth) is treated at elevated temperatures and pressures in a closed apparatus comprising of a stainless-steel pressure vessel called an autoclave (Fig. 3). The hydrothermal synthesis of photocatalysts could be done in a wide range of temperatures varying from room temperature to very high temperatures, while their morphologies could be controlled by optimizing the pressure conditions that are dependent on the vapor pressure of the composition in the solution mixture [3]. The most significant advantage of the hydrothermal technique is that it could produce photocatalysts that are not stable at elevated temperatures. Additionally, photocatalysts that possess high vapor pressures could be easily synthesized hydrothermally, with minimal loss of materials. Further, composition of the synthesized photocatalysts could be well controlled with the hydrothermal technique.

https://www.twirpx.org & http://chemistry-chemists.com

Up to the time of writing, numerous photocatalysts were reported to be synthesized on a large scale by employing the hydrothermal technique in different morphologies. For instance, Wang et al. synthesized microspheres of ZnS on a large scale via hydrothermal process using $ZnSO_4{\cdot}7H_2O$ and $SC(NH_2)_2$ as precursors, along with poly(vinyl pyrrolidone) as the surfactant [4]. The synthesized ZnS microspheres were studied for their photocatalytic performance toward methylene blue degradation in water. In another work, nanorods of ZnO with surface defects were developed on a glass substrate through the microwave-assisted hydrothermal technique, and their efficacy for photocatalytic phenol degradation was studied in an aqueous medium [5]. Recently, ZnO nanotubes have been synthesized on graphene-coated polyethylene terephthalate substrates using the hydrothermal technique [6]. The nanotubes of ZnO showed good photocatalytic activity toward photocatalytic decomposition of reactive yellow-15 (RY15) solution. Large-scale synthesized photocatalysts with other morphologies such as $Na_2V_6O_{16}.xH_2O$ nanoribbons (for photocatalytic CO_2 reduction into renewable hydrocarbon fuel, viz. CH_4) [7], $CdMoO_4$@CdS core/shell hollow superstructures (for photocatalytic aqueous Rhodamine B solution degradation) [8], graphitic carbon-nitride microtubes (for photocatalytic production of H_2 in lactic acid aqueous solutions) [9], etc. have also been reported to be synthesized via the hydrothermal approach.

2.2 Solvothermal method

The solvothermal method is another commonly used synthetic technique that could produce photocatalysts on a large scale. Solvothermal synthesis involves chemical reactions being carried out within sealed containers (e.g., bomb or autoclave) in a solvent (nonaqueous) at a temperature above its boiling point and under autogenous pressure. The solvothermal technique is analogous to the hydrothermal technique, except for the use of organic solvents in the solvothermal method, while the hydrothermal method employs water as the solvent. Solvothermal syntheses that employ alcohol and glycerol as the reaction media are termed as alcohothermal and glycothermal, respectively. The most important advantage of solvothermal synthesis is that it enables almost any material to be dissolved in the solvent by raising the temperature and pressure to their critical points. Additionally, this method facilitates precise control over the crystallinity, shape, and size of the photocatalysts, by altering experimental parameters such as reaction temperature and time, surfactant type, solvent type, and precursor type. Numerous photocatalysts have been reported to be synthesized on a large scale via the solvothermal method. For instance, a combination of solvothermal and sol-gel techniques have been used to synthesize a graphene-TiO_2 mesocrystal composite on a large scale and the photocatalytic property was assessed for photocatalytic Rhodamine B degradation in water [10]. Zheng et al. synthesized hierarchical microarchitectures of $CuInS_2$ photocatalyst via the solvothermal method and studied their efficacy for the photocatalytic evolution of hydrogen [11]. In another work, ultrathin nanosheet superstructures of TiO_2 were developed on a large scale via the solvothermal technique using n-propanol as

https://www.twirpx.org & http://chemistry-chemists.com

the solvent. The synthesized TiO_2 photocatalysts were studied for photocatalytic Rhodamine B degradation in an aqueous medium [12]. The solvothermal technique has also been used to develop photocatalysts on a large scale with other morphologies, such as an iron-based magnetic metal organic framework (for photocatalytic methylene blue degradation in an aqueous medium) [13], β-Bi_2O_3 nanospheres (for photocatalytic degradation of acetaminophen) [14], nanocomposites of a CdS metal-organic framework (for photocatalytic selective benzyl alcohol oxidation into benzaldehyde) [15], etc.

2.3 Thermal method

The thermal technique involves chemical decomposition or combustion of materials at elevated temperatures, either in the absence of oxygen or in the presence of oxygen. The thermal method includes simultaneous variation in both physical phase and chemical composition of the material. The key advantage of the thermal method is that it is a facile, inexpensive technique with no requirement of any solvent. Additionally, it produces well-crystallized products in less time and also reduces the production of wastes. Up to the time of writing, the thermal method has been widely employed to develop photocatalysts of graphitic carbon nitride (g-C_3N_4) on a large scale, particularly via pyrolysis [16–20]. Graphitic carbon nitride photocatalysts have also been developed via thermal treatment in the presence of air for different photocatalytic applications [21–23]. Nanocomposites of g-C_3N_4/Fe_3O_4/AgCl with magnetic properties were also reported to be synthesized on a large scale by the thermal method for photocatalytic Rhodamine B degradation [24]. The thermal method has also been employed to synthesize other photocatalysts on a large scale such as $AgVO_3$ nanorods (for methylene blue photodegradation) [25], micrometer-scaled ZnO/$ZnFe_2O_4$ coupled photocatalyst (for photodegradation of methyl orange and *Escherichia coli* K-12 inactivation) [26], three-dimensional mesoporous metal oxide networks (for photocatalytic azo dye degradation) [27], etc.

2.4 Wet chemical method

Another commonly used technique for synthesizing photocatalysts in nano-dimensions on a large scale is the wet chemical method. It is termed "wet" because it involves reactions as well as analyses in liquid phase. The wet chemical method involves the execution of chemical reactions in the solution phase between one or more reactants that undergoes transformation under certain specific experimental conditions to yield one or more products. The chemical reactions are usually carried out in reaction vessels, either in chemical reactors or in simple round-bottom flasks and beakers. There are several wet chemical synthesis routes for producing photocatalysts in nano dimensions, viz. the precipitation method, self-assembly, template synthesis, hot-injection, oriented attachment, interface-mediated synthesis, etc. Each of these synthetic routes differs from the others; hence, one cannot propose a general rule for these synthetic processes. The advantage of the wet chemical method is that it provides a high degree of controllability and reproducibility for nano-photocatalysts. The wet chemical synthetic technique has been used to produce

https://www.twirpx.org & http://chemistry-chemists.com

several nano-photocatalysts on a large scale for different photocatalytic applications. For instance, the chemical precipitation technique was employed to synthesize Bi_2S_3 nanorods/graphene composite photocatalyst material for photocatalytic malachite green dye degradation in an aqueous medium using visible light irradiation [28]. The chemical precipitation method has also been utilized to synthesize a Ag_2O/graphene oxide nanocomposite photocatalyst on a large scale for visible light-induced photocatalytic methylene blue degradation in water [29]. Alternatively, the coprecipitation technique was used to synthesize hierarchical Zn-Ti layered double-hydroxide photocatalysts with microspherical morphology, comprising of two-dimensional thin nanoflakes [30]. The photocatalysts were subsequently studied for photocatalytic decomposition of methylene blue in an aqueous medium. Nguyen et al. produced CuO combined-graphene-TiO_2 nanocomposite photocatalysts via the self-assembly technique for the photocatalytic decomposition of aqueous methylene blue trihydrate, Rhodamine B, and reactive black B solutions, using visible light irradiation [31]. Another wet chemical synthesis route, viz. the self-template method, was adopted to synthesize core/shell ZnO@zeolitic imidazolate frameworks-8 nanosphere photocatalysts for photocatalytic methylene blue degradation in water [32]. In another work, Ag-modified TiO_2 hollow octahedra photocatalysts were developed through the template-induced synthetic technique with Ag_2O octahedra as the template and TiF_4 as the precursor [33]. The developed photocatalysts were studied for photocatalytic methyl orange degradation in an aqueous medium.

2.5 Other synthetic strategies

In ion exchange synthetic methodology, ions (either cations or anions) are equivalently exchanged between the ionized species of the reaction system, wherein the ionized species are present in different phases. The exchange of ions does not involve any chemical bond formation. This method has been used to synthesize photocatalysts on a large scale. Sun et al. adopted the cation exchange technique to develop a CuS-decorated CdS nanorod photocatalyst for visible light-assisted photocatalytic production of hydrogen in water [34]. In another work, the anion-exchange method was used, along with the chemical method, to develop binary photocatalysts comprising of S-doped CeO_2 hollow spheres sensitized with an ultrathin CdS shell [35]. The composite photocatalyst was subsequently studied for photocatalytic hydrogen evolution using visible light illumination.

The microwave-assisted technique is a simple unique approach involving the application of microwave electromagnetic radiation for chemical reactions, resulting in rapid and efficient completion of the chemical reactions with high reproducibility. Microwave-assisted synthesis is a facile economic means for the reduction of particle size and improvement in dissolution. This technique has emerged as an efficient tool for the synthesis of nano-photocatalysts of desired sizes and shapes. Xia et al. reported microwave-assisted preparation of hollow MoS_2/BiOBr microsphere photocatalysts for visible light-aided photodegradation of ciprofloxacin and Rhodamine B [36]. Nanorods of ZnO have been prepared by the microwave-assisted hydrothermal technique and their photocatalytic

https://www.twirpx.org & http://chemistry-chemists.com

performance toward the degradation of phenol was investigated in water [5]. In another work, crystalline polyimide was obtained via microwave-assisted heating synthesis within minutes, without the requirement of any tedious washing process [37]. The obtained polyimide revealed improved photocatalytic production of H_2 using visible light irradiation.

The refluxing method is another synthetic technique that has been used to synthesize photocatalysts on a large scale. This technique basically involves the condensation and return of vapors to the reaction mixture from where it originated. The refluxing technique was used to develop Cu-doped α-FeOOH nanoflowers comprising of nanorods, where the nanoflower photocatalyst was studied for visible light-mediated decomposition of diclofenac sodium in water in the presence of H_2O_2 [38]. In another work, a nanocomposite of AgBr-ZnO was synthesized in water via the refluxing approach, where the reaction mixture was treated at 90°C for 3 h [39]. Subsequently, the nanocomposites were studied for photocatalytic methylene blue degradation in water using visible light irradiation. Nanocomposite photocatalysts of graphitic carbon nitride/SnO_2 were also developed on a large scale via the refluxing technique, for the visible light-driven photocatalytic decomposition of Rhodamine B in an aqueous medium [40].

The electrochemical method, particularly anodization, is a facile versatile electrolytic technique for the formation of functional materials (mostly oxides) onto the metal substrate's surface, upon providing the optimum voltage. The term "anodizing" is used because the metal substrate, on which the functional material is formed, acts as the anode electrode of an electrolytic cell. Owing to the ease of variability in the components, viz. metal substrate, electrolyte, etc., electrochemical anodization has been used to synthesize different photocatalysts for large-scale photocatalytic applications. Recently, ultrathin Cu_2O nanowires were synthesized via the anodizing method using nanoporous Cu as a substrate [41]. The Cu_2O nanowire photocatalysts were then investigated for their photocatalytic decomposition rate of Rhodamine B in water. In another work, nanoporous tungsten oxide films were prepared on a tungsten substrate through the anodizing technique in an ammonium nitrate/ethylene glycol/water mixture [42]. The developed photocatalyst was studied for photocatalytic methylene blue decomposition in water. The anodizing technique has also been used to synthesize photocatalysts of titania on a large scale, viz. pine-cone TiO_2 nanostructures (for photocatalytic hydrogen production using water and degradation of methyl orange) [43], TiO_2 nanotubes layers (for photocatalytic hexane degradation) [44], nitrogen-doped TiO_2 nanotubes (for photocatalytic phenol degradation) [45], etc.

3 Applications of large-scale produced photocatalysts

3.1 Degradation of pollutants

The exponential growth of industrialization to meet the demands of the increasing human population has led to an exponential increase in environmental contamination with various harmful pollutants, ranging from dyes and organic chemicals to different toxic metal

https://www.twirpx.org & http://chemistry-chemists.com

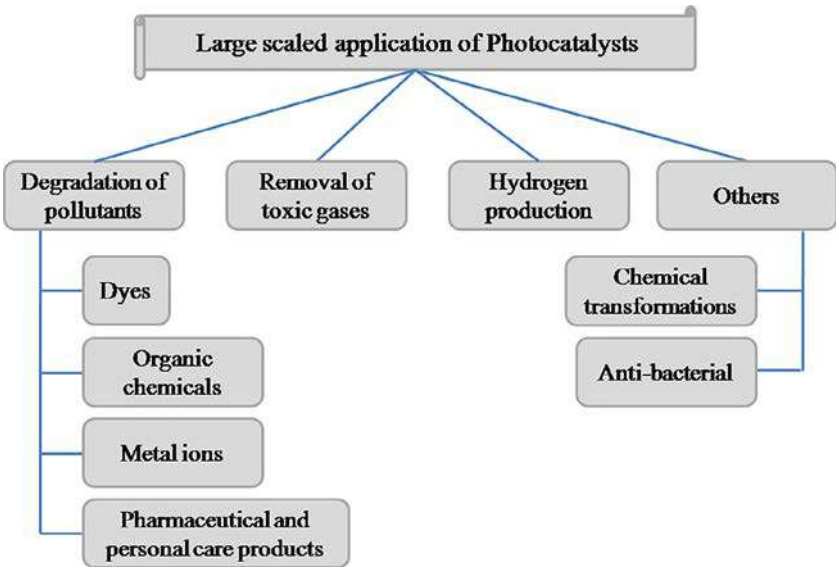

FIG. 4 Different applications of large-scale synthesized photocatalysts. *No permission required.*

ions. Photocatalysis is therefore an effective tool to combat these harmful environmental pollutants, by utilizing a major renewable source of energy, viz. solar energy (Fig. 4).

Dyes constitute a major fraction of the harmful pollutants released into the surrounding from various industries such as textiles, dying, printing, cosmetics, papermaking, etc. Most of the synthetic dyes and pigments used in various industries are toxic in nature and hence the untreated dye contaminated wastewater that is released into the water bodies is a great threat to the aquatic ecosystem. Photocatalysis that employs solar energy is therefore a very economical remediation technique for the degradation and removal of dyes from water bodies, which in turn requires the photocatalyst to be synthesized on a large scale for extensive commercial application. In this respect, numerous studies have already been reported that explained the effectiveness of large-scale synthesized photocatalysts in the disposal of harmful dyes from water bodies. For instance, Nguyen et al. reported the large-scale preparation of a frost-like CuO combined graphene-TiO_2 nanocomposite catalyst via the self-assembly technique for the photodegradation of methylene blue trihydrate, Rhodamine B, and reactive black B in aqueous solutions using visible light irradiation [31]. A large-scale synthesized macroscopic 3D structured aerogel hybrid of graphene oxide and graphitic-carbon nitride has been studied for photocatalytic methyl blue and methyl orange decomposition in an aqueous medium [46]. It was observed that decomposition of the dyes (20 mg L^{-1}) reached a value of ~90% in <40 min of visible light illumination when the mass ratio of graphitic carbon nitride and graphene oxide was 3:5. In a different approach, core-shell hollow superstructures of $CdMoO_4$@CdS were synthesized on a large scale via the ion exchange hydrothermal method with diameters of 2–3 μm

https://www.twirpx.org & http://chemistry-chemists.com

for the photocatalytic decomposition of Rhodamine B aqueous dye solution using visible light irradiation [8]. In another work, core-shell nanospheres of ZnO@zeolitic imidazolate frameworks-8, prepared on a large scale through a self-template technique, were used as photocatalyst for methylene blue decomposition in water [32]. Large-scale 3D mesoporous networks of metal oxides such as SnO_2, WO_3, Fe_2O_3, CeO_2, CuO, NiO, Co_3O_4, and TiO_2/WO_3 were prepared via the furfural alcohol-derived polymerization-carbonization-combustion approach for large-scale photocatalytic decomposition of aqueous methyl orange and Rhodamine B solutions [27]. The 3D mesoporous networks were reported to comprise of a large exposed surface area and a large pore volume that enhances their photocatalytic activity.

Organic chemicals such as phenol and its derivatives (viz. 2,4-dinitrophenol, 4-nitrophenol, and 2-nitrophenol) are other major pollutants of industrial wastewater, that are being released in high quantities from different manufacturing and petroleum industries. Being nonvolatile in nature, phenol and its derivatives could accumulate over years when untreated and could cause a serious threat to both aquatic life and human health, along with causing drinking water to become toxic. Numerous photocatalysts have therefore been synthesized on a large scale for disposal of phenols from aqueous solutions. For instance, Wang and coworkers reported nanoparticles of TiO_2 treated with NaH via a low-temperature solution-based method for photocatalytic phenol degradation in water [47]. In another work, anodically synthesized nitrogen-doped TiO_2 nanotubes were used for the photodegradation of phenol in water using visible light illumination [45]. Nanorods of zinc oxide, prepared on a glass substrate through the microwave-assisted hydrothermal technique, also showed efficient photocatalytic performance toward photodegradation of phenol using visible light irradiation [5]. In a different approach, graphitic carbon nitride with porous nanostructures, which were synthesized on a large scale by the pyrolysis technique, showed effective visible light photocatalytic activity toward the photocatalytic decomposition of phenol pollutants in water [21]. Large-scale synthesized Ag/AgCl nanoparticles on layered-titanate honeycomb structures were also studied for visible light photocatalytic aqueous phenol degradation [48].

The tremendous progress in the area of health care, in the last few decades, has led to the development of numerous effective pharmaceutical and personal care products (such as diclofenac sodium, acetaminophen, etc.) that are extensively used all round the world. However, improper disposal of these products has contaminated the environment, particularly water bodies including groundwater and surface water, and has posed a severe menace to the aquatic environment and human health. It is reported that the presence of even minute concentrations of these products can cause endocrine disruption, chronic toxicity, and development of pathogen resistance. Moreover, a few of these products are bioactive, environmentally persistent, and have the potential of bio-accumulation. These products are usually added to the aquatic ecosystem from the inadequately treated wastewater from chemical manufacturing plants, hospitals, and excreta of humans/animals. Most of these pharmaceutical and personal care products are not degraded completely by conventional wastewater treatments, and therefore require advanced treatment

https://www.twirpx.org & http://chemistry-chemists.com

technologies for their effective removal from the environment. In this context, the photocatalytic technique is an excellent tool for the complete and large-scale removal of these products from the environment with high efficiency under ambient conditions. An antipyretic and analgesic drug, acetaminophen (*N*-acetyl-*p*-aminophenol), popularly known as paracetamol, was reported to be photocatalytically degraded on a large scale under visible light irradiation by using β-Bi_2O_3 nanosphere photocatalysts [14]. Another pharmaceutical product, diclofenac sodium, which is an analgesic and antiinflammatory drug, was reported to be degraded in an aqueous medium through visible light photocatalysis in the presence of H_2O_2 by using Cu-doped α-FeOOH nanoflowers as photocatalysts [38]. The nanoflower-shaped photocatalyst comprises of a nanorod with a length of 200–400 nm. The Cu-doped α-FeOOH nanoflower photocatalyst showed optimal visible light photocatalytic activity when doped with 3% Cu (molar ratio of Cu to Fe). The overuse and improper disposal of antibiotics such as ciprofloxacin into the aquatic environment has also aroused global concern. Ciprofloxacin was reported to be photocatalytically degraded using visible light irradiation, upon utilizing ultrathin graphitic carbon nitride nanosheets as the photocatalyst [49]. The nanosheets photocatalyst was synthesized on a large scale via a facile hydrogen bond-assisted technique and exhibits few-layered thickness of 2–3 nm. In another work, few-layered MoS_2/BiOBr hollow microspheres were prepared on a large scale through the microwave-assisted method and subsequently used for photocatalytic ciprofloxacin degradation in an aqueous solution with visible light illumination [36].

Industrial wastewater also comprises of various toxic metal ions such as chromium, arsenic, etc. that are detrimental to both the environment and human bodies. Although the hexavalent form of chromium, i.e., Cr(VI), is the most toxic form of chromium, arsenic exhibits more toxicity and carcinogenic effects in its As(III) state. The arsenic removal processes/techniques developed until now—ion exchange, adsorption, precipitation, and membrane systems—could remove As(V) only [50]. Hence, As(III) oxidation to As(V) and Cr(VI) reduction to Cr(III) are vital for reducing their toxicity and facilitating their removal from contaminated water bodies. Photocatalysis was observed to be an effective means to achieve these goals, as photocatalysts were observed to get activated using UV and/or visible light irradiation and produce active species, viz. photoexcited hydroxyl radicals, holes, electrons, and superoxide radicals [51] that could trigger the oxidation/reduction of metal ions. Numerous studies of photocatalysis have been reported in this regard. For instance, Cu-doped ZnO photocatalysts have been synthesized by the precipitation technique for photocatalytic As(III) oxidation to As(V) under visible light irradiation [50]. Alternatively, porous Ag_2S-Ag heterostructure nanotubes were prepared via the microwave-assisted technique for visible light photocatalytic Cr(VI) species reduction in an aqueous solution [52]. Additionally, algae-decorated TiO_2/Ag hybrid nanofiber membranes [53] and terbium oxide-loaded TiO_2-oriented nanosheets [54] were synthesized on a large scale and studied for photocatalytic Cr(VI) reduction to Cr(III) using visible light illumination. Other inorganic heavy metals, such as mercury, have also been reported to be removed from industrial wastewater through photocatalysis. In aquatic

https://www.twirpx.org & http://chemistry-chemists.com

ecosystems, Hg(II) is converted into methyl mercury by bacteria that eventually magnify its toxicity after it progresses through the aquatic food chain [55]. Hence, reduction of Hg(II) is important to facilitate its removal from mercury-contaminated wastewater. Mohamed and Gazzaz [55] synthesized an SnO_2-Co_3O_4 nanocomposite through a simple coprecipitation technique and studied its photocatalytic efficiency in the visible light photo-reduction of Hg(II) to Hg(0). In another work, a Pd-ZnO/multiwalled carbon nanotubes nanocomposite was developed by a modified sol-gel technique, and was used for photocatalytic aqueous Hg(II) reduction with visible light irradiation [56].

3.2 Removal of toxic gases

Growing industrialization, increasing traffic, and rising demands for energy to meet the requirements of the growing population have led to an equivalent emission of various toxic gases as well as greenhouse gases into the environment. Toxic gases such as sulfur oxides (SO_x) and nitrogen oxides (NO_x) not only affect human health, but also lead to different environmental problems, such as photochemical smog, acid rain, and ozone layer destruction. In addition, greenhouse gases such as CH_4 and CO_2 have led to the greenhouse effect and global warming problems. Methane, the primary component of natural gas and a widely used chemical feedstock and fuel, is reported to exhibit a greenhouse gas effect that is more than 20 times greater than the effect of carbon dioxide by mass [57]. Hence, oxidation of methane to equimolar carbon dioxide is an important strategy for reducing the effects of global warming caused by methane. In this context, $SrCO_3$-decorated $SrTiO_3$ nano-photocatalysts were prepared by the sol-gel technique and studied for the photocatalytic oxidation of methane [58]. It was observed that both $SrCO_3$ and $SrTiO_3$ are inactive toward methane photo-oxidation when used alone, but they show a synergistic effect when used together as a composite material. In another work, Chen et al. synthesized silver-decorated zinc oxide nanostructured photocatalysts for CH_4 photo-oxidation using simulated solar light irradiation [57]. Carbon dioxide, another greenhouse gas that is produced mainly from fossil fuels' combustion, contributes significantly to global warming, and photocatalytic reduction is an effective strategy to combat its concentration in the atmosphere. Reli et al. [59] synthesized TiO_2/graphitic carbon nitride photocatalysts in varying concentrations through simple mechanical mixing of the constituents and studied the photocatalysts for photocatalytic carbon dioxide reduction. Apart from greenhouse gases, the removal of toxic gas, viz. SO_2, involves desulfurization techniques that could be attained efficiently by photocatalysis. In this regard, TiO_2-aluminum silicate fiber nanocomposites were synthesized through the sol-gel technique and their photocatalytic oxidation performance was studied for the desulfurization of SO_2 from simulated coal combustion flue gas [60]. Other toxic gases, viz. nitrogen oxides (NO_x), particularly NO and NO_2 that are emitted from different anthropogenic activities, are also a major threat to the environment, and photocatalytic NO_x oxidation/reduction is an efficient and economic means for their removal from the environment. Duan et al. [61] synthesized plasmonic Ag-TiO_{2-x} nanocomposites via a photochemical reduction

https://www.twirpx.org & http://chemistry-chemists.com

method, with subsequent postannealing, and studied their photocatalytic performance toward the removal of NO using visible light illumination. The Ag-TiO_{2-x} photocatalysts simultaneously undergo NO photo-oxidation and selective NO photo-reduction to N_2 during the NO removal course, where oxidation results from the synergic effect between h^+ and $\bullet O_2^-$, and reduction is due to the oxygen vacancies in TiO_2. In another work, graphitic carbon nitride/TiO_2 nanocomposites coupled with $CaCO_3$ were synthesized through the annealing technique and studied for the complete oxidation of NO to NO_3^- without the formation of intermediate toxic NO_2 gas [62]. Hematite (α-Fe_2O_3) has also been studied as a photocatalyst for the encapsulation and photo-oxidation of toxic NO_x gases, viz. NO and NO_2 [63]. Another toxic indoor air pollutant, formaldehyde, is reported to be removed through the photocatalytic oxidation technique. Formaldehyde is known to be a carcinogen and irritant that causes allergic symptoms even at very low concentrations. Zhou and coworkers [64] synthesized carbon-doped ZnO photocatalysts for the effective photo-mineralization of formaldehyde to CO_2 using visible light irradiation. The efficient photocatalytic performance of the photocatalyst was ascribed to its high efficacy of generating electron-hole pairs and low recombination rate of the generated pairs in the visible region.

3.3 Production of hydrogen

The concerns over the rising needs of the erupting population, escalating environmental issues, and tackling the growing global energy crisis have led to increasing demand for an environmentally benign and sustainable energy source, which could reduce both fossil fuel dependency and related environmental damage. Recently, hydrogen (a carbon-free solution) has been recognized as a promising, clean, and renewable fuel that exhibits high energy density and is convenient for transport and storage. Nonetheless, hydrogen is presently generated commercially either from fossil fuel combustion or high-energy consumption processes that are costly and lead to environmental pollution. In this context, photocatalysis has emerged as an alternative economical and environmentally benign approach of converting clean, renewable, and abundant solar energy into clean and renewable hydrogen fuel through water splitting, where solar energy gets converted into chemical energy of fuel. Since solar-driven photocatalytic water splitting uses two renewable and abundant sources, solar energy and water, it is considered to be an economical, green, and sustainable technique for large-scale hydrogen generation. During solar-driven photocatalytic water splitting, photons from solar irradiation hit the photocatalyst and generates electron-hole pairs [65]. The resultant electric charges subsequently dissociate water molecules. For solar-driven water splitting, the photocatalysts should exhibit a suitable bandgap along with proper location of conduction and valence bands for oxidation-reduction reaction, and there should be rapid generation as well as separation of electron-hole pairs [65] (Fig. 5). The photo-oxidation and photo-reduction reactions involved during photocatalytic water splitting are as follows [65].

Photo-oxidation: $2H_2O + h\nu \rightarrow O_2 + 4H^+ + 4e^-$

Photo-reduction: $2H_2O + 2e^- + h\nu \rightarrow H_2 + 2OH^-$

https://www.twirpx.org & http://chemistry-chemists.com

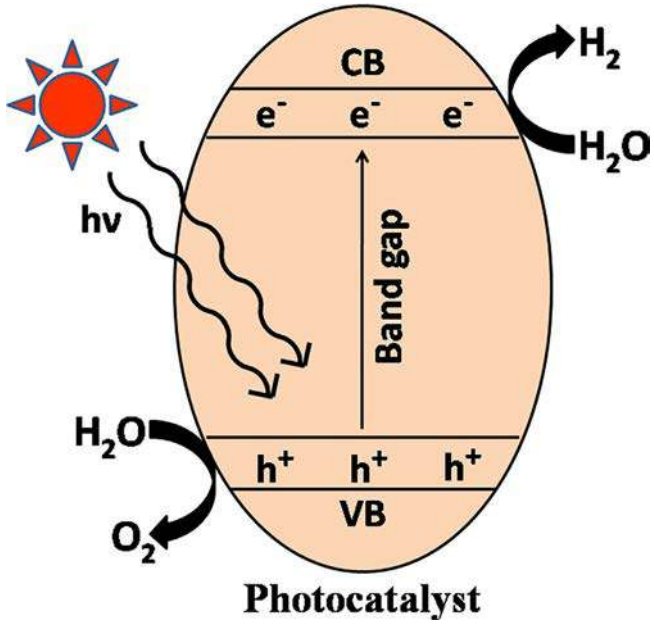

FIG. 5 Schematic diagram for photocatalytic water splitting into H_2 and O_2. (VB, valence band; CB, conduction band; h^+, hole; e^-, electron; $h\nu$, solar energy; h, Planck's constant; ν, frequency.) *No permission required.*

At the time of writing, numerous photocatalysts have been reported for the photocatalytic splitting of water for hydrogen production on a large scale. In this regard, recyclable and highly stable metal organic framework-derived ZnO/ZnS heterostructured nanophotocatalysts have been synthesized with superior photocatalytic hydrogen evolution reaction (HER) activity using visible light illumination ($\lambda > 420$ nm) [66]. In another work, a metal-free photocatalyst was synthesized involving the integration of CdS nanorods/ZnS heterojunction material with amorphous NiS for the solar-driven photocatalytic generation of hydrogen from water using visible light [67]. The average quantum yield was observed to be ~43.2% after 5 h illumination with a monochromatic light (420 nm). Ma et al. [68] prepared melamine-assisted exfoliated quasi-2D polymeric graphitic carbon nitride photocatalysts with high specific surface area (116.76 $m^2\ g^{-1}$) and large bandgap (0.13 eV) for large-scale photocatalytic hydrogen production using visible light irradiation. Nanosheet-structured photocatalysts of $MnSb_2S_4$ [69], graphitic carbon nitride [70], MoS_2/CdS [71], etc. have also been synthesized and studied for solar-driven photocatalytic hydrogen generation from water using visible light illumination.

3.4 Other applications

In the last few years, the search for effective and sustainable pollution-free techniques has been widened by rapidly growing industrialization to circumvent environmental issues and expand the commercial manufacture of essential products to meet the demands of the increasing population. One such attempt is the application of visible light

https://www.twirpx.org & http://chemistry-chemists.com

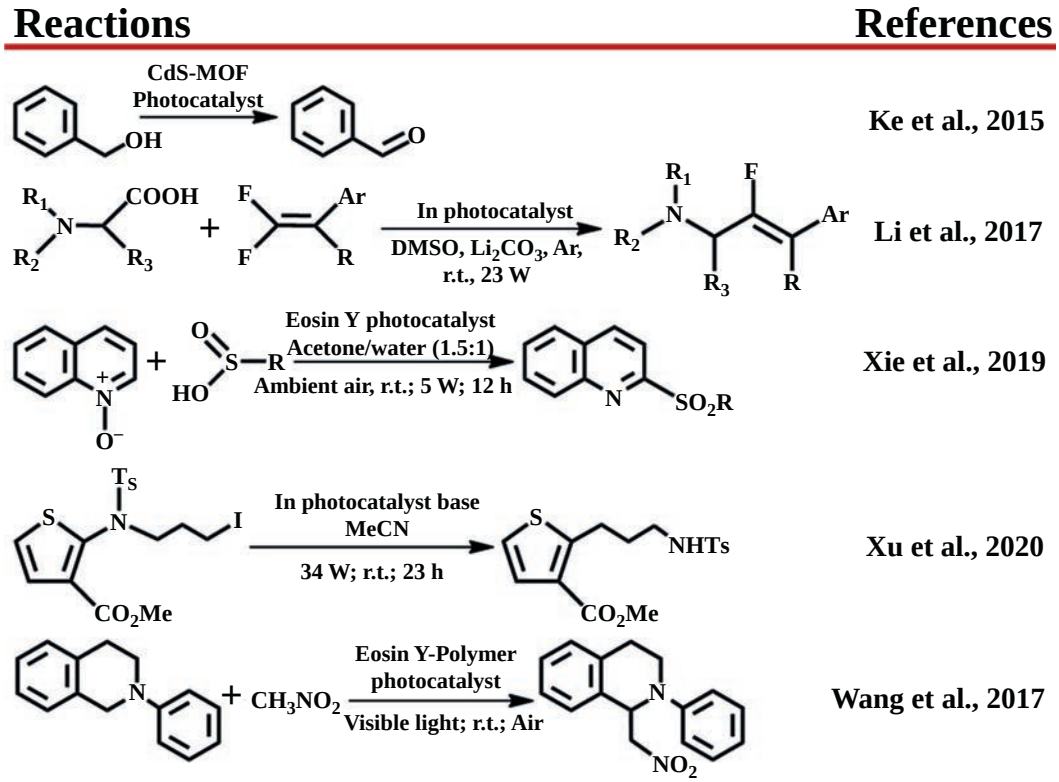

FIG. 6 A few chemical transformations that employed large-scale synthesized visible light photocatalysts. *No permission required.*

photocatalysis in synthetic organic chemistry for transformation of organic compounds from one to another. The use of naturally abundant solar energy, its environmental friendliness, and the ease of use make photocatalysis a powerful tool for carrying out organic reaction transformations on a large scale (Fig. 6). Ke et al. [15] carried out visible light-driven photocatalytic benzyl alcohol oxidation to benzaldehyde using CdS/metal organic framework (MOF) nanocomposites. The porous photocatalysts was prepared through the solvothermal technique using cadmium acetate [$Cd(Ac)_2$] as the CdS precursor and MIL-100(Fe) as the support. The photocatalytic conversion was observed to be ~54%, while the selectivity was found to be ~99%. In another work, Li et al. [72] carried out photocatalytic N-protected α-amino acids' decarboxylative monofluoroalkenylation with gem-difluoroalkene to get the corresponding α-amino monofluoroalkene, under visible light irradiation. The chemical transformation involves $Ir[dF(CF_3)ppy]_2(dtbpy)PF_6$ as the photocatalyst, DMSO as the solvent, and Li_2CO_3 as the base using an argon atmosphere at room temperature. In an alternative approach, visible light-induced deoxygenative C2-sulfonylation of quinoline N-oxide was carried out with sulfinic acid, in the presence of

https://www.twirpx.org & http://chemistry-chemists.com

ambient air as the sole oxidant, organic dye as the photocatalyst, and an acetone aqueous solution as the solvent [73]. This radical organic reaction produces 2-sulfonylquinoline in good to excellent yields at ambient temperature on a large scale. Recently, two heterogeneous visible light photocatalysts comprising of iridium-based porous organic polymers were prepared using two [Ir(ppy)2(dtbbpy)]-based bitopic linkers and tetraphenylmethane tetraborate [74]. The synthesized heterogeneous visible light photocatalysts were highly stable and were used to carry out different organic transformations such as desulfurative conjugate addition to Michael acceptor, Smiles-Truce rearrangement of alkyliodide, and aerobic oxidations of sulfide and arylboronic acid, with good recyclability of 8–19 times. Wang et al. [75] reported a facile "bottom-up" approach to prepare two Eosin Y dye-based porous organic polymer frameworks for heterogeneous organic photocatalysis. The photocatalysts effectively photocatalyzed the aza-Henry reaction using visible light irradiation and displayed good recyclability of 12 cycles with a yield of 94%–98%.

The presence of bacteria and the toxins produced by them not only contaminate water bodies, but also are responsible for poisoning humans and animals that come in contact with them. Some of the bacteria and their toxins are quite stable and cannot be removed efficiently by conventional water treatment techniques. The search for advanced techniques for their effective removal has shown that solar photocatalysis is a powerful tool in this context. Several studies have already been reported for solar photocatalysts with antibacterial properties. For instance, large-scaled synthesized AgI/TiO_2 nanocomposites through the ultrasound-assisted preparation approach [76] and a ZnO/$ZnFe_2O_4$ coupled photocatalyst via the thermal technique [26] were studied for the disinfection of wastewater from *E. coli* using visible light irradiation. In another work, three-phase TiO_2/Ag_3PO_4/graphene composites were prepared on a large scale through the combination of hydrothermal and ion-exchange techniques that showed excellent bactericidal performance [77]. The photo-induced antibacterial performance of the photocatalyst was examined on six different bacterial strains: *E. coli*, *Salmonella typhi*, *Staphylococcus aureus*, *Bacillus subtilis*, *B. pumilus*, and *Pseudomonas aeruginosa*. Microcystin-LR, a common cyanobacterial toxin, was reported to be degraded in water using doped visible light-absorbing photocatalysts, comprising of C, Pt, and Rh as the dopants in TiO_2 [78]. The study showed that Rh-doped TiO_2 possessed the highest photocatalytic performance using visible light irradiation of 20 min with 90% toxin removal.

4 Photocatalysts synthesized so far on a large scale

4.1 Titania-based photocatalysts

Titania (TiO_2) is the most widely studied semiconductor photocatalyst at the time of writing. The heterogeneous nature of TiO_2 makes it a very promising candidate for photocatalytic reactions with good reusability. Although TiO_2 was discovered as a promising catalyst ~90 years ago, extensive study of its catalytic activity commenced only after

https://www.twirpx.org & http://chemistry-chemists.com

Fujishima and Honda reported that TiO_2 electrodes could be used for photocatalytic splitting of water in 1972 [79]. TiO_2 photocatalysts can be used over a wide pH range. They are highly stable, biocompatible, environmentally benign, and abundant low-cost metal oxide photocatalysts that can be used for effective degradation of a wide spectrum of contaminants on a large scale. Additionally, they offer the possibility of being immobilized on different supports with no considerable loss to their photocatalytic performance. This feature enables TiO_2 photocatalysts to be used in the construction of effective photochemical reactors for purification of water and air.

During photocatalysis, the semiconductor TiO_2 is bombarded with photons, which results in excitation of electrons in the valence band that subsequently goes to the conduction band and creates positive holes in the valence band (Fig. 7). The excited electrons in the conduction band react with oxygen to give superoxide radicals, hydroperoxide radicals, hydroxyl radicals, and hydrogen peroxide, while the positive hole in the valence band reacts with water to generate hydroxyl radicals and hydrogen ions. These radicals subsequently participate in various photocatalytic reactions and degradation mechanisms. Among the three TiO_2 phases, viz. anatase, brookite, and rutile, the anatase phase is the most active photocatalytic phase owing to its large bandgap of 3.2 eV. However, this large bandgap restricts its use in the ultraviolet region (<390 nm) only, which comprises ~4% of the solar radiation. In order to enhance the photocatalytic activity, tremendous research work has been carried out on TiO_2 photocatalysts to shift their optical response from ultraviolet to the visible light region (400–700 nm) that comprises ~42% of the solar light. The modified TiO_2 photocatalysts have hence been studied for different visible light photocatalytic applications. For instance, TiO_2/Ag chitosan hybrid nanofiber mats were loaded with algae cells and the bio-nano hybrid photocatalyst was utilized for visible light-driven photocatalytic Cr(VI) removal from an aqueous medium [53]. In another approach, the light absorption ability of TiO_2 was shifted from the ultraviolet to the visible light region by the introduction of elemental red phosphorus [80]. The red phosphorus-TiO_2 photocatalyst was subsequently studied for visible light photocatalytic Rhodamine B pollutant degradation in water. Zhu and coworkers synthesized stable blue-colored titania nanoparticles on a large scale that are comprised of Ti^{3+} localized in a TiO_{2-x} core based on Le Chatelier's principle [81]. The presence of Ti^{3+} in the nanoparticles explains the visible light photocatalytic performance of the titania photocatalyst toward methylene blue

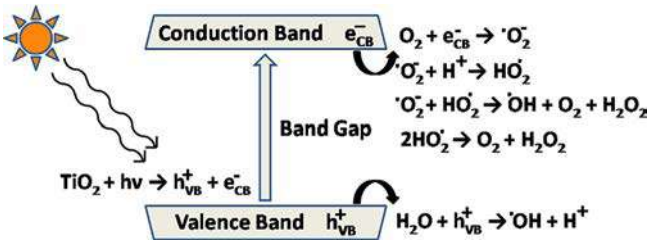

FIG. 7 Schematic diagram showing the photocatalysis mechanism of TiO_2. *No permission required.*

https://www.twirpx.org & http://chemistry-chemists.com

photo-oxidation using visible light irradiation. For the highest visible light photocatalytic performance, the optimal molar ratio of Ti^{4+}:Ti^{3+} was observed to be 1:40.

4.2 Graphitic carbon nitride-based photocatalysts

A metal-free polymeric organic semiconductor, graphitic carbon nitride (g-C_3N_4), is the most stable allotrope of carbon nitrides with a bandgap of ∼2.7 eV. The excellent thermal, chemical, and photo-chemical stability, abundant availability of precursors, environmentally friendly nature, 2D layered structure, low cost, and a low bandgap value have drawn enormous attention for the use of g-C_3N_4 in large-scale visible light-driven photocatalysis. Moreover, the preparation of g-C_3N_4 does not require any expensive materials or techniques, but can be easily prepared by the thermal polycondensation reaction of a nitrogen-rich precursor such as dicyandiamide, cyanamide, trithiocyanuric acid, melamine, thiourea, urea, and their mixtures. Despite exhibiting so many excellent characteristics, the large-scale use of g-C_3N_4 for visible light photocatalysis is limited by some shortcomings [82]. The major limitation is the high recombination rate of the photo-generated electron-hole pairs. Another limitation is the low specific surface area, which results in poor harvesting of visible light illumination. The excellent thermal and chemical stability enables the modifications of g-C_3N_4 with other suitable materials to overcome these shortcomings. Various modifications of g-C_3N_4 have already been proposed to improve their large-scale visible light photocatalytic activity via different approaches [19], such as integration with other semiconductors (e.g., TiO_2, WO_3, $DyVO_4$, ZnO, AgBr, Bi_2WO_6, $ZnWO_4$, CdS), loading with noble metal (e.g., Au, Ag, Fe, Pd), doping with non-metallic elements (e.g., B, S, F, P), and variation of g-C_3N_4 morphology (e.g., nanotubes, nanorods, nanospheres, mesoporous structure). Currently, many reports are available that describes the use of modified g-C_3N_4 for various large-scale visible light photocatalytic application such as degradation of dyes [19, 24, 46, 82], removal of toxic gases [59, 62], decomposition of metal ions [51], production of hydrogen [68, 70], decomposition of pharmaceutical products [49], etc.

4.3 ZnO-based photocatalysts

The n-type semiconductor zinc oxide (ZnO), exhibits a bandgap value of 3.37 eV, similar to that for TiO_2. Owing to its unique characteristics—such as nontoxic nature, environmentally benign features, low cost, high activity, good electric conductivity, strong oxidation ability, excellent optical transparency, and piezo electricity—ZnO has been extensively studied as a heterogeneous photocatalyst. Additionally, it exhibits good antibacterial and antifouling properties. Although ZnO has been widely studied in photocatalysis, it faces some serious drawbacks that limit its effective and economical visible light photocatalytic applications on a large scale. First, the wide bandgap value, similar to that for TiO_2, restricts its use to the ultraviolet region only. Second, the charge-carrier recombination of the photo-generated electron-hole pair in ZnO is very high. Thus, it becomes necessary to overcome these limitations of high recombination rate and restricted use in the

https://www.twirpx.org & http://chemistry-chemists.com

ultraviolet region only, to get efficient large-scale visible light photocatalysts of ZnO. The two limitations of ZnO have been reported to be surmounted by various techniques such as doping ZnO with another metal/nonmetal, self-doping by crystal defects, plasmon coupling, integration with other semiconductors, etc. Modified ZnO photocatalysts have been used in numerous large-scale visible light photocatalytic applications, such as removal of toxic gas [57], degradation of dye [32, 83], removal of metal ions [50, 56], antibacterial activity [26], hydrogen production [66], etc.

During photocatalysis, the semiconductor ZnO is excited with photonic energy that results in the promotion of electrons from the filled valence band to the empty conduction band, thereby generating electron-hole pairs [84]. These electron-hole pairs subsequently migrate to the ZnO surface and participate in various redox reactions. The H^+ in the valence band reacts with hydroxide ions and water to generate hydroxyl radicals, whereas the electrons in the conduction band react with oxygen to generate superoxide radical anions, followed by the formation of hydrogen peroxide. The generated reactive radicals then undergo various catalytic reactions [84].

4.4 Other large-scale synthesized photocatalysts

Apart from TiO_2- and ZnO-based photocatalysts, many other inorganic materials have also been studied for large-scale visible light photocatalysis. For instance, microwave-assisted synthesized Ag_2S-Ag porous hybrid nanotubes have been reported for large-scale visible light photocatalytic methyl orange degradation and aqueous Cr^{VI} reduction [52]. In other work, $AgVO_3$ nanorods [25] and 3D graphene oxide-Ag@Ag_3PO_4 hydrogel nanocomposites [85] have been used for visible light photocatalytic dye degradation. Anodically synthesized hierarchical structured ultrathin Cu_2O nanowires@nanoporous copper nanocomposite ribbon [41] and mechanochemically synthesized CuS quantum dots [86] have been reported for visible light photocatalytic degradation of dye. CdS nanostructures with hexagonal wurtzite phase, prepared using CdO and thiourea, have been used for large-scale visible light photocatalytic H_2 production and organic dye degradation [87]. CdS has also been integrated with other compounds and studied for large-scale visible light photocatalysis, viz. CdS/MoS_2 for hydrogen production [71], CdS/$CdMoO_4$ for dye degradation [8], CdS/Cu_xS for hydrogen production [34], CdS/$CeO_{2-x}S_x$ for hydrogen production [35], CdS/carbon nanotubes/diethylenetriamine for dye degradation [88], etc. In a different approach, the most stable n-type semiconducting iron oxide, i.e., α-Fe_2O_3 (hematite), was observed to be an effective visible light photocatalyst for the decontamination of NO_x gases [63]. Feng et al. [13] synthesized an iron-based magnetic metal organic framework MIL-53(Fe), comprising of embedded γ-Fe_2O_3 nanoparticles, for large-scale visible light photocatalytic degradation of dye. MoS_2/BiOBr hollow microspheres were studied for large-scale visible light photocatalytic removal of ciprofloxacin [36]. Large-scale visible light photocatalytic H_2 generation was also achieved by using an NiS/CdS/ZnS cocatalyst [67] and 2D monolayer $MnSb_2S_4$ nanosheets [69]. In a different work, indium oxide ($In_2O_{3-x}(OH)_y$) hydroxylated nanoparticle photocatalysts were studied for the large-scale photocatalytic gas-phase CO_2 reduction for solar fuel production [89].

https://www.twirpx.org & http://chemistry-chemists.com

5 Summary and future perspective

The two most important global concerns of today's world are environmental pollution and energy crisis. To meet the demands of the ever-increasing human population, exponentially growing industrialization has contaminated the environment with many tons of harmful pollutants and toxic gases. The proper functioning of these industries depends on the scarce nonrenewable fossil fuels, viz. coal and petroleum, which has subsequently led to the problems of the energy crisis. Hence, alternative routes are urgently sought to combat these serious global issues. In this context, photocatalysis is a promising economical, environmentally friendly, and effective approach to cope with these problems, as it employs an abundant renewable source of energy, viz. solar energy, which can be scaled up sufficiently to solve all these issues under ambient conditions. At the time of writing, numerous photocatalysts have already been developed for large-scale removal of different pollutants such as dyes, organic chemicals, pharmaceutical and personal care products, toxic metal ions, and toxic gases, along with the removal of harmful bacteria. Additionally, photocatalysis has been employed for large-scale production of hydrogen fuel and carrying out various organic transformations. Although solar light-driven photocatalysis has been widely used to solve many alarming problems of present times, such as environmental pollution, energy crisis, etc., it is in its infancy. We still have a long way to go to achieve a world that is both pollution-free and self-sufficient with essential commodities by employing this excellent technique. Owing to the excellent versatile and moldable properties of photocatalysts, the photocatalysis technique could be of great demand for industrial applications in years to come.

Acknowledgment

Himani Kalita would like to acknowledge University Grants Commission, New Delhi, India for providing the Dr. D.S. Kothari postdoctoral fellowship.

References

[1] Braslavsky SE, et al. Glossary of terms used in photocatalysis and radiation catalysis (IUPAC recommendations 2011). Pure Appl Chem 2011;83:931–1014.

[2] Richter R, et al. Removal of non-CO_2 greenhouse gases by large-scale atmospheric solar photocatalysis. Prog Energy Combust Sci 2017;60:68–96.

[3] Gan YX, et al. Hydrothermal synthesis of nanomaterials. J Nanomater 2020;2020:8917013.

[4] Wang X, et al. Large-scale synthesis well-dispersed ZnS microspheres and their photoluminescence, photocatalysis properties. Mater Charact 2008;59:1765–70.

[5] Al-Sabahi J, et al. Controlled defects of zinc oxide nanorods for efficient visible light photocatalytic degradation of phenol. Materials 2016;9:238.

[6] Yu Q, et al. Fabrication and photocatalysis of ZnO nanotubes on transparent conductive graphene-based flexible substrates. Sci China Mater 2018;61:1007–11.

[7] Feng S, et al. $Na_2V_6O_{16}.xH_2O$ nanoribbons: Large-scale synthesis and visible-light photocatalytic activity of CO_2 into solar fuels. Nanoscale 2014;6:1896–900.

https://www.twirpx.org & http://chemistry-chemists.com

[8] Madhusudan P, et al. Fabrication of $CdMoO_4$@CdS core-shell hollow superstructures as high performance visible-light driven photocatalysts. Phys Chem Chem Phys 2015;17:15339–47.

[9] Zhou C, et al. Template-free large-scale synthesis of g-C_3N_4 microtubes for enhanced visible light-driven photocatalytic H_2 production. Nano Res 2018;11:3462–8.

[10] Yang X, et al. Graphene-spindle shaped TiO_2 mesocrystal composites: facile synthesis and enhanced visible light photocatalytic performance. J Hazard Mater 2013;261:342–50.

[11] Zheng L, et al. Nearly monodisperse CuInS2 hierarchical microarchitectures for photocatalytic H_2 evolution under visible light. Inorg Chem 2009;48:4003–9.

[12] Hu C, et al. Large-scale, ultrathin and (001) facet exposed TiO_2 nanosheet superstructures and their applications in photocatalysis. J Mater Chem A 2014;2:2040–3.

[13] Feng X, et al. In-situ ethylenediamine-assisted synthesis of a magnetic iron-based metal-organic framework MIL-53(Fe) for visible light photocatalysis. J Colloid Interface Sci 2017;494:32–7.

[14] Xiao X, et al. Facile large-scale synthesis of β-Bi_2O_3 nanospheres as a highly efficient photocatalyst for the degradation of acetaminophen under visible light irradiation. Appl Catal Environ 2013;140–141:433–43.

[15] Ke F, et al. Facile fabrication of CdS-metal-organic framework nanocomposites with enhanced visible-light photocatalytic activity for organic transformation. Nano Res 2015;8:1834–46.

[16] Liu J, et al. Simple pyrolysis of urea into graphitic carbon nitride with recyclable adsorption and photocatalytic activity. J Mater Chem 2011;21:14398–401.

[17] Fang HB, et al. Facile large-scale synthesis of urea-derived porous graphitic carbon nitride with extraordinary visible-light spectrum photodegradation. Ind Eng Chem Res 2016;55:4506–14.

[18] Chen J, et al. One-step synthesis of sulfur-doped and nitrogen-deficient g-C_3N_4 photocatalyst for enhanced hydrogen evolution under visible light. Mater Lett 2015;145:129–32.

[19] Qiu P, et al. Fabrication of an exfoliated graphitic carbon nitride as highly active visible light photocatalyst. J Mater Chem A 2015;3:24237–44.

[20] Jiang J, et al. A comparison study of alkali metal-doped g-C_3N_4 for visible-light photocatalytic hydrogen evolution. Chinese J Catal 2017;38:1981–9.

[21] Zhang M, et al. Enhancement of visible light photocatalytic activities via porous structure of g-C_3N_4. Appl Catal Environ 2014;147:229–35.

[22] Dong F, et al. Efficient synthesis of polymeric g-C_3N_4 layered materials as novel efficient visible light driven photocatalysts. J Mater Chem 2011;21:15171–4.

[23] Dong F, et al. Facile transformation of low cost thiourea into nitrogen-rich graphitic carbon nitride nanocatalyst with high visible light photocatalytic performance. Cat Sci Technol 2012;2:1332–5.

[24] Akhundi A, Yangjeh AH. Novel magnetic g-C_3N_4/Fe_3O_4/AgCl nanocomposites: facile and large-scale preparation and highly efficient photocatalytic activities under visible-light irradiation. Mater Sci Semicond Process 2015;39:162–71.

[25] Sivakumar V, et al. $AgVO_3$ nanorods: synthesis, characterization and visible light photocatalytic activity. Solid State Sci 2015;39:34–9.

[26] Li Y, et al. Facile synthesis of highly efficient ZnO/$ZnFe_2O_4$ photocatalyst using earth-abundant sphalerite and its visible light photocatalytic activity. Appl Catal Environ 2018;226:324–36.

[27] Bai H, et al. Large-scale, three-dimensional, free-standing, and mesoporous metal oxide networks for high-performance photocatalysis. Sci Rep 2013;3:2204.

[28] Vadivel S, et al. Facile large scale synthesis of Bi_2S_3 nano rods-graphene composite for photocatalytic photoelectrochemical and supercapacitor application. Appl Surf Sci 2015;351:635–45.

[29] Ji Z, et al. Graphene oxide modified Ag_2O nanocomposites with enhanced photocatalytic activity under visible-light irradiation. Eur J Inorg Chem 2013;2013:6119–25.

https://www.twirpx.org & http://chemistry-chemists.com

[30] Shao M, et al. The synthesis of hierarchical Zn-Ti layered double hydroxide for efficient visible-light photocatalysis. Chem Eng J 2011;168:519–24.

[31] Nguyen DCT, et al. Synthesis of frost-like CuO combined graphene-TiO_2 by self-assembly method and its high photocatalytic performance. Appl Surf Sci 2017;412:252–61.

[32] Yu B, et al. Self-template synthesis of core-shell ZnO@ZIF-8 nanospheres and the photocatalysis under UV irradiation. Mater Lett 2015;156:50–3.

[33] Wang X, et al. Facile template-induced synthesis of Ag-modified TiO_2 hollow octahedra with high photocatalytic activity. Chinese J Catal 2015;36:2211–8.

[34] Sun Z, et al. Cadmium sulfide nanorods decorated with copper sulfide via one-step cation exchange approach for enhanced photocatalytic hydrogen evolution under visible light. ChemCatChem 2016;8:157–62.

[35] Zheng N-C, et al. Ultrathin CdS shell-sensitized hollow S-doped CeO_2 spheres for efficient visible-light photocatalysis. Cat Sci Technol 2019;9:1357–64.

[36] Xia J, et al. Microwave-assisted synthesis of few-layered MoS_2/BiOBr hollow microspheres with superior visible-response photocatalytic activity for ciprofloxacin removal. CrstEngComm 2015;17:3645–51.

[37] Lin L, et al. Rapid microwave-assisted green production of a crystalline polyimide for enhanced visible-light induced photocatalytic hydrogen production. J Mater Chem A 2015;3:10205–8.

[38] Xu J, et al. Large scale preparation of Cu-doped α-FeOOH nanoflowers and their photo-Fenton-like catalytic degradation of diclofenac sodium. Chem Eng J 2016;291:174–83.

[39] Pirhashemi M, Habibi-Yangjeh A. Simple and large scale one-pot method for preparation of AgBr–ZnO nanocomposites as highly efficient visible light photocatalyst. Appl Surf Sci 2013;283:1080–8.

[40] Akhundi A, Yangjeh AH. A simple large-scale method for preparation of g-C_3N_4/SnO_2 nanocomposite as visible-light-driven photocatalyst for degradation of an organic pollutant. Mater Express 2015;5:309–18.

[41] Li M, et al. Formation and evolution of ultrathin Cu_2O nanowires on NPC ribbon by anodizing for photocatalytic degradation. Appl Surf Sci 2020;506:144819.

[42] Kikuchi T, et al. Fabrication of porous tungsten oxide via anodizing in an ammonium nitrate/ethylene glycol/water mixture for visible light-driven photocatalyst. Appl Surf Sci 2017;422:130–7.

[43] Liu Y, et al. Fast and large-scale anodizing synthesis of pine-cone TiO_2 for solar-driven photocatalysis. Catalysts 2017;7:229.

[44] Sopha H, et al. Scaling up anodic TiO_2 nanotube layers for gas phase photocatalysis. Electrochem Commun 2018;97:91–5.

[45] Mazierski P, et al. Photocatalytic activity of nitrogen doped TiO_2 nanotubes prepared by anodic oxidation: the effect of applied voltage, anodization time and amount of nitrogen dopant. Appl Catal Environ 2016;196:77–88.

[46] Tang L, et al. Fabrication of compressible and recyclable macroscopic g-C_3N_4/GO aerogel hybrids for visible-light harvesting: a promising strategy for water remediation. Appl Catal Environ 2017;219:241–8.

[47] Wang M, et al. Low-temperature fabrication of brown TiO_2 with enhanced photocatalytic activities under visible light. Chem Commun 2016;52:2988–91.

[48] Tang Y, et al. In situ formation of large-scale Ag/AgCl nanoparticles on layered titanate honeycomb by gas phase reaction for visible light degradation of phenol solution. Appl Catal Environ 2011;106:577–85.

[49] Xing W, et al. Construction of large-scale ultrathin graphitic carbon nitride nanosheets by a hydrogen-bond-assisted strategy for improved photocatalytic hydrogen production and ciprofloxacin degradation activity. ChemCatChem 2016;8:1–9.

https://www.twirpx.org & http://chemistry-chemists.com

[50] Vaiano V, et al. Cu-doped ZnO as efficient photocatalyst for the oxidation of arsenite to arsenate under visible light. Appl Catal Environ 2018;238:471–9.

[51] Hu C, et al. Photocatalytic dye and Cr(VI) degradation using a metal-free polymeric g-C_3N_4 synthesized from solvent-treated urea. Polymers 2019;11:182.

[52] Yang W, et al. Microwave-assisted synthesis of porous Ag_2S-Ag hybrid nanotubes with high visible-light photocatalytic activity. Angew Chem Int Ed 2012;51:11501–4.

[53] Wang L, et al. Algae decorated TiO_2/Ag hybrid nanofiber membrane with enhanced photocatalytic activity for Cr(VI) removal under visible light. Chem Eng J 2017;314:622–30.

[54] Lu D, et al. Enhanced photocatalytic degradation of aqueous phenol and Cr(VI) over visible-light-driven TbxOy loaded TiO_2-oriented nanosheets. Appl Surf Sci 2017;399:167–84.

[55] Mohamed RM, Gazzaz H. Environmental remediation from aqueous mercury (II) by photocatalytic reduction using a coupled SnO_2-Co_3O_4 nanocomposite. Desalin Water Treat 2013;53:2712–9.

[56] Mohamed RM, Salam MA. Photocatalytic reduction of aqueous mercury (II) using multi-walled carbon nanotubes/Pd-ZnO nanocomposite. Mater Res Bull 2014;50:85–90.

[57] Chen X, et al. Photocatalytic oxidation of methane over silver decorated zinc oxide nanocatalysts. Nat Commun 2016;7:12273.

[58] Pan X, et al. Photocatalytic oxidation of methane over $SrCO_3$ decorated $SrTiO_3$ nanocatalysts via a synergistic effect. Phys Chem Chem Phys 2016;18:31400–9.

[59] Reli M, et al. Novel TiO_2/C_3N_4 photocatalysts for photocatalytic reduction of CO_2 and for photocatalytic decomposition of N_2O. J Phys Chem A 2016;120:8564–73.

[60] Yuan Y, et al. Simultaneous removal of SO_2, NO and mercury using TiO_2-aluminum silicate fiber by photocatalysis. Chem Eng J 2012;192:21–8.

[61] Duan Y, et al. Plasmonic Ag-TiO_2-x nanocomposites for the photocatalytic removal of NO under visible light with high selectivity: the role of oxygen vacancies. Appl Catal Environ 2017;204:67–77.

[62] Papailias I, et al. Photocatalytic activity of modified g-C_3N_4/TiO_2 nanocomposites for NO_x removal. Catal Today 2017;280:37–44.

[63] Sugranez R, et al. Efficient behaviour of hematite towards the photocatalytic degradation of NO_x gases. Appl Catal Environ 2015;165:529–36.

[64] Zhou X, et al. Synthesis, characterization and its visible-light-induced photocatalytic property of carbon doped ZnO. Mater Lett 2009;63:1747–9.

[65] Acar C, et al. Review of photocatalytic water-splitting methods for sustainable hydrogen production. Int J Energy Res 2016;40:1449–73.

[66] Zhao X, et al. Metal-organic framework-derived ZnO/ZnS heteronanostructures for efficient visible-light-driven photocatalytic hydrogen production. Adv Sci 2018;5:1700590.

[67] Jiang D, et al. Integrating noble-metal-free NiS cocatalyst with a semiconductor heterojunction composite for efficient photocatalytic H2 production in water under visible light. Chinese J Catal 2017;38:2102–9.

[68] Ma L, et al. A simple melamine-assisted exfoliation of polymeric graphitic carbon nitrides for highly efficient hydrogen production from water under visible light. J Mater Chem A 2015;3:22404–12.

[69] Lin Z, et al. Large-scale preparation of heterometallic chalcogenide $MnSb_2S_4$ monolayer nanosheets with a high visible-light photocatalytic activity for H_2 evolution. Chem Commun 2016;52:13381–4.

[70] Yang S, et al. Exfoliated graphitic carbon nitride nanosheets as efficient catalysts for hydrogen evolution under visible light. Adv Mater 2013;25:2452–6.

[71] Yin X-L, et al. MoS_2/CdS nanosheets-on-nanorod heterostructure for highly efficient photocatalytic H_2 generation under visible light irradiation. ACS Appl Mater Interfaces 2016;8:15258–66.

https://www.twirpx.org & http://chemistry-chemists.com

[72] Li J, et al. Visible light photocatalytic decarboxylative monofluoroalkenylation of α-amino acids with gem-difluoroalkenes. Chem Commun 2017;53:10299–302.

[73] Xie L-Y, et al. Visible-light-induced deoxygenative C_2-sulfonylation of quinoline N-oxides with sulfinic acids. Green Chem 2019;21:3858–63.

[74] Xu Z-Y, et al. Iridium complex-linked porous organic polymers for recyclable, broad-scope photocatalysis of organic transformations. Green Chem 2020;22:136–43.

[75] Wang C-A, et al. Eosin Y dye-based porous organic polymers for highly efficient heterogeneous photocatalytic dehydrogenative coupling reaction. RSC Adv 2017;7:408–14.

[76] Xue B, et al. AgI/TiO_2 nanocomposites: ultrasound-assisted preparation, visible-light induced photocatalytic degradation of methyl orange and antibacterial activity. Ultrason Sonochem 2015;22:1–6.

[77] Yang X, et al. Bifunctional TiO_2/Ag_3PO_4/graphene composites with superior visible light photocatalytic performance and synergistic inactivation of bacteria. RSC Adv 2014;4:18627–36.

[78] Graham D, et al. The degradation of microcystin-LR using doped visible light absorbing photocatalysts. Chemosphere 2010;78:1182–5.

[79] Byrne C, et al. Recent advances in photocatalysis for environmental applications. J Environ Chem Eng 2018;6:3531–55.

[80] Ansari SA, et al. Highly visible light responsive, narrow band gap TiO_2 nanoparticles modified by elemental red phosphorus for photocatalysis and photoelectrochemical applications. Sci Rep 2016;6:25405.

[81] Zhu Q, et al. Stable blue TiO_{2-x} nanoparticles for efficient visible light photocatalysts. J Mater Chem A 2014;2:4429–37.

[82] Mousavi M, Habibi-Yangjeh A. Magnetically separable ternary g-C_3N_4/Fe_3O_4/BiOI nanocomposites: novel visible-light-driven photocatalysts based on graphitic carbon nitride. J Colloid Interface Sci 2016;465:83–92.

[83] Sinha AK, et al. Fabrication of large-scale hierarchical ZnO hollow spheroids for hydrophobicity and photocatalysis. Chem A Eur J 2010;16:7865–74.

[84] Ong CB, et al. A review of ZnO nanoparticles as solar photocatalysts: synthesis, mechanisms and applications. Renew Sustain Energy Rev 2018;81:536–51.

[85] Li Z, et al. Large-scale pattern fabrication of 3D rGO-Ag@Ag_3PO_4 hydrogel composite photocatalyst with the excellent synergistic effect of adsorption and photocatalysis degradation. Catal Today 2018. https://doi.org/10.1016/j.cattod.2018.07.016.

[86] Li S, et al. Mechanochemically synthesized sub-5 nm sized CuS quantum dots with high visible-light-driven photocatalytic activity. Appl Surf Sci 2016;384:272–8.

[87] Apte AK, et al. A facile template-free approach for the large-scale solid-phase synthesis of CdS nanostructures and their excellent photocatalytic performance. Small 2011;7:957–64.

[88] Lv J, et al. Multi-walled carbon nanotube supported CdS-DETA nanocomposite for efficient visible light photocatalysis. Mater Chem Phys 2017;186:372–81.

[89] Hoch LB, et al. The rational design of a single-component photocatalyst for gas-phase CO_2 reduction using both UV and visible light. Adv Sci 2014;1:1400013.

https://www.twirpx.org & http://chemistry-chemists.com

https://www.twirpx.org & http://chemistry-chemists.com

20

Industrial problems and solution towards visible light photocatalysis

Maya Devi*, Swetapadma Praharaj*, and Dibyaranjan Rout

DEPARTMENT OF PHYSICS, SCHOOL OF APPLIED SCIENCES, KIIT DEEMED TO BE UNIVERSITY, BHUBANESWAR, ODISHA, INDIA

1 Introduction

1.1 Photocatalysis and its importance

Photocatalysis is coined from the words "photo" and "catalysis." "Photo" signifies light and "catalysis" is generally the action of modifying a chemical reaction in presence of a catalyst. Precisely, photocatalysis can be described as a type of catalysis that results in altering the rate of photoreaction by electron transfer and coupled redox reaction. Photocatalysis may be a homogeneous or heterogeneous catalytic process depending on the type of catalyst used. In homogeneous photocatalysis, the catalyst units are soluble homogeneous molecules having photosensitizers and catalytic sites for performing oxidation and reduction reactions. This kind of reaction can occur in two ways; one of the paths refers to excitation of the photosensitizer by incident light, which eventually transfers electrons to the catalyst and creates active states to promote reduction reaction. The second method involves a single molecule photocatalyst acting as both catalyst and light absorber. On the incidence of light, electrons in the molecular photocatalyst are excited from the highest occupied molecular orbital (abbreviated as HOMO) to the lowest unoccupied molecular orbital (abbreviated as LUMO) making the catalyst excited. The excited catalyst acts as a good reductant as well as a good oxidant, which is responsible for carrying out the redox reaction. Several sacrificial reagents are used in such reactions for quenching the excited states which also act as electron donors during the reduction step [1]. In homogeneous photocatalysis, usually transitions metal complexes as used as a catalyst. However, there are several limitations of this type of photocatalysis:

(i) the solubility of homogeneous photocatalyst makes it difficult for reuse as they cannot be separated from the solution;
(ii) the homogeneous catalyst with well-defined HOMO-LUMO is capable of absorbing a small part of the solar radiation spectrum; and

*Both authors have equal contribution.

Nanostructured Materials for Visible Light Photocatalysis. https://doi.org/10.1016/B978-0-12-823018-3.00018-X
Copyright © 2022 Elsevier Inc. All rights reserved.

https://www.twirpx.org & http://chemistry-chemists.com

(iii) this type of photocatalyst is prone to rapid deactivation due to its intrinsic chemical activity, which limits photocatalytic activity.

In heterogeneous photocatalysis, when light is incident on the photocatalysts suspended in a solution, the electrons are excited from the valence band (VB) to the conduction band (CB), leading to the creation of electron-hole pairs. These electron-hole pairs move to the surface and facilitate the electrocatalytic reduction and oxidation reaction. Here the light-induced transformation takes place on the surface of the photocatalyst. Most of the heterogeneous photocatalysts have semiconductor properties. Usually, heterogeneous photocatalysis is preferred over homogeneous photocatalysis for the purpose of wastewater treatment and clean energy harvesting purposes. Though the process of photocatalysis has a long history, its importance in practical applications was only really felt following the discovery of the famous Honda Fujishima effect (1972), which deals with the production of H_2 from photo-assisted H_2O oxidation in the presence of a TiO_2 electrode [2]. After this initial thrust, Frank and Brad reported the photo-assisted decomposition of CN^- and SO_3^{2-} by TiO_2, ZnO, and CdS [3]. Further, Fujishima et al. in 1979 reported the photocatalytic decomposition of CO_2 utilizing various inorganic semiconductors as photocatalysts [4]. From that point, research continued in the direction of environmental applications of photocatalysis. It has been identified that photocatalysis finds several applications ranging from the production of clean energy to organic pollutant removal from wastewater. Some of the industrial applications of photocatalysis are shown in Fig. 1. One of the major challenges in the global scenario is the removal of contaminants from wastewater discharged from several industries that are hazardous to mankind as well as aquatic animals due to their toxicity [5]. Industrial water contains both organic and inorganic pollutants. The inorganic pollutants can be easily removed by the process of sedimentation, whereas out of the organic pollutant as per report 15% of the industrial effluents are colorants that are discharged annually to water from different industries like paper, paint, textiles, food, and pharmaceuticals [6, 7]. The coloring agents in synthetic dyes are responsible for the prevention of penetration of light into water and also for the reduction in dissolved oxygen levels, affecting aquatic life severely [8]. These dyes lead to allergic reactions like dermatitis and have carcinogenic, mutagenic, and genotoxicity effects in humans [9–11]. Several methods including physical, chemical, and biological have been tried to remove these synthetic dyes but they have certain limitations, such as being expensive or inefficient. Processes like coagulation-flocculation, reverse osmosis, and carbon-activated adsorption have been tried, but it has been observed that the contaminant is only transferred from one stage to another [12].

Thus for the removal of synthetic dyes, photocatalysis, which is an advanced oxidation procedure, has increasingly received attention over the last few decades [13], owing to its several advantages such as: capability of using renewable and pollution-free sunlight; mild reaction conditions and moderate reaction time; lower chemical input requirements; and minimal secondary waste generation. Synthetic dyes comprise one of the major organic contaminants in the water. Dyes are classified in different ways; here we classify them based on their applications.

https://www.twirpx.org & http://chemistry-chemists.com

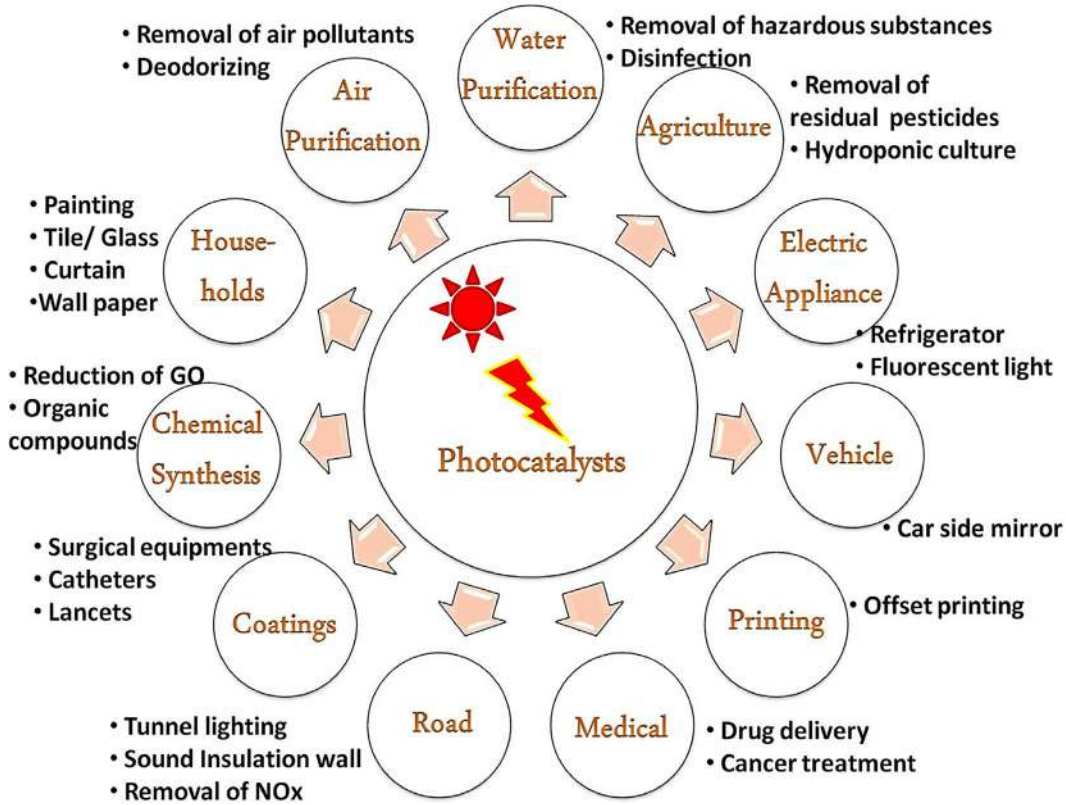

FIG. 1 Industrial applications of photocatalysis.

1.2 Types of industrial dyes

Dyes are usually organic molecules having a complex aromatic structure. Based on their application characteristic, they have been classified as represented in Fig. 2 [14]. Out of all these, water-soluble dyes are difficult to remove by separation methods. Therefore, the heterogeneous photocatalytic method should be adopted for the removal of these types of dyes.

2 Photocatalysis mechanism

Heterogeneous photocatalysis mainly includes four different steps, as shown in Fig. 3.

2.1 Light absorption for the generation of electron-hole pairs

Light absorption is dependent on the structure and surface morphology of the photocatalyst. The macroporous and mesoporous structures are preferred as they are capable of providing multiple reflections and scattering sites for maximum utilization of light [15].

https://www.twirpx.org & http://chemistry-chemists.com

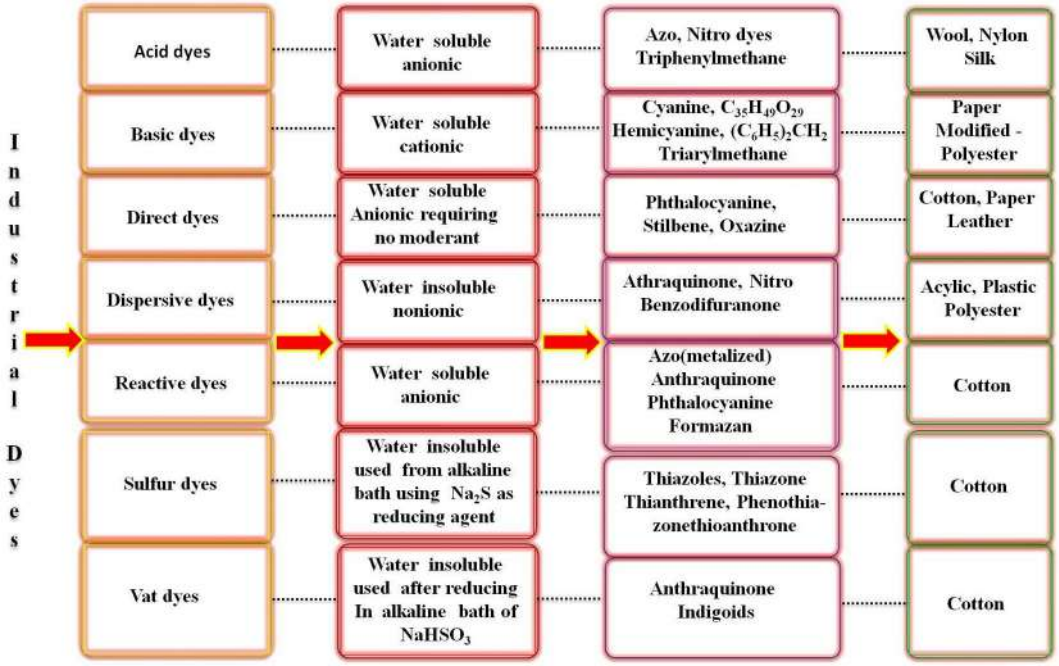

FIG. 2 Classification of industrial dyes based on their complex aromatic structure along with application to different fabrics.

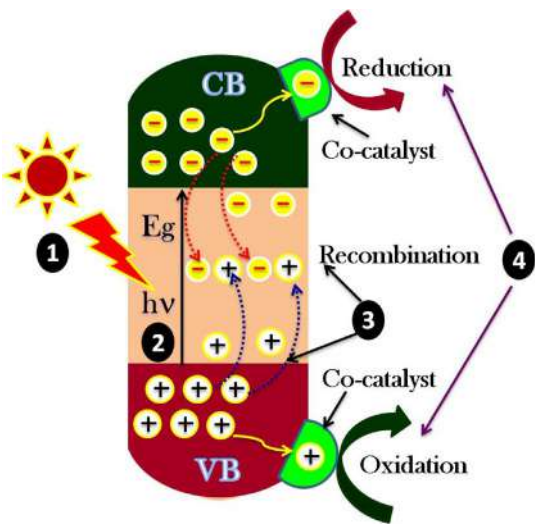

FIG. 3 Different steps of heterogeneous photocatalysis.

https://www.twirpx.org & http://chemistry-chemists.com

The excitation of the electrons takes place on the absorption of light and the excited electron moves from the VB of semiconductors to the CB. Therefore, the incident radiation must have an energy value higher than the bandgap of the semiconductor.

2.2 Separation of the excited charges

The separation and transfer of charge to the surface is mainly dependent on the charge recombination in the bulk and on the surface of the semiconductor. It plays a vital role in determining the photocatalytic quantum efficiency. The quantum efficiency can be improved by reducing the recombination rate, which can be achieved by bringing down the diffusion length of photogenerated charge carriers [16].

2.3 Electron and hole transportation to the surface of the photocatalyst

The electrons and holes that are highly energetic can only move to the surface without recombination. These excited electrons/holes can interact with the adsorbed molecules on the surface and transfer the absorbed photon energy.

2.4 The redox reaction on the surface

The excited electrons reduce the electron acceptor at the surface and the holes oxidize the electron donor adsorbed on the surface. The electron transfer between the surface and the adsorbed molecule is governed by the relation between band-edge alignments of semiconductors with the redox potential of the adsorbent. The reactions on the surface are only possible when the reduction and oxidation potentials are more positive and negative than the CB potential and VB potential, respectively [17]. The steps involved in the photocatalytic reaction are represented as Refs. [18, 19].

3 Basic requirements for photocatalysis

The basic requirements for heterogeneous catalysis for water splitting are discussed in this section. (i) The catalyst must have a suitable bandgap for the absorption of sunlight ($>$2 eV) because the electron-hole pairs are generated only when the absorbed photon energy is more than the bandgap energy. (ii) The thermodynamic redox potential is expected to be close to the band edges for effective charge transfer during the process. The thermodynamic potential of the electron acceptor must be more positive than the CB potential while the potential of the electron donor should be more negative than the VB potential of a semiconductor. So for water splitting application, the CB minimum must be more than the redox potential of H^+/H_2 [NHE] (where NHE is normal hydrogen electrode), and the VB maximum must be more positive than the redox potential of O_2/H_2O [20]. (iii) To avoid the recombination of generated electron and holes, the density of bulk defects is to be reduced so that the diffusion length is reduced [21]. (iv) Photocatalysts should have a low activation energy barrier and have more active sites

https://www.twirpx.org & http://chemistry-chemists.com

on the surfaces to facilitate the reduction of protons and oxidation of water, which represent the two halves of the redox reaction. (v) It is necessary that the catalyst is stable under appropriate reaction conditions, since in some cases it has been observed that some of the materials even after having a suitable bandgap react with the OH^- group and undergo corrosion. This becomes a great disadvantage and limits their use as photocatalysts. Thus a suitable catalyst has to be chosen which does not undergo photocorrosion [21]. (vi) The photocatalyst should be chemically and biologically inert. (vii) The catalyst should also be cost-effective. In addition, photocatalytic degradation is also dependent on parameters like pH, the intensity of light, amount of catalyst per dye, and the presence of the interfering compound.

4 Classification of photocatalysts

The past few years have witnessed the emergence of several categories of photocatalysts such as semiconductor-metal oxides, metal-organic frameworks, carbon nanostructures, magnetic-cored dendrimers, quantum dots, and many others, which have been extensively investigated for wastewater dye degradation. The timeline of the literature depicts that these photocatalysts gradually evolved with suitable modifications in order to overcome the limitations of their predecessors. Basing on the evolution of these materials (especially metal oxides), they can be broadly categorized into three generations, as shown in Fig. 4.

4.1 First-generation photocatalysts

First-generation oxide photocatalysts (e.g., TiO_2 and other single component oxides, nitrides, sulfides, phosphates) were the most debated ones in 1980–2000 in terms of: (i) nature of the oxidative agent; (ii) site at which reaction takes place; (iii) turnover numbers; and (iv) performance improvement and assessment of process efficiencies. This class of materials usually consists of a pair of the CB and VB, and on absorbing visible or UV light,

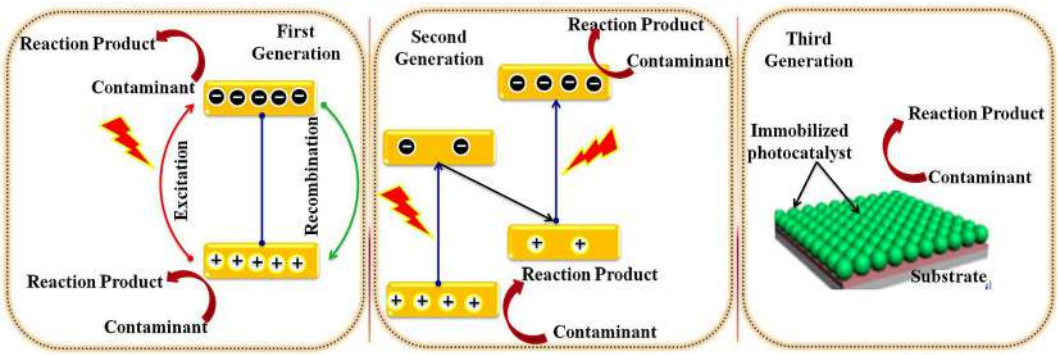

FIG. 4 Three generations of photocatalysts.

https://www.twirpx.org & http://chemistry-chemists.com

the electrons in the VB are promoted to CB generating holes. The formation of holes subsequently oxidizes the dye molecules. The most widely known photocatalysts under this category are TiO_2 or ZnO, which are used because of their improved quantum yield and figure of merit in comparison to other oxides and sulfides [22]. However, due to their large bandgap, i.e., ∼3.2 eV, TiO_2-based systems are mostly operated under UV irradiation (250–350 nm). In spite of the large bandgap, TiO_2 in both anatase (preferred) and rutile phase is engaged in the degradation of cationic dyes, anionic dyes, and dyes with different chromophores. Similarly, ZnO is largely employed for the decolorization of wastewater by the degradation of anionic dyes such as acid red, acid orange and methyl orange; other first-generation dyes include ZrO_2, ZnS, SnO_2, and NiO. Owing to the large bandgap of these pristine materials, irradiation by visible light is not common. Nevertheless, Vinodgopal et al. [23, 24] explored the photosensitization approach for visible light-induced degradation of acid orange 7 (textile azo dye) and naphthol blue-black (textile diazo dye) on TiO_2 nanoparticles. Further, a TiO_2/vis system was developed by Epling and Lin [25] for the removal of 15 different kinds of dyes (methylene blue, methylene green, dinitro methylene blue, rose Bengal, etc.) using various light sources (natural sunlight, 150 W spotlight, 90 W halogen floodlight). They suggested that both photocatalytic and photosensitization mechanisms were responsible for the degradation process. Reports on the removal of effluents by first-generation photocatalysts employing a visible range of light are rare in the literature. In a nutshell, the major limitation of this generation of materials is the existence of a single pair of CB and VB with a wide bandgap. While a large bandgap (∼ 3–5 eV) requires UV irradiation, the absence of multiple energy bands increases the probability of electrons falling back into the VB without generating reactive species. In addition, there are maximal chances of charge recombination minimizing the formation of reactive species for dye degradation. Hence, a large bandgap of these materials, the capability of limited utilization of solar radiation (only 5%), and fast recombination of charges limit the application of these materials. Such drawbacks actually triggered the search for the next generation of photocatalysts, i.e., second-generation photocatalysts.

4.2 Second-generation photocatalysts

In order to enhance the photocatalytic action of the first-generation materials, some of the major steps taken in this direction were: (i) doping of metal and nonmetal elements; (ii) coupling of different semiconductors to form a heterojunction; and (iii) surface modification by organic acids [26, 27]. Forming heterojunctions with suitable semiconductor nanostructures in the form of quantum dots, nanowires, or nanofibers [28] has emerged as a prospective technique of achieving significant enhancement in visible light-driven photocatalytic efficiency. To utilize visible light for photocatalytic action, the bandgap of this class of materials had to be tailored by doping with suitable oxide/nitride/sulfide to design multicomponent systems. In such heterojunction catalysts, the semiconductors are excited to generate charge carriers and the flow direction of these charge carriers mainly depends on the relative position of VBs and CBs. The electron movement takes

https://www.twirpx.org & http://chemistry-chemists.com

place between the CBs of a material having a high Fermi level to other material having a low Fermi level. Similarly, the holes move from the VB of a material having a low Fermi level to a material having a high Fermi level [29]. In this process, the charge carriers are separated by electrostatic forces but the redox potentials of electrons and holes are reduced [30], involving the *Z*-scheme mechanism of dye degradation. The reduction in redox potential is prevented by the transfer of an electron from one HOMO to the other HOMO of different semiconductors. The electrons from the HOMO move to the LUMO of the same semiconductor, creating a hole in the HOMO of the first semiconductor. In the above process, the diffusion length between the charge carriers is changed by generating active sites that are responsible for dye degradation. Recently, g-C3N_4 (graphite carbon nitride) has drawn the attention of many researchers due to its low cost and facile synthesis methodology. In addition, it is promising from the point of view of second-generation catalysts due to its lower bandgap energy (∼2.65 eV), which is within the upper limit of the energy bandgap (theoretical) of visible light photocatalysts (∼2.8 eV) [31]. Hence, for dye degradation purposes, g-C_3N_4-based photocatalysts have been extensively studied.

Shi et al. synthesized a series of g-C_3N_4/$BiOCl_xBr_{1-x}$ hybrid photocatalysts by facile preparation techniques. The photodegradation performance of the as-prepared hybrid catalyst improved substantially due to the synergetic effect, where the excited photoelectrons from g-C_3N_4 were efficiently transferred to the CB of $BiOCl_xBr_{1-x}$. The highest photoactivity was obtained for an optimum amount of g-C_3N_4 ($w = 0.2$) combined with $BiOCl_{0.8}Br_{0.2}$. The composite also showed excellent stability and efficiency even after eight runs of the photodegradation process [32]. Meanwhile, Zhu et al. also reported that a heterojunction nanocomposite of g-C_3N_4/Ag_2WO_4 displayed better photoactivity than the pristine compounds. The introduction of β-Ag_2WO_4 not only augmented the absorption of light but also reduced the formation of electron-hole pairs, thus proving it to be a superior photocatalyst composite for methyl orange degradation [33].

Over time, many other multicomponent systems have surfaced as potential photocatalysts. In this regard, modified porous boron nitride (a-BN) with uniformly distributed CdS prepared by a facile hydrothermal synthesis technique has been investigated for its adsorption and photocatalytic activities. The photocatalytic activity of this nanocomposite was examined on a highly concentrated Rhodamine B (RhB) target organic pollutant. The data showed that the performance of the system depends strongly on CdS concentration and the removal ability of RhB for a-BN coupling with CdS arises due to the synergetic effect of the composites [34]. Similarly, a hybrid of g-C_3N_4, CdS nanoparticles, and reduced graphene sheets was also found to be beneficial for RhB degradation and Congo red dyes using visible light [35].

4.3 Third-generation photocatalysts

Although photocatalytic efficiency is enhanced by using second-generation catalysts, the separation and recycling of the catalyst from the suspension is a hazardous task since the separation process cannot remove the catalyst completely from the suspension and also

https://www.twirpx.org & http://chemistry-chemists.com

accelerates the leaching of the catalyst into water [36]. In addition, the separation process requires extra energy and equipment, increasing the cost of effluent treatment. Many times the recycled composites engaged in wastewater treatment have exhibited a loss of photocatalytic activity. Hence, to find a viable solution to the abovementioned problems, many studies have recently focused on the third generation of photocatalysts, which are designed to be immobilized on a substrate to facilitate the postseparation problem. Metallic nanocrystals, semiconductors, carbon/boron nitrides, metal oxides, and many other composite systems, including both first- and second-generation materials, are deposited on the substrate surface for photocatalytic degradation of dye. The immobilization of the photocatalyst on different substrates can be done in two ways. The approach may be with or without a binder (popularly known as the binder-free and binderless approach, respectively). The binder-through approach leads to the deposition of films of organic or inorganic binders to the photocatalytic surface, which reduces the number of reactive sites and lowers the active surface area.

Using the binder-through approach, Fengquan et al. [37] deposited TiO_2/Ag composite thin film onto FTO glass by spin coating, and the binder, in this case, was colloidal silica. However, the photocatalytic activity was monitored for methylene blue degradation under UV illumination instead of visible light. It was observed that the composite was efficient in suspension form rather than the photocatalytic thin film since it required a long irradiation time (almost 3 h) to degrade 90% of the effluent. This shows that binder-through methodology leads to a reduction in dye decomposition efficiency and hence the adoption of a binder-free approach is highly recommended. However, the challenge comes in the process of deposition of multi-component heterogeneous photocatalyst on a substrate. Many strategies have been adopted by different researchers to overcome such complications. Shen et al. [38] reported an impregnation technique to grow BiOCl nanosheets and rutile TiO_2 nanorod arrays on a transparent, conductive substrate of fluorine-doped tin oxide (FTO). As per the degradation efficiency of immobilized BiOCl/TiO_2 tested with RhB, a photocatalytic efficiency of 99.1% could be achieved compared to pristine BiOCl (42.7%) and TiO_2 (44.8%). Tian et al. reported the cost-effective large-scale synthesis of a ZnO photocatalyst with excellent performance for dye photodegradation [39]. Furthermore, a peculiar kind of floating photocatalyst was synthesized by Bibova et al. [40] in which a very lightweight substrate like expanded clay, natural cork, and volcanic porous glass was coated with an SiO_2/TiO_2 nanocomposite. Some of the representatives of first-, second-, and third-generation photocatalysts are given in Table 1 [23, 24, 39, 41–67], Table 2 [33–35, 68–90], and Table 3 [38, 41, 91–102], respectively.

5 Industrial problems

Over the past few decades, though the importance of photocatalysis has increased significantly from a technological and economic viewpoint, the process of photocatalysis has not been completely adapted for industrial applications. Treatment of industrial wastewater is one of the areas that requires massive attention due to its hazardous environmental

https://www.twirpx.org & http://chemistry-chemists.com

Table 1 Some examples of first-generation photocatalysts.

Photo-catalyst	Dye	Reaction condition	Irradiation condition	Important results	References
Colloidal $TiO_2 + WO_3$	Acid orange 7 Direct blue 1	WO_3 (0.14 M) and TiO_2 (1.3 mM) Orange dye: 0, 2.4, 10.6, 16.5, and 33 μM. Oxidative rate constant: 8.6×10^8 M^{-1} s^{-l} (acid orange 7) 2.4×10^8 M^{-1} s^{-1} (direct blue 1)	Laser pulses: Lambda Physik EMG 101 MCS excimer laser system (−10-ne pulse width, −5 mJ)	The quantum efficiency for such a reductive process has been determined to be 4.7%	[41]
TiO_2	Basic yellow 15	Temp.: 30–40°C, 0.1 g/L TiO_2 powder pH: 3, 5, 11, oxidation rate constants: 0.0138, 0.007, and 0.0013 (mM/min)	17 UV lamps inside a chamber each with an intensity of 9200 watts/cm^2		[42]
TiO_2	Acid orange 7	0.10 mmol of AO_7/g of TiO_2 adsorption isotherm equilibrium constants are deduced from the slope of the best fit line 2.48×10^2 for AO_7 on TiO_2, reaction rate constant 2.1×10^{-2} and 3.0×10^{-2}/min	24 W halogen lamp	Charge injection from the excited dye molecule into the conduction band of the semiconductor as the primary mechanism for producing oxidized dye radicals	[23]
TiO_2	Reactive blue 221	0.06 g/100 mL solution, at 28°C and pH 9, rate constant for degradation of six organic compounds ranges from 0.026 to 0.114 min^{-1}, optimum concentration of H_2O_2 ranges from $1 \times 1O^{-2}$ to 0.5×10^{-2} M for 10–4 M organic solution	Three 20 W black light fluorescent lamps (General Electric F 20 T12 BLB)	Mineralization for 10^{-4} M of each organic result approximately 50–110 min whereas this period was shortened to 6–28 min by the addition of an optimum amount of H_2O_2	[43]
TiO_2	Napthol blue black	Dye coverage was 4 μmol of NBB/g of TiO_2. Rate constant (k): 8.8×10^{-4} min^{-1}	30 W halogen lamp (Fiber-Lite Model 190)	Complete bleaching of the absorption band at 615 nm in ∼42 h	[24]
TiO_2	Acid yellow 25	Solution concentration: 0.1 mM pH: 3, 7, and 11 catalyst flow rate 0.1 g/L	16 UV lamps	58% dye removed in 60 mins	[44]
TiO_2	Basic red 29	k: 0.127, 0.0424, and 0.0628 m^{-1}	16 UV lamps	98% dye removal in 60 mins at pH 3	[44]
TiO_2	Basic blue 41	k: 0.0839, 0.049, and 0.075 m^{-1}	16 UV lamps	99% dye removal in 60 mins at pH 3	[44]
TiO_2	Acid orange 8	k: 0.0827, 0.126, and 0.13 m^{-1}	16 UV lamps	80% dye degraded in 60 mins	[44]

https://www.twirpx.org & http://chemistry-chemists.com

TiO_2	Acid red 8	k: 0.0325, 0.134, and 0.0395 m^{-1}	16 UV lamps	60% dye removed in 60 mins	[44]
TiO_2	Acid red 3B	Dye concentration 500 ppm and catalyst 70 mg/100 mL solution pH 3.32, 7.05, and 9.97. The rate constants are 2.21×10^{-3}, 2.58×10^{-3}, and 3.11×10^{-3} m^{-1}	High-pressure Hg 300 W lamp	Dye removal efficiency increase with increasing pH	[45]
TiO_2	Reactive black 5	Dye concentration 0.0166 mM, catalyst flow rate 2 g/L, k: 0.0154, 0.0156, and 0.0154 min^{-1} for new, first, and second recycled TiO_2	75 W high-pressure mercury lamp (Toshiba-SHL-UVQ), visible light source used was a 100 W 587 Philips lamp (Philux)	Dye molecules were degraded to colorless but still toxic intermediates during first 120 mins of the experiment, and reduction in toxicity increased in last 60 mins	[46]
TiO_2	H/K acid-based azo dyes	Concentration of the aqueous solutions of the dyes in the study was 2.5×10^{-5} M. pH 9.2	200 W Hg lamp	Degradation of the dyes are of the order of 10^3/min	[47]
TiO_2	Tetrazine	75 mg of TiO_2 were suspended in 25 mL of dye solution. Rate constant is 0.013×10^{-4} min− 1. Amount of dye adsorbed to gm of TiO_2 is 0.51×10^{-5} mol/g	500 W superhigh-pressure mercury lamp	In 117 mins, 75% of the dye was removed	[48]
TiO_2	Direct fast scarlet	Catalyst flow rate 2.0 ± 1.5 g/L, pH 2.5	500 W medium-pressure mercury lamp	Photo reactivity does not increase with increasing TiO_2%	[49]
TiO_2	Acid orange 20	Dye concentration is 5×10^{-5} M, adsorption constant 7.3×10^{-4} M	18 W black light Hg lamp	At natural pH visible light strong adsorption of dye on TiO_2	[50]
TiO_2	Acid blue 80	Catalyst flow rate 2 g/L, pH 6.4	A 1500 W xenon source, equipped with a 340 nm cutoff filter	In 4 h, complete decomposition occurred	[51]
TiO_2	Red acid G	pH 6, temperature 20°C, dye flow rate 0.50 mmol/dm^3, catalyst flow rate 1 g/dm^3	500 W halogen lamp for visible light and 100 W Hg lamp for UV-vis light		[52]
TiO_2/ Degaussa-25	Reactive yellow 17	Natural pH of dye = 3.5, dye concentration 1.2×10^{-4} M, catalyst was coated as thin film	6 × 8 W low-pressure mercury arc lamp	Complete degradation in 12 h with UV light	[53]
TiO_2/ Degaussa-25	Reactive red 2	Natural pH of dye = 3.5, dye concentration 1.2×10^{-4} M, catalyst was coated as thin film	6 × 8 W low-pressure mercury arc lamp	Complete degradation in 18 h with UV light	[53]
TiO_2/ Degaussa-25	Reactive blue 4	Natural pH of dye = 3.5, dye concentration 1.2×10^{-4} M, catalyst was coated as thin film	6 × 8 W low-pressure mercury arc lamp	Complete degradation in 24 h with UV light	[53]

Continued

https://www.twirpx.org & http://chemistry-chemists.com

Table 1 Some examples of first-generation photocatalysts—cont'd

Photo-catalyst	Dye	Reaction condition	Irradiation condition	Important results	References
TiO_2	Alizarins	Catalyst flow rate 0.5 g/L, dye concentration 84.2 μmol/L, temperature 30°C	High-pressure Hg lamp (Philips HPK-125 W)	COD disappeared in < 3 h	[54]
TiO_2	Methyl red	Catalyst flow rate 0.5 g/L, dye concentration 84.2 μmol/L, temperature 30°C	High-pressure Hg lamp (Philips HPK-125 W)	COD disappeared in < 3 h, TOC reduced in < 2 h	[54]
TiO_2	Congo red	Catalyst flow rate 0.5 g/L, dye concentration 84.2 μmol/L, temperature 30°C	High-pressure Hg lamp (Philips HPK-125 W)	COD disappeared in < 3 h, TOC reduced in < 6 h	[54]
TiO_2	Methylene blue	Catalyst flow rate 0.5 g/L, dye concentration 84.2 μmol/L, temperature 30°C	High-pressure Hg lamp (Philips HPK-125 W)	COD disappeared in < 3 h, TOC reduced in < 6 h	[54]
TiO_2	Acid red 27	25 mL of a 0.1 mM solution of dye and 1 g/L of TiO_2	Sylvania 150 W indoor spotlight and a general electric (GE) energy-saving 90 W halogen floodlight	Degrades faster	[25]
TiO_2	Acid red 33	25 mL of a 0.1 mM solution of dye and 1 g/L of TiO_2	Sylvania 150 W indoor spotlight and a general electric (GE) energy-saving 90 W halogen floodlight	Degrades slowly in comparison to FD&C	[25]
TiO_2	Allura red AC	25 mL of a 0.1 mM solution of dye and 1 g/L of TiO_2	Sylvania 150 W indoor spotlight and a general electric (GE) energy-saving 90 W halogen floodlight	Degrades faster	[25]
TiO_2	Acid black 1	Quantity of photocatalyst 0.5 g/dm^3, dye concentration 0.01 gm/dm^3	VT-400 (Poland) mercury lamp with a power of 180 W	Photocatalytic degradation is preferred in acidic medium	[55]
TiO_2	Safira HEXL	At pH 5,catalyst 1 g/L, when initial dye concentration is 30 mg/L and light intensity 1.6×10^{-4} E/m	80, 125, or 150 W medium-pressure mercury lamp	Relative photonic efficiency in dye degradation is 41.88	[56]
TiO_2	Porcion red MX 5B	Initial dye concentration 40-mg/L. These conditions at a temperature of 23°C, TiO_2, 500 mg/L; H_2O_2, 10 mM; initial pH 5.0	UV intensity of 17 mW/cm^2	90% dye was mineralized in 80 mins	[57]
TiO_2	Acid red 14	Dye concentration 20 ppm, catalyst concentration 40 ppm, pH neutral. Rate constant of dye degradation is $= 1.41 \times 10^{-2}$/min	Mercury lamp Philips 30 W (UV-C)	In 2.5 h irradiation, 88% of the dye degraded. Addition of small amount of H_2O_2 makes the process faster	[58]

https://www.twirpx.org & http://chemistry-chemists.com

TiO_2	Lanasol blue	Dye concentration 100 mg/L, pH 3, temperature 85°C, 400 mg/L H_2O_2	50 W tungsten halogen lamp (KOTAS)	Efficiency of degradation of dye is lower in nanoporousTiO_2 compared to TiO_2/CdO-ZnO coupled nanoporous films	[59]
TiO_2	Reactive brilliant red K 2G	Initial dye concentration 40 mg/L, pH 10.8, catalyst concentration 500 mg/L, light intensity 4.2 mW/cm^2	Eight 365 nm UV fluorescent tubes (Viber-lourmat, model T-15 L/8D	Adsorption rate decreased but photodegradation rate increased with increase in pH	[60]
ZnO	Acid red 14	Photocatalyst was 160 ppm, with dye concentration of 20 ppm, neutral pH, rate constant of degradation is 0.0548 min^{-1}	Mercury lamp Philips 30 W (UV-C)	Complete color removal in 1 h	[61]
TiO_2	Reactive black 5	Temperature: 212°C, dye concentration: 40 ppm pH 3	25 W low pressure vapor mercury fluorescent lamp (Philips PL-S 2P)	After 5 h of irradiation, degradation is 64%	[62]
TiO_2	Reactive yellow 145	Temperature: 212°C, dye concentration: 40 ppm pH 3	25 W low pressure vapor mercury fluorescent lamp (Philips PL-S 2P)	After 5 h of irradiation, degradation is 62%	[62]
ZnO	Rhodamine 6G	Catalyst dose is 0.5 g/L, dye concentration 25 mg/L, pH 10, rate constant is 2.7×10^{-4} s^{-1}	Five UV tubes each of 30 W (Philips)	100% decolorization occurs in 3 h	[63]
TiO_2	Fast green FCF	Dye concentration 0.031 mM, neutral pH catalyst dose 1 g/L	125 W medium-pressure mercury lamp (Philips)	In presence of H_2O_2, the degradation efficiency increase	[64]
TiO_2	Bromo-cresol purple	Dye concentration: 0.0185 mM, pH 4.5 and 8, catalyst concentration 2.5 g/dm^3. k: 0.2085 and 0.0536 m^{-1}	4 UV lamps (Philips TL-40 W/05)	Efficiency percentages in adsorption in catalyst surface are 6.4 and 1 at pH 4.5 and pH 8, respectively.	[65]
ZnO	Congo red	Initial dye concentration 10 ppm, pH 12, quantity of catalyst is 2 mg/1 mL	UV light source of 125 W	Complete dye degradation occurred at about 8 mins	[66]
ZnO	Rhodamine B	Rate constant is 0.0215 min^{-1}		Dye fully degrades at 2 h	[39]
ZnO	Methyl orange	Initial dye concentration = 10 mg/L and pH 2, catalyst dose 1 g/L, rate constant of reaction 0.01076 min^{-1}	150 W mercury light	Maximum degradation using ZnO was 86%	[67]

https://www.twirpx.org & http://chemistry-chemists.com

Table 2 Some examples of second-generation photocatalysts.

Photo-catalyst	Dye	Reaction condition	Irradiation condition	Important results	References
S-doped TiO_2	Malachite green	Initial dye concentration: 20 mg/L	40 W UV bulb	An anatase to rutile ratio 81:19 showed the best results for degradation	[68]
S-doped TiO_2	Methyl orange	k: 1.17×10^{-2} $min^{-1,}$ 10 mg/20 mL of dye Temperature: 20°C	6 lamps (Philips visible light lamps), 15 W	Degradation efficiency is 94.3% in 240 mins of irradiation	[69]
C-doped TiO_2	Nitric oxide Methyl orange	Initial dye concentration is 15 mg/L, catalyst flow rate is 1 g/L	300 W simulated solar light (ASAHI SPECTRA HAL302)	Better photocatalytic ability at visible light range	[70]
Fe-doped TiO_2	Paranitro-phenol	Initial dye concentration is 10 mg/L at pH 4, catalyst loading rate 0.5 g/L	A 150 W Philips CFL bulb was used as a visible light source	Maximum degradation rate: 92% in 5 h when the Fe molar concentration was 0.05 mol%	[71]
Cu-doped TiO_2	Methyl orange	0.5 wt% Cu at incubation temp. 50°C and time 2 h	10 W UV lamp	82% dye removal efficiency	[72]
In-doped TiO_2	CO_2 reduction	Catalyst loading 0.25 g, temperature 373 k, pressure 0.02 bar	500 W mercury (Hg) flash lamp with irradiation intensity of 40 mW/cm^2	The yields of CH_4 and CO over In-doped TiO_2 catalysts were 7.9- and 2-fold higher than TiO_2, respectively	[73]
Pt/TiO_2 nanocomposite	Dichloroacetic acid	Photocatalyst loading, 0.5 g/L; 1 mM aqueous solution of DCA O_2^- saturated, pH 3; $T = 25$°C, reaction volume, 60 mL	UV(A) light by a Philips Hg lamp at 350 nm, 2.0 mW cm^{-2}	Photonic efficiency of nonporous TiO_2 P 25 was increased from 3.92% to 5.71% after Pt photo deposition. Photonic efficiencies of mesoporous TiO_2 P 25 is 4.2% and it is increased to 7.58% by Pt addition.	[74]
Au/TiO_2 nanocomposite	Ascorbic acid	10 mg composite photocatalysts were dispersed into 10 mL aqueous solution of L-ascorbic acid (0.1 M, pH 6), pure nitrogen gas used for 30 mins to drive away oxygen	300 W Xe lamp (MAX302, Asahi Spectra Co. Ltd.) coupled with a UV cutoff filter	Under irradiation at 500 20 nm, the 2AueTiO_2 sample still exhibits steady hydrogen evolution with a rate of 1.35 μmol h^{-1} g^{-1}	[75]
Ag/TiO_2 nanocomposite	Rhodamine B	30 mg photocatalysts were dispersed in 30 mL of 10 mg/L dye solution, irradiated 4 h	500 W xenon arc lamp with a 420 nm cutoff filter	100% dye degraded within 2 h	[76]
TiO_2/ZnO nanocomposite	Methyl orange	Dye concentration is 20 mg/mL^3	500 W Hg lamp	97% dye degradation within 30 mins	[77]

https://www.twirpx.org & http://chemistry-chemists.com

SnO_2/TiO_2 heterojunction	Rhodamine blue	100 mL of dye solution with an initial concentration of 10 mg/L in the presence of solid catalyst 0.01 g	50 W high-pressure mercury lamp with an average light intensity of 2.85 mW cm^{-2}	Dye removal occurs in 60 mins. SnO_2/TiO_2 composite possesses higher photocatalytic activity than the bare TiO_2 for the degradation of RB dye under UV light irradiation	[78]
α Fe_2O_3/TiO_2 nanocomposite	Congo red Methylene blue Methyl orange Eosin red	0.05 g of catalyst suspended in 200 mL dye aqueous solution (10 mg/L)	A xenon lamp (HSX-F/UV300), with a 400 nm cutoff filter placed above the reactor to cut off UV light	For dye concentration to 50 mg/L, the degradation capability increased to 94.0 mg g^{-1} after 160 mins exposure to visible light. After five cycles, 90% purification of the dye can be achieved	[79]
In_2O_3/TiO_2 nanocomposite	Rhodamine B	100 mL of the dye solution with an initial concentration of 10 mg/L in the presence of 0.05 g solid catalyst	Xenon lamp (XHA 150 W) equipped with a cutoff glass filter transmitting $\lambda > 420$ nm	After 4 h of exposure to visible light, the degradation efficiency of the catalyst is 90%	[80]
V^+, Mn^+, Fe^+ ion implanted TiO_2	2-Propanol	Ion-implanted TiO_2 photocatalysts for the degradation of 2-propanol diluted in water under visible light irradiation ($\lambda > 450$ nm). Amounts of implanted ions 13.2×10^{-7} mol/g-cat	100 W high-pressure Hg lamp with a colored filter	Exhibit an effective photocatalytic reactivity for the liquid-phase degradation of 2-propanol diluted in water at 275 K under visible light	[81]
V ion implanted P25 TiO_2	Formic acid	Initial concentration of formic acid 15 ppm, quantity of implanted V ions of 6.61×10^{-7} mol/g cat shows the highest photoactivity	500 W xenon lamp (SAN-EI XEF-501S) with a cutoff filter (Toshiba glass, Y-45), cutoff wavelength 450 nm	–	[82]
Cr ion implanted TiO_2	Formaldehyde	–	250 W metal halide lamp (Philips)	Photocatalytic degradation efficiency reaches 18% at a Cr loading of 1×10^{16} ions cm^{-2} and when intensity is increased to 3 $mWcm^{-2}$	[83]
g C_3N_4-$BiOCl_xBr_{(1-x)}$ heterojunction	Rhodamine B	0.05 g of sample was dispersed in an aqueous dye solution ($V = 200$ mL), initial concentration 9 mg/L	300 W Xe lamp	Catalysts showed almost complete photodecomposition of RhB in 60 mins under visible light exposure	[32]

Continued

https://www.twirpx.org & http://chemistry-chemists.com

Table 2 Some examples of second-generation photocatalysts—cont'd

Photo-catalyst	Dye	Reaction condition	Irradiation condition	Important results	References
Graphene quantum dot/ TiO_2 heterojunction	Rhodamine B	0.02 g of photocatalyst in 50 mL of 10 mg/L dye solution at room temperature	350 W xenon lamp with a cutoff filter ($\lambda > 420$ nm)	Dye completely degraded by visible light in the presence of 1.0 wt% GQD/TiO_2 photocatalyst for 120 mins. Presence of scavengers reduces the efficiency of dye degradation. The stability of the catalyst remains for four cycles	[84]
SnO_2-ZnO heterojunction	Methyl orange	Initial dye concentration 10 mg/L, catalyst concentration is 1 g/L. Photocatalysis is conducted in natural or basic media. The rate constant is 0.0931 min^{-1}	125 W high-pressure mercury lamp (Philips, HPL-N 125 W/ 542 E27)	Degradation efficiency is 88% in 20 mins. Photocatalyst can be easily recycled	[85]
WO_3/$NiWO_4$ heterojunction	Methylene blue	Dye concentration 20 ppm, 350 mL of dye, catalyst amount 200 mg at room temperature	125 W UV high-pressure mercury lamp	NiW_4 synthesized by triblock copolymer template showed 92.5% photocatalytic activity	[86]
BiOI/$Bi_2Sn_2O_7$ composite	Rhodamine blue	50 mL of dye solution with initial dye concentration 0.5 mg/L, 50 mg of catalyst powder	300 W Xenon arc lamp (LTIC 300BF, Boyi Ltd., China), equipped with wavelength cutoff filters for $\lambda \leqq 420$ nm	Optimal photocatalytic activity was achieved when the theoretical molar percentage of BiOI to initial $Bi_2Sn_2O_7$ reached 4% with the photodegradation efficiency being 99.9% after 6 h irradiation	[87]
CuO/$BiVO_4$	Rhodamine blue	CuO/$BiVO_4$ heterogeneous nanostructures (200 mg) were dispersed into an aqueous solution (100 mL) of dye (10 mg/L)	300 W Xe lamp (MAX-302, Asahi Spectra, USA) coupled with UV cutoff filter ($\lambda > 420$ nm)	About 99.8% of dye degraded after irradiating for 2.5 h with visible light irradiation	[88]
$AgPO_4$/MOS_2	Methylene blue	30 mg of the photocatalyst was ultrasonically dispersed in 30 mL of MB aqueous solution (20 mg/L)	35 W simulated solar Xe arc lamp with a 420 nm cutoff filter	Ag_3PO_4/MoS_2 photocatalyst with 0.648 wt% MoS_2 shows highest photocatalysis (98.2%) with rate constant 0.06548 min^{-1}. The time taken for complete dye degradation is 60 mins	[89]

https://www.twirpx.org & http://chemistry-chemists.com

g-C_3N_4/Ag_2WO_4	Methyl orange	0.03 g of the prepared photocatalyst was dispersed in 30 mL of dye solution (10 mg/L)	300 W Xe lamp	95% dye removal after mins of exposure	[33]
BN/CdS	Rhodamine blue	(0.1 g) of catalyst added to 160 mL of dye aqueous solution with an initial concentration of 100 mg/L, optimal loading CdS content is 0.5%	300 W Xe light with a 420 nm cutoff filter	In 80 mins the photocatalytic degradation is 74%	[34]
ZnS/CdS	Methylene blue	0.6 L of 10 mg/L of dye solution, 100 mg/L of catalyst, pH is 5	500 W halogen lamp	Degradation efficiency after 3 h is 54% with a rate constant of 4.1×10^{-3}/min	[90]
C_3N_4/CdS/ reduced graphene oxide	Rhodamine B	100 mg of the photocatalyst was dispersed in 250 mL of the dye solution, 4 mg/L solution of dye, The rate constant under visible and UV light are 21.92×10^{-3} and 66.12×10^{-3}, respectively	100 W halogen lamp for visible light and 300 W UV lamp for UV light	Dye was degraded completely in 1 h in visible light but in UV light it degraded in 20 mins	[35]

https://www.twirpx.org & http://chemistry-chemists.com

Table 3 Some examples of third-generation photocatalysts.

Substrate/ photocatalyst	Dye	Reaction condition	Irradiation condition	Important results	References
FTO/WO_3-ZnO	Methylene blue	The catalyst was added to a reactor having 200 mL of 16 mg/L dye. Catalyst mass 0.015 g	500 W xenon lamp	After 10 min irradiation under the visible light, about 42% of MB is sharply degraded	[91]
Al/ZnO	Methyl orange	1.0 cm^2 of the sample was immersed into 20 mL aqueous solution of dye with initial concentration 5 ppm, reaction rate is in order of the lamellar ZnO films > meshy ZnO films > granular ZnO films with k: 1.7×10^{-2}/min, 1.3×10^{-2}/min and 4.6×10^{-3}/min	300 W high-pressure mercury vapor lamp at 365 nm	91.5% and 94.4% of methyl orange can be decomposed in the presence of the meshy and lamellar ZnO films	[92]
FTO/BiOBr	Methyl orange	Experiments were carried out at 25 ± 3°C, catalyst film suspended in 10 mL of aqueous solution of dye with a concentration of 10 mg/L	150 W tungsten-halogen lamp at 200 mW/cm^2	Films prepared at 130°C, 160°C, and 180°C have degradation rates of 27.7%, 40.2%, and 47.2%, respectively, after irradiation by visible light for 5 h	[93]
Ni/TiO_2	Methyl orange	950 mL aqueous dye solution. Initial dye concentration 5 mg/L. Rate constant is 0.0098/min	Ultraviolet (UV) lamp (power 28 W with wavelength of 254 nm)	Noncalcined TiO_2 coated nickel network exhibited much higher degradation rate of $75.2 \pm 1.7\%$ ($n = 3$) at pH 7 and $95.5 \pm 1.5\%$ ($n = 3$) at pH 2	[94]
FTO/BiOCl-TiO_2	Rhodamine B	100 mL dye with the concentration of 2.5 mg/L. Immobilized catalyst substrate of size (3 cm*7 cm) is loaded	150 W Xenon lamp with a cutoff glass filter ($\lambda > 420$ nm)	BiOCl/TiO_2 composite having 0.60 g $BiCl_3$ shows optimal degradation of dye (99.1%) after 3 h of irradiation. k of reaction is 2.59 h^{-1}. After eight cycles the percentage of dye degradation is 91.7%	[38]
Bi/BiOCl	Rhodamine B	100 mL of dye solution with an initial concentration of 10 mg/L	350 W Xenon lamp as the simulated solar light and with a 420 nm filter	The dye degradation efficiencies were 98.2% and 88.9% in 210 mins under simulated solar light and visible light irradiation, respectively	[95]

https://www.twirpx.org & http://chemistry-chemists.com

Ti/BiOCl	Rhodamine B	50 mL dye solution with initial concentration 5 mg/L	UV and visible light	100% and more than 90% color removal efficiencies were achieved under UV and visible light in 120 mins and 180 mins; 90% and 70% TOC could also be removed under UV and visible light in the same conditions	[96]
Ce/TiO_2	Basic blue	Catalyst mass was 50 mg	Four black light or fluorescent tubes of 4 W nominal power	Pure and slightly modified (0.5%–2% Ce) TiO_2 films exhibit a photocatalytic activity after 80 mins of radiation	[97]
Glass/P-TiO_2	Benzyl butyl phthalate	200 mL of aqueous dye solution with initial concentration 20 mg/L. Temperature: 30°C	300 W Xe lamp with a 400 nm cutoff filter	More than 98% dye degraded with the thin film	[98]
Volcanic porous glass/SiO_2-TiO_2 composites	Methylene B oxalic acid	3.3×10^{-3} mol·dm^{-3} of dye is taken	Solar light is used	0.082 mol of OA were mineralized by 1.23 mol of photons, quantum efficiency 6.67%	[41]
Porous Ni/γ Fe_2O_3	Methyl orange	3 mL of dye is added to the catalyst. The initial concentration of dye is 20 mg/L		Complete dye degradation takes place in 12 h with UV light radiation but 98% dye degradation takes place in 9 h with natural sunlight. Higher photocatalytic performance is repeated for three cycles	[99]
Polydimethylsiloxane/TiO_2	Methylene blue	0.3 g of TiO_2/PDMS beads floating in 20 mL of 30-μM dye solution cycled constantly ~50 mL min^{-1}	Unfiltered 300 W Xe-arc lamp, 40 mW/m^2	Very low amount of photocatalyst is used for high-quality degradation because of the exposure of significant portion of catalyst by the PDMS substrate	[100]
Polyethylene terephthalate/TiO_2 (PTS TiO_2)	Acid brown 83 Direct blue 1	Immobilization of TiO_2 was done on PET at pH 2.5. A 50 ppm dye solution was prepared and pH was adjusted at 2.5, and 20 mL of dye solution were prepared and treated with the immobilized catalyst	Two Sylvania UV lamps (8 W, 254 nm)	The highest rate constant of the photocatalytic degradation reaction of AB83 (0.0922/min) was obtained at pH 2.5 with supported TiO_2. The rate constant for DB1 degradation at pH 2.5 using TiO_2 0.0529 min^{-1}	[101]

Continued

https://www.twirpx.org & http://chemistry-chemists.com

Table 3 Some examples of third-generation photocatalysts—cont'd

Substrate/ photocatalyst	Dye	Reaction condition	Irradiation condition	Important results	References
Polyethylene terephthalate/ZnO (PTS ZnO)	Acid brown 83 Direct blue 1	Immobilization of ZnO was done on PET at pH 9. A 50 ppm dye solution was prepared and pH was adjusted at 11, and 20 mL of dye solution were prepared and treated with the immobilized catalyst	Two Sylvania UV lamps (8 W, 254 nm)	For AB83, the higher degradation rate constants using supported ZnO were achieved at pH 7.0 (0.0694 min^{-1}). Rate constants of DB1 showed no significant differences between pH 7 and 9, but there was a significant decrease at pH 11	[101]
Polystyrene/TiO_2 (PS TiO_2)	Acid brown 83 Direct blue 1	Immobilization of TiO_2 was done on PS at pH 2.5. A 50 ppm dye solution was prepared and pH was adjusted at 2.5, and 20 mL of dye solution were prepared and treated with the immobilized catalyst	Two Sylvania UV lamps (8 W, 254 nm)	For AB83 the degradation rate constant increases at pH 2.5. Rate constant does not show significant change for DB1 dye	[101]
Polystyrene/ZnO (PS ZnO)	Acid brown 83 Direct blue1	Immobilization of ZnO was done on PS at pH 11. A 50 ppm dye solution was prepared and pH was adjusted at 11, and 20 mL of dye solution were prepared and treated with the immobilized catalyst	Two Sylvania UV lamps (8 W, 254 nm)	Treatment at pH 11.0 using ZnO (0.0845 min^{-1})	[101]
Nanoporous Cu/CuO_2	Methyl orange Methylene blue	10–20 mg Cu_2O@NP Cu catalysts into 5 mL 10 mg/L MB dye aqueous solution and 8–12 mg Cu_2O@NP Cu catalysts into 5 mL 20 mg/L MO aqueous solution	Exposed to sunlight for 80 mins	The highest degradation efficiencies for both the dyes are obtained by the nanobelts prepared in 3 days. Degradation efficiency of MB and MO dyes are 95.9% and 93.6%, respectively. The rate constants are 0.0544 and 0.0624 min^{-1}, respectively	[102]

https://www.twirpx.org & http://chemistry-chemists.com

effects and is expected to be resolved on a large scale by a cost-effective photocatalytic process in future. However, the foremost roadblock in photocatalytic water treatment is low photo-conversion efficiency. This lower efficiency is attributed to the loss in each step of photocatalysis [103]. The reaction efficiency is maximized by minimizing the recombination of charge carriers. Therefore, efforts are put into the modification of widely used TiO_2 by doping with metals or nonmetals, designing heterojunctions with lower bandgap materials, or sensitizing with chromophores which can widen the absorption capability to the visible range.

One more difficulty that hinders the commercialization of photocatalytic processes is the availability of a small number of systems currently being applied for wastewater treatment. The system used most often is TiO_2, whose performance remains unmatched by any of the systems investigated to date. Although other materials have been tried as a replacement for TiO_2, they have their limitations, such as toxicity (CdS), chemical instability (C_3N_4), or instability in wet conditions (most of the perovskites). However, some materials like platinized tungsten oxide and $BiPO_4$ have shown excellent improvement in terms of harvesting visible light, i.e., the larger part of solar radiation as an alternative to TiO_2 [103].

In addition, the studies conducted so far are limited to bench scale, which underrepresents the shortcomings of the available materials and related technology and at the same time overrepresent the opportunities. For large-scale industrial applications, many other factors such as cost of production of the photocatalytic material, long-term stability, and ease of separation from water have to be seriously considered. The parameters that also influence the performance of photocatalyst performance are pH, light intensity, rate of airflow, the concentration of catalyst, dopant content, and temperature [104]. It has been noticed that pH affects the formation of OH^- radicals and the rate of reaction. The variation of pH modifies the solid-electrolyte interface, which is responsible for photogenerated electron-hole separation at the catalyst surface. Again, poor oxygen flow can affect photocatalysis adversely, so the airflow into the photocatalytic system should be well regulated. Furthermore, some researchers have remarked that initially, the photocatalytic reaction is directly proportional to the catalyst concentration, but then the rate of reaction decreases. Similarly, dopant content is also observed to affect the photocatalytic property. Usually, up to a certain optimum concentration of dopant, photocatalytic activity is enhanced and thereafter reduces. Photocatalytic application on an industrial scale requires an innovative reactor design which is essential for proper illumination of photoactive material. The material acting as the catalyst shows activity when irradiated with photons of suitable energy. Thus the irradiation factor plays an important role in the design of the photocatalytic reactor (Fig. 5) because the amount of activated catalyst decides the capacity of the reactor for water treatment. The volume of the reactor is inversely proportional to the illuminated surface area of the catalyst in contact with the solution and the average mass destruction rate of the pollutant [105]. Therefore, the reactor size can be minimized if the illuminated surface area is enhanced. The enhanced morphological property of the catalyst can increase the mass destruction rate, thereby reducing the reactor size. Scaling up, the reactor configuration faces two major challenges:

https://www.twirpx.org & http://chemistry-chemists.com

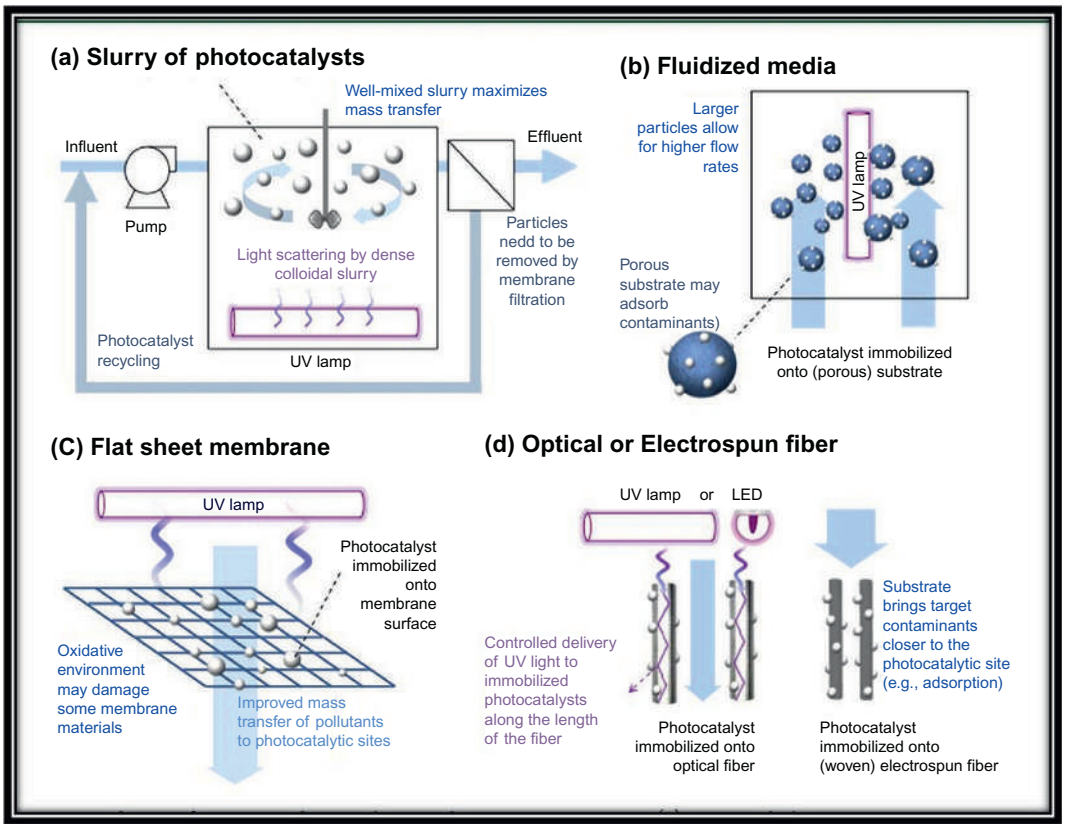

FIG. 5 Different types of photocatalytic reactors. *From Loeb, S. K., Alvarez, P. J. J., Brame, J. A., Cates, E. L., Choi, W., Crittenden, J., Dionysiou, D. D., Li, Q., Li-Puma, G., Quan, X., Sedlak, D. L., Waite, T. D., Westerhoff, P., Kim, J. H. The technology horizon for photocatalytic water treatment: sunrise or sunset? Environ Sci Technol 2019;53:2937–2947. https://doi.org/10.1021/acs.est.8b05041.*

(i) proper light distribution to the catalyst, which is influenced by two processes: elastic scattering and absorption; and
(ii) providing a large surface area for catalyst coating per unit volume of the reactor.

The reactors are generally categorized into two major classes depending on the deployed state of the catalyst. In one, the suspended photocatalyst particles are present, and in the other, the photocatalyst is immobilized onto an inert carrier [106]. The first category includes a slurry-type reactor in which the catalyst is in suspension form, providing a large surface area for reaction. Nevertheless, the major difficulty in this type of reactor is the separation of the ultrafine catalyst from the effluents. It requires an additional separation unit for the recovery of the photocatalyst. This in turn requires a greater degree of sophistication in the reactor design, which is perhaps achieved in the other kind of reactor design in which the catalyst is immobilized on a solid support. Depending on the method of immobilization of catalyst, the reactors are of five different types. For example, in a fixed

https://www.twirpx.org & http://chemistry-chemists.com

bed type reactor, the catalyst is immobilized onto the walls of the quartz tubes or onto the surface of light sources. Here no extra separation unit is required. However, it is often associated with the mass transfer limitation over the immobilized catalyst. However, a synergetic effect of photocatalysis in combination with membrane technology may be a good solution to outshine the typical photoreactors.

Conventionally, membrane technology was used as a physical separation process for pollutants in water. Based on the pore size of the membrane, the technology can be termed as microfiltration, nanofiltration, ultrafiltration, or reverse osmosis. This method can effectively be used for the removal of suspended solids, colloids, and microorganisms. By coupling this technology with heterogeneous photocatalysis, photocatalytic membrane reactors (PMRs) were developed [107]. It has several advantages in comparison to photocatalytic reactors:

(i) It confines the catalyst in the reaction environment.
(ii) It maintains the process continuity by separation of catalyst from the product.
(iii) It reduces the size of installation because no extra unit is required for the removal of the catalyst from the treated solution.

PMRs may have the catalyst suspended in a feed solution or immobilized on the membrane. PMRs with immobilized catalysts are of three types:

(i) photocatalyst coated on membrane;
(ii) catalyst blended with membrane; and.
(iii) freestanding photocatalytic membrane.

PMRs with immobilized catalyst have lower efficiency compared to those with suspended catalyst, and the photocatalyst loading cannot be adjusted according to wastewater composition. Thus slurry PMRs are usually preferred for wastewater treatment. Slurry PMRs are of two types depending on the method of coupling the photocatalytic module and membrane module. When the photocatalytic reaction and membrane separation process occurs in the same apparatus, it is called an integrative type PMR, and if occurs in separate apparatus, it is called a split type PMR. Some examples of different PMRs are provided in Table 4 [108–115].

6 Advancements and solutions

The process of photocatalysis based on nanocatalysts is an encouraging technique for contaminated water treatment. Researchers usually distinguish two types of photocatalytic applications in wastewater remediation: solar/visible light photocatalysis and photocatalytic systems equipped with artificial UV light. In this regard, visible light/solar irradiation has been identified as one of the breakthroughs in water remediation technologies (including both wastewaters generated from industries and drinking water) for removing traces of organic matter, heavy metal ions, microbes, etc. from water, especially in remote locations. Solar photocatalysis has the added advantages of being

https://www.twirpx.org & http://chemistry-chemists.com

Table 4 The uses of different PMR in laboratory scale.

Configuration	Photo catalyst membrane	Contaminant	Light source	Results	References
Immobilized	N-doped TiO_2 film on an Al_2O_3 membrane	Carbamazepine	Solar light simulator	N-doped film showed better reaction rate than undoped TiO_2	[108] Lab Scale
Immobilized	LiCl-TiO_2-doped PVDF membrane	Humic acid	UV radiation of 254 nm	At pH 7.5, 80%–84% rejected	[109] Lab Scale
Immobilized	Ag-TiO_2/HAP/Al_2O_3 composite membrane	Humic acid	400 W adjustable high-pressure Hg UV lamp	At 20°C, with optimum catalyst loading 15 mg/L 90% dye removal	[110] Lab Scale
Immobilized	PVDF/graphene oxide (GO) membrane	Methylene blue	Visible light 150 watt Xenon lamp with UV filter	At pH 7, 80% dye removal	[111] Lab scale
Slurry	TiO_2/Degussa	Congo red Patent blue	Immersed UV light	At optimum catalyst loading of 0.3 g/L, immersed UV lamp showed 50 times better result than external lamp	[112] Lab Scale
Integrated slurry PMR	TiO_2/ polyethersulfone (PES)	Phenanthrene	UV light (low-pressure Hg Lamp)	At optimum catalyst loading 0.5 g/L and pH 7 82%–100% color removed	[113] Lab Scale
Immobilized	ZnO/polyvinyl pyrrolidone (PVP)	Congo red	UV light	100% dye removal at optimum catalyst loading 0.3 g/L and pH 7	[114] Lab scale
Slurry	TiO_2/poly ethersulfone (PES), ZnO/PES	Textile water	UV-C and UV-A lamp	100% color removal at 25°C and optimum catalyst loading 0.5 g/L	[115] Lab Scale

low-cost, eco-friendly, easily accessible, and universally available. The need for equipment is also minimal, which is most pertinent for areas with remote access. Furthermore, such an arrangement in combination with the filtration membrane can reduce fouling of the membrane and enhance the efficiency of water cleaning to a great extent. A survey of the literature found that photocatalytic water remediation has already reached a mature market though systems using solar/visible light which are at the demonstration stage (http://www.raywox.com) and industrial projects on a pilot scale for drinking water purification in some developing countries have just begun (http://www.rcsi.ie/sodis). Fig. 6 compares the conversion efficiencies of UV light and visible (solar) light. A rough estimate of technology readiness levels is mapped for three selected applications in Fig. 7.

https://www.twirpx.org & http://chemistry-chemists.com

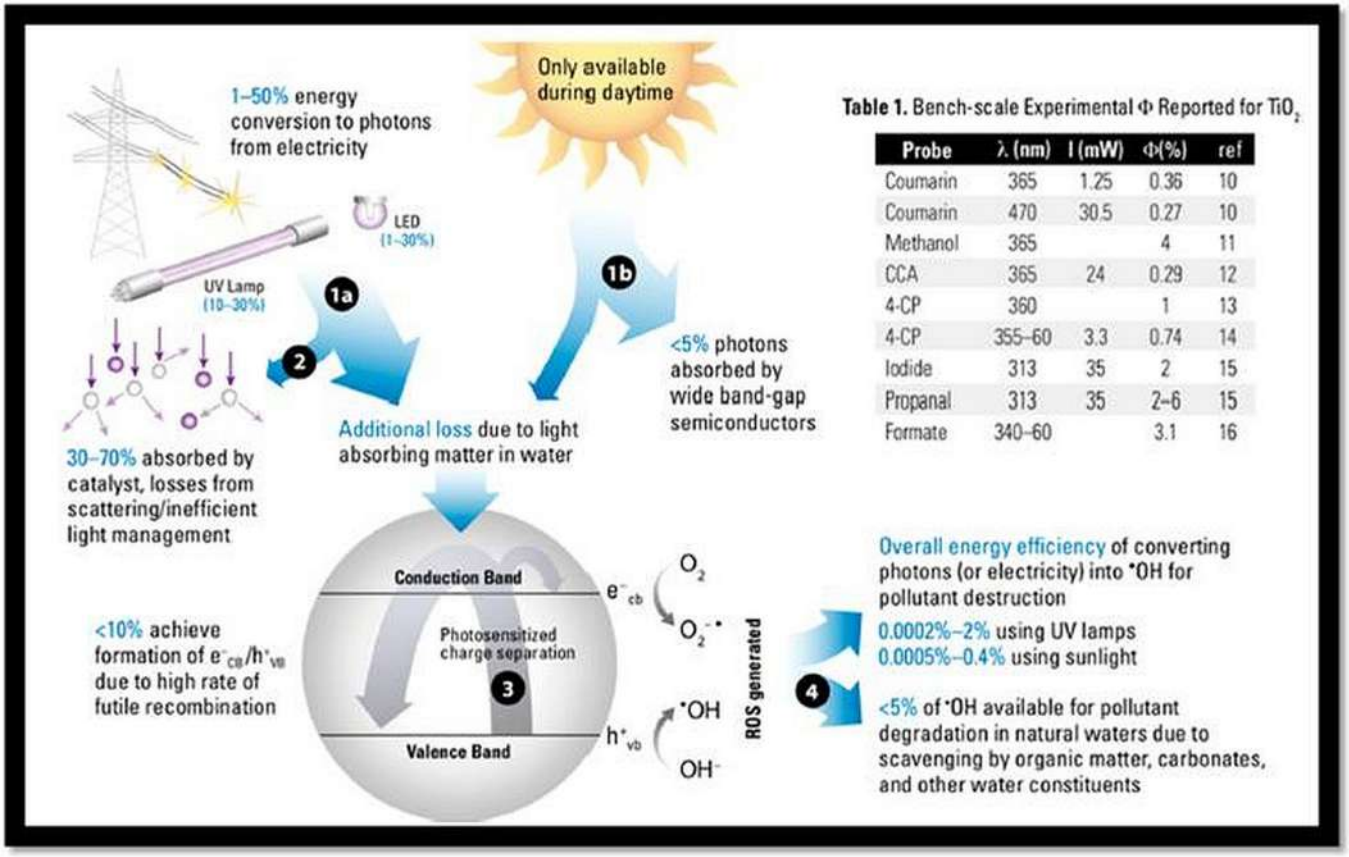

Table 1. Bench-scale Experimental Φ Reported for TiO_2

Probe	λ (nm)	I (mW)	Φ(%)	ref
Coumarin	365	1.25	0.36	10
Coumarin	470	30.5	0.27	10
Methanol	365		4	11
CCA	365	24	0.29	12
4-CP	360		1	13
4-CP	355–60	3.3	0.74	14
Iodide	313	35	2	15
Propanal	313	35	2–6	15
Formate	340–60		3.1	16

FIG. 6 A schematic diagram showing conversion efficiency of UV light versus visible light. *From Loeb, S. K., Alvarez, P. J. J., Brame, J. A., Cates, E. L., Choi, W., Crittenden, J., Dionysiou, D. D., Li, Q., Li-Puma, G., Quan, X., Sedlak, D. L., Waite, T. D., Westerhoff, P., Kim, J. H. The technology horizon for photocatalytic water treatment: sunrise or sunset? Environ Sci Technol 2019;53:2937–2947.* https://doi.org/10.1021/acs.est.8b05041.

https://www.twirpx.org & http://chemistry-chemists.com

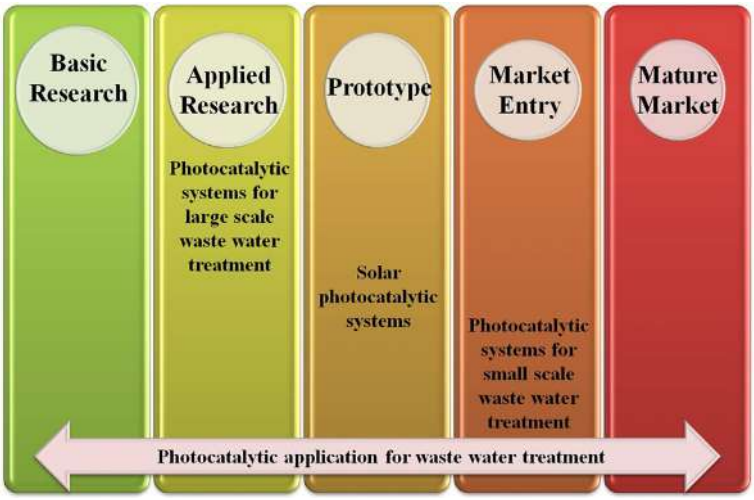

FIG. 7 Mapping of rough estimate of technology readiness levels for three selected applications.

7 Summary

Industries release various effluents (organic/inorganic dyes, heavy metals, etc.) that continuously pollute water bodies and pose a great danger to the ecosystem. In such circumstances, photocatalysis especially using solar/visible light seems to be a prospective technique that can act as a trump card in the water treatment process. Keeping in view the identified areas of concern, this chapter has summarized the importance of photocatalysis in wastewater remediation. With the advancements in photocatalysis for water treatment, photocatalysts have been bracketed into three generations depending on their suitability. Materials falling into the first-generation category proved to be inadequate for the removal of effluents owing to their large bandgap and could not efficiently utilize the visible range of electromagnetic spectrum for the generation of reactive species. In addition, they faced the challenges of interfacial electron-hole recombination. To minimize the drawbacks of these pristine classes of compounds, they were doped with different metals and nonmetals; semiconductors to form heterojunctions or surfaces modified by different organic compounds. Such customizations helped to reduce the bandgap to a large extent and these materials were called second-generation catalysts. These materials were studied extensively for visible light utilization, efficient charge separation, faster reaction kinetics, and a significant increase in photocatalytic efficiency. However, both the first and second generations of catalysts faced tremendous problems due to the separation stage. Hence, to expand the horizons of photocatalyst applications to a large industrial scale, the difficulties faced during the complicated separation process could be effectively addressed by the third-generation catalysts. The low quantum yield of these third-generation catalysts (due to a smaller surface area and fewer reaction sites after

https://www.twirpx.org & http://chemistry-chemists.com

deposition) opened up new avenues to develop immobilization techniques. Furthermore, the problems and challenges encountered in bringing solar/visible light photocatalysis from the laboratory scale to the industrial scale were discussed clearly. The critical and recent issues described in this chapter will definitely draw the attention of analytic minds to come up with viable solutions for transferring the technology from the laboratory scale to the industrial scale.

References

[1] Wang M, Shen S, Li L, Tang Z, Yang J. Effects of sacrificial reagents on photocatalytic hydrogen evolution over different photocatalysts. J Mater Sci 2017;52:5155–64. https://doi.org/10.1007/s10853-017-0752-z.

[2] Fujishima A, Honda K. Electrochemical photolysis of water at a semiconductor electrode. Nature 1972;238:37–8. https://doi.org/10.1038/238037a0.

[3] Frank SN, Bard AJ. Heterogeneous photocatalytic oxidation of cyanide and sulfite in aqueous solutions at semiconductor powders. J Phys Chem 1977;81:1484–8. https://doi.org/10.1021/j100530a011.

[4] Inoue T, Fujishima A, Konishi S, Honda K. Photoelectrocatalytic reduction of carbon dioxide in aqueous suspensions of semiconductor powders. Nature 1979;277:637–8.

[5] Chong MN, Jin B, Chow CWK, Saint C. Recent developments in photocatalytic water treatment technology: a review. Water Res 2010;44:2997–3027. https://doi.org/10.1016/j.watres.2010.02.039.

[6] Ajmal A, Majeed I, Malik RN, Idriss H, Nadeem MA. Principles and mechanisms of photocatalytic dye degradation on TiO2 based photocatalysts: a comparative overview. RSC Adv 2014;4:37003–26. https://doi.org/10.1039/c4ra06658h.

[7] Silveira E, Marques PP, Silva SS, Lima-Filho JL, Porto ALF, Tambourgi EB. Selection of Pseudomonas for industrial textile dyes decolourization. Int Biodeter Biodegr 2009;63:230–5. https://doi.org/10.1016/j.ibiod.2008.09.007.

[8] Islam MA, Ali I, Karim SMA, Hossain Firoz MS, Chowdhury AN, Morton DW, et al. Removal of dye from polluted water using novel nano manganese oxide-based materials. J Water Process Eng 2019;32. https://doi.org/10.1016/j.jwpe.2019.100911.

[9] Hunge K, editor. Industrial dyes: chemistry, properties, applications. John Wiley & Sons; 2007.

[10] Lacasse K, Baumann W. Textile chemicals: environmental data and facts. Springer; 2012.

[11] Chequer FMD, Lizier TM, de Felício R, Zanoni MVB, Debonsi HM, Lopes NP, et al. Analyses of the genotoxic and mutagenic potential of the products formed after the biotransformation of the azo dye Disperse Red 1. Toxicol In Vitro 2011;25:2054–63. https://doi.org/10.1016/j.tiv.2011.05.033.

[12] Robinson T, McMullan G, Marchant R, Nigam P. Remediation of dyes in textile effluent: a critical review on current treatment technologies with a proposed alternative. Bioresour Technol 2001;77:247–55. https://doi.org/10.1016/S0960-8524(00)00080-8.

[13] Legrini O, Oliveros E, Braun AM. Photochemical processes for water treatment. Chem Rev 1993;93:671–98. https://doi.org/10.1021/cr00018a003.

[14] Lau WJ, Ismail AF. Polymeric nanofiltration membranes for textile dye wastewater treatment: preparation, performance evaluation, transport modelling, and fouling control—a review. Desalination 2009;245:321–48. https://doi.org/10.1016/j.desal.2007.12.058.

[15] Li X, Yu J, Jaroniec M. Hierarchical photocatalysts. Chem Soc Rev 2016;45:2603–36. https://doi.org/10.1039/c5cs00838g.

https://www.twirpx.org & http://chemistry-chemists.com

[16] Li X, Yu J. Heterogeneous photocatalysis. Berlin Heidelberg: Springer; 2016.

[17] Laursen S, Poudyal S. Photo- and electro-catalysis: CO2 mitigation technologies. In: Novel materials for carbon dioxide mitigation technology. Elsevier; 2015. p. 233–68. https://doi.org/10.1016/B978-0-444-63259-3.00008-2.

[18] Ibhadon AO, Fitzpatrick P. Heterogeneous photocatalysis: recent advances and applications. Catalysts 2013;3:189–218. https://doi.org/10.3390/catal3010189.

[19] Viswanathan B. Photocatalytic degradation of dyes: an overview. Curr Catal 2018;99–121. https://doi.org/10.2174/2211544707666171219161846.

[20] Wang X, Maeda K, Thomas A, Takanabe K, Xin G, Carlsson JM, Domen K, Antonietti M. A metal-free polymeric photocatalyst for hydrogen production from water under visible light. Nat Mater 2009;8:76–80. https://doi.org/10.1038/nmat2317.

[21] Toe CY, Scott J, Amal R, Ng YH. Recent advances in suppressing the photocorrosion of cuprous oxide for photocatalytic and photoelectrochemical energy conversion. J Photochem Photobiol C Photchem Rev 2019;40:191–211. https://doi.org/10.1016/j.jphotochemrev.2018.10.001.

[22] Anwer H, Mahmood A, Lee J, Kim KH, Park JW, Yip ACK. Photocatalysts for degradation of dyes in industrial effluents: opportunities and challenges. Nano Res 2019;12:955–72. https://doi.org/10.1007/s12274-019-2287-0.

[23] Vinodgopal K, Wynkoop DE, Kamat PV. Environmental photochemistry on semiconductor surfaces: photosensitized degradation of a textile azo dye, Acid Orange 7, on TiO2 particles using visible light. Environ Sci Tech 1996;30:1660–6. https://doi.org/10.1021/es950655d.

[24] Nasr C, Vinodgopal K, Fisher L, Hotchandani S, Chattopadhyay AK, Kamat PV. Environmental photochemistry on semiconductor surfaces. Visible light induced degradation of a textile diazo dye, naphthol blue black, on TiO2 nanoparticles. J Phys Chem 1996;100:8436–42. https://doi.org/10.1021/jp953556v.

[25] Epling GA, Lin C. Photoassisted bleaching of dyes utilizing TiO2 and visible light. Chemosphere 2002;46:561–70. https://doi.org/10.1016/S0045-6535(01)00173-4.

[26] Yang J, Zhang X, Liu H, Wang C, Liu S, Sun P, et al. Heterostructured TiO2/WO3 porous microspheres: preparation, characterization and photocatalytic properties. Catal Today 2013;201:195–202. https://doi.org/10.1016/j.cattod.2012.03.008.

[27] Gao W, Dickinson L, Grozinger C, Morin FG, Reven L. Self-assembled monolayers of alkylphosphonic acids on metal oxides. Langmuir 1996;12:6429–35. https://doi.org/10.1021/la9607621.

[28] Chaguetmi S, Mammeri F, Nowak S, Decorse P, Lecoq H, Gaceur M, et al. Photocatalytic activity of TiO2 nanofibers sensitized with ZnS quantum dots. RSC Adv 2013;3:2572–80. https://doi.org/10.1039/c2ra21684a.

[29] Jing L, Zhou W, Tian G, Fu H. Surface tuning for oxide-based nanomaterials as efficient photocatalysts. Chem Soc Rev 2013;42:9509–49. https://doi.org/10.1039/c3cs60176e.

[30] Bard AJ, Fox MA. Artificial photosynthesis: solar splitting of water to hydrogen and oxygen. Acc Chem Res 1995;28:141–5. https://doi.org/10.1021/ar00051a007.

[31] Giannakopoulou T, Papailias I, Todorova N, Boukos N, Liu Y, Yu J, et al. Tailoring the energy band gap and edges' potentials of g-C3N4/TiO2composite photocatalysts for NOxremoval. Chem Eng J 2017;310:571–80. https://doi.org/10.1016/j.cej.2015.12.102.

[32] Shi S, Gondal MA, Rashid SG, Qi Q, Al-Saadi AA, Yamani ZH, et al. Synthesis of g-C3N4/BiOClxBr1-x hybrid photocatalysts and the photoactivity enhancement driven by visible light. Colloids Surf A Physicochem Eng Asp 2014;461:202–11. https://doi.org/10.1016/j.colsurfa.2014.07.024.

[33] Zhu B, Xia P, Li Y, Ho W, Yu J. Fabrication and photocatalytic activity enhanced mechanism of direct Z-scheme g-C3N4/Ag2WO4 photocatalyst. Appl Surf Sci 2017;391:175–83. https://doi.org/10.1016/j.apsusc.2016.07.104.

https://www.twirpx.org & http://chemistry-chemists.com

[34] Li X, Qi F, Xue Y, Yu C, Jia H, Bai Y, et al. Porous boron nitride coupled with CdS for adsorption-photocatalytic synergistic removal of RhB. RSC Adv 2016;6:99165–71. https://doi.org/10.1039/c6ra20671a.

[35] Pawar RC, Khare V, Lee CS. Hybrid photocatalysts using graphitic carbon nitride/cadmium sulfide/reduced graphene oxide (g-C3N4/CdS/RGO) for superior photodegradation of organic pollutants under UV and visible light. Dalton Trans 2014;43:12514–27. https://doi.org/10.1039/c4dt01278j.

[36] Munshi AM, Shi M, Thomas SP, Saunders M, Spackman MA, Iyer KS, et al. Magnetically recoverable Fe3O4@Au-coated nanoscale catalysts for the A3-coupling reaction. Dalton Trans 2017;46:5133–7. https://doi.org/10.1039/c7dt00058h.

[37] Gao F, Yang Y, Wang T. Preparation of porous TiO2/Ag heterostructure films with enhanced photocatalytic activity. Chem Eng J 2015;270:418–27. https://doi.org/10.1016/j.cej.2015.02.048.

[38] Shen Y, Yu X, Lin W, Zhu Y, Zhang Y. A facile preparation of immobilized BiOCl nanosheets/TiO2 arrays on FTO with enhanced photocatalytic activity and reusability. Appl Surf Sci 2017;399:67–76. https://doi.org/10.1016/j.apsusc.2016.12.076.

[39] Tian C, Zhang Q, Wu A, Jiang M, Jiang B, Fu H. Cost-effective large-scale synthesis of ZnO photocatalyst with excellent performance for dye photodegradation. Chem Commun 2012;48:2858–60. https://doi.org/10.1039/c2cc16434e.

[40] Bíbová H, Hykrdová L, Hoang H, Eliáš M, Jirkovský J. SiO2/TiO2 composite coating on light substrates for photocatalytic decontamination of water. J Chem 2019;2019:11. https://doi.org/10.1155/2019/2634398.

[41] Vinodgopal K, Bedja I, Hotchandani S, Kamat PV. A photocatalytic approach for the reductive decolorization of textile azo dyes in colloidal semiconductor suspensions. Langmuir 1994;10:1767–71. https://doi.org/10.1021/la00018a024.

[42] Tang WZ, An H. UV/TiO2 photocatalytic oxidation of commercial dyes in aqueous solutions. Chemosphere 1995;31:4157–70. https://doi.org/10.1016/0045-6535(95)80015-D.

[43] Balcioğlu IA, Inel Y. Photocatalytic degradation of organic contaminants in semiconductor suspensions with added H2O2. J Environ Sci Health A Tox Hazard Subst Environ Eng 1996;31:123–38.

[44] Tang WZ, Zhang Z, An H, Quintana MO, Torres DF. TiO2/UV photodegradation of azo dyes in aqueous solutions. Environ Technol 1997;18:1–12. https://doi.org/10.1080/09593330.1997.9618466.

[45] Shourong Z, Qingguo H, Jun Z, Bingkun W. A study on dye photoremoval in TiO2 suspension solution. J Photochem Photobiol A Chem 1997;108:235–8. https://doi.org/10.1016/S1010-6030(97)00014-2.

[46] Reutergådh LB, Iangphasuk M. Photocatalytic decolourization of reactive azo dye: a comparison between TiO2 and CdS photocatalysis. Chemosphere 1997;35:585–96. https://doi.org/10.1016/S0045-6535(97)00122-7.

[47] Zhan H, Tian H. Photocatalytic degradation of acid azo dyes in aqueous TiO2 suspension I. The effect of substituents. Dyes Pigments 1998;37:231–9. https://doi.org/10.1016/S0143-7208(97)00060-0.

[48] Tanaka K, Padermpole K, Hisanaga T. Photocatalytic degradation of commercial azo dyes. Water Res 2000;34:327–33. https://doi.org/10.1016/S0043-1354(99)00093-7.

[49] Zhu C, Wang L, Kong L, Yang X, Wang L, Zheng S, et al. Photocatalytic degradation of AZO dyes by supported TiO22 + UV in aqueous solution. Chemosphere 2000;41:303–9. https://doi.org/10.1016/S0045-6535(99)00487-7.

[50] Galindo C, Jacques P, Kalt A. Photooxidation of the phenylazonaphthol AO20 on TIO2: kinetic and mechanistic investigations. Chemosphere 2001;45:997–1005. https://doi.org/10.1016/S0045-6535(01)00118-7.

https://www.twirpx.org & http://chemistry-chemists.com

[51] Bianco Prevot A, Baiocchi C, Brussino MC, Pramauro E, Savarino P, Augugliaro V, Marci G, Palmisano L. Photocatalytic degradation of acid blue 80 in aqueous solutions containing TiO2 suspensions. Environ Sci Technol 2001;35:971–6. https://doi.org/10.1021/es000162v.

[52] Chen F, Xie Y, Zhao J, Lu G. Photocatalytic degradation of dyes on a magnetically separated photocatalyst under visible and UV irradiation. Chemosphere 2001;44:1159–68. https://doi.org/10.1016/S0045-6535(00)00277-0.

[53] Neppolian B, Choi HC, Sakthivel S, Arabindoo B, Murugesan V. Solar/UV-induced photocatalytic degradation of three commercial textile dyes. J Hazard Mater 2002;89:303–17. https://doi.org/10.1016/S0304-3894(01)00329-6.

[54] Lachheb H, Puzenat E, Houas A, Ksibi M, Elaloui E, Guillard C, et al. Photocatalytic degradation of various types of dyes (Alizarin S, Crocein Orange G, Methyl Red, Congo Red, Methylene Blue) in water by UV-irradiated titania. Appl Catal Environ 2002;39:75–90. https://doi.org/10.1016/S0926-3373(02)00078-4.

[55] Grzechulska J, Morawski AW. Photocatalytic decomposition of azo-dye acid black 1 in water over modified titanium dioxide. Appl Catal Environ 2002;36:45–51. https://doi.org/10.1016/S0926-3373(01)00275-2.

[56] Sauer T, Cesconeto Neto G, José HJ, Moreira RFPM. Kinetics of photocatalytic degradation of reactive dyes in a TiO2 slurry reactor. J Photochem Photobiol A Chem 2002;149:147–54. https://doi.org/10.1016/S1010-6030(02)00015-1.

[57] So CM, Cheng MY, Yu JC, Wong PK. Degradation of azo dye Procion Red MX-5B by photocatalytic oxidation. Chemosphere 2002;46:905–12. https://doi.org/10.1016/S0045-6535(01)00153-9.

[58] Daneshvar N, Salari D, Khataee AR. Photocatalytic degradation of azo dye acid red 14 in water: investigation of the effect of operational parameters. J Photochem Photobiol A Chem 2003;157:111–6. https://doi.org/10.1016/S1010-6030(03)00015-7.

[59] Suarez-Parra R, Hernández-Pérez I, Rincon ME, Lopez-Ayala S, Roldan-Ahumada MC. Visible light-induced degradation of blue textile azo dye on TiO2/CdO–ZnO coupled nanoporous films. Sol Energy Mater Sol Cells 2003;76:189–99. https://doi.org/10.1016/S0927-0248(02)00346-X.

[60] Hu C, Yu JC, Hao Z, Wong PK. Photocatalytic degradation of triazine-containing azo dyes in aqueous TiO2 suspensions. Appl Catal Environ 2003;42:47–55. https://doi.org/10.1016/S0926-3373(02)00214-X.

[61] Daneshvar N, Salari D, Khataee AR. Photocatalytic degradation of azo dye acid red 14 in water on ZnO as an alternative catalyst to TiO2. J Photochem Photobiol A Chem 2004;162:317–22. https://doi.org/10.1016/S1010-6030(03)00378-2.

[62] Aguedach A, Brosillon S, Morvan J, Lhadi EK. Photocatalytic degradation of azo-dyes reactive black 5 and reactive yellow 145 in water over a newly deposited titanium dioxide. Appl Catal Environ 2005;57:55–62. https://doi.org/10.1016/j.apcatb.2004.10.009.

[63] Kansal SK, Singh M, Sud D. Studies on photodegradation of two commercial dyes in aqueous phase using different photocatalysts. J Hazard Mater 2007;141:581–90. https://doi.org/10.1016/j.jhazmat.2006.07.035.

[64] Saquib M, Abu Tariq M, Faisal M, Muneer M. Photocatalytic degradation of two selected dye derivatives in aqueous suspensions of titanium dioxide. Desalination 2008;219:301–11. https://doi.org/10.1016/j.desal.2007.06.006.

[65] Baran W, Makowski A, Wardas W. The effect of UV radiation absorption of cationic and anionic dye solutions on their photocatalytic degradation in the presence TiO2. Dyes Pigments 2008;76:226–30. https://doi.org/10.1016/j.dyepig.2006.08.031.

[66] Nagaraja R, Kottam N, Girija CR, Nagabhushana BM. Photocatalytic degradation of Rhodamine B dye under UV/solar light using ZnO nanopowder synthesized by solution combustion route. Powder Technol 2012;215–216:91–7. https://doi.org/10.1016/j.powtec.2011.09.014.

https://www.twirpx.org & http://chemistry-chemists.com

[67] Anil IK, Shankar SV. Photocatalytic degradation of methylene blue using ZnO and 2%Fe–ZnO semiconductor nanomaterials synthesized by sol–gel method: a comparative study. SN Appl Sci 2019. https://doi.org/10.1007/s42452-019-1279-5.

[68] McManamon C, O'Connell J, Delaney P, Rasappa S, Holmes JD, Morris MA. A facile route to synthesis of S-doped TiO2 nanoparticles for photocatalytic activity. J Mol Catal A Chem 2015;406:51–7. https://doi.org/10.1016/j.molcata.2015.05.002.

[69] Bakar SA, Ribeiro C. Rapid and morphology controlled synthesis of anionic S-doped TiO2 photocatalysts for the visible-light-driven photodegradation of organic pollutants. RSC Adv 2016;6:36516–27. https://doi.org/10.1039/c6ra03819k.

[70] Wu X, Yin S, Dong Q, Sato T. Preparation and visible light induced photocatalytic activity of C-NaTaO3 and C-NaTaO3-Cl-TiO2 composite. Phys Chem Chem Phys 2013;15:20633–40. https://doi.org/10.1039/c3cp53437e.

[71] Sood S, Umar A, Mehta SK, Kansal SK. Highly effective Fe-doped TiO2 nanoparticles photocatalysts for visible-light driven photocatalytic degradation of toxic organic compounds. J Colloid Interface Sci 2015;450:213–23. https://doi.org/10.1016/j.jcis.2015.03.018.

[72] Pei LY, Chin LY. Synthesis of hybrid Cu-doped TiO_2 photocatalyst for dye removal. Key Eng Mater 2019;84–91. https://doi.org/10.4028/www.scientific.net/kem.797.84.

[73] Tahir M, NAS A. Indium-doped TiO2 nanoparticles for photocatalytic CO2 reduction with H2O vapors to CH4. Appl Catal Environ 2015;162:98–109. https://doi.org/10.1016/j.apcatb.2014.06.037.

[74] Ismail AA, Bahnemann DW. Mesostructured pt/tio2 nanocomposites as highly active photocatalysts for the photooxidation of dichloroacetic acid. J Phys Chem C 2011;115:5784–91. https://doi.org/10.1021/jp110959b.

[75] Fang J, Cao SW, Wang Z, Shahjamali MM, Loo SCJ, Barber J, et al. Mesoporous plasmonic Au-TiO 2 nanocomposites for efficient visible-light-driven photocatalytic water reduction. Int J Hydrogen Energy 2012;37:17853–61. https://doi.org/10.1016/j.ijhydene.2012.09.023.

[76] Yang D, Sun Y, Tong Z, Tian Y, Li Y, Jiang Z. Synthesis of Ag/TiO2 nanotube heterojunction with improved visible-light photocatalytic performance inspired by bioadhesion. J Phys Chem C 2015;119:5827–35. https://doi.org/10.1021/jp511948p.

[77] Zha R, Nadimicherla R, Guo X. Ultraviolet photocatalytic degradation of methyl orange by nanostructured TiO2/ZnO heterojunctions. J Mater Chem A 2015;3:6565–74. https://doi.org/10.1039/c5ta00764j.

[78] Wang C, Shao C, Zhang X, Liu Y. SnO2 nanostructures-tio2 nanofibers heterostructures: controlled fabrication and high photocatalytic properties. Inorg Chem 2009;48:7261–8. https://doi.org/10.1021/ic9005983.

[79] Li X, Lin H, Chen X, Niu H, Liu J, Zhang T, et al. Dendritic α-Fe2O3/TiO2 nanocomposites with improved visible light photocatalytic activity. Phys Chem Chem Phys 2016;18:9176–85. https://doi.org/10.1039/c5cp06681f.

[80] Mu J, Chen B, Zhang M, Guo Z, Zhang P, Zhang Z, et al. Enhancement of the visible-light photocatalytic activity of In2O3-TiO2 nanofiber heteroarchitectures. ACS Appl Mater Interfaces 2012;4:424–30. https://doi.org/10.1021/am201499r.

[81] Yamashita H, Harada M, Misaka J, Takeuchi M, Ikeue K, Anpo M. Degradation of propanol diluted in water under visible light irradiation using metal ion-implanted titanium dioxide photocatalysts. J Photochem Photobiol A Chem 2002;148:257–61. https://doi.org/10.1016/S1010-6030(02)00051-5.

[82] Zhou J, Takeuchi M, Ray AK, Anpo M, Zhao XS. Enhancement of photocatalytic activity of P25 TiO2 by vanadium-ion implantation under visible light irradiation. J Colloid Interface Sci 2007;311:497–501. https://doi.org/10.1016/j.jcis.2007.03.007.

[83] Humayun M, Raziq F, Khan A, Luo W. Modification strategies of TiO2 for potential applications in photocatalysis: a critical review. Green Chem Lett Rev 2018;11:86–102. https://doi.org/10.1080/17518253.2018.1440324.

https://www.twirpx.org & http://chemistry-chemists.com

[84] Pan D, Jiao J, Li Z, Guo Y, Feng C, Liu Y, et al. Efficient separation of electron-hole pairs in graphene quantum dots by TiO2 heterojunctions for dye degradation. ACS Sustain Chem Eng 2015;3:2405–13. https://doi.org/10.1021/acssuschemeng.5b00771.

[85] Uddin MT, Nicolas Y, Olivier C, Toupance T, Servant L, Müller MM, et al. Nanostructured SnO 2-ZnO heterojunction photocatalysts showing enhanced photocatalytic activity for the degradation of organic dyes. Inorg Chem 2012;51:7764–73. https://doi.org/10.1021/ic300794j.

[86] Mohamed MM, Ahmed SA, Khairou KS. Unprecedented high photocatalytic activity of nanocrystalline WO3/NiWO4 hetero-junction towards dye degradation: effect of template and synthesis conditions. Appl Catal Environ 2014;150–151:63–73. https://doi.org/10.1016/j.apcatb.2013.12.001.

[87] Xu W, Fang J, Zhu X, Fang Z, Cen C. Fabricaion of improved novel p-n junction BiOI/Bi2Sn2O7 nanocomposite for visible light driven photocatalysis. Mater Res Bull 2015;72:229–34. https://doi.org/10.1016/j.materresbull.2015.07.033.

[88] Wang W, Wang J, Wang Z, Wei X, Liu L, Ren Q, et al. P-n junction CuO/BiVO4 heterogeneous nanostructures: synthesis and highly efficient visible-light photocatalytic performance. Dalton Trans 2014;43:6735–43. https://doi.org/10.1039/c3dt53613k.

[89] Zhu C, Zhang L, Jiang B, Zheng J, Hu P, Li S, Wu M, Wu W. Fabrication of Z-scheme Ag3PO4/MOS2 composites with enhanced photocatalytic activity and stability for organic pollutant degradation. Appl Surf Sci 2016;377:99–108. https://doi.org/10.1016/j.apsusc.2016.03.143.

[90] Soltani N, Saion E, Yunus WMM, Erfani M, Navasery M, Bahmanrokh G, et al. Enhancement of visible light photocatalytic activity of ZnS and CdS nanoparticles based on organic and inorganic coating. Appl Surf Sci 2014;290:440–7. https://doi.org/10.1016/j.apsusc.2013.11.104.

[91] Zheng F, Lu H, Guo M, Zhang M, Zhen Q. Hydrothermal preparation of WO3 nanorod array and ZnO nanosheet array composite structures on FTO substrates with enhanced photocatalytic properties. J Mater Chem C 2015;3:7612–20. https://doi.org/10.1039/c5tc01125f.

[92] Wang HJ, Sun YY, Wang CF, Cao Y. Controlled synthesis, cytotoxicity and photocatalytic comparison of ZnO films photocatalysts supported on aluminum matrix. Chem Eng J 2012;198–199:154–62. https://doi.org/10.1016/j.cej.2012.05.088.

[93] Liu Z, Wu B, Niu J, Huang X, Zhu Y. Solvothermal synthesis of BiOBr thin film and its photocatalytic performance. Appl Surf Sci 2014;288:369–72. https://doi.org/10.1016/j.apsusc.2013.10.034.

[94] Zhang Y, Wan J, Ke Y. A novel approach of preparing TiO2 films at low temperature and its application in photocatalytic degradation of methyl orange. J Hazard Mater 2010;177:750–4. https://doi.org/10.1016/j.jhazmat.2009.12.095.

[95] Zhang X, Li R, Wang Y, Zhang X, Wang Y, Fan C. Slow-releasing Cl- to prepare BiOCl thin film on Bi plate and its photocatalytic properties. Mater Lett 2016;174:126–8. https://doi.org/10.1016/j.matlet.2016.03.109.

[96] Li K, Tang Y, Xu Y, Wang Y, Huo Y, Li H, et al. A BiOCl film synthesis from Bi2O3 film and its UV and visible light photocatalytic activity. Appl Catal Environ 2013;140–141:179–88. https://doi.org/10.1016/j.apcatb.2013.04.005.

[97] Rapsomanikis A, Apostolopoulou A, Stathatos E, Lianos P. Cerium-modified TiO2 nanocrystalline films for visible light photocatalytic activity. J Photochem Photobiol A Chem 2014;280:46–53. https://doi.org/10.1016/j.jphotochem.2014.02.009.

[98] Mohamed RM, Aazam E. Synthesis and characterization of P-doped TiO2 thin-films for photocatalytic degradation of butyl benzyl phthalate under visible-light irradiation. Chin J Catal 2013;1267–73. https://doi.org/10.1016/s1872-2067(12)60572-5.

[99] Ahmed SN, Inam A, Haider W. γ-Fe2O3 photocatalyst immobilized on a porous Ni substrate for recyclable solar photocatalysis. J Nanopart Res 2019;21:238.

[100] Bertram JR, Nee MJ. A buoyant, microstructured polymer substrate for photocatalytic degradation applications. Catalysts 2018;8.

https://www.twirpx.org & http://chemistry-chemists.com

[101] Sandoval C, Molina G, Vargas Jentzsch P, Pérez J, Muñoz F. Photocatalytic degradation of azo dyes over semiconductors supported on polyethylene terephthalate and polystyrene substrates. J Adv Oxid Technol 2017;20. https://doi.org/10.1515/jaots-2017-0006.

[102] Li Y, Ji C, Chi YC, Dan ZH, Zhang HF, Qin FX. Fabrication and photocatalytic activity of Cu 2O nanobelts on nanoporous Cu substrate. Acta Metall Sin 2019;32:63–73. https://doi.org/10.1007/s40195-018-0813-6.

[103] Loeb SK, Alvarez PJJ, Brame JA, Cates EL, Choi W, Crittenden J, Dionysiou DD, Li Q, Li-Puma G, Quan X, Sedlak DL, Waite TD, Westerhoff P, Kim JH. The technology horizon for photocatalytic water treatment: sunrise or sunset? Environ Sci Technol 2019;53:2937–47. https://doi.org/10.1021/acs.est.8b05041.

[104] Konstantinou IK, Albanis TA. TiO2-assisted photocatalytic degradation of azo dyes in aqueous solution: kinetic and mechanistic investigations: a review. Appl Catal Environ 2004;49:1–14. https://doi.org/10.1016/j.apcatb.2003.11.010.

[105] Ray AK. Design, modelling and experimentation of a new large-scale photocatalytic reactor for water treatment. Chem Eng Sci 1999;54:3113–25. https://doi.org/10.1016/S0009-2509(98)00507-7.

[106] Hossain MF. Sustainable design and build: building, energy, roads, bridges, water and sewer systems; 2018.

[107] Zheng X, Shen ZP, Shi L, Cheng R, Yuan DH. Photocatalytic membrane reactors (PMRs) in water treatment: configurations and influencing factors. Catalysts 2017;7. https://doi.org/10.3390/catal7080224.

[108] Horovitz I, Avisar D, Baker MA, Grilli R, Lozzi L, Di Camillo D, et al. Carbamazepine degradation using a N-doped TiO2 coated photocatalytic membrane reactor: influence of physical parameters. J Hazard Mater 2016;310:98–107. https://doi.org/10.1016/j.jhazmat.2016.02.008.

[109] Song H, Shao J, Wang J, Zhong X. The removal of natural organic matter with LiCl-TiO2-doped PVDF membranes by integration of ultrafiltration with photocatalysis. Desalination 2014;344:412–21. https://doi.org/10.1016/j.desal.2014.04.012.

[110] Ma N, Zhang Y, Quan X, Fan X, Zhao H. Performing a microfiltration integrated with photocatalysis using an Ag-TiO2/HAP/Al2O3 composite membrane for water treatment: evaluating effectiveness for humic acid removal and anti-fouling properties. Water Res 2010;44:6104–14. https://doi.org/10.1016/j.watres.2010.06.068.

[111] Alyarnezhad S, Marino T, Parsa JB, Galiano F, Ursino C, Garcìa H, et al. Polyvinylidene fluoride-graphene oxide membranes for dye removal under visible light irradiation. Polymers 2020;12:1–19. https://doi.org/10.3390/polym12071509.

[112] Molinari R, Pirillo F, Falco M, Loddo V, Palmisano L. Photocatalytic degradation of dyes by using a membrane reactor. Chem Eng Process Process Intensif 2004;43:1103–14. https://doi.org/10.1016/j.cep.2004.01.008.

[113] Rani CN, Karthikeyan S. Performance of an indigenous integrated slurry photocatalytic membrane reactor (PMR) on the removal of aqueous phenanthrene (PHE). Water Sci Technol 2018;77:2642–56. https://doi.org/10.2166/wst.2018.220.

[114] Hairom NHH, Mohammad AW, Kadhum AAH. Effect of various zinc oxide nanoparticles in membrane photocatalytic reactor for Congo red dye treatment. Sep Purif Technol 2014;137:74–81. https://doi.org/10.1016/j.seppur.2014.09.027.

[115] Doruk N, Yatmaz HC, Dizge N. Degradation efficiency of textile and wood processing industry wastewater by photocatalytic process using in situ ultrafiltration membrane. Clean (Weinh) 2016;44:224–31. https://doi.org/10.1002/clen.201400203.

https://www.twirpx.org & http://chemistry-chemists.com

https://www.twirpx.org & http://chemistry-chemists.com

21

Current status, research gaps, and future scope for nanomaterials toward visible light photocatalysis

So Jeong Park[a], Ju Hyun Yang[a,b], Min Hee Joo[a,b], and Youngku Sohn[a,b]

[a]DEPARTMENT OF CHEMISTRY, CHUNGNAM NATIONAL UNIVERSITY, DAEJEON, REPUBLIC OF KOREA [b]DEPARTMENT OF CHEMICAL ENGINEERING AND APPLIED CHEMISTRY, CHUNGNAM NATIONAL UNIVERSITY, DAEJEON, REPUBLIC OF KOREA

1 Introduction

For energy and environmental issues, hydrogen production, CO_2 reduction, pollutant removal, and photocatalysts have been the main keywords in the scientific community. A tremendous number of related articles have been introduced to show diverse photocatalysts synthesized by combination with diverse elements in the periodic table [1–74]. Because of human overpopulation and overconsumption of fuels, environmental living conditions have become worse over time. The consequent issues are basically energy shortage, the increase in global CO_2 levels, air pollution, and water pollution. Furthermore, the outbreak of the COVID-19 pandemic in 2020 has driven human life to a more severe situation. For energy solutions, hydrogen has been considered an alternative fuel and easily applied in hydrogen fuel cells [1–26]. Many countries have taken significant steps toward a hydrogen economy. Currently hydrogen is mainly produced from natural hydrocarbons. However, the current production price is high and CO_2 emission is a major problem. For future solutions, scientists keep trying to find hydrogen production photocatalysts with commercial efficiency [1–26]. However, the developed photocatalysts still show much lower efficiency than the minimum practical efficiency levels. Photoelectrochemical water splitting has become closer to a commercial application level since the first finding of electrochemical water splitting by Fujishima and Honda in 1972 [74]. Currently, carbon-free photoelectrochemical hydrogen production methods are of active active research projects supported by a national hydrogen energy policy.

Because of increases in global CO_2 levels, a lot of CO_2 waste from industry, and abundant levels on earth, scientists have suggested a solution in the form of CO_2 recycling such as chemical fixation and CO_2 reduction [27–49]. Because CO_2 is the most stable final product produced by consuming fossil fuels, the conversion to energetic fuels such as methane and methanol is a large and challenging project. CO_2 reduction recycling

Nanostructured Materials for Visible Light Photocatalysis. https://doi.org/10.1016/B978-0-12-823018-3.00001-4
Copyright © 2022 Elsevier Inc. All rights reserved.

https://www.twirpx.org & http://chemistry-chemists.com

uses water and light (and optionally electrical energy or solar cell electric energy) [45–48]. A general CO_2 reduction reaction is expressed as $xCO_2 + yH^+ + ze^- \rightarrow$ organic products + mH_2O [27]. This process resembles the photosynthesis process (e.g., $6CO_2 + 6H_2O + \text{light} \rightarrow C_6H_{12}O_6 + 6O_2$) in plants [27, 46, 49]. Thus, mimicking the natural photosynthesis system is regarded as a way to obtain a commercial efficiency level for a photocatalyst. Since the first discovery of CO_2 reduction using various semiconducting photocatalysts in 1979 by Inoue et al. [50], tremendous efforts have been made, but the efficiency remains on a starting level. There is a lot of scope to develop, but this is a significant and challenging task.

Pollution has been accelerated by humans' reckless activities in the pursuit of personal profits, without regard to public health and safety. Air pollution can be solved using hydrogen clean energy and CO_2 recycling. Water pollution such as dye wastes and toxic metals/chemicals has been solved by developing adsorbents and photocatalysts [51–73].

Motivated by the ongoing energy and environmental issues, this chapter deals with the current status of diverse photocatalysts such as metal oxides, sulfides, nitrides, and carbon-based materials working under visible light irradiation by discussing recent review articles. The fundamentals and the application areas of photocatalysts are first discussed, and the application areas mainly include water splitting, CO_2 reduction, and pollutant removal. For current trends of photocatalysts, (1) the design of photo(electro)catalyst reactors and (2) photocatalyst efficiency and modification of photocatalysts are discussed. The modification methods are categorized into (i) crystal phase/facet/crystallinity/morphology; (ii) sizes/defects/catalyst supports; (iii) heterojunction interface engineering; (iv) Z-scheme interfacing, (v) plasmonic photocatalysts; and (vi) metal/nonmetal-doping and sensitizers. Finally, nonmetallic-based photocatalysts, photoelectrochemistry, and mimicking nature are discussed.

2 Fundamentals and application areas of photocatalysts

2.1 Basic concepts

To achieve higher catalytic performance in energy production and pollutant removal, visible light has been used to produce initial activators of electrons and holes. To play a role, a catalyst has a valence band (VB) and a conduction band (CB) with a bandgap energy smaller than the incoming light. As shown in Fig. 1, the first step is that the electron-hole pairs (e^-/h^+) are created in the CB and VB, respectively. At this first stage, many challenging works for the photocatalyst are needed: (1) a tailored bandgap of the catalyst for visible light absorption; (2) high visible light absorption coefficient of the nature of the catalyst for producing a large number of electron-hole (e^--h^+) pairs; and (3) high light exposure area by controlling the catalyst surface area and designing a photocatalytic system.

For the second step, the electron and hole have several pathways: (1) radiative and nonradiative (surface and volume) recombination of electron and hole; (2) migration of separated charges to the catalyst surface; (3) charge trapping at some sites; and (4) redox

https://www.twirpx.org & http://chemistry-chemists.com

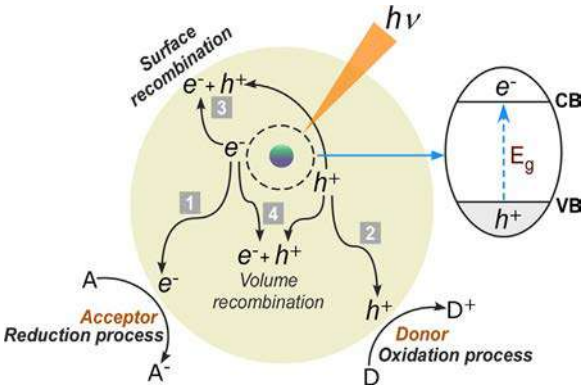

FIG. 1 Schematic diagram of several kinetic pathways for photoexcited charge carriers [4].

reaction on the donor and acceptor sites. At this second stage, several challenging tasks are: (1) good charge separation and poor recombination rate of e^- and h^+ for good photocatalysis; (2) tailoring for efficient migration and transport of separated charges to surface with any loss such as trapping and scattering loss; (3) tuned energy interfacial energy level alignment for good charge transfer; and (4) donor and acceptor sites for good surface redox reactions.

For the third stage, electrons and holes transfer to a well-matched energy level which is either a desired or undesired reaction pathway. Then, the questions at this stage are (1) what material has the well-matched desired energy band as depicted in Fig. 2; and (2) what energy the material absorbs. Fig. 2 displays valence and conduction band (VB and CB) energy levels of some selected materials relative to the energy levels of CO_2 reduction and oxygen/hydrogen evolution reactions. There are diverse multielectron/proton processes with narrow energy differences, and the hydrogen production level is positioned in the middle of the CO_2 reduction levels (HCOOH, CO, HCHO, CH_3OH, and CH_4). The light absorption energy and the energy band are highly dependent on the nature of a material. For this reason, material design is a key issue for increasing photocatalyst efficiency. Titanium oxide has been a model photocatalyst because of its chemical stability, abundance, low cost, and low toxicity [14, 27, 33, 34, 75]. However, diverse metal oxides and their hybrids have been utilized for tuning desired energy levels.

For photocatalysis on a desired reaction with well-matched energy level as shown in Fig. 2, adsorption of a molecule on the photocatalyst surface should first occur, and the separated electron and hole are then consumed for a desired reaction. As an example, for H_2 evolution, adsorption of H should occur via $H^+ + e^- \rightarrow H_{ad}$ followed by H_2 evolution [76]. For CO_2 reduction, better surface adsorption of CO_2 is required and a catalyst with higher CO_2 adsorption is needed as well as higher catalytic activity. Then, the question at this stage is: "How to increase CO_2 adsorption?" For pollutant removal on a catalyst

https://www.twirpx.org & http://chemistry-chemists.com

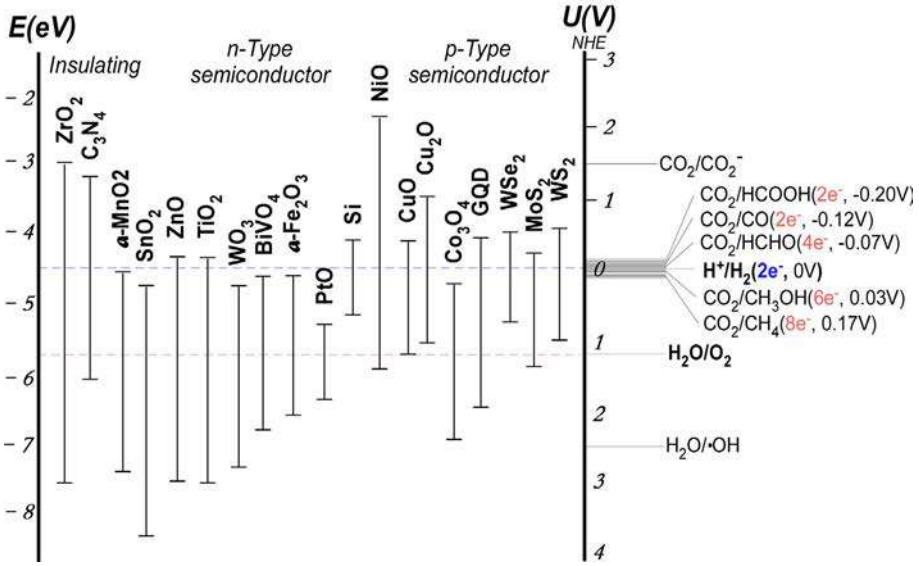

FIG. 2 Basic schematic energy diagram of some selected materials relative to the energy levels of CO_2 reduction and oxygen/hydrogen evolution reactions.

surface, the initial adsorption process is important [51–73]. To do this, many parameters such as surface area, morphology, and material surface charge have been considered.

Many reaction pathways exist with different energy potentials for the consumption of electrons and holes. Thereby, energy level tuning is used to increase efficiency as well as selectivity. Ideally, the CB and VB energy levels should well match the reduction and oxidation potentials, respectively. For overall water splitting, finding a photocatalyst that matches the redox potential for both H^+/H_2 (0 V vs NHE) and H_2O/O_2 (1.23 V vs NHE) is a challenging task. For the generally expressed CO_2 reduction as $xCO_2 + yH^+ + ze^- \rightarrow C_n$ products $+ mH_2O$ [27, 77], the energy potential for single electron capture of CO_2 is positioned at -1.48 V vs the normal hydrogen electrode (NHE). The energy potential is generally much higher than the CB of a catalyst. For this reason, the CO_2 reduction process commonly proceeds via other multielectron channels. There are several competitive pathways and their energy potentials are closely spaced. For an unwanted side channel, a kinetically favored hydrogen production channel ($2H^+ + 2e^- \rightarrow H_2$) exists among the CO_2 reduction channels. When H^+ is consumed, other CO_2 reductions using H^+ are suppressed. The H^+-consuming channels are HCOOH ($2e^-$ reaction), HCHO ($4e^-$ reaction), CH_3OH ($6e^-$ reaction), and CH_4 ($8e^-$ reaction). In addition, achieving higher electron density on a photocatalyst surface is required because they are multielectron processes. Therefore, both increasing selectivity and production efficiency are significant and challenging tasks.

2.2 Application areas of photocatalysts

Photocatalysis is really one of God's great gifts (for example, photosynthesis in plants) from the creation of Earth. Photocatalysis now plays an indispensable role in water

https://www.twirpx.org & http://chemistry-chemists.com

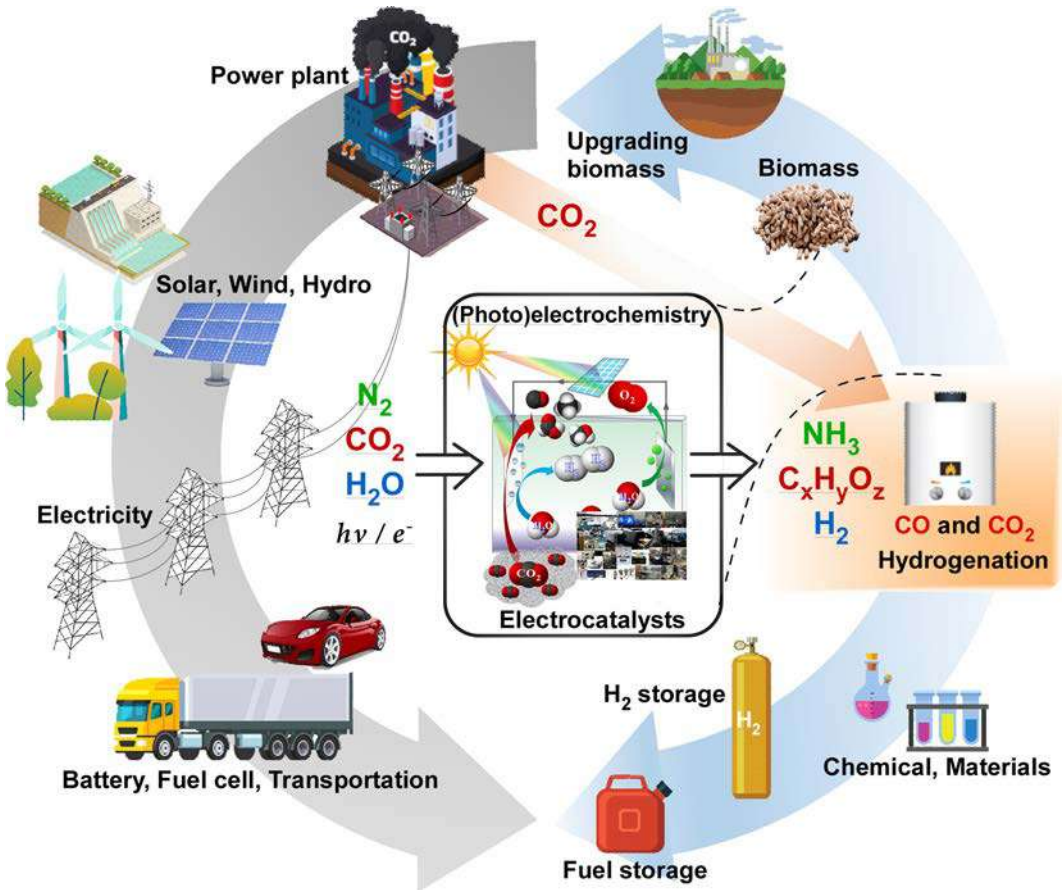

FIG. 3 Hydrogen and CO_2 recycle energy flow. *Modified from Seh ZW, Kibsgaard J, Dickens CF, Chorkendorff I, Nørskov JK, Jaramillo TF. Combining theory and experiment in electrocatalysis: insights into materials design. Science 2017;355:4998.*

splitting, CO_2 reduction, and pollutant removal. Because human activity and nature's self-purification are unbalanced, a driving force for balanced-cycling [78] has continuously been developed (Fig. 3).

2.2.1 Water splitting

The current status of photocatalysis on water splitting is in what might be termed the middle age of research [5–26]. However, the solar-to-hydrogen (STH) conversion efficiency (~1%) is far from practical application (>10%). Explosive amounts of photocatalysts have been developed to satisfy both hydrogen (H^+/H_2, 0 V vs NHE) and oxygen (O_2/H_2O, 1.23 V vs NHE) generation potentials [8]. Acar et al. first introduced various hydrogen production methods (electrolysis, thermolysis, thermochemical processes, photocatalysis, photoelectrochemical cells, dark fermentation, high-temp

https://www.twirpx.org & http://chemistry-chemists.com

electrolysis, photoelectrolysis, biophotolysis, and artificial photosynthesis), and then emphasized the advantage of photocatalytic water-splitting methods [10]. They compared hydrogen production rates (μmol/m^2 or μmol/g) and quantum yields with bandgaps for 49 selected photocatalysts. Suitable bandgaps in the literature for water splitting were summarized as being between 1.9 and 2.4 eV and the quantum yield reached 17% [10]. Hosseini and Wahid also discussed hydrogen production in depth using diverse methods of steam reforming of fossil fuels, biomass conversion/pyrolysis/gasification, biological production, supercritical water gasification, and hydrogen production using wind, thermal, and solar energies [5]. They concluded that the carbon-free hydrogen production method needs cost reduction and technology improvement for future hydrogen economy. Fajrina and Tahir thoroughly investigated H_2 production over recently developed TiO_2 and g-C_3N_4-based photocatalysts [6]. Metal/nonmetal modified, semiconductors coupled, ternary TiO_2, and heterojunction construction were discussed, including the factors that influence photocatalyst activity. Various reactors, their reaction parameters, and H_2 production yields were reported for the diverse photocatalysts. Fang and Shangguan reviewed hydrogen generation mainly with diverse bismuth-based composite oxides of Bi_2O_3, Bi_2MO_6(M = Cr, Mo, and W), $BiMO_4$(M = P, V, Nb, and Ta), BiOX (X = Cl, Br, and I), $BiFeO_3$, $BiYO_3$, $(BiO)_2CO_3$, $Sr_{1-x}Bi_xTi_{1-x}Fe_xO_3$, $CuBi_2O_4$, Bi_4NbO_8Cl, Bi_4YNbO_8Cl, $Na(Bi_xTa_{1-x})O_3$, $Bi_{0.5}Na_{0.5}TiO_3$, Bi_3NbO_7, and pentavalent bismuthates [8]. Their energy band positions were discussed for energy band engineering and the bandgaps were commonly controlled by doping, quantum size effect, and solid solution methods. Conclusively, the design of the Z-scheme system was a future direction for solving the limitations of bismuth-based composite oxides [8]. Yu et al. focused more on Bi_2MoO_6-based materials for photocatalytic water splitting [9]. Graphitic carbon nitride (g-C_3N_4) has high potential for application to photocatalytic hydrogen production [7, 11–13]. Mishra et al. introduced synthesis of 1D, 2D, and 3D g-C_3N_4 nanostructures and summarized hydrogen production yields in the literatures [11]. Diverse metal-free doped and hybrid g-C_3N_4 nanostructures were introduced with yields and stability. However, the yields and stability were reported to be poor. Metal oxide-based photocatalysts have been extensively demonstrated including Ti-oxide based catalysts [14, 15], Zn oxide [16], Zn sulfide [17], and Bi_2MoO_6-based materials [9].

Photoelectrochemistry is a more practical method for achieving higher hydrogen production rates, although some electrical energy is consumed [18–26]. Fabrication of photoelectrodes is a major task for water splitting in an electrolyte [18, 19]. For photoelectrochemical water splitting using metal oxide-based photocatalysts, Reddy et al. mainly discussed hetero-nanostructured metal oxides of titanium dioxide (TiO_2), zinc oxide (ZnO), and tungsten trioxide (WO_3) [20]. Other photoelectrodes include WO_3/$BiVO_4$ heterojunction [21], Bi-based nanomaterials [22], hematite [23, 24], Fe/Co/Ni sulfide/selenide/phosphides [25], and titanate-based perovskites [26]. Table 1 summarizes some metal- and nonmetal-based photocatalysts reviewed in the literature for water splitting.

https://www.twirpx.org & http://chemistry-chemists.com

Table 1 Literature summary of metal- and nonmetal-based photocatalysts for water splitting.

Metal-based	Nonmetal-based
Transition metals/oxides-TiO_2, precious metals-TiO_2, Al-$SrTiO_3$, Au-$SrTiO_3$, Au-Bi_2MoO_6/TiO_2, Au-TiO_2-AC, Bi_2S_3/TiO_2, $Ba_{5/6}Zn_{1/6}TiO_3$, $CaTi_{0.98}Cu_{0.02}O_3$, CdS/TiO_2, Cr/B-$SrTiO_3$, Cr/N-$SrTiO_3$, Cr/N-TiO_2, Cu/N/TiO_2, Cu_2O/TNAs, Cu-$SrTiO_3$, $CuTiO_3$, Cu-TiO_2/porphyrin, Cu/TiO_2/Ti_3C_2, Fe-Ni/TiO_2, F-Pt-TiO_2, $FeTiO_3$, g-C_3N_4-$SrTiO_3$, g-C_3N_4-TiO_2, g-C_3N_4-TiO_2/rGO, GO-TiO_2, Ir-C-N-TiO_2, K/TiO_2, $K_2La_2Ti_3O_{10}$, $K_2Ti_4O_9$, $La_2Ti_2O_7$-Cr, $La_2Ti_2O_7$-Fe, $MgTiO_3$, $MnTiO_3$, MoS_2/CdS/TiO_2, MoS_2/TiO_2, MWCNTs/TiO_2/MMT, N/Au/TiO_2, Nb-$SrTiO_3$, N-TiO_2, Na-$SrTiO_3$, $NiFe_2O_4$@TiO_2, Ni/TiO_2, $NiTiO_3$, PbS/$K_2Ti_4O_9$, PtO/CdS/$SrTiO_3$, Pt-RuO_2-TiO_2, Pt-TiC@C-TiO_2, Pt-WO_3-TiO_2, rGO/TiO_2, Sb_2TiO_5, Sn-containing TiO_2, $Sr_{0.9}Bi_{0.1}Ti_{0.9}Fe_{0.1}O_3$, perovskite oxides and hybrids, $SrTiO_3$: Ni/Ta/La, $Sr_{2/3}Zn_{1/3}TiO_3$, $Ti_3C_2(TiO_2)$@CdS/MoS_2, TiO_2-C-362, TiO_2/rGO/Pt, TiO_2-SnO_2, TiO_2-Ni$(OH)_2$/CNT/CdS, TiO_2-NiS, TiO_2-SiO_2, TiO_2/WO_3@MoS_2, Y-$SrTiO_3$, $ZnFe_2O_4/SrTiO_3$, Bi_2O_3-QDS-TiO_2, $Ag_{0.03}Mn_{0.40}Cd_{0.60}S$, Ag_2S QD, $Cd_{0.1}Zn_{0.9}S$, $Cd_{0.4}Zn_{0.6}S$, (transition) metal sulfides/nitrides, $Zr_3O_3N_2$, CdS/Cr/Pd, CdS/Ta_2O_5, CdS/Ti, CdS/$ZnFe_2O_4$, Co sulfides, $(Co_{0.59}Ni_{0.41})S_2$, CdSe QD, CdTe QD, $CuInS_2$ QD, $(Fe_{0.48}Co_{0.52})S_2$, FeNiS, $K_4Nb_6O_{17}$/CdS, Ni_2P/CdS, Pt-PdS-CdS, $Bi_{1.5}Zn_{0.99}Cu_{0.01}Ta_{1.5}O_7$, Bi_2S_3/Pt/ZnO, transition metals/oxides-ZnO, $(CuAg)_{0.15}In_{0.3}Zn_{1.4}S_2$, In(OH)yS:Ag-Zn, K-ZnO, N-$In_2Ga_2ZnO_7$, $ZnIn_2S_4$, ZnO/ZnS, $Zn_{0.9}Ti_{0.1}S$, $GaFeO_{2.98}S_{0.02}$, $Ga_{1-x}Zn_xN_{1-x}O_x$, In_2O_3/Ta_2O_5/ZnO, $ZnIn_2S_4$, CuO_x/Bi_2MoO_6, transition metals/oxides-ZnS, $Zn_2In_2S_5$, Ag/Bi_2MoO_6, Ag_3PO_4, Ag-rGo-Bi_2MoO_6, Ag_3VO_4, $BaZr_{0.96}Ta_{0.04}O_3$, $BiFeO_3$, Bi_2MoO_6, Bi-$NaTaO_3$, Bi_2O_3, BiOX (X=Br, Cl, I), BiOX/BiOX′, $BiPO_4$, Bi_2S_3, $BiTaO_4$, $BiVO_4$, $CaTa_{0.8}Zr_{0.2}O_{2.2}N_{0.8}$, $CeO_2/CoSe_2$, $Co_{0.13}Ni_{0.87}Se_2$/Ti, Co_2P, Co_9S_8-Ni_xS_y/NiF, CoP, CoP/Ti mesh, $CoSe_2$/CP, $CuBi_2O_4$, Er-Bi_2MoO_6, GaN, GaP, Gd-Bi_2MoO_6, Ge/Fe_2O_3, $K_{1.025}Sr_2Nb_{2.9875}Cr_{0.0125}O_{10}$, $KTaO_3$, Mn_3O_4-$CoSe_2$, $MoS_2/CoSe_2$, Nb_2O_5, Ni/NiO/$CoSe_2$, $Ni_{2.3\%}CoS_2$/CC, Ni_3S_2@Ni, Ni_3Se_2/CF, NiCoS/CC NSs, Ni$(OH)_2$/TaON, NiP_2/Ni/NF, NiSe/NF, $NiSe_2$, Ni_xP_y, PbS QD, Pt-Bi_2MoO_6, Pt/LaOF, Rh/Cr_2O_3/GaZn, $RuO_2/MgFe_2O_4$/Pt, $SnNb_2O_6$, Ta_3N_5, Ta_2O_5, TaON, Tb-Bi_2MoO_6	g-C_3N_4, ACTN/g-C_3N_4, $AgNbO_3$/g-C_3N_4, precious metals/g-C_3N_4, AuPd/g-C_3N_4, B/g-C_3N_4, B/F/g-C_3N_4, Br/g-C_3N_4, carbon dots, C/g-C_3N_4, C_3N_4, $C_3N_{4-x}S_x$, Carbon nanotubes (CNT), SiC CNTs/$ZnFe_2O_4$, transition metals and oxides/g-C_3N_4, Co_2P/NCNT, Co_3S_4/NCNTs, CoP/CNT, CoS_2 NS/RGO/CNT, Cu/g-C_3N_4, Cu_2O/g-C_3N_4, $Fe_{0.9}Co_{0.1}S_2$/CNT, g-C_3N_4-PEDOT, Graphene oxide (GO), Graphene QD, K/g-C_3N_4, Mo/g-C_3N_4, MoS_2/g-C_3N_4, N/g-C_3N_4, Ni/g-C_3N_4, Ni_2P/g-C_3N_4, $Ni_2P_2O_7$/g-C_3N_4, Ni_2P-$Cd_{0.9}Zn_{0.1}S$/g-C_3N_4, O/g-C_3N_4, P/g-C_3N_4, Pt/g-C_3N_4, ZnO/ZnS/g-C_3N_4, CNTs/MnO_2-C_3N_4

https://www.twirpx.org & http://chemistry-chemists.com

2.2.2 CO_2 reduction

The recycling of CO_2 has attracted a great deal of attention because of excess CO_2 levels on Earth. In view of this mission, huge amounts of research have been published, but the photocatalytic efficiency is extremely low and increasing its selectivity is one of various difficult tasks, as shown in Fig. 2 [27–50]. The current status of production rates is in the μmol/h range and a leap in activity is needed in the form of finding a new material. This is a very labor-intensive task. There are several closely spaced CO_2 reaction pathways and their reactions consist of multielectron reaction processes. To overcome the obstacles, there are many missions: (1) understanding the exact mechanism toward a desired reaction; (2) tuning energy levels; and (3) enhancing electron transfer processes.

Ti oxide-based materials are also the most studied catalysts for CO_2 reduction [33–35]. Sohn et al. fully reviewed recent progress and perspectives of photocatalytic CO_2 reduction over Ti oxide-based nanomaterials from reactor design, catalyst engineering, and the various strategies of improving efficiency and selectivity [27]. They also summarized major CO_2 reduction products over diverse Ti-oxide-based photocatalysts used under different reactor conditions. Nontitania based materials such as g-C_3N_4 and graphene have been proven to achieve the goal [27, 28, 36, 37, 39]. Tabish et al. introduced various perovskites ($CsPbBr_3$ quantum dots, $CsPb(Br_{0.5}/Cl_{0.5})_3$ nanocrystals, N-doped graphene quantum dots/Na tantalate nanocubes, $Cs_2AgBiBr_6$ nanocrystals, $CsPbBr_3$ nanocrystals/Pd nanosheets, $CsPbBr_3$ quantum dots/UiO-66 (NH_2) composites, $PbBiO_2Br$/carbonized polymer dots, B-doped $SrTiO_3$, Ag-loaded $H_2SrTa_2O_7$, sodium tantalate nanocubes) as photocatalyst materials for CO_2 reduction in their review article [28]. CO and CH_4 were found to be major products with both yields much less than 100 μmol/g under various reactor conditions. Perovskite oxides are of high interest as visible light photoelectrodes, as shown in Fig. 4 [31, 32]. Zeng et al. reviewed photocatalytic CO_2 reduction using perovskite oxides of titanates, niobates, tantalates, cobaltates, and double perovskite-type oxides. They focused mainly on synthesis methods, morphology, bandgap engineering, and the performances of various reported perovskite oxide nanomaterials [31]. Nahar et al. introduced modified TiO_2, plasmonic photocatalysts, layered Ag/A(=Ca, Ba, Sr) $La_4Ti_4O_{15}$ perovskites, and $LiNbO_3$ for photocatalytic CO_2 reduction [29]. Selectivity is a prime concern when designing a catalyst. Fu et al. introduced diverse photocatalysts in view of the main reduction products and reaction pathways [39]. For example, ZnO/ZnSe, MoS_2-TiO_2, O-doped g-C_3N_4, $CeO_3/ZnIn_2S_4$, and Bi_2S_3 produced CH_3OH as a main reduction product while TiO_2 photonic crystals and La_2O_3-modified $LaTiO_2N$ produced CH_4 [39]. Metal-organic frameworks (MOFs) have shown high potential diverse applicability to energy and the environment [40]. Zhan et al. introduced MOF-derived porous metal oxides, porous metal sulfides, and porous carbon materials, and then applied them to photocatalytic HER, water oxidation, CO_2 reduction, and pollutant removal [40]. Table 2 summarizes some metal- and nonmetal-based photocatalysts reviewed in the literature for CO_2 reduction.

When electrochemistry is combined with photocatalysis, CO_2 reduction production rates increase [39, 41, 42, 44]. Kumar et al. reviewed CO_2 reduction in view of

https://www.twirpx.org & http://chemistry-chemists.com

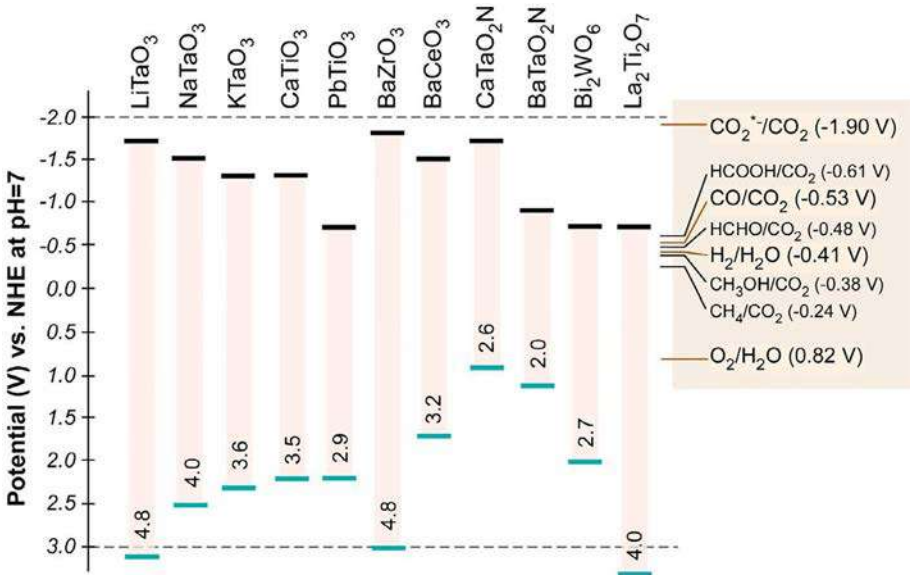

FIG. 4 Band structures for selected perovskite oxides and oxynitrides.

Table 2 Literature summary of metal- and nonmetal-based photocatalysts for CO_2 reduction.

Metal-based	Nonmetal-based
$Ag/CaTiO_3$, Ag/TiO_2, Au/TiO_2, $Au@CdS/TiO_2$, $Au/Pt/TiO_2$, $BaLa_4Ti_4O_{15}$, Bi_2S_3/TiO_2, $CaLa_4Ti_4O_{15}$, $CaTiO_3$, CdS/TiO_2, $CdSe/Pt/TiO_2$, CeO_2/TiO_2, Co-ZIF-9/TiO_2, CPO-Mg/TiO_2, $Cu/Fe/TiO_2$, $CuGaS_2$/RGO-TiO_2, Cu/TiO_2, Cu/TiO_2-SiO_2, Cu@V-TiO_2, CuN/TiO_2, CuO/TiO_2, Cu-Pt coated PMTiNT, Cu-Zn/TiO_2, DCQ-TiO_2/SBA-15, $FeTiO_2$, fluorinated TiO_2-SiO_2, $LaTiO_2$, MgAl-LDO/TiO_2, MgO/TiO_2, MgO-Pt/TiO_2, MoS_2/TiO_2, NaOH-TiO_2, N/Zr/TiO_2, N_3/TiO_2, NiS/TiO_2, Pb@TiO_3, Pd@TiO_2, $Pt/Cu/TiO_2$, Pt@TiO_2, Pt/Ti-MCM, Pt/TiO_2/Zeolite, $SrLa_4Ti_4O_{15}$, $SrTiO_3$, Ti-MCM, TiO_2/Zeolite, ZIF/TiO_2, ZnPC/TiO_2, Zr/TiO_2, Ag_2SO_3, $AgIO_3$, $BaCeO_3$, $BaTaO_2N$, $BaZrO_3$, Bi_2S_3/CdS, Bi_2WO_6, $BiVO_4$, $CaTaO_2N$, CdS, CdS/Co_9S_8, CdSe, Ce@$ZnFe_2O_4$, C-$LaCoO_3$, Co_9S_8@$ZnIn_2S_4$, Co-ZIF, Cu/GO, CuO, Fe_2O_3, GaN, HNb_3O_8, In_2O_3-$ZnIn_2S_4$, In_2S_3-$CdIn_2S_4$, In_2S_3-$CuInS_2$, $KNbO_3$, $KTaO_3$, $LiNbO_3$, $LiTaO_3$, $MnCo_2O_4$, MnS, $NaNbO_3$, $NaTaO_3$, NiO/Ni-GR, NC@$NiCo_2O_4$, NiO, NiO-RuRe, Pt/$NaNbO_3$, Rh/Cr_2O_3@GaN, Si, SiO_2-HNb_3O_8, $SrNb_2O_6$, $SrTaO_2N$, TaNO, WO_3, Zn_2GeO_4, Zn_2SnO_4, $ZnGa_2O$, ZnO, ZnS	$Ag_3PO_4/Ag/g\text{-}C_3N_4$, AgX/g-$C_3N_4$ (X = Cl and Br), Ag/g-C_3N_4 nanofibers, AgBr-g-C_3N_4/N-GR, Amine-g-C_3N_4, Bi@Ru/Ag@C_3N_4, $Cd_{0.2}Zn_{0.8}S$@UiO-66-NH_2, cobalt-cyclam, $CsPbBr_3$-QDs/GO, Cu/GO hybrids, Cu_2O/g-C_3N_4/RGO, Pt-G/RBT, Cu_2O/GR/TNA, CuO/Cu_2O NWAs@RGO, Fe(III)-porphyrin, GR/g-C_3N_4, $FeV_2O_{6.5}$/CdS/RGO, GA-CQDs/CNN, g-C_3N_4 hydrogel, g-$C_3N_4/KNbO_3$, g-C_3N_4/$NaNbO_3$, g-C_3N_4/rGH, g-C_3N_4/rGO, g-C_3N_4/ZIF-8, g-C_3N_4@UIO66, g-C_3N_4-agar hybrid hydrogels, $GOs@TiO_2$, GR/WO_3, HNb_3O_8/GR, HP-CN, Mn(CN)(bpy)$(CO)_3$, MOF-253-Ru$(CO)_2Cl_2$, P25/B-GR, porous N-doped g-C_3N_4, (Pt/TiO_2)/RGO, RGO/Pt-TNT, Ru complex/C_3N_4, SEG-TiO_2, SWCNT-TiO_2, TiO_2/RGO, ZnO-RGO, ZnTPP

https://www.twirpx.org & http://chemistry-chemists.com

photochemical and photoelectrochemical methods [30]. Yaashikaa et al. discussed photocatalytic transformation of CO_2 using metal complexes such as Re(I), Ru(II), Co(II), Ir(III), and Ni(II) [43]. They also discussed influencing factors of electrolyte (cations and anions), electrode (e.g., single or hybrid), gas adsorbent material, and CO_2 concentration (or pressure). Pawar et al. introduced various CO_2 reduction systems and discussed their advantages and disadvantages [41]. Conclusively, the solar PEC system was found to be superior to other methods and several methods were suggested for improving efficiency in view of visible photocatalyst design and reaction (or reactor) parameters. Huang et al. discussed photochemical and electrochemical CO_2 reduction mainly in terms of diverse materials, which include metals (e.g., Cu, Au, Ag, and Sn), metal chalcogenides, and carbonaceous materials, metal oxides, metal sulfides, metal nitrides, layered double hydroxide, MOFs, and metal-free materials [44]. For material design, they included Z-scheme construction, cocatalyst loading, defect engineering, heterostructure design, and bandgap engineering.

2.2.3 Pollutant removal

Photocatalysts have played a more practical role in pollutant treatments [51–73], compared with those of water splitting and CO_2 reduction [5–50]. This area is historically long and many practical catalysts have already been commercialized. For general pollutant removal, because pollutants should be adsorbed on catalysts' surfaces, large surface area and strongly interacted materials have been considered. The roles of photogenerated electrons and holes under visible light illumination are extremely important, as shown in Fig. 5. The electrons in the CB migrate to the catalyst surface, and react with adsorbed surface oxygen to form active $\bullet O_2^-$ radicals. The holes in the VB react with adsorbed H_2O/OH^- species to form •OH radicals. Consequently, active O_2^-, h^+ and •OH species play important roles in pollutant degradation.

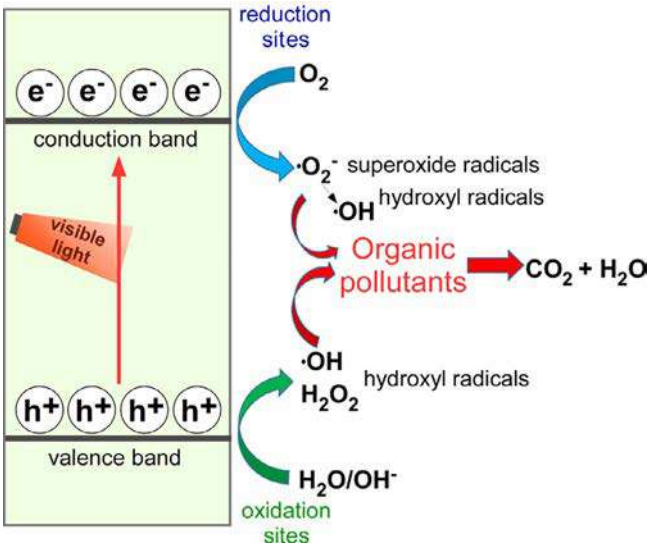

FIG. 5 Organic pollutant degradation mechanism under visible light illumination.

https://www.twirpx.org & http://chemistry-chemists.com

$$\text{Photocat} + \text{visible light} \rightarrow \text{photocat}\,(e^{-}{}_{\text{CB}} + h^{+}{}_{\text{VB}})$$

$$\text{Photocat}\,(e^{-}{}_{\text{CB}}) + \text{adsorbed}\,O_2 \rightarrow \bullet O_2{}^{-}$$

$$\text{Photocat}\,(h^{+}{}_{\text{VB}}) + \text{pollutant} \rightarrow \text{pollutant}\,(h^{+}{}_{\text{VB}})\ \text{hole transfer process} \rightarrow \text{degradation}$$

$$H_2O \rightarrow H^{+} + OH^{-}$$

$$OH^{-} + \text{photocat}\,(h^{+}{}_{\text{VB}}) \rightarrow \bullet OH$$

$$\bullet O_2{}^{-}\ (\text{or}\ \bullet O^{-}) + H^{+} \rightarrow \bullet OOH$$

$$\bullet OOH + e^{-} + H^{+} \rightarrow H_2O_2$$

$$H_2O_2 + e^{-} \rightarrow \bullet OH + OH^{-}$$

$$H_2O + \text{photocat}\,(h^{+}{}_{\text{VB}}) \rightarrow \bullet OH + H^{+}$$

$$\bullet O_2{}^{-}, \bullet OH\ \text{or}\ h^{+} + \text{pollutant}/\text{pollutant}^{+} \rightarrow \text{degraded products}$$

Among many developed pollutant removal photocatalysts, Ti oxide-based catalysts have been the most studied [56, 57], and transition metal oxides have also been actively demonstrated [58–61] to achieve pollutant removal. Layered double hydroxides (LDHs)-based visible light photocatalysts have been extensively demonstrated for photodegradation of organic pollutants [62]. Zhang et al. introduced LDHs with the general formula of $[M^{2+}_{1-x}\cdot M^{3+}_{x}(OH)_2]^{x+}(A^{n-}_{x/n})\cdot yH_2O$, where M^{2+} is a divalent metal ion (e.g., Zn^{2+}, Mg^{2+}, Cu^{2+}), and M^{3+} is a trivalent ion (e.g., Al^{3+}, Cr^{3+}, Fe^{3}) [62]. Further, they discussed photocatalytic degradation efficiency of organic pollutants (e.g., azo dyes, phenols) using LDHs-based photocatalysts which include LDHs-derived mixed metal oxides, supporting LDHs, intercalated, modified, and core-shell structured LDHs. Factors governing activity include structural/chemical/electronic properties, adsorption effect, acid-base property of LDHs, and vacancy sites. Bismuth vanadate-based and BiOX (X=Cl, Br, I, F) nanostructure-based photocatalysts have shown very high visible light photocatalytic activity and commercial applicability for water treatment [63–65]. Carbon-based materials with high potential applicability have been actively demonstrated and include graphene [66], MWCNT [68], g-C_3N_4 [67, 69, 70], and carbon quantum dots [71]. In view of activity, separation, and recycling of photocatalyst, magnetic photocatalysts have attracted much attention [72, 73]. Singh et al. have discussed in detail various synthesis methods and application tests of diverse magnetic iron oxide-integrated visible light photocatalysts [73]. Table 3 summarizes some metal and nonmetal-based photocatalysts reviewed in the literature for pollutant removal.

3 Current trends of photocatalysts

3.1 Photo(electro)catalyst reactors

Photocatalyst evaluation tests have been very important to reach the best performance of a prepared photocatalyst by improving a reactor design. Small- and large-scale reactors are commercially available and home-built designs have been reported. However, more efficient experimental setup is still required to minimize the efficiency loss from the

https://www.twirpx.org & http://chemistry-chemists.com

Table 3 Literature summary of metal- and nonmetal-based photocatalysts for pollutant removal.

Metal-based	Nonmetal-based
Diverse transition metal oxides/sulfides/nitrides, Al-doped TiO_2, Ag-doped TNH, CdS-TNTA, Cr/TiO_2 nanosphere, Cu-doped-TiO_2, CdS-TiO_2, $CuBi_2O_4$-TiO_2, Mn/TiO_2nanoparticle, N-TiO_2, transition metals/oxides-TiO_2, precious metals-TiO_2, Pt/TiO_2, S-doped TiO_2, Sn/TiO_2 nanoparticle, perovskite oxides, Fe/TiO_2, $SrTiO_3$, BiOX (X = Br, Cl, I), BiOX/BiOX′, AgBr/BiOCl, Bi_2O_3/BiOCl, $BiFeO_3$/BiOI, BiOBr/graphene oxide, BiOX/ZnO, $BiVO_4$/BiOCl, CdS/BiOCl, $CdWO_4$/BiOBr, Fe, Nb-doped BiOCl, La^{3+}-doped BiOBr, TiO_2/BiOX, $CoFe_2O_4$, $CoFe_2O_4$/AgBr, $CoFe_2O_4$/Ag_3PO_4, $CoFe_2O_4$/$BiVO_4$, $CoFe_2O_4$/ZnO, $CoFe_2O_4$/ZnS, Ag/AgBr/$CoFe_2O_4$, $CoFe_2O_4$, MoS_2/$CoFe_2O_4$, Au- $CoFe_2O_4$/MoS_2, Fe_3O_4@Au, Fe_3O_4/Cr_2O_3, Fe_3O_4@MnO_2, Fe_3O_4@SiO_2@Bi_2MoO_6, Fe_3O_4@SiO_2@TiO_2@Ho, Fe_3O_4@SnO_2, Fe_3O_4@MnO_2, Fe_3O_4@ZnO@Ag_3VO_4@AgI, $NiFe_xO_4$, WO_3/TiO_2/Fe_3O_4, ZnO@AgI@ Fe_3O_4, precious metals-SnO_2, BiOCl/SnO_2, CdS/SnO_2, F-doped SnO_2, Fe/SnO_2, Gd/SnO_2, I-doped SnO_2, La/SnO_2, Ni/Sb/SnO_2, Sb/SnO_2, rare-earth metals/SnO_2, Sn/SnO_2, transition metals and oxides-SnO_2, ZnO/TiO_2/SnO_2, SnO_2/V_2O_5, Ag-Au-ZnO, Ag-ZMNWA, Al-ZnO, Bi-ZnO, Bi_2O_3/ZnO, BiOI/ZnO (1:1), Cd-ZnO, CdO/ZnO, CdS/ZnO, Ce-Ag-ZnO, Er-Al-ZnO, transition metals and oxides-ZnO, rare-earth metals-ZnO, Hf-ZnO, alkali metal-ZnO, MoO_3/ZnO, $NaNbO_3$/ZnO, Ni-Th-ZnO, Pd-ZnO, Sb-ZnO, Se-ZnO, SiO_2/ZnO, Sn-ZnO, Sr-ZnO, WO_3/ZnO, ZnO/$ZnWO_4$, ZnO@Ag@ Cu_2O, ZnO-CeO_2, Zr-Ag-ZnO, Zr-Ag-ZnO, ZrO_2/ZnO, CdO, CdS, CdS-Bi_2S_3, CdSe, CeO_2, CeO_2-CdO, Cu_2O-$BiVO_4$, Cu-Au-ZnS, MoS_2, WO_x, ZnS, $ZnWO_4$, ZrO_2	CQDs/Ag/Ag_2O, CQDs/Ag/Ag_3PO_4, CQDs/Bi_2MoO_6, CQDs/Bi_2WO_6, CQDs/BiOBr, CQDs/BiOCl/BiOBr, CQDs/CdS, CQDs/$KNbO_3$, CQDs/TiO_2, CQDs/ZnO, Ag/CQDs/$Bi_2O_2CO_3$, Bi/BiOCl/TiO_2/CQDs, CdS/CQDs/BiOCl, TiO_2/BiOI/CQD, g-C_3N_4/Ag_3PO_4, g-C_3N_4/CdS/RGO, g-C_3N_4/GO/AgBr, g-C_3N_4/GO/Ag_3PO_4, g-C_3N_4/RGO/Bi_2WO_6, g-C_3N_4@Fe_3O_4@Ag_2CrO_4, g-C_3N_4@ Fe_3O_4@BiOI, g-C_3N_4@Fe_3O_4@$MnWO_4$, Ag_2O/g-C_3N_4, Ag_2MoO_4/g-C_3N_4, Ag_3VO_4/g-C_3N_4, Bi_2MoO_6/g-C_3N_4, Bi_2WO_6/g-C_3N_4, BiOCl@ g-C_3N_4@Cu_2O@Fe_3O_4, CdS/g-C_3N_4, $CdWO_4$/g-C_3N_4, CeO_2/g-C_3N_4, $CoFe_2O_4$/g-C_3N_4, Fe_3O_4/g-C_3N_4, $GdVO_4$/g-C_3N_4, MoS_2/g-C_3N_4, V_2O_5/g-C_3N_4, WO_3/g-C_3N_4, ZnO-g-C_3N_4/GO, BiOBr/$CoFe_2O_4$/graphene, $CoFe_2O_4$/graphene, CdS-ZnO-graphene, P25@graphene@Fe_3O_4, rGO-$CoFe_2O_4$, TiO_2/graphene, TiO_2/graphene/porphyrin, ZnO/graphene, G-CdS, GO/ZnO, GO-Ag_3PO_4, GO-TiO_2 NRCs, GO-TiO_2-Ag, MGO-TiO_2, MWCNT-ZnO, MWCNT@$CoFe_2O_4$, SGO-ZnO-Ag, Au-ZnO-rGO, Bi_2MoO_6-RGO, Bi_2WO_6/GO, CdS/GO, $CNRGOS_8$, P25/Ag_3PO_4/GO, TiO_2/Ag_3PO_4/GO, TiO_2/RGO, Ag@Fe_3O_4@C, Fe_3O_4@C@ZnO, Ag_3PO_4@polyaniline, Fe_3O_4-β-cyclodextrin, ZnO-PMMA, Fe_3O_4-PVA@PHB-PCL, Polyaniline-ZnO, Chitosan-Cu-TiO_2, PAN-CNTs

reactor condition. There are many reactor parameters, which include fluid mechanics, mass transfer, reactor type, light source type, and flow rates [7]. Photocatalytic efficiencies vary significantly in reports in the literature, and no direct comparisons are available because no standardization was established [27, 79–81]. For the design of a photoreactor, several parameters include efficient light (e.g., selection of wavelength and power) irradiation to a catalyst surface and efficient catalyst dispersion to harvest maximum amounts of incident photons. The photocatalytic reactor design includes maximum harvesting of incoming light. Photocatalysts are dispersed in liquid (called an S-L mode) or on a support (called an S-G mode) [27, 79–81] (Fig. 6).

The reactors can be operated under a closed (with atmospheric or high pressures) or a continuous-flow condition of reactant molecules. For CO_2 reduction in the S-L mode,

https://www.twirpx.org & http://chemistry-chemists.com

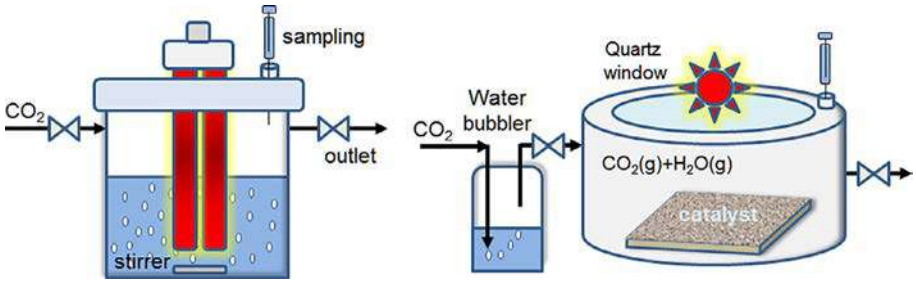

FIG. 6 Two typical photocatalytic CO_2 reduction reactors: (A) an S-L mode reactor design and (B) an S-G mode reactor. *From Sohn Y, Huang W, Taghipour F. Recent progress and perspectives in photocatalytic CO_2 reduction of Ti-oxide based nanomaterials. Appl Surf Sci 2017;396:1696–1711, with Copyright permission.*

catalyst powder is commonly dispersed in an aqueous solution and CO_2 gas is saturated in the reactor, or CO_2 gas is flowed continuously. For photocatalytic hydrogen production, only inert gas flowed or the reactor with catalyst-dispersed solution is closed. For increasing CO_2 adsorption probability on a photocatalyst, bicarbonates, ethylenediaminetetraacetic acid (EDTA), and monoethanolamine (MEA) solutions have commonly been used [27]. However, in many cases photocatalytic hydrogen production is superior in an aqueous solution. For the solid-gas mode, a gaseous H_2O/CO_2 mixture is saturated or flowed in a reactor for CO_2 reduction. For hydrogen production, gaseous H_2O is saturated in a closed system or flowed using a carrier gas. Bulk H_2O is not directly in contact with the catalyst. Fajrina and Tahir introduced a design of various reactor systems for H_2 production in their review article [6]. They discussed thoroughly the advantages and limitations of the various photoreactors of slurry, fluidized, optical fiber, monolith, and fixed bed reactors. The optical fiber honeycomb (or monolithic) reactor system is desirable to use incoming light efficiently, thereby increasing the photocatalytic efficiency [27, 79–81]. The advantages and disadvantages of various reactor designs have also been discussed in several review articles [79–81] (Figs. 7 and 8).

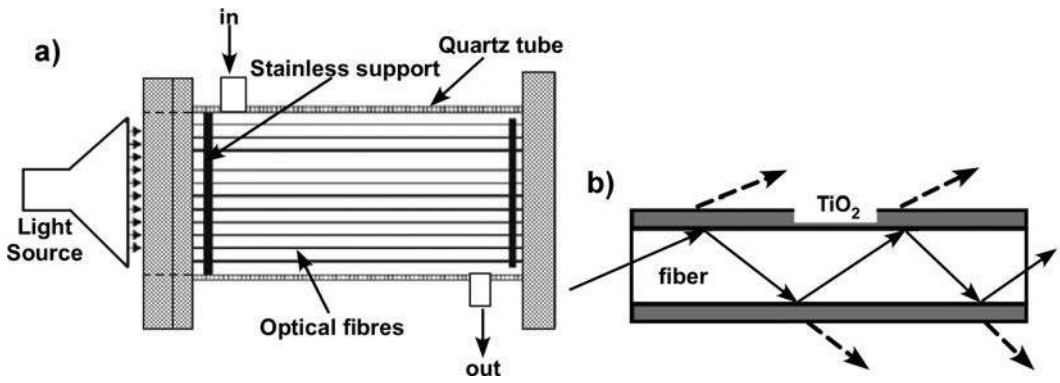

FIG. 7 (A) Schematic of an optical-fiber photoreactor and (B) light transmission in a TiO_2 coated-optical fiber [81].

https://www.twirpx.org & http://chemistry-chemists.com

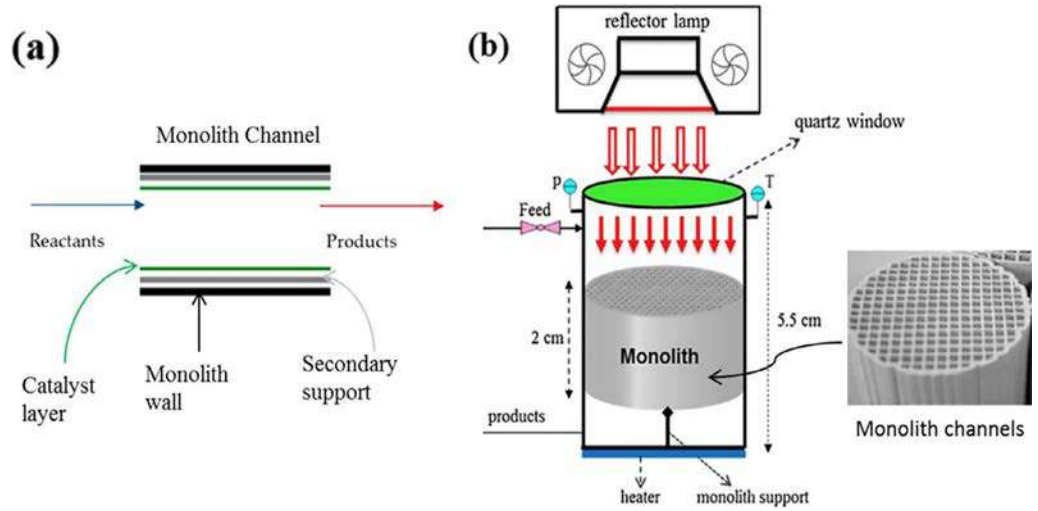

FIG. 8 (A) Schematic of single monolith channel and (B) monolith photo reactor. *From Fajrina N, Tahir M. A critical review in strategies to improve photocatalytic water splitting towards hydrogen production. Int J Hydrog Energy 2019;44:540–577, with Copyright permission.*

Singh et al. reported that the CO_2 reduction performance was dependent on the configuration of electrochemical cell systems: PEC, a tandem PEC, and a PV-electrolyzer [82]. Ahmed and Dincer reviewed diverse designs of photoelectrochemical reactors; single and dual photoelectrodes (P-, T-, wired T-, and wireless T-modes) as depicted in Fig. 9, photoelectrochemical/photovoltaic multijunction designs, solar-concentrator-PEC design, and an integrated hybrid PEC-chloroalkali system [83]. For comparison between parallel (P) mode and tandem (T) mode in Fig. 9, it was reported that the P-mode shows higher efficiency than the T-mode, especially for photoanodes [83].

3.2 Photocatalyst efficiency

Because many studies have used different reactors and reactor conditions, it is very difficult to compare directly the experimental data reported. For photocatalysis reaction using the solid-gas mode (or a fixed bed reactor), the production yield has been reported as mol/cm^2/h at a given powder density (mW/cm^2), but the photon flux has not been actively considered. The light power and wavelength have not been reported in a standardized format. The photocatalyst efficiency should consider the area (cm^2) of catalyst-dispersed support, light exposure time (s or h), the generated amount (mol) of a desired product, and photon flux (or light power density, W/cm^2 or J s/cm^2).

$$E(\text{joule}) = \frac{h(=6.626\times10^{-34}\,\text{J s})c(=2.998\times10^{8}\,\text{m/s})}{\lambda}$$

https://www.twirpx.org & http://chemistry-chemists.com

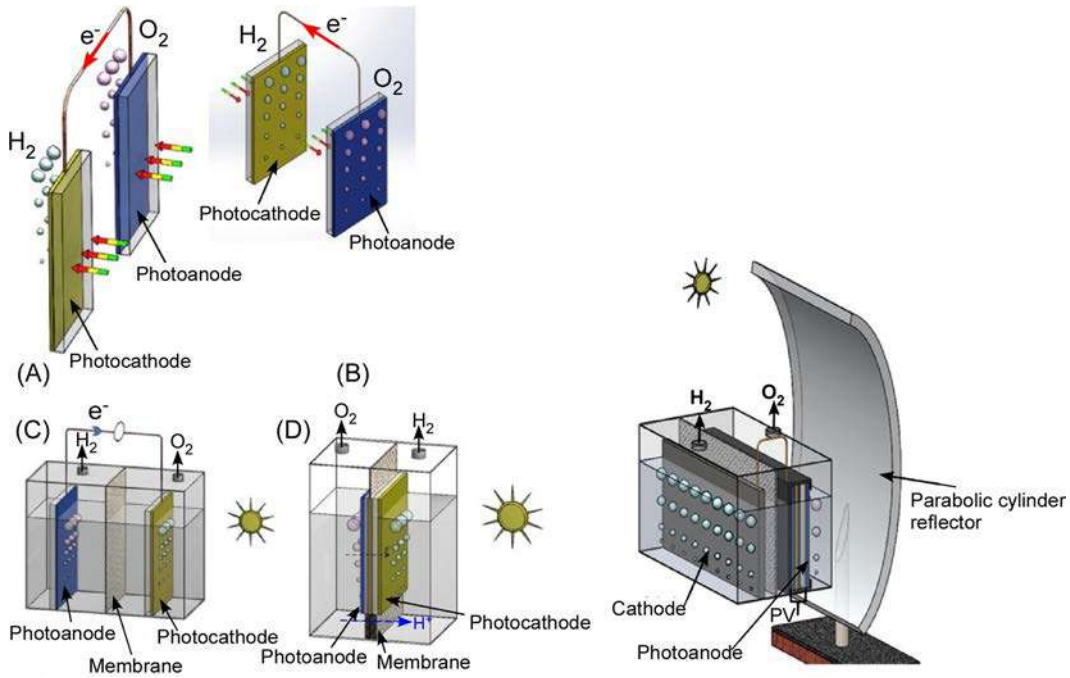

FIG. 9 Dual cell photoelectrodes: (A) parallel mode, (B) tandem, (T) mode, (C) wired T-mode, and (D) wireless T-mode and solar-concentrator-coupled PEC design. *From Ahmed M, Dincer I. A review on photoelectrochemical hydrogen production systems: challenges and future directions. Int J Hydrog Energy 2019;44:2474–2507, with Copyright permission.*

$$\text{Rate of photons (mol) per area} = \frac{\text{power density}\,(\text{W/cm}^2)}{E(\text{J})} = \frac{\#\text{photons}/N_A}{\text{s cm}^2} = \frac{\text{mol}}{\text{s cm}^2}$$

$$\text{Photocatalysis efficiency}\,(\%) = \frac{\text{generated amount (mol) of a desired product}}{(\text{Rate of photons per area, mol/s/cm}^2) \times (\text{catalyst area, cm}^2) \times (\text{totoal reaction time, s})}$$

For photocatalyst efficiency using the solid-liquid mode, one should consider the amount (L) of liquid, the amount (g) of photocatalyst, light exposure time (s or h), the generated amount (mol) of a desired product, and rate of photons per area (or light power density at a given wavelength, W/cm^2 or J s/cm^2). The production yield has commonly been reported as mol/g/h. The standardization was slightly more difficult.

The standardization of photoelectrochemical water splitting and CO_2 reduction results and efficiencies are required for absolute evaluation of the reported results [84]. Many literature experimental data have not been validated. In this sense, for electrochemical water splitting for hydrogen generation, Anantharaj et al. discussed in detail "the ten important parameters, 1) overpotential at a defined current density, 2) iR-corrected

https://www.twirpx.org & http://chemistry-chemists.com

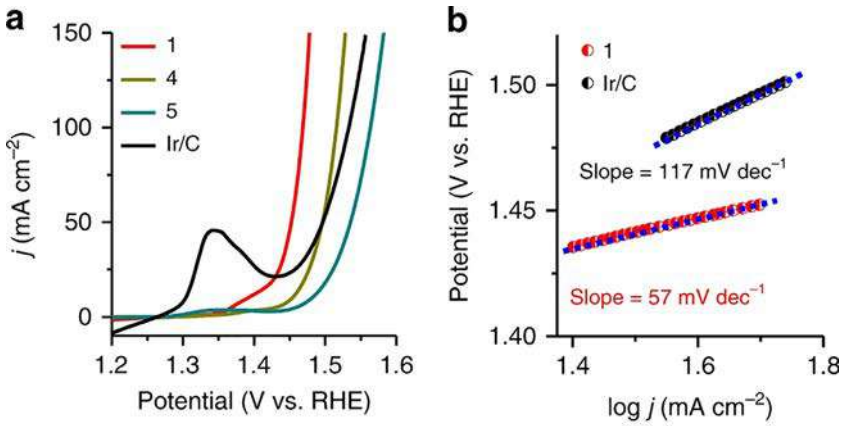

FIG. 10 (A) Typical linear sweep voltammograms curves and (B) Tafel slopes [85].

overpotential at a defined current density, 3) Tafel slope, 4) exchange current density (j_0), 5) mass activity, 6) specific activity, 7) faradaic efficiency (FE), 8) turnover frequency (TOF), 9) electrochemically active surface area, and 10) measurement of double layer capacitance (C_{dl})" in their review article [84].

Under dark conditions, obtaining linear sweep voltammetry curve (current density, A/cm^2 versus applied potential, e.g., $E_{vs\cdot RHE} = E_{vs\cdot Ag/AgCl} + 1.009$ V) for a given reference electrode is a starting point for an evaluation electrode efficiency, as shown in Fig. 10. The Tafel equation is expressed as $\eta = b \log J + c$, where η is the overpotential, b is the Tafel slope, c is the intercept, and J is the measured current density. A higher current density with a lower overpotential ($\eta = 0 - E_{vs\cdot RHE}$ for HER and $\eta = E_{vs\cdot RHE} - 1.23\ \text{V} = E_{vs\cdot Ag/AgCl} - 0.221$ V for OER) and a lower Tafel slope are generally indications of a better catalyst electrode (Fig. 10). Reduction of overpotential is crucial in electrochemistry.

The PEC efficiency was well discussed in the review article by Jiang et al. [86]. Faradaic efficiency is a useful method of determining that if the measured photocurrent (or current) is purely due to water splitting (or CO_2 reduction), not due to other side reactions. The efficiency of a product is calculated from the ratio of the measured amount divided by the theoretical amount based on the measured photocurrent.

$$\text{Faradaic efficiency} = \frac{\text{Experimental gas evolution}}{\text{Theoretical gas evolution}} = \frac{n_{\text{measured}}}{(\text{I} \times t)/(z \times F)} \times 100\%$$

where n_{measured} is the number of moles of gas generated, I is the current (A), t is the time (s), z is the transfer of electrons ($z = 2$ for H_2, $z = 4$ for O_2), and F is the Faraday constant (96485 C/mol).

$$\text{Quantum yield}\,(\%)\ \text{for}\ CO_2\ \text{reduction product} = \frac{n \times \#\ \text{of product molecules}}{\#\ \text{of incident photons}} \times 100\,(\%)$$

https://www.twirpx.org & http://chemistry-chemists.com

where n is 2, 2, 4, 6, and 8 for CO, HCOOH, HCHO, CH_3OH, and CH_4 molecules, respectively [29].

The incident photon-to-current efficiency (IPCE) at a fixed light wavelength has been used to evaluate a photoelectrode performance as a quantum efficiency for water splitting. The IPCE is calculated using the following equation [86, 87]:

$$\mathrm{IPCE}\,(\lambda) = \frac{\text{Total } E \text{ of converted electrons}}{\text{Total } E \text{ of incident photons}} = \frac{\left(\frac{J(\lambda)}{e}\right) \times \left(\frac{hc}{\lambda}\right)}{P(\lambda)} \times 100\%$$

where J is the photocurrent density (mA/cm^2) at a fixed light wavelength, h is Planck's constant (6.626×10^{-34} J s), c is the speed of light ($3.0 \times 10^8 \times 10^9$ nm/s), e is an electron charge (1.602×10^{-19} C), λ (nm) is the light wavelength, and $P(\lambda)$ is the incident light intensity (mW/cm^2 or 1 mJ/s/cm^2) at the light wavelength. For correction of optical losses such as reflection (R) and transmission (T), the absorbed photon-to-current conversion efficiency (APCE) is introduced using the following equation [86]:

$$\mathrm{APCE}\,(\lambda) = \frac{\mathrm{IPCE}\,(\lambda)}{1 - R - T} \times 100\%.$$

The solar to hydrogen (STH) conversion efficiency (η) is estimated by using the following equation:

$$\eta\,(\%) = \frac{J \times \left(1.23 - V_{\text{applied}}\right) \times \text{Fardaic efficiency}}{\text{Light intensity}\,(AM\,1.5G)}$$

For real application of hydrogen, Maeda and Domen briefly mentioned that more important tasks were required such as the construction of a large-scale solar water splitting reactor, an H_2/O_2 gas separator, a hydrogen storage plant, and so on [88]. They suggested that an area of 250,000 km^2 is required to provide one-third of the energy needs in 2050, based on 10% STH conversion efficiency, as depicted in Fig. 11 [88, 89].

3.3 Modification of photocatalysts

Many factors influence photocatalytic activity. The factors are commonly experimental (called here extrinsic) parameters (e.g., photoreactor design, temperature, pH, and sacrificial agent) and fundamental (called here intrinsic) properties (e.g., bandgap, surface area, crystal phase, defects, etc.) of a photocatalyst. The parameters are like an interdependent 3D cube puzzle. Engineering technology and strategies are large and challenging tasks in photocatalyst development, as illustrated in Fig. 12 [90].

For material design, crystal phase, crystallinity, morphology, exposed facets, sizes, defects, catalyst supports, and guest-introduction into a host material are all parameters that have been commonly considered [81–93]. Different crystal facets have different densities of exposed cations and anions, and consequently different surface electronic structures and interactions toward reactant molecules [94, 95]. Controlling catalyst particle size has been an essential parameter for increasing surface area, high active sites, and

https://www.twirpx.org & http://chemistry-chemists.com

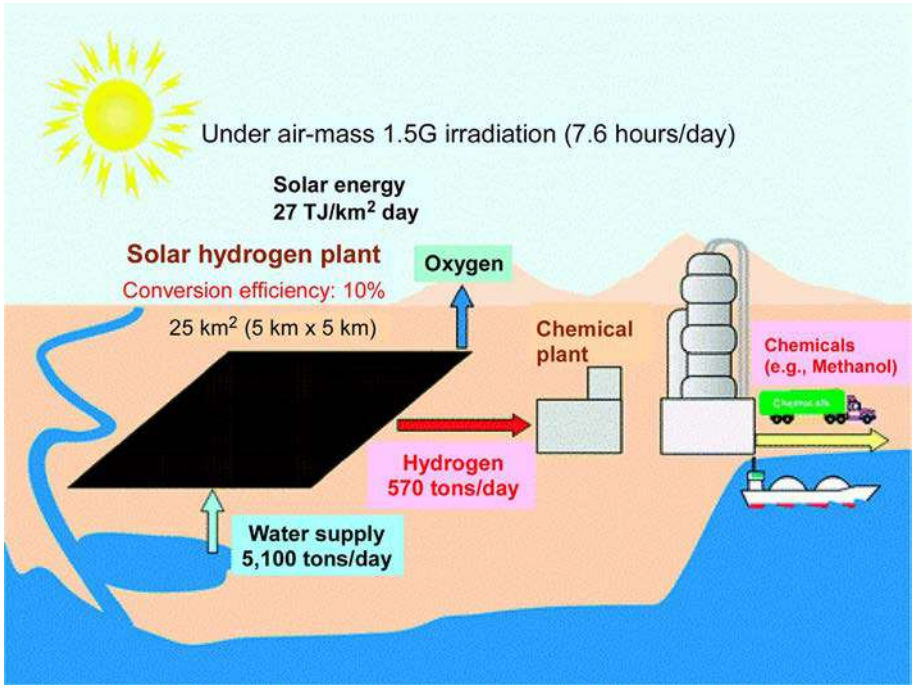

FIG. 11 Future large-scale H_2 production scheme via solar water splitting [88].

enhanced visible light absorption. The optimum size needs to be obtained because bandgaps, electronic structures, and charge-carrier dynamics are size-dependent in the quantum size region [96]. Defect creation has been used to increase active sites for increasing adsorption and reaction and to produce localized electronic mid-gap states for enhancing visible light absorption and energy level alignment [70, 97]. Liu et al. fully discussed the surface sites engineering of visible photocatalysts in their review article [91].

3.3.1 Heterojunction interface engineering

Fruitful experimental data of a single-phase catalyst are already available for diverse application areas. However, a single crystal phase material cannot achieve commercial efficiency. The single-phase catalyst has a continuum limit value although it reaches a maximum surface area, highly exposed active crystal facets, and active defect sites. It is very difficult to achieve the desired practical efficiency using a pure single-phase catalyst material. To overcome the limitations of the single phase, two or more different materials have been employed to fabricate heterojunction materials. Diverse research keywords include coupling, mixing, binding, bridging and hybridization of metal oxides, semiconductors, metals, and nonmetals. Then, the magic puzzle cube becomes $N \times N \times N$ as the experimental parameters increase to N. Many challenging questions arise here: (1) whether the energy levels well match at the interface; (2) what the direction of the charge

https://www.twirpx.org & http://chemistry-chemists.com

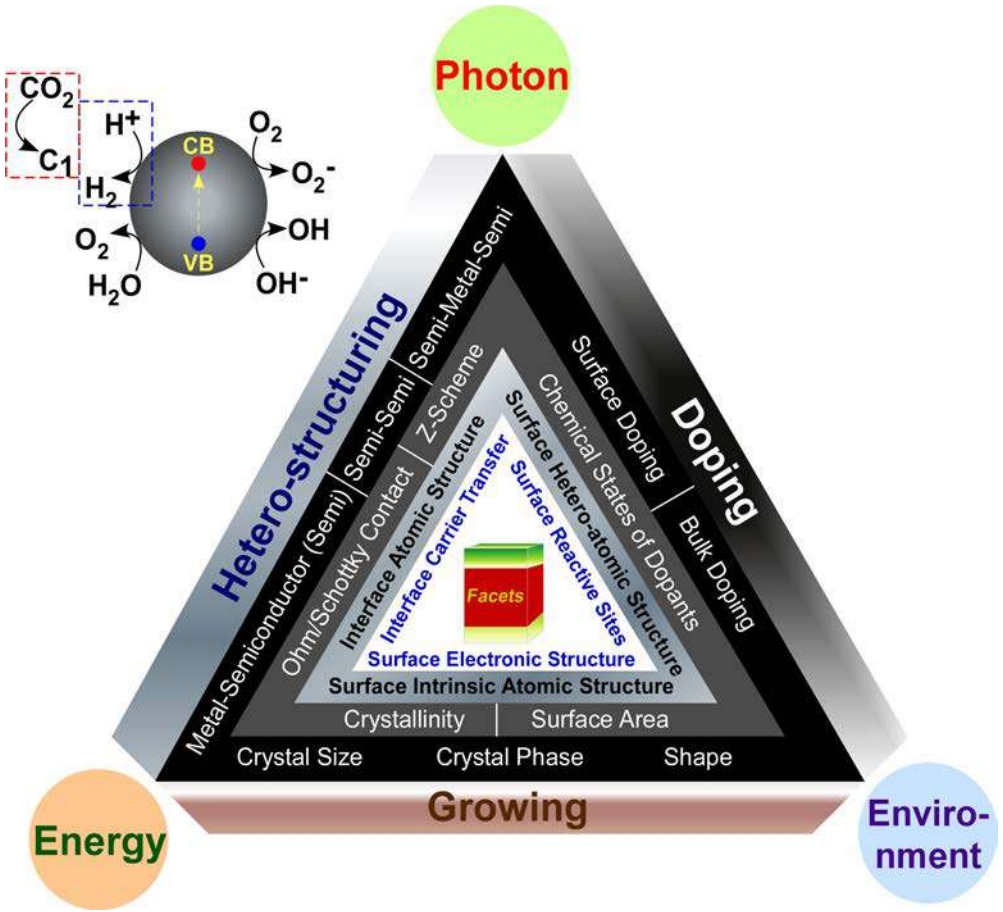

FIG. 12 Diverse material engineering strategies of photocatalysts. *From Liu G, Yu JC, Lu GQM, Cheng HM. Crystal facet engineering of semiconductor photocatalysts: motivations, advances and unique properties. Chem Commun 2011;47:6763–6783, with Copyright permission.*

carrier transfer is; and (3) what type of energy level alignment is present. When a heterojunction is made, two materials with different dimensions are considered to be an important factor, as shown in Fig. 13.

Among the contacts shown in Fig. 13, the major advantage of 2D/2D heterojunctions is the high interfacial contact area between two different materials, resulting in much stronger interactions and high charge-transfer rates [98–100]. 2D materials include graphene, g-C_3N_4, $MoTe_2/MoS_2$, WS_2/MoS_2, and WS_2/h-BN layer/MoS_2. Liang focused on H_2 production over diverse 2D MoS_2 cocatalysts [100]. In their summarized tables, they introduced different synthesis strategies (e.g., doping heteroatoms, interfacial coupling, controlling of thickness/size/defects/pores, exposing reactive facets/edge sites, cocatalyst heterojunctions, and engineering interfacial bonds/confinement effects) for more than 80 2D MoS_2 cocatalysts, reactor conditions, resultant photocatalytic activities (in unit of mol/g/h), and quantum efficiencies.

https://www.twirpx.org & http://chemistry-chemists.com

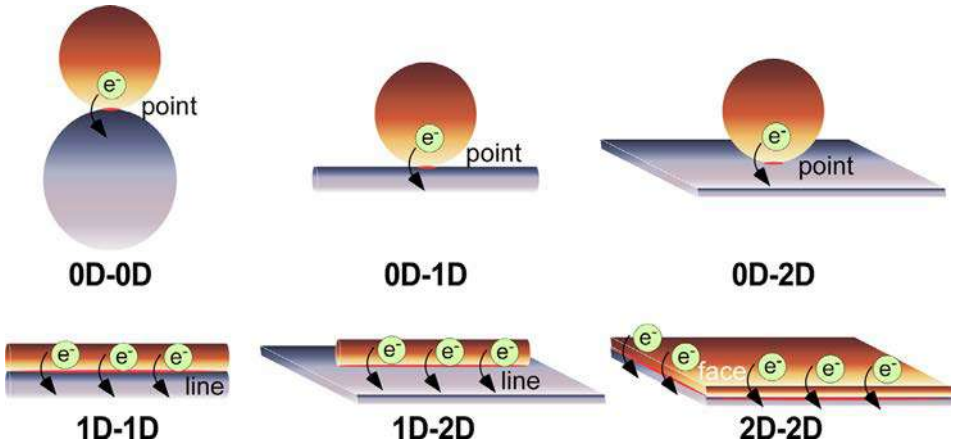

FIG. 13 Heterojunctions of two different materials with different dimensions and the charger transfer at the interface with point, line, and face contacts.

When two materials with different natures contact each other, redistribution of electron distribution occurs until an equilibrium is reached. The energy levels are then realigned and the charge carrier transfer rate can be engineered to increase photocatalytic activity. A great deal of various interface engineering has been carried out, such as metal/semiconductor interfacing and semiconductor/semiconductor interfacing [86, 101, 102]. Diverse engineered materials were shown in Tables 1–3 for water splitting, CO_2 reduction, and pollutant removal, respectively. Fig. 15 depicts energy band bending upon contact at the interface of metal and n- and p-type semiconductors. The interfacial energy level is then governed by Schottky (Fig. 14A and C) and ohmic (Fig. 14B and D) contacts, depending on the Fermi level and the work function differences between the two different materials. Therefore, when a hybrid metal-semiconductor is made, the plausible band bending should be plotted to better understand charge carrier dynamics.

When two semiconductors of different bandgaps and Fermi levels are junctioned, different types of interfacial energy level and charge carrier flow direction occur. Fig. 15 shows four different types of semiconductor-semiconductor junctions: (a) straddling (type 1); (b) staggered (type 2); (c) p/n junction; and (d) Z-scheme junction [101]. For the first three heterojunctions (Fig. 15A–C), electrons and holes flow between the CBs and VBs of two different materials, respectively. For the Z-scheme heterojunction, electrons flow between the CB and the VB of two different materials, respectively (Fig. 15D). For this reason, when a heterojunction is made, an appropriate material choice is needed. Band bending also occurs by induction of surface state, adsorption of a molecule, and applied bias voltage [86]. Zhong et al. discussed bridge engineering of different materials for the enhancement of photocatalytic and photoelectrochemical (PEC) processes [102].

https://www.twirpx.org & http://chemistry-chemists.com

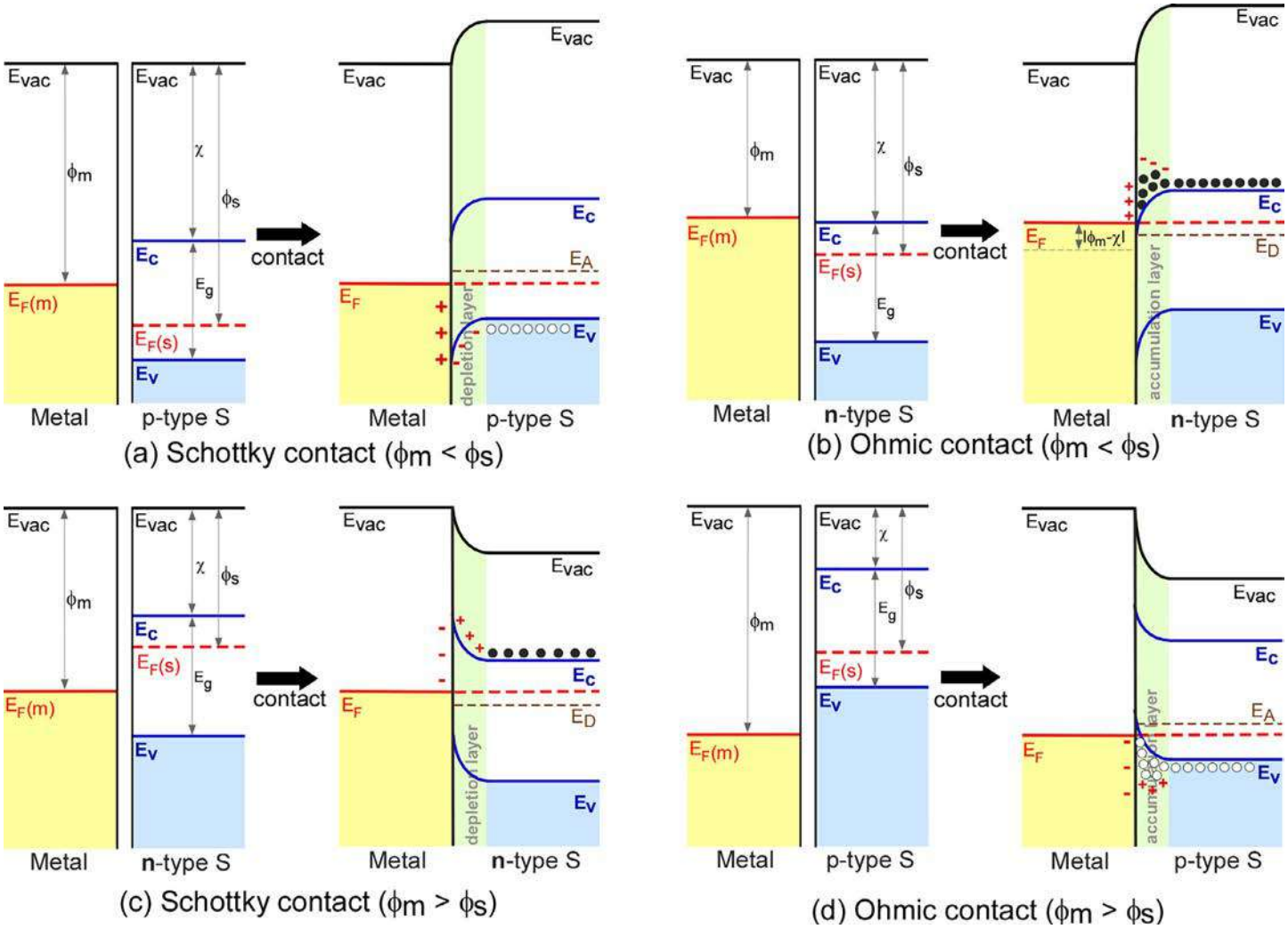

FIG. 14 Energy band bending upon contact at the interface of metal and n- and p-type semiconductors, where ϕ_m = metal work function, ϕ_s = metal work function, $E_F(m)$ = Fermi level of metal, $E_F(s)$ = Fermi level of semiconductor, E_c = energy of conduction band minimum, E_v = energy of valence band maximum, E_c = bandgap energy, and χ = electron affinity.

https://www.twirpx.org & http://chemistry-chemists.com

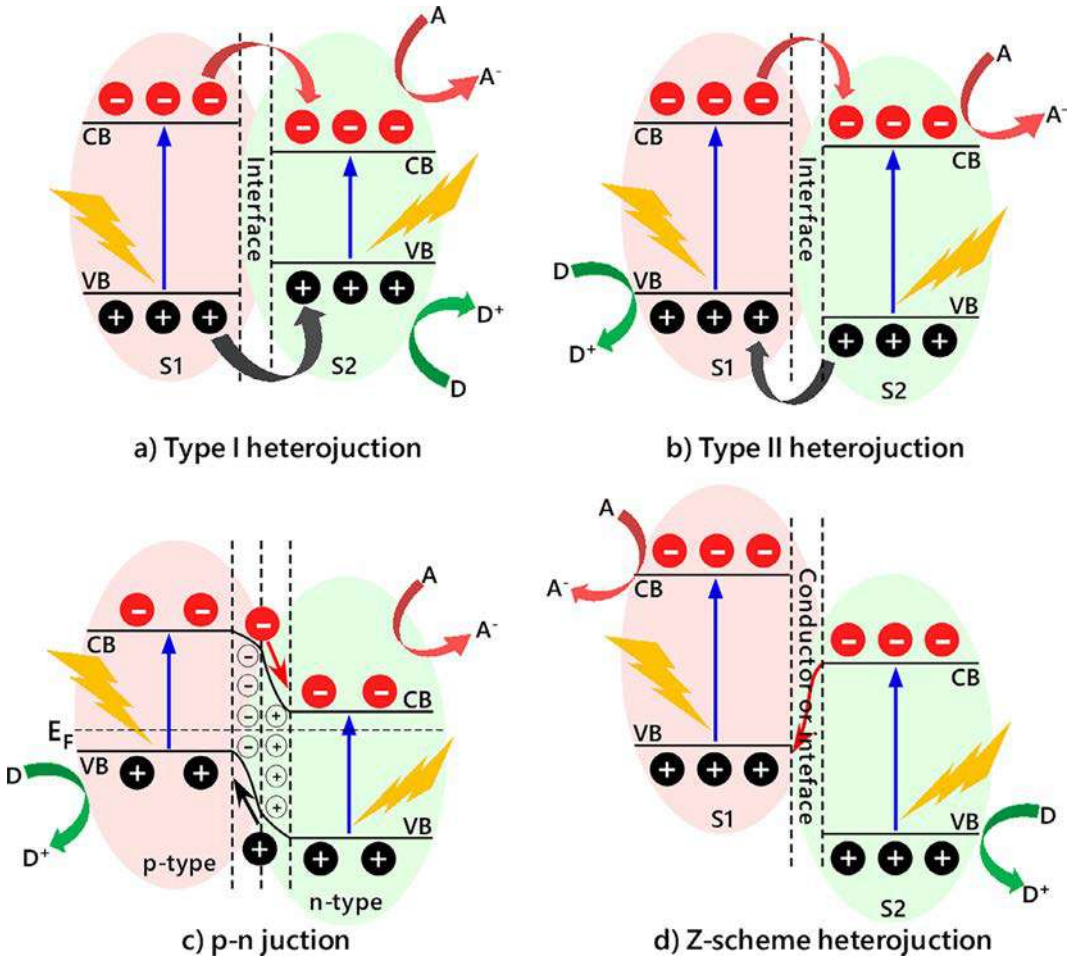

FIG. 15 Energy level alignments at the interface of two different semiconductors.

3.3.2 Z-scheme interfacing

Z-scheme interfacing has been a good way of tuning redox potentials for both hydrogen and oxygen evolutions as well as CO_2 reduction potential [6, 103–106]. Xia et al. summarized all-solid-state Z-scheme photocatalysts for water splitting in view of new morphologies and connection modes, thereby improving light absorption and carrier transport efficiency [103]. Li et al. reviewed Z-scheme photocatalytic systems in view of a natural photosynthesis system [104, 105]. They discussed diverse connection modes of different materials for increasing visible light absorption and promoting charge separation and transportation, thereby enhancing photocatalytic efficiency. The connection modes include Z-scheme systems as shown in Figs. 16 and 17: (1) without mediators (or direct junction); (2) with solid-state electron mediators; and (3) shuttle redox mediators [6, 104, 105].

https://www.twirpx.org & http://chemistry-chemists.com

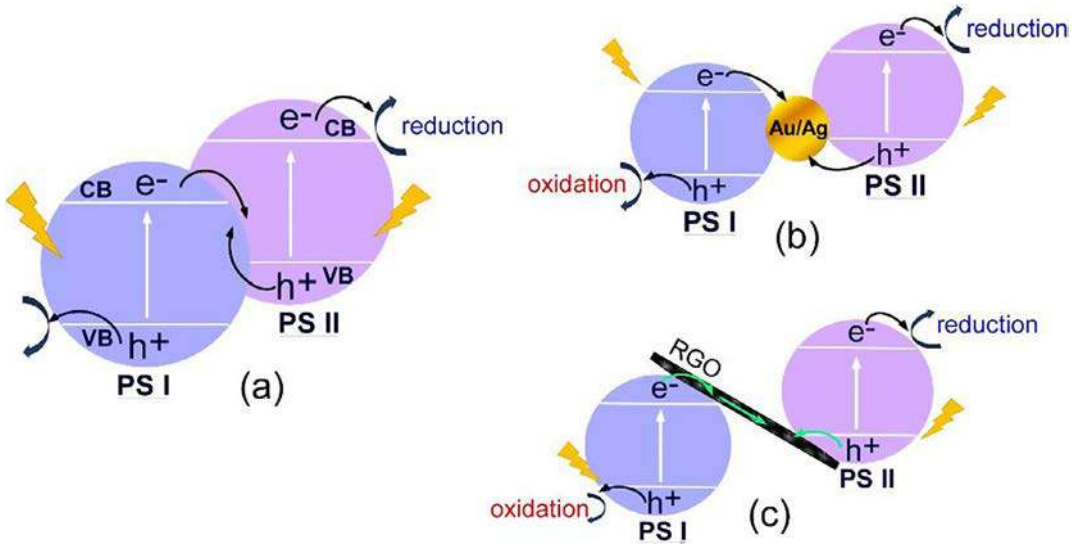

FIG. 16 Schematic illustrations of direct Z-scheme without a mediator (A), Z-scheme with an Au/Ag electron-mediator (B), and Z-scheme with an RGO electron-mediator (C).

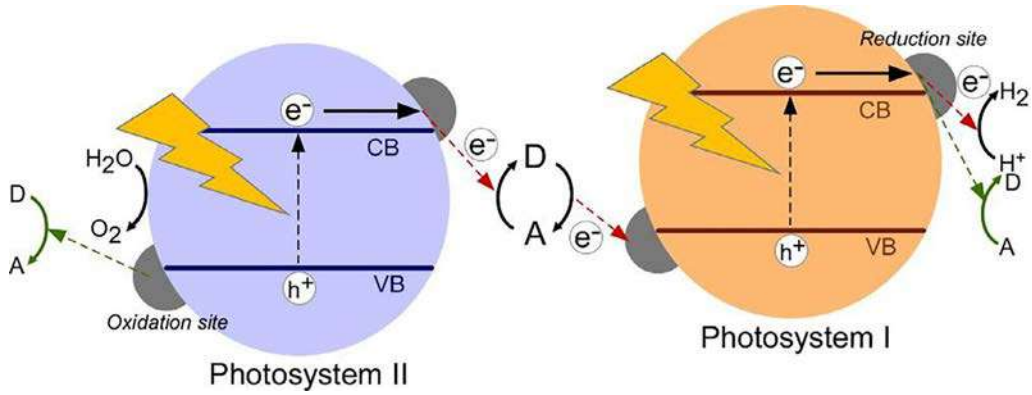

FIG. 17 Schematic illustrations of Z-scheme with shuttle redox mediators.

3.3.3 Plasmonic photocatalysts

Coherent delocalized electron oscillation exists at the interface between some small-scale noble metals (e.g., Au, Ag, and Pt) and dielectric, as shown in Fig. 18 [107–110]. The so-called surface plasmon plays an important role in increasing photocatalytic activity by enhancing the photoexcited charge carriers as well as ensuring good charge transfer onto a desired energy level. At this stage, several questions arise: (1) what surface plasmonic (SP) metals are employed for a selected support material; (2) what the optimum size (or thickness) of the SP metal is; (3) what mechanism is involved; and (4) what interfacial

https://www.twirpx.org & http://chemistry-chemists.com

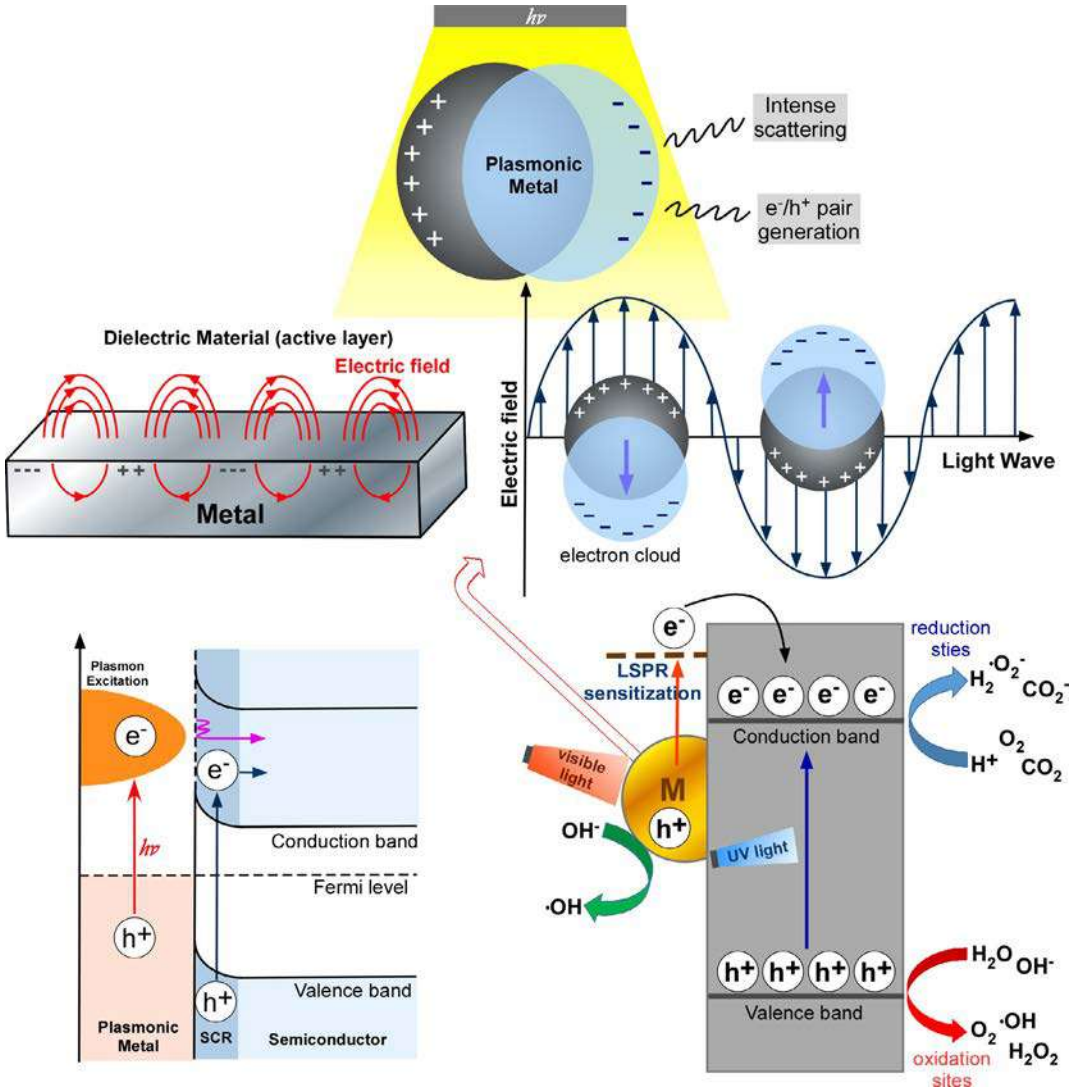

FIG. 18 Schematic diagram of coherent delocalized electron oscillation, energy level alignment of plasmonic metal-semiconductor system, and the charge transfer process for reactions at the redox sites.

energy level alignment is appropriate for a desired catalytic reaction. Several review articles deal with plasmonic metal-semiconductor photocatalysts and their design and mechanism involved in catalytic enhancement [107, 108]. Reddy et al. reviewed plasmonic nano-photocatalysts for hydrogen production [109]. In their review article, they discussed various synthesis methods of photo-deposition, chemical reduction, precipitation, hydrothermal, sol-gel, impregnation, and solid-state reaction methods. Different noble metals of Au, Ag, Pt, Pd, Ru, and Rh were discussed with various metal oxides of TiO_2, ZnO, V_2O_5,

https://www.twirpx.org & http://chemistry-chemists.com

and Fe_2O_3 showing diverse morphologies. For high performance of plasmonic photocatalysts, the major fundamental efforts were reported to be visible light response, enhanced UV-visible absorption, reduced e^- and h^+ diffusion length, enhanced local electric field, LSPR-powered e^- and h^+ generation, local heating effect, and molecule polarization effect [109].

3.3.4 Metal/nonmetal-doping and sensitizers

Introducing metals, nonmetals, and sensitizers creates new energy states for charge carrier transfer and light absorption, as depicted in Fig. 19. When photosensitizers are introduced (Fig. 19A) to make semiconductor/dye and semiconductor/metal-complex photocatalyst systems, visible light absorption can be enhanced. Photosensitizers include various dyes, porphyrins, and metal-organic complexes [111–113]. A photogenerated electron from the CB of a sensitizer transfers to the CB of the photocatalyst, where reduction reactions take place. The charge transfer can occur from the photocatalyst to the photosensitizer. When plasmonic and nonplasmonic metals are loaded into the host matrix, vacancies can be created depending on the oxidation states of metals [114, 115]. In addition, metals are electron scavenger sites. Therefore, the electrons are accumulated in the metal site, where reduction reactions take place, as depicted in Fig. 19B. The valence electrons of the nonmetals (e.g., C, N, and halogens) mainly occupy p orbitals which can be

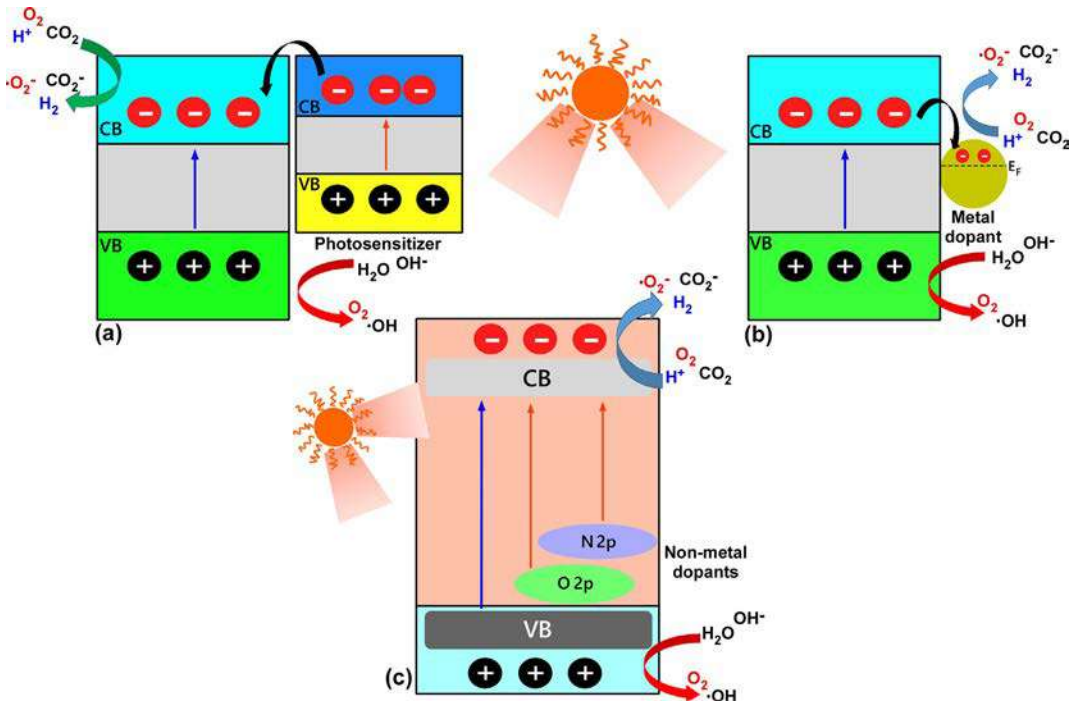

FIG. 19 Schematic energy levels upon introducing (A) sensitizer, (B) metal dopants, and (C) nonmetal dopants.

https://www.twirpx.org & http://chemistry-chemists.com

occupied mid-gap states in Fig. 19C. The (surface) electronic states are altered by nonmetal doping, and therefore the resultant activity is also altered [114, 115].

For a good example in this section, quantum dots (2–10 nm) of metals, metal oxides, metal chalcogenides, and carbon-based nanostructures, and their hybrids, have been extensively designed for hydrogen production photocatalysts [115]. Several quantum dots include CdS/GO, CdS/RGO, CdS/sulfonated graphene, CdS-Al_2O_3/GO, CdS quantum dots-ZnO/RGO, g-C_3N_4/CoO, TiO_2/GQDs, Ni-Ni_3C@C/g-C_3N_4, and ZnS/g-C_3N_4. The dots act as photocatalysts, cocatalysts, and photo-sensitizers that help visible absorption, charge separation, and the quantum confinement effect. Rao et al. reviewed quantum dot (more deliberately for carbon dots) hydrogen production photocatalysts from diverse synthesis methods, the roles of dots, and their energy transfer mechanism [115].

3.4 Nonmetallic-based photocatalysts

Nonmetallic-based photocatalysts and their heterostructures have been developed extensively. Graphene, carbon nanotube, C_{60}, and carbon nitride are of great interest. Graphene-based photocatalysts have been reviewed by Li et al. [116]. Carbon quantum dot-(CQD)-based photocatalysts have been developed because of their good light absorption and electron transfer ability. Makama et al. reviewed CQD-based composites especially in view of water purification [117]. They discussed the design of CQD-based catalysts and introduced various types of CQD/semiconductor composites which include CQD/Bi_2MoO_6, CQDs/Ag/Ag_2O, CQD-TiO_2, CQD-TiO_2, CQD-TiO_2, CQD-SiO_2, Fe_2O_3-CQD, Cu_2O-CQD, N-CQD, Bi_2MoO_6-CDQ, CDQ/Bi_2WO_6, CQD/BiOBr, Bi_2MoO_6-CDQ, CQDs/BiOI, Bi_2WO_6-CDQ, CQD/BiOBr, Bi_2MoO_6-CDQ, CQDs/BiOI, Bi_2WO_6-CDQ, $MoSe_2$-CDQ, Ag_3PO_4-CQD, CQD-TiO_2, CQDs/BiOI, CQD/BiOBr, CQDs/Ag/Ag_2O, Bi_2WO_6-CDQ, CQDs/BiOI, and CQDs/CdS. The future scope discussed for water purification includes: (1) utilization of a large portion of solar light; (2) cost-effective catalyst immobilization strategy without extra addition of oxidants; (3) catalyst operation in a wide pH range; (4) new heterojunction coupling systems for enhancing photocatalytic activity; and (5) design of a photocatalytic reactor and parabolic solar collector. Semiconducting graphitic carbon nitride has attracted great attention for the development of a new photocatalyst material [87, 118–122]. Jiang discussed photocatalysis (e.g., H_2 evolution and pollutant degradation) and diverse synthesis methods for metal (alkali and transition metals) and nonmetal (phosphorous, sulfur, oxygen, carbon, nitrogen, boron, and halogen)-doped g-C_3N_4 including codoped and heterojunction materials [123]. Liu et al. introduced a diverse g-C_3N_4 family with diverse micro-/nanostructures: bulky, mesoporous, nanosheets, thin films, 1D nanowires/nanorods/nanotubes, 0D quantum dots, and composites [87]. In view of CO_2 reduction, graphene, graphene oxide, and g-C_3N_4 have comprehensively been discussed including various modification methods [121, 122].

https://www.twirpx.org & http://chemistry-chemists.com

3.5 Photoelectrochemistry

Photocatalysis has popularly been commercialized in pollutant degradation. However, hydrogen production and CO_2 reduction using photocatalysis itself are still far from commercialization. One strategic solution is a combination of electrochemistry [83, 123, 124] and photocatalysis, known as photoelectrochemistry (PEC), using photoelectrode materials as depicted in Fig. 20. The electrochemical reaction is assisted by photocatalysis. The details are also found in the review article, "A review on photoelectrochemical hydrogen production systems: Challenges and future directions" by Ahmed and Dincer [83]. The commercialization of PEC hydrogen production is very positive. Many visible light photocatalysts with high efficiency have frequently been reported in the studies introduced above. Theoretical calculations assist the development of these photocatalysts by providing plausible mechanistic reaction pathways [125].

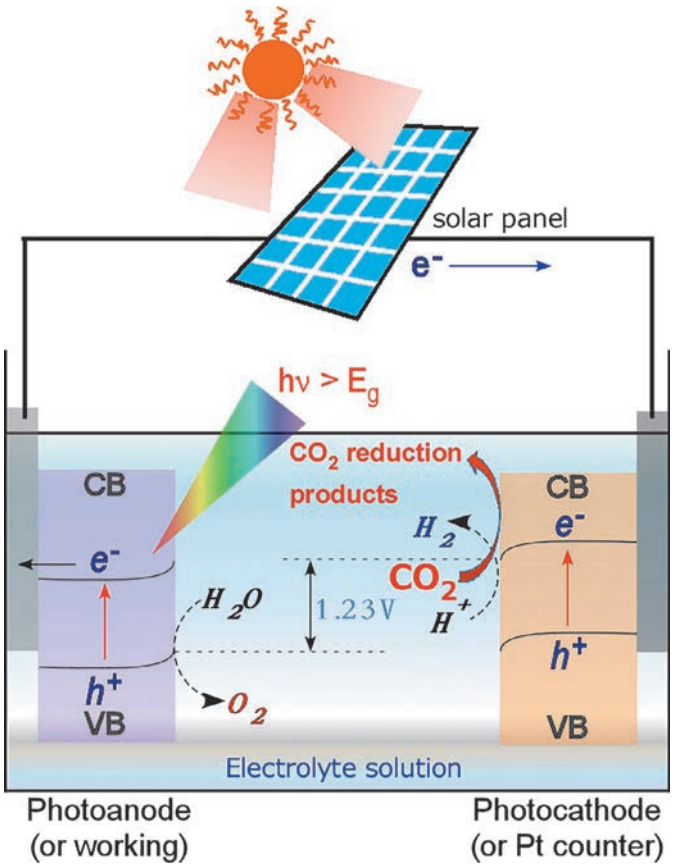

FIG. 20 Energy diagram of a PV-photoelectrochemical cell for water splitting and CO_2 reduction. The electrical energy source is from a solar cell.

https://www.twirpx.org & http://chemistry-chemists.com

Jiang et al. reviewed PEC devices for solar water splitting and future challenges [86]. They first discussed induced band bending with an energy diagram for (1) metal/semiconductor contact, (2) surface-state, (3) adsorption, and (4) applied bias, and explained the physics of semiconductor/electrolyte contacts and the PEC water-splitting process. They also discussed energy level alignment for various types of PEC water-splitting devices, as shown in Fig. 21. For photoelectrode materials, photoanode materials include TiO_2, α-Fe_2O_3, $BiVO_4$, CdS, and group III–V compounds, and photocathode materials Cu_2O, group II–IV metal phosphides (e.g., GaP and InP), and Si. In addition, cocatalyst selection was discussed. The authors suggest that type-II and IV PEC tandem cells (using first-row transition metal cocatalysts and earth-abundant semiconductors) have the greatest potential for future energy solutions [86].

Generally, the LSV curves for HER and OER in the PEC water-splitting systems are first obtained to evaluate the HER and OER efficiencies of a catalyst [76, 126]. A typical polarization curve is shown in Fig. 22, and the overpotential at a current density of 10 mA/cm^2 has been regarded as experimental value that evaluates a photoelectrode performance [126]. The mechanistic hydrogen and oxygen evolutions are also depicted in Fig. 22. More details are described elsewhere [76, 126].

Electrochemical CO_2 reduction ($xCO_2 + yH^+ + ze^- \rightarrow \text{products} + mH_2O$) is an even more difficult task since the first discovery of formic acid formation on a *p*-type GaP cathode in 1978 [127]. For photoelectrochemical CO_2 reduction, challenging tasks are: (1) how to minimize hydrogen evolution channel and enhance the faradaic efficiency for the desired product; (2) how to increase faradaic efficiency and selectivity; and (3) what photoelectrode materials are chosen and designed. Crucially, although CO_2 reduction products are in the liquid phase, the products can be reoxidized by active holes. To overcome these barriers, reaction pathways over a developed catalyst need to be understood [128]. Moreover, many other factors should be carefully examined including light absorption, energy level engineering, charge carrier generation and transport, and surface physics/chemistry [129]. The application of photocatalysts and reactor designs are discussed in Sections 2.2 and 3.1, respectively. Fig. 23 depicts various methods of CO_2 recycling. For direct CO_2 reduction into fuels, electrocatalytic, photoelectrochemical, and photocatalytic methods are included from CO_2 capture. These are fully discussed in "A general framework for the assessment of solar fuel technologies" by Herron et al. [130].

3.6 Mimicking nature

Many efforts have been devoted to mimicking the natural plant system (also called the natural photosynthetic system) and achieving achieving maximum performance such as water transportation, light harvesting, and CO_2 gas adsorption/diffusion to a desired catalytic site. The achievement of an artificial photocatalytic system is extremely challenging. For this mission, the question is what roles of a plant we have to mimic. The leaf in a plant is ideally designed for light harvesting and mass (CO_2, O_2, and H_2O) flow, as depicted in Fig. 24A. The diffusion and adsorption of the reactant molecules and desorption of the

https://www.twirpx.org & http://chemistry-chemists.com

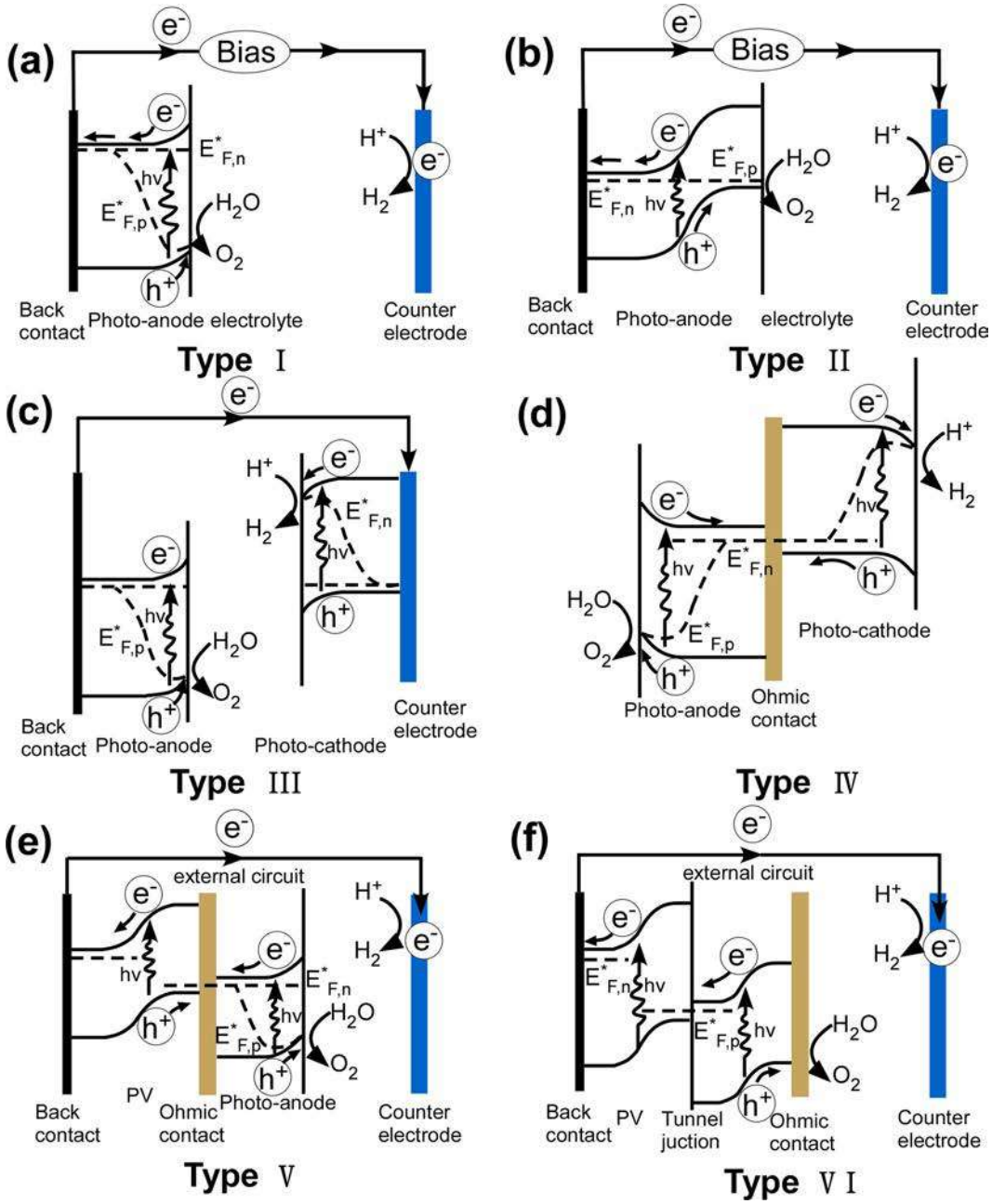

FIG. 21 Various types of PEC water-splitting devices: (A) type-I single light absorber, (B) type-II heterojunction photoelectrode, (C) wired type-III PEC tandem cell, (D) wireless type-IV PEC tandem cell, (E) type-V PV-PEC tandem cell, and (F) type-VI PV-electrolyzer cell [86].

https://www.twirpx.org & http://chemistry-chemists.com

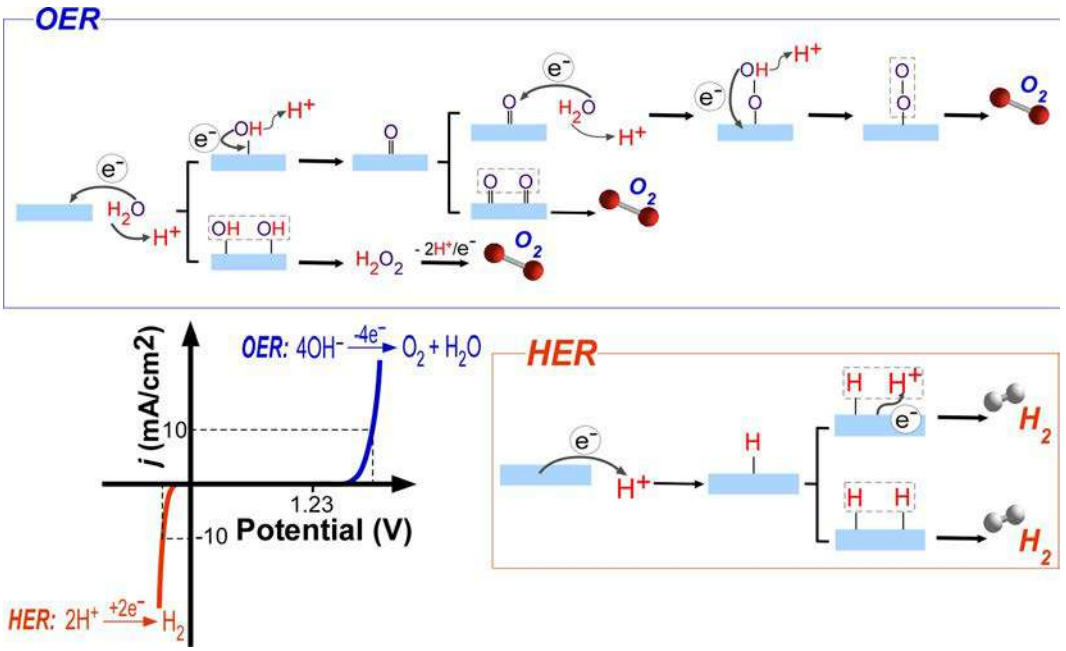

FIG. 22 Typical polarization curves (left). HER and OER mechanisms in acidic and basic conditions.

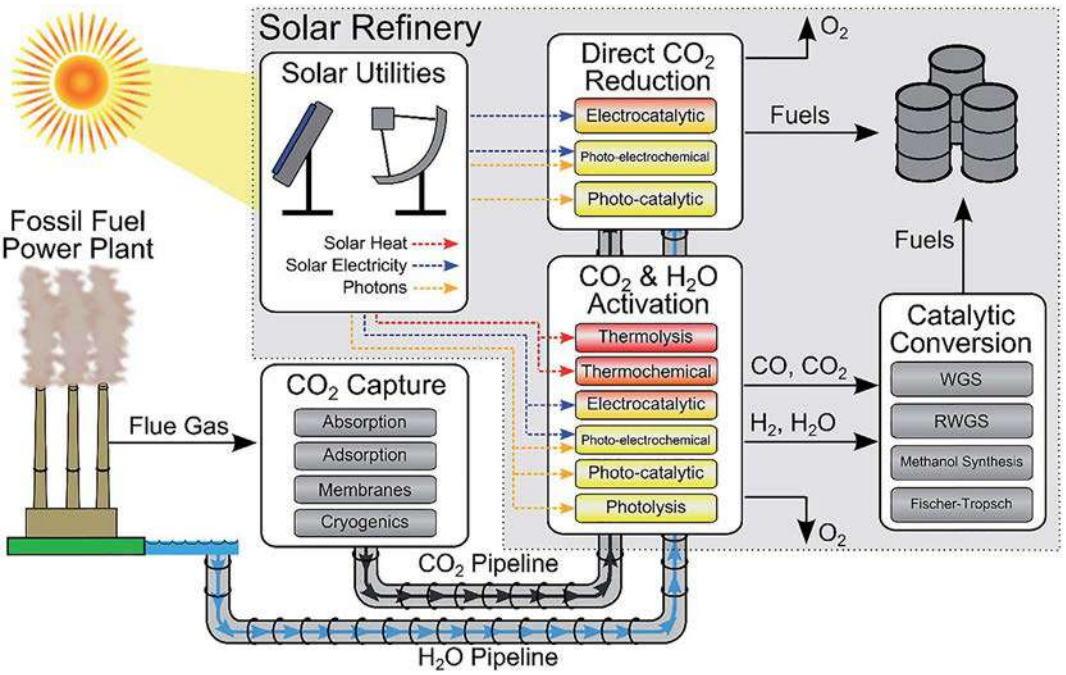

FIG. 23 Various energy production methods for CO_2 recycling. *From Herron JA, Kim J, Upadhye AA, Huber GW, Maravelias CT, A general framework for the assessment of solar fuel technologies. Energy Environ Sci 2015;8:126–157, with Copyright permission.*

https://www.twirpx.org & http://chemistry-chemists.com

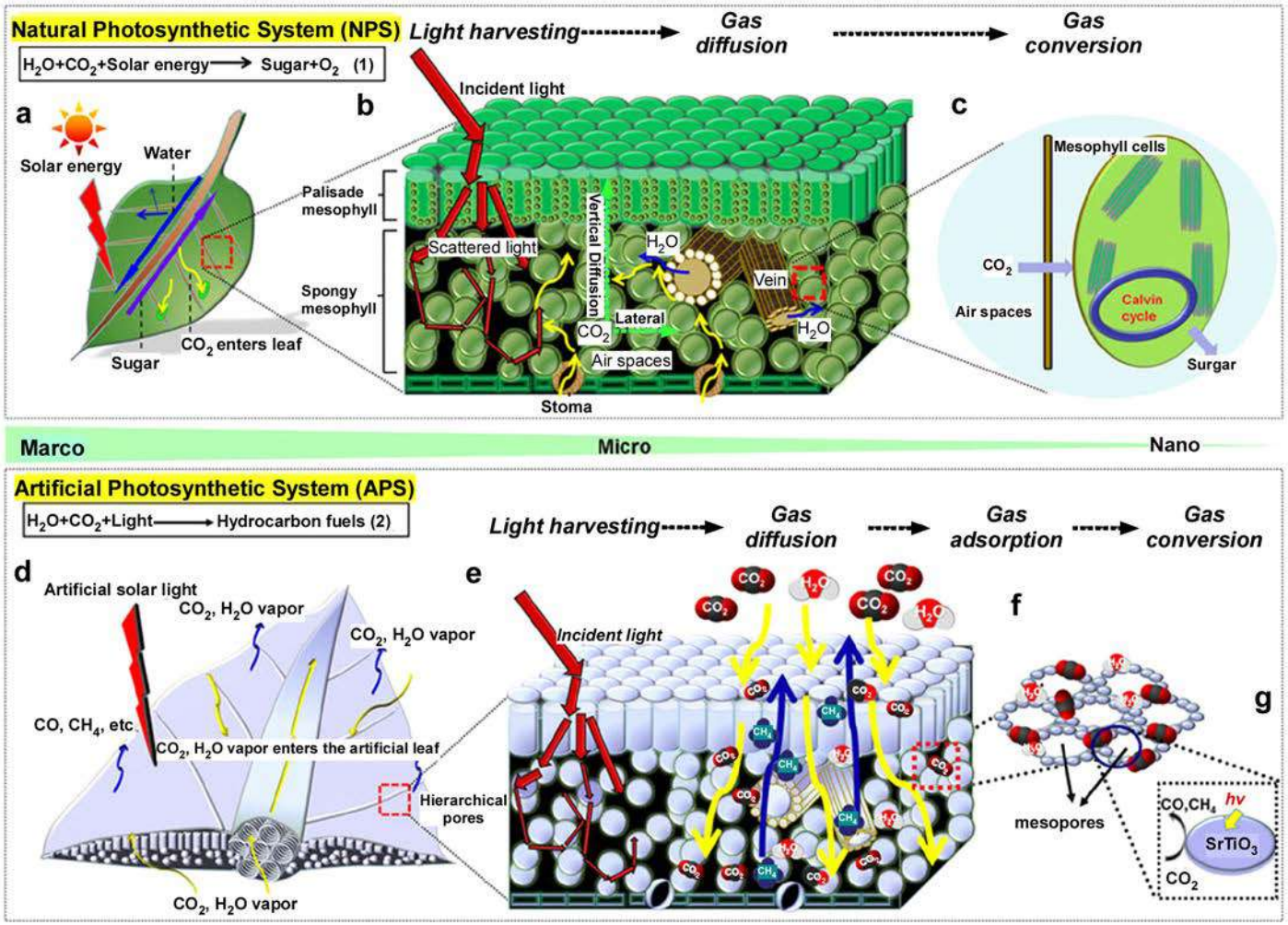

FIG. 24 Detailed description of natural and artificial photosynthetic processes [49].

https://www.twirpx.org & http://chemistry-chemists.com

product molecules are also ideal. Therefore, the photocatalytic conversion is maximized. Zhou et al. introduced mesopore perovskite titanates A(=Sr, Ca, and Pb)TiO_3 as artificial leaves (Fig. 24B) where light harvesting, gas (CO_2 and H_2O) diffusion, gas adsorption, and gas conversion (CO_2 reduction products) are efficient [49]. For mimicking nature, hierarchical nanostructures need to be understood. These were fully discussed by Li et al. in view of the roles of natural leaves [131]. Qi et al. discussed the progress of water splitting in terms of photosynthesis in green plants [126]. They first discussed a typical "Z-scheme" photosynthesis process in plants including electron and proton migrations, and then photocatalytic, PEC, and photovoltaic-electrolysis water splitting.

4 Summary and future scope

Photocatalysts will keep receiving increasing attention from scientists for solving energy and environmental issues. Scientists will continue to develop better and better visible light photocatalysts which have long-term stability, higher efficiency, and low economic input cost for practical applications. This is a very challenging area, with high opportunities for development.

Hydrogen appears to have a bright future as an alternative energy. In addition to the development of photocatalysts, hydrogen storage/transportation technology, hydrogen to electrical energy conversion, and all the related hydrogen technologies will also be assisted and developed. In particular, scientists will focus more on developing carbon-free hydrogen production technology mainly using solar light photoelectrochemical hydrogen production.

The conversion of thermodynamically stable CO_2 to valuable carbon compounds is a large and challenging task in view of thermodynamic and kinetic barriers. On the basis of the current status for CO_2 energy production efficiency, the recycling process by photocatalytic CO_2 reduction appears to be impractical for future energy solutions. However, there are many scientific depths to be researched. There is ample room for the development of candidate photocatalysts. To attain a commercial level, electrochemistry should be employed in a photocatalytic system. Because CO_2 reduction occurs in an aqueous solution, minimizing the hydrogen production channel is extremely important to increase the CO_2 reduction products. Because CO_2 reduction commonly proceeds via multielectron reaction steps, electron collection on a catalyst surface by efficient electron-hole pair separation is important to enhance the multistep processes. In addition, various CO_2 reduction channels exist with narrow energy differences. For this reason, the reaction pathways, mechanism, surface binding chemistry of reactants, intermediates, and products, and the rate-determining step should be better understood. By doing this, minimization of unwanted side reactions can be suppressed. A full understanding of the reaction mechanism and charge transfer dynamics is crucial for the development of photocatalysts in diverse application areas. For these efforts, sophisticated experimental techniques and density functional theory (DFT) calculations are essential to evaluate and increase

https://www.twirpx.org & http://chemistry-chemists.com

photocatalytic activity. Scientists with theoretical backgrounds have offered increasing contributions to development in this area.

Material engineering technology is of utmost important. Diverse synthetic parameters have been employed to synthesize photocatalysts that are stable in working conditions. For environmental remediation such as water and air purification, working conditions are much harder than those for hydrogen production and CO_2 reduction. When electrochemistry is employed, the developed catalysts should be stable in electrolyte conditions. All the experimental parameters are like an interdependent 3D cube puzzle, as discussed above. The Z-scheme photocatalytic system seems to be effective for the achievement of photocatalysts with a commercial efficiency level. Photoreactor design is also a very important issue, where maximization of light utilization and proper choice of reactant phases (e.g., gas or liquid) need to be considered. Light harvesting is a major parameter in the photocatalyst reaction. However, a unified standard unit and methodology for reporting the catalyst yield are required to keep track of the permeances of an uncountable number of photocatalysts and to collect big data.

One breakthrough for getting closer to commercialization is the introduction of electrochemistry into photocatalysis. Desired products such as hydrogen, oxygen, and CO_2 recycling reduction products are more easily produced by photoelectrocatalytic reactions with higher efficiency than those expected by photocatalytic reactions. For this purpose, the configuration of photoelectrochemical (PEC) devices and stability of photoelectrodes in a liquid electrolyte condition should be considered, and also highly efficient electrodes with low cost.

Concerning artificial photosynthesis, mimicking the natural photosynthesis system is extremely difficult, sophisticated, and challenging work, but a promising strategy. Progress in this area is still in the early stages and there is a lot of scope for mimicking nature, which uses sunlight, CO_2, and water very efficiently. For catalyst engineering, it has commonly been examinedthat the efficient delivery of gaseous CO_2 and liquid water into catalyst reactive center and efficient solar light usage for higher quantum yield. Multidisciplinary teamwork collaboration and artificial intelligence-based big-data are also required for a new breakthrough in the photocatalysis era. Conclusively, visible light photocatalysis under continuous financial support is a breakthrough for developing energy and environmental solutions.

Acknowledgments

This study was supported financially by a National Research Foundation of Korea (NRF) grant funded by the Korea government (MEST) (2016K2A9A2A06004534).

References

[1] Wang Z, Li C, Domen K. Recent developments in heterogeneous photocatalysts for solar-driven overall water splitting. Chem Soc Rev 2019;48:2109–25.

https://www.twirpx.org & http://chemistry-chemists.com

[2] Chandrasekaran S, Chung JS, Kim EJ, Hur SH. Advanced nano-structured materials for photocatalytic water splitting. J Electrochem Sci Technol 2016;7:1–12.

[3] Hossain A, Sakthipandi K, Ullah AKMA, Roy S. Recent progress and approaches on carbon-free energy from water splitting. Nano-Micro Lett 2019;11:103.

[4] Usubharatana P, McMartin D, Veawab A, Tontiwachwuthikul P. Photocatalytic process for CO_2 emission reduction from industrial flue gas streams. Ind Eng Chem Res 2006;45:2558–68.

[5] Hosseini SE, Wahid MA. Hydrogen production from renewable and sustainable energy resources: promising green energy carrier for clean development. Renew Sust Energ Rev 2016;57:850–66.

[6] Fajrina N, Tahir M. A critical review in strategies to improve photocatalytic water splitting towards hydrogen production. Int J Hydrog Energy 2019;44:540–77.

[7] Tentu RD, Basu S. Photocatalytic water splitting for hydrogen production. Curr Opin Electrochem 2017;5:56–62.

[8] Fang W, Shangguan W. A review on bismuth-based composite oxides for photocatalytic hydrogen generation. Int J Hydrog Energy 2019;44:895–912.

[9] Yu H, Jiang L, Wang H, Huang B, Yuan X, Huang J, Zhang J, Zeng G. Modulation of Bi_2MoO_6-based materials for photocatalytic water splitting and environmental application: a critical review. Small 2019;15:1901008.

[10] Acar C, Dincer I, Naterer GF. Review of photocatalytic water-splitting methods for sustainable hydrogen production. Int J Energy Res 2016;40:1449–73.

[11] Mishra A, Mehta A, Basu S, Shetti NP, Reddy KR, Aminabhavi TM. Graphitic carbon nitride ($g–C_3N_4$)–based metal-free photocatalysts for water splitting: a review. Carbon 2019;149:693–721.

[12] Wen J, Xie J, Chen X, Li X. A review on $g\text{-}C_3N_4$-based photocatalysts. Appl Surf Sci 2017;391:72–123.

[13] Mun SJ, Park S-J. Graphitic carbon nitride materials for photocatalytic hydrogen production via water splitting: a short review. Catalysts 2019;9:805.

[14] Humayun M, Raziq F, Khan A, Luo W. Modification strategies of TiO_2 for potential applications in photocatalysis: a critical review. Green Chem Lett Rev 2018;11:86–102.

[15] Singh R, Dutta S. A review on H_2 production through photocatalytic reactions using TiO_2/TiO_2-assisted catalysts. Fuel 2018;220:607–20.

[16] Kegel J, Povey IM, Pemble ME. Zinc oxide for solar water splitting: a brief review of the material's challenges and associated opportunities. Nano Energy 2018;54:409–28.

[17] Lee G-J, Wu JJ. Recent developments in ZnS photocatalysts from synthesis to photocatalytic applications—a review. Powder Technol 2017;318:8–22.

[18] Joy J, Mathew J, George SC. Nanomaterials for photoelectrochemical water splitting—review. Int J Hydrog Energy 2018;43:4804–17.

[19] Li D, Shi J, Li C. Transition-metal-based electrocatalysts as cocatalysts for photoelectrochemical water splitting: a mini review. Small 2018;14:1704179.

[20] Reddy CV, Reddy KR, Shetti NP, Shim J, Aminabhavi TM, Dionysiou DD. Hetero-nanostructured metal oxide-based hybrid photocatalysts for enhanced photoelectrochemical water splitting—a review. Int J Hydrog Energy 2020;45:18331–47.

[21] Kalanoor BS, Seo H, Kalanur SS. Recent developments in photoelectrochemical water-splitting using $WO_3/BiVO_4$ heterojunction photoanode: a review. Mater Sci Energy Technol 2018;1:49–62.

[22] Bhat SSM, Jang HW. Recent advances in bismuth-based nanomaterials for photoelectrochemical water splitting. ChemSusChem 2017;10:3001–18.

[23] Tamirat AG, Rick J, Dubale AA, Su W-N, Hwang B-J. Using hematite for photoelectrochemical water splitting: a review of current progress and challenges. Nanoscale Horiz 2016;1:243–67.

https://www.twirpx.org & http://chemistry-chemists.com

[24] Phuan YW, Ong W, Chong MN, Ocon JD. Prospects of electrochemically synthesized hematite photoanodes for photoelectrochemical water splitting: a review. J Photochem Photobiol C 2017;33:54–82.

[25] Anantharaj S, Ede SR, Sakthikumar K, Karthick K, Mishra S, Kundu S. Recent trends and perspectives in electrochemical water splitting with an emphasis on sulfide, selenide, and phosphide catalysts of Fe, Co, and Ni: a review. ACS Catal 2016;6:8069–97.

[26] Adnan MAB, Arifin K, Minggu LJ, Kassim MB. Titanate-based perovskites for photochemical and photoelectrochemical water splitting applications: a review. Int J Hydrog Energy 2018;43:23209–20.

[27] Sohn Y, Huang W, Taghipour F. Recent progress and perspectives in photocatalytic CO_2 reduction of Ti-oxide based nanomaterials. Appl Surf Sci 2017;396:1696–711.

[28] Tabish A, Varghese AM, Wahab MA, Karanikolos GN. Perovskites in the energy grid and CO_2 conversion: current context and future directions. Catalysts 2020;10:95.

[29] Nahar S, Zain MFM, Kadhum AAH, Hasan HA, Hasan MR. Advances in photocatalytic CO_2 reduction with water: a review. Materials 2017;10:629.

[30] Kumar B, Llorente M, Froehlich J, Dang T, Sathrum A, Kubiak CP. Photochemical and photoelectrochemical reduction of CO_2. Annu Rev Phys Chem 2012;63:541–610.

[31] Zeng S, Kar P, Thakur UK, Shankar K. A review on photocatalytic CO_2 reduction using perovskite oxide nanomaterials. Nanotechnology 2018;29, 052001.

[32] Shi R, Waterhouse GIN, Zhang T. Recent progress in photocatalytic CO_2 reduction over perovskite oxides. Sol RRL 2017;1:1700126.

[33] Shehzad N, Tahir M, Johari K, Murugesan T, Hussain M. A critical review on TiO_2 based photocatalytic CO_2 reduction system: strategies to improve efficiency. J CO_2 Util 2018;26:98–122.

[34] Low J, Cheng B, Yu J. Surface modification and enhanced photocatalytic CO_2 reduction performance of TiO_2: a review. Appl Surf Sci 2017;392:658–86.

[35] Abdullah H, Khan MMR, Ong HR, Yaakob Z. Modified TiO_2 photocatalyst for CO_2 photocatalytic reduction: An overview. J CO_2 Util 2017;22:15–32.

[36] Tan JZY, Maroto-Valer MM. A review of nanostructured non-titania photocatalysts and hole scavenging agents for CO_2 photoreduction processes. J Mater Chem A 2019;7:9368–85.

[37] Sun Z, Wang H, Wu Z, Wang L. g-C_3N_4 based composite photocatalysts for photocatalytic CO_2 reduction. Catalysis 2018;300:160–72.

[38] Ali S, Razzaq A, In S. Development of graphene based photocatalysts for CO_2 reduction to C1 chemicals: a brief overview. Catal Today 2019;335:39–54.

[39] Fu J, Jiang K, Qiu X, Yu J, Liu M. Product selectivity of photocatalytic CO_2 reduction reactions. Mater Today 2020;32:222–43.

[40] Zhan W, Sun L, Han X. Recent progress on engineering highly efficient porous semiconductor photocatalysts derived from metal–organic frameworks. Nano-Micro Lett 2019;11.

[41] Pawar AU, Kim CW, Nguyen-Le M, Kang YS. General review on the components and parameters of photoelectrochemical system for CO_2 reduction with in situ analysis. ACS Sustain Chem Eng 2019;7:7431–55.

[42] Vu N, Kaliaguine S, Do T. Critical aspects and recent advances in structural engineering of photocatalysts for sunlight-driven photocatalytic reduction of CO_2 into fuels. Adv Funct Mater 2019;29:1901825.

[43] Yaashikaa PR, Kumara PS, Varjani SJ, Saravanan A. A review on photochemical, biochemical and electrochemical transformation of CO_2 into value-added products. J CO_2 Util 2019;33:131–47.

[44] Wu J, Huang Y, Ye W, Li Y. CO_2 reduction: from the electrochemical to photochemical approach. Adv Sci 2017;4:1700194.

https://www.twirpx.org & http://chemistry-chemists.com

[45] Chang X, Wang T, Gong J. CO_2 photo-reduction: insights into CO_2 activation and reaction on surfaces of photocatalysts. Energy Environ Sci 2016;9:2177–96.

[46] House RL, Iha NYM, Coppo RL, Alibabaei L, Sherman BD, Kang P, Brennaman MK, Hoertz PG, Meyer TJ. Artificial photosynthesis: where are we now? where can we go? J Photochem Photobiol C 2015;25:32–45.

[47] Yuan L, Xu Y-J. Photocatalytic conversion of CO_2 into value-added and renewable fuels. Appl Surf Sci 2015;342:154–67.

[48] Passalacqua R, Centi G, Perathoner S. Solar production of fuels from water and CO_2: perspectives and opportunities for a sustainable use of renewable energy. Oil Gas Sci Technol 2015;70:799–815.

[49] Zhou H, Guo J, Li P, Fan T, Zhang D, Ye J. Leaf-architectured 3D hierarchical artificial photosynthetic system of perovskite titanates towards CO_2 photoreduction into hydrocarbon fuels. Sci Rep 2013;3:1667.

[50] Inoue T, Fujishima A, Konishi S, Honda K. Photoelectrocatalytic reduction of carbon dioxide in aqueous suspensions of semiconductor powders. Nature 1979;277:637–8.

[51] Zhu D, Zhou Q. Action and mechanism of semiconductor photocatalysis on degradation of organic pollutants in water treatment: a review. Environ Nanotechnol Monit Manage 2019;12:100255.

[52] Ahmed SN, Haider W. Heterogeneous photocatalysis and its potential applications in water and wastewater treatment: a review. Nanotechnology 2018;29:342001.

[53] Yahya N, Aziz F, Jamaludin NA, Mutalib MA, Ismail AF, Salleh WNW, Jaafar J, Yusof N, Ludin NA. A review of integrated photocatalyst adsorbents for wastewater treatment. J Environ Chem Eng 2018;6:7411–25.

[54] Long Z, Li Q, Wei T, Zhang G, Ren Z. Historical development and prospects of photocatalysts for pollutant removal in water. J Hazard Mater 2020;395:122599.

[55] Reddy PAK, Reddy PVL, Kwon E, Kim K-H, Akter T, Kalagara S. Recent advances in photocatalytic treatment of pollutants in aqueous media. Environ Int 2016;91:94–103.

[56] Al-Mamun MR, Kader S, Islam MS, Khan MZH. Photocatalytic activity improvement and application of UV-TiO_2 photocatalysis in textile wastewater treatment: A review. J Environ Chem Eng 2019;7:103248.

[57] Khalid NR, Majid A, Tahir MB, Niaz NA, Khalid S. Carbonaceous-TiO_2 nanomaterials for photocatalytic degradation of pollutants: a review. Ceram Int 2017;43:14552–71.

[58] Al-Hamdi AM, Rinner U, Sillanpää M. Tin dioxide as a photocatalyst for water treatment: a review. Process Saf Environ Prot 2017;107:190–205.

[59] Lee KM, Lai CW, Ngai KS, Juan JC. Recent developments of zinc oxide based photocatalyst in water treatment technology: a review. Water Res 2016;88:428–48.

[60] Khaki MRD, Shafeeyan MS, Raman AAA, Daud WMAW. Application of doped photocatalysts for organic pollutant degradation—A review. J Environ Manag 2017;198:78–94.

[61] Ma R, Zhang S, Wen T, Gu P, Li L, Zhao G, Niu F, Huang Q, Tang Z, Wang X. A critical review on visible-light-response CeO_2-based photocatalysts with enhanced photooxidation of organic pollutants. Catal Today 2019;335:20–30.

[62] Zhang G, Zhang X, Meng Y, Pan G, Ni Z, Xia S. Layered double hydroxides-based photocatalysts and visible-light driven photodegradation of organic pollutants: a review. Chem Eng J 2020;392:123684.

[63] Samsudin MFR, Sufian S, Hameed BH. Epigrammatic progress and perspective on the photocatalytic properties of $BiVO_4$-based photocatalyst in photocatalytic water treatment technology: a review. J Mol Liq 2018;268:438–59.

[64] Monfort O, Plesch G. Bismuth vanadate-based semiconductor photocatalysts: a short critical review on the efficiency and the mechanism of photodegradation of organic pollutants. Environ Sci Pollut Res 2018;25:19362–79.

https://www.twirpx.org & http://chemistry-chemists.com

[65] Singh S, Sharma R, Khanuja M. A review and recent developments on strategies to improve the photocatalytic elimination of organic dye pollutants by BiOX (X = Cl, Br, I, F) nanostructures. Korean J Chem Eng 2018;35:1955–68.

[66] Singh P, Shandilya P, Raizada P, Sudhaik A, Rahmani-Sani A, Hosseini-Bandegharaei A. Review on various strategies for enhancing photocatalytic activity of graphene based nanocomposites for water purification. Arab J Chem 2020;13:3498–520.

[67] Zhang S, Gu P, Ma R, Luo C, Wen T, Zhao G, Cheng W, Wang X. Recent developments in fabrication and structure regulation of visible-light-driven g-C_3N_4-based photocatalysts towards water purification: a critical review. Catal Today 2019;335:65–77.

[68] Gangu KK, Maddila S, Jonnalagadda SB. A review on novel composites of MWCNTs mediated semiconducting materials as photocatalysts in water treatment. Sci Total Environ 2019;646:1398–412.

[69] Lam S-M, Sin J-C, Mohamed AR. A review on photocatalytic application of g-C_3N_4/semiconductor (CNS) nanocomposites towards the erasure of dyeing wastewater. Mater Sci Semicond Process 2016;47:62–84.

[70] Zhang C, Li Y, Shuai D, Shen Y, Xiong W, Wang L. Graphitic carbon nitride (g-C_3N_4)-based photocatalysts for water disinfection and microbial control: a review. Chemosphere 2019;214:462–79.

[71] Sharma S, Dutta V, Singh P, Raizada P, Rahmani-Sani A, Hosseini-Bandegharaei A, Thakur VK. Carbon quantum dot supported semiconductor photocatalysts for efficient degradation of organic pollutants in water: a review. J Clean Prod 2019;228:755–69.

[72] Sonu, Dutta V, Sharma S, Raizada P, Hosseini-Bandegharaei A, Gupta VK, Singh P. Review on augmentation in photocatalytic activity of $CoFe_2O_4$ via heterojunction formation for photocatalysis of organic pollutants in water. J Saudi Chem Soc 2019;23:1119–36.

[73] Singh P, Sharma K, Hasija V, Sharma V, Sharma S, Raizada P, Singh M, Saini AK, Hosseini-Bandegharaei A, Thakur VK. Systematic review on applicability of magnetic iron oxides–integrated photocatalysts for degradation of organic pollutants in water. Mater Today Chem 2019;14:100186.

[74] Fujishima A, Honda K. Electrochemical photolysis of water at a semiconductor electrode. Nature 1972;238:37–8.

[75] Ge M, Cao C, Huang J, Li S, Chen Z, Zhang K-Q, Al-Deyab SS, Lai Y. A review of one-dimensional TiO_2 nanostructured materials for environmental and energy applications. J Mater Chem A 2016;4:6772–801.

[76] Wei J, Zhou M, Long A, Xue Y, Liao H, Wei C, Xu ZJ. Heterostructured electrocatalysts for hydrogen evolution reaction under alkaline conditions. NanoMicro Lett 2018;10:75.

[77] Kortlever R, Shen J, Schouten KJP, Calle-Vallejo F, Koper MTM. Catalysts and reaction pathways for the electrochemical reduction of carbon dioxide. J Phys Chem Lett 2015;6:4073–82.

[78] Seh ZW, Kibsgaard J, Dickens CF, Chorkendorff I, Nørskov JK, Jaramillo TF. Combining theory and experiment in electrocatalysis: insights into materials design. Science 2017;355:4998.

[79] Ola O, Maroto-Valer MM. Review of material design and reactor engineering on TiO_2 photocatalysis for CO_2 reduction. J Photochem Photobiol C 2015;24:16–42.

[80] Tahir M, Amin NS. Advances in visible light responsive titanium oxide-based photocatalysts for CO_2 conversion to hydrocarbon fuels. Energy Convers Manag 2013;76:194–214.

[81] Li K, An X, Park KH, Khraisheh M, Tang J. A critical review of CO_2 photoconversion: catalysts and reactors. Catal Today 2014;224:3–12.

[82] Singh MR, Clark EL, Bell AT. Thermodynamic and achievable efficiencies for solar-driven electrochemical reduction of carbon dioxide to transportation fuels. PNAS 2015;112:6111–8.

[83] Ahmed M, Dincer I. A review on photoelectrochemical hydrogen production systems: challenges and future directions. Int J Hydrog Energy 2019;44:2474–507.

https://www.twirpx.org & http://chemistry-chemists.com

[84] Anantharaj S, Ede SR, Karthick K, Sankar SS, Sangeetha K, Karthik PE, Kundu S. Precision and correctness in the evaluation of electrocatalytic water splitting: revisiting activity parameters with a critical assessment. Energy Environ Sci 2018;11:744–71.

[85] Sultan S, Ha M, Kim DY, Tiwari JN, Myung CW, Meena A, Shin TJ, Chae KH, Kim KS. Superb water splitting activity of the electrocatalyst $Fe_3Co(PO_4)_4$ designed with computation aid. Nat Commun 2019;10:5195.

[86] Jiang C, Moniz SJA, Wang A, Zhang T, Tang J. Photoelectrochemical devices for solar water splitting—materials and challenges. Chem Soc Rev 2017;46:4645–60.

[87] Liu J, Wang H, Antonietti M. Graphitic carbon nitride "reloaded": emerging applications beyond (photo)catalysis. Chem Soc Rev 2016;45:2308–26.

[88] Maeda K, Domen K. Photocatalytic water splitting: recent progress and future challenges. J Phys Chem Lett 2010;1:2655–61.

[89] Maeda K. Photocatalytic water splitting using semiconductor particles: history and recent developments. J Photochem Photobiol C 2011;12:237–68.

[90] Liu G, Yu JC, Lu GQM, Cheng HM. Crystal facet engineering of semiconductor photocatalysts: motivations, advances and unique properties. Chem Commun 2011;47:6763–83.

[91] Liu L, Wang S, Huang H, Zhang Y, Ma T. Surface sites engineering on semiconductors to boost photocatalytic CO_2 reduction. Nano Energy 2020;75:104959.

[92] Wang Z, Monny SA, Wang L. Hollow structure for photocatalytic CO_2 reduction. ChemNanoMat 2020;6:881–8.

[93] Ma Y, Wang Z, Xu X, Wang J. Review on porous nanomaterials for adsorption and photocatalytic conversion of CO_2. Chin J Catal 2017;38:1956–69.

[94] Chen W, Kuang Q, Wang Q, Xie Z. Engineering a high energy surface of anatase TiO_2 crystals towards enhanced performance for energy conversion and environmental applications. RSC Adv 2015;5:20396–409.

[95] Liu G, Yang HG, Pan J, Yang YQ, Lu GQM, Cheng HM. Titanium dioxide crystals with tailored facets. Chem Rev 2014;114:9559–612.

[96] Koci K, Obalova L, Matejova L, Placha D, Lacny Z, Jirkovsky J, Solcova O. Effect of TiO_2 particle size on the photocatalytic reduction of CO_2. Appl Catal B Environ 2009;89:494–502.

[97] Chen D, Zhang X, Lee AF. Synthetic strategies to nanostructured photocatalysts for CO_2 reduction to solar fuels and chemicals. J Mater Chem A 2015;3:14487–516.

[98] Su J, Li GD, Li XH, Chen JS. 2D/2D heterojunctions for catalysis. Adv Sci 2019;6:1801702.

[99] Ong WJ. 2D/2D graphitic carbon nitride (g-C_3N_4) heterojunction nanocomposites for photocatalysis: why does face-to-face interface matter? Front Mater 2017;4:1–10.

[100] Liang Z, Shen R, Ng YH, Zhang P, Xiang Q, Li X. A review on 2D MoS_2 cocatalysts in photocatalytic H_2 production. J Mater Sci Technol 2020. https://doi.org/10.1016/j.jmst.2020.04.032.

[101] Low J, Yu J, Jaroniec M, Wageh S, Al-Ghamdi AA. Heterojunction photocatalysts. Adv Mater 2017;29:1601694.

[102] Zhong S, Xi Y, Chen Q, Chen J, Bai S. Bridge engineering in photocatalysis and photoelectrocatalysis. Nanoscale 2020;12:5764–91.

[103] Xia X, Song M, Wang H, Zhang X, Sui N, Zhang Q, Colvin VL, Yu WW. Latest progress in constructing solid-state Z scheme photocatalysts for water splitting. Nanoscale 2019;11:11071–82.

[104] Li H, Tu W, Zhou Y, Zou Z. Z-scheme photocatalytic systems for promoting photocatalytic performance: recent progress and future challenges. Adv Sci 2016;3:1500389.

[105] Li H, Zhou Y, Tu W, Ye J, Zou Z. State-of-the-art progress in diverse heterostructured photocatalysts toward promoting photocatalytic performance. Adv Funct Mater 2015;25:998–1013.

https://www.twirpx.org & http://chemistry-chemists.com

[106] Zhang W, Mohamed AR, Ong WJ. Z-scheme photocatalytic systems for carbon dioxide reduction: Where are we now? Angew Chem 2020.

[107] Huang HJ, Wu JCS, Chiang HP, Chou Chau YF, Lin YS, Wang YH, Chen PJ. Review of experimental setups for plasmonic photocatalytic reactions. Catalysts 2020;10:46.

[108] Wu N. Plasmonic metal–semiconductor photocatalysts and photoelectrochemical cells: a review. Nanoscale 2018;10:2679–96.

[109] Reddy NL, Rao VN, Vijayakumar M, Santhosh R, Anandan S, Karthik M, Shankar MV, Reddy KR, Shetti NP, Nadagouda MN, Aminabhavi TM. A review on frontiers in plasmonic nano-photocatalysts for hydrogen production. Int J Hydrog Energy 2019;44:10453–72.

[110] Vu NN, Kaliaguine S, Do TO. Plasmonic photocatalysts for sunlight-driven reduction of CO_2: details, developments, and perspectives. ChemSusChem 2020;13:1–26.

[111] Yamazaki Y, Takeda H, Ishitani O. Photocatalytic reduction of CO_2 using metal complexes. J Photochem Photobiol C: Photochem Rev 2015;25:106–37.

[112] Zhang Y, Xia B, Ran J, Davey K, Qiao SZ. Atomic-level reactive sites for semiconductor-based photocatalytic CO_2 reduction. Adv Energy Mater 2020;10:1903879.

[113] Maeda K. Metal-complex/semiconductor hybrid photocatalysts and photoelectrodes for CO_2 reduction driven by visible light. Adv Mater 2019;31:1808205.

[114] Ran J, Jaroniec M, Qiao SZ. Cocatalysts in semiconductor-based photocatalytic CO_2 reduction: achievements, challenges, and opportunities. Adv Mater 2018;30:1704649.

[115] Rao VN, Reddy NL, Kumari MM, Cheralathan KK, Ravi P, Sathish M, Neppolian B, Reddy KR, Shetti NP, Prathap P, Aminabhavi TM, Shankar MV. Sustainable hydrogen production for the greener environment by quantum dots-based efficient photocatalysts: a review. J Environ Manag 2019;248:109246.

[116] Li X, Shen R, Ma S, Chen X, Xie J. Graphene-based heterojunction photocatalysts. Appl Surf Sci 2018;430:53–107.

[117] Makama AB, Umar M, Saidu SA. CQD-based composites as visible-light active photocatalysts for purification of water. In: Visible-light photocatalysis of carbon-based materials. IntechOpen; 2018. p. 111–35. https://doi.org/10.5772/intechopen.74245.

[118] Masih D, Ma Y, Rohani S. Graphitic C_3N_4 based noble-metal-free photocatalyst systems: a review. Appl Catal B Environ 2017;206:556–88.

[119] Mamba G, Mishra AK. Graphitic carbon nitride (g-C_3N_4) nanocomposites: a new and exciting generation of visible light driven photocatalysts for environmental pollution remediation. Appl Catal B Environ 2016;198:347–77.

[120] Ren Y, Zeng D, Ong WJ. Interfacial engineering of graphitic carbon nitride (g-C_3N_4)-based metal sulfide heterojunction photocatalysts for energy conversion: A review. Chin J Catal 2019;40:289–319.

[121] Ye S, Wang R, Wu MZ, Yuan YP. A review on g-C_3N_4 for photocatalytic water splitting and CO_2 reduction. Appl Surf Sci 2015;358:15–27.

[122] Low J, Cheng B, Yu J, Jaroniec M. Carbon-based two-dimensional layered materials for photocatalytic CO_2 reduction to solar fuels. Energy Storage Mater 2016;3:24–35.

[123] Jiang L, Yuan X, Pan Y, Liang J, Zeng G, Wu Z, Wang H. Doping of graphitic carbon nitride for photocatalysis: a review. Appl Catal B Environ 2017;217:288–406.

[124] Seitz LC, Chen Z, Forman AJ, Pinaud BA, Benck JD, Jaramillo TF. Modeling practical performance limits of photoelectrochemical water splitting based on the current state of materials research. ChemSusChem 2014;7:1372–85.

[125] Kumar S, Ojha K, Ganguli AK. Interfacial charge transfer in photoelectrochemical processes. Adv Mater Interfaces 2017;4:1600981.

https://www.twirpx.org & http://chemistry-chemists.com

[126] Qi J, Zhang W, Cao R. Solar-to-hydrogen energy conversion based on water splitting. Adv Energy Mater 2018;8:1701620.

[127] Halmann M. Photoelectrochemical reduction of aqueous carbon-dioxide on p-type gallium-phosphide in liquid junction solar-cells. Nature 1978;275:115–6.

[128] Tu W, Zhou Y, Zou Z. Photocatalytic conversion of CO_2 into renewable hydrocarbon fuels: state-of-the-art accomplishment, challenges, and prospects. Adv Mater 2014;26:4607–26.

[129] Liao P, Carter EA. New concepts and modeling strategies to design and evaluate photo-electro-catalysts based on transition metal oxides. Chem Soc Rev 2013;42:2401–22.

[130] Herron JA, Kim J, Upadhye AA, Huber GW, Maravelias CT. A general framework for the assessment of solar fuel technologies. Energy Environ Sci 2015;8:126–57.

[131] Li X, Yu J, Jaroniec M. Hierarchical photocatalysts. Chem Soc Rev 2016;45:2603–36.

https://www.twirpx.org & http://chemistry-chemists.com

Index

Note: Page numbers followed by *f* indicate figures and *t* indicate tables.

https://www.twirpx.org & http://chemistry-chemists.com

https://www.twirpx.org & http://chemistry-chemists.com

https://www.twirpx.org & http://chemistry-chemists.com

https://www.twirpx.org & http://chemistry-chemists.com

https://www.twirpx.org & http://chemistry-chemists.com

https://www.twirpx.org & http://chemistry-chemists.com

https://www.twirpx.org & http://chemistry-chemists.com

https://www.twirpx.org & http://chemistry-chemists.com

https://www.twirpx.org & http://chemistry-chemists.com

https://www.twirpx.org & http://chemistry-chemists.com

https://www.twirpx.org & http://chemistry-chemists.com

https://www.twirpx.org & http://chemistry-chemists.com

NANOSTRUCTURED MATERIALS FOR VISIBLE LIGHT PHOTOCATALYSIS

Edited by Arpan Kumar Nayak and Niroj Kumar Sahu

Nanostructured Materials for Visible Light Photocatalysis describes the various methods of synthesizing different classes of nanostructured materials that are used as photocatalysts for the degradation of organic hazardous dyes under visible light irradiation. The first three chapters include a general introduction, basic principles, mechanisms, and synthesis methods of nanomaterials for visible light photocatalysis. Recent advances in carbon, bismuth series, transition metal oxide and chalcogenides-based nanostructured materials for visible light photocatalysis are discussed. Later chapters describe the role of phosphides, nitrides, and rare earth-based nanostructured-based materials in visible light photocatalysis, as well as the characteristics, synthesis, and fabrication of photocatalysts. The role of doping, composites, defects, different facets, morphology of nanostructured materials and green technology for efficient dye removal under visible-light irradiation are also explored. Other topics covered include large-scale production of nanostructured materials, the challenges in present photocatalytic research, the future scope of nanostructured materials regarding environmental hazard remediation under visible light, and solar light harvesting. This book is a valuable reference for researchers and enables them to learn more about designing advanced nanostructured materials for wastewater treatment and visible light irradiation.

Key Features

- Covers all the recent developments of nanostructured photocatalytic materials
- Provides a clear overview of the mechanism of visible light photocatalysis and the controlled synthesis of nanostructured materials
- Assesses the major challenges of creating visible light photocatalysis systems at the nanoscale

Arpan Kumar Nayak is Assistant Professor in the School of Advanced Sciences, at the Vellore Institute of Technology Vellore in India. His research interests are nanostructured materials synthesis for environment and energy applications (present and future), high-performance energy storage and/or energy production applications, and photocatalysis.

Niroj Kumar Sahu is Associate Professor in the Centre for Nanotechnology Research at the Vellore Institute of Technology in India. His areas of research include physics and chemistry of nanomaterials; magnetism and magnetic materials; fabrication, surface functionalization and self-assembly of metallics, oxides and alloy nanostructured materials and their applications in biomedicine, energy storage and removal of environmental hazards.

ELSEVIER elsevier.com/books-and-journals

ISBN 978-0-12-823018-3

9 780128 230183